SLAC-R-508
CONF-9608101
UC-414

PROCEEDINGS
OF THE
SUMMER INSTITUTE ON PARTICLE PHYSICS

August 19–30, 1996

The Strong Interaction, from Hadrons to Partons

Program Directors:
David Burke
Lance Dixon
David W.G.S. Leith

Edited by Jennifer Chan, Lilian DePorcel, and Lance Dixon

Sponsored by Stanford University and Stanford Linear Accelerator Center under
contract with the U.S. Department of Energy. Contract DE-AC03-76SF00515.

June 1997

Printed in the United States of America. Available from National Technical Information Service, U.S. Department of Commerce,
5285 Port Royal Road, Springfield, VA 22161.

DISCLAIMER

This report was prepared as an account of work sponsored by an agency of the United States Government. Neither the United States Government nor any agency thereof, nor any of their employees, makes any warranty, express or implied, or assumes any legal liability or responsibility for the accuracy, completeness, or usefulness of any information, apparatus, product, or process disclosed, or represents that its use would not infringe privately owned rights. Reference herein to any specific commercial product, process, or service by trade name, trademark, manufacturer, or otherwise does not necessarily constitute or imply its endorsement, recommendation, or favoring by the United States Government or any agency thereof. The views and opinions of authors expressed herein do not necessarily state or reflect those of the United States Government or any agency thereof.

DISCLAIMER

Portions of this document may be illegible in electronic image products. Images are produced from the best available original document.















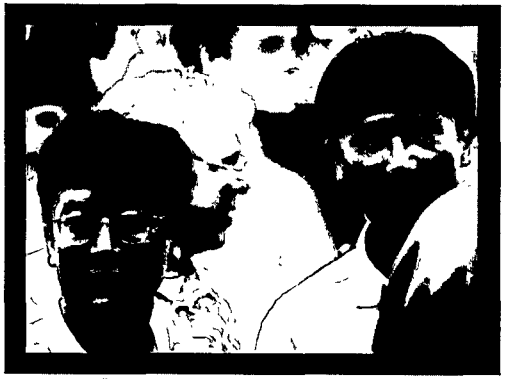


TABLE OF CONTENTS

Part I. SUMMER SCHOOL LECTURES

J. D. Bjorken
"QCD: Questions, Challenges, and Dilemmas" 1

D. E. Soper
"Basics of QCD Perturbation Theory" 15

A. F. Falk
"The Heavy Quark Expansion of QCD" 43

M. G. Albrow
"QCD in Hadron-Hadron Collisions" 67

P. N. Burrows
"Precise Tests of QCD in e^+e^- Annihilation" 101

W. Toki
"Search for Glueballs" 141

T. DeGrand
"Lattice Gauge Theory for QCD" 169

W. H. Smith
"QCD Studies in *ep* Collisions" 203

A. H. Mueller
"Small-x Physics" 237

J. Wiss
"QCD in Heavy Quark Production and Decay" 251

Part II. TOPICAL CONFERENCE

R. C. Welsh
"Precision Measurement of the Neutron Spin Structure Function" ... 297

G. Grindhammer
"F_2 and Test of the Standard Model at HERA" 313

G. Barbiellini
"Experimental Measurements of the Anti-Matter Component in Cosmic Rays" 315

N. Cartiglia
"Diffraction at HERA" 337

J. Conrad
"Precision Structure Function Measurements from CCFR/NUTEV" .. 365

L. Littenberg
"The BNL Rare Kaon Decay Program" 381

M. Doser
"Recent Results from LEAR" 395

N. Cason
"Search for Exotic Mesons in BNL E852" 403

S. Willocq
"Physics at the Z Pole with SLD" 405

K. Mönig
"Recent Results from LEP at the Z on Electroweak and Heavy Flavor Physics" 429

E. P. Solodov
"Recent Results from the VEPP-2M Collider at Novosibirsk" 457

R. Kass
"Some Recent Results from CLEO II" 473

M. Paulini
"Heavy Flavor Physics from Top to Bottom" 499

C. D. Buchanan
"New Accurate Ideas on Flavor Formation in Hadronization and Connections to QCD" 525

M. Beneke
"Nonrelativistic Effective Theory for Quarkonium Production in Hadron Collisions" 549

C. Klopfenstein
"Electroweak Tests and Searches for New Phenomena from the Tevatron" 575

D. M. Pierce
"The Strong Coupling Constant in Grand Unified Theories" 589

J. Mnich
"Recent Results from LEP" 599

APPENDICES

List of Participants 631

Previous SLAC Summer Institute Titles and Speakers 641

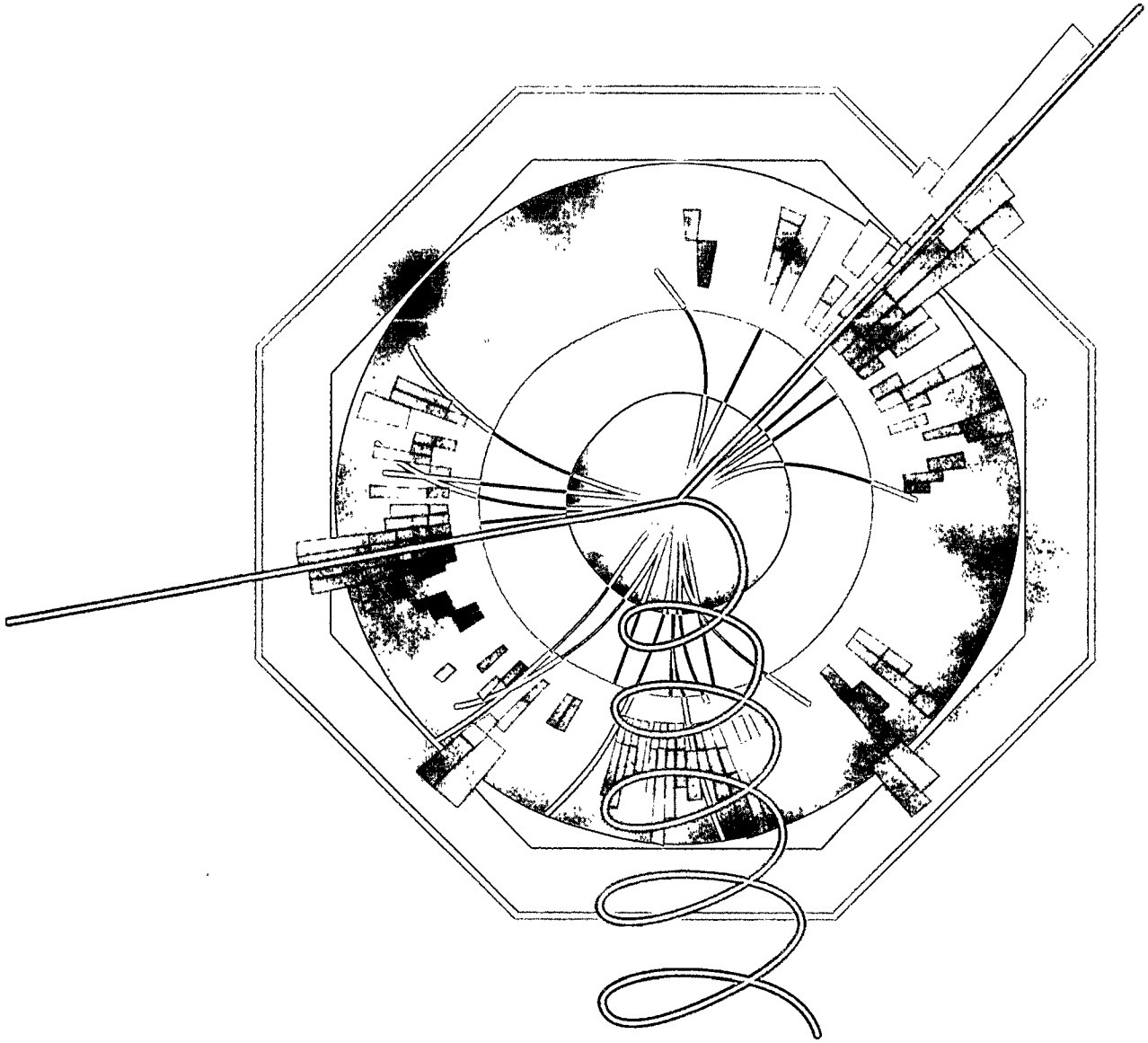
Author Index 645

PREFACE

The XXIV SLAC Summer Institute on Particle Physics explored the role of the strong interaction in the physics of hadrons and partons. The Institute attracted 239 physicists from 16 countries to hear lectures on the underlying theory of Quantum Chromodynamics, modern theoretical calculational techniques, and experimental investigation of the strong interaction as it appears in various phenomena. Different regimes in which one can calculate reliably in QCD were addressed in series of lectures on perturbation theory, lattice gauge theories, and heavy quark expansions. Studies of QCD in hadron–hadron collisions, electron–positron annihilation, and electron–proton collisions all give differing perspectives on the strong interaction—from low-x to high-Q^2. Experimental understanding of the production and decay of heavy quarks as well as the lighter meson states has continued to evolve over the past years, and these topics were also covered at the School. Attendance at the morning lectures was excellent, and the lively nature of the afternoon discussion sessions revealed a totally new aspect to the strong interaction—the passion of the physicists working to understand this remarkable force.

We are grateful to all speakers for their efforts to prepare clear and stimulating lectures, and to all those who presented the latest results in the field of particle physics at the Topical Conference that concluded the Institute. We are once again indebted to Lilian DePorcel and Jennifer Chan for creating such an enjoyable atmosphere for the Summer School and for their attention to the needs of so many who attend.

David Burke
Lance Dixon
David Leith



Summer School

QCD: QUESTIONS, CHALLENGES, AND DILEMMAS

James D. Bjorken*
Stanford Linear Accelerator Center
Stanford University, Stanford, CA 94309

ABSTRACT

An introduction to some outstanding issues in QCD is presented, with emphasis on work by Diakonov and co-workers on the influence of the instanton vacuum on low-energy QCD observables. This includes the calculation of input valence-parton distributions for deep-inelastic scattering.

*Supported by DOE Contract DE–AC03–76SF00515.

© 1996 by James D. Bjorken.

1 Introduction

Quantum electrodynamics (QED) is the correct theory of electromagnetism.

Quantum Chromodynamics (QCD) is the correct theory of the strong force.

These bold, bald statements are slightly unscientific. Nevertheless, they are not far from the truth, in the sense that to challenge either is a very serious enterprise, and one that is likely not to bear fruit unless the challenge is an especially incisive one.

It is remarkable to me that in the short span of two decades, QCD has attained a degree of credibility competitive with QED: the truth and the degree of falsity of the lead sentences above are at a comparable level for the two theories. In fact, we know that QED at short distances does break down. The noble photon becomes the offspring of an ugly, unaesthetic $U(1)$ gauge boson and the neutral $SU(2)$ electroweak boson. Nothing like that fate appears to await the gluons, at least this side of the GUT scale.

Both QED and QCD live in the family of gauge theories and are structurally similar. Their Lagrangian densities both are $E^2 - B^2$. Both require the gauge-invariant substitution $p \to p - eA$. The Heavy-Quark Effective Theory of QCD has its counterpart in the Heavy-Nucleon Effective Theory of QED, responsible for the nonrelativistic limit of electrodynamics, which contains the foundations of condensed matter theory, chemistry, biology, and more.

Both QED and QCD have their Feynman-diagram perturbation-theory processes, leading to incisive precision tests—which work. Their coupling constants run and are seen to run. QED and QCD are very well "tested."

But just as nonperturbative QED contains very interesting phenomena, as mentioned above, nonperturbative QCD is a most interesting portion of that theory as well. To me, it is *the* most interesting and most important portion of QCD to address, despite the evident difficulty in doing so. The lectures in this school emphasize the doable, perturbation-theory based piece of QCD, because that is where most of the work is occurring. In this introduction, I have decided to try to highlight the opposite extreme, with emphasis on material not covered in the other lectures, as well as on the troubles, not successes. I will omit some other unconventional QCD topics which I regard as especially relevant to future high-energy collider experimentation, because they are covered in another talk given to the Snowmass workshop earlier this summer.[1]

2 Questions

These are rather random, just to set the tone. First some easy ones:

Q1. Does the force between quarks get weaker at short distances?

A1. You had better answer no. The force follows an approximate inverse-square law, with a coefficient which at short distances very slowly gets smaller (asymptotic freedom). Please don't accuse me of nit-picking. It may be acceptable for us to use sloppy language to each other, but it is definitely very wrong when trying to explain QCD to the outside world at the *Scientific American* level.

Say it right! When you do, it becomes perfectly clear why there are so many high-p_t jets in hadron-hadron collisions, jets that justify the livelihood of so many experimentalists and theorists. The forces between quarks get so incredibly strong that 500 GeV partons which collide head-on can make the right-angle turn at rates high enough to be detected.

Q2: In idealized QCD, with light quarks omitted, does the force between quarks grow as their separation becomes very large?

A2: Again, no. It's the potential energy that grows linearly.

Q3: Is the QCD strong force CP conserving?

A3: In general, no. There is a CP-violating term $E{\cdot}B$ in the Lagrangian which is allowed and admits observable effects like a nonvanishing neutron electric dipole moment. Renormalization effects make the coefficient of the CP-violating term formally divergent, but the actual coefficient is very small, less than 10^{-9}. What to do remains an unsolved problem, probably not mentioned again in this school.

Q4: Do instantons matter?

A4: Yes. These will not appear in other lectures but will be mentioned in this one later on. They impact on, among other things, the CP-violation issue mentioned above.

Q5: Does old-fashioned pre-QCD S-matrix theory have anything to do with QCD?

A5: Yes. While there seems to be a feeling that quarks, QCD, and parton ideology have rendered that body of work obsolete, this is not true. The S-matrix techniques were built from general principles (analyticity, unitarity, microscopic causality, crossing symmetry, spectrum, ...) which are rigorously true in QCD.[2] Much can still be salvaged from these ideas in describing the nonperturbative, confining, low-energy limit of QCD. It is still something worth learning, and I

fear that it is taught less and less, much being eventually lost and having to be someday rediscovered afresh.

Q6: Does Regge-Pole theory have anything to do with QCD?

A6: This question is a special case of the previous one, with the same answer, but with very clear implications, for example, in main-line QCD structure-function phenomenology. Nonsinglet deep-inelastic structure functions in the limit of small x should be describable by exchange of well-established Regge-trajectories like the ρ or ω. These Reggeons are very well-established experimentally and precisely parametrized. There is much less uncertainty in the theoretical underpinnings of the asymptotic limit of nonsinglet structure functions than there is in the related world of soft and hard Pomeron physics, to be described by Al Mueller in this school.[3] Nevertheless, there is very little work going on to understand this problem in the context of QCD, perturbative or otherwise.[4] It is becoming of special current interest because of the experimental situation regarding the small-x behavior of the polarized structure functions.[5]

Q7: Is the boundary between what is legally calculable from perturbation theory and what is not well-defined?

A7: I believe not. Furthermore, it seems to be crossed more and more indiscriminately as time goes on. Many calculations treat initial and final quarks and gluons as on-shell, asymptotic states. This is illegal; there is no S matrix for quark and gluon interactions. At a less fundamental level, some perturbative-QCD-inspired models for hadronization push shamelessly into regions of parameter space (small momenta, large distance scales) which are indefensible. While boldness in this regard is in itself no vice, an uncritical attitude is. It is not enough to say "It agrees with data, therefore it makes sense and is a prediction of the perturbative theory."

Q8: Will these questions ever end?

A8: Yes, right now.

3 Challenges

The basic challenges in understanding QCD can be seen very clearly in a spacetime description: it is how to link the phenomena at short distances with phenomena at large distances. The simplest case is the static limit, with all light quark degrees of freedom left out. The short-distance limit is that of onium physics—a Coulomb-like interaction between heavy quarks with a weak coupling constant. This is under very good theoretical control. As the heavy quarks are pulled apart, there emerges a linear potential between them, something described quite well via the lattice calculations.[6] The microscopic picture is believed to be that there is a color-electric flux tube of smallish diameter between quark and antiquark in this limit. However, the dynamics creating it is the essence of the problem of confinement and not "understood" well. And if light quarks are included, long flux tubes invariably break and are terminated by constituent quarks or antiquarks. Pull apart bottomonium and you get a B meson and anti-B meson. A B meson is (by definition!) a constituent quark plus a heavy spectator b quark which can be treated perturbatively. Therefore, the B-meson dynamics is an especially simple way in principle (alas, not so much in experimental practice) of learning about the properties of single, "isolated," constituent quarks.[7]

Challenges for "pure" QCD with light quarks excluded include the understanding of the glueball spectrum,[8] as well as the details of the flux tube. When the light quarks are introduced, there are major changes to deal with: the glueballs mix with the myriad of ordinary meson excitations of $q-\overline{q}$ pairs, perhaps toward the limit of total extinction. Flux tubes break, but the microscopic description is obscure. Perhaps the flux-tube concept is likewise driven to the edge of extinction.

Another very basic challenge for the static picture is the nature of chiral symmetry breaking. Because the bare masses of up and down quarks are so small, the QCD Lagrangian has an almost exact $SU(2)_L \times SU(2)_R = O(4)$ chiral symmetry. These $SU(2)$'s describe independent isospin rotations of left- and right-handed up and down quarks. There is a vacuum condensate $\langle 0|\sigma|0\rangle \neq 0$, with σ the fourth component of an internal-symmetry four-vector $(\sigma, \vec{\pi})$ built from the quark densities. The situation is very analogous to the Higgs sector of electroweak theory. In QCD the spontaneous symmetry breakdown leads to nearly massless Goldstone bosons (the pions) as well as the 300–400 MeV of constituent-quark mass. So in the large distance limit (momentum scales smaller than 500–1000 MeV), the QCD dynamics is best described by an effective chiral Lagrangian containing the σ, π, and constituent-quark degrees of freedom (plus some glue) rather than the partonic quark-gluon degrees of freedom which form the basis of perturbative-QCD phenomenology.[9]

It is an extremely basic question to relate this long-distance chiral description to the short-distance Lagrangian. The boundary between large and short distances needs to be sharpened and quantified. And the connection of this chiral-symmetry breaking phenomenon to confinement needs elucidation. So far, the main clue comes from the lattice: the chiral phase transition and deconfinement phase transition in finite-temperature QCD are indistinguishable so far.

I have devoted the final section of this talk to a description of a specific attack on the above questions by Diakonov and his co-workers. I am no expert in this topic. But their work strikes me as a promising attack on the question at an impressively fundamental level, work which respects a variety of fundamental principles. Right or wrong, I think it is well-worth careful attention and study.

Much closer to most of the material contained in the lectures at this school is what goes on in QCD in the high-energy limit. Again, we may look at this in spacetime. But for high-energy collision dynamics, the important action is in the neighborhood of the light cone. Near the past light cone, there is perturbative "evolution"; it is here where each incoming hadron is replaced, in parton-model ideology, by an incoherent beam of incident partons which eventually scatter off a similar "beam" of partons in the other projectile. Near the future light cone, there occur perturbative branching processes which create the multijet structure of typical QCD final states. Further into the interior of the future light cone, things get messy because the partons must find their way into final-state hadrons without violating the nonperturbative demand of perfect confinement; never must a single quark escape into an isolated final state. Finally, deep inside the future light cone, there may also be dynamics: some of us speculate that this region contains a vacuum state with a rotated value of its order parameter (disoriented chiral condensate) which decays into coherent states of pions with curious properties.[10] It is conceivable that there could be other mechanisms of particle production from this region of spacetime as well. This need not happen, but if it does, it is novel physics not contained in existing event generators.

The time scale for evolution of the final state in high-energy collisions is very large, proportional to the energies involved. The time scale for hadronization of leading particles in a jet, in reference frames where the nearest neighboring jet is 90° away (The correct way, in fact, to define what is and is not in jets is to do it in such frames.[11]), is proportional to the transverse momentum or transverse energy of the jet. Thus, there is a direct correspondence between the configuration-space and momentum-space description of jets: the production angles are, of course, the same, while the (large) p_t's and (large) jet-hadronization time scales T are in direct proportion.

Indeed, since one can simultaneously describe the gross properties of jet contents in both momentum space and spacetime, it is clear that the description must be macroscopic, quasi-classical in nature. The vital region for phenomenology is the region of spacetime where the real observed hadrons are produced. In QCD, this is typically a fractal surface, because there can be jets within jets within jets. ... Recall that in the absence of QCD jet phenomena, hadrons are produced with rather uniform density in the lego plot. Since the lego plot area is proportional to $\log s$, the multiplicity should rise with s in a similar way. When additional jets populate the lego plot, they increase the phase space area by an amount equal to $\log\ p_t$ (or $\log T$) per jet. The jets themselves can contain additional jets in their (extended) phase space, leading to a branching structure and fractality by the time all jet evolution is accounted for. The hadron multiplicity is then proportional to the total area of this extended phase space, which thereby acquires fractal properties,[12] and the multiplicity growth with s becomes more rapid.

It is, of course, a challenge to provide a sharp description of all this. And the situation is, in fact, quite good. There is the phenomenon of "preconfinement," which is a perturbative mechanism which keeps color and anticolor close together (most of the time) in momentum space as the branching scale becomes soft and hadronization is invoked.[13] The Monte Carlo programs which employ QCD branching mechanisms work well, and subtle, QCD-specific phenomena like the "string effect" are predicted and seen.[14] Nevertheless, some of the other claimed successes are consequences of phase space and little more. And a purely perturbatively based approach cannot be complete, because confinement is neglected and confinement is important. For example, much is made of "local parton-hadron duality" which is the statement that the perturbatively computed momentum-space densities of "produced" soft partons matches smoothly to the corresponding densities of produced hadrons. This principle is reasonable almost always, especially when the densities are not small. But now and then, the phase space densities of produced partons will fluctuate to small values, and some nonperturbative mechanism (*e.g.*, flux tubes) must intervene. For example, the Z occasionally will decay into two pions and nothing else. Local parton-hadron duality asserts that with

comparable probability, the Z will evolve into two final-state partons and nothing else, *e.g.*, a q and $\overline{q}$; no gluons choose to be emitted. But this is a disaster because at the hadronization time of the quarks, they are 50 to 100 fermis apart. The local duality should apply to spacetime as well as momentum space, and there is a clear problem with simple causality. One cannot be satisfied with a theory of hadronization which accounts for confinement only most of the time.

Finally, there are challenges even within the perturbative sector. These need only be mentioned here briefly, because they will get a lot of attention in the other lectures. It turns out that despite the phenomenon of asymptotic freedom, the interaction of partons at extreme cms energies and a fixed, small-distance scale (say, of impact parameter) is supposed to grow as a power of energy, perhaps almost linearly with cms energy.[3] Thus at extremely high values of s/t, the parton-parton interactions might become strong, with a breakdown of perturbation theory and lots of diffractive phenomena. This is focusing much-needed attention on diffractive phenomena, especially short-distance, high-p_t diffractive processes. The buzz words are hard diffraction, soft and hard Pomerons, BFKL Pomerons, etc. It is an exciting new field, as the proceedings of this school exhibit.[3,15,16]

4 Dilemmas

It is the challenges facing QCD that makes its investigation so much fun. But with the challenges come the dilemmas, which can sometimes make the investigations frustrating. What follows is a rather random potpourri of dilemmas.

On the experimental side, many of the greatest challenges lie in the nonperturbative sector: low-energy spectroscopy (*e.g.*, of glueballs) and collision dynamics, as well as the problems of hadronization and soft diffraction at high energies. Unfortunately, these problems nowadays have little sex appeal, and the interest in—and resources for doing—low-energy spectroscopy and soft-collision dynamics is simply insufficient. For example, a low-energy full-acceptance spectrometer with modern capability would not be costly in comparison with most modern detectors, and could by itself augment the spectroscopy data base—much of which was established long ago via bubble chamber techniques—by orders of magnitude. There is not even an initiative anywhere for doing this. I am informed by Bill Dunwoodie that there actually was a proposal not so long ago for a full-acceptance spectrometer[17] at the proposed Canadian facility KAON. But it did not survive the death of KAON itself and is now abandoned. What a pity!

I also bemoan the lack of interest in full-acceptance, large-cross-section physics at hadron-hadron collider energies. The bemoanings are made in my Snowmass talk[1] and elsewhere,[18] and will not be repeated here.

Most of the challenges for theorists mentioned in the previous section are low-energy or soft phenomena which go beyond perturbation theory. And there are not too many good options for theorists under those circumstances. Lattice QCD is a very powerful way of going beyond perturbation theory, but it is very difficult to apply to high-energy collision dynamics.

A basic dilemma at higher energies is the problem of hadronization, where as already mentioned there is a fuzzy boundary between what is perturbative and what is not. The techniques for creating a precise understanding are still lacking.

Finally, there is the problem of QCD vacuum structure. Understanding the QCD vacua (there are many of them) is the key to the question of confinement and is important for the phenomenology of the effective chiral theory valid in the low-energy limit. Again, the available techniques are limited; nevertheless, the problem is being attacked and progress is being made. The next section on the recent work of Diakonov and his co-workers is evidence of some of the best of this work, and, right or wrong, is an exemplar of the kind of thing that is sorely needed to really make major new inroads into the full understanding of QCD.

5 Diakonov *et al.*: Instantons and their Consequences

The starting point of Diakonov's work[19] was to study the influence of instantons on low-energy QCD. The instanton, something not easy to explain even at length,[20] no less in a short summary like this, is a classical solution of the (Euclidean) QCD field equations, which physically is related to the mixing (via a tunneling mechanism) of various QCD vacua which differ by gauge transformations of nontrivial topology. All this was discovered 20 or so years ago,[21] but at that time, infrared divergences in the calculations[22] made quantitative consequences near impossible to attain. More recently, Shuryak determined phenomenologically the properties that the instanton "fluid" should have in order to be consistent with known data.[23]

Diakonov and Petrov[24] then performed variational calculations which supported the Shuryak picture. Since then, there have appeared some lattice calculations of instanton effects which, although still somewhat controversial, appear to lend support as well.[25] The net result is that by now there is a credible picture of what the instanton effects are. The immediate ones are the solution of the $U(1)$ problem (why the η' meson is so heavy) and the existence of a gluon condensate (seen in QCD sum rules, yet another piece of QCD not discussed at this school[26]).

All this, however, is still rather abstract; it is not clear what more these abstruse considerations have to say to the experimentalists in the trenches. However, the next steps taken are more directly related to QCD phenomenology. The most relevant features, in my opinion, are as follows:

1. The quark-parton degrees of freedom are influenced by the presence of the instantons, and they get a "constituent-quark" mass as a consequence of having to propagate through the instantons.
2. The above mechanism leads naturally to spontaneous breaking of the strong-interaction chiral symmetry.
3. Therefore, there must be the Goldstone degrees of freedom (almost massless pions) in the spectrum as well as the constituent quarks.
4. The low-energy chiral effective Lagrangian can be constructed. The lowest order terms are universal (model independent) in form, depending only on symmetry considerations. However, higher order terms are also present and can be estimated. The magnitudes of these terms are in agreement with what is needed for the phenomenology.
5. The Goldstone pions can be shown to be composites of the constituent quarks. This is an improvement on the scheme put forward by Manohar and Georgi[27] some time ago. They argued for the chiral constituent-quark-plus-pion picture based on the success of the additive quark model. They had, however, an awkward time in understanding whether their Goldstone pion is the same as, or distinct from, the ${}^1S_1$ partner of the ${}^3S_1$ ρ. In the Diakonov instanton picture, they are not distinct.
6. Diakonov *et al.* in addition put forward an interesting model of baryons, which is a variant of the somewhat popular Skyrmion picture, and to my eye, an improvement.[28] They assume that the pion cloud surrounding the three constituent quarks of the baryon has a nontrivial "hedgehog" topology, as originally suggested by Skyrme long, long ago[29] [see Eq. (14) below]. Then it can be shown that in such an external field, there will be one and only one quark-bound state with energy in the gap between the continua starting at $E = +m$ and $E = -m$. This state can be populated with one quark of each color to make objects with the quantum numbers of the nucleons. In the large N_c limit, the combined wave functions of these quarks can be treated *à la* Thomas-Fermi atomic theory as a source of the "hedgehog" pion field, leading to a self-consistent semiclassical description of the nucleon. To recover quantum mechanics, in particular the classification of the energy levels, the "cranking-model" techniques of nuclear theory can be employed to give a reasonable description.[30] So this picture has a quite good formal justification in the large N_c limit.
7. Finally, with this picture of the nucleon, they calculate[31] the distributions of the "primordial" partons within the nucleon, namely the leading-twist parton distributions at a low value of $Q^2 \approx 0.5\ GeV^2$, which when evolved to higher Q^2 via the DGLAP evolution equations give the leading-twist contributions to the structure functions. Their results agree reasonably with the Glück, Reya, Vogt[32] primordial parton distribution functions which are input by hand in order to reproduce deep-inelastic scattering data. But more important in my opinion is the way Diakonov *et al.* can maintain the internal consistency of the formalism. The validity of a variety of current algebra sum rules is established. This is highly nontrivial, because relativistic effects are very important, and valence antiquark distributions must be present; they are created by the back reaction of the nucleon valence quarks on the pionic "hedgehog" sea. The techniques which are employed provide valuable lessons for all bag-model descriptions of hadrons.

There remains a major missing link: an understanding of confinement. The effects of gluons in this low-energy limit are formally of "higher order." In one sense this is good, because in the low-energy constituent-quark spectroscopic world, the gluon degrees of freedom do not seem to play a central role. On the other hand, their effects cannot be omitted, because confinement depends on them. Probably some of the effective quark mass is accounted by something akin to color flux-tube energy, and the dynamical effects of fluctuations about an average value are not

too important. I think the ideal arena for studying this problem is that of heavy-flavor mesons and baryons, where the source of color is static and understood (a stationary heavy b-quark, or Wilson line), and only how the color finds its way into the single constituent quark degree of freedom of the B-meson, or alternatively into the "Skyrmionic" quark-baryon wave function, needs to be solved. Some work has been done, but more is needed.[33]

While there may well be reason to exhibit skepticism regarding the whole Diakonov program, I still want to emphasize that this kind of work is at the most important forefront of QCD. It links the confining world to the perturbative sector. Most of the known nonperturbative QCD phenomena are involved, and the work touches upon the edge of some of the best perturbative phenomenology which exists, namely the information on deep-inelastic structure functions. The level of attack is much deeper than mere phenomenological model building. It deserves, I believe, close attention and constructive criticism.

6 Some More Details on the Diakonov Program

The preceding description was very general in nature, and what follows is a slightly more technical version of some of the same material. It is far from definitive, if for no other reason than the limited competence of yours truly. However, there are recent lecture notes[19] to consult for a more detailed and authoritative version.

6.1 What about these Instantons?

As already mentioned, an instanton is a solution of the QCD classical field equations in Euclidean spacetime with finite action. It contains a "topological knot" and is localized in spacetime. It also has a size parameter which can take any value in principle. The immediate function of these instantons is to create couplings, via tunneling, between different Minkowski-space QCD vacua, vacua which differ from each other by a gauge transformation which also contains a "topological knot." Because of these nonperturbative tunneling couplings, the many initially degenerate QCD vacua, which can be classified in terms of the number of gauge knots they contain, are coupled together and must be diagonalized, leading to the so-called θ-vacua, which are the true energy eigenfunctions of the vacuous QCD theory.

When theorists initially attempted to estimate the magnitude of these effects, they were thwarted by the presence of large numbers of large instantons, whose effects were not under control. Shuryak, working phenomenologically, argued that if instantons with sizes larger than about 0.3 fermis (or a momentum scale $\approx 600\ MeV$) were suppressed, instanton-induced phenomenology could be understood. Furthermore, were this true, the instanton "liquid" in Euclidean spacetime would be dilute, in the sense that the mean separation R between instantons would be two to three times larger than the important instanton size ρ. As already mentioned, Diakonov and Petrov,[24] using variational techniques, found a candidate mechanism for this to happen, namely medium-range instanton-antiinstanton repulsion.

The bottom line is that the effects of large instantons are arguably damped out at a known scale, with a bonus of a small parameter (the instanton packing fraction in Euclidean spacetime) in the formalism. This then becomes the working hypothesis for going further. It is not rigorously established but is credible.

6.2 How Do the Instantons Induce Chiral Symmetry Breaking?

The next step is to introduce the quarks and calculate their influence. The equation of motion of quarks in a classical instanton field (again in Euclidean spacetime) also shows a remarkable feature—the existence of "zero-mode" solutions of the Dirac equation of the quark in the presence of the instanton (with zero eigenvalue of the Euclidean Dirac operator) which are localized around the instanton. Just as for the instanton itself, the implication of these solutions for physics is subtle and deep. For example, they influence the presence (or absence) of CP violation in the strong interactions. The vital buzzword here is "spectral flow": a filled negative-energy level (now in Minkowski space) in the negative energy sea can, because of the knotty gauge potentials, be pushed above zero (in the chiral limit of massless quarks), while other empty positive energy levels with different quantum numbers can be pushed into the negative energy sea.[34] The net result is that there can be net pair-creation induced, with the pair not necessarily having vacuum quantum numbers. All this activity is quite sufficient to create the mechanism of spontaneous symmetry breakdown.

In the calculations which argue for spontaneous symmetry breaking, it is necessary to include the mixings of zero modes associated with different instantons, something rather nontrivial. What follows are a few equations for theorists and well-educated experimentalists to give a flavor of what is done. The information about all this kind of thing is to be extracted from the Euclidean partition function

$$\begin{aligned} Z &\sim \int \mathcal{D}A\, e^{-\frac{1}{g^2}\int d^4x\, F^2} \int \mathcal{D}\psi\, \mathcal{D}\overline{\psi} e^{\int d^4x \overline{\psi}(\not\nabla - g\not A - m)\psi} \\ &\equiv \langle \det(\not\nabla - g\not A - m)\rangle \Rightarrow \left\langle e^{\frac{1}{2}\sum_n \ell n(\lambda_n^2+m^2)}\right\rangle , \end{aligned} \tag{1}$$

where in the second line the Gaussian integral over fermionic quark fields is performed, and where

$$\lambda_n = n_{th} \text{ eigenvalue of } (\not\nabla - g\not A) \tag{2}$$

and m is the small quark-parton mass of a few MeV.

There is one zero eigenvalue per instanton per quark flavor in the dilute-instanton approximation. But when the effect of the overlapping of zero modes from separate instantons is taken into account, the zero eigenvalues repel. The typical values become

$$\langle\lambda\rangle \sim \frac{\rho^2}{R^3} . \tag{3}$$

Now, by definition, the chiral order parameter is

$$\begin{aligned} V\left\langle\overline{\psi}\psi\right\rangle &\simeq \frac{\partial}{\partial m}\ell n\, Z\,\Big|_{m=0} \\ &= \frac{\partial}{\partial m}\left\langle \frac{1}{2}\int d\lambda\, \nu(\lambda)\, \ell n\,(\lambda^2+m^2)\right\rangle \\ &= \left\langle \int d\lambda\, \nu(\lambda)\left(\frac{m}{\lambda^2+m^2}\right)\right\rangle_{m\to 0} \end{aligned} \tag{4}$$

where we go to continuum normalization via

$$\sum_n \Leftrightarrow \int d\lambda\, \nu(\lambda) \tag{5}$$

and V is the (Euclidean) spacetime volume.

This shows that chiral symmetry breaking will occur provided the density of zero modes $\nu(\lambda)$ at $\lambda = 0$ is nonvanishing. But this is what is estimated to occur,

$$\left\langle\overline{\psi}\psi\right\rangle \sim \frac{\nu(0)}{V} = \frac{N}{\langle\lambda\rangle V} \sim \left(\frac{R^2}{\rho}\right)\left(\frac{1}{R}\right)^4 = \frac{1}{\rho R^2} . \tag{6}$$

The factor ρ/R^2 for $\langle\lambda\rangle$ occurs because

$$\langle\lambda\rangle^2 \Rightarrow \left\langle\lambda^2\right\rangle = N\left\langle\lambda^2\right\rangle_0 = N\int\frac{d^4R}{V}\left(\frac{\rho^2}{R^3}\right)^2 = \frac{N\rho^2}{V} = \frac{\rho^2}{R^4} \tag{7}$$

with $\langle\lambda^2\rangle_0$ the contribution to λ^2 from one instanton. Note that this happens because we have added the contributions to splittings from all the neighboring instantons in quadrature. This rough argument, due to Diakonov, actually can be refined, so that the conclusion is quite robust.

The parameters of the constituent quarks can be estimated from the instanton parameters, which are

$$\text{instanton size:} \qquad \overline{\rho} \approx 0.3\, f \tag{8}$$

$$\text{instanton spacing:} \qquad R \approx 1\, f\ . \tag{9}$$

This means that the fraction of Euclidean spacetime occupied by instantons is

$$\pi^2\left(\frac{\rho}{R}\right)^4 \approx 0.1\ . \tag{10}$$

The quark mass, in order of magnitude, turns out to be

$$M_Q \sim \frac{\rho}{R^2} = \frac{1}{\rho}\left(\frac{\rho}{R}\right)^2 , \tag{11}$$

and the careful calculations produce a reasonable value of constituent quark mass of 350–400 MeV.

The pion decay constant F_π can also be estimated

$$F_\pi \cong \frac{\text{const}}{\rho}\cdot\left(\frac{\rho}{R}\right)^2\sqrt{\ell n\,\frac{R}{\rho}} \approx 100\ MeV\ . \tag{12}$$

In the very low momentum limit, the constituent quark degrees of freedom can be integrated out of the partition function, leaving a chiral effective action of the form

$$Z = e^{iS(\pi)} = \int \mathcal{D}\psi\mathcal{D}\overline{\psi}\,\exp i\int d^4x\left(\overline{\psi}_L\left[i\not\nabla - M\, e^{i\vec{\tau}\cdot\vec{\pi}}\right]\psi_R\ +\text{h.c.}\right)\ . \tag{13}$$

There is also a "gap equation" relating how the pionic degrees of freedom are related to the quarks, but I have had difficulty dredging the details out of the easily available literature.

6.3 How Does This Lead to a Model of the Nucleon?

Thus far, it has been sufficient to look at the theory in Euclidean spacetime, a clear indicator that phenomenology is somewhat distant. The reason for the success is that the theory has been about the vacuum properties much more than about excitations of the vacuum, where Minkowski-space description is essential. (If the energy of the system is zero, then its analytic continuation to imaginary energies does not change too many things.) Nevertheless, the Euclidean analysis has led to an effective action, which can be continued to Minkowski spacetime and used for dynamics.

The model of the nucleon is built from this action via the Skyrme ansatz for the pion "condensate":

$$U \equiv e^{i\vec{\tau}\cdot\vec{\pi}} = e^{i\vec{\tau}\cdot\hat{r}f(r)} \tag{14}$$

with

$$f(0) = \pi \qquad f(\infty) = 0\ . \tag{15}$$

Because

$$U(0) = -1 \tag{16}$$

and

$$U(\infty) = +1, \tag{17}$$

the pion field contains the "topological knot"; U cannot be continuously deformed to the unit matrix.

Now the Dirac equation is solved in this pion field

$$i\,\partial\!\!\!/ - MU(r) = 0, \tag{18}$$

and as already advertised, one bound state is found to exist with $|E| < M$. The bound-state wave function is then determined by calculating the summed energy of the negative-energy Dirac sea and the bound state contribution as a function of the trial function $f(r)$, and then minimizing with respect to the choice of f. The resulting structure is classical, and the quantum structure is built by using the "cranking model," *i.e.*, projecting the constructions on eigenfunctions of rotations and translations. The nucleon and Δ masses can be calculated; the nucleon mass is somewhat on the high side (1200 MeV or so), although there are several candidate apologies for this situation. With this model, a variety of nucleon static properties are calculated with reasonable success.

6.4 What Implications Does This Have for Deep-Inelastic Structure Functions?

An especially interesting application of the model is in the construction of the primordial parton distributions, defined as follows[35]:

$$\left.\begin{array}{ll} q(x) & x > 0 \\ -\bar{q}(-x) & x < 0 \end{array}\right\} = \frac{1}{4\pi}\int_{-\infty}^{\infty} dt\, e^{ixMt} \left\langle P \,|\, \psi^\dagger(0)(1+\gamma^0\gamma^2)\,\psi(y) \,|\, P \right\rangle \tag{19}$$

with

$$y = (t, -t, 0, 0)\ . \tag{20}$$

This is to be interpreted as the input parton distributions at the highest value of the scale allowed by the effective chiral theory, namely the scale associated with the typical instanton size, 600 MeV, or $Q^2 \approx 0.4\ GeV^2$. Note that it is defined in the nucleon rest frame, but when boosted to an infinite-momentum frame becomes the usual correlation function defining the parton distributions.

Note that the definition in Eq. (19) admits the introduction by necessity of valence antiquark distributions. And, as mentioned earlier, the contribution of the discrete level by itself leads to negative-definite valence antiquark distributions. It is necessary to calculate the (distorted) negative-energy continuum contributions before obtaining sensible results. When this is carefully done, the antiquark distributions happily are positive definite. Some of these are shown in Figs. 1–5. In particular, in Fig. 3, which exhibits the flavor singlet antiquark distributions, is sketched the negative contribution of the discrete level, as well as the summed result.

A variety of deep-inelastic sum rules are also tested and shown to be in principle (as well as numerically) satisfied. These include the sum rules for baryon number, momentum (at this level, all momentum is carried by quarks), isospin, and flavor-nonsinglet polarized distributions. Also, the Gottfried sum, which measures the flavor nonsinglet antiquark distribution, is calculated and has a nonvanishing right-hand side, with the sign needed to account for the data. The argumentation for these results goes deep into the basic structure of the model, and the consistency is very satisfying.

It would be a great advance if the description of mesons, for which there is no Skyrmionic topological starting point, could be carried to the same level of sophistication. Are mesons really so different from baryons? I think the best

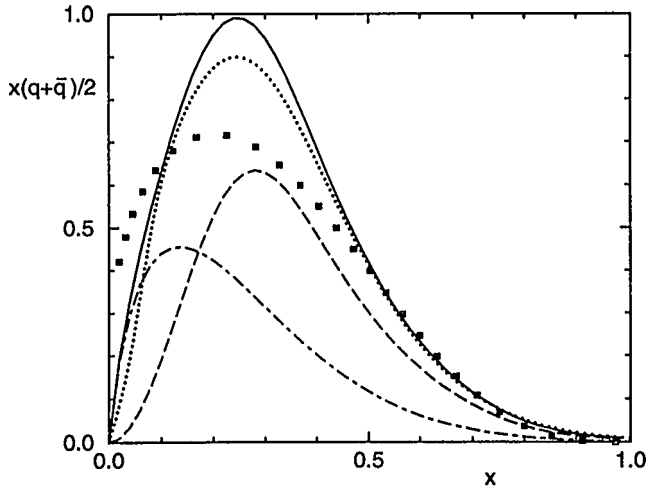


Figure 1: The singlet unpolarized distribution, $x[u(x) + d(x) + \overline{u}(x) + \overline{d}(x)]/2$. Dashed line: regularized contribution from the discrete level; dash-dotted line: contribution from the Dirac continuum; solid line: the total distribution, namely the sum of the dashed and dash-dotted curves; dotted line: the exact total distribution; squares: the parametrization of Ref. 32.

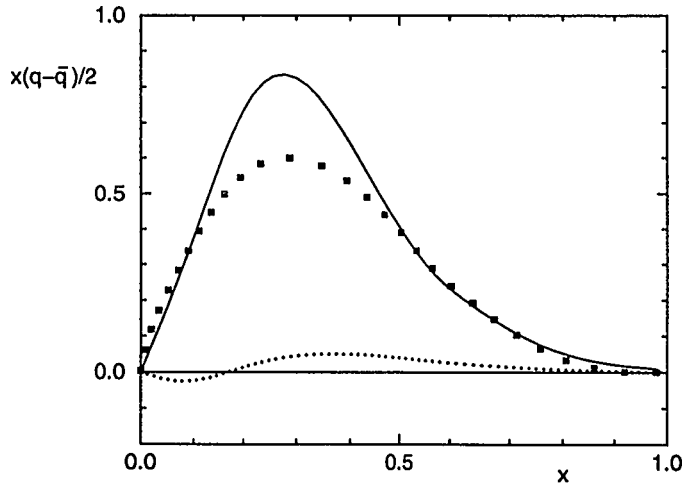


Figure 2: The baryon number distribution, $x[u(x) + d(x) - \overline{u}(x) - \overline{d}(x)]/2$. Solid line: distribution from the unregularized discrete level; dotted line: exact Dirac continuum contribution; squares: the parametrization of Ref. 32.

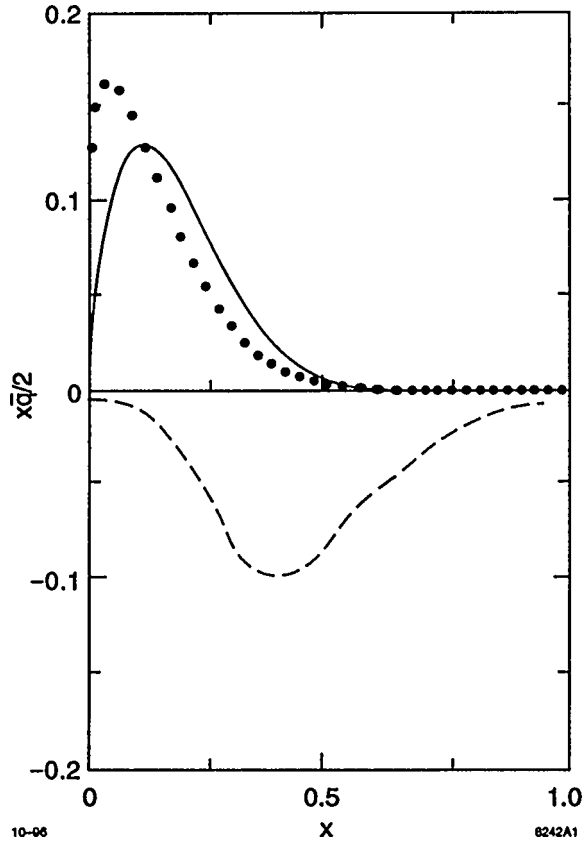


Figure 3: The antiquark distribution, $x[\overline{u}(x) + \overline{d}(x)]/2$. Solid line: theory; dotted line: the parametrization of Ref. 32; dashed line: contribution from the discrete level only.

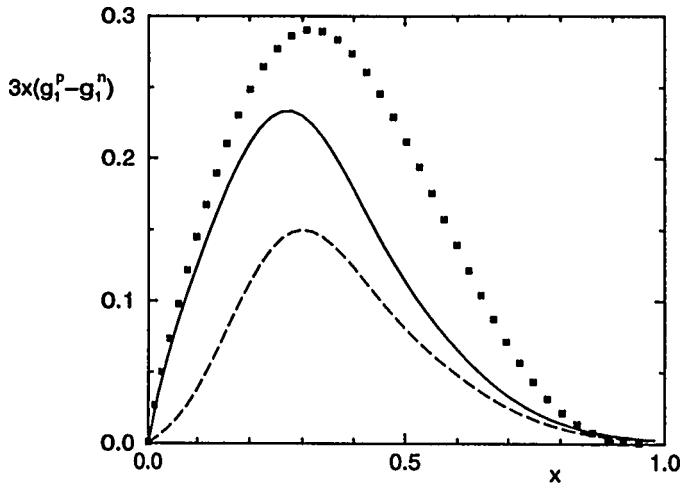


Figure 4: The isovector polarized distribution, $x[\Delta u(x) - \Delta d(x) + \Delta\overline{u}(x) - \Delta\overline{d}(x)]/2$. Dashed line: regularized contribution from the discrete level; solid line: the sum of the contributions from the discrete level and from the continuum; squares: the parametrization of Ref. 32.

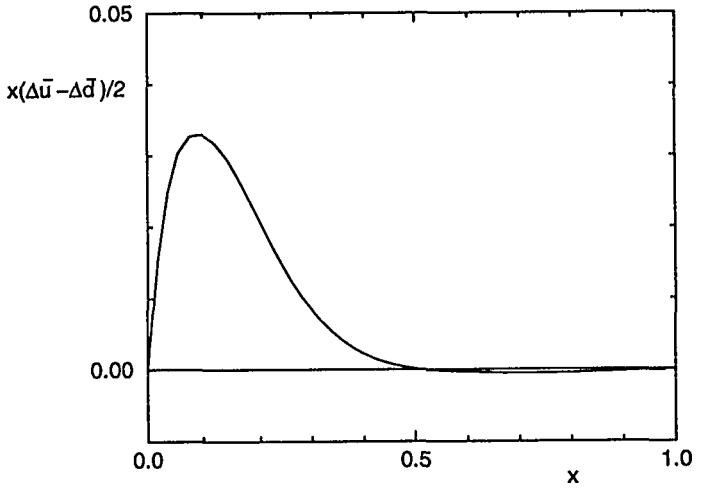


Figure 5: The isovector polarized distribution of antiquarks, $x[\Delta\overline{u}(x) - \Delta\overline{d}(x)]/2$. Reference 32 assumes this quantity to be zero.

candidate for study is the B meson. If progress can be made there, it may also shed light on the confinement issue, which so far has remained beyond the scope of these methods.

References

[1] J. Bjorken, *Proceedings of the 1996 DPF/DPB Summer Study of New Directions for High-Energy Physics* (Snowmass '96), to be published.

[2] See, *e.g.*, R. Oehme, Int. J. Mod. Phys. A **10**, 2014 (1995).

[3] A. Mueller, these proceedings.

[4] There are exceptions, see, *e.g.*, R. Kirschner, preprint hep-ph/9605391 and references therein.

[5] See the talk of R. Welsh, these proceedings.

[6] T. DeGrand, these proceedings.

[7] See, for example, J. Bjorken, Acta Physica Pol. B **23**, 637 (1992).

[8] W. Toki, these proceedings.

[9] For a review, see, *e.g.*, A. Manohar, *Proceedings of the Tenth Lake Louise Winter Institute: Quarks and Colliders*, edited by A. Astbury *et al.* (World Scientific, 1995), p. 274.

[10] For an introduction, see C. Taylor, *Proceedings of the Fourth International Workshop: Relativistic Aspects of Nuclear Physics*, CBPF Brazil, 28–30 August 1995, edited by T. Kodama *et al.* (World Scientific), p. 87.

[11] J. Bjorken, Phys. Rev. D **45**, 4077 (1992).

[12] B. Andersson, P. Dahlqvist, and G. Gustafsson, Phys. Lett. B **214**, 604 (1988).

[13] D. Amati and G. Veneziano, Phys. Lett. B **83**, 87 (1979).

[14] Y. Azimov, Y. Dokshitzer, V. Khoze, and S. Troyan, Phys. Lett. B **165**, 147 (1985).

[15] D. Soper, these proceedings.

[16] M. Albrow, these proceedings.

[17] See the talk of K. Crowe in the *Proceedings of a Workshop on Science at the Kaon Factory*, July 23–28, 1990, edited by D. Grill (TRIUMF); also S. Godfrey *et al.*, Guelph University preprint GIPP 89-8.

[18] J. Bjorken, Int. J. Mod. Phys. A **7**, 4189 (1992).

[19] See the recent Varenna lectures of Diakonov for an overview: D. Diakonov, hep-ph/9602375.

[20] A classic introduction is given by Sidney Coleman, *The Uses of Instantons*, "The Whys of Subnuclear Physics," edited by A. Zichichi (Plenum, 1979), p. 805.

[21] A. Belavin, A. Polyakov, A. Schwartz, and Y. Tyupkin, Phys. Lett. **59**, 85 (1975); G. 't Hooft, Phys. Rev. D **14**, 3432 (1976).

[22] C. Callan, R. Dashen, and D. Gross, Phys. Rev. D **17**, 2717 (1978).

[23] For a review, see E. Shuryak, Phys. Reports **115**, 151 (1985).

[24] D. Diakonov and V. Petrov, Nucl. Phys. B **245**, 259 (1984).

[25] M.-C. Chu, J. Grandy, S. Huang, and J. Negele, Phys. Rev. D **49**, 6039 (1994).

[26] M. Shifman, A. Vainstein, and V. Zakharov, Nucl. Phys. B **147**, 385 (1979).

[27] A. Manohar and H. Georgi, Nucl. Phys. B **234**, 189 (1984).

[28] D. Diakonov, V. Petrov, and P. Pobylitsa, Nucl. Phys. B **306**, 809 (1988).

[29] T. H. R. Skyrme, Nucl. Phys. **31**, 556 (1962).

[30] See, *e.g.*, P. Ring and P. Schuck, *The Nuclear Many-Body Problem* (Springer, 1980).

[31] D. Diakonov, V. Petrov, P. Pobylitsa, M. Polyakov, and C. Weiss, preprint hep-ph/9606314.

[32] M. Glück, E. Reya, and A. Vogt, Z. Phys. C **67**, 433 (1995).

[33] S. Chernyshev, M. Nowak, and I. Zahed, preprint hep-ph/9409207.

[34] A reasonable entry-level discussion of the relationship of the zero modes to Minkowski-space physics is given by N. Christ, Phys. Rev. D **21**, 1591 (1980) and references therein.

[35] J. Collins and D. Soper, Nucl. Phys. B **194**, 445 (1982).

BASICS OF QCD PERTURBATION THEORY

Davison E. Soper*
Institute of Theoretical Science
University of Oregon, Eugene, OR 97403

ABSTRACT

This is an introduction to the use of QCD perturbation theory, emphasizing generic features of the theory that enable one to separate short-time and long-time effects. I also cover some important classes of applications: electron-positron annihilation to hadrons, deeply inelastic scattering, and hard processes in hadron-hadron collisions.

*Supported by DOE Contract DE-FG03-96ER40969.

© 1996 by Davison E. Soper.

1 Introduction

A prediction for experiment based on perturbative QCD combines a particular calculation of Feynman diagrams with the use of general features of the theory. The particular calculation is easy at leading order, not so easy at next-to-leading order, and extremely difficult beyond the next-to-leading order. This calculation of Feynman diagrams would be a purely academic exercise if we did not use certain general features of the theory that allow the Feynman diagrams to be related to experiment:

- the renormalization group and the running coupling;
- the existence of infrared safe observables;
- the factorization property that allows us to isolate hadron structure in parton distribution functions.

In these lectures, I discuss these structural features of the theory that allow a comparison of theory and experiment. Along the way, we will discover something about certain important processes:

- e^+e^- annihilation;
- deeply inelastic scattering;
- hard processes in hadron-hadron collisions.

By discussing the particular along with the general, I hope to arm the reader with information that speakers at research conferences take to be collective knowledge—knowledge that they assume the audience already knows.

Now here is the disclaimer. We will not learn how to do significant calculations in QCD perturbation theory. Three lectures is not enough for that.

I hope that the reader may be inspired to pursue the subjects discussed here in more detail. A good source is the *Handbook of Perturbative QCD*[1] by the CTEQ Collaboration. More recently, Ellis, Stirling, and Webber have written an excellent book[2] that covers most of the subjects sketched in these lectures. For the reader wishing to gain a mastery of the theory, I can recommend the recent books on quantum field theory by Brown,[3] Sterman,[4] Peskin and Schroeder,[5] and Weinberg.[6] Another good source, including both theory and phenomenology, is the lectures in the 1995 TASI proceedings, *QCD and Beyond*.[7]

2 Electron-Positron Annihilation and Jets

In this section, I explore the structure of the final state in QCD. I begin with the kinematics of $e^+e^- \to 3$ *partons*, then examine the behavior of the cross section for $e^+e^- \to 3$ *partons* when two of the parton momenta become collinear or one parton momentum becomes soft. In order to illustrate better what is going on, I introduce a theoretical tool, null-plane coordinates. Using this tool, I sketch a space-time picture of the singularities that we find in momentum space. The singularities of perturbation theory correspond to long-time physics. We see that the structure of the final state suggested by this picture conforms well with what is actually observed.

I draw the distinction between short-time physics, for which perturbation theory is useful, and long-time physics, for which the perturbative expansion is out of control. Finally, I discuss how certain experimental measurements can probe the short-time physics while avoiding sensitivity to the long-time physics.

2.1 Kinematics of $e^+e^- \to 3$ *Partons*

Consider the process $e^+e^- \to q\,\bar{q}\,g$, as illustrated in Fig. 1. Let $\sqrt{s}$ be the total energy in the c.m. frame and let q^μ be the virtual photon (or Z boson) momentum, so $q^\mu q_\mu = s$. Let p_i^μ be the momenta of the outgoing partons $(q, \bar{q}, g)$ and let $E_i = p_i^0$ be the energies of the outgoing partons. It is useful to define energy fractions x_i by

$$x_i = \frac{E_i}{\sqrt{s}/2} = \frac{2p_i \cdot q}{s}. \tag{1}$$

Then

$$0 < x_i. \tag{2}$$

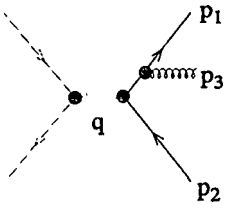


Figure 1: *Feynman diagram for* $e^+e^- \to q\bar{q}g$.

Energy conservation gives

$$\sum_i x_i = \frac{2(\sum p_i)\cdot q}{s} = 2. \tag{3}$$

Thus only two of the x_i are independent.

Let θ_{ij} be the angle between the momenta of partons i and j. We can relate these angles to the momentum fractions as follows:

$$2p_1\cdot p_2 = (p_1+p_2)^2 = (q-p_3)^2 = s - 2q\cdot p_3, \tag{4}$$

$$2E_1E_2(1-\cos\theta_{12}) = s(1-x_3). \tag{5}$$

Dividing this equation by $s/2$ and repeating the argument for the two other pairs of partons, we obtain three relations for the angles θ_{ij}:

$$\begin{aligned} x_1x_2(1-\cos\theta_{12}) &= 2(1-x_3), \\ x_2x_3(1-\cos\theta_{23}) &= 2(1-x_1), \\ x_3x_1(1-\cos\theta_{31}) &= 2(1-x_2). \end{aligned} \tag{6}$$

We learn two things immediately. First,

$$x_i < 1. \tag{7}$$

Second, the three possible collinear configurations of the partons are mapped into x_i space very simply:

$$\begin{aligned} \theta_{12}\to 0 &\Leftrightarrow x_3\to 1, \\ \theta_{23}\to 0 &\Leftrightarrow x_1\to 1, \\ \theta_{31}\to 0 &\Leftrightarrow x_2\to 1. \end{aligned} \tag{8}$$

The relations $0 \le x_i \le 1$, together with $x_3 = 2-x_1-x_2$, imply that the allowed region for (x_1, x_2) is a triangle, as shown in Fig. 2. The edges $x_i = 1$ of the allowed region correspond to two partons being collinear, as shown in Fig. 3. The corners $x_i = 0$ correspond to one parton momentum being soft ($p_i^\mu \to 0$).

2.2 Structure of the Cross Section

One can easily calculate the cross section corresponding to Fig. 1 and the similar amplitude in which the gluon attaches to the antiquark line. The result is

$$\frac{1}{\sigma_0}\frac{d\sigma}{dx_1dx_2} = \frac{\alpha_s}{2\pi}C_F\frac{x_1^2+x_2^2}{(1-x_1)(1-x_2)}, \tag{9}$$

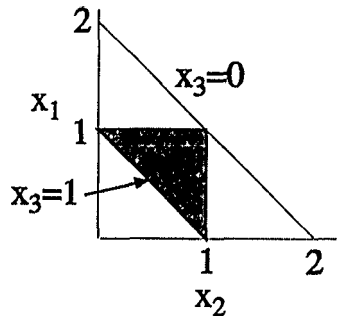


Figure 2: *Allowed region for (x_1, x_2). Then x_3 is $2-x_1-x_2$.*

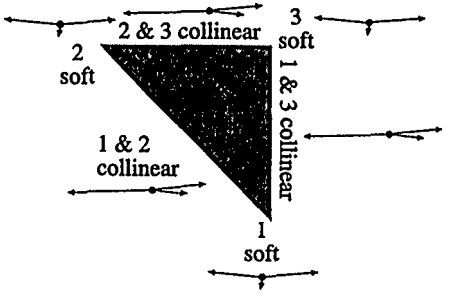


Figure 3: *Allowed region for (x_1, x_2). The labels and small pictures show the physical configuration of the three partons corresponding to subregions in the allowed triangle.*

where $C_F = 4/3$ and $\sigma_0 = (4\pi\alpha^2/s)\sum Q_f^2$ is the total cross section for $e^+e^- \to$ *hadrons* at order α_s^0. The cross section has collinear singularities:

$$\begin{aligned} (1-x_1) &\to 0, \qquad (2\ \&\ 3 \text{ collinear}); \\ (1-x_2) &\to 0, \qquad (1\ \&\ 3 \text{ collinear}). \end{aligned} \tag{10}$$

There is also a singularity when the gluon is soft: $x_3 \to 0$. In terms of x_1 and x_2, this singularity occurs when

$$(1-x_1)\to 0, \quad (1-x_2)\to 0, \quad \frac{(1-x_1)}{(1-x_2)} \sim const. \tag{11}$$

Let us write the cross section in a way that displays the collinear singularity at $\theta_{31} \to 0$ and the soft singularity at $E_3 \to 0$:

$$\frac{1}{\sigma_0}\frac{d\sigma}{dE_3\, d\cos\theta_{31}} = \frac{\alpha_s}{2\pi} C_F \frac{f(E_3,\theta_{31})}{E_3(1-\cos\theta_{31})}. \tag{12}$$

Here, $f(E_3,\theta_{31})$, is a rather complicated function. The only thing that we need to know about it is that it is finite for $E_3 \to 0$ and for $\theta_{31} \to 0$.

Now look at the collinear singularity, $\theta_{31} \to 0$. If we integrate over the singular region holding E_3 fixed, we find that the integral is divergent:

$$\int_a^1 d\cos\theta_{31}\, \frac{d\sigma}{dE_3\, d\cos\theta_{31}} = \log(\infty). \tag{13}$$

Similarly, if we integrate over the region of the soft singularity, holding θ_{31} fixed, we find that the integral is divergent:

$$\int_0^a dE_3\, \frac{d\sigma}{dE_3\, d\cos\theta_{31}} = \log(\infty). \tag{14}$$

Evidently, perturbation theory is telling us that we should not take the perturbative cross section too literally. The total cross section for $e^+e^- \to$ *hadrons* is certainly finite, so this partial cross section cannot be infinite. What we are seeing is a breakdown of perturbation theory in the soft and collinear regions, and we should understand why.

Where do the singularities come from? Look at Fig. 4 (in a physical gauge). The scattering matrix element $\mathcal{M}$ contains a factor $1/(p_1+p_3)^2$ where

$$(p_1+p_3)^2 = 2p_1\cdot p_3 = 2E_1E_3(1-\cos\theta_{31}). \tag{15}$$

Evidently, $1/(p_1+p_3)^2$ is singular when $\theta_{31} \to 0$ and when $E_3 \to 0$. The collinear singularity is somewhat softened because the numerator of the Feynman diagram contains a factor proportional to θ_{31} in the collinear limit. (This is not exactly obvious, but is easily seen by calculating. If you like symmetry arguments, you can derive this factor from quark helicity conservation and overall angular momentum conservation.) We thus find that

$$|\mathcal{M}|^2 \propto \left[\frac{\theta_{31}}{E_3\theta_{31}^2}\right]^2 \tag{16}$$

for $E_3 \to 0$ and $\theta_{31} \to 0$. Note the universal nature of these factors.

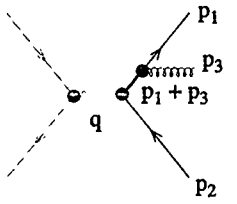


Figure 4: *Cross section for $e^+e^- \to q\bar{q}g$, illustrating the singularity when the gluon is soft or collinear with the quark.*

Integration over the double singular region of the momentum space for the gluon has the form

$$\int \frac{E_3^2 dE_3 d\cos\theta_{31} d\phi}{E_3} \sim \int E_3 dE_3 d\theta_{31}^2 d\phi. \tag{17}$$

Combining the integration with the matrix element squared gives

$$d\sigma \sim \int E_3 dE_3 d\theta_{31}^2 d\phi \left[\frac{\theta_{31}}{E_3\theta_{31}^2}\right]^2 \sim \int \frac{dE_3}{E_3}\,\frac{d\theta_{31}^2}{\theta_{31}^2}\, d\phi. \tag{18}$$

Thus we have a double logarithmic divergence in perturbation theory for the soft and collinear region. With just a little enhancement of the argument, we see that there is a collinear divergence from integration over θ_{31} at finite E_3 and a separate soft divergence from integration over E_3 at finite θ_{31}. Essentially the same argument applies to more complicated graphs. There are divergences when two final state partons become collinear and when a final state gluon becomes soft. Generalizing further,[8] there are also divergences when several final state partons become collinear to one another or when several (with no net flavor quantum numbers) become soft.

We have seen that if we integrate over the singular region in momentum space with no cutoff, we get infinity. The integrals are logarithmically divergent, so if we integrate with an infrared cutoff M_{IR}, we will get big logarithms of M_{IR}^2/s. Thus the collinear and soft singularities represent perturbation theory out of control. Carrying on to higher orders of perturbation theory, one gets

$$1 + \alpha_s \times (\text{big}) + \alpha_s^2 \times (\text{big})^2 + \cdots. \tag{19}$$

If this expansion is in powers of $\alpha_s(M_Z)$, we have $\alpha_s \ll 1$. Nevertheless, the big logarithms seem to spoil any chance of the low order terms of perturbation

theory being a good approximation to any cross section of interest. Is the situation hopeless? We shall have to investigate further to see.

2.3 Interlude: Null Plane Coordinates

In order to understand better the issue of singularities, it is helpful to introduce a concept that is generally quite useful in high-energy quantum field theory, null plane coordinates (see Fig. 5). The idea is to describe the momentum of a particle using momentum components $p^\mu = (p^+, p^-, p^1, p^2)$ where

$$p^\pm = (p^0 \pm p^3)/\sqrt{2}. \tag{20}$$

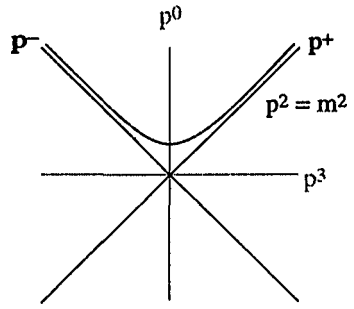


Figure 5: *Null plane axes in momentum space.*

For a particle with large momentum in the $+z$ direction and limited transverse momentum, p^+ is large and p^- is small. Often one *chooses* the plus axis so that a particle or group of particles of interest have large p^+ and small p^- and p_T.

Using null plane components, the covariant square of p^μ is

$$p^2 = 2p^+p^- - \mathbf{p}_T^2. \tag{21}$$

Thus, for a particle on its mass shell, p^- is

$$p^- = \frac{\mathbf{p}_T^2 + m^2}{2p^+}. \tag{22}$$

Note also that, for a particle on its mass shell,

$$p^+ > 0, \qquad p^- > 0. \tag{23}$$

Integration over the mass shell is

$$(2\pi)^{-3} \int \frac{d^3\vec{p}}{2\sqrt{\vec{p}^2 + m^2}} \cdots = (2\pi)^{-3} \int d^2\mathbf{p}_T \int_0^\infty \frac{dp^+}{2p^+} \cdots . \tag{24}$$

We also use the plus/minus components to describe a space-time point x^μ: $x^\pm = (x^0 \pm x^3)/\sqrt{2}$. In describing a system of particles moving with large momentum in the plus direction, we are invited to think of x^+ as "time." Classically, the particles in our system follow paths nearly parallel to the x^+ axis, evolving slowly as it moves from one $x^+ = const.$ plane to another.

We relate momentum space to position space for a quantum system by Fourier transforming. In doing so, we have a factor $\exp(ip \cdot x)$, which has the form

$$p \cdot x = p^+x^- + p^-x^+ - \mathbf{p}_T \cdot \mathbf{x}_T. \tag{25}$$

Thus x^- is conjugate to p^+, and x^+ is conjugate to p^-. That is a little confusing, but it is simple enough.

2.4 Space-Time Picture of the Singularities

We now return to the singularity structure of $e^+e^- \to q\bar{q}g$. Define $p_1^\mu + p_3^\mu = k^\mu$. Choose null plane coordinates with k^+ large and $\mathbf{k}_T = \mathbf{0}$. Then $k^2 = 2k^+k^-$ becomes small when

$$k^- = \frac{\mathbf{p}_{3,T}^2}{2p_1^+} + \frac{\mathbf{p}_{3,T}^2}{2p_3^+} \tag{26}$$

becomes small. This happens when $\mathbf{p}_{3,T}$ becomes small with fixed p_1^+ and p_3^+, so that the gluon momentum is nearly collinear with the quark momentum. It also happens when $\mathbf{p}_{3,T}$ and p_3^+ both become small with $p_3^+ \propto |\mathbf{p}_{3,T}|$, so that the gluon momentum is soft. (It also happens when the quark becomes soft, but there is a numerator factor that cancels the soft quark singularity.) Thus the singularities for a soft or collinear gluon correspond to small k^-.

Now consider the Fourier transform to coordinate space. The quark propagator in Fig. 6 is

$$S_F(k) = \int dx^+dx^-d\mathbf{x}\, \exp(i[k^+x^- + k^-x^+ - \mathbf{k} \cdot \mathbf{x}])\, S_F(x). \tag{27}$$

When k^+ is large and k^- is small, the contributing values of x have small x^- and large x^+. Thus the propagation of the virtual quark can be pictured in space-time as in Fig. 6. The quark propagates a long distance in the x^+ direction

before decaying into a quark-gluon pair. That is, the singularities that can lead to divergent perturbative cross sections arise from interactions that happen a long time after the creation of the initial quark-antiquark pair.

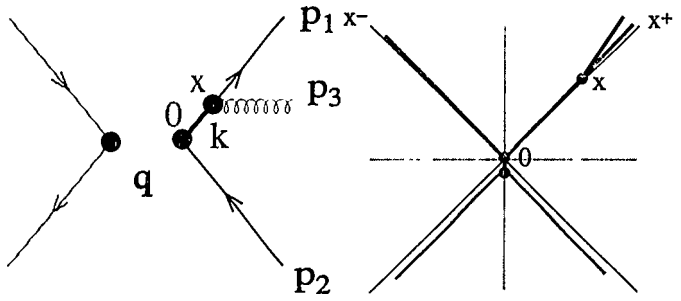


Figure 6: *Correspondence between singularities in momentum space and the development of the system in space-time.*

2.5 Nature of the Long-Time Physics

Imagine dividing the contributions to a scattering cross section into long-time contributions and short-time contributions. In the long-time contributions, perturbation theory is out of control, as indicated in Eq. (19). Nevertheless, the generic structure of the long-time contribution is of great interest. This structure is illustrated in Fig. 7. Perturbative diagrams have big contributions from space-time histories in which partons move in collinear groups and additional partons are soft and communicate over large distances, while carrying small momentum.

The picture of Fig. 7 is suggested by the singularity structure of diagrams at any fixed order of perturbation theory. Of course, there could be nonperturbative effects that would invalidate the picture. Since nonperturbative effects can be invisible in perturbation theory, one cannot claim that the structure of the final state indicated in Fig. 7 is known to be a consequence of QCD. One can point, however, to some cases in which one can go beyond fixed order perturbation theory and sum the most important effects of diagrams of all orders (for example, Ref. 9). In such cases, the general picture suggested by Fig. 7 remains intact.

We thus find that perturbative QCD suggests a certain structure of the final state produced in $e^+e^- \to$ *hadrons*: the final state should consist of jets of nearly

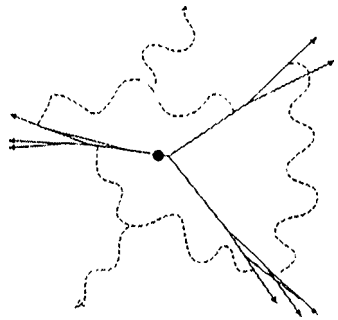


Figure 7: *Typical paths of partons in space contributing to $e^+e^- \to$ hadrons, as suggested by the singularities of perturbative diagrams. Short wavelength fields are represented by classical paths of particles. Long wavelength fields are represented by wavy lines.*

collinear particles plus soft particles moving in random directions. In fact, this qualitative prediction is a qualitative success.

Given some degree of qualitative success, we may be bolder and ask whether perturbative QCD permits quantitative predictions. If we want quantitative predictions, we will somehow have to find things to measure that are not sensitive to interactions that happen long after the basic hard interaction. This is the subject of the next section.

2.6 The Long-Time Problem

We have seen that perturbation theory is not effective for long-time physics. But the detector is a long distance away from the interaction, so it would seem that long-time physics has to be present.

Fortunately, there are some measurements that are *not* sensitive to long-time physics. An example is the total cross section to produce hadrons in e^+e^- annihilation. Here, effects from times $\Delta t \gg 1/\sqrt{s}$ cancel because of unitarity. To see why, note that the quark state is created from the vacuum by a current operator J at some time t; it then develops from time t to time ∞ according to the interaction picture evolution operator $U(\infty, t)$, when it becomes the final state $|N\rangle$. The cross section is proportional to the sum over N of this amplitude times

a similar complex conjugate amplitude with t replaced by a different time t'. We Fourier transform this with $\exp(-i\sqrt{s}\,(t-t'))$, so that we can take $\Delta t \equiv t - t'$ to be of order $1/\sqrt{s}$. Now, replacing $\sum |N\rangle\langle N|$ by the unit operator and using the unitarity of the evolution operators U, we obtain

$$\sum_N \langle 0|J(t')U(t',\infty)|N\rangle\langle N|U(\infty,t)J(t)|0\rangle \qquad (28)$$
$$= \langle 0|J(t')U(t',\infty)U(\infty,t)J(t)|0\rangle = \langle 0|J(t')U(t',t)J(t)|0\rangle.$$

Because of unitarity, the long-time evolution has canceled out of the cross section, and we have only evolution from t to t'.

There are three ways to view this result. First, we have the formal argument given above. Second, we have the intuitive understanding that after the initial quarks and gluons are created in a time Δt of order $1/\sqrt{s}$, *something* will happen with probability 1. Exactly what happens is long-time physics, but we don't care about it since we sum over all the possibilities $|N\rangle$. Third, we can calculate at some finite order of perturbation theory. Then we see infrared infinities at various stages of the calculations, but we find that the infinities cancel between real gluon emission graphs and virtual gluon graphs. An example is shown in Fig. 8.

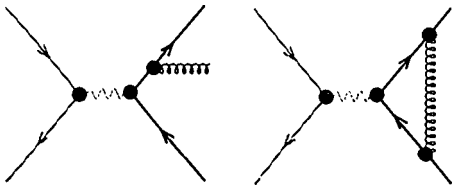


Figure 8: *Cancellation between real and virtual gluon graphs. If we integrate the real gluon graph on the left times the complex conjugate of the similar graph with the gluon attached to the antiquark, we will get an infrared infinity. However, the virtual gluon graph on the right times the complex conjugate of the Born graph is also divergent, as is the Born graph times the complex conjugate of the virtual gluon graph. Adding everything together, the infrared infinities cancel.*

We see that the total cross section is free of sensitivity to long-time physics. If the total cross section were all you could look at, QCD physics would be a little boring. Fortunately, there are other quantities that are not sensitive to infrared effects. They are called infrared safe quantities.

To formulate the concept of infrared safety, consider a measured quantity that is constructed from the cross sections,

$$\frac{d\sigma[n]}{d\Omega_2 dE_3 d\Omega_3 \cdots dE_n d\Omega_n}, \qquad (29)$$

to make n hadrons in e^+e^- annihilation. Here, E_j is the energy of the jth hadron and $\Omega_j = (\theta_j, \phi_j)$ describes its direction. We treat the hadrons as effectively massless and do not distinguish the hadron flavors. Following the notation of Ref. 10, let us specify functions $\mathcal{S}_n$ that describe the measurement we want, so that the measured quantity is

$$\begin{aligned}\mathcal{I} \;=\; & \frac{1}{2!}\int d\Omega_2 \,\frac{d\sigma[2]}{d\Omega_2}\,\mathcal{S}_2(p_1^\mu, p_2^\mu) \\ & + \frac{1}{3!}\int d\Omega_2 dE_3 d\Omega_3 \,\frac{d\sigma[3]}{d\Omega_2 dE_3 d\Omega_3}\,\mathcal{S}_3(p_1^\mu, p_2^\mu, p_3^\mu) \\ & + \frac{1}{4!}\int d\Omega_2 dE_3 d\Omega_3 dE_4 d\Omega_4 \times \frac{d\sigma[4]}{d\Omega_2 dE_3 d\Omega_3 dE_4 d\Omega_4}\mathcal{S}_4(p_1^\mu, p_2^\mu, p_3^\mu, p_4^\mu) \\ & + \cdots. \end{aligned} \qquad (30)$$

The functions $\mathcal{S}$ are symmetric functions of their arguments. In order for our measurement to be infrared safe, we need

$$\mathcal{S}_{n+1}(p_1^\mu, \ldots, (1-\lambda)p_n^\mu, \lambda p_n^\mu) = \mathcal{S}_n(p_1^\mu, \ldots, p_n^\mu) \qquad (31)$$

for $0 \le \lambda \le 1$.

What does this mean? The physical meaning is that the functions $\mathcal{S}_n$ and $\mathcal{S}_{n-1}$ are related in such a way that the cross section is not sensitive to whether or not a mother particle divides into two collinear daughter particles that share its momentum. The cross section is also not sensitive to whether or not a mother particle decays to a daughter particle carrying all of its momentum and a soft daughter particle carrying no momentum. The cross section is also not sensitive to whether or not two collinear particles combine, or a soft particle is absorbed by a fast particle. All of these decay and recombination processes can happen with large probability in the final state long after the hard interaction. But, by construction, they don't matter as long as the sum of the probabilities for something to happen or not to happen is one.

Another version of the physical meaning is that for an IR-safe quantity, a physical event with hadron jets should give approximately the same measurement

as a parton event with each jet replaced by a parton, as illustrated in Fig. 9. To see this, we simply have to delete soft particles and combine collinear particles until three jets have become three particles.

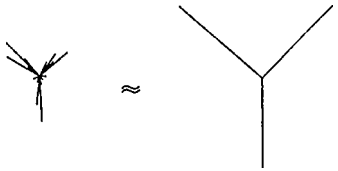


Figure 9: *Infrared safety. In an infrared safe measurement, the three-jet event shown on the left should be (approximately) equivalent to an ideal three-jet event shown on the right.*

In a calculation of the measured quantity $\mathcal{I}$, we simply calculate with partons instead of hadrons in the final state. The calculational meaning of the infrared safety condition is that the infrared infinities cancel. The argument is that the infinities arise from soft and collinear configurations of the partons, that these configurations involve long times, and that the time evolution operator is unitary.

I have started with an abstract formulation of infrared safety. It would be good to have a few examples. The easiest is the total cross section, for which

$$\mathcal{S}_n(p_1^\mu, \ldots, p_n^\mu) = 1. \tag{32}$$

A less trivial example is the thrust distribution. One defines the thrust $\mathcal{T}_n$ of an n particle event as

$$\mathcal{T}_n(p_1^\mu, \ldots, p_n^\mu) = \max_{\vec{u}} \frac{\sum_{i=1}^n |\vec{p}_i \cdot \vec{u}|}{\sum_{i=1}^n |\vec{p}_i|} \ . \tag{33}$$

Here $\vec{u}$ is a unit vector, which we vary to maximize the sum of the absolute values of the projections of $\vec{p}_i$ on $\vec{u}$. Then the thrust distribution $(1/\sigma_{tot})\, d\sigma/dT$ is defined by taking

$$\mathcal{S}_n(p_1^\mu, \ldots, p_n^\mu) = (1/\sigma_{tot})\ \delta(T - \mathcal{T}_n(p_1^\mu, \ldots, p_n^\mu)) \ . \tag{34}$$

It is a simple exercise to show that the thrust of an event is not affected by collinear parton splitting or by zero momentum partons. Therefore, the thrust distribution is infrared safe.

Another infrared safe quantity is the cross sections to make n jets. Here one has to define what one means by a jet. The definitions used in electron-positron annihilation typically involve successively combining particles that are nearly collinear to make the jets. A description can be found in Ref. 11. I discuss jet cross sections for hadron collisions in Sec. 5.4.

A final example is the energy-energy correlation function,[12] which measures the average of the product of the energy in one calorimeter cell times the energy in another calorimeter cell. One looks at this average as a function of the angular separation of the calorimeter cells.

Before leaving this subject, I should mention another way to eliminate sensitivity to long-time physics. Consider the cross section

$$\frac{d\sigma(e^+e^- \to \pi + X)}{dE_\pi}. \tag{35}$$

This cross section can be written as a convolution of two factors, as illustrated in Fig. 10. The first factor is a calculated "hard scattering cross section" for $e^+e^- \to quark + X$ or $e^+e^- \to gluon + X$. The second factor is a "parton decay function" for $quark \to \pi + X$ or $gluon \to \pi + X$. These functions contain the long-time sensitivity and are to be measured, since they cannot be calculated perturbatively. However, once they are measured in one process, they can be used for another process. This final state factorization is similar to the initial state factorization involving parton distribution functions, which we will discuss later. (See Refs. 1, 2, and 13 for more information.)

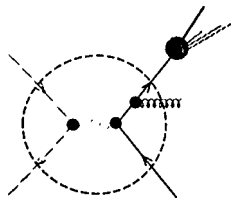


Figure 10: *The cross section for $e^+e^- \to \pi + X$ can be written as a convolution of a short-distance cross section (inside the dotted line) and a parton decay function.*

3 The Smallest Time Scales

In this section, I explore the physics of time scales smaller than $1/\sqrt{s}$. One way of looking at this physics is to say that it is plagued by infinities and we can manage to hide the infinities. A better view is that the short-time physics

contains wonderful truths that we would like to discover—truths about grand unified theories, quantum gravity, and the like. However, quantum field theory is arranged so as to effectively hide the truth from our experimental apparatus, which can probe with a time resolution of only an inverse half TeV.

I first outline what renormalization does to hide the ugly infinities or the beautiful truth. Then I describe how renormalization leads to the running coupling. Because of renormalization, calculated quantities depend on a renormalization scale. I look at how this dependence works and how the scale can be chosen. Finally, I discuss how one can use experiment to look for the hidden physics beyond the Standard Model, taking high E_T jet production in hadron collisions as an example.

3.1 What Renormalization Does

In any Feynman graph, one can insert perturbative corrections to the vertices and the propagation of particles, as illustrated in Fig. 11. The loop integrals in these graphs will get big contributions from momenta much larger than $\sqrt{s}$. That is, there are big contributions from interactions that happen on time scales much smaller than $1/\sqrt{s}$. I have tried to illustrate this in the figure. The virtual vector boson propagates for a time $1/\sqrt{s}$, while the virtual fluctuations that correct the electroweak vertex and the quark propagator occur over a time Δt that can be much smaller than $1/\sqrt{s}$.

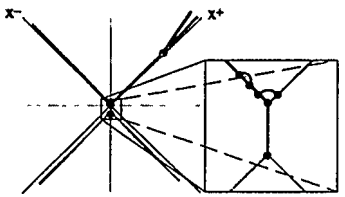


Figure 11: *Renormalization. The effect of the very small time interactions pictured are absorbed into the running coupling.*

Let us pick an ultraviolet cutoff M that is much larger than $\sqrt{s}$, so that we calculate the effect of fluctuations with $1/M < \Delta t$ exactly, up to some order of perturbation theory. What, then, is the effect of virtual fluctuations on smaller time scales, Δt with $\Delta t < 1/M$ but, say, Δt still larger than $t_{\rm Planck}$, where gravity takes over? Let us suppose that we are willing to neglect contributions to the cross section that are of order $\sqrt{s}/M$ or smaller compared to the cross section itself. Then there is a remarkable theorem[14]: the effects of the fluctuations are not particularly small, but they can be absorbed into changes in the couplings of the theory. (There are also changes in the masses of the theory and adjustments to the normalizations of the field operators, but we can concentrate on the effect on the couplings.)

The program of absorbing very short-time physics into a few parameters goes under the name of renormalization. There are several schemes available for renormalizing. Each of them involves the introduction of some scale parameter that is not intrinsic to the theory but tells how we did the renormalization. Let us agree to use $\overline{\rm MS}$ renormalization (see Ref. 14 for details). Then we introduce an $\overline{\rm MS}$ renormalization scale μ. A good (but approximate) way of thinking of μ is that the physics of time scales $\Delta t \ll 1/\mu$ is removed from the perturbative calculation. The effect of the small time physics is accounted for by adjusting the value of the strong coupling, so that its value depends on the scale that we used: $\alpha_s = \alpha_s(\mu)$. (The value of the electromagnetic coupling also depends on μ.)

3.2 The Running Coupling

We account for time scales much smaller than $1/\mu$ by using the running coupling $\alpha_s(\mu)$. That is, a fluctuation such as that illustrated in Fig. 12 can be dropped from a calculation and absorbed into the running coupling that describes the probability for the quark in the figure to emit the gluon. The μ dependence of $\alpha_s(\mu)$ is given by a certain differential equation, called the renormalization group equation (see Ref. 14):

$$\frac{d}{d\ln(\mu^2)}\frac{\alpha_s(\mu)}{\pi} = \beta(\alpha_s(\mu)) = -\beta_0\left(\frac{\alpha_s(\mu)}{\pi}\right)^2 - \beta_1\left(\frac{\alpha_s(\mu)}{\pi}\right)^3 + \cdots . \qquad (36)$$

One calculates the beta function $\beta(\alpha_s)$ perturbatively in QCD. The first coefficient, with the conventions used here, is

$$\beta_0 = (33 - 2N_f)/12 , \qquad (37)$$

where N_f is the number of quark flavors.

Of course, at time scales smaller than a very small cutoff $1/M$ (at the "GUT scale," say), there is completely different physics operating. Therefore, if we use

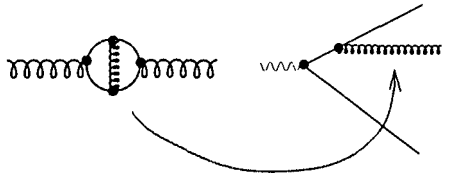


Figure 12: *Short-time fluctuations in the propagation of the gluon field absorbed into the running strong coupling.*

just QCD to adjust the strong coupling, we can say that we are accounting for the physics between times $1/M$ and $1/\mu$ (see Fig. 13). The value of α_s at $\mu_0 \approx M$ is then the boundary condition for the differential equation.

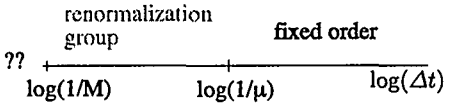


Figure 13: *Distance scales accounted for by explicit fixed order perturbative calculation and by use of the renormalization group.*

The renormalization group equation sums the effects of short-time fluctuations of the fields. To see what one means by "sums" here, consider the result of solving the renormalization group equation with all of the β_i beyond β_0 set to zero:

$$\begin{aligned} \alpha_s(\mu) &\approx \alpha_s(M) - (\beta_0/\pi)\ln(\mu^2/M^2)\ \alpha_s^2(M) \\ &\quad +(\beta_0/\pi)^2\ln^2(\mu^2/M^2)\ \alpha_s^3(M) + \cdots \\ &= \frac{\alpha_s(M)}{1+(\beta_0/\pi)\,\alpha_s(M)\ln(\mu^2/M^2)}. \end{aligned} \tag{38}$$

A series in powers of $\alpha_s(M)$—that is, the strong coupling at the GUT scale—is summed into a simple function of μ. Here $\alpha_s(M)$ appears as a parameter in the solution.

Note a crucial and wonderful fact. The value of $\alpha_s(\mu)$ decreases as μ increases. This is called "asymptotic freedom." Asymptotic freedom implies that QCD acts like a weakly interacting theory on short time scales. It is true that quarks and gluons are strongly bound inside nucleons, but this strong binding is the result of weak forces acting collectively over a long time.

In Eq. (38), we are invited to think of the graph of $\alpha_s(\mu)$ versus μ. The differential equation that determines this graph is characteristic of QCD. There could, however, be different versions of QCD with the same differential equation but different curves, corresponding to different boundary values $\alpha_s(M)$. Thus, the parameter $\alpha_s(M)$ tells us which version of QCD we have. To determine this parameter, we consult experiment. Actually, Eq. (38) is not the most convenient way to write the solution for the running coupling. A better expression is

$$\alpha_s(\mu) \approx \frac{\pi}{\beta_0 \ln(\mu^2/\Lambda^2)}. \tag{39}$$

Here we have replaced $\alpha_s(M)$ by a different (but completely equivalent) parameter Λ. A third form of the running coupling is

$$\alpha_s(\mu) \approx \frac{\alpha_s(M_Z)}{1+(\beta_0/\pi)\,\alpha_s(M_Z)\ln(\mu^2/M_Z^2)}. \tag{40}$$

Here the value of $\alpha_s(\mu)$ at $\mu = M_Z$ labels the version of QCD that is valid in our world.

In any of the three forms of the running coupling, one should revise the equations to account for the second term in the beta function in order to be numerically precise.

3.3 The Choice of Scale

In this section, we consider the choice of the renormalization scale μ in a calculated cross section. Consider, as an example, the cross section for $e^+e^- \to$ *hadrons* via virtual photon decay. Let us write this cross section in the form

$$\sigma_{\rm tot} = \frac{4\pi\alpha^2}{s}\left(\sum_f Q_f^2\right)[1+\Delta]. \tag{41}$$

Here s is the square of the c.m. energy, α is $e^2/(4\pi)$, and Q_f is the electric charge in units of e carried by the quark of flavor f, with $f = u, d, s, c, b$. The nontrivial part of the calculated cross section is the quantity Δ, which contains the effects of the strong interactions. Using $\overline{\rm MS}$ renormalization with scale μ, one finds (after a lot of work) that Δ is given by[15]

$$\Delta = \frac{\alpha_s(\mu)}{\pi} + \left[1.4092 + 1.9167\ \ln\left(\mu^2/s\right)\right]\left(\frac{\alpha_s(\mu)}{\pi}\right)^2 + \left[-12.805 + 7.8186\ \ln\left(\mu^2/s\right) + 3.674\ \ln^2\left(\mu^2/s\right)\right]\left(\frac{\alpha_s(\mu)}{\pi}\right)^3 + \cdots. \tag{42}$$

Here, of course, one should use for $\alpha_s(\mu)$ the solution of the renormalization group Eq. (36) with at least two terms included.

As discussed in the preceding subsection, when we renormalize with scale μ, we are defining what we mean by the strong coupling. Thus, α_s in Eq. (42) depends on μ. The perturbative coefficients in Eq. (42) also depend on μ. On the other hand, the physical cross section does not depend on μ:

$$\frac{d}{d\ln\mu^2}\Delta = 0. \tag{43}$$

That is because μ is just an artifact of how we organize perturbation theory, not a parameter of the underlying theory.

Let us consider Eq. (43) in more detail. Write Δ in the form

$$\Delta \sim \sum_{n=1}^{\infty} c_n(\mu)\ \alpha_s(\mu)^n. \tag{44}$$

If we differentiate not the complete infinite sum but just the first N terms, we get minus the derivative of the sum from $N+1$ to infinity. This remainder is of order α_s^{N+1} as $\alpha_s \to 0$. Thus

$$\frac{d}{d\ln\mu^2}\sum_{n=1}^{N} c_n(\mu)\ \alpha_s(\mu)^n \sim \mathcal{O}(\alpha_s(\mu)^{N+1}). \tag{45}$$

That is, the harder we work calculating more terms, the less the calculated cross section depends on μ.

Since we have not worked infinitely hard, the calculated cross section depends on μ. What choice shall we make for μ? Clearly, $\ln(\mu^2/s)$ should not be big. Otherwise the coefficients $c_n(\mu)$ are large and the "convergence" of perturbation theory will be spoiled. There are some who will argue that one scheme or the other for choosing μ is the "best." You are welcome to follow whichever advisor you want. I will show you below that for a well-behaved quantity like Δ, the precise choice makes little difference, as long as you obey the common sense prescription that $\ln(\mu^2/s)$ not be big.

3.4 An Example

Let us consider a quantitative example of how $\Delta(\mu)$ depends on μ. This will also give us a chance to think about the theoretical error caused by replacing Δ by the sum Δ_n of the first n terms in its perturbative expansion. Of course, we do not know what this error is. All we can do is provide an estimate. (Our discussion will be rather primitive. For a more detailed error estimate for the case of the hadronic width of the Z boson, see Ref. 16.)

Let us think of the error estimate in the spirit of a "1 σ" theoretical error: we would be surprised if $|\Delta_n - \Delta|$ were much less than the error estimate and we would also be surprised if this quantity were much more than the error estimate. Here, one should exercise a little caution. We have no reason to expect that theory errors are Gaussian distributed. Thus a $4\,\sigma$ difference between Δ_n and Δ is not out of the question, while a $4\,\sigma$ fluctuation in a measured quantity with purely statistical, Gaussian errors *is* out of the question.

Take $\alpha_s(M_Z) = 0.117$, $\sqrt{s} = 34$ GeV, five flavors. In Fig. 14, I plot $\Delta(\mu)$ versus p defined by

$$\mu = 2^p\sqrt{s}. \tag{46}$$

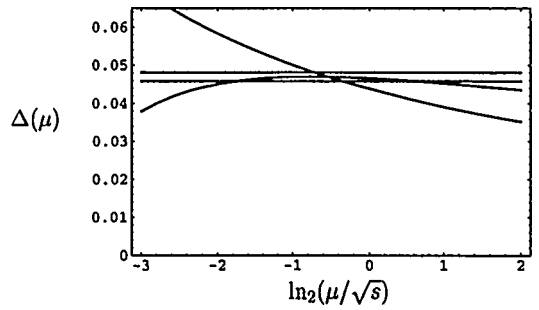


Figure 14: *Dependence of $\Delta(\mu)$ on the $\overline{\rm MS}$ renormalization scale μ. The falling curve is Δ_1. The flatter curve is Δ_2. The horizontal lines indicate the amount of variation of Δ_2 when μ varies by a factor of 2.*

The steeply falling curve is the order α_s^1 approximation to $\Delta(\mu)$, $\Delta_1(\mu) = \alpha_s(\mu)/\pi$. Notice that if we change μ by a factor of two, $\Delta_1(\mu)$ changes by about 0.006. If we

had no other information than this, we might pick $\Delta_1(\sqrt{s}) \approx 0.044$ as the "best" value and assign a ± 0.006 error to this value. (There is no special magic to the use of a factor of two here. The reader can pick any factor that seems reasonable.)

Another error estimate can be based on the simple expectation that the coefficients of α_s^n are of order of one for the first few terms. (Eventually, they will grow like $n!$ Reference 16 takes this into account, but we ignore it here.) Then the first omitted term should be of order of $\pm 1 \times \alpha_s^2 \approx \pm 0.020$ using $\alpha_s(34 \text{ GeV}) \approx 0.14$. Since this is bigger than the previous ± 0.006 error estimate, we keep this larger estimate: $\Delta \approx 0.044 \pm 0.020$.

Returning now to Fig. 14, the second curve is the order α_s^2 approximation, $\Delta_2(\mu)$. Note that $\Delta_2(\mu)$ is less dependent on μ than $\Delta_1(\mu)$.

What value would we now take as our best estimate of Δ? One idea is to choose the value of μ at which $\Delta_2(\mu)$ is least sensitive to μ. This idea is called the *principle of minimal sensitivity*[17]:

$$\Delta_{PMS} = \Delta(\mu_{PMS}), \qquad \left[\frac{d\Delta(\mu)}{d\ln\mu}\right]_{\mu=\mu_{PMS}} = 0. \tag{47}$$

This prescription gives $\Delta \approx 0.0470$. Note that this is about 0.003 away from our previous estimate, $\Delta \approx 0.0440$. Thus our previous error estimate of 0.020 was too big, and we should be surprised that the result changed so little. We can make a new error estimate by noting that $\Delta_2(\mu)$ varies by about 0.0012 when μ changes by a factor of two from μ_{PMS}. Thus, we might estimate that $\Delta \approx 0.0470$ with an error of ± 0.0012. This estimate is represented by the two horizontal lines in Fig. 14.

An alternative error estimate can be based on the next term being of order of $\pm 1 \times \alpha_s^3$ (34 GeV) ≈ 0.003. Since this is bigger than the previous ± 0.0012 error estimate, we keep this larger estimate: $\Delta \approx 0.0470 \pm 0.003$.

I should emphasize that there are other ways to pick the "best" value for Δ. For instance, one can use the BLM method,[18] which is based on choosing the μ that sets to zero the coefficient of the number of quark flavors in $\Delta_2(\mu)$. Since the graph of $\Delta_2(\mu)$ is quite flat, it makes very little difference which method one uses.

Now let us look at $\Delta(\mu)$ evaluated at order α_s^3, $\Delta_3(\mu)$. Here we make use of the full formula in Eq. (42). In Fig. 15, I plot $\Delta_3(\mu)$ along with $\Delta_2(\mu)$ and $\Delta_1(\mu)$. The variation of $\Delta_3(\mu)$ with μ is smaller than that of $\Delta_2(\mu)$. The improvement is not overwhelming, but is apparent particularly at small μ.

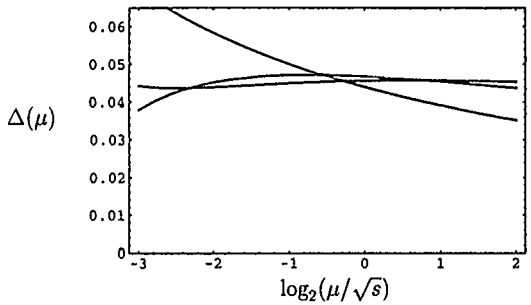


Figure 15: *Dependence of $\Delta(\mu)$ on the $\overline{\text{MS}}$ renormalization scale μ. The falling curve is Δ_1. The flatter curve is Δ_2. The still flatter curve is Δ_3.*

It is a little difficult to see what is happening in Fig. 15, so I show the same thing with an expanded scale in Fig. 16. (Here the error band based on the μ dependence of Δ_2 is also indicated. Recall that we decided that this error band was an underestimate.) The curve for $\Delta_3(\mu)$ has zero derivative at two places. The corresponding values are $\Delta \approx 0.0436$ and $\Delta \approx 0.0456$. If I take the best value of Δ to be the average of these two values and the error to be half the difference, I get $\Delta \approx 0.0446 \pm 0.0010$. The alternative error estimate is $\pm 1 \times \alpha_s^4$ (34 GeV) ≈ 0.0004. We keep the larger error estimate of ± 0.0010.

Was the previous error estimate valid? We guessed $\Delta \approx 0.0470 \pm 0.003$. Our new best estimate is 0.0446. The difference is 0.0024, which is in line with our previous error estimate. Had we used the error estimate ± 0.0012 based on the μ dependence, we would have underestimated the difference, although we would not have been too far off.

3.5 Beyond the Standard Model

We have seen how the renormalization group enables us to account for QCD physics at time scales much smaller than $\sqrt{s}$, as indicated in Fig. 17. However, at some scale $\Delta t \sim 1/M$, we run into the unknown!

How can we see the unknown in current experiments? First, the unknown physics affects α_s, α_{em}, $\sin^2(\theta_W)$. Second, the unknown physics affects masses of $u, d, \ldots, e, \mu, \ldots$. That is, the unknown physics (presumably) determines the

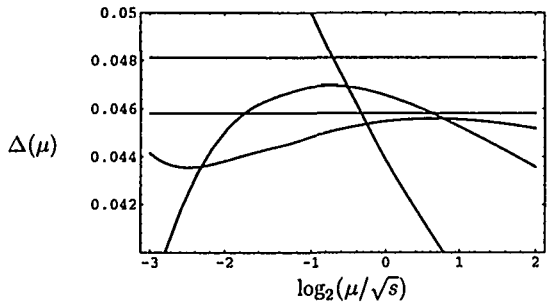


Figure 16: *Dependence of $\Delta(\mu)$ on the $\overline{\rm MS}$ renormalization scale μ with an expanded scale. The falling curve is Δ_1. The flatter curve is Δ_2. The still flatter curve is Δ_3. The horizontal lines represent the variation of Δ_2 when μ varies by a factor two.*

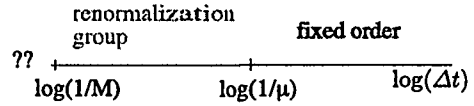


Figure 17: *Time scales accounted for by fixed order perturbative calculations and by use of the renormalization group.*

parameters of the Standard Model. These parameters have been well-measured. Thus, a Nobel prize awaits the physicist who figures out how to use a model for the unknown physics to predict these parameters.

There is another way that as yet unknown physics can affect current experiments. Suppose that quarks can scatter by the exchange of some new particle with a heavy mass M, as illustrated in Fig. 18, and suppose that this mass is not too enormous, only a few TeV. Perhaps the new particle isn't a particle at all, but is a pair of constituents that live inside of quarks. As mentioned above, this physics affects the parameters of the Standard Model. However, unless we can predict the parameters of the Standard Model, this effect does not help us. There is, however, another possible clue. The physics at the TeV scale can introduce new terms into the Lagrangian that we can investigate in current experiments.

In the second diagram in Fig. 18, the two vertices are never at a separation in time greater than $1/M$, so that our low-energy probes cannot resolve the details of the structure. As long as we stick to low-energy probes, $\sqrt{s} \ll M$, the effect of the new physics can be summarized by adding new terms to the Lagrangian of QCD. A typical term might be

$$\Delta\mathcal{L} = \frac{\tilde{g}^2}{M^2}\ \bar{\psi}\gamma^\mu\psi\ \bar{\psi}\gamma_\mu\psi. \tag{48}$$

There is a factor $\tilde{g}^2$ that represents how well the new physics couples to quarks. The most important factor is the factor $1/M^2$. This factor must be there: the product of field operators has dimension 6 and the Lagrangian has dimension 4, so there must be a factor with dimension -2. Taking this argument one step further, the product of field operators in $\Delta\mathcal{L}$ must have a dimension greater than 4 because any product of field operators having dimension equal to or less than 4 that respects the symmetries of the Standard Model is already included in the Lagrangian of the Standard Model.

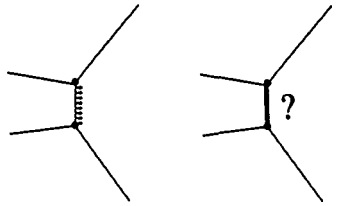


Figure 18: *New physics at a TeV scale. In the first diagram, quarks scatter by gluon exchange. In the second diagram, the quarks exchange a new object with a TeV mass, or perhaps exchange some of the constituents out of which quarks are made.*

3.6 Looking for New Terms in the Effective Lagrangian

How can one detect the presence in the Lagrangian of a term like that in Eq. (48)? These terms are small. Therefore we need either a high-precision experiment, or an experiment that looks for some effect that is forbidden in the Standard Model, or an experiment that has moderate precision and operates at energies that are as high as possible.

Let us consider an example of the last of these possibilities, $p + \bar{p} \to jet + X$ as a function of the transverse energy ($\sim P_T$) of the jet. The new term in the

Lagrangian should add a little bit to the observed cross section that is not included in the standard QCD theory. When the transverse energy E_T of the jet is small compared to M, we expect

$$\frac{\text{Data} - \text{Theory}}{\text{Theory}} \propto \tilde{g}^2 \frac{E_T^2}{M^2}. \tag{49}$$

Here the factor $\tilde{g}^2/M^2$ follows because $\Delta\mathcal{L}$ contains this factor. The factor E_T^2 follows because the left-hand side is dimensionless and E_T is the only factor with dimension of mass that is available.

In Fig. 19, I show a plot comparing experimental jet cross sections from CDF[20] and DØ (Ref. 21) compared to next-to-leading order QCD theory. The theory works fine for $E_T < 200$ GeV, but for 200 GeV $< E_T$, there appears to be a systematic deviation of just the form anticipated in Eq. (49).

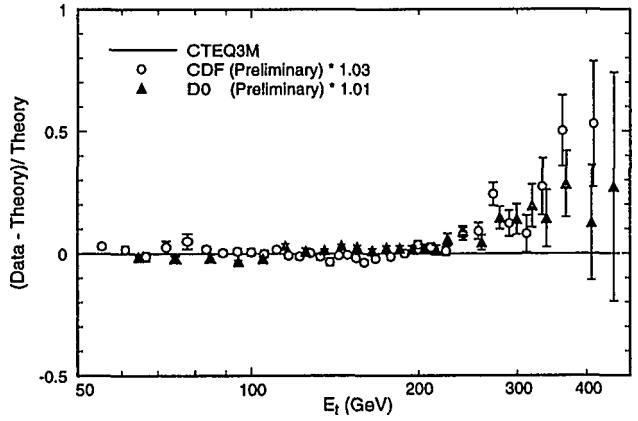


Figure 19: *Jet cross sections from CDF and DØ compared to QCD theory. (Data–Theory)/Theory is plotted versus the transverse energy E_T of the jet. The theory here is next-to-leading order QCD using the CTEQ3M parton distribution. Source: Ref. 19.*

This example illustrates the idea of how small distance physics beyond the Standard Model can leave a trace in the form of small additional terms in the effective Lagrangian that controls physics at currently available energies. However, in this case, there is some indication that the observed effect might be explained by some combination of the experimental systematic error and the uncertainties inherent in the theoretical prediction.[22] In particular, the prediction is sensitive to the distributions of quarks and gluons contained in the colliding protons, and the gluon distribution in the kinematic range of interest here is rather poorly known. In the next section, we turn to the definition, use, and measurement of the distributions of quarks and gluons in hadrons.

4 Deeply Inelastic Scattering

Until now, I have concentrated on hard scattering processes with leptons in the initial state. For such processes, we have seen that the hard part of the process can be described using perturbation theory because $\alpha_s(\mu)$ gets small as μ gets large. Furthermore, we have seen how to isolate the hard part of the interaction by choosing an infrared safe observable. But what about hard processes in which there are hadrons in the initial state? Since the fundamental hard interactions involve quarks and gluons, the theoretical description necessarily involves a description of how the quarks and gluons are distributed in a hadron. Unfortunately, the distribution of quarks and gluons in a hadron is controlled by long-time physics. We cannot calculate the relevant distribution functions perturbatively (although a calculation in lattice QCD might give them, in principle). Thus, we must find how to separate the short-time physics from the parton distribution functions, and we must learn how the parton distribution functions can be determined from the experimental measurements.

In this section, I discuss parton distribution functions and their role in deeply inelastic lepton scattering (DIS). This includes $e + p \to e + X$ and $\nu + p \to e + X$ where the momentum transfer from the lepton is large. I first outline the kinematics of deeply inelastic scattering and define the structure functions F_1, F_2, and F_3 used to describe the process. By examining the space-time structure of DIS, we will see how the cross section can be written as a convolution of two factors, one of which is the parton distribution functions and the other of which is a cross section for the lepton to scatter from a quark or gluon. This factorization involves a scale μ_F that, roughly speaking, divides the soft from the hard regime; I discuss the dependence of the calculated cross section on μ_F. With this groundwork laid, I give the $\overline{\text{MS}}$ definition of parton distribution functions in terms of field operators and discuss the evolution equation for the parton distributions. I close the section

with some comments on how the parton distributions are, in practice, determined from experiment.

4.1 Kinematics of Deeply Inelastic Lepton Scattering

In deeply inelastic scattering, a lepton with momentum k^μ scatters on a hadron with momentum p^μ. In the final state, one observes the scattered lepton with momentum k'^μ as illustrated in Fig. 20. The momentum transfer

$$q^\mu = k^\mu - k'^\mu \tag{50}$$

is carried on a photon, or a W or Z boson.

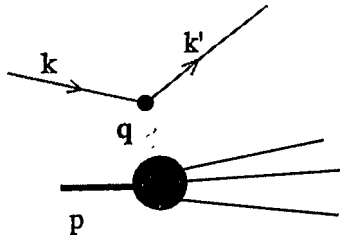


Figure 20: *Kinematics of deeply inelastic scattering.*

The interaction between the vector boson and the hadron depends on the variables q^μ and p^μ. From these two vectors, we can build two scalars (not counting $m^2 = p^2$). The first variable is

$$Q^2 = -q^2, \tag{51}$$

where the minus sign is included so that Q^2 is positive. The second scalar is the dimensionless Bjorken variable,

$$x_{\rm bj} = \frac{Q^2}{2p\cdot q}. \tag{52}$$

[In the case of scattering from a nucleus containing A nucleons, one replaces p^μ by p^μ/A and defines $x_{\rm bj} = A\,Q^2/(2p\cdot q)$.]

One calls the scattering *deeply inelastic* if Q^2 is large compared to 1 GeV^2. Traditionally, one speaks of the *scaling limit*, $Q^2 \to \infty$ with $x_{\rm bj}$ fixed. Actually, the asymptotic theory to be described below works pretty well if Q^2 is bigger than, say, 4 GeV^2 and $x_{\rm bj}$ is anywhere in the experimentally accessible range, roughly $10^{-4} < x_{\rm bj} < 0.5$.

The invariant mass squared of the hadronic final state is $W^2 = (p+q)^2$. In the scaling regime of large Q^2, one has

$$W^2 = m^2 + \frac{1-x_{\rm bj}}{x_{\rm bj}}\,Q^2 \gg m^2. \tag{53}$$

This justifies saying that the scattering is not only inelastic but deeply inelastic.

We have spoken of the scalar variables that one can form from p^μ and q^μ. Using the lepton momentum k^μ, one can also form the dimensionless variable

$$y = \frac{p\cdot q}{p\cdot k}. \tag{54}$$

4.2 Structure Functions for DIS

One can make quite a lot of progress in understanding the theory of deeply inelastic scattering without knowing anything about QCD except its symmetries. One expresses the cross section in terms of three structure functions, which are functions of $x_{\rm bj}$ and Q^2 only.

Suppose that the initial lepton is a neutrino, ν_μ, and the final lepton is a muon. Then in Fig. 20, the exchanged vector boson, call it V, is a W boson, with mass $M_V = M_W$. Alternatively, suppose that both the initial and final leptons are electrons and let the exchanged vector boson be a photon, with mass $M_V = 0$. This was the situation in the original DIS experiments at SLAC in the late 1960s. In experiments with sufficiently large Q^2, Z boson exchange should be considered along with photon exchange, and the formalism described below must be augmented.

Given only the electroweak theory to tell us how the vector boson couples to the lepton, one can write the cross section in the form

$$d\sigma = \frac{4\alpha^2}{s}\frac{d^3{\rm k}'}{2|{\rm k}'|}\frac{C_V}{(q^2-M_V^2)^2}\,L^{\mu\nu}(k,q)\,W_{\mu\nu}(p,q), \tag{55}$$

where C_V is 1 in the case that V is a photon and $1/(64\,\sin^4\theta_W)$ in the case that V is a W boson. The tensor $L^{\mu\nu}$ describes the lepton coupling to the vector boson and has the form

$$L^{\mu\nu} = \frac{1}{2}{\rm Tr}\,(k\cdot\gamma\;\gamma^\mu k'\cdot\gamma\;\gamma^\nu) \tag{56}$$

in the case that V is a photon. For a W boson, one has

$$L^{\mu\nu} = \mathrm{Tr}\,(k\cdot\gamma\,\Gamma^{\mu}k'\cdot\gamma\,\Gamma^{\nu})\,, \tag{57}$$

where Γ^{μ} is $\gamma^{\mu}(1-\gamma_5)$ for a W^+ boson ($\nu\to W^+\ell$) or $\gamma^{\mu}(1+\gamma_5)$ for a W^- boson ($\bar{\nu}\to W^-\bar{\ell}$). See Ref. 1.

The tensor $W^{\mu\nu}$ describes the coupling of the vector boson to the hadronic system. It depends on p^{μ} and q^{μ}. We know that it is Lorentz invariant and that $W^{\nu\mu} = W^{\mu\nu *}$. We also know that the current to which the vector boson couples is conserved (or in the case of the axial current, conserved in the absence of quark masses, which we neglect here) so that $q_{\mu}W^{\mu\nu} = 0$. Using these properties, one finds three possible tensor structures for $W^{\mu\nu}$. Each of the three tensors multiplies a structure function, F_1, F_2, or F_3, which, since it is a Lorentz scalar, can depend only on the invariants $x_{\rm bj}$ and Q^2. Thus

$$\begin{aligned} W_{\mu\nu} &= -\left(g_{\mu\nu}-\frac{q_{\mu}q_{\nu}}{q^2}\right)F_1(x_{\rm bj},Q^2) \\ &\quad +\left(p_{\mu}-q_{\mu}\frac{p\cdot q}{q^2}\right)\left(p_{\nu}-q_{\nu}\frac{p\cdot q}{q^2}\right)\frac{1}{p\cdot q}\,F_2(x_{\rm bj},Q^2) \\ &\quad -i\epsilon_{\mu\nu\lambda\sigma}p^{\lambda}q^{\sigma}\frac{1}{p\cdot q}\,F_3(x_{\rm bj},Q^2). \end{aligned} \tag{58}$$

If we combine Eqs. (55–58), we can write the cross section for deeply inelastic scattering in terms of the three structure functions. Neglecting the hadron mass compared to Q^2, the result is

$$\frac{d\sigma}{dx_{\rm bj}\,dy} = \tilde{N}(Q^2)\left[yF_1+\frac{1-y}{x_{\rm bj}y}F_2+\delta_V\,(1-\frac{y}{2})F_3\right]. \tag{59}$$

Here the normalization factor $\tilde{N}$ and the factor δ_V multiplying F_3 are

$$\begin{aligned} \tilde{N} &= \frac{4\pi\alpha^2}{Q^2}, && \delta_V = 0, \quad e^-+h\to e^-+X, \\ \tilde{N} &= \frac{\pi\alpha^2Q^2}{4\sin^4(\theta_W)\,(Q^2+M_W)^2}, && \delta_V = 1, \quad \nu+h\to\mu^-+X, \\ \tilde{N} &= \frac{\pi\alpha^2Q^2}{4\sin^4(\theta_W)\,(Q^2+M_W)^2}, && \delta_V = -1, \quad \bar{\nu}+h\to\mu^++X. \end{aligned} \tag{60}$$

In principle, one can use the y dependence to determine all three of F_1, F_2, F_3 in a deeply inelastic scattering experiment.

4.3 Space-Time Structure of DIS

So far, we have used the symmetries of QCD in order to write the cross section for deeply inelastic scattering in terms of three structure functions, but we have not used any other dynamical properties of the theory. Now we turn to the question of how the scattering develops in space and time.

For this purpose, we define a convenient reference frame, which is illustrated in Fig. 21. Denoting components of vectors v^{μ} by $(v^+, v^-, \mathbf{v}_T)$, we chose the frame in which

$$(q^+, q^-, \mathbf{q}) = \frac{1}{\sqrt{2}}\,(-Q, Q, 0). \tag{61}$$

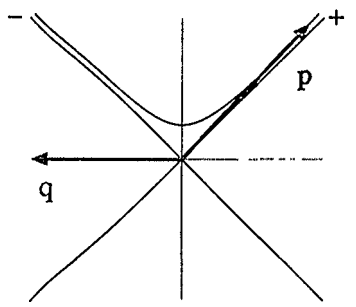


Figure 21: *Reference frame for the analysis of deeply inelastic scattering.*

We also demand that the transverse components of the hadron momentum be zero in our frame. Then

$$(p^+, p^-, \mathbf{p}) \approx \frac{1}{\sqrt{2}}\,(\frac{Q}{x_{\rm bj}}, \frac{x_{\rm bj}m_h^2}{Q}, 0). \tag{62}$$

Notice that in the chosen reference frame, the hadron momentum is big and the momentum transfer is big.

Consider the interactions among the quarks and gluons inside a hadron, using x^+ in the role of "time" as in Sec. 2.3. For a hadron at rest, these interactions happen in a typical time scale $\Delta x^+ \sim 1/m$, where $m \sim 300$ MeV. A hadron that will participate in a deeply inelastic scattering event has a large momentum, $p^+ \sim Q$, in the reference frame that we are using. The Lorentz transformation from the rest frame spreads out interactions by a factor Q/m, so that

$$\Delta x^+ \sim \frac{1}{m}\times\frac{Q}{m} = \frac{Q}{m^2}. \tag{63}$$

This is illustrated in Fig. 22.

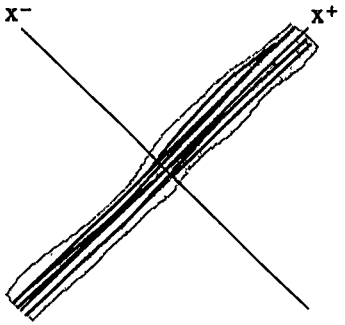


Figure 22: *Interactions within a fast moving hadron. The lines represent world lines of quarks and gluons. The interaction points are spread out in x^+ and pushed together in x^-.*

I offer two caveats here. First, I am treating $x_{\rm bj}$ as being of order of one. To treat small $x_{\rm bj}$ physics, one needs to put back the factors of $x_{\rm bj}$, and the picture changes rather dramatically. Second, the interactions among the quarks and gluons in a hadron at rest can take place on time scales Δx^+ that are much smaller than $1/m$, as we discussed in Sec. 3. We will discuss this later on, but for now we start with the simplest picture.

What happens when the fast moving hadron meets the virtual photon? The interaction with the photon carrying momentum $q^- \sim Q$ is localized to within

$$\Delta x^+ \sim 1/Q. \tag{64}$$

During this short time interval, the quarks and gluons in the proton are effectively free, since their typical interaction times are comparatively much longer (see Fig. 23).

We thus have the following picture. At the moment x^+ of the interaction, the hadron effectively consists of a collection of quarks and gluons (*partons*) that have momenta $(p_i^+, \mathbf{p}_i)$. We can treat the partons as being free. The p_i^+ are large, and it is convenient to describe them using momentum fractions ξ_i:

$$\xi_i = p_i^+/p^+, \qquad 0 < \xi_i < 1. \tag{65}$$

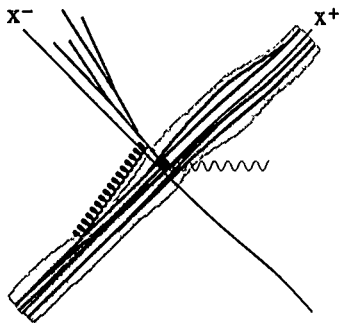


Figure 23: *The virtual photon meets the fast moving hadron. One of the partons is annihilated and recreated as a parton with a large minus component of momentum. This parton develops into a jet of particles.*

(This is convenient because the ξ_i are invariant under boosts along the z axis.) The transverse momenta of the partons, $\mathbf{p}_i$, are small compared to Q and can be neglected in the kinematics of the γ-parton interaction. The "on-shell" or "kinetic" minus momenta of the partons, $p_i^- = \mathbf{p}_i^2/(2p_i^+)$, are also very small compared to Q and can be neglected in the kinematics of the γ-parton interaction. We can think of the partonic state as being described by a wave function

$$\psi(p_1^+, \mathbf{p}_1; p_2^+, \mathbf{p}_2; \cdots), \tag{66}$$

where indices specifying spin and flavor quantum numbers have been suppressed.

This approximate picture is represented in Feynman diagram language in Fig. 24. The larger filled circle represents the hadron wave function ψ. The smaller filled circle represents a sum of subdiagrams in which the particles have virtualities of order Q^2. All of these interactions are effectively instantaneous on the time scale of the intra-hadron interactions that form the wave function. The approximate picture also leads to an intuitive formula that relates the observed cross section to the cross section for γ-parton scattering:

$$\frac{d\sigma}{dE'\,d\omega'} \sim \int_0^1 d\xi \sum_a f_{a/h}(\xi,\mu)\, \frac{d\hat{\sigma}_a(\mu)}{dE'\,d\omega'} + \mathcal{O}(m/Q). \tag{67}$$

In Eq. (67), the function f is a parton distribution function: $f_{a/h}(\xi,\mu)\,d\xi$ gives probability to find a parton with flavor $a = g, u, \bar{u}, d, \ldots$, in hadron h, carrying

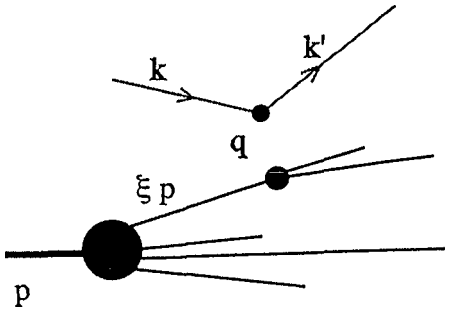


Figure 24: *Feynman diagram for deeply inelastic scattering.*

momentum fraction within $d\xi$ of $\xi = p_i^+/p^+$. If we knew the wave functions ψ, we would form f by summing over the number n of unobserved partons, integrating $|\psi_n|^2$ over the momenta of the unobserved partons, and also integrating over the transverse momentum of the observed parton.

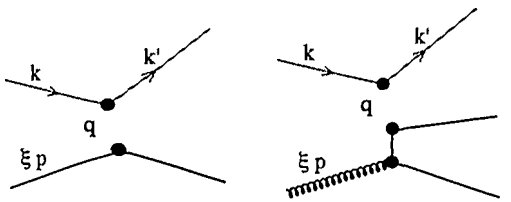
The second factor in Eq. (67), $d\hat{\sigma}_a/dE'\,d\omega'$, is the cross section for scattering the lepton from the parton of flavor a and momentum fraction ξ.

I have indicated a dependence on a factorization scale μ in both factors of Eq. (67). This dependence arises from the existence of virtual processes among the partons that take place on a time scale much shorter than the nominal $\Delta x^+ \sim Q/m^2$. I will discuss this dependence in some detail shortly.

4.4 The Hard Scattering Cross Section

The parton distribution functions in Eq. (67) are derived from experiment. The hard scattering cross sections $d\hat{\sigma}_a(\mu)/dE'\,d\omega'$ are calculated in perturbation theory, using diagrams like those shown in Fig. 25. The diagram on the left is the lowest order diagram. The diagram on the right is one of several that contributes to $d\hat{\sigma}$ at order α_s; in this diagram, the parton a is a gluon.

One can understand a lot about deeply inelastic scattering from Fig. 26, which illustrates the kinematics of the lowest order diagram. Recall that in the reference frame that we are using, the virtual vector boson has zero transverse momentum. The incoming parton has momentum along the plus axis. After the scattering, the parton momentum must be on the cone $k_\mu k^\mu = 0$, so the only possibility is



Lowest order. Higher order.

Figure 25: *Some Feynman diagrams for the hard scattering part of deeply inelastic scattering.*

that its minus momentum is nonzero and its plus momentum vanishes. That is

$$\xi p^+ + q^+ = 0. \tag{68}$$

Since $p^+ = Q/(x_{\rm bj}\sqrt{2})$ while $q^+ = -Q/\sqrt{2}$, this implies

$$\xi = x_{\rm bj}. \tag{69}$$

The consequence of this is that the lowest order contribution to $d\hat{\sigma}$ in Eq. (67) contains a delta function that sets ξ to $x_{\rm bj}$. Thus deeply inelastic scattering at a given value of $x_{\rm bj}$ provides a determination of the parton distribution functions at momentum fraction ξ equal to $x_{\rm bj}$, as long as one works only to leading order. In fact, because of this close relationship, there is some tendency to confuse the structure functions $F_n(x_{\rm bj}, Q^2)$ with the parton distribution functions $f_{a,h}(\xi,\mu)$. I will try to keep these concepts separate: the structure functions F_n are something that one measures directly in deeply inelastic scattering; the parton distribution functions are determined rather indirectly from experiments like deeply inelastic scattering, using formulas that are correct only up to some finite order in α_s.

4.5 Factorization for the Structure Functions

We will look at DIS in a little detail since it is so important. Our object is to derive a formula relating the measured structure functions to structure functions calculated at the parton level. Then we will look at the parton level calculation at lowest order.

Start with Eq. (67), representing Fig. 24. We change variables in this equation from (E', ω') to $(x_{\rm bj}, y)$. We relate $x_{\rm bj}$ to the momentum fraction ξ and a new

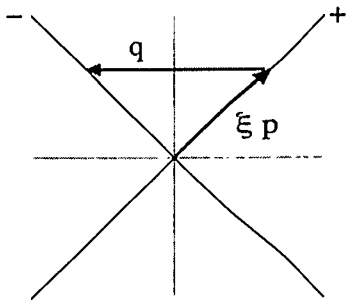


Figure 26: *Kinematics of lowest order diagram.*

variable $\hat{x}$ that is just $x_{\rm bj}$ with the proton momentum p^μ replaced by the parton momentum ξp^μ:

$$x_{\rm bj} = \frac{Q^2}{2p\cdot q} = \xi\,\frac{Q^2}{2\xi p\cdot q} = \xi\hat{x}. \tag{70}$$

That is, $\hat{x}$ is the parton level version of $x_{\rm bj}$. The variable y is identical to the parton level version of y because p^μ appears in both the numerator and denominator:

$$y = \frac{p\cdot q}{p\cdot k} = \frac{\xi p\cdot q}{\xi p\cdot k}. \tag{71}$$

Thus Eq. (67) becomes

$$\frac{d\sigma}{dx_{\rm bj}\,dy} \sim \int_0^1 d\xi \sum_a f_{a/h}(\xi)\,\frac{1}{\xi}\left[\frac{d\hat{\sigma}_a}{d\hat{x}\,dy}\right]_{\hat{x}=x_{\rm bj}/\xi} + \mathcal{O}(m/Q). \tag{72}$$

Now recall that, for γ exchange, $d\sigma/(dx_{\rm bj}dy)$ is related to the structure functions by Eq. (59):

$$\frac{d\sigma}{dx_{\rm bj}\,dy} = \tilde{N}(Q^2)\left[y\,F_1(x_{\rm bj},Q^2) + \frac{1-y}{x_{\rm bj}\,y}\,F_2(x_{\rm bj},Q^2)\right] + \mathcal{O}(m/Q). \tag{73}$$

We define structure functions $\hat{F}_n$ for partons in the same way:

$$\frac{d\hat{\sigma}_a}{d\hat{x}\,dy} = \tilde{N}(Q^2)\left[y\,\hat{F}_1^a(x_{\rm bj}/\xi,Q^2) + \frac{1-y}{(x_{\rm bj}/\xi)y}\,\hat{F}_2^a(x_{\rm bj}/\xi,Q^2)\right]. \tag{74}$$

We insert Eq. (74) into Eq. (72) and compare to Eq. (73). We deduce that the structure functions can be factored as

$$F_1(x_{\rm bj},Q^2) \sim \int_0^1 d\xi \sum_a f_{a/h}(\xi)\,\frac{1}{\xi}\hat{F}_1^a(x_{\rm bj}/\xi,Q^2) + \mathcal{O}(m/Q), \tag{75}$$

$$F_2(x_{\rm bj},Q^2) \sim \int_0^1 d\xi \sum_a f_{a/h}(\xi)\;\hat{F}_2^a(x_{\rm bj}/\xi,Q^2) + \mathcal{O}(m/Q). \tag{76}$$

A simple calculation gives $\hat{F}_1$ and $\hat{F}_2$ at lowest order:

$$\hat{F}_1^a(x_{\rm bj}/\xi,Q^2) = \frac{1}{2}Q_a^2\;\delta(x_{\rm bj}/\xi - 1) + \mathcal{O}(\alpha_s), \tag{77}$$

$$\hat{F}_2^a(x_{\rm bj}/\xi,Q^2) = Q_a^2\;\delta(x_{\rm bj}/\xi - 1) + \mathcal{O}(\alpha_s). \tag{78}$$

Inserting these results into Eqs. (75) and (76), we obtain the lowest order relation between the structure functions and the parton distribution functions:

$$F_1(x_{\rm bj},Q^2) \sim \frac{1}{2}\sum_a Q_a^2\;f_{a/h}(x_{\rm bj}) + \mathcal{O}(\alpha_s) + \mathcal{O}(m/Q), \tag{79}$$

$$F_2(x_{\rm bj},Q^2) \sim \sum_a Q_a^2\;x_{\rm bj}\,f_{a/h}(x_{\rm bj}) + \mathcal{O}(\alpha_s) + \mathcal{O}(m/Q). \tag{80}$$

The factor $1/2$ between $x_{\rm bj}F_1$ and F_2 follows from the Feynman diagrams for spin $1/2$ quarks.

4.6 μ_F Dependence

I have so far presented a rather simplified picture of deeply inelastic scattering in which the hard scattering takes place on a time scale $\Delta x^+ \sim 1/Q$, while the internal dynamics of the proton take place on a much longer time scale $\Delta x^+ \sim Q/m^2$. What happens when one actually computes Feynman diagrams and looks at what time scales contribute? Consider the graph shown in Fig. 27. One finds that the transverse momenta k range from order m to order Q, corresponding to energy scales $k^- = \mathrm{k}^2/2k^+$ between $k^- \sim m^2/Q$ and $k^- = Q^2/Q \sim Q$, or time scales $1/Q \lesssim \Delta x^+ \lesssim Q/m^2$.

The property of factorization for the cross section of deeply inelastic scattering, embodied in Eq. (67), is established by showing that the perturbative expansion can be rearranged so that the contributions from long time scales appear in the parton distribution functions, while the contributions from short time scales appear in the hard scattering functions. (See Ref. 23 for more information.) Thus, in Fig. 27, a gluon emission with $\mathrm{k}^2 \sim m^2$ is part of $f(\xi)$, while a gluon emission with $\mathrm{k}^2 \sim Q^2$ is part of $d\hat{\sigma}$.

Breaking up the cross section into factors associated with short and long time scales requires the introduction of a *factorization scale*, μ_F. When calculating the diagram in Fig. 27, one integrates over k. Roughly speaking, one counts

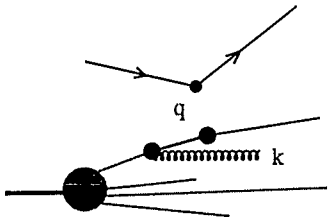


Figure 27: *Deeply inelastic scattering with a gluon emission.*

the contribution from $k^2 < \mu_F^2$ as part of the higher order contribution to $\phi(\xi)$, convoluted with the lowest order hard scattering function $d\hat{\sigma}$ for deeply inelastic scattering from a quark. The contribution from $\mu_F^2 < k^2$ then counts as part of the higher order contribution to $d\hat{\sigma}$ convoluted with an uncorrected parton distribution. This is illustrated in Fig. 28. (In real calculations, the split is accomplished with the aid of dimensional regularization, and is a little more subtle than a simple division of the integral into two parts.)

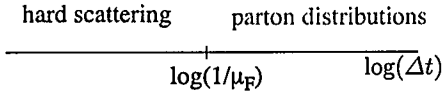


Figure 28: *Distance scales in factorization.*

A consequence of this is that both $d\hat{\sigma}_a(\mu_F)/dE'\,d\omega'$ and $f_{a/h}(\xi,\mu_F)$ depend on μ_F. Thus we have two scales, the factorization scale μ_F in $f_{f/h}(\xi,\mu_F)$ and the renormalization scale μ in $\alpha_s(\mu)$. As with μ, the cross section does not depend on μ_F. Thus there is an equation $d(\textit{cross section})/d\mu_F = 0$ that is satisfied to the accuracy of the perturbative calculation used. If you work harder and calculate to higher order, then the dependence on μ_F is less.

Often one sets $\mu_F = \mu$ in applied calculations. In fact, it is rather common in applications to deeply inelastic scattering to set $\mu_F = \mu = Q$.

4.7 Contour Graphs of Scale Dependence

As an example, look at the one-jet inclusive cross section in proton-antiproton collisions. Specifically, consider the cross section $d\sigma/dE_T d\eta$ to make a collimated spray of particles, a *jet*, with transverse energy E_T and rapidity η. [Here, E_T is essentially the transverse momentum carried by the particles in the jet, and η is related to the angle between the jet and the beam direction by $\eta \equiv \ln(\tan(\theta/2))$.] We will investigate this process and discuss the definitions in the next section. For now, all we need to know is that the theoretical formula for the cross section at next-to-leading order involves the strong coupling $\alpha_s(\mu)$ and two factors $f_{a/h}(x,\mu_F)$ representing the distribution of partons in the two incoming hadrons. There is a parton level hard scattering cross section that also depends on μ and μ_F.

How does the cross section depend on μ in $\alpha_s(\mu)$ and μ_F in $f_{a/h}(x,\mu_F)$? In Fig. 29, I show contour plots of the jet cross section versus μ and μ_F at two different values of E_T. The center of the plots corresponds to a standard choice of scales, $\mu = \mu_F = E_T/2$. The axes are logarithmic, representing $\log_2(2\mu/E_T)$ and $\log_2(2\mu_F/E_T)$. Thus μ and μ_F vary from $E_T/8$ to $2E_T$ in the plots.

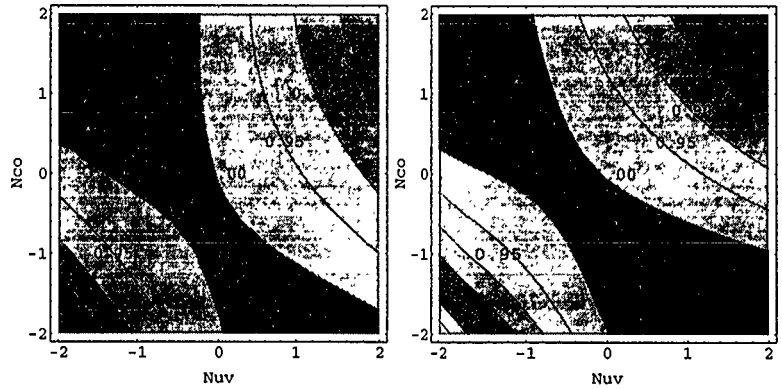


Figure 29: *Contour plots of the one-jet inclusive cross section versus the renormalization scale μ and the factorization scale μ_F. The cross section is $d\sigma/dE_T d\eta$ at $\eta = 0$ with $E_T = 100$ GeV in the first graph and $E_T = 500$ GeV in the second. The horizontal axis in each graph represents $N_{UV} \equiv \log_2(2\mu/E_T)$ and the vertical axis represents $N_{CO} \equiv \log_2(2\mu_F/E_T)$. The contour lines show 5% changes in the cross section relative to the cross section at the center of the figures. The c.m. energy is $\sqrt{s} = 1800$ GeV.*

Notice that the dependence on the two scales is rather mild for the next-to-leading order cross section. The cross section calculated at leading order is quite sensitive to these scales, but most of the scale dependence found at order α_s^2 has been canceled by the α_s^3 contributions to the cross section. One reads from the figure that the cross section varies by roughly $\pm 15\%$ in the central region of the graphs, both for medium and large E_T. Following the argument of Sec. 3.4, this leads to a rough estimate of 15% for the theoretical error associated with truncating perturbation theory at next-to-leading order.

4.8 $\overline{\rm MS}$ Definition of Parton Distribution Functions

The factorization property, Eq. (67), of the deeply inelastic scattering cross section states that the cross section can be approximated as a convolution of a hard scattering cross section that can be calculated perturbatively and parton distribution functions $f_{a/A}(x,\mu)$. But what are the parton distribution functions? This question has some practical importance. The hard scattering cross section is essentially the physical cross section divided by the parton distribution function, so the precise definition of the parton distribution functions leads to the rules for calculating the hard scattering functions.

The definition of the parton distribution functions is to some extent a matter of convention. The most commonly used convention is the $\overline{\rm MS}$ definition, which arose from the theory of deeply inelastic scattering in the language of the "operator product expansion."[24] Here I will follow the (equivalent) formulation of Ref. 13. For a more detailed pedagogical review, the reader may consult Ref. 25.

Using the $\overline{\rm MS}$ definition, the distribution of quarks in a hadron is given as the hadron matrix element of certain quark field operators:

$$f_{i/h}(\xi,\mu_F) = \frac{1}{2}\int \frac{dy^-}{2\pi}\, e^{-i\xi p^+ y^-} \langle p|\bar\psi_i(0,y^-,\mathbf{0})\gamma^+ F \psi_i(0)|p\rangle. \tag{81}$$

Here $|p\rangle$ represents the state of a hadron with momentum p^μ aligned so that $p_T = 0$. For simplicity, I take the hadron to have spin zero. The operator $\psi_i(0)$, evaluated at $x^\mu = 0$, annihilates a quark in the hadron. The operator $\bar\psi_i(0,y^-,\mathbf{0})$ recreates the quark at $x^+ = \mathbf{x}_T = 0$ and $x^- = y^-$, where we take the appropriate Fourier transform in y^- so that the quark that was annihilated and recreated has momentum $k^+ = \xi p^+$. The motivation for the definition is that this is the hadron matrix element of the appropriate number operator for finding a quark.

There is one subtle point. The number operator idea corresponds to a particular gauge choice, $A^+ = 0$. If we are using any other gauge, we insert the operator

$$F = \mathcal{P}\exp\left(-ig\int_0^{y^-} dz^- A_a^+(0,z^-,\mathbf{0})\,t_a\right). \tag{82}$$

The $\mathcal{P}$ indicates a path ordering of the operators and color matrices along the path from $(0,0,\mathbf{0})$ to $(0,y^-,\mathbf{0})$. This operator is the identity operator in $A^+ = 0$ gauge and it makes the definition gauge invariant.

The physics of this definition is illustrated in Fig. 30. The first picture (from Fig. 23) illustrates the amplitude for deeply inelastic scattering. The fast proton moves in the plus direction. A virtual photon knocks out a quark, which emerges moving in the minus direction and develops into a jet of particles. The second picture illustrates the amplitude associated with the quark distribution function. We express F as F_2F_1 where

$$\begin{aligned} F_2 &= \bar{\mathcal{P}}\exp\left(+ig\int_{y^-}^{\infty} dz^- A_a^+(0,z^-,\mathbf{0})\,t_a\right), \\ F_1 &= \mathcal{P}\exp\left(-ig\int_{0}^{\infty} dz^- A_a^+(0,z^-,\mathbf{0})\,t_a\right), \end{aligned} \tag{83}$$

and write the quark distribution function including a sum over intermediate states $|N\rangle$:

$$f_{i/h}(\xi,\mu_F) = \frac{1}{2}\int \frac{dy^-}{2\pi}\, e^{-i\xi p^+ y^-} \sum_N \langle p|\bar\psi_i(0,y^-,\mathbf{0})\gamma^+ F_2|N\rangle\langle N|F_1\psi_i(0)|p\rangle. \tag{84}$$

Then the amplitude depicted in the second picture in Fig. 30 is $\langle N|F_1\psi_i(0)|p\rangle$. The operator ψ annihilates a quark in the proton. The operator F_1 stands in for the quark moving in the minus direction. The gluon field A evaluated along a lightlike line in the minus direction absorbs longitudinally polarized gluons from the color field of the proton, just as the real quark in deeply inelastic scattering can do. Thus, the physics of deeply inelastic scattering is built into the definition of the quark distribution function, albeit in an idealized way. The idealization is not a problem because the hard scattering function $d\hat\sigma$ systematically corrects for the difference between real deeply inelastic scattering and the idealization.

There is one small hitch. If you calculate any Feynman diagrams for $f_{i/h}(\xi,\mu_F)$, you are likely to wind up with an ultraviolet-divergent integral. The operator product that is part of the definition needs renormalization. This hitch is only a small one. We simply agree to do all of the renormalization using the $\overline{\rm MS}$ scheme

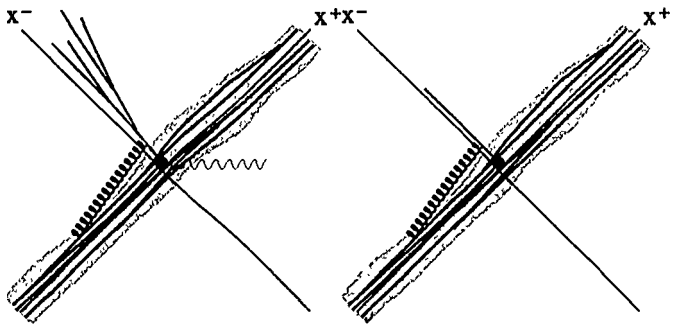


Figure 30: *Deeply inelastic scattering and the parton distribution functions.*

for renormalization. It is this renormalization that introduces the scale μ_F into $f_{i/h}(\xi, \mu_F)$. This role of μ_F is in accord with Fig. 28: roughly speaking, μ_F is the upper cutoff for what momenta belong with the parton distribution function; at the same time, it is the lower cutoff for what momenta belong with the hard scattering function.

What about gluons? The definition of the gluon distribution function is similar to the definition for quarks. We simply replace the quark field ψ by suitable combinations of the gluon field A^μ, as described in Refs. 13 and 25.

4.9 Evolution of the Parton Distributions

Since we introduced a scale μ_F in the definition of the parton distributions in order to define their renormalization, there is a renormalization group equation that gives the μ_F dependence

$$\frac{d}{d\ln \mu_F} f_{a/h}(x, \mu_F) = \sum_b \int_x^1 \frac{d\xi}{\xi}\, P_{ab}(x/\xi, \alpha_s(\mu_F))\; f_{b/h}(\xi, \mu_F). \tag{85}$$

This is variously known as the evolution equation, the Altarelli-Parisi equation, and the DGLAP (Dokshitzer-Gribov-Lipatov-Altarelli-Parisi) equation. Note the sum over parton flavor indices. The evolution of, say, an up quark ($a = u$) can involve a gluon ($b = g$) through the element P_{ug} of the kernel that describes gluon splitting into $\bar{u}u$.

The equation is illustrated in Fig. 31. When we change the renormalization scale μ_F, the change in the probability to find a parton with momentum fraction x and flavor a is proportional to the probability to find such a parton with large transverse momentum. The way to get this parton with large transverse momentum is for a parton carrying momentum fraction ξ and much smaller transverse momentum to split into partons carrying large transverse momenta, including the parton that we are looking for. This splitting probability, integrated over the appropriate transverse momentum ranges, is the kernel P_{ab}.

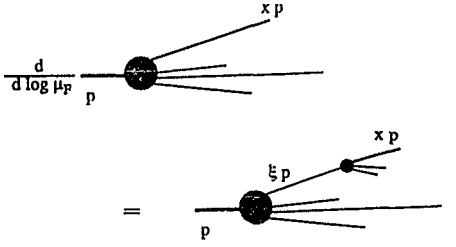


Figure 31: *The renormalization for the parton distribution functions.*

The kernel P in Eq. (85) has a perturbative expansion

$$P_{ab}(x/\xi, \alpha_s(\mu_F)) = P_{ab}^{(1)}(x/\xi)\, \frac{\alpha_s(\mu_F)}{\pi} + P_{ab}^{(2)}(x/\xi)\, \left(\frac{\alpha_s(\mu_F)}{\pi}\right)^2 + \cdots. \tag{86}$$

The first two terms are known and are typically used in numerical solutions of the equation. To learn more about the DGLAP equation, the reader may consult Refs. 1 and 25.

4.10 Determination and Use of the Parton Distributions

The $\overline{\rm MS}$ definition giving the parton distribution in terms of operators is process independent—it does not refer to any particular physical process. These parton distributions then appear in the QCD formula for any process with one or two hadrons in the initial state. In principle, the parton distribution functions could be calculated by using the method of lattice QCD (see Ref. 25). Currently, they are determined from experiment.

Currently, the most comprehensive analyses are being done by the CTEQ[19] and MRS[26] groups. These groups perform a "global fit" to data from experiments

of several different types. To perform such a fit, one chooses a parameterization for the parton distributions at some standard factorization scale μ_0. Certain sum rules that follow from the definition of the parton distribution functions are built into the parameterization. An example is the momentum sum rule:

$$\sum_a \int_0^1 d\xi\ \xi\ f_{a/h}(\xi,\mu) = 1. \tag{87}$$

Given some set of values for the parameters describing the $f_{a/h}(x,\mu_0)$, one can determine $f_{a/h}(x,\mu)$ for all higher values of μ by using the evolution equation. Then the QCD cross section formulas give predictions for all of the experiments that are being used. One systematically varies the parameters in $f_{a/h}(x,\mu_0)$ to obtain the *best* fit to all of the experiments. One source of information about these fits is the World Wide Web pages of Ref. 27.

If the freedom available for the parton distributions is used to fit all of the world's data, is there any physical content to QCD? The answer is yes: there are lots of experiments, so this program won't work unless QCD is right. In fact, there are roughly 1400 data points in the CTEQ fit and only about 25 parameters available to fit these data.

5 QCD in Hadron-Hadron Collisions

When there is a hadron in the initial state of a scattering process, there are inevitably long time scales associated with the binding of the hadron, even if part of the process is a short-time scattering. We have seen, in the case of deeply inelastic scattering of a lepton from a single hadron, that the dependence on these long time scales can be factored into a parton distribution function. But what happens when two high-energy hadrons collide? The reader will not be surprised to learn that we then need two parton distribution functions.

I explore hadron-hadron collisions in this section. I begin with the definition of a convenient kinematical variable, rapidity. Then I discuss, in turn, production of vector bosons (γ^*, W, and Z), heavy quark production, and jet production.

5.1 Kinematics: Rapidity

In describing hadron-hadron collisions, it is useful to employ a kinematic variable y that is called *rapidity*. Consider, for example, the production of a Z boson plus anything, $p + \bar{p} \to Z + X$. Choose the hadron-hadron c.m. frame with the z axis along the beam direction. In Fig. 32, I show a drawing of the collision. The arrows represent the momenta of the two hadrons; in the c.m. frame, these momenta have equal magnitudes. We will want to describe the process at the parton level, $a + b \to Z + X$. The two partons a and b each carry some share of the parent hadron's momentum, but generally these will not be equal shares. Thus, the magnitudes of the momenta of the colliding partons will not be equal. We will have to boost along the z axis in order to get to the parton-parton c.m. frame. For this reason, it is useful to use a variable that transforms simply under boosts. This is the motivation for using rapidity.

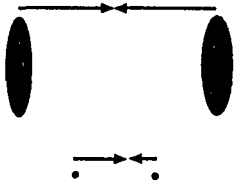


Figure 32: *Collision of two hadrons containing partons producing a Z boson. The c.m. frame of the two hadrons is normally not the c.m. frame of the two partons that create the Z boson.*

Let $q^\mu = (q^+, q^-, \mathbf{q})$ be the momentum of the Z boson. Then the rapidity of the Z is defined as

$$y = \frac{1}{2}\ln\left(\frac{q^+}{q^-}\right). \tag{88}$$

The four components $(q^+, q^-, \mathbf{q})$ of the Z boson momentum can be written in terms of four variables, the two components of the Z boson's transverse momentum $\mathbf{q}$, its mass M, and its rapidity:

$$q^\mu = (e^y\sqrt{(\mathbf{q}^2 + M^2)/2},\ e^{-y}\sqrt{(\mathbf{q}^2 + M^2)/2},\ \mathbf{q}). \tag{89}$$

The utility of using rapidity as one of the variables stems from the transformation property of rapidity under a boost along the z axis:

$$q^+ \to e^\omega q^+, \quad q^- \to e^{-\omega} q^-, \quad \mathbf{q} \to \mathbf{q}. \tag{90}$$

Under this transformation,

$$y \to y + \omega. \tag{91}$$

This is as simple a transformation law as we could hope for. In fact, it is just the same as the transformation law for velocities in nonrelativistic physics in one dimension.

Consider now the rapidity of a massless particle. Let the massless particle emerge from the collision with polar angle θ, as indicated in Fig. 33. A simple calculation relates the particle's rapidity y to θ:

$$y = -\ln(\tan(\theta/2)), \qquad (m = 0). \tag{92}$$

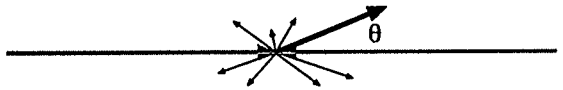


Figure 33: *Definition of the polar angle θ used in calculating the rapidity of a massless particle.*

Another way of writing this is

$$\tan\theta = 1/\sinh y, \qquad (m = 0). \tag{93}$$

One also defines the *pseudorapidity* η of a particle, massless or not, by

$$\eta = -\ln(\tan(\theta/2)) \qquad \text{or} \qquad \tan\theta = 1/\sinh\eta. \tag{94}$$

The relation between rapidity and pseudorapidity is

$$\sinh\eta = \sqrt{1 + m^2/q_T^2}\ \sinh y. \tag{95}$$

Thus, if the particle isn't quite massless, η may still be a good approximation to y.

5.2 γ^*, W, Z Production in Hadron-Hadron Collisions

Consider the process

$$A + B \to Z + X, \tag{96}$$

where A and B are high-energy hadrons. Two features of this reaction are important for our discussion. First, the mass of the Z boson is large compared to 1 GeV, so that a process with a small time scale $\Delta t \sim 1/M_Z$ must be involved in the production of the Z. At lowest order in the strong interactions, the process is $q + \bar{q} \to Z$. Here the quark and antiquark are constituents of the high-energy hadrons. The second significant feature is that the Z boson does not participate in the strong interactions, so that our description of the observed final state can be very simple.

We could equally well talk about $A + B \to W + X$ or $A + B \to \gamma^* + X$ where the virtual photon decays into a muon pair or an electron pair that is observed, and where the mass of the γ^* is large compared to 1 GeV. This last process,[28] $A+B \to \gamma^*+X \to \ell^+ + \ell^- + X$, is historically important because it helped establish the parton picture as being correct. The W and Z processes were observed later. In fact, these are the processes by which the W and Z bosons were first directly observed.[29]

In process (96), we allow the Z boson to have any transverse momentum $\mathbf{q}$. (Typically, then, $\mathbf{q}$ will be much smaller than M_Z.) Since we integrate over $\mathbf{q}$ and the mass of the Z boson is fixed, there is only one variable needed to describe the momentum of the Z boson. We choose to use its rapidity y, so that we are interested in the cross section $d\sigma/dy$.

The cross section takes a factored form similar to that found for deeply inelastic scattering. Here, however, there are two parton distribution functions:

$$\frac{d\sigma}{dy} \approx \sum_{a,b} \int_{x_A}^1 d\xi_A \int_{x_B}^1 d\xi_B\ f_{a/A}(\xi_A, \mu_F)\ f_{b/B}(\xi_B, \mu_F)\ \frac{d\hat{\sigma}_{ab}(\mu, \mu_F)}{dy}. \tag{97}$$

The meaning of this formula is intuitive: $f_{a/A}(\xi_A, \mu_F)\, d\xi_A$ gives the probability to find a parton in hadron A; $f_{b/B}(\xi_B, \mu_f)\, d\xi_B$ gives the probability to find a parton in hadron B; $d\hat{\sigma}_{ab}/dy$ gives the cross section for these partons to produce the observed Z boson. The formula is illustrated in Fig. 34. The hard scattering cross section can be calculated perturbatively. Figure 34 illustrates one particular order α_s contribution to $d\hat{\sigma}_{ab}/dy$. The integrations over parton momentum fractions have limits x_A and x_B, which are given by

$$x_A = e^y\sqrt{M^2/s}, \qquad x_B = e^{-y}\sqrt{M^2/s}. \tag{98}$$

Equation (97) has corrections of order m/M_Z, where m is a mass characteristic of hadronic systems, say 1 GeV. In addition, when $d\hat{\sigma}_{ab}/dy$ is calculated to order α_s^N, then there are corrections of order α_s^{N+1}.

There can be soft interactions between the partons in hadron A and the partons in hadron B, and these soft interactions can occur before the hard interaction that creates the Z boson. It would seem that these soft interactions do not fit into

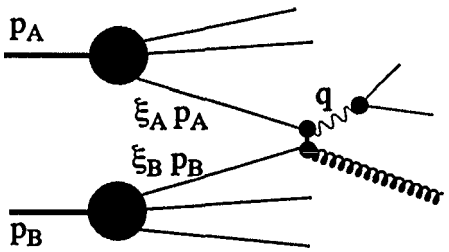


Figure 34: *A Feynman diagram for Z boson production in a hadron-hadron collision. Two partons, carrying momentum fractions ξ_A and ξ_B, participate in the hard interaction. This particular Feynman diagram illustrates an order α_s contribution to the hard scattering cross section: a gluon is emitted in the process of making the Z boson. The diagram also shows the decay of the Z boson into an electron and a positron.*

the intuitive picture that comes along with Eq. (97). It is a significant part of the factorization property that these soft interactions do not modify the formula. These introductory lectures are not the place to go into how this can be. For more information, the reader is invited to consult Ref. 23.

5.3 Heavy Quark Production

We now turn to the production of a heavy quark and its corresponding antiquark in a high-energy hadron-hadron collision:

$$A + B \to Q + \bar{Q} + X. \tag{99}$$

The most notable example of this is top quark production. A Feynman diagram for this process is illustrated in Fig. 35.

The total heavy quark production cross section takes a factored form similar to that for Z boson production,

$$\sigma_T \approx \sum_{a,b} \int_{x_A}^1 d\xi_A \int_{x_B}^1 d\xi_B \; f_{a/A}(\xi_A, \mu_F) \; f_{b/B}(\xi_B, \mu_F) \; \hat{\sigma}_T^{ab}(\mu_F, \mu). \tag{100}$$

As in the case of Z production, $Q\bar{Q}$ production is a hard process, with a time scale determined by the mass of the quark: $\Delta t \sim 1/M_Q$. It is this hard process that is represented by the calculated cross section $\hat{\sigma}_T^{ab}$. Of course, the heavy quark and

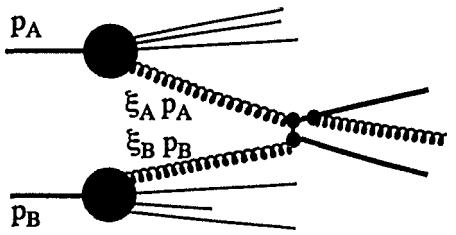


Figure 35: *Feynman graph for heavy quark production. The lowest order hard process is $g + g \to Q + \bar{Q}$, which occurs at order α_s^2. This particular Feynman diagram illustrates an order α_s^3 process in which a gluon is emitted.*

antiquark have strong interactions, and can radiate soft gluons or exchange them with their environment. These effects do not, however, affect the cross section: once the $Q\bar{Q}$ pair is made, it is made. The probabilities for it to interact in various ways must add to one. For an argument that Eq. (100) is correct, see Ref. 30.

5.4 Jet Production

In our study of high-energy electron-positron annihilation, we discovered three things. First, QCD makes the qualitative prediction that particles in the final state should tend to be grouped in collimated sprays of hadrons called jets. The jets carry the momenta of the first quarks and gluons produced in the hard process. Second, certain kinds of experimental measurements probe the short-time physics of the hard interaction, while being insensitive to the long-time physics of parton splitting, soft gluon exchange, and the binding of partons into hadrons. Such measurements are called infrared safe. Third, among the infrared safe observables are cross sections to make jets.

These ideas work for hadron-hadron collisions too. In such collisions, there is sometimes a hard parton-parton collision, which produces two or more jets, as depicted in Fig. 36. Consider the cross section to make one jet plus anything else,

$$A + B \to jet + X. \tag{101}$$

Let E_T be the *transverse energy* of the jet, defined as the sum of the absolute values of the transverse momenta of the particles in the jet. Let y be the rapidity of the jet. Given a definition of exactly what it means to have a jet with transverse

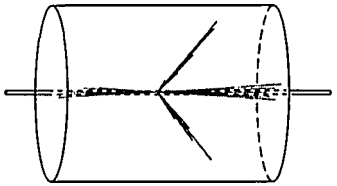


Figure 36: *Sketch of a two-jet event at a hadron collider. The cylinder represents the detector, with the beam pipe along its axis. Typical hadron-hadron collisions produce beam remnants, the debris from soft interactions among the partons. The particles in the beam remnants have small transverse momenta, as shown in the sketch. In rare events, there is a hard parton-parton collision, which produces jets with high transverse momenta. In the event shown, there are two high P_T jets.*

energy E_T and rapidity y, the jet production cross section takes the familiar factored form

$$\frac{d\sigma}{dE_T d\eta} \approx \sum_{a,b} \int_{x_A}^1 d\xi_A \int_{x_B}^1 d\xi_B \; f_{a/A}(\xi_A,\mu_F)\; f_{b/B}(\xi_B,\mu_F)\; \frac{d\hat{\sigma}^{ab}(\mu,\mu_F)}{dE_T d\eta}. \quad (102)$$

What shall we choose for the definition of a jet? At a crude level, high E_T jets are quite obvious and the precise definition hardly matters. However, if we want to make a quantitative measurement of a jet cross section to compare to next-to-leading order theory, then the definition does matter. There are several possibilities for a definition that is infrared safe. The one most used in hadron-hadron collisions is based on cones.

In the standard *Snowmass Accord* definition,[31] one imagines that the experimental calorimeter is divided into small angular cells labeled i in η-ϕ space, as depicted in Fig. 37. We can say that a jet consists of all the particles that fall into certain calorimeter cells, or we can measure the E_T in each cell and build the jet parameters from the cell variables (E_{Ti}, η_i, ϕ_i). We then say that a jet consists of the cells inside a certain circle in η-ϕ space. The circle has a radius R, usually chosen as 0.7 radians, and is centered on a direction (η_J, ϕ_J). Thus, the calorimeter cells i included in the jet obey

$$(\eta_i - \eta_J)^2 + (\phi_i - \phi_J)^2 < R^2. \quad (103)$$

The transverse energy of the jet is defined to be

$$E_{T,J} = \sum_{i\in\text{cone}} E_{T,i}. \quad (104)$$

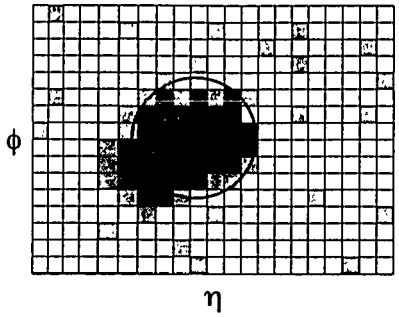


Figure 37: *Jet definition according to the Snowmass algorithm. The shading of the squares represents the density of transverse energy as a function of azimuthal angle ϕ and pseudorapidity η. The cells inside the circle constitute the jet.*

The direction of the jet is defined to be the direction (η_J, ϕ_J) of the jet axis, which is chosen to obey

$$\phi_J = \frac{1}{E_{T,J}} \sum_{i\in\text{cone}} E_{T,i}\; \phi_i, \quad (105)$$

$$\eta_J = \frac{1}{E_{T,J}} \sum_{i\in\text{cone}} E_{T,i}\; \eta_i. \quad (106)$$

Of course, if one picks a trial jet direction (η_J, ϕ_J) to define the meaning of "$i \in$ cone" and then computes (η_J, ϕ_J) from these equations, the output jet direction will not necessarily match the input cone axis. Thus one has to treat the equations iteratively until a consistent solution is found.

Note that the Snowmass algorithm for computing $E_{T,J}, \phi_J, \eta_J$ is infrared safe. Infinitely soft particles do not affect the jet parameters because they enter the equations with zero weight. If two particles have the same angles η, ϕ, then it does not matter if we join them together into one particle before applying the algorithm. For example,

$$E_{T,1}\phi + E_{T,2}\phi = (E_{T,1} + E_{T,2})\,\phi. \quad (107)$$

Note, however, that the Snowmass definition given above is not complete. It is perfectly possible for two or more cones that are solutions to Eqs. (104–106) to overlap. One must then have an algorithm to assign calorimeter cells to one of the competing jets, thus splitting the jets, or else to merge the jets. When

supplemented by an appropriate split/merge algorithm, the Snowmass definition is not as simple as it seemed at first.

In an order α_s^3 perturbative calculation, one simply applies this algorithm at the parton level. At this order of perturbation theory, there are two or three partons in the final state (see Fig. 38). In the case of three partons in the final state, two of them are joined into a jet if they are within R of the jet axis computed from the partonic momenta. The split/merge question does not apply at this order of perturbation theory.

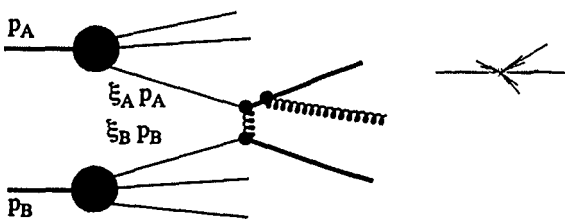


Figure 38: *A Feynman diagram for jet production in hadron-hadron collisions. The leading order diagrams for $A+B \to jet+X$ occur at order α_s^2. This particular diagram is for an interaction of order α_s^3. When the emitted gluon is not soft or nearly collinear to one of the outgoing quarks, this diagram corresponds to a final state like that shown in the small sketch, with three jets emerging in addition to the beam remnants. Any of these jets can be the jet that is measured in the one-jet inclusive cross section.*

I showed a comparison of the theory and experiment for the one-jet inclusive cross section in Fig. 19.

I should record here that the actual jet definitions used in current experiments are close to the Snowmass definition given above but are not exactly the same. Furthermore, there are other definitions available that may come into use in the future. There is not time here to explore the issues of jet definitions in detail. What I hope to have done is give the outline of one definition and to explore what the issues are.

6 Epilogue

QCD is a rich subject. The theory and the experimental evidence indicate that quarks and gluons interact weakly on short time and distance scales. But the net effect of these interactions extending over long time and distance scales is that the chromodynamic force is strong. Quarks are bound into hadrons. Outgoing partons emerge as jets of hadrons, with each jet composed of subjets. Thus, QCD theory can be viewed as starting with simple perturbation theory, but it does not end there. The challenge for both theorists and experimentalists is to extend the range of phenomena that we can relate to the fundamental theory.

I thank F. Hautmann for reading the manuscript and helping to eliminate some of the mistakes.

References

[1] G. Sterman *et al.*, "Handbook of perturbative QCD," Rev. Mod. Phys. **67**, 157 (1995).

[2] R. K. Ellis, W. J. Stirling, and B. R. Webber, *QCD and Collider Physics* (Cambridge University Press, Cambridge, 1996).

[3] L. Brown, *Quantum Field Theory* (Cambridge University Press, Cambridge, 1992).

[4] G. Sterman, *An Introduction to Quantum Field Theory* (Cambridge University Press, Cambridge, 1993).

[5] M. Peskin and D. V. Schroeder, *An Introduction to Quantum Field Theory* (Addison-Wesley, Reading, 1995).

[6] S. Weinberg, *The Quantum Theory of Fields* (Cambridge University Press, Cambridge, 1995).

[7] *QCD and Beyond, Proceedings of the 1995 Theoretical Advanced Studies Institute*, edited by D. E. Soper, Boulder, 1995 (World Scientific, Singapore, 1996).

[8] G. Sterman, Phys. Rev. D **17**, 2773 (1978); **17**, 2789 (1978).

[9] J. C. Collins and D. E. Soper, Nucl. Phys. B **193**, 381 (1981).

[10] Z. Kunszt and D. E. Soper, Phys. Rev. D **46**, 192 (1992).

[11] S. Bethke, Z. Kunszt, D. E. Soper, and W. J. Stirling, Nucl. Phys. B **370**, 310 (1992).

[12] C. L. Basham, L. S. Brown, S. D. Ellis, and S. T. Love, Phys. Rev. D **19**, 2018 (1979).

[13] J. C. Collins and D. E. Soper, Nucl. Phys. B **194**, 445 (1982); G. Curci, W. Furmanski, and R. Petronzio, Nucl. Phys. B **175**, 27 (1980).

[14] J. C. Collins, *Renormalization* (Cambridge University Press, Cambridge, 1984).

[15] L. Surguladze and M. Samuel, Rev. Mod. Phys. **68**, 259 (1996).

[16] D. E. Soper and L. Surguladze, Phys. Rev. D **54**, 4566 (1996).

[17] P. M. Stevenson, Phys. Rev. D **23**, 2916 (1981).

[18] S. J. Brodsky, G. P. Lepage, and P. MacKenzie, Phys. Rev. D **28**, 228 (1983).

[19] H. Lai *et al.*, e-Print Archive hep-ph/9606399, Phys. Rev. D **55** (to be published).

[20] CDF Collaboration (F. Abe *et al.*), Phys. Rev. Lett. **77**, 438 (1996); B. Flaugher, CDF Collaboration, *Proceedings of the XI Topical Workshop on $p\bar{p}$ Collider Physics*, Padova, Italy, May 1996.

[21] DØ Collaboration: N. Varelas, *Proceedings of the International Conference on High Energy Physics*, Warsaw, July 1996.

[22] J. Huston *et al.*, Phys. Rev. Lett. **77**, 444 (1996).

[23] J. C. Collins, D. E. Soper, and G. Sterman, in *Perturbative QCD*, edited by A. Mueller (World Scientific, Singapore, 1989).

[24] W. A. Bardeen, A. J. Buras, D. W. Duke, and T. Muta, Phys. Rev. D **18**, 3998 (1978).

[25] D. E. Soper, in *Lattice '96 International Symposium on Lattice Field Theory*, edited by M. Golterman *et al.*, St. Louis, June 1996 (Elsevier Science, Amsterdam, to be published).

[26] A. D. Martin, R. G. Roberts, and W. J. Stirling, Phys. Lett. B **387**, 419 (1996).

[27] P. Anandam and D. E. Soper, "A Potpourri of Partons," http://zebu.uoregon.edu/~parton/.

[28] S. D. Drell and T.-M. Yan, Ann. Phys. **66**, 578 (1971).

[29] UA1 Collaboration (G. Arnison *et al.*), Phys. Lett. B **122**, 103 (1983); UA2 Collaboration (G. Banner *et al.*), Phys. Lett. B **122**, 476 (1983).

[30] J. C. Collins, G. Sterman, and D. E. Soper, Nucl. Phys. B **263**, 37 (1986).

[31] J. Huth *et al.*, in *Proceedings of the Summer Study on High Energy Physics in the 1990s, Research Directions for the Decade*, edited by E. Berger, Snowmass, Colorado, 1990 (World Scientific, Singapore, 1992), p. 134.

THE HEAVY QUARK EXPANSION OF QCD

Adam F. Falk
Department of Physics and Astronomy
Johns Hopkins University
3400 North Charles Street
Baltimore, Maryland 21218

ABSTRACT

These lectures contain an elementary introduction to heavy quark symmetry and the heavy quark expansion. Applications such as the expansion of heavy meson decay constants and the treatment of inclusive and exclusive semileptonic B decays are included. Heavy hadron production via nonperturbative fragmentation processes is also discussed.

© 1996 by Adam F. Falk.

1 Heavy Quark Symmetry

In these lectures, I will introduce the ideas of heavy quark symmetry and the heavy quark limit, which exploit the simplification of certain aspects of QCD for infinite quark mass, $m_Q \to \infty$. We will see that while these ideas are extraordinarily simple from a physical point of view, they are of enormous practical utility in the study of the phenomenology of bottom and charmed hadrons. One reason for this is the existence not just of an interesting new limit of QCD, but of a systematic expansion about this limit. The technology of this expansion is the Heavy Quark Effective Theory (HQET), which allows one to use heavy quark symmetry to make accurate predictions of the properties and behavior of heavy hadrons in which the theoretical errors are under control. While the emphasis in these lectures will be on the physical picture of heavy hadrons which emerges in the heavy quark limit, it will be important to introduce enough of the formalism of the HQET to reveal the structure of the heavy quark expansion as a simultaneous expansion in powers of $\Lambda_{\rm QCD}/m_Q$ and $\alpha_s(m_Q)$. However, what I hope to leave you with, above all, is an appreciation for the simplicity, elegance, and coherence of the ideas which underlie the technical results which will be presented. The interested reader is also encouraged to consult a number of excellent reviews,[1] which typically cover in more detail the material in the first two sections of these lectures.

1.1 Introduction

Why is an understanding of QCD crucial to the study of the properties of the bottom and charmed quarks? As an example, consider semileptonic b decay, $b \to c\ell\bar{\nu}$. This process is mediated by a four-fermion operator,

$$\mathcal{O}_{bc} = \frac{G_F V_{cb}}{\sqrt{2}} \bar{c}\gamma^\mu(1-\gamma^5) b\, \bar{\nu}\gamma_\mu(1-\gamma^5)\ell\,. \tag{1}$$

The weak matrix element is easy to calculate at the quark level,

$$\mathcal{A}_{\rm quark} = \langle c\ell\bar{\nu}|\,\mathcal{O}_{bc}|b\rangle = \frac{G_F V_{cb}}{\sqrt{2}} \bar{u}_c(p_c)\gamma^\mu(1-\gamma^5)u_b(p_b)\,\bar{u}_\ell(p_\ell)\gamma_\mu(1-\gamma^5)v_\nu(p_\nu)\,. \tag{2}$$

However, $\mathcal{A}_{\rm quark}$ is only relevant at very short distances; at longer distances, QCD confinement implies that free b and c quarks are not asymptotic states of the theory. Instead, nonperturbative QCD effects "dress" the quark level transition $b \to c\ell\bar{\nu}$ to a hadronic transition, such as

$$B \to D\ell\bar{\nu} \quad \text{or} \quad B \to D^*\ell\bar{\nu} \quad \text{or} \quad \ldots\,. \tag{3}$$

(In these lectures, we will use a convention in which a B meson contains a b quark, not a $\bar{b}$ antiquark.) The hadronic matrix element $\mathcal{A}_{\rm hadron}$ depends on nonperturbative QCD as well as on $G_F V_{cb}$, and is difficult to calculate from first principles. To disentangle the weak interaction part of this complicated process requires us to develop some understanding of the strong interaction effects.

There are a variety of methods by which one can do this. Perhaps the most popular, historically, has been use of various quark potential models.[2] While these models are typically very predictive, they are based on uncontrolled assumptions and approximations, and it is virtually impossible to estimate the theoretical errors associated with their use. This is a serious defect if one builds such a model into the experimental extraction of a weak coupling constant such as V_{cb}, because the uncontrolled theoretical errors then infect the experimental result.

Another approach, the one to be discussed here, is to exploit as much as possible the fact that the b and c quarks are *heavy*, by which we mean that $m_b, m_c \gg \Lambda_{\rm QCD}$. The scale $\Lambda_{\rm QCD}$ is the typical energy at which QCD becomes nonperturbative, and is of the order of hundreds of MeV. The physical quark masses are approximately $m_b \approx 4.8\,{\rm GeV}$ and $m_c \approx 1.5\,{\rm GeV}$. The formalism which we will develop will not make as many predictions as do potential models. However, the compensation will be that we will develop a *systematic* expansion in powers of $\Lambda_{\rm QCD}/m_{b,c}$, within which we will be able to do concrete error analysis. In particular, we will be able to estimate the error associated with the fact that m_c may not be very close to the asymptotic limit $m_c \gg \Lambda_{\rm QCD}$. Even where this error may be substantial, the fact that it is under control allows us to maintain predictive power in the theory.

1.2 The Heavy Quark Limit

Consider a hadron H_Q composed of a heavy quark Q and "light degrees of freedom," consisting of light quarks, light antiquarks, and gluons, in the limit $m_Q \to \infty$. The Compton wavelength of the heavy quark scales as the inverse of the heavy quark mass, $\lambda_Q \sim 1/m_Q$. The light degrees of freedom, by contrast, are characterized by momenta of order $\Lambda_{\rm QCD}$, corresponding to wavelengths $\lambda_\ell \sim 1/\Lambda_{\rm QCD}$. Since $\lambda_\ell \gg \lambda_Q$, the light degrees of freedom cannot resolve features of the heavy quark other than its conserved gauge quantum numbers. In particular, they cannot probe the actual *value* of λ_Q, that is, the value of m_Q.

We draw the same conclusion in momentum space. The structure of the hadron H_Q is determined by nonperturbative strong interactions. The asymptotic freedom of QCD implies that when quarks and gluons exchange momenta p much larger than $\Lambda_{\rm QCD}$, the process is perturbative in the strong coupling constant $\alpha_s(p)$. On the other hand, the typical momenta exchanged by the light degrees of freedom with each other and with the heavy quark, are of order $\Lambda_{\rm QCD}$, for which a perturbative expansion is of no use. For these exchanges, however, $p < m_Q$, and the heavy quark Q does not recoil, remaining at rest in the rest frame of the hadron. In this limit, Q acts as a static source of electric and chromoelectric gauge fields. The chromoelectric field, which holds H_Q together, is nonperturbative in nature, but it is independent of m_Q. The result is that the properties of the light degrees of freedom depend only on the presence of the static gauge field, independent of the flavor and mass of the heavy quark carrying the gauge charge.*

There is an immediate implication for the spectroscopy of heavy hadrons. Since the interaction of the light degrees of freedom with the heavy quark is independent of m_Q, then so is the spectrum of their excitations. It is these excitations which determine the spectrum of heavy hadrons H_Q. Hence, the *splittings* $\Delta_i \sim \Lambda_{\rm QCD}$ between the various hadrons H_Q^i are independent of Q, and in the limit $m_Q \to \infty$, do not scale with m_Q.

For example, the spectra of bottom and charmed mesons are shown schematically in Fig. 1, in the limit $m_b, m_c \gg \Lambda_{\rm QCD}$. The light degrees of freedom are in exactly the same state in the mesons B_i and D_i, for a given i. The offset $B_i - D_i = m_b - m_c$ is just the difference between the heavy quark masses; in no way does the relationship between the spectra rely on an approximation $m_b \approx m_c$.

We can enrich this picture by recalling that the heavy quarks and light degrees of freedom also carry spin. The heavy quark has spin quantum number $S_Q = \frac{1}{2}$, which leads to a chromomagnetic moment

$$\mu_Q = \frac{g}{2m_Q}. \tag{4}$$

Note that $\mu_Q \to 0$ as $m_Q \to \infty$, and the interaction between the spin of the heavy quark and the light degrees of freedom is suppressed. Hence, the light degrees of freedom are insensitive to S_Q; their state is independent of whether $S_Q^z = \frac{1}{2}$ or

*Top quarks decay too quickly for a static chromoelectric field to be established around them, so the simplifications discussed here are not relevant to them.

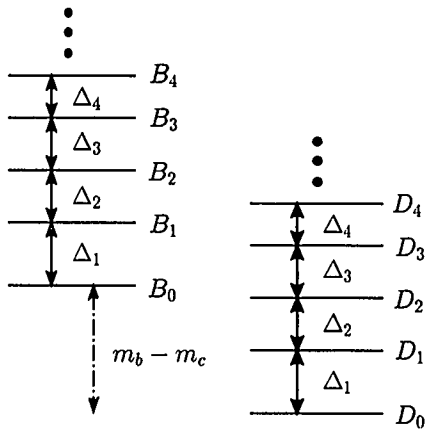


Figure 1: Schematic spectra of the bottom and charmed mesons in the limit $m_b, m_c \gg \Lambda_{\rm QCD}$. The offset of the two spectra is not to scale; in reality, $m_b - m_c \gg \Delta_i \sim \Lambda_{\rm QCD}$.

$S_Q^z = -\frac{1}{2}$. Thus each of the energy levels in Fig. 1 is actually doubled, one state for each possible value of S_Q^z.

To summarize, what we see is that the light degrees of freedom are the same when combined with any of the following heavy quark states:

$$Q_1(\uparrow),\quad Q_1(\downarrow);\quad Q_2(\uparrow),\quad Q_2(\downarrow);\quad \ldots\quad Q_{N_h}(\uparrow),\quad Q_{N_h}(\downarrow), \tag{5}$$

where there are N_h heavy quarks (in the real world, $N_h = 2$). The result is an $SU(2N_h)$ symmetry which applies to the light degrees of freedom.[3-7] A new symmetry means new nonperturbative relations between physical quantities. It is these relations which we wish to understand and exploit.

The light degrees of freedom have total angular momentum J_ℓ, which is integral for baryons and half-integral for mesons. When combined with the heavy quark spin $S_Q = \frac{1}{2}$, we find physical hadron states with total angular momentum

$$J = \left| J_\ell \pm \tfrac{1}{2} \right|. \tag{6}$$

If $S_\ell \neq 0$, then these two states are degenerate. For example, the lightest heavy mesons have $S_\ell = \frac{1}{2}$, leading to a doublet with $J = 0$ and $J = 1$. Indeed, in the

charm system, we find that the states of lowest mass are the spin-0 D and the spin-1 D^*; the corresponding bottom mesons are the B and B^*.

When effects of order $1/m_Q$ are included, the chromomagnetic interactions split the states of given S_ℓ but different J. This "hyperfine" splitting is not calculable perturbatively, but it is proportional to the heavy quark magnetic moment μ_Q. This gives its scaling with m_Q:

$$\begin{aligned} m_{D^*} - m_D &\sim 1/m_c \\ m_{B^*} - m_B &\sim 1/m_b . \end{aligned} \tag{7}$$

From this fact, we can construct a relation which is a nonperturbative prediction of heavy quark symmetry,

$$m_{B^*}^2 - m_B^2 = m_{D^*}^2 - m_D^2 . \tag{8}$$

Experimentally, $m_{B^*}^2 - m_B^2 = 0.49\,\mathrm{GeV}^2$ and $m_{D^*}^2 - m_D^2 = 0.55\,\mathrm{GeV}^2$, so this prediction works quite well. Note that this relation involves not just the heavy quark symmetry, but the systematic inclusion of the leading symmetry violating effects.

So far, we have formulated heavy quark symmetry for hadrons in their rest frame. Of course, we can easily boost to a frame in which the hadrons have arbitrary four-velocity $v^\mu = \gamma(1, \vec{v})$. For heavy quarks Q_1 and Q_2, the symmetry will then relate hadrons $H_1(v)$ and $H_2(v)$ with the same velocity but with different momenta. This distinguishes heavy quark symmetry from ordinary symmetries of QCD, which relate states of the same momentum. To remind ourselves of this distinction, henceforth we will label heavy hadrons explicitly by their velocity: $D(v)$, $D^*(v)$, $B(v)$, $B^*(v)$, and so on.

1.3 Semileptonic Decay of a Heavy Quark

Now let us return to the semileptonic weak decay $b \to c\,\ell\bar{\nu}$, but now consider it in the heavy quark limit for the b and c quarks. Suppose the decay occurs at time $t = 0$. For $t < 0$, the b quark is embedded in a hadron H_b; for $t > 0$, the c quark is dressed by light degrees of freedom to H_c'. Let us consider the lightest hadrons, $H_b = B(v)$ and $H_c' = D(v')$. Note that since the leptons carry away energy and momentum, in general $v \neq v'$.

What happens to the light degrees of freedom when the heavy quark decays? For $t < 0$, they see the chromoelectric field of a point source with velocity v. At $t = 0$, this point source recoils instantaneously† to velocity v'; the color-neutral leptons do not interact with the light hadronic degrees of freedom as they fly off. The light quarks and gluons then must reassemble themselves about the recoiling color source. This nonperturbative process will generally involve the production of an excited state or of additional particles; the light degrees of freedom can exchange energy with the heavy quark, so there is no kinematic restriction on the excitations (of energy $\sim \Lambda_{\mathrm{QCD}}$) which can be formed. There is also some chance that the light degrees of freedom will reassemble themselves back into a ground-state D meson. The amplitude for this to happen is a function only of the inner product $w = v \cdot v'$ of the initial and final velocities of the color sources. This amplitude, $\xi(w)$, is known as the Isgur-Wise function.[3]

Clearly, the kinematic point $v = v'$, or $w = 1$, is a special one. In this corner of phase space, where the leptons are emitted back to back, there is no recoil of the source of color field at $t = 0$. As far as the light degrees of freedom are concerned, *nothing happens!* Their state is unaffected by the decay of the heavy quark; they don't even notice it. Hence, the amplitude for them to remain in the ground state is exactly unity. This is reflected in a nonperturbative normalization of the Isgur-Wise function at zero recoil,[3]

$$\xi(1) = 1 . \tag{9}$$

As we will see, this normalization condition is of enormous phenomenological use. It will be extremely important to understand the corrections to this result for finite heavy quark masses m_b, and especially, m_c.

The weak decay $b \to c$ is mediated by a left-handed current $\bar{c}\gamma^\mu(1-\gamma^5)b$. Not only does this operator carry momentum, but it can change the orientation of the spin S_Q of the heavy quark during the decay. For a fixed light angular momentum J_ℓ, the relative orientation of S_Q determines whether the physical hadron in the final state is a D or a D^*. However, the light degrees of freedom are insensitive to S_Q, so the nonperturbative part of the transition is the same whether it is a D or a D^* which is produced. Hence, heavy quark symmetry implies relations between the hadronic matrix elements which describe the semileptonic decays $B \to D\ell\bar{\nu}$ and $B \to D^*\ell\bar{\nu}$.

†The weak decay occurs over a very short time $\delta t \sim 1/M_W \ll 1/\Lambda_{\mathrm{QCD}}$.

It is conventional to parameterize these matrix elements by a set of scalar form factors. These are defined separately for the vector and axial currents, as follows:

$$\begin{aligned}
\langle D(v')|\,\bar{c}\gamma^\mu b\,|B(v)\rangle &= h_+(w)(v+v')^\mu + h_-(w)(v-v')^\mu \\
\langle D^*(v',\epsilon)|\,\bar{c}\gamma^\mu b\,|B(v)\rangle &= h_V(w)i\epsilon^{\mu\nu\alpha\beta}\epsilon^*_\nu v'_\alpha v_\beta \\
\langle D(v')|\,\bar{c}\gamma^\mu\gamma^5 b\,|B(v)\rangle &= 0 \\
\langle D(v',\epsilon)|\,\bar{c}\gamma^\mu\gamma^5 b\,|B(v)\rangle &= h_{A_1}(w)(w+1)\epsilon^{*\mu} - \epsilon^*\cdot v[h_{A_2}(w)v^\mu + h_{A_3}(w)v'^\mu]\,.
\end{aligned} \tag{10}$$

The set of form factors $h_i(w)$ is the one appropriate to the heavy quark limit. Other linear combinations are also found in the literature. In any case, the form factors are independent nonperturbative functions of the recoil, or equivalently, for fixed m_b and m_c, of the momentum transfer. However, in the heavy quark limit, they correspond to a *single* transition of the light degrees of freedom, being distinguished from each other only by the relative orientation of the spin of the heavy quark. Hence, they may all be written in terms of the single function $\xi(w)$ which describes this nonperturbative transition. As we will derive later, the result is a set of relations,[3]

$$\begin{aligned}
h_+(w) = h_V(w) = h_{A_1}(w) = h_{A_3}(w) = \xi(w) \\
h_-(w) = h_{A_2}(w) = 0\,,
\end{aligned} \tag{11}$$

which follow solely from the heavy quark symmetry. Of course, all of the form factors which do not vanish inherit the normalization condition (9) at zero recoil. This result is a powerful constraint on the structure of semileptonic decay in the heavy quark limit.

1.4 Heavy Meson Decay Constant

As a final example of the utility of the heavy quark limit, consider the coupling of the heavy meson field to the axial vector current. This is conventionally parameterized in terms of a decay constant; for example, for the B^- meson, we define f_B via

$$\langle 0|\,\bar{u}\gamma^\mu\gamma^5 b\,|B^-(p_B)\rangle = if_B p_B^\mu\,. \tag{12}$$

What is the dependence of the nonperturbative quantity f_B on m_B? To address this question, we rewrite Eq. (12) in a form appropriate to taking the heavy quark limit, $m_B \to \infty$ (which is equivalent to $m_b \to \infty$). This entails making explicit the dependence of all quantities on m_B. First, we trade the B^- momentum for its velocity,

$$p_B^\mu = m_B v^\mu\,. \tag{13}$$

Second, we replace the usual B^- state, whose normalization depends on m_B,

$$\langle B(p_1)|B(p_2)\rangle = 2E_B\,\delta^{(3)}(\vec{p}_1 - \vec{p}_2)\,, \tag{14}$$

by a mass-independent state,

$$|B(v)\rangle = \frac{1}{\sqrt{m_B}}|B(p_B)\rangle\,, \tag{15}$$

satisfying

$$\langle B(v_1)|B(v_2)\rangle = 2\gamma\,\delta^{(3)}(\vec{p}_1 - \vec{p}_2)\,. \tag{16}$$

Then Eq. (12) becomes

$$\sqrt{m_B}\langle 0|\,\bar{u}\gamma^\mu\gamma^5 b\,|B^-(v)\rangle = if_B m_B v^\mu\,. \tag{17}$$

The nonperturbative matrix element $\langle 0|\,\bar{u}\gamma^\mu\gamma^5 b\,|B^-(v)\rangle$ is independent of m_B in the heavy quark limit. Hence, we see that in this limit, f_B takes the form

$$f_B = m_B^{-1/2} \times (\text{independent of } m_B)\,. \tag{18}$$

This makes explicit the scaling of f_B with m_B. It is more interesting to write this as a prediction for the ratio of charmed and bottom meson decay constants. We find[3,4,6]

$$\frac{f_B}{f_D} = \sqrt{\frac{m_D}{m_B}} + O\left(\frac{\Lambda_{\rm QCD}}{m_D}, \frac{\Lambda_{\rm QCD}}{m_B}\right)\,. \tag{19}$$

For the physical bottom and charm masses, of course, the correction terms proportional to $\Lambda_{\rm QCD}/m_Q$ could be important.

2 Heavy Quark Effective Theory

We have already extracted quite a bit of nontrivial information from the heavy quark limit. We have found the scaling of various quantities with m_Q, we have studied the implications for heavy hadron spectroscopy, and we have found nonperturbative relations among the hadronic form factors which describe semileptonic $b \to c$ decay. However, all of these results have been obtained in the strict

limit $m_Q \to \infty$. If the heavy quark limit is to be of more than academic interest and is to provide the basis for quantitative phenomenology, we have to understand how to include corrections systematically. There are actually two types of corrections which we would like to include. *Power corrections* are subleading terms in the expansion in $\Lambda_{\rm QCD}/m_Q$; those proportional to $\Lambda_{\rm QCD}/m_c$ are the most worrisome, because of the relatively small charm quark mass. *Logarithmic corrections* arise from the implicit dependence of quantities on m_Q through the strong coupling constant $\alpha_s(m_Q) \sim 1/\ln(m_Q/\Lambda_{\rm QCD})$. For the physical values of m_b and m_c, either of these could be important. What we need is a formalism which can accommodate them both.

In short, we need to go from a set of heavy quark symmetry predictions in the $m_Q \to \infty$ limit to a reformulation of QCD which provides a controlled expansion about this limit. The formalism which does the job is the Heavy Quark Effective Theory, or the HQET. The purpose of the HQET is to allow us to extract, explicitly and systematically, all dependence of physical quantities on m_Q, in the limit $m_Q \gg \Lambda_{\rm QCD}$. In these lectures, we will develop only enough of the technology to treat the dominant leading effects, providing indications along the way of how one would carry the expansion further.

The HQET, as formulated here, was developed in a series of papers going back to the late 1980s (Refs. 3, 4, 6, and 8–15), which the reader who is interested in tracking its historical development may consult.

2.1 The Effective Lagrangian

Consider the kinematics of a heavy quark Q, bound in a hadron with light degrees of freedom to make a color singlet state. The small momenta which Q typically exchanges with the rest of the hadron are of order $\Lambda_{\rm QCD} \ll m_Q$, and they never take Q far from its mass shell, $p_Q^2 = m_Q^2$. Hence, the momentum p_Q^μ can be decomposed into two parts,

$$p_Q^\mu = m_Q v^\mu + k^\mu \,, \tag{20}$$

where $m_Q v^\mu$ is the constant on-shell part of p_Q^μ, and $k^\mu \sim \Lambda_{\rm QCD}$ is the small, fluctuating "residual momentum." The on-shell condition for the heavy quark then becomes

$$m_Q^2 = (m_Q v^\mu + k^\mu)^2 = m_Q^2 + 2 m_Q v\cdot k + k^2 \,. \tag{21}$$

In the heavy quark limit, we may neglect the last term, and we have the simple condition

$$v \cdot k = 0 \tag{22}$$

for an on-shell heavy quark. Here, the velocity v^μ functions as a label; since soft interactions cannot change v^μ, there is a ***velocity superselection rule*** in the heavy quark limit, and v^μ is a good quantum number of the QCD Hamiltonian.

We find the same result by taking the $m_Q \to \infty$ limit of the heavy quark propagator,

$$\frac{i}{\not p - m_Q + i\epsilon} \to \frac{1+\not v}{2}\,\frac{i}{v\cdot k + i\epsilon} \,. \tag{23}$$

In this limit, the propagator is independent of m_Q. The projection operators

$$P_\pm = \frac{1 \pm \not v}{2} \tag{24}$$

project onto the positive (P_+) and negative (P_-) frequency parts of the Dirac field Q. This is clear in the Dirac representation in the rest frame, in which P_+ and P_- project, respectively, onto the upper two and lower two components of the heavy quark spinor. In the limit $m_Q \to \infty$, in which Q remains almost on shell, only the "large" upper components of the field Q propagate; mixing via zitterbewegung with the "small" lower components is suppressed by $1/2m_Q$. Hence, the action of the projectors on Q is

$$P_+ Q(x) = Q(x) + O(1/m_Q) \,, \qquad P_- Q(x) = 0 + O(1/m_Q) \,. \tag{25}$$

The momentum dependence of the field Q is given by its action on a heavy quark state,

$$Q(x)\,|Q(p)\rangle = e^{-ip\cdot x}\,|0\rangle \,. \tag{26}$$

If we now multiply both sides by a phase corresponding to the on-shell momentum,

$$e^{im_Q v\cdot x} Q(x)\,|Q(p)\rangle = e^{-ik\cdot x}\,|0\rangle \,, \tag{27}$$

the right side of this equation is independent of m_Q. Hence, the left side must be, as well. Combining this observation with the argument of the previous paragraph, we are motivated to define a m_Q-*independent* effective heavy quark field $h_v(x)$,

$$h_v(x) = e^{im_Q v\cdot x}\, P_+ \, Q(x) \,. \tag{28}$$

Note that the effective field carries a velocity label v and is a two-component object. The modifications to the ordinary field $Q(x)$ project out the positive

frequency part and ensure that states annihilated by $h_v(x)$ have no dependence on m_Q. Hence, these are reasonable candidate fields to carry representations of the heavy quark symmetry. Of course, the small components cannot be neglected when effects of order $1/m_Q$ are included. In the HQET, they are represented by a field

$$H_v(x) = e^{im_Q v\cdot x}\, P_-\, Q(x)\,. \tag{29}$$

The field $H_v(x)$ vanishes in the $m_Q \to \infty$ limit.

The ordinary QCD Lagrange density for a field $Q(x)$ is given by

$$\mathcal{L}_{\rm QCD} = \overline{Q}(x)\,(i\not{D} - m_Q)\,Q(x)\,, \tag{30}$$

where $D_\mu = \partial_\mu - igA^a_\mu T^a$ is the gauge covariant derivative. To find the Lagrangian of the HQET, we substitute

$$Q(x) = e^{-im_Q v\cdot x} h_v(x) + \ldots \tag{31}$$

into $\mathcal{L}_{\rm QCD}$ and expand. With the aid of the projection identity $P_+\gamma^\mu P_+ = v^\mu$, we find

$$\mathcal{L}_{\rm HQET} = \bar h_v(x) iv\cdot D h(x)\,. \tag{32}$$

This simple Lagrangian leads to the propagator we derived earlier,

$$\frac{i}{v\cdot k + i\epsilon}\,, \tag{33}$$

and to an equally simple quark-gluon vertex,

$$igT^a v^\mu A^a_\mu\,. \tag{34}$$

Note that both the propagator and the vertex are independent of m_Q, reflecting the heavy quark flavor symmetry. They also have no Dirac structure, reflecting the heavy quark spin symmetry. Our intuitive statements about the structure of heavy hadrons have been promoted to explicit symmetries of the QCD Lagrangian in the limit $m_Q \to \infty$.

It is straightforward to include power corrections to $\mathcal{L}_{\rm HQET}$. Write $Q(x)$ in terms of the effective fields,

$$Q(x) = e^{-im_Q v\cdot x}\left[h_v(x) + H_v(x)\right]\,, \tag{35}$$

and apply the classical equation of motion $(i\not{D} - m_Q)Q(x) = 0$:

$$i\not{D}\, h_v(x) + (i\not{D} - 2m_Q)H_v(x) = 0\,. \tag{36}$$

Multiplying by P_- and commuting $\not{v}$ to the right, we find

$$(iv\cdot D + 2m_Q)H_v(x) = i\not{D}_\perp\, h_v(x)\,, \tag{37}$$

where $D^\mu_\perp = D^\mu - v^\mu v\cdot D$. We then substitute $Q(x)$ into $\mathcal{L}_{\rm QCD}$ as before, eliminate $H_v(x)$, and expand in $1/m_Q$ to obtain

$$\begin{aligned}\mathcal{L}_{\rm HQET} &= \bar h_v iv\cdot D h_v + \bar h_v i\not{D}_\perp \frac{1}{iv\cdot D + 2m_Q} i\not{D}_\perp h_v \\ &= \bar h_v iv\cdot D h_v + \frac{1}{2m_Q}\left[\bar h_v (iD_\perp)^2 h_v + \frac{g}{2}\bar h_v \sigma^{\alpha\beta} G_{\alpha\beta} h_v\right] + \ldots\,.\end{aligned} \tag{38}$$

The leading corrections have a simple interpretation, which becomes clear in the rest frame, $v^\mu = (1,0,0,0)$. The spin-independent term is

$$\frac{1}{2m_Q}\mathcal{O}_K = \frac{1}{2m_Q}\bar h_v (iD_\perp)^2 h_v \to -\frac{1}{2m_Q}\bar h_v (i\vec D)^2 h_v\,, \tag{39}$$

which is the negative of the nonrelativistic kinetic energy of the heavy quark. Because of the explicit factor of $1/2m_Q$, this term violates the heavy flavor symmetry. The spin-dependent part is

$$\frac{1}{2m_Q}\mathcal{O}_G = \frac{1}{2m_Q}\frac{g}{2}\bar h_v \sigma^{\alpha\beta} G_{\alpha\beta} h_v \to \frac{1}{4m_Q}\bar h_v \sigma^{ij} T^a h_v \times g G^a_{ij} = g\vec\mu^a_Q\cdot\vec B^{\,a}\,, \tag{40}$$

which is the coupling of the spin of the heavy quark to the chromomagnetic field. Because it has a nontrivial Dirac structure, this term violates both the heavy flavor symmetry and the heavy spin symmetry. For example, $\mathcal{O}_G$ is responsible for the $D - D^*$ and $B - B^*$ mass splittings. These correction terms will be treated as part of the *interaction* Lagrangian, even though $\mathcal{O}_K$ has a piece which is a pure bilinear in the heavy quark field.

2.2 Effective Currents and States

The expansion of the weak interaction current $\bar c\gamma^\mu(1-\gamma^5)b$ is analogous. However, here we must introduce separate effective fields for the charm and bottom quarks, each with its own velocity:

$$b \to h^b_v\,, \qquad c \to h^c_{v'}\,. \tag{41}$$

Then a general flavor-changing current becomes, to leading order,

$$\bar c\,\Gamma\, b \to \bar h^c_{v'}\,\Gamma\, h^b_v\,, \tag{42}$$

where Γ is a fixed Dirac structure. With the leading power corrections, this is

$$\bar{c}\,\Gamma\,b \to \bar{h}^c_{v'}\,\Gamma\,h^b_v + \frac{1}{2m_b}\,\bar{h}^c_{v'}\Gamma(i\not{D}_\perp)h^b_v + \frac{1}{2m_c}\,\bar{h}^c_{v'}(-i\overleftarrow{\not{D}}_\perp)\Gamma h^b_v + \dots\,. \tag{43}$$

The effective currents, and other operators which appear in the HQET, may often be simplified by use of the classical equation of motion,

$$iv\cdot D h_v(x) = 0\,. \tag{44}$$

However, it is only safe to apply these equations naively at order $1/m_Q$; at higher order, the application of the equations of motion involves additional subtleties.[16–18]

To complete the effective theory, we need m_Q-independent hadron states which are created and annihilated by currents containing the effective fields. For example, there is an effective pseudoscalar meson state $|M(v)\rangle$ which couples to the effective axial current $\bar{q}\gamma^\mu\gamma^5 h_v$, with a coupling F_M which is independent of m_Q,

$$\langle 0|\,\bar{q}\gamma^\mu\gamma^5 h_v\,|M(v)\rangle = iF_M v^\mu\,. \tag{45}$$

At lowest order, F_M is related to a conventional decay constant such as f_B by

$$f_B = F_M/\sqrt{m_B}\,, \tag{46}$$

from which we immediately find the relationship [Eq. (19)] between f_D and f_B.

2.3 Radiative Corrections

We can use the effective Lagrangian $\mathcal{L}_{\rm HQET}$ to compute the radiative corrections to the matrix element [Eq. (45)]. In particular, we would like to extract the dependence of F_M on $\ln m_Q$. This dependence comes through the one-loop renormalization of the current $\bar{q}\gamma^\mu\gamma^5 Q$. At lowest order, of course, the renormalization is straightforward: we simply compute the set of graphs found in Fig. 2. The result is finite, because the current is (partially) conserved, and we extract a result of the form

$$\bar{q}\gamma^\mu\gamma^5 Q\,\left(1 - \bar{\gamma}_0\frac{\alpha_s}{\pi}\ln(m_Q/m_q) + \dots\right)\,. \tag{47}$$

Note that there is no explicit dependence on the renormalization scale μ, since there is no divergence to be subtracted.

The same result may be obtained in the effective theory. In this case, we must match the currents in full QCD onto HQET currents of the form $\bar{q}\gamma^\mu\gamma^5 h_v$.

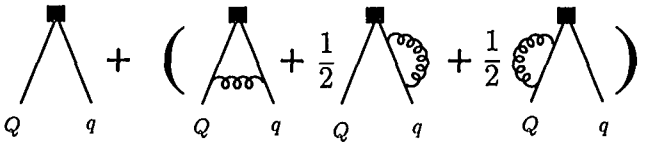


Figure 2: Tree level plus the one-loop renormalization of the current $\bar{q}\Gamma Q$ in QCD. The box represents the current insertion.

This step will induce a matching coefficient containing the explicit dependence on m_Q, which is absent, by construction, from the operators and Lagrangian of the HQET.[‡] In addition, the effective current will not necessarily be conserved, since the ultraviolet properties of QCD and the HQET differ. Hence, the form of the matching, once radiative corrections are included, is

$$\bar{q}\gamma^\mu\gamma^5 Q \to C(m_Q,\mu)\,\bar{q}\gamma^\mu\gamma^5 h_v\,. \tag{48}$$

We can deduce the form of $C(m_Q,\mu)$ by considering the renormalization of the effective current $\bar{q}\gamma^\mu\gamma^5 h_v$, shown in the last three terms of Fig. 3. These diagrams, computed in the effective theory, are independent of m_Q. However, in general they are divergent, so they depend on the renormalization scale μ; the renormalization takes the form

$$\bar{q}\gamma^\mu\gamma^5 h_v\,\left(C(m_Q,\mu) - \gamma_0\frac{\alpha_s}{\pi}\ln(\mu/m_q) + \dots\right)\,, \tag{49}$$

where m_q acts as an infrared cutoff. The μ dependence in the second term must be canceled by $C(m_Q,\mu)$. Since the logarithm depends on a dimensionless ratio, $C(m_Q,\mu)$ must be of the form

$$C(m_Q,\mu) = 1 - \gamma_0\frac{\alpha_s}{\pi}\ln(m_Q/\mu) + \dots\,. \tag{50}$$

Comparing the dependence on m_Q of $C(m_Q,\mu)$ and the expansion [Eq. (47)], we see that $\bar{\gamma}_0 = \gamma_0$.

However, the effective theory allows us to go beyond leading order and to resum all corrections of the form $\alpha_s^n \ln^n m_Q$. We do this with the renormalization group equations, which express the independence of physical observables on the

[‡] In general, the matching procedure at order α_s can also induce new Dirac structures $\bar{q}\Gamma h_v$. They do not affect the leading logarithms discussed here.

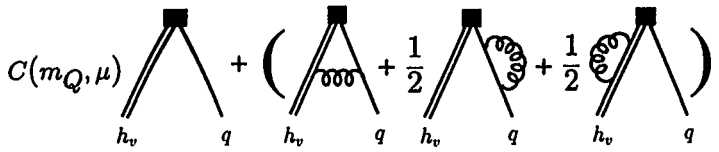


Figure 3: Tree level plus the one-loop renormalization of the current $\bar{q}\gamma^\mu\gamma^5 h_v$ in HQET. The double line is the propagator of the effective field h_v.

renormalization scale μ. In this case, they require that the μ dependence of $C(m_Q,\mu)$ cancel that of the one-loop diagrams in Fig. 3, under small changes in μ:

$$\mu\frac{\mathrm{d}}{\mathrm{d}\mu}C(m_Q,\mu) = \gamma_0\frac{\alpha_s(\mu)}{\pi}\,. \tag{51}$$

Here, the total derivative with respect to μ includes the implicit dependence on μ of the coupling constant $\alpha_s(\mu)$:

$$\begin{aligned}
\mu\frac{\mathrm{d}}{\mathrm{d}\mu} &= \mu\frac{\partial}{\partial\mu} + \beta(g)\frac{\partial}{\partial g}\\
\beta(g) &= -\beta_0\frac{g^3}{16\pi^2} + \ldots\\
\beta_0 &= 11 - \frac{2}{3}N_f = \frac{25}{3} \quad \text{for } N_f = 4\,,
\end{aligned} \tag{52}$$

where N_f is the number of light flavors. We compute the anomalous dimension γ_0 from the divergent parts of the one-loop diagrams shown in Fig. 3. From the three terms we find, respectively,[4,6]

$$\gamma_0 = \frac{8}{3} + \frac{1}{2}\left(-\frac{8}{3}\right) + \frac{1}{2}\left(\frac{16}{3}\right) = 4\,. \tag{53}$$

The solution of the renormalization group equation is

$$C(m_Q,\mu) = \left(\frac{\alpha_s(m_Q)}{\alpha_s(\mu)}\right)^{\gamma_0/2\beta_0} = \left(\frac{\alpha_s(m_Q)}{\alpha_s(\mu)}\right)^{6/25}\,. \tag{54}$$

This then yields the leading logarithmic correction to the ratio f_B/f_D:

$$\frac{f_B}{f_D} = \sqrt{\frac{m_D}{m_B}}\left(\frac{\alpha_s(m_b)}{\alpha_s(m_c)}\right)^{6/25}\,. \tag{55}$$

The radiative correction is approximately a ten percent effect. In fact, it has a simple physical interpretation. For virtual gluons of "intermediate" energy, $m_c < E_g < m_b$, the bottom quark is heavy but the charm quark is light. Such gluons contribute to the difference between f_B and f_D even in the heavy quark limit.

In summary, then, the purpose of the HQET is to make explicit all dependence of observable quantities on m_Q. The logarithmic dependence, through $\alpha_s(m_Q)$, arises from intermediate virtual gluons with $m_c < E_g < m_b$. We obtain these corrections by computing perturbatively with the HQET Lagrangian, then using the renormalization group to resum the logarithms to all orders. The power dependence, $1/m_Q$, is extracted systematically in the heavy quark expansion. We have seen how to expand the Lagrangian and the states to subleading order; the application of the expansion to a physical decay rate will be presented in the next section.

These lectures are meant to be pedagogical, so we will only treat the leading corrections to a few processes. However, the state of the art goes significantly beyond what will be presented here. For many quantities, not only the leading logarithms, $\alpha_s^n \ln^n m_Q$, but the subleading (two-loop) logarithms, of order $\alpha_s^{n+1}\ln^n m_Q$, have been resummed. Similarly, many power corrections are known to relative order $1/m_Q^2$. It is particularly important phenomenologically to take into account the corrections of order $1/m_c^2$.

3 Exclusive B Decays

We now have the tools we need for an HQET treatment of the exclusive semileptonic transitions $B \to D\,\ell\bar{\nu}$ and $B \to D^*\,\ell\bar{\nu}$. Earlier, we argued on physical grounds that in the heavy quark limit, all of the hadronic matrix elements which appear in these decays are related to a single nonperturbative function $\xi(w)$. Now we will sharpen this analysis to actually *derive* these relations, and to include radiative and power corrections. In fact, almost all of our effort will go into the power corrections, since the radiative corrections to the transition currents are computed just as in the previous section.

3.1 Matrix Element Relations at Leading Order

The transitions in question require the nonperturbative matrix elements

$$\langle D(v')|\,\bar{c}\gamma^\mu b\,|B(v)\rangle\,, \qquad \langle D^*(v',\epsilon)|\,\bar{c}\gamma^\mu b\,|B(v)\rangle\,, \qquad \langle D^*(v',\epsilon)|\,\bar{c}\gamma^\mu\gamma^5 b\,|B(v)\rangle\,, \tag{56}$$

parameterized in terms of form factors as in Eq. (10). Our first task is to derive the relations between these form factors, as promised earlier. These relations depend on the heavy quark symmetry, that is, on the fact that the spin quantum numbers of Q and of the light degrees of freedom are separately conserved by the soft physics. Hence, we need a representation of the heavy meson states in which they have well-defined transformations separately under the angular momentum operators S_Q and J_ℓ. In particular, the representation must reflect the fact that a rotation by S_Q can exchange the pseudoscalar meson $M(v)$ with the vector meson $M^*(v,\epsilon)$.

The solution is to introduce a "superfield" $\mathcal{M}(v)$, defined as the 4×4 Dirac matrix[11,19]

$$\mathcal{M}(v) = \frac{1+\not{v}}{2}\left[\gamma^\mu M^*_\mu(v,\epsilon) - \gamma^5 M(v)\right]. \tag{57}$$

Under heavy quark spin rotations S_Q, $\mathcal{M}(v)$ transforms as

$$\mathcal{M}(v) \to D(S_Q)\mathcal{M}(v)\,, \tag{58}$$

and under Lorentz rotations Λ, as

$$\mathcal{M}(v) \to D(\Lambda)\mathcal{M}(\Lambda^{-1}v)D^{-1}(\Lambda)\,. \tag{59}$$

Here $D(\cdots)$ is the spinor representation of $SO(3,1)$. The superfield satisfies the matrix identity

$$P_+\,\mathcal{M}(v)\,P_- = \mathcal{M}(v)\,, \tag{60}$$

so it transforms the same way as the product of spinors $h_v\,\bar{q}$, representing a heavy quark and a light antiquark moving together at velocity v^μ.

A current which mediates the decay of one heavy quark (Q) into another (Q') is of the form $\bar{h}_{v'}\,\Gamma\,h_v$. Under a rotation by S_Q, the effective field h_v transforms as

$$h_v \to D(S_Q)\,h_v\,, \tag{61}$$

while $h_{v'}$ is unchanged. The current would remain invariant if we took Γ to transform as

$$\Gamma \to \Gamma\,D^{-1}(S_Q)\,. \tag{62}$$

On the other hand, the matrix element of superfields

$$\langle\mathcal{M}'(v')|\,\bar{h}_{v'}\,\Gamma\,h_v\,|\mathcal{M}(v)\rangle \tag{63}$$

is invariant if we rotate *both* h_v and $\mathcal{M}(v)$ by the *same* S_Q. With the transformation law [Eq. (58)] for $\mathcal{M}(v)$, it follows that the S_Q-invariant matrix element must be proportional to $\Gamma\mathcal{M}(v)$. When we also consider rotations under $S_{Q'}$, we find that the matrix element is restricted to the general form

$$\langle\mathcal{M}'(v')|\,\bar{h}_{v'}\,\Gamma\,h_v\,|\mathcal{M}(v)\rangle = -\,[M_M M_{M'}]^{1/2}\,\mathrm{Tr}\left[\overline{\mathcal{M}}'(v')\,\Gamma\,\mathcal{M}(v)\,\hat{F}(v,v')\right]. \tag{64}$$

The product of masses in front is a convention which restores the relativistic normalization of the states. Note that the heavy quark symmetry allows an arbitrary 4×4 Dirac matrix $\hat{F}(v,v')$ to act on the "light quark" part of the superfields. Its presence reflects the fact that, other than the constraint of Lorentz symmetry, the behavior of the spin of the light degrees of freedom during the decay is unknown.

A general expansion of $\hat{F}(v,v')$ in terms of scalar functions $F_i(w = v\cdot v')$ takes the form

$$\hat{F}(v,v') = F_1(w) + F_2(w)\not{v} + F_3(w)\not{v}' + F_4(w)\not{v}\not{v}'\,. \tag{65}$$

However, the identity [Eq. (60)] applied to the matrix element [Eq. (64)] yields

$$\hat{F}(v,v') = P_-\,\hat{F}(v,v')\,P'_- = [F_1(w) - F_2(w) - F_3(w) + F_4(w)]\,P_-\,P'_-\,. \tag{66}$$

In other words, $F(v,v')$ is actually a *scalar*, which we identify with the Isgur-Wise function,

$$\hat{F}(v,v') = \xi(w)\,. \tag{67}$$

As an exercise, let us apply this formalism to the matrix elements for $B \to (D,D^*)\,\ell\bar{\nu}$. For a given matrix element, we pick out the part of the superfield $\mathcal{M}(v)$ which is relevant. Hence, we find

$$\begin{aligned}\langle D(v')|\,\bar{c}\gamma^\mu b\,|B(v)\rangle &= \langle M_D(v')|\,\bar{h}^c_{v'}\gamma^\mu h^b_v\,|M_B(v)\rangle \\ &= -\,[m_D m_B]^{1/2}\,\mathrm{Tr}\left[\gamma^5 P'_+\gamma^\mu P_+(-\gamma^5)\right]\,\xi(w) \\ &= [m_D m_B]^{1/2}\,\xi(w)\,(v+v')^\mu\end{aligned} \tag{68}$$

$$\begin{aligned}\langle D^*(v',\epsilon)|\,\bar c\gamma^\mu\gamma^5 b\,|B(v)\rangle &= \langle M_D^*(v',\epsilon)|\,\bar h^c_{v'}\gamma^\mu\gamma^5 h^b_v\,|M_B(v)\rangle \\ &= -\left[m_{D^*}m_B\right]^{1/2}\,\mathrm{Tr}\left[\not\epsilon^* P'_+\gamma^\mu\gamma^5 P_+(-\gamma^5)\right]\,\xi(w) \\ &= \left[m_{D^*}m_B\right]^{1/2}\,\xi(w)\,\left[(w+1)\epsilon^{*\mu}-\epsilon^*\cdot(v+v')^\mu\right] \qquad (69)\end{aligned}$$

$$\begin{aligned}\langle D^*(v',\epsilon)|\,\bar c\gamma^\mu b\,|B(v)\rangle &= \langle M_D^*(v',\epsilon)|\,\bar h^c_{v'}\gamma^\mu h^b_v\,|M_B(v)\rangle \\ &= -\left[m_{D^*}m_B\right]^{1/2}\,\mathrm{Tr}\left[\not\epsilon^* P'_+\gamma^\mu P_+(-\gamma^5)\right]\,\xi(w) \\ &= \left[m_{D^*}m_B\right]^{1/2}\,\xi(w)\,i\varepsilon^{\mu\nu\alpha\beta}\epsilon^*_\nu v'_\alpha v_\beta\,, \qquad (70)\end{aligned}$$

reproducing explicitly the relations [Eq. (11)] between the independent form factors $h_i(w)$. We can also derive the normalization condition at $w=1$. Consider the matrix element of the b number current $\bar b\gamma^\mu b$ between B-meson states. In QCD, the matrix element of this current is exactly normalized,

$$\langle B(v)|\,\bar b\gamma^\mu b\,|B(v)\rangle = 2p_B^\mu = 2m_B v^\mu\,. \qquad (71)$$

But in HQET, we have

$$\begin{aligned}\langle B(v)|\,\bar b\gamma^\mu b\,|B(v)\rangle &= \langle M_B(v)|\,\bar h_v\gamma^\mu h_v\,|M_B(v)\rangle \\ &= m_B\xi(v\cdot v)(v+v)^\mu \\ &= 2m_B v^\mu\,\xi(1)\,. \qquad (72)\end{aligned}$$

Hence, the normalization condition at zero recoil,

$$\xi(1)=1\,, \qquad (73)$$

follows directly from the conservation of the heavy quark number current.

3.2 Power Corrections to the Matrix Elements

The matrix elements we have derived are computed in the strict limit $m_{b,c}\to\infty$. How are they affected by corrections of order $1/m_b$ and $1/m_c$? There are two sources of $1/m_Q$ corrections in the effective theory: the corrections [Eq. (43)] to the heavy quark currents, and the corrections [Eq. (38)] to the Lagrangian.

When radiative corrections are included, the expansion of the heavy quark current $\bar c\Gamma b$ in terms of HQET operators has a form which is somewhat more general than Eq. (43),

$$\bar c\Gamma b \to a_0(\alpha_s)\,\bar h^c_{v'}\Gamma h^b_v + \frac{a_1(\alpha_s)}{2m_b}\,\bar h^c_{v'}\Gamma_1^\alpha iD_\alpha h^b_v + \frac{a_1'(\alpha_s)}{2m_c}\,\bar h^c_{v'}(-i\overleftarrow{D}_\alpha)\Gamma_1'^\alpha h^b_v + \ldots\,. \qquad (74)$$

The matrix elements of the power corrections are constrained by heavy quark symmetry in a manner completely analogous to the leading current. In terms of traces over the superfields, we have[13]

$$\langle\mathcal{M}'(v')|\,\bar h_{v'}\,\Gamma^\alpha iD_\alpha\,h_v\,|\mathcal{M}(v)\rangle = -\left[M_M M_{M'}\right]^{1/2}\,\mathrm{Tr}\left[\overline{\mathcal{M}}'(v')\,\Gamma^\alpha\,\mathcal{M}(v)\,\hat G_\alpha(v,v')\right]\,, \qquad (75)$$

where $\hat G_\alpha(v,v')$ is another arbitrary 4×4 Dirac matrix. The matrix element

$$\langle\mathcal{M}'(v')|\,\bar h_{v'}\,(-i\overleftarrow{D}_\alpha)\Gamma_1'^\alpha h_v\,|\mathcal{M}(v)\rangle \qquad (76)$$

may also be written in terms of $\hat G_\alpha(v,v')$, using charge conjugation.

The $1/m_Q$ corrections $\mathcal{O}_K$ and $\mathcal{O}_G$ to the Lagrangian contribute somewhat differently. In order to apply heavy quark symmetry, the matrix elements of the local currents, both leading and subleading, must be written in terms of the *effective* states $|M(v)\rangle$. However, these states are not eigenstates of the Hamiltonian, once $\mathcal{O}_K$ and $\mathcal{O}_G$ are included in the Lagrangian. Hence, we must allow for the possibility that if an effective state $|M(v)\rangle$ is created at time $t=-\infty$, then $\mathcal{O}_K$ or $\mathcal{O}_G$ could act on the state before its decay at $t=0$. This possibility is accounted for by including time-ordered products in which $\mathcal{O}_K$ or $\mathcal{O}_G$ is inserted along the incoming or outgoing heavy quark line. If we are keeping terms of order $1/m_Q$, only one insertion of $\mathcal{O}_K$ or $\mathcal{O}_G$ needs to be included. The time-ordered products are of the form[13]

$$\begin{aligned}\langle D^{(*)}(v)|\,\bar c\Gamma b\,|B(v)\rangle = \ldots &+ \frac{1}{2m_c}\,\langle\mathcal{M}'(v')|\,i\int\mathrm{d}y T\left\{\bar h^c_{v'}\Gamma h^b_v,\mathcal{O}_K^{v'}+\mathcal{O}_G^{v'}\right\}|\mathcal{M}(v)\rangle \\ &+ \frac{1}{2m_b}\,\langle\mathcal{M}'(v')|\,i\int\mathrm{d}y T\left\{\bar h^c_{v'}\Gamma h^b_v,\mathcal{O}_K^{v}+\mathcal{O}_G^{v}\right\}|\mathcal{M}(v)\rangle\,, \qquad (77)\end{aligned}$$

where the ellipses refer to the current corrections computed earlier. The evaluation of the matrix elements of the time-ordered products will lead to still more nonperturbative functions like $\hat F(v,v')$ and $\hat G_\alpha(v,v')$.

3.3 Corrections at Zero Recoil

It is straightforward, but not very illuminating, to expand all of the new nonperturbative functions which arise at order $1/m_Q$ in terms of scalar form factors. In

the end, the corrections may be parameterized in terms of four functions of the velocity transfer w, and a single nonperturbative parameter $\bar{\Lambda}$, all proportional to the mass scale $\Lambda_{\rm QCD}$. The new parameter has a simple interpretation as the "energy" of the light degrees of freedom and is given by

$$\bar{\Lambda} = \lim_{m_b \to \infty} (m_B - m_b) \,. \tag{78}$$

Instead of a general treatment, however, we will consider the $1/m_Q$ corrections at the zero recoil point $w = 1$. This is clearly the most important case, because it is at this point that the nonperturbative matrix elements are absolutely normalized in the heavy quark limit. What happens to this normalization condition when $1/m_Q$ corrections are included?

Let us study the corrections to the current in detail. They are described by the nonperturbative function $\hat{G}_\alpha(v, v')$. At $v = v'$, $\hat{G}_\alpha(v, v)$ may be expanded as

$$\hat{G}_\alpha(v, v) = G_1 v_\alpha + G_2 \gamma_\alpha + G_3 v_\alpha \not{v} + G_4 \gamma_\alpha \not{v} \,. \tag{79}$$

But $\hat{G}_\alpha(v, v)$ is subject to the same constraint as $\hat{F}(v, v')$,

$$\hat{G}_\alpha(v, v) = P_- \hat{G}_\alpha(v, v) P_- = (G_1 - G_2 - G_3 + G_4) v_\alpha P_- \equiv G\, v_\alpha P_- \,, \tag{80}$$

and it, too, is equivalent to a Dirac scalar (the same is *not* true of the general function $\hat{G}_\alpha(v, v')$). Now consider the matrix element where we take $\Gamma^\alpha = v^\alpha$. Then we have

$$\begin{aligned} \langle \mathcal{M}'(v) | \bar{h}_{v'}\, iv \cdot D\, h_v \, | \mathcal{M}(v) \rangle &= -[M_M M_{M'}]^{1/2} \,\mathrm{Tr}\left[\overline{\mathcal{M}}'(v)\, v^\alpha\, \mathcal{M}(v) \right] G\, v_\alpha \\ &= -G [M_M M_{M'}]^{1/2} \,\mathrm{Tr}\left[\overline{\mathcal{M}}'(v)\, \mathcal{M}(v) \right] . \end{aligned} \tag{81}$$

But this matrix element *vanishes* by the classical equation of motion in the effective theory,

$$v \cdot D\, h_v(x) = 0 \,. \tag{82}$$

Hence, $G = 0 = \hat{G}_\alpha(v, v)$. There are no $1/m_Q$ corrections from the current to the normalization condition at zero recoil.[13,20]

The same is true of insertions of the corrections $\mathcal{O}_K$ and $\mathcal{O}_G$ to the Lagrangian: their contribution vanishes at $w = 1$. To show this requires the imposition of the conservation of the b number current at order $1/m_b$, much as we derived the normalization of the Isgur-Wise function at leading order. The complete derivation is found in the literature.[13]

In the end, we have an extremely exciting result, known as *Luke's Theorem*. There are no corrections at zero recoil to the hadronic matrix elements responsible for the semileptonic decays $B \to D\, \ell\bar{\nu}$ and $B \to D^*\, \ell\bar{\nu}$. The leading power corrections to the normalization of zero recoil matrix elements are only of order $1/m_c^2$. Given that $\Lambda_{\rm QCD}/m_c \sim 30\%$ and $\Lambda_{\rm QCD}^2/m_c^2 \sim 10\%$, the implication is that the leading order predictions at $w = 1$ are considerably more accurate than one might have expected. In addition, away from zero recoil, the $1/m_c$ corrections must be suppressed at least by $(w - 1)$.

On closer inspection, this result is more interesting for $B \to D^*\, \ell\bar{\nu}$ than for $B \to D\, \ell\bar{\nu}$. This is because the leading order matrix element for $B \to D\, \ell\nu$ vanishes kinematically at zero recoil for a massless lepton in the final state. Hence, in this case, the $1/m_c$ corrections are not suppressed as a fractional correction to the lowest order term.[21]

3.4 Extraction of $|V_{cb}|$ from $B \to D^*\, \ell\bar{\nu}$

An immediate application of these results is the extraction of $|V_{cb}|$ from the exclusive decay $B \to D^*\, \ell\bar{\nu}$. This process is mediated by the weak operator $\mathcal{O}_{bc}$ [Eq. (1)], whose matrix element factorizes as

$$\langle D^*\, \ell\bar{\nu} | \, \mathcal{O}_{bc} \, | B \rangle = \frac{G_F V_{cb}}{\sqrt{2}} \langle D^* | \, \bar{c} \gamma^\mu (1 - \gamma^5) b \, | B \rangle \, \langle \ell\bar{\nu} | \, \bar{\ell} \gamma_\mu (1 - \gamma^5) \nu \, | 0 \rangle \,. \tag{83}$$

The leptonic matrix element may be computed perturbatively, while we treat the hadronic matrix element in the heavy quark expansion. The result is a differential decay rate of the form[22]

$$\begin{aligned} \frac{\mathrm{d}\Gamma}{\mathrm{d}w} &= \frac{G_F^2}{48\pi^3} |V_{cb}|^2 \, (m_B - m_{D^*})^2 m_{D^*}^3 (w + 1)^3 \sqrt{w^2 - 1} \\ &\quad \times \left[1 + \frac{4w}{w + 1} \, \frac{m_B^2 - 2w m_b m_{D^*} + m_{D^*}^2}{(m_B - m_{D^*})^2} \right] F^2(w) \,. \end{aligned} \tag{84}$$

All of the HQET analysis goes into the factor $F(w)$, which has an expansion

$$F(w) = \xi(w) + (\text{radiative corrections}) + (\text{power corrections}) \,. \tag{85}$$

We extract $|V_{cb}|$ by studying the differential decay rate near $w = 1$, where the hadronic matrix elements are known. Of course, this requires extrapolation of the experimental data, since the rate vanishes kinematically at $w = 1$. For massless

leptons, only the matrix element $\langle D^*|\,\bar{c}\gamma^\mu\gamma^5 b\,|B\rangle$ of the axial current contributes at this point. The analysis of this quantity in the HQET yields an expansion of the form

$$F(1) = \eta_A\left[1 + \frac{0}{m_c} + \frac{0}{m_b} + \delta_{1/m^2} + \ldots\right]. \tag{86}$$

The correction δ_{1/m^2}, which contains terms proportional to $1/m_c^2$, $1/m_b^2$, and $1/m_c m_b$, is intrinsically nonperturbative. It has been estimated from a variety of models to be small and negative,[17,23,24]

$$\delta_{1/m^2} \approx -0.055 \pm 0.035\,. \tag{87}$$

Note that the model dependence in the result has been relegated to the estimation of the sub-subleading terms. The radiative correction η_A has now been computed to two loops,[25,26]

$$\eta_A = 0.960 \pm 0.007\,. \tag{88}$$

The result is a value for $F(1)$ with errors at the level of 5%,

$$F(1) = 0.91 \pm 0.04\,. \tag{89}$$

This is the theory error which the experimental determination of $|V_{cb}|$ will inherit. It is dominated by the uncertainty in the nonperturbative corrections, and it is difficult to see how this can be improved much in the future.

All that is left experimentally is to extrapolate the data to $w = 1$ and extract

$$\lim_{w\to 1} \frac{1}{\sqrt{w-1}}\frac{d\Gamma}{dw}. \tag{90}$$

Once the kinematic factors in Eq. (84) have been included, this amounts to a direct measurement of the combination $|V_{cb}|F(1)$. Four experiments recently have reported results for this quantity[27–30]:

$$\begin{aligned}
\text{ALEPH}: &\quad (31.4 \pm 2.3 \pm 2.5)\times 10^{-3}\\
\text{ARGUS}: &\quad (38.8 \pm 4.3 \pm 2.5)\times 10^{-3}\\
\text{CLEO}: &\quad (35.1 \pm 1.9 \pm 2.0)\times 10^{-3}\\
\text{DELPHI}: &\quad (35.0 \pm 1.9 \pm 2.3)\times 10^{-3}\,.
\end{aligned} \tag{91}$$

Neubert[31] has combined these measurements to find a "world average" of $(35.3 \pm 1.8)\times 10^{-3}$, from which we extract

$$|V_{cb}| = (38.8 \pm 2.0_{\rm exp} \pm 1.6_{\rm th})\times 10^{-3}\,. \tag{92}$$

This value of $|V_{cb}|$ has almost no dependence on hadronic models. In contrast to model-based "measurements," here the theoretical error is meaningful, in that it is based on a systematic expansion in small quantities.

4 Inclusive B Decays

An exclusive semileptonic B decay, such as $B \to D\,\ell\bar{\nu}$, is one in which the final hadronic state is fully reconstructed. An inclusive decay, by contrast, is one in which only certain kinematic features, and perhaps the flavor, of the hadron are known. In this case, we need a theoretical analysis in which we sum over all possible hadronic final states allowed by the kinematics. Fortunately, this is possible within the structure of the HQET.

As in the case of exclusive decays, the key theme is the separation of short-distance physics, associated with the heavy quark, from long-distance physics, associated with the light degrees of freedom. We will also rely on heavy quark spin and flavor symmetry. However, the new ingredient will be the idea of "parton-hadron duality," which, as we will see, also relies on the heavy quark limit $m_b \gg \Lambda_{\rm QCD}$.

4.1 The Inclusive Decay $B \to X_c\,\ell\bar{\nu}$

Let us consider the inclusive decay

$$B(p_B) \to X_c(p_X)\,\ell(p_\ell)\nu(p_\nu)\,, \tag{93}$$

where all that is known about the state X_c is its energy and momentum, and the fact that it contains a charm quark. This decay is mediated by the weak operator $\mathcal{O}_{bc}$. It is easy to generalize our discussion to inclusive decays of other heavy quarks, such as $b \to u\,\ell\nu$ and $c \to s\,\bar{\ell}\nu$, by replacing $\mathcal{O}_{bc}$ with the appropriate weak operator.

The treatment of exclusive decays required both the b and c quarks to be heavy. For inclusive decays, we can relax this condition on the c quark, requiring only $m_b \gg \Lambda_{\rm QCD}$. What does the weak decay of the b, at time $t = 0$, look like to the light degrees of freedom? For $t < 0$, there is a heavy hadron composed of a point-like color source and light quarks and gluons. At $t = 0$, the point source disappears, releasing both its color and a large amount of energy into

the hadronic environment. Eventually, for $t > 0$, this new collection of strongly interacting particles will materialize as a set of physical hadrons. The probability of this hadronization is unity; there is no interference between the hadronization process and the heavy quark decay. There are subleading effects in powers of $\Lambda_{\rm QCD}/m_b$, but they do not alter the probability of hadronization. Rather, they reflect the fact that the b quark is not exactly a static source of color: it has a small nonrelativistic kinetic energy and it carries a spin, both of which affect the kinematic properties of its decay.

As in the case of exclusive decays, we will compute the inclusive semileptonic width $\Gamma(B \to X_c\,\ell\bar{\nu})$ as a double expansion in $\alpha_s(m_b)$ and $\Lambda_{\rm QCD}/m_b$.[18,32–34] The expansion in $\alpha_s(m_b)$ reflects the applicability of perturbative QCD to the short-distance part of the process. The heavy quark expansion will be continued to relative order $1/m_b^2$, as there is an analogue of Luke's Theorem which eliminates power corrections to the rate of order $1/m_b$. The $1/m_b^2$ corrections will be written in terms of three nonperturbative parameters. The first, $\bar{\Lambda}$, is defined in Eq. (78). It is essentially the mass of the light degrees of freedom in the heavy hadron, but we will see that it is plagued by an ambiguity of order $\Lambda_{\rm QCD}$ in the definition of the b quark mass. The other two parameters are the expectation values in the B meson of the leading corrections $\mathcal{O}_K$ and $\mathcal{O}_G$ to $\mathcal{L}_{\rm HQET}$. They are defined as[17]

$$\begin{aligned} \lambda_1 &= \frac{1}{2m_B}\langle B|\,\mathcal{O}_K\,|B\rangle \\ \lambda_2 &= -\frac{1}{6m_B}\langle B|\,\mathcal{O}_G\,|B\rangle\,, \end{aligned} \tag{94}$$

where we take the usual relativistic normalization of the states. Hence, λ_1 may be thought of roughly as the negative of the b quark kinetic energy, and λ_2 as the energy of its hyperfine interaction with the light degrees of freedom.

Now let us outline the computation. The inclusive decay involves a sum over all possible final states, which is actually a sum over exclusive modes (such as $D, D^*, D\pi, \ldots$), followed by a phase space integral for each mode. We write

$$\Gamma(B \to X_c\,\ell\bar{\nu}) = \sum_{X_c} \int {\rm d[P.S.]}\,\left|\langle X_c\,\ell\bar{\nu}|\,\mathcal{O}_{bc}\,|B\rangle\right|^2 . \tag{95}$$

There is an Optical Theorem for QCD, which follows from the analyticity of the scattering matrix as a function of the momenta of the asymptotic states. Its content is that a transition rate is proportional to the imaginary part of the forward scattering amplitude with two insertions of the transition operator,

$$\Gamma(B \to X_c\,\ell\bar{\nu}) = -2\,{\rm Im}\,i\int {\rm d}x\, e^{ik\cdot x}\,\langle B|\,T\left\{\mathcal{O}_{bc}^\dagger(x), \mathcal{O}_{bc}(0)\right\}\,|B\rangle \equiv 2\,{\rm Im}\,T\,. \tag{96}$$

In what follows, we will write the time-ordered product $T\{\mathcal{O}_{bc}^\dagger, \mathcal{O}_{bc}\}$ as a series of local operators, using the Operator Product Expansion. As we will see, the applicability of this expansion, and its computation in perturbation theory, will rest on the limit $m_b \gg \Lambda_{\rm QCD}$. We will then use this limit again to expand the matrix elements of these local operators in the HQET.

The first step is to factorize the integration over the lepton momenta, which can be performed explicitly. Written as a product of currents, $\mathcal{O}_{bc}$ takes the form

$$\mathcal{O}_{bc} = \frac{G_F V_{cb}}{\sqrt{2}}\,J_{bc}^\mu\,J_{\ell\mu}\,, \tag{97}$$

where

$$\begin{aligned} J_{bc}^\mu &= \bar{c}\gamma^\mu(1-\gamma^5)b \\ J_\ell^\mu &= \bar{\ell}\gamma^\mu(1-\gamma^5)\nu\,. \end{aligned} \tag{98}$$

Then T can be decomposed as an integral over the total momentum $q^\mu = p_\ell^\mu + p_\nu^\mu$ transferred to the leptons,

$$T = \frac{1}{2}G_F^2|V_{cb}|^2 \int {\rm d}q\,T^{\mu\nu}(q)\,L_{\mu\nu}(q)\,. \tag{99}$$

Here the lepton tensor is

$$\begin{aligned} L_{\mu\nu}(q) &= \int {\rm d[P.S.]}\,\langle 0|\,J_{\ell\mu}^\dagger\,|\ell\bar{\nu}\rangle\,\langle \ell\nu|\,J_{\ell\nu}\,|0\rangle \\ &= \frac{1}{3\pi}\left(q_\mu q_\nu - q^2 g_{\mu\nu}\right), \end{aligned} \tag{100}$$

and the hadron tensor is

$$T^{\mu\nu}(q) = -i\int {\rm d}x\,e^{iq\cdot x}\,\langle B|\,T\left\{J_{bc}^{\mu\dagger}(x), J_{bc}^\mu(0)\right\}\,|B\rangle\,. \tag{101}$$

We will need the imaginary part, Im $T^{\mu\nu}$. Where is it nonvanishing? In quantum field theory, a scattering amplitude develops an imaginary part when there can be a real intermediate state, that is, the intermediate particles can all go on their mass shell. Whether this is possible, of course, depends on the kinematics of the external states.

In this case, there are two avenues for creating a physical intermediate state.[32] The first is to act on the external state $|B\rangle$ with the transition current J^μ_{bc}. The state which is created has no net b number and a single charm quark; the simplest possibility is the decay process $b \to c$. The momentum of the intermediate state is $p_X = p_B - q$; the condition that it could be on mass shell is simply

$$p_X^2 = (p_B - q)^2 \geq m_D^2 \,. \tag{102}$$

If we define scaled variables

$$p_B^\mu = m_B v^\mu \,, \qquad \hat{q}^\mu = q^\mu / m_B \,, \qquad \hat{m}_D = m_D / m_B \,, \tag{103}$$

this condition becomes

$$v \cdot \hat{q} \leq \frac{1}{2}\left(1 + \hat{q}^2 - \hat{m}_D^2\right) . \tag{104}$$

Another possibility is to act on $|B\rangle$ with the conjugate operator $J^{\mu\dagger}_{bc}$. This operation would produce an intermediate state with two b quarks and one $\bar{c}$. For this state to be on shell, the momentum transfer has to satisfy

$$p_X^2 = (p_B + q)^2 \geq (2m_B + m_D)^2 \,, \tag{105}$$

that is,

$$v \cdot \hat{q} \geq \frac{1}{2}\left(3 - \hat{q}^2 + 4\hat{m}_D + \hat{m}_D^2\right) . \tag{106}$$

The physical intermediate states are shown as cuts in the $v \cdot \hat{q}$ plane in Fig. 4. Also shown is the contour corresponding to the phase space integration over the lepton momentum q. For physical (massless) leptons which are the product of a heavy quark decay, this integral runs over the top of the lower cut, for the range

$$\sqrt{\hat{q}^2} + i\epsilon \leq v \cdot \hat{q} \leq \frac{1}{2}\left(1 + \hat{q}^2 - \hat{m}_D^2\right) + i\epsilon \,. \tag{107}$$

As indicated by the dotted line, we can continue this contour around the end of the cut and back along the bottom, to $v \cdot \hat{q} = \sqrt{\hat{q}^2} - i\epsilon$. Since $T^{\mu\nu}(v \cdot \hat{q}^*) = -T^{\mu\nu}(v \cdot \hat{q})$ for real $\hat{q}^2$, we compensate for extending the contour by dividing the new integral by two.

We now encounter our central problem. The integral over $v \cdot \hat{q}$ runs over physical intermediate hadron states, which are color-neutral bound states of quarks and gluons. Hence, the integrand depends intimately on the details of QCD at long distances, which is intrinsically nonperturbative. A perturbative calculation of $T^{\mu\nu}$, which is all we have at our disposal, would appear to be of no use.

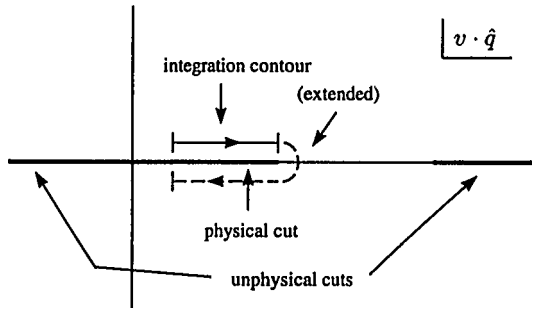


Figure 4: Analytic structure of $T^{\mu\nu}$ in the complex $v \cdot \hat{q}$ plane, for fixed, real $\hat{q}^2$. The integration contour is over the "physical cut," corresponding to real decay into leptons. The unphysical cuts correspond to other processes.

The solution is to deform the contour away from the cut, into the complex $v \cdot \hat{q}$ plane, as shown in Fig. 5. Since the scale of momenta is set by m_b, the contour is now a distance $\sim m_b$ away from the resonances.[32] Since $m_b \gg \Lambda_{\rm QCD}$, it is reasonable to hope that a perturbative treatment in this region is valid. Essentially, we are saved because we do not need to know $T^{\mu\nu}(q)$ for every value of q, just suitable integrals of $T^{\mu\nu}$. That we can use such arguments to compute perturbatively the *average* value of a hadronic quantity, where at each point the quantity depends on nonperturbative physics, is known as (global) *parton-hadron duality*.

Parton-hadron duality has the status of being somewhat more than an assumption, since it is known to hold in QCD in the limit $m_b \to \infty$, but somewhat less than an approximation, since it is not known how to compute systematically the leading corrections to it. In any case, the limit $m_b \gg \Lambda_{\rm QCD}$ plays a crucial role here. By deforming the integration contour a distance $\sim m_b$ away from the resonance regime, we find the correspondence in QCD of our earlier intuitive statement: the probability of the decay products materializing as physical hadrons is unity, independent of the kinematics of the short-distance process. The local redistribution of probability in phase space due to the presence of hadronic resonances is irrelevant to the total decay. Finally, we should note that since we do not have control over the corrections to local duality, it might work better in some processes than in others, for reasons that need not be apparent from within the calculation.

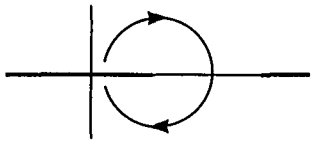


Figure 5: The deformation of the integration contour into the complex $v \cdot \hat{q}$ plane.

Hence, one must be particularly wary of drawing dramatic conclusions from any surprising results of these inclusive calculations.[35]

Let us perform the operator product expansion at tree level and for decay kinematics. The Feynman diagram is given in Fig. 6, which yields the expression

$$T^{\mu\nu} = \bar{b}\gamma^\mu(1-\gamma^5)\,\frac{\not{p}_b - \not{q} + m_c}{(p_b-q)^2 - m_c^2 + i\epsilon}\,\gamma^\nu(1-\gamma^5)b\,. \tag{108}$$

We now write

$$\begin{aligned} p_b^\mu &= m_b v^\mu + k^\mu = m_b(v^\mu + \hat{k}^\mu) \\ \hat{q}^\mu &= q^\mu/m_b \\ \hat{m}_c &= m_c/m_b \\ b(x) &= e^{-im_b v\cdot x}\,h_v(x) + O(1/m_b)\,, \end{aligned} \tag{109}$$

and expand in powers of $1/m_b$. Since the operator product expansion is in terms of the effective field h_v, a factor of k^μ corresponds to an insertion of the covariant derivative iD^μ. Operator ordering ambiguities are to be resolved by considering graphs with external gluon fields.

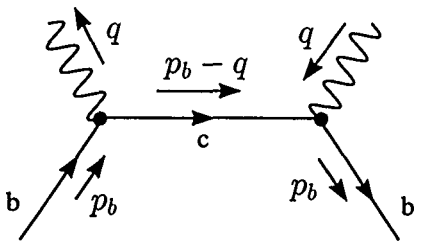


Figure 6: The operator product expansion at tree level.

As an example of the procedure, let us expand the propagator to order $1/m_b^2$. (There are also corrections to the currents at this order, which are included in a full calculation.) It is convenient to define the scaled hadronic invariant mass,

$$\hat{s} = (p_b - q)^2/m_b^2 = 1 - 2v\cdot\hat{q} + \hat{q}^2\,. \tag{110}$$

Then we find a contribution to $T^{\mu\nu}$ of the form

$$T^{\mu\nu} = \frac{1}{m_b}\,\bar{h}_v\gamma^\mu(\not{p} - \not{q})\gamma^\nu(1-\gamma^5)\left[\frac{1}{\hat{s}-\hat{m}_c^2+i\epsilon} + \frac{2\hat{k}\cdot\hat{q} - \hat{q}^2}{(\hat{s}-\hat{m}_c^2+i\epsilon)^2} + \ldots\right] h_v + \ldots\,. \tag{111}$$

From this expression, we can read off the operators which appear in the operator product expansion. Since

$$\mathrm{Im}\,\frac{1}{(\hat{s}-\hat{m}_c^2+i\epsilon)^n} \propto \delta^{(n-1)}(\hat{s}-\hat{m}_c^2)\,, \tag{112}$$

we see that the effect of taking the imaginary part in each term is to put the charm quark on its mass shell. The leading term is a quark bilinear,

$$\frac{1}{m_b}\,\bar{h}_v\gamma^\mu(\not{p} - \not{q})\gamma^\nu(1-\gamma^5)h_v\,. \tag{113}$$

It is straightforward to compute its matrix element in the HQET using the trace formalism,

$$\begin{aligned} &\langle B|\,\bar{h}_v\gamma^\mu(\not{p} - \not{q})\gamma^\nu(1-\gamma^5)h_v\,|B\rangle \\ &\qquad = 2m_B\,(2v^\mu v^\nu - g^{\mu\nu} - v^\mu\hat{q}^\nu - v^\nu\hat{q}^\mu + g^{\mu\nu}\,v\cdot\hat{q} + \ldots)\,. \end{aligned} \tag{114}$$

The ellipses denote terms of order $1/m_b^2$; there are no corrections of order $1/m_b$, by Luke's Theorem. Finally, we contract the tensor $T^{\mu\nu}$ with $L_{\mu\nu}$ and perform the phase space integration [Eq. (99)]. In the end, the result is the same as we would have gotten directly by computing free quark decay.

Of course, if we only intended to reproduce the free quark decay result, we would never have introduced so much new formalism. The value of the HQET framework is that it allows us to go beyond leading order and compute the next terms in the series in $1/m_b^n$. For example, consider the operators induced by the expansion of the propagator (111). The correction of order $1/m_b$ comes from the operator

$$\frac{1}{m_b^2}\,\frac{2}{(\hat{s}-\hat{m}_c^2+i\epsilon)^2}\,\bar{h}_v\gamma^\mu(\not{p} - \not{q})\gamma^\nu(1-\gamma^5)\hat{q}\cdot iD\,h_v\,. \tag{115}$$

However, the matrix element of this operator is of the form

$$\langle B|\,\bar{h}_v \Gamma^\alpha(v,q)\, iD_\alpha\, h_v\,|B\rangle\,, \tag{116}$$

which, as we have seen, vanishes by the classical equation of motion. In fact, since all $1/m_b$ corrections, from any source, have a single covariant derivative, they all vanish in the same way. This is the analogue of Luke's Theorem for inclusive decays.[32] The correction of order $1/m_b^2$ in Eq. (111) is

$$-\frac{1}{m_b^3}\,\frac{1}{(\hat{s}-\hat{m}_c^2+i\epsilon)^2}\,\bar{h}_v\gamma^\mu(\not{p}-\not{q})\gamma^\nu(1-\gamma^5)(iD)^2\,h_v\,. \tag{117}$$

The matrix element of this operator is related by the heavy quark symmetry to λ_1, the expectation value of $\mathcal{O}_K$. The full expansion of $T^{\mu\nu}$ also induces operators with explicit factors of the gluon field, whose matrix elements are related to λ_2.

We now present the result for the inclusive semileptonic decay rate, up to order $1/m_b^2$ in the heavy quark expansion, and with the complete radiative correction of order α_s. We also include that part of the two-loop correction which is proportional to $\beta_0\alpha_s^2$. Since $\beta_0 \approx 9$, perhaps this term dominates the two-loop result. In any case, it is interesting for other reasons, as we will see below.

Let us first consider the decay $B \to X_u\,\ell\bar{\nu}$, for which the decay rate simplifies since $m_u = 0$. We find[33,34,36,37,40]

$$\begin{aligned}\Gamma(B\to X_u\,\ell\bar{\nu}) = \frac{G_F^2|V_{ub}|^2}{192\pi^3}\,m_b^5\Bigg[1 \;&+\; \left(\frac{25}{6}-\frac{2\pi^2}{3}\right)\frac{\alpha_s(m_b)}{\pi} \\ &-\; (2.98\beta_0 + C_u)\left(\frac{\alpha_s(m_b)}{\pi}\right)^2 + \ldots \\ &+\; \frac{\lambda_1 - 9\lambda_2}{2m_b^2} + \ldots\Bigg]\,.\end{aligned} \tag{118}$$

When we include the charm mass, it is convenient to write the unknown quark masses in terms of the measured meson masses and the parameters of the HQET. In terms of the spin averaged mass $\overline{m}_B = (m_B + 3m_{B^*})/4$, we have

$$m_b = \overline{m}_B - \bar{\Lambda} + \frac{\lambda_1}{2m_B} + \ldots\,, \tag{119}$$

and analogously for m_c. We then find[33,34,38,39]

$$\begin{aligned}\Gamma(B\to X_c\,\ell\bar{\nu}) = \frac{G_F^2|V_{cb}|^2}{192\pi^3}\,m_B^5 \times 0.369\Bigg[1 &- 1.54\frac{\alpha_s(m_b)}{\pi} \\ &- (1.43\beta_0 + C_c)\left(\frac{\alpha_s(m_b)}{\pi}\right)^2 + \ldots \\ &- 1.65\frac{\bar{\Lambda}}{m_B}\left(1 - 0.87\frac{\alpha_s(m_b)}{\pi}\right) \\ &- 0.95\frac{\bar{\lambda}^2}{m_B^2} - 3.18\frac{\lambda_1}{m_B^2} + 0.02\frac{\lambda_2}{m_B^2} + \ldots\Bigg]\,.\end{aligned} \tag{120}$$

All the coefficients which appear in this expression are known functions of $\overline{m}_D/\overline{m}_B$ and are evaluated at the physical point $\overline{m}_D/\overline{m}_B = 0.372$. In both $B \to X_u\,\ell\bar{\nu}$ and $B \to X_c\,\ell\bar{\nu}$, the power corrections proportional to λ_1 and λ_2 are numerically small, at the level of a few percent.

4.2 Renormalons and the Pole Mass

The inclusive decay rate depends on the heavy quark mass m_b, either explicitly, as in Eq. (118), or implicitly through $\bar{\Lambda}$, as in Eq. (120). At tree level, m_b is just the coefficient of the $\bar{b}\,b$ term in the QCD Lagrangian, but beyond that, we are faced with the question of what exactly we mean by m_b. Should we take an $\overline{\rm MS}$ mass, such as $\overline{m}_b(m_b)$? Or should we take the pole mass $m_b^{\rm pole}$, or maybe some other quantity? The various prescriptions for m_b can vary by hundreds of MeV, and since the total rate is proportional to m_b^5, the question is of practical importance if we hope to make accurate phenomenological predictions.

At a fixed order in QCD perturbation theory, the answer is clear. The heavy quark masses which appear come from poles in quark propagators, so we should take $m_b^{\rm pole}$ (and $m_c^{\rm pole}$). This is also the prescription for the mass which cancels out the on-shell part of the heavy quark field in the construction of $\mathcal{L}_{\rm HQET}$. Hence, the difference of heavy quark pole masses is known quite well,

$$\begin{aligned} m_b^{\rm pole} - m_c^{\rm pole} &= \left(\overline{m}_B - \bar{\Lambda} + \frac{\lambda_1}{2m_B} + \ldots\right) - \left(\overline{m}_D - \bar{\Lambda} + \frac{\lambda_1}{2m_D} + \ldots\right) \\ &= 3.34\,{\rm GeV} + O(\Lambda_{\rm QCD}^2/m_Q^2)\,. \end{aligned} \tag{121}$$

Since $\Gamma(B \to X_c\,\ell\bar{\nu})$ depends approximately as $m_b^2(m_b - m_c)^3$, the uncertainty due to quark mass dependence is reduced.

The problem, of course, is that there is no sensible nonperturbative definition of $m_b^{\rm pole}$, since due to confinement, there is no actual pole in the quark propagator. Hence, a direct experimental determination of a value for $m_b^{\rm pole}$ to insert into the theoretical expressions Eq. (118) and Eq. (120) is not possible. How, then, can we do phenomenology?

One approach would be to define $m_b^{\rm pole}$ to be the pole mass as computed in perturbation theory, truncate at some order, and then estimate the theoretical error from the uncomputed higher order terms. However, it turns out that even *within* perturbation theory, the concept of a quark pole mass is ambiguous. Consider a particular class of diagrams which contribute to $m_b^{\rm pole}$, shown in Fig. 7. The perturbation theory is developed as an expansion in the small parameter $\alpha_s(m_b)$, so we hope that it will be well-behaved. Each of the bubbles represents an insertion of the gluon self-energy, which is proportional at lowest order to $\alpha_s(m_b)\beta_0$. Of course, the infinite sum of the graphs in Fig. 7 can be absorbed into the one-loop graph, with a compensating change in the coupling from $\alpha_s(m_b)$ to $\alpha_s(q)$, where q is the loop momentum. The result is an expansion for $m_b^{\rm pole}$ of the form

$$m_b^{\rm pole} = \overline{m}_b(m_b)\Big[1 + a_1\alpha_s(m_b) + (a_2\beta_0 + b_2)\alpha_s^2(m_b) + (a_3\beta_0^2 + b_3\beta_0 + c_3)\alpha_x^3(m_b) + \ldots\Big]. \qquad (122)$$

The graphs in Fig. 7 contribute the terms proportional to $\alpha_s^{n+1}(m_b)\beta_0^n$. Since $\beta_0 \approx 9$, these terms are "intrinsically" larger than ones with fewer powers of β_0, and we might hope that their sum approximates the full series. However, it is important to realize that the only limit of QCD in which such terms actually dominate is that of a large number of light quark flavors, in which case the sign of β_0 is opposite to that of QCD. Although this is a physical limit of an Abelian theory, we are certainly not close to that limit here. The ansatz of keeping only the terms proportional to $\alpha_s^{n+1}(m_b)\beta_0^n$ is known as "naive non-Abelianization" (NNA).[41]

What is most interesting about the series of terms shown in Fig. 7,

$$\sum a_n \alpha_s^n(m_b)\beta_0^{n-1}, \qquad (123)$$

is that it does not converge. Already in the graphs kept in the NNA ansatz, we are sensitive to the fact that QCD is an asymptotic, rather than a convergent expansion. For large n, the coefficients a_n diverge as $n!$, much stronger than any

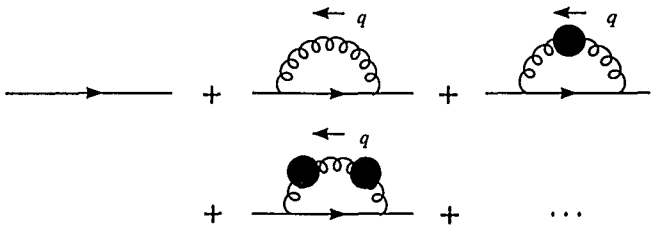


Figure 7: The radiative corrections to $m_b^{\rm pole}$ of order $\alpha_s(m_b)^{n+1}\beta_0^n$.

convergence due to the powers $\alpha_s^n(m_b)$. The series can only be made meaningful if this divergence is subtracted. As with many subtraction prescriptions, there is a residual finite ambiguity.[§] This ambiguity, known as an "infrared renormalon," leads to an ambiguity in the pole mass of order[41–43]

$$\delta m_b^{\rm pole} \sim 100\,{\rm MeV}. \qquad (124)$$

By the definition [Eq. (78)], $\bar{\Lambda}$ also inherits this ambiguity.

The expressions Eq. (118) and Eq. (120) are plagued by two problems. The first is the renormalon ambiguity in $m_b^{\rm pole}$ and $\bar{\Lambda}$. The second is that the perturbative expansion for the rate Γ is itself divergent, and *also* has an infrared renormalon. In the expansion

$$\Gamma = \Gamma_0\left[\sum a'_n \alpha_s^n(m_b)\beta_0^{n-1} + (\text{power corrections})\right], \qquad (125)$$

the coefficients a'_n also diverge as $n!$ However, it turns out that these two problems actually cure each other, because the infrared renormalons in $m_b^{\rm pole}$ and in the perturbation series for Γ cancel.[42,44] We can exploit this cancellation to improve the predictive power of the theoretical computation of the rate. Without this improvement, the infrared renormalons render the expressions Eq. (118) and Eq. (120) of dubious phenomenological utility.

The most reliable approach, theoretically, is to eliminate $m_b^{\rm pole}$ or $\bar{\Lambda}$ explicitly from the rate by computing and measuring another quantity which also depends on it. For example, let us consider the charmless decay rate $\Gamma(B \to X_u\,\ell\bar{\nu})$ and

[§] In a formal treatment, this ambiguity arises from a choice of contour in the Borel plane.

the average invariant mass $\langle s_H \rangle$ of the hadrons produced in the decay. Each of these expressions suffers from a poorly behaved perturbation series in the NNA approximation. Ignoring terms of relative order $1/m_b^2$ and writing the rate in terms of $\bar{\Lambda}$ instead of $m_b^{\rm pole}$, we find to five-loop order,[41]

$$\begin{aligned}\Gamma &= \frac{G_F^2|V_{ub}|^2}{192\pi^3} m_B^5 \Big[1 - 2.41\frac{\alpha_s}{\pi} - 2.98\left(\frac{\alpha_s}{\pi}\right)^2\beta_0 - 4.43\left(\frac{\alpha_s}{\pi}\right)^3\beta_0^2 \\ &\qquad - 7.67\left(\frac{\alpha_s}{\pi}\right)^4\beta_0^3 - 15.7\left(\frac{\alpha_s}{\pi}\right)^5\beta_0^4 + \ldots - 5\frac{\bar{\Lambda}}{m_B} + \ldots\Big] \\ &= \frac{G_F^2|V_{ub}|^2}{192\pi^3} m_B^5 \left[1 - 0.061 - 0.120 - 0.107 - 0.111 - 0.136 + \ldots \right. \\ &\qquad \left. - 5\bar{\Lambda}/m_B + \ldots\right], \end{aligned} \tag{126}$$

for $\alpha_s(m_b) = 0.21$ and $\beta_0 = 9$. As we see, not only does the perturbation series fail to converge, it does not even have an apparent smallest term, where one should truncate to minimize the error of the asymptotic series. The series for $\langle s_H \rangle$ exhibits a similar behavior,[40]

$$\begin{aligned}\langle s_H \rangle &= m_B^2\Big[0.20\frac{\alpha_s}{\pi} + 0.35\left(\frac{\alpha_s}{\pi}\right)^2\beta_0 + 0.64\left(\frac{\alpha_s}{\pi}\right)^3\beta_0^2 + 1.29\left(\frac{\alpha_s}{\pi}\right)^4\beta_0^3 \\ &\qquad + 2.95\left(\frac{\alpha_s}{\pi}\right)^5\beta_0^4 + \ldots + \frac{7}{10}\frac{\bar{\Lambda}}{m_B} + \ldots\Big] \\ &= m_B^2\left[0.0135 + 0.0141 + 0.0156 + 0.0189 + 0.0261 + \ldots \right. \\ &\qquad \left. - 7\bar{\Lambda}/10m_B + \ldots\right]. \end{aligned} \tag{127}$$

However, the situation improves dramatically if we eliminate $\bar{\Lambda}$ and write Γ directly in terms of $\langle s_H \rangle$,

$$\Gamma = \frac{G_F^2|V_{ub}|^2 m_B^5}{192\pi^3}\left[1 - 7.14\frac{\langle s_H\rangle}{m_B^2} - 0.064 - 0.020 - 0.0002 - 0.022 - 0.047 + \ldots\right]. \tag{128}$$

By truncating this series at its smallest term, 0.0002, we obtain a new expression in which the theoretical errors are under control. The price is that we must now measure a second quantity, $\langle s_H \rangle$, in the same decay.

An analogous approach works for inclusive decays to charm, in which case the new quantity which we must measure is $\langle s_H - \overline{m}_D^2 \rangle$. Let us apply this analysis to the extraction of V_{cb} from the inclusive decay $B \to X_c \ell\bar{\nu}$. Eliminating $\bar{\Lambda}$ as before, we find[40]

$$\begin{aligned}\Gamma(B \to X_c\ell\nu) &= \frac{G_F^2|V_{cb}|^2}{192\pi^3} m_B^5 \times 0.369\Big[1 - 1.17\frac{\alpha_s(m_b)}{\pi} - 0.74\beta_0\frac{\alpha_s^2(m_b)}{\pi^2} \\ &\qquad - 7.17\frac{\langle s_H - \overline{m}_D^2\rangle}{m_B^2} + \ldots\Big], \end{aligned} \tag{129}$$

plus small terms of order $\lambda_{1,2}/m_B^2$. The current data on $\langle s_H - \overline{m}_D^2 \rangle$ are still inconclusive, but they will improve in the future. As an illustration of the utility of the method, however, let us consider the physical limit $\langle s_H - \overline{m}_D^2 \rangle \geq 0$. In that case, we can already obtain the bound

$$V_{cb} \geq 0.037 \times \left(\frac{\tau_B}{1.54\ {\rm ps}}\right)^{-1/2}, \tag{130}$$

where we have used the observed B semileptonic branching ratio of 10.7%. As the data on $\langle s_H - \overline{m}_D^2 \rangle$ improve, so will this bound. Note that it is entirely consistent with the value [Eq. (92)] obtained from exclusive decays.

An alternative approach is to express the width Γ in terms of the running mass $\overline{m}_b(m_b)$ instead of another inclusive observable.[42,45] Since the $\overline{\rm MS}$ mass is a short-distance quantity, this also eliminates the infrared renormalon, which is associated with long-distance physics. However, from a phenomenological point of view, it begs the question of how the running mass is to be determined from experiment. Possibilities include quarkonium spectroscopy, QCD sum rules, and lattice calculations, but in all of these cases, it is unclear both how to determine reliably the accuracy of the method, and how to deal with renormalon ambiguities in a manner that is *consistent* with their treatment in the calculation of Γ. With additional progress, however, such an approach might eventually prove fruitful.

5 Heavy Hadron Production in Fragmentation

So far, we have applied the idea of heavy quark symmetry to heavy hadron spectroscopy and to heavy hadron decay. We can also apply it to heavy hadron production via fragmentation. Although there is not yet available the wealth of detailed data for production processes that there is for spectroscopy and decays,

the study of heavy quark fragmentation is an elegant application of the heavy quark limit in a new regime.[46]

5.1 The Physics of Heavy Quark Fragmentation

The production of a heavy hadron proceeds in two steps. First, the heavy quark itself must be created; because of its large mass, this process takes place over a time scale τ_Q which is very short, $\tau_Q \leq 1/m_Q$. Second, some light degrees of freedom assemble themselves about the heavy quark to make a color-neutral heavy hadron, a process which involves nonperturbative strong interactions and typically takes much longer, $\tau_F \sim 1/\Lambda_{\rm QCD} \gg \tau_Q$. If the heavy quark is produced with a large velocity in the center-of-mass frame, and if there is plenty of available energy, then production of these light degrees of freedom will be local in phase space and independent of the initial state. This is the fragmentation regime. We will see that heavy quark symmetry simplifies the description of heavy hadron production via fragmentation, because, as before, it allows us to separate certain properties of the heavy quark from those of the light degrees of freedom. This is particularly important in the production of excited heavy hadrons, for which the behavior of the spin of the light degrees of freedom can be quite interesting.

Heavy quark symmetry simplifies the picture of fragmentation in several ways. First, since the fragmentation process involves the exchange only of soft momenta, the velocity v^μ of the hadron H_Q which is produced is the same as the velocity of the heavy quark Q. Second, the angular momenta S_Q and J_ℓ of the heavy quark and the light degrees of freedom are well-defined and can be followed individually through the processes of production and decay. Third, the typical precession time τ_S of S_Q and J_ℓ about each other is of order $\tau_S \sim m_Q/\Lambda_{\rm QCD}^2 \gg 1/\Lambda_{\rm QCD}$, since the precession is induced by the chromomagnetic interaction. Hence, $\tau_S \gg \tau_F$, and during the fragmentation process, S_Q can essentially be taken to be frozen in direction.

Suppose that Q fragments initially to a state with light degrees of freedom with spin J_ℓ. This could correspond to two possible hadronic states: H_Q, with spin $J = J_\ell - \frac{1}{2}$, or H_Q^*, with spin $J = J_\ell + \frac{1}{2}$. Let the states $H_Q^{(*)}$ have lifetime τ. How should we treat the interaction of S_Q with J_ℓ?

The answer depends critically on the relationship of τ to the precession time τ_S. While the order of magnitude of τ_S is essentially fixed at $m_Q/\Lambda_{\rm QCD}^2$, the lifetime τ can vary widely, depending on the channel in which $H_Q^{(*)}$ primarily decays. Of course, if $H_Q^{(*)}$ decays weakly, then $\tau \gg \tau_S$. But if $H_Q^{(*)}$ decays strongly, then τ depends critically on the phase space available for the transition. In the absence of phase space factors, $\tau \sim 1/\Lambda_{\rm QCD} \ll \tau_S$. But since the pion, the lightest hadron, is not massless, it is possible to have a situation where an allowed strong decay is either forbidden by phase space (as with $B^* \to B + \pi$) or severely suppressed (as with $D^* \to D + \pi$).

The treatment of a given hadron doublet depends on the relative size of τ and τ_S. Let us consider the two extreme possibilities. The first corresponds to a strong decay with plenty of phase space, so $\tau_S \gg \tau$. Here, H_Q and H_Q^* are formed and then decay before the angular momenta S_Q and J_ℓ have a chance to interact. The fact that there is no precession means that there is no change in the orientation of S_Q and J_ℓ. If, for example, either spin was polarized before or during the fragmentation process, this polarization would be undisturbed by passing through the resonance $H_Q^{(*)}$. The strong decay of the heavy hadron then would reflect the orientation of the light degrees as they were produced.

Note that it is the very same spin exchange interaction which is inhibited here which is responsible for the splitting Δ_H between H_Q and H_Q^*. Hence, under these conditions, the resonances are almost completely *overlapping*, with widths $\Gamma = 1/\tau$ satisfying $\Gamma \gg \Delta_H$. This is another consequence of the effective decoupling of S_Q and J_ℓ, which are independent good quantum numbers of the resonances. It also provides a convenient criterion for determining directly whether we are in the regime $\tau_S \gg \tau$: we cannot distinguish separate resonances for H_Q and H_Q^*.

The second possibility is the opposite extreme, $\tau_s \ll \tau$. This corresponds to heavy hadrons which decay weakly or electromagnetically, or to strong decays which are severely suppressed by phase space. Here the spins S_Q and J_ℓ have plenty of time to interact, precessing about each other many times before H_Q and H_Q^* decay. There is at least a partial degradation of any initial polarization of S_Q, as well as a degradation of any information about the fragmentation process which may be carried by the light degrees of freedom. The signature of this situation is that the states H_Q and H_Q^* are well-separated resonances, since the chromomagnetic interactions have ample opportunity to produce a hyperfine splitting much larger than the width, $\Delta_H \gg \Gamma$. In contrast with the first case, here the heavy and light spins are resolved into states of definite total spin $J = |J_\ell \pm \frac{1}{2}|$. This resolution destroys information about the individual angular momenta S_Q and J_ℓ,

and the decays of H_Q and H_Q^* only partially reflect the features of the production process.

5.2 Production and Decay of D_1 and D_2^*

We will illustrate these ideas with two examples. The first concerns the production and decay of the excited charmed mesons D_1 and D_2^*. These are states with light degrees of freedom with angular momentum and parity $J_\ell^P = \frac{3}{2}^+$; in the quark model, this would correspond to a light antiquark with a unit of orbital angular momentum. The physical states are the D_1, with mass 2423 MeV and width 18 MeV, and the D_2^*, with mass 2458 MeV and width 21 MeV. The splitting between them is 35 MeV; although this is not much larger than the individual widths, for simplicity, we will treat them in this limiting case $\tau \gg \tau_S$.

Let us review the sequence of events. First, the charm quark is created in some hard interaction, with a time scale $\tau_c \sim 1/m_c$. Second, light degrees of freedom with $J_\ell = \frac{3}{2}$ are created in a fragmentation process, over a time $\tau_F \sim 1/\Lambda_{\rm QCD}$, forming a color-neutral charmed hadron. Third, the angular momenta S_c and J_ℓ precess about each other, resolving the individual D_1 and D_2^* states, which requires a time $\tau_S \sim m_c/\Lambda_{\rm QCD}^2$. Then, finally, after a time τ greater than $m_c/\Lambda_{\rm QCD}^2$, the D_1 or D_2^* emits a pion and decays to a D or D^*. One question we might ask about this process is, what is the alignment of the light degrees of freedom produced in the fragmentation? Of course, the answer depends on nonperturbative QCD and is difficult to calculate from first principles. Still, we can explore the question experimentally.

Since the total angular momentum of the light degrees of freedom is $J_\ell = \frac{3}{2}$, they can be produced with helicity $h = \pm\frac{3}{2}$ or $h = \pm\frac{1}{2}$ along the fragmentation axis. While parity invariance of the strong interactions requires that the probabilities for helicities h and $-h$ are identical, the relative production of light degrees of freedom with $|h| = \frac{3}{2}$ versus $|h| = \frac{1}{2}$ is determined in some complicated way by nonperturbative dynamics. Let the quantity $w_{3/2}$ denote the probability that $|h| = \frac{3}{2}$,

$$w_{3/2} = P(h = \tfrac{3}{2}) + P(h = -\tfrac{3}{2}) . \qquad (131)$$

Then $1 - w_{3/2}$ is the probability that $|h| = \frac{1}{2}$. Completely isotropic production corresponds to $w_{3/2} = \frac{1}{2}$. The observable $w_{3/2}$ is a new nonperturbative parameter of QCD, which is well-defined only in the heavy quark limit.

This new parameter can be measured directly in the strong decay of the D_2^* or D_1. For example, consider the angular distribution of the pion with respect to the fragmentation axis in the decay $D_2^* \to D + \pi$. This is a decay of the light degrees of freedom in the excited hadron, so it will depend on their initial orientation (that is, on $w_{3/2}$) and on the details of the precession of J_ℓ around S_Q during the lifetime of the D_2^*. Following the direction of J_ℓ through the sequence of fragmentation, precession, and decay, we find the distribution[46]

$$\frac{1}{\Gamma}\frac{d\Gamma}{d\cos\theta} = \tfrac{1}{4}\left[1 + 3\cos^2\theta - 6w_{3/2}(\cos^2\theta - \tfrac{1}{3})\right] . \qquad (132)$$

This distribution is isotropic only when $w_{3/2} = \frac{1}{2}$, that is, when the light degrees of freedom are produced isotropically in the fragmentation process. Similar distributions are found in the decays $D_2^* \to D^* + \pi$ and $D_1 \to D^* + \pi$.

A fit of ARGUS data[47] to the expression Eq. (132) seems to indicate that a small value of $w_{3/2}$ is preferred; while the errors are large, we find that $w_{3/2} < 0.24$ at the 90% confidence level. It would be nice to confirm this result with a sharper measurement, and not only for the charmed mesons but in the bottom system as well. Since $w_{3/2}$ is intrinsically nonperturbative, we do not have any real theoretical understanding of why it should be small, although one can construct a qualitative understanding based on a string picture of fragmentation.[48]

5.3 Polarization of Λ_b at SLC/LEP

The second example springs from a practical question: What is the polarization of Λ_b baryons produced at the Z pole? This question is motivated by the fact that b quarks produced in the decay of the Z are 94% polarized left-handed. Since the Λ_b is composed of a b quark and light degrees of freedom with $J_\ell = 0$, the orientation of a Λ_b is identical to the orientation of the b quark inside it. Similarly, the b quark spin does not precess inside a Λ_b. Hence, if a b quark produced at the Z fragments to a Λ_b, then those baryons should inherit the left-handed polarization of the quarks and reveal it in their weak decay.

Unfortunately, life is not that simple. Two recent measurements of Λ_b polarization $P(\Lambda_b)$ from LEP are[49,50]

$$\begin{aligned} \text{DELPHI}: &\quad 0.08\,{}^{+0.35}_{-0.29}(\text{stat.})\,{}^{+0.18}_{-0.16}(\text{syst.}) \\ \text{ALEPH}: &\quad 0.26\,{}^{+0.20}_{-0.25}(\text{stat.})\,{}^{+0.12}_{-0.13}(\text{syst.}) , \end{aligned}$$

both a long way from $P(\Lambda_b) = 0.94$. The reason is that not all b quarks which wind up as Λ_b baryons get there directly. There is a competing process, in which they fragment first to the excited baryons Σ_b and Σ_b^*, which then decay to Λ_b via pion emission. These new states have light degrees of freedom with $J_\ell = 1$. If they have a lifetime $\tau > \tau_S$, then the b quark will have time to precess about J_ℓ and its polarization will be degraded. The result will be a net sample of Λ_b's with a polarization less than 94%, as is in fact observed.

In addition to the requirement that $\tau > \tau_S$ for the $\Sigma_b^{(*)}$, any depolarization of Λ_b's by this mechanism depends on two unknown quantities. First, there is the production rate f of $\Sigma_b^{(*)}$ relative to Λ_b. Isospin and spin counting enhance f by a factor of nine, while the mass splitting between $\Sigma_b^{(*)}$ and Λ_b suppresses it; studies based on the Lund Monte Carlo [51] indicate $f \approx 0.5$ with a very large uncertainty. Of course, it would be preferable to measure f directly. Second, there is the orientation of the spin J_ℓ with respect to the fragmentation axis. This orientation, which is nonperturbative in origin, allows the helicities $h = 1, 0, -1$. By analogy with the treatment of the D_1 and D_2^*, let us define

$$w_1 = P(h = 1) + P(h = -1) . \tag{133}$$

In this case, isotropic production corresponds to $w_1 = \frac{2}{3}$. We may measure w_1 from the angle of the pion with respect to the fragmentation axis in the decay $\Sigma_b^* \to \Lambda_b + \pi$ (Ref. 46),

$$\frac{1}{\Gamma}\frac{d\Gamma}{d\cos\theta} = \tfrac{1}{4}\left[1 + 3\cos^2\theta - \tfrac{9}{2}w_1(\cos^2\theta - \tfrac{1}{3})\right] . \tag{134}$$

It turns out that the decay $\Sigma_b \to \Lambda_b + \pi$ is isotropic in $\cos\theta$ for any value of w_1.

The polarization retention of the Λ_b may be computed in terms of f and w_1. As before, we will consider the simpler situation in which the Σ_b and the Σ_b^* do not overlap, so $\tau \gg \tau_S$. Then the polarization of the observed Λ_b's is $P(\Lambda_b) = R(f, w_1)P(b)$, where $P(b) = 94\%$ is the initial polarization of the b quarks, and[46]

$$R(f, w_1) = \frac{1 + \frac{1}{9}(1 + 4w_1)f}{1 + f} . \tag{135}$$

Note that for $f = 0$ (no $\Sigma_b^{(*)}$'s are produced), $R(0, w_1) = 1$ and there is no depolarization. For the Lund value $f = 0.5$, R ranges between 0.70 and 0.85 for $0 \le w_1 \le 1$.

Can the very low measured values of $P(\Lambda_b)$ be accommodated by the present data on the $\Sigma_b^{(*)}$? The situation is still unclear, because not much is known about the Σ_b and Σ_b^* states. DELPHI[52] has reported the observation of these states, but with masses which deviate significantly from those that one would expect based on heavy quark symmetry and the observed Σ_c and Σ_c^* (Ref. 54). Along with the masses, DELPHI also reports $w_1 \approx 0$ and $1 < f < 2$. If this is confirmed, then a polarization in the range $P(\Lambda_b) \approx 40\% - 50\%$ is easy to accommodate. On the other hand, the CLEO analysis[53] of the decay of the Σ_c^* yields $w_1 = 0.71 \pm 0.13$, consistent with isotropic fragmentation. Recall that by heavy quark symmetry, w_1 measured in the charm and bottom systems must be the same, so this result is inconsistent with the report from DELPHI. Clearly, further measurements are needed to resolve this situation.

6 Concluding Remarks

Unfortunately, we have had time in these lectures only to introduce a very few of the many applications of heavy quark symmetry and the HQET to the physics of heavy hadrons. Since its development less than ten years ago, it has become one of the basic tools of QCD phenomenology. Much of the popularity and utility of the HQET certainly come from its essential simplicity. The elementary observation that the physics of heavy hadrons can be divided into interactions characterized by short and long distances gives us immediately a clear and compelling intuition for the properties of heavy-light systems. The straightforward manipulations which lead to the HQET then allow this intuition to form the basis for a new systematic expansion of QCD. The deeper understanding of heavy hadrons which we thereby obtain will become increasingly important as the end of the second millenium approaches and the B Factory Era begins.

Acknowledgments

I would like to thank the organizers of the Summer Institute for the opportunity to present these lectures, and for arranging a most interesting and pleasant summer school. This work was supported by the National Science Foundation under Grant No. PHY-9404057 and National Young Investigator Award No. PHY-9457916, by

the Department of Energy under Outstanding Junior Investigator Award No. DE-FG02-94ER40869, and by the Alfred P. Sloan Foundation.

References

[1] H. Georgi in *Proceedings of TASI-91,* edited by R. K. Ellis *et al.* (World Scientific, Singapore, 1991); B. Grinstein in *High Energy Phenomenology,* edited by R. Huerta and M. A. Peres (World Scientific, Singapore, 1991); N. Isgur and M. B. Wise in *Heavy Flavors,* edited by A. Buras and M. Lindner (World Scientific, Singapore, 1992); T. Mannel in *QCD – 20 Years Later,* edited by P. Zerwas and H. Kastrup (World Scientific, Singapore, 1993); M. Neubert, Phys. Rep. **245**, 259 (1994); M. Shifman, preprint TPI-MINN-95-31-T, to appear in *QCD and Beyond, Proceedings of TASI-95.*

[2] For example, see M. Wirbel, B. Stech, and M. Bauer, Z. Phys. C **29**, 637 (1985); J. G. Körner and G. A. Schuler, Z. Phys. C **38**, 511 (1988); N. Isgur, D. Scora, B. Grinstein, and M. B. Wise, Phys. Rev. D **39**, 799 (1989).

[3] N. Isgur and M. B. Wise, Phys. Lett. B **232**, 113 (1989); Phys. Lett. B **237**, 527 (1990).

[4] M. B. Voloshin and M. A. Shifman, Yad. Fiz. **45**, 463 (1987); Yad. Fiz. **47**, 511 (1988).

[5] S. Nussinov and W. Wetzel, Phys. Rev. D **36**, 130 (1987).

[6] H. D. Politzer and M. B. Wise, Phys. Lett. B **206**, 681 (1988); Phys. Lett. B **208**, 504 (1988).

[7] E. V. Shuryak, Phys. Lett. B **93**, 134 (1980).

[8] E. Eichten and B. Hill, Phys. Lett. B **234**, 511 (1990); Phys. Lett. B **243**, 427 (1990).

[9] H. Georgi, Phys. Lett. B **240**, 447 (1990).

[10] B. Grinstein, Nucl. Phys. B **339**, 253 (1990).

[11] A. F. Falk, H. Georgi, B. Grinstein, and M. B. Wise, Nucl. Phys. B **343**, 1 (1990).

[12] A. F. Falk and B. Grinstein, Phys. Lett. B **247**, 406 (1990).

[13] M. Luke, Phys. Lett. B **252**, 247 (1990).

[14] A. F. Falk, B. Grinstein, and M. Luke, Nucl. Phys. B **357**, 185 (1991).

[15] T. Mannel, W. Roberts, and Z. Ryzak, Nucl. Phys. B **355**, 38 (1991).

[16] H. D. Politzer, Nucl. Phys. B **172**, 349 (1980).

[17] A. F. Falk and M. Neubert, Phys. Rev. D **47**, 2965 (1993).

[18] A. F. Falk, M. Luke, and M. J. Savage, Phys. Rev. D **49**, 3367 (1994).

[19] A. F. Falk, Nucl. Phys. B **378**, 79 (1992).

[20] P. Cho and B. Grinstein, Phys. Lett. B **285**, 153 (1992).

[21] M. Neubert and V. Rieckert, Nucl. Phys. B **382**, 97 (1992).

[22] M. Neubert, Phys. Lett. B **264**, 455 (1991).

[23] M. A. Shifman, N. G. Uraltsev, and A. I. Vainshtein, Phys. Rev. D **51**, 2217 (1995); Erratum, D **52**, 3149 (1995).

[24] M. Neubert, Phys. Lett. B **338**, 84 (1994).

[25] A. Czarnecki, Phys. Rev. Lett. **76**, 4124 (1996).

[26] For earlier one-loop and one-loop improved calculations, see A. F. Falk and B. Grinstein, Phys. Lett. B **247**, 406 (1990); Phys. Lett. B **249**, 314 (1990); M. Neubert, Phys. Rev. D **46**, 2212 (1992); Phys. Rev. D **51**, 5924 (1995); Phys. Lett. B **341**, 367 (1995).

[27] D. Buskulic *et al.* (ALEPH Collaboration), Phys. Lett. B **359**, 236 (1995).

[28] H. Albrecht *et al.* (ARGUS Collaboration), Z. Phys. C **57**, 533 (1993).

[29] B. Barish *et al.* (CLEO Collaboration), Phys. Rev. D **51**, 1041 (1995).

[30] P. Abreu *et al.* (DELPHI Collaboration), CERN report CERN-PPE/96-11 (1996).

[31] M. Neubert, Int. J. Mod. Phys. A **11**, 4173 (1996).

[32] J. Chay, H. Georgi, and B. Grinstein, Phys. Lett. B **247**, 399 (1990).

[33] I. I. Bigi, N. G. Uraltsev, and A. I. Vainshtein, Phys. Lett. B **293**, 430 (1992); I. I. Bigi, M. A. Shifman, N. G. Uraltsev, and A. I. Vainshtein, Phys. Rev. Lett. **71**, 496 (1993).

[34] A. V. Manohar and M. B. Wise, Phys. Rev. D **49**, 1310 (1994).

[35] A. Falk, I. Dunietz, and M. B. Wise, Phys. Rev. D **51**, 1183 (1995).

[36] B. Guberina, R. D. Peccei, and R. Ruckl, Nucl. Phys. B **171**, 333 (1980).

[37] M. Luke, M. J. Savage, and M. B. Wise, Phys. Lett. B **343**, 329 (1995).

[38] Y. Nir, Phys. Lett. B **221**, 184 (1989).

[39] M. Luke, M. J. Savage, and M. B. Wise, Phys. Lett. B **345**, 301 (1995).

[40] A. F. Falk, M. Luke, and M. J. Savage, Phys. Rev. D **53**, 2491 (1996); Phys. Rev. D **53**, 6316 (1996).

[41] M. Beneke and V. M. Braun, Nucl. Phys. B **426**, 301 (1994); M. Beneke, V. M. Braun, and V. I. Zakharov, Phys. Rev. Lett. **73**, 3058 (1994).

[42] I. I. Bigi, M. A. Shifman, N. G. Uraltsev, and A. I. Vainshtein, Phys. Rev. D **50**, 2234 (1994).

[43] M. Neubert and C. T. Sachrajda, Nucl. Phys. B **438**, 235 (1995).

[44] M. Luke, A. V. Manohar, and M. J. Savage, Phys. Rev. D **51**, 4924 (1995).

[45] P. Ball, M. Beneke, and V. M. Braun, Phys. Rev. D **52**, 3929 (1995).

[46] A. F. Falk and M. E. Peskin, Phys. Rev. D **49**, 3320 (1994).

[47] H. Albrecht *et al.* (ARGUS Collaboration), Phys. Lett. B **221**, 422 (1989).

[48] C. K. Chow, Cornell report CLNS-96-1432 (1996).

[49] P. Brückman (DELPHI Collaboration), DELPHI 96-95 CONF, 24 (1996).

[50] D. Buskulic *et al.* (ALEPH Collaboration), Phys. Lett. B **365**, 437 (1996).

[51] T. Sjöstrand, Comput. Phys. Commun. **39**, 347 (1996).

[52] M. Feindt *et al.* (DELPHI Collaboration), CERN report CERN-PPE/95-139 (1995).

[53] G. Brandenburg *et al.* (CLEO Collaboration), Cornell report CLEO CONF. 96–13 (1996).

[54] A. F. Falk, Phys. Rev. Lett. **77**, 223 (1996).

QCD IN HADRON-HADRON COLLISIONS

Michael G. Albrow*
Fermi National Accelerator Laboratory, MS 318
P.O. Box 500, Wilson Road, Batavia, IL 60510

ABSTRACT

Quantum Chromodynamics provides a good description of many aspects of high energy hadron-hadron collisions, and this will be described, along with some aspects that are not yet understood in QCD. Topics include high E_T jet production, direct photon, W, Z, and heavy flavor production, rapidity gaps, and hard diffraction.

*Supported by DOE contract through Fermilab contracts.

© 1996 by Michael G. Albrow.

1 Quarks and Gluons in Hadrons

In the Standard Model, the strongly interacting particles, or *hadrons*, are composites of the more fundamental quarks q, antiquarks $\bar{q}$, and gluons g. While the hadrons are extended objects with dimensions of order 1 fm (10^{-13} cm), their constituents $q, \bar{q}$, and g, generically called partons,[1] are point-like at all scales presently accessible. With a resolving power of order 10^{-17} cm, reached in hadron-hadron collisions at the Fermilab Tevatron, they still behave like points. However, if you "observe" a proton, by probing it with a photon or any other particle, what you "see" depends very much on the wavelength λ of the probe. If you probe the proton with x-rays ($\lambda \approx 10^{-8}$ cm) you will see a point-like object. If you use photons with a wavelength of about 1 fm, the experiments will show a fuzzy blob [quantified by the electromagnetic form factor $F(Q^2)$, where Q^2 is $(\hbar c)^2\lambda^{-2}$]. If you further decrease the wavelength of the photon (increasing Q^2), you begin to see that the proton is lumpy, and three *valence quarks* become apparent. This was the famous experiment at SLAC in 1969 (for which Friedman, Kendall, and Taylor received the Nobel Prize in 1990), scattering electrons on protons and finding "point-like" structures. As you continue to decrease the wavelength of the photons, the quarks always appear smaller than the resolution, but additional partons appear. The fraction of the proton's momentum carried by quarks and antiquarks decreases as they radiate gluons. Gluons convert into $q\bar{q}$ or gg pairs which in turn can radiate gluons, and we have a branching tree of q and g. The smaller the probe wavelength (the larger the Q^2), the better the resolution, and the more of these low-momentum-fraction partons you observe. This is called *evolution*. Thus, the proton (like all other hadrons) has an ever-changing structure and composition; it just depends how *hard* you look. Larger Q^2 means harder.

What are the quarks and gluons? The quarks are fermions, spin $\frac{1}{2}\hbar$ point-like electric charges. There are six types, called *flavors*, named down (d), up (u), strange (s), charm (c), bottom or beauty (b), and top (t). With the electric charge of the electron defined to be -1, the u, c, and t quarks have charge $+\frac{2}{3}$, and the d, s, and b quarks have charge $-\frac{1}{3}$. The quarks have another kind of charge for the strong, Quantum Chromodynamics or QCD, interaction. This is called a *color* charge by analogy with the fact that three lights (red, green, and blue) together make white (colorless) light.* Quarks are said to be in a color triplet state. At any time a quark can be, with equal probability, in a R, G, or B state. A triplet of quarks, one of each color, makes a colorless composite or hadron, such as a proton. Antiquarks carry anticolor charges: $\bar{R}, \bar{G}$, or $\bar{B}$. Three quark states qqq are called *baryons*, and three antiquarks $\bar{q}\bar{q}\bar{q}$ are antibaryons. Mesons are hadrons consisting primarily of a quark and an antiquark; the color and anticolor (e.g., $R\bar{R}$) cancel to make a colorless composite. Gluons are continually exchanged between the q and $\bar{q}$. Gluons are in color octet states, having a color and an anticolor, e.g., $R\bar{G}$. The "octet" comes from group theory arithmetic:

$$3 \times \bar{3} = 8 + 1$$

The singlet $R\bar{R} + G\bar{G} + B\bar{B}$ decouples from the theory; it is not part of the group $SU(3)$. Exchanged gluons, in the space-like t-channel, having no defined direction of propagation, can be equally $R\bar{G}$ and $G\bar{R}$; these are indistinguishable. The net effect is to change the color of the coupling quarks. In the t-channel we have, e.g., $q_R q_B \rightarrow q_B q_R$. Gluons can also be "exchanged" in the time-like s channel, for $q\bar{q}$ annihilation, and they carry the color of the quark and the anticolor of the antiquark. However, a quark and antiquark of opposite color cannot annihilate into a single gluon; they can, however, annihilate by the electromagnetic or weak interaction into a photon, W, or Z.

The strength of the coupling between quarks and gluons depends on the four-momentum-transfer-squared Q^2 involved in the process and is denoted by $\alpha_S(Q^2)$ to reflect the notation α_{em} of QED. The coupling $\alpha_S(Q^2)$ is large (of order 1) at very small Q^2 (of order 1 GeV^2) and falls with Q^2 to become about 0.12 at $Q^2 = M_Z^2$. The particle Z is the neutral weak intermediate vector boson, with mass 91.19 GeV. Probes of progressively shorter wavelength see the strong interaction becoming weaker, and the quarks and gluons behaving more like free particles. This is known as *asymptotic freedom*. On the other hand at small Q^2, or long wavelengths, the coupling becomes so large that we do not know how to calculate interactions (the *nonperturbative* regime) except by approximating space-time by a discrete set of points and using vast computing power. This is the approach called *Lattice QCD*.

We can in principle make hadronic states out of any colorless composite, hence not only qqq, $\bar{q}\bar{q}\bar{q}$, and $q\bar{q}$, but also gg and ggg. The latter are called *gluonia* and *glueballs* and have resisted unambiguous identification for nearly two decades. Recently, a picture is emerging[2] which has candidate states at 1.5 GeV and 1.9 GeV.

*An anthropocentric statement, the human eye happens to have three different color sensors.

The main technique is "central hadron production," with the beam and target particles quasielastically scattered and a cluster of hadrons well-separated in momentum space (or more correctly, rapidity, defined in Sec. 2.1) in the center. At high enough energies, this is dominated by double Pomeron exchange, discussed in Sec. 11.2.2.

A proton, observed with a probe with wavelength $\lambda < 0.1$ fm, or $Q^2 > 5$ GeV^2, therefore consists of three valence (constituent) quarks uud, an indefinite number of gluons g which carry about half the total momentum of the proton, and an indefinite number of $q_s\bar{q}_s$ pairs called the sea (s stands for sea). The momentum fraction carried by a parton is called Bjorken-x, or usually just x. Most of the sea quarks are u and d, while strange s-quarks make up about 20% of the total, and charmed quarks, because of their relatively high mass, are present at a lower level. The ratio of c/s quarks depends on Q^2, tending more towards equality at high Q^2, and on x, being predicted to rise from about 0.4 at $x = 0.1$ to 0.8 at $x = 10^{-4}$. At very high Q^2 and very small x, we can expect quark democracy! Even sea top quarks can become nonnegligible at the Very Large Hadron Collider (VLHC, up to 100 TeV/beam).[3]

Phenomenologically, we can consider two hadrons colliding at high energy (such as at the Tevatron, with 900 GeV p and $\bar{p}$ giving a center-of-mass energy $\sqrt{s} = 1800$ GeV) to be colliding broad-band beams of quarks, antiquarks, and gluons. Figure 1 shows a model for a collision involving a hard process.

The spectra of quarks and gluons are dependent, because of evolution, on the Q^2 of the interactions that take place between them. To first (leading) order, these are $2 \to 2$ "elastic" scattering processes: $q\bar{q} \to q\bar{q}$, $q\bar{q} \to gg$, $gg \to q\bar{q}$, and $gg \to gg$. Given that QCD *is* the theory of quark and gluon interactions, we could expect that hadron-hadron collisions are ideal for testing the theory. While hadron-hadron collisions provide a very fertile hunting ground for QCD phenomena (as I hope to convince you), e^+e^- collisions and ep collisions are superior in some respects,[4,5] such as measuring α_S from many features of the final state in e^+e^-. However, quark and gluon scattering processes can only be studied in hadron-hadron collisions, and this is central to QCD.

The scattered quarks and gluons do not emerge from the collisions farther than about 10^{-13} cm, the so-called confinement radius. They have color charge, and as they try to escape, a strong color field builds up in their wake. Unlike the force between two electric charges, which decreases like $1/R^2$, the force between

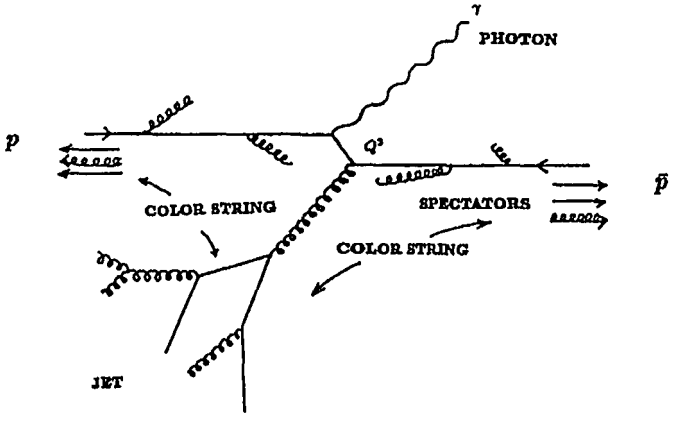


Figure 1: Schematic representation of a hard hadron-hadron collision, as described in the text. A photon is produced opposite a jet.

two color charges remains approximately constant (the potential is linear) with separation, and so the energy in the string-like field increases. (String-like, because if we think in terms of lines of force, these lines behave as if they attract each other, unlike lines of force in QED which behave as if they repel each other.) When the energy in this stretching color field increases, it becomes energetically favorable for a $q\bar{q}$ pair to "pop out" of the vacuum, to be created. This process repeats itself until many quarks and antiquarks with small relative energies, able to form hadrons ... perhaps not yet pions but resonances and low mass colorless clusters ... dominate. The process is called *fragmentation*. In the next stage, the resonances and clusters decay to ground state hadrons, namely $\pi, K, p, \bar{p}, \Lambda$, etc. The above description is a simplified "string model"; the color field is seen as a string which can break, and q and $\bar{q}$ are the ends of the string.

Another picture of fragmentation sees it rather as a branching process, a *tree diagram*. A gluon branches into a quark-antiquark pair $q\bar{q}$ or two gluons gg, a quark branches into qg. At each vertex, a price $\alpha_S(Q^2)$ must be paid in the amplitude, but as the tree evolves Q^2 decreases, α_S increases, and the branching becomes more prolific. Eventually, all these partons assemble themselves into hadrons, and colorless clusters which decay into hadrons, and the proliferation ceases. This is similar in many ways to the string model, and both seem to

be quite good approximations to reality. (Of course, *every* model is at best an approximation to reality.[6])

1.1 Structure Functions

The structure functions or Parton Distribution Functions, PDF's, give the probabilities of finding a quark q_i of type i or a gluon g carrying a momentum fraction x of the hadron, when it is probed with four-momentum-transfer-squared Q^2. Perturbative QCD cannot predict the absolute normalization of parton distributions. However, if given (for example, from a measurement) the distributions at one value of the scale Q^2, QCD *can* calculate them at any other value, provided that both Q^2 are large enough that $\alpha_S(Q^2)$ is small. The name of the game is therefore to choose some *input* PDF, normally at low Q^2, and *evolve* it to larger Q^2 applying the QCD rules of evolution which involve the branching processes $q \to qg, g \to gg$, and $g \to q\bar{q}$.† After the pioneers of evolution calculations Dokshitzer, Gribov, Lipatov, Altarelli, and Parisi,[7] this is called the DGLAP equation. As the evolution occurs, the valence quarks (on average) take lower fractional momentum x, so that the probability of finding a valence quark at high x decreases with Q^2 while the probability of finding one at low x increases. Near $x = 0.2$, the losses and gains cancel out and the quark structure functions are almost independent of Q^2. Dependence only on x, not on Q^2, was a prediction of the parton model and was observed[8] in the Deep Inelastic electron Scattering (DIS) experiments at SLAC in 1969 that gave the first real experimental evidence for the partonic structure of nucleons. However, this observation of DIS scaling was mostly in the region around $x = 0.2$ and was therefore somewhat fortuitous; at both larger and smaller x, the scaling deviations expected in QCD evolution were seen (and were later mapped out) at SLAC.

Unfortunately, we do not have just one arbitrary input structure function, we have one for each quark type $u, \bar{u}, d, \bar{d}, s, \bar{s}$ if we ignore the charm, beauty, and top quarks (which we are normally allowed to do) and one for the gluons g. It is not common, especially in hadron-hadron collisions, to do experiments sensitive to quark helicities, but in principle different helicities can have different structure functions. I shall ignore that complication, but that still leaves seven unknown input functions, which are parameterized with functions typically of the form $q(x) = Ax^B(1-x)^C(1+Dx)$. Usually, the three antiquarks $\bar{u}, \bar{d}$, and $\bar{s}$ are taken to have the same x-dependence and differ only in their normalization, and $s(x) = \bar{s}(x)$. While the u and d quark distributions may be equated with a sum of valence quarks u_v and d_v and sea quarks, the valence distributions u_v and d_v do not have quite the same shape. This can be demonstrated using the rapidity dependence, in $p\bar{p}$ collisions, of the $W^{\pm}$ (the W is the charged weak boson, mass $M_W = 80.3$ GeV) charge asymmetry. The ratio $R(\frac{e^+}{e^-})$ versus η is closely related to the ratio $R(\frac{u}{d})$ versus x.

Despite arbitrariness in the input structure functions (QCD prides itself on calculating their evolution, not the low-Q^2 starting point), there are other constraints. Some of these are sum rules, e.g., because a proton has two u_v and one d_v valence quarks, we must have:

$$\int_0^1 u_v(x)dx = 2 \tag{1}$$

and

$$\int_0^1 d_v(x)dx = 1. \tag{2}$$

There is also a momentum sum rule, integrating over all parton types:

$$\int_0^1 [xq(x) + x\bar{q}(x) + xg(x)]dx = 1. \tag{3}$$

There are also relationships with the phenomenology of Regge exchanges,[45] applied, e.g., to elastic $\gamma^* p$ scattering which involves both *Pomeron* (vacuum quantum number exchange) and *Reggeon* (virtual ρ, f^0, A_2, etc., exchanges). These relations lead one[45] to expect, as $x \to 1$, a behavior $q_v(x) \sim (1-x)^3$. Given the paucity of data for $x \geq 0.75$, this is not contradicted by data. Regge phenomenology also predicts the behavior of the structure functions at the other extreme $x \to 0$ which is now being studied most intensively at HERA.[5] I shall argue that building bridges between QCD (**The** Theory of Strong Interactions, but with limited applicability!) and Regge Theory (which organized a wealth of strong interaction data, mostly outside the domain of applicability—or calculability—of QCD) is now an important and exciting task.

So, the parameterizations of the input structure functions can be (and usually are) constrained by sum rules and perhaps Regge behavior. It is also possible

†Think about the similarities and differences between these branchings in the parton structure of hadrons (hadron→parton) and the branchings in the process parton→hadron described in the previous section. There is a "parton-hadron duality" here.

to say, as Glück, Reya, and Vogt (GRV) did,[9] "What if we just suppose three valence quarks at very low Q^2, sharing the momentum democratically, and let that evolve?" They tried this starting at $Q^2 = 0.5$ GeV^2, but it does not work well . . . of course, using QCD evolution from such low Q^2 is brave. However, if they allow some 50% of the low-Q^2 momentum to be carried by gluons and then evolve, the resulting structure functions are quite reasonable considering the small amount of input. Figure 2 shows the evolved GRV structure functions at very low Q^2 (0.23–0.34 GeV^2) using two evolution procedures, LO and NLO. The Leading Order (LO) calculations compute all the tree diagrams, the branching processes, but do not try to compute diagrams with closed loops. The Next-to-Leading Order (NLO) calculations do allow one-loop diagrams (and must effectively integrate over all possible momenta running inside the loop). The difference between the LO and NLO curves is an indicator that QCD is not a theory with the precision predictive power of QED, basically because $\alpha_S \gg \alpha_{em}$. Allowing two loops (NNLO) and looking for convergence is an obvious progression but is a major piece of work.

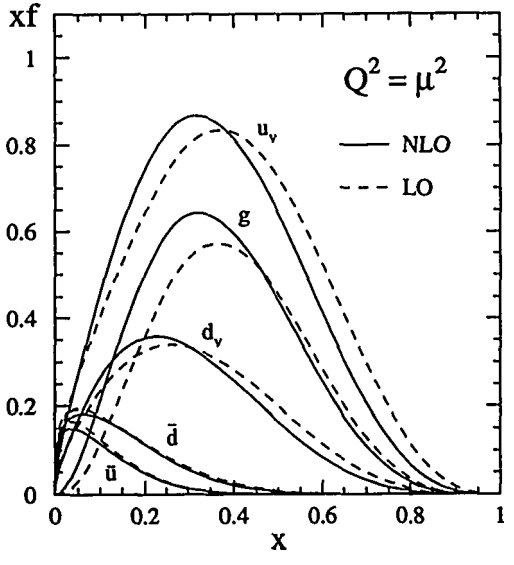


Figure 2: Proton structure functions according to Glück, Reya, and Vogt, at low Q^2.

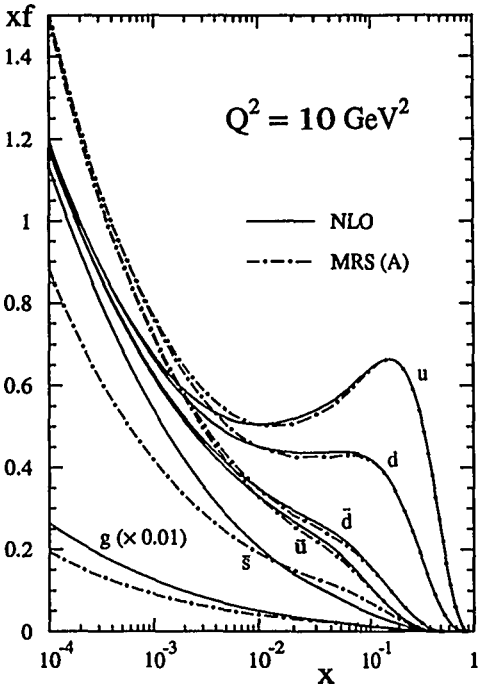


Figure 3: Proton structure functions according to Glück, Reya, and Vogt, on a logarithmic x-scale to show the low-x region.

To see the behavior of the proton structure function at very small x, Fig. 3 shows a plot on a logarithmic x-scale, at $Q^2 = 10$ GeV^2. The antiquarks rise steeply as x decreases from 10^{-2} to 10^{-4}, meeting the quarks as there are no valence quarks here, only sea. The GRV curves show a different trend from an extrapolation of the MRS (Martin, Roberts, and Stirling)[10] fits; there is now HERA data in this region (not available when this plot was made). It is important to be aware that the $xg(x)$ gluon distribution has been scaled down by a factor 0.01 to be shown on this plot! Gluons dominate at small x, by a factor more than three (over the sum of all q and $\bar{q}$ species) at $x = 10^{-4}$. What will happen at still smaller x? When x gets very small, the center of momentum (CM) collision energy of the $\gamma^* p$ collision becomes large; in fact, there is a direct relation between the

low-x structure function and the $\gamma^* p$ total cross section at high energy. In Regge Theory, the total cross section $\sigma_T(s)$ at high energy is determined by the value of the Pomeron trajectory $\alpha(t)$ at $t = 0$. $\alpha(t)$ is the (complex) angular momentum exchanged, and $\sigma_T(s) \sim s^{\alpha(0)-1}$. For the Pomeron $\alpha(0) \approx 1.08$, above 1.0, so $\sigma_T(s)$ increases with (CM energy)^2, s. There is a bound called the Froissart Bound which limits the rise of total cross sections to $ln^2 s$; if they would rise faster, unitarity (the principle that there is no free lunch) would be violated. The interesting question is now "What will happen to $xg(x)$ and $xq(x)$ so that unitarity is not violated as x gets smaller?" Presumably, a flattening or turnover will come in, and will there then be interesting new associated phenomena? Presumably, when this begins to happen, the gluon densities are so high that recombination $gg \rightarrow g$ becomes important and cancels the DGLAP branchings $g \rightarrow gg$. One also talks about *screening* of color fields becoming important. It is not unreasonable to suppose that this is a frontier (very low x, very high g-density) where new interesting phenomena will show up.

I should not leave this section without referring to "modern" structure function representations which are popular for comparing with hadron collider data. One frequently used set comes from the Martin-Roberts-Stirling (MRS) group in the UK.[10] In addition, a collaboration of theorists and experimenters was formed in the early 1990s, called the CTEQ Collaboration. One of its aims was to provide best-fit QCD-based structure functions to as large a database as possible. These structure functions are labelled CTEQ2M, CTEQ2ML, and so on; Ref. 11 is a useful guide.

2 Quark and Gluon Scattering Processes

We have seen how hadrons can be viewed as microbeams of quarks, antiquarks, and gluons with Q^2-dependent momentum spectra. These partons are continually interacting, but in a frame where the hadron momenta are very large (ideally, the "infinite momentum frame"), due to time dilation these interactions become negligible and we can think of the partons as quasi-independent. When two hadrons collide, a parton carrying momentum fraction x_1 from one hadron can scatter with a parton carrying momentum fraction x_2 from the other hadron. It is usually simplest to think in the center-of-momentum frame, the normal frame of colliders, so that if $x_1 = x_2$, we are also in the parton-parton CM frame. In the center-of-momentum frame, the parton collision energy squared $\hat{s} = x_1 x_2 s = (p_1 + p_2)^2$, where p_i is the four momentum of the parton i in the process $1 + 2 \rightarrow 3 + 4$. We also have the four-momentum transfer squared variable $\hat{t} = (p_1 - p_3)^2$ and the crossed variable $\hat{u} = (p_1 - p_4)^2$. For massless partons, $\hat{s} + \hat{t} + \hat{u} = 0$.

There is a simple basic equation for parton-parton scattering in QCD, which is as follows:

$$\frac{d\sigma}{d\hat{t}} = \frac{\pi \alpha_S^2}{\hat{s}^2} |\mathcal{M}|^2. \tag{4}$$

In this equation, $d\sigma$ [cm^2] is an elemental cross section, which if you multiply by the *luminosity* gives the rate of scattering into an elemental $\hat{t}$ bin of size $d\hat{t}$. On the right-hand side, the strong coupling α_S is not a constant (let us **not** call it the strong coupling constant!) but gets smaller as the hardness of the collision Q^2 increases, $\alpha_S(Q^2)$, the so-called running of the strong coupling. What is Q^2 in terms of the Mandelstam variables $\hat{s}, \hat{t}, \hat{u}$? In DIS, it is rather clear that it should be identified with the four-momentum transfer squared of the probing photon/W/Z. Here it is not so clear. $Q^2 = \hat{s}$ would be bad as we can have very soft but very large $\hat{s}$ collisions. On the other hand, for high mass Drell-Yan, $q + \bar{q} \rightarrow \mu^+ \mu^-$, $Q^2 = \hat{s}$ would be natural, as the hard photon is in the $\hat{s}$-channel. Choosing $\hat{t}$ is probably good, but should we not have $\hat{t}\hat{u}$ symmetry? The choice

$$Q^2 = \frac{\hat{s}\hat{t}\hat{u}}{\hat{s}^2 + \hat{t}^2 + \hat{u}^2} \tag{5}$$

gives that, and is sometimes used. There is not a unique answer; in fact, theoretically it should not matter which choice is made if one could do the calculations to all orders. The predictions would then be independent of the choice of Q^2 scale. As we are not in that situation, we make a choice, but one that is hopefully not very dependent on the number of orders calculated. One often-used solution is to identify Q^2 with p_T^2 or $(2p_T)^2$ where p_T is the largest p_T object (hadron jet, e.g.) in the event. Given that collider experiments are all central and would not see high mass Drell-Yan giving low-p_T leptons, this should be all right!

There are two other elements of our basic scattering equation: $|\mathcal{M}|^2$ and $\hat{s}^2$, where $|\mathcal{M}|^2$ is a dimensionless number, process dependent, the matrix element for each particular process. From the dimensions of the l.h.s., we can see that the r.h.s. has to have dimensions [GeV^{-4}] as given by the $\hat{s}^2$ in the denominator.

The matrix elements $|\mathcal{M}|$ can be calculated[12] from the Feynman rules for quark and gluon propagators and vertices in QCD, but that would take more theoretical

lectures to explain. Here I will just show the end results for three sample cases. They depend on the quark spins ($\pm\frac{1}{2}$) and colors (3) and gluon spins (-1, 0, +1) and colors (8). These can just be averaged over (initial state) and summed over (final state) if we are not doing spin (color!)-dependent measurements. To give you an idea of what the matrix elements look like, for the elastic scattering of identical type quarks $q_iq_i \to q_iq_i$:

$$|\mathcal{M}|^2 = \frac{4}{9}\left(\frac{\hat{s}^2+\hat{u}^2}{\hat{t}^2}\frac{\hat{s}^2+\hat{t}^2}{\hat{u}^2}\right) - \frac{8}{27}\frac{\hat{s}^2}{\hat{t}\hat{u}}. \tag{6}$$

The annihilation of same-flavor quarks by an $\hat{s}$-channel gluon into a pair of different flavor, $q_i\bar{q}_i \to q_j\bar{q}_j$ is simpler:

$$|\mathcal{M}|^2 = \frac{4}{9}\frac{\hat{t}^2+\hat{u}^2}{\hat{s}^2}, \tag{7}$$

and as a final example, gluon elastic scattering $gg \to gg$ through the four-gluon coupling or $\hat{s}, \hat{t}$, or $\hat{u}$ channel gluon exchange is

$$|\mathcal{M}|^2 = \frac{9}{2}\left(3 - \frac{\hat{u}\hat{t}}{\hat{s}^2} - \frac{\hat{u}\hat{s}}{\hat{t}^2} - \frac{\hat{s}\hat{t}}{\hat{u}^2}\right), \tag{8}$$

and there are similar formulae for several other $2 \to 2$ quark and gluon scattering processes in leading order.

2.1 Rapidity

Rapidity is an important variable and should therefore be defined. Longitudinal rapidity y is just the particle's velocity component along the beam axis, but transformed in such a way that while for small values it is identical to the usual speed $\beta \cdot c = \frac{dx}{dt}$, at large values it does not "saturate" ($\beta \to 1.00\dot{0}$) but keeps going: as $\beta \to 1.00\dot{0}, y \to \infty$. The law of addition of speeds, $\beta_{13} = \beta_{12} + \beta_{23}$ which is only valid at small β, is valid for all values of rapidity: $y_{13} = y_{12} + y_{23}$. So rapidity differences are invariant under Lorentz boosts, and a pion and a proton with the same rapidity are moving with zero relative speed, but have different momenta. We could use a three-dimensional rapidity, and this would be natural in a three-dimensional relativistic world. But generally in particle collisions, one axis has special significance: in hadron-hadron it is the beam-beam axis z and in e^+e^- it is the dijet axis (or thrust axis, defined later). So we choose that as the axis to define a one-dimensional (longitudinal) rapidity, and measure transverse momenta p_T, and transverse energies E_T, with respect to that axis. The linear addition law comes from the following.

From elementary relativity, we have the law for addition of speeds:

$$\beta_{13} = \frac{\beta_{12}+\beta_{23}}{1+\beta_{12}\cdot\beta_{23}}.$$

Where else have we seen this formula? It occurs when adding hyperbolic tans!

$$tanh(A+B) = \frac{tanhA + tanhB}{1 + tanhA \cdot tanhB}.$$

So we just make the identification:

$$\beta_{12} \equiv tanhA,$$

i.e.,

$$tanh^{-1}\beta_{12} = A.$$

This formula has a unique solution:

$$A = \frac{1}{2}ln\frac{1+\beta}{1-\beta}$$

which, as $\beta = p/E$, can be rewritten:

$$y = \frac{1}{2}ln\frac{E+p}{E-p}.$$

A particle of mass m traveling along the rapidity axis with a momentum p has a rapidity $y = ln\frac{E+p_L}{m}$ which is 7.5 for a proton in a 900 + 900 GeV collision. The full rapidity coverage is $\Delta y = ln\frac{s}{m^2}$. If you set $m = 0$ in the above formula for y, you can derive a special case:

$$y_{m=0} \equiv \eta = ln(tan\frac{\theta}{2}).$$

This is called the *pseudorapidity* η and is a good approximation to y as long as the mass m is small compared to p_T. This is perfect for photons but is bad for high E_T jets; never mind, we use it for jets too.

Longitudinal rapidity is a very natural variable in describing final states in hadron-hadron collisions. Particles have an average density of about four charged particles per unit of rapidity, and there are short-range rapidity correlations between particles. To describe jet events, we frequently use E_T, η, and ϕ.

2.2 Event Generators

Given that the strong coupling α_S is not very small, 10^{-1} rather than say 10^{-3}, higher order processes with additional vertices and additional gluons must be considered, the NLO or Next-to-Leading Order processes. This is routinely done, but makes life much more complicated than the nice LO formulae displayed above. The Next-to-Next-to Leading Order (NNLO) processes are now being addressed by theorists, and will eventually take us another step in precision in comparing data with theory.

How are comparisons with theory made in this field? Generally, one copes with the very large number of variables using Monte Carlo methods, *event generators* which simulate interactions on a computer. Basically, one tries to generate interactions taking account of everything we know about parton distribution functions (the relation hadrons $\rightarrow$ partons), scattering processes, initial and final state radiation (gluon bremsstrahlung), and fragmentation (the relation partons $\rightarrow$ jets $\rightarrow$ hadrons). These Monte Carlo generated events must then be confronted with a computer model of the experimental detector, with all its cracks, resolution smearing, etc. Then one can compare data with theoretical expectations, and if one finds significant disagreements, one can try variations of the inputs to, e.g., learn that the received wisdom on PDF's should be modified. Of course, any such changes must not result in significant disagreement with other experiments.

Examples of currently popular event generators are called ISAJET, HERWIG, and PYTHIA. These are big programs developed over perhaps 20 years. Being based on QCD, they, of course, have a great deal in common, but there are also many differences in the way they handle some not yet well-understood subprocesses, for example, fragmentation. These event generators actually have several applications. One is to make predictions, already before an accelerator (SSC, LHC) is approved, for the rates and shapes of diverse event types. For example, a 300 GeV Higgs should decay to W^+W^- and ZZ, and these to four high-p_T jets, but there will be many four-jet events from $gg \rightarrow gggg$, so can we still find a signal? Then, when we design the big detectors for such a machine, we use a Monte Carlo simulation to help optimize the detector performance for desired goals (e.g., discovering supersymmetry). While designing the detectors, but more realistically much later, one should use these simulations to devise analysis strategies to optimize signal (SUSY, Higgs) to noise (QCD, Electroweak). Once data exist, observed rates must be corrected for acceptance and resolution and perhaps for subtle effects to derive true cross sections. Because this tends to be a multi-dimensional problem, Monte Carlo methods are the appropriate tool. Finally, the event generators, as a Standard Model benchmark, are compared to the data to look for new physics. The process is iterative and any new physics (which may just be a significant change of the PDF's) will become part of a new benchmark. Where generators differ in their predictions, comparison with experiment can shed light on the not-well-known parts of the physics, e.g., the fragmentation.

Without going into details, let us just look over the main steps in PYTHIA as an example. The parton distribution functions $q_i(x, Q^2)$, $\bar{q}_i(x, Q^2)$, and $g(x, Q^2)$ are built in, with a switch to any particular PDF, and in a pp collision, one can select a parton from each proton with suitable weights (corresponding to the PDF's and the parton cross sections). Initial state gluon radiation from the incoming partons, e.g., $P_{q\rightarrow qg}(z)$, where z is the momentum fraction of the quark carried by the gluon, will be simulated. Earlier branchings have smaller Q^2—one starts at a cut-off of about $Q^2 = 1$ GeV^2—and the closer to the hard scattering, the larger is the Q^2 of the radiation. Final state radiation goes the other way, the first branches having highest Q^2.

This description of initial state radiation, scattering, and final state radiation is not quantum mechanically correct. To ask whether a particular hard gluon was radiated just before or just after the scatter is the same as asking which slit the photon went through! But we cannot yet do the calculations properly, with quantum mechanics in all its glory, so we approximate.

The incident partons that do not participate in the hard scattering, the *spectators*, are simulated; as they carry color, color strings may form between these forward moving spectator partons and central scattered partons. The hard scattering uses the QCD matrix elements discussed above, in NLO. The final state partons again form a branching tree, until their *virtualities* (basically Q^2 of the branches) is small. Then comes the part we do not really know how to calculate in QCD, to go from partons to hadrons. So we use some phenomenology, to make the transition to hadrons, not just pions but especially resonances, such as rho-mesons $\rho \rightarrow \pi\pi$. PYTHIA also includes some subtler effects such as *color coherence*, which tracks the color fields and gives rise to enhancements or depletions in particle density in certain angular regions, and *color strings*.

3 Experimental Interlude

Experimental lectures should at least say a few words about experiments! The accelerator wizards inject and circulate bunches of protons and antiprotons in opposite directions around the ring, four miles around for the Tevatron and 17 miles for the LHC. The bunches collide at set places around the ring, but they are steered apart electrostatically so that they only meet head-on where there are experiments. The Fermilab Tevatron has two experiments, CDF and DØ. There are about 10^{11} p and $\bar{p}$ per bunch, and they are focused down to transverse dimensions of 30 μm, but only about one $p\bar{p}$ collision takes place per bunch crossing: these particles are very small! However, there are so many bunch crossings per second that the overall rate of interactions is very high (*much* higher than in e^+e^- or ep machines). The rate is

$$R_T = L \cdot \sigma_T, \tag{9}$$

where σ_T is the total cross section, about 80 mb = 8×10^{-26} cm^2 and L is the luminosity, of order 10^{32} cm^{-2} sec^{-1}. The product gives a large number of interactions per second to observe, select, and record. Typically, only tens of events per second are recorded so the combination of the detector and its electronics (*triggers*) must do an amazing job in real time of recognizing which are the events of most interest. After about 15 hours, the beams are degraded in density, so they are dumped and fresh beams are injected. The total *integrated* luminosity over a run is given in units of pb^{-1} or events per picobarn (note that an inverse microbarn is much *smaller* than an inverse nanobarn!).

Hadron collider detectors have evolved but not diverged; most of the so-called general purpose detectors look similar in plan to Fig. 4.

I shall just say a few words about each element with emphasis on their roles in QCD. The figure shows a quarter of the detector; imagine rotating it around the beam pipe to make a cylindrical object and then reflecting in the transverse plane at the left. We really want to detect and identify everything that could come out of a collision: hadrons and leptons (electrons e, muons μ, taus τ, and neutrinos ν), and measure their energies and directions. Starting from the collision point inside the vacuum pipe, the first detector is a *microtracker*, in CDF called a Silicon Vertex Detector. This measures charged particle tracks with very high precision so that one can see the vertices of B-hadron (containing b-quarks) decays displaced from the collision point (although the displacement is only of order

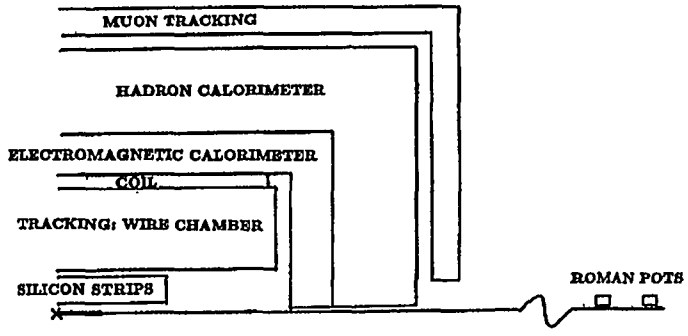


Figure 4: Schematic diagram of a general-purpose hadron collider detector.

of 1 mm). Then the particles pass through a larger tracking volume of lower precision, the whole tracking region being in a magnetic field so the momenta of charged particles can be obtained from their track curvature. The particles then enter two calorimeters; absorbing material that will cause them to shower and deposit all their energy, containing every cm or so a detector layer (liquid argon in DØ and scintillator in CDF, other media are possible). These calorimeters are the heart of the detector for most QCD studies, as they measure the energies of neutral as well as charged particles, and you can see jets (see next section) rather directly in their energy content versus angle. The front part is a separately read out "electromagnetic calorimeter" which detects photons and electrons (a track and shower with $p = E$). This is followed by a thicker "hadronic" calorimeter that contains showers from $\pi^\pm, K^\pm, K^0_L, p, n$, etc. Not all particles get absorbed in the calorimeters. Muons deposit a few GeV but normally emerge where they can be tracked. Neutrinos emerge (there's not much one can do about that!) but they carry away energy, and in the transverse plane, that can often be detected as missing E_T. If there is more than one large E_T neutrino, only their sum can be measured, but in single W production, the ν can usually be measured quite well by adding the energies vectorially in the whole calorimeter to find the missing E_T.

Way off to the right are two small detectors labeled *Roman Pots*. These are often added to large detectors to detect very small angle and high momentum scattered protons, for studying *diffraction*. This will be discused in Chap. 11.

4 High E_T Jets in Hadron-Hadron Collisions

The first hadron collider was the ISR, Intersecting Storage Rings, at CERN. The first collisions took place in 1971, just 25 years ago, in the same year that an important paper was published by Berman, Bjorken, and Kogut[13] (BBK) predicting high p_T jets in hadron collisions. At that time, the highest energy (fixed target) pp collisions were at 30 GeV beam energy, i.e., 7.6 GeV in the center of mass. The ISR was to take us to 63 GeV in the CM, equivalent to 2000 GeV with a beam + fixed target. The conventional wisdom then was that in hadron-hadron collisions, particles are produced with limited p_T, with a typical distribution e^{-6p_T}. The chance of finding a particle with p_T as high as 5 GeV/c from such a distribution is rather small! The main "facility" magnet, called the Split Field Magnet (SFM), was chosen to have a good field only in the forward (beam) directions, because "that is where all the physics would be," and a proposal for a central axial field magnet was not approved. The BBK paper pointed out that in the then-new parton model, which was looking good because the SLAC experiments[8] seemed to be seeing charged partons by the electromagnetic interaction, we should also have strong interaction scattering between the partons. Strong $qq \to qq$ scattering (assuming partons are quarks) was not yet calculable (this was pre-QCD), but BBK estimated that the strong scattering could be as much as 10^4 times stronger than electromagnetic (an overestimate because BBK did not know $\alpha_S \approx 0.1$). So what would events look like if two partons made a large angle scatter? BBK said the partons would turn into jets of hadrons! (They actually used the word "cores.") They were absolutely right, and although this paper inspired high p_T jet searches at the ISR, the wheels turned painfully slowly. An abundance of hadrons, both π^0 and identified charged hadrons π, K, p, and $\bar{p}$ at large p_T (of order 4–10 GeV), was discovered, and eventually only the hard parton scattering explanation survived. At Fermilab with its lower energy ($\sqrt{s} = 24$ GeV) fixed-target collisions, one looked[14] for jets by triggering on total transverse energy E_T in limited solid angle calorimeters, but this had a very strong bias making the results difficult to interpret. It was agreed that the trigger solid angle must be much larger than the eventual jet solid angle, so that the jets are much more localized than had been required in the trigger. It was finally 11 years after the BBK paper, in 1982, that really convincing evidence for high p_T jets was presented from the ISR,[15] made possible by a really good (uranium-scintillator) large aperture hadron calorimeter and very high luminosity from the machine. An example is shown in Fig. 5, an early example of a so-called LEGO plot.[16]

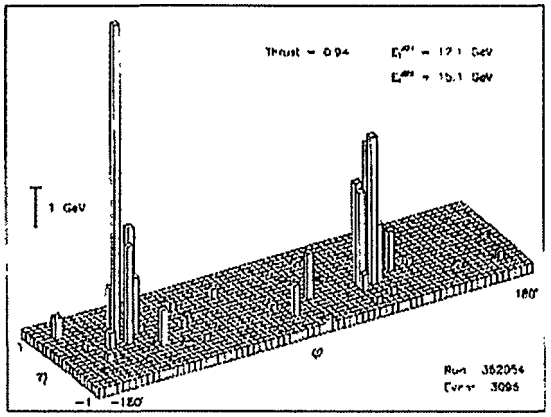


Figure 5: A high E_T jet event at the ISR. The E_T detected in cells in η and ϕ is shown; the trigger/selection was just large total E_T.

Each calorimeter cell (tower) is shown as a cell in the $\eta\phi$ plane with a vertical bar proportional to the $E_T = E \cdot sin\theta$ in the tower. On the figure, the quantity Thrust = 0.94 is noted. Thrust, T, is a quantity defined as:

$$T = Max\left(\frac{\sum|\hat{e}.\vec{p}_i|}{\sum|\vec{p}_i|}\right), \tag{10}$$

where the sums are over all clusters with vector momenta $\vec{p}_i$ in the transverse plane and $\hat{e}$ is a unit vector in the transverse plane. It can range from $2/\pi = 0.64$ for an isotropic event to 1.0 for a perfectly collimated two-jet event. The event in the figure is not atypical once ΣE_T in this central region exceeds about 35 GeV (out of $\sqrt{s} = 63$ GeV), although this only happens in about one in 10^9 collisions.

By this time, experiments UA1 and UA2 at the CERN $p\bar{p}$ Collider were beginning to present their first results. Even though their luminosity was still very low, thanks to the much higher $\sqrt{s} = 540$ GeV, events with dramatically high (at that time) p_T jets could be clearly seen.[17,18] So the discovery of high p_T jets in hadron collisions was shared between the ISR and $Sp\bar{p}S$, but the latter was in the limelight and provided a dramatic and exciting first look at the new era of

jet physics. At the new generation of colliders ($Sp\bar{p}S$, Tevatron, LEP, LHC), we would come to treat jets like particles.

In the early days of measuring jets, one much-discussed question was: "What is the best way to define a jet?" and various *jet algorithms* were proposed. A typical and still much used algorithm is to find a cone in $\eta\phi$ space ... actually, it is a *circle* in $\eta\phi$ space which is two-dimensional ... chosen to contain a local maximum in ΣE_T, the total transverse energy of all hadrons, or calorimeter towers, in the circle. This is called a *cone algorithm*; in the central region, the $\eta\phi$ circle corresponds to a good approximation to a circular cone in space, although when it is very forward, the cone gets distorted. Actual procedures are usually iterative, starting with the highest E_T calorimeter cluster and putting a cone around it, adding the "energy vectors" inside to define a new cone axis, and repeating if necessary until some condition is satisfied. Once the procedure is defined, the only parameter to be chosen is the cone radius $R = r_{max}$, where $R^2 = \Delta\eta^2 + \Delta\phi^2$ and $\Delta\eta$ and $\Delta\phi$ are the distances of a particle (or calorimeter tower) to the cone axis. Cone radii are typically chosen in the range 0.4 to 0.7, values which hopefully give an optimum correspondence between the measured jet four-momentum and the "initiating hard parton" (even though the latter is not theoretically well-defined because of Quantum Mechanics). If you make the defining cone too small, particles obviously associated with the hard scatter are excluded, and if it is too large, more of what is often called the *underlying event* is included. The underlying event is also not a well-defined concept; in reality, color connections are everywhere in an event, and it does not make sense to ask whether a pion with $p_T = 600$ MeV/c and $r = 0.8$ is part of the jet or of the "underlying event." The color-string model takes this holistic view. But cone algorithms ideally choose a cone size where (a) leakage of "jet particles" out is on average balanced by an "underlying event" taken in. (b) A hard, perturbatively radiated gluon will be reconstructed as a separate jet and not merged in. Again, there is no sharp cut-off between hard and soft radiation, so finally one must just do the same things with the same cuts in data and Monte Carlo generated events and compare them. For any "reasonable" choice, it should not matter what cone size is chosen. CDF and DØ normally (but not always) use 0.7 independent of E_T. For a multijet process like $t\bar{t} \to 6$ jets, 0.4 is preferred. As jets tend to shrink in $\eta\phi$ space with E_T, one could make $R(E_T)$, but this complication is not normally worth making. What about the low E_T end, how far down can one go in E_T and still talk meaningfully about jets? This is a complicated question and there is no sharp boundary. It is also a machine-dependent question. In e^+e^- collisions, the first two-jet structures were observed at $\sqrt{s} = 6.2$–7.4 GeV (Ref. 19), but they became much more obvious at higher energies, e.g., when PEP and PETRA operated at $\sqrt{s} = 30$ GeV. These are intrinsically clean final states with a q and $\bar{q}$ back-to-back. In hadron-hadron collisions, it is a different matter, with a large number of final state partons, most going forward-backward (and giving rise to the so-called underlying event). Jets obviously will need higher E_T to stick out of this "background." This statement will also be dependent on $\sqrt{s}$. At the lowest $\sqrt{s}$ hadron collider, the ISR, the AFS Collaboration measured jets down to 6 GeV in fair agreement with hard scattering models, but only by about 10–12 GeV were they the dominant feature in a large solid angle trigger. At the $Sp\bar{p}S$ and Tevatron, it is generally considered that jets above about 10 GeV E_T "make sense," i.e., the measured jet momentum corresponds reasonably well to a hard parton, while jets below about 5 GeV do not, i.e., the correspondence is very washed out. However, a recent CDF study has found that if you select collisions with exactly two "jets," both with $5 \leq E_T \leq 7$ GeV, they will nearly always be back-to-back in azimuth, showing that even at the Tevatron (not just at the ISR) such a low E_T cut can sometimes be used. Where one chooses to cut depends on the physics under study. In events at the Tevatron with $\Sigma E_T > 500$ GeV, jets of 5 GeV are lost, but in double Pomeron events with $\Sigma E_T \sim 20$ GeV, they stick out.

Jet E_T spectra rise dramatically with $\sqrt{s}$. The ISR was put out of business by the $Sp\bar{p}S$, and the $Sp\bar{p}S$ by the Tevatron, and you can see a comparison[20] between the latter two in Fig. 6.

Actually, the data is all from CDF at the Tevatron, but the two lower energies were chosen to coincide with the $Sp\bar{p}S$. At $E_T = 100$ GeV, the $\sqrt{s} = 1800$ GeV (Tevatron) jet production cross section is 40 times what it was at $Sp\bar{p}S$. The rise is because at the higher $\sqrt{s}$, the scattering partons are at lower x where the parton density is much higher (and more are gluons, which helps). At 1800 GeV, the data span eight orders of magnitude in rate (using 1/5 of the data to date) and reach above 400 GeV in E_T. On nearly every point, the statistical error bars are smaller than the symbols. Experiment DØ has data that agree extremely well with this 1800 GeV spectrum. What is very impressive is the agreement with a typical theoretical calculation as shown by the lines. Only at the largest E_T, above say 250 GeV, does a disagreement appear at the level of a factor of about 1.5.

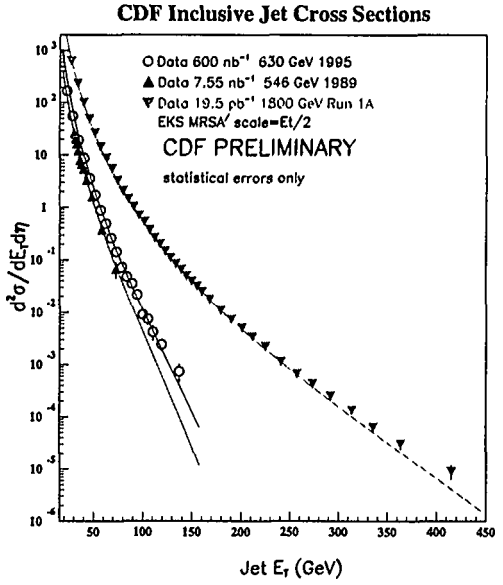


Figure 6: Inclusive jet cross section at three s values, as measured by CDF in the central region. The two lower energies correspond to the $Sp\bar{p}S$.

The disagreement is seen more clearly on a linear scale by dividing data by theory and subtracting 1, or (DATA-THEORY)/THEORY, and this is shown in Fig. 7. The points below 200 GeV are low but if you include systematic errors which are about 20% (largely E_T independent), they agree. The so-called "excess" at high E_T is clearly not a statistical fluctuation, and CDF could not find a systematic (or detector) effect which would account for it. A real excess that could not be explained by QCD would be exciting as these jets are probing quarks (mainly) at smaller distances than ever before, and if quarks were really composite at the scale of order $(1.5\text{–}2.0\ \text{TeV})^{-1}$ (about 10^{-17} cm), this is the sort of thing one might see. The DØ jet data could not quite either confirm or deny an excess: their high E_T data points were lower than CDF's but not by more than 1–2 σ.

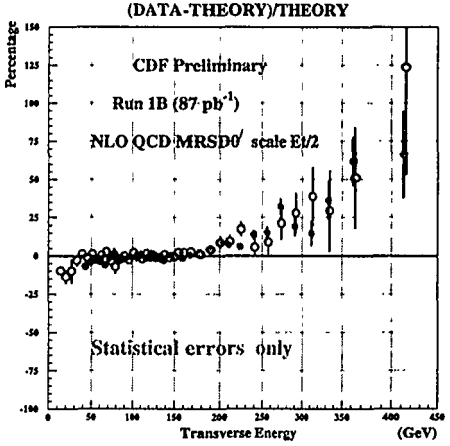


Figure 7: A comparison of the inclusive jet cross section with the NLO QCD calculation using the MRSD0′ structure function.

Before jumping to conclusions about dramatic new physics, one has to see whether some not-so-dramatic new physics can explain the discrepancy. There are two worthy contenders: (1) the density of gluons in the $p/\bar{p}$ at large x is more than in the structure functions being used for comparison (CTEQ3M, MRSD0′, and others) or (2) soft and colinear gluon corrections are important.[24] As to the former possibility, of course, one cannot just try adding in more gluons at high x because that will change all the fits to other data, such as DIS data. A new global fit has to be tried to find a solution consistent with all good data. Normally, the high E_T jet data would have little relative weight in such a fit and would not pull the structure functions. So CTEQ tried a fit giving extra weight to the high E_T data by artificially decreasing their errors, and found a solution CTEQ4HJ, shown in Fig. 8 with both CDF and DØ data. This makes the excess insignificant without significantly worsening the fit to the rest of the world. In their fit, the normalizations of CDF and DØ were left floating, but they only moved 2% which is impressive. So, one simple solution to the excess puzzle is to

modify the structure functions mostly at high x by just about doubling the glue. More data to shed light on this could come from probing the high rapidity tails of the jet distributions at lower E_T.

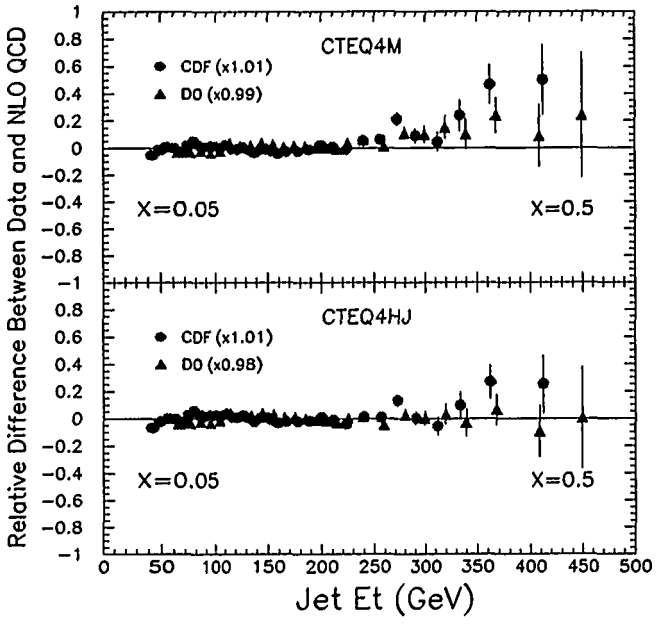


Figure 8: Linearized comparison [(DATA-THEORY)/THEORY] of inclusive jet data.

An alternative, or perhaps additional, way[24] of explaining the jet rate at very large E_T is to consider higher order corrections. While the full NNLO calculations have not been done (and it may be some time!), direct estimates of higher order corrections are sometimes possible by a process called resummation. This generally requires two hard scales in the process with one much larger than the other, say $Q \gg \mu$ where μ is the inverse wavelength of emitted gluons. Soft colinear gluons cannot know about the hard scattering taking place on the much smaller scale $1/Q$. In such cases, it is sometimes possible to resum the large corrections which have the form $\alpha_S \cdot log^k(Q/\mu)$ (resumming large logarithms). See Refs. 22 and 23 for more information. Very high $x_T = 2E_T/\sqrt{s}$ requires partons from very high Bjorken-x where the parton densities are falling fast and the phase space for gluon emission is reduced; this will affect the jet cross sections in the right direction to explain the excess, but according to Mangano,[24] "it seems unlikely that the full 30–50% excess reported by CDF ...could be explained by resummation effects."

The CDF two-jet mass spectrum, shown in Fig. 9, perhaps not surprisingly, shows the same excellent agreement at low mass with a growing excess compared to PYTHIA (CTEQ2L) at large mass. It is to a large extent the same data, so this is not independent. It is still impressive to note that we are now detecting parton collisions at $\sqrt{\hat{s}} = 1000$ GeV, and if there were strongly produced new particles, such as *"axigluons"* up to a mass of 870 GeV, they would be visible in this plot as a significant bump.[25] Several other types of hypothetical massive particles can also be excluded, thanks to our knowledge (or assumed knowledge) of their strong interactions, namely QCD. This search will be continued in the Tevatron Run II (1999–?), but a really large extension of the mass range will only come with the LHC.

Naturally, one of the first questions to ask, faced with a possible large E_T jet excess, is whether the angular (or η) distribution of these jets is normal. It is. To see this for dijets, we can calculate a variable χ defined as:

$$\chi = \frac{1 + cos\theta^*}{1 - cos\theta^*} = |e^{\eta_1 - \eta_2}|. \tag{11}$$

Figure 10 shows some χ distributions together with NLO predictions, and the fit is good for all mass ranges. From this, a lower limit can be put on a parameter Λ_C which is called the *compositeness scale*, namely Λ_C >1.8 TeV at 95% confidence level. Thus at a resolution of about 1.1×10^{-17} cm, the partons still appear point-like.

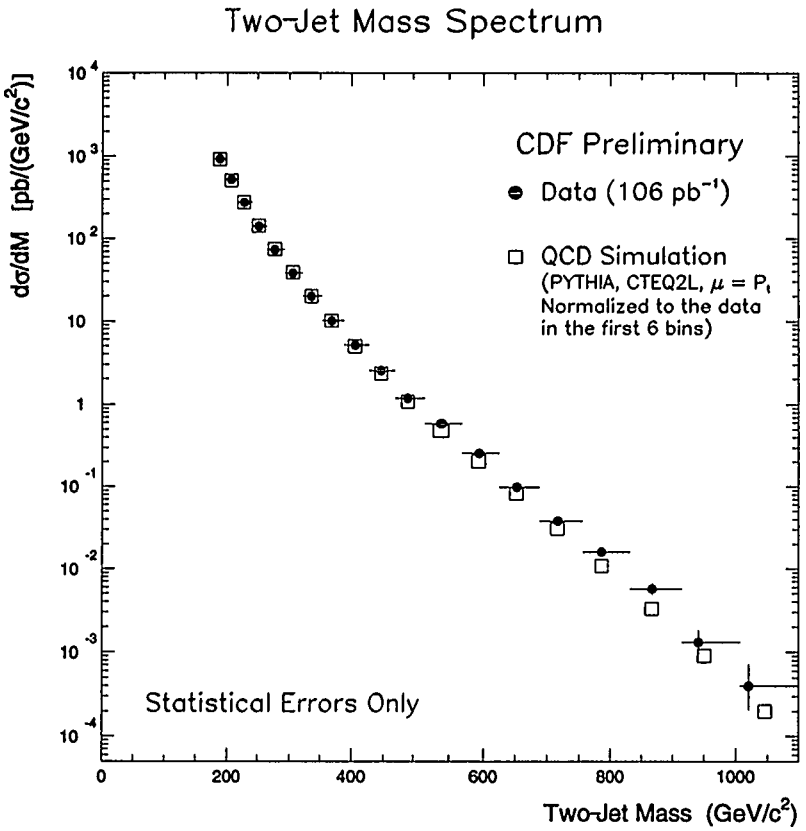


Figure 9: Spectrum of the invariant mass of the two highest jets.

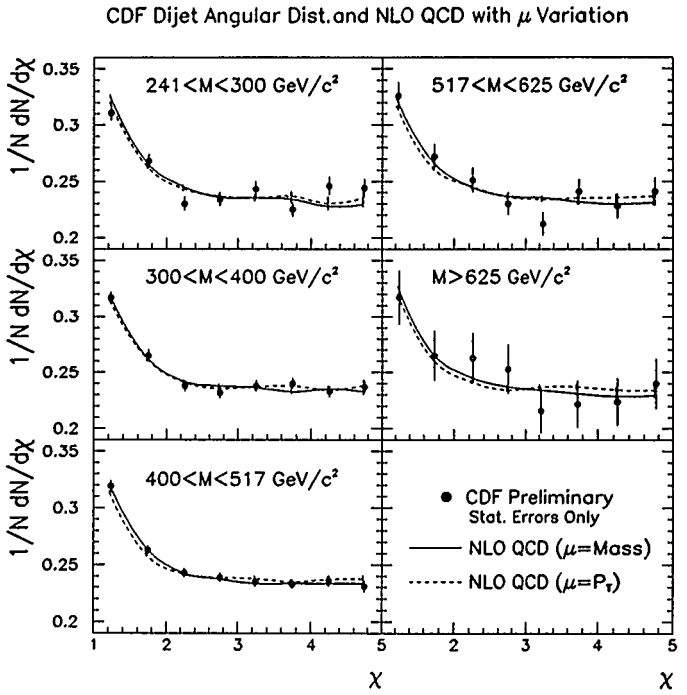


Figure 10: Angular distribution of the two highest jets in terms of the variable χ (see text).

Another place where large logarithms appear is when two balancing jets are at large opposite rapidity, or small angles. Then $log\left(\frac{\hat{s}}{Q^2}\right)$ is large and we can apply resummation schemes. Important progress in this direction came with the BFKL formalism from Balitsky, Fadin, Kuraev, and Lipatov.[26] A picture emerges of gluons scattering by t-channel gluon exchange, the latter also emitting gluons, so that this diagram times its complex conjugate is like a *ladder*. This is a perhaps naïve description of the BFKL Pomeron, not the same as the standard Pomeron giving diffraction with rapidity gaps (about which more will be said later), but related. The BFKL Pomeron is much discussed in relation to very low-x physics. DØ searched[27] for evidence in the form of a decorrelation between a pair of hadron jets as the rapidity interval between the jets increases. Figure 11 shows the azimuth angle difference $(1 - \Delta\phi/\pi)$; the back-to-back peaking has a tendency to wash out as $\Delta\eta$ increases. However, as seen in Fig. 12, the effect is not as strong as predicted by BFKL and is actually in agreement with the HERWIG Monte Carlo (but not NLO JETRAD). BFKL effects are seen elsewhere (e.g., at HERA) and more studies are clearly needed.

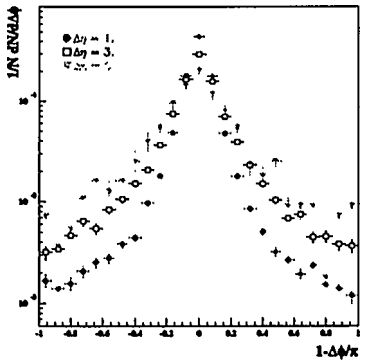


Figure 11: The azimuthal difference between the two leading jets (DØ) for three different values of their rapidity separation. The back-to-back balance gets washed out as $\Delta\eta$ increases.

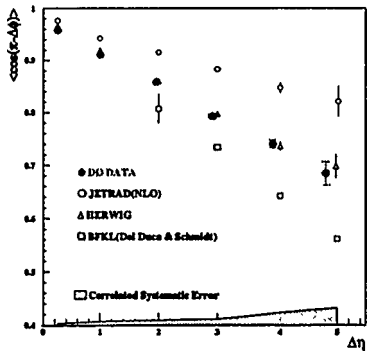


Figure 12: The mean value of $< cos(\pi - \Delta\phi) >$ versus $\Delta\eta$ showing the decorrelation of the previous plot, compared with three predictions.

4.1 Multiple Jets: Very High E_T

In the previous section, I discussed inclusive one-jet and two-jet data, but events with many high E_T jets are not rare at the Tevatron, and they provide an interesting testing ground for the QCD predictions *via* MC. One can study both the total rates and the structure of the events, e.g., sub-energies and angles between jets. Figure 13 shows CDF data, ignoring everything in the events except jets above $E_T = 20$ GeV and making a scalar sum of those above that threshold. The data are only plotted above $\sum E_T = 300$ GeV, far above any threshold effects, and extend to about 1000 GeV. The shape compares well with the two Monte Carlos (JETRAD and HERWIG) apart from being slightly flatter at large E_T, the same effect we saw in the one-jet inclusive spectrum (it is, of course, essentially the same data). The relative normalization of 1.4 applied to the MC to get best agreement is probably as good as could be expected for these far-from-simple events. Still, although the highest $\sum E_T$ events frequently have several jets, the two highest E_T jets usually dominate.

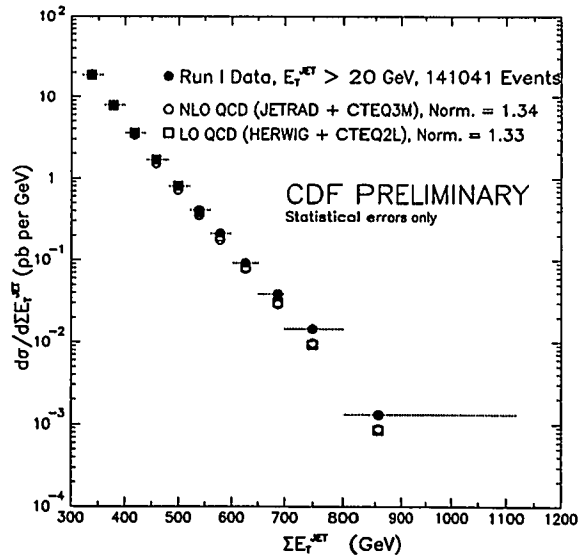


Figure 13: Distributions of total E_T including all jets above 20 GeV.

CDF did a study[21] of events with $\sum E_T$ above 420 GeV and three jets each above 20 GeV. There are many ways to study data with many variables, so one should try to choose plots that have a clear physical meaning, or which make incisive tests among models. Figure 14 (Ref. 21) shows the mass distribution of the three, four, or five highest E_T jets compared with HERWIG and NJETS; both give good descriptions. For three jets, one can go to their rest frame, calculate the energy fraction

$$X_j = \frac{2E_j}{m_{3j}}, \tag{12}$$

and make a Dalitz plot of X_1, X_2, and X_3. This sort of study can also be done for four-jet events by merging the two jets with the smallest invariant mass m_{ij} to get a three-body system (with an additional variable m_{ij}). Any number of jets can be sequentially reduced this way to a three-body system which can then be studied more simply. For example, the distribution of X_3 for three-jet events (all above 20 GeV) seems to be a variable with little discriminating power, both phase space and QCD Monte Carlo having similar behavior and agreeing with data, apart from a wave in HERWIG which the data does not show. Phase space models do not describe the data as well as the QCD calculations which predict large contributions from initial or final state gluon radiation.

5 Direct Photon Production: γ and $\gamma\gamma$

As quarks carry electromagnetic charge as well as strong charge, in any diagram involving gluon emission from a quark $q \to qg$, we can also have photon emission $q \to q\gamma$. The leading order diagrams are $qg \to \gamma q$ and $q\bar{q} \to \gamma g$, and there are also bremsstrahlung photons radiated off quark lines. The latter are usually considered as a background and are harder to measure, being close to (or in) a hadron jet. Therefore, experiments usually require the photon candidates to be *isolated*, to have very little accompanying energy in a cone of $R = 0.4$ (typically). This cut also minimizes background from π^0; most detectors cannot resolve the two photons from $\pi^0 \to \gamma\gamma$ at high p_T, but π^0 tends to be in jets.

Direct photon production at high p_T was first observed at the ISR.[29] As they had done for jets, the $Sp\bar{p}S$ and Tevatron extended the reach in p_T dramatically, up to about 120 GeV in the latter case as shown in Fig. 15. It is not enough to require an isolated electromagnetic shower; the background from π^0 is still high.

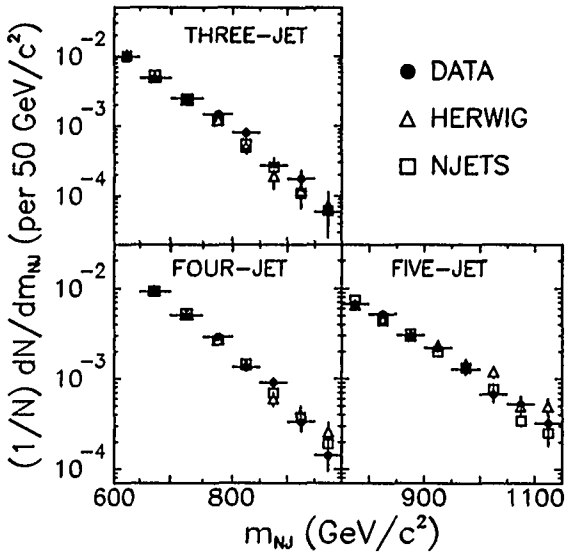


Figure 14: Distributions of the effective masses of the three leading jets, four leading jets, and five leading jets (if present, above 20 GeV). The data are compared with HERWIG and NJETS and agree well.

A method of statistically separating the γ and π^0 pioneered by UA2 (Ref. 30) is to start the calorimeter with a converter and then a separately read-out layer to see whether a photon conversion occurred. The probability for the two photons from a π^0 to convert is about twice the probability for a single direct photon, so it is easy to calculate the fraction of γ in the sample (although not on an event-by-event basis). This method can be used at arbitrarily high p_T. The CDF calorimeter also has a so-called Shower Maximum detector, a layer of strip elements after a few radiation lengths (near the maximum of a typical shower) which can measure the projected profile. The two photons from low energy π^0 are resolved into two peaks (depending on the decay orientation), but even at higher E_T when they merge (typically, in CDF, the shower separation is $d_{\gamma\gamma} = 50\ \text{cm}/E_{\pi^0}$), the profile is broader for π^0. The figure shows that both methods agree where they overlap, and also that the data agree well with NLO QCD, at least at high p_T, with the CTEQ2M structure function. We could expect that photons are better probes of

structure functions than jets; there are none of the complications of final state radiation, jet fragmentation, or questions about the correspondence between the jet and hard parton. Calorimetric detectors also have better resolution for photons than for hadrons, and it is intrinsically a clean process. So it was hoped that the diagram $gq \to q\gamma$ would be a good way to measure the gluon distribution $g(x, Q^2)$. However, higher order diagrams muddy the predictions, and they are not as precise a probe as once thought.

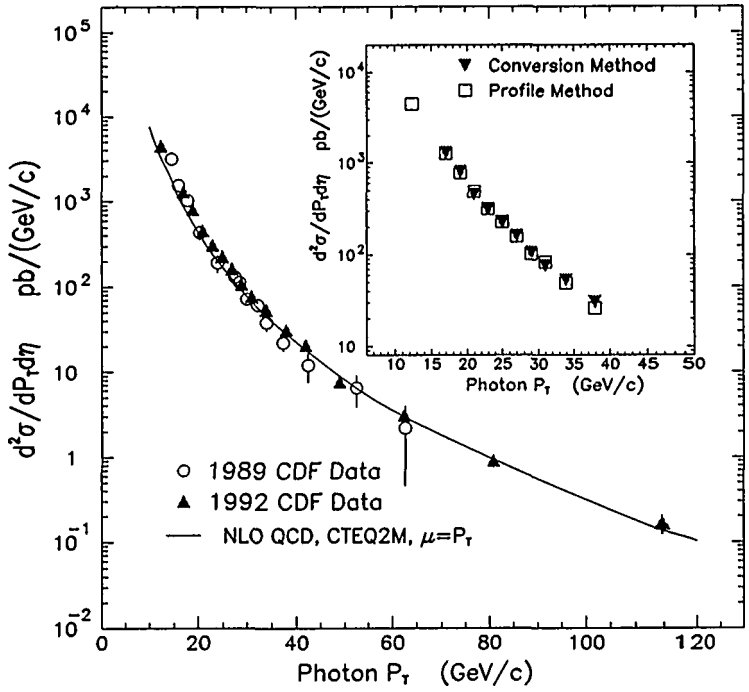


Figure 15: The p_T spectrum of direct photons as measured by CDF, compared to a NLO calculation which underestimates the rate at low p_T. The inset shows the agreement between two methods of identifying photons (conversion probability and shower profile).

In detail, the photon data lie systematically above the QCD line below 40 GeV. *All* direct photon data are systematically high at their lowest p_T values. If this were

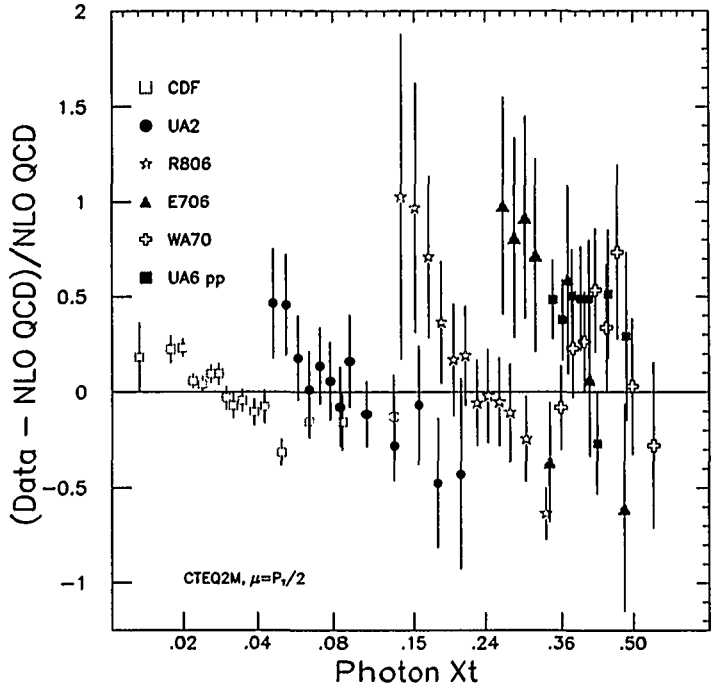


Figure 16: The x_t spectrum of direct photons in different experiments (data-theory/theory). The lowest p_T data are systematically high.

due to a structure function behavior, we would expect the trend to be common, to experiments at different $\sqrt{s}$, if plotted against the scaled p_T, namely, $x_T = 2p_T/\sqrt{s}$. In Fig. 16, (Data-NLOQCD)/NLOQCD are plotted and show that this is not the simple solution; at the same x_T, a low $\sqrt{s}$ point is higher than QCD, and a high $\sqrt{s}$ point is lower. Admittedly, these points differ in Q^2, but the Q^2 dependence is supposed to be well-handled by the QCD calculation. It looks like an effect that to first order is a p_T dependence, the lowest p_T being enhanced at any $\sqrt{s}$. A likely explanation is that the QCD predictions fail because they assume that the incoming partons are colinear. We know that cannot be strictly true because protons have a finite size, so the uncertainty principle will give an *intrinsic* k_T of a few hundred MeV/c to the partons. But more than that, there

are nonperturbative (and therefore not well-calculable) effects, namely, soft gluon emission, that can give k_T which may be larger than a GeV and will smear the production cross section. This k_T (which I would not call intrinsic, I reserve that for the proton size effect) will depend on $\sqrt{s}$ at fixed x and could account for much or perhaps all of the behavior in Fig. 16. But the jury is still out. One good test should be two photon production.

The production of two back-to-back high p_T direct photons was first seen at the ISR,[31] but the signals there were very small. Even at the Tevatron, very few events were found by CDF in 90 pb^{-1} as shown by the plot of $M_{\gamma\gamma}$, Fig. 17. In this plot, the rise to $M_{\gamma\gamma} \approx 30$ GeV is entirely a trigger threshold and data selection effect; presumably the cross section is very high for low mass pairs, all the way down to the GeV region and below, but the experiment has not been done. (It might be very interesting.) Can we conclude anything about k_T from this limited data? The diphoton system p_T is well-measured, but the poor statistics can be seen in Fig. 18. What can you say?

On a separate issue, note that $M_{\gamma\gamma}$ is well-determined by good electromagnetic calorimeters, obviously much better determined than M_{JJ}. For best resolution, one needs to know also the production point, not always easy at a high luminosity hadron collider such as LHC. But this is why the two-photon channel is considered an interesting channel for searching for Higgs H^0 even though the branching fraction of $H \to \gamma\gamma$ is very small, less than 10^{-4} depending on M_H. Between about 80 GeV and 150 GeV (the intermediate mass Higgs region), the full width of the Higgs is only a few MeV, much narrower than conceivable resolutions (so an experiment with super resolution has a major advantage). There is a very interesting thing about this decay which makes it important even if the H^0 is discovered in another channel. The H^0 being neutral does not actually couple to photons, so this decay proceeds through loops of anything that couples both to H^0 and γ, and the heavier the better. This means the decay rate will depend on the existence of heavy things such as W, t, $\tilde{q}$, and even charged particles of many TeV, or even hundreds of TeV. But it will be difficult! Very!

6 Vector Bosons: W/Z + Jets

Just as direct photons can be used as probes of hard QCD processes, so can vector bosons, namely, $W^{\pm}$ and Z. In lowest order, the perturbative diagrams are simply

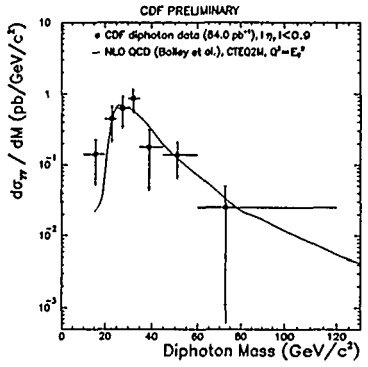


Figure 17: The diphoton mass spectrum measured in CDF. The rise at low $M_{\gamma\gamma}$ is due to threshold/acceptance effects.

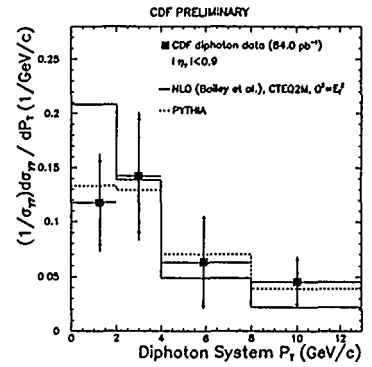


Figure 18: The distribution in p_T of the $\gamma\gamma$ pair. This should be a useful probe of k_T effects.

$q\bar{q}$ annihilation, $q\bar{q} \to W$, and the W have low p_T which is given by, and provides information on, nonperturbative initial state gluon radiation and k_T (I do not now distinguish these). This process is like Drell-Yan ($q\bar{q} \to l^+l^-$) and is sometimes also called Drell-Yan. Given that a colored quark from the proton annihilates with a colored antiquark, with a large rapidity separation, perhaps the associated hadrons in these events would show interesting differences with, e.g., typical soft collisions. To the extent that people have looked (which does not include the forward regions), there are no striking differences.

More study has been done of events containing both a W/Z and high p_T jets. Apart from the intrinsic interest for QCD, $W + jets$ is the most important channel for studying the top quark. The dominant process for creating top quarks is $q\bar{q} \to t\bar{t}$ and then $t\bar{t} \to W^+bW^-\bar{b}$. The W then decay either hadronically $W \to q\bar{q}$ or leptonically $W \to l\nu$. If both W decay hadronically, which happens 46% of the time, we have a six jet final state. Strong QCD production of six jets has a much higher cross section, but a $t\bar{t}$ signal can still be observed[32] by demanding that one or two of the jets have characteristics of b jets (leptons from semileptonic b decay, or displaced vertices). When both W decay leptonically (10% of the time for each of e, μ, or τ for each W), the signature is relatively clean, but two neutrinos are undetected so the kinematics is poorly constrained. The best compromise between

signal:background and reconstruction ability is with the 44% fraction which are hadronic+leptonic, called the *lepton + jets* mode. There is still a large background from non-top W + jets, hence the importance of being sure we understand the QCD aspects. Note, however, that two of the jets in $t\bar{t}$ production will be b-jets, so b-tagging is very important. Unfortunately, b-tagging efficiencies are typically only about 30%–40%.

The cross section for $W + \geq n$ jets and $Z + \geq n$ jets[33] as functions of the number (actually $\geq n$) of jets is shown in Fig. 19. Jets are counted if their E_T exceeds 15 GeV and they are in the pseudorapidity region $|\eta| \leq 2.4$. Note the excellent fit to a pure exponential, with a factor of five decrease for each additional jet. This factor will depend on the minimum jet E_T. Note also that the Z cross sections are just about a factor of ten below the W (mostly because of the mass difference), and show the same behavior. Leading order QCD predictions using VECBOS and MRSA and CTEQ3M structure functions and two different choices of Q^2 are also shown, giving some idea of the uncertainty coming from the choice of renormalization scale. The cross section for W + 4 jets (with the above cuts) is about 5 pb^{-1}. Compare this with the cross section for $t\bar{t}$ [$7.7^{+1.8}_{-1.5}$ pb from CDF, and 5.8 ± 1.8 pb from DØ (for $M_t = 170$ GeV)] times the 0.43 combined branching fraction. I do not go into additional complications in the top studies such as: one or more of the wanted jets from top decays may be below threshold or at too large η, and additional jets from gluon radiation may be in the selected region. These effects are all supposed to be modeled correctly in the Monte Carlo simulations.

There are many measurements one can make and compare with perturbative QCD in W/Z + multijets events. I will just show one and mention a few more. Figure 20 shows the E_T of the highest E_T jet associated with a W. There are a few events with a jet above 150 GeV.

The spectrum includes the estimated contribution from $t\bar{t}$ events *(background!)*, from jets from other interactions (pile-up), and "QCD background" which means that a hadron jet fakes a W. The sum of all these fits the data reasonably well, but the data above 120 GeV are systematically high. Other plots agree remarkably well; these include:

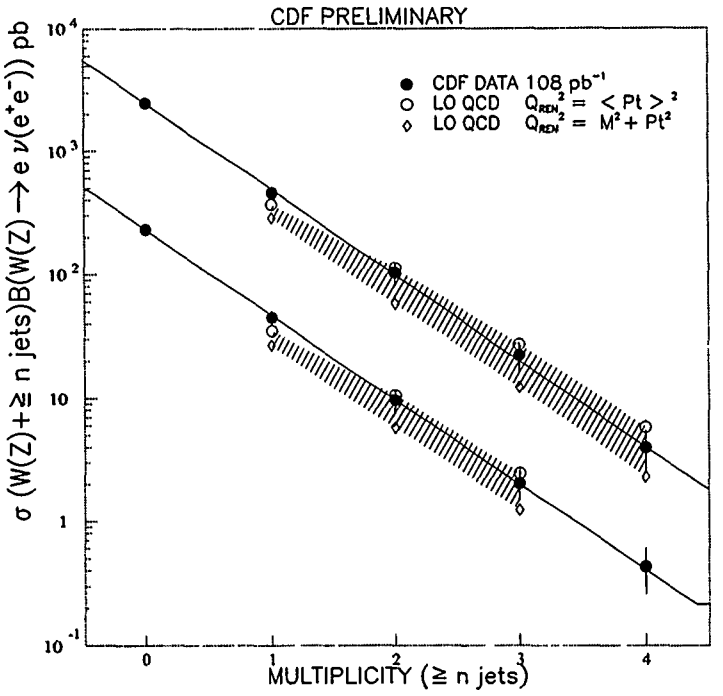


Figure 19: The multiplicity of jets in events with a W (top curve) and Z (bottom curve). The lines are simply exponential fits. The shaded band shows LO QCD and the effect of varying Q^2 within the range shown.

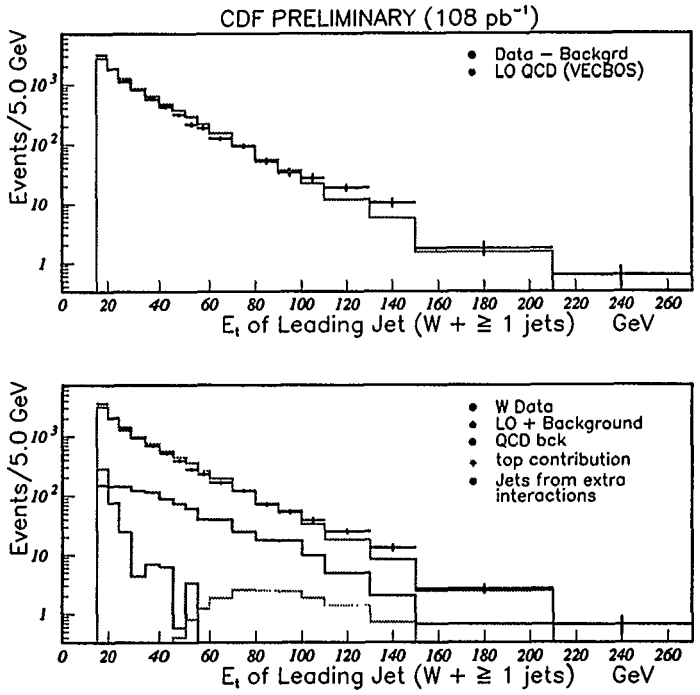


Figure 20: In a study of jets associated with W, the top plot shows the E_T spectrum of the leading jet and the bottom plot shows the predictions for how this is composed.

- The E_T distributions of jets two and three if present.
- The dijet mass distributions if two or more jets are present. It extends to about 650 GeV. There is no sign of any extra events in the W/Z region from WW or WZ production!
- The distance ΔR_{ij} in the $\eta\phi$ plane between two jets.
- $E_{T2} + E_{T3}$ . . . and so on.

7 Heavy Quark Production: Charm, Beauty, and Top

In this section, we consider c, b, and t quark production; these are normally considered the heavy quarks. The production of strange s quarks, including $\phi(s\bar{s})$ mesons, cannot be calculated in perturbative QCD. Such small mass means too large α_S to handle. For top ($M_t \approx 175$ GeV) and bottom ($M_b \approx 4.1$–4.5 GeV), perturbative QCD should work rather well, and we can test that. The charm quark case ($M_c \approx 1.0$–1.6 GeV) is marginal; perhaps charm can be used as a bridge between perturbative and nonperturbative QCD?

A set of diagrams for $b\bar{b}$ production is shown in Fig. 21.

The leading order diagrams, $O(\alpha_S^2)$ (two strong vertices), are $q\bar{q}$ annihilation to a massive virtual gluon, or $gg \to Q\bar{Q}$ with t-channel Q exchange. Higher order diagrams are gluon splitting $g \to Q\bar{Q}$, in which the $Q\bar{Q}$-pair will be close in $\eta\phi$ (probably in the same jet), flavor excitation in which only one of the $Q\bar{Q}$-pairs is at high p_T, and hard gluon radiation off any parton line.

What experimental techniques are used to study b production? The b-quark lifetime is *much* longer (about 10^{-12} s) than the formation time of hadrons (about 10^{-23} s). The b quark therefore emerges from the interaction in a hadron (B). The "average flight path" $c\tau$ for B mesons is about 460 μm, so a high-p_T B meson with a γ-factor E/M frequently travels a few mm before it decays. High-precision tracking close to the interaction point, usually with silicon strips (as in the CDF Silicon VerteX detector SVX) can reconstruct these secondary vertices and kill the overwhelming combinatorial background one would otherwise have. One can inspect the $c\tau$ distributions for prompt, charm, and bottom components and select the latter. This can be done, for b quarks, with a typical efficiency of around 30%. Another technique for tagging b hadrons or c hadrons is to use their semileptonic

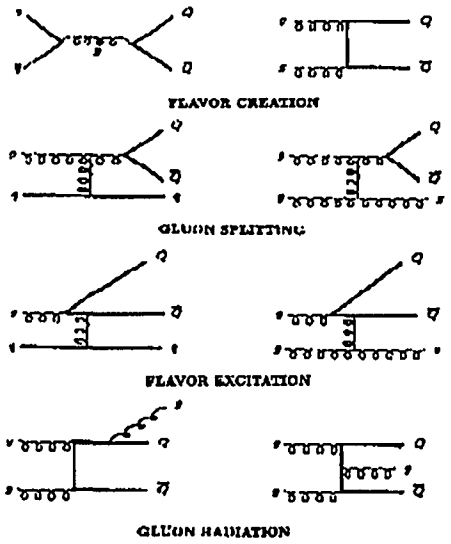


Figure 21: Feynman diagrams for leading and next-to-leading order b-quark production. Please attribute the fuzziness to quantum fluctuations!

decays. The branching fraction is about 10% to each lepton. (Of course, this is the same as for W; indeed, the process is $b \to Wc$ where the W is virtual, followed by the virtual W decay.) It is hard to use τ, but high p_T electrons or muons in or close to a hadron jet and coming from within mm of the interaction vertex make a good signature for c or b decays. Distinguishing c from b is not easy [they have similar branching fractions to leptons as you would expect, and the lifetimes are not *greatly* different: $c\tau(D^{\pm}) = 317$ μm, $c\tau(D^0) = 124$ μm, $c\tau(B) = 465$ μm]. However, the more massive b quark kicks the lepton out with larger Q than the c quark does, and this kinematic difference is quite powerful for c/b discrimination.

Figure 22 shows CDF data[34] on the production cross section for B hadrons in the central region, $|\eta| \leq 1.0$ as a function of p_T. Three different techniques were used: two look for high-p_T muons with a nearby reconstructed charmed meson (D^0, D^{*+}) and the other uses a high p_T ψ as seen in $\mu^+\mu^-$, together with a K or K^*. The latter mode has only about a 1% branching fraction—it occurs through $b \to$ "W"c followed by "W" $\to \bar{c}s$ and the c and $\bar{c}$ make a ψ—but it has a good signature. In fact, 20% of all $p_T > 5$ GeV/c ψ come from b decay. The data on B production is higher than the theory prediction by a factor three to four, more than the systematic errors on the theory (dashed lines). Experiment DØ sees a similar (although less significant) discrepancy.

If we study J/ψ production from any source (prompt, b decays, χ decays), the data is also a factor of several times higher than the predictions. To investigate this, we can separate the components. Displaced vertices in the CDF SVX select the component from b decays, which is found to be 20% for $p_T > 5$ GeV/c. The other J/ψ are "prompt," with the decay muons apparently coming from the production vertex. These can again be separated into J/ψ coming from χ decay: $\chi \to \psi\gamma$, by looking for an associated photon in the electromagnetic calorimeter with acceptable combined masses, or not coming from χ. The surprising result is that the rate of prompt ψ and ψ' production is much larger than the theoretical expectation, in the case of ψ' by a factor of 50! Here is a good example of experiment telling theory that some aspect of the theoretical calculations was badly wrong! A factor of about 50 wrong! The simplest explanation is probably that the theoretical calculations assumed that to make a J/ψ, you have to produce a c and $\bar{c}$ in a color singlet state, with the right spins and orbital angular momenta. This is asking quite a lot! Perhaps instead one can produce a c and $\bar{c}$ in any color state, e.g., color octet, and the color can be radiated away by soft gluons (which

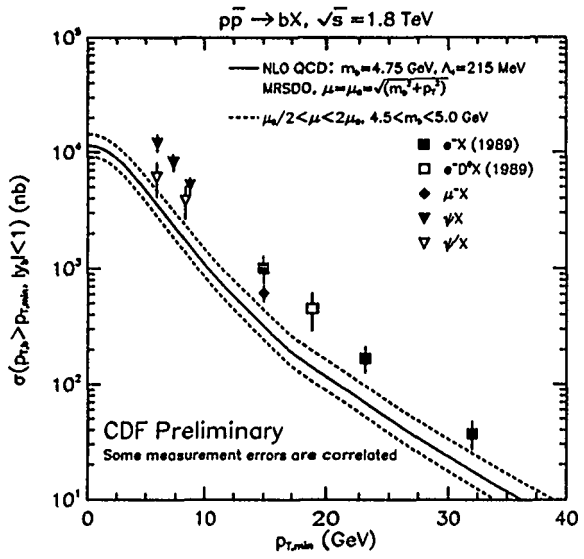


Figure 22: Cross section for B-hadron production vs p_T at the Tevatron.

is difficult to calculate) until the $c\bar{c}$ pair is colorless. Similarly, angular momenta can be radiated away until we get to the ground state. This is the *color octet model*, and it seems to do a good job of calculating the spectrum shape, but does not have much to say about the normalization (except that it should be much higher than the old *color singlet model*). One interesting test will be to study the nearby hadron density. The isolation of the J/ψ should be less in the color octet model, but being a nonperturbative effect, there are no precise predictions.

Data on open charm production at the Tevatron are meager, but as described above, the hidden charm $c\bar{c}$ sector is very interesting. What about hidden beauty, $\Upsilon(b\bar{b})$? Figure 23 shows the nicely separated peaks in the dimuon spectrum for $\Upsilon(1S)$, $\Upsilon(2S)$, and $\Upsilon(3S)$. The Υ are all prompt; they can be decay products of excited states like χ_b, but these are prompt decays. Again, we can get a handle on them by looking for associated photons (direct photon detection capability is very useful!). The data are about an order of magnitude higher in cross section than the predictions of the color singlet model, see Figs. 24 and 25. Color octet production may account for the discrepancy.[35]

The trend towards improved agreement between theory and experiment as M_Q increases continues to the top quark. Figure 26 shows a comparison between predictions and CDF data, which are at most a factor of two higher (about 1.5 standard deviations) while DØ data agree with theory. Now we only have to consider open top production; the top quark lifetime is so short that it decays before it can form bound states. There are no top hadrons. At the Tevatron, $t\bar{t}$ pairs are produced mostly by $q\bar{q}$ annihilation. At LHC, $M/\sqrt{s}$ is seven times lower, therefore so is the x of the incident partons, and $gg \rightarrow t\bar{t}$ is dominant.

I finish this section with the search for the six-jet decays of $t\bar{t}$, which is very difficult given the large QCD six-jet background. The CDF analysis[32] selected events with six jets above 15 GeV in E_T, central, and required at least one of the jets to be b-tagged. This, of course, kills a lot of the background, which is then of a similar magnitude to the signal. One fits all jet combinations to the hypothesis

$$M_1 + M_1 \rightarrow (M_W + b) + (M_W + \bar{b}) \rightarrow (J + J)_W + b + (J + J)_W + \bar{b} \qquad (13)$$

with the two jets from each W constrained to have the right mass. M_1 is left as an unknown. The jet combination with best χ^2 is chosen, and the mass M_1 plotted in Fig. 27. The data by themselves could hardly be taken as evidence for top, so this is not a discovery channel. However, our QCD studies give us confidence in the

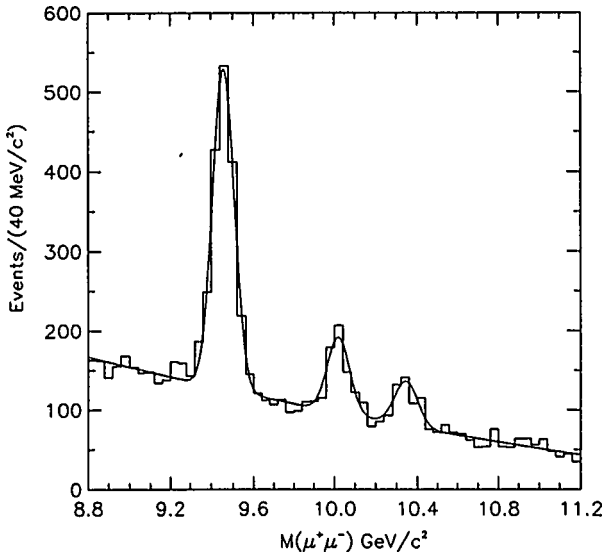


Figure 23: The dimuon $\mu^+\mu^-$ mass spectrum in CDF showing the $b\bar{b}$ resonances $\Upsilon, \Upsilon', \Upsilon''$ on top of a smooth background.

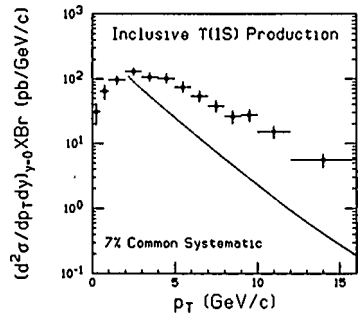


Figure 24: The cross section × branching fraction to $\mu^+\mu^-$ of the Υ compared with a QCD calculation.

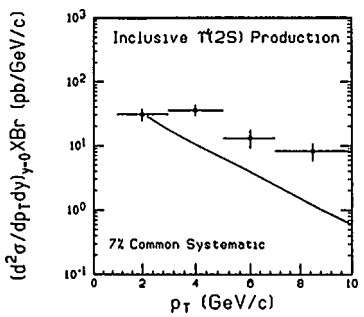


Figure 25: The cross section × branching fraction to $\mu^+\mu^-$ of the $\Upsilon'(2S)$ compared with a QCD calculation.

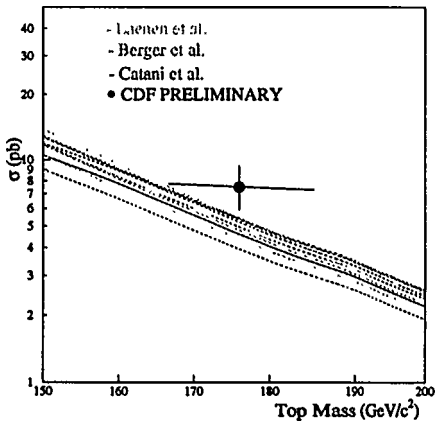


Figure 26: The cross section for production of the top quark as a function of the assumed mass M_t, together with the central value of the CDF M_t measurement and some theoretical predictions.

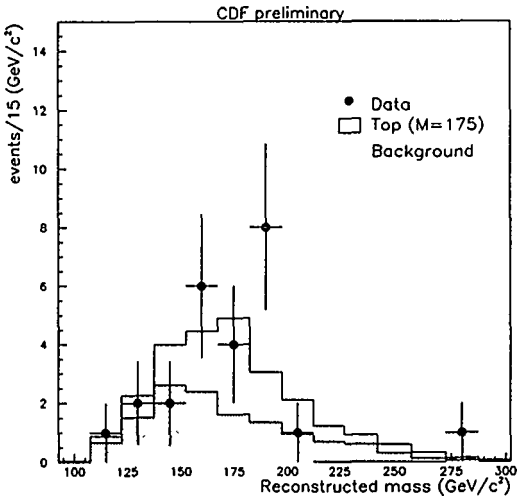


Figure 27: Six jet events (including b jets) treated as $t\bar{t}$ candidates, plotted as a function of the fitted mass M_t. The shaded area is the expected QCD $\rightarrow$ 6 jets background, and the open area the fit to a top contribution.

estimate of the non-top background, and the excess can be used to measure both M_t and $\sigma_{t\bar{t}}$ which are consistent with (but have larger errors than) measurements in the other channels.

8 Double Parton Scattering

All the hard process cross sections discussed so far have depended on the single parton distribution functions, and have ignored possible correlations between partons. The basis of the parton model is that they are non-interacting, but of course, this is not true in QCD. There are still some "trivial" correlations such as: (1) $\sum x = 1.0$ so if you find a parton with $x = 0.6$, there will be no others with $x \geq 0.4$. (2) The cloud of partons which constitute a proton has a limited radial distribution. Measuring the probability of *Double Parton Scattering, DPS,* where two independent hard scatters take place in the same $p\bar{p}$ collision, gives information on this spatial extension in the transverse plane. Obviously, the probability of a second hard scattering, given a first, will be small if the parton cloud is large, and greater if it is small. We can write schematically:

$$\sigma_{DP} \equiv \frac{\sigma_A \sigma_B}{A_{eff}}. \tag{14}$$

σ_A and σ_B are the cross sections for the two single hard scatterings, and σ_{DP} is the cross section for both in a single interaction. A_{eff} is a parameter with dimensions of area; the smaller A is, the more compact is the parton cloud and the larger the rate of double parton scattering. Commonly, σ_{eff} is used for the area A_{eff} but could be confusing as we are used to σ meaning a cross section and to event rates rising with σ rather than the inverse. So I prefer A_{eff}.

The first measurement of DPS was a study by the Axial Field Spectrometer[36] which selected events with four jets with $E_T(jet) \geq 4$ GeV and $\sum E_T(jet) \geq 25$ GeV. A jet threshold of only 4 GeV is dangerously low, but not as shocking at the ISR ($\sqrt{s} = 63$ GeV) as it would be at collider energies ten to 30 times higher. The background to DPS is "double bremsstrahlung," DBS, where a $2 \rightarrow 2$ hard collision is accompanied by radiation of two gluons. DPS and DBS are statistically distinguishable because in DPS, one pair of jets tends to balance (same E_T, opposite in ϕ) and so does the other pair, while in DBS this is not normally the case. Distributions of an *imbalance parameter* are best fit by a mixture of the processes, and from the amount of DPS, one could derive an effective radius of the

proton's parton cloud to be 0.3 fm. The fraction of four-jet events which are DPS falls rapidly with the E_T of the jets, but close to the lower cuts in the AFS data was as high as 60%. Large $\sum E_T$ triggers at fixed target energies $\sqrt{s} \leq 30$ GeV never showed the dominance of a two-jet structure, probably because with a steeply falling x distribution and parton scattering cross section, it was easier to get large $\sum E_T$ by DPS and TPS (Triple Parton Scattering) events. On the other hand, if one requires four *large* E_T jets as done by UA2 (Ref. 37) (15 GeV) or CDF[38] (25 GeV), the DPS fraction is very small. UA2 gave only an upper limit, while CDF found a signal at the significance level 2.7 σ, 5.4% for DPS/DBS.

The DPS fraction will rise strongly as the jet E_T threshold is decreased, both because of the structure function rising and because the partonic cross sections rise. CDF has a new analysis[39] which requires exactly three jets with $E_T > 5$ GeV and a direct photon candidate (it could be a π^o) above 16 GeV. Starting as low as 5 GeV was shown to still give good behavior, e.g., in terms of di-jet balancing, so the parton-jet relationship seems still to be acceptable. Having a photon (or narrow em jet) as one of the "jets" has advantages despite the lower rate. Perhaps more important, the cuts allow the two jet pairs to have rather different E_T, which reduces the allowed combinations in the $2 \times (2 \rightarrow 2)$ reconstruction. It is found that about half the events in this sample are DPS; the significance of the signal is not in doubt. Figure 28 shows the distribution of ΔS, the azimuth angle between the jet pairs, the pairs being chosen to have the best balance. This is very peaky (at $\Delta S = \pi$) for DBS but is rather flat for DPS. The area parameter is measured to be $A_{eff} = 14.5 \pm 2.6$ mb, significantly larger than the AFS result. Although we might expect A_{eff} to be rather independent of $\sqrt{s}, x$, etc., there can be some dependence. It would be interesting to have more information on this process. In fact, with the right selections, even TPS $= 3 \times (2 \rightarrow 2)$ should have a good signal:background (e.g., events with two jets above 25 GeV, two with E_T = 15 GeV–25 GeV and two with E_T = 7 GeV–15 GeV. (The staggering in E_T is, of course, just to reduce background; events with six jets above 7 GeV will have a much larger TPS signal but much larger $2 \rightarrow 6$ background.)

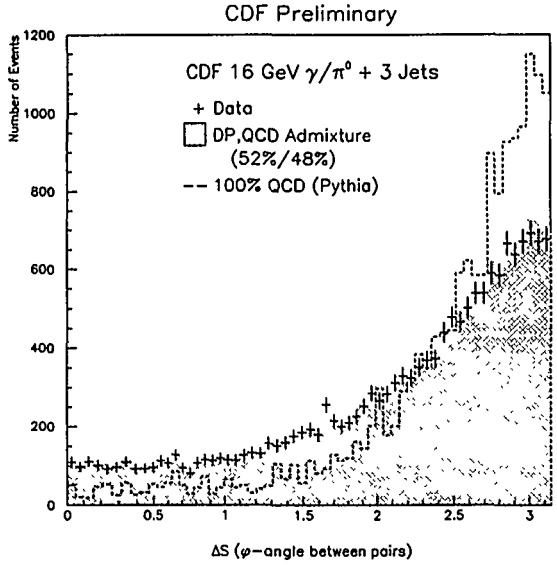


Figure 28: The azimuth angle is plotted between the best balancing pairs in γJJJ events. Double parton scattering gives a flat distribution.

9 Color Coherence

Among the other interesting phenomena which are being studied at the Tevatron, *color coherence* deserves attention. A proper simulation of strong interactions

would compute all the color wavefunctions in space-time, and derive probabilities of finding particles by adding and then squaring the wavefunctions. As in optics, we have destructive or constructive interference, giving rise to "fringes" or at least angular regions that tend to be depleted or enhanced (extremely broad fringes if you like). We do not generate our Monte Carlo events at this level, but the effects of this color coherence can be seen. One manifestation is a *string effect* in $e^+e^- \to q\bar{q}g$ three-jet events where some angular regions get enhanced, others depleted. Another is *angular ordering* in a parton cascade, where successive opening angles are progressively smaller ($\theta_1 \geq \theta_2 \geq \theta_3$, etc.). As usual, $p\bar{p}$ interactions are more complicated than e^+e^- because we have gluon radiation in both the initial and final states, and interference occurs between them. Some Monte Carlo programs include angular ordering effects [HERWIG, PYTHIA+, PYTHIA5.6 (final state only)] and others (ISAJET, JETRAD) do not. One can look[40] at events with one stiff leading jet (Jet1) and two others (Jet2, Jet3). Jet3 is normally near Jet2, and we can plot its distribution around Jet2 as an angle in the η, ϕ plane. Preliminary data from DØ show that the third jet is much more likely to be between Jet2 and the beam directions than orthogonal (i.e., at the same η as Jet2). HERWIG seems to get this right while ISAJET (with no color coherence) does not.

10 Jet Fragmentation

Studies of jet fragmentation have received a lot more attention recently at LEP,[4] from $e^+e^- \to q\bar{q}$, than at the Tevatron. It is an interesting arena for pushing QCD to its soft limits, and understanding how a hard quark in a color field transforms into isolated colorless soft hadrons. Modeled as a branching tree of quarks and gluons, one has to handle the problems of α_S diverging as four-momenta Q become smaller, giving so-called *soft divergences* and *colinear divergences*. (These are not important for a calorimetric jet measurement, but here we are discussing the hadronic structure.) One normally puts a cut-off scale Q_0 of several GeV on the cascade, to keep emission probabilities small:

$$w \approx \alpha_S \cdot ln^2 \frac{E}{Q_0} \cdot \tag{15}$$

In the 1970s and 1980s, tools for summing divergencies were developed especially by the "Russian school"[41] which led to the Leading Log Approximation, LLA, and recently to the Modified LLA or MLLA by Mueller,[42] Dokshitzer, and Troyan.[43] This results in a formula for jet fragmentation into hadrons with essentially only two parameters, an effective cut-off Q_{eff} of the parton cascade and the ratio of hadron multiplicity to parton multiplicity (at the cut-off scale). Color interference, giving angular ordering, is incorporated. The MLLA manages to get very reasonable fits to many fragmentation variables. One such is the variable

$$\xi = ln\frac{1}{z} \tag{16}$$

where

$$z = \frac{p_{had}}{p_{JET}} \tag{17}$$

is the fractional momentum of the hadron along the jet axis. $\xi = 0$ then corresponds to a single hadron jet, while a soft hadron with $z = 0.0025$ has $\xi \approx 6$. In a CDF study,[44] all the charged hadrons within a cone around the jet axis of radius 0.466 rad are counted, and the ξ distributions are plotted in Fig. 29 for several values of the leading dijet mass from 105 to 625 GeV. Good fits are obtained to a form derived from the MLLA. Surprisingly, the parameter Q_{eff} for these fits is very low, about 240 MeV, but this should not be interpreted as "QCD works down to 240 MeV." However, the parameterizations given by the MLLA methods can apparently be extrapolated with some success even down to this soft region.

Studies show that the cone size θ can be varied and the fits remain good with stable parameters. The position of the peaks in Fig. 29 depend both on E_J and θ, but it is just the product $E_J\theta$ which matters. If we define

$$Y = ln\frac{E_J\theta}{Q_{eff}}, \tag{18}$$

then the position ξ_0 of the peak is given by

$$\xi_0 = \frac{1}{2}Y + \sqrt{cY} - c, \tag{19}$$

where c is a constant; 0.292 fits the data. We then can show a universal curve of ξ_0 versus $M_{JJ}\theta$ with CDF points for several dijet masses together with LEP e^+e^- data, see Fig. 30. This emphasizes the similarity of the internal structure of jets at the Tevatron ($p\bar{p}$) and LEP (e^+e^-).

11 Diffraction and Rapidity Gaps

Essentially everyone agrees that QCD is The Theory of Strong Interactions. Nevertheless, we actually know how to calculate only a very small fraction of strong

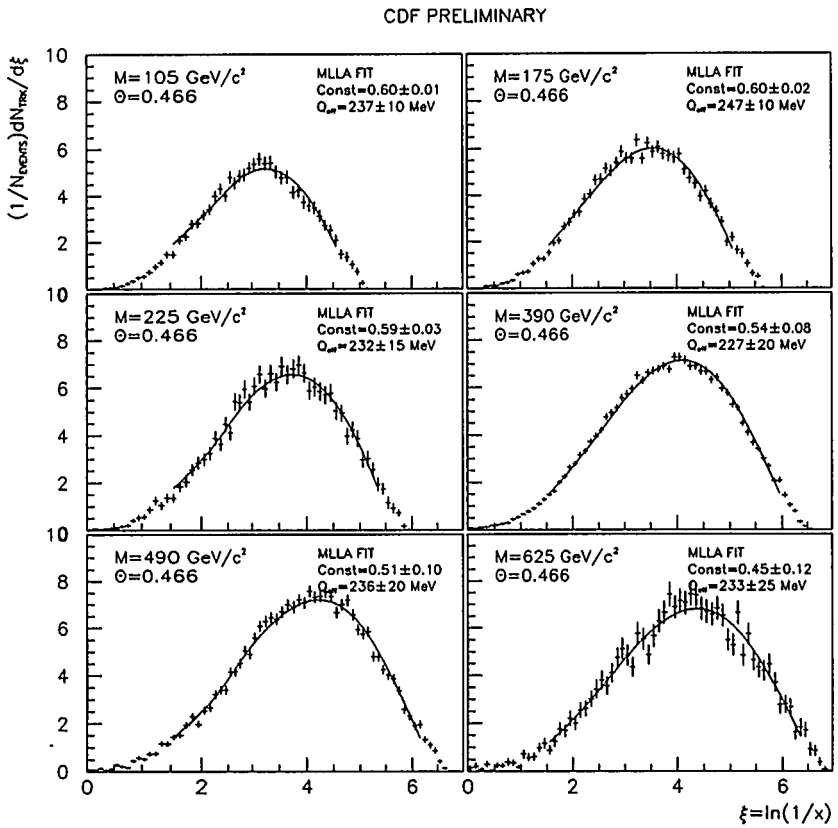


Figure 29: For six different dijet masses, the distribution of the jet fragmentation variable ξ is shown and compared to a fit derived from the MLLA formalism.

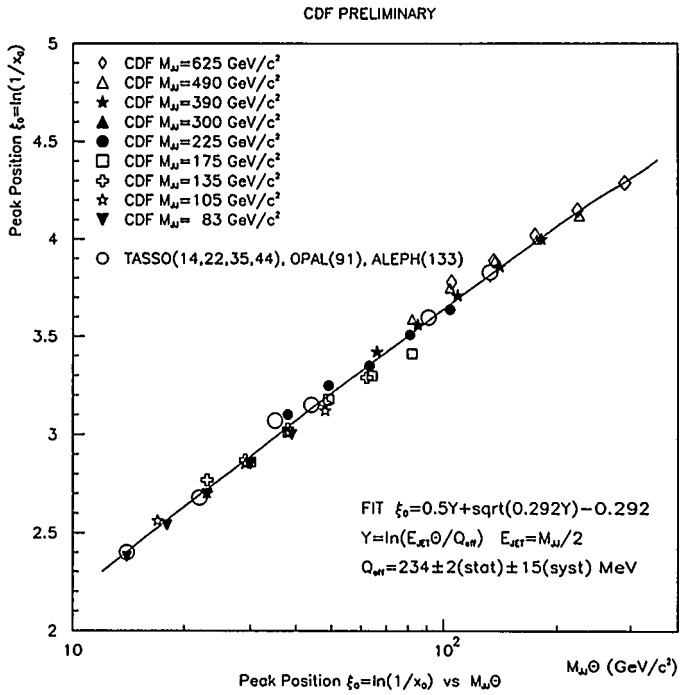


Figure 30: The jet fragmentation parameter ξ_o vs $M_{JJ}\theta$ for Tevatron and LEP jets.

interaction physics (large Q^2) and therefore do not have a good understanding of such "soft" phenomena as the total cross section σ_T, elastic scattering $\frac{d\sigma}{dt}$, diffractive dissociation, and double Pomeron exchange. The *Pomeron*, $I\!P$, can be defined[46] operationally as the dominant strongly interacting entity exchanged over large rapidity gaps. In elastic scattering at the Tevatron, the p and $\bar{p}$ are separated by 15 units of rapidity, and the four-momentum transfer exchanged is carried by the Pomeron, except at very small t where photon exchange dominates *(Coulomb scattering)*. The imaginary (absorptive) part of the elastic scattering amplitude at $t \to 0$ is proportional to the total cross section σ_T; this is the famous optical theorem. The Pomeron therefore "drives" the total cross section. Regge theory is not much taught now, but it is more successful than QCD at "explaining" much soft strong interaction data. Could it one day be "derived" from QCD? In Regge theory,[45] Pomerons and other *Reggeons* are exchanged carrying complex angular momentum $\alpha(t)$. At any t, the highest α tends to dominate, and at $t \approx 0$, this is the Pomeron. Total cross sections behave like:

$$\sigma_T = C \cdot s^{\alpha_{I\!P}(0)-1}, \tag{20}$$

so as $\alpha_{I\!P}(0)$ exceeds 1.0 total cross sections rise with energy $\sqrt{s}$. In fact, a more theoretical definition of the Pomeron[46] is: "The highest Regge trajectory, with the quantum numbers of the vacuum, responsible for the growth in hadronic total cross sections at high energy." It has the quantum numbers of the vacuum (zero I-spin, no charges), which is not surprising as a proton can "emit" a Pomeron and remain a proton. The relation between the Pomeron and the QCD vacuum (gluon condensates?) is interesting. So now I have defined it (twice!), but what is it? QCD has quark and gluon fields, so presumably the Pomeron should be describable in the same terms.

There is currently much progress in trying to understand the Pomeron by studying hard diffractive processes, i.e., events with both a Pomeron and a large Q^2 process such as high E_T jet production or W production. The idea is to think of the Pomeron as a *quasiparticle*. Think of it as a particle, Pomeron ($I\!P$) that can be emitted with some flux and absorbed, and that has a structure function $g_{I\!P}(\beta, Q^2, t)$ and $q_{I\!P}(\beta, Q^2, t)$ where β is the fraction of the Pomeron momentum carried by the parton. This may not be a very sound theoretical concept but it seems to work, and by trying to measure the Pomeron partonic structure in different processes, we put it to the test.

11.1 Jet-Gap-Jet Events

In 1993, Bjorken predicted[47] that hard scattering between two partons, leading to two high E_T jets, could occur not only by gluon or quark exchange but also by a color singlet exchange, most simply by two-gluon exchange with gluons of opposite color. In the early days of QCD, Low[48] and Nussinov[49] had proposed that the Pomeron is two gluons. Because no color is exchanged between the right-moving and left-moving systems, there is no color field between them and hadrons are not formed; hence we should have a rapidity gap, defined as a region of rapidity containing no particles. To be dominated by color singlet exchange, rather than just a fluctuation in the rapidity separations of particles in a normal "non-diffractive" event, the rapidity gap Δy should be larger than about three units. Bjorken could calculate the probability for the two-hard-gluon exchange, but could only estimate the probability that the rapidity gap would not be spoiled by some additional soft color exchange in the event. This he called the *Survival Probability, S,* and estimated it to be about 10%, leading to an expected fraction of events with gaps between jets in the range $0.003 < R_{gap} < 0.03$. Both DØ and CDF found[50,51] such events at a level near 1%. One technique is to select events with two forward jets on opposite sides ($\eta_1 \eta_2 < 0$) and to count charged hadrons in a central rapidity region $-1 < \eta < 1$. Figure 31 shows such a plot (solid line) compared with the multiplicity distribution when the two jets are on the same side ($\eta_1 \eta_2 > 0$). An excess is seen in the bin of zero tracks, at the level of $(1.13 \pm 0.16)\%$. It is interesting to know whether this gap fraction depends on the E_T and/or η of the jets, and also whether, if we could discriminate between quark and gluon jets (not easy), the q/g mix is the same for gap and nongap events. The point is whether the hard color singlet exchange differentiates between quarks and gluons. Between about 20 GeV and 45 GeV, CDF sees[52] no significant change in the gap fraction with E_T, while DØ sees an increase, from 18 GeV to 50 GeV, from 0.4% to 1.4% (Ref. 53). However, the errors on both measurements are such that the data are not in significant disagreement and more study is required. The same statement is true for the dependence of the gap fraction on rapidity separation between the jets; CDF sees a hint of a decrease in gap fraction at the largest $< |\eta| >$ (3.0–3.4) which is not seen by DØ. These issues should be resolved, and we should extend the data to lower E_T and eventually study the transition to

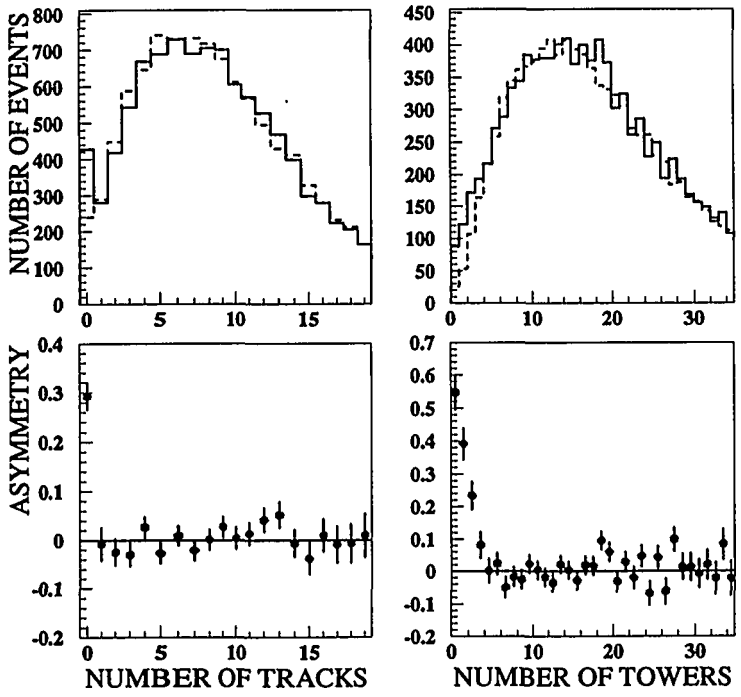


Figure 31: Track (left) and calorimeter tower (right) multiplicity distributions (top) in the central region ($|\eta| < 1$) between two high-p_T (> 25 GeV) jets (solid lines, OS jets). The dashed lines show the same when the two jets have the same rapidity, far from the central region (SS jets). The bottom figures show the difference (OS-SS)/SS with the evidence for a rapidity gap.

double diffractive dissociation without jets, a subject not yet properly studied at colliders.

Another topic for future study, but which will probably be difficult, is that of rapidity gaps with double parton scattering. The idea is to select events with two jets at large positive rapidity and two at large negative rapidity, use the pairwise balancing techniques discussed above to select a DPS component, and then look for rapidity gaps in the center. We should learn something about the dynamics of the color singlet exchange.

11.2 Single Diffractive Excitation

While the events with gaps between jets were first published[50] only two years ago, single diffractive excitation has a long history. Before the ISR started in 1971, it was known that an incident hadron could be excited into a low mass resonance with the same quantum numbers, and the cross section stays up as the energy increases. Good and Walker[54] (experimentalists!) had much earlier proposed this phenomenon. Their mechanism was basically that the beam particle is actually a superposition of virtual states ($p/n\pi^+/p\pi^+\pi^-/\Lambda K^+$/etc.), which are differentially absorbed by the target so the beam "particle" can emerge in a different state. This was an s-channel, optical model viewpoint which went out of fashion in favor of the t-channel Pomeron, but Bjorken[55] is advocating its revival.

In 1973, experiments at the ISR found that the range of diffractive masses scales with $\sqrt{s}$, extending to about 14 GeV there, and later at the CERN $Sp\bar{p}S$ Collider to 140 GeV. The $Sp\bar{p}S$ was therefore in the energy regime where high-p_T jets might be seen also in diffractive events. Ingelman and Schlein[56] proposed that such events could be considered as Pomeron-proton collisions, and thus by measuring jets, we could learn about the parton structure of the Pomeron. Schlein and collaborators installed "Roman pots" (special vacuum pots with detectors to measure protons scattered at very small angles and with nearly the full beam momentum, see Fig. 4, first used by the CERN-Rome Collaboration at the ISR) next to the UA2 detector which was used to look for jets. They found such events, with two jets above 7 GeV, and from the E_T and η distribution of the jets, they concluded that the parton distribution in the Pomeron is rather hard, like $\beta(1-\beta)$ where $\beta = p_{parton}/p_{I\!P}$. They also claimed a "superhard" component with a single parton carrying nearly all of the Pomeron momentum, but smeared by resolution

and acceptance effects. This would be very interesting, suggesting a picture of the Pomeron behaving like a single hard gluon with its color "bleached" by a soft gluon cloud. Data from H1 at HERA[57] also derive a structure of the Pomeron at very low Q^2 which is a quasi-δ-function gluon at $\beta \approx 1$. This is not directly measured but inferred from the pattern of scaling violations in the quark structure. Even at very high β, the quark density rises with Q^2, so it must be fed by gluons at even higher β. If the Pomeron really appears to be a single high-β gluon with an accompanying soft cloud, that would be very strange. According to Alan White[58] "gauge invariance requires that all the gluons in a color zero vacuum exchange are identical." His solution to this dilemma is to introduce a quantum number: *color charge parity* C_c. The hard and soft gluons carry different values of C_c.

Recently, both CDF and DØ have also found diffractively produced dijets. The method is to select events with a pair of jets at similar forward η (SS = Same Side, $|\eta| > 1.8$ or so) and to look at the multiplicity distribution (calorimeter towers or tracks) on the far opposite side, say $2 < \eta < 5$. This distribution shows[59,60] a distinctive spike in the zero-multiplicity bin which is the diffractive signature, at the level of 0.7% of the dijet sample. CDF also had Roman pot detectors located 57 m downstream along the outgoing $\bar{p}$ pipe and took data with the diffractively scattered $\bar{p}$ detected. This tags the mass of the $I\!Pp$ system and measures the t of the Pomeron. Jets are observed; the data are still being studied, and it will be interesting to compare with the UA8 studies and look for the "δ-function" component.

11.2.1 Diffractive W Production

The study of diffractive dijets tells us about the Pomeron structure but without distinguishing between quark and gluon constituents, both of which produce jets. Experiments at HERA on diffractive DIS probe the Pomeron with photons and hence select the quark component. In hadron colliders, one can look for Drell-Yan lepton pair production, $q\bar{q} \to l^+l^-$, $W^\pm$, or Z production to probe the quarks. CDF have now done this[61] and find that (1.15±0.55)% of all W are diffractively produced at the Tevatron. This is very much less than one particular prediction[62] which said that *if* the Pomeron were only $q\bar{q}$, as much as 15%–24% of all produced W could be diffractive. How could it be so high, when the total diffractive cross section is only about 10% of the total cross section? The answer might be that the Pomeron is more efficient than the proton at producing W (on another proton) as it is smaller ($\sigma_{I\!Pp} \approx$ few mb), but the partonic cross sections are the same.

We can now put four *diffractive* results together: DIS cross section at HERA,[63] jet production at HERA, jet production at the Tevatron, and W production at the Tevatron, to see whether we get a consistent picture for the Pomeron. We can choose as two parameters $\Sigma_{I\!P}$, the momentum fraction of the Pomeron carried by hard (participating) partons, and $g_{I\!P}$, the fraction of those hard partons which are gluons. The form $\beta(1-\beta)$ is assumed. Each of these results constrains us to a band in the plane $(\Sigma_{I\!P}, g_{I\!P})$, processes favoring quarks going up to the right, and processes favoring gluons going up to the left, see Fig. 32.

The intersections of these bands are the favored regions (at the 1σ level). Both ZEUS and CDF favor $g_{I\!P} \approx 0.5$–0.7 but differ in the estimate of $\Sigma_{I\!P}$. We could be seeing here a breakdown of factorization, or a breakdown of the (perhaps naïve) picture of the Pomeron as a quasiparticle with a structure function, or an indication that the Pomeron *flux* is not correctly calculated. Goulianos has proposed[64] the latter solution, suggesting that the Pomeron flux from high energy hadrons must be renormalized such that it never exceeds 1.0 (otherwise the diffractive cross sections become large, even compared to the total cross sections). This may bring ZEUS and CDF $\Sigma_{I\!P}, g_{I\!P}$ values into agreement, although it is not clear how the ZEUS data should be renormalized, and of course, we need better data. Schlein has also recently proposed[65] a Pomeron flux renormalization but not global (like Goulianos), but preferentially damping small $\xi = 1 - x_F$ values.

The use of the parameters $\Sigma_{I\!P}, g_{I\!P}$ is one way of treating data which is not good enough to properly measure the full structure functions $g_{I\!P}(\beta, Q^2, t)$ and $q_{I\!P}(\beta, Q^2, t)$; this is our ambition but it needs very high statistics. As previously stated, H1 and ZEUS at HERA are measuring $q_{I\!P}(\beta, Q^2)$, and H1 suggest that it may derive from what looks like (90%) a single gluon at low Q^2, rapidly evolving into a q/g mixture.

11.2.2 Double Pomeron Exchange

Finally, a few words about the reaction called *Double Pomeron Exchange*. A Pomeron is emitted from each incident hadron, the hadrons scatter quasielastically, and the two Pomerons interact in the central region. The final state has the two beam particles with x_F greater than about 0.95, followed by rapidity

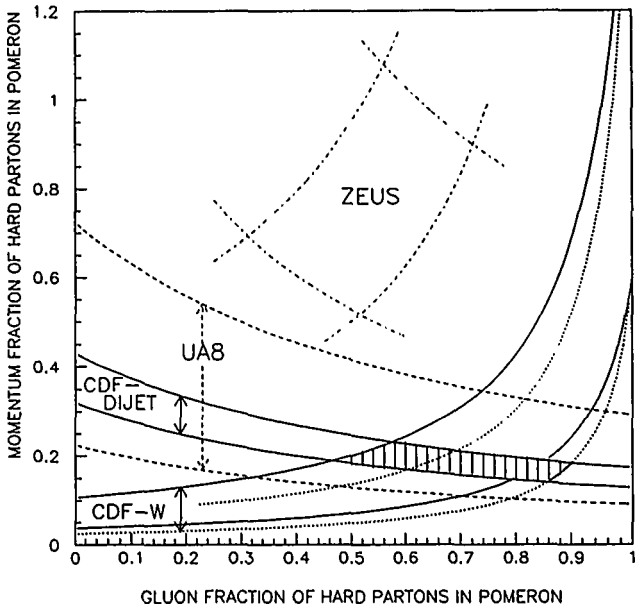


Figure 32: Allowed areas in the plane $\Sigma_{I\!P}$, the fraction of the Pomeron momentum carried by hard partons, and $g/I\!P$, the fraction of hard partons which are gluons. The CDF W and JJ production constrain the region to the hatched area; ZEUS data imply a larger $\Sigma_{I\!P}$.

gaps of three or more units, and central hadrons, with central mass $M_\odot$. The rule of thumb relation, for which double Pomeron exchange dominates over other exchanges (e.g., Pomeron-Reggeon), is

$$M_\odot < 0.05\sqrt{s}, \tag{21}$$

which means:

- 3 GeV at the ISR (hadrons, glueball spectroscopy[66]),
- 90 GeV at the Tevatron (high E_T jets),
- 700 GeV at the LHC (W? H? $SUSY$?).

Double Pomeron exchange is still very little studied at the Tevatron, and not much was done at the $Sp\bar{p}S$ Collider either,[67,68] but it could be very interesting. The rate of double Pomeron events should help resolve issues about Pomeron flux renormalization. Hard scattering dijet events should be sensitive to the question of a δ-function gluon, through observing events where the central system is just two jets (like an e^+e^- event, but from gg!). It should be noted that the interesting LHC process of Higgs production via $W^+W^- \to H^0$ fusion also can leave rapidity gaps, since the W's are colorless. $I\!P I\!P$ processes can be a background to this. However, any processes with rapidity gaps will be difficult to study in the big "high mass" experiments ATLAS and CMS because they require single interactions and therefore modest luminosity. The FELIX experiment will cover this field better, with very large rapidity acceptance and deliberately modest luminosity.

12 Concluding Remarks

I hope I have communicated a sense that hadron-hadron colliders are a gold mine for QCD studies and a great deal is going on. Of course, a glance at these proceedings will show that e^+e^- and ep collisions are also great places to study QCD, and the three types of colliders complement one another nicely. Nearly everyone now agrees that **QCD is the theory of strong interactions**. Nevertheless, QCD being "right" does not mean that there will be no more surprises. On the contrary, we saw that prompt J/ψ are being produced at a rate about *50* times higher than anticipated. From this, we are learning about the subtle behavior of color in a soft, nonperturbative regime. B-quark production is higher than predicted by a

factor of a few, and $t\bar{t}$ production by a factor less than about 50%. Searching for new physics beyond the Standard Model often demands excellent understanding of QCD. Even more challenging is the fact that high cross section processes like diffraction dissociation, elastic scattering, and the total cross section itself are not yet calculable and therefore not yet well-understood. It is very exciting that we are now learning to extend the domain of calculability of QCD to phenomena such as very low-x partons, the Pomeron, and other color magic. I am reminded about other fields of physics, where collective phenomena like superfluidity and superconductivity were not predicted from basic atomic theory and Quantum Mechanics but were experimental discoveries. Perhaps there are exciting new strong interaction phenomena just waiting to be found!

Acknowledgments

I am aware that I have not kept a fair balance between different experiments. I hardly mentioned the major experiments UA1 and UA2 at the CERN $Sp\bar{p}S$ Collider, and most of my illustrations were from CDF rather than DØ. I apologize, but only a little; these lectures were meant to be pedagogical and not to be a review.

I would like to thank Steve Behrends and Dino Goulianos for comments on the manuscript; Keith Ellis, Heidi Schellman, and Andreas Vogt for some figures; and Sue, Cele, and Randy Herber for technical help with figures.

References

[1] R. P. Feynman, Phys. Rev. Lett. **23**, 1415 (1969).

[2] F. E. Close, *The Current Picture of Glueballs*, hep–ph/9610426 RAL-96-085 (1995). D. Barberis *et al.* (WA102), CERN-PPE-96-197, submitted to Phys. Lett.

[3] *The "Pipetron," a Low-Field Approach to a Very Large Hadron Collider*, edited by E. Malamud, selected papers (Fermilab, 1997).

[4] P. Burrows, lectures on "Precision Tests of QCD in e^+e^- Annihilations," these proceedings.

[5] W. Smith, lectures on "QCD Studies in ep Collisions," these proceedings.

[6] A. Pickering, *Constructing Quarks* (Univ. Chicago Press, 1984).

[7] L. N. Lipatov, Sov. J. Nucl. Phys. **20**, 95 (1975); V. N. Gribov and L. N. Lipatov, Sov. J. Nucl. Phys. **15**, 438 (1972); G. Altarelli and G. Parisi, Nucl. Phys. B **126**, 298 (1977); Y. L. Dokshitzer, Sov. Phys. JETP **46**, 641 (1977).

[8] E. D. Bloom *et al.* (SLAC-MIT), Phys. Rev. Lett. **23**, 930 (1969); G. Miller *et al.* (SLAC-MIT), Phys. Rev. D **5**, 528 (1972).

[9] G. Parisi and R. Petronzio, Phys. Lett. B **62**, 331 (1976). M. Glück, E. Reya, and A. Vogt, Z. Phys. C **67**, 433 (1995).

[10] A. D. Martin, R. G. Roberts, and W. J. Stirling (MRS), Phys. Lett. B **306**, 145 (1993); Phys. Rev. D 50, 6734 (1994); Phys. Lett. B **354**, 155 (1995).

[11] J. Botts *et al.* (CTEQ), Phys. Lett. B **304**, 159 (1993).

[12] R. K. Ellis, W. J. Stirling, and B. R. Webber, *QCD and Collider Physics* (Cambridge, 1996), an excellent and up-to-date textbook.

[13] S. M. Berman, J. D. Bjorken, and J. B. Kogut, Phys. Rev. D **4**, 3388 (1971).

[14] C. Bromberg *et al.*, Phys. Rev. Lett. **38**, 1447 (1977); M. Corcoran *et al.*, Phys. Rev. D **21**, 641 (1980).

[15] T. Akesson *et al.* (AFS Collaboration), Phys. Lett. B **118**, 185, 193 (1982).

[16] T. Akesson *et al.* (AFS Collaboration), Z. Phys. C **30**, 27 (1986).

[17] M. Banner *et al.* (UA2), Phys. Lett. B **118**, 203 (1982); J. Appel *et al.* (UA2), Phys. Lett. B **160**, 349 (1995).

[18] G. Arnison *et al.* (UA1), Phys. Lett. B **123**, 115 (1983); Phys. Lett. B **172**, 461 (1986).

[19] G. Hanson *et al.*, Phys. Rev. Lett. **35**, 1609 (1975).

[20] F. Abe *et al.* (CDF), Phys. Rev. Lett. **70**, 1376 (1993). The $\sqrt{s} = 630$ GeV data are not yet published.

[21] F. Abe *et al.* (CDF), Phys. Rev. D **54**, 4421 (1996).

[22] G. Sterman, in *Proceedings of the 10th Workshop on Proton-Antiproton Collider Physics* (Batavia, 1995), hep-ph/950835.

[23] W. Giele, in *Proceedings of the 10th Workshop on Proton-Antiproton Collider Physics* (Batavia, 1995), Fermilab-Conf-95-169-T.

[24] M. L. Mangano, CERN-TH/96-278, hep-ph/9610234. "Topics in jet physics," in *Proceedings of the XI Topical Workshop on Hadron Collider Physics* (Padova, 1996).

[25] F. Abe *et al.* (CDF), Phys. Rev. Lett. **74**, 3538 (1995).

[26] E. A. Kuraev, L. N. Lipatov, and V. S. Fadin, Phys. Lett. B **60**, 50 (1975); Sov. Phys. JETP **45**, 199 (1977); Y. Y. Balitsky and L. N. Lipatov, Sov. J. Nucl. Phys. **28**, 822 (1978).

[27] S. Abachi *et al.* (DØ), Phys. Rev. Lett. **77**, 595 (1996).

[28] F. Abe *et al.* (CDF), Phys. Rev. D **54**, 4221 (1996).

[29] M. Diakonou *et al.* (R806), Phys. Lett. B **87**, 292 (1979).

[30] J. Alitti *et al.* (UA2), Phys. Lett. B **263**, 544 (1991).

[31] C. Kourkoumelis *et al.* (R806), Z. Phys. C-Particles and Fields, **16**, 101 (1982).

[32] F. Abe *et al.* (CDF), "First observation of the all hadronic decay of $t\bar{t}$ pairs," CDF/4025, submitted to Phys. Rev. Lett., March 1997.

[33] F. Abe *et al.* (CDF), Phys. Rev. Lett. **77**, 448 (1996).

[34] J/ψ and ψ' Production at CDF, FERMILAB-CONF-96/156-E, CDF Note 3721 (1996).

[35] P. Cho and A. K. Liebovich, Cal. Tech preprint CALT-68-1988, hep-ph-9505329; E. Braaten and S. Fleming, Phys. Rev. Lett. **74**, 3327 (1995).

[36] T. Akesson *et al.* (AFS), Z. Phys. C-Particles and Fields **34**, 163 (1987).

[37] J. Alitti *et al.* (UA2), Phys. Lett. B **268**, 145 (1991).

[38] F. Abe *et al.* (CDF), Phys. Rev. D **47**, 4857 (1993).

[39] F. Abe *et al.* (CDF), "Measurement of double parton scattering in $p\bar{p}$ collisions at $\sqrt{s} = 1.8$ TeV," CDF/4053, to be submitted to Phys. Rev. Lett.

[40] S. Abachi *et al.* (DØ), XVII Int. Symp. on Lepton Photon Interactions (LP95), Beijing, China, Aug. 1995.

[41] Y. L. Dokshitzer, V. A. Khoze, A. H. Mueller, and S. I. Troyan, *Basics of Perturbative QCD* (Editions Frontieres, 1991).

[42] A. H. Mueller, Nucl. Phys. B **213**, 85 (1983).

[43] Y. L. Dokshitzer and S. I. Troyan, in *Proceedings of the XIX Winter School of LNPI* **1**, 144 (1984).

[44] F. Abe *et al.* (CDF), MLLA paper in preparation.

[45] P. D. B. Collins, *An Introduction to Regge Theory and High Energy Scattering* (Cambridge Univ. Press, Cambridge, 1977).

[46] M. G. Albrow *et al.*, FERMILAB-Conf-96/377-E, in *Proceedings of the Snowmass '96 Summer Study on New Directions for Particle Physics* (1996).

[47] J. D. Bjorken, Phys. Rev. D **47**, 101 (1993).

[48] F. Low, Phys. Rev. D **12**, 163 (1975).

[49] S. Nussinov, Phys. Rev. D **14**, 246 (1976).

[50] F. Abe *et al.* (CDF), Phys. Rev. Lett. **74**, 855 (1995).

[51] S. Abachi *et al.* (DØ), Phys. Rev. Lett. **72**, 2332 (1994).

[52] F. Abe *et al.* (CDF), "Events with a rapidity gap between jets at the Tevatron," paper in preparation.

[53] T. Taylor Thomas (DØ), in *Proceedings of the Small-x and Diffractive Physics Workshop* (Argonne, Sept. 1996).

[54] M. L. Good and W. D. Walker, Phys. Rev. **120**, 1854 (1960).

[55] J. D. Bjorken, in *Proceedings of the Small-x and Diffractive Physics Workshop* (Argonne, Sept. 1996).

[56] G. Ingelman and P. Schlein, Phys. Lett. B **152**, 256 (1985).

[57] P. Biddulph (H1), in *Proceedings of the Small-x and Diffractive Physics Workshop* (Argonne, Sept. 1996).

[58] A. R. White, in *Proceedings of the Small-x and Diffractive Physics Workshop* (Argonne, Sept. 1996).

[59] S. Bagdasarov (CDF), in *Proceedings of the Small-x and Diffractive Physics Workshop* (Argonne, Sept. 1996).

[60] K. Mauritz (DØ), in *Proceedings of the Small-x and Diffractive Physics Workshop* (Argonne, Sept. 1996).

[61] F. Abe *et al.* (CDF), "Observation of diffractive W-boson production at the Tevatron," submitted to Phys. Rev. Lett. (1997). CDF-3799.

[62] P. Bruni and G. Ingelman, Phys. Lett. B **311**, 317 (1993).

[63] M. Derrick *et al.*, Phys. Lett. B **356**, 129 (1995).

[64] K. Goulianos, Phys. Lett. B **358**, 379 (1995).

[65] P. Schlein, in *Proceedings of the Small-x and Diffractive Physics Workshop* (Argonne, Sept. 1996).

[66] T. Akesson *et al.* (AFS), Nucl. Phys. B **264**, 154 (1986).

[67] D. Joyce *et al.* (UA1), Phys. Rev. D **48**, 1943 (1993).

[68] A. Brandt *et al.* (UA8), Singapore Conference (1990), "Observation of Double Pomeron Exchange. . . ."

PRECISE TESTS OF QCD IN e^+e^- ANNIHILATION*

P. N. Burrows

Laboratory for Nuclear Science
Massachusetts Institute of Technology
Cambridge, MA 02139, USA

burrows@slac.stanford.edu

ABSTRACT

A pedagogical review is given of precise tests of QCD in electron-positron annihilation. Emphasis is placed on measurements that have served to establish QCD as the correct theory of strong interactions, as well as measurements of the coupling parameter α_s. An outlook is given for future important tests at a high-energy e^+e^- collider.

*Work supported by Department of Energy contracts DE–FC02–94ER40818 (MIT) and DE–AC03–76SF00515 (SLAC).

©1996 by P. N. Burrows.

1. Introduction: e^+e^- Colliders

The production of hadronic final states by a variety of interactions is illustrated in Fig. 1. In electron-positron annihilation, hadronic activity is, by construction, limited to the final state, making the study of hadronic events cleaner and simpler relative to lepton-hadron and hadron-hadron collisions, from both the experimental and theoretical points of view. On the experimental side, there are no remnants of the beam particles to add confusion to the interpretation of hadronic structures, and, apart from initial and final-state photon radiation effects, the hadronic center-of-mass frame coincides with the laboratory frame. On the theoretical side, the absence of hadrons in the incoming beams removes dependence on the limited knowledge of the parton density functions of hadrons, as well as rendering QCD calculations at a given order of perturbation theory easier to perform because there are generally fewer strong-interaction Feynman diagrams to consider. Electron-positron annihilation thus provides an ideal environment for precise tests of QCD.

A large number of e^+e^- colliders have been constructed over the past 25 years; these are listed in Table 1. The range of c.m. energies Q extends from a few GeV at the very first colliders up to almost 200 GeV at the CERN LEP-II collider. The first generation of colliders was built on speculation of allowing exciting high-energy physics studies. They did not disappoint, the J/Ψ being discovered at SPEAR, the gluon being observed at PETRA, and a wealth of strong- and electroweak-interaction studies being performed at PETRA, PEP, and TRISTAN, all of which served to establish the validity of the Standard Model. A second generation of colliders has been designed to serve as particle "factories": DAΦNE in the vicinity of the Φ resonance; BEPC near the charmonium threshold; DORIS, CESR, PEP-II, and KEKB around the bottomonium resonances; SLC and LEP at the Z^0 resonance; and LEP-II at the W^+W^- threshold.

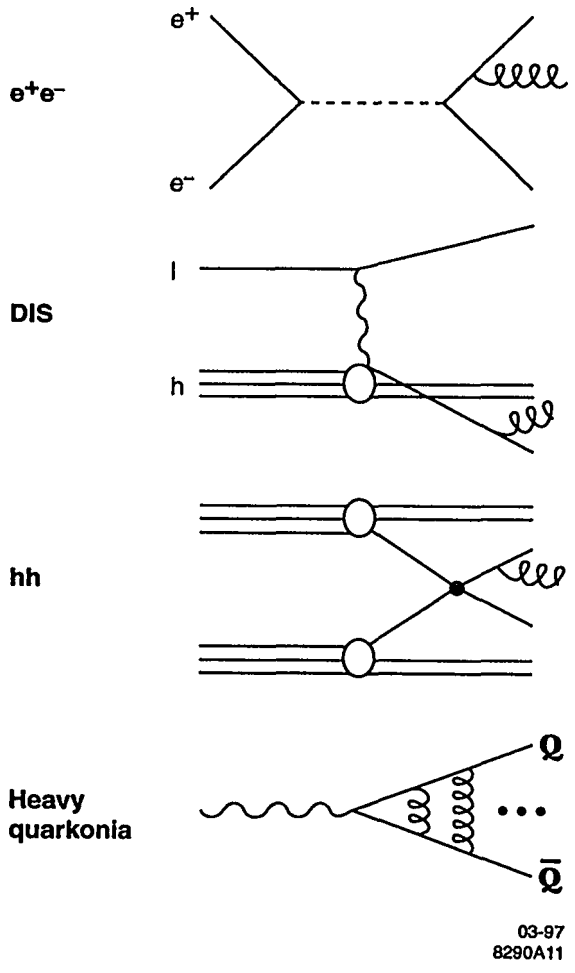


Figure 1: Schematic of the production of hadronic final states by different interactions: e^+e^- annihilation, deep inelastic lepton-hadron scattering, hadron-hadron collisions, and production and decay of heavy quarkonia.

With the exception of the SLC, all of these colliders have been of the storage-ring type, the largest, LEP-II with a circumference of 27 km, probably marking the limit of the energy that can be achieved with current storage-ring technology for an acceptable cost. The SLC is the first example of a high-energy *linear* e^+e^- collider; it achieves the same collision energy as LEP, but has an effective length of about three miles and was considerably cheaper to construct. Because of their intrinsically lower cost/GeV, linear colliders represent the obvious path towards construction of higher-energy e^+e^- colliders with current acceleration technology. A number of proposals for such an accelerator are represented by "XLC" in Table 1; they all aim to achieve c.m. energies between 500 and 1500 GeV, which is believed to cover the interesting range for study of electroweak-symmetry-breaking processes. Some examples of QCD tests that could be made at the XLC will be given towards the end of these lectures.

	Collider	Location	c.m. energy Q (GeV)
	ADONE	Frascati	1 – 3
	DCI	Orsay	1 – 2.4
•	VEPP-2M	Novosibirsk	1 – 1.5
•	DAΦNE	Frascati	1 – 1.5
	SPEAR	SLAC	2 – 8
•	BEPC	Beijing	2 – 3
	DORIS	DESY	3 – 11
•	VEPP-4M	Novosibirsk	10 – 12
•	CESR	Cornell	10 – 11
•	PEP-II	SLAC	$9 \otimes 3.1$
•	KEKB	KEK	$8 \otimes 3.5$
	PETRA	DESY	12 – 47
	PEP	SLAC	29
	TRISTAN	KEK	50 – 64
•	SLC	SLAC	88 – 93
	LEP	CERN	88 – 93
•	LEP-II	CERN	130 – 192
	XLC	????	500 – 1500

Table 1: e^+e^- colliders 1972–200? • denotes running/under construction.

It would require a semester-long lecture series to do full justice to QCD studies in e^+e^- annihilation, so some hard choices have been made as to the material to be covered here; I apologize well in advance for all that has been omitted. No attempt has been made to give a complete review of all of the experimental results in any of the areas covered; usually, one or two results or figures are shown as examples. For this purpose, I have drawn heavily on material from TASSO and SLD, the two experiments with which I have been involved since 1985; no disrespect is intended to the many other experiments whose results may not be shown. Tests of QCD in hadron-hadron and lepton-hadron collisions will not be discussed here as they are covered in other lectures [1, 2] at this Institute.

In the interests of pedagogy, I shall review the fundamental properties of QCD and the important experimental measurements from e^+e^- annihilation that have been key historically to establishing the theory. Having verified QCD, in a qualitative sense, as being the only viable theory for describing strong interactions, I shall then review quantitative tests in the form of measurements of α_s, the single parameter of the theory, and put the e^+e^- measurements into context with determinations from other processes. I shall focus on measures of the event topology, especially on jet definition and the relation between the jets observed in detectors and the "true" underlying parton-jet structure. This will introduce the problem of hadronization, as well as the difficulty of relating finite-order perturbative QCD calculations to the "all-orders" data. I shall conclude by looking forward to the precise QCD tests that could be made at a high-energy e^+e^- collider and to the qualitatively new $t\bar{t}g$ system accessible at such a facility.

2. Our Theory of Strong Interactions—QCD

Quantum Chromodynamics (QCD) [3] is our theory of the strong interaction between quarks and gluons. It is a non-Abelian Yang-Mills gauge theory that describes the interactions of a triplet of spin-1/2 quarks possessing the color quantum number (c = r, b, g) via an octet of vector gluons. The spinor quark fields $q_c(x)$ transform as the fundamental representation of the SU(3) group, whilst the gluon fields $A^a_\mu(x)$ (a = 1, 2, ..., 8) transform according to the adjoint representation. The SU(3) color transformations are generated by the 3×3 matrices $T^a = \lambda^a/2$, where λ^a are the Gell-Mann matrices [4] which obey the commutation relations:

$$[T^a, T^b] \quad = \quad i\, f^{abc}\, T^c \tag{1}$$

and f^{abc} are the structure constants of SU(3). The Lagrangian has the form:

$$\mathcal{L} \quad = \quad -\frac{1}{4} F^a_{\mu\nu} F^{\mu\nu\, a} \; + \; \overline{q}\; (i\gamma_\mu D^\mu \; - \; m)\; q, \tag{2}$$

where $F_{\mu\nu}$ is the field strength tensor:

$$F^a_{\mu\nu} \quad = \quad \partial_\mu A^a_\nu - \partial_\nu A^a_\mu + g f^{abc} A^b_\mu A^c_\nu \tag{3}$$

and D_μ is the covariant derivative:

$$D_\mu \quad = \quad \partial_\mu - igT^a A^a_\mu(x), \tag{4}$$

g is the bare coupling of the theory, m the bare mass of the quark field, and the gluons are massless.

Following Ref. [5], the "essential features" of QCD may be summarized as:

- quarks with spin 1/2 exist as color triplets,
- gluons with spin 1 exist as color octets,
- the coupling $q\overline{q}g$ exists,
- the couplings ggg and gggg exist,
- the couplings are equal,
- the coupling decreases as $1/\ln Q^2$.

For most of the first lecture, I shall review the evidence, from e^+e^- annihilation alone, that QCD *is* the correct theory of strong interactions.

3. Establishing the QCD Lagrangian

3.1 Two-Jet Events and $q\overline{q}$ Production

Quarks were first postulated in 1964 by Gell-Mann and Zweig [6] as a calculational device to explain the rich spectroscopy of recently discovered mesons and baryons in terms of bound $q\overline{q}$ and qqq (or $\overline{q}\overline{q}\overline{q}$) states. The first direct evidence for quarks came from the observations at SLAC in the late 1960s that in electron-nucleon scattering experiments at high Q^2, the electron scatters from quasi-free pointlike particles. In e^+e^- annihilation, a convincing demonstration of the existence of quarks was provided by the observation of jets in the Mark I experiment at SPEAR in 1975 (Ref. [7]). This analysis represents the first use of an *event shape observable* which, as will be discussed later, is a key component in the study of hadronic final states, so I shall briefly describe it.

By eye, the spatial distribution of particles in hadronic events recorded in the Mark I detector operating at c.m. energies between 3.0 and 7.4 GeV looked more-or-less isotropic, and it was hard to distinguish any clear jet structure. The quantity sphericity,

$$S \quad = \quad \frac{\mathrm{Min}\,(\Sigma_i p^2_{\perp i})}{\Sigma_i \vec{p}_i^{\,2}}, \tag{5}$$

where $\vec{p}_i$ represents the momentum of particle i and the sums run over all particles in each event, was invented [8] to characterize the degree of isotropy in the particle flow. In each event, an axis, the sphericity axis, is defined so as to minimize the

quantity in brackets in the numerator; Eq. (5) then defines the sphericity of the event. A completely isotropic distribution of particles, or spherical event, would yield $S \sim 1$, whilst a perfectly-collimated back-to-back two-jet event would have $S = 0$. Sphericity distributions from Mark I are shown in Fig. 2 for data taken at several different c.m. energies. As the energy was raised from 3.0 to 7.4 GeV, a clear change in the sphericity distribution was observed, the distribution shifting to lower values at higher energies. This was interpreted in terms of an increasing degree of collimation of particle production with c.m. energy, namely the onset of the production of two back-to-back jets of hadrons. At higher energies, the jet structure is much more apparent by eye, as indicated in the Z^0 decay event from SLD shown in Fig. 3, and is striking evidence for the production of a back-to-back quark and antiquark in e^+e^- annihilation.

The Mark I analysis was also able to establish the nature of the spin of the quark and antiquark. Shown in Fig. 4 is the distribution of the azimuthal-angle, ϕ, of the sphericity axis w.r.t. the beamline, at two c.m. energies. At Q = 7.4 GeV, the electron and positron beams in the SPEAR ring built up a degree of transverse polarization P via the Sokolov-Ternov synchrotron radiation effect [9] and a clear modulation in ϕ is visible. This is in contrast to the flat ϕ distribution at $Q = 6.2$ GeV which corresponds to a beam-depolarizing resonance ($P = 0$) in the accelerator. A fit of the function:

$$\frac{dN}{d\Omega} \propto 1 + \alpha\cos^2\theta + P^2\alpha\sin^2\theta\cos 2\phi \qquad (6)$$

to the 7.4 GeV data yielded $\alpha = 0.78 \pm 0.12$; this is close to unity, which is expected for production of two spin-1/2 particles [10].

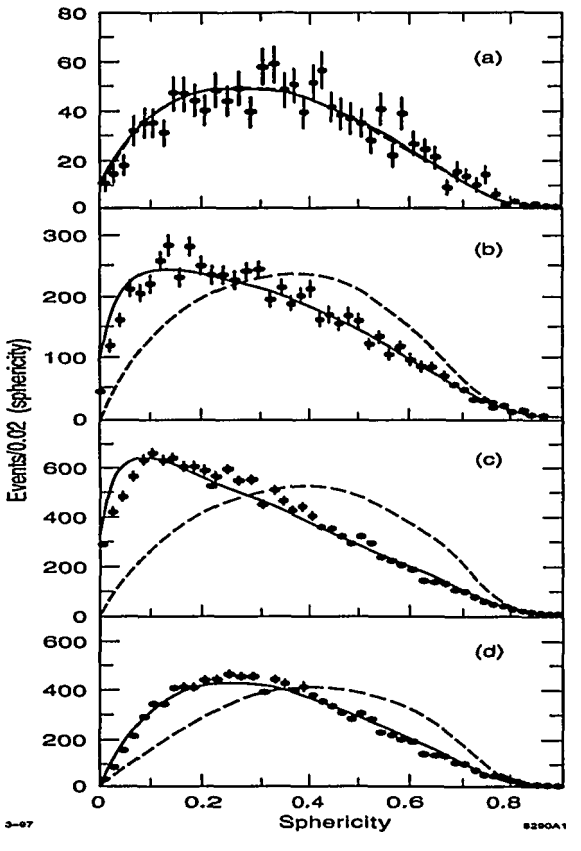


Figure 2: Sphericity distributions measured by the Mark I experiment at SPEAR [7] at c.m. energies of (a) 3.0, (b) 6.2, and (c) 7.4 GeV. The narrowing of the distribution, and the trend towards smaller values as the c.m. energy is raised, represent evidence for collimated production of hadrons in e^+e^- annihilation. The dashed line represents the expectation from a "phase-space model" of hadron production. (d) is as (c) but for a subset of events containing particles with scaled momentum, $2p/Q$, less than 0.4.

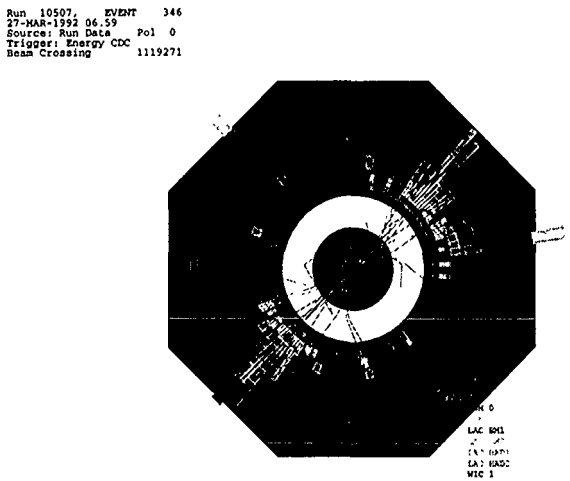


Figure 3: A contemporary two-jet event recorded by SLD: the process $e^+e^- \to Z^0 \to q\bar{q}$.

These studies were subsequently extended at the higher-energy PETRA collider, and examples from TASSO [11] are shown in Fig. 5. Here the distribution of the polar-angle (θ_S) of the sphericity axis is shown at c.m. energies of 14, 22, and 35 GeV. A fit to the functional form:

$$\frac{dN}{d\cos\theta} \propto 1 + a_{S,T}\cos^2\theta_{S,T} \qquad (7)$$

yields, at 35 GeV for example, $a_S = 1.03 \pm 0.07$, again characteristic of the production of two spin-1/2 particles in the e^+e^- annihilation. Also shown in Fig. 5 is our second example of an event shape observable in the form of the thrust-axis [12] polar-angle (θ_T) distribution. Thrust will be discussed later; it is qualitatively similar to sphericity in that it can be used to quantify the degree of collimation of particle production, although it has properties that make it more attractive theoretically. The thrust-axis polar-angle distribution in Fig. 5 was fitted to obtain,

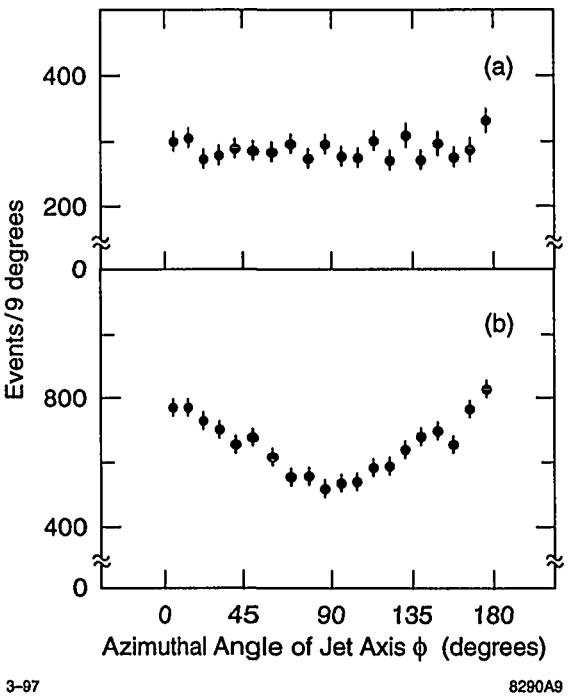


Figure 4: Azimuthal-angle distribution of the sphericity axis from Mark I (Ref. [7]). At $Q = 6.2$ GeV, (a) the SPEAR beams were unpolarized, and at $Q = 7.4$ GeV, (b) the polarization-product was 0.47; the modulation in (b) is characteristic of the production of two spin-1/2 particles in e^+e^- annihilation.

at 35 GeV for example, $a_T = 1.01 \pm 0.06$, in good agreement with the result using the sphericity axis.

So far, spin-1/2 quarks and antiquarks would appear to be well-established, and their color-triplet nature, $N_C = 3$, is required in the quark-parton model (QPM) of hadrons to explain the existence of spin-3/2 baryon states such as the Δ^{++} ($u\uparrow u\uparrow u\uparrow$) and Ω^- ($s\uparrow s\uparrow s\uparrow$), which would otherwise contain three identical fermions in the same quantum state, in violation of the Pauli exclusion principle.

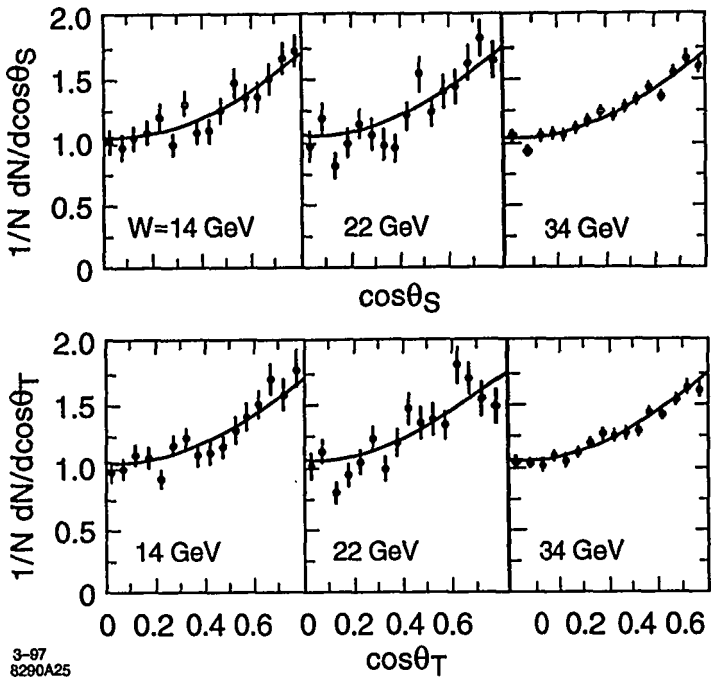


Figure 5: Polar-angle distributions of the sphericity and thrust axes from TASSO [11]. The $1+\cos^2\theta$ form is characteristic of the production of two spin-1/2 particles in the e^+e^- annihilation.

In e^+e^- annihilation, evidence for $N_C = 3$ is provided by the quantity:

$$R \equiv \frac{\sigma(e^+e^- \to \text{hadrons})}{\sigma_{QED}(e^+e^- \to \mu^+\mu^-)}$$

which, according to QED and the QPM, should be equal to $N_C\ \Sigma_f\ q_f^2$, where q_f is the charge of the quark of flavor f and the sum runs over all active flavors at a given c.m. energy.

A summary of R measurements made up to 1988, as a function of c.m. energy, is presented in Fig. 6 (Ref. [13]). This is a tremendously information-rich figure.

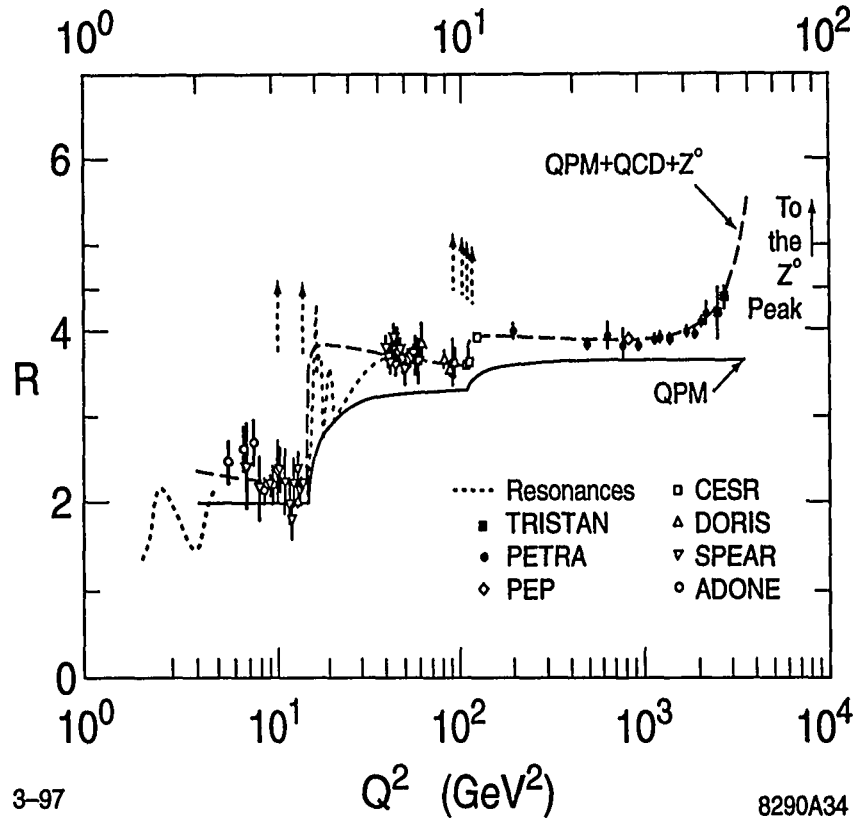


Figure 6: The R ratio as a function of c.m. energy [13]. The expectation for $N_C = 3$ is shown as the solid line.

First, increases in R just above $Q^2 = 10$ and 100 GeV^2 represent the $c\bar{c}$ and $b\bar{b}$ production thresholds—further evidence, were it needed, for the existence of quarks. Secondly, the QED + QPM prediction comes close to the data only if the quarks are assigned fractional charges *and* the number of colors $N_C = 3$ is used; the "color singlet" expectation ($N_C = 1$) is simply too low by a factor of about three!

Thirdly, above $Q^2 = 1000$ GeV^2, the data points rise as Q^2 increases, representing the onset of contributions to e^+e^- annihilation from Z^0 exchange. Finally, in regions between quark flavor thresholds and below the tail of the Z^0 resonance, there is a residual excess in the data relative to the QED + QPM expectation, and the excess appears to decrease as Q^2 increases. In other words, some mechanism causes an increase in the "phase-space" for hadron production beyond QED + QPM, but at a rate that decreases with Q^2. In the language of the 1990s, we know that the extra contribution is due to gluon emission in the final state, and that the probability for this process, α_s, decreases roughly logarithmically with Q^2. The R ratio thus provides indirect evidence for the existence of the gluon, as well as for the non-Abelian "running" of the strong coupling.

3.2 Three-Jet Events and the Gluon

In e^+e^- annihilation, events containing *three* distinct jets of hadrons were first observed in 1979 at the PETRA storage ring [14] at c.m. energies around 20 GeV. Such events were interpreted [15] in terms of the fundamental process $e^+e^- \to q\bar{q}g$, providing direct evidence for the existence of the gluon and its coupling to quarks. A modern example of a three-jet event, in fact, the very event used to advertise this Summer Institute, is shown in Fig. 7.

Counting the number of jets per event, and then comparing the numbers of two- and three-jet events, it was found [16] that around $Q = 20$ GeV

$$\frac{\#3-\text{jet events}}{\#2-\text{jet events}} \approx 0.15. \qquad (8)$$

Since, at lowest order in perturbative QCD, this ratio is simply the probability for gluon emission, or α_s, the strong coupling parameter, simple event counting indicated that the strong coupling at 20 GeV was around 0.15, *i.e.*, about ten times larger than the electromagnetic coupling α. More systematic determinations of α_s will be discussed later.

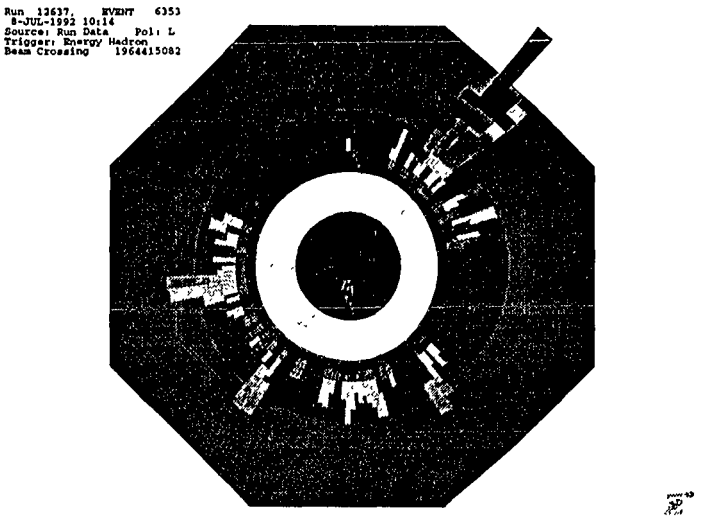


Figure 7: A contemporary three-jet event recorded by SLD: the process $e^+e^- \to Z^0 \to q\bar{q}g$.

Having observed the gluon directly in three-jet events, one still needs to know whether it is the gluon of QCD, namely a color-octet vector particle. Many studies of the nature of the gluon spin were performed at the PETRA and PEP storage rings and involved analysis of the partition of energy among the three jets. Ordering the three jets in $e^+e^- \to q\bar{q}g$ according to their energies $E_1 > E_2 > E_3$, and normalizing by the c.m. energy Q, we obtain the scaled jet energies

$$x_i = \frac{2E_i}{Q} \qquad (i = 1,2,3), \qquad (9)$$

represented in Fig. 8, where $x_1 + x_2 + x_3 = 2$. Making a Lorentz boost of the event into the rest frame of jets 2 and 3, the historically important Ellis-Karliner angle θ_{EK} is defined [17] to be the angle between jets 1 and 2 in this frame. For

massless partons at tree-level:

$$cos\theta_{EK} = \frac{x_2 - x_3}{x_1}. \tag{10}$$

The results of an early study by TASSO [18] are shown in Fig. 9, where the Ellis-Karliner angle distribution is compared, for data taken at $Q \sim 30$ GeV, with the prediction of QCD. One can also consider alternative "toy" models of strong interactions, for example, a model incorporating spin-0 (scalar) gluons [19]. From Fig. 9, the scalar-gluon model is clearly excluded.

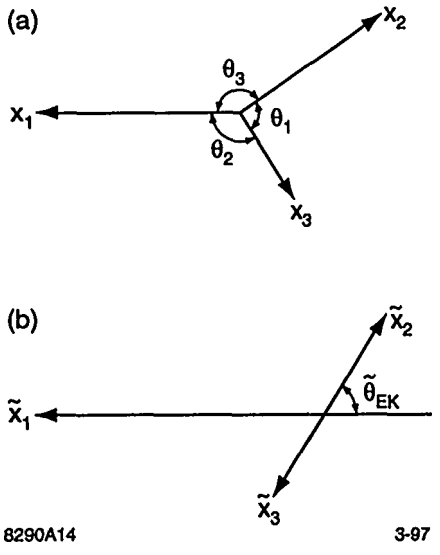


Figure 8: (a) Representation of the momentum vectors in a three-jet event, and (b) definition of the Ellis-Karliner angle.

Similar studies have been extended at the Z^0 resonance by the LEP and SLC experiments. In this case, the inclusive differential cross sections, calculated at leading order and assuming massless partons, can be written for vector gluons [5]:

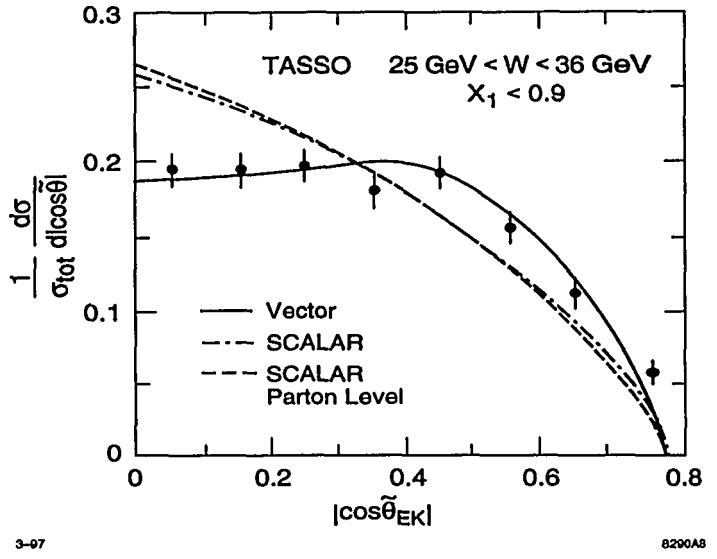


Figure 9: The Ellis-Karliner angle distribution of three-jet events recorded by TASSO at $Q \sim 30$ GeV (Ref. [18]); the data favor spin-1 (vector) gluons.

$$\frac{1}{\sigma}\frac{d^2\sigma^V}{dx_1 dx_2} \propto \frac{x_1^3 + x_2^3 + (2 - x_1 - x_2)^3}{(1 - x_1)(1 - x_2)(x_1 + x_2 - 1)}, \tag{11}$$

for scalar gluons [19]:

$$\frac{1}{\sigma}\frac{d^2\sigma^S}{dx_1 dx_2} \propto \left[\frac{x_1^2(1 - x_1) + x_2^2(1 - x_2) + (2 - x_1 - x_2)^2(x_1 + x_2 - 1)}{(1 - x_1)(1 - x_2)(x_1 + x_2 - 1)} - R\right], \tag{12}$$

where

$$R = \frac{10\,\Sigma_j a_j^2}{\Sigma_j (v_j^2 + a_j^2)} \tag{13}$$

and a_j and v_j are the axial and vector couplings, respectively, of quark flavor j to the Z^0, and for a model of strong interactions incorporating spin-2 (tensor) gluons [20, 21]:

$$\frac{1}{\sigma}\frac{d^2\sigma^T}{dx_1 dx_2} \propto \frac{(x_1 + x_2 - 1)^3 + (1 - x_1)^3 + (1 - x_2)^3}{(1 - x_1)(1 - x_2)(x_1 + x_2 - 1)}. \tag{14}$$

Singly-differential cross sections for x_1, x_2, x_3, or $\cos\theta_{EK}$ can be obtained by numerical integrations of Eqs. (11), (12), and (14) and are compared with SLD data [21] in Fig. 10. The shapes are different for the vector, scalar, and tensor gluon cases, and only the vector case describes the data.

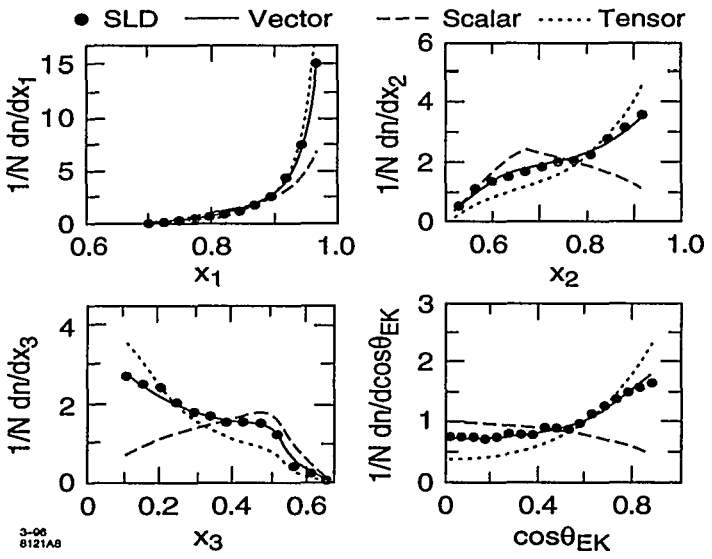


Figure 10: Comparison of leading-order scalar-, vector-, and tensor-gluon models with SLD data [21]; the scalar and tensor hypotheses are clearly excluded.

An additional interesting observable in three-jet events is the orientation of the event plane w.r.t. the beam direction, which can be described by three Euler angles (Fig. 11). These angular distributions were studied first by TASSO [22], and more recently by L3 (Ref. [23]) and DELPHI [24]. Again, the data were compared with the predictions of perturbative QCD and a scalar gluon model, but the Euler angles are less sensitive than the jet energy distributions to the differences between the two cases [23]. One can parameterize the angular distributions in the form:

$$\frac{d\sigma}{d\cos\theta} \propto 1 + \alpha(T)\cos^2\theta \qquad (15)$$

$$\frac{d\sigma}{d\cos\theta_N} \propto 1 + \alpha_N(T)\cos^2\theta_N \qquad (16)$$

$$\frac{d\sigma}{d\chi} \propto 1 + \beta(T)\cos 2\chi, \qquad (17)$$

where T is the thrust value [12] of the event. As an example, fits of Eq. (16) to SLD distributions of $\cos\theta_N$ are shown in Fig. 12 (Ref. [21]) in four bins of thrust. The coefficients $\alpha(T)$, $\alpha_N(T)$, and $\beta(T)$ depend on the gluon spin; they are shown in Fig. 13 for leading-order calculations incorporating vector, scalar, and tensor gluons. The measured $\alpha(T)$, $\alpha_N(T)$, and $\beta(T)$ are also shown in Fig. 13 and confirm that only vector gluons are compatible with the data.

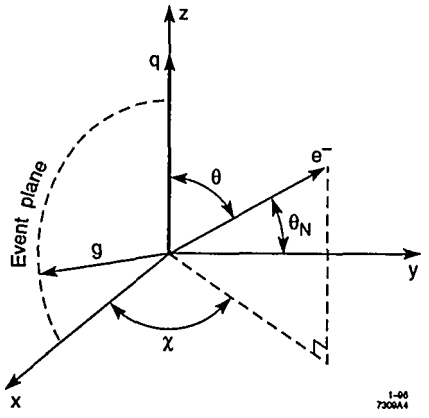


Figure 11: Definition of event-plane orientation angles.

At this point, it is worth pausing to take stock of what has been learned so far. The $e^+e^- \to$ two-jet events have provided direct evidence for $q\bar{q}$ production, and the jet axis angular distribution indicates that the quark and antiquark have spin-1/2. From the inclusive R-ratio, we can confirm the fractional nature of the quark charges, and know that the quarks must exist as color triplets since $N_C = 3$ is the only value that brings QED + the quark-parton model close to the data.

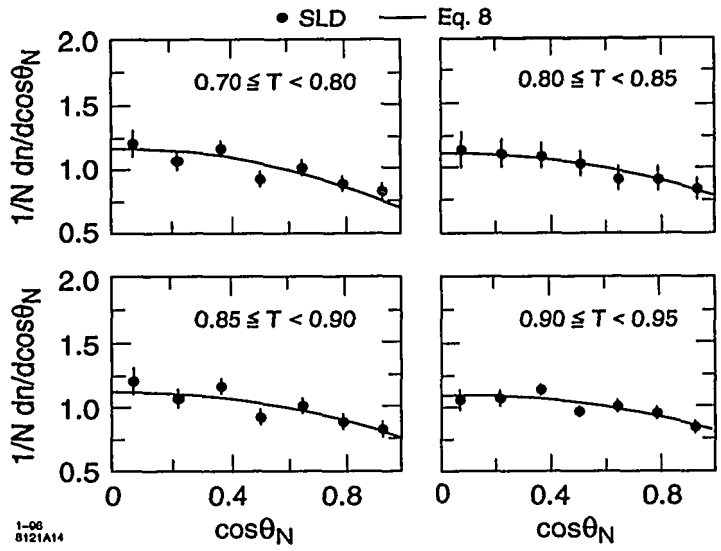


Figure 12: Distributions of $\cos\theta_N$ as a function of event thrust from SLD [21].

The value of the R-ratio also tells us that there must be contributions to hadronic final states in addition to $q\bar{q}$ production, and we know that these are provided by three-jet events, which represent direct evidence for the existence of the gluon and its coupling to quarks and antiquarks. The distributions of jet energies, or equivalently of jet angles within the event plane, as well as of the event plane orientation itself, confirm that the only hypothesis that fits the data is that the gluon has spin-1, and therefore, that it is the vector boson of QCD. Finally, from counting the relative rates of three- and two-jet events at $Q \sim 30$ GeV, we know that the coupling strength of the gluon to quarks is about 0.15. Checking the list of "essential features" of QCD, we see that we have verified about half of them! The next item in the list refers to the triple- and quartic-gluon couplings; in order to study these, we need to examine multijet final states.

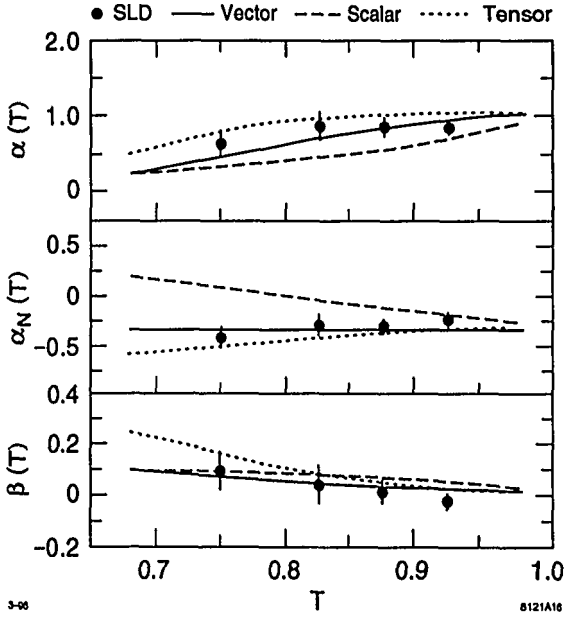


Figure 13: Dependence of the coefficients of the three-jet event plane orientation angular distributions on event thrust value [21].

3.3 Multijet Events and Gluon Self-Couplings

Consider the Feynman diagrams for production of four-jet final states shown in Fig. 14. Figures 14(a) and 14(b) illustrate the gluon bremsstrahlung process, whilst Fig. 14(d) shows the splitting of a gluon into a quark and an antiquark; the latter may be thought of as a QCD analogue of the QED process whereby a photon converts into an electron and a positron. Figures 14(a), 14(b), and 14(d) are sometimes referred to as "Abelian" diagrams. Figure 14(c) illustrates the lowest order diagram for a gluon to split into two gluons. This process has no analogue in QED since the photon does not couple to itself, and is a consequence of the non-Abelian nature of QCD in that the gluons, by virtue of possessing color charge, can interact among themselves.

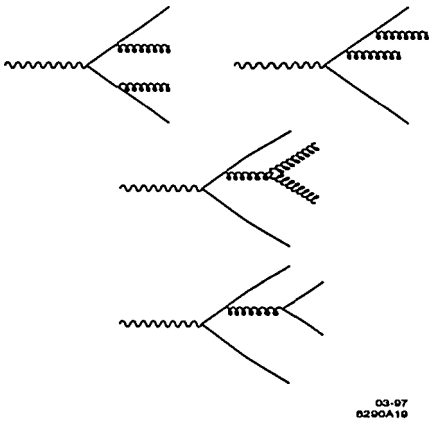


Figure 14: Tree-level Feynman diagrams for four-jet production in e^+e^- annihilation.

Group	N_C	C_F	T_F
U(1)	0	1	1
$U(1)_3$	0	1	3
SU(N)	N	$(N^2-1)/2N$	1/2
SU(3)	3	4/3	1/2

Table 2: Casimir factors for some common gauge groups.

Now consider the formal properties of the SU(3) group. The group can be characterized by constants known as Casimir factors that are defined by:

$$\Sigma_a (T^a T^a)_{ij} = \delta_{ij} C_F \tag{18}$$

$$\Sigma_{a,b} (f^{abc} f^{abd}) = \delta^{cd} N_C \tag{19}$$

$$Tr[T^a T^b] = \delta^{ab} T_F. \tag{20}$$

The Casimir factors for several common groups are shown in Table 2. We see that in the case of SU(3), N_C corresponds to the now-familiar "number of colors" that we have already encountered several times. The tree-level couplings appearing in Fig. 14 may be classified in terms of the Casimir factors, as illustrated in Fig. 15. The amplitude-squared corresponding to the bremsstrahlung diagrams [Figs. 14(a) and 14(b)] is proportional to C_F, that corresponding to $g \to q\bar{q}$ is proportional to T_F, and that corresponding to the non-Abelian process $g \to gg$ is proportional to N_C.

It is interesting to consider whether the Casimir factors of SU(3) QCD can be measured. Clearly, nature does not deliver events corresponding to the tree-level vertices shown in Fig. 15! Instead, one must write down the Feynman amplitudes for the four-jet event diagrams shown in Fig. 14, add them to those for two-

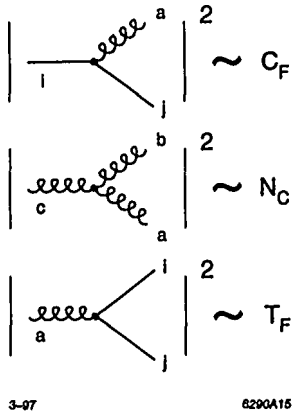


Figure 15: Casimir classification of tree-level QCD couplings.

and three-jet production at the same order of perturbation theory, and square them to derive the total hadronic cross section. The terms corresponding to four-jet production can then be identified in a gauge-invariant manner, and yield a differential cross section of the form:

$$\frac{1}{\sigma_0} d\sigma^4 = \left(\frac{\alpha_s C_F}{\pi}\right)^2 \left[F_A + \left(1 - \frac{1}{2}\frac{N_C}{C_F}\right) F_B + \frac{N_C}{C_F} F_C\right] + \left(\frac{\alpha_s C_F}{\pi}\right)^2 \left[\frac{T_F}{C_F} N_f F_D + \left(1 - \frac{1}{2}\frac{N_C}{C_F}\right) F_E\right], \quad (21)$$

where $F_A \ldots F_E$ are kinematical functions. We see that the overall normalization of the cross section is proportional to $(\alpha_s C_F)^2$, and that the kinematical distribution of the four jets depends on the ratios N_C/C_F and T_F/C_F, which can hence in principle be measured.

The issue of jet definition will be discussed in detail in Sec. 4.4. For now, let us assume that four-jet events can be defined and measured in particle detectors, and that they can be related meaningfully to the underlying four-jet parton structure described by Eq. (21). Two important physical characteristics underly the definition of four-jet observables that are sensitive to N_C/C_F and T_F/C_F: the first is that the two jets resulting from the primary quark and antiquark produced in the Z^0 decay tend to be more energetic than the jets produced by the two radiated gluons or the radiated $q\bar{q}$; the second is that in the "non-Abelian" process [Fig. 14(c)], the two gluons tend to be produced in the plane of the primary quark and antiquark, whereas in the "Abelian" process [Fig. 14(d)], the radiated quark and antiquark tend to be produced along an axis normal to this plane [25].

With this in mind, a number of four-jet observables that are potentially sensitive to the ratios of Casimir factors have been proposed over the years. If one orders and labels the four jets in an event in terms of their momenta (or energies) such that $p_1 > p_2 > p_3 > p_4$, one can define the Bengtsson-Zerwas angle [26] (Fig. 16):

$$\cos\chi_{BZ} \propto (\vec{p_1} \times \vec{p_2}) \cdot (\vec{p_3} \times \vec{p_4}) \quad (22)$$

and the Nachtmann-Reiter angle [25] (Fig. 17):

$$\cos\theta^*_{NR} \propto (\vec{p_1} - \vec{p_2}) \cdot (\vec{p_3} - \vec{p_4}). \quad (23)$$

The sensitivity of these observables is illustrated in Fig. 18, where the distributions of these angles are shown for SU(3) QCD, as well as for a straw-person $U(1)_3$ Abelian model of strong interactions, and are compared with L3 data [27]; the Abelian model is clearly excluded.

A more recent analysis by OPAL [28] is summarized in Fig. 19; here a simultaneous fit was performed to the Nachtmann-Reiter and Bengtsson-Zerwas angle distributions, as well as to the angle α_{34} between jets 3 and 4. The resulting values of N_C/C_F and T_F/C_F are displayed in Fig. 20, where they are compared with the expectations from numerous gauge groups. The SU(3) QCD expectation is clearly in good agreement with the data. The expectations from several other gauge models, such as SU(4), Sp(4), and Sp(6), also appear to be compatible with the experimental results. Note, however, that none of these models contains

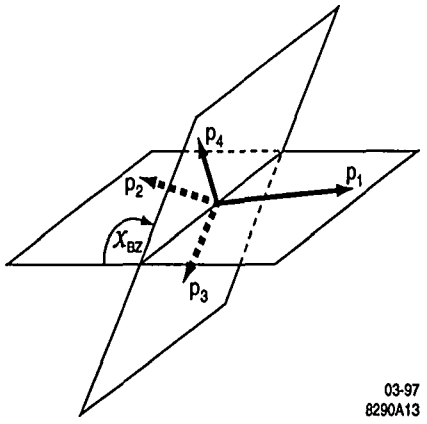


Figure 16: Definition of the Bengtsson-Zerwas angle.

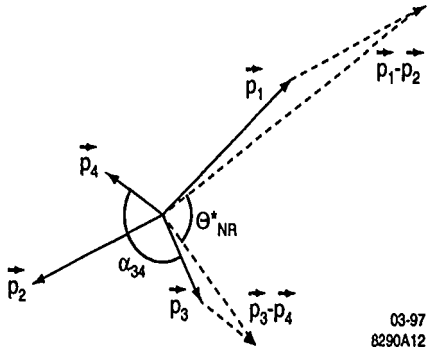


Figure 17: Definition of the Nachtmann-Reiter angle.

three color degrees of freedom for quarks, and hence all can be ruled out on that basis. Besides SU(3), only the $U(1)_3$ and SO(3) models contain three quark colors, but both are inconsistent with the measured values of N_C/C_F and T_F/C_F.

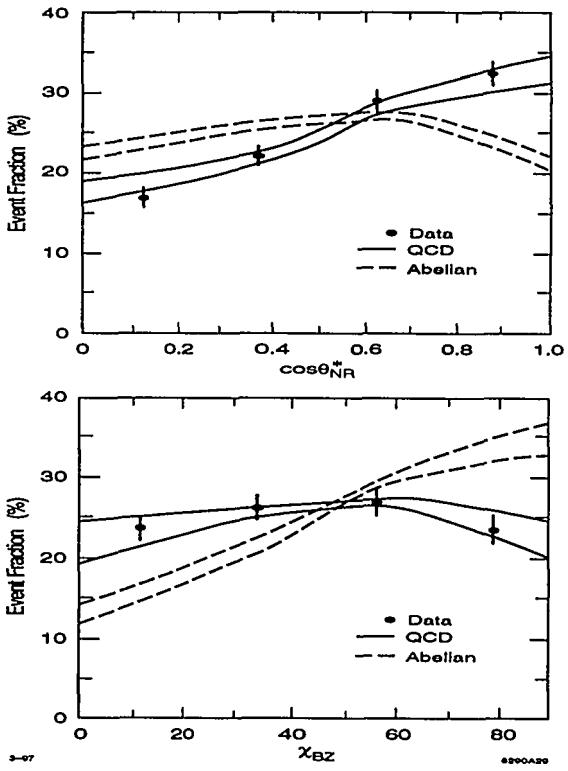


Figure 18: Illustration of the sensitivity of the Nachtmann-Reiter and Bengtsson-Zerwas angles to non-Abelian effects and comparison with L3 data [27].

The results shown in Fig. 20 hence yield the remarkable conclusion that SU(3) is the only known viable gauge model for strong interactions.

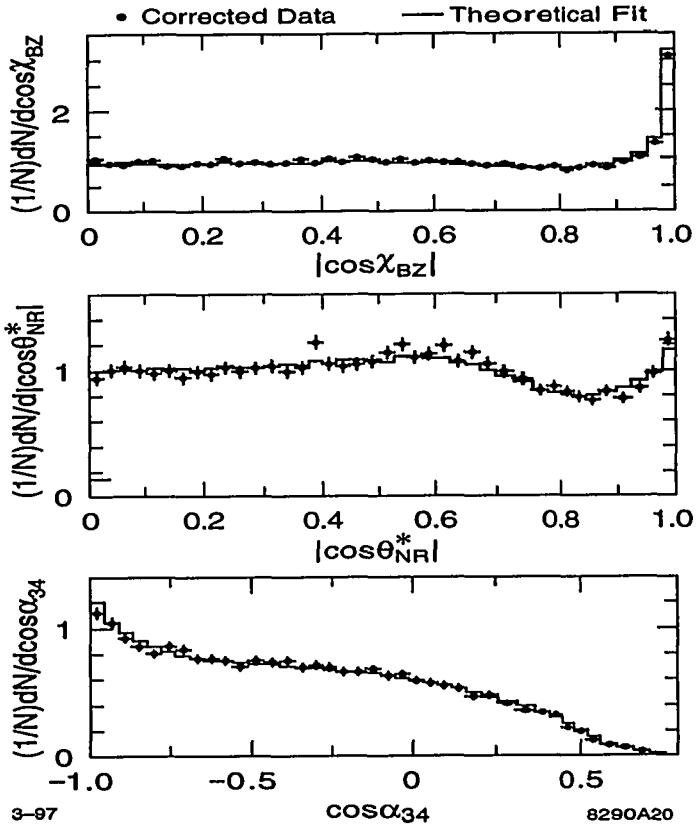


Figure 19: Simultaneous fit of QCD to OPAL measurements of χ_{BZ}, θ_{NR}, and α_{34} (Ref. [28]).

Recalling the "essential feature" of QCD that the ggg vertex must exist, we see from Fig. 20 that the nonzero measured value of N_C/C_F provides direct evidence for its contribution to four-jet production. Now consider the existence of the gggg

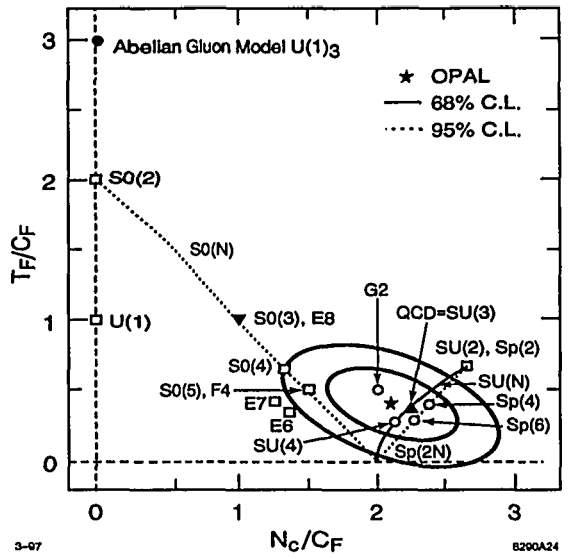


Figure 20: The T_F/C_F vs N_C/C_F plane showing the fitted values derived from Fig. 19, as well as the expectations from numerous gauge groups [28]; QCD is in good agreement with the data.

vertex; it should come as no surprise that we need to study events of yet higher jet multiplicity in order to be sensitive to it. The tree-level Feynman diagrams for five-jet production in e^+e^- annihilation are shown in Fig. 21; the gggg vertex can be seen in the two diagrams just left of center on the bottom row.

Performing a similar exercise to that for the four-jet cross section, one finds:

$$\frac{1}{\sigma_0}d\sigma^5 = \frac{1}{\sigma_0}d\sigma^{2q3g} + \frac{1}{\sigma_0}d\sigma^{4q1g}. \quad (24)$$

The first term contributes about 85% of the five-jet cross section, and may be written:

$$\frac{1}{\sigma_0}d\sigma^{2q3g} = \left(\frac{\alpha_s C_F}{\pi}\right)^3\left[G_A + \frac{N_C}{C_F}G_B + \left(\frac{N_C}{C_F}\right)^2 G_C\right], \quad (25)$$

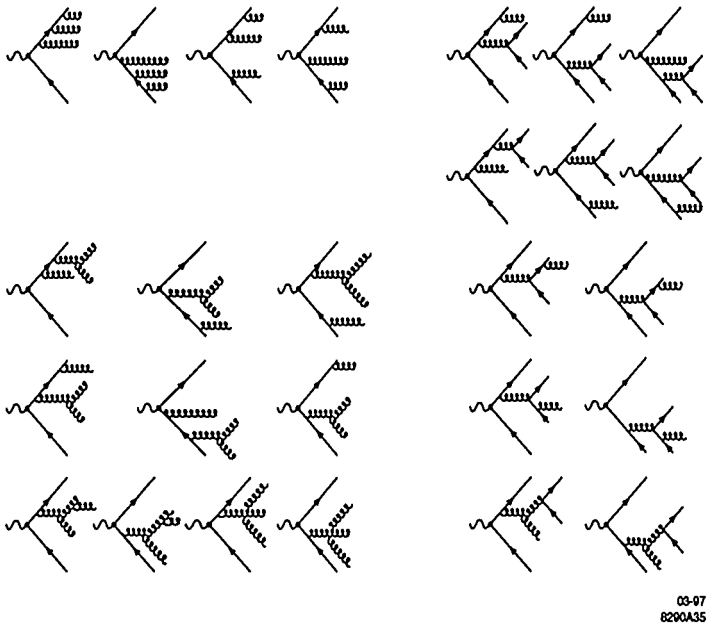


Figure 21: Tree-level Feynman diagrams for five-jet production in e^+e^- annihilation.

where G_A, G_B, and G_C are kinematical functions. The contribution of the gggg vertex is represented by the last term in Eq. (25), which is proportional to $(N_C/C_F)^2$. We have just seen that N_C/C_F must be nonvanishing in order to describe the four-jet data, so that the existence of the gggg vertex is absolutely required in QCD in order for the theory to be gauge-invariant and self-consistent. Pushing pedagogy to its limits, however, one can still ask if the data actually *require* the existence of the gggg vertex, from a phenomenological point-of-view. One can therefore define a set of *ad hoc* five-jet correlation observables, such as those illustrated in Fig. 22 (Ref. [29]). The measured distributions of the five of these observables that are most sensitive to the $(N_C/C_F)^2$ term are shown in Fig. 23, from the OPAL Collaboration [29].

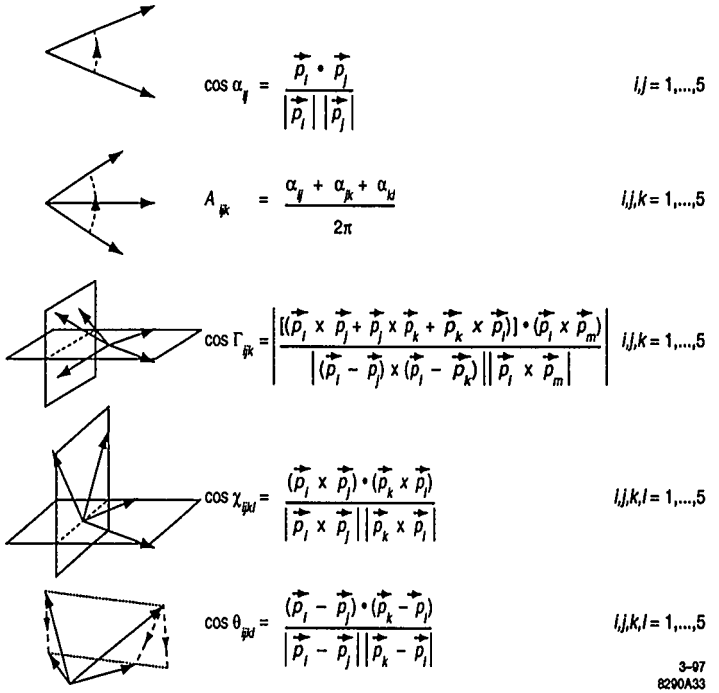


Figure 22: Illustration of correlation observables among the jets in five-jet events [29].

Two possible strategies now present themselves for testing the self-consistency of QCD. One could fit inclusively the quantity N_C/C_F to the five-jet data shown in Fig. 23 and compare it with the value determined from four-jet events; the results of such a comparison are shown in Fig. 24(a); the four-jet and five-jet events clearly yield consistent results. A second possibility is to fit phenomenologically only the gggg contribution proportional to $(N_C/C_F)^2$; the results are shown in

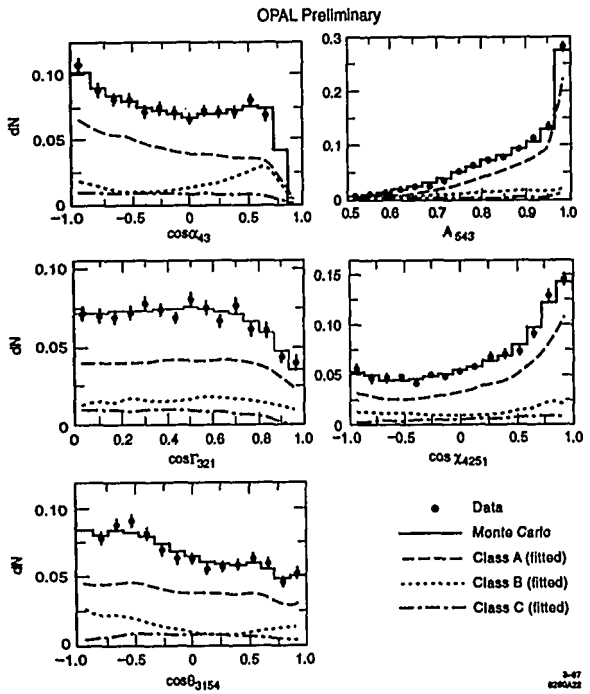


Figure 23: The five correlation observables in five-jet events that are most sensitive to contributions from the gggg vertex [29].

Fig. 24(b). In the latter case, the error bars are large due to the small number of five-jet events, as well as to the large uncertainties on multijet production that arise from hadronization effects (see Sec. 4.4). The measured value of $(N_C/C_F)^2$ is clearly consistent with the QCD expectation of $(9/4)^2 \approx 5$, but it is also consistent with zero, so that the existence of the gggg vertex has not yet been established from a phenomenological point-of-view.

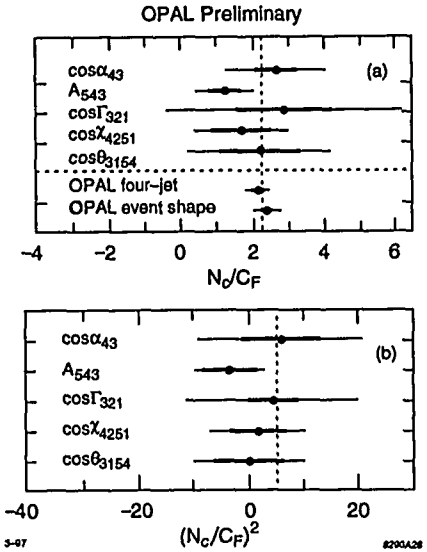


Figure 24: Measurements of (a) (N_C/C_F) and (b) $(N_C/C_F)^2$ made using five-jet events at OPAL [29].

3.4 Review of Strategy for QCD Tests

At this point, we have seen that most of the "essential features" of QCD have been established empirically, with the possible exception of the gggg coupling. Even in this case, given the existence of the ggg vertex, the gggg vertex must exist in QCD in order for the theory to be gauge-invariant. The last 20 years of hadronic-event studies at e^+e^- colliders have hence established, in a qualitative sense, that the QCD Lagrangian is the correct one to describe strong interactions. At this point, it therefore seems sensible to revise the strategy for testing QCD.

Since the theory contains in principle only one free parameter, the strong coupling α_s, QCD can be tested in a quantitative fashion by measuring α_s in different processes and at different hard scales Q. The precision of these measurements,

and the resulting degree of consistency among them, determine quantitatively the precision with which the theory has been tested. This philosophy is directly analogous to that used to test the electroweak theory by measuring a large number of observables that are sensitive to a few key unknown parameters of the theory. In addition to testing QCD, the precise measurement of α_s allows constraints on possible extensions to the Standard Model (SM) of elementary particles; see, *e.g.*, Ref. [30]. Measurements of α_s have been performed in e^+e^- annihilation, hadron-hadron collisions, and deep-inelastic lepton-hadron scattering, covering a range of Q^2 from roughly 1 to 10^5 GeV^2. In the next section, I shall describe the e^+e^- measurements, and compare them with those made in other hard processes; for a review of this field, see Ref. [31].

4. Measurements of α_s in e^+e^- Annihilation

4.1 Theoretical Considerations

An inclusive observable X may be written schematically:

$$X \quad = \quad X^{EW}\,(1 + \delta^{QCD}), \tag{26}$$

where X^{EW} represents the electroweak contribution. Since, with observables of this type, α_s enters via the small QCD radiative correction, δ^{QCD}, a precise measurement of α_s generally requires a large data sample. Observables can also be defined that are directly proportional to δ^{QCD} and hence potentially more sensitive to α_s. In either case, δ^{QCD} can be separated into perturbative and nonperturbative contributions:

$$\delta^{QCD} \quad = \quad \delta^{pert} + \delta^{non-pert}. \tag{27}$$

The perturbative contribution can in principle be calculated as a power series in α_s, though in practice the large number of Feynman diagrams involved renders a complete calculation beyond the first few orders intractable. The nonperturbative contribution, often called a "hadronization correction" in e^+e^- annihilation or a "higher twist effect" in lepton-hadron scattering, is expected to have the form of a series of inverse powers of the physical scale (see Sec. 5).

In practice, most QCD calculations of observables are performed using finite-order perturbation theory, and calculations beyond leading order depend on the *renormalization scheme* employed, implying a scheme-dependent strong-interaction scale Λ. It is conventional to work in the modified minimal subtraction scheme ($\overline{MS}$ scheme) [32], and to use the strong interaction scale $\Lambda_{\overline{MS}}$ for five active quark flavors. If one knows $\Lambda_{\overline{MS}}$, one may calculate the strong coupling $\alpha_s(Q^2)$ from the solution of the QCD renormalization group equation [33]:

$$\alpha_s(Q^2) \quad = \quad \frac{4\pi}{\beta_0 \ln(Q^2/\Lambda^2_{\overline{MS}})}\{\,1 - \frac{2\beta_1}{\beta_0^2}\,\frac{\ln(\ln(Q^2/\Lambda^2_{\overline{MS}}))}{\ln(Q^2/\Lambda^2_{\overline{MS}})} + \ldots\,\}. \tag{28}$$

Because of the large data samples taken in e^+e^- annihilation at the Z^0 resonance, it has become conventional to use as a yardstick $\alpha_s(M_Z^2)$, where M_Z is the mass of the Z^0 boson; $M_Z \approx 91.2$ GeV (Ref. [34]). Tests of QCD can therefore be quantified in terms of the consistency of the values of $\alpha_s(M_Z^2)$ measured in different experiments. The "QCD-challenged" reader may like to think of $\alpha_s(M_Z^2)$ as being "the $\sin^2\theta_W$ of strong interactions."

In e^+e^- annihilation, $\alpha_s(M_Z^2)$ has been measured from inclusive observables relating to the Z^0 lineshape and to hadronic decays of the τ lepton, as well as from jet-related hadronic event shape observables, and scaling violations in inclusive hadron fragmentation functions.

4.2 R and the Z^0 Lineshape

For the inclusive ratio $R = \sigma(e^+e^- \to \text{hadrons})/\sigma(e^+e^- \to \mu^+\mu^-)$, the SM electroweak contributions are well-understood theoretically and the perturbative QCD series has been calculated up to $O(\alpha_s^3)$(Ref. [35]) for massless quarks and up to

$O(\alpha_s^2)$ including quark mass effects [36]; the large size of the $O(\alpha_s^3)$ term is potentially a cause for concern about the degree of convergence of the series. Closely-related observables at the Z^0 resonance are:

- the Z^0 total width, Γ_Z,
- the pole cross section, $\sigma_h^0 \equiv 12\pi\Gamma_{ee}\Gamma_{had}/M_Z^2\Gamma_Z^2$,
- the ratio of hadronic to leptonic Z^0 decay branching ratios $R_l \equiv \Gamma_{had}/\Gamma_{ll}$,

which all depend on the Z^0 hadronic width:

$$\Gamma_{had} = 1.671\left(1 + a_1\left(\frac{\alpha_s}{\pi}\right) + a_2\left(\frac{\alpha_s}{\pi}\right)^2 + a_3\left(\frac{\alpha_s}{\pi}\right)^3 + \ \ldots\right) \quad (29)$$

where: $a_1 = 1$, $a_2 = 0.75$, and $a_3 = -15.3$. In these cases, the nonperturbative contributions are expected to be $O(1/M_Z)$ and are usually ignored. A concern is that recent measurements of observables that probe the electroweak couplings of the Z^0 to b and c quarks deviate slightly from SM expectations [37]. Since these couplings must be known in order to extract $\alpha_s(M_Z^2)$, this effect, whatever its origin, is a potential source of bias [33]. Further analysis is in progress from the SLC and LEP experiments, and the situation is not yet resolved.

Proceeding nonetheless, the procedure adopted [37] is to perform a global SM fit to a panoply of electroweak data that includes the W and top quark masses as well as the Z^0 observables relating to the lineshape, left-right production asymmetry, decay fermion forward-backward asymmetries, branching ratios to heavy quarks, and τ polarization. The free parameters are the Higgs mass, M_{Higgs}, which contributes to X^{EW}, and $\alpha_s(M_Z^2)$. Data presented at the 1996 summer conferences yield the results shown in Fig. 25 (Ref. [37]), from which the positively-correlated results $M_{Higgs} = 149^{+190}_{-82}$ GeV and

$$\alpha_s(M_Z^2) = 0.1202 \pm 0.0033 \ \text{(exp.)} \quad (30)$$

are obtained. The $\alpha_s(M_Z^2)$ value is lower than the corresponding results presented at the 1995 conferences [38], $\alpha_s(M_Z^2) = 0.123 \pm 0.005$, and at the 1994 conferences, $\alpha_s(M_Z^2)$ 0.125 ± 0.005 (Ref. [39]), whose large central values were partly responsible for a supposed discrepancy between "low-Q^2" and "high-Q^2" $\alpha_s(M_Z^2)$ measurements [40]. The change between 1995 and 1996 is due to a combination of shifts in the values of the Z^0 lineshape parameters, redetermined in light of the recalibration of the LEP beam energy due to the "TGV effect" [37], and a change in the central value of M_{Higgs} at which $\alpha_s(M_Z^2)$ is quoted, from 300 GeV (1995) to the fitted value 149 GeV (1996). A detailed study of theoretical uncertainties implies [41] that they contribute at a level substantially below ± 0.001. Since data-taking at the Z^0 resonance has now been completed at the LEP collider, the precision of this result is not expected to improve further.

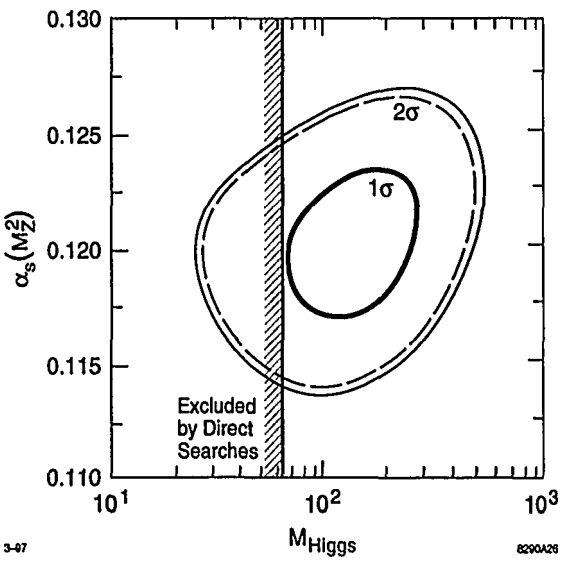


Figure 25: Results of a global fit of the Standard Model to electroweak observables [37]; the one- and two-standard deviation contours are shown in the $\alpha_s(M_Z^2)$ vs M_{Higgs} plane.

4.3 Hadronic τ Decays

An inclusive quantity similar to R is the ratio R_τ of hadronic to leptonic decay branching ratios, B_h and B_l respectively, of the τ lepton:

$$R_\tau \equiv \frac{B_h}{B_l} = \frac{1 - B_e - B_\mu}{B_e}, \quad (31)$$

where B_e and B_μ can either be measured directly, or deduced from a measurement of the τ lifetime τ_τ. In addition, a family of observables known as "spectral moments" of the invariant mass-squared s of the hadronic system has been proposed [42]:

$$R_\tau^{kl} \equiv \frac{1}{B_e}\int_0^{M_\tau^2} ds \left(1 - \frac{s}{M_\tau^2}\right)^k \left(\frac{s}{M_\tau^2}\right)^l \frac{dB_h}{ds}, \quad (32)$$

where M_τ is the τ mass. In this case, the integrand can be measured independently of B_e. It is easily seen that $R_\tau = R_\tau^{00}$.

R_τ and R_τ^{kl} have been calculated perturbatively up to $O(\alpha_s^3)$. However, because $M_\tau \sim 1$ GeV, one expects [Eq. (28)] $\alpha_s(M_\tau) \sim 0.3$ and it is not *a priori* obvious that the perturbative calculation can be expected to be reliable, or that the non-perturbative contributions of $O(1/M_\tau)$ will be small. In recent years, a large theoretical effort has been devoted to this subject; see, *e.g.*, Refs. [42, 43, 44].

The ALEPH Collaboration derived R_τ from its measurements of B_e, B_μ, and τ_τ, and also measured the (10), (11), (12), and (13) spectral moments. A combined fit yielded (Ref. [45]) $\alpha_s(M_Z^2) = 0.124 \pm 0.0022 \pm 0.001$, where the first error receives equal contributions from experiment and theory, and the second derives from uncertainties in evolving α_s across the c and b thresholds. The OPAL Collaboration measured R_τ from B_e, B_μ, and τ_τ, and derived (Ref. [46]) $\alpha_s(M_Z^2) = 0.1229^{+0.0016}_{-0.0017}$ (exp.) $^{+0.0025}_{-0.0021}$ (theor.). The CLEO Collaboration measured the same four spectral moments as ALEPH and also derived R_τ using 1994 Particle Data Group values for B_e, B_μ, and τ_τ. A combined fit yielded (Ref. [47]) $\alpha_s(M_Z^2) = 0.114 \pm 0.003$. This central value is slightly lower than the ALEPH and OPAL values. If more recent world average values of B_e and B_μ are used, CLEO obtains a higher central $\alpha_s(M_Z^2)$ value [47]. Averaging the second CLEO result and the ALEPH and OPAL results by weighting with the experimental errors, assuming they are uncorrelated, yields:

$$\alpha_s(M_Z^2) = 0.122 \pm 0.001 \text{ (exp.)} \pm 0.002 \text{ (theor.)}. \quad (33)$$

This is nominally a very precise measurement, although recent studies have suggested that additional theoretical uncertainties may be as large as ± 0.006 (Ref. [48]).

4.4 Hadronic Event Shape Observables

As discussed in Sec. 3.2, in e^+e^- annihilation the rate of three-jet production:

$$R_3 \equiv \frac{\sigma_{3-jet}}{\sigma_{had}} \quad (34)$$

is directly proportional to α_s and can hence be used to determine α_s. In order to make a meaningful measurement that can be compared with those just discussed, one must calculate R_3 to at least next-to-leading order in α_s, *i.e.*, to $O(\alpha_s^2)$. The relevant contributing Feynman diagrams are shown in Fig. 26; these form the basis of the $O(\alpha_s^2)$ calculation of R_3 (Refs. [49, 50, 51]).

4.4.1 Definition of Jets and Event Shape Measures

The task is, in principle, straightforward. One must count the number of three-jet events and divide by the total number of hadronic events to obtain R_3, then compare with the theoretical prediction to obtain α_s. However, it is immediately apparent that one cannot simply define the jet multiplicity of events on the basis of a visual inspection! On the experimental side, the classic "Mercedes-Benz" three-jet event measured in a detector is rather rare; many events contain broad particle flows that might be classified as a single jet by one observer but as two or more jets by another observer. Moreover, in QCD the bremsstrahlung spectrum of parton radiation peaks at small angles and is continuous. Hence, even theoretically the

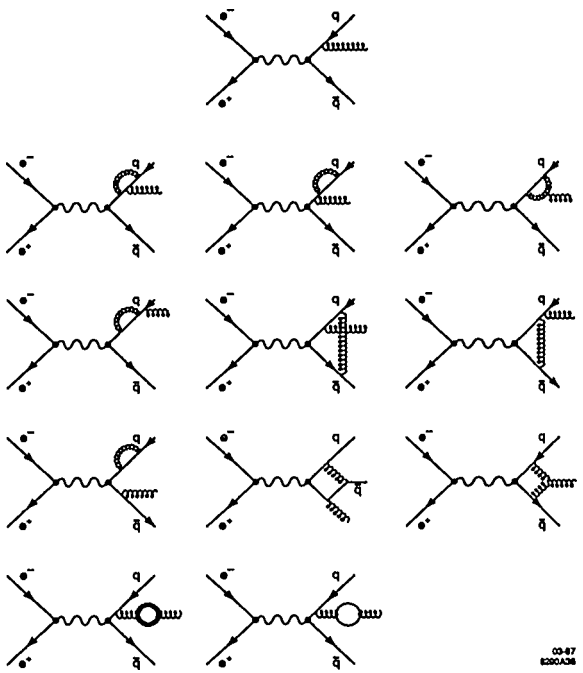


Figure 26: Tree-level and one-loop Feynman diagrams that contribute to three-jet observables up to $O(\alpha_s^2)$ in QCD perturbation theory.

issue of when a radiated parton is sufficiently energetic, and at a sufficiently wide angle relative to its parent, so as to be resolved as a separate jet, is not without ambiguity. After due Cartesian deliberation, one pragmatically concludes that one needs an algorithmic definition of a jet that can be applied to hadrons recorded in a detector, as well as to partons in perturbative QCD calculations, and a sensible recipe to translate between the two.

A convenient solution is provided by iterative clustering algorithms in which a measure y_{ij}, such as invariant mass-squared/Q^2, is calculated for all pairs of particles i and j in an event, and the pair with the smallest y_{ij} is combined into a single "particle." This process is repeated until all pairs have y_{ij} exceeding a value y_c, and the jet multiplicity of the event is defined as the number of particles remaining. For a sample of events, the n-jet rate R_n is then defined as the number of n-jet events divided by the total number of events. This number is not a constant, but rather depends on the choice of algorithm and on the y_c value. The y_c-dependence is illustrated in Fig. 27 for jets defined using the JADE algorithm [52] applied to SLD data [53]. One can think of y_c as the "jet resolution" scale. Large y_c values correspond to poor eyesight, most events look two-jet-like, and hence $R_2 \approx 1$. Small y_c values correspond to good eyesight, a richer jet structure is discernible, and R_3 and R_4 are nonzero. It should be noted, however, that from an operational point of view, the data points shown in Fig. 27 are awkward to handle in that they are correlated between different y_c values. A more convenient observable is the *differential* two-jet rate:

$$D_2(y_c) \equiv (R_2(y_c) - R_2(y_c - \Delta y_c))/\Delta y_c \qquad (35)$$

which is a measure of the rate of events that *change* their classification between 2-jet-like and $\geq$ 3-jet-like as y_c is varied across the range Δy_c. $D_2(y_c)$ is illustrated in Fig. 28.

In fact, several variations of the JADE algorithm have been suggested [54]; these differ in the definition of the resolution measure y_{ij}, and/or in the "recombination scheme" prescription for combining two particles that are unresolvable. A full discussion is beyond the scope of these lectures, but it is important to note that the "E," "E0," "P," and "P0" variations of the JADE algorithm, as well as the "Durham" ("D") and "Geneva" ("G") algorithms, are all *collinear- and infra-red-safe* observables, which, for our purposes, means that they can be calculated in perturbative QCD [55].

More generally, one can define other infra-red- and collinear-safe measures of the topology of hadronic final states; a list of 15 such observables is given in Table 3. Thrust has already been encountered in Sec. 3 and is related to the

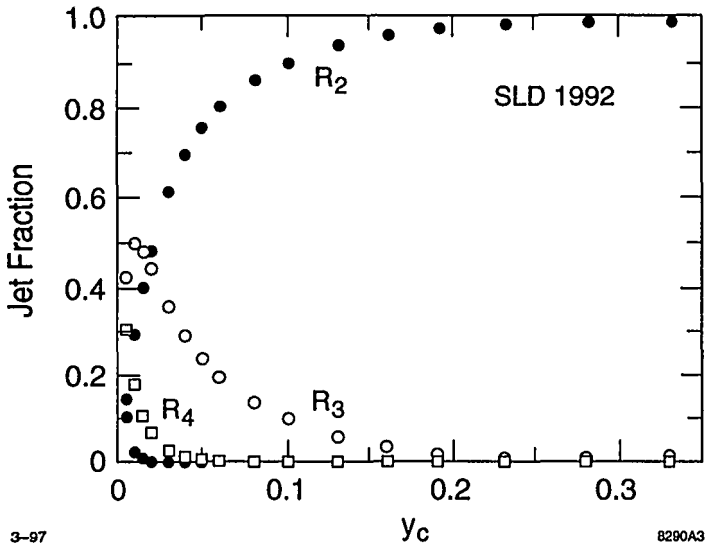


Figure 27: Dependence on the jet resolution parameter y_c of the n-jet rates R_n measured using SLD data [53] with the JADE algorithm.

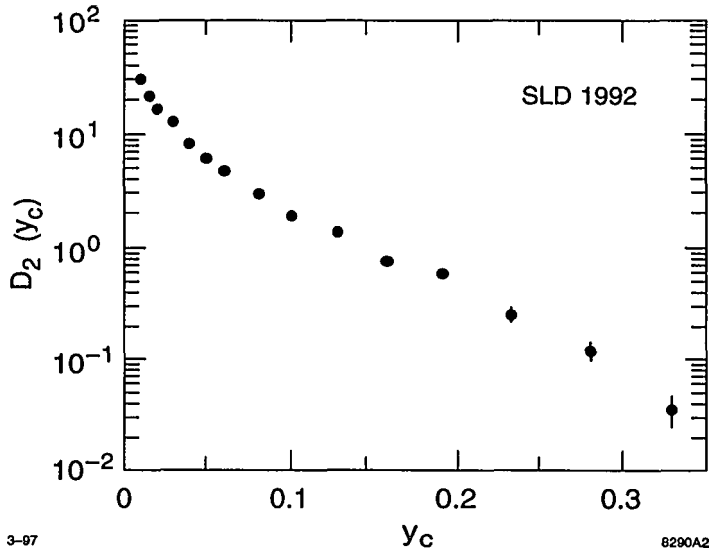


Figure 28: Dependence on the jet resolution parameter y_c of the differential two-jet rate D_2 (Ref. [53]).

longitudinal momentum flow in events:

$$T = \max \frac{\sum_i | \vec{p}_i \cdot \vec{n}_T |}{\sum_i | \vec{p}_i |}, \tag{36}$$

where $\vec{p}_i$ is the momentum vector of particle i, and $\vec{n}_T$ is the thrust axis to be determined. It is useful to define $\tau \equiv 1 - T$. For back-to-back two-parton final states, τ is zero, while $0 \leq \tau \leq \frac{1}{3}$ for planar three-parton final states. Spherical events have $\tau = \frac{1}{2}$. An axis $\vec{n}_{maj}$ can be found to maximize the momentum sum transverse to $\vec{n}_T$, and an axis $\vec{n}_{min}$ is defined to be perpendicular to the two axes $\vec{n}_T$ and $\vec{n}_{maj}$. The variables thrust-major T_{maj} and thrust-minor T_{min} are obtained by replacing $\vec{n}_T$ in Eq. (36) by $\vec{n}_{maj}$ or $\vec{n}_{min}$, respectively. The oblateness O is then defined by Ref. [56]

$$O = T_{maj} - T_{min}. \tag{37}$$

Other measures are related to jet masses, and energy-energy correlations between particles; for a discussion see, *e.g.*, Ref. [57].

The observables are all constructed to be directly proportional to α_s at leading order, and so are potentially sensitive measures of the strong coupling. The $O(\alpha_s^2)$ QCD prediction for each of these observables X can be written [51]:

$$\frac{1}{\sigma_0}\frac{\mathrm{d}\sigma}{\mathrm{d}X} = A(X)\left(\frac{\alpha_s}{2\pi}\right) + B(X)\left(\frac{\alpha_s}{2\pi}\right)^2, \tag{38}$$

so that α_s can be determined from each. Though these observables are intrinsically highly correlated, by using all 15 to study α_s, one is attempting to maximize the use of the information in complicated multihadron events, and in some sense, is making a more demanding test of QCD than by using only one or two observables.

Observable	Symbol
1 – Thrust	τ
Heavy jet mass	ρ
Jet broadening:	
Total	B_T
Wide	B_W
Oblateness	O
C-parameter	C
Differential jet rates:	
$D_2(y_c) = \frac{\Delta R_2(y_c)}{\Delta y_c}$	E
	E0
	P
	P0
	D
	G
Energy-energy correlations	EEC
Asymmetry of EEC	$AEEC$
Jet cone energy fraction	$JCEF$

Table 3: Fifteen infra-red- and collinear-safe measures of the topology of e^+e^- hadronic final states.

Moreover, it will be seen that the study of many observables is essential, as it may expose systematic effects. Finally, the α_s determination from hadronic event shape observables is based on the information content within three-jet-like events, and is essentially uncorrelated with the measurements from the Z^0 lineshape which are based on event-counting of predominantly two-jet-like final states.

The technology of this approach has been developed over the past 15 years of analysis at the PETRA, PEP, TRISTAN, SLC, and LEP colliders, so that the method is considered to be well-understood both experimentally and theoretically.

Note, however, that before they can be compared with perturbative QCD predictions, it is necessary to correct the measured distributions for any bias effects originating from the detector acceptance, resolution, and inefficiency, as well as for the effects of initial-state radiation and hadronization, to yield "parton-level" distributions.

4.4.2 Hadronization and Monte Carlo Models

A schematic of hadron production in e^+e^- annihilation is shown in Fig. 29. One may divide this process into several phases:

1. A hard electroweak process in which the primary quark and antiquark may be produced off mass-shell:
   $e^+e^- \rightarrow q\bar{q}$.
2. Perturbative QCD evolution of the primary $q\bar{q}$ via parton bremsstrahlung:
   $q\bar{q} \rightarrow$ several q, $\bar{q}$, g.
3. Hadronization of partonic system:
   (q, $\bar{q}$, g)s $\rightarrow$ primary resonances.
4. Decays of primary resonances into "stable" particles:
   B, C, K^0_s, ϕ, Δ, ρ ... $\rightarrow \pi^\pm$, $K^\pm$, p, $\bar{p}$ ... ($e^\pm$, $\mu^\pm$, $\tau^\pm$, ν).

Phases 1 and 2 are generally agreed to be calculable "respectably" using perturbative techniques applied to the electroweak theory and QCD, respectively. Phases 3 and 4 are more problematic in that they are intrinsically nonperturbative processes that cannot in general be calculated from first principles. In the absence of nonperturbative calculations, we are forced to rely on phenomenological models.

Since it is also necessary in phase 4 to simulate the interaction of particles with detectors, which can only be done in a deterministic fashion, Monte Carlo event

generators have been developed for the complete simulation of hadronic event production in e^+e^- annihilation and are now essential components of data analysis. I shall discuss only the two most widely used generators JETSET [58] and HERWIG [59]; other generators are described in Ref. [60], and will be discussed later by Buchanan [61]. I shall not discuss at all the GEANT program [62], which is widely used for the simulation of the geometry and material response of particle detectors. The philosophy here is to outline the main features of these generators in the context of their use as tools in understanding and correcting the data; no attempt will be made to justify these models on phenomenological grounds, and the outline will necessarily be brief.

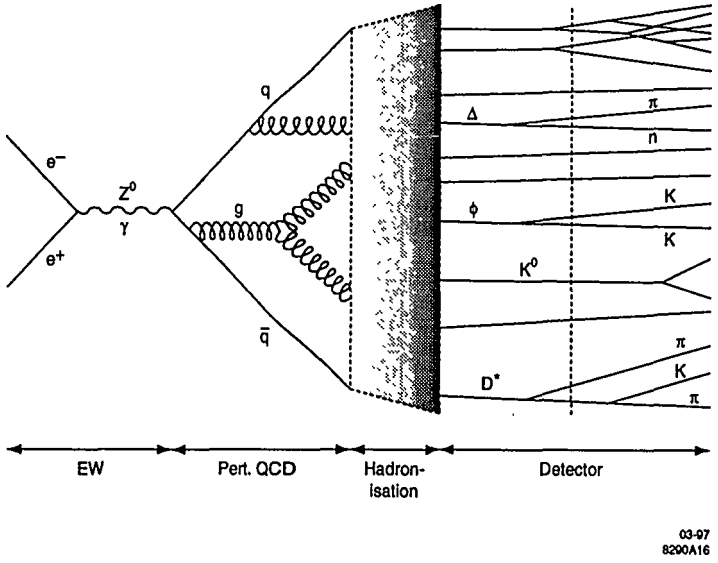


Figure 29: Schematic of hadron production in e^+e^- annihilation.

Both JETSET and HERWIG implement electroweak matrix elements for the production of a primary $q\bar{q}$, as well as a perturbative QCD "parton shower" evolution of the system into a set of low-virtual-mass quarks and gluons. More formally, the latter is based on a probabilistic parton branching process that is derived from a leading + partial next-to-leading logarithmic resummation of the QCD matrix elements [63]. JETSET and HERWIG implement the parton branching process slightly differently, a discussion of which is beyond the scope of these lectures, but both generators have a parameter Λ that characterizes the scale of strong interactions, as well as a parameter Q_0 that characterizes the minimum virtual-mass scale of the parton evolution.

A schematic of the hadronization process as implemented in HERWIG is shown in Fig. 30. At the termination of the parton shower, pairs of partons are associated into colorless clusters; these then undergo phase-space decay to produce stable pions, kaons, and baryons. Clusters with mass larger than a parameter M_{cl} are split into two before the phase-space decay. Additional parameters control the properties of heavy (B or C) hadron decay [59].

JETSET implements the "Lund string model" of jet fragmentation [64], illustrated in Fig. 31. In this case, the color field between partons at the end of the parton shower is represented as a one-dimensional massless relativistic string. String pieces terminate at quarks and antiquarks, and gluons are represented by momentum-carrying "kinks" in the string. The string is fragmented iteratively according to the recipe:

$$f(z) \quad \propto \quad \frac{1}{z}(1-z)^a \exp(-b\frac{m_\perp^2}{z}), \tag{39}$$

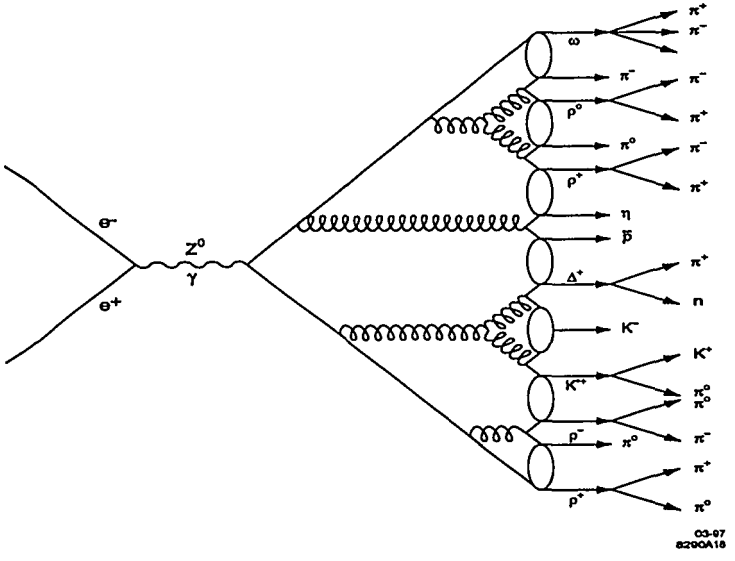


Figure 30: Schematic of hadronization in HERWIG.

where z is the fraction of the quantity $E + p_{\parallel}$ of a parent string piece taken by the daughter, $m_{\perp} = \sqrt{p_{\perp}^2 + m^2}$, "$\perp$" and "$\parallel$" refer to the string axis, and a and b are parameters. Momentum transverse to the string axis, $p_{\perp}$, is introduced in an *ad hoc* fashion using a Gaussian probability distribution. A large number of additional parameters is used to fine-tune the relative production of particles such as strange, pseudoscalar, and vector mesons, as well as strange and nonstrange, octet and decuplet baryons [58].

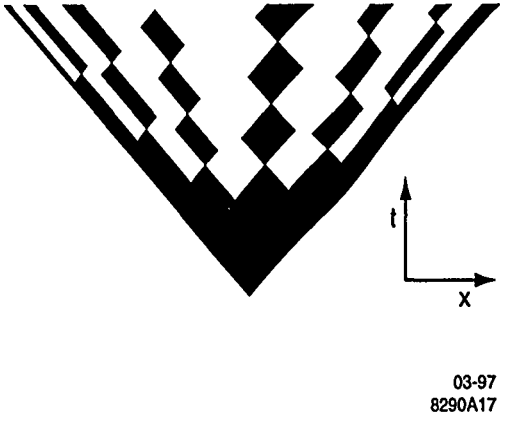


Figure 31: Schematic of hadronization in JETSET.

4.4.3 Data Correction

For the α_s analysis, we wish to use these event generators to understand the effect of the hadronization process on the hadronic momentum flow in events, and to correct for any bias, as well as to understand the influence of the response of the detector. One conventional approach involves using a sample of Monte Carlo events to calculate bin-by-bin correction factors, and then applying these to the

measured distribution. For a distribution $D(X)$, the correction for detector effects is defined:

$$C_{DET}^{MC}(X) \quad = \quad \frac{D_{HAD}^{MC}(X)}{D_{DET}^{MC}(X)}, \tag{40}$$

where HAD and DET refer to the simulated distribution at the hadron-level and detector-level phases, respectively. The correction for hadronization effects is analogously defined:

$$C_{HAD}^{MC}(X) \quad = \quad \frac{D_{PART}^{MC}(X)}{D_{HAD}^{MC}(X)}, \tag{41}$$

where $PART$ refers to the simulated distribution at the parton-level. The data distribution corrected back to the parton-level is given by:

$$D^{Data'}(X) \quad = \quad C_{HAD}^{MC}(X) \cdot C_{DET}^{MC}(X) \cdot D^{Data}(X), \tag{42}$$

and $D^{Data'}(X)$ can be compared with perturbative QCD. More sophisticated correction procedures can also be defined; see, *e.g.*, Ref. [65].

As with any correction procedure, one must take care not to introduce bias from implicit model-dependence, and must estimate the systematic uncertainties involved. A prerequisite is that the simulation describe the distribution measured in the detector! The parameters of the detector simulation, as well as of the event generator itself, should then be varied, the stability of the correction factors examined, and systematic errors assigned accordingly. An example of a raw measured D_2 distribution from SLD [57], compared with simulations based on JETSET and HERWIG, is shown in Fig. 32. The corresponding corrected distribution, and the correction factors, are shown in Fig. 33.

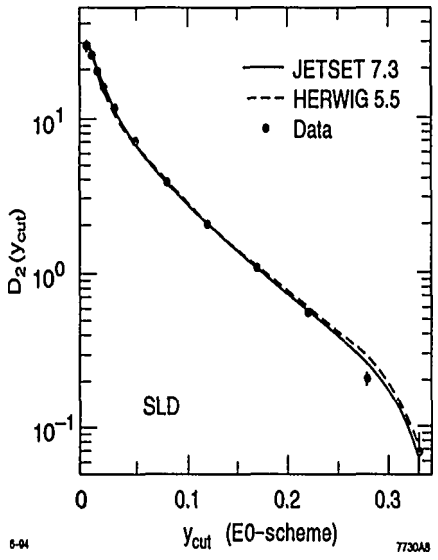


Figure 32: Measured D_2 distribution [57] compared with JETSET and HERWIG predictions.

4.4.4 Comparison with Perturbative QCD

A fit of $O(\alpha_s^2)$ perturbative QCD to the D_2 distribution is shown in Fig. 33; it yields $\alpha_s(M_Z^2) = 0.1175 \pm 0.0007$ (stat.) ± 0.0027 (syst.) [57]. One can repeat this procedure for all 15 observables listed in Table 3 and derive in each case a fitted value of $\alpha_s(M_Z^2)$; these are shown in Fig. 34(a). The distressing result of this exercise is that the $\alpha_s(M_Z^2)$ values so determined are not internally consistent with one another! A measure of the scatter among the results is given by the r.m.s. deviation of ± 0.008, which is much larger than the experimental error of ± 0.003 on a typical observable. An exciting, though remote, possibility is that we have observed a spectacular breakdown of QCD! A more likely explanation is that some systematic effect that we have not yet considered is at work. In fact,

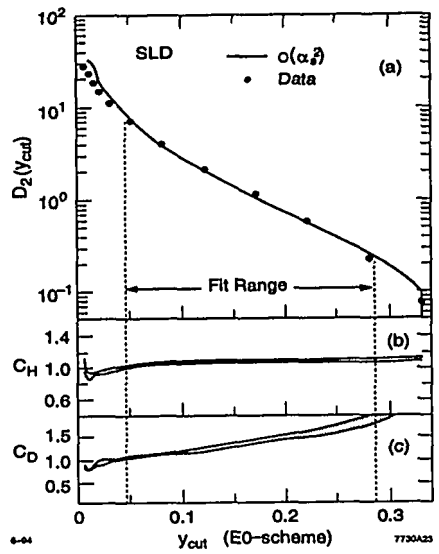


Figure 33: (a) Corrected D_2 distribution [57]; (b) hadronization correction factor; (c) detector effects correction factor. In (a), the line shows a fit to $O(\alpha_s^2)$ QCD.

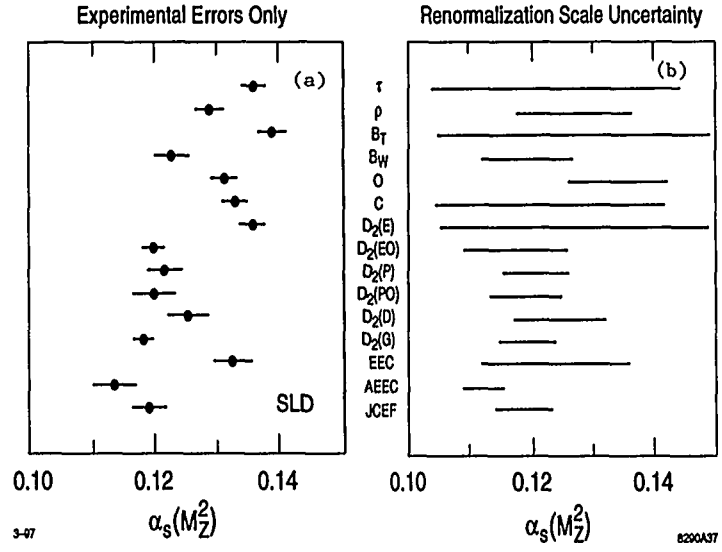


Figure 34: (a) Values of $\alpha_s(M_Z^2)$ determined [57] by fitting $O(\alpha_s^2)$ QCD predictions to 15 hadronic event shape observables using a fixed value of the renormalization scale $\mu = Q$; the results are clearly inconsistent within the experimental errors. (b) Renormalization scale uncertainties.

an implicit assumption was made in deriving the results shown in Fig. 34(a) that relates to the arcane issue of choosing the *renormalization scale* in QCD.

4.4.5 Renormalization Scale Uncertainty

For any observable, truncation of the QCD perturbation series at finite order causes a residual dependence on the (scheme-dependent) *renormalization scale* μ. This parameter is formally unphysical and should not enter at all into an exact infinite-order calculation, and its value is arbitrary. For the event shape observables, an explicit μ-dependence enters the next-to-leading coefficient:

$$\frac{1}{\sigma_0}\frac{d\sigma}{dX} = A(X)\left(\frac{\alpha_s(\mu^2)}{2\pi}\right) + (B(X) + A(X)2\pi b_0 \ln\mu^2/Q^2)\left(\frac{\alpha_s(\mu^2)}{2\pi}\right)^2 \quad (43)$$

so that a measurement of α_s must be in the context of some chosen value of μ. This is illustrated in Fig. 35, where the value of $\Lambda_{\overline{MS}}$ from fits to D_2 is shown as a function of the choice of μ; there is clearly a strong μ-dependence. The top portion of Fig. 35 shows the corresponding χ^2_{dof} for each fit; amusingly, the data show no preference for any particular value of μ provided it is larger than $\sqrt{0.001Q^2}$. A full discussion of the form of the μ-dependence is beyond the scope of these lectures; see Ref. [66]. Figures of the μ-dependence for the other observables can be found in Ref. [57].

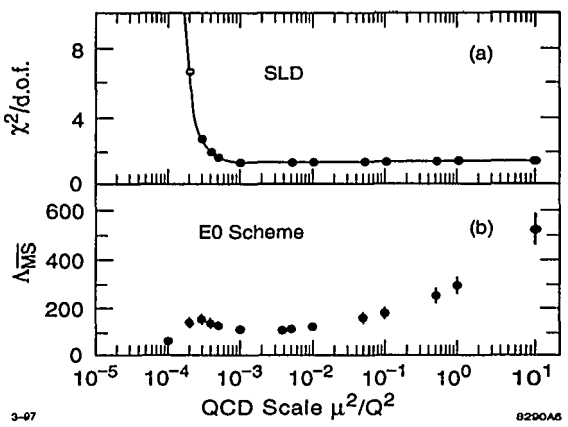


Figure 35: Dependence of (a) χ^2_{dof} and (b) $\Lambda_{\overline{MS}}$ on the value of μ chosen in fits to the SLD D_2 distribution [53].

A consensus has arisen among experimentalists that the effect of missing higher-order terms can hence be estimated from the dependence of $\alpha_s(M_Z^2)$ on the value of μ assumed in fits of the calculations to the data, and a *renormalization scale uncertainty* is often quoted. This procedure, well-motivated in that the μ-dependence caused by the truncation of the perturbation series would be cancelled by addition of the higher-order terms, is, however, arbitrary, and is not equivalent to knowledge of the size of the *a priori* unknown terms. In cases where scale uncertainties are considered, this arbitrariness is manifested in the wide variation among the ranges and central values of μ chosen by different experimental groups, see, *e.g.*, Ref. [67]; in other cases, this source of uncertainty is not included in the errors. Different $\alpha_s(M_Z^2)$ results with similar experimental precision can hence be quoted with different total errors depending on the procedure adopted for assigning the theoretical uncertainties. The interpretation of the central values and errors on $\alpha_s(M_Z^2)$ measurements is hence not always straightforward. The SLD estimate of the renormalization scale uncertainty for each observable is shown in Fig. 34(b). It is apparent that the scale uncertainty is much larger than the experimental error, and that the $\alpha_s(M_Z^2)$ values are consistent within these uncertainties. Though this is comforting, in that it indicates that QCD is self-consistent, the necessary addition of large theoretical uncertainties to otherwise precise experimental measurements is frustrating, at least to experimentalists!

The best resolution of the scale ambiguity would be to reduce its effect by calculating observables to higher order in perturbation theory. Though this is in principle possible, the large number of Feynman diagrams involved renders the task difficult and unattractive. In e^+e^- annihilation, only the R-related observables and the τ hadronic decay ratio R_τ have been calculated exactly up to $O(\alpha_s^3)$. For the hadronic event shape observables, $O(\alpha_s^3)$ contributions have not yet been calculated completely. However, for six observables (indicated in Table 3), improved calculations can be formulated that incorporate the resummation [68] of leading and next-to-leading logarithmic terms matched to the $O(\alpha_s^2)$ results. The matched calculations are expected *a priori* both to describe the data in a larger region of phase space than the fixed-order results, and to yield a reduced dependence of α_s on the renormalization scale. This is illustrated in Fig. 36 for the case of thrust (τ). Though not well-described by the $O(\alpha_s^2)$ calculation, the low-τ region is well-reproduced when resummed contributions are included.

Application of other approaches to circumvent the scale ambiguity in α_s measurement, involving the use of "optimized" perturbation theory [69] and Padé Approximants [70], can be found in Refs. [67, 71] respectively.

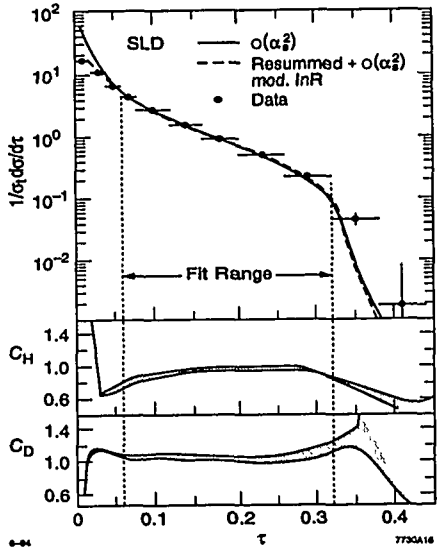


Figure 36: Illustration of the need for resummed contributions: the τ distribution measured by SLD [57]. At low τ, the $O(\alpha_s^2)$ calculation is unable to describe the data unless resummed terms are considered.

4.4.6 Summary of α_s Measurements

Hinchliffe has reviewed the various hadronic event shapes-based measurements from experiments performed in the c.m. energy range $10 \leq Q \leq 91$ GeV, utilizing both $O(\alpha_s^2)$ and resummed calculations, and quotes an average value of $\alpha_s(M_Z^2) = 0.122 \pm 0.007$ (Ref. [33]), where the large error is dominated by the renormalization scale uncertainty, which far exceeds the experimental error of about ± 0.002. Schmelling has also compiled the measurements, including the recent results from the LEP-II run at $Q \sim 133$ GeV (Ref. [72]), and quotes a global average (Ref. [73]) $\alpha_s(M_Z^2) = 0.121 \pm 0.005$, in agreement with Ref. [33], but assuming a more aggressive scale uncertainty.

4.5 Scaling Violations in Fragmentation Functions

Though distributions of final-state hadrons are not, in general, calculable in perturbative QCD, the Q^2-evolution of the scaled energy ($x_p = 2E/Q$) distributions of hadrons, or "fragmentation functions," can be calculated and used to determine α_s. In addition to the usual renormalization scale μ, a *factorization scale* μ_F must be defined that delineates the boundary between the calculable perturbative, and incalculable nonperturbative, domains. Additional complications arise from the changing composition of the underlying event flavor with Q due to the different Q-dependence of the γ and Z^0 exchange processes. Since B and C hadrons typically carry a large fraction of the beam momentum, and contribute a large multiplicity from their decays, it is necessary to consider the scaling violations separately in b, c, and light quark events, as well as in gluon jet fragmentation.

In an early analysis [74], the DELPHI Collaboration parameterized the fragmentation functions using the $O(\alpha_s^2)$ matrix elements and the string fragmentation model implemented in JETSET [58]. They fitted data in the range $14 \leq Q \leq 91$ GeV to determine $\alpha_s(M_Z^2) = 0.118 \pm 0.005$, where the error is dominated

by varying μ in the range $0.1 \leq \mu/Q \leq 1$. The ALEPH Collaboration used its Z^0 data to constrain flavor-dependent effects by tagging event samples enriched in light, c, and b quarks, as well as a sample of gluon jets [75]. The fragmentation functions for the different flavors and the gluon were parameterized at a reference energy, evolved with Q according to the perturbative DGLAP formalism calculated at next-to-leading order [76], in conjunction with a parameterization proportional to $1/Q$ to represent nonperturbative effects (Sec. 5), and fitted to data in the range $22 \leq Q \leq 91$ GeV (Fig. 37). They derived $\alpha_s(M_Z^2) = 0.126 \pm 0.007$ (exp.) ± 0.006 (theor.), where the theoretical uncertainty is dominated by variation of the factorization scale μ_F in the range $-1 \leq \ln\mu_F^2/Q^2 \leq 1$; variation of the renormalization scale in the same range contributed only ± 0.002. DELPHI has recently reported a similar analysis [77] yielding $\alpha_s(M_Z^2) = 0.121^{+0.006}_{-0.007}$ (exp.) ± 0.010 (theor.). Curiously, although a similar range as ALEPH, $0.3 \leq \mu/Q \leq 3$, was used to examine variation of the renormalization and factorization scales, here the renormalization scale dominates the theoretical uncertainty, with a contribution of ± 0.009, in contrast to ± 0.002 from factorization. Combining the ALEPH and later DELPHI results, assuming uncorrelated experimental errors, yields [31]:

$$\alpha_s(M_Z^2) \quad = \quad 0.124 \pm 0.005(\text{exp.}) \pm 0.010(\text{theor.}). \qquad (44)$$

4.6 Comparison with Other Measurements of $\alpha_s(M_Z^2)$

A summary of world α_s measurements, all evolved to $Q = M_Z$, is shown in Fig. 38 (Ref. [31]). These are drawn from lepton-hadron scattering, hadron-hadron collisions, heavy quarkonia decays and lattice gauge theory, as well as e^+e^- annihilation. In addition to being relatively precise, the e^+e^- results have the invaluable feature that they bracket the Q-range of the experiments, from around 1 GeV for τ decays to around 100 GeV for Z^0 production, providing the largest lever-arm for tests of consistency of $\alpha_s(M_Z^2)$ measured at different energy scales. It is clear that, within the uncertainties, all results are consistent with one another.

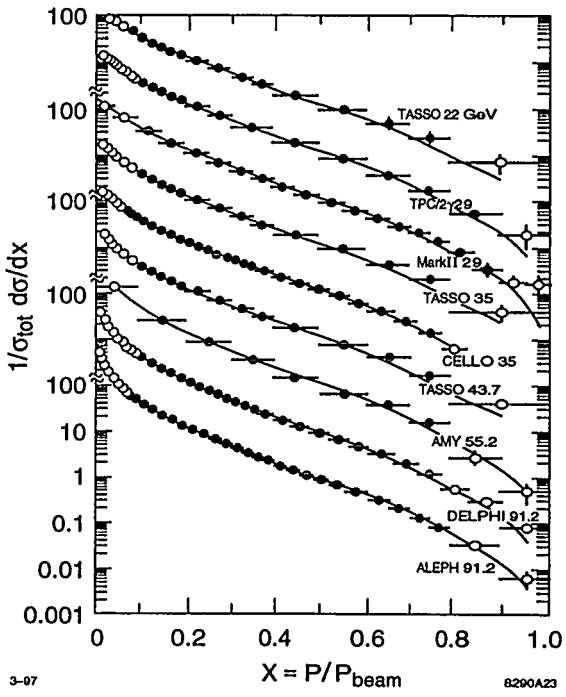


Figure 37: Illustration of scaling violations in e^+e^- fragmentation functions.

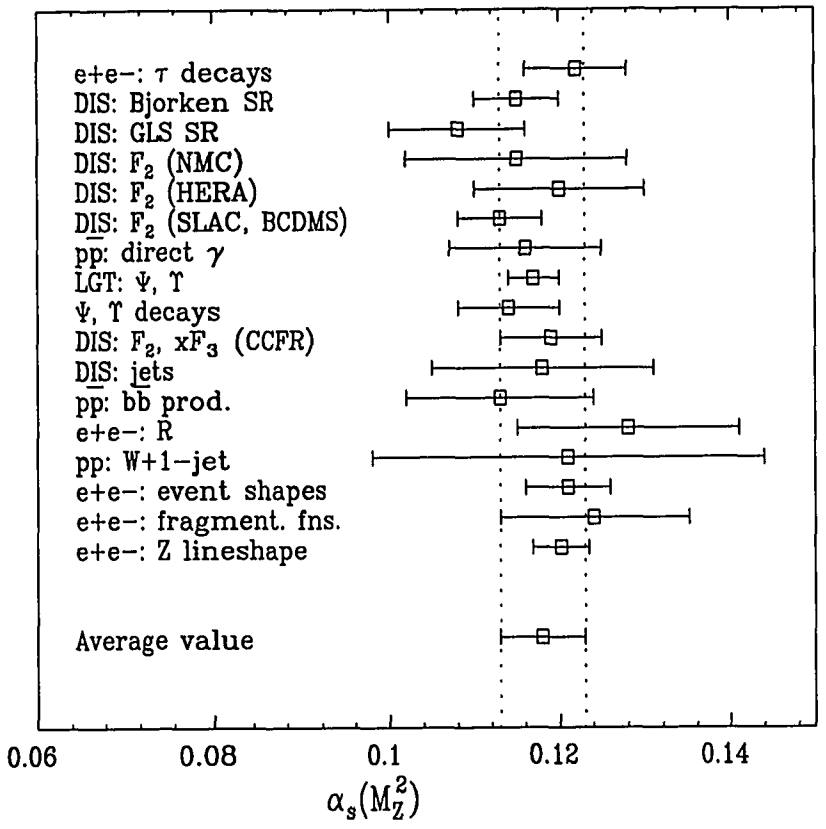


Figure 38: Summary of world $\alpha_s(M_Z^2)$ measurements [31]. The results are ordered vertically in terms of the hard scale Q of the experiment.

Taking an average over all 17 measurements *assuming* they are independent, by weighting each by its *total* error, yields $\alpha_s(M_Z^2) = 0.118$ with a χ^2 of 6.4; the low χ^2 value reflects the fact that most of the measurements are theoretical-systematics-limited. Taking an unweighted average, which in some sense corresponds to the assumption that all 17 measurements are completely correlated, yields the same result. The r.m.s. deviation of the 17 measurements w.r.t. the average value characterizes the dispersion, and is ±0.005. In a quantitative sense, therefore, QCD has been tested to a level of about 5%.

If further progress is to be made in testing QCD, future measurements of $\alpha_s(M_Z^2)$ should aim for substantially improved precision. The prospects for achieving 1%-level measurements are discussed in detail elsewhere [78]. Lattice QCD determinations may reach this precision within the next few years. A precise $\alpha_s(M_Z^2)$ measurement has yet to emerge from the TeVatron, but feasibility studies are in progress and appear promising. Deep-inelastic scattering and e^+e^- annihilation will probably require higher-energy facilities, as well as significant theoretical effort with regard to $O(\alpha_s^3)$ perturbative contributions. An $\alpha_s(M_Z^2)$ measurement at a high-energy e^+e^- collider will be discussed in Sec. 6.2.

5. Towards a Theory of Hadronization

We expect that the strong coupling becomes large in long-distance (low-Q) q−q interactions such that finite-order perturbation theory is no longer valid. Lattice gauge theory [79] is the only practical nonperturbative calculational tool available today. It is presently limited in applicability to static properties of hadrons, such as masses and decay constants, although in principle it might eventually be applied to the dynamical process of hadronization.

From the operator product expansion (OPE), one expects (see, *e.g.*, Ref. [80]) that the expectation value of an observable O may be written:

$$< O > \; = \; \sum_i a_i \left(\frac{\alpha_s}{\pi}\right)^i \; + \; \sum_j \frac{b_j}{Q^j}. \qquad (45)$$

During the past 15 years, much theoretical effort has been focused on the perturbative component represented by the first term in this equation. More recently, attention has turned to the "power corrections" represented by the second term, whose origin is intrinsically nonperturbative. In particular, attempts have been made to evaluate power corrections for e^+e^- observables. An illustration of the potential of such an approach is provided by Fig. 39 (Ref. [81]). The *ad hoc* addition of a $1/Q$ term to the $O(\alpha_s^2)$ QCD prediction describes the energy-dependence of $< 1 - T >$ remarkably well. It will be seen in Sec. 6.2 that the inverse power-law behavior of hadronization effects has important consequences for a precise α_s measurement at a high-energy e^+e^- collider. The explicit calculation of leading power corrections [80] hence represents our first tentative step towards a consistent theoretical treatment of hadronization.

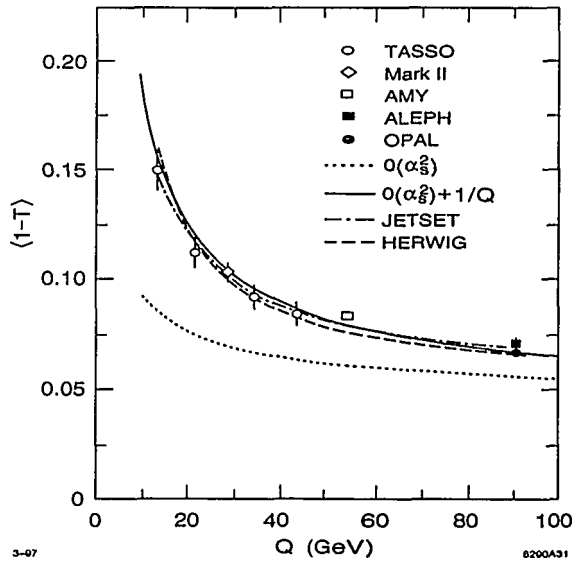


Figure 39: Energy-dependence of the mean value of $1 - T$. The *ad hoc* addition of a $1/Q$ term to the $O(\alpha_s^2)$ QCD prediction describes the data [81].

6. QCD at a High-Energy e^+e^- Collider

6.1 Introduction

Since QCD *is* our theory of strong interactions, it would be irresponsible not to test it at the highest energy scales available in different hard scattering processes. For this reason, testing QCD at a 0.5–1.5 TeV e^+e^- collider ("XLC") is mandatory. For a detailed discussion, see Ref. [82].

Precise determination of the strong coupling α_s is key to a better understanding of high-energy physics. The current precision of $\alpha_s(M_Z^2)$ measurements, limited to about 5% (Sec. 4.6), results in the dominant uncertainty on our prediction of the energy scale at which grand unification of the strong, weak, and electromagnetic forces takes place. An $\alpha_s(M_Z^2)$ measurement of 1% precision may be possible at a high-energy e^+e^- collider. Such a measurement would also allow improved determination of the mass and width of the top quark from the threshold behavior of the $t\bar{t}$ cross section. Measurements of hadronic event properties at high energies, combined with existing lower energy data, would allow one to test further the gauge structure of QCD by searching for anomalous "running" of observables, such as the rate of production of events containing three jets, and to set limits on models which predict such effects, for example, those involving light gluinos which are difficult to exclude by other means.

Gluon radiation in $t\bar{t}$ events is expected to be strongly regulated by the large mass and width of the top quark; $t\bar{t}g$ events will hence provide an exciting new domain for QCD studies. As a corollary, measurements of gluon radiation patterns in $t\bar{t}g$ events may provide valuable additional constraints on the top quark decay width. Furthermore, searches could be made for anomalous chromo-electric and chromo-magnetic moments of quarks [83], which effectively modify the rate and pattern of gluon radiation, and for which the effect increases as the c.m. energy is raised. Finally, polarized electron beams will be exploited at high-energy e^+e^- colliders and will allow tests of symmetries using multijet final states [84].

6.2 Is a 1%–Level Measurement of $\alpha_s(M_Z^2)$ Possible?

It is interesting to consider whether a measurement of $\alpha_s(M_Z^2)$ at the 1%–level of precision is possible at the XLC. Consider the SLD $\alpha_s(M_Z^2)$ measurement, discussed in Sec. 4.4, based on 15 hadronic event shape observables measured with a data sample comprising approximately 50,000 hadronic events [57]:

$$\alpha_s(M_Z^2) \quad = \quad 0.1200 \pm 0.0025\,(\text{exp.}) \pm 0.0078\,(\text{theor.}), \tag{46}$$

where the experimental error is composed of statistical and systematic components of about ±0.001 and ±0.002 respectively, and the theoretical uncertainty has components of ±0.003 and ±0.007 arising from hadronization and missing higher order terms, respectively. Now consider "scaling" this result to estimate the precision of a similar measurement at $Q = 500$ GeV.

• **Statistical error**: At design luminosity, the 500 GeV XLC would deliver roughly 100,000 $q\bar{q}$ (q = u, d, s, c, b) events per year (Sec. 6.4), implying that a statistical error on $\alpha_s(M_Z^2)$ well below ± 0.001 could be obtained.

• **Systematic error**: This results primarily from the uncertainty in modeling the jet resolution of the detector. The situation may be improved at the XLC by a combination of building better detectors and benefitting from improved calorimeter energy resolution for higher energy jets. It is not unreasonable to suppose that the current systematic error of roughly ±0.002 could be reduced by a factor of two.

• **Hadronization uncertainty**: From the discussion in Sec. 5, it can be seen that nonperturbative corrections to jet final states in e^+e^- annihilation can be parameterized in terms of inverse powers of the hard scale Q. At leading order, perturbative evolution is proportional to $1/\ln Q$. Hence, for a generic observable X, the ratio of nonperturbative to perturbative QCD contributions is dominated by a term of the form:

$$\frac{\delta X^{\text{non-pert}}}{X^{\text{pert}}} \quad \sim \quad \frac{\ln Q}{Q}. \tag{47}$$

Increasing Q from 91 GeV to 500 GeV causes this ratio to decrease by a factor of five, implying that hadronization corrections in the "3-jet region" of observables should be of order 2% at XLC. The conclusion of this analysis is reinforced by explicit simulation of hadronization effects, illustrated in Fig. 40 (Ref. [85]) for thrust. Assuming that these corrections can be estimated to better than ±50%, the hadronization *uncertainty* should contribute less than 1% to the error on $\alpha_s(M_Z^2)$.

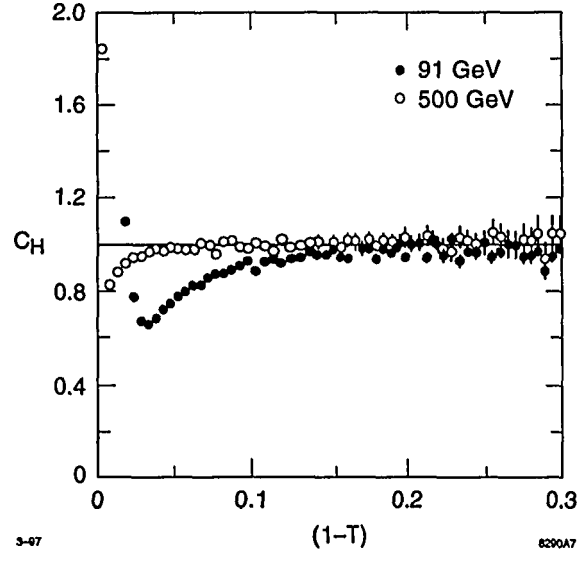


Figure 40: Estimate of the hadronization correction factor (Sec. 4.4.2) for thrust at $Q = 91$ GeV and 500 GeV (Ref. [85]). At 500 GeV, the factor barely deviates from unity for most of the kinematic range.

• **Uncertainty due to missing higher orders:** Currently, perturbative QCD calculations of hadronic event shapes are available complete up to $O(\alpha_s^2)$. Since the data contain knowledge of all orders, one must estimate the possible bias inherent in measuring $\alpha_s(M_Z^2)$ using the truncated QCD series (Sec. 4.4.5). Since the missing perturbative terms are $O(\alpha_s^3)$, and since at $Q = 500$ GeV α_s is expected to be about 25% smaller than its value at the Z^0, one naively expects the uncalculated terms to be almost a factor of two smaller at the higher energy, leading to an estimated uncertainty of ± 0.004 on $\alpha_s(500\ \text{GeV})$. However, translating to the yardstick $\alpha_s(M_Z^2)$ yields an uncertainty of ± 0.006, only slightly reduced compared with the current uncertainty.

From this simple analysis, it seems reasonable to conclude that achievement of the luminosity necessary for "discovery potential" at the XLC will result in a $q\bar{q}$ event sample of sufficient size to measure $\alpha_s(M_Z^2)$ with a statistical uncertainty of better than 1%. Construction of detectors superior in performance to those in operation today at SLC and LEP may be necessary in order to reduce systematic errors to the 1% level. Hadronization effects should be significantly smaller, implying a sub-1% uncertainty. However, unless $O(\alpha_s^3)$ contributions are calculated, $\alpha_s(M_Z^2)$ measurements at 500 GeV will be limited by theoretical uncertainties to a precision of ± 0.006, only marginally better than that achieved at present.

6.3 Top Quark Mass Determination and α_s

It is clear that the value of α_s controls the shape of the strong potential that binds quarkonia resonances. In the case of $t\bar{t}$ production near threshold, the large top mass m_t, and hence large decay width Γ, ensure that the top quarks decay in a time comparable with the classical period of rotation of the bound system, making the toponium resonance a very short-lived phenomenon, and washing out most of the resonant structure in the cross section. The shape of the $t\bar{t}$ cross section near threshold hence depends strongly not only on the top mass, but also on α_s.

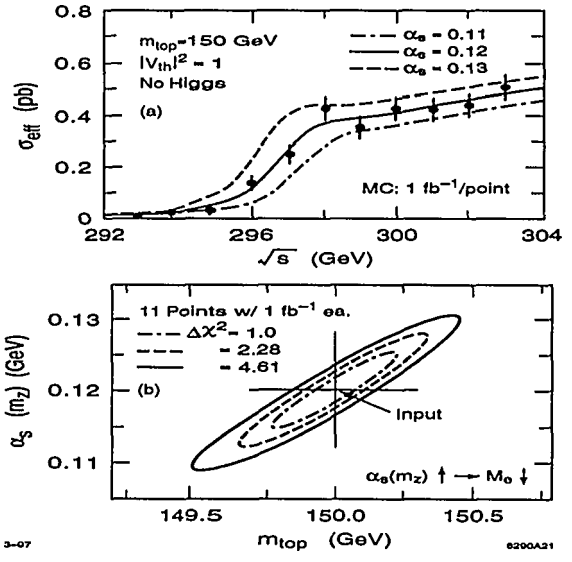


Figure 41: Simulation of a simultaneous measurement of $\alpha_s(M_Z^2)$ and m_t at a high-energy e^+e^- collider [86]: (a) $t\bar{t}$ production cross section; (b) correlation between fitted values.

Fits to simulations of measurements of this cross section have shown [86] that the top mass so determined is strongly correlated with the assumed value of $\alpha_s(M_Z^2)$. This is illustrated in Fig. 41. The European Top Quark Working Group has updated these simulations for the latest measured values of the top mass and has shown [87] that a simultaneous determination of m_t and $\alpha_s(M_Z^2)$ by fitting to the threshold cross section measured with one design-year of luminosity yields statistical precisions of $\pm 250\ \text{MeV}/c^2$ and ± 0.006 on m_t and $\alpha_s(M_Z^2)$, respectively. Fixing $\alpha_s(M_Z^2)$ to 0.120 reduces the error on m_t by a factor of two. Since this technique would yield a measurement of $\alpha_s(M_Z^2)$ no more precise than those made

today, and since systematic uncertainties may be large and have not yet been considered, a more sensible strategy would be to measure $\alpha_s(M_Z^2)$ as precisely as possible, as described in the previous section, and to use this value to allow better determination of the top quark parameters.

6.4 Energy Evolution Studies

The non-Abelian gauge structure of QCD implies that as the hard scattering scale Q increases, the strong coupling decreases roughly as $1/\ln Q$. Existing hadronic final states data from e^+e^- annihilation at the PETRA, PEP, TRISTAN, SLC, and LEP colliders span the range $14 \leq Q \leq 170$ GeV, although hadronization uncertainties are large on the data below 25 GeV. A 1.5 TeV e^+e^- collider would increase the lever-arm in $1/\ln Q$ by almost a factor of two, hence allowing detailed study of the energy evolution of QCD observables that are proportional to α_s, such as the rate of production of final states containing three hadronic jets, R_3. This would provide not only a test of the fundamental structure of SU(3) QCD, but also a searching ground for new physics that might produce "anomalous" running.

One such possibility is the existence of a light, electrically neutral, colored fermion that couples to gluons, often called a "light gluino" and denoted by $\tilde{g}$. The existence of such a particle would manifest itself via a modification of gluon vacuum polarization contributions involving fermion loops, effectively increasing the number of light fermions entering into the QCD β-function. At one-loop level, the effective number of flavors would change from N_F to $N_F + 3N_{\tilde{g}}$, where $N_{\tilde{g}}$ is the number of families of light gluinos, causing a decrease in the running of α_s as a function of Q. The existence of a light gluino of mass between 2 and 5 GeV/c^2 has not been excluded by searches with current data [85]. A simulated measurement of R_3 at $Q = 500$ GeV, corresponding to one design-luminosity-year, is shown in Fig. 42 (Ref. [85]), together with existing measurements, plotted as a function of $1/\ln Q$. The presence of one family of light gluinos of mass 2 GeV/c^2 would cause an increase in the predicted value of R_3 at 500 GeV by 10%. A 1%-level measurement of R_3, as discussed in the previous section, would allow this difference to be measured with a significance of many standard deviations.

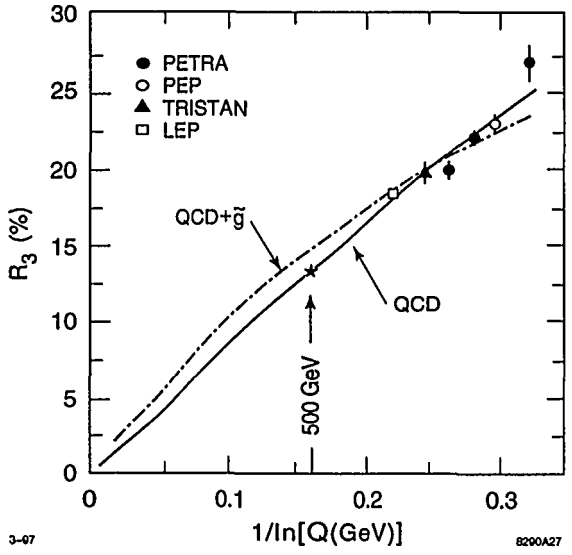


Figure 42: Energy-evolution of the three-jet rate R_3 (Ref. [85]). For illustration, an $O(\alpha_s^2)$ QCD fit, as well as a fit allowing the possibility of one family of light gluinos, is shown. The simulated data point at $Q = 500$ GeV would add considerable lever-arm.

It should be noted, however, that data from a number of experiments at different e^+e^- colliders contribute to Fig. 42. Some of these data were recorded more than ten years ago, were treated differently by the various experimental groups, and have relatively large systematic errors that are at least partly uncorrelated from point to point. Furthermore, the sophistication and performance of particle detectors constructed in the last decade has improved significantly, and it is reasonable to assume that future detectors will be even better. In addition, our

c.m. energy Q (GeV)	$q\bar{q}$ events/day
500	1750
91	20,000,000
60	75,000
35	150,000

Table 4: Number of $q\bar{q}$ events per day delivered by an e^+e^- collider operating at a luminosity of 5×10^{33} cm$^{-2}s^{-1}$.

understanding of the modeling of hadronization effects and theoretical uncertainties has improved enormously as a result of studies at the Z^0. Therefore, the precision of searches for anomalous running of QCD observables at XLC would be improved significantly if new data were taken at the lower c.m. energies with the *same* detector and analysis procedures.

In fact, if the luminosity of the 500 GeV XLC could be preserved at lower c.m. energies, very large data samples would be recorded. Table 4 (Ref. [85]) shows the number of $q\bar{q}$ events delivered per day at various c.m. energies by the XLC operating at the design luminosity of 5×10^{33} cm$^{-2}s^{-1}$. At each energy, more luminosity would be delivered *per day* than was recorded in total by the original dedicated colliders! This argument is of course naive, in that a collider designed to operate at a luminosity of 5×10^{33} cm$^{-2}s^{-1}$ at 500 GeV would not automatically be operable at the same luminosity at energies a factor of five or ten lower; such capability would have to be designed from the outset. Furthermore, the requirements on the triggering and data processing capabilities of the detector are extreme by the standards of e^+e^- annihilation, and this would also have to be designed from the start. Nevertheless, the prospect of running the XLC at the Z^0 resonance, or at even lower energies, for QCD studies, not to mention high-statistics electroweak physics measurements, is very attractive.

6.5 Gluon Radiation in $t\bar{t}$ Events

The large mass and decay width of the top quark serve to make the study of gluon radiation in $t\bar{t}$ events a new arena for testing QCD. The large mass acts as a cutoff for collinear gluon radiation, and the large decay width acts as a cutoff for soft gluon radiation, allowing reliable perturbative QCD calculations to be performed; these effects are of course correlated. The latter case is particularly interesting. If the top width were infinite, top quarks would decay immediately to bottom quarks, and any gluons would be radiated from the secondary b's. If the top width were zero, top quarks would live forever and all radiation would be from the primary t's. In the case of a large but finite width, expected to be around 2 GeV for a top mass of 180 GeV/c^2, gluon radiation in $t\bar{t}$ events will be a coherent sum of contributions from these two limiting cases, with a degree of coherence regulated by the top width itself.

A theoretical study of $t\bar{t}$ production above threshold, assuming $m_t = 175$ GeV/c^2 at $Q = 1$ TeV, is illustrated in Fig. 43 (Ref. [88]). This shows the angular distribution of 5 GeV gluons w.r.t. the $t\bar{t}$ axis for the kinematic configuration in which the decay b-quark travels backwards w.r.t. the t flight direction. The dependence of the radiation pattern on the top decay width is strong. Similar effects are predicted in the spectrum of gluon radiation in $t\bar{t}$ events around threshold [89]. Measurement of such effects would yield not only a dramatic demonstration of quantum interference in strong interactions, but might also provide an essential cross-check on the value of the top quark decay width, which may prove difficult to disentangle from measurements of the $t\bar{t}$ threshold cross section and top momentum distributions, which also depend on α_s and m_t (Sec. 6.3), as well as on the beam energy distribution.

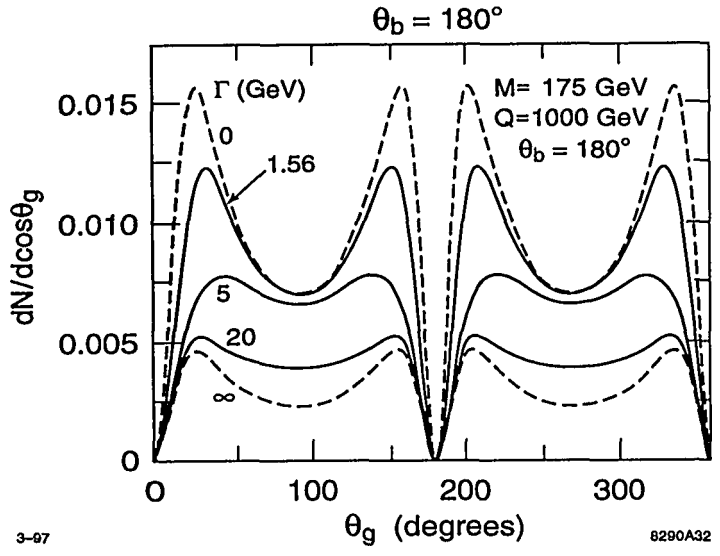


Figure 43: Angular distribution of 5 GeV gluons w.r.t. $t\bar{t}$ axis, at $Q = 1$ TeV, illustrating the dependence on the top width Γ (Ref. [88]).

7. Concluding Remarks

We have seen that e^+e^- annihilation is an ideal laboratory for precise studies of QCD. One observes jets indicating the primary production of quarks and gluons, and one can measure precisely the quark and gluon spins. Multijet events allow the very gauge structure of QCD to be tested via measurement of the Casimir factors N_C, T_F, and C_F, leading us to the conclusion that QCD *is* the theory of strong interactions. One can then measure the single parameter of QCD, the coupling α_s, from inclusive observables such as R, or equivalently the Z^0 line-shape parameters, and from hadronic τ decays, as well as from event shape measures and scaling violations in inclusive single-particle fragmentation functions. These $\alpha_s(M_Z^2)$ measurements are internally consistent, and agree with results from lepton-nucleon scattering, hadron-hadron collisions, and lattice gauge theory determined across a wide range of energy scales.

There was no time to cover many interesting topics, including: differences between quark and gluon jets, tests of the flavor-independence of strong interactions, polarization phenomena, particle multiplicities and correlations, production of B and C mesons and baryons, and production of identified hadrons such as $\pi^\pm$, K_s^0, $K^\pm$, $p/\bar{p}$, Λ, ϕ, K^*, *etc.* Some of these topics are discussed in other contributions to these proceedings [61, 90].

Looking towards the future, tests of QCD will provide an important component of the physics program at a future high-energy e^+e^- collider operating in the c.m. energy range $0.5 \leq Q \leq 1.5$ TeV. Measurement of $\alpha_s(M_Z^2)$ at the 1% level of precision appears feasible experimentally, but will require considerable theoretical effort to calculate $O(\alpha_s^3)$ contributions in QCD perturbation theory. A search for anomalous running of $\alpha_s(Q^2)$, by operating the collider at different c.m. energies, is an attractive prospect. Quantum coherence is expected to give rise to interesting gluon radiation patterns in $t\bar{t}$ events, which could be used to constrain the top quark decay width, and measurement of the gluon radiation spectrum would also constrain anomalous top quark chromomagnetic couplings.

More immediately, the next generation of *low* energy e^+e^- colliders, known as B factories, also has the potential to make a precise α_s measurement from the R-ratio at $Q \approx 10$ GeV, as well as from hadronic τ decays. Even more precise tests of QCD in e^+e^- annihilation will hence continue to enhance our confidence in the theory, and may even yield surprises. ...

Acknowledgments

I am grateful for the support of my colleagues in the SLD Collaboration and the SLAC Theory Group. I thank Lance Dixon and David Muller for careful reading of this manuscript.

References

[1] M. Albrow, "QCD studies in hadron-hadron collisions"; these proceedings.

[2] W. Smith, "QCD studies in lepton-hadron collisions"; these proceedings.

[3] H. Fritzsch, M. Gell-Mann, and H. Leutwyler, Phys. Lett. B **47**, 365 (1973);
D. J. Gross and F. Wilczek, Phys. Rev. Lett. **30**, 1343 (1973);
H. D. Politzer, Phys. Rev. Lett. **30**, 1346 (1973);
S. Weinberg, Phys. Rev. Lett. **31**, 494 (1973).

[4] M. Gell-Mann, Phys. Rev. **125**, 1067 (1962).

[5] G. Kramer, *Springer Tracts in Modern Physics*, Vol. 102 (1984).

[6] See, for example, M. Gell-Mann and Y. Ne'eman, *The Eightfold Way* (Benjamin, New York, 1972).

[7] Mark I Collaboration, G. Hanson *et al.*, Phys. Rev. Lett. **35**, 1609 (1975).

[8] J. D. Bjorken and S. J. Brodsky, Phys. Rev. D **1**, 1416 (1970).

[9] Mark I Collaboration, R. F. Schwitters *et al.*, Phys. Rev. Lett. **35**, 1320 (1975).

[10] See, for example, V. Barger and R. J. N. Phillips, *Frontiers in Physics*, Vol. 71, "Collider physics" (Addison-Wesley, 1987).

[11] TASSO Collaboration, M. Althoff *et al.*, Z. Phys. C **22**, 307 (1984).

[12] S. Brandt *et al.*, Phys. Lett. **12**, 57 (1964).
E. Farhi, Phys. Rev. Lett. **39**, 1587 (1977).

[13] R. Marshall, Z. Phys. C **43**, 595 (1989).

[14] TASSO Collaboration, R. Brandelik *et al.*, Phys. Lett. B **86**, 243 (1979).
MARK J Collaboration, D. P. Barber *et al.*, Phys. Rev. Lett. **43**, 830 (1979).
PLUTO Collaboration, C. Berger *et al.*, Phys. Lett. B **86**, 418 (1979).
JADE Collaboration, W. Bartel *et al.*, Phys. Lett. B **91**, 142 (1980).

[15] J. Ellis, M. K. Gaillard, and G. G. Ross, Nucl. Phys. B **111**, 253 (1976).

[16] S. L. Wu, Phys. Rep. **107**, 59 (1984).

[17] J. Ellis and I. Karliner, Nucl. Phys. B **148**, 141 (1979).

[18] TASSO Collaboration, M. Althoff *et al.*, Z. Phys. C **22**, 307 (1984).

[19] P. Hoyer, P. Osland, H. G. Sander, T. F. Walsh, and P. M. Zerwas, Nucl. Phys. B **161**, 349 (1979);
E. Laermann, K. H. Streng, and P. M. Zerwas, Z. Phys. C **3**, 289 (1980); *erratum ibid* C **52**, 352 (1991).

[20] T. G. Rizzo, private communications.

[21] SLD Collaboration, K. Abe *et al.*, Phys. Rev. D **55**, 2533 (1997).

[22] TASSO Collaboration, W. Braunschweig *et al.*, Z. Phys. C **47**, 181 (1990).

[23] L3 Collaboration, B. Adeva *et al.*, Phy. Lett. B **263**, 551 (1991).

[24] DELPHI Collaboration, P. Abreu *et al.*, Phys. Lett. B **274**, 498 (1992).

[25] O. Nachtmann and A. Reiter, Z. Phys. C **16**, 45 (1982).

[26] M. Bengtsson and P. M. Zerwas, Phys. Lett. B **208**, 306 (1988).

[27] L3 Collaboration, B. Adeva *et al.*, Phys. Lett. B **248**, 227 (1990).

[28] OPAL Collaboration, R. Akers *et al.*, Z. Phys. C **65**, 367 (1995).

[29] OPAL Collaboration, OPAL Physics Note PN-188 (July 1995).

[30] G. L. Kane *et al.*, Phys. Lett. B **354**, 350 (1995).

[31] P. N. Burrows, SLAC-PUB-7293 (1996); to appear in *Proceedings of the 3rd International Symposium on Radiative Corrections*, August 1-5 1996, Cracow, Poland.

[32] W. A. Bardeen, A. J. Buras, D. W. Duke, and T. Muta, Phys. Rev. **18**, 3998 (1978); D. W. Duke, Rev. Mod. Phys. **52**, 199 (1980).

[33] R. M. Barnett *et al.*, Phys. Rev. D **54**, 77 (1996).

[34] R. M. Barnett *et al.*, Phys. Rev. D**54**, 19 (1996).

[35] S. G. Gorishny, A. Kataev, and S. A. Larin, Phys. Lett. B **259**, 144 (1991);
L. R. Surguladze and M. A. Samuel, Phys. Rev. Lett. **66**, 560 (1991).

[36] K. H. Chetyrkin, J. H. Kühn, and A. Kwiatkowski, Berkeley preprint LBL 36678-Rev (1996); subm. to Phys. Rep.

[37] A. Blondel, "Experimental status of electroweak interactions," to appear in *Proceedings of the 28th International Conference on High Energy Physics*, 25-31 August 1996, Warsaw, Poland.

[38] P. B. Renton, in *Proceedings of the 17th International Symposium on Lepton-Photon Interactions*, 10-15 August 1995, Beijing, China, p. 35.

[39] D. Schaile, in *Proceedings of the XXVII International Conference on High Energy Physics*, July 20-27 1994, Glasgow, Scotland, IoP Publishing, edited by P. J. Bussey and I. G. Knowles, p. 27.

[40] See, for example, M. Shifman, Mod. Phys. Lett. A **10**, 605, No. 7 (1995).

[41] J. Chyla and A. L. Kataev, *Reports of the Working Group on Precision Calculations for the Z Resonance*, edited by D. Bardin, W. Hollik, and G. Passarino, CERN 95-03, 313 (1995).

[42] F. Le Diberder and A. Pich, Phys. Lett. B **289**, 165 (1992).

[43] E. Braaten, S. Narison, and A. Pich, Nucl. Phys. B **373**, 581 (1992); F. Le Diberder and A. Pich, Phys. Lett. B **286**, 147 (1992).

[44] M. Neubert, Nucl. Phys. B **463**, 511 (1996).

[45] L. Duflot (ALEPH Collaboration), Nucl. Phys. B (Proceedings of the Supp.), B **39**, 322 (1995).

[46] OPAL Collaboration, R. Akers *et al.*, Z. Phys. C **66**, 543 (1995).

[47] CLEO Collaboration, T. Coan *et al.*, Phys. Lett. B **356**, 580 (1995).

[48] G. Altarelli, P. Nason, and G. Ridolfi, Z. Phys. C **68**, 257 (1995).

[49] R. K. Ellis, D. A. Ross, and A. E. Terrano, Phys. Rev. Lett. **45**, 1226 (1980); Nucl. Phys. B **178**, 421 (1981).

[50] G. Kramer and B. Lampe, Z. Phys. C **39**, 101 (1988); Fortschr. Phys. **37**, 161 (1989).

[51] Z. Kunszt *et al.*, CERN 89-08 Vol. I, (1989) p. 373.

[52] JADE Collaboration, W. Bartel *et al.*, Z. Phys. C **33**, 23 (1996).

[53] SLD Collaboration, K. Abe *et al.*, Phys. Rev. Lett. **71**, 2528 (1993).

[54] S. Bethke *et al.*, Nucl. Phys. B **370**, 310 (1992).

[55] See, for example, D. Soper, "Basics of QCD perturbation theory"; these proceedings.

[56] MARK-J Collaboration, D. P. Barber *et al.*, Phys. Rev. Lett. **43**, 830 (1979); Phys. Lett. B **89**, 139 (1979).

[57] SLD Collaboration, K. Abe *et al.*, Phys. Rev. D **51**, 962 (1995).

[58] T. Sjöstrand, CERN–TH–7112/93 (1993).

[59] G. Marchesini *et al.*, Comp. Phys. Comm. **67**, 465 (1992).

[60] I. Knowles *et al.*, *QCD Event Generators*, hep-ph/9601212 (1996).

[61] C. D. Buchanan, "New accurate ideas on flavor production in hadronization and their connections to QCD"; these proceedings.

[62] R. Brun *et al.*, CERN-DD/EE/84-1 (1989).

[63] G. Marchesini and B. R. Webber, Nucl. Phys. B **238**, 1 (1984).

[64] B. Andersson, *et al.*, Phys. Rep. **97**, 33 (1983).

[65] V. Blobel, in *Proceedings of 8th CERN School of Computing*, Aiguablava, Spain, September 9–22, 1984, CERN 85–09 (1985).

[66] P. N. Burrows and H. Masuda, Z. Phys. C **63**, 235 (1994).

[67] P. N. Burrows *et al.*, Phys. Lett. B **382**, 157 (1996).

[68] S. Catani, G. Turnock, B. R. Webber, and L. Trentadue, Phys. Lett. B **263**, 491 (1991).

[69] P. M. Stevenson, Phys. Rev. D **23**, 2916 (1981);
G. Grunberg, Phys. Rev. D **29**, 2315 (1984);
S. J. Brodsky, G. P. Lepage, and P. B. Mackenzie, Phys. Rev. D **28**, 228 (1983).

[70] See, for example, G. A. Baker, Jr., *Essentials of Padé Approximants* (Academic Press, 1975).

[71] P. N. Burrows *et al.*, SLAC-PUB-7222 (1996); to appear in Phys. Lett. B.

[72] D. Duchesneau, "QCD results from LEP above and below the Z^0 peak," to appear in *Proceedings of the 28th International Conference on High Energy Physics*, Warsaw, Poland, 25-31 July 1996.

[73] M. Schmelling, "Status of the strong coupling constant," to appear in *Proceedings of the 28th International Conference on High Energy Physics*, Warsaw, Poland, 25-31 July 1996.

[74] DELPHI Collaboration, P. Abreu *et al.*, Phys. Lett. B **311**, 408 (1993).

[75] ALEPH Collaboration, D. Buskulic *et al.*, Phys. Lett. B **357**, 487 (1995).

[76] G. Gurci, W. Furmanski, and R. Petronzio, Nucl. Phys. B **175**, 27 (1980).

[77] DELPHI Collaboration, W. de Boer *et al.*, paper contributed to the *Proceedings of the 28th International Conference on High Energy Physics*, Warsaw, Poland, 25-31 July 1996, pa01-022.

[78] P. Burrows *et al.*, "Prospects for the precision measurement of α_s," SLAC-PUB-7371 (1996); to appear in *Proceedings of the Workshop on Future Directions in High Energy Physics*, June 25–July 12, 1996, Snowmass, CO, USA.

[79] See, for example, T. DeGrand, "Lattice gauge theory for QCD"; these proceedings.

[80] M. Beneke, SLAC-PUB-7277 (1996); to appear in *Proceedings of the 28th International Conference on High Energy Physics*, 25-31 August 1996, Warsaw, Poland.

[81] B. R. Webber, Cavendish-HEP-94/17 (1994).

[82] P. N. Burrows, in *Proceedings of the Workshop on Physics and Experiments with Linear Colliders*, September 8-12, 1995, Morioka-Appi, Iwate, Japan, edited by A. Miyamoto *et al.* (World Scientific, 1996), p. 179.

[83] T. G. Rizzo, Phys. Rev. D **50**, 4478 (1994).

[84] A. Brandenburg, L. Dixon, and Y. Shadmi, Phys. Rev. D **53**, 1264 (1996). SLD Collaboration, K. Abe *et al.*, Phys. Rev. Lett. **74**, 4173 (1995).

[85] S. Bethke, in *Proceedings of the Workshop on Physics and Experiments with Linear e^+e^- Colliders*, April 1993, Waikoloa, Hawaii, edited by F. A. Harris *et al.* (World Scientific, 1993), p. 687.

[86] JLC Group, S. Matsumoto *et al.*, KEK Report 92-16 (1992), p. 53.

[87] P. Comas *et al.*, in *Proceedings of the Workshop on Physics and Experiments with Linear Colliders*, September 8-12, 1995, Morioka-Appi, Iwate, Japan, edited by A. Miyamoto *et al.* (World Scientific, 1996), p. 455.

[88] L. Orr, private communication.

[89] L. Orr, in *Proceedings of the Workshop on Physics and Experiments with Linear e^+e^- Colliders*, 26-30 April 1993, Waikoloa, Hawaii; edited by F. A. Harris *et al.* (World Scientific), Vol. II, p. 670.

[90] S. Willocq, "Physics at the Z pole with SLD"; these proceedings.

*Search for Glueballs**

Walter Toki

Department of Physics
Colorado State University
Ft. Collins, CO 80523

Abstract

In these Summer School lectures, we review the results of recent glueball searches. We begin with a brief review of glueball phenomenology and meson spectroscopy, including a discussion of resonance behavior. The results on the $f_0(1500)$ and $f_J(1700)$ resonances from proton-antiproton experiments and radiative J/ψ decays are discussed. Finally, $\pi\pi$ and $\eta\pi$ studies from D_s decays and exotic meson searches are reviewed.

---

*Work supported in part by the Department of Energy, contract DE-FG03-96ER40788.

© 1996 by Walter Toki.

1. Introduction

In this Summer School lecture, we review the search for glueballs. This topic is of great interest in light of more precise lattice QCD calculations on glueball masses and new data and glueball candidates from the LEAR groups.

The review begins with an introduction to glueball phenomenology in Chap. 2, a review of the $q\bar{q}$ meson model and predictions in Chap. 3, and a discussion of experimental spin-parity techniques in Chap. 4. The discussion of experimental results focuses on the search for scalar glueballs which decay into two pseudoscalar mesons. The main two candidates are the $f_0(1500)$ from $p\bar{p}$ experiments, discussed in Chap. 5, and the $f_J(1700)$ from radiative J/ψ decays, discussed in Chap. 6. New results from weak decays of charm D_s mesons are covered in Chap. 7, and the search for the exotic $\eta\pi$ resonance in Chap. 8.

Very recent material (August 1996) to be covered in the Topical Conference from LEAR (see M. Doser's talk[1]) and from BNL (see N. Cason's talk[2]) will not be discussed here.

Major references for this report include *the 6th International Conference on Hadron Spectroscopy* (Hadron '95) *Proceedings*,[3] J/ψ decays in *Physics Reports*,[4] "Review of Meson Spectroscopy,"[5] *Review of Particle Physics*,[6] *An Introduction to Quarks and Partons*,[7] and *Proceedings*[8] *of the Second Biennial Workshop on Nucleon-Antinucleon Physics*.

2. Glueballs

2.1 What Are Glueballs?

In the theory of Quantum Chromodynamics, gluons carry color charge, and consequently, gluons can interact with other gluons. This feature leads to couplings between two and three gluons. Hence, it may be possible for gluons to form bound states entirely composed of gluons with no quarks. These bound states of gluons are called glueballs.

We can form possible candidate glueball states by examining the states formed from combinations of gluons. Gluons are spin-one vectors and members of a color octet. To form color singlet mesons, the spin, space, and color symmetries must be properly combined. Two spin-one gluons in an S wave ($L = 0$) must be symmetric and will form states of $J^{PC} = 0^{++}$ or 2^{++}. The $L = 1$ case must have the antisymmetric $S = 1$ case and will yield $J^{PC} = 0^{-+}, 1^{-+}, 2^{-+}$. The different combinations are shown in Table 1.

L	J^{PC}
0	$0^{++}, 2^{++}$
1	$0^{-+}, 1^{-+}, 2^{-+}$
2	$2^{++}, 0^{++}, 4^{++}$
3	$2^{-+}, 3^{-+}, 4^{-+}$

Table 1. Possible spin-parity combinations for glueball states.

Several modes in the table are impossible to form from $q\bar{q}$ meson states. These are the $J^{PC} = 1^{-+}, 3^{-+}$ combinations. These states are called exotic or odd balls.

From Lattice QCD theory,[9] we expect the mass of the lowest lying glueball to be a scalar, $J^{PC} = 0^{++}$. The mass is expected to be in the 1-2 GeV/c^2 region. For a detailed discussion of mass predictions, see the lectures by T. DeGrand. The glueball width is not predicted by Lattice QCD theory. There are very rough ideas that the width should be in between the width of conventional mesons and OZI suppressed decays.

$$\Gamma_G = \sqrt{\Gamma_{OZI}\Gamma_{q\bar{q}}} = \sim \text{few 10's MeV}. \qquad \text{[Eq. 1]}$$

The width of an OZI suppressed ϕ decay is 4 MeV and the width of a typical OZI allowed meson decay of the rho meson is 150 MeV.

Since the glueball is a flavor singlet, the decay modes should be quite different from conventional mesons. A flavor singlet has zero isospin, and in the case of decays into two pseudoscalar mesons, the rates are set by the SU(3) Clebsch-Gordan coefficients coupling between a singlet and a pair of octet members. A scalar glueball candidate would be a meson that decays in an S wave into a pair of pseudoscalars such as $\pi\pi$, K_sK_s, K^+K^-, and $\eta\eta$.

A pure gluonic state should not contain charge; hence, there should be little coupling to photons. As a result, the glueball candidate should have no radiative decays such as a radiative transition or a two photon decay.

In conventional $q\bar{q}$ mesons, mixing is possible between states of the same J^{PC}, and such a situation may apply between glueballs and $q\bar{q}$ mesons. This possibility will complicate isolating a glueball. Hence, a careful understanding of conventional $q\bar{q}$ mesons will be necessary to interpret any glueball candidate. In addition, there is the possibility of hybrid states of a gluon plus quarks, $g + q\bar{q}$, which could also mask the search for glueballs.

In summary, the features of a glueball are:

- flavor symmetry in decay
- no radiative decays and no two photon decays
- mass 1-2 GeV (scalar glueball)
- decays into $\pi\pi$, K_sK_s, K^+K^-, and $\eta\eta$ (scalar glueball)
- a width of order of ~10's of MeV.

2.2 How Are Glueballs Produced?

Glueballs may be produced in reactions shown in Figure 1. The reactions include:

- radiative J/ψ decays
- OZI violating decay channels
- Pomeron exchange channels in central production.

Radiative J/ψ decays proceed via one photon and two gluons. The two gluons should couple to the glueball. Hence, scalar resonances produced in J/ψ decays are primary glueball candidates.

Charge exchange reactions such as $\pi^-p \rightarrow nX$, $X \rightarrow KK$, $\phi\phi$, or $K^-p \rightarrow \Lambda X$, $X \rightarrow \pi\pi$ are possible reactions for producing glueballs. In these reactions, the resonance X should be coupled by gluons to the other quark lines. These OZI violating decays can provide a very high statistics search from fixed-target experiments.

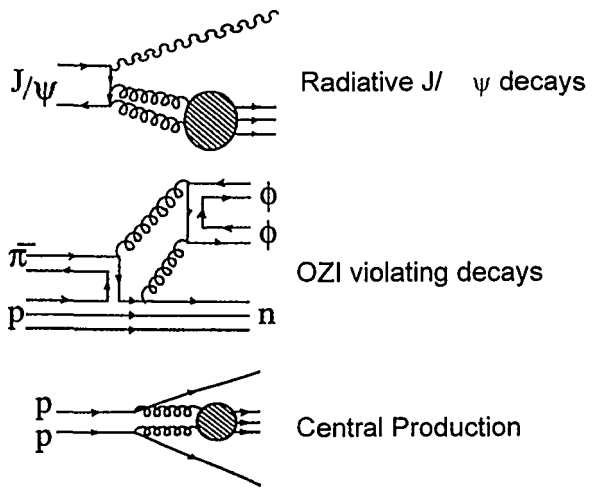


Figure 1. Gluon rich production reactions.

In high-energy reactions, peripheral collisions may be formed at small x_F. The proton-proton collisions may produce gluon collisions. This is called central production. The collision may also proceed via multiple gluons, and this is referred to as Pomeron exchange.

Other possible places for glueball production include nucleon-antinucleon annihilation. In this case, the quarks and antiquarks may rearrange themselves such that the final state produces multiple gluons plus a conventional $q\bar{q}$ meson. It is also possible that hybrid states and four quark states may be formed in this reaction as well.

Places where we DO NOT expect to produce glueballs are shown in Figure 2.

These reactions include:

- two-photon production
- meson exchange.

Two-photon production of a meson is due to quark charges. Any state produced in two-photon production should be made up of quarks.

In meson exchange, the produced states should contain dominantly the quarks in the exchange. In the lower Figure 2, the mesons with hidden strangeness should be abundantly produced.

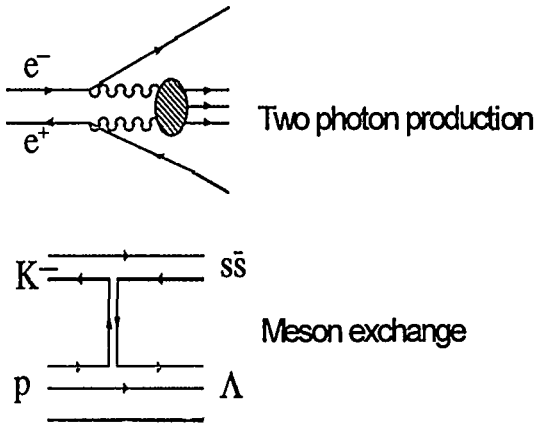


Figure 2. Reactions producing conventional $q\bar{q}$ mesons.

3. Quark-Antiquark Mesons

3.1 Review of Quark-Antiquark Mesons

The simple quark-antiquark model for mesons[10] is very successful in explaining virtually all meson properties, their quantum numbers, mass, and decay modes. In addition, there are few states that do not have a $q\bar{q}$ meson interpretation.

The properties of spin ½ quarks are listed in Table 2. Mesons are formed from quark q and antiquark $\bar{q}$ pairs. They form states similar to positronium like atoms with total spin S and angular spin L. The $q\bar{q}$ combination forms mesons with total spin $J = |L-S|, \ldots, |L+S|$. Since the quark and antiquark have opposite intrinsic parity, the meson parity depends on L and is $P = -(-1)^L$. For charge conjugation, only the neutral mesons can be eigenstates. If charge conjugation is applied to a neutral meson, the quarks switch to antiquarks and antiquarks to quarks. To form an eigenstate, the position and spins must be interchanged. The position interchange leads to a $(-1)^L$ dependence and the spin interchange leads to a $(-1)^{S+1}$ dependence. The combined operation yields a meson charge conjugation of $C = (-1)^{S+1}(-1)^L$. The flavor of the quark is defined to have the same sign as its charge.

Flavor	u	d	s	c	b	t
charge	+2/3	−1/3	-1/3	+2/3	−1/3	+2/3
I_3	+1/2	−1/2	0			
strangeness	0	0	−1			
charm				+1		
bottomness					−1	
topness						+1
mass (GeV)	0.3	0.3	0.5	1.5	5	160
spin	½	½	½	½	½	½
baryon number, B	1/3	1/3	1/3	1/3	1/3	1/3

Table 2. Quark properties with the constituent masses listed.

The quark and antiquark pair, when formed into special unitary (SU) multiplets, become mesons. A quark triplet of u, d, and s quarks, together with the corresponding antiquarks, form the SU(3) meson multiplets of an octet plus a singlet. These multiplets can be formed by constructing a triangle from the u, d, s triplet quarks on a plane with x and y axes of I_3 and hypercharge, $Y = (B+S)/2$, and an upside-down triangle of a triplet of antiquarks. Superimposing the triangle on the upside-down triangle leads to a six-sided octet on the I_3-Y plane. At the center of the diagram are two states, the eighth member of the octet and the singlet. In the quark model, these members can mix and the linear combinations are specified by an experimentally determined mixing angle. The mixed members of the SU(3) octet and singlet are the η and η' for the pseudoscalars and the ω and ϕ for the vectors.

If instead of a quark triplet we use a SU(4) quark quartet of u, d, s, c quarks and antiquarks, the SU(4) multiplets form a 16-plet. Using a similar scheme as in SU(3), the four quarks, u, d, s, c are plotted on a three-dimensional plot with variables, I_3-Y-C, forming a pyramid, and the antiquarks form an upside-down pyramid. Superimposing the center of the upside down pyramid on each corner of the pyramid leads to the 16-plet multiplet.

Table 3 lists the well-established mesons and their properties.

The simple quark model successfully explains

- meson mass splittings
- OZI allowed hadronic decays
- radiative and two photon decays.

Experimentally, every $q\bar{q}$ meson is accounted for except the light quark scalars! This may be related to some presently unknown reason that causes the scalar glueball to be experimentally hidden. We next discuss the scalar charmonium χ states and the experimentally known light quark scalars.

$N^{2S+1}L_J$	J^{PC}	I=1	I=0	I=0	I=0	I=1/2	I=1/2
1^1S_0	0^{-+}	π	η,η	η_c		K	D
1^3S_1	1^{--}	ρ	ω,ϕ	$J/\psi(1s)$	$\Upsilon(1s)$	$K^*(892)$	$D^*(2010)$
1^1P_1	1^{+-}	$b_1(1235)$	$h_1(1170)$, $h_1(1380)$	$h_c(1P)$		K_{1B}	$D_1(2420)$
1^3P_0	0^{++}			$\chi_{c0}(1P)$	$\chi_{b0}(1P)$	$K^*_0(1430)$	
1^3P_1	1^{++}	$a_1(1260)$	$f_1(1285)$, $f_1(1510)$	$\chi_{c1}(1P)$	$\chi_{b1}(1P)$	K_{1A}	
1^3P_2	2^{++}	$a_2(1320)$	$f_2(1270)$, $f_2(1525)$	$\chi_{c2}(1P)$	$\chi_{b2}(1P)$	$K^*_2(1430)$	$D^*_2(2460)$
1^1D_2	2^{-+}	$\pi_2(1670)$				$K_2(1770)$	
1^3D_1	1^{--}	$\rho(1700)$	$\omega(1600)$	$\psi(3770)$		$K^*(1680)$	
1^3D_2	2^{--}					$K_2(1820)$	
1^3D_3	3^{--}	$\rho_3(1690)$	$\omega_3(1670)$, $\phi_3(1850)$			$K^*_3(1780)$	
1^3F_4	4^{++}	$a_4(2040)$	$f_4(2050)$, $f_4(2020)$			$K^*_4(2045)$	
2^1S_0	0^{-+}	$\pi(1300)$	$\eta(1295)$	$\eta_c(2s)$		$K(1460)$	
2^3S_1	1^{--}	$\rho(1450)$	$\omega(1420)$, $\phi(1680)$	$\psi(2s)$	$\Upsilon(2s)$	$K^*(1410)$	
2^3P_2	2^{++}		$f_2(1810)$, $f_2(2010)$		$\chi_{b2}(2P)$	$K^*_2(1980)$	
3^1S_0	0^{-+}	$\pi(1770)$	$\eta(1760)$			$K(1830)$	

Table 3. Meson table, from the Particle Data Group tables.

3.2 χ States

The charmonium χ states are the three P wave ($L = 1$, $J^{PC} = 0^{++}, 1^{++}, 2^{++}$) members of the charm and anticharm quark mesons. Their masses are 3415, 3510, and 3556 MeV. The mass splitting is small and the electromagnetic transition rates from the electric dipole radiation from spin flip of the $\psi(3680)$ are predicted by theory and agree quite well with experimental measurements. The charmonium scalar is very well-understood, and we have no reason to expect mysterious behavior in the scalar P wave quark-antiquark states.

3.3 Scalar Mesons

If we now turn to the light quark scalar members, we find they are not listed in Table 3. The experimentally well-established scalars are the isovector, $a_o(980)$, and the isoscalars, $f_o(980)$ and $f_o(1370)$. The $f_o(980)$ predominantly decays into pion and kaon pairs, and the isovector, $a_o(980)$ into $\eta\pi$. The $f_o(1370)$ appears as a phase shift in S wave $\pi\pi$. These states were discovered 20 years ago. These states were formerly thought to be the light quark scalars, but recently this interpretation has been removed by the Particle Data Group. There are several reasons to suspect that these states are not the light $q\bar{q}$ scalar mesons. The mass splitting from the other light quark P wave states, $a_1(1260)$ and $a_2(1320)$, is very large. The real $q\bar{q}$ scalar should be close to these other P wave states. The $a_o(980)$ and $f_o(980)$ masses are at $K\bar{K}$ threshold. There has been a suggestion that these states are really $K\bar{K}$ molecules.[11] If in fact these presently known scalars are not the real $q\bar{q}$ scalars, we have two puzzles; namely, where are the real $q\bar{q}$ scalars and the glueball scalar?

3.4 What Is a Resonance?

What is a resonance? Most experimentalists look for peaks in invariant mass plots. However, many resonances are short-lived ($\tau \sim 10^{-24}$ sec.) and can have very large widths.

A resonance[12] is properly defined in terms of a phase shift. In classical electromagnetic theory,[13] if plane waves are incident on a metal or dielectric surface, the spherical scattered waves will get a phase shift that depends on the boundary conditions. In Quantum Mechanics, we consider plane waves incident on a target particle. A general solution from the Schrodinger Wave Equation will have the form $u_r(r,\theta,\phi) = e^{ikz} + e^{ikr} f(\theta,\phi)/r$, where

$$f(\theta) = \frac{1}{k}\sum_{l=0}^{\infty}(2l+1)T_l(E)P_l(\cos\theta). \qquad \text{[Eq. 2]}$$

We can rewrite T_l, the scattering amplitude, as

$$T_l(E) = \frac{\rho_l e^{2i\delta_l} - 1}{2i}, \qquad \text{[Eq. 3]}$$

where ρ_l and δ_l depend on the energy E. Using the cross section relation, we can obtain

$$\sigma(total) - \sigma(elastic\ scattering) = \frac{\pi}{k^2}\sum_{l=0}^{\infty}(2l+1)\left(1-\rho_l^2\right). \qquad \text{[Eq. 4]}$$

Thus, if $\rho_l = 1$, then the scattering is elastic and

$$T_l(E) = e^{i\delta_l}\sin\delta_l = \frac{1}{\cot\delta_l - i}, \qquad \text{[Eq. 5]}$$

then the cross section for the elastic case becomes

$$\sigma(a+b\rightarrow a+b;\text{elastic}) = \frac{\pi}{k^2}\sum_{l=0}^{\infty}(2l+1)\sin^2\delta_l. \qquad \text{[Eq. 6]}$$

The cross section reaches a maximum when δ_l goes to 90^0. For elastic scattering, $\rho_l = 1$, then

$$T_l = \frac{e^{2i\delta_l} - 1}{2i} = \frac{i}{2} + \frac{1}{2}\left(\sin 2\delta_l - i\cos 2\delta_l\right). \qquad \text{[Eq. 7]}$$

The plot of the real versus imaginary values of T_l is called an Argand diagram. This is shown in Figure 3 for the elastic case.

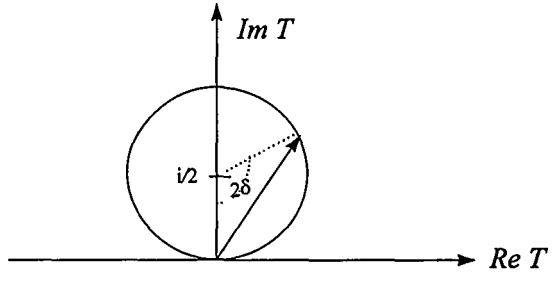


Figure 3. Argand diagram for elastic scattering.

If $\rho_l < 1$, for inelastic scattering, we have Figure 4 which simplifies to,

$$T_l = \frac{\rho_l e^{2i\delta_l} - 1}{2i} = \rho_l\left[\frac{e^{2i\delta_l} - 1}{2i}\right] + \frac{\rho_l - 1}{2i}. \qquad \text{[Eq. 8]}$$

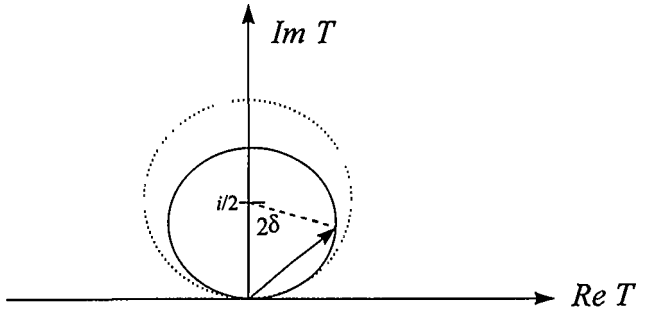


Figure 4. Argand diagram for inelastic scattering.

What is the connection with the Breit-Wigner form of a resonance in a mass plot? Since $T_l = 1/[\cot\delta_l - i]$ and the resonance is at $\delta_l(E_R) = 90°$, we have $\cos(\delta_l(E_R)) = 0$. We can expand the cotangent as

$$\cot(\delta_l(E)) \equiv \cot[\delta_l(E_R)] + (E_R - E)\left.\frac{d\cot(\delta_l(E))}{dE}\right|_{E=E_R} + \ldots \qquad \text{[Eq. 9]}$$

$$\cot(\delta_l(E)) \equiv (E_R - E)\left.\frac{d\cot(\delta_l(E))}{dE}\right|_{E=E_R} = (E_R - E)\frac{2}{\Gamma}.$$

Then, $T = [\Gamma/2]/[(E_R\text{-}E) + i\Gamma/2\ ]$. Figure 5 shows the scattering cross section versus the center-of-mass energy for a resonance. The half width, where the distribution falls to half its maximum, occurs at $E = E_R \pm \Gamma/2$.

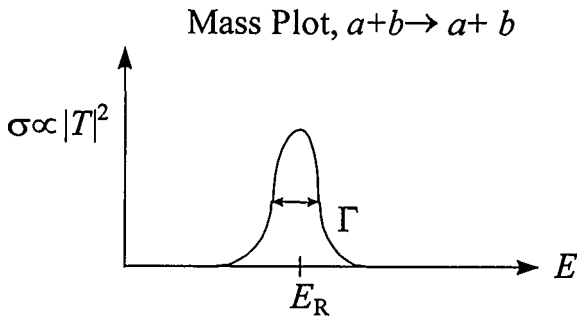


Figure 5. Mass plot and resonance width.

To determine a resonance, a δ_l phase shift of 180 degrees is required and the mass peak occurs at 90^0. To measure this phase shift in a particle physics experiment will require the phase shift to be measured *relative* to another partial wave. This is possible if there are other nearby resonances decaying into the same final state and whose Breit-Wigner shapes are already well-known.

There are cases where the resonance is very close to threshold,[14] such as the $f_o(980)$, and it is possible to have decays into $\pi\pi$ and $K\overline{K}$ In the case of the f_o, the mass is centered well above $\pi\pi$ threshold but for the decays into $K\overline{K}$, the mass is at $K\overline{K}$ threshold. In this case, unitarity and analyticity are used to extrapolate the $K\overline{K}$ threshold. The mass dependence is given in Eq. (10),

$$\frac{d\sigma}{dm} \propto \left| \frac{m_R\sqrt{\Gamma_o\Gamma_i}}{m_R^2 - m^2 - im_R(\Gamma_{\pi\pi} + \Gamma_{K\overline{K}})} \right|^2 \qquad \text{[Eq. 10]}$$

$$\Gamma_{\pi\pi} \propto g_\pi p$$

$$\Gamma_{K\overline{K}} \propto g_K\sqrt{m^2/4 - m_K^2}, \text{ above } K\overline{K} \text{ threshold}$$

$$\Gamma_{K\overline{K}} \propto ig_K\sqrt{m_K^2 - m^2/4}, \text{ below } K\overline{K} \text{ threshold}.$$

Above $K\overline{K}$ threshold, the $\pi\pi$ mass shape is depressed by rapidly increasing $\Gamma_{K\overline{K}}$, and below threshold, the $\pi\pi$ mass shape is depressed if g_K is large. This effect of

this width dependence near threshold is seen in the decay of J/ψ → $\phi f_o(980)$, $f_o(980) \rightarrow K\overline{K}$, ππ in Figure 6. In the ππ decay mode, the Breit-Wigner shape of the $f_o(980)$ is cut short as the $\Gamma_{K\overline{K}}$ threshold opens up and the denominator in $d\sigma/dm$ increases. For the $K\overline{K}$ decay mode, the shape of $d\sigma/dm$ can be obtained using the $\Gamma_{K\overline{K}}$ below threshold.

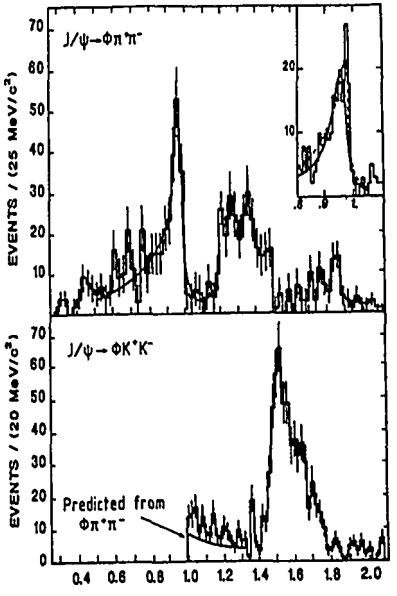


Figure 6. Mass plots of $\pi^+\pi^-$ from J/ψ → φππ and K^+K^- from J/ψ →φ *KK*. Results from the DM2 experiment.[4]

Threshold effects can create seemingly narrow peaks, as in the $f_o(980) \rightarrow \pi\pi$ case. This can occur any place near the threshold of the final secondary particles. For example, below are listed places were several peaks can occur due to threshold effects of a resonance. There are numerous such places and corresponding candidates.

- $K\overline{K}$ (~1 GeV); candidates, $f_o(980) \rightarrow \pi\pi$, $a_o(980) \rightarrow \eta\pi$
- $K^*\overline{K}$ (~1.4 GeV); candidates, $f_1(1420)$, $\eta(1440) \rightarrow K\overline{K}\,\pi$
- ρρ, ωω (~1.5 GeV); candidates, $f_o(1500) \rightarrow \pi\pi$
- $K^*\overline{K}^*$ (~1.8 GeV); candidates, $f_J(1710) \rightarrow K\overline{K}$
- $p\overline{p}$ (~2 GeV); candidates?
- $\Lambda\overline{\Lambda}$ (~2.23 GeV); candidates, $\xi(2230) \rightarrow K\overline{K}$.

4. Experimental Techniques

4.1 Spin-Parity Determination

Spin-parity determination can be understood fairly simply by using the helicity formalism[15] for two body decays. Decays with more than two secondaries can be extended by considering the decay in terms of sequential two body decays. If a particle *X* decays into particles *a* and *b* (see Fig. 7), the amplitude for the decay into two pseudoscalars is as follows:

$$\text{amplitude} \sim Y_{lm}(\theta,\phi). \qquad \text{[Eq. 11]}$$

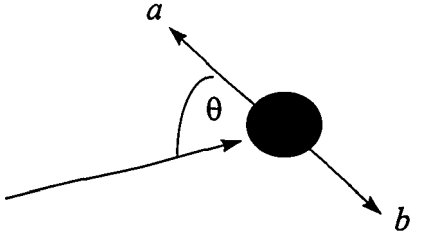


Figure 7. Decay angles of *X* decaying into *a* and *b* particles.

The amplitude for decay of a scalar *X* is simply $\sim Y_{00}$, which is constant. The amplitude for decay of a spin two-particle *X* is $\sim\Sigma\, a_m\, Y_{2m}(\theta,\phi)$, where the a_m are coefficients that depend on the magnitude of the different helicity states *m*. It is

possible to fit the distribution of decay angles θ and φ, and to find which Y_{lm} choice fits the best in order to determine the spin. If the particle has spin 2, we will need to fit the unknown helicity amplitudes a_m. Usually, they will become additional unknown parameters to fit.

A more sophisticated approach utilizes moments. The idea is to weight each event by Y_{lm}'s. Suppose an amplitude is given by $A = \sum a_{Jmm'} D^J_{mm'}(\Omega)$. Then the intensity in the amplitude is squared,

$$|A|^2 = \sum a_{Jm_1m_1'} D^J_{m_1m_1'}(W) \sum a^*_{Jm_2m_2'} D^{J*}_{m_2m_2'}(W). \qquad \text{[Eq. 12]}$$

The pair of D functions can be equated to a single D function using a summation relation,

$$D^{J_1}_{m_1m_1'}(\Omega) D^{J_2}_{m_2m_2'}(\Omega) = \sum_{J_3=|J_1-J_2|}^{J_1+J_2} \langle J_1m_1, J_2m_2 | J_3m_3 \rangle \langle J_1m_1', J_2m_2' | J_3m_3' \rangle D^{J_3}_{m_3m_3'}(\Omega). \qquad \text{[Eq. 13]}$$

Using this relation, the intensity $|A|^2$, can be written as a sum of a single D function.

$$|A|^2 = \sum_{J=|J_1-J_2|}^{J_1+J_2} T_{Jmm'} D^J_{mm'}(\Omega). \qquad \text{[Eq. 14]}$$

Now the coefficient $T_{Jmm'}$, is a complicated complex coefficient that is a sum of products of $a_{Jmm'}$. Also, although we have the intensity as a linear combination of a single D functions, the value of J will vary from $|J_1-J_2|$ to J_1+J_2. So to study spin 2 will require a J value of up to four. Since the intensity can be written as a sum of single D's, we can extract the value of the coefficient $T_{Jmm'}$ by weighting the data events by a particular $D^{*J_1}_{m_2m_3}(\Omega)$, which will project out the coefficient $T_{J_1m_2m_3}$. The other coefficients are associated with orthogonal D functions and will not contribute. This result assumes that the efficiency is uniform in angle. If the efficiency is not uniform, the coefficients can still be determined by a slightly more complicated correction procedure.

Once we obtain all the values of the coefficients, $T_{Jmm'}$, we can then invert the process to obtain the values of the $a_{Jmm'}$. In some cases, the inversion can have ambiguities.

4.2 Dalitz Plot Analysis

In spin-parity analyses of states that decay into three mesons, the study of the Dalitz plot has provided important information. If a particle X decays into mesons, a, b, and c, $X \rightarrow a + b + c$, it is possible that intermediate states are formed between any two of the three particles. For example, the reaction $J/\psi \rightarrow \rho\pi \rightarrow \pi^+\pi^-\pi^0$, has an intermediate state, $\rho \rightarrow \pi\pi$. These intermediate states can be studied with the use of the Dalitz plot. In a Dalitz plot, the invariant mass squared of two of the particles is plotted versus the invariant mass squared of a second pair of the particles (at least one particle is common to the two pairs). A schematic Dalitz plot is shown in Figure 8 with bands created by two-body resonances. Figure 9 is a Dalitz plot of the $\pi^+\pi^0$ mass squared versus the $\pi^-\pi^0$ mass squared.

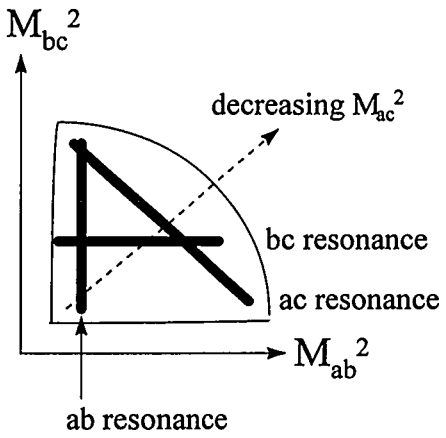


Figure 8. Schematic diagram of a Dalitz plot.

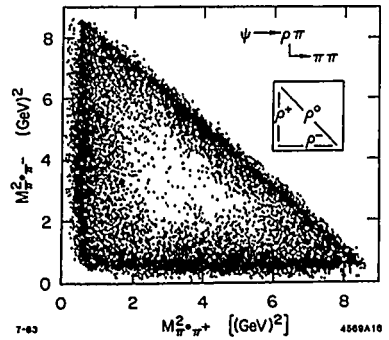


Figure 9. Dalitz plot of $J/\psi \to \rho\pi \to \pi^+\pi^-\pi^0$, from Mark III.[4]

The concentration of events on the vertical band corresponds to $\rho^+ \to \pi^+\pi^0$, the horizontal bank corresponds to $\rho^- \to \pi^-\pi^0$, and the diagonal band corresponds to $\rho^0 \to \pi^+\pi^-$. The density of the events along the line depends upon the spin of the intermediate particle. In this case, the ρ has spin one and the density peaks at the middle of the band and drops to zero at the ends of the band. If the two body resonance has spin zero, the band will have a uniform distribution.

The spin of a particle that decays into three mesons can be determined by trying different spin-parity hypotheses and comparing the probability for each hypothesis.

4.3 K Matrix Formalism

The general idea of the K matrix formalism[16] is to include unitarity in a convenient manner. Suppose a resonance X decays into two bodies such as $\pi\pi$, KK, $\eta\eta$. We can write the unitarity requirement on the S matrix as $\Sigma|S_{ij}|^2 = 1$. If we use the transition matrix T, defined from the S matrix as $S = I + 2iT$, where I is the identity matrix, then unitarity is given by $Im\ T_{if} = \Sigma\, q_j\, T_{ji}^*\, T_{jf}$ where q_j is the momentum in the cms for channel j.

It turns out that imposing unitarity directly on the T matrix is not a convenient approach. Instead, we can redefine T in terms of another matrix called the K matrix via $T = K(I - iQK)^{-1}$, where $Q_{ij} = q_i\delta_{ij}$. With this definition, unitarity is automatically satisfied. This can be checked by substituting this equation into $Im\ T_{if} = \Sigma\, q_j\, T_{ji}^*\, T_{jf}$. Hence, a convenient method is to approximate T (or S) by representing T in terms of K. If time invariance holds, K will be real and symmetric. In older textbooks,[17] this matrix is also called the reaction or reactance matrix.

5. Proton-Antiproton Searches

In recent years, the most important new data on the search for glueballs and new hadronic states have come from the study of $p\bar{p}$ reactions at LEAR, and notably, the Crystal Barrel experiment with its very high statistics data. A scalar resonance at a mass of 1.5 GeV has been observed. It may have been seen in an earlier low statistics BNL experiment. In early LEAR runs, it was perhaps overlapping and

misidentified with a tensor meson called the AX. Later, after analysis of the very high statistics Crystal Barrel data, clear evidence for a scalar was obtained. Confirming evidence has not yet been obtained from the charmonium experiment E760 at FNAL. In this section, we discuss the $p\bar{p}$ results in historical order and discuss in detail the study of the resonance at a mass of 1500 MeV.

5.1 Early Results

The early results in $p\bar{p}$ physics are from BNL low statistics data studying the reaction, $p\bar{n} \rightarrow 2\pi^+\pi^-$. The results indicated a ρ and $f_2(1270)$ signal and a bump at 1527 MeV with a width of Γ = 101 MeV. This data is shown in Figure 10.

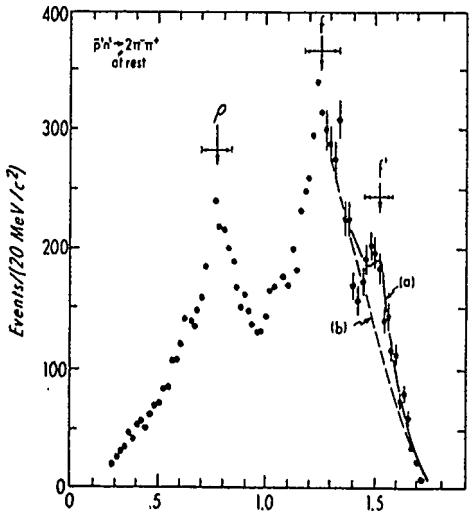


Figure 10. $\pi^+\pi^-$ mass from BNL.[18]

At LEAR, the ASTERIX experiment sent an antiproton beam into a gaseous H_2 target and observed a peak near 1500 MeV. The OBELIX experiment studied $\bar{n}p \rightarrow \pi^+\pi^+\pi^-$ in flight. The $\pi^+\pi^-$ mass plot is shown in Figure 11. The observed peak includes the ρ, the $f_2(1270)$, and a peak at ~1.5 GeV. This resonance was called the AX and the initial spin-parity studies suggested $J^{PC} = 2^{++}$.

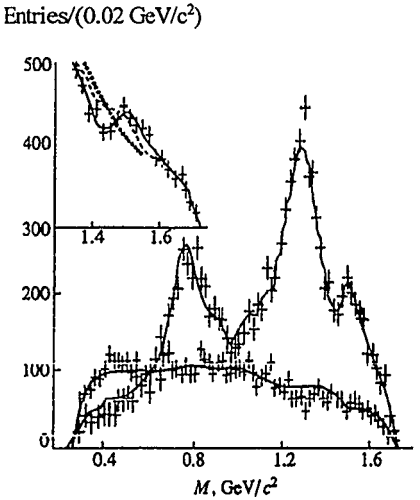


Figure 11. $\pi^+\pi^-$ mass results from the OBELIX experiment.[19]

GROUP	Channel	Mass	Width	*BR* (10^{-3})	*JPC*
ASTERIX	$\pi^+\pi^-\pi^0$	1565 ± 20	170 ± 40	3.7 ± 0.6	2^{++}
CRYSTAL BARREL	$\pi^0\pi^0\pi^0$	1515 ± 10	120 ± 10	2.0 ± 0.6	2^{++}
OBELIX	$\pi^+\pi^-\pi^+$	1502 ± 9	130 ± 10	-	2^{++}
E760	$\pi^0\pi^0\pi^0$	1498 ± 4	141 ± 10	-	
BNL	$\pi^+\pi^-\pi^0$, $\pi^0\pi^0\pi^0$, $\pi^+\pi^-\pi^+$	1527 ± 5	101 ± 13	1.6 ± 0.5 2.6 ± 0.4	
Bridge *et al.*	$2\pi^+3\pi^-$ (ρρ)	1477 ± 5	116 ± 9	37 ± 0.3	2^{++}

Table 4. "AX" results.

5.2 High Statistics Crystal Barrel Results

The Crystal Barrel group published early results on $p\bar{p} \rightarrow \pi^0\pi^0\pi^0$ in May 1991 based on 55K events. This analysis obtained a spin parity result of $J^{PC} = 2^{++}$ for a resonance at a mass of 1515 MeV decaying into $\pi^0\pi^0$.

In December 1993, a complicated analysis simultaneously fit a resonance $X \rightarrow \pi^0\pi^0$ in the reaction $p\bar{p} \rightarrow \pi^0\pi^0\pi^0$, and $X \rightarrow \eta\eta$ in the reaction $p\bar{p} \rightarrow \eta\eta\pi^0$. This resulted in the first evidence for two separate scalar signals with masses and widths at $M = 1565$ MeV, $\Gamma = 268$ MeV and $M = 1520$ MeV, $\Gamma = 148$ MeV.

In January 1995, based on 712K events, the reaction on $p\bar{p} \rightarrow \pi^0\pi^0\pi^0$ was analyzed with an amplitude analysis utilizing the K matrix formalism. The amplitude fitted was

$$A\left[{}^{2S+1}L_J\right](p,q) = \sum_{L,l} Z\left[{}^{2S+1}L_J\right]_{,L,l}(p,q) B^L(p) F^l(q)$$

$$A\left[{}^{2S+1}L_J\right](p,q) = \sum_{L,l} Z\left[{}^{2S+1}L_J\right]_{,L,l}(p,q) B^L(p) F^l(q)$$

$F^l(q)$ are the dynamical functions containing the K matrix

$B^L(p)$ are the angular momentum barrier factors

$Z\left[{}^{2S+1}L_J\right]_{,L,l}$ are the Zemach spin parity functions

The sequential decay was set up as shown in Figure 12.

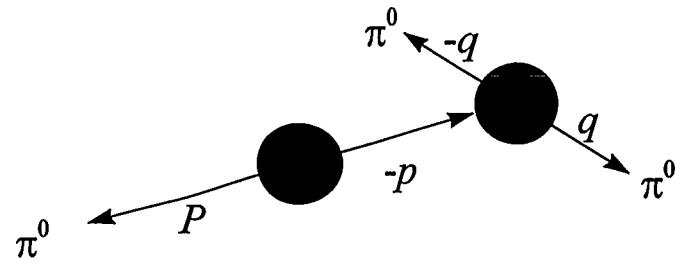


Figure 12. Decay chain of $p\bar{p} \rightarrow X \rightarrow \pi^0\pi^0$.

A total of 34 parameters are used to fit the Dalitz plot in 1338 nonzero cells. The K matrix poles are obtained, and then using the relation $T = (I - iKQ)^{-1}K$, the mass and width are obtained from the T matrix. The results of this fit are shown in Table 5.

Spin	Mass (MeV)	Γ (MeV)	*BR*	Comments
0	994 ± 5	26 ± 1	42%	old S^*
0	1330	760		old ε
0	1490 ± 13	120 ± 15	12%	new scalar
2	1285	195	29%	$f_2(1270)$
2	1520	135	17%	old AX

Table 5. Results for T matrix poles in Crystal Barrel data.

In the high statistics Dalitz plot in Figure 13, we can observe several features:

- a flat band at M~1500 MeV
- a high spin at M~1540 MeV
- a dip at the $f_0(980)$
- a peak in the $f_2(1270)$ mass region.

There is clear evidence for a scalar at 1500 MeV. The K matrix analysis reveals a scalar with a mass of 1490 MeV and a broad scalar at 1330 MeV which may be the old ε scalar. The tensors $f_2(1270)$ and the AX at 1520 MeV are also obtained.

The Crystal Barrel group also studied the decay $p\bar{p} \rightarrow \pi^0\eta\eta$. The Dalitz plots are shown in Figure 14 and Figure 15. A couple of features are apparent:

- a $\delta^0 \rightarrow \eta\pi^0$ signal
- an $\eta\eta$ resonance in the 1.3–1.5 GeV mass region.

Utilizing the K matrix formalism, similar results of a scalar at 1360 MeV and 1500 MeV are obtained for the $\eta\eta$ channel.

The decay modes of the $f_0(1500)$ are listed in Table 6. The upper limit in the $K\bar{K}$ mode is obtained from old BNL results.

Decay Mode X	Branching Fraction of f_0
$\pi^0\pi^0$, $\pi^+\pi^-$	$[38 \pm 10] \times 10^{-4}$
$\eta\eta$	$[6.2 \pm 2.8] \times 10^{-4}$
$\eta'\eta$	$[1.5 \pm 0.5] \times 10^{-4}$
$4\pi^0$	$3.4 \times [3.8 \pm 10] \times 10^{-4}$
$K\bar{K}$	$< [5\text{-}6] \times 10^{-4}$ (from Gray *et al.*[18])

Table 6. Product branching fractions $B(p\bar{p} \rightarrow \pi^0 f_0) \times B(f_0 \rightarrow X)$.

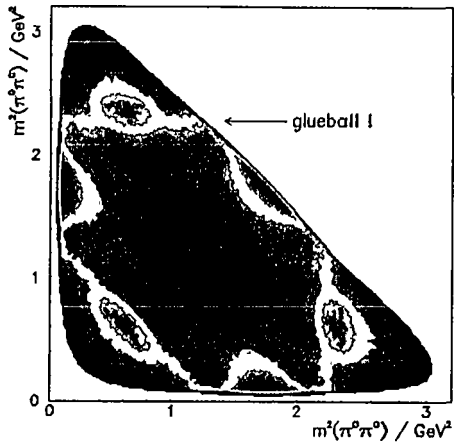


Figure 13. Dalitz plot for $p\bar{p} \rightarrow \pi^0\pi^0\pi^0$ from the Crystal Barrel.[20]

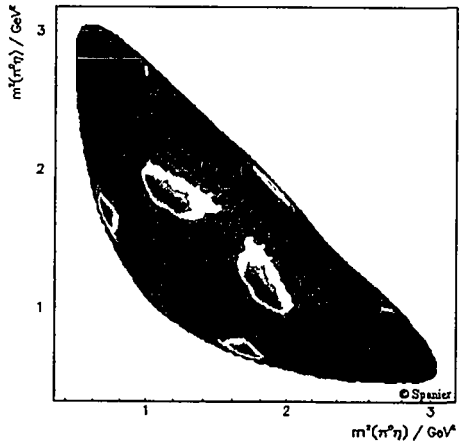


Figure 14. Dalitz plot for $p\bar{p} \rightarrow \eta\pi^0\pi^0$ from the Crystal Barrel.[21]

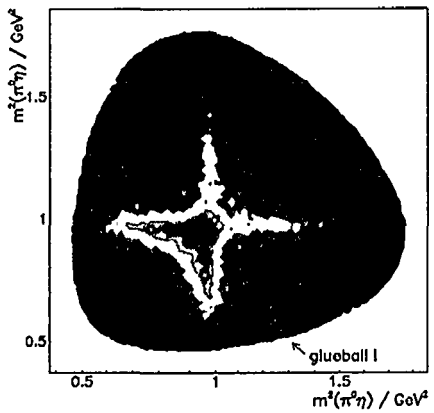


Figure 15. Dalitz plot for $p\bar{p} \rightarrow \eta\eta\pi^0$ from the Crystal Barrel.

5.3 E760 Results

The E760 experiment at FNAL collides antiprotons on a proton gas jet target at center-of-mass energies of 2.98 and 3.526 GeV to study charmonium states. The group has studied the $3\pi^0$ and $\pi^0\eta\eta$ decays. The Dalitz plots from E760 are shown in Figure 16 and Figure 17. We can see the following:

- in $3\pi^0$, there are $2\pi^0$ peaks at 1270, 1500, and 2000 MeV
- in $\pi^0\eta\eta$, there are $\pi^0\eta$ peaks at 980 and 1320 MeV
- in $\pi^0\eta\eta$, there are $\eta\eta$ peaks at 1500 and 2100 MeV.

Since the center-of-mass energy is higher than for Crystal Barrel, the resonances seen by E760 are not caused by reflections on the Dalitz plot. Since the center-of-mass energy is different, perhaps the production rate of the $f_0(1500)$ and the AX(1520) is different, so they may not be able to confirm the existence of the scalar. A spin-parity determination has not yet been published by the E760 group. However, a fit to the $\pi\pi$ mass plot has been performed including seven resonances and is shown in Figure 18.

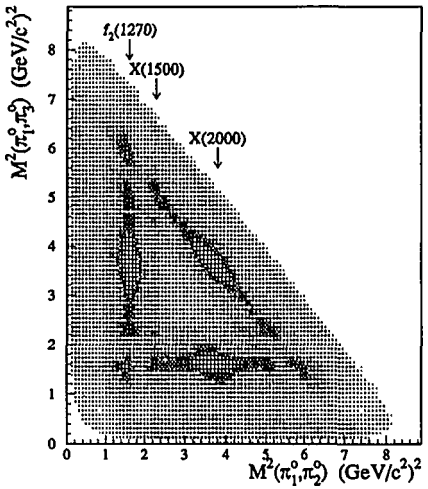


Figure 16. Dalitz plot for $p\bar{p} \rightarrow \pi^0\pi^0\pi^0$ from E760 (Ref. 22).

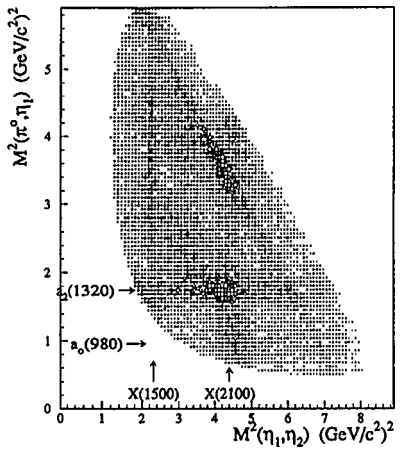


Figure 17. Dalitz plot for $p\bar{p} \rightarrow \eta\eta\pi^0$ from E760.

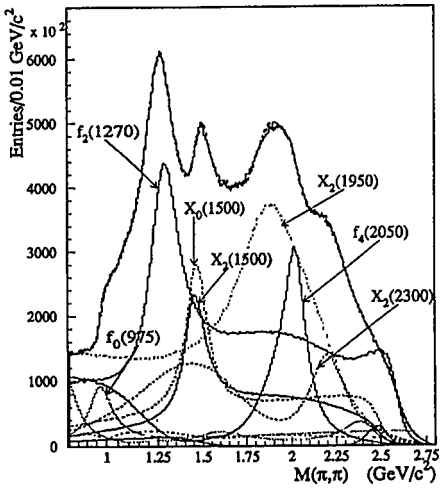


Figure 18. Fit to the $\pi\pi$ mass spectrum from E760.

5.4 Other Developments

A very important question is: Does the $f_0(1500)$ appear in radiative J/ψ decays? In the radiative decays into four pions from the DM2 group, a peak appears near 1500 MeV as shown in Figure 19.

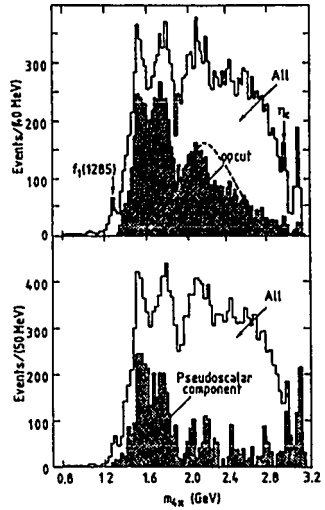


Figure 19. $J/\psi \rightarrow \gamma 4\pi$ from the DM2 group.[23]

D. Bugg *et al.*,[24] have analyzed the $J/\psi \rightarrow \gamma 4\pi$ channel from the Mark III group. The Mark III four pion mass distribution, however, does look different from the DM2 data and there is no visible peak at 1500 MeV. Using a four body partial wave analysis and assuming that the pion pairs form scalars, they conclude there is evidence for a scalar near 1500 MeV. In Figure 20, the left plot is the fit result including the $f_0(1500)$ and right plot is the fit result not including the $f_0(1500)$. In Figure 21, the lower left and right plots are the scalar and tensor intensities. The scalar intensity is fit with resonances at 1505, 1750, and 2104 MeV.

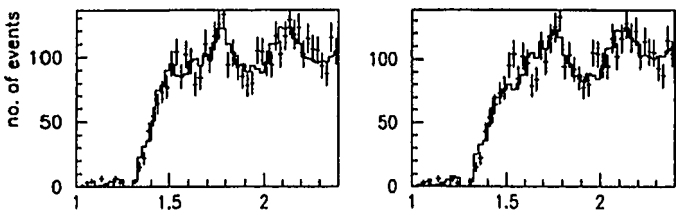


Figure 20. Mass plot fits to the Mark III data.

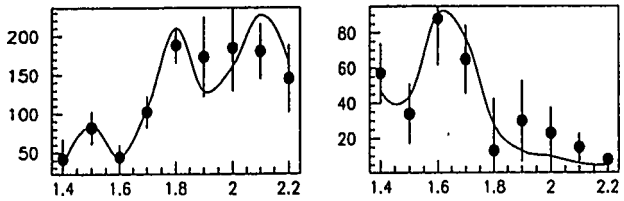


Figure 21. Partial wave analysis of Mark III data.[24]

From the Bugg *et al.* analysis, the branching ratio the $B(J/\psi \rightarrow \gamma f_o(1500) \rightarrow \pi\pi) = 5.7 \times 10^{-4}$ is obtained. Using a Crystal Barrel branching ratio of $B(f_o \rightarrow 4\pi)/B(f_o \rightarrow 2\pi) = 3.4 \pm 0.8$, we can compare the rate to the $f_2(1270)$ and find that the radiative J/ψ decays have a rate of $f_o \rightarrow \pi\pi$ that is 15% of the $f_2(1270)$. If we look at the Crystal Ball results on $J/\psi \rightarrow \gamma\pi^o\pi^o$ in Figure 22, we observe a clear $f_2(1270)$ signal. At 1500 MeV, there is a dip where we would expect the f_o signal that is 15% of the neighboring $f_2(1270)$ signal. There is a peak of 14 events at 1450 MeV which appears below the $f_o(1500)$.

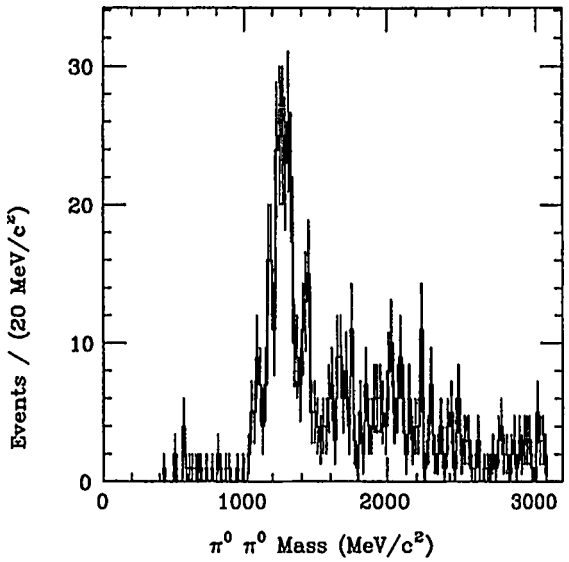


Figure 22. $J/\psi \rightarrow \gamma\pi^0\pi^0$ from the Crystal Ball.[25]

5.5 Discussion of $f_o(1500)$

The $f_o(1500)$ results are summarized below:

- mass ~1500 MeV
- width ~120 MeV
- decays to $\pi^0\pi^0$, 4π, $\eta\eta$, $\eta\eta'$ (possibly related to the GAMS resonance at 1590 MeV)
- does not decay to $K\overline{K}$
- $J^{PC}=0^{++}$, a 2^{++} resonance is nearby
- produced in $p\overline{p}$,

not seen in:

- two photon, fixed-target $\pi\pi$ scattering, central production.
- J/ψ evidence in 4π, but 2π may be controversial?

Possible interpretations of this state include glueball, threshold effect, four quark state, and antinucleon-nucleon bound state.

In a glueball interpretation, f_0 is a strong candidate. The main puzzles, however, are the lack of SU(3) flavor singlet symmetry[26] and the lack of any large $\pi\pi$ signal in radiative J/ψ decays. It is possible that mixing may be suppressing the $K\bar{K}$ mode; however, none of the radiative J/ψ results show any hint of a $\pi\pi$ signal at 1.5 GeV.

The $f_0(1500)$ mass is near the $\omega\omega$ and $\rho\rho$ thresholds. This may be accidental or may support evidence that it is a molecule or a threshold effect, although there is little evidence for direct $\omega\omega$ or $\rho\rho$ decay.

Since the f_0 is seen in $p\bar{p}$ annihilation, there should be many up and down quarks available to form four-quark states. If four-quark states are being formed, there may be $I = 0$ and possibly $I = 2$ states. As a long shot, we took a brief look for charge two pion pairs in Figure 23, but no evidence for a mass bump in double charged pion pairs is seen.

Another interpretation[27] has been put forward that the f_0 is a quasi nuclear antinucleon-nucleon bound state. In this model, $p\bar{p}$ annihilation radiates a π to form a lower mass bound state, which is below $p\bar{p}$ threshold and decays into two pions. This model predicts both scalar and tensor states.

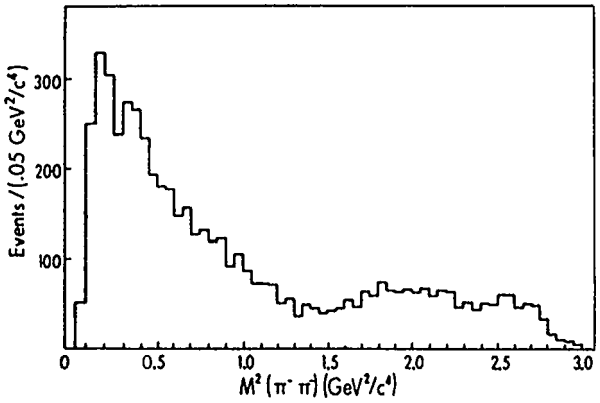


Figure 23. $M^2(\pi^-\pi^-)$ distribution from BNL.[28]

6. $f_J(1700)$ Resonance

The $f_J(1700)$ resonance was first observed in radiative J/ψ decays into K^+K^- and K_sK_s. Early spin-parity tests suggested spin two, but recently spin zero has been obtained. The $f_J(1700)$ may also be seen in central production, although the analysis suggests spin two. Here we discuss the early observations in radiative J/ψ decays, the fixed-target experiments, and finally, the spin parity tests.

6.1 J/ψ Radiative Decays

The first evidence for a new resonance in radiative J/ψ decays into two pseudoscalars came from Mark II[29] studying $J/\psi \to \gamma KK$. The KK mass plot is shown in Figure 24. The Mark II mass was m = 1708 ± 30 MeV.

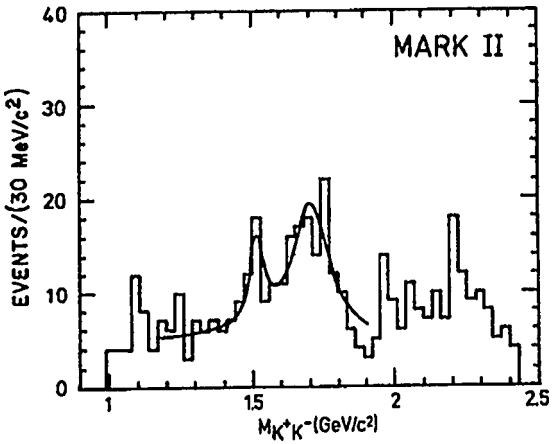


Figure 24. KK mass distribution from J/ψ → γKK from Mark II.[29]

Soon afterwards, the Crystal Ball group[30] observed an ηη signal at $m = 1670 \pm 50$ MeV in $J/\psi \rightarrow \gamma\eta\eta$. A spin-parity analysis provided evidence for spin two. The mass and fit to the decay angles are shown in Figure 25.

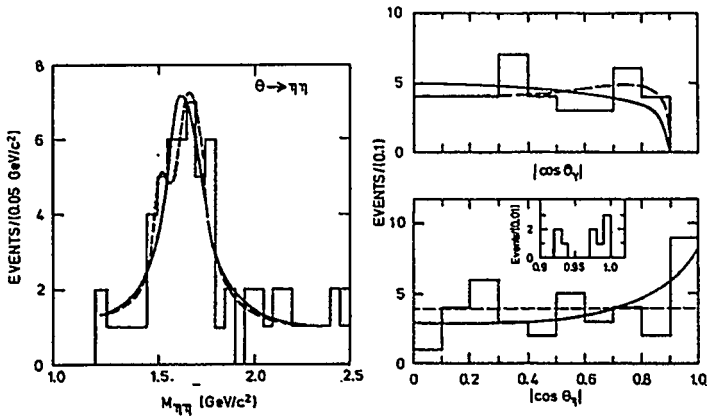


Figure 25. ηη mass distribution from $J/\psi \rightarrow \gamma\eta\eta$, from the Crystal Ball.[30]

Later, the Mark III and DM2 group observed with higher statistics this signal in radiative J/ψ decays in the K^+K^- and K_sK_s modes. The plots from the Mark III for the KK and $\pi\pi$ radiative decays are shown in the upper plots in Figure 26. In the radiative J/ψ decays, there is some evidence in the $\pi\pi$ mode for the $f_J(1700)$, but there is no evidence for the $f_0(980)$. In the hadronic decays of $J/\psi \rightarrow \phi+X$, we observe the $f_0(980)$ and $f_2(1500)$. And in the hadronic decays of $J/\psi \rightarrow \omega+X$, we observe the $f_2(1270)$ and an enhancement in the KK channel in the 1700 MeV mass region.

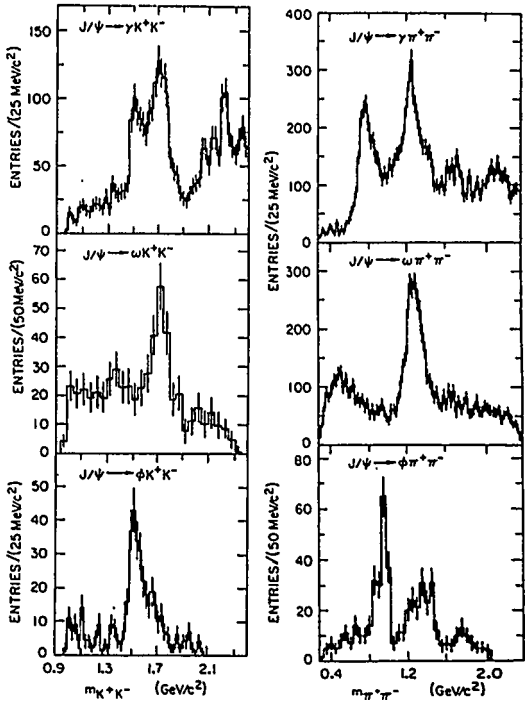


Figure 26. Mass distributions from $J/\psi \rightarrow KK+[\gamma, \omega, \phi]$, $\pi\pi + [\gamma, \omega, \phi]$ from Mark III.

In the Mark III data,[31] a simple maximum likelihood fit was applied to the events in the 1700 MeV region, and it was determined that it was more likely that all the events in that region were spin two instead of all spin zero. This primitive analysis did not allow for overlapping resonances but only all spin zero or all spin two in the mass region.

6.2 *Fixed-Target Results*

In fixed-target experiments, there is a mixture of evidence for a resonance decaying into two pseudoscalars in the 1700 MeV mass region. The LASS group studied the reaction $K^- p \to KK\Lambda$. In Figure 27 is shown the $K_S K_S$ mass plots from the radiative J/ψ decays and the $K^- p$ reaction. Here, we see in both experiments the conventional $s\bar{s}$ spin two resonance, the $f_2(1500)$, but the $f_J(1700)$ is missing in the LASS result. This would indicate that the $f_J(1700)$ is not an $s\bar{s}$ state.

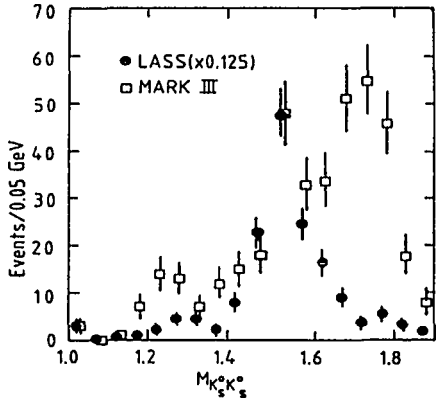


Figure 27. Comparison of KK mass distributions between Mark III and LASS.

From the BNL experiment studying the reaction $\pi^- p \to n K_s K_s$ at 23 GeV incident pion momentum, a scalar signal was claimed at 1730 MeV. There is an excess of events in the scalar wave intensity at 1.7 GeV as shown in Figure 28. This signal was attributed to a radial excitation [called the $S^{*\prime}(1770)$ in their paper] of the $f_0(980)$ which was seen in this reaction at BNL but not in radiative J/ψ decays. A mass and width of 1771^{+11}_{-53} MeV and 200^{+156}_{-9} MeV was obtained.[32]

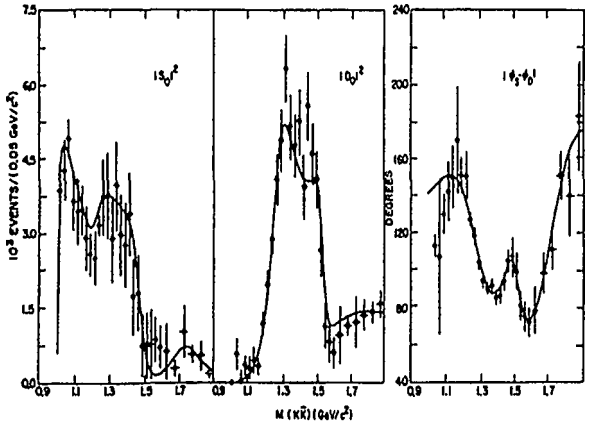


Figure 28. Partial wave analysis results from BNL.[33]

The WA76 experiment studies the reaction $pp \to p_f (KK)\, p_s$. In this reaction, centrally produced resonances may be coupled to gluons. In Figure 29 is the $K_s K_s$ mass plot from WA76 showing a clear $f_2(1500)$ signal and events at 1700 MeV. A fit of this signal yielded m = 1748 ± 10 MeV and Γ = 264 ± 25. A WA76 spin-parity study[34] prefers spin two for the resonance.

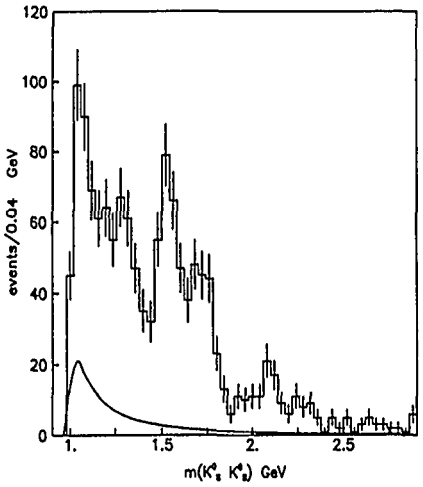


Figure 29. K_sK_s mass from WA76 (Ref. 35).

6.3 *Spin-Parity Analysis*

The spin-parity test of the *KK* signal in the radiative *J*/ψ data has been performed on the Mark III and BES data. The analysis of the *KK* signal is complicated due to the overlapping tensor and scalar signals and also due to the backgrounds from other channels such as $J/\psi \rightarrow K^*K$. In Figure 30 is a Dalitz plot of the mass squared of γK^+ versus γK_s^- and γK_s versus γK_s from the reaction $J/\psi \rightarrow \gamma K^+K^-$ and γK_SK_S. In the K^+K^- plot, there are backgrounds from K^*K which appear as bands (vertical and horizontal) near $m^2 = 0.5$ GeV^2.

A proper analysis of this complex channel required a moment analysis. Below in Figure 31 are the decay angles for a *J*/ψ radiative decay into two pseudoscalars. In this case, there are two sets of angles and this will require a set of double moments.

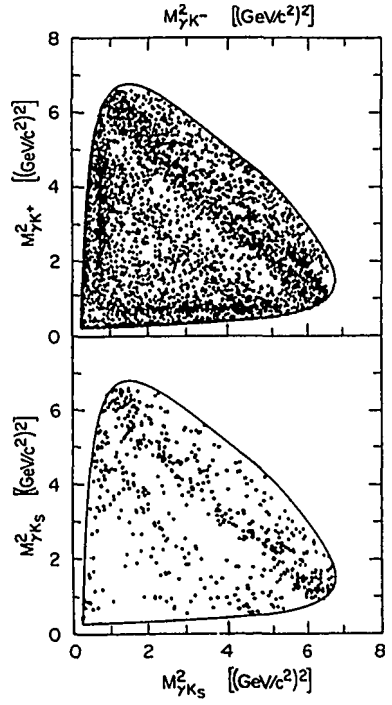


Figure 30. Dalitz plot $J/\psi \rightarrow \gamma KK$ and γK_sK_s from Mark III.

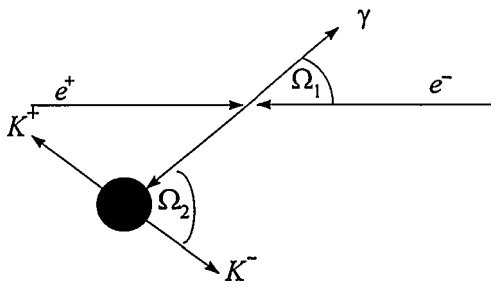


Figure 31. Schematic diagram of $ee \rightarrow J/\psi \rightarrow X, X \rightarrow KK$.

The Mark III data[36] is for the K_sK_s, K^+K^-, and $\pi^+\pi^-$ channels are shown in Figure 32. After fitting the moments, the amplitudes are extracted and the intensities for the scalar and tensor decay are derived which are plotted for the three channels in Figure 32 and Figure 33.

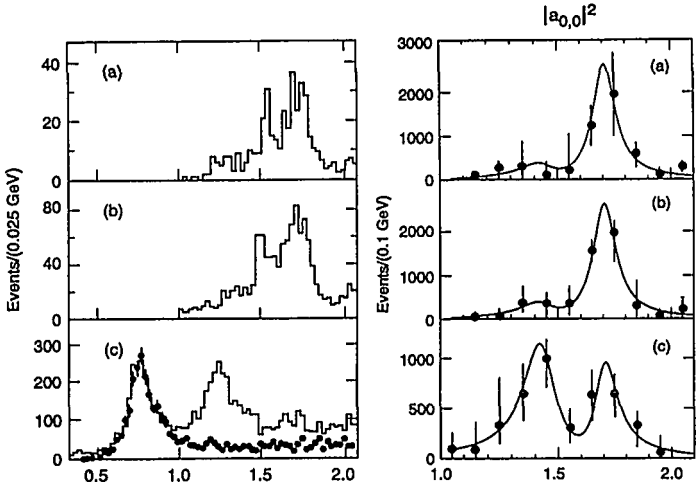


Figure 32. Mass distributions in GeV (left) and scalar intensities (right) of (a) K_sK_s, (b) K^+K^-, and (c) $\pi^+\pi^-$.

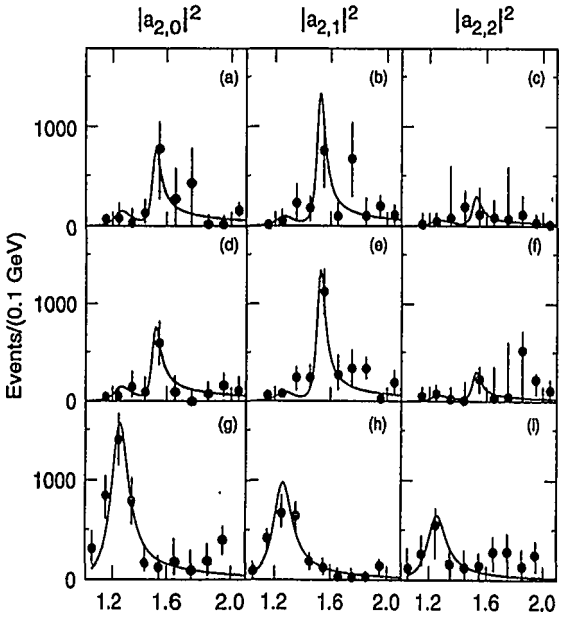


Figure 33. Tensor intensities for helicities 0,1,2 for (a)–(c) K_sK_s, (d)–(f) K^+K^-, and (g)–(i) $\pi^+\pi^-$ from Mark III.

The intensity of the different channels reveal the following:

- $f_2(1270)$ in the tensor $\pi\pi$ channel
- $f_2(1500)$ in the tensor K^+K^- and K_sK_s channels
- $f_J(1700)$ in the scalar $\pi\pi$, K^+K^-, and K_sK_s channels
- a signal at ~1400 MeV in the scalar $\pi\pi$ channel.

The conventional $f_2(1270)$ and $f_2(1500)$ mesons appear in the correct channel. The $f_J(1700)$ is found to be scalar, although there is nonzero spin two intensity in the 1700 MeV region. There is a scalar $\pi\pi$ signal ~1400 MeV which may be related

to the Crystal Barrel signal which was identified at 1330 MeV with a broad Γ = 760 MeV width. The $f_0(1500)$ is not observed.

Signal	Mass (MeV)	Width (MeV)	BR (10^{-4})
$f_0(1430)$	1429^{+43}_{-37}	169^{+111}_{-76}	$4.3^{+2\,7}_{-1\,7}$
$f_J(1700)$	1704^{+16}_{-23}	124^{+52}_{-44}	$9.5^{+2\,5}_{-2\,0}$

Table 7. Results of K_sK_s, K^+K^-, and $\pi\pi$ fits from Mark III.

Additional evidence for a scalar signal is provided by certain linear combinations of moments which contain only scalar amplitudes. These are plotted in Figure 34 and demonstrate consistency in the analysis procedure.

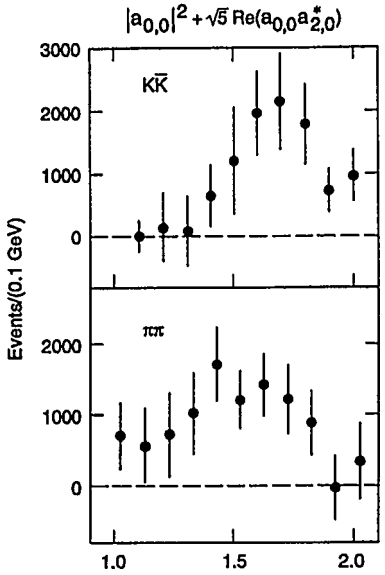


Figure 34. Scalar linear combinations of moments for K_sK_s and K^+K^- from the Mark III.

The BES group has recently published a moment analysis of the K^+K^- channel. The results of the scalar intensity are shown in Figure 35. There is a clear excess of scalar intensity near 1.8 GeV. However, the results of the tensor fit indicate an $f_2(1500)$ signal and a large tensor signal at 1700 MeV in disagreement with the Mark III results. The BES results are listed in Table 8.

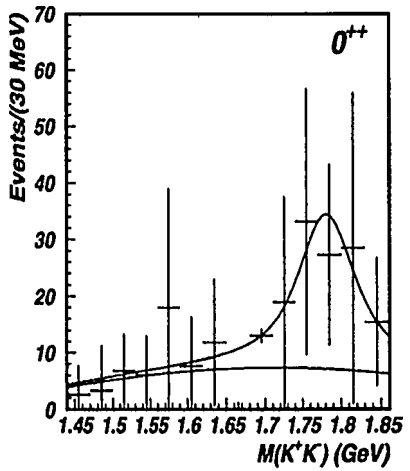


Figure 35. KK scalar wave intensity from BES.[37]

Spin	Mass (MeV)	Width (MeV)	BR (10^{-4})
scalar	$1781 \pm 8^{+10}_{-31}$	$85 \pm 25^{+22}_{-19}$	$0.8 \pm 0.1^{+0\,3}_{-0\,1}$
tensor	$1696 \pm 5^{+9}_{-34}$	$103 \pm 18^{+30}_{-11}$	$2.5 \pm 0.4^{+0\,9}_{-0\,4}$
$f_2(1525)$	$1516 \pm 5^{+9}_{-15}$	$60 \pm 23^{+13}_{-20}$	$1.6 \pm 0.2^{+0.6}_{-0\,2}$

Table 8. Results of fits to KK analysis from BES.

6.4 $f_J(1700)$ Summary

The $f_J(1700)$ results include:

- production in radiative J/ψ and central production
- scalar spin in radiative J/ψ decays
- decay modes KK, $\eta\eta$, $\pi\pi$
- KK decays appear in recoil of $J/\psi \rightarrow \omega KK$.
- approximate SU(3) flavor singlet behavior, favors KK.

6.5 $\xi(2.2)$ Evidence

Evidence for the $\xi(2.2)$, a narrow resonance with a mass near 2.2 GeV observed in radiative J/ψ decays and decaying into K^+K^- and K_sK_s, was first obtained by Mark III[38] in 1985. Subsequently, the DM2[39] did not find the $\xi(2.2)$, but a broad signal in the 2.2 GeV region and concluded that the Mark III evidence may have been a fluctuation. Later evidence of a 2.2 GeV signal in K_sK_s and $\eta\eta'$ has been reported from the LASS[40] and GAMS[41] groups.

Recently, the BES group[37] reported evidence for the $\xi(2.2)$ in K^+K^-, K_sK_s, $\pi^+\pi^-$, and $p\bar{p}$. This new evidence of nonstrange decay modes appears to provide evidence that the $\xi(2.2)$ is more flavor symmetric.

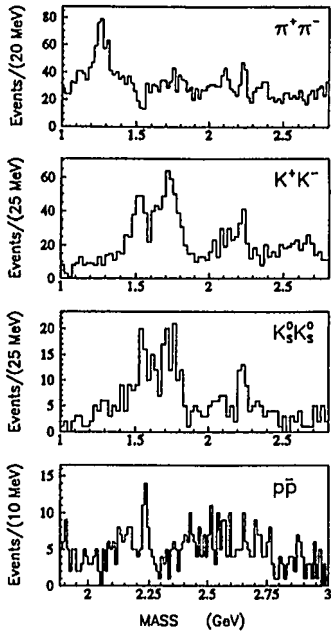


Figure 36. $J/\psi \rightarrow \gamma\pi\pi$, γK^+K^-, γK_sK_s, γpp from BES.[42]

New evidence[43] for the $\xi(2.2)$ comes from preliminary results from the L3 experiment at LEP. In the gluon jet, which is the least energetic jet in a three-jet decay of the Z^0, an excess of events in K_sK_s are observed at $M = 2.234$ GeV. In the more energetic jets, which are expected to be the quark jets, the signal is absent.

7. Study of D_s Decays

The study of hadronic physics in the weak decays of charm mesons provide a new and possibly clean method to study mesons. This is now possible due to the high statistics data from charm fixed-target experiments. From the E791 experiment comes a clean $f_0(980)$ signal from the weak D_s decays. Figure 37 is the 3π mass where charged D and D_s signals are observed from the E791 group.

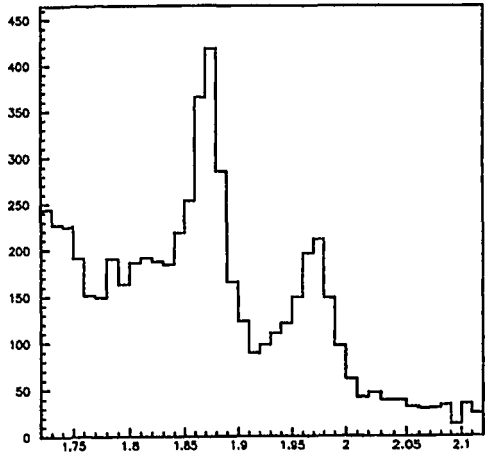


Figure 37. 3π mass from E791 (Ref. 44).

Restricting to the events at the D_s mass, the $\pi^+\pi^-$ mass squared is plotted in Figure 38. A clear peak is seen near 1 GeV which is most likely the $f_0(980)$. A broader peak is seen at m^2 = 1.9 GeV^2 (m = 1.35 GeV) which may be related to the 1.4 GeV resonance seen by the Crystal Barrel. No evidence is seen for the $f_0(1500)$ which would appear at m^2 = 2.25 GeV^2 in the figure.

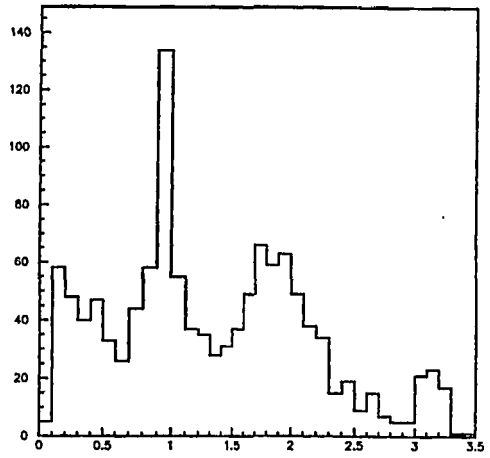


Figure 38. Mass $\pi^+\pi^-$ squared from experiment E791.

In Figure 39 is a folded Dalitz plot of the decay $D_s \rightarrow 3\pi$. Where the $f_0(980)$ overlaps at 1 GeV^2, there is a constructive interference. There are also enhancements at low $\pi\pi$ mass below 0.5 GeV and near $m^2 = 2$ GeV^2.

The $\pi\pi$ mass distribution is very similar to the one produced in $J/\psi \rightarrow \phi\pi\pi$, in Figure 6, where we expect the $\pi\pi$ states to couple to $s\bar{s}$. The D_s weak decay should also produce a recoiling $s\bar{s}$ quark pair. Hence, the $\pi\pi$ recoil should be very similar to the $\pi\pi$ recoil in $J/\psi \rightarrow \phi\pi\pi$. This provides qualitative agreement between the quark content produced in the OZI decay of the J/ψ and the weak decay of the D_s.

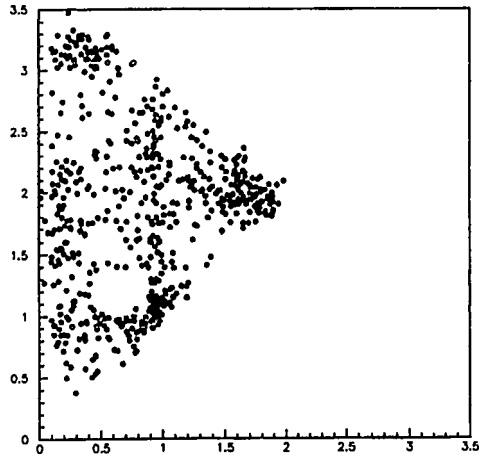


Figure 39. Dalitz plot of $\pi^+\pi^-$ vs $\pi^+\pi^-$ from E791.

Since we find that the $f_0(980)$ and possibly other higher $\pi\pi$ states are visible in the D_s, it is likely the KK mass from $J/\psi \rightarrow \phi$KK, will be similar to the KK mass in $D_s \rightarrow \pi KK$. This information may be useful to isolate the $D_s \rightarrow \phi\pi$ contributions from $KK\pi$ and to correct the absolute D_s branching ratios.

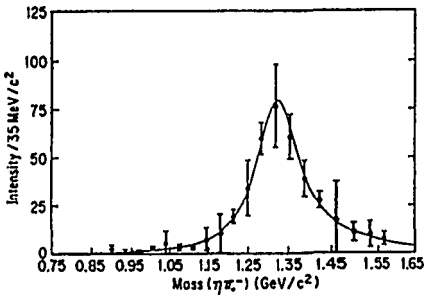
8. Search for Exotic States

The most promising candidate for an exotic state has been evidence of a resonance decaying into $\eta\pi$ in a P wave with a mass near ~1.3 GeV. Such a state would have $J^{PC} = 1^{-+}$.

The first evidence came from the GAMS experiment[45] which studied the reaction, $\pi^- p \rightarrow nX$, $X \rightarrow \eta\pi^0$ with incident pion momentum of 100 GeV. A partial wave analysis indicated a forward-backward asymmetry between a P wave signal and the D wave from the nearby $a_2(1320)$. The P wave signal had a mass and width of 1406 ± 20 MeV and 180 ± 30 MeV.

Another experiment from the BENKEI group[46] at KEK, studied the reaction $\pi^- p \rightarrow pX$, $X \rightarrow \eta\pi^+$ at 6.3 GeV incident pion momentum. A clear P wave signal near the a_2 at 1325 ± 5 MeV with a width of 126 ± 14 MeV was observed. In Figure 40 is shown the results from the BENKEI experiment. The upper plot is the D wave intensity of the a_2 resonance. The middle plot is the P wave signal showing a clear excess at the same place as the a_2. The lower plot is the phase variation between the P wave and the D wave where the D wave signal is assumed to be constant. Apparently, there is no phase variation seen between the P and D waves.

A new experiment at BNL has also studied this reaction, and this will be reported at the topical conference of this meeting by N. Cason[2].



Fitting of the Breit-Wigner formula to the D_s wave.

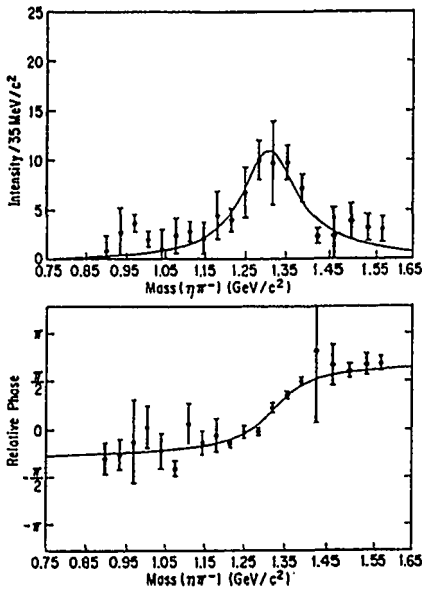


Figure 40. Partial wave results on ηπ from BENKEI.[46]

9. Summary and Outlook

The $f_0(1500)$ and $f_J(1700)$ resonances are strong glueball candidates. However, more experimental work will be very important to consolidate and confirm the evidence.

For the $f_0(1500)$, the search for non-$p\bar{p}$ production and a $K\bar{K}$ decay mode will be very important. In the future, more BES data on J/ψ decays may reveal $f_0(1500)$ evidence in 4π and 2π decays. Also, high statistics hadronic searches at BNL may add new information. Unfortunately, LEAR is no longer running, so the only hope for more $p\bar{p}$ data is from the E760 group which will still be running for charmonium physics. Perhaps they can confirm the scalar spin and find a KK decay mode.

For the $f_J(1700)$, new data will be available from BES in J/ψ decays. Much higher statistics are required for convincing spin-parity tests. Also, the $\pi\pi$ decay modes and the hadronic production of the $f_J(1700)$ require confirming measurements.

In the future, the B factories and charm experiments (E835) will provide more charm data. The weak semileptonic D_s and D decays may add much needed evidence for scalars.

REFERENCES

[1] M. Doser, these proceedings.

[2] N. Cason, these proceedings.

[3] *Hadron '95, 6th Int. Conf. On Hadron Spectroscopy*, Manchester, UK, July 10-14, 1995, edited by. M. Birse, G. Lafferty, and J. McGovern.

[4] L. Kopke and N. Wermes, Physics Reports **174**, 67 (1989).

[5] M. Chanowitz, SLAC Summer School Lectures, July 27-29, 1981.

[6] Particle Data Group, Phys. Rev. D **54**, 1 (1996).

[7] F. Close, *An Introduction to Quarks and Partons* (Academic Press, 1979).

[8] Physics of Atomic Nuclei, **57**, 1465 (1994), edited by Y. Kalashnikova, L. Kondratyuk, A. Kudryavtsev, and N. Smorodinskaya.

[9] See the talk by Thomas DeGrand in these proceedings.

[10] For a treatment of the quark model see Ref. 7.

[11] J. Weinstein, Phys. Rev. D 27,588 (1983).

[12] See the introductory treatment by W. Burcham and M. Jobes, *Nuclear and Particle Physics* (Longman Scientific & Technical, 1995).

[13] J. D. Jackson, *Classical Electrodynamics* (Wiley, New York, 1975).

[14] S. Flatte, Phys. Lett. B **63**, 224 (1976).

[15] J. Richman, *An Experimentalist's Guide to the Helicity Formalism*, CALT-60-1148, June 1984.

[16] H. Pilkuhn, *The Interactions of Hadrons* (North-Holland Publishing, 1967).
For an application of this technique, see R. Longacre, T. Lasinski, R. Rosenfeld, G. Smadja, D. Leith, and R. Cashmore, Phys. Rev. D **17**, 1795 (1978).

[17] T. Lasinski and R. Levi-Setti, *Strongly Interacting Particles*, (University of Chicago Press, 1973).

[18] L. Gray *et al.*, Phys. Rev. D 27, 307 (1983).

[19] A. Adamo *et al.*, Phys. Lett. B **287**, 368 (1992).

[20] C. Amsler *et al.*, Phys. Lett. B **342**, 433 (1995).

[21] C. Amsler *et al.*, Phys. Lett. B **353**, 571 (1995).

[22] M. Abul Hasal in, *Hadron '95 Proceedings*, July 10-14, 1995, Manchester, UK, edited by M. Birse, G. Lafferty, and J. McGovern.

[23] D. Bisello *et al.*, contributed paper to the 1987 Int. Lepton and Photon Meeting, Hamburg, July 1987.

[24] D. Bugg *et al.*, Phys. Lett. B **353**, 378 (1995).

[25] Roger Lee, Ph.D thesis, Stanford University, SLAC-Report 282, 1985.

[26] See C. Amsler and F. Close, Phys. Lett. B **353**, 385 (1995).

[27] C. Dover *et al.*, Nucl. Phys. **43**, 379 (1991).

[28] T. Kalogeropoulos *et al.*, Phys. Rev. D **24**, 1759 (1981).

[29] M. Franklin, preprint SLAC-254, 1982.

[30] C. Edwards *et al.*, Phys. Rev. Lett. **48**, 458 (1982).

[31] R. Baltrusaitus *et al.*, Phys. Rev. D **35**, 2077 (1987).

[32] A. Etkin *et al.*, Phys. Rev. D **25**, 1786 (1982)

[33] A. Etkin *et al.*, Phys. Rev. D **25**, 1786 (1982); A. Etkin *et al.*, Phys. Rev. D **25**, 2446 (1982).

[34] T. Armstrong *et al.*, Phys. Lett. B **227**,186 (1989).

[35] T. A. Armstrong *et al.*, Z. Phys. C **51**, 351(1991).

[36] This analysis is from L. Chen's Ph.D. thesis, University of Vanderbilt. The fits in this review have been performed by W. Dunwoodie on the moments from L. Chen's thesis.

[37] J. Z. Bai *et al.*, Phys. Rev. Lett. **77**, 3959 (1996).

[38] R. Baltrusaitis *et al.*, Phys. Rev. Lett. **56**, 107 (1986)

[39] J. Augustin *et al.*, Phys. Rev. Lett. **60**, 2238 (1988)

[40] D. Aston *et al.*, Phys. Lett. B **215**, 199 (1988)

[41] D. Alde *et al.*, Phys. Lett. B **177**, 120 (1986)

[42] J. Z. Bai *et al.*, Phys. Rev. Lett. **76**, 3502 (1996).

[43] G. Forconi, DPF96, Minnesota, Minn., August 1996.

[44] Preliminary results from M. Sokoloff.

[45] D. Alde *et al.*, Phys. Lett. B **205**, 205 (1988).

[46] H. Aoygi *et al.*, Nuovo Cimento A **107**, 1925 (1994).

LATTICE GAUGE THEORY FOR QCD

Thomas DeGrand
Department of Physics
University of Colorado, Boulder, CO 80309

ABSTRACT

These lectures provide an introduction to lattice methods for nonperturbative studies of Quantum Chromodynamics. Lecture 1 (Ch. 2): Basic techniques for QCD and results for hadron spectroscopy using the simplest discretizations; lecture 2 (Ch. 3): "improved actions"—what they are and how well they work; lecture 3 (Ch. 4): SLAC physics from the lattice—structure functions, the mass of the glueball, heavy quarks and $\alpha_s(M_Z)$, and $B - \bar{B}$ mixing.

© 1996 by Thomas DeGrand.

1 Introduction

The lattice[1] version of QCD was invented by Wilson[2] in 1974. It has been a fruitful source of qualitative and quantitative information about QCD, the latter especially in the years since Creutz, Jacobs, and Rebbi[3] performed the first numerical simulations of a lattice gauge theory. Lattice methods are presently the only way to compute masses and matrix elements in the strong interactions beginning with the Lagrangian of QCD and including no additional parameters. In the past few years, the quality of many lattice predictions has become very high, and they are beginning to have a large impact in the wide arena of "testing the standard model." My goal in these lectures is to give enough of an overview of the subject that an outsider will be able to make an intelligent appraisal of a lattice calculation when s/he encounters one later on.

The first lecture will describe why one puts QCD on a lattice, and how it is done. This is a long story with a lot of parts, but at the end, I will show you "standard" lattice results for light hadron spectroscopy. The main problem with these calculations is that they are so unwieldy: to get continuum-like numbers requires very large-scale numerical simulations on supercomputers, which can take years to complete (sort of like the high-energy experiments themselves, except that we do not have to stack lead bricks). We would like to reduce the computational burden of our calculations. In Lecture Two, I will describe some of the different philosophies and techniques which are currently being used to invent "improved actions." Some of these methods actually work: some QCD problems can be studied on very large work stations. Finally, in Lecture Three, I will give a survey of recent lattice results for matrix elements, using physics done at SLAC as my unifying theme.

2 Gauge Field Basics

2.1 Beginnings

The lattice is a cutoff which regularizes the ultraviolet divergences of quantum field theories. As with any regulator, it must be removed after renormalization. Contact with experiment only exists in the continuum limit, when the lattice spacing is taken to zero.

We are drawn to lattice methods by our desire to study nonperturbative phenomena. Older regularization schemes are tied closely to perturbative expansions: one calculates a process to some order in a coupling constant; divergences are removed order by order in perturbation theory. The lattice, however, is a nonperturbative cutoff. Before a calculation begins, all wavelengths less than a lattice spacing are removed. Generally, one cannot carry out analytical studies of a field theory for physically interesting parameter values. However, lattice techniques lend themselves naturally to implementation on digital computers, and one can perform more-or-less realistic simulations of quantum field theories, revealing their nonperturbative structure, on present-day computers. I think it is fair to say that little of the quantitative results about QCD which have been obtained in the last decade, could have been gotten without the use of numerical methods.

On the lattice, we sacrifice Lorentz invariance but preserve all internal symmetries, including local gauge invariance. This preservation is important for nonperturbative physics. For example, gauge invariance is a property of the continuum theory which is nonperturbative, so maintaining it as we pass to the lattice means that all of its consequences (including current conservation and renormalizability) will be preserved.

It is very easy to write down an action for scalar fields regulated by a lattice. One just replaces the space-time coordinate x_μ by a set of integers n_μ ($x_\mu = an_\mu$, where a is the lattice spacing). Field variables $\phi(x)$ are defined on sites $\phi(x_n) \equiv \phi_n$. The action, an integral over the Lagrangian, is replaced by a sum over sites

$$\beta S = \int d^4x \mathcal{L} \to a^4 \sum_n \mathcal{L}(\phi_n), \tag{1}$$

and the generating functional for Euclidean Green's functions is replaced by an ordinary integral over the lattice fields

$$Z = \int (\prod_n d\phi_n) e^{-\beta S}. \tag{2}$$

Gauge fields are a little more complicated. They carry a space-time index μ in addition to an internal symmetry index a ($A^a_\mu(x)$) and are associated with a path in space $x_\mu(s)$: a particle traversing a contour in space picks up a phase factor

$$\psi \to P(\exp\ ig \int_s dx_\mu A_\mu)\psi \tag{3}$$

$$\equiv U(s)\psi(x). \tag{4}$$

P is a path-ordering factor analogous to the time-ordering operator in ordinary quantum mechanics. Under a gauge transformation g, $U(s)$ is rotated at each end:

$$U(s) \to g^{-1}(x_\mu(s))U(s)g(x_\mu(0)). \tag{5}$$

These considerations led Wilson[2] to formulate gauge fields on a space-time lattice, as follows:

The fundamental variables are elements of the gauge group G which live on the links of a four-dimensional lattice, connecting x and $x+\mu$: $U_\mu(x)$, with $U_\mu(x+\mu)^\dagger = U_\mu(x)$

$$U_\mu(n) = \exp(igaT^a A^a_\mu(n)) \tag{6}$$

for $SU(N)$ (g is the coupling, a the lattice spacing, A_μ the vector potential, and T^a is a group generator).

Under a gauge transformation, link variables transform as

$$U_\mu(x) \to V(x)U_\mu(x)V(x+\hat{\mu})^\dagger \tag{7}$$

and site variables as

$$\psi(x) \to V(x)\psi(x), \tag{8}$$

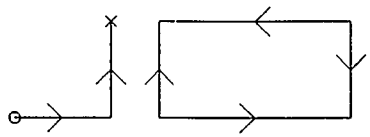
so the only gauge invariant operators we can use as order parameters are matter fields connected by oriented "strings" of U's [Fig. 1(a)]

$$\bar{\psi}(x_1)U_\mu(x_1)U_\mu(x_1+\hat{\mu})\ldots\psi(x_2) \tag{9}$$

or closed-oriented loops of U's [Fig. 1(b)]

$$\mathrm{Tr}\ldots U_\mu(x)U_\mu(x+\hat{\mu})\ldots \to \mathrm{Tr}\ldots U_\mu(x)V^\dagger(x+\hat{\mu})V(x+\hat{\mu})U_\mu(x+\hat{\mu})\ldots. \tag{10}$$

An action is specified by recalling that the classical Yang-Mills action involves the curl of A_μ, $F_{\mu\nu}$. Thus, a lattice action ought to involve a product of U_μ's around some closed contour. There is enormous arbitrariness at this point. We are trying to write down a bare action. So far, the only requirement we want to impose is gauge invariance, and that will be automatically satisfied for actions built of powers of traces of U's around closed loops, with arbitrary coupling constants. If we assume that the gauge fields are smooth, we can expand the link variables in a power series in gaA_μ's. For almost any closed loop, the leading term in the expansion will be proportional to $F^2_{\mu\nu}$. We might want our action to have the same normalization as the continuum action. This would provide one constraint among the lattice coupling constants.



(a) (b)

Figure 1: Gauge invariant observables are either (a) ordered chains ("strings") of links connecting quarks and antiquarks, or (b) closed loops of link variables.

The simplest contour has a perimeter of four links. In $SU(N)$,

$$\beta S = \frac{2N}{g^2}\sum_n\sum_{\mu>\nu}\mathrm{Re\ Tr}\ (1 - U_\mu(n)U_\nu(n+\hat{\mu})U^\dagger_\mu(n+\hat{\nu})U^\dagger_\nu(n)). \tag{11}$$

This action is called the "plaquette action" or the "Wilson action" after its inventor. The lattice parameter $\beta = 2N/g^2$ is often written instead of $g^2 = 4\pi\alpha_s$.

Let us see how this action reduces to the standard continuum action. Specializing to the U(1) gauge group, and slightly redefining the coupling,

$$S = \frac{1}{g^2}\sum_n\sum_{\mu>\nu}\mathrm{Re}\ (1 - \exp(iga[A_\mu(n) + A_\nu(n+\hat{\mu}) - A_\mu(n+\hat{\nu}) - A_\nu(n)])). \tag{12}$$

The naive continuum limit is taken by assuming that the lattice spacing a is small, and Taylor expanding

$$A_\mu(n+\hat{\nu}) = A_\mu(n) + a\partial_\nu A_\mu(n) + \ldots, \tag{13}$$

so the action becomes

$$\beta S = \frac{1}{g^2}\sum_n\sum_{\mu>\nu} 1 - \mathrm{Re}\ (\exp(iga[a(\partial_\nu A_\mu - \partial_\mu A_\nu) + O(a^2)])) \tag{14}$$

$$= \frac{1}{4g^2}a^4\sum_n\sum_{\mu\nu} g^2F^2_{\mu\nu} + \ldots \tag{15}$$

$$= \frac{1}{4}\int d^4x F^2_{\mu\nu} \tag{16}$$

transforming the sum on sites back to an integral.

2.2 Relativistic Fermions on the Lattice

Defining fermions on the lattice presents a new problem: doubling. The naive procedure of discretizing the continuum fermion action results in a lattice model with many more low energy modes than one originally anticipated. Let's illustrate this with free field theory.

The free Euclidean fermion action in the continuum is

$$S = \int d^4x[\bar{\psi}(x)\gamma_\mu\partial_\mu\psi(x) + m\bar{\psi}(x)\psi(x)]. \tag{17}$$

One obtains the so-called naive lattice formulation by replacing the derivatives by symmetric differences: we explicitly introduce the lattice spacing a in the denominator and write

$$S_L^{naive} = \sum_{n,\mu}\bar{\psi}_n\frac{\gamma_\mu}{2a}(\psi_{n+\mu} - \psi_{n-\mu}) + m\sum_n\bar{\psi}_n\psi_n. \tag{18}$$

The propagator is:

$$G(p) = (i\gamma_\mu \sin p_\mu a + ma)^{-1} = \frac{-i\gamma_\mu \sin p_\mu a + ma}{\sum_\mu \sin^2 p_\mu a + m^2a^2}. \tag{19}$$

We identify the physical spectrum through the poles in the propagator, at $p_0 = iE$:

$$\sinh^2 Ea = \sum_j \sin^2 p_j a + m^2a^2. \tag{20}$$

The lowest energy solutions are the expected ones at $p = (0,0,0)$, $E \simeq \pm m$, but there are other degenerate ones, at $p = (\pi,0,0)$, $(0,\pi,0,)$, $\ldots(\pi,\pi,\pi)$. This is a model for eight light fermions, not one.

(a) Wilson Fermions

There are two ways to deal with the doublers. The first way is to alter the dispersion relation so that it has only one low-energy solution. The other solutions are forced to $E \simeq 1/a$ and become very heavy as a is taken to zero. The simplest version of this solution (and almost the only one seen in the literature until recently) is due to Wilson: add a second-derivative-like term

$$S^W = -\frac{r}{2a}\sum_{n,\mu}\bar{\psi}_n(\psi_{n+\mu} - 2\psi_n + \psi_{n-\mu}) \tag{21}$$

to S^{naive}. The parameter r must lie between 0 and 1; $r = 1$ is almost always used and "$r = 1$" is implied when one speaks of using "Wilson fermions." The propagator is

$$G(p) = \frac{-i\gamma_\mu \sin p_\mu a + ma - r\sum_\mu(\cos p_\mu a - 1)}{\sum_\mu \sin^2 p_\mu a + (ma - r\sum_\mu(\cos p_\mu a - 1))^2}. \tag{22}$$

It has one pair of poles at $p_\mu \simeq (\pm im, 0, 0, 0)$, plus other poles at $p \simeq r/a$. In the continuum, these states become infinitely massive and decouple (although decoupling is not trivial to prove).

With Wilson fermions, it is conventional to use not the mass but the "hopping parameter" $\kappa = \frac{1}{2}(ma + 4r)^{-1}$, and to rescale the fields $\psi \to \sqrt{2\kappa}\psi$. The action for an interacting theory is then written

$$S = \sum_n \bar{\psi}_n\psi_n - \kappa\sum_{n\mu}(\bar{\psi}_n(r - \gamma_\mu)U_\mu(n)\psi_{n+\mu} + \bar{\psi}_n(r + \gamma_\mu)U_\mu^\dagger\psi_{n-\mu}). \tag{23}$$

Wilson fermions are closest to the continuum formulation—there is a four-component spinor on every lattice site for every color and/or flavor of quark. Constructing currents and states is just like in the continuum.

However, the Wilson term explicitly breaks chiral symmetry. This has the consequence that the zero bare quark mass limit is not respected by interactions; the quark mass is additively renormalized. The value of κ_c, the value of the hopping parameter at which the pion mass vanishes, is not known a priori before beginning a simulation; it must be computed. This is done in a simulation involving Wilson fermions by varying κ and watching the pion mass extrapolate quadratically to zero as $m_\pi^2 \simeq \kappa_c - \kappa$ ($\kappa_c - \kappa$ is proportional to the quark mass for small m_q). For the lattice person, this is unpleasant since preliminary calculations are required to find "interesting" κ values. For the outsider trying to read lattice papers, it is unpleasant because the graphs in the lattice paper typically list κ, and not quark (or pion) mass, so the reader does not know "where" the simulation was done. Note also that the relation between κ and physical mass changes with lattice coupling β.

(b) Staggered or Kogut-Susskind Fermions

In this formulation, one reduces the number of fermion flavors by using one-component "staggered" fermion fields rather than four-component Dirac spinors. The Dirac spinors are constructed by combining staggered fields on different lattice sites. Staggered fermions preserve an explicit chiral symmetry as $m_q \to 0$

even for finite lattice spacing, as long as all four flavors are degenerate. They are preferred over Wilson fermions in situations in which the chiral properties of the fermions dominate the dynamics—for example, in studying the chiral restoration/deconfinement transition at high temperature. They also present a computationally less intense situation from the point of view of numerics than Wilson fermions, for the trivial reason that there are less variables. However, flavor symmetry and translational symmetry are all mixed together. Construction of meson and baryon states (especially the Δ) is more complicated than for Wilson fermions.[4]

2.3 Enter the Computer

A "generic" Monte Carlo simulation in QCD breaks up naturally into two parts. In the "configuration generation" phase, one constructs an ensemble of states with the appropriate Boltzmann weighting: we compute observables simply by averaging N measurements using the field variables $\phi^{(i)}$ appropriate to the sample

$$\langle\Gamma\rangle \simeq \bar{\Gamma} \equiv \frac{1}{N}\sum_{i=1}^{N}\Gamma[\phi^{(i)}]. \tag{24}$$

As the number of measurements N becomes large, the quantity $\bar{\Gamma}$ will become a Gaussian distribution about a mean value. Its standard deviation is[5]

$$\sigma_\Gamma^2 = \frac{1}{N}\left(\frac{1}{N}\sum_{i=1}^{N}|\Gamma[\phi^{(i)}]|^2 - \bar{\Gamma}^2\right). \tag{25}$$

The idea of essentially all simulation algorithms is that one constructs a new configuration of field variables from an old one. One begins with some simple field configuration and monitors observables while the algorithm steps along. After some number of steps, the value of observables will appear to become independent of the starting configuration. At that point, the system is said to be "in equilibrium" and Eq. (24) can be used to make measurements.

The simplest method for generating configurations is called the Metropolis[6] algorithm. It works as follows: From the old configuration $\{\phi\}$ with action βS, transform the variables (in some reversible way) to a new trial configuration $\{\phi\}'$ and compute the new action $\beta S'$. Then, if $S' < S$, make the change and update all the variables; if not, make the change with probability $\exp(-\beta(S'-S))$.

Why does it work? In equilibrium, the rate at which configurations i turn into configurations j is the same as the rate for the back reaction $j \to i$. The rate of change is (number of configurations) $\times$ (probability of change). Assume for the sake of the argument that $S_i < S_j$. Then the rate $i \to j$ is $N_i P(i \to j)$ with $P(i \to j) = \exp(-\beta(S_j - S_i))$ and the rate $j \to i$ is $N_j P(j \to i)$ with $P(j \to i) = 1$. Thus, $N_i/N_j = \exp(-\beta(S_i - S_j))$.

If you have any interest at all in the techniques I am describing, you should write a little Monte Carlo program to simulate the two-dimensional Ising model. Incidentally, the favorite modern method for pure gauge models is overrelaxation.[7]

One complication for QCD which spin models don't have is fermions. The fermion path integral is not a number and a computer can't simulate fermions directly. However, one can formally integrate out the fermion fields. For n_f degenerate flavors of staggered fermions,

$$Z = \int [dU][d\psi][d\bar{\psi}]\exp(-\beta S(U) - \sum_{i=1}^{n_f}\bar{\psi}M\psi) \tag{26}$$

$$= \int [dU](\det M)^{n_f/2}\exp(-\beta S(U)). \tag{27}$$

(One can make the determinant positive-definite by writing it as $\det(M^\dagger M)^{n_f/4}$.) The determinant introduces a nonlocal interaction among the U's:

$$Z = \int [dU]\exp(-\beta S(U) - \frac{n_f}{4}\mathrm{Tr}\ln(M^\dagger M)). \tag{28}$$

All large-scale dynamical fermion simulations today generate configurations using some variation of the microcanonical ensemble. That is, they introduce momentum variables P conjugate to the U's and integrate Hamilton's equations through a simulation time t

$$\dot{U} = iPU \tag{29}$$

$$\dot{P} = -\frac{\partial S_{eff}}{\partial U}. \tag{30}$$

The integration is done numerically by introducing a timestep Δt. The momenta are repeatedly refreshed by bringing them in contact with a heat bath, and the method is thus called Refreshed or Hybrid Molecular Dynamics.[8]

For special values of n_f (multiples of two for Wilson fermions or of four for staggered fermions), the equations of motion can be derived from a local Hamiltonian, and in that case, Δt systematics in the integration can be removed by an extra Metropolis accept/reject step. This method is called Hybrid Monte Carlo.[9]

The reason for the use of these small timestep algorithms is that for any change in any of the U's, $(M^\dagger M)^{-1}$ must be recomputed. When Eq. (30) is integrated, all

of the U's in the lattice are updated simultaneously, and only one matrix inversion is needed per change of all the bosonic variables.

The major computational problem dynamical fermion simulations face is inverting the fermion matrix M. It has eigenvalues with a very large range—from 2π down to $m_q a$—and in the physically interesting limit of small m_q, the matrix becomes ill-conditioned. At present, it is necessary to compute at unphysically heavy values of the quark mass and to extrapolate to $m_q = 0$. The standard inversion technique today is one of the variants of the conjugate gradient algorithm.[10]

2.4 Taking the Continuum Limit, and Producing a Number in MeV

When we define a theory on a lattice, the lattice spacing a is an ultraviolet cutoff and all the coupling constants in the action are the bare couplings defined with respect to it. When we take a to zero, we must also specify how $g(a)$ behaves. The proper continuum limit comes when we take a to zero holding physical quantities fixed, not when we take a to zero holding the couplings fixed.

On the lattice, if all quark masses are set to zero, the only dimensionful parameter is the lattice spacing, so all masses scale like $1/a$. Said differently, one computes the dimensionless combination $am(a)$. One can determine the lattice spacing by fixing one mass from experiment. Then all other dimensionful quantities can be predicted.

Now imagine computing some masses at several values of the lattice spacing. (Pick several values of the bare parameters at random and calculate masses for each set of couplings.) Our calculated mass ratios will depend on the lattice cutoff. The typical behavior will look like

$$(am_1(a))/(am_2(a)) = m_1(0)/m_2(0) + O(m_1 a) + O((m_1 a)^2) + \dots . \qquad (31)$$

The leading term does not depend on the value of the UV cutoff, while the other terms do. The goal of a lattice calculation (like the goal of almost any calculation in quantum field theory) is to discover the value of some physical observable as the UV cutoff is taken to be very large, so the physics is in the first term. Everything else is an artifact of the calculation. We say that a calculation "scales" if the a-dependent terms in Eq. (31) are zero or small enough that one can extrapolate to $a = 0$, and generically refer to all the a-dependent terms as "scale violations."

We can imagine expressing each dimensionless combination $am(a)$ as some function of the bare coupling(s) $\{g(a)\}$, $am = f(\{g(a)\})$. As $a \to 0$, we must tune the set of couplings $\{g(a)\}$ so

$$\lim_{a\to 0} \frac{1}{a} f(\{g(a)\}) \to \text{constant}. \qquad (32)$$

From the point of view of the lattice theory, we must tune $\{g\}$ so that correlation lengths $1/ma$ diverge. This will occur only at the locations of second- (or higher-) order phase transitions in the lattice theory.

Recall that the β-function is defined by

$$\beta(g) = a\frac{dg(a)}{da} = \frac{dg(a)}{d\ln(1/\Lambda a)}. \qquad (33)$$

(There is actually one equation for each coupling constant in the set. Λ is a dimensional parameter introduced to make the argument of the logarithm dimensionless.) At a critical point, $\beta(g_c) = 0$. Thus, the continuum limit is the limit

$$\lim_{a\to 0}\{g(a)\} \to \{g_c\}. \qquad (34)$$

Continuum QCD is a theory with one dimensionless coupling constant. In QCD, the fixed point is $g_c = 0$, so we must tune the coupling to vanish as a goes to zero.

Pushing this a little further, the two-loop β-function is prescription independent,

$$\beta(g) = -b_1 g^3 + b_2 g^5, \qquad (35)$$

and so if we think that the lattice theory is reproducing the continuum, and if we think that the coupling constant is small enough that the two-loop β-function is correct, we might want to observe perturbative scaling, or "asymptotic scaling," m/Λ fixed, or a varying with g as

$$a\Lambda = \left(\frac{1}{g^2(a)}\right)^{b_2/(2b_1^2)} \exp\left(-\frac{1}{b_1 g^2(a)}\right). \qquad (36)$$

Asymptotic scaling is not scaling. Scaling means that dimensionless ratios of physical observables do not depend on the cutoff. Asymptotic scaling involves perturbation theory and the definition of coupling constants. One can have one without the other. (In fact, one can always define a coupling constant so that one quantity shows asymptotic scaling.)

And this is not all. There are actually two parts to the problem of producing a number to compare with experiment. One must first see scaling. Then one needs

to set the scale by taking some experimental number as input. A complication that you may not have thought of is that the theory we simulate on the computer is different from the real world. For example, a commonly used approximation is called the "quenched approximation": one neglects virtual quark loops but includes valence quarks in the calculation. The pion propagator is the propagator of a $\bar{q}q$ pair, appropriately coupled, moving in a background of gluons. This theory almost certainly does not have the same spectrum as QCD with six flavors of dynamical quarks with their appropriate masses. (In fact, an open question in the lattice community is what is the accuracy of quenched approximation?) Using one mass to set the scale from one of these approximations to the real world might not give a prediction for another mass which agrees with experiment. We will see examples where this is important.

2.5 Spectroscopy Calculations

"In a valley something like a race took place. A little crowd watched bunches of cars, each consisting of two 'ups' and a 'down' one, starting in regular intervals and disappearing in about the same direction. 'It is the measurement of the proton mass,' commented Mr. Strange, 'they have done it for ages. A very dull job, I am glad I am not in the game.'"[11]

Masses are computed in lattice simulations from the asymptotic behavior of Euclidean-time correlation functions. A typical (diagonal) correlator can be written as

$$C(t) = \langle 0|O(t)O(0)|0\rangle. \tag{37}$$

Making the replacement

$$O(t) = e^{Ht}Oe^{-Ht} \tag{38}$$

and inserting a complete set of energy eigenstates, Eq. (37) becomes

$$C(t) = \sum_n |\langle 0|O|n\rangle|^2 e^{-E_n t}. \tag{39}$$

At large separation, the correlation function is approximately

$$C(t) \simeq |\langle 0|O|1\rangle|^2 e^{-E_1 t}, \tag{40}$$

where E_1 is the energy of the lightest state which the operator O can create from the vacuum. If the operator does not couple to the vacuum, then in the limit of large t, one hopes to find the mass E_1 by measuring the leading exponential falloff of the correlation function, and most lattice simulations begin with that measurement. If the operator O has poor overlap with the lightest state, a reliable value for the mass can be extracted only at a large time t. In some cases, that state is the vacuum itself, in which $E_1 = 0$. Then one looks for the next higher state—a signal which disappears into the constant background. This makes the actual calculation of the energy more difficult.

This is the basic way hadronic masses are found in lattice gauge theory. The many calculations differ in important specific details of choosing the operators $O(t)$.

2.6 Recent Results

Today's supercomputer QCD simulations range from $16^3 \times 32$ to $32^3 \times 100$ points and run from hundreds (quenched) to thousands (full QCD) of hours on the fastest supercomputers in the world.

Results are presented in four common ways. Often one sees a plot of some bare parameter versus another bare parameter. This is not very useful if one wants to see continuum physics, but it is how we always begin. Next, one can plot a dimensionless ratio as a function of the lattice spacing. These plots represent quantities like Eq. (31). Both axes can show mass ratios. Examples of such plots are the so-called Edinburgh plot (m_N/m_ρ versus m_π/m_ρ) and the Rome plot (m_N/m_ρ versus $(m_\pi/m_\rho)^2$). These plots can answer continuum questions (how does the nucleon mass change if the quark mass is changed?) or can be used to show (or hide) scaling violations. Plots of one quantity in MeV versus another quantity in MeV are typically rather heavily processed after the data comes off the computer.

Let's look at some examples of spectroscopy, done in the "standard way," with the plaquette gauge action and Wilson or staggered quarks. I will restrict the discussion to quenched simulations because only there are the statistical errors small enough to be interesting to a nonlattice audience. Most dynamical fermion simulations are unfortunately so noisy that it is hard to subject them to detailed questioning.

Figure 2 shows a plot of the rho mass as a function of the size of the simulation, for several values of the quark mass (or m_π/m_ρ ratio in the simulation) and lattice

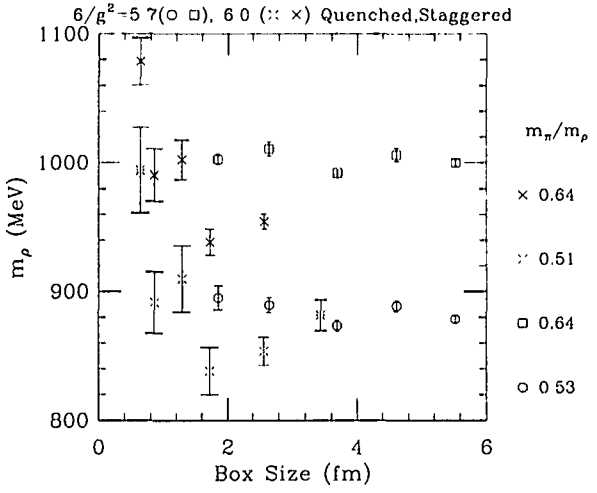


Figure 2: Rho mass vs box size.

spacing ($\beta = 6.0$ is $a \simeq 0.1$ fm and $\beta = 5.7$ is about twice that).[12] This picture shows that if the box has a diameter bigger than about 2 fm, the rho mass is little affected, but if the box is made smaller, the rho is "squeezed" and its mass rises.

Next, we look at an Edinburgh plot, Fig. 3 (Ref. 12). The different plotting symbols correspond to different bare couplings or (equivalently) different lattice spacings. This plot shows large scaling violations: mass ratios from different lattice spacings do not lie on top of each other. We can expose the level of scaling violations by taking "sections" through the plot and plot m_N/m_ρ at fixed values of the quark mass (fixed m_π/m_ρ) versus lattice spacing, in Fig. 4.

Now for some examples of scaling tests in the chiral limit. (Extrapolating to the chiral limit is a whole can of worms on its own, but for now, let's assume we can do it.) Figure 5 shows the nucleon to rho mass ratio (at chiral limit) versus lattice spacing (in units of $1/m_\rho$) for staggered[12] and Wilson[13] fermions. The "analytic" result is from strong coupling. The two curves are quadratic extrapolations to zero lattice spacing using different sets of points from the staggered data set. The burst is from a linear extrapolation to the Wilson data. The reason I show

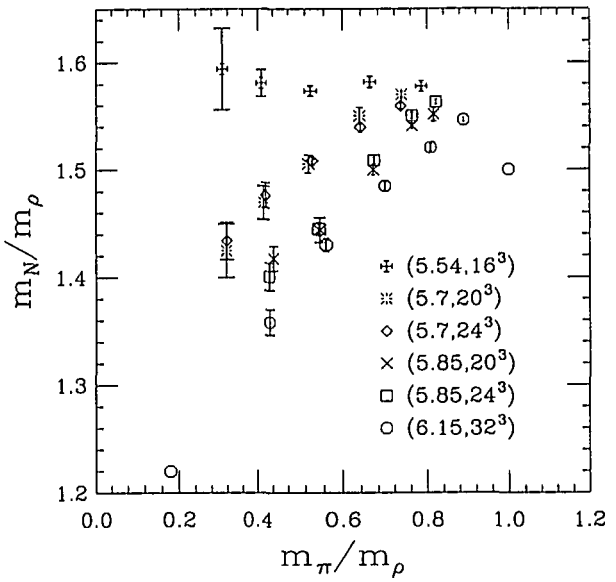


Figure 3: An Edinburgh plot for staggered fermions, from the MILC Collaboration.

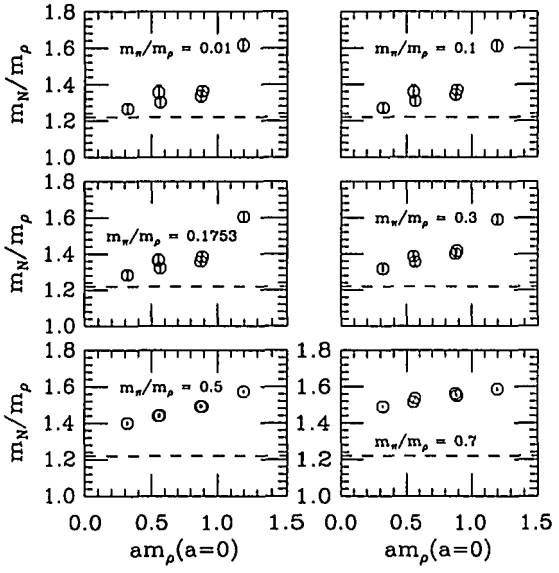


Figure 4: "Sections" through the Edinburgh plot.

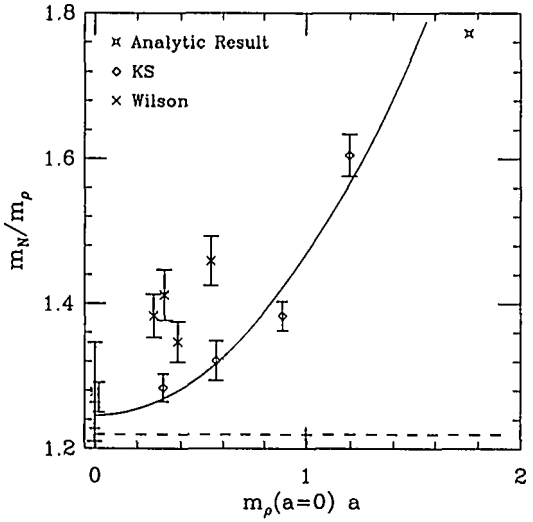


Figure 5: Nucleon to rho mass ratio (at chiral limit) vs lattice spacing (in units of $1/m_\rho$).

this figure is that one would like to know if the continuum limit of quenched spectroscopy "predicts" the real-world N/ρ mass ratio of 1.22 or not. The answer (unfortunately) depends on how the reader chooses to extrapolate.

Another test[14] is the ratio of the rho mass to the square root of the string tension, Fig. 6. Here the diamonds are staggered data and the crosses from the Wilson action. Scaling violations are large, but the eye extrapolates to something close to data (the burst).

Finally, despite Mr. Strange, very few authors have attempted to extrapolate to infinite volume, zero lattice spacing, and to physical quark masses, including the strange quark. One group which did, Butler *et al.*,[13] produced Fig. 7. The squares are lattice data, the octagons are the real world. They look quite similar within errors. Unfortunately, to produce this picture, they had to build their own computer.

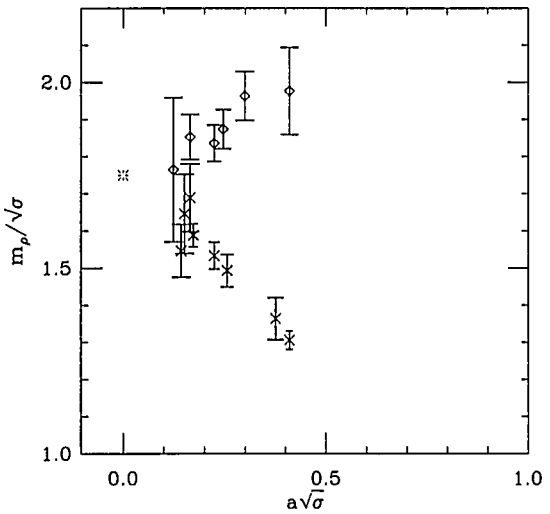


Figure 6: Scaling test for the rho mass in terms of the string tension, with data points labeled as in Fig. 5.

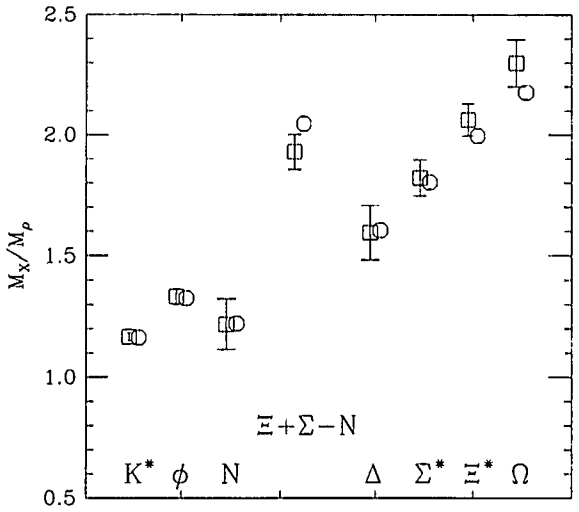


Figure 7: Quenched approximation mass ratios from Ref. 13.

3 Doing a Better Job—Maybe!

The slow approach to scaling presents a practical problem for QCD simulations, since it means that one needs to work at small lattice spacing. This is expensive. The cost of a Monte Carlo simulation in a box of physical size L with lattice spacing a and quark mass m_q scales roughly as

$$(\frac{L}{a})^4(\frac{1}{a})^{1-2}(\frac{1}{m_q})^{2-3}, \tag{41}$$

where the 4 is just the number of sites, the 1–2 is the cost of "critical slowing down"—the extent to which successive configurations are correlated, and the 2–3 is the cost of inverting the fermion propagator, plus critical slowing down from the nearly massless pions. The problem is that one needs a big computer to do anything.

However, all the simulations I described in the last lecture were done with a particular choice of lattice action: the plaquette gauge action, and either Wilson or staggered quarks. While those actions are the simplest ones to program, they

are just particular arbitrary choices of bare actions. Can one invent a better lattice discretization, which has smaller scaling violations?

People are trying many approaches. One could just write down a slightly more complicated action, include some parameters which can be tuned, do a spectroscopy calculation, and see if there is any improvement as the parameters are varied. The problem with this method is that it is like hunting for a needle in a multidimensional haystack—there are so many possible terms to add. One needs an organizing principle.

3.1 Improvement Based on Naive Dimensional Analysis

The simplest idea is to use the naive canonical dimensionality of operators to guide us in our choice of improvement. If we perform a naive Taylor expansion of a lattice operator like the plaquette, we find that it can be written as

$$\begin{aligned} 1-\frac{1}{3}\mathrm{Re\ Tr}U_{plaq} = \; & r_0 \mathrm{Tr}F_{\mu\nu}^2 + a^2[r_1 \textstyle\sum_{\mu\nu} \mathrm{Tr}D_\mu F_{\mu\nu} D_\mu F_{\mu\nu} + \\ & r_2 \textstyle\sum_{\mu\nu\sigma} \mathrm{Tr}D_\mu F_{\nu\sigma} D_\mu F_{\nu\sigma} + \\ & r_3 \textstyle\sum_{\mu\nu\sigma} \mathrm{Tr}D_\mu F_{\mu\sigma} D_\nu F_{\nu\sigma}] + \\ & + O(a^4). \end{aligned} \tag{42}$$

The expansion coefficients have a power series expansion in the coupling, $r_j = A_j + g^2 B_j + \ldots$ and the expectation value of any operator T computed using the plaquette action will have an expansion

$$\langle T(a) \rangle = \langle T(0) \rangle + O(a) + O(g^2 a) + \ldots . \tag{43}$$

Other loops have a similar expansion, with different coefficients. Now the idea is to take the lattice action to be a minimal subset of loops and systematically remove the a^n terms for physical observables order by order in n by taking the right linear combination of loops in the action.

$$S = \sum_j c_j O_j \tag{44}$$

with

$$c_j = c_j^0 + g^2 c_j^1 + \ldots . \tag{45}$$

This method was developed by Symanzik and co-workers[15-17] ten years ago.

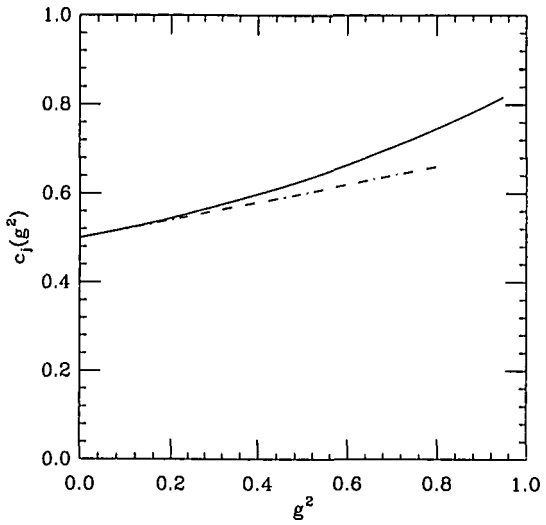


Figure 8: The value of some parameter in a lattice action for which physical observables have no a^n errors. The dotted line is the lowest order perturbative expectation.

To visualize this technique, look at Fig. 8. We imagine parameterizing the coefficients of various terms in the lattice action, which for a pure gauge theory could be a simple plaquette, a 1×2 closed loop, the square of the 1×2 loop, and so on, as some function of g^2. "Tree-level improvement" involves specifying the value of the j-th coefficient $c_j(g^2)$ at $g^2 = 0$. As we move away from $g^2 = 0$, the value of $c_j(g^2)$ for which observables calculated using the lattice action have no errors through the specified exponent n (no a^n errors) will trace out a trajectory in coupling constant space. For small g^2, the variation should be describable by perturbation theory, Eq. (45), but when g^2 gets large, we would not expect that perturbation theory would be a good guide.

The most commonly used "improved" fermion action is the "Sheikholeslami-Wohlert"[18] or "clover" action, an order a^2 improved Wilson action. The original Wilson action has $O(a)$ errors in its vertices, $S_W = S_c + O(a)$. This is corrected by making a field redefinition

$$\psi(x) \to \psi'(x) = \; \psi(x) + \tfrac{ia}{4}\gamma_\mu D_\mu \psi \tag{46}$$

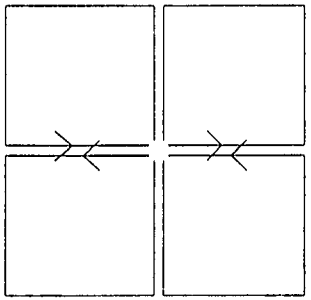


Figure 9: The "clover term."

$$\bar{\psi}(x) \to \bar{\psi}'(x) = \bar{\psi}(x) + \tfrac{ia}{4}\gamma_\mu \bar{\psi} D_\mu, \tag{47}$$

and the net result is an action with an extra lattice anomalous magnetic moment term,

$$S_{SW} - \frac{iag}{4}\bar{\psi}(x)\sigma_{\mu\nu}F_{\mu\nu}\psi(x). \tag{48}$$

It is called the "clover" action because the lattice version of $F_{\mu\nu}$ is the sum of paths shown in Fig. 9.

Studies performed at the time showed that this program did not improve scaling for the pure gauge theory (in the sense that the cost of simulating the more complicated action was greater than the savings from using a larger lattice spacing.) The whole program was re-awakened in the last few years by Lepage and collaborators,[19] and variations of this program give the most widely used "improved" lattice actions.

3.2 Nonperturbative Determination of Coefficients

Although I am breaking chronological order, the simplest approach to Symanzik improvement is the newest. The idea[20] is to force the lattice to obey various desirable identities to some order in a, by tuning parameters until the identities are satisfied by the simulations. That is, we try to find the solid line in Fig. 8 by doing simulations. Then use the action to calculate other things and test to see if scaling is improved. One example is the PCAC relation

$$\partial_\mu A^a_\mu = 2m^a_P + O(a), \tag{49}$$

where the axial and pseudoscalar currents are just

$$A^a_\mu(x) = \bar{\psi}(x)\gamma_\mu\gamma_5\frac{1}{2}\tau^a\psi(x) \tag{50}$$

and

$$P^a(x) = \bar{\psi}(x)\gamma_5\frac{1}{2}\tau^a\psi(x) \tag{51}$$

(τ^a is an isospin index.) The PCAC relation for the quark mass is

$$m \equiv \frac{1}{2}\frac{\langle\partial_\mu A^a_\mu O^a\rangle}{\langle P^a O^a\rangle} + O(a). \tag{52}$$

Now the idea is to take some Symanzik-improved action, with the improvement coefficients allowed to vary, and perform simulations in a little box with some particular choice of boundary conditions for the fields. Parameters which can be tuned include the c_{SW} in the clover term $i/4c_{SW}a\sigma_{\mu\nu}F_{\mu\nu}$ and the ones used for more complicated expressions for the currents

$$A_\mu = Z_A[(1 + b_A am_q)A^a_\mu + c_A a\partial_\mu P^a] \tag{53}$$

$$P^a = Z_P(1 + b_P am_q)P^a. \tag{54}$$

They are varied until the quark mass, defined in Eq. (52), is independent of location in the box or of the boundary conditions. Figures 10 and 11 illustrate what can be done with this tuning procedure. It is still too soon for definitive tests of scaling with this procedure.

3.3 Improving Perturbation Theory

The older version of Symanzik improvement uses lattice perturbation theory to compute the coefficients of the operators in the action. The idea here is to find a new definition of g^2 for which the solid line in Fig. 8 is transformed into a straight line (compare Fig. 12).

Let's make a digression into lattice perturbation theory.[21] It has three major uses. First, we need to relate lattice quantities (like matrix elements) to continuum

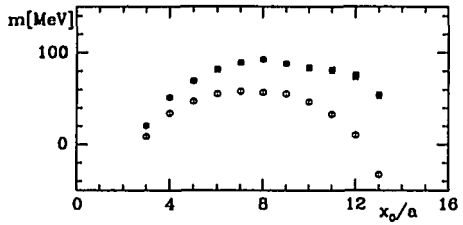


Figure 10: Values of the quark mass as computed from the axial and pseudoscalar currents, using the Wilson action. The open and full symbols correspond to different boundary conditions on the gauge fields.

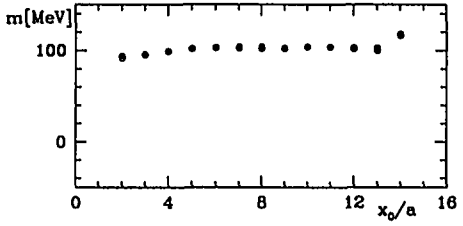


Figure 11: Same as previous figure, but now with improved action and operators.

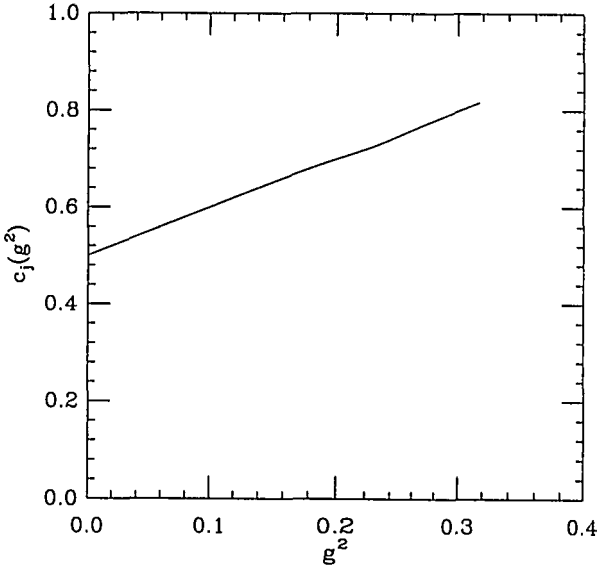


Figure 12: Same as Fig. 8, but now with a redefined coupling constant g_R^2, to make the "improvement line" linear in g_R^2.

ones: $O^{cont}(\mu) = Z(\mu a, g(a))O^{latt}(a)$. This happens because the renormalization of an operator is slightly different in the two schemes. In perturbation theory, Z has an expansion in powers of g^2. Second, we can use perturbation theory to understand and check numerical calculations when the lattice couplings are very small. Finally, one can use perturbative ideas to motivate nonperturbative improvement schemes.[22]

Perturbation theory for lattice actions is just like any other kind of perturbation theory (only much messier). One expands the Lagrangian into a quadratic term and interaction terms, and constructs the propagator from the quadratic terms:

$$\mathcal{L} = A_\mu(x)\rho_{\mu\nu}(x-y)A_\nu(y) + gA^3 + \ldots \quad (55)$$

$$= \mathcal{L}_0 + \mathcal{L}_I. \quad (56)$$

For example, the gluon propagator in Feynman gauge for the Wilson action is

$$D_{\mu\nu}(q) = \frac{g_{\mu\nu}}{\sum_\mu(1-\cos(q_\mu a))}. \quad (57)$$

To do perturbation theory for any system (not just the lattice), one has to do three things: one has to fix the renormalization scheme (RS) (define a coupling), specify the scale at which the coupling is defined, and determine a numerical value for the coupling at that scale. All of these choices are arbitrary, and any perturbative calculation is intrinsically ambiguous.

Any object which has a perturbative expansion can be written

$$O(Q) = c_0 + c_1(Q/\mu, RS)\alpha_s(\mu, RS) + c_2(Q/\mu, RS)\alpha_s(\mu, RS)^2 + \ldots . \quad (58)$$

In perturbative calculations, we truncate the series after a fixed number of terms and implicitly assume that's all there is. The coefficients $c_i(Q/\mu, RS)$ and the coupling $\alpha_s(\mu, RS)$ depend on the renormalization scheme and choice of scale μ. The guiding rule of perturbation theory[21] is "For a good choice of expansion the uncalculated higher order terms should be small." A bad choice has big coefficients.

There are many ways to define a coupling: The most obvious is the bare coupling; as we will see shortly, it is a poor expansion parameter. Another possibility is to define the coupling from some physical observable. One popular choice is to use the heavy quark potential at very high momentum transfer to define

$$V(q) \equiv 4\pi C_f \frac{\alpha_V(q)}{q^2}. \quad (59)$$

There are also several possibilities for picking a scale: One can use the bare coupling, then $\mu = 1/a$ the lattice spacing. One can guess the scale or play games just like in the continuum. One game is the Lepage-Mackenzie q^* prescription: find the "typical" momentum transfer q^* for a process involving a loop graph by pulling $\alpha_s(q)$ out of the loop integral and set

$$\alpha_s(q^*)\int d^4q\xi(q) = \int d^4q\xi(q)\alpha_s(q). \quad (60)$$

To find q^*, write $\alpha_s(q) = \alpha_s(\mu) + b\ln(q^2/\mu^2)\alpha_s(\mu)^2 + \ldots$, and similarly for $\alpha_s(q^*)$, insert these expressions into Eq. (60) and compare the $\alpha_s(\mu)^2$ terms, to get

$$\ln(q^*) = \int d^4q \ln(q)\xi / \int d^4q\xi. \quad (61)$$

This is the lattice analog of the Brodsky-Lepage-Mackenzie[23] prescription in continuum PT.

Finally, one must determine the coupling: If one uses the bare lattice coupling, it is already known. Otherwise, one can compute it in terms of the bare coupling:

$$\alpha_{\overline{MS}}(s/a) = \alpha_0 + (5.88 - 1.75\ln s)\alpha_0^2 + (43.41 - 21.89\ln s + 3.06\ln^2 s)\alpha_0^3 + \ldots . \quad (62)$$

Or one can determine it from something one measures on the lattice, which has a perturbative expansion. For example,

$$-\ln\langle\frac{1}{3}\mathrm{Tr}U_{plaq}\rangle = \frac{4\pi}{3}\alpha_P(3.41/a)(1 - 1.185\alpha_P) \quad (63)$$

(to this order, $\alpha_P = \alpha_V$). Does "improved perturbation theory" actually improve perturbative calculations? In many cases, yes: some examples are shown in Fig. 13 from Ref. 22: On the upper left, we see a calculation of the average link in Landau gauge, from simulations (octagons) and then from lowest-order perturbative calculations using the bare coupling (crosses) and α_V and $\alpha_{\overline{MS}}$ (diamonds and squares). In the upper right panel, we see how the lattice prediction of an observable involving the two-by-two Wilson loop depends on the choice of momentum q^*/a (at $\beta = 6.2$, a rather weak value of the bare coupling) in the running coupling constant. The burst is the value of the prescription of Eq. (61). In the lower panel are perturbative predictions, the same observables as a function of lattice coupling. These pictures illustrate that perturbation theory in terms of the bare coupling does not work well, but that using other definitions for couplings, one can get much better agreement with the lattice "data."

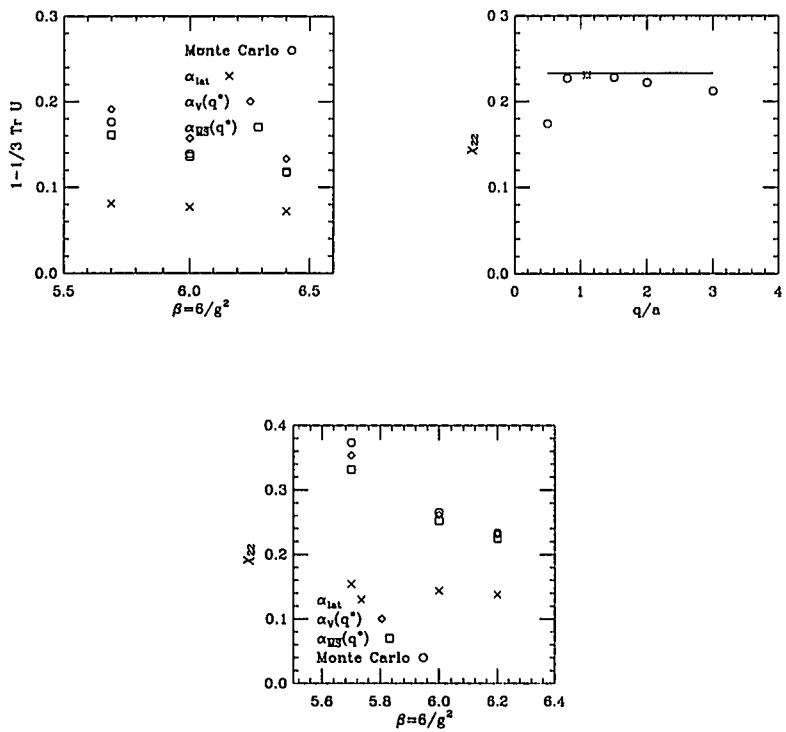


Figure 13: Examples of "improved perturbation theory."

Straight perturbative expansions by themselves for the commonly used lattice actions are typically not very convergent. The culprit is the presence of U_μ's in the action. One might think that for weak coupling, one could expand

$$\bar{\psi}U\psi = \bar{\psi}[1 + igaA + \ldots]\psi \tag{64}$$

and ignore the ..., but the higher order term $\bar{\psi}\frac{1}{2}g^2a^2A^2\psi$ generates the "tadpole graph" of Fig. 14. The UV divergence in the gluon loop $\simeq 1/a^2$ cancels the a^2 in the vertex. The same thing happens at higher order, and the tadpoles add up to an effective $a^0 \sum c_n g^{2n}$ contribution. Parisi[24] and later Lepage and Mackenzie[22] suggested a heuristic way to deal with this problem: replace $U_\mu \to u_0(1 + igaA)$ where u_0, the "mean field term" or "tadpole improvement term" is introduced phenomenologically to sum the loops. Then one rewrites the action as

$$S = \frac{1}{g^2u_0^4}\sum \mathrm{Tr}U \leftrightarrow \frac{1}{g_{lat}^2}\sum \mathrm{TrU}, \tag{65}$$

where $g^2 \equiv g_{lat}^2/u_0^4$ is the new expansion parameter. Is $u_0^4 \equiv \langle \mathrm{Tr}U_{plaq}/3\rangle$? This choice is often used; it is by no means unique.

A "standard action" (for this year, anyway) is the "tadpole-improved Lüscher-Weisz[17] action," composed of a 1 by 1, 1 by 2, and "twisted" loop (+x, +y, +z, −x, −y, −z),

$$\beta S = -\beta[\mathrm{Tr}(1\times 1) - \frac{1}{20u_0^2}(1 + 0.48\alpha_s)\mathrm{Tr}(1\times 2) - \frac{1}{u_0^2}0.33\alpha_s\mathrm{Tr}U_{tw}] \tag{66}$$

with $u_0 \equiv \langle \mathrm{Tr}U_{plaq}/3\rangle^{1/4}$ and $3.068\alpha_s \equiv -\ln\langle \mathrm{Tr}U_{plaq}/3\rangle$ determined self-consistently in the simulation.

3.4 Fixed-Point Actions

Let's recall the question we were trying to answer in the previous sections: Can one find a trajectory in coupling constant space, along which the physics has no corrections to some desired order in a^n or $g^m a^n$? Let's take the question one step further: Is there a trajectory in coupling constant space in which there are *no* corrections at all, for any n or m?

To approach the answer, let's think about the connection between scaling and the properties of some arbitrary bare action, which we assume is defined with some UV cutoff a (which does not have to be a lattice cutoff, in principle). The

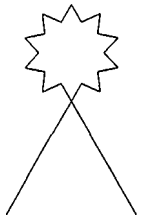


Figure 14: The "tadpole diagram."

action is characterized by an infinite number of coupling constants, $\{c\}$. (Many of them could be set to zero.) When the c's take on almost any arbitrary values, the typical scale for all physics will be the order of the cutoff: $m \simeq 1/a$, correlation length $\xi \simeq a$. There will be strong cutoff effects.

The best way to think about scaling is through the renormalization group.[25] Take the action with cutoff a and integrate out degrees of freedom to construct a new effective action with a new cutoff $a' > a$ and fewer degrees of freedom. The physics at distance scales $r > a$ is unaffected by the coarse-graining (assuming it is done exactly.) We can think of the effective actions as being similar to the original action, but with altered couplings. We can repeat this coarse-graining and generate new actions with new cutoffs. As we do, the coupling constants "flow":

$$S(a, c_j) \to S(a', c'_j) \to S(a'', c''_j) \to \ldots . \tag{67}$$

If under repeated blockings the system flows to a fixed point

$$S(a_n, c_j^n) \to S(a_{n+1}, c_j^{n+1} = c_j^n), \tag{68}$$

then observables are independent of the cutoff a, and in particular, the correlation length ξ must either be zero or infinite.

This can only happen if the original c's belong to a particular restricted set, called the "critical surface." It is easy to see that physics on the critical surface is universal: at long distances, the effective theory is the action at the fixed point, to which all the couplings have flowed, regardless of their original bare values.

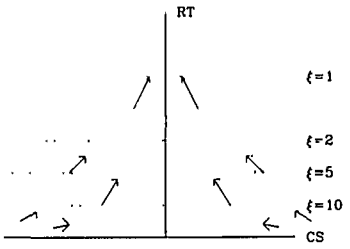


Figure 15: A schematic picture of renormalization group flows along a one-dimensional critical surface, with the associated renormalized trajectory, and superimposed contours of constant correlation length.

In particular, physics at the fixed point is independent of the underlying lattice structure.

But $\xi = \infty$ is not ξ large. Imagine tuning bare parameters close to the critical surface, but not on it. The system will flow towards the fixed point, then away from it. The flow lines in coupling constant space will asymptotically approach a particular trajectory, called the renormalized trajectory (RT), which connects (at $\xi = \infty$) with the fixed point. Along the renormalized trajectory, ξ is finite. However, because it is connected to the fixed point, it shares the scaling properties of the fixed point—in particular, the complete absence of cutoff effects in the spectrum and in Green's functions. (To see this remarkable result, imagine doing QCD spectrum calculations with the original bare action with a cutoff equal to the Planck mass and then coarse-graining. Now exchange the order of the two procedures. If this can be done without making any approximations, the answer should be the same.)

A Colorado analogy is useful for visualizing the critical surface and renormalized trajectory: think of the critical surface as the top of a high mountain ridge. The fixed point is a saddle point on the ridge. A stone released on the ridge will roll to the saddle and come to rest. If it is not released exactly on the ridge, it will roll near to the saddle, then go down the gully leading away from it. For a cartoon, see Fig. 15.

So the ultimate goal of "improvement programs" is to find a true perfect action, without cutoff effects, along the renormalized trajectory of some renormalization group transformation. At present, finding an RT has not been done in a convincing way for any renormalization group transformation. However, an action at the fixed point might also be an improved action, and fixed-point actions really can be constructed and used.

In lattice language, a bare action for QCD is described by one overall factor of $\beta = 2N/g^2$ and arbitrary weights of various closed loops,

$$\beta S = \frac{2N}{g^2} \sum_j c_j O_j. \tag{69}$$

Asymptotic freedom is equivalent to the statement that the critical surface of any renormalization group transformation is at $g^2 = 0$. The location of a fixed point involves some relation among the c_j's.

A direct attack on the renormalized trajectory begins by finding a fixed-point action. Imagine having a set of field variables $\{\phi\}$ defined with a cutoff a. Introduce some coarse-grained variables $\{\Phi\}$ defined with respect to a new cutoff a', and integrate out the fine-grained variables to produce a new action

$$e^{-\beta S'(\Phi)} = \int d\phi e^{-\beta(T(\Phi,\phi)+S(\phi))}, \tag{70}$$

where $\beta(T(\Phi,\phi)$ is the blocking kernel which functionally relates the coarse and fine variables. Integrating Eq. (70) is usually horribly complicated. However, P. Hasenfratz and F. Niedermayer[26] noticed an amazing simplification for asymptotically free theories: Their critical surface is at $\beta = \infty$, and in that limit, Eq. (70) becomes a steepest-descent relation

$$S'(\Phi) = \min_\phi((T(\Phi,\phi) + S(\phi)) \tag{71}$$

which can be used to find the fixed-point action

$$S_{FP}(\Phi) = \min_\phi((T(\Phi,\phi) + S_{FP}(\phi)). \tag{72}$$

The program has been successfully carried out for $d = 2$ sigma models[26] and for four-dimensional pure gauge theories.[27] These actions have two noteworthy properties: First, not only are they classically perfect actions (they have no a^n scaling violations for any n), but they are also one-loop quantum perfect: that is, as one moves out of the renormalized trajectory,

$$\frac{1}{g^2} S_{RT}(g^2) = \frac{1}{g^2}(S_{FP} + O(g^4)). \tag{73}$$

Physically, this happens because the original action has no irrelevant operators, and they are only generated through loop graphs. Thus, these actions are an extreme realization of the Symanzik program. Second, because these actions are at the fixed point, they have scale invariant classical solutions. This fact can be used to define a topological charge operator on the lattice in a way which is consistent with the lattice action.[28]

These actions are "engineered" in the following way: one picks a favorite blocking kernel, which has some free parameters, and solves Eq. (72), usually approximately at first. Then one tunes the parameters in the kernel to optimize the action for locality and perhaps refines the solution. Now the action is used in simulations at finite correlation length (i.e., do simulations with a Boltzmann factor $\exp(-\beta S_{FP})$). Because of Eq. (73), one believes that the FP action will be a good approximation to the perfect action on the RT; of course, only a numerical test can tell. As we will see in the next section, these actions perform very well. At this point in time, no nonperturbative FP action which includes fermions has been tested, but most of the formalism is there.[29]

3.5 Examples of "Improved" Spectroscopy

I would like to show some examples of the various versions of "improvement" and remind you of the pictures at the end of the last chapter to contrast results from standard actions.

Figure 16 shows a plot of the string tension measured in systems of constant physical size (measured in units of $1/T_c$, the critical temperature for deconfinement), for SU(3) pure gauge theory. In the quenched approximation, with $\sqrt{\sigma} \simeq 440$ MeV, $T_c = 275$ MeV and $1/T_c = 0.7$ fm. Simulations with the standard Wilson action are crosses, while the squares show FP action results[27] and the octagons from the tadpole-improved Lüscher-Weisz action.[30] The figure illustrates that it is hard to quantify improvement. There are no measurements with the Wilson action at small lattice spacing of precisely the same observables that the "improvement people" measured. The best one can do is to take similar measurements (the diamonds) and attempt to compute the $a = 0$ prediction for the observable we measured (the fancy cross at $a = 0$). This attempt lies on a straight line with the FP action data, hinting strongly that the FP action is indeed scaling. The FP action seems to have gained about a factor of three to four in

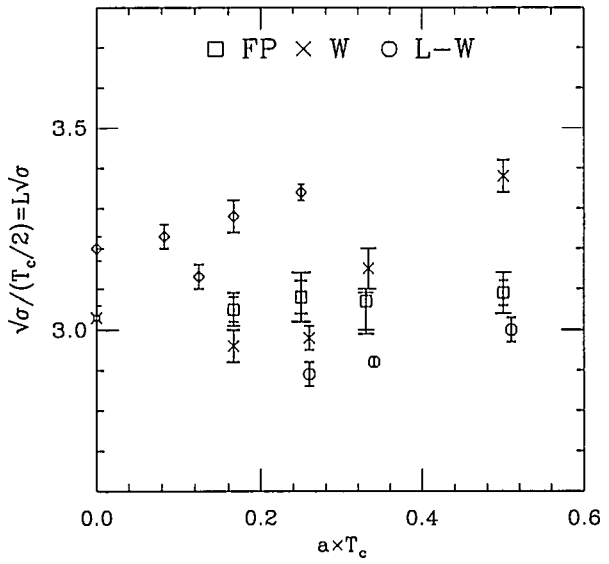


Figure 16: The square root of the string tension in lattices of constant physical size $L = 2/T_c$, but different lattice spacings (in units of $1/T_c$).

lattice spacing, or a gain of $(3-4)^6$ compared to the plaquette action, according to Eq. (41), at a cost of a factor of seven per site because it is more complicated to program. The tadpole-improved Lüscher-Weisz action data lie lower than the FP action data and do not scale as well. As $a \to 0$, the two actions should yield the same result; that is just universality at work. However, there is no guarantee that the approach to the continuum is monotonic.

Figure 17 shows the heavy quark-antiquark potential in SU(2) gauge theory, where $V(r)$ and r are measured in the appropriate units of T_c, the critical temperature for deconfinement. The Wilson action is on the left and an FP action is on the right. The vertical displacements of the potentials are just there to separate them. Notice the large violations of rotational symmetry in the Wilson action data when the lattice spacing is $a = 1/2T_c$, which are considerably improved in the FP action results.

Next, we consider nonrelativistic QCD. A comparison of the quenched charmonium spectrum from Ref. 19 using data from Ref. 31 is shown in Fig. 18.

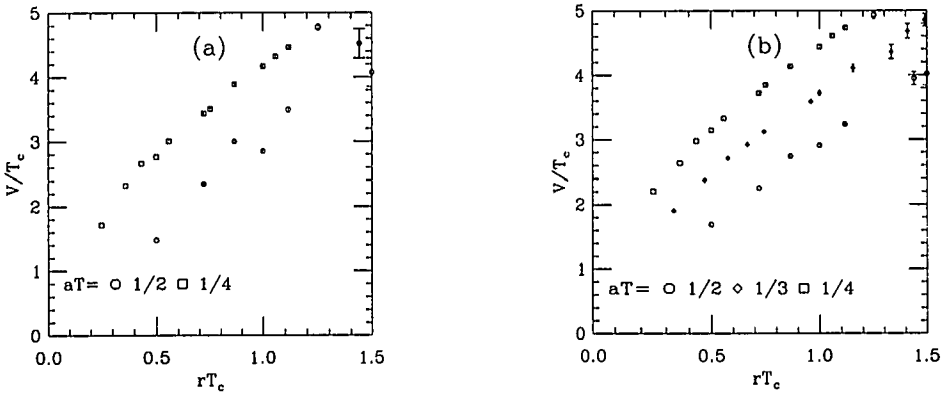


Figure 17: The heavy quark potential in SU(2) pure gauge theory measured in units of T_c. (a) Wilson action, and (b) an FP action.

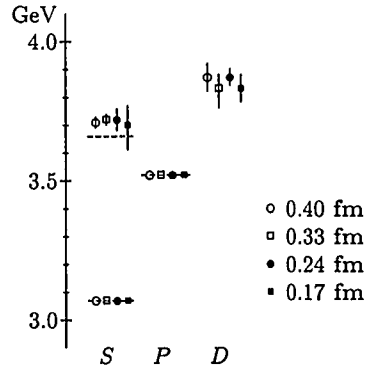


Figure 18: S, P, and D states of charmonium computed on lattices with: a = 0.40 fm (improved action, $\beta_{plaq} = 6.8$); $a = 0.33$ fm (improved action, $\beta_{plaq} = 7.1$); $a = 0.24$ fm (improved action, $\beta_{plaq} = 7.4$); and $a = 0.17$ fm (Wilson action, $\beta = 5.7$, from Ref. [31]), from Ref. 19. The dashed lines indicate the true masses.

When the tadpole-improved L-W action is used to generate gauge configurations, the scaling window is pushed out to $a \simeq 0.4$ fm for these observables.

Now we turn to tests of quenched QCD for light quarks. The two actions which have been most extensively tested are the S-W action, with and without tadpole improvement, and an action called the D234(2/3) action, a higher-order variant of the S-W action.[32] Figures 19 and 20 are the analogs of Figs. 5 and 6. Diamonds[33] and plusses[34] are S-W actions, ordinary and tadpole-improved, squares are the D234(2/3) action. They appear to have about half the scaling violations as the standard actions but they don't remove all scaling violations. It's a bit hard to quantify the extent of improvement from these pictures because a chiral extrapolation is hidden in them. However, one can take one of the "sections" of Fig. 4 and overlay the new data on it, Fig. 21. It looks like one can double the lattice spacing for an equivalent amount of scale violation. However, the extrapolation in a is not altogether clear. Figure 22 is the same data as Fig. 21, only plotted versus a^2, not a. All of the actions shown in these figures are supposed to have $O(a^2)$ (or better) scaling violations. Do the data look any straighter in Fig. 22 than in Fig. 21?

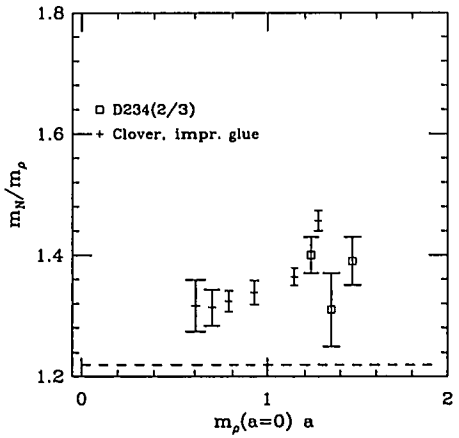


Figure 19: Nucleon to rho mass ratio (at chiral limit) vs lattice spacing (in units of $1/m_\rho$).

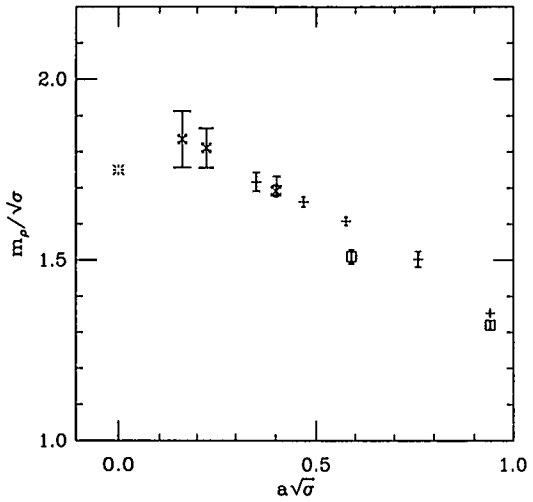


Figure 20: Rho mass scaling test with respect to the string tension.

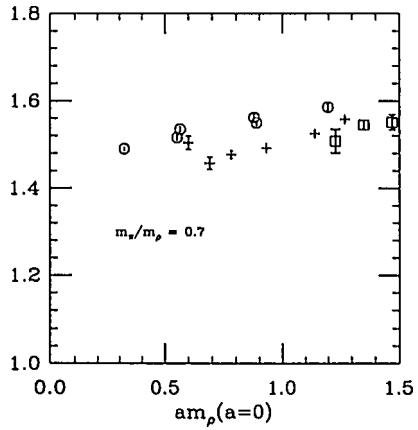


Figure 21: m_N/m_ρ vs am_ρ at fixed quark mass (fixed m_π/m_ρ). Interpolations of the S-W and D234(2/3) data were done by me.

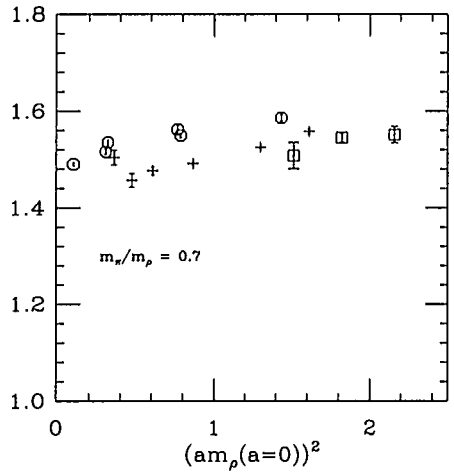


Figure 22: m_N/m_ρ vs $(am_\rho)^2$ at fixed quark mass (fixed m_π/m_ρ).

3.6 The Bottom Line

At the cost of enormous effort, one can do fairly high-precision simulations of QCD in the quenched approximation with standard actions. The actions I have shown you appear to reduce the amount of computation required for pure gauge simulations from supercomputers to very large work stations, probably a gain of a few hundreds. All of the light quark data I showed actually came from supercomputers. According to Eq. (41), a factor of two in the lattice spacing gains a factor of 64 in speed. The cost of either of the two improved actions I showed is about a factor of eight to ten times the fiducial staggered simulation. Improvement methods for fermions are a few years less mature than ones for pure gauge theory, and so the next time you hear a talk about the lattice, things will have changed for the better (maybe).

4 SLAC Physics from the Lattice

One of the major goals of lattice calculations is to provide hadronic matrix elements which either test QCD or can be used as inputs to test the Standard Model. In many cases, the lattice numbers have uncertainties which are small enough that they are interesting to experimentalists. I want to give a survey of lattice calculations of matrix elements, and what better way at this summer school, than to recall science which was done here at SLAC, as the framework?

4.1 Generic Matrix Element Calculations

Most of the matrix elements measured on the lattice are expectation values of local operators composed of quark and gluon fields. The mechanical part of the lattice calculation begins by writing down some Green's functions which contain the local operator (call it $J(x)$) and somehow extracting the matrix element. For example, if one wanted $\langle 0|J(x)|h\rangle$, one could look at the two-point function

$$C_{JO}(t) = \sum_x \langle 0|J(x,t)O(0,0)|0\rangle. \tag{74}$$

Inserting a complete set of correctly normalized momentum eigenstates

$$1 = \frac{1}{L^3}\sum_{A,\vec{p}} \frac{|A,\vec{p}\rangle\langle A,\vec{p}|}{2E_A(p)} \tag{75}$$

and using translational invariance and going to large t gives

$$C_{JO}(t) = e^{-m_A t}\frac{\langle 0|J|A\rangle\langle A|O|0\rangle}{2m_A}. \tag{76}$$

A second calculation of

$$C_{OO}(t) = \sum_x \langle 0|O(x,t)O(0,0)|0\rangle = e^{-m_A t}\frac{|\langle 0|O|A|\rangle|^2}{2m_A} \tag{77}$$

is needed to extract $\langle 0|J|A\rangle$ by fitting two correlators with three parameters.

Similarly, a matrix element $\langle h|J|h'\rangle$ can be gotten from

$$C_{AB}(t,t') = \sum_x \langle 0|O_A(t)J(x,t')O_B(0)|0\rangle \tag{78}$$

by stretching the source and sink operators O_A and O_B far apart on the lattice, letting the lattice project out the lightest states, and then measuring and dividing out $\langle 0|O_A|h\rangle$ and $\langle 0|O_B|h\rangle$.

These lattice matrix elements are not yet the continuum matrix elements. The lattice is a UV regulator, and changing from the lattice cutoff to a continuum regulator (like $\overline{MS}$) introduces a shift

$$\langle f|O^{cont}(\mu = 1/a)|i\rangle_{\overline{MS}} = a^D(1 + \frac{\alpha_s}{4\pi}(C_{\overline{MS}} - C_{latt}) + \ldots)\langle f|O^{latt}(a)|i\rangle + O(a) + \ldots. \tag{79}$$

The factor a^D converts the dimensionless lattice number to its continuum result. The $O(a)$ corrections arise because the lattice operator might not be the continuum operator: $df/dx = (f(x+a) - f(x))/a + O(a)$. The C's are calculable in perturbation theory, and the "improved perturbation theory" described in the last section is often used to reduce the difference $C_{\overline{MS}} - C_{latt}$.

4.2 Structure Functions

In the beginning, there was deep inelastic scattering. The lattice knows about structure functions through their moments:

$$\int_0^1 dx x^{n-2}F_2(x,Q^2) \equiv M_n(Q^2) = \sum c_n^f v_n^{(f)} \tag{80}$$

has a representation in terms of matrix elements of fairly complicated quark (for the nonsinglet structure function) or gluon bilinears: for quarks

$$\mathcal{O}^{(q)}_{\mu_1\cdots\mu_n} = \left(\frac{i}{2}\right)^{n-1}\bar{q}\gamma_{\mu_1}\overleftrightarrow{D}_{\mu_2}\cdots\overleftrightarrow{D}_{\mu_n}q \tag{81}$$

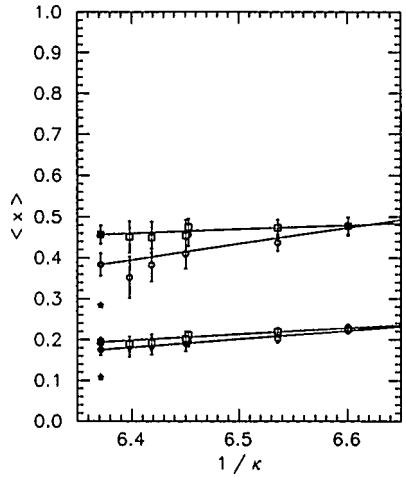


Figure 23: $\langle x\rangle$ for the proton (MOM scheme) from Ref. 35. The circles (boxes) correspond to different choices of lattice operators. The upper (lower) band of data represents the results for the up- (down-) quark distribution.

$$\sum_s \langle p,s|\mathcal{O}^{(f)}_{\{\mu_1\ldots\mu_n\}}|p,s\rangle \simeq v_n^{(f)}(p_{\mu_1}\ldots p_{\mu_n} + \ldots). \tag{82}$$

D is a lattice covariant derivative, which is approximated by a finite difference. The Wilson coefficients $c_{i,n}^{(f)}$ are calculated in perturbation theory and depend on μ^2/Q^2 as well as on the coupling constant $g(\mu)$. The lattice calculation is done by sandwiching the operator in Eq. (78).

It is presently possible to calculate the two lowest moments of the proton structure function on the lattice. Two groups[35,36] presented results at this year's lattice conference. Figure 23 shows $\langle x\rangle$ from Ref. 35, a calculation done in quenched approximation. In this picture, the massless quark limit is the left edge of the picture. There are several different lattice operators which serve as discretizations of the continuum operator, and the figure shows two possibilities.

Unfortunately, the calculation is badly compromised by the quenched approximation. It shows $\langle x\rangle_u = 0.38$ and $\langle x\rangle_d = 0.19$, while in the real world, we expect about 0.28 and 0.10, respectively. In the computer, there are no sea quarks, and their momentum is obviously picked up (at least partly) by the valence quarks.

One nice feature about the lattice calculation is that the spin structure function can be calculated in essentially the same way; the operator $\mathcal{O}$ has an extra

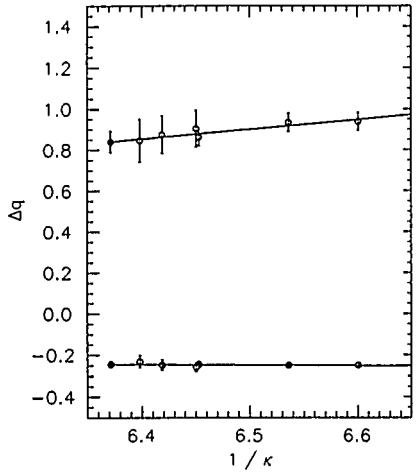


Figure 24: Δu (upper values) and Δd (lower values) for the proton from Ref. 35.

gamma-5 in it. Reference 35 computed $\Delta u = 0.84$ and $\Delta d = -0.24$ (in contrast to 0.92 and -0.34 in the real world). A plot versus quark mass is shown in Fig. 24.

There is no problem in principle which prevents extending these calculations to full QCD (with dynamical sea quarks). It will probably be very expensive to push beyond the lowest moments.

4.3 Heavy Quark Physics

Then there was the November revolution. Twenty years later, systems with one or more heavy quarks remain interesting objects for study. The lattice is no exception. Many groups study spectroscopy, decay amplitudes, form factors, etc., with the goal of confronting both experiment and analytic theoretical models.

There are several ways to study heavy quarks on the lattice. If the quark has infinite mass (the "static limit"), its propagator is very simple: the quark is confined to one spatial location, and as it evolves in time, its color "twinkles." The propagator is just a product of link matrices going forward in time.

One can simulate nonrelativistic quarks directly on the lattice.[31] This has evolved into one of the most successful (and most elaborate) lattice programs.

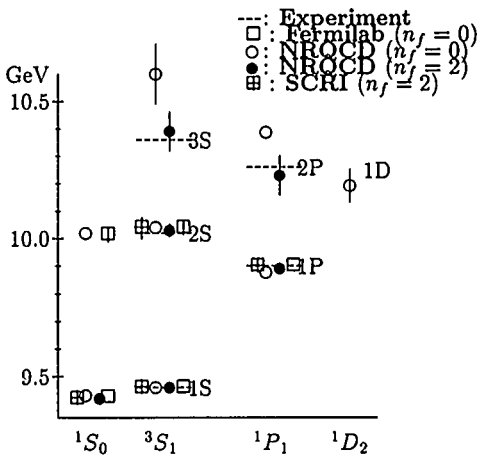


Figure 25: Υ spectrum.

The idea is to write down lattice actions which are organized in an expansion of powers of the quark velocity and to systematically keep all the terms to some desired order. For example, one might write

$$S = \psi^\dagger [iD_t - \frac{D^2}{2m} + \vec{\mu} \cdot \vec{B} + \ldots]\psi \tag{83}$$

including kinetic and magnetic moment terms, suitably (and artistically) discretized. Tadpole-improved perturbation theory is heavily used to set coefficients. Figures 25 and 26 show the Upsilon spectrum and its hyperfine splittings from various NRQCD calculations (from a recent summary by Shigemitsu[37]).

The main shortcoming of nonrelativistic QCD is, of course, that when the quark mass gets small, the nonrelativistic approximation breaks down. For charmonium, $v/c \simeq 0.3$, so the method is less safe for this system than for the Upsilon.

Finally, one can take relativistic lattice quarks and just make the mass heavy. If the quark mass gets too heavy ($ma \simeq 1$), lattice artifacts dominate the calculation. For Wilson fermions, the dispersion relation breaks down: $E(p) \simeq m_1 + p^2/2m_2$ where $m_2 \neq m_1$. The magnetic moment is governed by its own different mass, too.

Another signal of difficulty is that all these formulations have their own pattern of scale violations. That is, nonrelativistic quarks and Wilson quarks approach

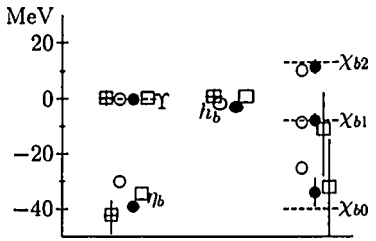


Figure 26: Υ spin splittings: Symbols have the same meaning as in Fig. 25.

their $a \to 0$ limits differently. This is often described in the literature by the statement that "the lattice spacing is different for different observables." For example, in one data set,[38] the inverse lattice spacing (in MeV) is given as 2055 MeV from fitting the heavy $q\bar{q}$ potential, 2140 MeV from the rho mass, 1800 MeV from the proton mass, and 2400 MeV from the Upsilon spectrum. These simulations are just sitting in the middle of figures like Fig. 5 with only one point, trying to guess where the left-hand edge of the picture will be. This is a problem for calculations of B meson and baryon spectroscopy, where the heavy quarks might be treated nonrelativistically and the light quarks are relativistic. What observable should be used to set the overall scale?[39]

One of the major uses of heavy quark systems by the lattice community is to try to calculate the strong coupling constant at $Q^2 = M_Z^2$. This topic deserves its own section.

4.4 $\alpha_s(M_Z)$

Now we are at the SLC and LEP. For some time now, there have been claims that physics at the Z pole hints at a possible breakdown in the Standard Model.[40] A key question in the discussion is whether or not the value of $\alpha_{\overline{MS}}$ inferred from the decay width of the Z is anomalously high relative to other determinations of the strong coupling (which are usually measured at lower Q and run to the Z pole).

The most recent analysis of $\alpha_s(M_Z)$ I am aware of is due to Erler and Langacker.[41] Currently, $\alpha_{\overline{MS}}^{lineshape} = 0.123(4)(2)(1)$ for the Standard Model Higgs mass range, where a first, second, and third uncertainty is from the inputs, Higgs mass, and estimate of α_s^4 terms, respectively. The central Higgs mass is assumed to be 300 GeV, and the second error is for $M_H = 1000$ GeV (+), 60 GeV (-). For the SUSY Higgs mass range (60-150 GeV), one has the lower value $\alpha_{\overline{MS}} = .121(4)(+1-0)(1)$. A global fit to all data gives 0.121(4)(1). Hinchcliffe in the same compilation quotes a global average of 0.118(3).

The lattice can contribute to this question by predicting $\alpha_{\overline{MS}}$ from low-energy physics. The basic idea is simple: The lattice is a (peculiar) UV cutoff. A lattice mass $\mu = Ma$ plus an experimental mass M give a lattice spacing $a = \mu/M$ in fm. If one can measure some quantity related to α_s at a scale $Q \simeq 1/a$, one can then run the coupling constant out to the Z.

The best (recent) lattice number, from Shigemitsu's Lattice '96 summary talk,[37] is

$$\alpha_{\overline{MS}}(M_Z) = 0.1159(19)(13)(19), \tag{84}$$

where the first error includes both statistics and estimates of discretization errors, the second is due to uncertainties from the dynamical quark mass, and the third is from conversions of conventions. The lattice number is about one standard deviation below the pure Z-physics number. Lattice results are compared to other recent determinations of $\alpha_{\overline{MS}}(Z)$ in Fig. 27, a figure provided by P. Burrows.[42]

Two ways of calculating $\alpha_s(M_Z)$ from lattice have been proposed: The first is the "small loop method."[43] This method uses the "improved perturbation theory" described in Chap. 2: One assumes that a version of perturbation theory can describe the behavior of short-distance objects on the lattice: in particular, that the plaquette can be used to define $\alpha_V(q = 3.41/a)$. With typical lattice spacings now in use, this gives the coupling at a momentum $Q_0 = 8 - 10$ GeV. One then converts the coupling to $\alpha_{\overline{MS}}$ and runs out to the Z using the (published) three-loop beta function.[44]

Usually, the lattice spacing is determined from the mass splittings of heavy $Q\bar{Q}$ states. This is done because the mass differences between physical heavy quark states are nearly independent of the quark mass—for example, the S-P mass splitting of the ψ family is about 460 MeV, and it is about 440 MeV for the Υ. A second reason is that the mass splitting is believed to be much less sensitive to sea quark effects than light quark observables, and one can estimate the effects of sea quarks through simple potential models. The uncertainty in the lattice spacing is three to five per cent, but systematic effects are much greater (as we will see below).

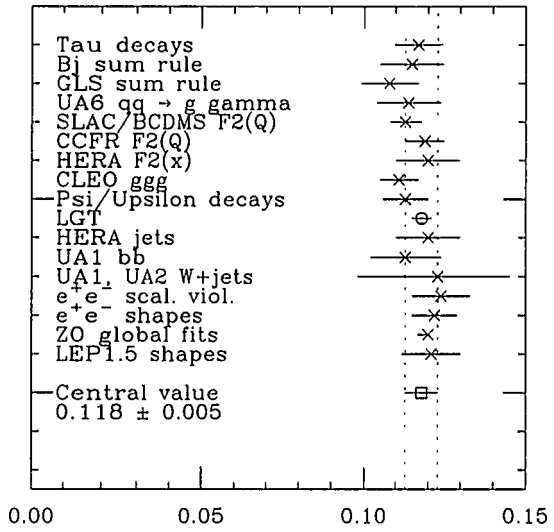


Figure 27: Survey of $\alpha_{\overline{MS}}(M_Z)$ from Ref. 42.

The coupling constant comes from Eq. (63). The plaquette can be measured to exquisite accuracy (0.01 per cent is not atypical) and so the coupling constant is known essentially without error. However, the scale of the coupling is uncertain (due to the lattice spacing).

The next problem is getting from lattice simulations, which are done with $n_f = 0$ (quenched) or $n_f = 2$ (but unphysical sea quark masses) to the real world of $n_f = 3$. Before simulations with dynamical fermions were available, the translation was done by running down in Q to a "typical gluonic scale" for the psi or the upsilon (a few hundred MeV) and then matching the coupling to the three-flavor coupling (in the spirit of effective field theories). This produced a rather low $\alpha_s \simeq 0.105$. Now we have simulations at $n_f = 2$ and can do better. Recall that in lowest order

$$\frac{1}{\alpha_s} = (\frac{11 - \frac{2}{3}n_f}{4\pi}) \ln \frac{Q^2}{\Lambda^2}. \tag{85}$$

One measures $1/\alpha_s$ in two simulations, one quenched, the other at $n_f = 2$, runs one measurement in Q to the Q of the other, then extrapolates $1/\alpha$ linearly in n_f to $n_f = 3$. Then one can convert to $\overline{MS}$ and run away.

Pictures like Fig. 27 are not very useful when one wants to get a feel for the errors inherent in the lattice calculation. Instead, let's run our expectations for $\alpha_s(M_Z)$ down to the scale where the lattice simulations are done, and compare. Figure 28 does that. The squares are the results of simulations of charmed quarks and the octagons are from bottom quarks, both with $n_f = 0$. The crosses and diamond are $n_f = 2$ bottom and charm results. (The bursts show upsilon data when the 1S-2S mass difference gives a lattice spacing.) Note the horizontal error bars on the lattice data. Finally, the predicted $n_f = 3$ coupling α_P is shown in the fancy squares, with error bars now rotated because the convention is to quote an error in α_s. The lower three lines in the picture (from top to bottom) are $\alpha_{\overline{MS}}(M_Z) = 0.118$, 0.123, and 0.128 run down and converted to the lattice prescription.

The two top lines are predictions for how quenched α should run.

Now for the bad news. All of the $n_f = 2$ data shown here were actually run on the same set of configurations. The bare couplings are the same, but the lattice spacings came out different. What is happening is that we are taking calculations at some lattice spacing and inferring continuum numbers from them, but the lattice predictions have scale violations which are different. (The Υ calculations use nonrelativistic quarks, the ψ calculations use heavy Wilson quarks.) Notice also that the bottom and charm quenched lattice spacings are different. This discrepancy is thought to be a failure of the quenched approximation: the characteristic momentum scale for binding in the ψ and Υ are different, and because n_f is not the real world value, α runs incorrectly between the two scales. Said differently, in the quenched approximation, the spectrum of heavy quark bound states is different from the real world.

There is a second method of determining a running coupling constant which actually allows one to see the running over a large range of scales. It goes by the name of the "Schrödinger functional," (referring to the fact that the authors study QCD in a little box with specified boundary conditions) but "coupling determined by varying the box size" would be a more descriptive title. It has been applied to quenched QCD but has not yet been extended to full QCD,[45] and so it has not yet had an impact on phenomenology. This calculation does not use perturbation theory overtly. For a critical comparison of the two methods, see Ref. 46.

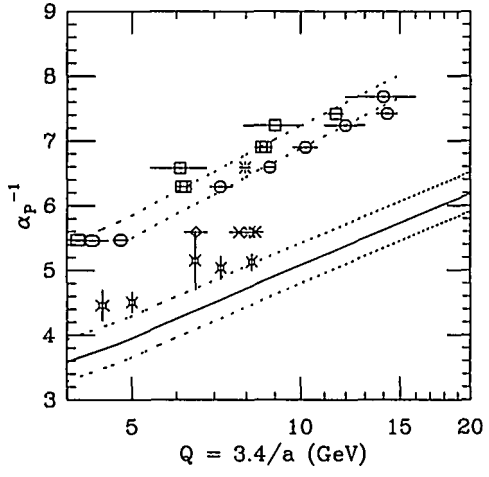


Figure 28: Survey of $\alpha_{\overline{MS}}(Q)$ at the scale where lattice simulations are actually done.

4.5 Glueballs

I have been hearing people talk about glueballs from psi decay for almost 20 years. Toki[47] has summarized the experimental situation for glueballs. What do theorists expect for a spectrum? The problem is that any nonlattice model requires making uncontrolled approximations to get any kind of an answer: there are no obvious zeroth order solutions with small expansion parameters. The lattice is the only game in town for a first-principles calculation.

People have been trying to measure the masses of the lightest glueballs (the scalar and the tensor) using lattice simulations for many years. The problem has proven to be very hard, for several reasons.

Recall how we measure a mass from a correlation function [Eq. (40)]. The problem with the scalar glueball is that the operator O has nonzero vacuum expectation value, and the correlation function approaches a constant at large t:

$$\lim_{t\to\infty} C(t) \to |\langle 0|O|\vec{p}=0\rangle|^2 \exp(-mt) + |\langle 0|O|0\rangle|^2. \tag{86}$$

The statistical fluctuations on $C(t)$ are given by Eq. (25), and we find after a short calculation that

$$\sigma \to \frac{C(0)}{\sqrt{N}}. \tag{87}$$

Thus, the signal-to-noise ratio collapses at large t like $\sqrt{N}\exp(-mt)$ due to the constant term.

A partial cure for this problem is a good trial wave function O. While in principle the plaquette itself could be used, it is so dominated by ultraviolet fluctuations that it does not produce a good signal. Instead, people invent "fat links" which average the gauge field over several lattice spacings, and then make interpolating fields which are closed loops of these fat links. The lattice glueball is a smoke ring.

The second problem is that lattice actions can have phase transitions at strong or intermediate coupling, which have nothing to do with the continuum limit, but mask continuum behavior.[48] As an example of this, consider the gauge group $SU(2)$, where a link matrix can be parameterized as $U = 1\cos\theta + i\vec{\sigma}\cdot\vec{n}\sin\theta$, so $\mathrm{Tr}U = 2\cos\theta$. Now consider a generalization of the Wilson action $-S = \beta\mathrm{Tr}U + \gamma(\mathrm{Tr}U)^2$. (This is a mixed fundamental-adjoint representation action.) At $\gamma\to\infty$, $\mathrm{Tr}U \to \pm 1$ and the gauge symmetry is broken down to $Z(2)$. But $Z(2)$ gauge theories have a first-order phase transition. First-order transitions are stable

under perturbations, and so the phase diagram of this theory, shown in Fig. 29, has a line of first-order transitions which terminate in a second-order point. At the second-order point, some state with scalar quantum numbers becomes massless. However, now imagine that you are doing Monte Carlo along the $\gamma = 0$ line, that is, with the Wilson action. When you come near the critical point, any operator which couples to a scalar particle (like the one you are using to see the scalar glueball) will see the nearby transition and the lightest mass in the scalar channel will shrink. Once you are past the point of closest approach, the mass will rise again. Any scaling test which ignores the nearby singularity will lie to you.

This scenario has been mapped out for $SU(3)$, and the place of closest approach is at a Wilson coupling corresponding to a lattice spacing of 0.2 fm or so, meaning that very small lattice spacings are needed before one can extrapolate to zero lattice spacing. A summary of the situation is shown in Fig. 30 (Ref. 49). Here the quantity r_0 is the "Sommer radius,"[50] defined through the heavy quark force, $F(r) = -dV(r)/dr$, by $r_0^2 F(r_0) = -1.65$. In the physical world of three colors and four flavors, $r_0 = 0.5$ fm.

Finally, other arguments suggest that a small lattice spacing or a good approximation to an action on an RT are needed to for glueballs: the physical diameter of the glueball, as inferred from the size of the best interpolating field, is small, about 0.5 fm. Shäfer and Shuryak[51] have argued that the small size is due to instanton effects. Most lattice actions do bad things to instantons at large lattice spacing.[28]

Two big simulations have carried calculations of the glueball mass close to the continuum limit: the UKQCD Collaboration[52] and a collaboration at IBM which built its own computer.[53] (The latter group is the one with the press release last December announcing the discovery of the glueball.) Their predictions in MeV are different, and they each favor a different experimental candidate for the scalar glueball (the one which is closer to their prediction, of course). It is a useful object lesson because both groups say that their lattice numbers agree before extrapolation, but they extrapolate differently to $a = 0$.

The UKQCD group sees that the ratio $m(0^{++})/\sqrt{\sigma}$ can be well-fitted with a form $b + ca^2\sigma$ (σ is the string tension) and a fit of this form to the lattice data of both groups gives $m(0^{++})/\sqrt{\sigma} = 3.64 \pm 0.15$. To turn this into MeV, we need σ in MeV units. One way is to take $m_\rho/\sqrt{\sigma}$ and extrapolate that to $a = 0$ using $b + ca\sqrt{\sigma}$. Averaging and putting 770 MeV for m_ρ, one gets $\sqrt{\sigma} = 432 \pm 15$ MeV,

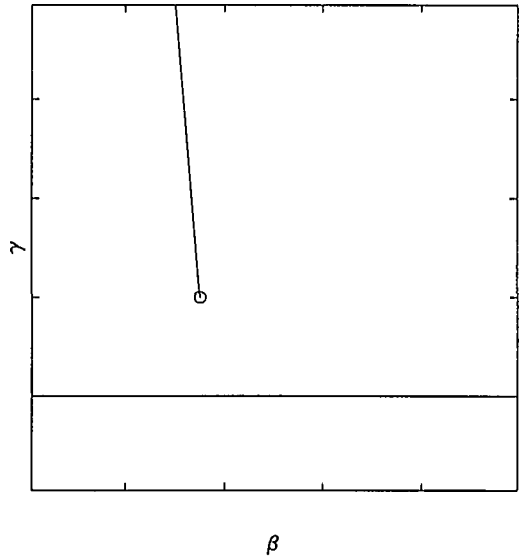


Figure 29: Phase transitions in the fundamental-adjoint plane.

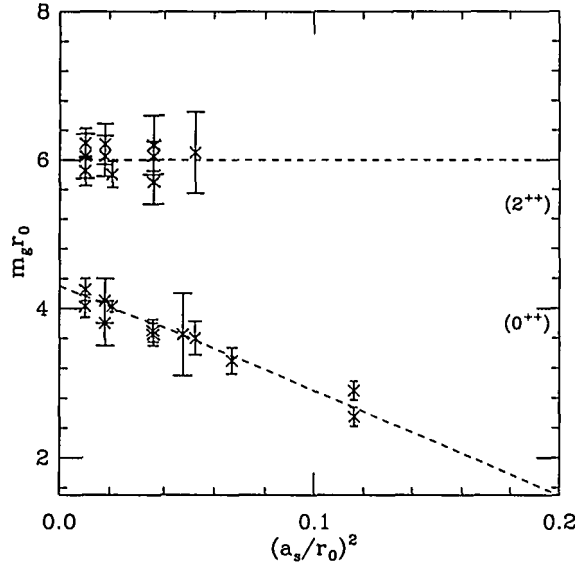


Figure 30: Glueball mass vs r_0 with the Wilson action, from a summary picture in Ref. 49.

which is consistent with the usual estimate (from extracting the string tension from the heavy quark potential) of about 440 MeV. Using the total average, they get $m(0^{++}) = 1572 \pm 65 \pm 55$ MeV where the first error is statistical and the second comes from the scale.

The IBM group, on the other hand, notices that $m_\rho a$ and $m_\phi a$ scale asymptotically, and uses the phi mass to predict quenched $\Lambda_{\overline{MS}}$, then extrapolates $m(0^{++})/\Lambda = A + B(a\Lambda)^2$. They get 1740(41) MeV from their data; when they analyze UKQCD data, they get 1625(94) MeV; and when they combine the data sets, they get 1707(64) MeV.

A neutral reporter could get hurt here. It seems to me that the lattice prediction for the scalar glueball is 1600 ± 100 MeV, and that there are two experimental candidates for it, the $f_0(1500)$ and the $f_J(1710)$.

Masses are not the end of the story. The IBM group has done two interesting recent calculations related to glueballs, which strengthen their claim that the $f_J(1710)$ is the glueball.

The first one of them[54] was actually responsible for the press release. It is a calculation of the decay width of the glueball into pairs of pseudoscalars. This is done by computing an unamputated three-point function on the lattice, with an assumed form for the vertex, whose magnitude is fitted. The result is shown in Fig. 31. The octagons are the results of the simulation, and the diamonds show interpolations in the quark mass. The "experimental" points (squares) are from a partial wave analysis of isoscalar scalar resonances by Longacre and Lindenbaum.[55]

The response of a member of the other side is that the slope of the straight line that one would put through the three experimental points is barely, if at all, compatible with the slope of the theoretical points. Since they argue theoretically for a straight line, the comparison of such slopes is a valid one.

If one of the experimental states is not a glueball, it is likely to be a $^3P_0$ orbital excitation of quarks. Weingarten and Lee[56] are computing the mass of this state on the lattice and argue that it is lighter than 1700 MeV; in their picture, the $f_0(1500)$ is an $s\bar{s}$ state. I have now said more than I know and will just refer you to recent discussions of the question.[57]

Both groups predict that the 2^{++} glueball is at about 2300 MeV.

Can "improved actions" help the situation? Recently, Peardon and Morningstar[49] implemented a clever method for beating the exponential signal-to-noise ratio: make the lattice spacing smaller in the time direction than in the space

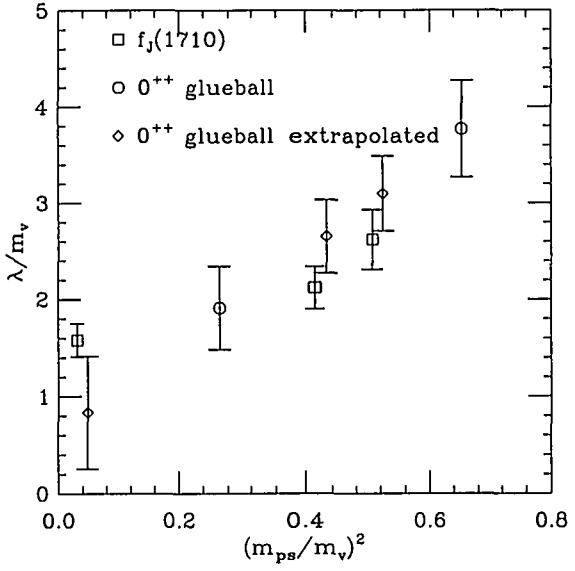


Figure 31: Scalar glueball decay couplings from Ref. 54.

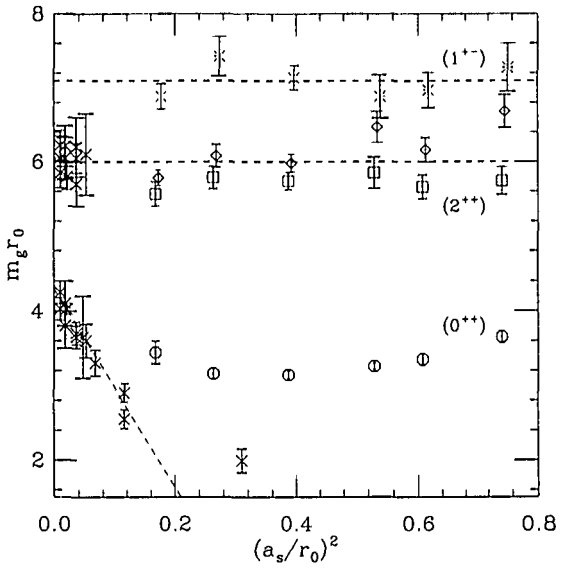


Figure 32: Glueball mass vs r_0 from Ref. 49, including large lattice spacing data.

direction. Then the signal, which falls like $\exp(-ma_t L_t)$ after L_t lattice spacings, dies more slowly because a_t is reduced. Their picture of the glueball mass versus r_0 is shown in Fig. 32. They are using the tadpole-improved Lüscher-Weisz action. The pessimist notes the prominent dip in the middle of the curve; this action also has a lattice-artifact transition (somewhere); the optimist notes that the dip is much smaller than for the Wilson action, and then the pessimist notes that there is no Wilson action data at large lattice spacing to compare. I think the jury is still out.

4.6 The B Parameter of the B Meson

And finally we are at BaBar. $\bar{B} - B$ mixing is parameterized by the ratio

$$x_d = \frac{(\Delta M)_{b\bar{d}}}{\Gamma_{b\bar{d}}} = \tau_{b\bar{d}} \frac{G_F^2}{6\pi^2} \eta_{QCD} F(\frac{m_t^2}{m_W^2}) |V_{tb}^* V_{td}|^2 b(\mu) \{\frac{3}{8} \langle \bar{B}|\bar{b}\gamma_\rho(1-\gamma_5)d\bar{b}\gamma_\rho(1-\gamma_5)d|B\rangle\}. \quad (88)$$

Experiment is on the left, theory on the right. Moving into the long equation from the left, we see many known (more or less) parameters from phase space integrals

or perturbative QCD calculations, then a combination of CKM matrix elements, followed by a four-quark hadronic matrix element.[58] We would like to extract the CKM matrix element from the measurement of x_d (and its strange partner x_s). To do so, we need to know the value of the object in the curly brackets, defined as $3/8 M_{bd}$ and parameterized as $m_B^2 f_{B_d}^2 B_{b_d}$ where B_{b_d} is the so-called B parameter, and f_B is the B-meson decay constant

$$\langle 0|\bar{b}\gamma_0\gamma_5 d|B\rangle = f_B m_B. \tag{89}$$

Naive theory, which is expected to work well for the B system, suggests that $B_B = 1$ to good accuracy. Of course, the stakes are high and a good determination of M_{bd} is needed to test the Standard Model. The lattice can do just that.

In Eq. (88) $b(\mu)$, the coefficient which runs the effective interaction down from the W-boson scale to the QCD scale μ, and the matrix element $M(\mu)$ both depend on the QCD scale, and one often sees the renormalization group invariant quantities $\hat{M}_{bd} = b(\mu)M_{bd}(\mu)$ or $\hat{B}_{bd} = b(\mu)B_{bd}(\mu)$ quoted in the literature.

Decay constants probe very simple properties of the wave function: in the nonrelativistic quark model,

$$f_M = \frac{\psi(0)}{\sqrt{m_M}}, \tag{90}$$

where $\psi(0)$ is the $\bar{q}q$ wave function at the origin. For a heavy-quark (Q) light-quark (q) system, $\psi(0)$ should become independent of the heavy quark's mass as the Q mass goes to infinity, and in that limit, one can show in QCD that $\sqrt{m_M} f_M$ approaches a constant.

One way to compute the decay constant is to put a light quark and a heavy quark on the lattice and let them propagate. It is difficult to calculate f_B directly on present day lattices with relativistic lattice fermions because the lattice spacing is much greater than the b quark's Compton wavelength (or the UV cutoff is below m_b). In this limit, the b quark is strongly affected by lattice artifacts as it propagates. However, one can make m_b infinite on the lattice and determine the combination $\sqrt{m_B} f_B$ in the limit. Then one can extrapolate down to the B mass and see if the two extrapolations up and down give the same result. (Nonrelativistic b quarks can solve this problem in principle, but the problem of setting the lattice spacing between light and nonrelativistic quarks has prevented workers from quoting a useful decay constant from these simulations.)

Among the many lattice decay constant calculations, the one of Ref. 59 stands out in my mind for being the most complete. These authors did careful quenched

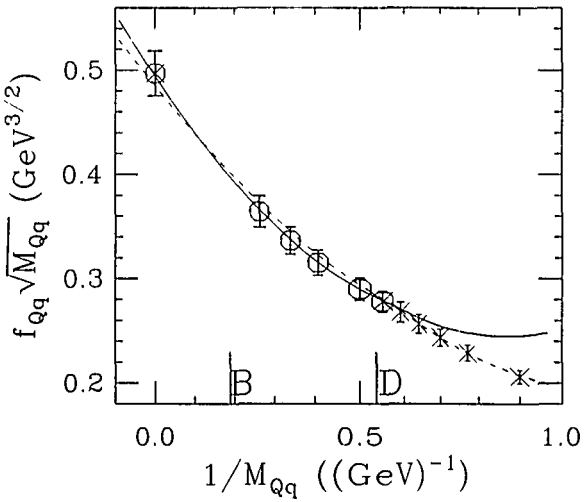


Figure 33: Pseudoscalar meson decay constant vs $1/M$, from Ref. 59.

simulations at many values of the lattice spacing, which allows one to extrapolate to the continuum limit by brute force. They have also done a less complete set of simulations which include light dynamical quarks, which should give some idea of the accuracy of the quenched approximation.

The analysis of all this data is quite involved. One begins with a set of lattice decay constants measured in lattice units, from simulations done with heavy quarks which are probably too light and light quarks which are certainly too heavy. One has to interpolate or extrapolate the heavy quark masses to their real world values, extrapolate the light quarks down in mass to their physical values, and finally try to extrapolate to $a \to 0$. It is not always obvious how to do this. Complicating everything are the lattice artifacts in the fermion and gauge actions, and the lattice-to-continuum renormalization factors as in Eq. (79).

The (still preliminary) results of Ref. 59 are shown in Figs. 33 and 34. The $N_f = 2$ dynamical fermion data in Fig. 34 have moved around a bit in the past year and may not have settled down yet.

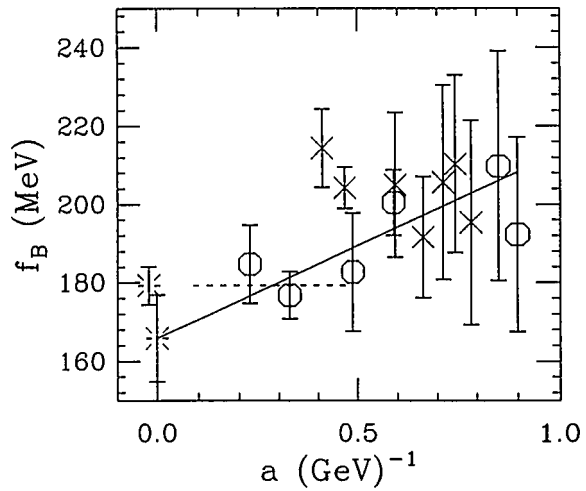


Figure 34: f_B vs a from Ref. 59. Octagons are quenched data; crosses, $N_F = 2$. The solid line is a linear fit to all quenched points; the dashed line is a constant fit to the three quenched points with $a < 0.5$ GeV^{-1}. The extrapolated values at $a = 0$ are indicated by bursts. The scale is set by $f_\pi = 132$ MeV throughout.

The numerical results of Ref. 59 are:

$$f_B = 166(11)(28)(14) \quad f_D = 196(9)(14)(8)$$
$$f_{B_s} = 181(10)(36)(18) \quad f_{D_s} = 211(7)(25)(11)$$
$$\frac{f_{B_s}}{f_B} = 1.10(2)(5)(8) \quad \frac{f_{D_s}}{f_D} = 1.09(2)(5)(5),$$

where the first error includes statistical errors and systematic effects of changing fitting ranges; the second, other errors within the quenched approximation; the third, an estimate of the quenching error. Decay constants are in MeV.

Note that the error bars for the B system are small enough to be phenomenologically interesting. The Particle Data Group's[60] determination of CKM matrix elements, which does not include this data, says, "Using $\hat{B}_{B_d} f_{B_d}^2 = (1.2 \pm 0.2)(173 \pm 40$ MeV$)^2$..., $|V_{tb}^* V_{td}|^2 = 0.009 \pm 0.003$, where the error bar comes primarily from the theoretical uncertainty in the hadronic matrix elements."

Can we trust these numbers? Lattice calculations have been predicting $f_{D_s} \simeq 200$ MeV for about eight years. The central values have changed very little, while the uncertainties have decreased. So far, four experiments have reported measurements of this quantity. The most recent is the Fermilab E653 Collaboration[61] $f_{D_s} = 194(35)(20)(14)$ MeV. The older numbers, with bigger errors, were 238(47)(21)(43) from WA75 (1993) (Ref. 62); 344(37)(52)(42) from CLEO (1994) (Ref. 63); 430 (+150 −130)(40) from BES (1995) (Ref. 64).

Now back to the mixing problem. On the lattice, one could measure the decay constants and B parameter separately and combine them after extrapolation, or measure M directly and extrapolate it. In principle, the numbers should be the same, but in practice, they will not be.

A recent calculation illustrates this point.[65] The authors computed the four fermion operators M_{bs} and M_{bd} directly on the lattice. Figure 35 shows the behavior of M as a function of hadron mass at one of their lattice spacings.

The ratio $r_{sd} = M_{bs}/M_{bd}$ is presumably much less sensitive to lattice spacing or to quark mass extrapolation. The authors' result for the lattice spacing dependence of this ratio is shown in Fig. 36, along with an extrapolation to zero lattice spacing. They find $1.54 \pm .13 \pm .32$ from their direct method, compared to $r_{sd} \approx 1.32 \pm .23$ from separate extrapolations of the decay constants and the B parameter. (They measure equal B parameters for strange and nonstrange B mesons, $B(\mu) = 1.02(13)$ for $\mu = 2$ GeV.)

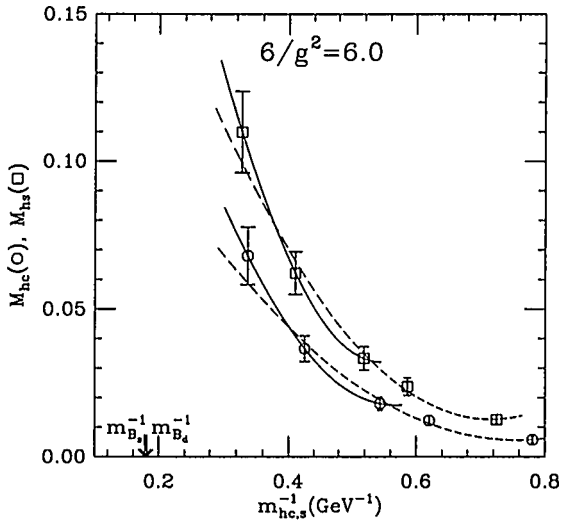


Figure 35: M_{hc} (octagons) and M_{hs} (squares) as a function of the inverse heavy-down (strange) meson mass, at $\beta = 6.0$. The dashed line shows the effect of the lightest points on the fit.

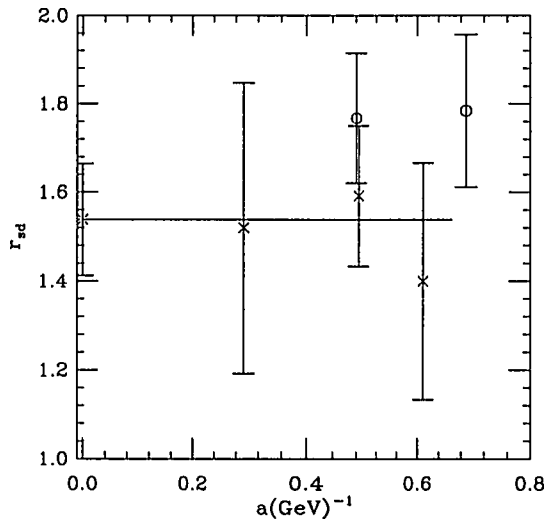


Figure 36: The SU(3) flavor breaking ratio M_{bs}/M_{bd} vs the lattice spacing a. The points denoted by crosses were used in the fit (solid line). The burst shows the extrapolation to $a = 0$.

It looks like $SU(3)$ breaking is fairly large, and if that is so, it looks like the parameter x_s, the strange analog of Eq. (88), might be about 20, unmeasurably large.[66]

5 Conclusions

Lattice methods have arrived. There are so many lattice calculations of different matrix elements that it is impossible to describe them all, and in many cases, the quality of the results is very high. One can see plots showing extrapolations in lattice spacing which show that the control of lattice spacing has become good enough to make continuum predictions with small uncertainties. Calculations with dynamical fermions and a small lattice spacing are still nearly impossibly expensive to perform, and "quenching" remains the dominant unknown in all lattice matrix element calculations.

There are two major tasks facing lattice experts. I believe that all the people in our field would agree that the first problem is to reduce the computational burden, so that we can do more realistic simulations with smaller computer resources. I have illustrated several of the approaches people are using to attack this problem. I believe that some of them have been shown to be successful and that "improvement" will continue to improve.

There is a second question for lattice people, which I have not discussed, but I will mention at the end: Is there a continuum phenomenology of light hadron structure or confinement, which can be justified from lattice simulations? The motivation for asking this question is that there are many processes which cannot be easily addressed via the lattice, but for which a QCD prediction ought to exist. For examples of such questions, see the talk of Bjorken in this conference,[67] or Shuryak's article.[11] Few lattice people are thinking about this question. Part of the lattice community spends its time looking for "structure" in Monte Carlo-generated configurations of gauge fields: instantons, monopoles, etc. This effort is not part of the mainstream because the techniques either involve gauge fixing (and so it is not clear whether what is being seen is just an artifact of a particular gauge), or they involve arbitrary decisions during the search (perform a certain number of processing operations, no more, no less). To answer this question requires new ideas and a controlled approach to simulation data. Will an answer be found?

Acknowledgments

I would like to thank M. Alford, C. Bernard, T. Blum, P. Burrows, S. Gottlieb, A. Hasenfratz, P. Hasenfratz, U. Heller, P. Langacker, P. Lepage, P. Mackenzie, J. Negele, F. Niedermayer, J. Shigemitsu, J. Simone, R. Sommer, R. Sugar, M. Teper, D. Toussaint, D. Weingarten, U. Wiese, and M. Wingate for discussions, figures, and correspondence. I would also like to thank Brian Greene, the organizer of the 1996 TASI Summer School for asking me to lecture there: it means that I had already written most of the material for these lectures well in advance of the deadline! I would also like to thank the Institute for Theoretical Physics at the University of Bern for its hospitality, where these lectures were written. Finally, it was a pleasure to be able to visit SLAC again, talk to many of my old friends, and present my subject to a wider audience. This work was supported by the U. S. Department of Energy.

References

[1] Some standard reviews of lattice gauge theory are M. Creutz, *Quarks, Strings, and Lattices* (Cambridge, 1983); *Quantum Fields on the Computer,* (World Scientific, 1992) edited by M. Creutz; I. Montvay and G. Munster, *Quantum Fields on a Lattice* (Cambridge, 1994). The lattice community has a large annual meeting, and the proceedings of those meetings (Lattice XX, published so far by North Holland) are the best places to find the most recent results.

[2] K. Wilson, Phys. Rev. D **10**, 2445 (1974).

[3] M. Creutz, L. Jacobs, and C. Rebbi, Phys. Rev. Lett. **42**, 1390 (1979).

[4] M. Golterman and J. Smit, Nucl. Phys. B **255**, 328 (1985).

[5] G. P. Lepage, in *From Actions to Answers–Proceedings of the 1989 Theoretical Advanced Summer Institute in Particle Physics*, edited by T. DeGrand and D. Toussaint (World Scientific, 1990).

[6] N. Metropolis, A. Rosenbluth, M. Rosenbluth, A. Teller, and E. Teller, J. Chem. Phys. **21**, 1087 (1953).

[7] F. Brown and T. Woch, Phys. Rev. Lett. **58**, 2394 (1987); M. Creutz, Phys. Rev. D **36**, 55 (1987). For a review, see S. Adler in the *Proceedings of the 1988 Symposium on Lattice Field Theory*, edited by A. Kronfeld and P. Mackenzie [Nucl. Phys. B (Proc. Suppl.) 9 (1989)].

[8] H. C. Andersen, J. Chem. Phys. **72**, 2384 (1980); S. Duane, Nucl. Phys. B **257**, 652 (1985); S. Duane and J. Kogut, Phys. Rev. Lett. **55**, 2774 (1985); S. Gottlieb, W. Liu, D. Toussaint, R. Renken, and R. Sugar, Phys. Rev. D **35**, 2531 (1987).

[9] S. Duane, A. Kennedy, B. Pendleton, and D. Roweth, Phys. Lett. B **194**, 271 (1987).

[10] For a recent review, see A. Frommer, talk presented at Lattice '96, hep-lat/9608074.

[11] E. Shuryak, "Why is a nucleon bound?" hep-ph/9603354, to appear in Festschrift for Gerry Brown's 70.

[12] The MILC Collaboration, presented at Lattice '96, hep-lat/9608012.

[13] F. Butler *et al.*, Phys. Rev. Lett. **70**, 2849 (1993).

[14] This plot was kindly provided by R. Sommer.

[15] K. Symanzik, in *Recent Developments in Gauge Theories*, edited by G. 't Hooft *et al.* (Plenum, New York, 1980), p. 313; in *Mathematical Problems in Theoretical Physics*, edited by R. Schrader *et al.* (Springer, New York, 1982); Nucl. Phys. B **226**, 187, 205 (1983).

[16] P. Weisz , Nucl. Phys. B **212**, 1 (1983); M. Lüscher and P. Weisz, Comm. Math. Phys. **97**, 59 (1985).

[17] M. Lüscher and P. Weisz, Phys. Lett. B **158**, 250 (1985).

[18] B. Sheikholeslami and R. Wohlert, Nucl. Phys. B **259**, 572 (1985).

[19] M. Alford, W. Dimm, G. P. Lepage, G. Hockney, and P. Mackenzie, Phys. Lett. B **361**, 87 (1995); G. P. Lepage, to appear in the *Proceedings of Lattice '95*, and his Schladming lectures, hep-lat/9607076.

[20] K. Jansen *et al.*, Phys. Lett. B **372**, 275 (1996) (hep-lat/9512009); M. Lüscher *et al.*, hep-lat/9605038, hep-lat/9608049.

[21] C. Morningstar, to appear in the *Proceedings of Lattice '95*, hep-lat/9509073.

[22] G. P. Lepage and P. Mackenzie, Phys. Rev. D **48**, 2250 (1993).

[23] S. Brodsky, G. P. Lepage, and P. Mackenzie, Phys. Rev. D **28**, 228 (1983).

[24] G. Parisi, in *High Energy Physics-1980, XX Int. Conf.*, edited by L. Durand and L. G. Pondrom (AIP, New York, 1981).

[25] The classic reference is K. Wilson and J. Kogut, Phys. Repts. **12** C, 77 (1974).

[26] P. Hasenfratz and F. Niedermayer, Nucl. Phys. B **414**, 785 (1994); P. Hasenfratz, Nucl. Phys. B (Proc. Suppl.) **34**, 3 (1994); F. Niedermayer, *ibid.*, 513; A. Farchioni, P. Hasenfratz, F. Niedermayer, and A. Papa, Nucl. Phys. B **454**, 638 (1995).

[27] T. DeGrand, A. Hasenfratz, P. Hasenfratz, and F. Niedermayer, Nucl. Phys. B **454**, 587 (1995); Nucl. Phys. B **454**, 615 (1995).

[28] T. DeGrand, A. Hasenfratz, and D. Zhu, COLO-HEP-369, hep-lat/9603015.

[29] U.-J. Wiese, Phys. Lett. B **315**, 417 (1993); W. Bietenholz, E. Focht, and U.-J. Wiese, Nucl. Phys. B **436**, 385 (1995); W. Bietenholz and U.-J. Wiese, MIT preprint, CTP 2423 (1995).

[30] D. Bliss *et al.*, hep-lat/9605041.

[31] C. Davies *et al.*, Phys. Rev. D **52**, 6519 (1995); Phys. Lett. B **345**, 42 (1995); Phys. Rev. D **50**, 6963 (1994); Phys. Rev. Lett. **73**, 2654 (1994); and G. P. Lepage *et al.*, Phys. Rev. D **46**, 4052 (1992).

[32] M. Alford, T. Klassen, and G. P. Lepage, presentations at Lattice '95, hep-lat/9509087, and in Lattice '96, hep-lat/9608113.

[33] UKQCD Collaboration, presentation at Lattice '96, hep-lat/9608034.

[34] S. Collins, R. Edwards, U. Heller, and J. Sloan, presentation at Lattice '96, hep-lat/9608021.

[35] M. Göckeler *et al.*, talk presented at Lattice '95, hep-lat/9608046, plus references therein.

[36] R. C. Brower *et al.*, talk presented at Lattice '95, hep-lat/9608069.

[37] J. Shigemitsu, talk at Lattice '96, hep-lat/9608058.

[38] Compare M. Wingate *et al.*, Nucl. Phys. B (Proc. Suppl.) **42**, 373 (1995).

[39] See S. Collins *et al.*, preprint FSU-SCRI-96-43, hep-lat/9607004.

[40] For one example of this idea, see M. Shifman, Int. J. Mod. Phys. A **11**, 3195 (1996), hep-ph/9511469.

[41] L. Montonet *et al.*, Phys. Rev. D **50**, 1173 (1994) and 1995 off-year partial update for the 1995 edition available on the PDG WWW pages (URL: http://pdg.lbl.gov/).

[42] P. Burrows, in these proceedings.

[43] A. El-Khadra, G. Hockney, A. Kronfeld, and P. Mackenzie, Phys. Rev. Lett. **69**, 729 (1992).

[44] G. Rodrigo and A. Santamaria, Phys. Lett. B **313**, 441 (1993).

[45] M. Lüscher, P. Weisz, and U. Wolff, Nucl. Phys. B **359**, 221 (1991); M. Lüscher, R. Narayanan, P. Weisz, and U. Wolff, Nucl. Phys. B **384**, 168 (1992); M. Lüscher, R. Sommer, U. Wolff, and P. Weisz, Nucl. Phys. B **389**, 247 (1993); M. Lüscher, R. Sommer, P. Weisz, and U. Wolff, Nucl. Phys. B **413**, 491 (1994).

[46] P. Weisz, in the *Proceedings of Lattice '95*, hep-lat/9511017.

[47] For a review of the experimental situation, see W. Toki, in these proceedings.

[48] G. Bhanot and M. Creutz, Phys. Rev. D **24**, 3212 (1981); for recent work, see U. Heller, Phys. Lett. B **362**, 123 (1995) (hep-lat/9508009).

[49] C. Morningstar and M. Peardon, contribution to Lattice '96, hep-lat/9608050.

[50] R. Sommer, Nucl. Phys. B **411**, 839 (1994).

[51] T. Schäfer and E. Shuryak, Phys. Rev. Lett. **75**, 1707 (1995).

[52] G. Bali *et al.*, Phys. Lett. B **309**, 378 (1993).

[53] H. Chen, J. Sexton, A. Vaccarino, and D. Weingarten, Nucl. Phys. B (Proc. Suppl.) **34**, 347 (1994).

[54] J. Sexton, A. Vaccarino, and D. Weingarten, Phys. Rev. Lett. **75**, 4563 (1995).

[55] S. Lindenbaum and R. Longacre, Phys. Lett. B **274**, 492 (1992).

[56] W. Lee and D. Weingarten, contribution to Lattice '96, hep-lat/9608071.

[57] For the UKQCD/$f_0(1500)$ picture, see F. Close and M. Teper, RAL-96-040, contribution to the 1996 International Conference on High Energy Physics, C. Amsler and F. Close, Phys. Lett. B **353**, 385 (1995) and Phys. Rev. D **53**, 295 (1996); while for the IBM/$f_J(1710)$ picture, see D. Weingarten, contribution to Lattice '96, hep-lat/9608070.

[58] For a nice derivation of this formula, see the lectures of J. Rosner in the *Proceedings of the 1990 Theoretical Advanced Study Institute*, edited by M. Cvetič and P. Langacker (World Scientific, 1991).

[59] C. Bernard and the MILC Collaboration, presentation at Lattice '96, hep-lat/9608092.

[60] R. M. Barnett *et al.* , Phys. Rev. D **54**, 1 (1996).

[61] K. Kodama *et al.*, DPNU-96-33, hep-ex/9696017.

[62] S. Aoki *et al.*, Prog. Theor. Phys. **89**, 1 (1993).

[63] D. Acosta *et al.*, Phys. Rev. D **49**, 5690 (1994).

[64] J. Z. Bai *et al.*, Phys. Rev. Lett. **74**, 4599 (1995).

[65] C. Bernard, T. Blum, and A. Soni, presentation at Lattice '96, hep-lat/9609005.

[66] J. Flynn, talk presented at Lattice '96, hep-lat/9610010.

[67] J. D. Bjorken, in these proceedings.

QCD Studies in *ep* Collisions

Wesley H. Smith*
Physics Department
University of Wisconsin, Madison, WI 53706 USA

ABSTRACT

These lectures describe QCD physics studies over the period 1992–1996 from data taken with collisions of 27 GeV electrons and positrons with 820 GeV protons at the HERA collider at DESY by the two general-purpose detectors H1 and ZEUS.

The focus of these lectures is on structure functions and jet production in deep inelastic scattering, photoproduction, and diffraction. The topics covered start with a general introduction to HERA and *ep* scattering. Structure functions are discussed. This includes the parton model, scaling violation, and the extraction of F_2, which is used to determine the gluon momentum distribution. Both low and high Q^2 regimes are discussed. The low Q^2 transition from perturbative QCD to soft hadronic physics is examined.

Jet production in deep inelastic scattering to measure α_s, and in photoproduction to study resolved and direct photoproduction, is also presented. This is followed by a discussion of diffraction that begins with a general introduction to diffraction in hadronic collisions and its relation to *ep* collisions, and moves on to deep inelastic scattering, where the structure of diffractive exchange is studied, and in photoproduction, where dijet production provides insights into the structure of the Pomeron.

*Supported by DOE Contract DE-FG02-95ER40896.

© 1996 by Wesley H. Smith.

1. Introduction

The H1 and ZEUS experiments at the HERA *ep* collider, located in the DESY Laboratory in Hamburg, Germany, observe interactions of 27 GeV electrons with 820 GeV protons. The study of electron-proton collisions at HERA is but the most recent in a long and productive series of investigations begun at Stanford by R. Hofstadter in the '50s. The results obtained in *t*-channel (momentum transfer) investigations have provided much of our present knowledge of the structure of the nucleon as well as several fundamental discoveries. Among the milestones are:

(i) Proton and neutron form factors. The measurement of the dipole form factor led to the search and discovery of the ρ, ω , *etc.*

(ii) The two-neutrino experiment, which established lepton flavors.

(iii) Bjorken scaling, an entirely experimental discovery, which gave reality to the hitherto imaginary quarks which had been used empirically to successfully classify the resonances.

(iv) Measurement of the properties of the quark constituents. The experimental verification of the number, charge, spin, and momentum of the constituents established their identification as quarks and predicted the existence of the gluon.

(v) Discovery of prompt leptons produced in neutrino interactions indicating the production of a new quantum number by the weak interaction.

(vi) Discovery of the neutral weak current in neutrino-nucleon collisions.

Two recent important milestones from the H1 and ZEUS experiments at DESY are:

(vii) Observation of the strong rise of the structure F_2 with decreasing x, attributed to a singular gluon momentum distribution in the proton at low x.

(viii) Observation of deep inelastic scattering events characterized by a "large rapidity gap," attributed to diffractive scattering of the virtual photon from proton, proceeding through the exchange of a Pomeron. The study of these events yields information on the flux of Pomerons in the proton and the structure of the Pomeron itself.

The size of a target feature that can be distinguished in the scattering process is inversely proportional to the square of the four-momentum, Q^2, transferred to the object being probed. Thus the ability to resolve smaller features requires higher momentum transfers. The construction of the first *ep* collider (HERA) provides a window to this physics at center-of-mass energies of 300 GeV, as compared to 30 GeV reached in fixed-target experiments. This has brought about a new era in the physics of lepton-nucleon scattering, in which both Q^2 and energy transfer ν are increased by two orders of magnitude (equivalent to a fixed-target experiment with a 52 TeV lepton beam). Viewing the collisions at HERA in the Breit Frame, where the quark reverses upon impact with the virtual photon or boson, the interactions resemble those found in e^+e^- colliders, but with energies greater than LEP200.

1.1. HERA Data

The HERA collider was commissioned with the first *ep* collisions in the Fall of 1991. First luminosity was observed in the H1 and ZEUS detectors at the end of May 1992 with 26.7 GeV electrons and 820 GeV protons. Since then, there have been four successful data runs, in the summer and the fall of 1992, from June to November 1993, from May to November 1994, and from May to December of 1995. Another run began in July 1996 and is scheduled for completion in December. H1 and ZEUS have had similar data exposures. The '92 summer and fall runs collected about 27 nb^{-1}, and the '93 run about 550 nb^{-1}. During 1994, ZEUS collected about 800 nb^{-1} with electrons. HERA then switched to running with positrons to increase the luminosity and ZEUS collected about 4.5 pb^{-1}. In 1995, ZEUS collected more than 7 pb^{-1} of luminosity with positrons.

2. Deep Inelastic Scattering

Deep inelastic scattering (DIS) at HERA typically involves the exchange of a virtual photon as shown in Figure 1. The kinematic variables are defined as:

$$s = (k + P)^2 = \text{ center-of-mass energy}$$

$$Q^2 = -q^2 = -(k-k')^2 = \text{(momentum transferred)}^2$$

$$x = \frac{Q^2}{2P \bullet q}, \quad y = \frac{P \bullet q}{P \bullet k}, \quad Q^2 = sxy,$$

where x is the fraction of the proton's momentum carried by the struck quark and y is the fraction of the electron's energy lost in the proton rest frame. The topology of a DIS event is shown in Figure 2, illustrated with a ZEUS event in Figure 3. The electron

and the current jet from the struck quark are observed in the central detector, while the proton remnant travels unobserved down the forward beampipe in the proton direction.

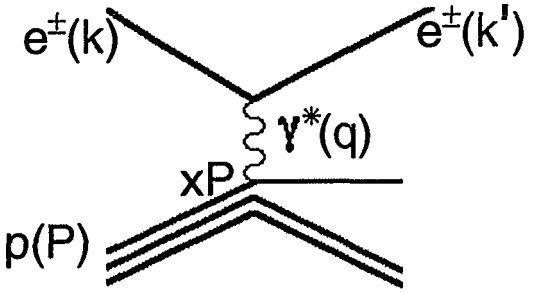


Figure 1. A deep inelastic scattering event.

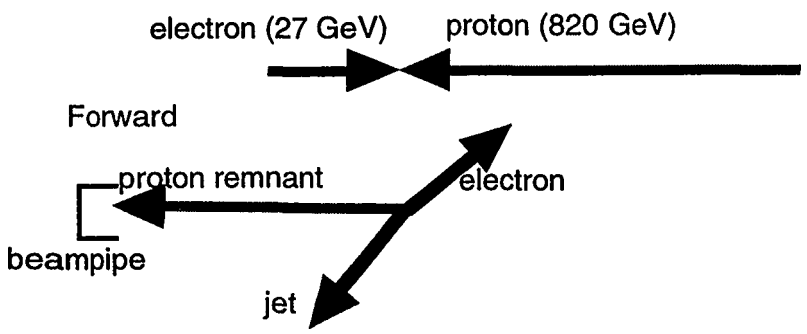


Figure 2. Topology of a deep inelastic scattering event at HERA.

The reconstruction of the x and Q^2 of DIS events is determined from the energy and angle of the scattered electron (E_e', θ_e) and the energy and angle of the current jet (E_h,γ_h). Only two of these four measured quantities are required to reconstruct x and Q^2. For example, in terms of the scattered electron energy and angle (E_e', θ_e), we have:

$$Q^2 = 4E_e E_e' \cos^2\frac{\theta}{2}, \quad x = \frac{E_e \cos^2\frac{\theta}{2}}{E_p\left[1-\frac{E_e'}{E_e}\right]}, \quad y = 1-\frac{E_e'}{E_e}\sin^2\frac{\theta}{2}.$$

The reconstruction methods using various combinations of the variables E_e', θ_e', E_h, and γ_h have different responses to detector effects and vary in accuracy for different kinematic regions. The optimal reconstruction method, called the P_T method, provides the best performance for the full kinematic range using all four variables, conservation of $E - P_z$ (see Sec. 2.1.1), and P_T balance between the electron and current jets.

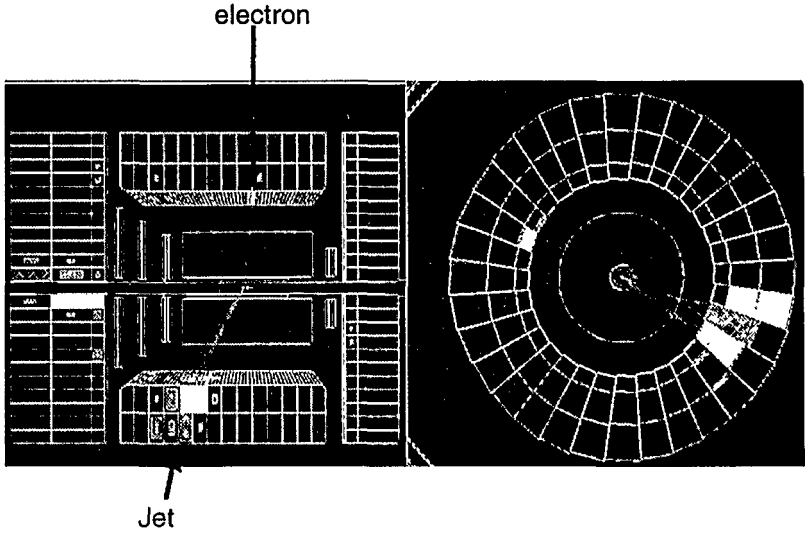


Figure 3. A deep inelastic scattering event observed in ZEUS with Q^2 = 1600 GeV^2.

2.1. Backgrounds

2.1.1. Photoproduction

Photoproduction is not only a large source of background to DIS events, especially at high y, but also is the source of many interesting physics results that will be discussed in Sec. 2.3.3. Photoproduction in *ep* scattering occurs when the electron is scattered at very small angles ($\theta < 1.0°$) and Q^2 is very close to zero ($Q^2 < 0.2$ GeV^2). Since the

outgoing electron in photoproduction events is emitted at very low angles, in most cases it escapes undetected down the beampipe in the electron direction. However, even though the outgoing electron is missing, some photoproduction events can contaminate the DIS sample through false identification of hadronic activity as the scattered electron. Since the *ep* interaction cross section via virtual photon exchange is proportional to $1/Q^2$, photoproduction is the dominant source of physics events at HERA, and even a small fraction of contamination from photoproduction events creates a sizable background.

There are several techniques used to suppress the photoproduction background. If the falsely identified electron is caused by a deposit of hadronic energy near the forward beampipe, the event will have a large reconstructed *y*, which can be removed by a *y* cut. We can also use conservation of the difference between the energy of the event and the energy in the proton beam direction:

$$(E_{tot} - P_{z\ tot})_{final} = (E_{tot} - P_{z\ tot})_{initial} = (E_p + E_e) - (E_p + E_e) = 2E_e.$$

Since the proton remnant jet contributes very little to this expression due to its small forward angle, we expect the value of $(E_{tot} - P_{z\ tot})$ for DIS events to be $2E_e$. For photoproduction events, the scattered electron of energy E_e' escapes undetected in the electron direction, yielding a lower value of $(E_{tot} - P_{z\ tot}) = 2E_e - E_e'$.

2.1.2. Beam-Gas Background

A large source of background comes from interactions of the proton beam with the residual beampipe gas. Events from protons that interact after passing through the detector are not seen. Events from protons that interact before passing through the detector can be eliminated by measurement of the event time. The topology of a typical proton beam-gas interaction is shown in Figure 4. Beam-gas events can create energy deposits that mimic both the scattered electron and the current jet. However, the timing of these events is different than events from the interaction point, which deposit energy in the rear calorimeter (direction of the electron beam) after the proton has traveled to the interaction point and the scattered electron has traveled back to the detector. Beam-gas interactions upstream of the detector directly strike the detector at a time different from the round-trip time of flight from the detector to the interaction point and back, which is about 13 ns.

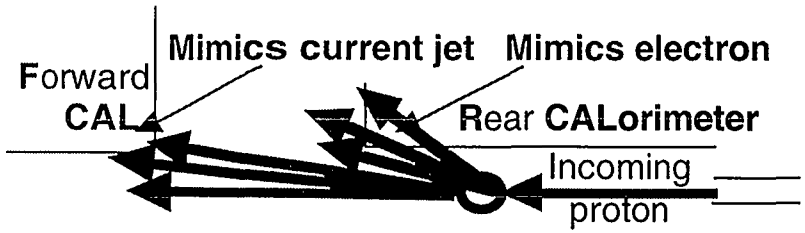


Figure 4. Topology of a typical upstream proton beam-gas interaction.

Proton beam-gas events that originate in the detector can be eliminated with cuts on $(E_{tot} - P_{z\ tot})$ as described in Sec. 2.1.1. The very small background remaining after these cuts and the very small background from electron beam-gas background is calculated from the event rate for special noncolliding bunches of electrons and protons that are not paired with a corresponding proton or electron bunch.

2.2. Phenomenology of Deep Inelastic Scattering

2.2.1. Deep Inelastic Scattering Cross Section

The neutral current *ep* DIS differential cross section is:

$$\frac{d\sigma^{NC}(e^{\pm}p)}{dxdQ^2} = \frac{2\pi\alpha^2}{xQ^4} Y_+ \left[F_2 - \frac{y^2}{Y_+} F_L \mp \frac{Y_-}{Y_+} xF_3 \right],$$

where $Y_\pm = 1 \pm (1 - y^2)$. The virtual photon is either longitudinally or transversely polarized. The structure function $F_2(x, Q^2)$ gives the interaction between transversely polarized photons and spin-1/2 partons, and equals the charge weighted sum of the quark distributions. The structure function $F_L(x, Q^2)$ gives the cross section due to longitudinally polarized photons that interact with the proton. The partons that interact with these photons need to have high transverse momentum, which happens predominantly at high *y*. The structure function $F_3(x, Q^2)$ is the parity violating structure function which is due to Z^0 exchange, which is only an appreciable part of the cross section at high Q^2.

2.2.2. Parton Model

Beginning in 1967, a series of *ep* scattering experiments at SLAC[1] showed that the DIS cross section fell weakly with increasing Q^2 and that the momentum distributions of

the proton constituents (i.e., the structure functions), depended only on x. The Q^2 independence of the structure functions, called *scaling,* had been predicted by Bjorken[2] and was incorporated by Feynman[3] into the *parton model,* which assumed the proton was composed of non-interacting point-like partons, from which the electron scatters incoherently.

In the parton model, the structure function F_2 is given by the charge-weighted sum of the parton momentum densities, $F_2(x) = \sum_i e_i^2 x f_i(x)$. For spin-1/2 partons, $F_L = 0$ and for spin-zero partons, $F_L = F_2$. The parton densities are not calculable in this model and therefore are derived from experiment. DIS provides an excellent laboratory for the extraction of the parton densities because the electromagnetic probe is well-understood.

In the quark-parton model,[4] partons are identified with fractionally charged quarks that come in several flavors. The proton is made of three valence quarks, and a distribution of quark-antiquark pairs called the sea quarks. The singlet and nonsinglet quark flavor combinations are defined as:

$$q^{SI}(x) = \sum_i \left(q_i(x) + \bar{q}_i(x) \right), \qquad q^{NS}(x) = \sum_i \left(q_i(x) - \bar{q}_i(x) \right),$$

where the subscript i runs over all flavors. Under the assumption that $u(x) = u^v(x) + u^s(x)$ and $\bar{u}(x) = u^s(x)$, we have $q^{NS}(x) = u^v(x) + d^v(x)$ where v and s stand for valence and sea, respectively. The measurement of the momentum sum rule, $\int_0^1 x q^{SI}(x) dx < 1$, and its experimental determination[5] as ~0.5, led to acceptance of the addition of the electrically neutral gluons, the field quanta responsible for the binding of the quarks to the proton constituents,[6] *i.e.*, $\int_0^1 \left(x q^{SI}(x) + x g(x) \right) dx = 1$. Therefore, measurement of the gluon momentum density, $xg(x)$, is required to fully understand the structure of the proton. It is also particularly important at low x, where gluon scattering dominated the proton collision cross sections.

2.2.3. Perturbative QCD

QCD produces interactions between quarks and gluons which cause the quarks to acquire transverse momentum, which causes scaling violation: $F_2(x) \rightarrow F_2(x,Q^2)$. Examples of these interactions are shown in Figure 5. The probabilities for these interactions are called splitting functions and have a $\ln(Q^2)$ behavior.

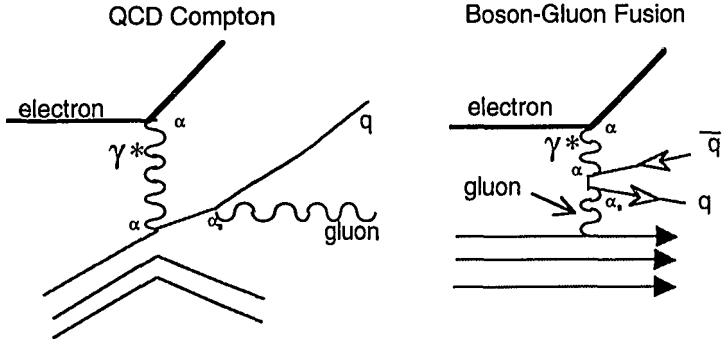


Figure 5. QCD interactions between quarks and gluons.

As Q^2 increases, the photon is able to resolve finer structure in the proton and interacts with the cloud of partons (quarks and gluons) around each valence quark that shares the proton's momentum. As x decreases, the fraction of proton momentum needed to be carried by the struck parton decreases, increasing the likelihood that such a parton is present. Therefore, we expect the number of quarks to increase with decreasing x, and we expect this effect to be more pronounced at higher Q^2. The detailed expectations for these changes are discussed below.

The evolution of the quark and gluon densities of the proton with Q^2 and x is given by perturbative QCD. Given an empirical parameterization for the parton densities at some $Q^2 = Q_0^2$: $xg(x) = A_g x^{\delta_g}(1-x)^{\eta_g}(1+\gamma_g x)$, $xq^{NS}(x) = A_{NS} x^{\delta_{NS}}(1-x)^{\eta_{NS}}$, and $xq^{SI}(x) = A_{SI} x^{\delta_{SI}}(1-x)^{\eta_{SI}}(1+\varepsilon_{SI}\sqrt{x}+\gamma_{SI}x)$, the Dokshitzer-Gribov-Lipatov-Altarelli-Parisi (DGLAP)[7] equations describe the evolution of the parton densities to higher Q^2:

$$\frac{dq_i(x,Q^2)}{d\ln Q^2} = \frac{\alpha_s(Q^2)}{2\pi}\int_x^1 \frac{dw}{w}\left[q_i(w,Q^2) P_{qq}\left(\frac{x}{w}\right) + g(w,Q^2) P_{qg}\left(\frac{x}{w}\right)\right]$$

$$\frac{dg(x,Q^2)}{d\ln Q^2} = \frac{\alpha_s(Q^2)}{2\pi}\int_x^1 \frac{dw}{w}\left[\sum_i q_i(w,Q^2) P_{gq}\left(\frac{x}{w}\right) + g(w,Q^2) P_{gg}\left(\frac{x}{w}\right)\right],$$

where the functions $P_{ij}(x/y)$ are called the splitting functions, which give the probability that a parton (either a quark or a gluon) i with momentum fraction x originated from a parton j with momentum fraction y, where $x < y < 1$. The coupling constant α_s of the

strong force is given in lowest order by: $\alpha_s(Q^2) = \frac{12\pi}{(33-2n_f)\log(Q^2/\Lambda^2)}$, where n_f is the number of flavors and Λ is a QCD parameter that governs the Q^2 dependence, and in particular, sets the boundary for $Q^2 \gg \Lambda^2$ where α_s is sufficiently small to justify a perturbative treatment in terms of quasifree quarks and gluons. The logarithmic radiative QCD processes and their subsequent parton evolution as characterized by the DGLAP equations result in the logarithmic scaling violations that render the structure functions dependent on both x and Q^2. Even though the structure function F_2 is given by $F_2(x,Q^2) = \sum_i e_i^2 x q_i(x,Q^2)$, since the DGLAP equations couple the quark and gluon distributions, F_2 also depends on the gluon distribution as well as the quark distributions. Moreover, since the structure function is extracted from the cross section, and the calculation of the DIS cross section requires F_L,

$$F_L(x,Q^2) = \frac{\alpha_s(Q^2)}{\pi}\int_x^1 \frac{dw}{w}\left(\frac{x}{w}\right)^2\left\{\frac{4}{3}F_2(w,Q^2) + 2\sum_i e_i^2\left(1-\frac{x}{w}\right)wg(w,Q^2)\right\},$$

the parameterization of the gluon density can be determined by fitting QCD evolution to the DIS data.

2.2.4. Parton Distribution Functions

Parton Distribution Functions (PDF's) describe the sharing of the proton's momentum amongst its partons (gluons, valence, and sea quarks). Martin, Roberts, and Stirling[8] (MRS) and the Coordinated Theoretical/Experimental Project on QCD[9] (CTEQ) assume $g(x,Q_0^2) \sim x^{\gamma_1}$ and $F_2(x,Q_0^2) \sim x^{\gamma_2}$, where $Q_0^2 = 4$ GeV^2, and they evolve in Q^2 according to the DGLAP equations, using the single parameterization to produce a global fit to the world DIS data. Glück, Reya, and Vogt[10] (GRV) start with valence-like parton (gluon, valence, and sea quark) distributions at $Q_0^2 = 0.3$ GeV^2 and they evolve in Q^2 using the DGLAP equations. This dynamically generated growth in the parton distribution functions (PDF's) predicts a rapid rise at low-x with $g(x,Q^2)$ and $F_2(x,Q_0^2) \sim x^{\gamma}$, where $\gamma \ll -0.08$.

2.2.5. Models for Low Q^2 and Low x

In the low-Q^2 region where the proton is mostly sea quarks and gluons, perturbative QCD cannot be used and other models must be used to predict the behavior of the structure functions. One approach is to use Regge theory, which describes hadron-hadron and real photoproduction cross sections in terms of the exchange of a non-perturbative particle, or "Reggeon" in the t-channel. In the limit as $s \to \infty$, only one of these Reggeons survives, the Pomeron. The Pomeron has the quantum numbers of the vacuum. Donnachie and Landshoff[11] (DL) extended the Regge picture to virtual photoproduction cross sections for $Q^2 < 10$ GeV^2. This approach assumes that

since: $F_2 = \frac{Q^2}{4\pi\alpha^2}\sigma(\gamma^* p)$ but at $Q^2 = 0$: $\sigma(\gamma^* p) = C \times (W^2)^{+0.08}$,

and at low x : $W^2 = \frac{Q^2}{x} \to \sigma(\gamma^* p) = C'(Q^2)x^{-0.08}$, then : $\lim_{Q^2\to 0} F_2(x,Q^2) = f(Q^2)x^{-0.08}$.

Therefore, they relate the structure function to Reggeon exchange phenomena which successfully describe the slow rise of total cross sections with center-of-mass energy in hadron-hadron and photoproduction reactions.

In the limit $x \to 0$, the splitting functions become singular and the $\ln(1/x)$ terms become important. The Balitsky, Fadin, Kuraev, and Lipatov[12] (BFKL) equation is a perturbative QCD approach that resums the leading powers of $\ln(1/x)$, producing an evolution equation in x. The analytic solution to this equation results in a gluon distribution:

$$g(x,Q_0^2) \sim x^{\gamma} \text{ and } \gamma = -\frac{12\ln(2)}{\pi}\alpha_s \sim -0.5.$$

The BFKL approach may be viewed as the exchange of many gluons, which corresponds to the same quantum numbers as the Pomeron. This multigluon system is referred to as the BFKL Pomeron. Since this perturbative QCD process is taking place at relatively high t, the BFKL Pomeron is called a "hard Pomeron" in contrast to the "soft Pomeron" referred to above in the nonperturbative DL model, which is exchanged at low t.

2.3. Measurement of F_2 and Gluon Extraction

2.3.1. Technique and Kinematic Range

The measurement of F_2 at HERA starts by binning the data in x and Q^2 and subtracting the background. The cross section is multiplied by a QCD calculation of F_L using parameterizations of $q(x, Q^2)$ and $g(x, Q^2)$. The acceptance is measured by a Monte Carlo calculation. F_2 is then unfolded iteratively until the Monte Carlo matches the data.

Finally, the systematic errors are estimated by repetition of the analysis with excursions within the error envelope.

The H1 (Ref. 13) and ZEUS[14] F_2 data cover a large kinematic range with Q^2 from 0.16 to 15,000 GeV^2 and x values between 3×10^{-6} and 0.8. The experiments have been able to explore the low-x, low-Q^2 regime through several techniques. Both H1 and ZEUS have taken shifted vertex (SVX) runs with the interaction point moved in the proton direction to give an extended lever arm for electrons striking their rear calorimeters, thereby reducing the acceptance cutoff for low Q^2. In addition, both experiments analyzed data with initial state radiation (ISR) from the electron, which reduced the energy of the incoming electron, which also permits access to lower Q^2 scattering within the detector acceptance. Finally, ZEUS added a calorimeter behind and between the rear calorimeter and the beampipe. This beampipe calorimeter (BPC) detects electrons scattering at very shallow angles that would otherwise be unobserved.

Figure 6 compares the range of structure function measurements from H1 and ZEUS with deep inelastic fixed target electron scattering at SLAC and muon scattering at CERN (BCDMS,[15] NMC[16]) and Fermilab [E665 (Ref. 17)]. This shows that the HERA experiments have extended the range of both x and Q^2 measurements by more than two orders of magnitude. There is also considerable overlap between the HERA results and those of E665 and NMC, providing for comparisons with the fixed target regime.

2.3.2. F_2 Results

Figure 7 shows the final results for F_2 versus x in Q^2 bins from the H1 and ZEUS 1994 data sets, along with the fixed target muon scattering experiments BCDMS, NMC, and E665. The dramatic rise in F_2 with decreasing x is evident over a wide Q^2 range from 1.5 to 5000 GeV^2. This rise is attributed to a sharp increase in the gluon content with decreasing x at low values of x. This singular gluon behavior is further discussed in Sec. 2.3.3.

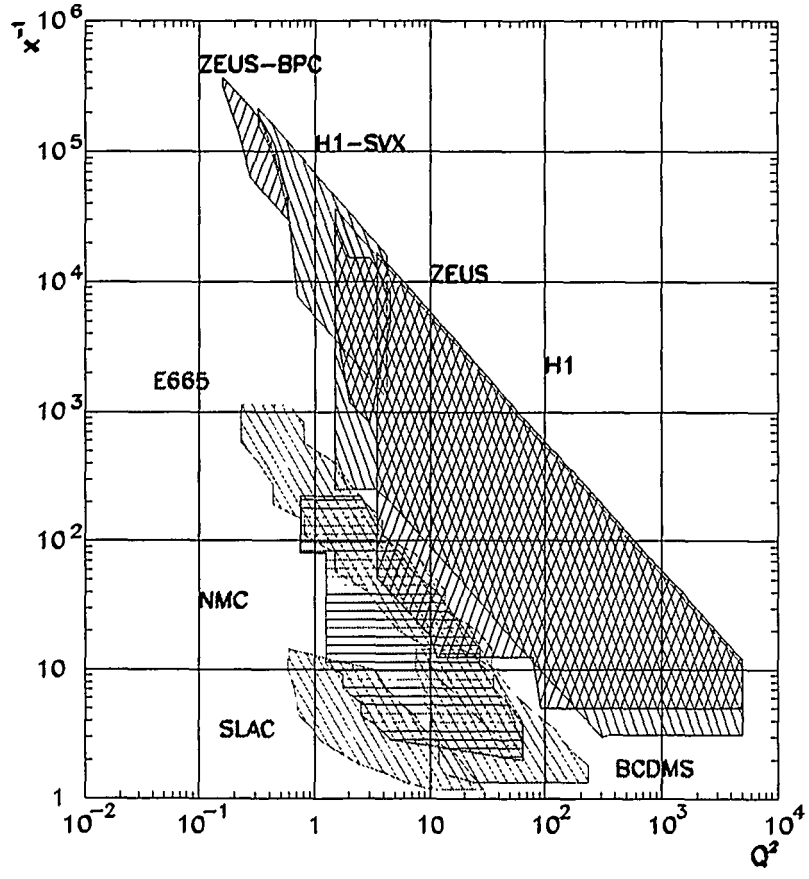


Figure 6. Kinematic range of structure function measurements.

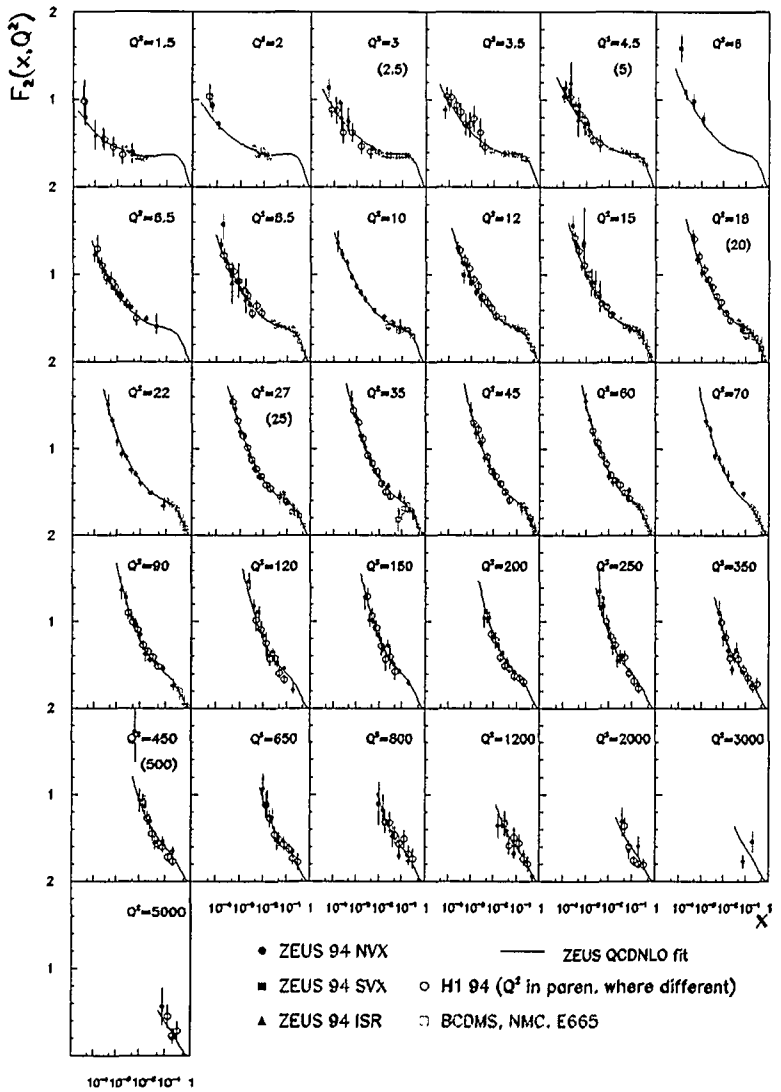


Figure 7. Measurements of F_2 versus x for various Q^2 bins from H1, ZEUS (Normal VerteX, Shifted VerteX, and Initial State Radiation samples), and fixed target muon scattering experiments at CERN (NMC, BCDMS) and Fermilab (E665).

There is good agreement between H1 and ZEUS, as well as between the HERA results and the fixed target muon scattering data of BCDMS, NMC, and E665. Also shown is a next-to-leading order (NLO) QCD fit used for the acceptance calculation for ZEUS. This fit agrees well with the data, showing that the QCD evolution characterized by the DGLAP equations describes that data well down to $x = 3 \times 10^{-5}$. The agreement between the data and the ZEUS QCD NLO fit indicates that the DGLAP evolution approaches of MRS, CTEQ, and GRV are sufficient to explain the data shown in Figure 7 and that it is not necessary to invoke the BFKL equation to resum the ln(1/x) terms in the kinematic regime covered by the HERA data thus far. Further investigation at low x and low Q^2 is discussed in Sec. 2.3.4.

At large x and at Q^2 values up to 70 GeV^2, where the HERA data reach the x range covered by the fixed-target experiments, good agreement with the muon scattering results is observed. The agreement of the QCD NLO fit with both the HERA and fixed target muon scattering data shows a consistent picture between QCD evolution and the experiments over a wide kinematic range. This observation is further underscored by the good agreement between the HERA data and the latest parton distribution functions from the global data analyses produced by CTEQ[18] and MRS.[19]

2.3.3. Extraction of the Gluon Density

Figure 8 shows measurements of F_2 as a function of Q^2 for various bins of x from H1, ZEUS, and fixed target muon scattering experiments at CERN (NMC, BCDMS) and Fermilab (E665). There is good agreement between ZEUS and H1, as well as good agreement between the HERA measurements and the fixed target results where they overlap from $x = 0.004$ through 0.081. The QCD NLO fit is also shown. It agrees well with the HERA and muon scattering data, indicating that the measured x-Q^2 behavior of F_2 is described by QCD using DGLAP evolution over the full kinematic range. The plot also shows the variation of F_2 with Q^2, showing strong QCD-predicted scaling violations for $x < 0.02$. Since these scaling violations are caused by gluon radiation, they can be used to determine the gluon distribution.

As pointed out in Sec. 2.2.3, the logarithmic slope $dF_2/d\ln Q^2$ provides a measurement of the gluon distribution. An example of the fitting technique can be taken from the ZEUS analysis of the 1994 F_2 data. The NMC data was used to constrain the fit at larger values of x. The momentum sum rule was used to constrain

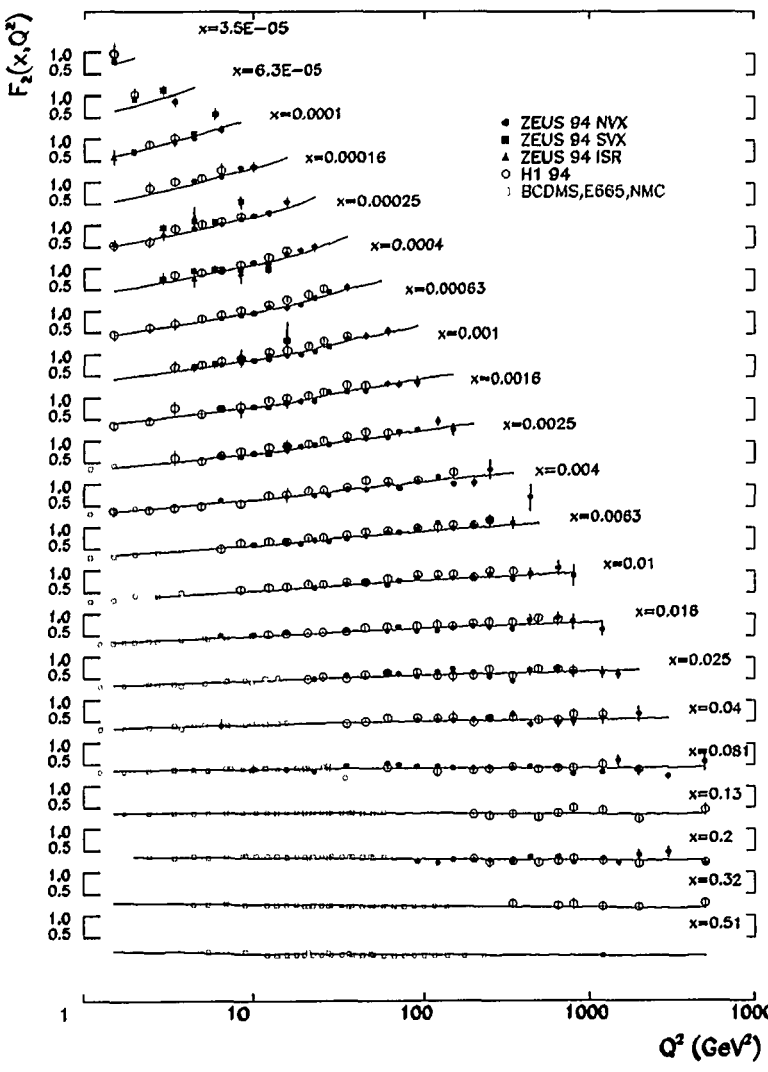


Figure 8. F_2 versus Q^2 for various bins of x for H1, ZEUS, and for fixed target muon scattering (BCDMS, E665, NMC) along with the NLO QCD fit to ZEUS data.

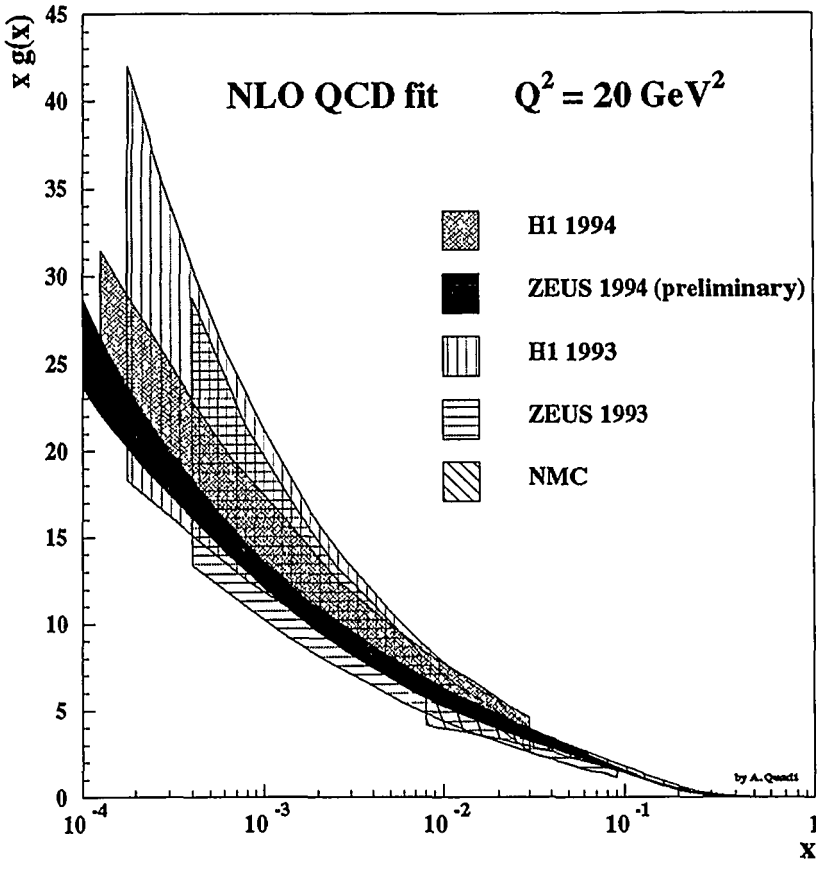


Figure 9. Results for fits to the gluon distribution from H1 and ZEUS from the 1993 and 1994 data sets.

the gluon density. The functional forms of the quark and gluon densities shown in Sec. 2.2.3 were assumed. The SLAC/BCDMS value of $\alpha_s(M_Z^2) = 0.113$ was assumed and evolved in Q^2. The quark and gluon distributions were evolved using the DGLAP equations to measured Q^2 bins to calculate F_2, and this was compared to the data by computing a χ^2 with statistical errors only. A nonlinear minimization of the χ^2 was then used to find the fit parameters of the assumed functional forms of the quark and gluon distributions. Finally, the systematic uncertainty was estimated separately by varying each of the 31 different systematic effects individually and performing a new fit.

Figure 9 shows the results of NLO QCD fits for the gluon density from H1 (Ref. 20), ZEUS,[21] and NMC[16] data for $Q^2 = 20$ GeV^2. The most striking effect is the more than an order of magnitude increase in the gluon content of the proton from about one gluon per unit of rapidity to more than 20 for x approaching 10^{-4}. It is also important to notice the major increase in range from that of the NMC experiment to the HERA results, as well as the significant improvement in the uncertainty and validity range in the kinematic plane between the 1993 and 1994 HERA measurements, while the agreement between the 1993 and 1994 HERA measurements remains quite good. The ZEUS measurement found an exponent of the gluon distribution (see Sec. 2.2.3) $\delta_g = 0.24 \pm 0.02$, and the momentum sum rule at $Q^2 = 7$ GeV^2 determined contributions of 0.555 quarks + 0.445 gluons.

There are some general caveats in order, concerning the extraction of F_2 and the gluon density. These analyses involve a priori assumptions for α_s and the quark-gluon parameterization in order to compute the F_L and F_3 corrections to the DIS cross section. The extracted F_2 is sensitive to these assumptions, particularly for the high-y kinematic range data, which is sensitive to the gluon. Therefore, it is more prudent to perform an assumption-independent analysis by directly fitting the cross-section data. The results of such an analysis can yield consistent values for α_s and the quark and gluon parameterizations.

2.3.4. Low Q^2 Measurements

The use of techniques such as shifted vertex running and initial state radiation analysis, as well as the data from the ZEUS beampipe calorimeter (BPC), have enabled measurements at lower Q^2 in the low-x region. This allows the study of the transition between DIS and photoproduction. At $Q^2 = 0$, the dominant processes are non-perturbative and described by Regge theory. As Q^2 increases, it is expected to observe the onset of perturbative QCD. The nature of the transition from a soft process of low virtuality to a hard process of high virtuality should provide understanding of both types of interactions. Knowledge of the low x and low Q^2 region is also needed for the calculation of radiative corrections.

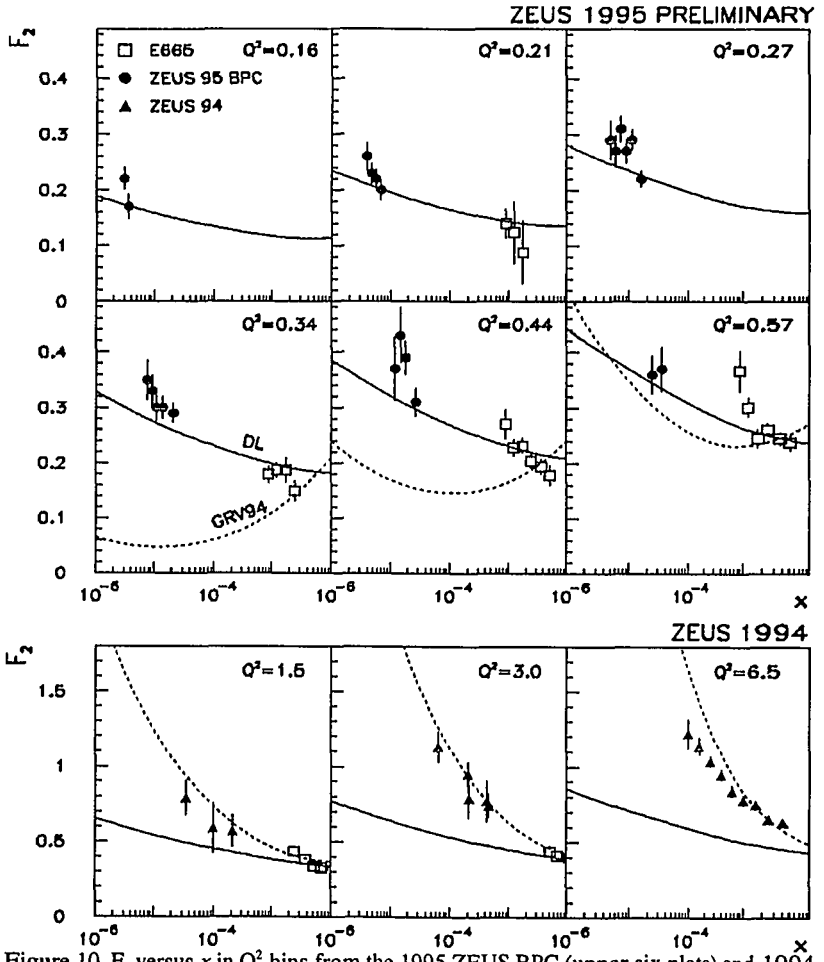


Figure 10. F_2 versus x in Q^2 bins from the 1995 ZEUS BPC (upper six plots) and 1994 shifted and normal vertex (lower three plots) data shown with E665 muon scattering results at the closest Q^2 values. Also shown are the theoretical predictions of GRV (dotted lines) and DL (solid lines).

The top six plots of Fig. 10 show the preliminary ZEUS BPC F_2 results for $0.16 \leq Q^2 \leq 0.57$ GeV^2. Also shown are the data from the E665 (Ref. 17) measurement at a similar Q^2, but much larger x. There is a rise in F_2 of approximately 1.5 to 2 from x near 10^{-3} to x near 10^{-5}. The bottom of Fig. 10 shows F_2 values from ZEUS and E665 for $Q^2 = 1.5$, 3.0, and 6.5 GeV^2 showing a rapid rise of F_2 as Q^2 increases. The rise of F_2 over two to three decades in x from E665 to ZEUS for $0.16 \leq Q^2 \leq 0.57$ GeV^2 agrees with the expectations of the DL model discussed in Sec. 2.2.5. However, at

higher Q^2, the DL prediction falls substantially below the ZEUS result. The GRV perturbative QCD prediction for F_2 accounts for about 40% of the measured F_2 at Q^2 = 0.44 GeV^2 and about 80% at Q^2 = 0.57 GeV^2. At larger Q^2 values, the GRV prediction reproduces the rapid rise of F_2, but is somewhat higher. We therefore observe the transition from a region of $Q^2 \leq 0.5$ GeV^2, where the DL soft Pomeron model describes almost real photoproduction and the perturbative QCD picture does not describe the measured behavior, to a region of $Q^2 \geq 1.5$ GeV^2, where a perturbative QCD prediction is valid and the Regge picture is no longer appropriate.

A useful way to display the results for F_2 is to plot the total γ^*p cross section using the relation: $\sigma^{\gamma^* p}(W^2,Q^2) = \frac{4\pi^2\alpha}{Q^2}\frac{1}{1-x}\left(1+\frac{4M^2x^2}{Q^2}\right)F_2(x,Q^2)$. Figure 11 shows $\sigma(\gamma^*p)$ as measured by ZEUS[21,22] and E665 (Ref. 17) as a function of W^2 for Q^2 bins from 0.15 through 6.5 GeV^2. The total real photon-proton cross-section measurements from ZEUS[22], H1 (Ref. 23), and fixed-target experiments[24] are also shown. The curves show the DL soft Pomeron model and the GRV perturbative QCD model. As discussed in Sec. 2.2.5, the DL model predicts $\sigma(\gamma^*p) \sim (W^2)^{0.08}$. The GRV model predicts a stronger variation with Q^2 and W^2. At low Q^2, the DL model describes the data well, but fails at $Q^2 \geq 1.5$ GeV^2. At $Q^2 \geq 1.5$ GeV^2, the GRV prediction agrees with the rapid rise in $\sigma(\gamma^*p)$ with W^2 observed in the data.

Figure 12 explores the dependence of the exponent λ in $\sigma_{tot}^{\gamma^* p}(W^2,Q^2) \sim (W^2)^{\lambda}$ as a function of Q^2 from the H1 F_2 data.[25] There is a steady decrease in λ with decreasing Q^2. The data show a smooth transition from the higher to lower Q^2 regions in the Q^2 range covered by the H1 data from 0.35 to 3.5 GeV^2 down to 6 x 10^{-6}. The H1 experiment also reports[25] that the distinct rise in F_2 with decreasing x that is observed for $Q^2 > 2$ GeV^2 is sharply reduced with decreasing Q^2 until the rise observed at small Q^2 is close to that expected by Regge models.

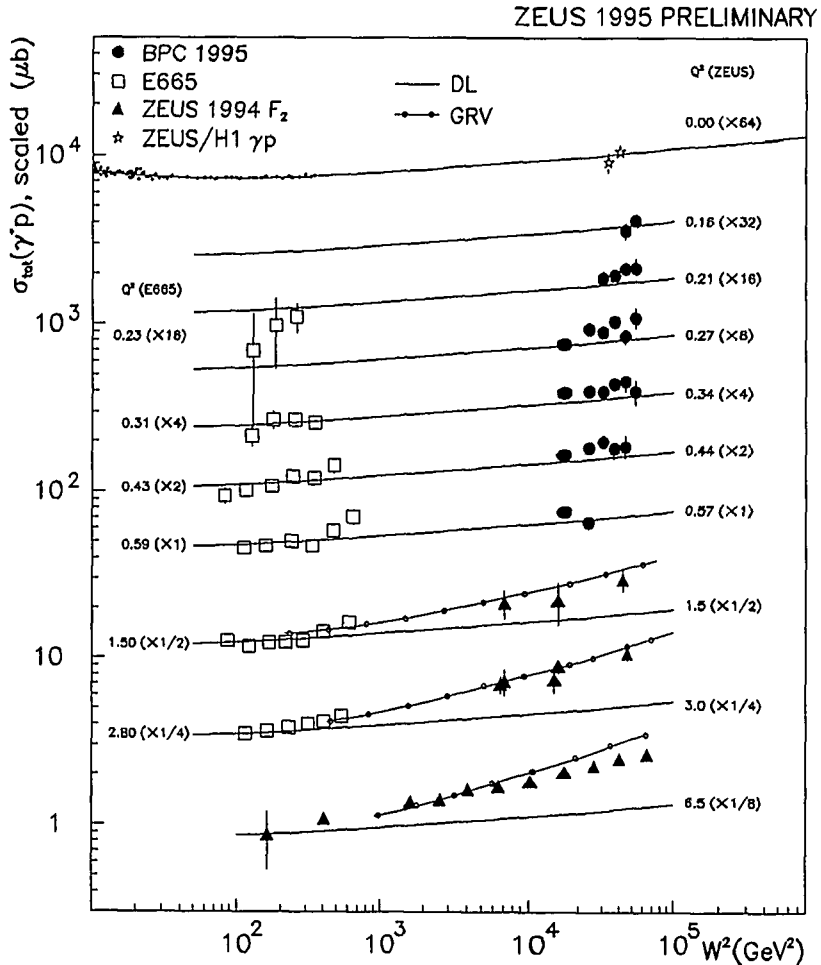


Figure 11. Total γ^*p cross section, $\sigma_{tot}^{\gamma^* p}(W^2,Q^2) = \frac{4\pi^2\alpha}{Q^2}F_2(x,Q^2)$ as a function of W^2 for ZEUS and E665. The total cross section for real photon-proton scattering from ZEUS, H1, and fixed-target experiments at low W are also shown.

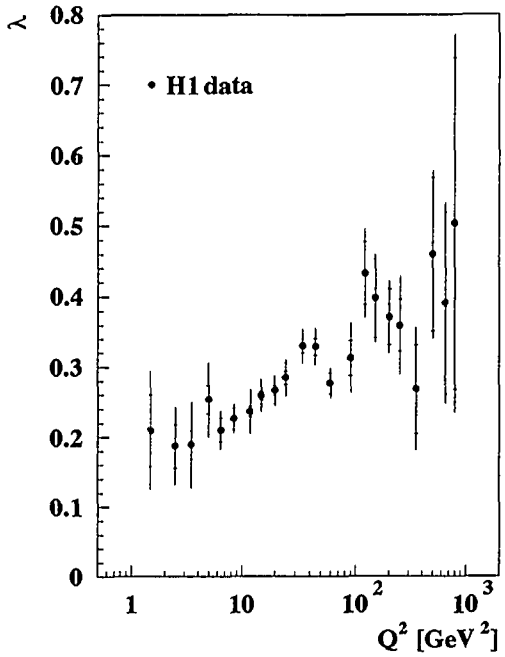


Figure 12. Dependence of λ in $\sigma_{tot}^{\gamma^* p}(W^2, Q^2) \sim (W^2)^{\lambda}$ on Q^2 from H1.

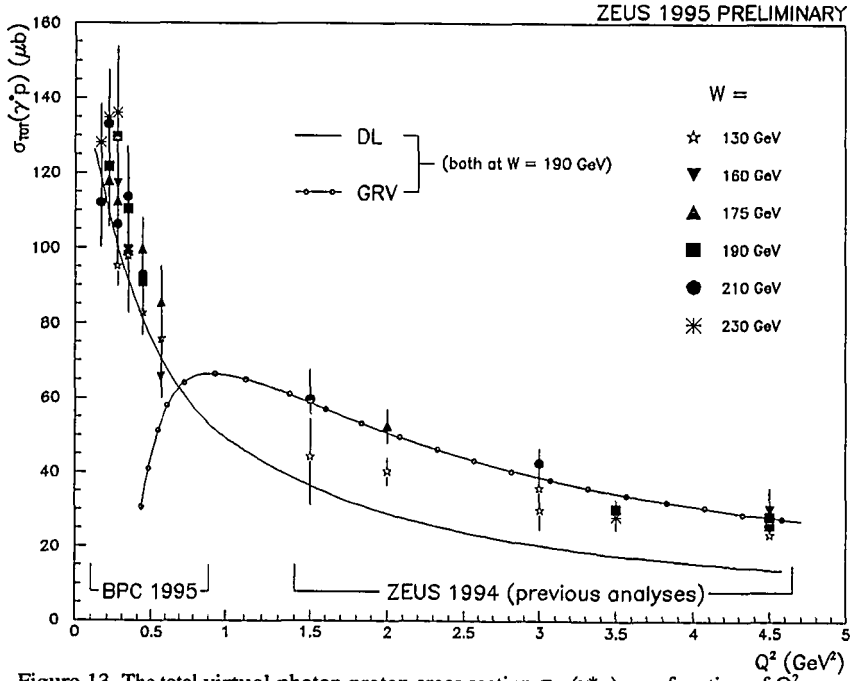


Figure 13. The total virtual photon-proton cross section σ_{tot} (γ*p) as a function of Q^2 from ZEUS 1995 BPC and 1994 SVX and NVX data for various mean W^2 values. Also shown are the predictions of GRV (upper curve for $Q^2 > 1.5$) and DL.

Figure 13 shows σ(γ*p) as a function of Q^2 with the cross sections at different W values indicated by different symbols. The data between Q^2 = 0.16 and 0.57 GeV² show the same decrease with increasing Q^2 for all values of W between 130 GeV and 230 GeV. This is consistent with the Regge picture as shown by the agreement with the DL model. For $Q^2 \geq 1.5$ GeV², we again observe behavior consistent with a perturbative QCD picture as shown by the agreement with the GRV model.

Therefore, we see that the rapid rise in F_2 with decreasing x observed by H1 and ZEUS for $Q^2 \geq 1.5$ GeV² and $x \ll 10^{-2}$ changes to a moderate rise in the low Q^2 region. This indicates a transition from the high-Q^2 perturbative QCD region to the low Q^2 region where Regge models provide a good description, while perturbative QCD does not. We also see that the transition region between these two regimes is smooth with an interplay between the two in the intermediate Q^2 range.

2.4. Charged and Neutral Current Cross Sections at High Q^2

At high Q^2 (> 200 GeV²), the charged current and neutral current cross sections reported by H1 (Ref. 26) and ZEUS[27] have established that the Q^2 dependence of the CC and NC cross sections are consistent with the W and Z propagators and that the CC and NC cross sections have a similar magnitude for $Q^2 \geq M_W^2$. ZEUS has shown that the NC DIS cross section $d\sigma/dQ^2$, for e^+p and e^-p collisions at 200 < Q^2 < 50,000

GeV^2 shows good agreement with the Standard Model and uses this to set limits of 1.0 to 2.5 TeV at 95% CL on the effective mass of contact interactions and to place a limit of 1.4 x 10^{-16} cm at 95% CL on the effective quark radius. H1 have measured the integrated CC cross section and the differential cross section for e^+p collisions with missing transverse momentum above 25 GeV. These results are summarized in Figure 14. Both H1 and ZEUS have used these cross sections to extract the W mass: $M_W^{H1} = 84^{+9+5}_{-6-4} GeV$, $M_W^{ZEUS} = 79^{+8+4}_{-7-4} GeV$, in good agreement with the 80.22 ± 0.26 GeV on-shell W mass measured at the Tevatron.[28]

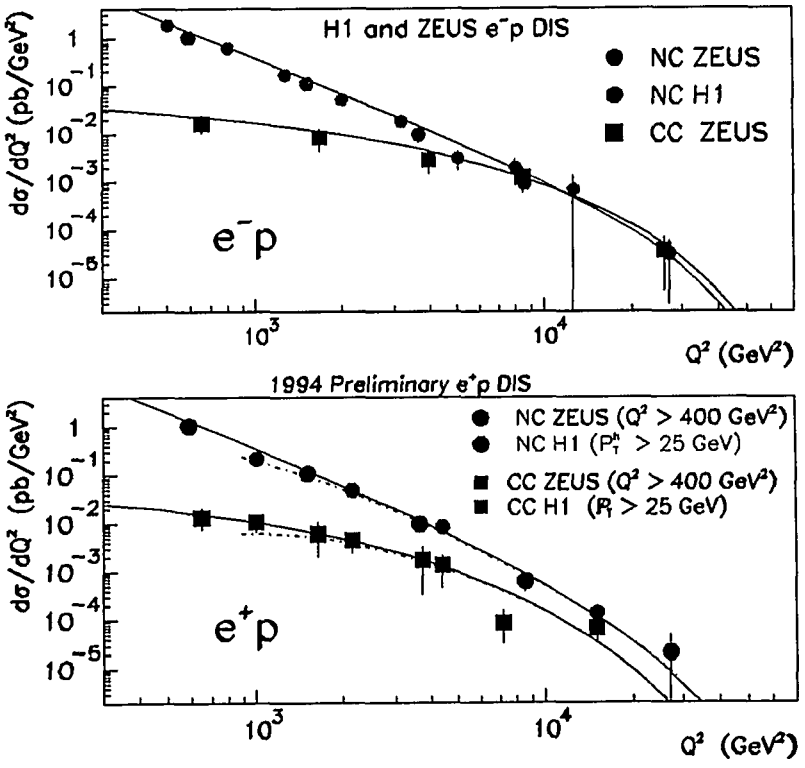


Figure 14. CC and NC DIS cross sections at high Q^2 from H1 and ZEUS for e^-p and e^+p collisions, compared with Standard Model predictions.

2.5. Jets in Deep Inelastic Scattering

In the naive quark-parton model, DIS virtual photoproduction gives rise to one jet from the struck quark and one jet from the proton remnant, which at HERA escapes undetected down the beampipe. We denote such events as 1+1, where the +1 refers to the unseen remnant jet. The production of additional jets in DIS beyond 1+1 involves QCD since it is due to the involvement of gluons in the hard scattering process. In particular, dijet or 2+1 jet production, to leading order in α_s, proceeds via QCD-Compton scattering (QCDC) characterized by the emission of a gluon from the struck quark and Boson-Gluon-Fusion, where a gluon from the proton and the virtual boson fuse to form a quark-antiquark pair. The basic DIS parton emission processes up to leading order in α_s are shown in Figure 15. Shown are (a) the Born process where a single quark is emitted, (b) BGF, (c) QCDC where the gluon is emitted in the final state and (d) in the initial state, and (e) gluon emission in the final and initial state as viewed in the Breit Frame.[29] In the naive quark parton model, the Breit Frame is the frame where the struck quark is scattered exactly backwards to its original direction and has no transverse momentum component. However, QCD processes introduce a net transverse momentum component to the incoming parton or the struck quark itself.

The strong coupling constant, α_s, can be measured at HERA from the relative rate of 2+1 jet events to 1+1 jet events. This measurement can be performed for different values of Q^2 so that it is possible to see the evolution of α_s within a single experiment over a wide range of Q^2. For the extraction of α_s to be reliable, the 2+1 jet rate must be calculated to NLO and the jet definition must be treated in the same way for experiment and theory.

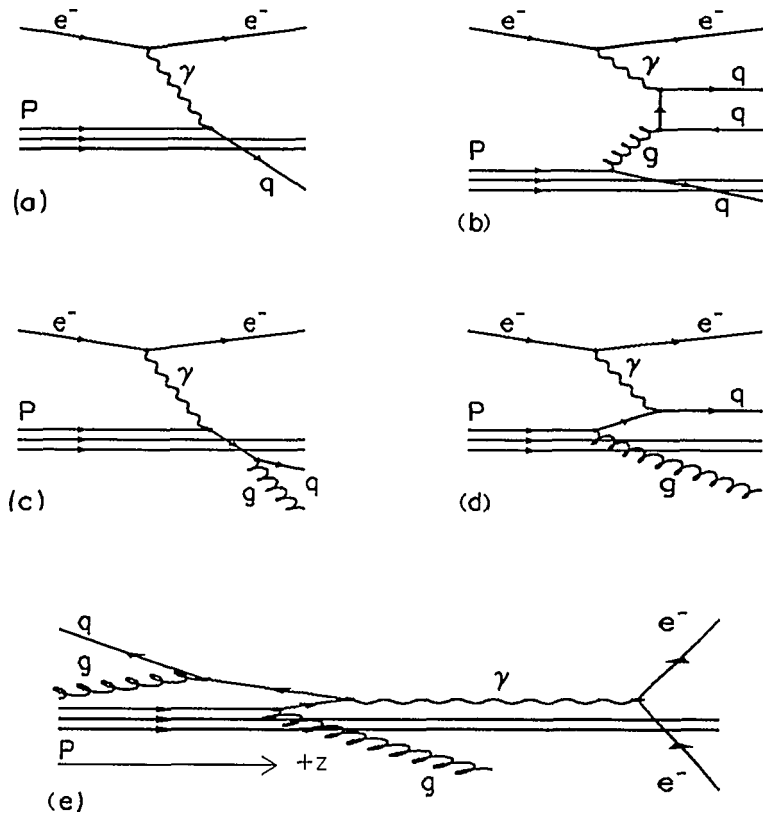


Figure 15. DIS parton emission processes to leading order in α_s: (a) Born process, (b) Boson Gluon Fusion, (c) final state gluon radiation, (d) initial state gluon radiation, (e) Breit Frame view of initial and final state gluon radiation.

Both H1(Ref. 30) and ZEUS[31] have extracted α_s from multijet production. They used the JADE[32] algorithm to assemble the jets and relate the hadronic final state measured in the detector to the hard scattering process. The algorithm employs a scaled invariant mass $y_{ij} = m_{ij}^2/W^2 = 2E_iE_j(1-cos\theta_{ij})/W^2$, where m_{ij} is the invariant mass of objects i and j, which are assumed massless and E_i, E_j are their energies. Objects are merged into jets by adding their four-momenta until y_{ij} for all objects exceed a jet resolution parameter y_{cut}. To prevent the detected fraction of the proton remnant jet from forming spurious jets, a pseudo-particle[33] was inserted along the z-axis (proton direction) and the missing longitudinal momentum in each event was assigned to it. Both H1 and ZEUS extracted values of α_s at $y_{cut} = 0.02$. Even this value of y_{cut}, which requires a large invariant mass between the jets, does not constrain the jets to be away from the beam direction. This is because one of the nonremnant 2+1 jets is often in the forward direction due to the forward singularity in the cross section. This forward direction has the greatest model uncertainty. Therefore H1 impose a cut in the jet polar angle in the laboratory system ($\theta_{jet} > 10°$). They also impose a cut in the backwards direction ($\theta_{jet} < 145°$) to ensure analysis in the hadronic calorimeter. In contrast, ZEUS uses a cut on $z = 1/2(1-cos\theta^*)$, where θ^* is the angle of the parton that produced the jet in the γ^*–parton center-of-mass system, of $0.1 < z < 0.9$. The variable z is a Lorentz invariant and a well-defined variable in the theory. These cuts on the jet position significantly reduce the statistics. In the case of the ZEUS cut, the loss is 50%.

Figure 16 shows the corrected jet rates R_{1+1}, R_{2+1}, and R_{3+1} as a function of y_{cut} for ZEUS data[31] compared with the DISJET[34] and PROJET[35] NLO QCD calculations for three Q^2 intervals between 120 and 3600 GeV^2 and the whole range. Both programs agree in their predictions for α_s and reproduce the shape of the measured jet rate distributions. H1 performed a similar analysis for two Q^2 intervals, 100–400 and 400–4000 GeV^2.

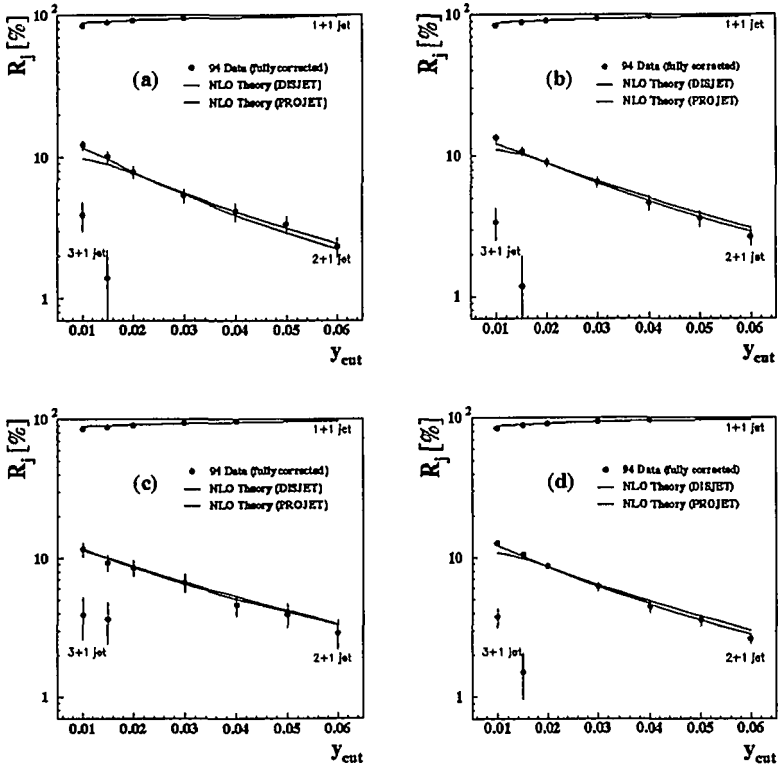


Figure 16. ZEUS results for jet production rates, R_j as a function of the jet resolution parameter y_{cut} for (a) $120 < Q^2 < 240$ GeV^2, (b) $240 < Q^2 < 720$ GeV^2, (c) $720 < Q^2 < 3600$ GeV^2, and (d) $120 < Q^2 < 3600$ GeV^2 with statistical errors only compared with two NLO QCD calculations, DISJET and PROJET.

The running of α_s depends on the renormalization group equation. The extraction of α_s in finite order QCD perturbative calculations depends on the renormalization scheme. H1 and ZEUS use the $\overline{MS}$ scheme. In second order, the dependence on other renormalization schemes is characterized by a single parameter, the value of the renormalization scale[35] where α_s is evaluated. H1 and ZEUS chose this to be Q^2. The same scale, Q^2, is chosen for the factorization scale where the parton densities are evaluated.

The ZEUS values[31] of α_s extracted using the JADE cluster algorithm are plotted in Figure 17 as a function of Q^2 for three Q^2 ranges. They are calculated from the fitted values of $\Lambda^{(5)}_{\overline{MS}}$ and plotted against the curves for $\Lambda^{(5)}_{\overline{MS}}$ = 100, 200, and 300 MeV. ZEUS uses five flavors in the calculation of Λ because the lower bound of the Q^2 range is above the b-quark mass threshold. The measured α_s decreases with increasing Q^2 as expected from the running of the strong coupling constant if Q^2 is taken as the scale. Extrapolating these measurements to $Q = M_{Z^0}$ yields the ZEUS result from the JADE algorithm that $\alpha_s(M_{Z^0}) = 0.117 \pm 0.005$ *(stat)* $^{+0.004}_{-0.005}$ *(syst$_{exp}$)* $\pm$ 0.007 *(syst$_{theory}$)*. H1 also extract their result[30] using the JADE algorithm, but with four flavors in the calculation of Λ and determine $\alpha_s(M_{Z^0}) = 0.123 \pm 0.018$, with statistics and systematic errors combined in quadrature. The difference in number of flavors should be a small effect since the contribution to the proton structure function from massive b-quarks in the kinematic region studied in these measurements is less than 2% (Ref. 37). The H1 and ZEUS values of α_s are in agreement with the world average result[28] of $\alpha_s(M_{Z^0}) = 0.117 \pm 0.005$. This constitutes an important test of QCD.

The ZEUS experiment also explored the dependence of the α_s measurement on use of another cluster algorithm, the k_t algorithm, which is evaluated in the Breit frame and uses a jet resolution parameter based on the minimum transverse energy of one particle relative to the other, $y_{ij} = 2\min(E_i^2, E_j^2)(1-\cos\theta_{ij})/M_{ref}^2$, where M_{ref}^2 is either Q^2 or a fixed value of 120 GeV^2 (Ref. 38). A second parameter, the transverse energy of the particle relative to the incoming proton direction, $y_{ip} = 2E_i^2(1-\cos\theta_{ip})/Q^2$, is used to distinguish particles that belong to the proton remnant jet from those which form jets by the condition $y_{ip} < y_{ij}$ for inclusion in the remnant jet. The k_t algorithm does not require a z cut with its loss of statistics nor a pseudo-particle to take care of the remnant jet. Its detector and hadronization corrections are smaller than those of the JADE algorithm. Finally, due to the definition of the energy-angle correlation of the particles with respect to the proton direction, initial state collinear singularities can be dealt with in a well-understood manner.[29] Figure 17 shows the extracted ZEUS values[38] of α_s extracted using the k_t cluster algorithm as a function of Q^2 for three Q^2 ranges , M_{ref}^2 is either equal to Q^2 or a fixed value of 120 GeV^2. Extrapolating these measurements to $Q = M_{Z^0}$ yields the ZEUS results from the k_t algorithm that $\alpha_s(M_{Z^0}) = 0.118 \pm 0.008$ *(stat)* for $M_{ref}^2 = Q^2$ and 0.120 ± 0.004 *(stat)* for $M_{ref}^2 = 120$ GeV^2. These values are close to the value of 0.117 extracted using the JADE algorithm, indicating only a small dependence on the choice between the JADE and k_t cluster algorithms.

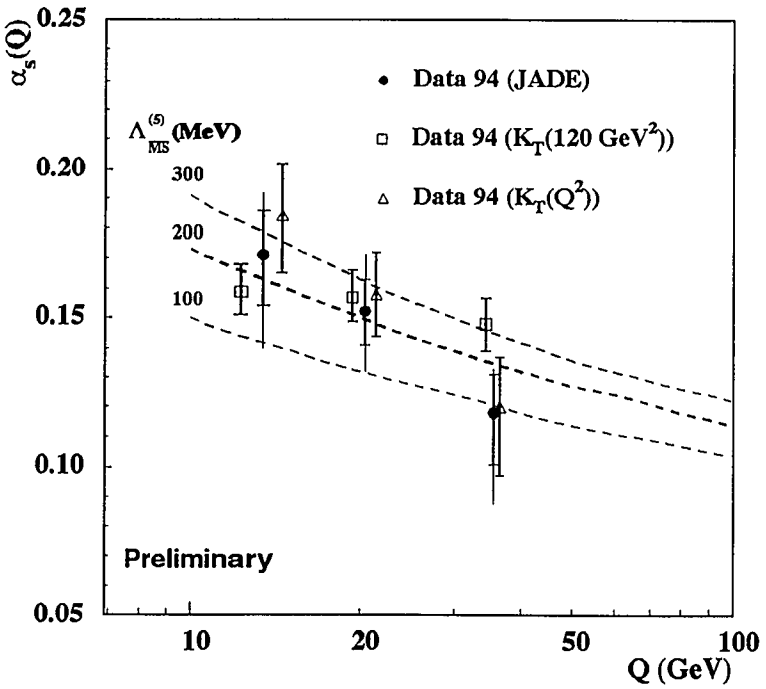


Figure 17. ZEUS measured values of $\alpha_s(Q)$ for three different Q^2 regions, extracted using three different jet algorithms. The statistical error corresponds to the inner bar and the thin bar shows the statistical and systematic error combined in quadrature. The dashed curves represent α_s with $\Lambda^{(5)}_{\overline{MS}}$= 100, 200, and 300 MeV.

3. Photoproduction

3.1. Introduction

For low Q^2 *ep* scattering, the photon is essentially real and the involvement of the electron can be essentially neglected. Such events are therefore called photoproduction events. Since the cross section has a $1/Q^4$ dependence, these events are the most common type of *ep* interaction. Although the center of mass of the *ep* collisions is 300 GeV at HERA, the center-of-mass energy of the photon-proton collisions, $W_{\gamma p}$= $\sqrt{4yE_eE_p}$, has a range from less than 130 GeV to more than 270 GeV. This is equivalent to a beam of 20 TeV photons striking a fixed proton target. These energies are sufficiently high to permit a photon that has fluctuated into a quark-antiquark pair to travel as a hadronic particle for hundreds of proton radii without violating the Heisenberg Uncertainty Principle.

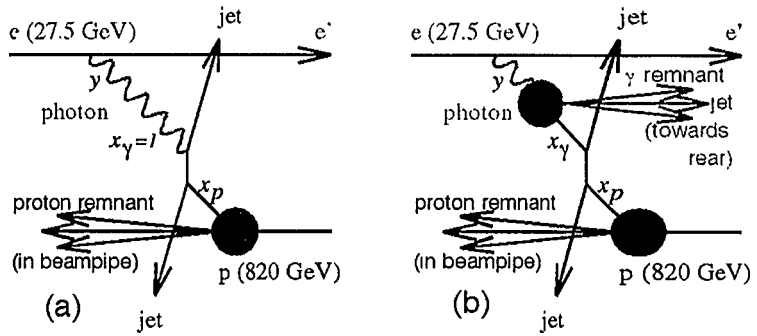


Figure 18. Topology of (a) direct photoproduction and (b) resolved photoproduction.

Photoproduction events are classified into direct and resolved[39] categories. The topology of a direct photoproduction event is shown in Figure 18(a). Direct photoproduction occurs when the photon interacts directly with a quark or gluon in the proton. In this case, the fraction of the photon momentum involved in the collision, x_γ, is close to one. Due to the low Q^2, the scattered electron emerges at a very low angle and travels undetected down the beampipe in the original electron direction. The hard scattering of the photon with a parton in the proton, carrying a fraction of proton momentum, x_p, can result in two outgoing partons with high E_t that manifest themselves as two jets in the main detector. The remaining particles from the proton, which form the proton remnant jet, travel down the beampipe in the proton direction. Figure 19 shows a high-E_t direct photoproduction dijet event as observed in the ZEUS detector.

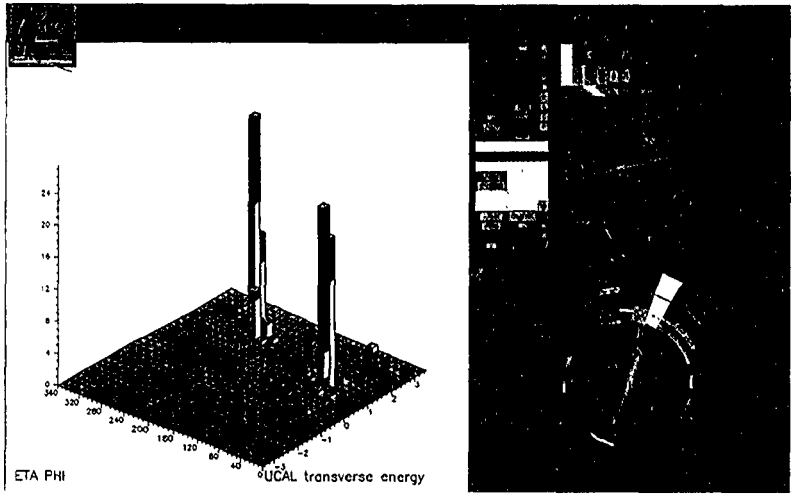


Figure 19. Direct photoproduction dijet event as seen in ZEUS.

Figure 18(b) shows the topology of a resolved photoproduction event. Here the scattered electron is also emitted at a very shallow angle. However, the high-energy photon fluctuates into a quark-antiquark pair, thereby resolving into a hadronic state before the collision. Hence, the photon acts like a source of quarks and gluons, one of which interacts with a parton from the proton. Therefore, only a fraction of the photon's momentum, x_γ, participates in the hard scatter, i.e., $x_\gamma < 1$. The remaining photon momentum is carried away by the other partons in the photon, which tend to travel close to the original photon direction, which is close to the scattered electron direction. The fragmentation of these remaining partons from the photon is called the photon remnant and is found toward the rear of the detector. As for the case of direct photoproduction, the fragmentation of the remaining partons in the proton form the proton remnant, which travels down the beampipe in the proton direction. Figure 20 shows a resolved photoproduction event from ZEUS with two high-E_t dijets and a photon remnant observable in the rear of the detector.

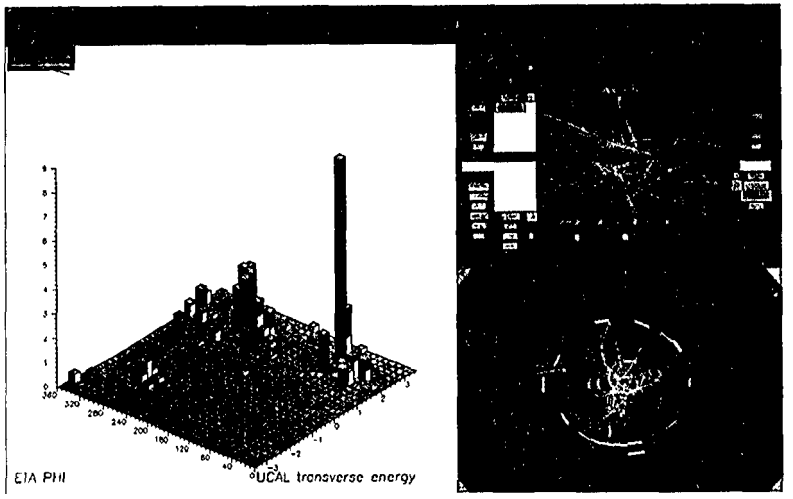


Figure 20. Resolved photoproduction high-E_t dijet event as seen in ZEUS. Note the presence of the photon remnant in the rear of the detector.

3.2. Models of Photoproduction

In Leading Order (LO) QCD, for direct photoproduction [Figure 21(a)], the photon interacts via boson-gluon fusion or QCD Compton scattering. These processes have a quark propagator in the *s*, *t*, or *u* channel, with the *t* and *u* channels dominating. For resolved photoproduction [Figure 21(b)], the dominant subprocesses (*e.g.*, $qg \rightarrow qg$, $gg \rightarrow gg$, $qq \rightarrow gg$) involve the *t*-channel exchange of a gluon. Since the Q^2 of the photon is generally below 1 GeV, perturbative QCD cannot be used to describe the fluctuation of the photon into a hadronic state. Therefore, the photon is treated as a strongly interacting particle and a parton distribution function (PDF) is used to describe its structure. This model is called vector-meson dominance (VMD)[40] since the photon must fluctuate into a meson with the same spin 1. Photon-PDF's are used to parameterize the probability to find a parton in the photon that carries a fraction of the

photon's momentum, x_γ. The circles in the diagrams in Figure 21 indicate the PDF's for the photon and proton.

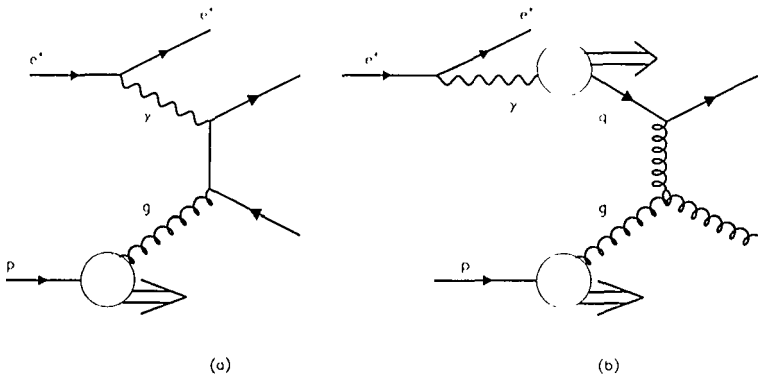


Figure 21. Examples of LO QCD diagrams for (a) direct photoproduction and (b) resolved photoproduction.

At Next-to-Leading-Order (NLO) in QCD, the distinction between direct and resolved photoproduction blurs. Therefore, a separation of resolved and direct photoproduction was developed,[41] based on the variable

$$x_\gamma^{OBS} = \frac{\sum_{jets} E_T^{jet} e^{-\eta^{jet}}}{2yE_e},$$

where the sum runs over the two highest E_T jets, $\eta_{jet} = -\ln(\tan\theta/2)$ is the pseudorapidity of the jet, where θ is the angle of the jet axis, and $y = E_\gamma/E_e$ is the fraction of the initial electron energy carried by the photon. x_γ^{OBS} is the fraction of the photon's energy participating in the production of the two highest E_T jets. This variable is calculable to all orders in perturbative QCD and is measurable. However, an additional complication to the measurement of the jet energy is the contribution to the underlying event energy from the spectator partons that produce the proton remnant jet. Such multiparton interactions in beam remnants[42] have been used to describe hadron collider data.[43] Since the dynamics of hadronic final state interactions in hadronic collisions should resemble those found in high-energy photoproduction in *ep* collisions, these models have been applied to HERA data.[44,45]

3.3. Jets in Photoproduction

Figure 22 shows the x_γ^{OBS} distribution for ZEUS data[46] using the k_T jet clustering algorithm described in Sec. 2.5. The peak at high x_γ^{OBS} is from direct photoproduction, while resolved photoproduction extends the tail down to low x_γ^{OBS}, where the forward rapidity acceptance for jets cuts off. Events from the HERWIG 5.8 Monte Carlo[47] are shown with and without multiparton interactions.[45,48] The Monte Carlo is normalized to agree with the data for $x_\gamma^{OBS} > 0.3$. Irrespective of the multiparton interactions, both Monte Carlo histograms do not match the data for $x_\gamma^{OBS} < 0.3$, although the inclusion of multiparton interactions moves the histogram closer. For $x_\gamma^{OBS} > 0.3$, the HERWIG Monte Carlo with multiparton interactions provides a good description of the data. Therefore, ZEUS measures resolved photoproduction for $x_\gamma^{OBS} > 0.3$. Also shown as the dark histogram is the HERWIG LO direct contribution, with a vertical line drawn at $x_\gamma^{OBS} = 0.75$ to define the region above this cut that corresponds to the LO definition of direct photoproduction. Therefore, for data and calculations, we define resolved and direct photoproduction by this cut in x_γ^{OBS}.

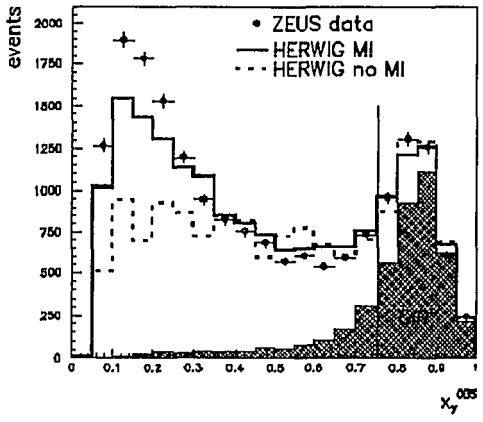


Figure 22. x_γ^{OBS} of ZEUS data without acceptance correction (black dots) compared to HERWIG Monte Carlo with and without multiparton interactions including all acceptance effects. The shaded histogram is the subset of LO direct HERWIG events.

3.3.1. Inclusive Jet Cross Sections

The photoproduction jet cross section as a function of transverse energy, $d\sigma/dE_T^{jet}$, falls steeply with E_T, as predicted by QCD. The measured cross section is described by matrix elements summed according to the quark and gluon distributions of the quark and gluon distributions in the proton and photon, and is relatively less sensitive to these distributions than to the features of the matrix elements. The photoproduction jet cross section as a function of the pseudo-rapidity, $d\sigma/d\eta^{jet}$, is sensitive to the parton distributions in the photon and can be used to extract them.

Figure 23 shows the inclusive differential jet photoproduction cross sections, $d\sigma/dE_T^{jet}$ and $d\sigma/d\eta^{jet}$, from H1 (Ref. 49). The H1 data is plotted using the pseudo-rapidity in the lab frame, where η(lab) - η(cms) = 0.5 $\ln(E_p/E_\gamma) \approx 2$. Figure 23(a) shows the E_T spectrum measured in two jet pseudo-rapidity intervals, $-1 < \eta_{jet} < 1$ and $-1 < \eta_{jet} < 2$. Figure 23(b) shows the jet cross section as a function of η_{jet} for three different jet E_T thresholds: $E_t^{jet} > 7$, 11, and 15 GeV. The cross section decreases as $(E_T^{jet})^{-n}$ with $n = 6.1 \pm 0.5$ between $7 < E_t^{jet} < 29$ GeV, and $-1 < \eta_{jet} < 2$. The ZEUS experiment also reports similar results[50] and has extended these measurements to higher E_T and compared them with NLO QCD calculations.[51] The H1 and ZEUS results are consistent with the jet cross sections measured in hadron collisions at the same cms energy of 200 GeV (Ref. 52), where an exponent of $n = 5.8$ was measured for the same E_t^{jet} range.

Figure 23 compares the H1 data with a calculation based on the PYTHIA 5.7 event generator for photon-proton interactions.[53] The PYTHIA model without multiple interactions (dashed line) does not describe the measured cross sections well at large

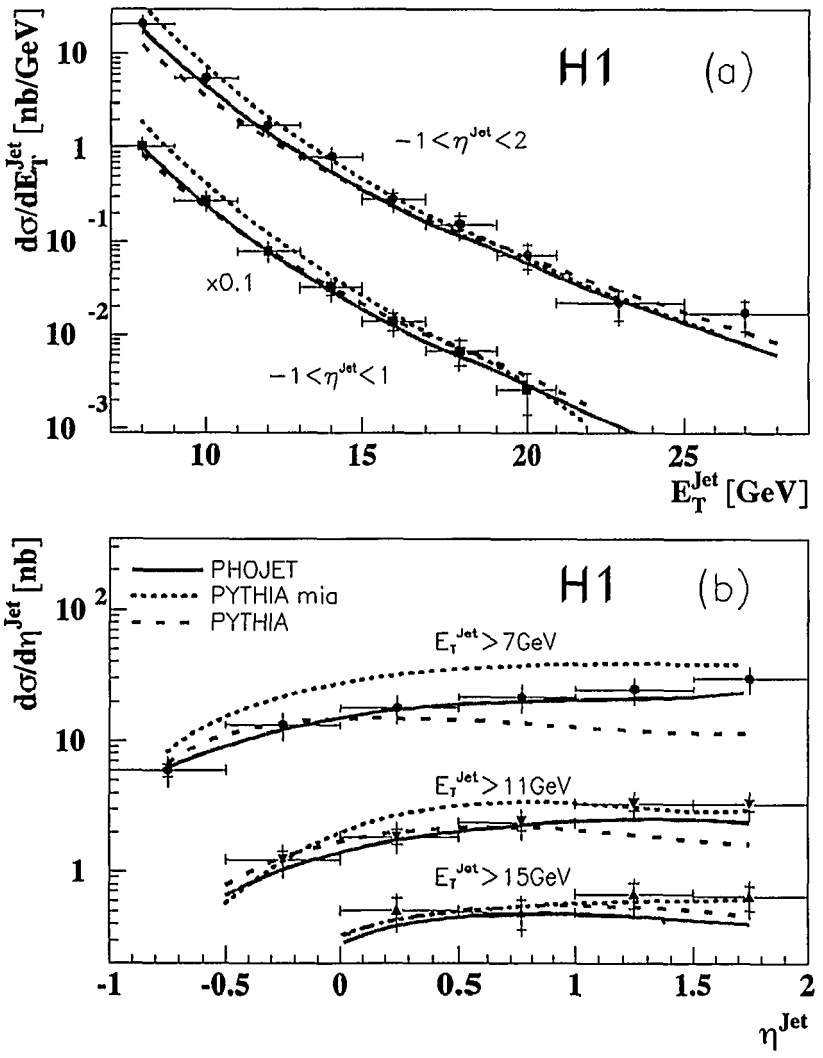


Figure 23.(a) Inclusive differential E_T^{jet} photoproduction jet cross sections for $E_T^{jet} > 7$ GeV from H1 for two η ranges compared with two QCD generators, PHOJET and PYTHIA, the latter with and without interactions of the beam remnants.(b) Inclusive differential η photoproduction cross section from H1 compared with the same 3 QCD generators for 3 different E_T^{jet} thresholds[49].

rapidities and at small transverse energies of the jets. The PYTHIA model with multiple interactions (dotted line) provides a good description of the shape of the measured $d\sigma/d\eta^{jet}$ cross section, but gives too large a cross section for small $E_t^{jet} > 7$ GeV, where x_γ is small ($x_\gamma \approx 0.1$). Figure 23 also compares the H1 data with the PHOJET 1.0 calculation,[54] which includes multiple interactions, but with softer beam-remnant interactions than PYTHIA, and adds a characterization of the transition to the nonperturbative soft-scattering. In addition, while PYTHIA contains hard initial state parton radiation, PHOJET does not. The PHOJET curves (solid lines) give a good description of both $d\sigma/dE_T^{jet}$ and $d\sigma/d\eta^{jet}$ distributions. The differences in these two models and their agreement with the data lead H1 to conclude that there are uncertainties on the order of a factor of two in conclusions about the parton content of the photon drawn from jet cross sections in the low x_γ region.[49] The data support the inclusion of interactions between the beam remnants since this produces a marked improvement in the agreement with QCD models.

3.3.2. Dijet Photoproduction Cross Sections

Figure 24 shows the kinematics of dijet production in the dijet center-of-mass system and the lab frame. In the dijet CMS, the average pseudo-rapidity of the two highest E_T jets, $\bar{\eta} = \frac{1}{2}(\eta_1 + \eta_2) = \frac{1}{2}\ln\frac{x_p E_p}{y x_\gamma E_e}$, provides information about the structure functions of the photon and proton. The sensitivity to the incoming particle parton distributions is increased by the requirement[55] that $|\Delta\eta| = |\eta_1 - \eta_2| < 0.5$. Under these conditions where $E_T^{jet1} \approx E_t^{jet2}$, for $2 \rightarrow 2$ scattering in LO QCD, we have: $x_\gamma \approx \frac{\left(E_T^{jet} e^{-\eta^{jet}}\right)}{yE_e} \propto \frac{\bar{\eta}}{y}$ for resolved photoproduction ($0.3 < x_\gamma^{OBS} < 0.75$, where the lower cut is placed to ensure a well-understood model) and $x_p \approx \frac{\left(E_T^{jet} e^{+\eta^{jet}}\right)}{E_p} \propto \bar{\eta}$ for direct photoproduction ($x_\gamma^{OBS} > 0.75$). This provides an opportunity, by separating direct from resolved photoproduction, to present cross sections sensitive to the gluon distributions in the proton and photon, respectively.

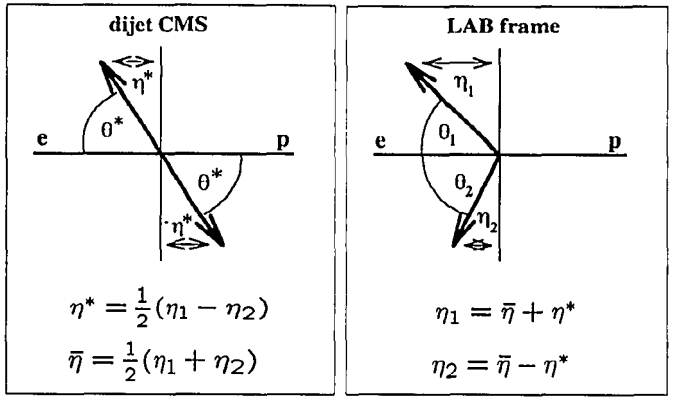


Figure 24. Jet kinematics for *ep* interactions in the center-of-mass system and the lab frame.

Figure 25 shows the differential dijet cross section, $d\sigma/d\bar{\eta}$, from ZEUS[56] integrated above $E_T^{jet} = 6$ GeV for the central rapidity range, $-1.375 < \eta_{jet} < 1.875$ using three different jet finders. EUCELL and PUCELL are cone algorithms[57] with radius R =1. EUCELL uses a sliding window in η and ϕ to define the seed, while PUCELL uses a calorimeter cell as a seed and merges nearby jets under certain conditions. KTCLUS[58] is a k_T cluster algorithm (see Sec. 2.5) selected[59] to closely resemble the cone algorithm in its use of $\Delta R = \sqrt{(\Delta\phi)^2 + (\Delta\eta)^2}$ and the E_T recombination scheme. Also shown is a full NLO QCD calculation of Klasen and Kramer[56] using the GRV[60] photon and CTEQ[61] proton PDF's for $R_{sep} = 1.0$ and 2.0, where R_{sep} (Ref. 62) determines the maximum distance in $\eta-\phi$ at which two partons can be merged into a single jet. For comparison with KTCLUS and PUCELL, $R_{sep} = 1.0$ should be used, and for comparison with EUCELL, R_{sep} should be in the range 1.5–2.0. In Figure 25(a), the direct photoproduction data is in fairly good agreement with the theory, particularly when the KTCLUS algorithm is used, with the exception of the forward rapidity region, where the data fall systematically above the theory. The choice of jet algorithm has an effect of about 25–30% for both theory and experiment. In Figure 25(b), the resolved cross section data is above the theory by a factor of two, although the systematic errors are large and the shape appears to be generally the same. The choice of jet algorithm has an effect of about 50% in both theory and experiment.

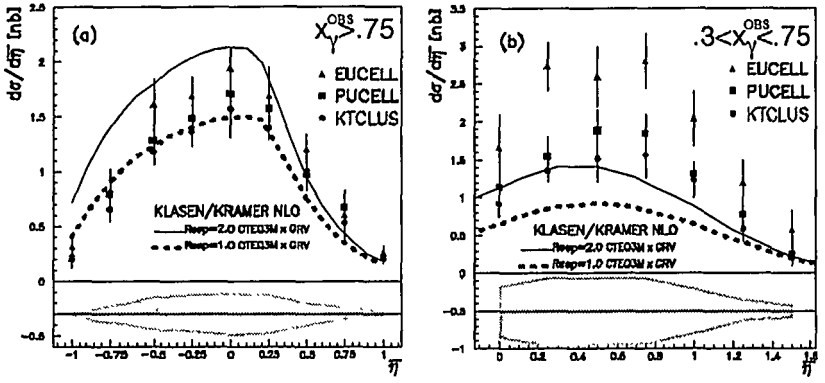


Figure 25. Differential dijet cross section, $d\sigma/d\bar{\eta}$, for three different jet algorithms from ZEUS for (a) direct photoproduction and (b) resolved photoproduction. The shaded band indicates the uncertainty due to the ±5% uncertainty in the calorimeter energy scale. The curves are from the full QCD NLO calculations described in the text.

3.3.3. Dijet Angular Distributions in Photoproduction

The difference between the pseudo-rapidity of the two highest E_T jets, η^*, where $\tanh(\eta^*) = \tanh(1/2(\eta_1 - \eta_2)) = \cos(\theta^*)$ and θ^* is the angle between the jet-jet axis and the beam direction in the dijet CMS (see Figure 24), provides information about the spin of the exchanged particle in the interaction. Only the absolute value of $\cos\theta^*$ can be measured since the outgoing jets are indistinguishable. As shown in Figure 21 and discussed in Sec. 3.2, LO QCD direct photoproduction involves a quark propagator, while resolved photoproduction processes are dominated by a gluon propagator. The angular dependence of the cross section for resolved processes with a spin-1 gluon propagator is approximately proportional to $(1-|\cos\theta^*|)^{-2}$, whereas the angular dependence of direct photoproduction with a spin-1/2 quark propagator is approximately proportional to $(1-|\cos\theta^*|)^{-1}$. Therefore, the cross section for resolved processes should rise more steeply with increasing $|\cos\theta^*|$ than direct processes. This behavior is also predicted by NLO QCD calculations[63].

In order to enhance the sensitivity to the parton dynamics, ZEUS makes a cut[64] on $\bar{\eta}$, which is a measure of the boost of the dijet scattering system in the HERA frame, $|\bar{\eta}| < 0.5$. This is in contrast to the requirement of $|\Delta\eta| = |\eta_1 - \eta_2| < 0.5$ used to enhance the sensitivity of the dijet cross sections to the incoming parton distributions. In addition, the dijet angular distributions are studied with a cut on the dijet invariant mass, $M_{jj} > 23$ GeV, where $M_{jj} = \sqrt{2E_T^{jet1}E_T^{jet2}\left[\cosh\left(\eta^{jet1}-\eta^{jet2}\right)-\cos\left(\phi^{jet1}-\phi^{jet2}\right)\right]}$, and ϕ^{jet} is the azimuthal angle of the jet in the HERA frame. For two jets back to back in ϕ and with equal E_T^{jet}, $M_{jj} \approx 2E_T^{jet}/\sqrt{1-|\cos\theta^*|^2}$. In a LO $2 \rightarrow 2$ scatter, the dijet invariant mass is related to x_p and x_γ by $M_{jj} = \sqrt{4E_\gamma E_p x_\gamma x_p} = \sqrt{4E_e E_p y x_\gamma x_p}$. Therefore, the requirements that the dijet system have high mass and small boost select events with γp center-of-mass energies mostly above 190 GeV and suppress events with low x_γ^{OBS}. This produces dijets with good acceptance over a wide range of scattering angles in a region of x_p and x_γ where photon and parton distributions are fairly well determined[64].

Figure 26(a) shows the ZEUS data[64] compared to LO and NLO QCD parton level calculations[63] using CTEQ3M[65] and GRV (LO)[60] PDF's for the proton and photon respectively. The resolved cross section rises more steeply with increasing $|\cos\theta^*|$ than the direct cross section. The good agreement between data and theory verifies the expected effects of the spins of the quark and gluon propagators. The same conclusion is drawn from Figure 26(b), where the ZEUS data is compared with HERWIG58 (Ref. 47) and PYTHIA57 (Ref. 42) predictions using the MRSA[66] and GRV (LO)[60] PDF's for the proton and photon respectively. The agreement of $|\cos\theta^*|$ dependence of the measured cross section with these QCD NLO calculations and Monte Carlo simulations, including parton showering and hadronization models, provides an important confirmation of fundamental aspects of QCD.

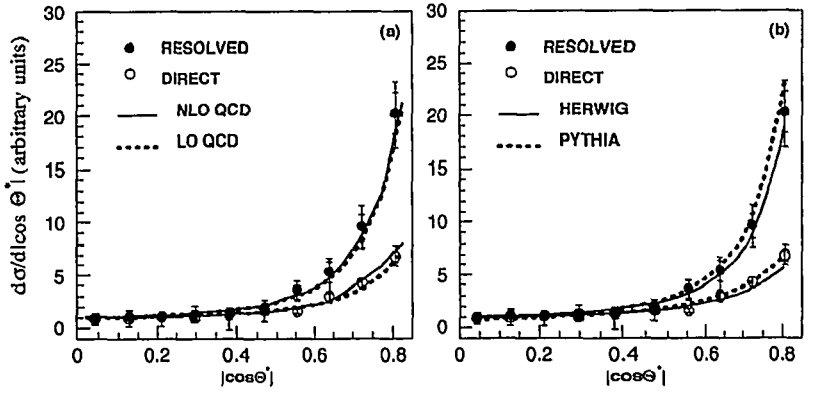


Figure 26. $d\sigma/d|\cos\theta^*|$ from ZEUS[64] normalized to one at $\cos\theta^* = 0$ for resolved (black dots) and direct (open circles) photoproduction. In (a), the data are compared to a LO (dashed line) and NLO (solid line) QCD prediction. In (b), the data are compared to PYTHIA (dashed line) and HERWIG (solid line) distributions. The inner error bars show the statistical errors and the outer error bars sum in quadrature the statistical and systematic errors excluding the energy scale and luminosity uncertainties.

4. Diffraction

4.1. Soft Diffractive Phenomenology

Soft diffractive *ep* physics involves the study of soft hadronic collisions. These processes have a scale of about 1 fm. An example is *pp* scattering. The total cross section is approximately constant above 5 GeV. The elastic cross section is a large fraction at low energy (below 1 GeV) and a small fraction at high energy (above 10 GeV). If one models this cross section as a totally absorbing disk, one concludes that the elastic cross section equals the inelastic cross section and corresponds to the optical diffractive or shadow scattering observed when a plane wave impinges on a totally absorbing target, where the angular distribution is the Fourier transform of the target.[67] In the case of the hadronic cross section, as for the optical case, minima occur at angular deflections corresponding to specific values of q^2. While the experimental hadronic elastic cross sections display this behavior, their magnitude and dependence on energy do not.

4.1.1. Regge Theory

The optical theorem relates the imaginary part of the forward scattering amplitude to the total cross section, Im $F(s,t=0) = (q/4\pi)\ \sigma_{tot}(s)$. Using the optical theorem with unitarity and analyticity properties of the scattering amplitude leads to the Froissart bound[68] on the scattering amplitude, $\sigma_{tot}(s) < c\ (\ln[s])^2$ as $s \rightarrow \infty$. A useful description of pion-nucleon scattering above the resonance region ($M_{\pi p} > 3$ GeV), where the energy dependence is smooth, is in terms of a *t*-channel exchange two-body scattering process mediated by a single virtual particle (e.g., a pion). However, such a scattering amplitude has dominant poles corresponding to the exchange of particles with a fixed angular momentum, *j*, producing a dependence E^j in the amplitude that violates the Froissart bound as $s \rightarrow \infty$.

Regge[69] showed that the usual partial wave decomposition of the scattering amplitude, $f(k,\theta) = \sum_l (2l+1) f_l(k) P_l(\cos\theta)$, could be extended to continuous complex angular momenta $f(j,k)$ with physically observable states for multiples of integral or half-integral angular momentum, $j(k)$, called Regge poles. Chew and Frautschi[70] extended this to relativistic field theory where the resonances at these values of angular momentum, $j(t)$, are organized in a family of particles, with different spin but the same internal quantum numbers, called Regge trajectories. These turn out to have a universal slope for both baryons and mesons of the form $j(t) = j(0) + \alpha' t$, where $\alpha' \approx 1$ GeV^{-2}. Crossing symmetry and with the assumption that an isolated Regge pole at lowest *j* for space-like *t* dominates the amplitude results in a prediction[71] for the asymptotic behavior of the scattering amplitude in the *s*-channel, $F(s,t) \propto \frac{1}{k}\beta(t)\left(\frac{s}{s_0}\right)^{\alpha(t)}$ and $d\sigma/dt = \beta^2(t) s^{2(\alpha(t)-1)}$. The forward direction is $t = 0$, and as we move away from the forward direction, *t* becomes negative and $d\sigma/dt$ decreases exponentially. This forward diffraction peak is an important feature of elastic scattering. Regge theory predicts that this diffraction peak should become increasingly narrower at higher *s*. This is called shrinkage.

A nearly constant total cross section at high *s* requires $\alpha(0)$ very close to one. Since a single Regge trajectory should account for all elastic scattering at high energy, where no quantum numbers save angular momentum may be exchanged, the trajectory must involve the exchange of no quantum numbers except angular momentum and therefore has the quantum numbers of the vacuum. This trajectory is called the Pomeron trajectory, where $\alpha(t) = \alpha_0 + \alpha' t = 1.085 + 0.25t$. Regge theory provides a good description[72] of total hadronic and photoproduction cross sections[73].

4.2. Hard Diffraction at Hadron Colliders

In 1984, the UA4 experiment at the CERN SPS $p\bar{p}$ collider reported[74] diffractive production of high mass systems at $\sqrt{s} = 540$ GeV. Ingelman and Schlein[75] suggested that high-p_t jets might be produced in such states and that such high-p_t structure would provide new information about the nature of Pomeron exchange. They suggested the possibility of probing the exchanged Pomeron in a hard scattering process such as between a gluon in the Pomeron and a parton in the proton, which would have the signature of two high-p_t jets and two low-p_t remnant or spectator jets. They also pointed out that if there were a Pomeron component in the proton that could be characterized by an effective structure function, this could be studied at HERA, where the probe would be well understood and with a clear experimental signature: "a quasi-elastically scattered proton (going down the beampipe) well separated from the hadronic system."

Subsequently, the UA8 experiment at the CERN SPS $p\bar{p}$ collider reported jet production in high-mass diffractive final states[76] that was in good agreement with a hard scattering model with a Pomeron dominated by gluons. They also reported[77] a "super-hard" component of the Pomeron, where it appeared that a "large fraction of the Pomeron's momentum participates in the hard scattering a significant amount of the time." There have also been recent measurements of diffractive scattering at the Fermilab Tevatron $p\bar{p}$ collider. These are discussed in the article by M. Albrow in these proceedings.

4.3. DIS Diffraction at HERA

In 1993, ZEUS reported[78] and H1 confirmed[79] DIS events that have an absence of energy deposition in the forward direction. Figure 27 shows an event observed in the ZEUS detector with no significant deposit of energy beyond $\theta > 90°$. The figure also shows the lines of pseudorapidity, η, at the boundary of the ZEUS forward, barrel, and rear calorimeters. Events with a large region in η with no energy deposits are called large rapidity gap events (LRG). In order to quantify the absence of energy in the detector, the ZEUS analysis defines a calorimeter cluster as an isolated set of adjacent cells with summed energy above 400 MeV. The η of the cluster closest to the forward direction, i.e., the highest η value, is called η_{max}. Figure 28 shows the η_{max} distribution of DIS events from ZEUS. There are two groups of events, one with large η_{max} values, and the other with $\eta_{max} < 2$. Also shown is the standard ZEUS DIS MC, which agrees with the data for $\eta_{max} > 2$, but not for $\eta_{max} < 2$, where there is a clear excess of events with large rapidity gaps, corresponding to ~ 10% of the total DIS cross section.

A natural interpretation of these events is that they are due to diffractive scattering of the virtual photon from the proton. This means that the proton does not fragment into a visible system of hadrons either because it remains intact or dissociates into a system which is closely confined to the proton direction. In addition, there is no appreciable amount of initial state QCD radiation, because that would also have produced hadrons visible in the forward calorimeter.

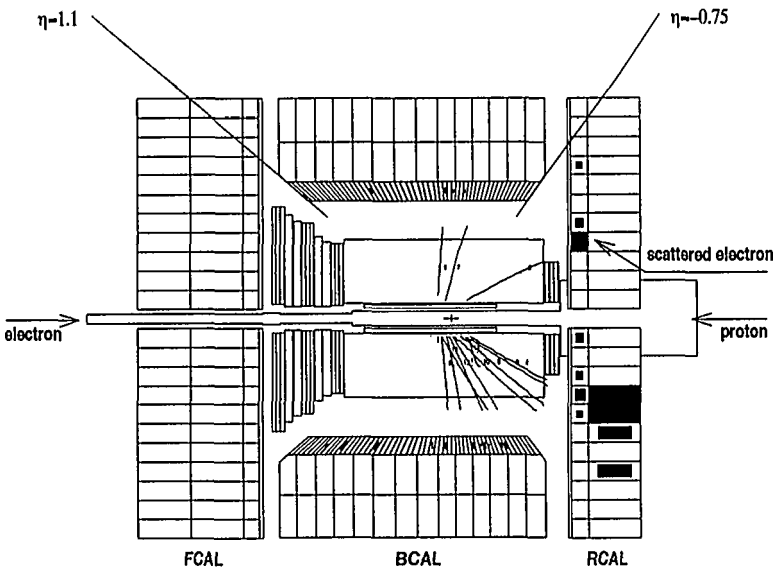


Figure 27. A ZEUS DIS event at Q^2=64 GeV^2 with a large rapidity gap.

Figure 29 shows a schematic picture of DIS events with no rapidity gap (NRG) and with a large rapidity gap (LRG). A typical NRG event has the phase space between the current jet and the proton remnant filled with particles produced by the emission of additional gluons and quarks created by the color flow between the struck quark and the proton remnant. An explanation for the LRG events is the emission of a color-neutral particle from the proton, which interacts with the exchanged virtual photon. In this case, there is no color flow that would produce particles between the struck quark and the proton remnant. Since diffraction is considered to proceed by the exchange of a Pomeron, with the quantum numbers of the vacuum, a model of the LRG events is to assume a flux of Pomerons in the proton. Figure 28 shows the prediction of a DIS model with a diffractive component (POMPYT[80]) modeled by a flux of Pomerons (where the Pomeron is considered to be composed of gluon constituents typically carrying a large fraction of the Pomeron's momentum), which does agree for all values of η_{max}.

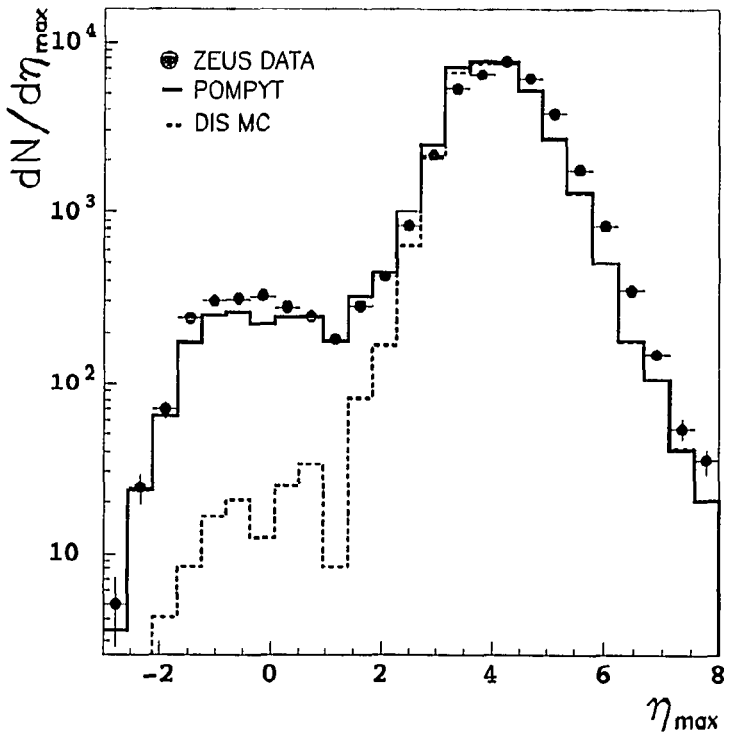


Figure 28. Distribution of the maximum rapidity η_{max} of a calorimeter cluster in ZEUS DIS events for data (points), the standard DIS MC, and MC calculations (POMPYT) adding a diffractive component to the standard DIS processes.

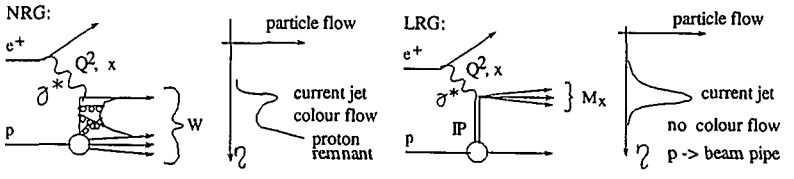


Figure 29. Comparison of *ep* events with no rapidity gap (NRG) and with a large rapidity gap (LRG), showing the absence of the particle and color flow in LRG events.

4.4. Analysis of Diffractive *ep* Scattering

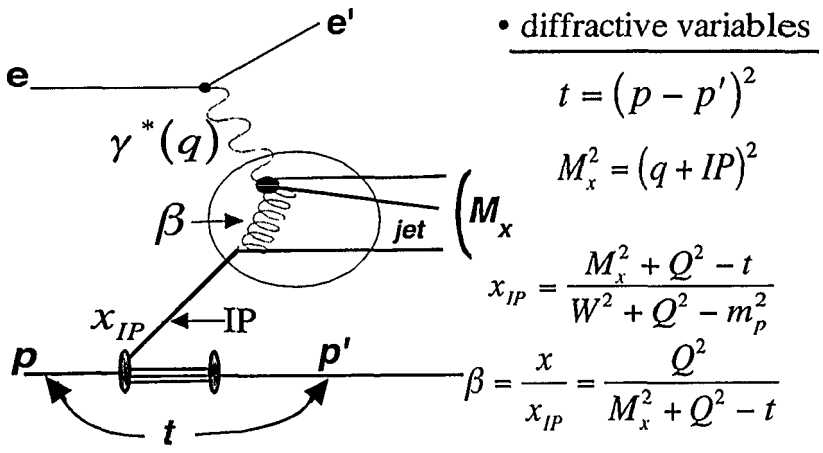
4.4.1. Introduction

Diffractive *ep* scattering provides the opportunity to explore the interplay of soft and hard QCD processes as well as to investigate the structure of the Pomeron. Soft hadronic processes occur on the scale of ~ 1 fm and are characterized by the Pomeron trajectory as described in Sec. 4.1. Hard QCD processes such as DIS, including hard diffraction, have their hard scale determined by the virtuality of the photon or jets and the soft scale set by the size of the proton of ~ 1 fm. In order to apply perturbative QCD to hard processes, the hard scale physics must factorize from the soft scale physics. This factorization, which allows the two scales of physics to be considered separately, is an assumption used to produce the DGLAP evolution equations described in Sec. 2.2.3.

Important distinguishing features of hard and soft QCD processes are the energy and t-dependence of the scattering cross sections and their variation with Q^2 or W^2. Another interesting question is the partonic structure of the Pomeron. This can be investigated by comparison with various models treating the parton as composed of combinations of soft and hard quarks and gluons. Another approach is to treat the Pomeron as a quasi-hadron with a flux factor and under diffractive conditions to replace the proton structure function by a diffractive structure function. Another indication of Pomeron partonic structure would be jet production in diffractive events. Each of these aspects is discussed below.

4.4.2. Kinematics of Diffractive *ep* Scattering

Figure 30 shows the definition of the kinematic variables used in *ep* scattering. The square of the momentum transfer at the proton vertex is $t = (p - p')^2$, where p' is the four-momentum of the outgoing proton, or if the proton dissociates, the four-momentum of the outgoing system. The Pomeron carries momentum IP, with a fraction of the proton momentum x_{IP}. M_X is the invariant mass of the hadronic system produced from the photon dissociation. β is the fraction of the Pomeron momentum carried by the parton in the Pomeron that interacts with the virtual photon, in analogy to the definition of x defined for the proton in DIS.



• diffractive variables

$$t = (p - p')^2$$

$$M_x^2 = (q + IP)^2$$

$$x_{IP} = \frac{M_x^2 + Q^2 - t}{W^2 + Q^2 - m_p^2}$$

$$\beta = \frac{x}{x_{IP}} = \frac{Q^2}{M_x^2 + Q^2 - t}$$

Figure 30. Definition of kinematics for diffractive *ep* scattering.

4.5. Diffractive Structure Function

For unpolarized beams, the differential cross section for single diffractive dissociation can be described[81] in terms of a diffractive structure function, $\frac{d^3\sigma_{diff}}{d\beta dQ^2 dx_{IP}} = \frac{2\pi\alpha^2}{\beta Q^4}\left(1+(1-y)^2\right)F_2^{D(3)}(\beta,Q^2,x_{IP})$, where an integration has been performed over t, corresponding to the (undetected) momentum transfer to the proton system, the effect of F_L has been neglected, and the relation $x = \beta x_{IP}$ has been used. In the model of Ingelman and Schlein,[75] the proton emits a Pomeron which is treated as a virtual hadron whose structure is probed by the virtual photon. The Pomeron is described by a structure function, $F_2^{IP}(\beta,Q^2)$, which is independent of the process of Pomeron emission Therefore $F_2^{D(3)}$ factorizes as: $F_2^{D(3)}(\beta,Q^2,x_{IP}) = f_{IP}(x_{IP}) \bullet F_2^{IP}(\beta,Q^2)$, where $f_{IP}(x_{IP})$ is the flux of Pomerons in the proton, which can be extracted[82] from diffractive hadron-hadron scattering within an uncertainty of about 30%. Regge theory[83] predicts that if the x_{IP} dependence corresponds to a flux of Pomerons associated with the proton, then $F_2^{D(3)} \propto 1/x_{IP}^n$, where $n = 2\alpha(t) - 1$, and $\alpha(t) = \alpha(0) + \alpha' t$ is the Pomeron trajectory. The first measurements of $F_2^{D(3)}$ by H1 (Ref. 84) and ZEUS[85] established the attribution of the rapidity gap events to a virtual photon-proton process that was dominantly diffractive. Figure 31 shows a recent measurement of $x_{IP} \bullet F_2^{D(3)}$ by H1 (Ref. 86) as a function of x_{IP} for different values of β and Q^2. The data is compared to a fit of the form $(x_{IP})^{-n(\beta)}$ with the normalization in each bin determined by the factor $A(\beta,Q^2)$.

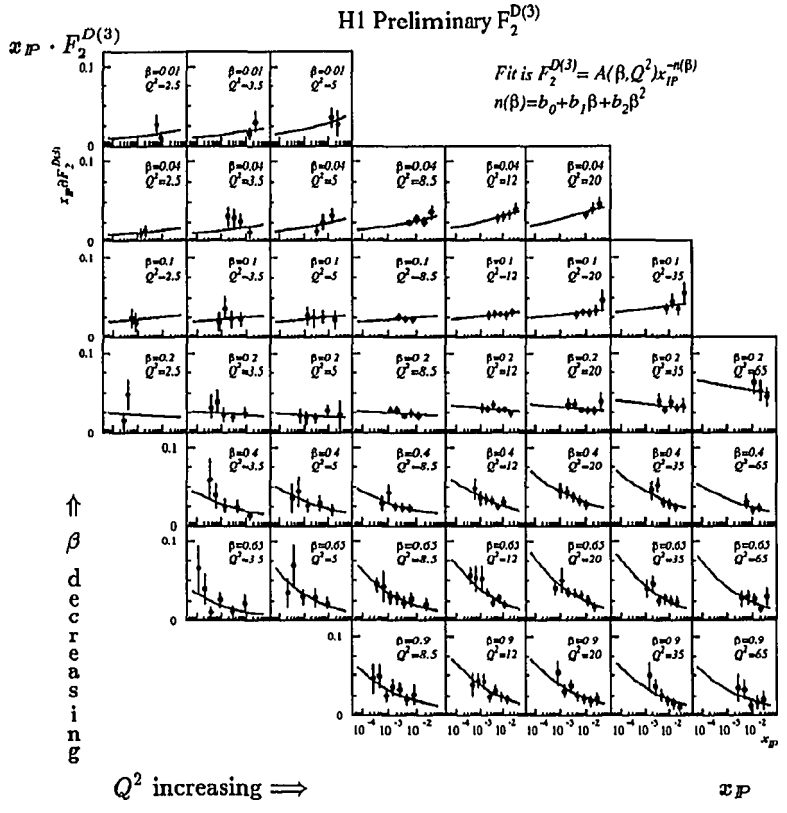


Figure 31. Preliminary measurement of $x_{IP} \bullet F_2^{D(3)}$ by H1 as a function of x_{IP} in bins of Q^2 and β with statistical and systematic errors added in quadrature. The curves are from the overall parameterization of the x_{IP} dependence described in the text.

Figure 32(a) shows the H1 (Ref. 86) result from fitting the data of Figure 31 to the polynomial dependence $1/x_{IP}^n$, where n is allowed to vary with β, but not with Q^2. The value of n decreases markedly with β for $\beta \leq 0.3$, which shows that the expectation of factorization of $F_2^{D(3)}$ is not valid over the full kinematic range. However, H1 note that these deviations from factorization are consistent with a contribution to $F_2^{D(3)}$ from meson exchange. An example of such a meson trajectory would be the $f_2^0(1270)$, which would have $n \sim 0$ and possibly a much softer β dependence than the Pomeron

trajectory. Figure 32(b) shows the result where n is allowed to vary with Q^2, but not with β. There is no evidence for dependence of β on Q^2.

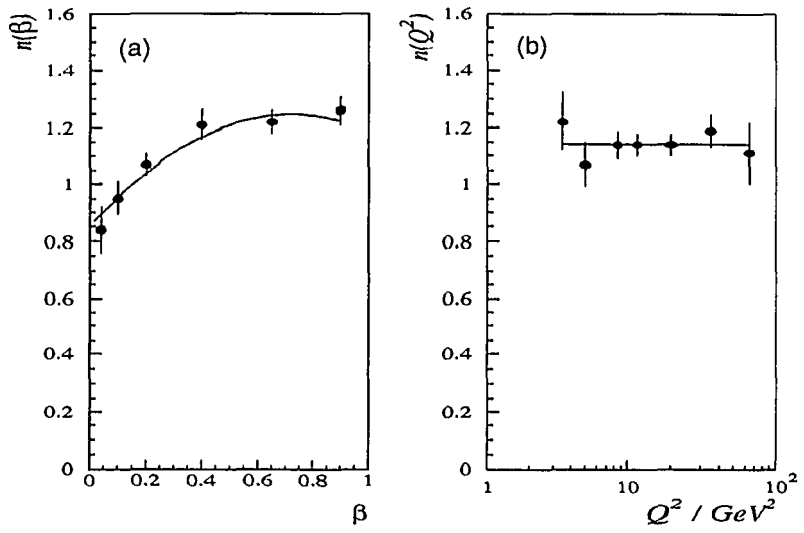


Figure 32. Preliminary H1 results from fitting $x_{IP} \cdot F_2^{D(3)}(\beta, Q^2, x_{IP})$ to the form $F_2^{D(3)} \propto 1/x_{IP}^n$. In (a), n is allowed to vary with β, but not with Q^2. In (b), n is allowed to vary with Q^2 but not with β. The error bars include statistical and systematic uncertainties folded in quadrature.

In spite of the lack of factorization of the measured diffractive cross section over the entire kinematic range, integrating over x_{IP} produces a measurement of the average deep inelastic structure of the total colorless, isospin-conserving exchanges involved.

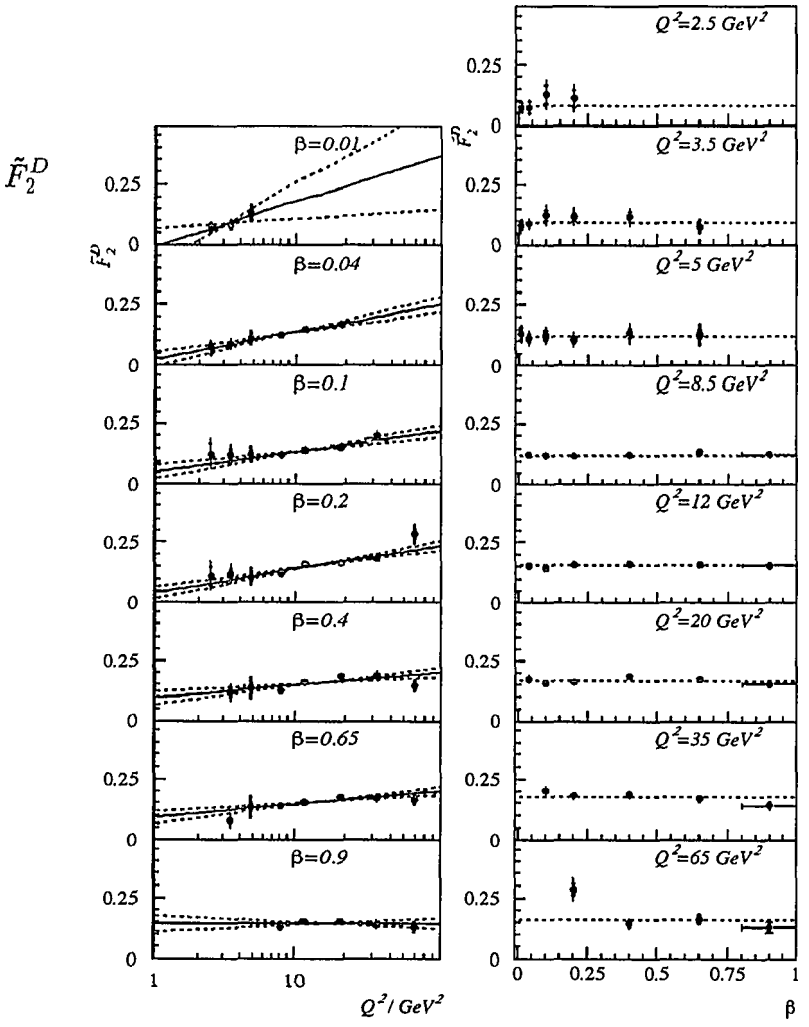


Figure 33. Preliminary measurement by H1 of $\tilde{F}_2^D(\beta, Q^2)$ as a function of Q^2 for different β values (left) and as a function of β for different Q^2 values (right). The solid lines in the Q^2 plots are the best fit to a linear dependence on $\ln Q^2$, with dashed lines at $\pm 1\sigma$. The dashed lines in the β plots show a constant dependence on β.

H1 defines[86] $\tilde{F}_2^D(\beta, Q^2) = \int_{x_{IP}=0.0003}^{x_{IP}=0.05} F_2^{D(3)}(\beta, Q^2, x_{IP}) dx_{IP}$. Figure 33 shows $\tilde{F}_2^D(\beta, Q^2)$ from H1 as a function of Q^2 for fixed β and as a function of β for fixed Q^2. At fixed Q^2,

$\tilde{F}_2^D(\beta,Q^2)$ shows little dependence on β. The dependence of $\tilde{F}_2^D(\beta,Q^2)$ on Q^2 shows clear evidence of scaling violation. Most notable is the persistence of the rise with $\ln Q^2$ that persists to values of β beyond the point where the proton structure function is dominated by valence quarks ($x \sim 0.15$) and not by gluons. These scaling violations are in agreement with a picture where there is a substantial gluon contribution to the diffractive exchange. H1 have performed a QCD analysis of $\tilde{F}_2^D(\beta,Q^2)$ using DGLAP evolution and conclude that at $Q^2 = 5$ GeV^2, "leading" gluon behavior is seen, where the exchange is mostly taking place through gluons carrying a large (> 0.9) fraction of the Pomeron's momentum, and that throughout the observed Q^2 range from 5 to 65 GeV^2, more than 80% of the momentum transfer in the diffractive exchange is due to gluons, with a decreasing momentum fraction with increasing Q^2.

4.6. Diffraction with a Tagged Leading Proton

ZEUS has used its Leading Proton Spectrometer (LPS) to measure scattered protons with small transverse momenta ($p_T < 1$ GeV) with respect to the proton beam direction. The LPS provides a direct measurement of $x_L = p'/p_{beam}$ with 0.4% resolution[87] at p_{beam} = 820 GeV, as well as $x_{IP} \sim 1 - x_L$ and $t = -\frac{1}{x_L}p_T^2 + m_p^2\frac{(1-x_L)}{x_L}$. This provides the opportunity to directly measure t with a resolution ~ 30%, dominated by the transverse spread in the proton beam. The identification of single diffractive events (where the proton remains intact) by the presence of rapidity gaps results in considerable backgrounds from nondiffractive DIS of up to 50% and proton dissociation (where the proton does not remain intact) of 10–15% (estimated from hadron scattering data). Figure 34 shows the x_L distribution for ZEUS data,[88] compared with MC calculations of events from diffraction (RAPGAP[89]) and the backgrounds from nondiffractive DIS, pion exchange, and proton dissociation. There is excellent agreement between the model and the data with a clear diffractive peak at high x_L. The backgrounds peak at low x_L values. Therefore, the LPS enables the selection of a clean sample of diffractive events by requiring $x_L > 0.97$, with a uniform acceptance in x_L, after averaging over an azimuthal angle of 6%. The remaining background for $x_L > 0.97$ is estimated to be ~ 5% and is subtracted from the subsequent LPS results.

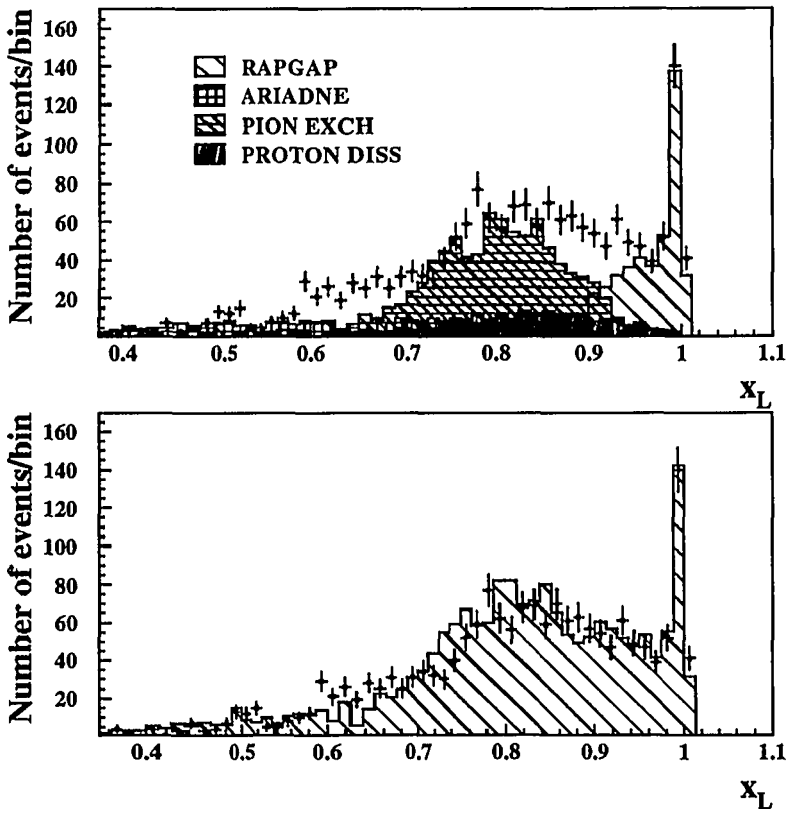


Figure 34. $x_L = p'/p_{beam}$ distribution for ZEUS data compared with individual (upper plot) and summed (lower plot) MC calculations of events from DIS (ARIADNE), pion exchange, proton dissociation, and diffraction (RAPGAP).

Figure 35 shows the ZEUS LPS measurement of the t-dependence of diffractive DIS events measured in the kinematic range $4 < Q^2 < 30$ GeV^2, $70 < W^2 < 210$ GeV^2, $0.02 < \beta < 0.4$, and $x_L > 0.97$. The bin width in t was selected to be larger than the resolution, producing four bins in the range $0.07 < |t| < 0.35$ GeV^2. The distribution was fit to a single exponential of the form $d\sigma/d|t| \sim e^{-b|t|}$ and is shown in Figure 35 as a solid line. The value of the fitted slope parameter $b = 5.9 \pm 1.3(stat)^{+1.1}_{-0.7}(syst)$ GeV^2.

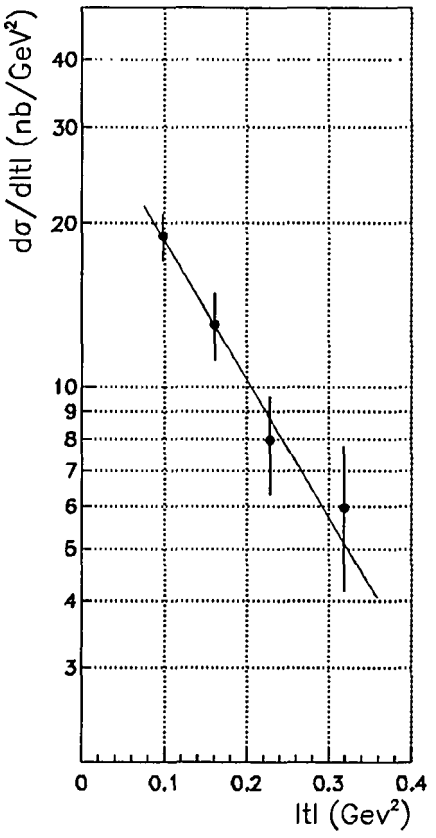


Figure 35. Differential cross section dσ/d|t| from ZEUS for diffractive DIS events with a tagged leading proton having $x_L > 0.97$, along with an exponential fit described in the text. The error bars include statistical and systematic errors added in quadrature.

Figure 36 shows the ZEUS measurement[88] of the diffractive structure function, $F_2^{D(3)}(\beta, Q^2, x_{IP})$, integrated over t due to the limited statistics, as a function of x_{IP} in bins of β for $0.006 < \beta < 0.5$, $4 \times 10^{-4} < x_I < 3 \times 10^{-2}$, and $4 < Q^2 < 20$ GeV^2 with a central value of $Q^2 = 12$ GeV^2. In order to investigate whether the factorization of $F_2^{D(3)}$ holds, fits were performed in the highest three β bins to the form $A_i(1/x_{IP})^a$, where the normalization constants A_i were allowed to vary in each bin. A very good fit is obtained (χ^2 of 10 for 11 degrees of freedom) in all three β bins with the value $a = 1.28 \pm 0.07$ *(stat.)* $\pm$ 0.15 *(syst.)*. Therefore, this result is compatible with factorization, which is significant considering the removal of backgrounds, particularly that of meson exchange, that could affect the H1 result.

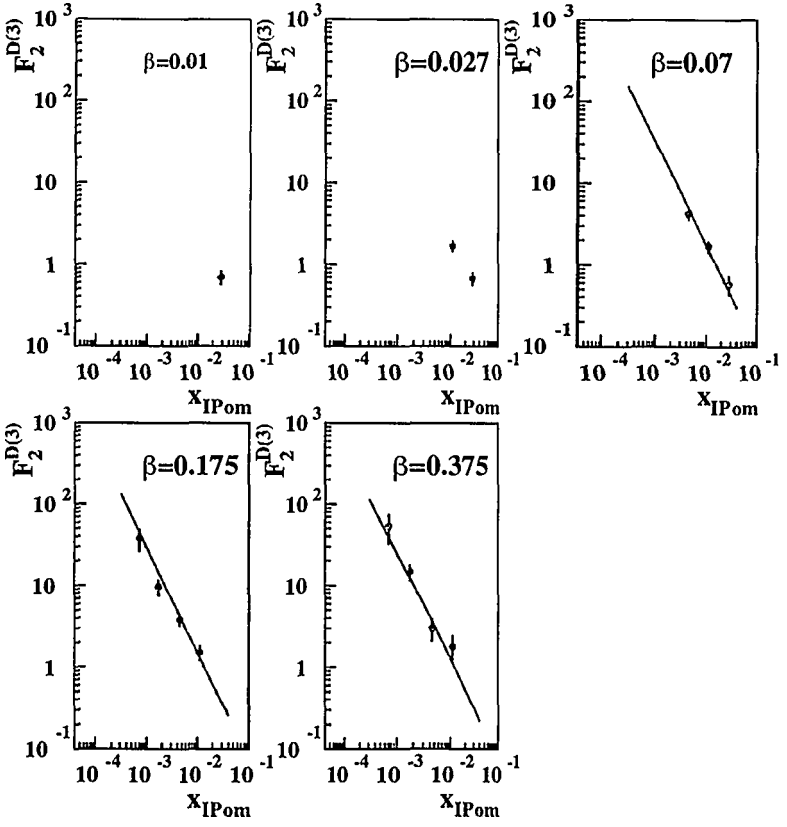


Figure 36. The diffractive structure function $F_2^{D(3)}(\beta, Q^2, x_{IP})$ from ZEUS, plotted as a function of x_{IP} in five bins of β at $Q^2 = 12$ GeV^2 compared with a fit described in the text. The errors are statistical only.

4.7. Diffractive Dijet Photoproduction

Diffractive hard photoproduction in *ep* collisions occurs with $Q^2 \approx 0$ and a final state hadronic system containing at least one jet. ZEUS has examined dijet photoproduction events with a forward rapidity gap.[90] Figure 37(a) shows a schematic representation of such an event that proceeds via Pomeron exchange at small t. The indicator of the photon dissociation is the final state proton's retention of a large fraction of the original longitudinal momentum. A large rapidity gap between the hadronic system and the

scattered proton is produced by the exchange of a colorless object, *i.e.*, the Pomeron. The typical topology of a diffraction dijet photoproduction event is shown in Figure 37(b).

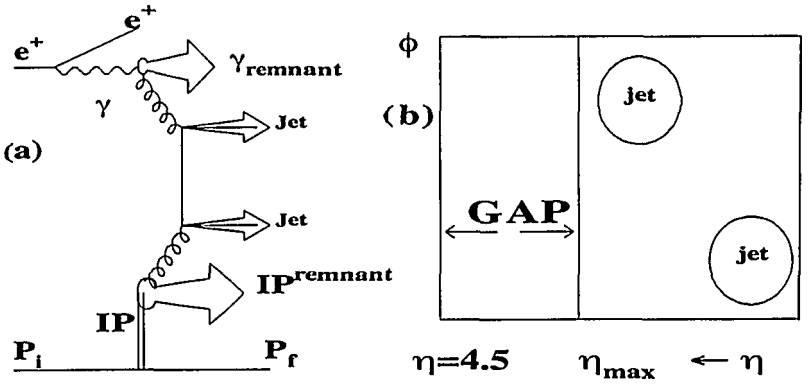


Figure 37. (a) Example of a two-jet diffractive process via Pomeron exchange at small *t*. (b) Typical topology of the event in (a) as seen by ZEUS.

ZEUS has measured[90] the dijet cross section for photoproduction events with the most forward-going hadron at $\eta < 1.8$, where the jets have $|\eta^{jet}| < 1.5$ and transverse energy, $E_t^{jet} > 6$ GeV, where $Q^2 < 4$ GeV^2 and $0.2 < E_\gamma/E_e < 0.8$, corresponding to photoproduction interactions with a center-of-mass energy in the range 134–269 GeV and a median $Q^2 \approx 10^{-3}$ GeV^2. This data has been compared with a factorizable Ingelman-Schlein (IS) model[91] where a parton from the Pomeron can directly scatter off the photon (direct photoproduction) or with a parton from the photon (resolved photoproduction). The flux of Pomerons in the proton is given by a parameterization of UA4 data.[92] A second model[93] from Donnachie and Landshoff (DL) calculates the Pomeron flux from fits to hadron-hadron data. The IS and DL Pomeron flux factors give similar results. ZEUS explored the effects of four different expressions for the density of partons in the Pomeron in terms of β, the momentum fraction of the struck parton in the Pomeron:

- super-hard gluon density: $\beta f_{g/IP}(\beta) = 0.1/(1-\beta)^{0.9}$ [similar to $\delta(1-\beta)$]
- hard gluon density: $\beta f_{g/IP}(\beta) = 6\beta(1-\beta)$
- soft gluon density: $\beta f_{g/IP}(\beta) = 6\,(1-\beta)^5$
- quark density (two flavors): $\beta f_{g/IP}(\beta) = 1.5\beta(1-\beta)$.

These were implemented in the framework of the POMPYT[80] model.

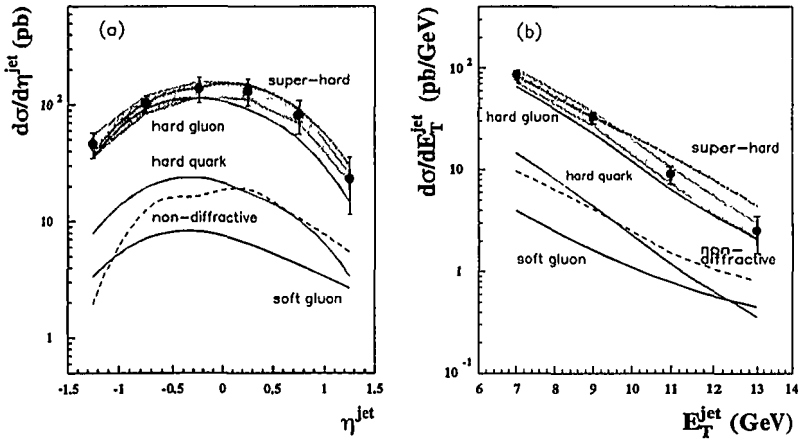


Figure 38. ZEUS differential dijet photoproduction cross section as a function of (a) η^{jet} and (b) E_T^{jet}. The thick error bars show the statistical error and the thin error bars show the statistical and systematic errors added in quadrature (excluding the jet energy scale error shown as a band). The data are compared with the POMPYT model using the inputs described in the text and with a calculation of the nondiffractive component.

The ZEUS-corrected differential dijet cross section $d\sigma/d\eta^{jet}$ with the cuts described above is shown in Figure 38(a). The cross section is flat in the central region and falls off as the jets approach the beam direction. The transverse energy differential cross section $d\sigma/dE_T^{jet}$ is shown in Figure 38(b). The cross section falls off exponentially as a function of E_t^{jet}. The figure shows that the expectation of the nondiffractive contribution caused by fluctuations in the final hadron system and estimated using PYTHIA including both direct and resolved, is three to eight times below the data for $d\sigma/dE_T^{jet}$ and seven times for $d\sigma/d\eta^{jet}$. Figure 38 also shows the diffractive model predictions using POMPYT, the DL Pomeron flux, and the parton distributions in the Pomeron listed above. The soft gluon density Pomeron parton distribution neither matches the data in shape nor normalization. The hard quark density describes the shape, but falls below the data. The hard and super-hard gluon densities provide reasonable descriptions of the data both in shape and magnitude.

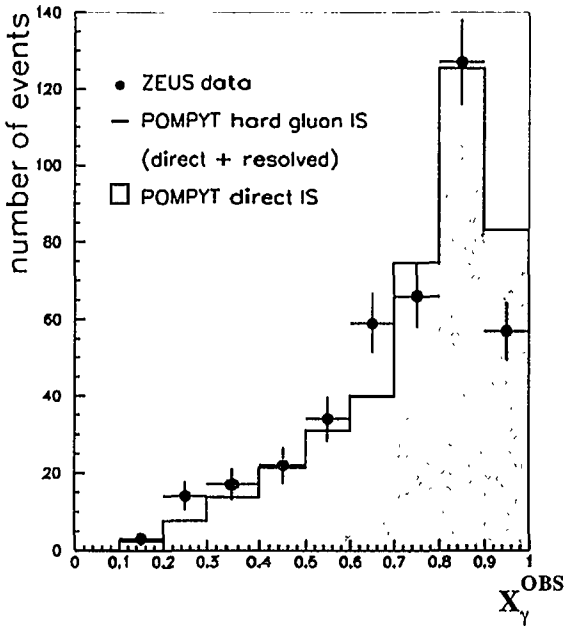


Figure 39. x_γ^{OBS} distribution from ZEUS for diffractive photoproduction of dijets. The solid line shows POMPYT with resolved and direct contributions for a hard gluon density in the Pomeron. The direct contribution is shown as the shaded area.

Figure 39 shows the x_γ^{OBS} distribution from ZEUS for diffractive photoproduction of dijets with the cuts described above. The x_γ^{OBS} distribution peaks at $x_\gamma^{OBS} = 0.85$ with a large tail at low x_γ^{OBS}. The background from nondiffractive hard photoproduction, as calculated from PYTHIA, is estimated to be about 18 ± 4 % and is concentrated at large x_γ^{OBS} values, so it cannot account for the amount of the data nor the low x_γ^{OBS} tail. The dependence of the relative amounts of direct and resolved contributions to standard hard photoproduction is predicted to depend on the jet transverse energy.[94] The resolved contribution is expected to dominate over the direct in the E_t^{jet} range of this sample. However, due to the limited center-of-mass energy, the direct contribution is expected to be enhanced.[90] Figure 39 shows that the sum of the direct and resolved contributions as predicted by POMPYT (histogram) with the hard gluon Pomeron parton density and IS Pomeron flux give a reasonable description of the data. In contrast, the prediction of the purely direct photoproduction contribution (shaded area) does not reproduce the data. This remains true when a hard quark density is used. Therefore, one can conclude that resolved diffractive photoproduction is being observed.

5. Conclusions

The HERA collider and the H1 and ZEUS experiments have unearthed a rich source of information on the structure of the proton and the photon. The extension of the range of the proton structure function measurements by two orders of magnitude has uncovered the dramatic rise in F_2 with decreasing x at low Q^2 that indicates a large increase in the gluon density. At low Q^2, we are observing the transition from perturbative QCD to the soft hadronic physics described by Regge theory. Studies of deep inelastic multijet events have shown the value and running of the strong coupling constant over a large Q^2 range within a single experiment. The observation of resolved and direct photoproduction, particularly in dijets, has provided new insight into the structure of the photon as well as the spin of the exchanged parton in these processes. The discovery of diffraction in *ep* collisions both in deep inelastic scattering and in photoproduction has produced information about the structure of the Pomeron and the characteristics of the diffractive process.

The future for the HERA program looms particularly bright. While all of the above physics discussed in these lectures is based on data samples up through 1995 of around 10 pb^{-1}, the DESY Directorate has endorsed an upgrade plan for HERA that should yield luminosities of 150 pb^{-1}/year, with polarized electrons and positrons, beginning in the year 2000. Already, the 1996 run with positrons is expected to yield more than 10 pb^{-1}, with more improvements expected in 1997 and beyond, including switching to electrons in 1998. This large increase in luminosity should yield substantial physics results in all realms of HERA physics.[95] We can look forward to a much deeper understanding of the structure of the proton and photon, and maybe even some surprises.

Acknowledgments

I am very grateful for the help of many people from H1 and ZEUS who assisted me in the preparation of these lectures with information, figures, references, and advice. In particular, I would like to thank E. Barberis, V. Boudry, J. Bulmahn, A. Caldwell, R. Cross, J. Dainton, S. Dasu, R. Eichler, L. Feld, C. Foudas, E. Gallo, G. Grindhammer, G. Iacobucci, S. Magill, A. Mehta, S. Mattingly, S. Nam,

P. Newman, A. Quadt, D. Reeder, J. Repond, S. Ritz, R. Sacchi, F. Sciulli, B. Surrow, S. Tapprogge, T. Trefzger, and many others. I would like to thank the DESY Directorate for their strong support and encouragement of the HERA program. I would also like to thank the HERA machine group for their operation of the collider and the computing staff for the data analysis environment. Finally, I would like to thank the organizers of the SLAC Summer School for continuing their fine tradition of superb meetings.

References

[1] E. Bloom *et al.*, Phys. Rev. Lett. **23**, 930 (1968); M. Breidenbach *et al.*, Phys. Rev. Lett. **23**, 935 (1968); R. Taylor, Rev. Mod. Phys. **63**, 573 (1991); H. Kendall, Rev. Mod. Phys. **63**, 597 (1991); J. Friedman, Rev. Mod. Phys. **63**, 615 (1991).

[2] J. D. Bjorken, Phys. Rev. **179**, 1547 (1969).

[3] R. P. Feynman, Phys. Rev. Lett. **23**, 1415 (1969).

[4] J. D. Bjorken and E. A. Paschos, Phys. Rev. **185**, 1975 (1969).

[5] J. Friedman *et al.*, Phys. Rev. D **5**, 528 (1972).

[6] J. Kuti and V. F. Weisskopf, Phys. Rev. D **4**, 3418 (1971).

[7] V. N. Gribov and L. N. Lipatov, Sov. J. Nucl. Phys. **15**, 438 (1972); L. N. Lipatov, Sov. J. Nucl. Phys. **20**, 94 (1975); G. Altarelli and G. Parisi, Nucl. Phys. B **126**, 298 (1977).

[8] A. D. Martin, R. G. Roberts, and W. J. Stirling, Phys. Lett. B **354**, 155 (1995).

[9] R. Brock *et al.*, Rev. Mod. Phys. **67**, 157 (1995).

[10] M. Glück, E. Reya, and A. Vogt, Z. Phys. C **65**, 157 (1995).

[11] A. Donnachie and P. V. Landshoff, Nucl. Phys. B **244**, 322 (1984); Phys. Lett. B **296**, 227 (1992); Phys. Lett. C **61**, 139 (1994).

[12] Y. Balitsky and L. Lipatov, Sov. J. Nucl. Phys. **28**, 822 (1978); E. Kuraev, L. Lipatov, and V. Fadin, Sov. Phys. JETP **44**, 443 (1976); Sov. Phys. JETP **45**, 443 (1977).

[13] T. Ahmed *et al.*, Nucl. Phys. B **349**, 471 (1995).

[14] M. Derrick *et al.*, Z. Phys. C **69**, 607 (1996).

[15] A. C. Benvenuti *et al.*, Phys. Lett. B **223**, 485 (1989).

[16] M. Arneodo *et al.*, Phys. Lett. B **364**, 107 (1995).

[17] M. R. Adams *et al.*, Phys. Rev. D **54**, 3006 (1996).

[18] H. L. Lai *et al.*, Phys. Rev. D **51**, 4768 (1996).

[19] A. D. Martin *et al.*, Phys. Lett. B **387**, 419 (1996).

[20] S. Aid *et al.*, Nucl. Phys. B **470**, 3 (1996).

[21] M. Derrick *et al.*, DESY 96-076, accepted by Z. Phys. (1996).

[22] M. Derrick *et al.*, Z. Phys. C **63**, 391 (1994).

[23] S. Aid *et al.*, Z. Phys. C **69**, 27 (1995).

[24] D. O. Caldwell *et al.*, Phys. Rev. Lett. **40**, 1222 (1978).

[25] H1 Collaboration, contributed paper PA02-70 to the 1996 International Conference on High Energy Physics, Warsaw, July 1996.

[26] S. Aid *et al.*, Phys. Lett. B **379**, 319 (1996); S. Aid *et al.*, Z. Phys. C **67**, 565 (1995); T. Ahmed *et al.*, Phys. Lett. B **324**, 241 (1994).

[27] M. Derrick *et al.*, Phys. Rev. Lett. **75**, 1006 (1995).

[28] L. Montanet *et al.*, Phys. Rev. D **50**, 1173 (1994).

[29] S. Magill, ZEUS Note 94-154.

[30] T. Ahmed *et al.*, Phys. Lett. B **346**, 415 (1995).

[31] M. Derrick *et al.*, Phys. Lett. B **363**, 201 (1995).

[32] W. Bartel *et al.*, Z. Phys. C **33**, 23 (1986); S. Bethke *et al.*, Phys. Lett. B **213**, 235 (1988).

[33] T. Brodkorb *et al.*, Z. Phys. C **44**, 415 (1989); D. Graudenz and N. Magnussen, *Proceedings of the HERA Workshop 1991*, DESY.

[34] T. Brodkorb and E. Mirkes, U. Wisconsin preprint MAD-PH-821, April 1994.

[35] D. Graudenz, Comp. Phys. Commun. **92**, 65 (1995).

[36] G. Ingelman and J. Rathsman, Z. Phys. C **59**, 213 (1994).

[37] E. Laenen *et al.*, Nucl. Phys. B **392**, 228 (1993); S. Riemersma, J. Smith, and W. L. van Neervan, Phys. Lett. B **347**, 143 (1995); M. Glück, E. Reya, and M. Stratmann, Nucl. Phys. B **422**, 37 (1994).

[38] T. Trefzger, ZEUS Note 96-075.

[39] J. F. Owens, Phys. Rev. D **21**, 54 (1980); M. Drees and F. Halzen, Phys. Rev. Lett. **61**, 275 (1988); M. Drees and R. M. Godbole, Phys. Rev. D **39**, 169 (1989); G. A. Schuler and T. Sjostrand, Phys. Lett. B **300**, 169 (1993).

[40] J. J. Sakurai, Phys. Rev. Lett. **22**, 981 (1969).

[41] M. Derrick *et al.*, Phys. Lett. B **348**, 665 (1995).

[42] T. Sjostrand and M. van Zijl, Phys. Rev. D **36**, 2019 (1987).
[43] S. D. Ellis, *Proceedings of the 28th Rencontre de Moriond*, 235 (1993).
[44] T. Ahmed *et al.*, Nucl. Phys. B **445**, 195 (1995).
[45] G. Schuler and T. Sjostrand, Nucl. Phys. B **407**, 539 (1993).
[46] ZEUS Collaboration, contributed paper pa02-040, *International Conference on High Energy Physics*, Warsaw, Poland, July 1996.
[47] G. Marchesini *et al.*, Comp. Phys. Comm. **67**, 465 (1992).
[48] J. M. Butterworth and J. R. Forshaw, J. Phys. G **19**, 1657 (1993).
[49] S. Aid *et al.*, Z. Phys. C **70**, 17 (1996).
[50] M. Derrick *et al.*, Phys. Lett. B **342**, 417 (1995).
[51] ZEUS Collaboration, contributed paper pa02-041, *International Conference on High Energy Physics*, Warsaw, Poland, July 1996.
[52] C. Albajar *et al.*, Nucl. Phys. B **309**, 405 (1988).
[53] T. Sjostrand, Comput. Phys. Comm. **82**, 74 (1994).
[54] R. Engel, Z. Phys. C **66**, 203 (1995).
[55] J. R. Forshaw and R. G. Roberts, Phys. Lett. B **319**, 539 (1993).
[56] ZEUS Collaboration, contributed paper pa02-040, *International Conference on High Energy Physics*, Warsaw, Poland, July 1996.
[57] J. Huth *et al., Proceedings of the 1990 DPF Summer Study on High Energy Physics* (World Scientific, Singapore, 1992), p. 134; G. Arnison *et al.*, Phys. Lett. B **123**, 115 (1983).
[58] S. Catani, Y. L. Dokshitzer, M. H. Seymour, and B. R. Webber, Nucl. Phys. B **406**, 187 (1993).
[59] S. D. Ellis and D. E. Soper, Phys. Rev. D **48**, 3160 (1993).
[60] M. Glück, E. Reya, and A. Vogt, Phys. Rev. D **46**, 1973 (1992).
[61] J. Huston *et al.*, Phys. Rev. D **51**, 6139 (1995).
[62] S. D. Ellis, Z. Kunszt, and D. E. Soper, Phys. Rev. Lett. **69**, 3615 (1992).
[63] H. Baer, J. Ohnemus, and J. F. Owens, Phys. Rev. D **40**, 2844 (1989).
[64] M. Derrick *et al.*, Phys. Lett. B **384**, 401 (1996).
[65] J. Botts *et al.*, Phys. Lett. B **304**, 15 (1993).
[66] A. Martin, W. J. Stirling, and R. G. Roberts, Phys. Rev. D **50**, 6734 (1994).
[67] D. Perkins, *Introduction to High Energy Physics* (J. Wiley, 1988).
[68] M. Froissart, Phys. Rev. **123**, 1053 (1961).
[69] T. Regge, Nuovo Cimento **16**, 951 (1959); Nuovo Cimento **18**, 947 (1960).
[70] G. F. Chew and S. C. Frautschi, Phys. Rev. Lett. **7**, 394 (1961) and **8**, 41 (1962).
[71] A good review is found in *Regge Theory of Low-p_T Interactions*, edited by L. Caneschi (North-Holland, 1989).
[72] A. Donnachie and P. V. Landshoff, Phys. Lett. B **296**, 227 (1992).
[73] Particle Data Group, Phys. Rev. D **54**, 191 (1966).
[74] M. Bozzo *et al.*, Phys. Lett. B **136**, 217 (1984).
[75] G. Ingelman and P. E. Schlein, Phys. Lett. B **152**, 256 (1985).
[76] R. Bonino *et al.*, Phys. Lett. B **211**, 239 (1988).
[77] A. Brandt *et al.*, Phys. Lett. B **297**, 417 (1992).
[78] M. Derrick *et al.*, Phys. Lett. B **316**, 207 (1993).
[79] A. DeRoeck, *Proceedings of the 1993 EPS Conference*, Marseille, DESY 94-005; J. Dainton, *Proceedings of the 1993 Lepton-Photon Conference*, Cornell.
[80] P. Bruni and G. Ingelman, *Proceedings of the 1993 EPS Conference*, Marseille, 595, DESY 93-187.
[81] G. Ingelman and K. Jansen-Prytz, Z. Phys. C **58**, 285 (1993).
[82] K. Prytz, Z. Phys. C **64**, 79 (1994).
[83] P. D. B. Collins, *An Introduction to Regge Theory and High Energy Physics* (Cambridge University Press, 1977) p. 418.
[84] T. Ahmed *et al.*, Phys. Lett. B **348**, 681 (1995).
[85] M. Derrick *et al.*, Z. Phys. C **68**, 569 (1995).
[86] H1 Collaboration, contributed paper pa02-061, 1996 Lepton-Photon Conference, Warsaw.
[87] ZEUS Collaboration, contributed paper pa02-050, 1996 Lepton-Photon Conference, Warsaw.
[88] ZEUS Collaboration, contributed paper pa02-026, 1996 Lepton-Photon Conference, Warsaw.
[89] H. Jung, DESY preprint DESY93-182.
[90] ZEUS Collaboration, contributed paper pa02-039, 1996 Lepton-Photon Conference, Warsaw.
[91] P. Bruni and G. Ingelman, *Proceedings of the International Europhysics Conference*, Marseille, France, 1993.
[92] M. Bozzo *et al.*, Phys. Lett. B**136**, 217 (1984).

[93] A. Donnachie and P. V. Landshoff, Nucl. Phys. B **303**, 634 (1988); Phys. Lett. B **285**, 172 (1992).

[94] Drees and Grassie, Z. Phys. C **28**, 451 (1985).

[95] Proceedings of the Workshop on Future Physics at HERA, edited by G. Ingelman, A. De Roeck, and R. Klanner, DESY Report (http://www.desy.de/~heraws96), 1996.

SMALL-x PHYSICS

A. H. Mueller*
Department of Physics, Columbia University
New York, New York 10027, USA

ABSTRACT

After a brief review of the kinematics of deep inelastic lepton-proton scattering, the parton model is described. Small-x behavior coming from DGLAP evolution and from BFKL evolution is discussed, and the two types of evolution are contrasted and compared. Then a more detailed discussion of BFKL dynamics is given. The phenomenology of small-x physics is discussed with an emphasis on ways in which BFKL dynamics may be discussed and measured.

*This research is supported in part by the Department of Energy under GRANT DE-FG02-94ER40819.

© 1996 by A. H. Mueller.

1 Introduction

Small-x physics encompasses those high-energy reactions where there is a hard scattering (at scale Q) and where $s/Q^2 >> 1$ with s the square of the center-of-mass energy of the reaction. Thus, deep inelastic lepton-proton scattering at small values of the Bjorken x-variable is a small-x reaction as is jet production at the Tevatron so long as the transverse momentum of the jet is much less than the center-of-mass energy. The new element which occurs in small-x reactions is that there are two large logarithms present, namely, $\ell nQ^2/\Lambda^2$ and $\ell n1/x$. We are used to summing $(\alpha\ \ell n\ Q^2/\Lambda^2)^n$ corrections as part of ordinary QCD evolution, and this summation is governed by the renormalization group, or equivalently by the Dokshitzer, Gribov, Lipatov, Altarelli, Parisi (DGLAP) [1-3] equation. The resummation of $(\alpha\ \ell n\ 1/x)^n$ terms is less familiar. The leading series of $\alpha\ \ell n\ 1/x$ terms is governed by the Balitsky, Fadin, Kuraev, Lipatov (BFKL) [4-6] equation, and one expects a generalization of the BFKL kernel also to apply to nonleading series of $(\alpha\ \ell n\ 1/x)$ logarithms. The BFKL resummation is more like that which occurs in Regge pole models than that of the renormalization group.

When Q^2 is large and when $\alpha\ell n1/x \geq 1$, in principle one must take into account both resummation in $\ell nQ^2/\Lambda^2$ and in $\ell n1/x$. The DGLAP formalism is sufficiently general to allow this, although resummation of $\ell n1/x$ terms means dealing with anomalous dimensions and coefficient functions to all orders in α. We shall come back to this question in some detail in Sec. 3.

Evolution in Q^2, coming from the DGLAP equation, has been studied and tested in great detail in moderate x reactions. The physics is that of revealing partonic substructure as one probes shorter distance scales, a physics that is well-understood in the framework of perturbative QCD.

Evolution in x, coming from the BFKL equation, has not yet been tested. As one goes to smaller and smaller values of x, at a given short-distance scale, BFKL evolution predicts a growth in hard scattering cross sections due to a growing number of partons. At very small values of x, unitarity corrections are expected to slow the rate of growth of these amplitudes while the growing numbers of overlapping partons (mainly gluons) are expected to initiate a strong field strength regime of QCD where $F_{\mu\nu} \geq 1/g$ and where new nonperturbative QCD effects may appear. The experimental study of BFKL evolution is the most pressing problem in small-x physics, and I shall discuss these issues in some detail in Sec. 6.

These lectures are meant to be an introduction to the theoretical and phenomenological issues in small-x physics with technical details suppressed as much as possible.

2 Structure Functions, the Parton Model, and DGLAP Evolution

2.1 Deep Inelastic Scattering Structure Functions

The cross section for deep inelastic lepton-proton scattering is given, in the proton rest system, by

$$\frac{d\sigma}{dE'd\Omega'} = \frac{4\alpha_{em}^2(E')^2}{Q^4}\left[W_2 cos^2\theta/2 + 2W_1 sin^2\theta/2\right], \tag{1}$$

where the process is illustrated in Fig. 1. E' and Ω' are the energy and scattering solid angle of the outgoing lepton, while θ is the scattering angle between the incoming and outgoing lepton directions. $Q^2 = -q_\mu q_\mu$ is the virtuality of the photon exchanged between the lepton and the proton. The structure functions W_1 and W_2 appear in the decomposition of

$$W_{\mu\nu} = \frac{4\pi^2 E_p}{M}\int d^4x e^{iq\cdot x}(p|j_\mu(x)j_\nu(0)|p) \tag{2}$$

as

$$W_{\mu\nu} = -(g_{\mu\nu} - \frac{q_\mu q_\nu}{q^2})W_1 + \frac{1}{M^2}[p_\mu p_\nu - \frac{p\cdot q}{q^2}(p_\mu q_\nu + p_\nu q_\mu) + (\frac{p\cdot q}{q^2})^2 q_\mu q_\nu]W_2. \tag{3}$$

W_1 and W_2 depend on Q^2 and on the scaling variable $x = \frac{Q^2}{2p\cdot q}$.

2.2 The Bjorken Frame

The parton picture is only manifest in a special infinite momentum (Bjorken) frame where

$$p_\mu = (p_0, p_1, p_2, p_3) \approx (p + \frac{M^2}{2p}, 0, 0, p) \tag{4a}$$

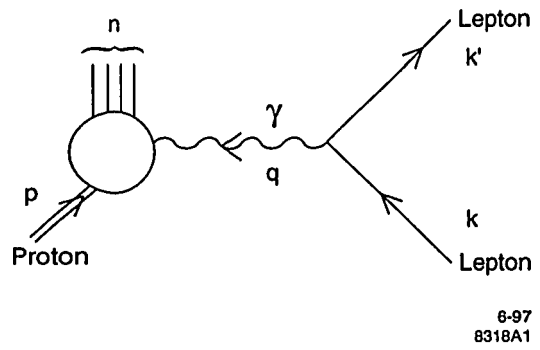


Figure 1.

with p very large and where

$$q_\mu = (q_0, \underline{q}, q_3 = 0). \tag{4b}$$

One can evaluate $q_0 \approx \frac{p \cdot q}{p} \to 0$ as $p \to \infty$ so that

$$Q^2 \approx \underline{q}^2. \tag{5}$$

2.3 The Parton Model (Physical Picture)

In order to describe how the parton model comes about, it is convenient to write

$$W_{\mu\nu} = 2Im\, T_{\mu\nu}, \tag{6}$$

where

$$T_{\mu\nu} = i\frac{4\pi^2 E_p}{M}\int d^4x e^{iq\cdot x}(p|Tj_\mu(x)j_\nu(0)|p) \tag{7}$$

is the time-ordered product of two electromagnetic currents in a proton state. $T_{\mu\nu}$ is given in terms of Feynman diagrams in contrast to $W_{\mu\nu}$ where certain intermediate states are put on mass shell, consistent with $W_{\mu\nu}$ being related to a cross section rather than a scattering amplitude. $T_{\mu\nu}$ is simply the forward Compton amplitude for virtual photon-proton scattering.

Let us follow the time-ordered sequence of a proton absorbing a virtual photon and then reemitting it as given by $T_{\mu\nu}$ in Eq. (7). Since the incoming photon has a transverse momentum Q, it must be absorbed over a transverse spatial size $\Delta x_\perp \sim 1/Q$. We view the proton as a collection of quarks and gluons spread over a transverse size of about one fermi. Because $\Delta x_\perp \sim 1/Q$ is much less than a fermi, the incoming photon will be absorbed by a single quark, the probability of finding two or more quarks in $\Delta x_\perp \sim 1/Q$ being very unlikely. The quark which absorbs the photon is called the struck quark. The lifetime of the struck quark, after absorbing the incoming photon, is

$$\tau \approx \frac{2}{Q}\cdot\frac{k}{Q} = \frac{2k}{Q^2}, \tag{8}$$

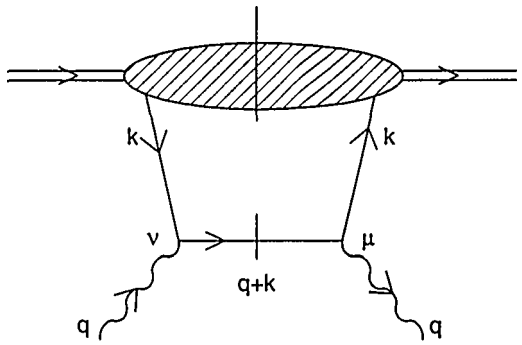
with the first factor being the typical virtuality of the struck quark and k/Q, with k the longitudinal momentum of the struck quark, being the time dilation factor. But the "normal" time scale for soft interactions between quarks in a high-momentum parton is $\tau_0 = \frac{2p}{\mu^2}$ with $\mu \approx 300\ MeV$. Thus, the struck quark is in the uncomfortable situation of having a lifetime much too short, and a transverse momentum much too large, to fit into the proton's infinite momentum wavefunction. In order to fit into the wavefunction, the struck quark will reemit the virtual photon, thus lowering its transverse momentum and increasing its lifetime to that of a normal quark in the light-cone wavefunction of a proton. The picture is illustrated in Fig. 2. Thus, in the Bjorken frame, the virtual photon resolves individual quarks and measures them with a resolution $\Delta x_\perp \sim 1/Q$.

2.4 The Parton Model (Formulas)

We have just seen that the virtual Compton amplitude can be viewed as the absorption of the photon by the struck quark followed by the reemission of the photon by the same quark. This suggests that the virtual photon actually determines, or measures, the single-quark distribution in the proton. This is stated quantitatively by the formula for the "QCD improved" parton model

$$\nu W_2(x, Q^2) = \sum_f e_f^2 x P_f(x, Q^2), \tag{9}$$

where $P_f(x, Q^2)$ is the number density of quarks, measured to be bare at scale $\Delta x_\perp = 1/Q$, having longitudinal momentum fraction x. In terms of local operators



6-97
8318A2

Figure 2.

$$\int_0^1 dx x^{n-1} P_f(x,Q^2) = \frac{(2\pi)^3 E_p}{p_+^n} (p|\tilde{q}_f \gamma_{\mu_1} i\partial_{\mu_2} \cdots i\partial_{\mu_n} q_f|p)|_{\mu_i=+}, \tag{10}$$

where the operator is renormalized at scale Q^2. In general, one should write $D_\mu = \partial_\mu - igA_\mu$ instead of ∂_μ in Eq. (10); however, in light-cone gauge $A_+ = 0$ and $D_\mu = \partial_\mu$. It is only in this gauge that the partonic picture of deep inelastic scattering is manifest.

The renormalization scale dependence, Q^2, in Eqs. (9) and(10) is governed by the DGLAP equation and is expressed most simply in terms of flavor singlet, flavor nonsinglet, and gluon distributions

$$\Delta_{ff'} = q_f(x,Q^2) - q_{f'}(x,Q^2) \tag{11a}$$

$$\Sigma = \Sigma_f \left(q_f(x,Q^2) + q\bar{f}(x,Q^2)\right) \tag{11b}$$

$$G(x,Q^2) \tag{11c}$$

as

$$Q^2 \frac{\partial}{\partial Q^2} \Delta(x,Q^2) = \frac{\alpha(Q^2)}{2\pi} \int_x^1 \frac{dx'}{x'} \gamma_{qq}(x/x') \Delta(x',Q^2) \tag{12a}$$

and

$$Q^2 \frac{\partial}{\partial Q^2} \begin{pmatrix} \Sigma(x,Q^2) \\ G(x,Q^2) \end{pmatrix} = \frac{\alpha(Q^2)}{2\pi} \int_x^1 \frac{dx'}{x'} \begin{pmatrix} \gamma_{qq}(x/x') & \gamma_{qG}(x/x') \\ \gamma_{Gq}(x/x') & \gamma_{GG}(x/x') \end{pmatrix} \cdot \begin{pmatrix} \Sigma(x',Q^2) \\ G(x',Q^2) \end{pmatrix}. \tag{12b}$$

3 Small-x Behavior from the DGLAP Equation

3.1 Leading Double Logarithms

For very small values of x, the gluon distribution and γ_{GG} dominate DGLAP evolution. The physical reason for this is clear. Soft gluons can be emitted from harder quarks or gluons, while in a gluon splitting into a quark-antiquark pair, the quark and antiquark share the momentum of the gluon equally. In the leading double-logarithm approximation, one requires a logarithm from transverse momentum integration along with a logarithm from longitudinal momenta for each power of α. In this approximation, gluons are not allowed to split into quark-antiquark pairs but only to break into an asymmetric pair consisting of a hard gluon and a soft gluon. Thus

$$Q^2 \frac{\partial}{\partial Q^2} G(x,Q^2) = \frac{\alpha(Q^2)}{2\pi} \int_x^1 \frac{dx'}{x'} \gamma_{GG}(x/x') G(x',Q^2) \tag{13}$$

is the DGLAP equation in the leading double-logarithmic approximation. Using

$$\alpha(Q^2) = \frac{1}{b\ \ell n\ Q^2/\Lambda^2}, \quad b = \frac{11N_c - 2N_f}{12\pi} \tag{14a}$$

$$\gamma_{GG}(x) = \frac{2N_c}{x} \tag{14b}$$

and writing $\ell n\ Q^2/\Lambda^2\ Q^2 \frac{\partial}{\partial Q^2} = \frac{\partial}{\partial \ell n\ \ell n\ Q^2/\Lambda^2}$, one finds

$$\frac{\partial}{\partial \ell n\ 1/x} \frac{\partial}{\partial \ell n\ \ell n\ Q^2/\Lambda^2} xG(x,Q^2) = \frac{N_c}{\pi b}\ xG(x,Q^2). \tag{15}$$

Equation (15) leads to a small-x dependence

$$xG(x,Q^2) \propto exp\left\{2\sqrt{\frac{N_c}{\pi b}\,\ell n\ 1/x \ell n(\frac{\ell n Q^2/\Lambda^2}{\ell n\ Q_0^2/\Lambda^2})}\right\}. \tag{16}$$

If one parametrizes $xG(x,Q^2)$ as a constant times $x^{-\lambda(x,Q^2)}$ in a local region of x and Q^2, then Eq. (16) leads to

$$\lambda(x,Q^2) = \sqrt{\frac{N_c}{\pi b}\,\frac{\ell n(\frac{\ell n Q/\Lambda^2}{\ell n Q_0^2/\Lambda^2})}{\ell n\ 1/x}}. \tag{17}$$

Since $\sqrt{\frac{N_c}{\pi b}} = \frac{6}{5}$ for $N_f = 3, \lambda$ need not be small so long as x is not too small and so long as Q_0^2/Λ^2 is not too large. Thus, DGLAP evolution can give a fairly steep rise of $xG(x,Q^2)$, and hence of $P_f(x,Q^2)$, as x becomes small.

3.2 Deep Inelastic Scattering from DGLAP in General

The DGLAP equations furnish a general formalism for describing deep inelastic scattering in QCD. From the operator product expansion (factorization)

$$\nu W_2(x,Q^2) = \sum_{i=f,G}\int_x^1 \frac{dx'}{x'} P_i(x',Q^2) E_i(x/x',\alpha(Q^2)), \tag{18}$$

with E_i the coefficient function and P_i the parton distribution. E_i is expressed as a power series in $\alpha(Q^2)$ with the first term being $e_i^2\delta(x/x'-1)$ and leading to Eq. (9). Although the separation between P and E in Eq. (18) is in the renormalization scheme department, as one goes beyond Eq. (9), the product is scheme independent up to powers in $1/Q^2$. The parton distributions satisfy the DGLAP equation

$$Q^2\frac{\partial}{\partial Q^2} P_i(x,Q^2) = \sum_j \int_x^1 \frac{dx'}{x'}\gamma_{ij}(x/x',\alpha(Q^2)) P_j(x',Q^2). \tag{19}$$

The anomalous dimension matrix has a perturbative expansion

$$\gamma(z,\alpha) = \alpha\gamma^{(1)}(z) + \alpha^2\gamma^{(2)}(z) + \cdots. \tag{20}$$

The level of approximation in solving Eq. (19) and in describing νW_2 in terms of Eq. (18) is as follows: (i) If one keeps only $\gamma^{(1)}$ in Eq. (20) and sets $E_i = e_i^2$, one has a first-order formalism, the leading logarithmic approximation. (ii) The second-order formalism keeps the α and α^2 terms in γ along with the constant and order α terms in E_i. This is the current level of precision of the QCD description of hard processes [7-9], though in the near future, we may expect to see the third-order formalism come into use.

So long as $\alpha\ \ell n\ 1/x$ is small, the second-order QCD formalism is quite accurate. However, $\gamma^{(n)}(x)$ has terms of size $(\ell n\ 1/x)^n$ so that one can no longer expect a second-order formalism to be adequate when $\alpha\ \ell n\ 1/x$ is of order one or greater. In this case, one might expect that one should try to resum all terms of size $(\alpha \ell n 1/x)^n$ in γ and also in E_i. This resummation can be done, at the leading $\ell n\ 1/x$ level [10-16], using the BFKL equation which we shall describe later.

3.3 Physical Picture of DGLAP Evolution

DGLAP evolution describes how parton distributions change as one measures the partons with better and better resolution in $x_\perp = 1/Q$. For example, a quark which looks bare at a scale Q_0 may actually be found to be a quark and a gluon when measured with a resolution $Q > Q_0$. The situation is pictured in Fig. 3. Although DGLAP evolution can lead to large parton distributions at small x and at large Q^2, a fixed-order DGLAP formalism, when consistently used, always leads to partons being dilute in the proton. Thus the DGLAP equation, even at small x, does not lead to any new domain of QCD. As we shall see later, BFKL

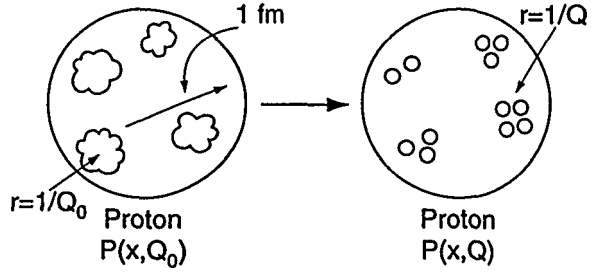


Figure 3.

evolution leads to large numbers of partons which become dense, and strongly overlap, leading to a new domain of QCD where partons can no longer be viewed as dilute and noninteracting.

4 DGLAP as BFKL

DGLAP evolution applies to two-scale problems where (at least) one of the scales is hard. For example, in deep inelastic lepton-proton scattering, the size of the proton, 1 fm, furnishes one scale while Q^2 furnishes the second, hard scale. DGLAP evolution, in a fixed-order formalism, furnishes the information on the hard-scale dependence in terms of initial conditions giving the parton distributions at a scale Q_0^2. The situation is illustrated in Fig. 4. In moving from lower Q^2 to higher Q^2 values, $\ell n\ 1/x$ always increases, as seen in Eq. (19). So long as the final x-value is not too small, the slope in Fig. 4 will not be large and a fixed-order formalism is quite adequate.

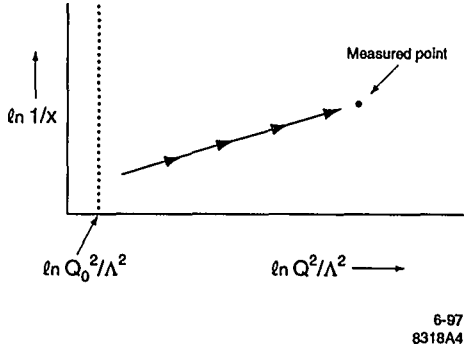


Figure 4.

If the final x-value is very small, DGLAP evolution may follow different types of paths as shown in Fig. 5. For path 1, the slope of the evolution is not large and a fixed-order DGLAP evolution should be adequate. However, for a path like 2, the AB part of that path should be well-described by low-order DGLAP evolution; however, the BC part of that path has a large slope and cannot be expected to be reliably described by fixed-order DGLAP. It is in such a circumstance where one must resum all $(\alpha \ell n\ 1/x)^n$ terms in the anomalous dimension when using Eq. (19) and do a corresponding resummation for the coefficient function in Eq. (18).

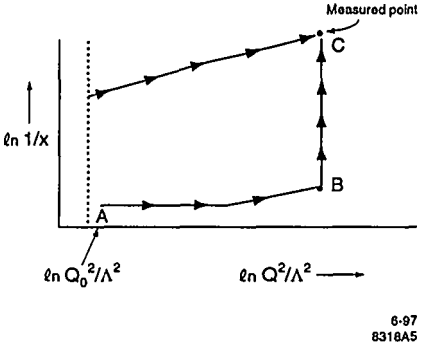


Figure 5.

While one use of the BFKL equation is to aid in the resummation of $(\alpha \ell n 1/x)^n$ terms in the anomalous dimensions and coefficient functions in a DGLAP description of deeply inelastic scattering, the BFKL equation applies directly to certain physical processes. The characteristics that a scattering process must have in order that BFKL evolution apply are: (i) there should be only one transverse momentum scale, Q, in the process; (ii) that scale should be hard enough that $\alpha(Q^2) << 1$; (iii) the center-of-mass energy squared, s, should be large enough so that $s/Q^2 >> 1$. In these circumstances, all $(\alpha \ell n\ s/Q^2)^n$ terms will be given by the BFKL equation, and thus predictions for the energy dependence will emerge. Such processes are not easy to find in practice. We shall describe several possibilities later on. *Conceptually*, the most straightforward process is heavy onium-heavy onium scattering at high energy. The only transverse scale is the size of the onium which, if the onium is heavy enough, will be in the domain of weak coupling. We shall use onium-onium scattering in the next section, as a means of describing the physics of the BFKL equation.

5 The BFKL Equation

As mentioned above, we shall use heavy onium-heavy onium scattering [17-18] as a means to describe BFKL evolution. Later on, we shall discuss specific ways that one might test BFKL evolution in more phenomenologically practical situations.

5.1 Lowest Order

Consider, in the center-of-mass system, the scattering of a heavy onium having momentum P on a heavy onium having momentum P'. We begin by treating the heavy onium state as simply a heavy quark-heavy antiquark state bound by Coulomb interactions. Then the square of the light-cone wavefunction for the state P can be described in terms of the transverse coordinates $\underline{x}_0$ and $\underline{x}_1$ of the heavy quark and heavy antiquark, respectively, along with $1-z_1$ and z_1 giving the (respective) longitudinal momentum fractions of the heavy quark and the heavy antiquark. Since the ground state wavefunction can only depend on $x_{01} = |\underline{x}_1 - \underline{x}_0|$, we may write $\Phi = \Phi(x_{01}, z_1)$ for the square of the wavefunction. Then, at lowest order, the cross section is given by the square of the one gluon exchange amplitude, shown in Fig. 6, and takes the form

$$\sigma = \int d^2x_{01} \int_0^1 dz_1 \Phi(x_{01}, z_1) \int d^2x'_{01} \int_0^1 dz'_1 \Phi(x'_{01}, z'_1) \sigma_{dipole} \tag{21}$$

with

$$\sigma_{dipole} = 2\pi\alpha^2 x_<^2 (1 + \ell n\ (x_>/x_<)) \tag{22}$$

the cross section for scattering a color dipole of size x_{01} on a color dipole of size x'_{01} at high energy. In Eq. (22), $x_< = min\{x_{01}, x'_{01}\}$ and $x_> = max\{x_{01}, x'_{01}\}$. The cross section in Eq. (21) is clearly proportional to $\alpha^2 R^2$ with R the radius of the onium.

In Coulomb gauge, the energy dependence of high-energy onium-onium scattering comes from the higher Fock space states of the onia, consisting of a heavy quark, a heavy antiquark, and some number of (virtual) transverse gluons. At the leading logarithmic level, one need only consider a single gluon exchange between the two onia in order to calculate the total onium-onium cross section.

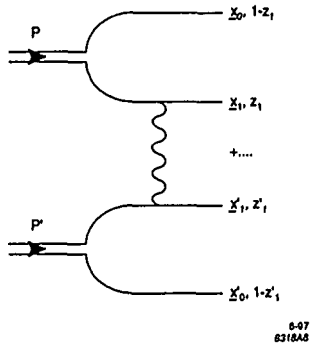


Figure 6.

5.2 One Soft Gluon in the Wavefunction in the Large-N_c Limit

In the leading logarithmic approximation, the gluons in the onium wavefunction carry a small fraction of the onium's momentum. Thus, in the one-gluon approximation, the gluon can be viewed as coming off either the heavy quark or heavy antiquark external leg as illustrated in the left-hand part of Fig. 7. In the large N_c limit, the gluon may be viewed as a quark-antiquark pair, as far as color factors are concerned. And since further soft gluon emission will only involve classical (eikonal) vertices, the gluon, in fact, acts exactly as a quark-antiquark pair at a definite transverse coordinate position. This is emphasized in the right-hand part of Fig. 7.

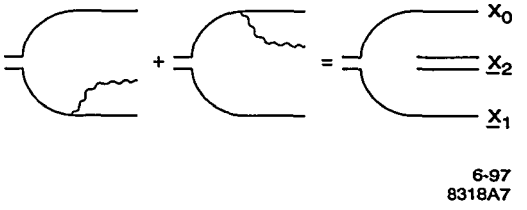


Figure 7.

5.3 Scattering in the Leading Logarithmic Approximation

In the large N_c limit, the n-gluon component of the onium wavefunction may be viewed as $n+1$ dipoles made of the (color connected) heavy quark-heavy antiquark and n "quark-antiquark pairs" corresponding to the n gluons. In an onium-onium scattering, one dipole in the right-moving onium interacts with one dipole in the left-moving onium with a cross section given by Eq. (22). Thus, we may express the total onium-onium cross section as

$$\sigma(Y) = \int \frac{d^2x d^2x'}{4\pi^2 x^2 x'^2} N(x, Y/2) N(x', Y/2) \sigma_{dipole}(x, x'), \tag{23}$$

where $N(x, Y/2)$ is number density of dipoles of transverse size $x = |\mathrm{x}|$ formed using gluons in a rapidity interval $Y/2$, where $Y = \ell n(s/M^2)$ with $s = p \cdot p'$ and with M the onium mass. Thus, in order to calculate the high-energy cross section, we need to know the dipole density in an onium state.

5.4 The BFKL Equation

In order to write an equation for N, it is convenient to first write

$$N(x, Y) = \int d^2x_{01} \int_0^1 dz_1 \Phi(x_{01}, z_1) n(x_{01}, x, Y), \tag{24}$$

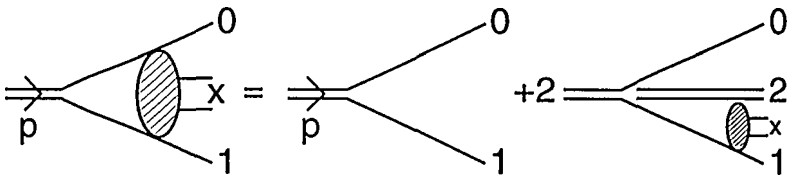
where $n(x_{01}, x, Y)$ has the simple interpretation of the number density of dipoles of size x in a rapidity interval Y starting with a (parent) dipole of size x_{01}. The creation of dipoles proceeds by one gluon emission which changes a single dipole into two dipoles as illustrated in Fig. 7.

The equation for n is given as

$$n(x_{01}, x, Y) = x\delta(x - x_{01}) exp\{-\frac{2\alpha N_c}{\pi} \ell n(\frac{x_{01}}{\rho}) Y\} +$$

$$+\frac{\alpha N_c}{\pi^2} \int_R \frac{x_{01}^2 d^2x_2}{x_{02}^2 x_{21}^2} \int_0^Y dy\, exp\{\frac{-2\alpha N_c}{\pi} \ell n\, (\frac{x_{01}}{\rho})(Y - y)\} n(x_{21}, x, y), \tag{25}$$

and is illustrated in Fig. 8. The gluon (x_2, y) is the hardest of the soft gluons in the wavefunction of the onium. The subscript R on the integral in Eq. (25) indicates that one is to integrate over the region $x_{02}, x_{21} \geq \rho$. The introduction of ρ serves to cut off ultraviolet divergences in the wavefunction. ρ appears correspondingly in the virtual corrections [the exponential factors in Eq. (25)] which are determined from probability conservation. As always in a BFKL description, only leading logarithms [terms of the type $(\alpha Y)^n$] are kept in Eq. (25), although transverse coordinate expressions are exact, up to powers of ρ which will be unimportant when the $\rho \to 0$ limit is taken for a physical quantity.



6-97
8318A8

Figure 8.

Taking a derivative with respect to Y on both sides of Eq. (25) gives

$$\frac{dn(x_{01}, x, Y)}{dY} = \frac{\alpha N_c}{\pi^2} \int_R d^2x_2 \{\frac{x_{01}^2}{x_{02}^2 x_{12}^2} - 2\pi\delta(\mathrm{x}_2 - \mathrm{x}_0) \ell n \frac{x_{01}}{\rho}\} n(x_{21}, x, Y). \tag{26}$$

The limit $\rho \to 0$ can be taken after performing the integration in Eq. (26). Equation (26) is the BFKL equation expressing the evolution of the number of gluons (dipoles) as one changes the available longitudinal momentum region which those gluons are allowed to occupy.

5.5 The Solution to the BFKL Equation

The solution to Eq. (26) is

$$n(x_{01}, x, Y) = \frac{x_{01}}{2x} \frac{e^{(\alpha_P - 1)Y}}{\sqrt{\frac{7}{2}\alpha\, N_c \zeta(3) Y}}\, exp\{\frac{-\pi \ell n^2(x_{01}/x)}{14\alpha\, N_c \zeta(3) Y}\} \tag{27}$$

with $\alpha_P - 1 = \frac{4\alpha N_c}{\pi}\ell n 2$. Using Eq. (27) in Eq. (23) and Eq. (24) gives

$$\sigma = \frac{16\pi R^2 \alpha^2 e^{(\alpha_P - 1)Y}}{\sqrt{\frac{7}{2}\alpha N_c \zeta(3) Y}} \tag{28}$$

with

$$R = 1/2 \int d^2 x_{01} \int_0^1 dz_1 x_{01} \Phi(x_{01} z_1) \tag{29}$$

the onium radius.

From Eq. (28), we see that σ becomes larger than the geometric cross section πR^2 when $Y \approx \frac{1}{\alpha_P - 1}\ell n\ 1/\alpha^2$ so it is at such rapidities that one expects strong (unitarity) corrections to the BFKL equation to become important.

5.6 The Physical Picture of BFKL Evolution

Earlier, we saw that DGLAP evolution corresponds to a growing number of gluons in a state as one looks to smaller and smaller transverse distances, and that this growth is especially strong when a large longitudinal phase space is available. In BFKL evolution, the focus is on evolution for a fixed transverse size as one increases the available longitudinal phase space. The picture is illustrated in Fig. 9 with the formula given in Eq. (27). Equation (27) shows that in addition to a growth in Y of the number of dipoles (gluons), there is also a diffusion of dipoles sizes away from the starting size, x_{01} in Eq. (27). In principle, this diffusion is slow enough, compared to the rate of growth of the number of gluons, that the picture of the growth of the number of gluons of a fixed size as shown in Fig. 9, a hot spot of gluons in the proton, is a reasonably good picture of BFKL evolution. However, there are circumstances where the diffusion inherent in BFKL evolution is very important and cannot be neglected [19].

5.7 Unitarity, Saturation, and High Field Strengths

With proper triggering on final-state characteristics, one should be able to discuss questions of unitarity, saturation, and high field strengths in the context of two hot spots colliding in a proton-proton collision. However, we prefer to keep the discussion simple and conceptual, so again, high-energy onium-onium scattering

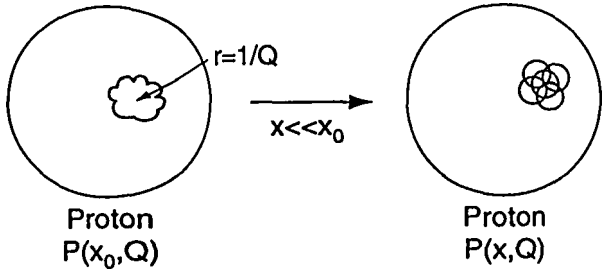


Figure 9.

will be our "theoretical laboratory" for these topics. In the center of mass, we may express, crudely, onium-onium scattering as

$$\sigma \approx [N(Y/2)]^2\, \sigma_{dipole}, \tag{30}$$

where we have simplified Eq. (23) by taking a typical dipole size in the integral appearing there. Again, crudely, $\sigma_{dipole} \approx \alpha^2 R^2$ so that σ is of size R^2, where unitarity corrections can be expected to become important, when Y is large enough so that $N(Y/2) \approx 1/\alpha$. As we have seen earlier, this corresponds to $Y \approx \frac{1}{\alpha_P - 1}\ell n\ 1/\alpha^2$. Thus, we expect the BFKL approximation to break down when the center-of-mass wavefunctions have on the order of $1/\alpha$ dipoles (gluons) spread over a rapidity interval $Y/2$. The number of dipoles (gluons) per unit rapidity, $\frac{dN(Y/2)}{d(Y/2)}$, is a constant when $N \approx 1/\alpha$ so that the field strength, $F_{\mu\nu}$, in the wavefunction is of order one for those gluons occupying the lowest unit of rapidity. (The field strengths coming from gluons in any other unit of rapidity in the wavefunction are even smaller.) Since $F_{\mu\nu}$ is not large, we expect unitarity corrections to be calculable perturbatively, and this is indeed the case. Including the dominant unitarity corrections in high-energy onium-onium scattering can be done, and numerical calculations are available [17,20,21]. Unitarity corrections in the center-of-mass system are just the multiple scattering corrections involving two or more dipoles.

Perturbation theory is expected to break down when $F_{\mu\nu}$ takes on values as large as $1/g$ for gluons occupying a unit of rapidity. This occurs, in the center-of-

mass frame, when $\frac{dN(Y/2)}{d(Y/2)} \approx 1/\alpha$ which corresponds to rapidity $Y = \frac{2}{\alpha_P - 1} \ell n\ 1/\alpha^2$, a rapidity twice that necessary for unitarity corrections to become important. At rapidities this large, the number of gluons in the wavefunctions becomes so large that our whole perturbative picture of the wavefunction breaks down and a new nonperturbative regime of QCD is reached. Unfortunately, one cannot expect to reach such a regime at Fermilab or HERA energies.

6 Phenomenology

6.1 The Soft Pomeron

There are clearly strong similarities between small-x physics and high-energy soft hadronic processes. Unfortunately, high-energy soft processes are very difficult to deal with in QCD. For example, $\sigma = \sigma_0(s/s_0)^\epsilon$, with $\epsilon \approx 0.08$, gives a good fit to many cross sections [22,23], including total photoabsorption as measured up through HERA energies. ϵ is a nonperturbative parameter which should be calculable in QCD. However, in the present Euclidean formulations of lattice QCD, one cannot give an algorithm for calculating ϵ, and in fact, it is likely that it is not possible to calculate ϵ in an Euclidean formulation of lattice QCD. So for the moment, it is difficult to make progress in soft hadronic physics, and we await a successful formulation of nonperturbative QCD where such extremely Minkowskian quantities, such as ϵ, can be calculated. A good candidate for such a formulation is discrete light-cone QCD.

6.2 $\nu W_2(x, Q^2)$, Quark and Gluon Distributions

For $Q^2 \geq 1.5\ GeV^2$, νW_2 rises rapidly with decreasing x with the rate of rise depending somewhat on the exact value of Q^2 (Ref. [24]). For $Q^2 \leq 0.6\ GeV^2$, νW_2 acts like a soft process with a moderate, $x^{-\epsilon}$, x-dependence which appears independent of Q^2. It will be interesting to have data in the $0.6 < Q^2 < 1.5$ region to see exactly how the transition from hard to soft physics comes about. Also, very precise data in the $1\ GeV^2 \leq Q^2 \leq 5\ GeV^2$ regime could give evidence for, or against, the necessity of resummation effects in a DGLAP description of deep inelastic scattering. This is clearly a phenomenology of pressing urgency at the moment.

On a more qualitative level, in the region $10\ GeV^2 \leq Q^2 \leq 20\ GeV^2$ and $x \approx 10^{-4}$, the number of quarks and antiquarks per unit of rapidity in the proton is about four while the number of gluons is likely between 20 and 30. These are rather extraordinary numbers when one recalls that a traditional gluon distribution $G(x) = \frac{3}{x}(1-x)^5$ used for intermediate values of x corresponds to three gluons per unit rapidity. It would be very interesting to have gluon densities in the lower Q^2 regime. It might be that gluon densities become large enough for saturation efffects [25] to become important in the $Q^2 \approx 1\ GeV^2$ regime.

6.3 Rapidity Gaps Bounded by Jets

We now turn to some specific processes of special interest in small-x physics. The first of these, rapidity gaps bounded by jets, may furnish a window to BFKL behavior. Such events have now been studied both at Fermilab [26,27] and at HERA [28]. In each case, one measures two jets having $k_\perp \geq Q$ with a rapidity gap between them. Except for the measured jets and the rapidity gap, the process is otherwise inclusive [29-31]. One might guess that such a cross section would take the form

$$\sigma_{2jet}^{gap} = x_1 q_1(x_1, Q^2) \hat{\sigma}(Y, Q^2) x_2 q_2(x_2, Q^2) \tag{31}$$

with x_1 and x_2 being the momentum fractions of the two jets and q_1 and q_2 being the quark and/or antiquark distributions from which the jets emerge. (For simplicity of discussion, we ignore gluons.) The process is illustrated in Fig. 10. Furthermore, one might suppose that

$$\hat{\sigma} \propto \frac{e^{2(\alpha_P - 1)Y}}{Y^3}, \tag{32}$$

thus furnishing a possibility of measuring the BFKL Pomeron.

However, the process is not inclusive enough to use the hard scattering formula (31). The problem is that requiring a rapidity gap destroys the delicate cancellation between real and virtual soft gluons, of which cancellation is key to a factorization such as expressed in Eq. (31). One knows how to write the cross section for the hard elastic quark-quark scattering $\hat{\sigma}$, but the probability that there are no accompanying soft interactions between the spectator quarks, which would fill in the gap, is not something which can be calculated perturbatively. What has

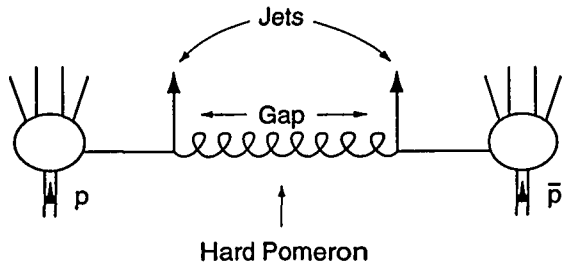


Fig. 10.

become traditional is to include a factor [32,33] $< S^2 >$ on the right-hand side of Eq. (31), interpreted as the survial probability of the gap, or equivalently, the probability of no soft spectator interactions.

Data from Fermilab show that about 1% of two-jet events have a gap of greater that two to three units of rapidity while at HERA that number is about 5%. This means that $< S^2 > \approx 0.1$ at Fermilab and $< S^2 > \approx 0.5$ at HERA. If $< S^2 >$ is not very energy dependent and this is likely, one can take ratios of gap events at $E = 1800\ GeV$ to those at $E = 630\ GeV$ now that Fermilab has data at two energies. Keeping x_1 and x_2 the same at the two energies, Eq. (31) leads to

$$\frac{\sigma_{2-jet}^{gap}(1800\ GeV)}{\sigma_{2-jet}^{gap}(630\ GeV)} = e^{4(\alpha_P-1)\ell n\ 3}\left[\frac{Y(630)}{Y(1800)}\right]^3 \frac{< S^2 >_{1800}}{< S^2 >_{630}}. \tag{33}$$

For example, if $Y(630) = 4$ then $Y(1800) \approx 6$ and

$$\frac{\sigma(1800)}{\sigma(630)} \approx \frac{8}{27}\frac{< S^2 >_{1800}}{< S^2 >_{630}} \cdot e^{4(\alpha_P-1)}, \tag{34}$$

or assuming that $< S^2 >$ does not increase with energy,

$$\frac{\sigma(1800)}{\sigma(630)} \leq \frac{8}{27}\, e^{4(\alpha_P-1)}. \tag{35}$$

If $\alpha_P - 1 = 1/2$, this ratio could be as large as 2. It will be interesting to see what happens when the data is analyzed.

6.4 Diffractive Vector Meson Production [34-37]

The process $\gamma(Q) + proton \to V + proton'$ with V a vector meson is illustrated in Fig. 11. We suppose that Q^2 is large, although for heavy vector mesons, this need not be the case in order to carry out an analysis similar to the one outlined here.

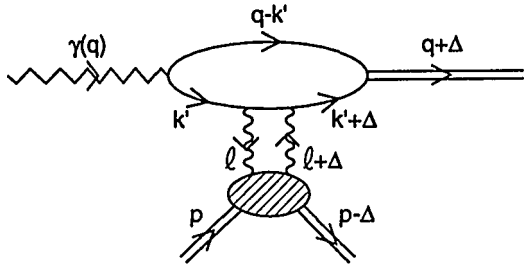


Fig. 11.

The amplitude is expected to be dominated by two-gluon exchange to the $\gamma - V$ system. We suppose that $t = \Delta^2$ is very small. In the rest system of the target proton, the process proceeds in three steps.

(i) Before reaching the target, $\gamma(Q)$ goes, virtually, into a quark-antiquark pair having lifetime

$$\tau_i = \frac{2qz(1-z)}{Q^2 z(1-z) + k_\perp^2 + m^2} \approx \frac{2q}{Q^2}, \tag{36}$$

where z is the fraction of the photon's momentum carried by the antiquark, $k_z = zq_z$. For example, for $Q^2 = 5\ GeV^2$ and $q = 100\ GeV, \tau_i = 8\ fm$.

(ii) The quark-antiquark pair scatters off the target. Since the $k_\perp^2$ integration is only cut off at Q^2, the quark-antiquark pair has $\Delta x_\perp \sim 1/Q$, meaning that the coupling of the gluons, lines ℓ and $\ell + \Delta$, occur with $\alpha(Q^2)$ strength. This justifies perturbation theory. In coupling to the small dipole moment of the quark-antiquark pair, one gets a factor of $\ell_\perp^2$ from lines ℓ and $\ell + \Delta$. This factor of $\ell_\perp^2$ gives a logarithmic $\ell_\perp^2-$ integral, again cut off at Q^2. The $\ell_\perp^2$-integral is exactly the same as appears in defining the gluon distribution.

(iii) The vector meson is formed from the quark-antiquark pair at a time

$$\tau_f = \frac{2qz(1-z)}{k_\perp^2 + m^2}, \tag{37}$$

with m the quark mass. One finds, for longitudinally polarized virtual photons,

$$\left.\frac{d\sigma_{\gamma^*+N\to V+N'}}{dt}\right|_{t=0} = \frac{12\pi^3}{\alpha_{em}Q^6N_c^2}\Gamma_{V\to e^+e^-}m_V\alpha^2(Q^2)\eta_V^2|xG(x,Q^2)+i\frac{\pi}{c}\frac{d}{dx}xG|^2 \tag{38}$$

with

$$x = \frac{Q^2+m_V^2}{s} \tag{39}$$

and

$$\eta_V = \frac{1}{2}\frac{\int_0^1 \frac{dz}{z(1-z)}\Phi_V(z)}{\int_0^1 dz\Phi_V(z)} \tag{40}$$

given in terms of the exclusive wavefunction Φ_V of the vector meson.

Equation (38) has been derived in a double-leading logarithmic approximation. Further refinements, necessary to confront data, can be found in Ref. 36. At the moment, perhaps the main use of Eq. (41) is to get an independent check on the gluon distribution which occurs quadratically in the diffractive cross section. Data at HERA [24] have already found the extremely rapid rise of the diffractive cross section with decreasing x expected from a gluon distribution now known to grow rapidly at small x.

6.5 The Search for the BFKL Pomeron

6.5.1 Deep Inelastic Scattering

Precise studies of νW_2 may give evidence for resummation effects [13-16]. This would be an indirect confirmation of BFKL dynamics, but one cannot directly measure $\alpha_P - 1$ from νW_2 data alone. Final state properties, such as transverse energy flow, may also prove useful in deciding how important BFKL dynamics is in deep inelastic scattering, but so far these analyses have not proved very definitive.

6.5.2 Gaps at Fermilab and HERA

I think the best hope here is a comparison of gaps bounded by jets in the two Fermilab energies as given by Eq. (33). The difficulty is that the Y^{-3} prefactors to BFKL behavior suppress the 1800 GeV to 630 GeV ratio so that this measurement will only prove successful if $\alpha_P - 1$ is near 1/2 and if the survival probability is not very energy dependent. However, a ratio of two or more in the gap cross section comparing 1800 GeV data to 630 GeV data would be a definitive sign of BFKL dynamics, and one could try to extract $\alpha_P - 1$, or at least bounds on that quantity.

6.5.3 Large-t Vector Meson Diffractive Photoproduction [38]

Earlier, we have seen that t=0 diffractive electroproduction of vector mesons gives a measurement of the gluon distribution of the proton, at least in the leading double logarithmic approximation. If one takes $-t$ large, say $-t \geq 3\ GeV^2$ or so, the diffractive cross section has the asymptotic form

$$\frac{d\sigma}{dt} \propto \frac{(s/(-t))^{2(\alpha_P-1)}}{(\ell n\ (s/(-t))^3)} \tag{41}$$

and could furnish a determination of $\alpha_P - 1$. The most favorable measurement is to allow the proton to break up so that a quark jet takes the recoil transverse momentum of the vector meson. In some respects, this process is like the gap events bounded by jets which were discussed earlier, now with one of the jets replaced by a vector meson. There is no survival probability factor because the incoming photon is pointlike and has no spectators to interact with the target proton. However, the cross sections here are small, and apparently, the asymptotic behavior sets in rather slowly. Nevertheless, it will be interesting to see what emerges from the HERA data.

6.5.4 Associated Jets in Proton-Antiproton and Electron-Proton Collisions

One straightforward way to measure the BFKL intercept, $\alpha_P - 1$, is to study the inclusive two-jet cross section at Fermilab [39,40] or the associated one-jet cross section at HERA [41-43]. Let me illustrate the idea in terms of the Fermilab process. In a proton-antiproton collision, one measures two jets, inclusively, having

momentum fractions x_1 and x_2 and transverse momenta $k_{1\perp}, k_{2\perp} \geq Q$ with Q a fixed (perturbative) scale. The process is illustrated in Fig. 12.

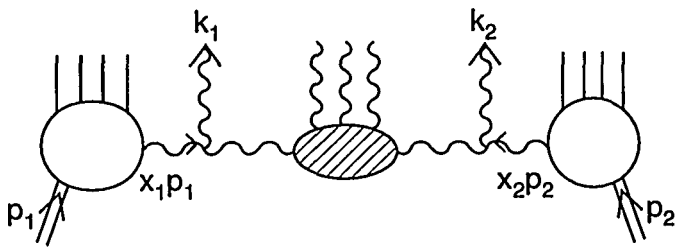


Figure 12.

The two-jet cross section is

$$\sigma_{2-jet} = x_1[G(x_1,Q^2) + \frac{4}{9}(q+\bar{q})(x_1,Q^2)]x_2[G(x_2,Q^2) + \frac{4}{9}(q+\bar{q})(x_2,Q^2)]$$

$$\cdot \left(\frac{\alpha N_c}{\pi}\right)^2 \frac{\pi^3}{2Q^2} \frac{e^{(\alpha_P - 1)Y}}{\sqrt{\frac{7}{2}\alpha N_c \zeta(3) Y}}, \qquad (42)$$

where Y is the relative rapidity of the two measured jets. If one takes the ratio of σ_{2-jet}, keeping x_1, x_2, and Q^2 fixed, at 1800 GeV and 630 GeV, the result is

$$\frac{\sigma_{2-jet}(1800)}{\sigma_{2-jet}(630)} = e^{2(\alpha_P - 1)\ell n 3} \sqrt{\frac{Y(630)}{Y(1800)}} \qquad (43)$$

so long as $Y(630)$ is large enough to use the asymptotic form (42). For example, for $Y(630) = 4$, one gets $Y(1800) = 6$, and the ratio in Eq. (43) is about 2 for $(\alpha_P - 1) = 1/2$. While Eq. (42) is only a leading logarithmic formula, a significant growth in the two-jet cross section with energy would be a significant beginning to a BFKL phenomenology. There should be a Fermilab result on this soon.

The corresponding measurement at HERA, a forward inclusive jet measurement, has been vigorously pursued by the H1 Collaboration [44]. The preliminary results are strongly encouraging and seem to agree reasonably with the BFKL prediction [44,45]. More definitive comparisons between theory and experiment can be expected soon and are eagerly awaited.

7 What Is Needed

From the experimental side, the most urgent issue is a measurement of the BFKL Pomeron, that is, a measurement of $\alpha_P - 1$. Also, extremely precise data in the low-x and low to intermediate Q^2-region for νW_2 will be very useful. We can expect the level of phenomenology to improve to the point of deciding how well second order DGLAP fits really work and to what level resummation effects are important. Also, a good direct measurement of $xG(x,Q^2)$ either from two forward jet production or from heavy quark production is important to test how well second order DGLAP evolution works and to have confidence in the values of xG.

From the theory side, the α^2 correction to $\alpha_P - 1$ is very important in order to do BFKL phenomenology with a good level of confidence. We desperately need a better understanding of the $Q^2 \approx 1$ regime, where perturbative and nonperturbative physics merge. Finally, from a purely theory point of view, clarification and a deeper understanding of unitarity corrections, saturation effects and their relationship to high field strength QCD are exciting areas where further progress should be possible.

References

[1] Y. L. Dokshitzer, Sov. Phys. JETP **73**, 1216 (1977).

[2] V. N. Gribov and L. N. Lipatov, Sov. J. Nucl. Phys. **15**, 78 (1972).

[3] G. Altarelli and G. Parisi, Nucl. Phys. B **126**, 298 (1977).

[4] E. A. Kuraev, L. N. Lipatov, and V. S. Fadin, Sov. Phys. JETP **45**, 199 (1978).

[5] Y. Y. Balitsky and L. N. Lipatov, Sov. J. Nucl. Phys. **28**, 22 (1978).

[6] L. N. Lipatov, "Small-x physics in perturbative QCD," hep-ph/9610276 (1996).

[7] A. D. Martin, R. G. Roberts, and W. J. Stirling, Phys. Rev. D **50**, 6734 (1994); Phys. Lett B **387**, 419 (1996).

[8] CTEQ Collaboration: J. Botts *et al.*, Phys. Lett. B **304**, 159 (1993); H. L. Lai *et al.*, Phys. Rev. D **51**, 4763 (1995); Phys. Rev. D **55**, 1280 (1997).

[9] M. Glück, E. Reya, and A. Vogt, Z. Phys. C **67**, 433 (1995).

[10] T. Jaroszewicz, Phys. Lett. B **116**, 291 (1982).

[11] S. Catani, M. Ciafaloni, and F. Hautmann, Nucl. Phys. B **366**, 135 (1991).

[12] S. Catani and F. Hautmann, Nucl. Phys. B **427**, 475 (1994).

[13] R. K. Ellis, F. Hautmann, and B. R. Webber, Phys. Lett. B **348**, 582 (1995).

[14] R. D. Ball and S. Forte, Phys. Lett. B **351**, 313 (1995); Phys. Lett. B **351**, 365 (1995).

[15] J. R. Forshaw, R. G. Roberts, and R. S. Thorne, Phys. Lett. B **356**, 79 (1995).

[16] R. S. Thorne, Phys. Lett. B **392**, 463 (1997).

[17] A. H. Mueller, Nucl. Phys. B **415**, 373 (1994); Nucl. Phys. B **437**, 107 (1995).

[18] A. H. Mueller and B. Patel, Nucl. Phys. B **425**, 471 (1994).

[19] J. Bartels and H. Lotter, Phys. Lett. B **309**, 400 (1993).

[20] G. Salam, Nucl. Phys. B **461**, 512 (1996).

[21] A. H. Mueller and G. Salam, Nucl. Phys. B **475**, 293 (1996).

[22] K. Goulianos, Phys. Reports **101**, 169 (1983).

[23] A. Donnachie and P. V. Landshoff, Nucl. Phys. B **244**, 322 (1984); B **267**, 690 (1985).

[24] See, for example, the lectures of W. Smith at this school.

[25] L. V. Gribov, E. M. Levin, and M. G. Ryskin, Phys. Reports **100**, 1 (1983).

[26] DØ Collaboration, S. Abachi *et al.*, Phys. Rev. Lett. **72**, 2332 (1994).

[27] CDF Collaboration, F. Abe *et al.*, Phys. Rev. Lett. **74**, 855 (1995).

[28] ZEUS Collaboration, M. Derrick *et al.*, Phys. Lett. B **369**, 55 (1996).

[29] J. D. Bjorken, Int. J. Mod. Phys. A **7**, 4189 (1992).

[30] A. H. Mueller and W.-K. Tang, Phys. Lett. B **284**, 123 (1992).

[31] V. Del Duca and W.-K. Tang, Phys. Lett. B **312**, 225 (1993).

[32] J. D. Bjorken, Phys. Rev. D **47**, 101 (1992).

[33] E. Gotsman, E. M. Levin, and U. Maor, Phys. Lett. B **309**, 199 (1993).

[34] M. G. Ryskin, Z. Phys. C **57**, 89 (1993).

[35] S. J. Brodsky, L. Frankfurt, J. F. Gunion, A. H. Mueller, and M. Strikman, Phys. Rev. D **50**, 3134 (1994).

[36] L. Frankfurt, W. Koepf, and M. Strikman, Phys. Rev. D **54**, 3194 (1996).

[37] A. D. Martin, M. G. Ryskin, and T. Teubner, Phys. Rev. D **55**, 4329 (1997).

[38] J. R. Forshaw and M. Ryskin, Z. Phys. C **68**, 137 (1995).

[39] A. H. Mueller and H. Navelet, Nucl. Phys. B **282**, 727 (1987).

[40] V. Del Duca and C. R. Schmidt, Phys. Rev. D **49**, 4510 (1994); D **51**, 2150 (1995).

[41] W.-K. Tang, Phys. Lett. B **278**, 363 (1992).

[42] J. Bartels, A. DeRoeck, and M. Loewe, Z. Phys. C **54**, 635 (1992).

[43] J. Kwiecinski, A. Martin, and P. J. Sutton, Phys. Rev. D **461**, 921 (1992).

[44] H1 Collaboration, paper pa 03-049 submitted to the *28th International Conference on High Energy Physics*, Warsaw, Poland, July 1996.

[45] J. Bartels *et al.*, Phys. Lett B **384**, 300 (1996).

QCD IN HEAVY QUARK PRODUCTION AND DECAY

Jim Wiss*
University of Illinois
Urbana, IL 61801

ABSTRACT

I discuss how QCD is used to understand the physics of heavy quark production and decay dynamics. My discussion of production dynamics primarily concentrates on charm photoproduction data which is compared to perturbative QCD calculations which incorporate fragmentation effects. We begin our discussion of heavy quark decay by reviewing data on charm and beauty lifetimes. Present data on fully leptonic and semileptonic charm decay is then reviewed. Measurements of the hadronic weak current form factors are compared to the nonperturbative QCD-based predictions of Lattice Gauge Theories. We next discuss polarization phenomena present in charmed baryon decay. Heavy Quark Effective Theory predicts that the daughter baryon will recoil from the charmed parent with nearly 100% left-handed polarization, which is in excellent agreement with present data. We conclude by discussing nonleptonic charm decay which are traditionally analyzed in a factorization framework applicable to two-body and quasi-two-body nonleptonic decays. This discussion emphasizes the important role of final state interactions in influencing both the observed decay width of various two-body final states as well as modifying the interference between interfering resonance channels which contribute to specific multibody decays.

*Supported by DOE Contract DE-FG0201ER40677.

© 1996 by Jim Wiss.

1 Introduction

A vast amount of important data on heavy quark production and decay exists for both the beauty and charm sector—far more than I could possibly cover in two lectures. For this reason, most of my talk will cover the production of charm in fixed target experiments with an emphasis on my own experiment—E687.*

Charmed mesons were discovered by the Mark I Collaboration which studied the e^+e^- annihilation process at SLAC about 21 years ago.[2] In the intervening years, a large number of collider as well as fixed-target experiments have heavily mined the field of heavy quark physics. The discovery paper by the Mark I group reported on the observation of $\approx$ 230 fully reconstructed decays of the D^o into the $K^{\mp}\pi^{\pm}$ and $K^{\mp}\pi^{\pm}\pi^{+}\pi^{-}$ final state. Recent experiments are capable of amassing clean, fully reconstructed charm data decays which are in excess of 100,000 events. Millions of fully reconstructed events are anticipated for several experiments presently taking data.

1.1 Charm and QCD

Charm provides a rich QCD phenomenology in both the perturbative and nonperturbative regimes. Studies of production dynamics test leading order (LO) and next-to-leading order (NLO) perturbative QCD. Charm lifetime measurements test models based on $1/M_Q$ QCD expansions. Heavy Quark Effective Theory (HQET) predicts a large degree of daughter baryon polarization in both semileptonic and two-body nonleptonic decay. Semileptonic form factors test nonperturbative QCD methods such as Lattice Gauge Theories (LGT). Finally, exclusive hadronic decay measurements test factorization models based on QCD renormalization group methods. Exclusive charm hadronic decays underscore the importance of final state interactions which should be important in unravelling the pattern of CP violations in the b sector.

While discussing the physics contained in the above topics and illustrating it with real data, I would like to give you some feeling on how measurements are actually made. You will probably find that these lectures tilt too much in the direction of fixed-target experiments. Perhaps they serve as a sort of swan song since the future of fixed-target charm experiments in the United States is very short.

*A general description of E687 can be found in Ref. 1.

1.2 Charm Mesons

Figure 1 is a crude sketch of the spectrum and properties of the low-lying D (pseudoscalar) and D^* (vector) mesons which consist of a charm quark and an up, down, or strange antiquark. There are a large number of baryon and higher excited mesons and baryons as well which are not shown. Several of the most

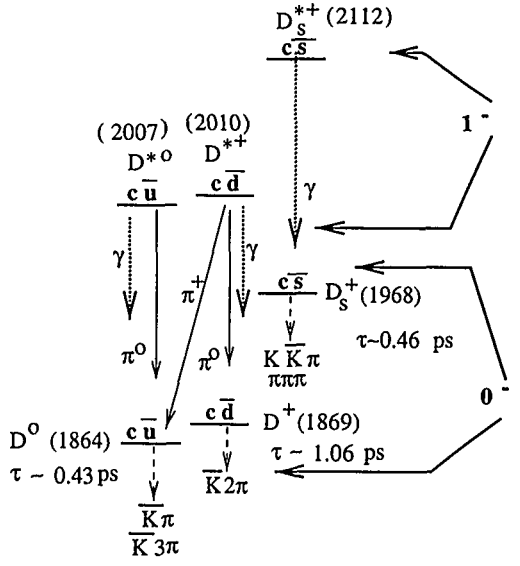


Fig. 1. Sketch of the spectrum of low lying charm mesons. The D^o amd D^+ mesons form a nearly degenerate strong isodoublet. The D_s^+ is shifted upwards by roughly 100 MeV. This mass splitting pattern is repeated for the D^*'s. Weak decays are shown by dashed arrows. Some strong and electromagnetic de-excitations of the D^* system into the ground state D system are shown by solid and dashed arrows. The approximate lifetimes of the ground state D system are indicated on the figure.

experimentally useful weak decay modes are shown in the figure. These are CKM-allowed decays where the charm quark is transformed to a strange quark resulting in a single kaon final state for the D^o and D^+, and a double kaon final state for the D_s^+. The D mesons have lifetimes ranging from about 1/2 to 1 psec. In a fixed-target experiment, a D^+ might typically be produced with a typical lab momenta of 100 GeV and will travel several centimeters before decaying. A high-quality vertex detector, such as a silicon microstrip detector, can readily measure a several centimeter decay path and thus cleanly tag a charm decay through its short but finite lifetime.

Perhaps the second best way of tagging charm particles is through the decay $D^{*+} \to \pi^+ D^o$ where the D^o decays into an easily reconstructible, all-charged decay mode such as the $K^{\mp}\pi^{\pm}$ final state. Owing to the small energy release in the decay $D^{*+} \to \underline{\pi}^+ D^o$, the soft (underlined) pion will carry only a small fraction of the lab momentum of the D and therefore can be very well-measured by a magnetic spectrometer. Most of the experimental smearing in reconstructing the D^{*+} mass is due to the D^o reconstruction which cancels in the mass difference $\Delta M \equiv M(D^o\pi^+) - M(D^o)$. This cancellation often results in a mass difference which is about ten times better resolved than the mass of the D^{*o}. By cutting on both $M(D^o)$ and ΔM, one can often get charm signals nearly as clean as those obtainable using lifetime tagging but without the technological inconvenience of having to build an expensive vertex tagging system. One can even extend the ΔM technique to tag semileptonic final states with a missing neutrino. Most of the data discussed in these lectures use either lifetime tagging or the $D^* \to D$ tagging trick to isolate and study charm.

2 The Physics of Charm Photoproduction

Charm photoproduction provides several nice illustrations of the successes and complications of applying perturbative QCD to production dynamics. We will begin on the most inclusive level by considering the center-of-mass energy dependence of the photoproduction cross section for charmed quarks. In order to delve deeper into the photoproduction process and study, *e.g.*, the P_t and X_f dependence for specific charm mesons, one must understand the hadronization process which describes the soft processes by which charmed quarks appear as charmed mesons and baryons. Studies of the kinematic dependence of photo- and hadroproduced charm-$\overline{\text{charm}}$ asymmetries provide surprisingly sensitive probes of QCD-inspired models of charm hadronization.

2.1 The Charm Quark Photoproduction Cross Section

At lowest order, and at energies significantly above charm threshold, the photoproduction of charmed quarks thought to be dominated by the photon-gluon fusion process is illustrated in lowest order by Fig. 2. The photon-gluon fusion

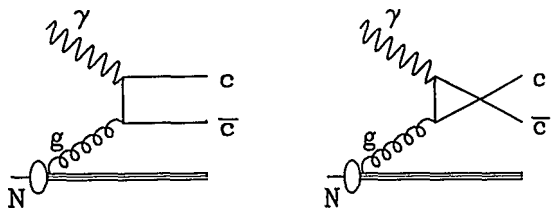


Fig. 2. Illustration of the lowest order contribution to the photon gluon fusion process. A gluon constituent of the nucleon interacts with a real photon to produce a $c\bar{c}$ pair. These graphs are both $\mathcal{O}(\alpha_{em}\alpha_s)$.

process is analogous to the pair production process $\gamma\mathcal{N} \to e^+e^-\,\mathcal{N}$, where a projectile photon interacts with a virtual photon from the nucleus to form an e^+e^- pair. Charm hadroproduction is thought to occur by a very similar process where a gluon from the projectile fuses with a gluon from target to form a $c\bar{c}$ pair.

The charm quark photoproduced cross section will depend linearly on the gluon density within the nucleon as well as the partonic cross section evaluated at the squared energy in the photon-gluon rest frame:

$$\sigma(\gamma p \to c\bar{c}) = \int_{4m_c^2/s}^{1} dx_g\; g(x_g, \mu^2)\;\; \hat{\sigma}(s\; x_g) \;\;,\;\; \hat{s} = s\; x_g. \qquad (1)$$

The variable of integration, x_g, represents the fraction of the nucleon momentum carried by the incident gluon. The lower limit of integration is due to the fact that $\hat{s} \equiv s\; x_g$; the squared center-of-mass energy in the photon-gluon rest frame must exceed $(2m_c)^2$. The lowest order PGF cross section will grow slowly with increasing $\hat{s}$ due to the contributions of increasingly softer (lower x_f) gluons.

At next-to-leading order (NLO), the graphs of Fig. 2 are joined by the $\mathcal{O}(\alpha_{em}\;\alpha_s^2)$ contributions which were recently calculated by Frixione, Mangano, Nason, and Ridolfi[3] (FMNR). The NLO graphs (Fig. 3) include contributions with extra

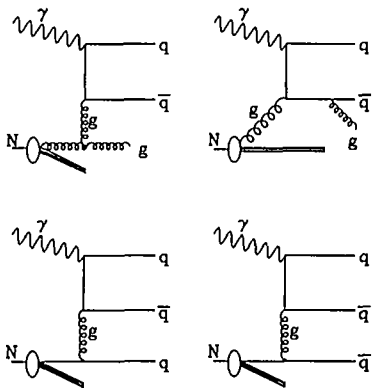


Fig. 3. NLO contributions to photon-gluon fusion which produce an additional gluon or quark in the final state.

quarks or gluons in the final state. Figure 4 compares the experimentally measured charm quark cross section to the FMNR predictions for several choices of renormalization scales, and gluon momentum distributions. The data are a reasonably good match to these predictions over a large kinematic range covering both fixed-target photoproduction experiments as well as the very recent data[4] on virtual photoproduction* of charm from HERA. The threshold condition $sx_g > 4\,m_c^2$ implies that the HERA data probes gluon density at fairly low x_g ($x_g > 1.6 \times 10^{-4}$) while fixed-target experiments typically probe in the more moderate x_g range ($x_g > 0.04$). Although the HERA charm event samples are fairly modest,† they carry an enormous kinematic lever arm which can be used to ultimately constrain parameters in the NLO description.

An apparent advantage of testing the QCD photoproduction model through the measurement of the $c\bar{c}$ cross-section energy dependence is that the theoretical cross section does not depend explicitly on a hadronization model, since ultimately the photoproduced quarks must somehow appear as charmed particles. Although some very nice models for hadronization exist (which we will discuss in Sec. 2.4),

*HERA defines the virtual photoproduction kinematic regime as $Q^2 < 4\ GeV^2$.

†For example, the ZEUS charm cross sections were based on 48 reconstructed $D^{*+} \to D^0\pi^+ \to (K^-\pi^+)\pi^+$ events.

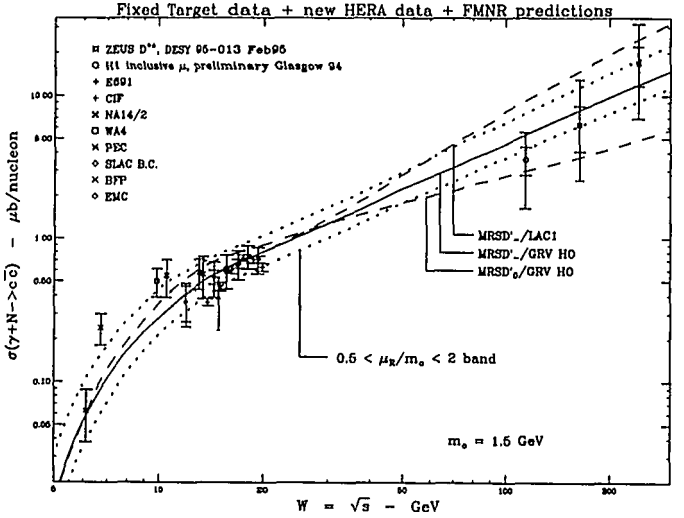


Fig. 4. Measured charm quark photoproduction cross sections compared to the FMNR NLO predictions for various gluon distribution parameterizations and renormalization scales.

they are phenomenological in the sense that although based on a general QCD-inspired framework, they parameterize many soft processes using inputs from experimental data.

Although hadronization assumptions may not enter directly into the predictions, they are required to experimentally measure the $c\bar{c}$ cross section. An experimenter will measure the yield of several different charm particles over a certain kinematic range where the experiment has a reasonably large, momentum-dependent reconstruction efficiency. To get a total $c\bar{c}$ cross section from such data, the experimenter must rely on a fragmentation model to know what fraction of the total charm cross section hadronizes into the final states being reconstructed. In addition, the hadronization model can affect the acceptance by controlling the fraction of charm particles with, *e.g.*, momenta outside of kinematic ranges of reasonable acceptance, or changing the overall reconstruction efficiency by affecting the multiplicity of particles which accompany the charm particle of interest.‡

‡This is an especially important effect in photoproduction where charm particles are tagged through the separation between a downstream (secondary) vertex containing the charm particle decay products and an upstream (primary) vertex which contains many of particles created through the hadronization process.

2.2 Nonperturbative Effects

In order to probe more deeply into charm photoproduction dynamics, one needs to consider the myriad of nonperturbative, soft-physics effects illustrated in Fig. 5. Fragmentation effects can change the direction of the charmed mesons relative to

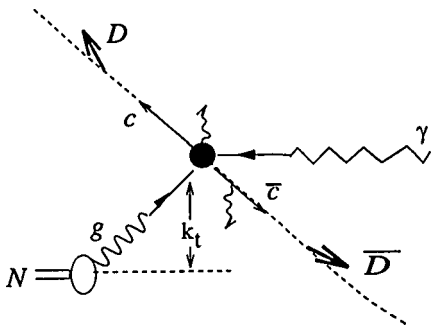


Figure 5: A cartoon of photoproduction of charm in the real world which illustrates several nonperturbative effects. The incident gluon can be thought to carry a small momentum component transverse to the incident nucleon called k_t. Soft gluon emission can accompany the charmed quark as it dresses, creating additional sources of relative $P_\perp$. A significant amount of quark energy is lost to the emerging D's while they hadronize.

the charmed quarks as well as significantly degrade their energy. A convenient variable to describe the energy fraction is called X_F for "Feynman X" which gives the fraction of available longitudinal momentum in the overall center of mass carried by an object divided by the maximum possible longitudinal momentum possible in that frame or:

$$X_F = \frac{2P_\parallel}{\sqrt{s}}. \qquad (2)$$

In a fixed-target experiment, X_F is approximately the fraction of the beam energy which appears in the charmed object.

Figure 6 compares the X_F distribution of charmed quarks and charmed mesons according to the JETSET-PYTHIA[6] string fragmentation model. Figure 6 shows that although each member of the $c\bar{c}$ pair carries an average of half of the incident beam energy, after fragmentation each charmed particle carries only about a quarter of the incident beam energy.

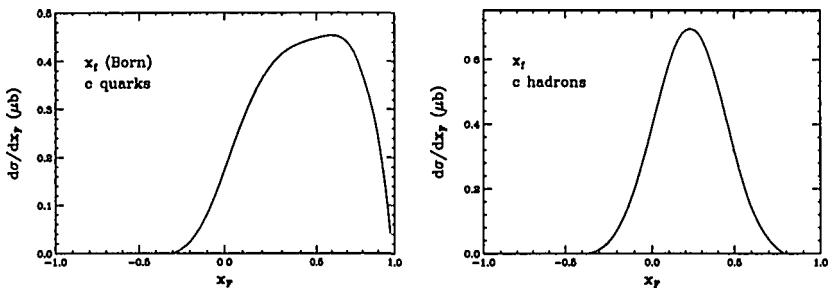


Figure 6: Comparison of the X_F distribution of charmed quarks (left) and charmed mesons (right) in LO photon-gluon fusion in the LO JETSET-PYTHIA model.

Figure 7 illustrates the importance of fragmentation effects by comparing the observed P_t^2 for photoproduced D^+ to the NLO FMNR predictions for charmed quarks (without fragmentation). The P_t^2 distribution of the data tracks fairly well with the PYTHIA MC which embeds LO PGF with LUND string fragmentation. The data clearly does not match the high end tail of the FMNR predictions for bare, charmed quarks where hard gluon emission is included in the NLO description. It is possible to match the P_t^2 spectrum of the data as shown in Fig. 8 by supplementing the NLO calculations with fragmentation effects such as intrinsic gluon k_t and momentum loss described by Peterson[5] fragmentation.

2.3 Correlations in Photoproduced $D\overline{D}$ Pairs

It is possible to fully reconstruct both members of a photoproduced $D\overline{D}$ pair in order to more fully probe photoproduction dynamics. As Fig. 9 shows, there are two ways of doing this. One can fully reconstruct both particles by detecting all of the decay products of both decays. Of course, one will necessarily pay a big price in statistics in acceptance and branching ratios to acquire a fully reconstructed double-D signal. Alternatively, one can kinematically tag the soft (underlined) pion from the decay $D^{*+} \to \underline{\pi}^+ D^o$ by exploiting charge and kinematic correla-

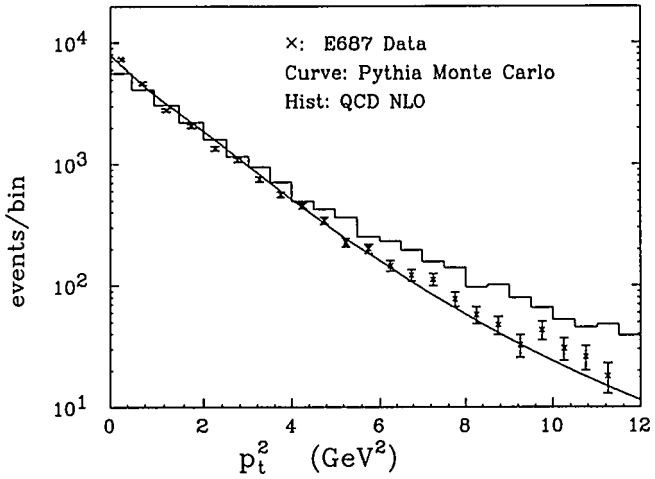


Figure 7: Overlay of the P_t^2 distribution for reconstructed D^+ mesons collected by E687 (with error bars) with the FMNR NLO predictions (histogram) and the PYTHIA Monte Carlo.

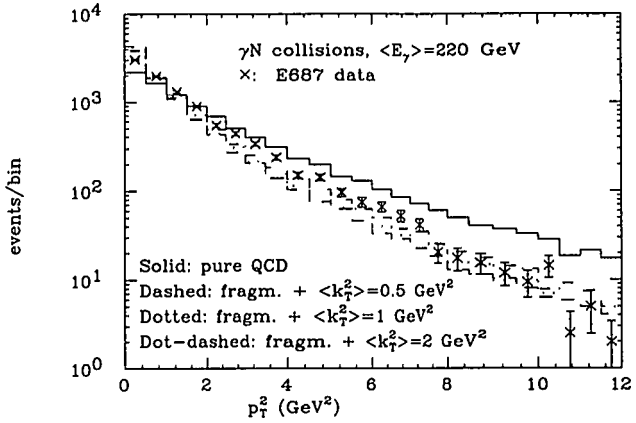


Figure 8: NLO calculations for various k_t and fragmentation options compared to E687 D^+ data. The Peterson fragmentation recipe is used which softens the momentum of the D^+ in the photon-gluon rest frame by a factor Z which is drawn from a QCD-inspired distribution. Fragmentation tends to soften the P_t^2 spectrum while k_t hardens this spectrum.

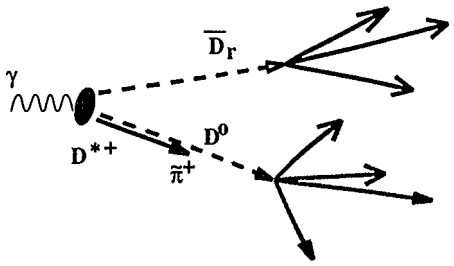


Figure 9: Two ways of studying photoproduced $D\overline{D}$ pairs. One can fully reconstruct both charmed particles. Alternatively, one can use a partially reconstructed double-D sample obtained by identifying the soft pion from $D^{*+} \to D^o\pi^+$ decay through the use of kinematic and charge correlation tagging.

tions between the pion and a fully reconstructed recoil $\overline{D_r}$. Because of the small energy release in $D^{*+} \to D^o\pi^+$, the soft pion, D^o, and D^{*+} all have approximately the same laboratory velocity. This allows one to estimate the momentum of a D^{*+} from just the soft pion by multiplying its momentum by the D^*/π mass ratio.[§] The charge of the soft pion is correlated with the charm of the fully reconstructed, recoil D state, and the scaled pion momentum should approximately balance P_t with the recoil $\overline{D_r}$. We use the P_t balance variable $\Delta_t^2 = |\, 13.8\, \vec{P}_t(\pi^+) + \vec{P}_t(\overline{D_r})\,|^2$. Figure 10 shows the signals for the fully reconstructed and partially reconstructed $D\overline{D}$ samples[7] which start with a baseline sample of $\approx 45,000$ inclusive D's reconstructed in the $K^{\mp}\pi^{\pm}$, $K^{\mp}\pi^{\pm}\pi^{\pm}$, and $K^{\mp}\pi^{\pm}\pi^{+}\pi^{-}$ final states.

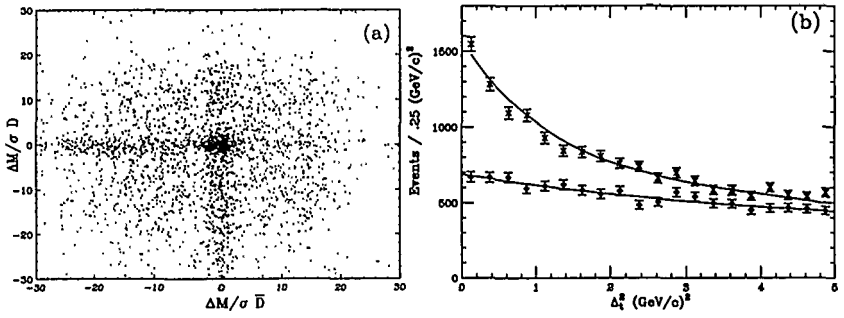


Fig. 10. (a) Scatter plot of the normalized mass of detached D candidates vs the normalized mass of the recoil $\overline{D}$ candidate. The normalized mass is the difference between the reconstructed and known D mass divided by the calculated event-by-event resolution. The accumulation near the origin consists of $\approx$ 320 fully reconstructed $D\overline{D}$ pairs. (b) Distribution of the P_t balance variable Δ_t^2 for right-sign and wrong-sign decay pion candidates. The upper curve is the form expected by fitting the net P_t^2 of fully reconstructed $D\overline{D}$ candidates and smearing slightly for errors due to reconstructing the P_t of the parent D^{*+} by scaling the P_t of the decay π^+. The right-sign excess below $\Delta_t^2 = 4\ GeV^2$ consists of $\approx$ 4530 events.

We have explored the kinematical correlations of the $D\overline{D}$ pair using several longitudinal and transverse variables. The acoplanarity angle, $\Delta\phi$, which is illustrated by Fig. 11, is used by many experimental groups since most experiments have excellent acceptance and resolution in this variable. A related variable is the net transverse momentum of the observed $D\overline{D}$ pair or $P_t^2(D\overline{D}) = |\vec{P}_t(D) + \vec{P}_t(\overline{D})|^2$.

[§]To take into account the very slight soft pion kinetic energy in the D^* rest frame, we actually use a scaling factor of 13.8 which is slightly smaller than the D^{*+}/π^+ mass ratio.

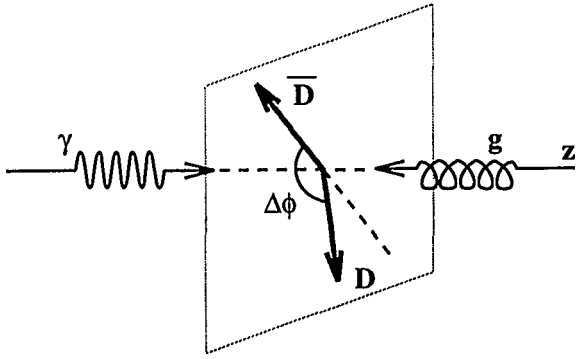


Fig. 11. The acoplanarity angle $\Delta\phi$ is the angle between the D and $\overline{D}$ in a plane transverse to the collision axis. If k_t or final-state gluon emission were negligible, the $\Delta\phi$ distribution would peak sharply at π radians.

A good longitudinal correlation variable is provided by rapidity difference $\Delta Y = Y(D) - Y(\overline{D})$. The rapidity or $Y = \frac{1}{2}\ln\left(\left(E + P_{\|}\right) / \left(E - P_{\|}\right)\right)$ approaches the longitudinal velocity in the nonrelativistic limit, but with the added virtue that a rapidity difference is relativistically invariant. Finally, the invariant mass of the $D\overline{D}$ pair measures transverse as well as longitudinal kinematic correlations.

Figure 12 compares the $D\overline{D}$ kinematic correlations observed in E687 data to the predictions of the JETSET-PYTHIA Monte Carlo[6] run with default parameters. There is good agreement between the ΔY and $M(D\overline{D})$ longitudinal correlation variables observed in the data to those predicted by the default JETSET-PYTHIA Monte Carlo. This longitudinal correlation data along with the P_t distribution for inclusive photoproduced D^+'s shown in Fig. 7, and the asymmetry data presented in Sec. 2.4, underscores this LO Monte Carlo's ability to successfully model the important soft physics effects of fragmentation. However, the PYTHIA Monte Carlo gives far too much peaking of $\Delta\phi$ distribution near π and the $P_t^2(D\overline{D})$ distribution near zero. Because the $\Delta\phi$ and $P_t^2(D\overline{D})$ distributions should be sensitive to hard gluon emission, it would be surprising if PYTHIA got these transverse correlations right since it does not incorporate the hard gluon emission processes[¶] at NLO illustrated in Fig. 3.

[¶]JETSET does include bremsstrahlung-like, soft gluon emission in its parton shower fragmentation model.

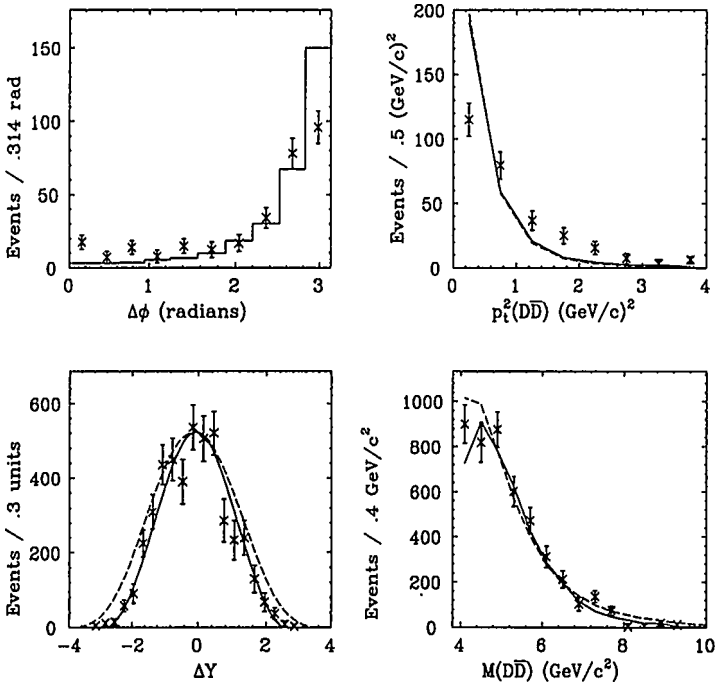


Fig. 12. $D\overline{D}$ kinematic correlations observed in E687 data overplotted with the predictions of the default PYTHIA model. We use the fully reconstructed $D\overline{D}$ sample for the upper row of transverse correlations, and (because of its larger kinematic acceptance domain) the partially reconstructed sample for the lower row which involves longitudinal correlations. The solid curves show acceptance-corrected predictions; the dashed curves show the predictions without acceptance effects.

Indeed, Fig. 13, which compares the NLO predictions of FMNR[3] to the $\Delta\phi$ and $P_t^2(D\overline{D})$ distributions observed by E687, shows that the NLO predictions agree with the data as long as reasonable $< k_t^2 >$ values are used.

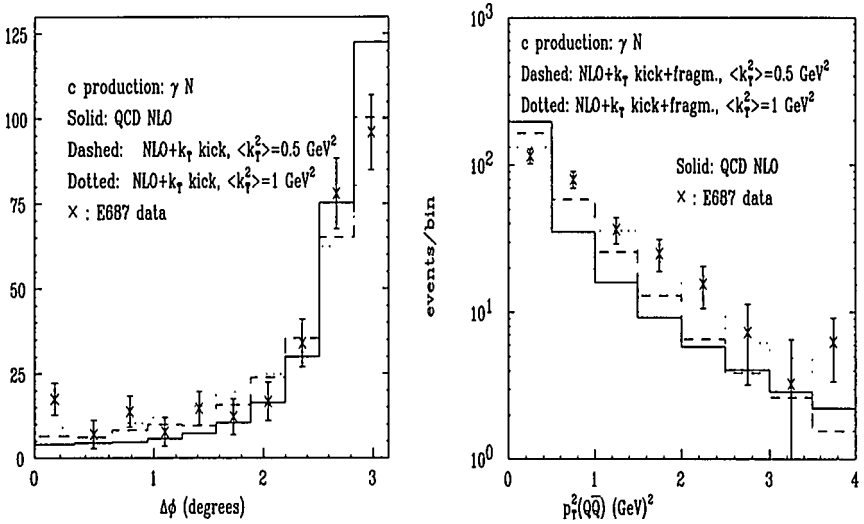


Fig. 13. Overlay of the NLO predictions for the $\Delta\phi$ and $P_t^2(D\overline{D})$ distributions to E687 data for several $< k_t^2 >$ choices.

2.4 Charm-Anticharm Asymmetries

In lowest order QCD, the charm and anticharm quark are produced symmetrically in photoproduction and hadroproduction. In hadroproduction, at next to leading order, QCD introduces small ($\approx 1\%$) asymmetries in quark momenta due

to interference between contributing amplitudes. As we shall see, however, a significant degree of $c\bar{c}$ asymmetries can naturally arise through the fragmentation process. Figure 14 illustrates the mechanism responsible for a photoproduced $c\bar{c}$ asymmetry in the JETSET-PYTHIA model. As shown in Fig. 14, the dominant source of charm-$\overline{\text{charm}}$ asymmetry in the JETSET-PYTHIA model for photoproduction arises through the differences between the momentum fraction of the target nucleon remnant carried by the effective quark and di-quark color poles. The di-quark and quark remnants should be viewed as effective color pole descriptions rather than actual quarks or di-quarks. As such, there is no reason to assume that their momentum fractions are the same as the quark momentum distributions measured in deep inelastic leptoproduction. In the default JETSET-PYTHIA, the effective quark is drawn with a momentum fraction given by $dN/dx \propto (1-x)^3/x$ which has the soft $1/x$ dependence expected for a sea quark distribution. Since at the energies employed by E687 the gluons are typically very soft as well, the default PYTHIA puts nearly all of the nucleon momentum fraction into the effective di-quark. The very different momentum fractions carried by the quarks and di-quarks in the default PYTHIA Monte Carlo leads to asymmetries in the charm-$\overline{\text{charm}}$ particle momentum distributions which are much stronger than those observed in the E687 (Ref. 8) data. On the other hand, an alternative PYTHIA effective quark distribution called the "counting rule" option draws the effective quark momentum fraction according to a much harder spectrum: $dN/dx \propto (1-x)$. When one uses the counting rule option, 1/3 of the nucleon remnant momentum on average is carried by the effective quark and 2/3 is carried by the di-quark. A counting-rule Monte Carlo predicts significantly less charm-$\overline{\text{charm}}$ asymmetry, which is in good agreement with the experimental data.

Figure 15 compares the kinematic variation of the photoproduced D^+/D^- measured asymmetry to the PYTHIA-JETSET Monte Carlo for sea-like (default) and counting rule effective quark momentum fractions. The more symmetrical counting rule model does a very good job at matching the kinematic trends and level of the D^+ asymmetry observed in the E687 data. It is also a reasonable match to the overall level of photoproduced asymmetry observed for other charm decay modes[‖] as shown in Table 1.

[‖]Note that different asymmetries are predicted for two different decay modes of the D^o. This is true since the asymmetries are not corrected for experimental acceptance and the two decay modes have different acceptance versus momentum curves.

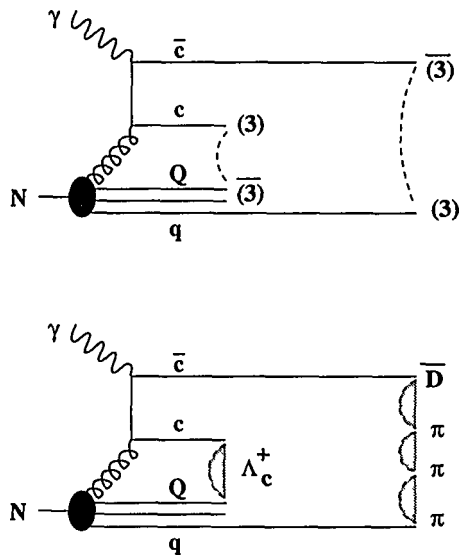


Figure 14: In JETSET, strings are drawn between the triplet and anti-triplet color poles. Final-state hadrons are produced as these strings fragment. Quarks are color triplets; antiquarks are color anti-triplets. In photon-gluon fusion, the initially colorless nucleon emits a color octet gluon. The nucleon remnants must therefore form a color octet to "cancel" the color of the gluon. JETSET achieves color conservation by resolving the nucleon remnants into an anti-triplet, effective di-quark (Q), and a triplet, effective quark (q). Because the c quark must dress with the q remnant and the $\bar{c}$ quark must dress with the Q remnant, a difference between the quark and di-quark momenta fraction distributions will lead to an asymmetry between the momenta spectra of the charmed and anti-charmed hadrons.

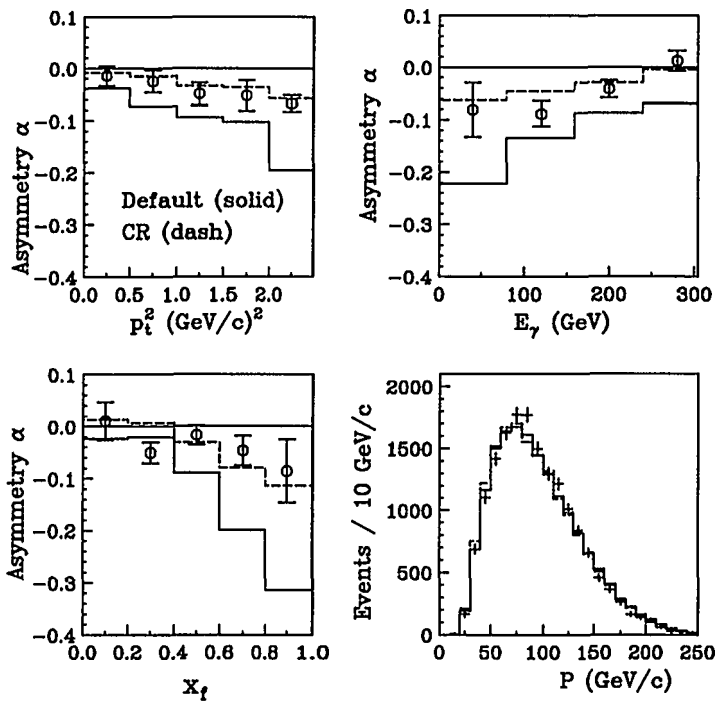


Figure 15: The asymmetry $\alpha = (N(D^+) - N(D^-)) / (N(D^+) + N(D^-))$ in bins of $P_t^2(D^\pm)$, incident photon energy, and $X_F(D^\pm)$ for accepted $D^\pm$ photoproduced from E687. The data is indicated with error bars, the sea-like effective quark predictions are solid and the counting rule effective quark predictions are dashed. The lower right corner compares the total lab momentum spectrum for $D^\pm$ candidates to the two models. In contrast to the asymmetry, the lab momentum spectrum is insensitive to the assumed effective quark momentum distribution.

Table 1. Observed asymmetry α (%) compared to predictions.

Decay Mode	E687 Data	Sea-Like	Counting Rule
$D^+ \to K^-\pi^+\pi^+$	-3.8 ± 0.9	-10.4 ± 0.4	-2.9 ± 0.3
$D^{*+} \to D^0\pi^+ \to (K^-\pi^+)\pi^+$	-6.4 ± 1.5	-9.2 ± 0.7	-2.4 ± 0.5
$D^{*+} \to D^0\pi^+ \to (K^-\pi^+\pi^+\pi^-)\pi^+$	-4.0 ± 1.7	-9.2 ± 0.8	-3.0 ± 0.5
$D^0 \to K^-\pi^+$ (no D^*-tag)	-2.0 ± 1.5	-5.1 ± 0.6	-1.6 ± 0.4
$D^0 \to K^-\pi^+\pi^+\pi^-$ (no D^*-tag)	-1.9 ± 1.5	-9.9 ± 0.5	-2.9 ± 0.4
$D_s^+ \to K^-K^+\pi^+$	2.5 ± 5.2	9.7 ± 1.7	2.5 ± 0.7
$\Lambda_c^+ \to pK^-\pi^+$	3.5 ± 7.6	21.5 ± 0.7	-7.7 ± 0.6

Recently, the E791 Collaboration[49] studied the kinematic asymmetry from their ≈74,000 event sample of D^+ produced with 500 GeV π^-'s incident on a target consisting of four diamonds and one platinum foil. The asymmetry measured by E791 (with the opposite convention as ours) is shown in Fig. 16. The basic trend of an asymmetry which favors more D^-'s at larger X_F is the same trend observed in the photoproduction data of Fig. 15, but the level of asymmetry is much larger in hadroproduction.

This asymmetry pattern has been previously observed by other groups[9] who study charm hadroproduction where it goes under the name of the leading particle effect (since the D^- contains the same $\overline{u}$ quarks found initially in the π^- projectile). As is the case for photoproduction, the asymmetry observed in hadroproduction is a sensitive probe of fragmentation effects since the $c\overline{c}$ asymmetry predicted in NLO for charm quarks is very small. Again, the overall level of asymmetry in the default PYTHIA Monte Carlo exceeds the data but can be matched once one increases the $< k_t^2 >$ to 1 GeV^2 and increases the charmed quark mass from 1.35 to 1.7 GeV. The pattern of asymmetry predicted by the Vogt-Brodsky[50] intrinsic model does not really match the data although a better match might possibly be obtained by varying some parameters.

2.5 Production Dynamics Summary

Although most of my discussion involved the QCD charm photoproduction process, many of the same conclusions apply to high-energy charm hadroproduction.

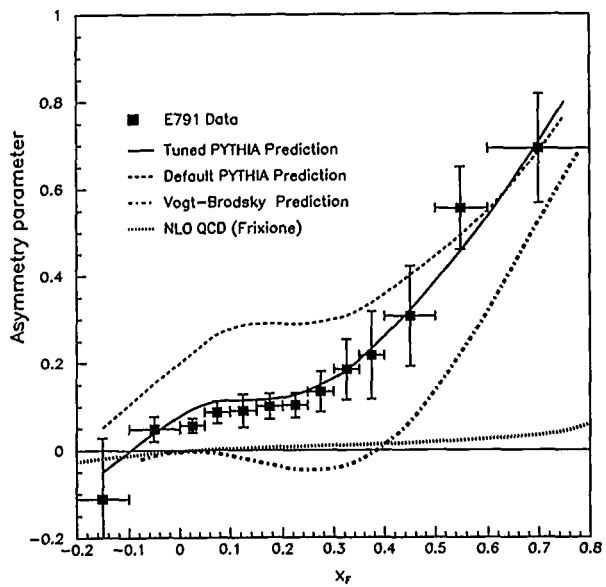


Fig. 16. Comparison of E791's (Ref. 49) measurement (error bars) to various models for the π^- hadroproduction asymmetry. Their asymmetry convention is a "leading particle" asymmetry with the D^- being the "leading particle," which has the opposite convention as that used in Fig. 15 and Table 1 for E687. Overlayed on the figure are the predictions of default PYTHIA, a tuned PYTHIA model, the intrinsic charm model of Vogt and Brodsky,[50] and the FMNR NLO prediction for charmed quarks which shows a very mild asymmetry for the bare charmed quarks.

The NLO photon-gluon fusion calculations of FMNR do a good job at reproducing the photoproduced cross section over a large range of photon energies from 20 GeV to over 30 TeV. Such calculations require a choice of charmed quark mass, renormalization scale, and gluon momentum fraction distribution.

Fragmentation effects play an important role in the P_t and X_F distribution for photoproduced charmed particles. In particular, in the absence of fragmentation effects, NLO calculations predict a significantly harder tail to the P_t^2 distribution for photoproduced charmed mesons than is observed in E687 data. Studies of the kinematic correlations between fully and partially reconstructed $D\overline{D}$ pairs provide incisive tests of QCD-inspired fragmentation models such as the LO JETSET-PYTHIA model. Longitudinal correlations such as the rapidity difference between the D and $\overline{D}$ are well-reproduced by PYTHIA, whereas transverse correlations such as the $D\overline{D}$ acoplanarity angle distributions show considerably more smearing in data compared to the PYTHIA Monte Carlo. This difference can be attributed to the hard gluon emission process which occurs at NLO. Indeed, the FMNR NLO calculations predict an acoplanarity distribution which is in good agreement with the data under reasonable fragmentation and k_t assumptions.

Finally, the asymmetry in the momentum spectrum between photoproduced and hadroproduced charmed and anticharmed particles primarily reflects the fragmentation process. The mechanism used in the JETSET-PYTHIA model for color conservation in photon-gluon fusion where the target nucleon remnants appear as effective quark and di-quark color poles provides a natural mechanism for charm-$\overline{\text{charm}}$ asymmetry. The asymmetry predicted by the JETSET-PYTHIA Monte Carlo does a good job at matching asymmetries seen in E687 data provided that a simple counting rule distribution which attributes (on average) 1/3 of the nucleon remnant momentum to the effective quark and 2/3 of the remnant momentum to the di-quark is used. JETSET-PYTHIA also does a good job of predicting the kinematic asymmetry observed in hadroproduction for particular parameter choices.

3 Heavy Quark Decay

A great many tools of QCD have been brought to bear on the issue of heavy quark decay. In this section, we will primarily review the physics of charm rather than beauty decay, since in charm, the QCD corrections to the weak decay process

are particularly important. On the most inclusive level, the lifetimes of weakly decaying charmed particles serve as measurements of the total decay rate. In the absence of QCD effects, the lifetimes of heavy flavor states would depend on the heavy quark alone, rather than the specific charm or beauty particle being considered. Although the lifetimes of the various beauty states are all comparable, the lifetimes of various weakly decaying charm states differ by roughly an order of magnitude. Recent progress has been made in predicting the deviations from a universal charm lifetime due to QCD corrections, through the use of heavy quark expansions in $1/M_Q$.

We will turn next to a discussion of leptonic and semileptonic decays of charmed mesons. These are the simplest exclusive decays to understand since all of the QCD effects can be expressed as modifications to a weak hadronic current through form factors which can be computable in principle using Lattice Gauge Theory. Since all semileptonic decay processes studied thus far have a single final-state daughter hadron, the complications of final-state interactions which plague nonleptonic decays are absent. We next discuss polarization phenomena in charmed baryon decay, an area of charm decay where HQET makes a very interesting prediction.

We conclude with a discussion of nonleptonic charm decays which are generally studied within a framework called factorization. In this framework, two-body charm decays are described by the interaction of two hadronic currents which are similar to those describing leptonic and semileptonic decays. Unfortunately, when several strongly interacting final-state particles are produced, they can continue to interact after their formation, via final-state interactions. These final-state interactions can significantly distort the factorization predictions for, *e.g.*, branching ratios into specific two pseudoscalar final states by creating an *a priori* unknown phase shift between interfering amplitudes. These same strong phase shifts can be independently studied through interference between the various quasi-two-body decay amplitudes which contribute to a particular three- or four-body charm decay.

3.1 Charm Particle Lifetimes

There are seven known weakly decaying charmed particles with experimentally measurable lifetimes. Last year, the lifetime for the heaviest of these, the Ω_c^o (css) (2704), was measured for the first time. As you can see from the compendium of lifetime results measured by E687 shown in Table 2, there is roughly an order of magnitude difference between these seven lifetimes.[10] Before discussing the physics implications of such measurements, I would like to use a few words to explain how such measurements are made.

Table 2. E687 lifetime measurements (in psec).

D^+	D^o	D_s^+
$1.048 \pm .015 \pm .011$	$0.413 \pm .004 \pm .003$	$0.475 \pm 0.020 \pm 0.007$
Λ_c^+ (udc)	Ξ_c^+ (csu)	Ξ_c^o (csd)
$0.215 \pm 0.016 \pm 0.008$	$0.41^{+0.11}_{-0.08} \pm 0.02$	$0.101^{+0.025}_{-0.017} \pm 0.005$
Ω_c^0 (css)		
$0.089^{+0.027}_{-0.020} \pm 0.028$		

3.1.1 Lifetime Measurement

Most experimental information on charmed particle lifetimes comes from fixed-target experiments employing vertexing techniques. In order to tag charm, one generally requires a minimal detachment between the primary and charm decay vertex of $\ell > \mathcal{N}\ \sigma_\ell$, where σ_ℓ is the event-by-event estimate of the experimental resolution on the detachment and $\mathcal{N}$ is the minimum detachment in units of the computed measurement error, σ_ℓ, deemed adequate to ensure a clean enough charm sample (often a 5-10 σ_ℓ cut is used). It might seem that the use of an event-dependent minimum lifetime cut which is required to isolate charm might complicate the process of measuring a charm particle lifetime. Actually, these complications are actually fairly minor. E687 and most other groups fit their lifetime evolution data using what is known as a reduced proper time variable, $t' \equiv (\ell - \mathcal{N}\ \sigma_\ell)\ /(c\beta\gamma)$, where the $(c\beta\gamma)^{-1}$ converts the distance to a proper time including time dilation, and the $\mathcal{N}\ \sigma_\ell$ piece effectively starts the clock at the point of the minimum detachment cut. An exponential decay distribution is exponential no matter when the clock is started. Given that the error on the detachment (σ_ℓ) is approximately independent of ℓ and that the acceptance usually has only a weak

dependence on ℓ, the reduced proper time for a decaying state will closely follow an exponential distribution expected for a state of lifetime τ: $dN/dt' \approx \exp(-t'/\tau)$.

We generally make binned likelihood fits to the reduced proper time (t') distributions by minimizing a log-likelihood variable w of the form:

$$w = -2\sum_{i}^{\text{bins}} \ln \mathcal{P}(n_i;\mu_i) - 2\ln \mathcal{P}(N_{\text{sidebands}};2B)$$

$$\text{where } \mathcal{P}(n_i;\mu_i) \equiv \frac{{\mu_i}^{n_i}\, e^{-\mu_i}}{n_i!} \text{ and } \mu_i = S\, f(t_i')\, e^{-t_i'/\tau} + B\, b_i. \qquad (3)$$

A few words on Eq. (3) might help. The departure from a pure $\exp(-t_i'/\tau)$ form due to acceptance variation and absorption of the charmed particles or decay products as they travel through the target are included through the factor $f(t_i')$ which is deduced via Monte Carlo simulation.* The fit maximizes the Poisson probability that t' bin populations $\{n_i\}$ of events in the signal region (about, *e.g.*, the D^o) matches the number expected $\{\mu_i\}$ for a given lifetime τ and background level B which are the two fit parameters. The fit accomplishes this by minimizing w with the extra factor of -2 included so that the $\pm 1\sigma$ errors correspond to changes of $w - w_{\min} = 1$. Figure 17 illustrates the background subtraction method used in this type of fit. This procedure should be valid and free of systematics to the extent that time evolution for the background under the signal can be adequately determined by events with masses near the signal peak and that proper time resolution is small compared to the lifetime.

For the case where $\sigma(\tau) \ll \tau$ † and the background level is small, the anticipated fractional statistical error on the lifetime is given by $\sigma_\tau/\tau = 1/\sqrt{N_{\text{sample}}}$. This means that a $\pm 1\%$ statistical error on τ (which is comparable to present systematic errors due to background uncertainties) would require about 10,000 reconstructed events. This yield has already been achieved in experiments such as E687 and E791. Interestingly enough, the lifetime knowledge for the D system is already comparable to that for kaons: $\sigma_\tau/\tau = 0.1\% \rightarrow 0.8\%$ for kaons.

*E687 uses a vertex finder which is efficient even at very small detachments, and hence the correction functions $f(t_i')$ for our experiment are nearly constant. The one exception is that $f(t_i')$ cuts off at long t' for the very long-lived D^+ since it has a nonnegligible probability of decaying downstream of our silicon microstrip vertex detector!

†In a fixed-target experiment, $\sigma_\ell \propto P(\text{charm state})$, and hence, one has a resolution on t' which is independent of momentum and about the same for all fully reconstructed charm states. For E687, $\sigma(t') \approx \tau(D^o)/10$, and hence for many of the measurements reported in Table 2, proper time resolution is unimportant.

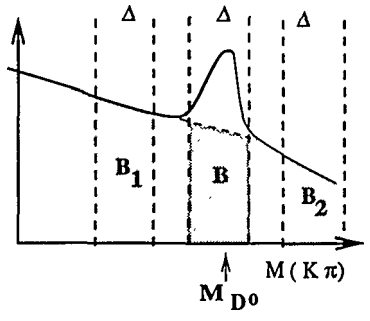


Fig. 17. A sketch of the histogram used to deduce parameters for the lifetime fit described by Equation 3. The log-likelihood variable w is constructed from the population of signal region events found in each bin of reduced proper time (t_i'). The normalized background shape b_i is taken directly from events falling in the equal width, sideband regions marked B_1 and B_2. Information which ties the fit parameter B to the average of the number of events in each sideband is communicated to the fit through the inclusion of the term $-2\ln\mathcal{P}(N_{\text{sidebands}};2B)$.

3.1.2 Lifetime Physics

Lifetimes represent the most inclusive way of looking at charm particle decay. The lifetime is related to the total decay width via the expression:

$$\Gamma_T(C_x) = \sum_i \Gamma_i = \frac{\hbar}{\tau(C_x)}. \qquad (4)$$

The partial width ratio (Γ_i/Γ_T) gives the fraction of times a given charm particle C_x will decay into a particular final state i. Theoretical predictions for the decay rate into a given final state, i, are generally expressed in terms of the partial width Γ_i. In the absence of the quark re-arrangement effects permitted by QCD, charm particles would be expected to proceed by the naive spectator model depicted in Fig. 18. We thus expect in the naive spectator model a universal charm decay width given (in the absence of HO corrections and QCD effects) by:

$$\Gamma_T = (2+3)\,\Gamma_o \text{ where } \Gamma_o = \frac{G_F^2 m_c^5}{192\pi^3}\,|V_{cs}|^2.$$

$$\text{Scaling from the muon : } \tau_C = \frac{1}{5}\left(\frac{0.105}{1.5}\right)^5 2.2\times 10^{-6} = 7\times 10^{-13}\ s. \qquad (5)$$

Of course, given the fact that the charm lifetimes are not universal but differ by an order of magnitude, there must be additional nonspectator diagrams which

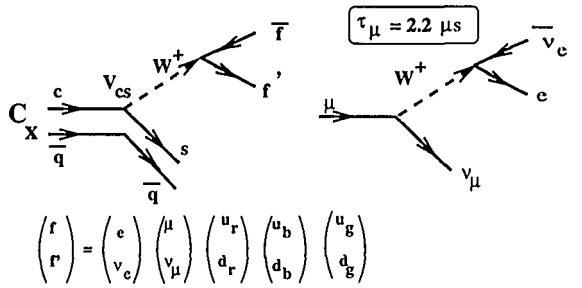


Figure 18: In the naive spectator model, the lifetime of charmed particles should have a universal value which can be estimated by scaling from the known muon lifetime of 2.2 μs. When scaling decay rates, one would need to consider the fact that five low mass final states are available for the charmed quark (two lepton generations and three color multiplets of the first quark generation), and that the charm quark has a much larger decay phase space owing to its much larger mass.

contribute differently for the various charm species. Figure 19 gives examples of nonspectator diagrams which could account for lifetime differences amongst the charmed mesons. Although it is relatively easy to imagine nonspectator decay processes that differentiate among the charmed particles, it has been more difficult to assess their relative importance until recently. Systematic progress has been made by the use of Heavy Quark expansion techniques which include QCD corrections as parameters of an expansion for the semileptonic and nonleptonic widths of the form[11-12]:

$$\Gamma_{SL} = \Gamma_0 \left(1 + \frac{B_2}{m_c^2} + \frac{B_3}{m_c^3} + ...\right)$$

$$\Gamma_{NL} = N_c\, \Gamma_0 \left(1 + \frac{C_2}{m_c^2} + \frac{C_3}{m_c^3} + ...\right)$$

$$\text{where } \Gamma_0 = \frac{G_F^2\, M_Q^5}{192\pi^3}\, |V_{Qq'}|^2. \qquad (6)$$

The expansion of Eq. (6) has some appealing as well as disturbing aspects. As $M_Q \to \infty$, one recovers the predictions of the naive spectator model illustrated in Fig. 5 which features a universal single-generation decay width Γ_0 which depends on the CKM matrix element and the quark mass that controls the size of phase space available to the decay products. Hence, the lifetimes of various beauty particles should be fractionally much closer than those for charm owing to the

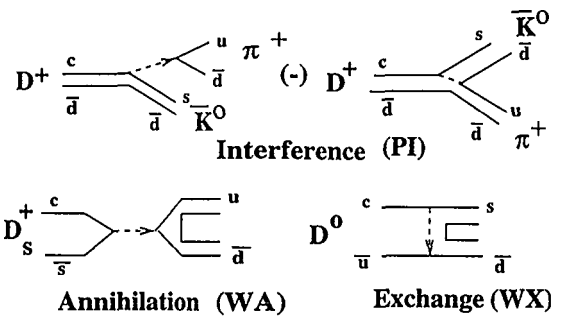


Figure 19: D^+ decays always have two ways of re-arranging the quarks $W^+ \to u\bar{d}$ into the final-state mesons. Because this involves fermion exchange, one expects a destructive (Pauli) interference between the interfering amplitudes which will suppress the rate for D^+ decay and enhance the D^+ lifetime. The $c\bar{s}$ quarks comprising the D_s^+ have a CKM-allowed coupling directly to a virtual W^+ giving a CKM-favored weak annihilation contribution unique among mesons to the D_s^+. Finally, the D^o has a CKM-allowed W^+ exchange contribution which among mesons is unique to the D^o.

heavier b-quark mass. The processes which differentiate among the various heavy quark species such as those depicted in Fig. 19 contribute to the coefficient C_3.

Tables 3 and 4, taken from Bigi,[12] compare various experimental lifetime ratios to the predictions of a $1/M_Q$ expansion which uses various inputs, including theoretical estimates for the leptonic decay constants of the D and the mass and mass splitting pattern among various charm hadrons.

As expected, the lifetimes are much closer between the species measured for the beauty sector than is the case for the charm sector. The rough factor of two difference between the D^+ and D^o lifetime suggests that the PI mechanism, shown in Fig. 19, is important, while the relative equality between the D^o and D_s^+ lifetime suggests that the WA process must not be very important.

To the heavy quark experimentalist, Eq. (6) contains the ominous prediction that the semileptonic widths are not universal among the various charm or beauty species. This is disturbing news since most of our present knowlege of charm particle branching ratios beyond the well-known D^+ and D^o absolute branching

Table 3: Comparison of data to $1/M_Q$ expansion in the charm sector.

Lifetime Ratio	QCD $1/M_c$ exp	Data
D^+/D^o	≈ 2	2.547 ± 0.043
D_s/D^o	≈ 1	1.125 ± 0.045
Λ_c/D^o	≈ 0.5	0.51 ± 0.05
Ξ_c^+/Λ_c	≈ 1.3	1.75 ± 0.36
Ξ_c^+/Ξ_c^o	≈ 2.8	3.57 ± 0.91
Ξ_c^+/Ω_c	≈ 4	3.9 ± 1.7

Table 4: Comparison of data to $1/M_Q$ expansion in the beauty sector.

Lifetime Ratio	QCD $1/M_b$ exp	Data
B^-/B_d	≈ 1	1.04 ± 0.05
B_s/B_d	≈ 1	0.98 ± 0.08
Λ_b/B_d	≈ 0.9	0.76 ± 0.06

fractions depend on the assumption of a universal semileptonic width.‡ The hope that there might be a universal semileptonic width is based on experience with the $D^+ - D^o$ system where it was noted that the ratio of the D^+/D^o semileptonic width was approximately the ratio of the D^+/D^o lifetime[13]:

$$\frac{\mathcal{B}_{SL}(D^+)}{\mathcal{B}_{SL}(D^o)} = 2.3 \pm 0.4 \pm 0.1 \quad \approx \quad \frac{\tau(D^+)}{\tau(D^o)} = 2.54 \pm 0.07. \tag{7}$$

This observation implies that $\Gamma_{SL}(D^+) \approx \Gamma_{SL}(D^o)$ since $\mathcal{B}_{SL} = \Gamma_{SL}/\Gamma_T$ and $\Gamma_T(D^o)/\ \Gamma_T(D^+) = \tau(D^+)/\tau(D^o)$. However, it is really not correct to infer a universal semileptonic width for all charm species based on this evidence since the D^+ and D^o are in the same isodoublet and the $c \to s$ transitions involved in semileptonic decays will transform as $\Delta I = 0$. Nonetheless encouraged by the possibility of a universal Γ_{SL}, groups have been estimating absolute branching fractions through the technique suggested by Eq. (8).

$$\mathcal{B}_x = \frac{\#C \to x}{\#C \to SL}\ \mathcal{B}_{SL}\ ,\ \mathcal{B}_{SL} = \frac{\Gamma_{SL}}{\Gamma_T}\ ,\ \Gamma_T = \frac{\hbar}{\tau_C}. \tag{8}$$

One can first infer the semileptonic branching ratio ($\mathcal{B}_{SL}$) using the measured lifetime of the state (τ_C) and the value of a "universal" Γ_{SL} measured from the average of the known D^+ and D^o values. Next, the absolute branching fraction into state x can be measured relative to the inferred $\mathcal{B}_{SL}$ by measuring the fraction of times the state decays into the x or SL final state. Although the assumption of a universal Γ_{SL} is invalid, the expected variance according to Bigi[12] is not too large. The expected relative ratios of Γ_{SL} are shown in Table 5.

Table 5. Expected relative values for Γ_{SL}.

D^+	D^o	D_s^+	Λ_c^+	Ω_c^o
1	1	≈ 1	≈ 1.5	≈ 1.2

‡Absolute branching fractions for the D^+ and D^o can be obtained in e^+e^- annihilation just above charm threshold by studying events where both charmed particles are reconstructed. Alternatively, one can tag the presence of a D by kinematically tagging pions from $D^* \to \pi D$ using techniques similar to those described in Sec. 2.3 and count the number of times the tagged D decays into a specfic final state.

3.2 Leptonic Decays of the D_s^+

There has recently been a new measurement of $D_s^+ \to \mu^+\nu$ by the E653 Collaboration. Figure 20 illustrates several features of the D_s^+ decay process. Nature

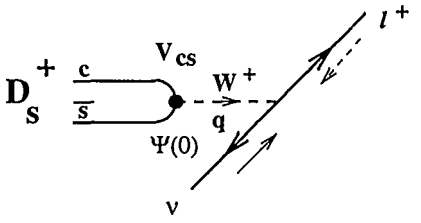


Figure 20: The D_s^+ leptonic decay has the $c\bar{s}$ quarks coupling to the virtual W^+ carrying a four-momentum q_μ with a CKM-favored coupling constant. The virtual W^+ then decays into an ℓ^+ and a left-handed ν. Since the D_s^+ is spinless, the ℓ^+ must emerge left-handed in order to conserve angular momentum along the lepton decay axis. A right-handed antilepton has a highly suppressed $V-A$ coupling. In the context of a quark model, this process provides information on the quark wave function near the origin.

handles the fact that the ℓ^+ is forced into the "wrong" helicity state by suppressing the decay width by two powers of the charged lepton mass as shown in Eq. (10). This means that the only nonnegligible leptonic decays for the D_s^+ will be into taus and muons (with tau's being favored by a factor of ≈ 10.) Because the $\tau^+\nu$ decay includes at least two missing final state neutrinos, it is very hard to experimentally reconstruct, which makes the muonic decay the decay of choice among experimentalists.

Equation (9) shows the structure of the leptonic decay amplitude which is a current $\times$ current interaction with one current being the familiar $V-A$ current comprised of the leptons and the other current being an *a priori* unknown current involving the D_s^+,

$$\mathcal{M} = \frac{G_f}{\sqrt{2}}\,\bar{u}_\ell\gamma^\mu\,(1-\gamma_5)v_\nu < 0|\,J_\mu^\dagger\,|D_s^+> \\ < 0|J_\mu^\dagger|D_s^+> = i\,V_{cs}\,f_{D_s}\,q_\mu. \qquad (9)$$

This current must be constructed out of the only available vector q_μ which is the four momentum carried by the virtual W^+. The current also contains a potentially

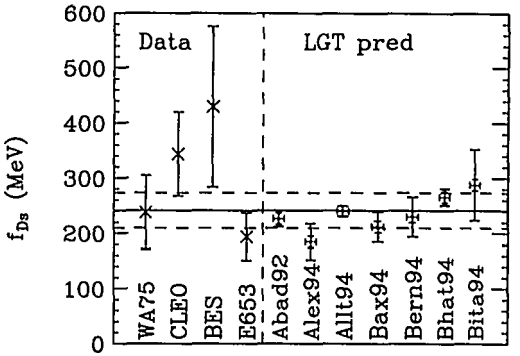


Figure 21: An informal weighted average of the four experimental results gives $f_{D_s} = 242 \pm 32\ MeV$ at $\approx 20\%$ CL level. This value and error form the dashed and solid horizontal lines. Also shown are the Lattice Gauge Theory predictions.

q^2 dependent form factor, but since $q^2 = M^2(D_s^+)$, this form factor just becomes the constant known as the D_s^+ leptonic decay constant. Equation (10) relates the leptonic decay constant to the D_s^+ leptonic width:

$$\Gamma(D_s \to \ell\nu) = \frac{G_f^2|V_{cs}|^2}{8\pi} f_{D_s}^2\, M_{D_s}\, M_\ell^2 \left(1 - \frac{M_\ell^2}{M_{D_s}^2}\right). \qquad (10)$$

Experimentally, one can measure $f_{D_s}^2$ through the decay width expression by measuring the yield of $D_s^+ \to \mu\nu$ decays to a reference state with a surmised decay width such as $\phi\ell^+\nu$ as discussed in Sec. 3.1.2. Data from BES infers the width directly from the lifetime using a double-tag technique.

Being the theoretically simplest charm decay, there are many theoretical estimates of leptonic decay constants which use a variety of techniques including Lattice Gauge Theory, QCD sum rules, and explicit quark models. The review by Richman and Burchat[14] contains a summary of these calculations and a fuller discussion of the experimental techniques. Figure 21 compares the experimental data[15–18] to the Lattice Gauge calculations. Agreement of the theory with experiment is quite good.

3.3 Semileptonic Decays

The basic heavy quark semileptonic process, depicted in Fig. 22, suggests that a major reason to study semileptonic decays is the measurement of $|V_{Qq}|^2$. Historically,

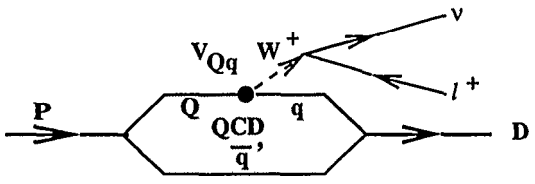


Fig. 22. The basic three-body, semileptonic process where a parent P transforms into a daughter hadron D while emitting a virtual W which materializes into a $\nu\ell^+$ pair. The QCD processes which govern the form factors are complicated but can be computed in principle using Lattice Gauge Theory.

it is true that many CKM matrix elements were first measured through semileptonic decay including nuclear β decay (V_{ud}), $K \to \pi e\nu$ (V_{us}), and more recently, inclusive beauty semileptonic decay at CLEO (V_{ub} and V_{cb}). The grey area of Fig. 22, meant to describe the QCD process by which the $\overline{q}'q$ appears as a fully dressed daughter hadron, is understood in principle but difficult to calculate in practice without approximation.

Only three-body semileptonic decay processes have been studied thus far. All the QCD effects for, *e.g.*, pseudoscalar $\ell^+\nu$ decays are contained in two q^2 dependent form factors which describe how the hadronic weak current between the parent and daughter is constructed from their four momenta:

$$< D|J^\dagger_\mu|P > \; = \; f_+(q^2)\;(P+D)_\mu + f_-(q^2)\;(P-D)_\mu. \qquad (11)$$

Most information is known about the $f_+(q^2)$ form factor since in width expressions, terms involving $f_-(q^2)$ always multiply the charged lepton mass (and hence, they are generally small except for the τ).

For charm semileptonic decays which represent heavy-to-light transitions, the primary theoretical tools have been Lattice Gauge Theory (LGT) and quark models.§ In LGT,[19] form factors are evaluated as the expectation value of three-point correlation functions describing the parent, current, and daughter. These expectation values involve evaluating integrals by summation over a four-dimensional

§In b to c decays, HQET provides considerable understanding of beauty semileptonic decay physics.

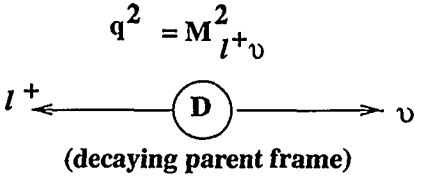


Fig. 23. LGT and Quark Model semileptonic form factor calculations work best when the hadron daughter is at rest. In this configuration, q^2, which is the $\ell^+\nu$ invariant mass, is at q^2_{max}.

space-time lattice of size L and spacing a. Naive computation times would scale as $(L/a)^4$, so there is a computational premium in keeping L as small as possible (but no smaller than the extent of the hadron wave function $\approx 1\ fm$), and a as large as possible (but smaller than the daughter wavelength). Generally, calculations are performed with the daughter at rest in the parent rest frame as depicted in Fig. 23. This is also true of Quark Model calculations which utilize quark wave functions. As the daughter momentum increases and $q^2 \to q^2_{min}$, the form factor probes the tail of the wave function which is the least accurately known part.

Unfortunately, as we will see, the decay intensity of the data is peaked near the maximum daughter momentum or $q^2 \to q^2_{min}$ where theory has the hardest time. For the case of pseudoscalar $\ell^+\nu$ decays, the current of Eq. (11) gives the differential width expression given by Eq. (12),

$$\frac{d\Gamma}{dq^2} = \frac{G_F^2|V_{Qq}|^2|\vec{h}^{(D)}|^3}{24\pi^3}\{|f_+(q^2)|^2 + m_\ell^2\;|f_-(q^2)|^2 ...\}, \qquad (12)$$

where $\vec{h}^{(D)}$ is the three-momentum of the daughter hadron in the D rest frame. These three powers of $|\vec{h}^{(D)}|$ (one from phase space and two from the squared amplitude modulus), severely deplete the intensity near q^2_{max}.

In order to bridge the gap between q^2_{min} where the data are measured and q^2_{max} where the data are predicted, most groups assume the pole form *ansatz* given by Eq. (13),

$$f(q^2) = \frac{f(0)}{1 - q^2/m^2_{\rm pole}}. \qquad (13)$$

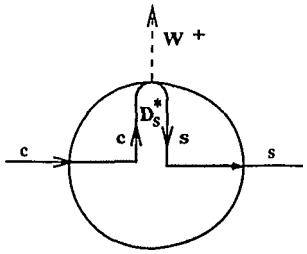


Figure 24: Illustration of the coupling of a virtual W^+ to the $c \to s$ quark. For pseudoscalar $\ell^+\nu$ decays, one can think of the hairpin as a virtual D_s^* vector state comprised of $c\bar{s}$ quarks which contributes a propagator of the form $1/(m^2(D_s^*) - q^2)$.

Expectations are that $m_{\rm pole}$ will be the lowest mass $Q\overline{q}$ resonance with the same spin-parity as the hadronic weak current proportional to V_{Qq}. Figure 24 gives a cartoonish "explanation" of why one might expect a pole-like q^2 dependence with a pole mass given by the spectrum of D^* and D^{**} mesons. Although my version of the pole dominance argument seems *ad hoc*, Burdman and Kambor[20] recently made a detailed dispersion relation calculation to show that contributions of higher poles should be negligible for charm.

Perhaps the most elegant way of thinking about the kinematics of three-body semileptonic processes is via the Dalitz plot which is sketched in Fig. 25. As shown in Eq. (14), the great virtue of the Dalitz plot is that the three-body decay phase space is doubly differential in the Dalitz variables which can be taken as any two of the three possible two-body invariant masses constructed from three final-state daughters. The form ensures that a process with a constant amplitude $\mathcal{M}$ will uniformly populate the Dalitz plot,

$$d^2\Gamma = \frac{|\mathcal{M}|^2}{256\pi^3\, M^3}\, dM_{h\ell}^2\, dM_{\ell\nu}^2 \;=\; \frac{|\mathcal{M}|^2}{256\pi^3\, M^3}\, dM_{hl}^2\, dq^2. \qquad (14)$$

For the case of pseudoscalar $\ell^+\nu$ decays, the $\mathcal{M}$ is not uniform but rather of the form given by Eq. (15),

$$\mathcal{M} \propto f_+(q^2)\, |\vec{h}^{(D)}|\, \sin\theta_{h\ell}^{(q)}. \qquad (15)$$

The $\sin\theta_{h\ell}^{(q)}$ dependence is an easy-to-understand consequence of the $V-A$ helicity rules as illustrated in Fig. 26. This angular factor will cause the decay

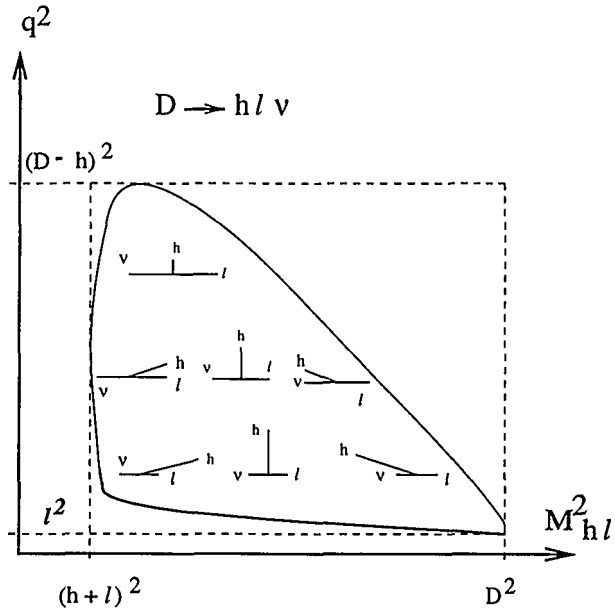


Figure 25: We chose $q^2 \equiv M_{\ell nu}^2$ and $M_{h\ell}^2$ as the two conjugate mass variables. The boundaries depend on the masses of the D, final state hadron, and charged lepton, abbreviated as D, h, and ℓ in the figure. Several decay configurations are drawn in the virtual W^+ or q rest frame. The momentum magnitudes of the ℓ, ν, h are fixed at a given fixed q^2 with the lepton momenta increasing and hadron momentum decreasing as q^2 increases. When ℓ^+ and the hadron are collinear, one reaches the left boundary of the plot; when ℓ^+ and the hadron are anticollinear, one reaches the right boundary of the plot. The expression for $M_{h\ell}^2$ is of the form $A - B\, \cos\theta_{h\ell}^{(q)}$.

intensity Dalitz to disappear at the Dalitz boundary where $\theta = 0$. Figure 27 shows simulated Dalitz plots for $D^+ \to K^-\mu^+\nu$, and $\pi^-\mu^+\nu$ decays.

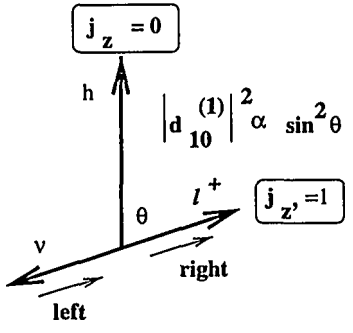


Figure 26: We view the decay in the virtual W^+ rest frame. Since the D is spinless and the hadron, h, is spinless, the virtual W^+ must have zero spin along the axis formed by the hadron. The ν is left-handed while the ℓ^+ is right-handed, which means the virtual W^+ has a spin of zero along the lepton axis. The amplitude for having the W^+ spin with a spin of one along the hadron axis and a spin of one along the lepton axis is proportional to the Wigner D-matrix $d^{(0)}_{10}(\theta) \propto \sin\theta$. The amplitude must clearly disappear when the hadron and lepton axes are either collinear or anticollinear, and the W^+ would need to have two different spin components along the same axes simultaneously.

3.3.1 Experimental Techniques

Semileptonic charm physics presents a real challenge to experimentalists because most experiments which can study charm cannot directly detect the missing neutrino. Although there is often a way of extracting information about the neutrino through missing P_t, the knowledge of the neutrino momentum is often ambiguous and inaccurate. This leaves the experimentalist in a double bind. In contrast to the case of a fully reconstructed final state, there is no well-resolved charm signal peak in the invariant mass distribution, and hence there are many backgrounds where one or more final state particles escapes detection and thus closely resembles the desired final state with a single missing neutrino. One is also faced with

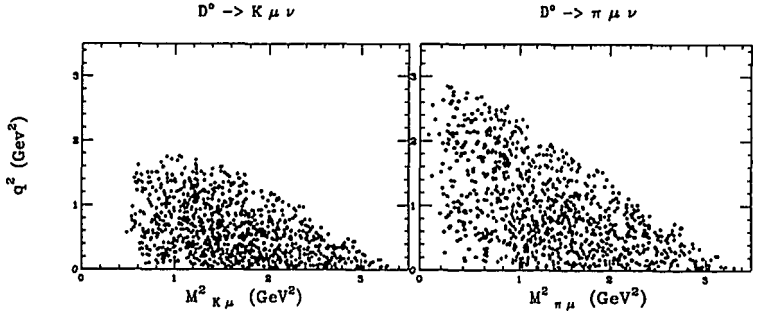


Figure 27: Simulated $D^+ \to K^-\mu^+\nu$ (left) and $D^+ \to \pi^-\mu^+\nu$ (right). The much larger phase space for the pion decay is evident. The point density decreases near the Dalitz boundary and is strongest at low q^2.

the problem of not being able to accurately measure the submasses needed to measure the form factors from the semileptonic final state.

Figure 28 shows how the missing neutrino is reconstructed from the measured D line of flight in a fixed-target experiment like E687. While the neutrino is equally likely to emerge in either hemisphere in the Fig. 28 frame, when the neutrino appears in the backward hemisphere, the charged system tends to be shot forward in the lab frame and gets accepted in the typical fixed-target forward spectrometer. For this reason, most fixed-target results resolve the ambiguity by selecting the solution with the neutrino in the backward hemisphere. Although this properly resolves the ambiguity most of the time, smearing on q^2 due to wrong choices and poor resolution on the D^o line of flight creates a highly significant smearing in q^2.

We turn next to the problem of fitting the semileptonic decay intensity to extract information on form factors. As an example, we describe the technique used by the E687 Collaboration[21] to extract information on $f_+(q^2)$ in Eq. (11) through a fit to the $D^o \to K^-\ell^+\nu$ Dalitz plot. A binned, likelihood fit is made to the $K^-\ell^+\nu$ Dalitz plot. The idea in such a binned fit is to maximize the agreement between the set of observed bin populations ($\{n_i\}$) and the set of expected populations ($\{\mu_i\}$) for a given set of form factor parameters. This is done by having

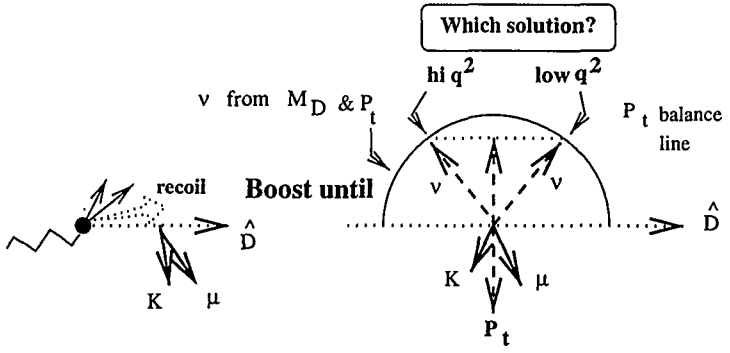


Figure 28: Consider the decay $D^0 \to K^-\mu^+\nu$. By observing tracks from an upstream primary vertex and the downstream vertex, one can reconstruct the D^o line of flight. One boosts the kaon and muon along the D line of flight until the sum of their longitudinal momentum vanishes: *i.e.*, the boosted visible momentum lies transverse to the D^o line of flight. The neutrino momentum must lie on the line which balances the visible P_t. The neutrino momentum must lie on a circle since the magnitude of the neutrino momentum can be calculated from its P_t and the D^o mass. The two circle-line intersections give two ambiguous solutions for the neutrino momentum. In this example, the backward hemisphere solution has the larger q^2 since the angle between the reconstructed neutrino and muon is larger.

the fit vary the form factors to minimize the log-likelihood parameter w given by Eq. (16)

$$w = -2\sum_{i}^{\text{bins}} \ln \mathcal{P}(n_i;\mu_i) \quad , \quad \text{where} \quad \mathcal{P}(n_i;\mu_i) \equiv \frac{{\mu_i}^{n_i}\, e^{-\mu_i}}{n_i!}. \tag{16}$$

The complication in the procedure is that the expected bin populations for a given set of form factors, $\{\mu_i\}$, must reflect the considerable diffusion of events into and out of a given reconstructed q^2 bin due to smearing. In order to properly handle the possible biases and error inflation due to q^2 smearing, most groups use some variant of the fitting technique developed by the E691 Collaboration (Ref. 22), which I will call Los Vegas weighting, and is illustrated in Fig. 29.

3.3.2 $D \to K\ell\nu$

The decays $D \to K\ell\nu$ give the best information on the q^2 dependence of the $f_+(q^2)$ form factor. The most recent, high statistics data comes from E687 (Ref. 21) and CLEO.[23] Figure 30 shows CLEO's $\approx$ 2700 event sample of D^* tagged $D \to K\ell\nu$ events. The (uncorrected) q^2 distribution of the CLEO $K\ell\nu$ sample is shown in Fig. 31.

Figure 32 shows the $D^{*+} - D^o$ mass difference distribution for E687's $\approx$ 430 event sample of $D^{*+} \to (K^-\mu^+\nu)\pi^+$ decays along with their uncorrected q^2 distribution. E687 augmented their D^* tagged sample with an $\approx$ 1900 event inclusive (untagged) event sample of $K^-\mu^+\nu$ decays. Because the $D^* - D$ mass difference cut cannot be applied, there is significantly more background in the untagged $K^-\mu^+\nu$ sample. However, because many of these backgrounds are well-understood, one can reliably subtract their effects by fitting to the $K^-\mu^+\nu$ Dalitz plot using the technique illustrated in Fig. 29. Figure 33 compares observed q^2 and $E_\mu \equiv (M^2_{K-\mu^+} + q^2 - M^2_K)/(2M_D)$ Dalitz projections to the results computed from the complete fit including backgrounds. Although the background contributions to the Dalitz projections of Fig. 33 are significant, the form factors and relevant branching ratios for each of the major physics backgrounds have already been accurately measured by our own[24,25] and other experiments. Muon misidentification probabilities can be reliably measured using known pions from the decay $K_s \to \pi^+\pi^-$. The parameterized misidentification level was fed into charm Monte Carlo calculations to estimate the shape and level of this background source. The expected population of events in the i'th bin, μ_i, was expressed as a function of the

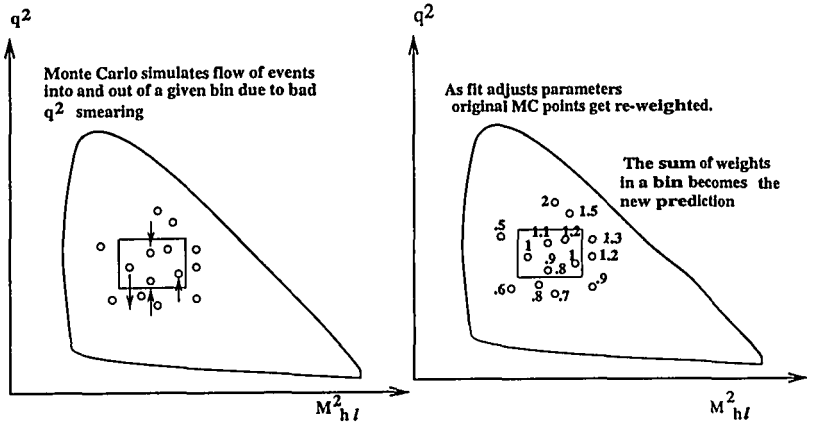


Figure 29: A Monte Carlo simulation using an initial guess for the relevant form factors is used to simulate the q^2 smearing due to neutrino reconstruction. This smearing will cause events to diffuse into and out of each bin. The program saves the generated Dalitz variables as well as the smeared Dalitz variables for each simulated event. As the fitter changes the form factors to minimize w, each simulated event is assigned a weight given by the ratio of the intensity with the new form factors divided by the ratio of the original intensity with the initial guess. The expected number of observed counts μ_i within a bin is computed from the sum of the weights for events falling within the i'th bin. This technique avoids prohibitively computer intensive, separate full Monte Carlo simulations for each iteration of the fit.

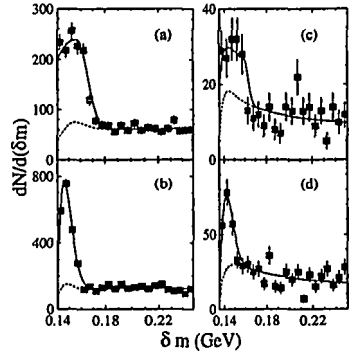


Figure 30: CLEO's $D^* - D$ mass difference for (a) $D^o \to K^- e^+ \nu$, (b) $D^o \to K^- \mu^+ \nu$, (c) $D^+ \to K_s e^+ \nu$, and (d) $D^+ \to K_s \mu^+ \nu$. The background estimates are given by the dashed curves.

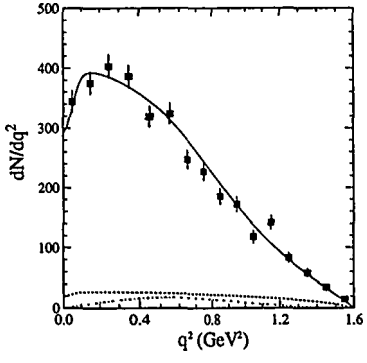


Figure 31: The uncorrected (for acceptance and smearing) q^2 spectrum measured by CLEO in their $\approx$ 2700 event sample of $D \to K\ell\nu$ decays. As suggested by Eq. (12), very few decays are observed near $q^2_{max} \approx 1.9\ GeV^2$.

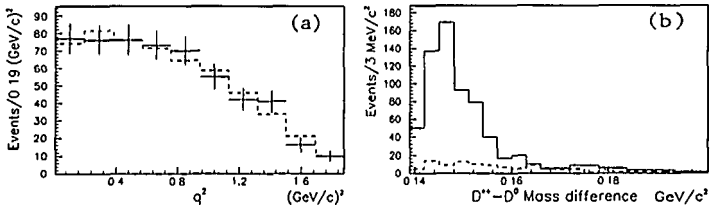


Fig. 32. The $\approx$ 430 event sample of D^* tagged $D^o \to K^-\mu^+\nu$ decays: (a) q^2 distribution, (b) $D^{*+} - D^o$ mass peaks and backgrounds.

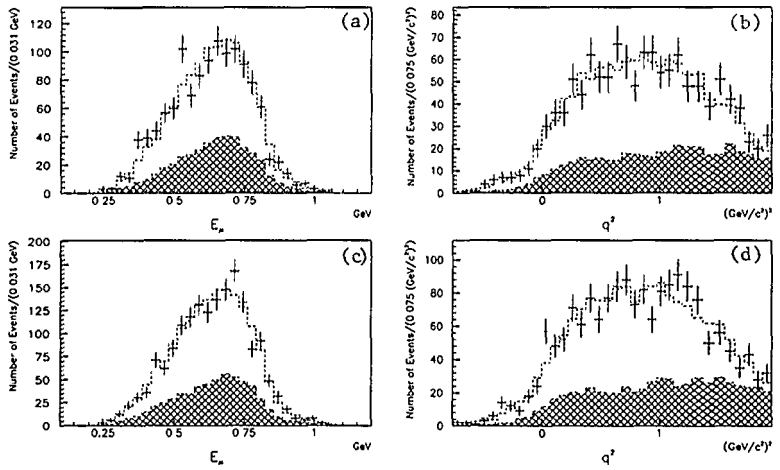


Fig. 33. Projections of the E687 $K^-\mu^+\nu$ Dalitz plot with fits overlayed on the data. Figures (a) and (b) compare projections obtained in 1990 data. Figures (c) and (d) compare projections obtained in 1991 data. A significant hole in our muon wall was inflicted upon us in 1991 to accommodate an experiment located downstream of our apparatus. The shaded region indicates background contributions from $D^+ \to (K^-\pi^+)\mu^+\nu$, $D^0 \to (K^-\pi^o)\mu^+\nu$, $D_s^+ \to \phi\mu^+\nu$, and nonleptonic charm decays where final-state hadrons were misidentified as muons.

yield of actual $D^o \to K^-\mu^+\nu$ events, the various background contributions, $\{b_k\}$, and the pole mass $m_{\rm pole}$ which parameterizes the q^2 dependence of the form factor $f_+(q^2)$.[¶] Although the known background contributions, $\{b_k\}$, were allowed to vary throughout the fit, *a priori* information on the anticipated background ($b_k^{(\rm meas)}$) was fed into the fit through the inclusion of a χ^2 contribution to the log likelihood of the form:

$$w = -2 \sum_i^{(bins)} \ln \mathcal{P}(n_i;\mu_i) + \sum_k^{(back)} \frac{(b_k - b_k^{(\rm meas)})^2}{\sigma_k^2}. \qquad (17)$$

The σ_k in Eq. (17) are the initial uncertainties in the background parameters $\{b_k\}$. We used this rather conservative technique so that final statistical errors on the form factors properly reflect uncertainties in the background estimation.

Once the yield of $D^o \to K^-\mu^+\nu$ signal events and pole mass are measured using the fit, the f_+ form factor can be measured via Eq. (18):

$$\Gamma_{K\ell\nu} = \underline{|V_{cs}|^2} \times |f_+(0)|^2 \times \int dq^2 \; H\left(q^2, m^2_{\rm pole}\right)$$
$$\Gamma_{K\ell\nu} = \frac{\hbar\, \mathcal{B}_{K\ell\nu}}{\underline{\tau_{D^o}}} \;, \quad \mathcal{B}_{K\ell\nu} = \frac{Y_{K\ell\nu}/\epsilon_{K\ell\nu}}{Y_{K\pi}/\epsilon_{K\pi}}\, \underline{\mathcal{B}_{K\pi}}. \qquad (18)$$

The underlined quantities in Eq. (18) are previously well-measured known inputs. The function $H(q^2)$ is the $d\Gamma/dq^2$ expression of Eq. (12) with the $f_+(0)$ and $|V_{cs}|^2$ factored out. By measuring the efficiency-corrected yield of $D^o \to K^-\mu^+\nu$ signal events relative to a reference state ($K^-\pi^+$) with a known branching fraction, $\mathcal{B}_{K\pi}$, observed in the same experiment with similar kinematic cuts, one can measure the branching fraction $\mathcal{B}_{K\ell\nu}$. This $\mathcal{B}_{K\ell\nu}$ can be combined with the D^o lifetime to form a decay width $\Gamma_{K\ell\nu}$. Finally, the integral expression for the decay width can be used to extract $f_+(0)$.

Table 6 gives a summary of the form factor and pole mass obtained in various experiments. Figure 34 shows excellent agreement between the experimental results. Figure 35 compares experimental results on $M_{\rm pole}$. Note that the more recent, high statistics data favors a pole mass which is lower (by $\approx 2\sigma$) than the spectroscopic pole mass.

It is important to point out that the pole mass determinations measure this parameter under the assumption of a pole form. As Fig. 36 shows, over the

[¶]In this measurement, the $f^-(q^2)/f_+(q^2)$ form factor ratio [see Eq. (11)] was set to the "mid-range" of theoretical expectations $f_-/f_+ \approx -1$. A small systematic error contribution due to uncertainty in this ratio was included.

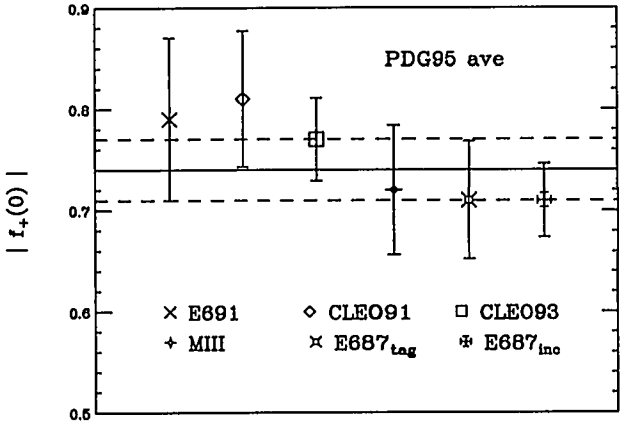


Figure 34: Comparison of the experimental results on $|f_+(0)|$. The weighted average and error are shown by the dashed and solid horizontal lines.

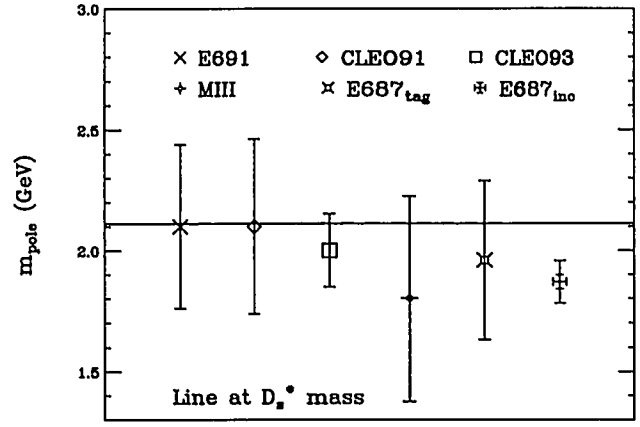


Figure 35: Comparison of the experimental results on $m_{\rm pole}$. The horizontal line is at the D_s^{*+} mass which is the expected pole mass value.

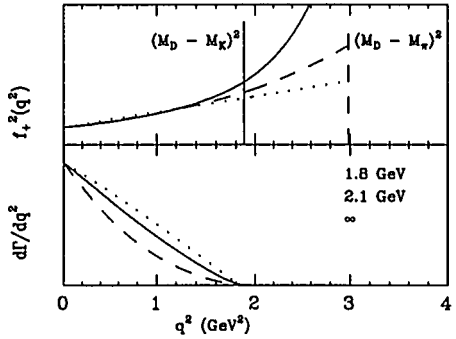


Fig. 36. Upper frame: $|f_+(q^2)|^2$ as a function of q^2 for various q^2 parameterizations which have been drawn to have the same slope and intercept at $q^2 \approx 0$. The kinematic limit for $D \to \overline{K}\ell^+\nu$ and $\pi\ell\nu$ are drawn with vertical dashed lines. The solid curve is the pole form; dashed is exponential; dotted is linear. Lower frame: $d\Gamma/dq^2$ as a function of q^2 for $D \to \overline{K}\ell^+\nu$ decay with three different pole masses. The dashed curve is for $m_{\rm pole} \to \infty$; the solid is for $m_{\rm pole} = 2.1\ GeV$ (the expected value); the dotted is for $m_{\rm pole} = 1.8\ GeV$. The influence of the pole mass on the overall q^2 dependence on $d\Gamma/dq^2$ is rather subtle over the kinematic range probed by $D \to \overline{K}\ell^+\nu$.

Table 6. $K\ell\nu$ form factor results.

Exp.	Mode	m_{pole}	$\mid f_+(0) \mid$
E691	$K^-e^+\nu_e$	$2.1^{+0.4}_{-0.3} \pm 0.2$	$0.79 \pm 0.05 \pm 0.06$
CLEO(91)	$K^-e^+\nu_e$	$2.1^{+0.4+0.3}_{-0.2-0.2}$	$0.81 \pm 0.03 \pm 0.06$
CLEO(93)	$K^-l^+\nu_l$	$2.00 \pm 0.12 \pm 0.18$	$0.77 \pm 0.01 \pm 0.04$
MKIII	$K^-e^+\nu_e$	$1.8^{+0.5+0.3}_{-0.2-0.2}$	$\mid V_{cs} \mid (0.72 \pm 0.05 \pm 0.04)$
E687	$K^-\mu^+\nu_\mu$ tag	$1.97^{+0.43+0.07}_{-0.22-0.06}$	$0.71 \pm 0.05 \pm .03$
E687	$K^-\mu^+\nu_\mu$ incl.	$1.87^{+0.11+0.07}_{-0.08-0.06}$	$0.71 \pm 0.03 \pm 0.02$

kinematic range accessible in $D \to \overline{K}\ell\nu$, a pole form q^2 dependence is nearly indistinguishable from an exponential or linear dependence. This is not true, however, for the decay $D \to \pi\ell\nu$ since the maximum q^2 range in this decay lies much closer to the spectroscopic pole. As Fig. 36 illustrates, over the limited q^2 range probed by the $\overline{K}\ell^+\nu$, the pole mass is essentially a measurement of the normalized slope $f_+^{-1}(0)\ df_+(q^2)/dq^2$. A real check of the pole parameterization in charm semileptonic decay must await a future, well-measured, high-statistics sample of $\pi\ell\nu$ decays.

Figure 37 compares the experimental average to several Quark Model and Lattice Gauge Theory predictions.[26] Agreement between theory and data are quite good. The recent calculations of the LANL (Los Alamos) group[26] which included a study of the q^2 dependence of the $f_+(q^2)$ form factor concluded that $m_{\rm pole} < M\,(D_s^{*+})$, in agreement with the recent trends of the data as shown in Fig. 35.

E687 (Ref. 24) has also presented the first experimental information on the f_- form factor which forms part of the hadronic weak current which is underlined in Eq. (19),

$$< D|J_\mu|K > \ = \ f_+(q^2)\ (D+K)_\mu + \underline{f_-(q^2)}\ (D-K)_\mu. \qquad (19)$$

As shown in Eq. (20), which gives a schematic rendering of partial width expression, the squared lepton mass multiplies the pure $|f_-(q^2)|^2$ as well as interference $2\ f_-(q^2)\ f_+(q^2)$ contributions. For the decay $D^o \to K^-\mu^+\nu$, the effects of $f_-(q^2)$ are to give very small gradients in the Dalitz plot intensity.

$$\frac{d^2\Gamma}{dq^2 dM^2_{K\ell}} = |f_+(q^2)|^2\ \mathcal{A} + \underline{M_\ell^2}\ \left(2\ f_-(q^2)\ f_+(q^2)\ \mathcal{B} + |f_-(q^2)|^2\ \mathcal{C}\right)$$
$$\mathcal{B} \propto M^2_{K\ell\ \rm max} - M^2_{K\ell}\ -\ \left(q^2 - q^2_{\rm min}\right)/2, \quad \mathcal{C} \propto q^2 - q^2_{\rm min}. \qquad (20)$$

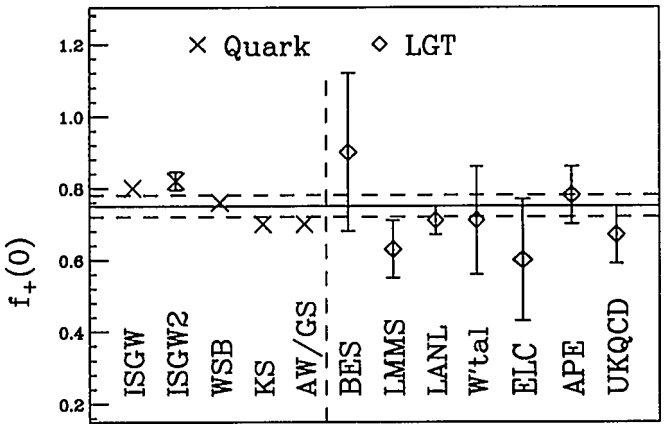


Fig. 37. Comparison of theoretical $f_+(0)$ predictions for $D \to \overline{K}\ell^+\nu$ to the world's data. The first points are quark-model estimates; the last are Lattice Gauge Theory calculations.

Of course, a small error in the m_{pole} parameter will induce a false competing gradient in the Dalitz plot along the q^2 axis by slightly changing the q^2 dependence of the $f_+(q^2)$ form factor. Figure 38 shows likelihood contours on f_-/f_+ versus m_{pole} based on the $\approx$ 430 event E687 sample of D^* tagged $D^o \to K^-\mu^+\nu$ events. From this contour, we conclude $f_-/f_+ = -1.3 \pm 3.5 \pm 0.6$, which is in good agreement with theoretical estimates.[21]

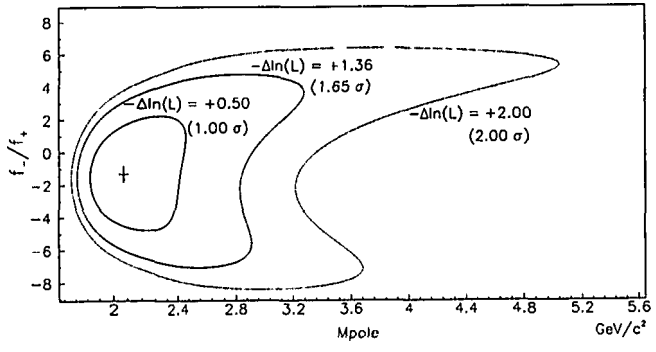


Fig. 38. Contours of constant likelihood for f_-/f_+ versus m_{pole} assuming that f_- and f_+ follow pole forms with the same pole mass. Note that the contour shape shows that a large f_-/f_+ ratio can be compensated by an increased value for m_{pole} which can be understood from Eq. (20) for the case where $|f_-(q^2)|^2 > 2\, f_-(q^2)\, f_+(q^2)$.

3.3.3 $D \to \pi\ell\nu$

As Fig. 39 shows, measurement of $D \to \pi\ell\nu$ / $D \to K\ell\nu$ would seem to provide useful information on the CKM ratio $|V_{cd}|^2/|V_{cs}|^2$. However, as illustrated in Fig. 40, (three-generation) unitarity of the CKM matrix along with experimental information on charm production by high-energy neutrinos on fixed targets and b decays from CLEO already provides V_{cd} measurements which are probably more accurate than the present ability to predict the $\pi\ell\nu/\overline{K}\ell\nu$ form factor ratio. For this reason, the principle motivation for studies of $D \to \pi\ell^+\nu$ decays is to test the ability of the QCD calculational tools to accurately predict the ratio of CKM

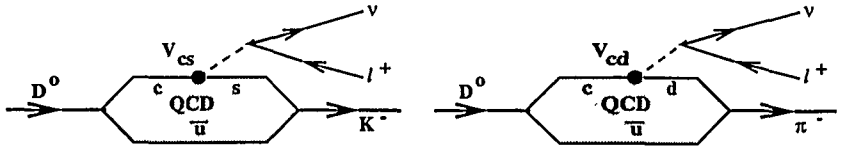


Fig. 39. Apart from possible QCD corrections, the difference between $D \to \pi\ell\nu$ and $D \to K\ell\nu$ are in the CKM matrix element couplings.

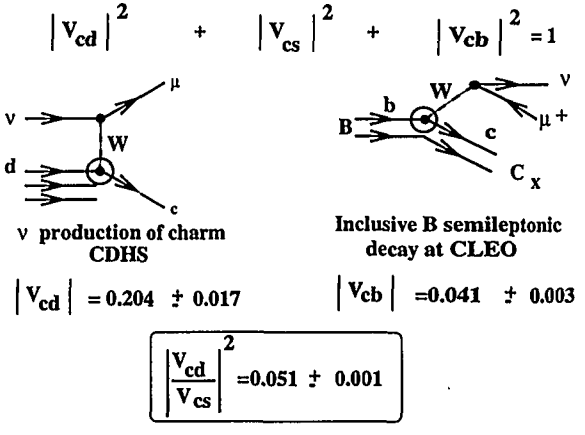


Fig. 40. V_{cd} can accurately be measured by studying the charmed particles produced from incident neutrinos interacting with d valence quarks. Neutrino experiments generally detect the semimuonic decays of charmed mesons. V_{cb} can be determined through measurements of lepton spectrum produced by B decay near threshold at CLEO.

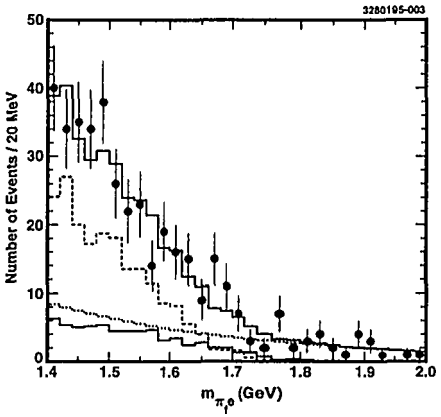


Fig. 41. CLEO $M_{e\pi}$ for events satisfying $M(D^*) - M(D) < 0.160$. The total fit to the $M_{e\pi}$ distribution is shown as a solid histogram. The contribution from backgrounds is shown as the dashed histogram.

favored over CKM suppressed form factors. One hopes that such calculations can ultimately be used to provide CKM information in the b sector.

Recent tagged $D^* \to (\pi^- \ell^+ \nu)\pi^+$ signals are shown in Figs. 41 (CLEO) and 42 (E687). Because the decay $D^o \to \pi^- \ell^+ \nu$ is CKM suppressed and therefore somewhat rare, background contamination is a major concern. In E687 (Ref. 28), a major source of background is $D^o \to K^- \ell^+ \nu$ where the kaon is misidentified by our Cherenkov system as a pion. Another important class of backgrounds involve semileptonic decays with missing (underlined) daughters such as $D^o \to K^{*-} \ell \nu$, $K^{*-} \to \underline{K^o}\pi^-$ or $D^o \to \rho^- \ell \nu$, $\rho^- \to \pi^- \underline{\pi^o}$. It is possible to significantly suppress missing daughter contributions by requiring a minimum hadron lepton-lepton mass value as illustrated by Fig. 43. The background $D^o \to K^- \ell^+ \nu$, $K^- \hookrightarrow \pi^-$, on the other hand, has a $\pi^- \ell^+$ invariant mass distribution which is nearly indistinguishable from that for $\pi^- \ell^+ \nu$ and will form a very similar peak in the $M(D^{*+}) - M(D^o)$ mass difference distribution. This means that there is no reasonable way of kinematically distinguishing between the signal and the $D^o \to K^- \ell^+ \nu$, $K^- \hookrightarrow \pi^-$ background. For this reason, we jointly fit the $M(D^{*+}) - M(D^o)$ mass difference histograms for both $K^- \ell^+ \nu$ and $\pi^- \ell^+ \nu$ by summing the binned log likelihoods from both distributions. The contribution of misidentified $D^o \to K^- \ell^+ \nu$ events into the $\pi^- \ell^+ \nu$

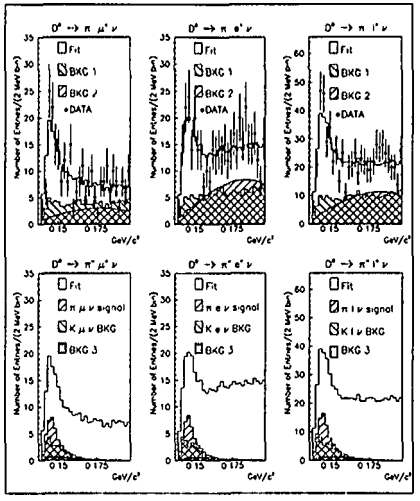


Fig. 42. E687 $M(D^*) - M(D)$ peaks for events satisfying the cut $M_{\ell\pi^-} > 1.1\ GeV$. The first column is $\pi^- \mu^+ \nu$ candidates, the second is for $\pi^- e^+ \nu$ candidates, and the third is the combined sample. In the legend: BKG1 is the background contribution for misidentified leptons, BKG2 is the background due to actual semileptonic D^o combined with random soft pions to form a false D^{*+}, and BKG3 are misidentified kaons from $D^o \to K^- \ell^+ \nu$.

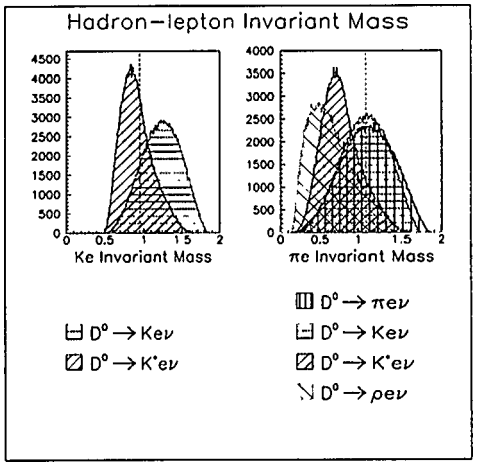


Fig. 43. Simulated hadron-lepton invariant mass distributions for the $D^o \to K^-\ell^+\nu$ signal (left) $D^o \to \pi^-\ell^+\nu$ signal (right) and several background contributions. Missing daughter type backgrounds typically peak below $M^2_{h\ell} < 1\ GeV^2$ and can be significantly reduced through the cut $M^2_{h\ell} > 1.1\ GeV^2$.

$M(D^{*+}) - M(D^o)$ mass difference histogram is proportional to the $D^o \to K^-\ell^+\nu$ signal yield and $K^- \hookrightarrow \pi^-$ misidentification probability, which was parameterized by studies of $D^{*+} \to D^o\pi^+ \to (K^-\pi^+)\pi^+$ which are misidentified in the data as $D^{*+} \to D^o\pi^+ \to (\pi^-\pi^+)\pi^+$ events.

Figure 44 illustrates an interesting systematic on the measurement of the $\pi^-\ell^+\nu/K^-\ell^+\nu$ branching ratio and form-factor ratio. Because the maximum $\sqrt{q^2}$ available in $D^o \to \pi^+\ell^-\nu$ lies only $\approx 300\ MeV$ below the expected D^{*+} pole mass, uncertainties in the effective pole mass‖ will cause significant variations in $|f_+(q^2)|^2$ which will cause intensity variations in the upper reaches of the $D^o \to \pi^-\ell^+\nu$ Dalitz plot. The $M_{\pi-\ell+}$ cut used to suppress daughters cuts off the q^2 range and thereby acts like a double-edged sword in measurements of $\pi^-\ell^+\nu/K^-\ell^+\nu$. The $M_{\pi-\ell+}$ cut exacerbates measurements of the relative branching fraction since one must extrapolate the number of $\pi^-\ell^+\nu$ below the $M_{\pi-\ell+}$ cut in order to measure the efficiency-corrected yield ratio of $\pi^-\ell^+\nu/K^-\ell^+\nu$ events

‖Perhaps several excited D_s^{**} states potentially contribute, or potentially there are contributions from complex cuts.

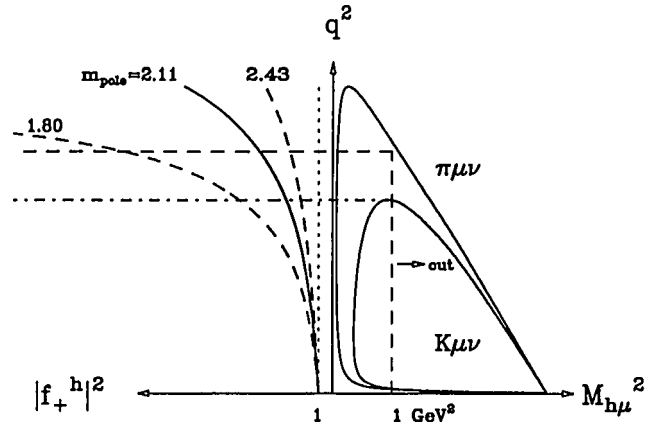


Fig. 44. We show Dalitz plots (right) and form factor variation (left) for several reasonable $m_{\rm pole}$'s. Because of its larger q^2 reach, the $\pi\ell\nu$ Dalitz plot extends into a q^2 range where the $m_{\rm pole}$ uncertainty becomes significant. The $M^2_{\pi-\ell+} > 1.1\ GeV^2$ cut eliminates the q^2 region beyond $2.3\ GeV^2$.

over the full Dalitz plot. The variation on the (full Dalitz plot) acceptance including the $M_{\pi-\ell+}$ cut as a function of $m_{\rm pole}$ is shown in Fig. 45.

By way of contrast, the $M_{\pi-\ell+}$ cut improves the pole mass systematic for the form factor ratio. This ratio follows from the corrected yields of $\pi\ell\nu$ and $K\ell\nu$ events which satisfy the $M_{\pi-\ell+}$ cut according to Eq. (21)

$$\frac{Y_{\pi\ell\nu}}{Y_{K\ell\nu}} = \frac{|V_{cd}\ f_+^\pi(0)|^2}{|V_{cs}\ f_+^K(0)|^2} \frac{\int dq^2\ |f_+^\pi(q^2)/f_+^\pi(0)|^2\ \mathcal{H}^\pi(q^2)}{\int dq^2\ |f_+^K(q^2)/f_+^K(0)|^2\ \mathcal{H}^K(q^2)},$$

where
$$\mathcal{H}^{(h)}(q^2) = \int_{M^2_{h\ell}\ \rm cut}^{M_D^2} dM^2_{h\ell}\ \ \epsilon(q^2, M^2_{h\ell})\ \ \left(\frac{d^2\Gamma}{dq^2 dM^2_{h\ell}}\right)_{f_+^{(h)}(q^2)=1}. \qquad (21)$$

The integrals of Eq. (21) are only over the q^2 range satisfying the $M^2_{h\ell}$ cut which limits them to regions farther from the expected $m_{\rm pole}$. The kernels under the integral of Eq. (21) are plotted in Fig. 46. Figure 47 shows the dependence of the final measured form factor × CKM ratio on $m_{\rm pole}$ or alternatively on a linear q^2 parameterization.

Experimental results[27–29] on the $\pi^-\ell^+\nu/K^-\ell^+\nu$ form factor and branching ratio are compared to predictions[30] in Figs. 48 and 49. Agreement between the measured form factor ratios and their predictions is satisfactory.

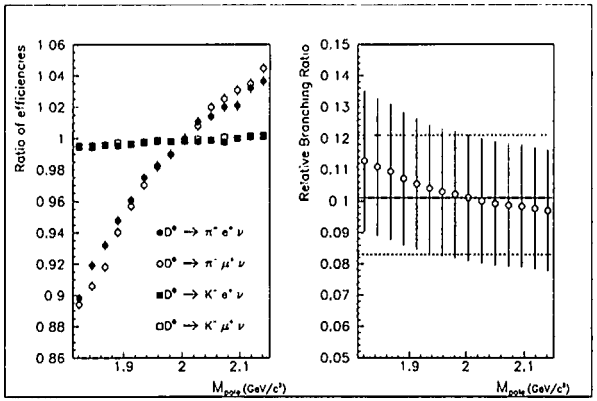


Fig. 45. The $\epsilon(M^2_{h\ell} > 1)$ cut varies by 15% for $\pi\ell\nu$. ϵ for $\overline{K}\ell\nu$ varies much less since its q^2 reach is much smaller.

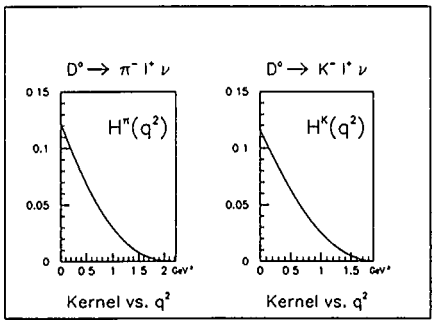


Fig. 46. $\mathcal{H}^\pi$ (left) and $\mathcal{H}^K$ (right). Our CKM-ff ratio is essentially the ratio of the weighted $<>_{\mathcal{H}}$'s over these functions.

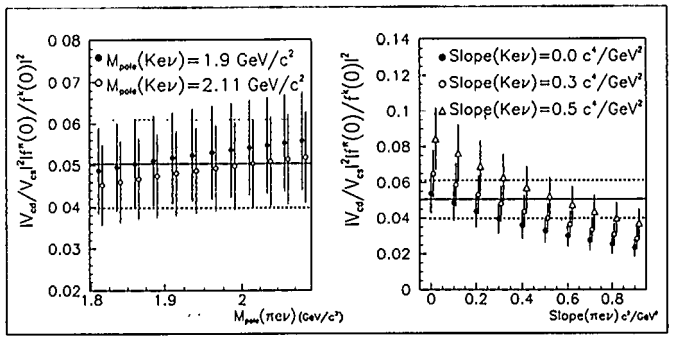


Fig. 47. CKM-ff ratio vs q^2 dependence of f_+^π and f_+^K. (Left) pole and (right) linear. $f_+(q^2) = f_+(0)\ (1 + a\ q^2)$. "Reasonable" choices give $\approx 10\%$ variation.

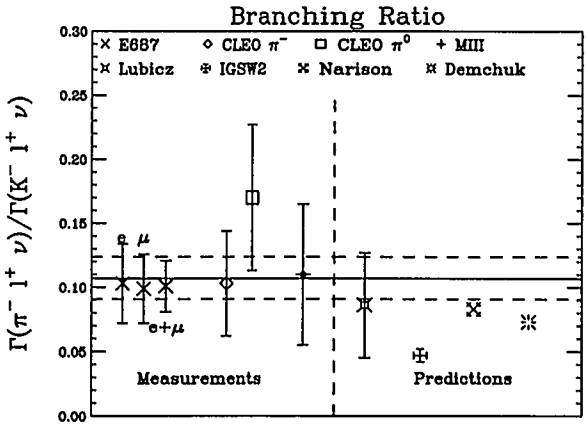


Fig. 48. An informal weighted average gives $\Gamma\,(\pi^-\ell^+\nu)\,/\Gamma\,(K^-\ell^+\nu) = 0.11 \pm 0.02$. The data slightly exceeds the predictions.

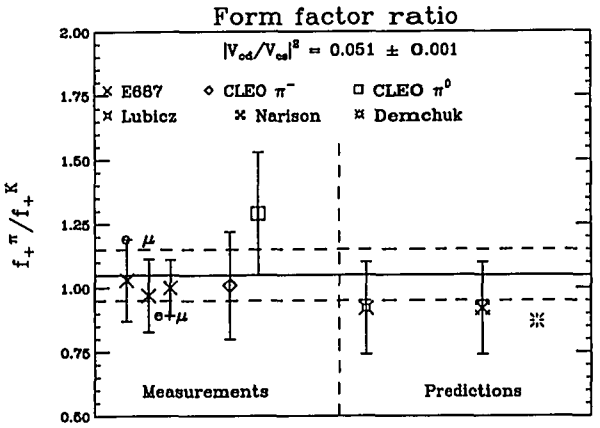


Fig. 49. An informal weighted average of the form-factor ratio is $|f_+^\pi/f_+^k| = 1.05 \pm 0.095$ (assuming $|V_{cd}/V_{cs}|^2 = 0.051$). The predictions are in reasonably good agreement with the prediction.

3.3.4 $D^+ \to K^{*0}\mu^+\nu$

This decay is one of the oldest and cleanest charm semileptonic decays. In fixed-target experiments, one begins with a detached vertex which contains the $K^-\pi^+\mu^+$ charged tracks. As Fig. 50 shows, the $K^-\pi^+$ mass distribution suggests that the four-body decay $D^+ \to K^-\pi^+\mu^+\nu$ is strongly dominated by the quasi-three-body process $D^+ \to K^{*0}\mu^+\nu$. By fitting the $M\,(K^-\pi^+)$ versus $M\,(K^-\pi^+\mu^+)$ for the detached events, E687 (Ref. 24) obtained the limit on nonresonant $D^+ \to K^-\pi^+\mu^+\nu$ decays given by Eq. (22),

$$\frac{\Gamma(K^-\pi^+\mu^+\nu)_{\rm nr}}{\Gamma(\{K^-\pi^+\}_{892}\,\mu^+\nu)} = 0.083 \pm 0.029 \;<\; 0.12\ {}_{90\%\ \text{C.L.}} \qquad (22)$$

The fact that the $\overline{K^*}$ is a vector particle significantly complicates the Lorentz structure of the weak current $< D^+|J_W|\overline{K^*} >$ which is now described by three q^2 dependent form factors ($A_1(q^2)$ $A_2(q^2)$ $V(q^2)$) (two axial and one vector).** The ratio of the form factors controls the decay angular distribution as illustrated in Fig. 51. Once the R_v and R_2 shape variables are determined, one can measure the overall scale of $A_1(q^2)$ from the decay width in a way highly analogous

**Experimentalists generally analyze their data assuming that the q^2 dependence of these form factors are of the pole form with the D_s^{*+} and D_s^{**+} poles.

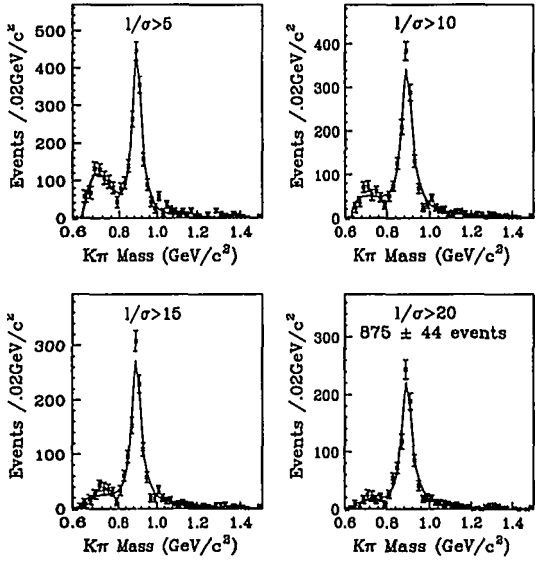


Fig. 50. The subtracted $K^-\pi^+$ invariant mass plot for $D^+ \to K^-\pi^+\mu^+\nu$ events from E687. The right sign–wrong sign subtraction tends to eliminate noncharm background. Increasing the ℓ/σ cut eliminates the low mass $D^{*+} \to (K^-\mu^+\nu)\pi^+$ bump, leaving a $K^-\pi^+$ mass distribution dominated by $\overline{K^*}(892)$.

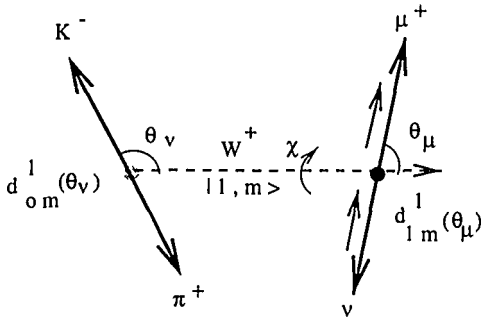


Fig. 51. The three form factors control the q^2 dependence of the virtual W^+ polarization. The spin states of the leptons favored by $V-A$ are shown. The three decay angles are θ_μ describing the virtual $W^+ \to \mu^+\nu$ decay in its rest frame, θ_v describing the $\overline{K}^{*0} \to K^-\pi^+$ in the $\overline{K^*}$ rest frame, and the acoplanarity, χ, between the W and $\overline{K^*}$ decay planes. The decay distribution $d^4\Gamma/\left(d\cos\theta_\mu d\cos\theta_v dq^2 d\chi\right)$ serves to measure $R_v = V(0)/A_1(0)$ and $R_2 = A_2(0)/A_1(0)$.

to the use of Eq. (18). Figures 52 and 53 compare the experimental data to theoretical predictions[26] for both the form factor ratios and $A_1(0)$. Since the initial predictions for the $f_+(q^2)$ form factor which governs $D^o \to K^-\ell^+\nu$ was in good agreement with experimental data, whereas Fig. 53 shows initially the $A_1(q^2)$ which sets the scale of $\Gamma\left(D^+ \to \overline{K^{*o}}\ell^+\nu\right)$ was overpredicted by $\approx \sqrt{2}$, the ratio $\Gamma\left(D_+ \to \overline{K^{*o}}\ell^+\nu\right)/\Gamma\left(D^0 \to K^-\ell^+\nu\right)$ was initially predicted to be a factor of two larger than the measured value of $< \Gamma_{\overline{K^*}\ell\nu}/\Gamma_{\overline{K}\ell\nu} >= 0.56 \pm 0.05$. As Fig. 53 shows, this apparently serious discrepancy with the predictions for A_1 is beginning to fade away as the recent LGT predictions are becoming available. Finally, the recently revised ISGW2 quark model[31] computes $\Gamma_{\overline{K^*}\ell\nu}/\Gamma_{\overline{K}\ell\nu} = 0.54$, which is in excellent agreement with the experimental value.

3.4 Polarization in Charm Baryon Decay

The CLEO and ARGUS Collaborations have studied both semileptonic decay processes such as $\Lambda_c^+ \to \Lambda\ell^+\nu$, and hadronic decay processes such as $\Lambda_c^+ \to \Lambda\pi^+$, and find in either case that the daughter Λ emerges with a spin which is nearly 100% left-handed (when viewed in the Λ_c^+ rest frame). This effect has also been observed in the decays $\Xi_c^o \to \Xi^-\pi^+$. Figure 54 gives an illustration of the effect

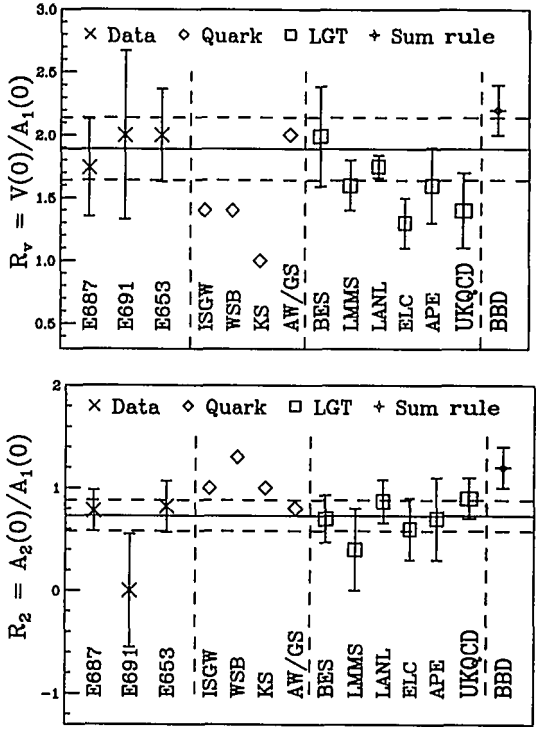


Fig. 52. Experimental averages compared to theoretical prediction for the form factor ratios $R_v = V(0)/A_1(0)$, $R_2 = A_2(0)/A_1(0)$. The horizontal lines give the average of the data. The Lattice Gauge predictions are in good agreement with the data.

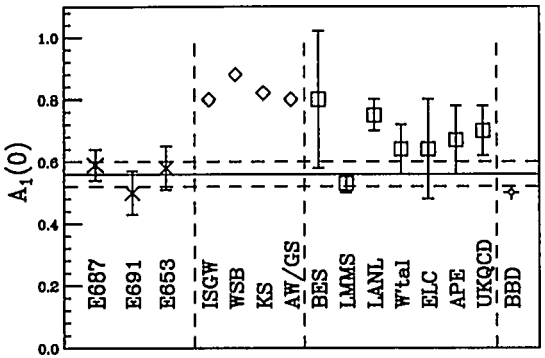


Fig. 53. Experimental averages compared to theoretical predictions for the $A_1(0)$ form factor. The points are in rough chronological order. The earliest quark model points were about 40% higher than the data. The more recent LGT points are in much closer agreement with experiment.

for the case of $\Lambda_c^+ \to \Lambda \ell^+ \nu$ with $\Lambda \to p\pi^-$. The observation of a nearly left-handed daughter baryon in charm decay can be predicted using HQET. Although HQET plays a dramatic role in understanding b-sector physics, to my knowledge, the charmed baryon polarization effect along with the predicted spectroscopy of excited charmed mesons and baryons are the main applications of HQET in the charm sector.

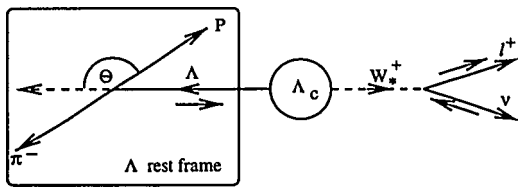


Fig. 54. When viewed in the Λ_c^+ rest frame, the daughter Λ emerges predominantly left-handed, *e.g.*, spinning against its momentum vector. I also indicate the preferred spin directions of the final state leptons in a $V-A$ decay. The Λ can be thought of as self-analyzing in the sense that in the decay $\Lambda \to p\pi^-$, the proton emerges primarily along the Λ spin direction when viewed in the Λ rest frame. See Fig. 55 as well.

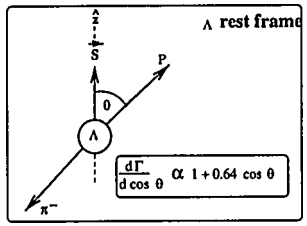


Fig. 55. We view the decay $\Lambda \to p\pi^-$ in the rest frame of a Λ and orientate our $\hat{z}$ axis to be along the Λ spin direction. The polar angle distribution for the proton daughter is of the form $d\Gamma/d\cos\theta \propto 1 + 0.64\cos\theta$. The asymmetry of 0.64 is sometimes called the analyzing power.

We begin by a discussion of the semileptonic decay results. Figure 56 shows the basic semileptonic process. The signature for baryon semileptonic decays is an

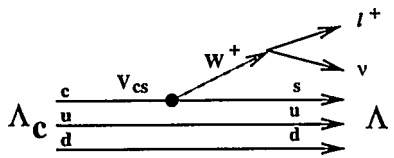


Fig. 56. In the decay $\Lambda_c^+ \to \Lambda \ell^+ \nu$, the daughter baryon is produced along with an ℓ^+ (right sign) rather than an ℓ^- (wrong sign).

excess of right-sign compared to wrong-sign leptons being produced along with the daughter hyperon as illustrated in Fig. 57. One can assign q^2 dependent, helicity form factors for the four ways of assigning spin to the virtual W^+ and daughter Λ which are illustrated by Fig. 58. We can define a Λ polarization asymmetry by Eq. (23). By this definition, $\alpha_{\Lambda_c} = -1$ implies a 100% left-handed daughter Λ.

$$\alpha_{\Lambda_c} = \frac{\Uparrow - \Downarrow}{\Uparrow + \Downarrow} \quad \text{where} \quad \begin{array}{l} \Uparrow \text{ means } \vec{S}_\Lambda \parallel \vec{\Lambda} \\ \Downarrow \text{ means } \vec{S}_\Lambda \parallel -\vec{\Lambda} \end{array}. \tag{23}$$

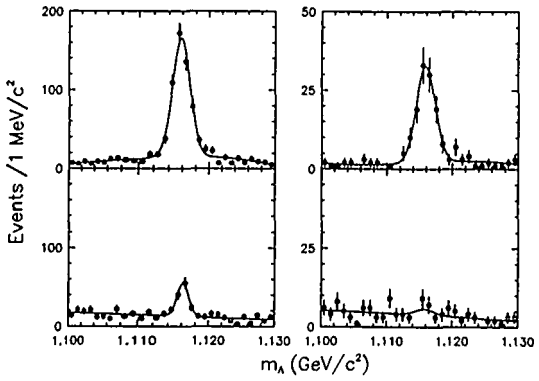


Fig. 57. CLEO right-sign and wrong-sign $\Lambda \to p\pi^-$ signals against an $e^\pm$ (left) or $\mu^\pm$ (right). More $\Lambda\ell^+$ events (top) are seen than $\Lambda\ell^-$ (bottom).

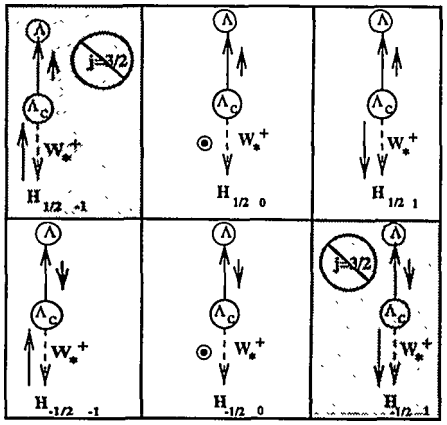


Fig. 58. Four q^2 dependent helicity amplitudes describe this decay. Two of the six possible spin alignments for the spin 1 virtual W^+ and spin 1/2 Λ cannot be produced through the decay of a spin 1/2 Λ_c^+.

Adding together the helicity possibilities shown in Fig. 58, we obtain Eq. (24).

$$\alpha_{\Lambda_c} = \frac{\left(|H^{q^2}_{\frac{1}{2}\,0}|^2 + |H^{q^2}_{\frac{1}{2}\,1}|^2\right) - \left(|H^{q^2}_{-\frac{1}{2}\,-1}|^2 + |H^{q^2}_{-\frac{1}{2}\,0}|^2\right)}{\left(|H^{q^2}_{\frac{1}{2}\,0}|^2 + |H^{q^2}_{\frac{1}{2}\,1}|^2\right) + \left(|H^{q^2}_{-\frac{1}{2}\,-1}|^2 + |H^{q^2}_{-\frac{1}{2}\,0}|^2\right)}. \tag{24}$$

HQET[32] applied to heavy $\to$ light quark transitions such as in charm decay are used to relate these four independent form factors to just two whose ratio $R = f_1/f_2$ controls the q^2 dependence of α_{Λ_c}.†† Angular momentum leads to an additional restriction as $q^2 \to 0$ which is independent of HQET. Figure 59 illustrates the fact that as $q^2 \to 0$, the leptons become collinear and form a spinless system, and only $J_z = 0$ W_*^+'s are formed. In this limit, only two of the four helicity form factors survive this limit. Combining both the angular momentum and HQET restriction, one has the prediction that $\alpha_{\Lambda_c} = -1$ as $q^2 \to 0$, independent of the form factor ratio R. Figure 60 illustrates the predictions of the polarization

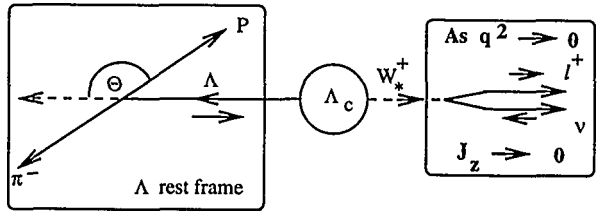


Fig. 59. As $q^2 \to 0$, the ℓ^+ and ν become collinear. By the $V-A$ rules, the neutrino is left-handed and the ℓ^+ becomes right-handed, and their spins cancel. Hence, only $H^{q^2}_{\frac{1}{2}\,0}$, $H^{q^2}_{-\frac{1}{2}\,0} \neq 0$ as $q^2 \to 0$.

asymmetry predicted in the Körner and Krämer model[32] for various values of the form factor ratio R. For the case of heavy $\to$ heavy transitions such as one would get in b-baryon decays, the four form factors are reduced to just one, and thus $\alpha_{\Lambda_b} = -1$ at all q^2.

Rather than going to the $q^2 \to 0$ limit in $\Lambda_c^+ \to \Lambda\ell^+\nu$ decays to form a $J_z(W_*^+) \to 0$, one could directly couple the W_*^+ to a π^+ as illustrated in Fig. 61.

††The two HQET allowed form factors, f_1 and f_2, are generally assumed to have the same q^2 dependence.

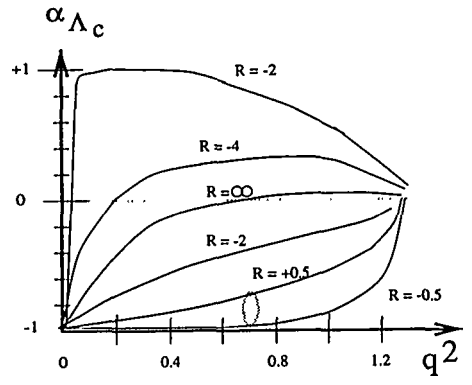


Fig. 60. A crude sketch of the Körner and Krämer predictions for α_{Λ_c} versus q^2 for various form factor ratios. The shaded region is relevant to $\Lambda_c^+ \to \Lambda\ell^+\nu$. Note $\alpha_{\Lambda_c} \to -1$ as $q^2 \to 0$ independent of the form factor ratio R. The basic prediction is that $\alpha_{\Lambda_c} \approx -1$.

Again, for this case of these nonleptonic charm baryon decays, angular momentum conservation combined with HQET applied to heavy $\to$ light transitions predicts a nearly complete left-handed daughter baryon polarization. These results can

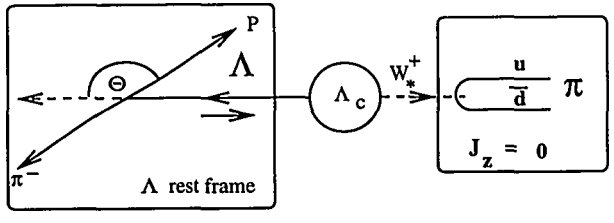


Fig. 61. For $\Lambda_c^+ \to \Lambda\pi^+$, $q^2 = m_\pi^2 \to 0$, HQET predicts $\alpha_{\Lambda_c} = -1$.

be extended to the decay $\Xi_c^o \to \Xi^-\pi^+$ where the hyperon daughter subsequently decays via $\Xi^- \to \Lambda\pi^-$. The Ξ^- decay is also self-analyzing with the Λ following a polar angle distribution of the form $(d\Gamma/d\cos\Theta)_\Lambda \propto 1 - 0.46\cos\Theta$. Figures 62 and 63 show acceptance-corrected polar distributions for the $\Lambda \to p\pi^-$ and $\Xi^- \to \Lambda\pi^-$ from $\Lambda_c^+ \to \Lambda\ell^+\nu$ and $\Xi_c^o \to \Xi^-\pi^+$ decays obtained by the CLEO Collaboration.

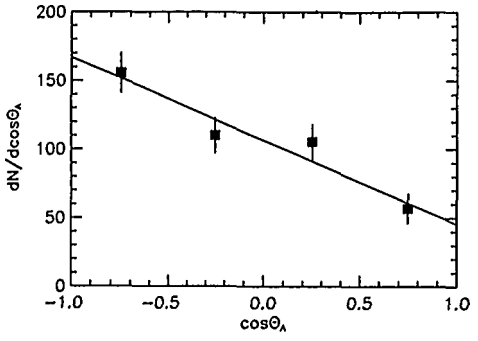


Fig. 62. CLEO's acceptance-corrected measurement of the proton polar angle distribution in the Λ rest frame with respect to the Λ helicity axis for $\Lambda_c^+ \to \Lambda\ell^+\nu$ decays. The Λ helicity axis points against the momentum of the Λ_c^+ when viewed in the Λ rest frame. The slope of this line divided by the Λ analysis power of 0.64 gives $\alpha_{\Lambda_c} \approx -1$.

Figure 64 summarizes the polarization asymmetry obtained for various charmed baryon decay modes. In each case, the asymmetry is consistent with a 100% left-handed polarization as predicted by HQET.

3.5 Nonleptonic Charm Decays

One can profitably study nonleptonic charm decays on several levels. On the most inclusive level, the rough order of magnitude difference between the charm particle lifetimes, discussed in Sec. 3.1, primarily reflects differences in the nonleptonic decay width. The semileptonic width is a small fraction of the total width in the first place, and secondly, although the semileptonic widths of the various charmed particles are not expected to be universal, Table 5 tells us that these widths are expected to be roughly the same.

On the next level of inclusiveness, one can study the partial decay widths of charm mesons into specific two-body final states. Factorization models have been proposed which predict the partial decay widths of two-body decays of charmed

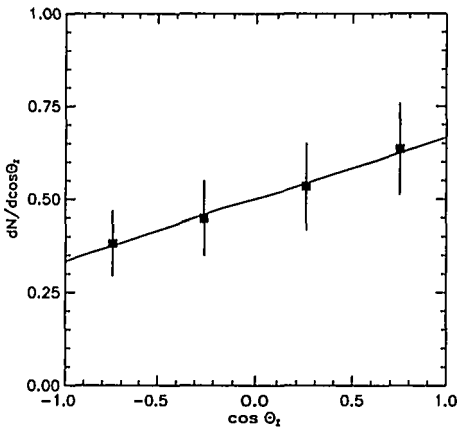


Fig. 63. CLEO's acceptance-corrected measurement of the Λ polar angle distribution in the Ξ^- rest frame with respect to the Ξ^- helicity axis in $\Xi_c^o \to \Xi^-\pi^+$ decays. The slope of this line divided by the Ξ^- analysis power of -0.46 gives $\alpha_{\Xi_c^o} \approx -1$.

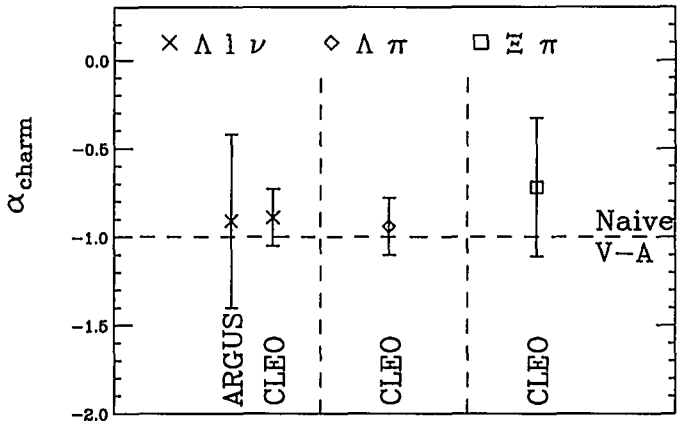


Fig. 64. The polarization asymmetry of the daughter hyperon observed for the charmed baryon decays studied thus far. The horizontal dashed line gives the $V-A$ left-handed helicity predicted by HQET.

mesons in the absence of final-state interactions. Final-state interaction effects become apparent in the interference between the various isospin amplitudes which contribute to different charged variants of a given final state. The simplest experimental tests of factorization involve pure two-body decays of charmed mesons into two pseudoscalar final states involving kaons and pions.

One can extend factorization tests to quasi-two-body decays such as pseudoscalar-vector decays as well as vector-vector decays by analyzing the resonance structure in multibody, nonleptonic, charmed meson decays. Experience has shown that the data is best fit by models where the various resonant channels contribute coherently to a decay amplitude, and thus, interfere in the differential decay width. These amplitude analyses provide additional handles on final-state interaction effects through interference of the amplitudes describing competing resonant channels in, *e.g.*, a three-particle decay Dalitz plot.

The factorization framework, in which nonleptonic charm decays have been traditionally analyzed, begins with an effective Hamiltonian such as that given by Eq. (25) describing CKM-allowed decays:

$$\mathcal{H} = \frac{G_f}{\sqrt{2}} V_{cs}^* V_{ud} \Big(\frac{C_+ + C_-}{2} (\,\bar{u}\, d)\,(\bar{s}\, c\,) + \frac{C_+ - C_-}{2} (\,\bar{s}\, d)\,(\,\bar{u}\, c) \Big). \qquad (25)$$

The Hamiltonian of Eq. (25) incorporates QCD corrections to the underlying weak decay process through the use of renormalization group methods. The coefficients $C_\pm$ are called "Wilson coefficients." In the absence of QCD corrections, $C_+ = C_-$, and one recovers a single weak process corresponding to the familiar spectator diagram of Fig. 65. The Wilson coefficients depend on the scale of the QCD-coupling

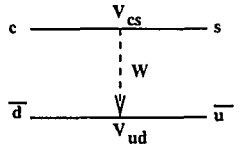


Fig. 65. When $C_+ = C_-$, the second term of Eq. (25) disappears, and one has the CKM spectator diagram.

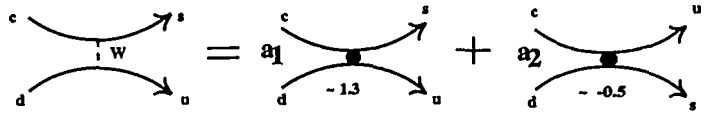


Fig. 66. The effective charged current whose amplitude $a_1 \approx (C_+ + C_-)/2$ (with a small color correction) describes the familiar spectator process. The effective neutral current process, with an amplitude $a_2 \approx (C_+ - C_-)/2$ which decreases as $M_Q \to \infty$, gives rise to nonspectator effects which are important in charm but less so in beauty.

constants. When taken at the charmed quark mass, the Wilson coefficients have the values given by Eq. (26)

$$\frac{C_+(M_Q) + C_-(M_Q)}{2} \approx 1.25\,, \quad \frac{C_+(M_Q) - C_-(M_Q)}{2} \approx -0.49. \qquad (26)$$

In 1987, Bauer, Stech, and Wirbel (BSW)[33] combined these ideas into an explicit model which applied two-body and quasi-two-body nonleptonic charmed meson decay. In the BSW model, the two terms of Eq. (25) are organized into an effective "charged" current and effective "neutral current" between the parent and daughter hadrons as illustrated in Fig. 66. If a given nonleptonic charm decay can only proceed through the effective charged current interaction, it is classified as a Class 1 process. Class 2 processes only proceed through the effective neutral current interactions. Class 3 processes have contributions from both interactions. In the process, $D^o \to K^-\pi^+$, illustrated by Fig. 67, one has a neutral parent and two charged daughters, and hence, this must be a Class 1 process. In the Class 2 process, $D^o \to \overline{K^o}\pi^o$, illustrated by Fig. 68, one has neutral parent D^o decaying into two neutral daughters. The CKM-allowed decays of the D^+ such as $D^+ \to \overline{K^o}\pi^+$, depicted in Fig. 69, are Class 3 processes.

According to the Watson theorem, the weak amplitudes predicted in factorization models such as BSW must all be relatively real. However, the final-state hadrons can continue to interact via long-range strong interactions and acquire complex phases. These final state interactions (FSI) can be accommodated by multiplying the bare (weak) amplitudes by the square root of a complex, unitary S matrix describing the strong rescattering. To illustrate the effects of FSI,

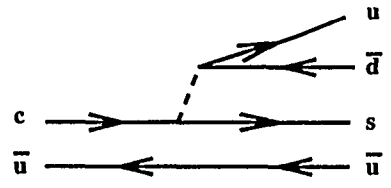


Fig. 67. In the BSW model, the amplitude for this decay is written as $a_1\, G_f\, 2^{-1/2} \; < \pi^+|(\bar{u}d)|0 >< K^-|(\bar{s}c)|D^o >= a_1\, G_f\, 2^{-1/2}\, (-if_\pi P_\pi) \times f_+(m_\pi^2)$. The coupling of the π^+ with respect to the virtual W^+ involves the same current as the leptonic decay $\pi^+ \to \ell^+\nu$ which is proportional to the pion-lepton decay constant. The CKM-allowed current which describes the process $D^o \to W^{+*}\, K^-$ is the same current involved in the semileptonic decay process $D^o \to K^-\ell^+\nu$ which is described by the form factor $f_+(q^2)$.

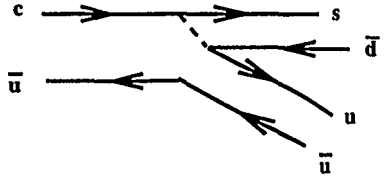


Fig. 68. In the BSW model, the amplitude for this decay is written as $a_2\, G_f\, 2^{-1/2} \; < \overline{K^o}|(\bar{s}d)|0 >< \pi^o|(\bar{u}c)|D^o >$ where again the currents involve the leptonic and semileptonic form factors. Note that the light $\bar{u}$ constituent of the D^o does not spectate as is the case in Fig. 67, but is actively rearranged into the final-state hadron.

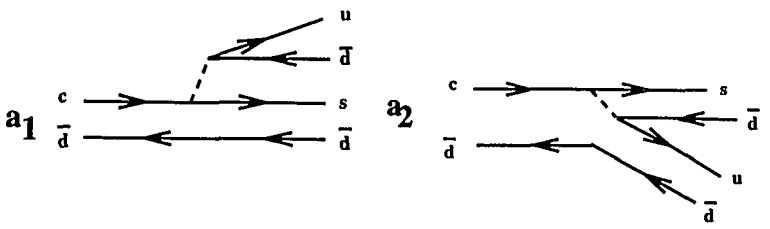


Fig. 69. The two processes depicted in the figure differ by the exchange of $\bar{d}$ quark fermion in the final state. Because a_1 and a_2 interfere with the opposite sign, one generally has destructive interference for D^+ decays which causes the D^+ to have a longer life than the D^o.

consider the isospin classification of three amplitudes related to $D \to \pi\pi$ decay:

$$A(D^o \to \pi^-\pi^+) = \frac{1}{\sqrt{3}}\left(\sqrt{2}\, a_o + a_2\right)$$

$$A(D^o \to \pi^o\pi^o) = \frac{1}{\sqrt{3}}\left(-a_o + \sqrt{2}\, a_2\right) \quad , \quad A(D^+ \to \pi^o\pi^+) = \sqrt{\frac{3}{2}}\, a_2. \qquad (27)$$

The measured a_o and a_2 amplitudes will acquire complex phases through the FSI S matrix as indicated in Eq. (28)

$$\begin{pmatrix} a_0 \\ a_2 \end{pmatrix} = \begin{pmatrix} \eta\, e^{2i\delta_0} & i\sqrt{1-\eta^2}e^{i(\delta_0+\delta_2)} \\ i\sqrt{1-\eta^2}e^{i(\delta_0+\delta_2)} & \eta\, e^{2i\delta_2} \end{pmatrix}^{1/2} \begin{pmatrix} a_0 \\ a_2 \end{pmatrix}_{\text{bare}}. \qquad (28)$$

Since QCD respects isospin symmetry, there should be no mixing between a_o and a_2, which means the elasticity parameter in Eq. (28) should be $\eta = 1$.‡‡ Even a purely elastic FSI can change the total width of charm decays into a particular final state by changing the value of $\cos(\delta_2 - \delta_0)$ when converting, *e.g.*, $A(D^o \to \pi^-\pi^+)$ into $\Gamma(D^o \to \pi^-\pi^+)$ via Eq. (29)

$$\Gamma(\pi^+\pi^-) = \frac{2}{3}\,|a_o|^2 + \frac{1}{3}\,|a_2|^2 + \frac{2\sqrt{2}}{3}|a_o|\,|a_2|\,\cos(\delta_2 - \delta_0). \qquad (29)$$

‡‡One can still have, however, inelastic final state interactions between final states such as $D \to \pi\pi$ and $D \to KK$ since a dipion final state can potentially scatter into a dikaon final state. One could accommodate such a case with a 4×4 matrix describing the two isospin amplitudes for the dipion and two isospin amplitudes for the dikaon.

The unexpectedly large branching ratio for the decay $D^o \to K^+K^-/\pi^+\pi^-$ provided an early example of the possible role of FSI affecting branching ratios. Table 7 summarizes recent data on $\Gamma(K^+K^-)/\Gamma(\pi^+\pi^-)$. As one can see from

Table 7. $\Gamma(D^o \to K^+K^-)/\Gamma(D^o \to \pi^+\pi^-)$.

E687 (Ref. 34)	WA82 (Ref. 35)
$2.53 \pm 0.46 \pm 0.19$	$2.23 \pm 0.81 \pm 0.46$
E691 (Ref. 36)	CLEO (Ref. 37)
$1.95 \pm 0.34 \pm 0.22$	$2.35 \pm 0.37 \pm 0.28$

Table 7, although both processes are CKM suppressed by the same amount and $D^o \to \pi^+\pi^-$ is favored by having a larger phase space, $D^o \to K^+K^-$ occurs at roughly twice the rate as $D^o \to \pi^+\pi^-$. Since these decays were the first CKM-suppressed decays to be studied, their width ratio was initially quite surprising. In the context of the BSW model, both decays are Class 1 processes, since no effective neutral currents are possible between the parent and either daughter, and the BSW model makes the prediction $\Gamma(K^+K^-)/\Gamma(\pi^+\pi^-) \approx 1.4$ independent of the Class 2 normalization. Conventional wisdom has it that discrepancy between the data and the BSW prediction is due to FSI changing the phase of interfering dipion or dikaon isospin amplitudes.

A more direct way of seeing the effects of final-state interactions is to measure the widths into various isospin-related channels such as $\Gamma(\pi^+\pi^-)$, $\Gamma(\pi^o\pi^o)$, and $\Gamma(\pi^+\pi^o)$, and extract a_0, a_2, and $\cos(\delta_2 - \delta_0)$ by solving Eq. (29) and the two similar equations. Table 8 taken from the upcoming *Annual Review* article by Pedrini, Browder, and Honschied[38] summarizes the results of such isospin analyses for many two-body and quasi-two-body charm decays. Table 8 shows that more often than not, a considerable phase shift is observed between the two isospin amplitudes. Watson's theorem tells us that phase shifts between interfering isospin amplitudes where $\sin(\delta_{I'} - \delta_I) \neq 0$ cannot arise from the weak processes alone and thus constitute direct evidence for FSI.

Several groups[40–43] have gone a step further and published resonant amplitude analyses of particular final states. Most of this work concerns three-body decays where all of the amplitude information resides in the Dalitz plot. Amplitude analyses allow one to extend factorization model tests to pseudoscalar-vector

Table 8. Isospin amplitude ratios and phase shifts for two-body charm decays.

Mode	Ratio of amplitudes	$\delta = \delta_I - \delta_{I'}$
$K\pi$	$\lvert A_{1/2}\rvert/\lvert A_{3/2}\rvert = 4.12 \pm 0.40$	$88° \pm 8°$
$K^*\pi$	$\lvert A_{1/2}\rvert/\lvert A_{3/2}\rvert = 5.23 \pm 0.59$	$90° \pm 16°$
$K\rho$	$\lvert A_{1/2}\rvert/\lvert A_{3/2}\rvert = 3.22 \pm 0.64$	$10° \pm 47°$
$K^*\rho$	$\lvert A_{1/2}\rvert/\lvert A_{3/2}\rvert = 4.93 \pm 1.95$	$33° \pm 57°$
KK	$\lvert A_1\rvert/\lvert A_0\rvert = 0.58 \pm 0.12$	$47° \pm 13°$
$\pi\pi$	$\lvert A_2\rvert/\lvert A_0\rvert = 0.63 \pm 0.13$	$81° \pm 10°$

and vector-vector nonleptonic decays of D mesons and provide new ways of studying FSI effects. A particularly clean and instructive example is provided by the E687 (Ref. 43) group's analysis of the $D^+, D_s^+ \to K^-K^+\pi^+$ final state. Mass histograms and the two Dalitz plots are shown in Fig. 70.

The D_s^+ Dalitz plot is dominated by the $\phi\pi^+$ and $\overline{K}^{0*}K^+$ channels, while the D^+ also has a significant contribution from a single or multiple broad resonances. We note that both the ϕ and $\overline{K}^*$ bands have a node due to angular momentum conservation in the center of each band as illustrated in Fig. 71. In order to extract information from Dalitz plots such as those illustrated in Fig. 70, the experimental groups fit the intensity across a Dalitz plot to a coherent sum of quasi-two-body or possible nonresonant contributions. For example, one can fit the D_s^+ Dalitz plot to the form $d^2\Gamma/(dM_1^2 dM_2^2) \propto |\mathcal{A}(D_s^+ \to K^+K^-\pi^+)|^2$, where the amplitude is given by Eq. (30)

$$\mathcal{A}(D_s^+ \to K^+K^-\pi^+) = a_{\overline{K}^*}\, e^{i\delta_{\overline{K}^*}} \mathcal{M}(\pi^+K^-K^+|\overline{K}^{*0}\, K^+) + a_\phi\, e^{i\delta_\phi} \mathcal{M}(K^+K^-\pi^+|\phi\pi^+) + \ldots . \quad (30)$$

Figure 72 illustrates the form of one of these quasi-two-body contributions. Each resonant channel contribution is multiplied by a complex amplitude coefficient whose modulus serves as a gauge to the relative "importance" of the channel.*

*In fitting to the shape of the relative event density across the Dalitz plot, one of the fitted amplitude factors is generally set to unity and serves as a reference channel. Clearly, since one is fitting to $|\mathcal{A}|^2$, the overall phase of $\mathcal{A}$ cannot be measured. The modulus of the reference amplitude can be determined if desired through the total decay width in a way similar in spirit to Eq. (18).

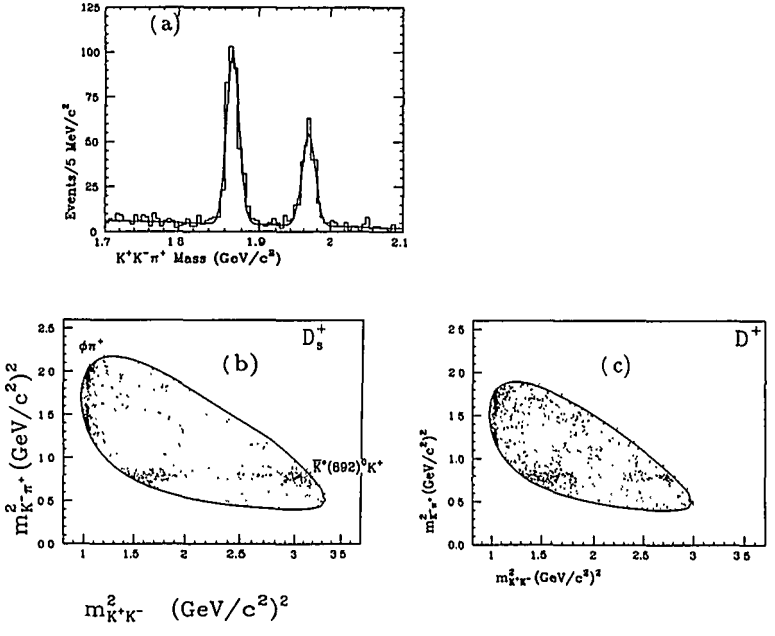


Fig. 70. (a) The mass spectrum for out-of-target $K^+K^-\pi^+$ decays. (b) and (c) The full sample $D_s^+, D^+ \to K^-K^+\pi^+$ Dalitz plots. The bands due to $\overline{K}^{*0}(890)K^+$ and $\phi(1019)\pi^+$ are quite visible for both the D_s^+ and D^+ Dalitz plots. Note the significant asymmetry between the population of the high and low $\overline{K}^{*0}(890)K^+$ lobes for the D^+ in sharp contrast with the symmetric appearance of the lobes for the D_s^+.

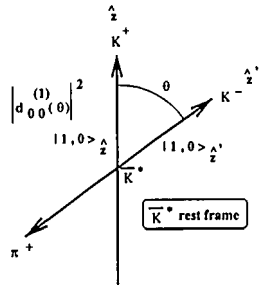


Fig. 71. When viewed in the $\overline{K^*}$ rest frame, the $\overline{K^*}$ has zero spin along the $\overline{K^*} \to K^-\pi^+$ decay axis since neither decay product carries spin. Since the D and D^+ are both spinless, the $\overline{K^*}$ must have zero spin along the K^+ axis. The amplitude for the $\overline{K^*}$ to have been in these two simultaneous spin states is given by $d^{(1)}_{00}(\theta) \propto \cos\theta$. This angular factor causes the Dalitz intensity to vanish in the center of the Dalitz band where $\cos\theta = 0$ as discussed in Fig. 25.

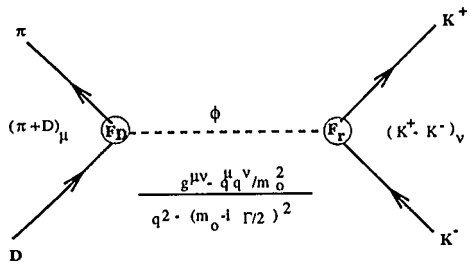


Fig. 72. We show a Feynman-like diagram for the process $D_s^+ \to \phi\pi^+$. A $D \to \pi^+$ current with a form factor F_D interacts with a kaon current with form factor F_r through an unstable ϕ propagator with an imaginary width contribution to the propagator mass. This diagram gives an amplitude contribution of the form $\mathcal{M} = F_D\, F_r \times |\vec{c}|^J |\vec{a}|^J P_J(\cos\theta^r_{ac}) \times BW(m_{ab})$, where the angular factor which gives rise to the Dalitz nodes follows from the structure of current × current contribution, and the Breit-Wigner represents the unstable propagator. The form factors are relatively unimportant.

Any nonreal phase differences are due to the influence of final state interactions which in a two resonant model would be given by Eq. (31)

$$\begin{pmatrix} a_{\overline{K}^*}\, e^{i\delta_{\overline{K}^*}} \\ a_\phi\, e^{i\delta_\phi} \end{pmatrix} = \begin{pmatrix} \eta\, e^{2i\delta_1} & i\sqrt{1-\eta^2}e^{i(\delta_1+\delta_2)} \\ i\sqrt{1-\eta^2}e^{i(\delta_1+\delta_2)} & \eta\, e^{2i\delta_2} \end{pmatrix}^{1/2} \begin{pmatrix} a_{K^*} \\ a_\phi \end{pmatrix}_{\text{bare}}. \tag{31}$$

One of the more interesting features of the Dalitz plots of Fig. 70 is the pronounced asymmetry between the two $\overline{K^*}$ lobes for the $D^+ \to K^-K^+\pi^+$. We believe that this lobe asymmetry is due to interference of the $\overline{K^{*0}}K^+$ channel with a broad, spinless resonance channel. From the interference pattern, one can infer that the data requires a nearly imaginary relative phase shift. For simplicity, we model the broad resonance in the vicinity of the $\overline{K^*}$ as a nearly constant amplitude which we write as $\cos\,\delta + i\sin\,\delta$. Equation (32) gives an explicit form for this interference term

$$Re\left\{(\cos\,\delta + i\sin\,\delta)^* \,\frac{\cos\,\theta}{M_r^2 - M_{K\pi}^2 - i\Gamma M_r}\right\} = \frac{(M_r^2 - M_{K\pi}^2)\,\cos\,\theta\,\cos\,\delta}{(M_r^2 - M_{K\pi}^2)^2 + \Gamma^2 M_r^2} + \frac{\Gamma M_r\,\cos\,\theta\,\sin\,\delta}{(M_r^2 - M_{K\pi}^2)^2 + \Gamma^2 M_r^2}. \tag{32}$$

The asymmetry comes about because the $\overline{K^{o*}}K^+$ decay amplitude contains an angular factor of $\cos\theta$, where θ is the angle between the two kaons in the $\overline{K^{o*}}$ rest frame. This $\cos\theta$ factor causes the interference term to change sign from the left lobe to the right lobe. We get an interference term from both the real part of the Breit-Wigner as well as the imaginary part. Since the real part of a Breit-Wigner reverses sign as one passes through the resonance (thus canceling the net interference across the lobe), any net interference is due to the second term which is proportional to $\sin\delta$. Figure 73 makes this argument graphically. The net lobe asymmetry thus provides visible evidence for final-state interactions since all bare amplitudes must be real ($\delta = 0$ or 180^o). After exploring many possibilities, E687 settled on the $\overline{K_0^*}(1430)$ K^+ channel as the most likely channel interfering with the $\overline{K^{*0}}K^+$ band.

We next discuss the $D_s^+ \to K^+K^-\pi^+$ Dalitz plot. A close examination of the Dalitz plot for the nearly background-free, out-of-target data (Fig. 74) shows an accumulation of events in (what should be) the ϕ band angular node. E691 (Ref. 44) discovered that the $D_s^+ \to \pi^+\pi^-\pi^+$ Dalitz plot is strongly dominated by the channel $D_s^+ \to f(980)\pi^+ \to (\pi^+\pi^-)\pi^+$. We therefore expect a contribution from the known dikaon decay of the $f(980)$ which should populate the ϕ node

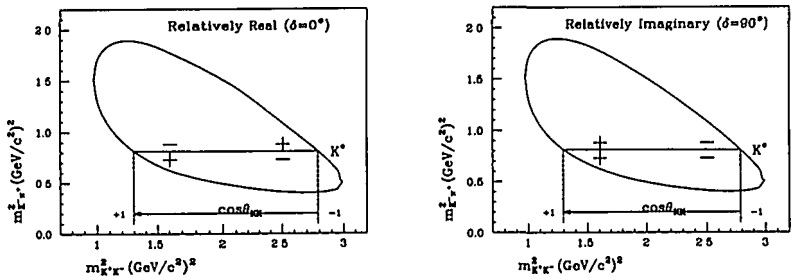


Fig. 73. The "+" and "−" indicate the sign of the interference term between a constant phase and the $\overline{K^{0*}}K^+$ Dalitz band for the case of relatively real (left) and relatively imaginary (right) phase shift. The sign alternates from the left to the right of the band owing to the $\cos\theta$ portion of the $\overline{K^{0*}}$ amplitude in Eq. (32). The real part of a Breit-Wigner amplitude reverses sign as one passes through the resonance which implies an additional sign change for the relatively real case. The relatively imaginary part has no such additional sign reversal.

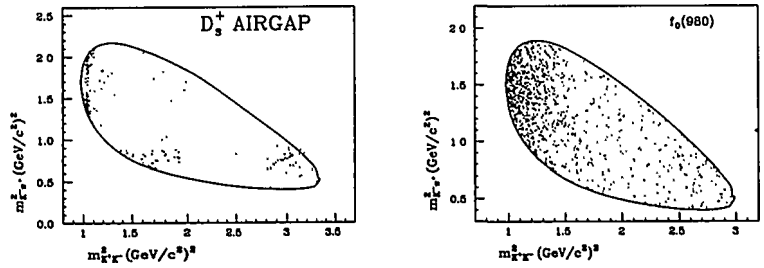


Fig. 74. The E687 D_s^+ Dalitz plot, and simulated $D_s^+ \to f(980)\pi^+ \to (K^+K^-)\pi^+$ decays.

region as shown in Fig. 74. Figure 75 shows us that the inclusion of additional contributions from the $f_J(1710)\pi^+$ and $\overline{K_0^*}(1430)$ K^+ significantly improved the quality of the fits in the vicinity of the K^* peak (R_1) and just above it (R_2).

Table 9 compares the E687 (Ref. 43) results on the channels common to both the $D^+, D_s^+ \to K^+K^-\pi^+$decays. The fractions, f_r, are known as decay fractions and represent the ratio of the integrated Dalitz intensity for a single resonance r divided by the intensity with all contributions present. The D^+ amplitude consists of nearly equal contributions of $\overline{K}^*K$, $\phi\pi$, and $\overline{K}^*(1430)^0K^+$; while the D_s^+ is strongly dominated by just the $\overline{K}^*K$ and $\phi\pi$. The decay fraction for the $f_o(980)$ and $f_J(1710)$ contributions to the D_s^+ sum to 14%.†

Table 9. Comparison of $D^+, D_s^+ \to K^+K^-\pi$ amplitudes.

Parameter	D^+	D_s^+
$\delta_{\overline{K}^*(892)^0K+}$	0° (fixed)	0° (fixed)
$\delta_{\phi\pi+}$	$-159 \pm 8 \pm 11°$	$178 \pm 20 \pm 24°$
$\delta_{\overline{K}^*(1430)^0K+}$	$70 \pm 7 \pm 4°$	$152 \pm 40 \pm 39°$
$f_{\overline{K}^*(892)^0K+}$	$0.301 \pm 0.020 \pm 0.025$	$0.478 \pm 0.046 \pm 0.040$
$f_{\phi\pi+}$	$0.292 \pm 0.031 \pm 0.030$	$0.396 \pm 0.033 \pm 0.047$
$f_{\overline{K}^*(1430)^0K+}$	$0.370 \pm 0.035 \pm 0.018$	$0.093 \pm 0.032 \pm 0.032$

Both the D^+ and D_s^+ could be fit entirely by quasi-two-body processes without the need to include a nonresonant contribution. It is interesting to note that both charm states have a real relative phase between the dominant $\overline{K}^*K$ and $\phi\pi$ channels which indicates absent or canceling FSI phase shifts.

Our amplitude fit for $D^+ \to K^-K^+\pi^+$ enables us to correct for acceptance variations across the Dalitz plot as well as the effects of resonant channel interference to obtain a much improved inclusive branching ratio $D^+ \to K^+K^-\pi^+/K^-\pi^+\pi^+ = 0.0976 \pm 0.0042 \pm 0.0046$. It has become common practice to quote "branching ratios" for resonant decay amplitudes such as $D^+ \to \phi\pi^+/K^-\pi^+\pi^+$, but because of quantum mechanical interference, only such inclusive ratios as $D^+ \to K^+K^-\pi^+/K^-\pi^+\pi^+$ are truly legitimate.

†I find it interesting to note that both the $f_o(980)$ and $f_J(1710)$ are often suspected to be non-$q\bar{q}$ states. There is a discussion of this in the 1996 summary by the Particle Data Group.[45]

Several groups have performed Dalitz analyses for the $D^o, D^+ \to K\pi\pi$ final state. Although these fits provide a good qualitative match to the data, often discrepancies are apparent in comparisons between the data and mass projections as shown in Fig. 76. The fit fractions obtained by the various experiments[46-48] are in excellent agreement; while there is little agreement concerning the relative phases, as illustrated in Fig. 77 for $D^o \to K^o_s\pi^+\pi^-$. There is excellent agreement, however, between phases obtained by E687 (Ref. 46) and Argus.[48] These analyses provide a wealth of information on new decay modes which can be compared to models based on factorization, QCD sum rules, and $1/N_c$ expansions. Generally, agreement of the models with the data is only at about the ± 60 % level. Often, the isospin amplitudes show nearly imaginary relative phases as reported in Table 8. It is interesting to note that all experimental groups report a sizable nonresonant contribution to the $D^+ \to K^-\pi^+\pi^+$ Dalitz plot which makes it unique among the plots discussed here.

3.6 Heavy Quark Decay Summary

Here is a very brief summary of this rather lengthy section. We began by discussing charm decay at the most inclusive level—the total decay rate or inverse lifetime of the charmed particles. The lifetime of the last measured weakly decaying charmed baryon, the Ω_c^o (css) (2704) state, was measured last year at 0.064 ± 0.020 ps. There is approximately an order of magnitude difference in the lifetime of the short-lived Ω_c^o (css) (2704) state and the long-lived (1.06 ps) D^+. In the absence of QCD effects, the naive spectator model predicts a universal charm lifetime of ≈ 0.7 ps. Recent progress in $1/M_Q$ expansions provides a systematic approach to estimating the effects of WA, WX, and PI diagrams which differentiate among the various charm particle species. The expansion approach does a credible job of reproducing observed lifetimes of the seven known weakly decaying charm states. By way of contrast, the lifetimes of the weakly decaying beauty states are much closer in value. More precise charm baryon measurements and b-sector measurements are needed to fully test these promising new approaches.

HQET predicts a very strong, backward polarization for the daughter baryon in $\Lambda_c \to \Lambda\ell\nu$, such as $\Lambda_c \to \Lambda\pi$, and $\Xi_c \to \Xi\pi$. The spin of the baryons are

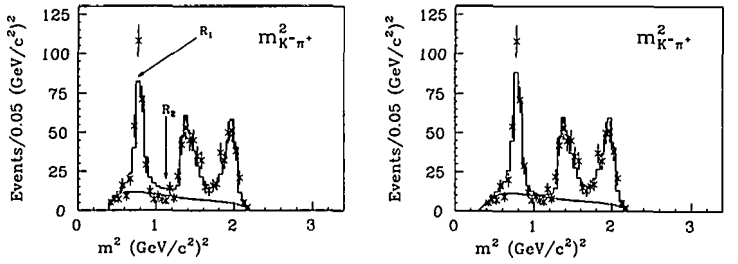


Fig. 75. Comparing the $m^2(K^-\pi^+)$ three amplitude (left) and five amplitude (right) D_s^+ fit to the data (error bars). The background, deduced from the mass sidebands, is shown in the lower histogram.

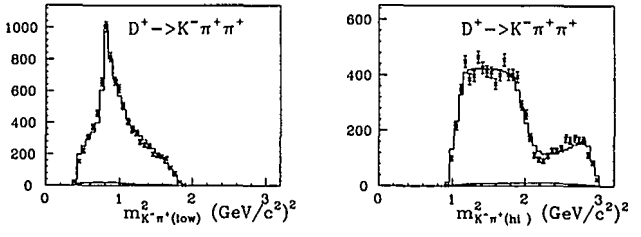


Fig. 76. Comparison of the lower and higher $K^-\pi^+$ mass projection in E687 data (error bars) and our fit (histogram). The high projection does not match near 2.5 GeV^2.

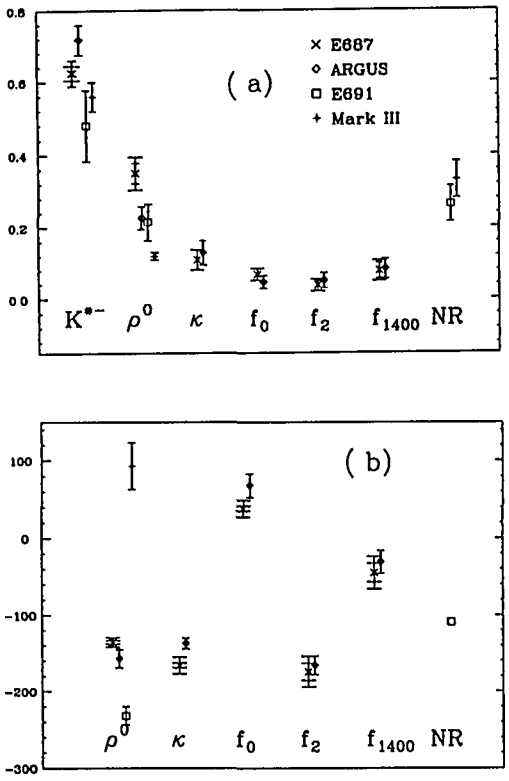


Fig. 77. Comparison of (a) the decay fractions and (b) phases obtained by different experiments for the decay $D^o \to K^o_s\pi^+\pi^-$.

self-analyzed through the decays: $\Lambda \to p\pi$ and $\Xi \to \Lambda\pi$. All three decays were measured by ARGUS and/or CLEO and found to be consistent with nearly complete, left-handed polarization.

A great deal of progress has been made in leptonic and semileptonic decays. There now exist several measurements of the $D_s^+ \to \mu^+\nu$ decay constant. Present data is internally consistent with a value of $f_{D_s} = 242 \pm 32\ MeV$ at $\approx 20\%$ CL level. This value is in good agreement with many of the predictions from Lattice Gauge Theory.

Charm form factors are exactly computable (in principle) by Lattice Gauge Theory and are frequently estimated by Quark Models. Both techniques are most effective when the daughter hadron is at rest relative to the parent, which means that they work best at $q^2 \approx q^2_{\rm max}$. Both the phase space and $V-A$ matrix element tend to force the data to values close to $q^2 \approx 0$. Most experimental groups use a VDM-inspired pole form to bridge the experimental and theoretical q^2 regimes, where the pole mass corresponds to the known D^* and D^{**} spectroscopy. The validity of these forms is unproven.

Theory does a good job predicting the f_+ form factor for $D \to K\ell\nu$. Data favors an $m_{\rm pole}$ slightly lower than the expected D_s^* mass. Crude experimental information on the lepton mass suppressed form factor, $f_-(q^2)$, has just become available. As expected, f_+^π for $D \to \pi\ell\nu$ is equal (to within $\pm 10\%$) to f_+^K for $D \to K\ell\nu$. Since $\pi\ell\nu$ probes q^2 much closer to the pole mass, pole mass uncertainty is an important source of systematics on the form factor and branching ratio measurements. It will be exciting to measure the q^2 dependence of $\pi\ell\nu$ decay in the future. Recent LGT and improved QM calculations are in much better agreement with the form factor magnitude in $D \to \overline{K^*}\ell\nu$ decay than the first predictions.

A factorization framework, the Bauer-Stech-Wirbel (BSW) model, was designed to incorporate QCD corrections into nonleptonic decays. The BSW model deals specifically with two-body and quasi-two-body decays. Predictions are made in terms of leptonic and semileptonic form factors. It has been known for some time that long-range, final-state interactions, FSI, can significantly distort BSW predictions for two-body-decay branching ratios. FSI is also responsible for creating complex phase shifts between isospin amplitudes. Amplitude analyses have confirmed the quasi-two-body nature of most three-body decays. FSI effects are evident in the interference between resonant channels. Amplitude analyses make possible vector-vector, and vector-pseudoscalar comparisons with the BSW model.

Only ±60% agreement exists between the models and resonance data. Extending these analyses to higher multiplicity meson and baryon decays and improving the physics of nonresonant terms is a future goal of charm physics.

4 A Final Word

I have tried throughout these lectures to capture some of the excitement of the present research on charm quark production and decay. Charm provides a unique window to test the calculations of QCD which is in many respects complementary to beauty owing to its intermediate mass scale. Charm lies somewhere between the light quark chiral limit and the limit where HQET is clearly applicable.

I have tried to show that the charm quark appears to be massive enough such that data on high-energy charm photoproduction and hadroproduction cross sections can be reasonably compared to the perturbative QCD calculations at next-to-leading order. The smaller mass of charm compared to beauty offers the experimentalist two distinct advantages. The low mass means that charm is copiously produced in high-energy fixed-target experiments. The reduced decay phase space of charm compared to beauty means that there exist easily reconstructible final states with appreciable ($\approx$ 5–10%) branching fractions. A copious sample of reconstructed charm decays allows one to make rather incisive tests of the QCD production mechanism and fragmentation models involving high-accuracy measurements of particle–antiparticle asymmetries and correlations.

Nonperturbative models have been successfully employed in understanding both the overall decay rate and details concerning form factors for both fully leptonic and semileptonic decays. The emerging calculational tool for charm decay appears to be Lattice Gauge theory since charm semileptonic decays are generally not in the proper domain of HQET. There still remains the problem of the q^2 gulf between where data exists and where the theories work best. Finally, many of the attempts to understand the bulk of charm decay—nonleptonic decay—are presently thwarted by the difficult-to-compute influence of final-state interactions. The final-state interactions will ultimately complicate future beauty physics, but at a hopefully reduced level. When viewed in this context, charm nonleptonic decay perhaps provides a "preview of coming distractions" for future beauty physics.

I would like to acknowledge the hospitality of the SLAC Summer Institute for arranging and maintaining this excellent school and conference. I would also like to acknowledge the prodigious efforts of my many E687 collaborators over the years.

References

[1] E687 Collaboration, P. L. Frabetti *et al.*, Nucl. Instrum. Methods, Phys. Res. Sec., A **320**, 519 (1992).

[2] Mark I Collaboration, G. Goldhaber *et al.*, Phys. Rev. Lett. **37**, 255 (1976).

[3] S. Frixione, M. Mangano, P. Nason, and G. Ridolfi, Nucl. Phys. B **405**, 507 (1993).

[4] H1 Collaboration, C. Kleinwort *et al.*, ICHEP-94 Glasgow, August (1994).
ZEUS Collaboration, M. Derrick *et al.*, DESY 95-013 (1995).
Also see the lectures of Wesley Smith in these proceedings.

[5] C. Peterson, D. Schlatter, I. Schmitt, and P. Zerwas, Phys. Rev. D **27**, 105 (1983).

[6] PYTHIA 5.6 and JETSET 7.3 *Physics Program and Manual*, CERN-TH.6488/92, and references: T. Sjöstrand, Computer Phys. Comm. **39**, **347** (1986); T. Sjöstrand and H. U.Bengtsson, Computer Phys. Comm. **43**, **367** (1987); H. U. Bengtsson and T. Sjöstrand, Computer Phys. Comm. **46**, **43** (1987).

[7] E687 Collaboration, P. L. Frabetti *et al.*, Phys. Lett. B **308**, 194 (1993).

[8] E687 Collaboration, P. L. Frabetti *et al.*, Phys. Lett. B **370**, 222 (1996).

[9] UCLA-Saclay Collaboration, S. Erhan *et al.*, Phys. Lett. B **85**, 447 (1979);
CERN-Bologna-Frascati Collaboration, M. Basile *et al.*, Lett. Nuovo Cimento **340**, 487 (1981).
E595 Collaboration, J. L. Ritchie *et al.*, Phys. Lett. B **138**, 213 (1984);
LEBC-EHS Collaboration, M. Aguilar-Benitez *et al.*, Z. Phys. C **31**, 489 (1986);
ACCMOR Collaboration, S. Barlag *et al.*, Z. Phys. C **49**, 555 (1991);
WA82 Collaboration, M. Adamovich *et al.*, Phys. Lett. B **305**, 402 (1993);
E769 Collaboration, G. A. Alves *et al.*, Phys. Rev. Lett. **72**, 812 (1994).

[10] E687 Collaboration, P. L. Frabetti *et al.*, Phys. Rev. Lett. **70**, 1381 (1993); Phys. Rev. Lett. **70**, 1775 (1993); Phys. Rev. Lett. **70**, 2058 (1993); Phys. Rev. Lett. **71**, 827 (1993); Phys. Lett. B **232**, 429 (1994); Phys. Lett B **357**, 678 (1995).

[11] V. Khoze and M. Shifman, Usp. Fiz. Nauk **140**, 3 (1983); Sov. J. Nucl. Phys. **41**, 120 (1985);
I. I. Bigi, N. G. Uraltsev, and A. Vainshtein, Phys. Lett. B **293**, 430 (1992); B **297**, 477 (1993);
B. Blok and M. Shifman, Nucl. Phys. B **399**, 441 (1993).

[12] I. I. Bigi, *Quo Vadis, Fascinum?* Workshop on the Tau/Charm Factory, Argonne, IL, June 21-23, 1995 (AIP Conference Proceedings 349), pp. 331-342.

[13] J. P. Cumalat, in *The Fermilab Meeting DPF92*, 10-14 November 1992, edited by Carl H. Albright, Peter H. Kasper, Rajendran Raja, and John Yoh (World Scientific Publishing Co.).

[14] Jeffrey D. Richman and Patrica R. Burchat to be published in Rev. Mod. Phys.

[15] WA75 Collaboration, S. Aoki *et al.*, Prog. Theor. Phys. **89**, 131.

[16] BES Collaboration, J. Z. Bai *et al.*, SLAC preprint no. SLAC-PUB-95-6746 (1995).

[17] CLEO Collaboration, D. Acosta *et al.*, Phys. Rev. D **49**, 5690 (1994).

[18] E653 Collaboration, K. Kodama *et al.*, Phys. Lett. B **382**, 299 (1996).

[19] See, for example, Anna Hasenfratz and Peter Hasenfratz, Ann. Ref. Nucl. Part. Sci **35**, 559-604 (1985).

[20] Gustavo Burdman and Joachim Kambor, http://xxx.lanl.gov/hep-ph/hep-ph/9602353.

[21] E687 Collaboration, P. L. Frabetti *et al.*, Phys. Lett. B **364**, 461 (1995).

[22] D. M. Schmidt, R. J. Morrison, and M. S. Witherell, Nucl. Instrum. Methods, A **328**, 547 (1993).

[23] CLEO Collaboration, A. Bean *et al.*, Phys. Lett. B **317**, 647 (1993).

[24] E687 Collaboration, P. L. Frabetti *et al.*, Phys. Lett. B **307**, 262 (1993).

[25] E687 Collaboration, P. L. Frabetti *et al.*, Phys. Lett. B **313**, 253 (1993); Phys. Lett. B **328**, 187 (1994).

[26] James N. Simone, *Semileptonic Decays: An Update Down Under*, plenary talk presented at Lattice '95 Melbourne, Australia, Fermilab-Conf-96.017-T.

[27] CLEO Collaboration, F. Butler *et al.*, Phys. Rev. D **52**, 2656 (1995).

[28] E687 Collaboration, P. L. Frabetti *et al.*, Phys. Lett. B **382**, 312 (1996).

[29] Mark III Collaboration, J. Adler *et al.*, Phys. Rev. Lett. **62**, 1821 (1989).

[30] D. Scorna and N. Isgur, Phys. Rev. D **62**, 2783 (1995);
V. Lubicz *et al.*, Phys. Lett. B **274**, 415 (1992);
S. Narison, Phys. Lett. B **377**, 163 (1994);
N. B. Debchuk *et al.*, INFN preprint INFN0ISS 95/18, (submitted to Sov. J. Nucl. Phys.).

[31] D. Scorna and N. Isgur, Phys. Rev. D **62**, 2783 (1995).

[32] J. G. Körner and M. Krämer, Phys. Lett. B **275**, 495 (1992).

[33] M. Bauer, B. Stech, and M. Wirbel, Z. Phys. C**29**, 637 (1985);
M. Bauer and M. Wirbel, Z. Phys. C **42**, 671 (1989).

[34] P. Frabetti *et al.*, Phys. Lett. B **321**, 295 (1994).

[35] M. Adamovich *et al.*, Phys. Lett.B **280**, 163 (1992).

[36] J. C. Anjos *et al.*, Phys. Rev. D **44**, R3371 (1991).

[37] J. Alexander *et al.*, Phys. Rev. Lett. B **65**, 1184 (1990).

[38] Thomas E. Browder, Klaus Honscheid, and Daniele Pedrini, to be submitted to Ann. Rev. Nucl. Part. Sci.

[39] P. Frabetti *et al.*, Phys. Lett. B **331**, 217 (1994).

[40] J. Adler *et al.*, Phys. Lett. B **196**, 107 (1987).

[41] J. C. Anjos *et al.*, Phys. Rev. D **48**, 56 (1993).

[42] H. Albrecht *et al.*, Phys. Lett. B **308**, 435 (1993).

[43] P. Frabetti *et al.*, Phys. Lett B **351**, 591 (1995).

[44] J. C. Anjos *et al.*, Phys. Rev. Lett. **62**, 125 (1989).

[45] Particle Data Group, R. M. Barnett *et al.*, Review of Particle Physics, Phys. Rev. D **54**, 557 (1996).

[46] P. Frabetti *et al.*, Phys. Lett. B **331**, 217 (1994).

[47] J. C. Anjos *et al.*, Phys. Rev. D **48**, 56 (1993).

[48] H. Albrecht *et al.*, Phys. Lett. B **308**, 435 (1993).

[49] E791 Collaboration, E. M. Aitala et al., Phys. Lett. B **371**, 157 (1996).

[50] R. Vogt and S. J. Brodsky, Nucl. Phys. B 438, 261 (1996).

Topical Conference

PRECISION MEASUREMENT OF THE NEUTRON SPIN STRUCTURE FUNCTION

Robert C. Welsh*
Physics Department
University of Michigan
Ann Arbor, MI 48109

Representing the SLAC E154 Collaboration

ABSTRACT

Deep inelastic scattering of electrons has been used for nearly three decades to probe the internal structure of nucleons. The vast majority of the available data on deep inelastic scattering comes from unpolarized experiments. These experiments have revealed the internal linear momentum structure of nucleons. However, not until the last decade and a half have experiments been carried out to elucidate the internal angular momentum structure of the nucleons. Recently, the experiment E154 at the Stanford Linear Accelerator Center has completed a two-month data taking run in which a large number ($\sim 10^8$) of spin–dependent deep inelastic scattering events were collected. The experiment covered the kinematic range of $0.014 \leq x \leq 0.70$ and $1\ (\mathrm{GeV/c})^2 \leq Q^2 \leq 17\ (\mathrm{GeV/c})^2$. The preliminary analysis of these data yields to date the most precise integral of $\int_{0.014}^{0.70} g_1^n(x)\ dx = -0.036 \pm 0.004(\mathrm{statistical}) \pm 0.005(\mathrm{systematic})$ at an average Q^2 of $5\ (\mathrm{GeV/c})^2$.

*Supported by NSF Grant PHY–9515418.

© 1996 by Robert C. Welsh.

1 Introduction

1.1 Spin–Averaged Deep Inelastic Scattering

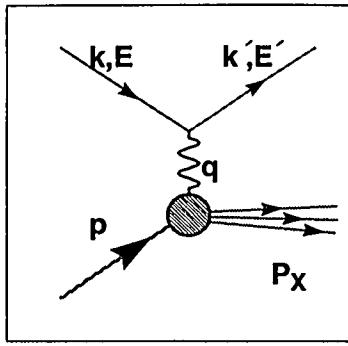
Deep Inelastic Scattering (DIS) experiments take advantage of the point–like nature and the relatively weak electromagnetic interaction of leptons to probe the internal structure of hadrons, specifically nucleons. I will speak mainly of electrons except when referring to other experiments such as the muon scattering experiments at CERN. In deep inelastic scattering experiments, a high-energy lepton beam impinges upon a nuclear target. The energy and momentum transfer to the target nucleon can be calculated by detecting the scattered electron and measuring its momentum. Experiments from the late 1960s established the parton model as a description of DIS. The 1990 Nobel Prize in Physics was awarded for these seminal experiments.[1-3] Further experimentation led to the observation of *Scale Invariance* as predicted by Bjorken[4] and the explanation of scaling in the context of the parton model by Feynman.[5]

The parton model lets the experimenter equate the fraction x of the momentum of the nucleon carried by the struck parton (quark) to a ratio of kinematic observables,

$$x = \frac{-q^2}{2\,M_{\rm N}\,\nu}\,, \tag{1}$$

where q^2 is the four–momentum transfer squared, $\nu = E - E'$ is the energy transfer, and $M_{\rm N}$ is the nucleon mass. In the Born approximation, the scattering is described by single photon exchange between the incoming lepton and the struck quark. This is schematically shown in Fig. 1. The internal momentum structure of the nucleon can be extracted from the x dependence of the scattering rates and summarized in the *structure functions*, $F_1(x)$ and $F_2(x)$.

In the years subsequent to the original DIS experiments, the theory of *Quantum Chromodynamics* (QCD) has become a good description of the dynamics of partons (quarks and gluons). QCD[6-8] has been quite successful in explaining the dynamics of scale violation in parton distributions.[9] Currently, high-precision data for the spin–averaged nucleon structure functions[10] are available and provide for a rigorous test of QCD. However, only recently have high-precision data for *spin–dependent* structure functions become available.



k, E	incoming electron
k', E'	scattered electron
$q^2 = (k-k')^2 = -4EE'\sin^2\frac{\theta}{2}$	
p	initial nucleon momentum
P_x	unobserved final hadron momentum

Fig. 1. Schematic of deep inelastic scattering.

1.2 Spin–Dependent DIS

The impetus for spin–dependent DIS is the desire to fully understand and describe the spin nature of the nucleon. We know from low Q^2 measurements that the nucleon is a spin 1/2 particle. From the parton description, we also know that the nucleon is comprised of spin 1/2 (quarks) and spin 1 (gluons) particles. From angular momentum conservation, we can then put forth the following

$$S_{\rm nucleon} \equiv \frac{1}{2} = \frac{1}{2}\Delta q + \Delta G + <L>\,, \tag{2}$$

where Δq is the portion of the nucleon's spin carried by the quarks, ΔG that carried by the gluons, and $<L>$ the internal orbital angular momentum.

This current experiment undertook the task of precisely measuring the neutron spin–dependent structure function $g_1^n(x)$[1]. To first order, the measurement of the spin–dependent structure function $g_1(x)$ is a probe of the longitudinal quark spin content of the nucleon. Since free neutrons are unstable and the use of a neutron beam from a facility such as a reactor is impracticable, preparation of a polarized neutron target requires the use of either a deuterated molecule, such as ND_4 or Butonal, or a nucleus in which an unpaired neutron can be effectively polarized, such as ^{3}He. A rather good approximation of the ^{3}He wave–function is that the two protons are paired off as a spin singlet and the unpaired neutron carries the spin of the nucleus. More exact treatments[11] show that the neutron polarization is $P_n = 0.87$ and the proton polarization is $P_p = -0.027$. Thus,

[1] Data primarily sensitive to $g_2^n(x)$ were also collected.

spin dependence is dominated by the neutron; while in the deuteron, the proton and the neutron have spins aligned. Measurement of the neutron spin–dependent structure function using the deuteron requires the subtraction of 100% of the proton spin structure function. Extraction of the neutron spin structure from deep inelastic data taken with ^{3}He targets requires a much smaller adjustment due to the proton contribution, though the asymmetry is smaller. The experiment E154 used polarized ^{3}He for the present measurement of the neutron spin structure.

Spin–dependent DIS is described by the following differential cross–section[12]

$$\begin{aligned}\frac{d\sigma}{dE'd\Omega} &= 4E'^2\frac{\alpha^2}{Q^2}\left[2\sin^2\left(\frac{\theta}{2}\right)W_1(Q^2,\nu)+\cos^2\left(\frac{\theta}{2}\right)W_2(Q^2,\nu)\right] \\ &-\frac{E'\alpha^2}{EQ^4}\left[\frac{2m_e\,[q^2\,S_P\cdot S_e - q\cdot S_e\; q\cdot S_p]}{P\cdot q}g_1(x,Q^2)\right. \\ &\left.+\frac{2m_e[q^2\,(q\cdot P\,S_p\cdot S_e - q\cdot S_p\,P\cdot S_e)]}{(P\cdot q)^2}g_2(x,Q^2)\right]. \qquad (3)\end{aligned}$$

The four–momentum transfer is q, the target nucleon four–momentum is P, and the beam and target polarization four–vectors are S_e and S_p respectively. Under change of sign of the beam helicity, the four–vector S_e changes overall sign. The differences in spin–dependent cross sections for the cases *(a)* the spins of the incoming electron and nuclear target are parallel and anti–parallel and *(b)* the spins of the incoming electron and the nuclear target are perpendicular and anti–perpendicular are

$$(a)\quad \frac{d^2\sigma(\downarrow\Uparrow-\uparrow\Uparrow)}{d\Omega dE'} = \frac{4\alpha^2E'}{EM\nu Q^2}\left([E+E'\cos\theta]g_1(x)-2xMg_2(x)\right)$$

$$(b)\quad \frac{d^2\sigma(\downarrow\Leftarrow-\uparrow\Leftarrow)}{d\Omega dE'} = \frac{4\alpha^2E'}{EM\nu Q^2}E'\sin\theta\left(g_1(x)+\frac{4xME}{Q^2}g_2(x)\right). \qquad (4)$$

In the scaling limit, the spin–dependent structure function $g_1(x)$ can be shown to be the difference of spin–dependent parton distributions

$$g_1(x)=\frac{1}{2}\sum_{\text{Flavors (i)}}q_i^2(f_i^{\uparrow}(x)-f_i^{\downarrow}(x))\;, \qquad (5)$$

where the charge of the parton (quark) is given by q_i. The i^{th} partonic structure function is denoted by f_i. Likewise, the spin–averaged structure function is the average of the spin–dependent parton distributions

$$F_1(x)=\frac{1}{2}\sum_{\text{Flavors (i)}}q_i^2(f_i^{\uparrow}(x)+f_i^{\downarrow}(x))\;. \qquad (6)$$

Furthermore, the individual spin–dependent structure functions $g_1(x)$ and $g_2(x)$ can be calculated from the above differential cross sections by making measurements of both the parallel/anti–parallel and perpendicular/anti–perpendicular scattering rates in a DIS experiment. The details of the manipulation are shown in Eqs. 10 through 13.

While there is no *a priori* determination of a particular structure function, spin–independent or spin–dependent, there is a rigorous prediction that relates the integral of the difference of the proton spin structure function and the neutron spin structure function. This is known as the Bjorken sum rule[13]

$$\lim_{Q^2\to\infty}\int_0^1\left(\,g_1^p(x)-g_1^n(x)\right)\,dx=\frac{1}{6}|g_A|, \qquad (7)$$

where $g_A=-1.2573\pm0.00281$ is the axial–vector coupling for neutron beta decay.[14] It is important to note that the integral is over the full range of x and that the integral should be evaluated at *infinite* Q^2. Calculable QCD corrections must be applied[15] at finite Q^2.

Ellis and Jaffe[16] proposed that the strange quark sea would be unpolarized

$$\int_0^1(s^{\uparrow}(x)-s^{\downarrow}(x))dx=0 \qquad (8)$$

and thus introduced the Ellis–Jaffe sum rule for the nucleon

$$\lim_{Q^2\to\infty}\int_0^1\;g_1^{p(n)}(x)\;dx=(\pm)\frac{1}{12}g_A\left[1(\pm)\frac{5}{3}\frac{3F-D}{F+D}\right]. \qquad (9)$$

Again, g_A comes from neutron beta decay, while F and D are constants of hyperon decay.[14] Originally, only the spin–dependent structure functions of the proton were measured by the E80 Collaboration[17] and E130 Collaboration.[18] Data from both of the original SLAC experiments were consistent with the Ellis–Jaffe sum rule for the proton. In 1989, the EMC Collaboration presented data consistent with a violation of the Ellis–Jaffe sum rule.[19] Subsequent experiments, both at CERN[20,21] and at SLAC,[22–24] have also shown that the Ellis–Jaffe sum rule is violated.[2] Figure 2 shows some of the world's data for the proton spin structure function. Once neutron spin–dependent structure functions became available, tests of the Bjorken sum rule by the SMC[20] and SLAC–E143[23] Collaborations[3]

[2] Indeed, a more careful QCD-based analysis results in the quark sea being polarized.[25,26]

[3] The SLAC experiment E142 made the first measurement of the neutron spin structure function $g_1^n(x)$ using a laser–polarized ^{3}He target; however, a test of the Bjorken sum rule would require use of either the SMC proton data or the SLAC E143 proton data. Both SMC and E143 measured the proton and the neutron spin structure functions $g_1^p(x)$ and $g_1^n(x)$.

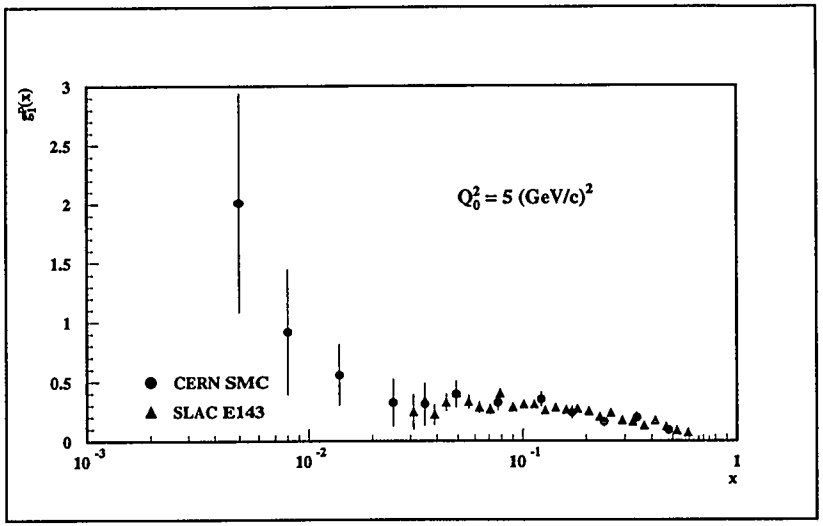


Fig. 2. Some of the currently published data for $g_1^p(x)$. Plotted is $g_1^p(x)$ as a function of x. The data were evolved to $Q_0^2 = 5$ (GeV/c)^2 using Eq. (26).

were possible. Summaries of both the Ellis–Jaffe sum rule tests and the Bjorken sum rule tests are shown in Table 1.

The amount of published world data for the neutron spin structure function $g_1^n(x)$ is limited due to the difficulty in preparation of an effectively polarized neutron target. To date, only the SMC Collaboration, SLAC E142, and SLAC E143 have published neutron data[4]. Figure 3 summarizes these data[5]. Naively, the proton structure function appears well-behaved in the low–x region ($x < 0.1$). However, the neutron data are not as precise as the proton data in this low–x region. For tests of the Bjorken sum rule, collaborations have assumed two things about the data: (a) that the quantity $g_1(x)/F_1(x)$ is Q^2 independent, and (b) that the low–x region not covered by data would assume a Regge–like form[27] resulting in $g_1^n(x) \sim$ constant. These two assumptions have been used to extrapolate the

[4]Currently, an experiment at DESY by the HERMES Collaboration has collected neutron spin structure function data with a polarized ^{3}He target, though the statistics are limited with respect to the current experiment.

[5]The shaded region in the figure indicates the kinematic coverage of the current experiment.

(a)	Ellis–Jaffe Sum (proton)	Prediction	Collaboration
	$0.126 \pm 0.010 \pm 0.015$	0.189 ± 0.005	EMC[19]
	$0.049 \pm 0.044 \pm 0.032$	0.187 ± 0.010	SMC[20] (deuteron)
	$0.136 \pm 0.011 \pm 0.011$	0.176 ± 0.006	SMC[21]
	$0.127 \pm 0.004 \pm 0.010$	0.160 ± 0.006	SLAC E143[22]
	$-0.031 \pm 0.006 \pm 0.009$	-0.011 ± 0.016	SLAC E142[24] (neutron)
(b)	Bjorken Sum	Prediction	Collaboration
	0.204 ± 0.029	0.185 ± 0.004	SMC[21]
	$0.163 \pm 0.010 \pm 0.016$	0.171 ± 0.008	SLAC E143[23]

Table 1. (a) Ellis–Jaffe sum rule tests and (b) Bjorken sum rule tests.

structure functions below the measured regions for the purpose of integrating the structure functions over the full x range. With the advent of precise data, such an extrapolation method can be tested, as can possibly the Q^2 dependence of $g_1(x)$.

2 Methodology

To precisely measure the neutron spin structure function $g_1^n(x)$, many systematic effects must be well-understood. These are summarized in Table 2. This contribution will address the *E154 Experimental Systematics* while the reader is referred to the literature for the best measurements of $F_1(x)$ (Ref. [28]), R (Ref. [29]), and $g_1^p(x)$ (Refs. [19], [21], and [22]).

E154 Experimental Systematics	
Beam Flux Stability	Beam Polarization
Target Dilution Factor	Target Polarization
Electron Identification	Background Subtraction
Radiative Corrections	
External Systematics	
$F_1(x)$	R $g_1^p(x)$

Table 2. Sources of systematic errors.

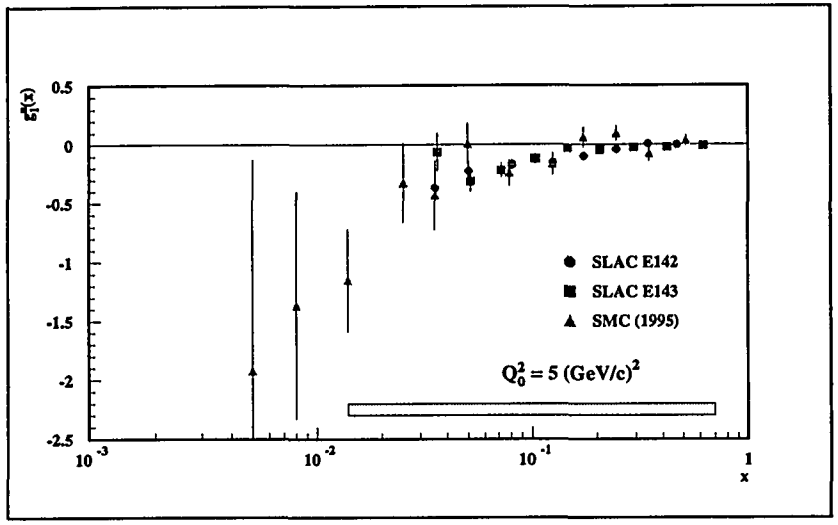


Fig. 3. Published data for $g_1^n(x)$. The shaded region indicates the x interval of the present experiment.

2.1 Cross–Sections or Ratio of Rates

To extract the spin–dependent structure functions, either the absolute differential cross sections must be measured or the asymmetry must be measured. The cross–section and asymmetry measurements are subject to different systematic errors. The advantage of the asymmetry measurement is that experimental conditions such as the spectrometer acceptance drop out in the ratio. Though eventually the absolute DIS cross section must be known, the value may be taken from precise measurements due to other experiments. The following equations illustrate the latter method.

First, we define some variables related to the experimental observables in Table 3. The explicit spin dependence is dropped for brevity. Additionally, the differential cross sections have implicit x and Q^2 dependence. The acceptance $\mathcal{A}$ in general is also a function of x and Q^2. Finally, the dilution factor f is a function of x and Q^2.

n	density of target	l	target length
$\mathcal{A}$	acceptance of spectrometer	F^e	electron beam flux
$d\sigma$	differential cross section	N^e	observed scattering rate
P_e	electron beam polarization	$P_{^3\mathrm{He}}$	target polarization
f	dilution factor	η	generic efficiency variable

Table 3. Experimental variables.

We can define the following two ratios, which we shall call the parallel, $A_\parallel$, and perpendicular, $A_\perp$, asymmetries

$$\begin{aligned} A_\parallel &= \frac{d\sigma(\downarrow\Uparrow - \uparrow\Uparrow)}{d\sigma(\downarrow\Uparrow + \uparrow\Uparrow)} \\ A_\perp &= \frac{d\sigma(\downarrow\Leftarrow - \uparrow\Leftarrow)}{d\sigma(\downarrow\Leftarrow + \uparrow\Leftarrow)}. \end{aligned} \tag{10}$$

The electron spin directions are denoted by $\uparrow$ and $\downarrow$, while the nuclear spin directions are shown by $\Uparrow$ and $\Leftarrow$. The experiment is able to measure these ratios by observing the scattering rates as a function of beam polarization state. A given rate can be expressed as

$$N^e = F^e\, n\, l\, \mathcal{A}\, \eta\, d\sigma. \tag{11}$$

Since the beam polarization (P_e) and target polarization ($P_{^3\mathrm{He}}$) are in general not 100% and the ^{3}He gas is confined to a glass target vessel, the observed rates relate to the parallel and perpendicular asymmetries according to

$$A_\parallel = \frac{1}{P_e\, P_{^3\mathrm{He}}\, f\, \eta'} \frac{N^e_{\downarrow\Uparrow}/F^e_\downarrow - N^e_{\uparrow\Uparrow}/F^e_\uparrow}{N^e_{\downarrow\Uparrow}/F^e_\downarrow + N^e_{\uparrow\Uparrow}/F^e_\uparrow}, \tag{12}$$

where η' represents efficiencies that do not necessarily cancel in the ratios[6] and f is the dilution factor defined in Sec. 2.5. A similar expression exists for the perpendicular asymmetry. Manipulation of Eq. (4) along with the definition of the asymmetries in Eq. (10) and the equations that relate the asymmetries to experimental observables such as Eq. (12) then lead to the structure functions $g_1(x)$ and $g_2(x)$

$$\begin{aligned} g_1(x) &= \frac{F_1(x)}{D}\left[A_\parallel + \tan\left(\frac{\theta}{2}\right) A_\perp\right] \\ g_2(x) &= \frac{y\, F_1(x)}{2\, D}\left[\frac{E + E'\cos(\theta)}{E'\sin(\theta)} A_\perp - A_\parallel\right]. \end{aligned} \tag{13}$$

[6]Such as any efficiencies that are dependent upon rate. If such efficiencies exist, then they will become dependent upon the asymmetry being measured.

D and y are kinematic factors defined by

$$y = \frac{E-E'}{E} \qquad D = \frac{(1-\epsilon)(2-y)}{y(1+\epsilon R)}$$
$$\epsilon = \left[1+2(1+\nu^2/Q^2)\tan^2(\frac{\theta}{2})\right]^{-1} \qquad R = \frac{\sigma_0}{\sigma_T}. \tag{14}$$

Finally, because the spin of the neutron in the ^{3}He nucleus is not 100% aligned with the nuclear spin, and because the protons have a residual polarization, the neutron spin structure function $g_1^n(x)$ takes the form

$$g_1^n(x) = \frac{1}{P_n}\left(g_1^{^3\mathrm{He}}(x) - 2\,P_p\,g_1^p(x)\right) \tag{15}$$

with $P_p = -0.027$ and $P_n = 0.87$.

2.2 Experimental Description

Two small acceptance magnetic spectrometers ($d\Omega \sim 5$ msr) were used to observe deep inelastic scattering rates of 48.3 GeV polarized electrons impinging on a gaseous laser-polarized ^{3}He target. Approximately 100 million events were collected over a period of two months (October and November of 1995) at the Stanford Linear Accelerator Center. The experiment ran in fixed target hall End Station A. The majority of the events were collected in a polarization configuration in which the beam was polarized along the direction of the beam axis and the target was polarized along the same axis. The asymmetry in this configuration of polarization vectors is dominated by the spin structure function $g_1^n(x)$. With the target polarization perpendicular to the electron beam, the asymmetry is dominated by the other spin structure function[7] $g_2^n(x)$. As previously stated, this talk only presents results on the measurement of $g_1^n(x)$.

2.3 Electron Beam

The electron beam originates at the polarized electron source.[30] This source utilizes a strained-lattice GaAs crystal in conjunction with a Ti-Sapphire laser system. Illumination of the strained crystal with a particular helicity of the laser light produces a current of highly polarized electrons which are accelerated to an energy of 48.3 GeV. The laser light was applied in a pulse mode, each pulse being 200–250 ns long. The helicity of the laser light was determined by the high voltage applied to two Pockels cells. For the present experiment, the helicity state of the laser for each pulse was determined by a random number generator. By doing this, random flipping of the beam polarization fluctuations in beam flux and experimental acceptance and efficiencies were averaged, and thus, systematic errors were reduced.

$$< A_\uparrow > = < A_\downarrow >$$
$$< \eta_\uparrow > = < \eta_\downarrow > . \tag{16}$$

For the experiment, we utilized a beam current between $3\cdot10^9$ and $9\cdot10^9$ electrons per pulse. The accelerator provided 120 pulses per second, though one pulse was used to monitor accelerator performance. The beam polarization was measured in dedicated runs using a single-arm Möller polarimeter.[31] Average beam polarization was stable at 0.825 and was measured with less than a 5% relative error. Off-line analysis cuts were used to prepare parent samples of DIS events which had beam flux distributions identical to better than 10^{-4}. Analysis examined both spatial and charge distributions of the pulses.

2.4 ^{3}He Polarized Target

To measure the neutron spin structure function $g_1^n(x)$, the experiment E154 chose to use a spin-exchange ^{3}He gaseous target[8]. The experiment utilized a sealed two-cell target system. The target system is schematically shown in Fig. 4. An upper cell was used for laser optical pumping of a Rb vapor. Rubidium density was controlled by heating the upper cell to $\sim 180°$ C. Circularly polarized light provided by three solid state laser diode arrays and four Ti-Sapphire lasers illuminated the upper cell. This results in an atomically polarized Rb vapor. The Rb vapor and the ^{3}He gas freely diffuse and undergo hyperfine interactions during collisions resulting in polarization transfer from the Rb atomic electron to the ^{3}He nucleus.[32] The ^{3}He polarization is governed by

$$P_{^3\mathrm{He}}(t) = P_{\mathrm{Rb}}\frac{\gamma_{SE}}{\gamma_{SE}+\Gamma}\left(1-e^{-(\gamma_{SE}+\Gamma)t}\right), \tag{17}$$

[7] Todd Averett for the E154 Collaboration, SPIN 96 *Proceedings*, Amsterdam, The Netherlands.

[8] In contrast to the experiment DESY/HERMES which uses a meta-stability exchange based ^{3}He polarization system.

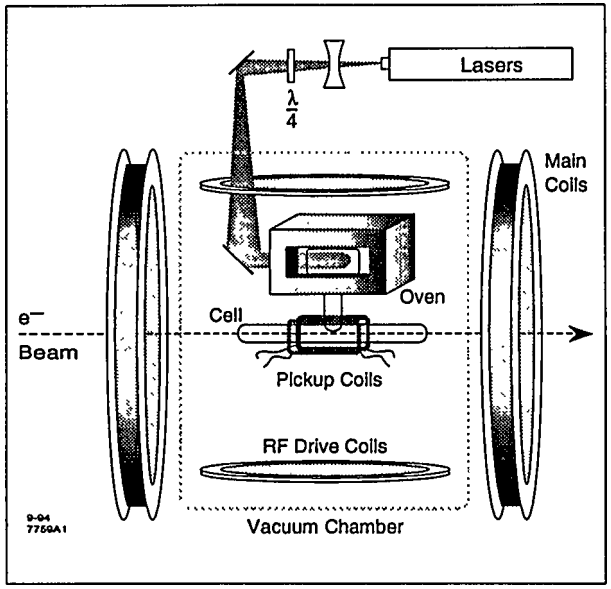


Fig. 4. Schematic of laser-polarized ^{3}He target.

where $P_{\rm Rb}$ is the average rubidium atomic polarization, γ_{SE} is the spin–exchange rate between the rubidium and the ^{3}He, and Γ is the intrinsic cell relaxation time. Typical values were $P_{\rm Rb} \sim 0.60$, $\gamma_{SE} \sim (16\ {\rm hr})^{-1}$, and $\Gamma \sim (70\ {\rm hr})^{-1}$. Figure 5 illustrates the atomic levels of the rubidium valence electron and the effect of optical pumping. A quantization axis is achieved with two sets of large helmholtz coils providing a holding field of $10 \sim 20$ gauss. Longitudinal target polarization is set by having the holding field parallel to the beam axis, while a transverse field results in perpendicular polarization[9]. The target cells were filled with ^{3}He to a pressure of approximately ten atmospheres. Additionally, each cell had in it a small amount of N_2 (~60 torr) to aid in the optical pumping process. The bottom (target) cell through which the high-energy electron beam passed was constructed with very thin entrance and exit windows ($\sim$ 50 μm). The lower, target cell

[9]During perpendicular running of the experiment, the target cell was permitted to cool and the lasers were turned off. The ^{3}He polarization was allowed to decay with a time constant on the order of many tens of hours. This was done because the optical path of the laser light was fixed for parallel pumping only.

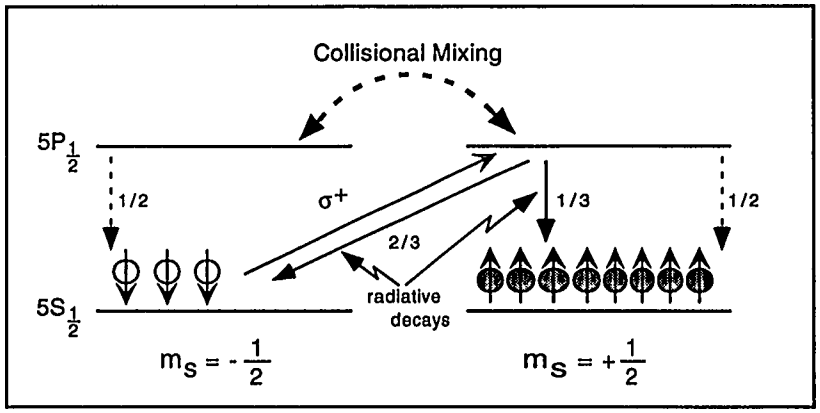


Fig. 5. Optical pumping of rubidium. The circularly polarized light is denoted by σ^+. In the absence of N_2, the $5P_{1/2}$ state deexcites with a ratio of relative rates of 2/3:1/3. Introduction of a small amount of N_2 results in collisional mixing and increases this ratio to 1/2:1/2.

was 30 cm long. Average target polarization over the two-month duration of the experiment was 38% ± 2% and as high as 50%. The target polarization was regularly measured throughout the course of the experiment using *adiabatic fast passage*, a NMR technique.[33] The NMR was calibrated by two methods: proton NMR and Rb EPR.[34] In the analysis of the data, the interpolated polarization for each run was used.

2.5 Target Dilution Factor f

The advantages of using a closed optical pumping cell for the nuclear target for DIS is the high densities achieved. However, this results in DIS events originating from nuclei other than the ^{3}He. The ratio of the events from the ^{3}He to the sum of events from all species is referred to as the dilution factor[10] f.

$$f = \frac{N_{\downarrow}^{^3{\rm He}} + N_{\uparrow}^{^3{\rm He}}}{N_{\downarrow}^{^3{\rm He}} + N_{\uparrow}^{^3{\rm He}} + (N_{\downarrow}^{\rm N_2} + N_{\uparrow}^{\rm N_2}) + (N_{\downarrow}^{\rm glass} + N_{\uparrow}^{\rm glass})}. \qquad (18)$$

[10]The nuclear spin directions ($\Uparrow$ and $\Leftarrow$) are not shown since this formula holds for all nuclear spin directions.

In the observed asymmetries, the numerator is only dependent upon the polarized ^{3}He as the glass target vessel and the N_2 gas are unpolarized. However, the denominator, which is a measure of the spin-averaged scattering rates, is sensitive to the presence of any matter in the electron beam. The ratio of the difference of the spin-dependent scattering rates from ^{3}He to the sum is

$$P_e\, P_{^3\mathrm{He}}\, A_{^3\mathrm{He}} = \frac{N_\downarrow^{^3\mathrm{He}} - N_\uparrow^{^3\mathrm{He}}}{N_\downarrow^{^3\mathrm{He}} + N_\uparrow^{^3\mathrm{He}}} = f\, \frac{N_\uparrow^{\mathrm{Total}} - N_\downarrow^{\mathrm{Total}}}{N_\uparrow^{\mathrm{Total}} + N_\downarrow^{\mathrm{Total}}}. \tag{19}$$

Because the glass target vessel is unpolarized as is the N_2 gas, the difference in the spin-dependent ^{3}He scattering rates is identical to the difference in the total spin-dependent scattering rates

$$N_\downarrow^{^3\mathrm{He}} - N_\uparrow^{^3\mathrm{He}} = N_\uparrow^{\mathrm{Total}} - N_\downarrow^{\mathrm{Total}}. \tag{20}$$

Precise determination of f is crucial to the measurement of $g_1^n(x)$. We used two methods: (1) physical characterization of the target cell with detailed calculation of expected rates from contributions due to different matter present, and (2) use of a variable pressure reference cell to directly measure rates of deep inelastic scattering from ^{3}He.

2.5.1 Dilution Factor Method 1: Calculated with Target Physical Characteristics

In method 1, each target cell was measured to determine the amount of glass in the path of the incoming high-energy electron beam. In addition to mechanical measurements of the target windows, thickness determination was done by performing X-ray absorption measurements and using laser–interferometric techniques. The gas density was measured at the time of target manufacture using standard pressure gauges. The gas density was also determined using an optical line broadening technique.[35] This information was used to construct a detailed mathematical model of each target used in the course of the experiment[11]. Published values of nucleon structure functions[28] for the proton and the neutron ($F_2^p(x,Q^2)$ and $F_2^n(x,Q^2)$) along with knowledge of the EMC effect[36] were used in conjunction with internal radiative corrections[12] to calculate deep inelastic scattering rates. These rates were calculated as distributions of both x and Q^2. Finally, these rates were corrected for effects of *external radiation*[13] due to the path of the scattered electrons through the target cell wall and the spectrometer detector components. Final distributions were used to calculate the dilution factor.

2.5.2 Dilution Factor Method 2: Measurements in Beam

The second method of dilution factor determination utilized variable pressure ^{3}He reference cells. An advantage of the reference cell method is that the internal and external radiative corrections are included since the cross sections are physical, to all orders. The variable pressure reference cells were constructed in the same manner as the target cells, with the exception that no optical pumping cell was attached. By recording the scattering rate into each spectrometer as a function of the ^{3}He density in the reference cell, the rate of electrons due to events originating in the ^{3}He and those originating in the glass target windows can be decoupled. This decoupling is illustrated below

$$N^e = F^e\; l_{^3\mathrm{He}}\; n_{^3\mathrm{He}}\; \mathcal{A}\; d\sigma_{^3\mathrm{He}} \;+\; F^e\; l_{\mathrm{glass}}\; n_{\mathrm{glass}}\; \mathcal{A}\; d\sigma_{\mathrm{glass}}, \tag{21}$$

where now the density $n_{^3\mathrm{He}}$ is varied by the experimenters. This can be summarized in the following equation,

$$N^e = \mathcal{M}\; n_{^3\mathrm{He}} + \mathcal{R}_{\mathrm{glass}}. \tag{22}$$

The reference cell can be pressurized to various densities and the rate per unit density $\mathcal{M}$ can be measured. Note that this rate variable ($\mathcal{M}$) is explicitly dependent[14] upon x and Q^2. The extracted rate can then be used to construct a dilution factor

$$f = \frac{\mathcal{M}\; \tilde{n}_{^3\mathrm{He}}}{N_{\mathrm{Total\ Rate}}}, \tag{23}$$

[11] Due to the thinness of the target windows $\sim 50\ \mu$m, the target cell windows had a limited life in the electron beam. Different target cells were used during the course of the experiment.

[12] Initial and final state radiation along with vertex corrections were calculated. Additionally, radiative corrections were applied to *elastic scattering* and *quasielastic scattering* to be combined with the radiative corrections of the deep inelastic scattering to calculate an overall *effective* radiative correction to the deep inelastic scattering.

[13] The radiative effects were calculated as prescribed by Mo and Tsai[37] and through the use of the Monte Carlo program GEANT.[38] In the latter method, a detailed model of the target was incorporated into the program. Additionally descriptions of the two spectrometers, including magnets, detector elements, vacuum windows, etcetera, were used.

[14] However, the narrow Q^2 range in any given x bin results in $\mathcal{M}$ being a function mainly of x.

where $\tilde{n}_{^3He}$ is the actual operating density of the polarized target while the electron beam is impinging. The total electron scattering rate given by $N_{\text{Total Rate}}$ is just the total rate as observed by each spectrometer.[15] Excellent agreement is found between the two methods of dilution factor determination, as illustrated by Fig. 6.

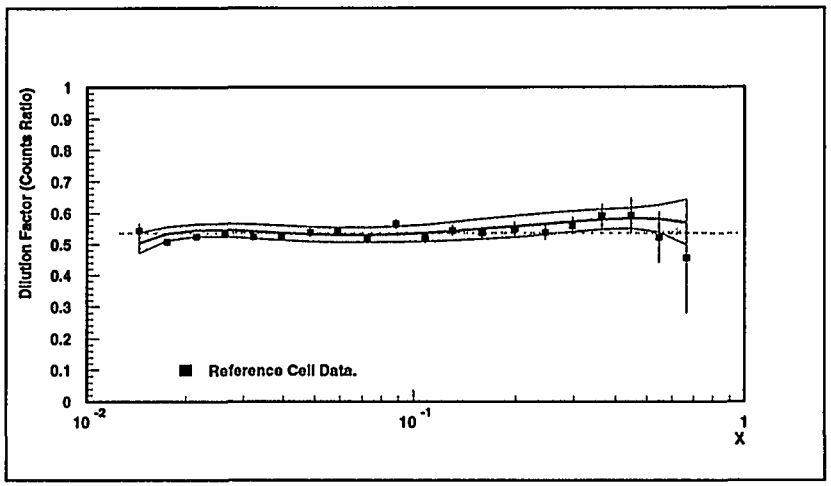


Fig. 6. Dilution factor as determined by mechanical measurement and as determined by reference cell rate measurement (symbols). The band is the result of the calculation based on the parameterization of the cell.

2.6 Electron Identification and Background Suppression

The experiment utilized magnetic spectrometers at forward angles.[16] The spectrometers were triggered by every pulse and the electronics were gated for a 400 ns duration. This mode of triggering enabled the experiment to record multiple events in any given pulse. Each spectrometer used magnets for momentum and charge selection of the scattered particles. Each spectrometer had nonvanishing acceptance for electrons above a momentum of 10 GeV/c. The momentum was reconstructed via the use of tracking hodoscopes.[17] The hodoscopes were instrumented with multiple-hit TDC's, thus permitting the recording of multiple events in a pulse. Electron identification was achieved with a combination of threshold gas Cherenkov detectors and lead-glass shower array detectors. As with the hodoscopes, the lead-glass detectors were also instrumented with multiple-hit TDC's. Each Cherenkov detector was instrumented with a high time resolution (1 nanosecond/bin) Flash ADC. Analysis of the digitized PMT waveforms led to e^- identification and π^- rejection for momentum below 19 GeV/c and 16 GeV/c for the 2.75° and 5.50° spectrometers respectively. Situated at the far end of each spectrometer, as shown in Fig. 7, was an array of lead-glass blocks in the *Fly's Eye* configuration sufficiently long for total containment of e^- (e^+) induced electromagnetic cascades. Particle energy reconstruction was done along with a shower development analysis using a neural network based algorithm. The energy value along with the momentum value were used to construct a ratio. For electrons, the ratio would have a mean of 1, while for π^-'s, the value would be different and less than 1. Further e^- identification was done by examining the results of the neural network analysis. Thus, a final e^- profile could be determined. A complementary analysis also led to π^- profiling. An interplay of the e^- and π^- analyses then led to an efficiency and background rate determination.[18]

2.7 Radiative Corrections

Equation 4 was written in the Born approximation (one photon exchange). What is actually observed is the cross section to all orders. In order to extract the spin-dependent structure functions, effects that are higher order than Born approximation must be taken into account. These corrections are referred to as internal and external radiative corrections. In addition to spin-averaged internal corrections, spin-dependent internal corrections must be calculated.

[15] Each spectrometer had a dilution factor calculated using both methods.

[16] The SLAC experiments E142 and E143 were precursors to the present experiment. A brief description has been published.[39]

[17] Thin fingers of scintillator material paired with a photo-multiplier tube (PMT).

[18] A residual sample of e^- in the final π^- sample and a residual sample of π^- in the final e^- sample are viewed as background contaminations. These background rates were measured to be small.

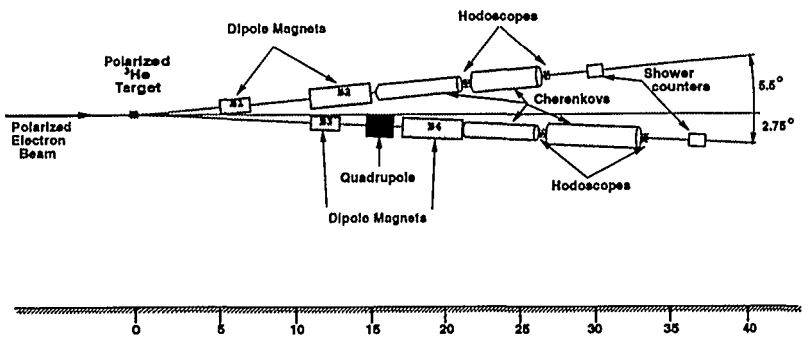


Fig. 7. Schematic of the 2.75° and 5.50° spectrometers as seen from above.

2.7.1 External Radiation

External radiative corrections include energy loss of the electron beam while traversing the target and energy loss of the scattered beams while exiting the target and traversing the detector elements. The incident beam energy loss is negligible in the thin target. Energy loss of the scattered electrons due to traversal through the target and the spectrometer elements can be explicitly calculated given the physical description of all matter encountered in the spectrometer line. In this way, each scattered electron can have its momentum corrected to the value just after the initial deep inelastic scattering.

2.7.2 Internal Radiation

There are two distinct sources of internal radiative corrections. Those that are calculated in the spin-averaged (unpolarized) case and those that are spin-dependent (polarized). Since the experiment measures an asymmetry which is the ratio of spin-dependent and spin-averaged processes, both polarized and unpolarized radiative corrections must be calculated. Polarized radiative corrections alone are a subject worthy of discussion at a conference or workshop. To this end, the reader is referred to the latest literature on the topic.[40,41] However, a brief description is warranted. Angular momentum conservation results in radiative corrections to deep inelastic scattering being different for the spin-dependent case compared to the spin-averaged case. The process of calculating the polarized radiative corrections entails the use of the observed deep inelastic scattering asymmetries. A polarized correction is calculated and applied to the asymmetry. The resulting asymmetry is then used to calculate a new correction. This iterative process is continued until the corrections converge.

3 Experimental Results

The analysis was carried out by two relatively independent subgroups of the collaboration. This allowed for a study of systematic effects possibly introduced by the analysis methods. The large data sets were analyzed on computer farms at SLAC and at The California Institute of Technology. Reduction of the data led to data summary tapes (DST's) with analysis cuts refined for e^- selection. Pion identification has already been discussed in Sec. 2.6; another background is *false* electrons. These are real electrons (not pions) that have an origin other than deep inelastic scattering.[19] The observed electrons can be described by

$$N^e_{\text{Total}} = N^e_{True} + N^e_{False}. \tag{24}$$

The *false* electrons have a charge symmetric origin, such as π^0 *Dalitz* decay,

$$\pi^0 \rightarrow \gamma\, e^-\, e^+\,. \tag{25}$$

Other sources would include pair production from high-energy γ's. In order to remove these *false* e^-'s, the polarity of each spectrometer was periodically reversed to accept positrons. The observed positron rate is a measure of these false electrons. Numerical asymmetries were constructed from the DST files. These were then corrected for π's and *false* e^-'s. Use of the dilution factor, beam polarization, and target polarization then results in the asymmetries $A_{\|}$ and $A_{\perp}$. These asymmetries were then corrected for radiative effects and the spin-dependent structure functions extracted.

Due to the finite acceptance of each spectrometer, the structure functions were measured in a range of Q^2 that is highly correlated with x. This correlation of Q^2 and x arises from the fixed angle of each spectrometer and the small entrance apertures. This Q^2 and x acceptance is shown for the two spectrometers in Fig. 8.

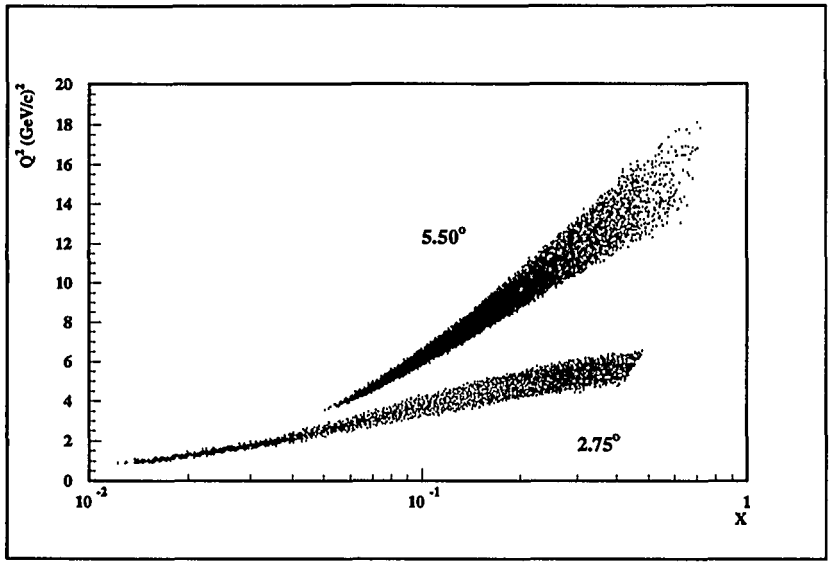


Fig. 8. Acceptance map of the 2.75° and 5.50° spectrometers in Q^2 and x.

In order to present $g_1(x)$ in a meaningful manner, the Q^2 value should be fixed to a common value for all x values. However, because of the acceptance correlation, the mean Q^2 values increase as a function of x. Early spin–dependent structure function experiments made an explicit check for Q^2 dependence for the ratio of the spin–dependent structure function to the spin–averaged structure function.[19] To the statistical and systematic precision of the experiment, no significant Q^2 dependence was found. That is

$$\left.\frac{g_1(x,Q^2)}{F_1(x,Q^2)}\right|_{x=x'} = \text{constant} \; . \tag{26}$$

Assuming validity of this relationship, the structure function $g_1^n(x,Q^2)$ can be evolved to a mean Q_0^2 to arrive at $g_1^n(x,Q_0^2)$. We chose to evolve to the average Q^2 observed in the data,[20] namely $Q_0^2 = 5$ (GeV/c)^2. Figure 9 shows the results of our experiment. The precision of the data is striking. An important feature of the data is the increase in the structure function at lower values of x. This is a possible indication of near divergent behavior of the structure function.

The data need to be evolved to a common Q^2 value in order to compare the current data to the world data for $g_1^n(x)$. Equation 26 was used to evolve the world data to the average Q^2 of 5 (GeV/c)^2. The results of this evolution are shown in Fig. 10. Additionally, the product $xg_1^n(x)$ as a function of x is shown rather than $g_1^n(x)$. This method of data presentation allows for a clearer comparison of experiments, an appreciation of the precision of each experiment, and a sense of the convergence of $\int_0^1 g_1^n(x)dx$. The precision of the current data in comparison to the world data cannot be overstated. The numerical integral over the covered data range is

$$\int_{0.014}^{0.70} g_1^n(x)\; dx = -0.036 \pm 0.004(\text{statistical}) \pm 0.005(\text{systematic}). \tag{27}$$

In order to integrate over the full x range, extrapolations below and above the covered data range must be done. For the high-x region, quark–counting arguments[42] may be followed that lead to an extrapolation of the form

$$g_1^n(x) \to (1-x)^3. \tag{28}$$

This form leads to a small contribution to the overall integral

$$\int_{0.70}^{1.0} g_1^n(x)dx \sim 0.0002. \tag{29}$$

The low–x behavior is, however, another matter. Since the data show an increase at low values of x, the extrapolation is more tenuous. The precision of the data brings into question the validity of naive low–x extrapolation models, such as the Regge–like behavior.

$$g_1(x) \sim x^{\alpha} \; . \tag{30}$$

Under the constraint that the exponent α in the Regge-inspired model is required to assume a value in the range $0 \leq \alpha \leq 0.5$, the best fit in the low–x ($x < 0.1$) interval of neutron data leads to an exponent of $\alpha = 0$. However, if the exponent

[19] In addition to deep inelastic scattering, radiated elastic and radiated quasielastic scattering are included in the definition of *true* electrons since these are accounted for in the radiative corrections.

[20] This is the current convention used by spin–dependent structure function experiments.

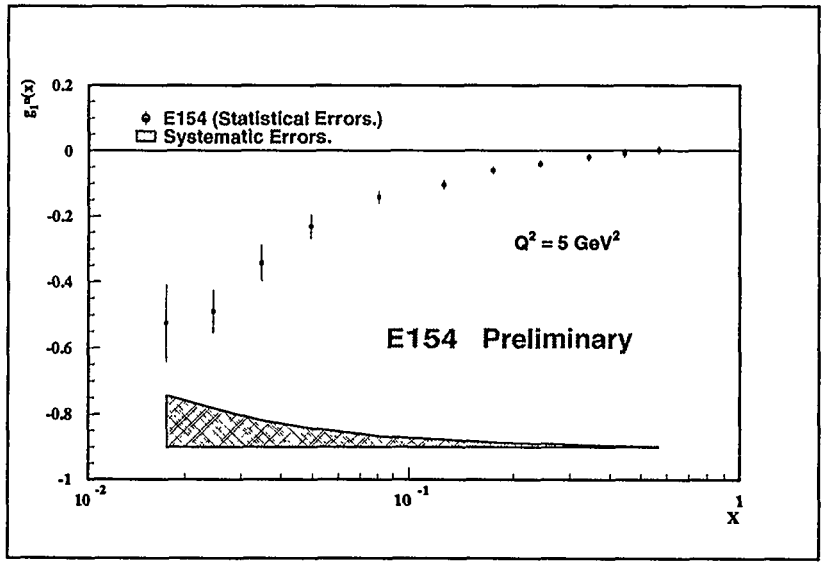


Fig. 9. Results of E154 measurement of the neutron spin structure function $g_1^n(x)$ evolved to a mean Q^2 of 5 (GeV/c)^2. The error bars are statistical only. The band near the bottom of the plot is the 1 σ systematic error.

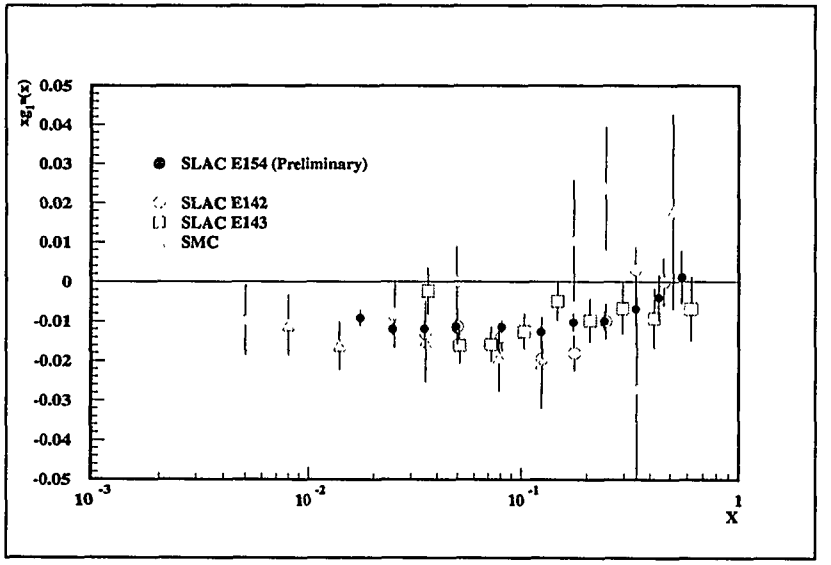


Fig. 10. Comparison of results of E154 and the rest of the world for the spin structure function $g_1^n(x)$ evolved to a common Q^2 of 5 (GeV/c)^2. Evolution is done with Eq. (26).

is allowed to assume any value, the fit leads to near divergent behavior. The two vastly different fits indicate the complexity of extrapolating.

The isovector difference in the structure functions is solely nonsinglet and is expected to have softer behavior.[43] Under this premise, the difference in structure functions takes the form

$$(g_1^p(x) - g_1^n(x)) \to C\, x^\alpha. \tag{31}$$

A combination of the SMC and E143 proton data may be taken along with the present neutron data to construct the difference. All points below $x < 0.1$ are used to calculate the fit parameters. The resulting fit is shown in Fig. 11. With this extrapolation, the form may be integrated and a Bjorken sum rule value calculated. In order to estimate the systematic error involved in the extrapolation, the fit can be done with and without the inclusion of the quantity $g_1^p(x) - g_1^n(x)$ below the E154 data range of $0.014 < x < 0.70$. The low–x extrapolation results in the following integral

$$\int_{0.0}^{0.014} (g_1^p(x) - g_1^n(x))dx = 0.041 \pm 0.007. \tag{32}$$

The average of the two extrapolations is taken as the integral, and half the difference is taken as an estimate of the extrapolation error. Due to the preliminary nature of the data, the Bjorken sum rule calculated here is viewed as more a qualitative check rather than a high-precision test. Evolution of the available data on the proton spin structure function leads to a global phenomenological fit resulting in an integral over the finite x range of

$$\int_{0.014}^{1.0} g_1^p(x)dx = 0.121 \pm 0.004 \pm 0.008. \tag{33}$$

Use of the high–x extrapolation found in Eq. (28) and the measured data range of the present experiment gives the neutron contribution in the same x region of

$$\int_{0.014}^{1.0} g_1^n(x)dx = -0.036 \pm 0.004 \pm 0.005. \tag{34}$$

These evaluations along with the low–x extrapolation on the difference of the structure functions gives a value of the Bjorken sum rule of

$$\int_0^1 (g_1^p(x) - g_1^n(x))dx = 0.198 \pm 0.006 \pm 0.011. \tag{35}$$

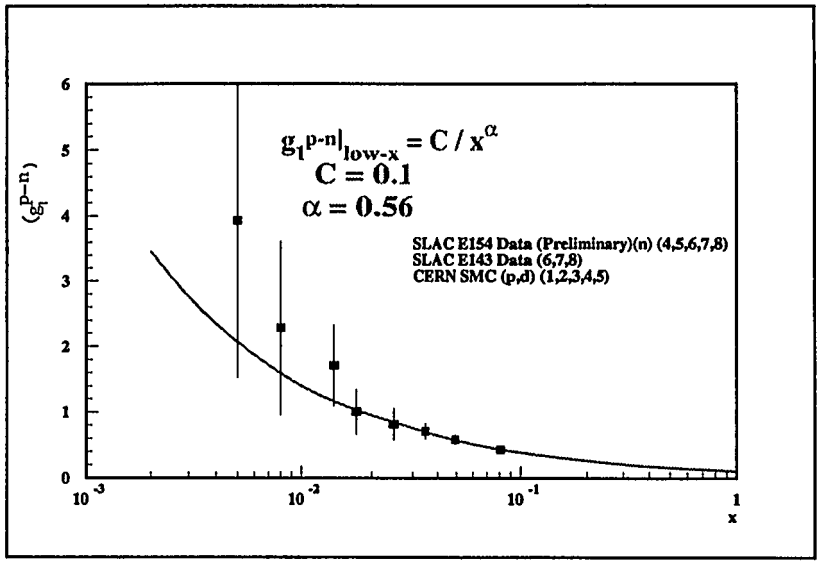


Fig. 11. Power law fit to $g_1^p(x) - g_1^n(x)$ in the low–x region using proton data from SMC and E142 along with neutron data of E154. For the x–region below the kinematic region of E154, the SMC data alone were used to construct $g_1^p(x) - g_1^n(x)$.

Consistent with the current Q^2 value of 5 (GeV/c)^2, the $O(\alpha_s^3)$ QCD corrected calculation of the Bjorken sum rule is

$$\int_0^1 (g_1^p(x) - g_1^n(x))dx = 0.181 \pm 0.003. \quad (36)$$

Certainly, the statistical precision of the available data is sufficient to test the Bjorken sum rule; however, the uncertainty in the extrapolation to low-x values ($x \to 0$) is high. Even though the low-x fit results in a reasonable value of χ^2/D.F., the assumptions of the extrapolation form might not be valid.

4 Conclusions

The experiment E154 has provided the scientific community with the most precise measurement of $g_1^n(x)$ in the kinematic range of $0.014 \leq x \leq 0.70$. An associated collaboration, E155, will be finished with a complementary set of high-precision $g_1^p(x)$ and $g_1^d(x)$ data in the spring of 1997. The experiment E155 will be using the same spectrometers with minor improvements. Additionally, a new spectrometer[44] has been constructed to detect scattered electrons at the angle of 10.5°. This will result in a data set that spans a much wider Q^2 range for a given value of x. By themselves, the high-precision results of E154 have brought into question the past methodology of handling extrapolations of the spin-dependent structure functions to regions in x below that which has been covered by experiments. Recent theoretical work in perturbative QCD has resulted in evolution equations in Next-to-Leading-Order for the spin-dependent structure functions which can be used to analyze the experimental data.[25,26] This manner of analysis should result in more reliable extrapolations to low-x regions and provide for an indirect measurement of the gluon angular momentum contribution to the spin of the nucleon. Until direct measurements at low x are undertaken, this will be the only method by which to probe the low-x realm of the spin-dependent structure functions. Such experiments will need the development of a new electron-nucleon colliding facility. The proposed *Next Linear Collider* could be such a facility; or low x could be probed by polarizing the protons at the collider facility at DESY. Spin-dependent gluon structure functions have yet to be directly measured; however, experiments at the *Relativistic Heavy Ion Collider* (RHIC) at Brookhaven National Laboratory are in preparation in which polarized protons will collide with polarized protons.

References

[1] R. E. Taylor, Rev. Mod. Phys. **63**(3), 573 (1991).

[2] H. W. Kendall, Rev. Mod. Phys. **63**(3), 597 (1991).

[3] J. I. Friedman, Rev. Mod. Phys. **63**(3), 615 (1991).

[4] J. D. Bjorken, Phys. Rev. **179**, 1547 (1969).

[5] R. P. Feynman, Phys. Rev. Lett. **23**, 1415 (1969).

[6] V. N. Gribov and L. N. Lipatov, Sov. J. Nucl. Phys. **15**, 438 (1972).

[7] Y. L. Dokshitzer, JETP **46**, 461 (1977).

[8] G. Altarelli and G. Parisi, Nucl. Phys. B **126**, 298 (1977).

[9] D. J. Fox *et al.*, Phys. Rev. Lett. **33**, 1504 (1974).

[10] W. Smith, "QCD studies in ep collisions," these proceedings.

[11] J. L. Friar, B. F. Gibson, G. L. Payne, A. M. Bernstein, and T. E. Chupp, Phys. Rev. C **42**(6), 2310 (1990).

[12] W. Greiner and A. Schäfer, *Quantum Chromodynamics,* (Springer, 1994).

[13] J. D. Bjorken, Phys. Rev. **148**(4), 1467 (1966).

[14] Particle Data Group, *Particle Physics Booklet* (1996).

[15] S. A. Larin and J. A. M. Vermaseren, Phys. Lett. B **259**, 345 (1991).

[16] J. Ellis and R. Jaffe, Phys. Rev. D **9**, 1444 (1974).

[17] M. J. Alguard *et al.*, Phys. Rev. Lett. **37**(19), 1261 (1976).

[18] G. Baum *et al.*, Phys. Rev. Lett. **51**(13), 1135 (1983).

[19] J. Ashman *et al.*, Nucl. Phys. B **328**, 1-35 (1989).

[20] B. Adeva *et al.*, Phys. Lett. B **302**, 533 (1993).

[21] D. Adams *et al.*, Phys. Lett. B **329**, 399 (1994).

[22] K. Abe *et al.*, Phys. Rev. Lett. **74**(3), 346 (1995).

[23] K. Abe *et al.*, Phys. Rev. Lett. **75**(1), 25 (1995).

[24] P. L. Anthony *et al.*, Phys. Rev. D **54**, 6620 (1996).

[25] M. Glück, E. Reya, M. Stratmann, and W. Vogelsang, Phys. Rev. D **53**(9), 4775 (1996).

[26] R. D. Ball, S. Forte, and G. Ridolfi, Phys. Lett. B **378**, 255 (1996).

[27] R. L. Heinmann, Nucl. Phys. B **64**, 429 (1973).

[28] M. Arneodo *et al.*, Phys. Lett. B **364**, 107 (1995).

[29] L. W. Whitlow *et al.*, Phys. Lett. B **250**, 193 (1990).

[30] H. Tang *et al.*, SLAC-PUB-6918 (1995).

[31] H. R. Band, G. Mitchell, R. Prepost, and T. Wright, *A Möller polarimeter for high-energy electron beams*, SLAC-PUB-7370 (1997).

[32] T. E. Chupp *et al.*, Phys. Rev. C **45**, 915 (1992).

[33] N. R. Newbury *et al.*, Phys. Rev. A **48**, 558 (1993).

[34] M. Romalis, *E154 Technical Note # 34* (1996).

[35] C. S. Yi, Phys. Rev. **58**, 1051 (1940).

[36] J. Aubert *et al.*, Phys. Lett. B **123**, 275 (1983).

[37] L. W. Mo and Y. S. Tsai, Rev. Mod. Phys. **41**(1), 205 (1969).

[38] R. Brun *et al.*, *GEANT—Detector Description and Simulation Tool* (1993).

[39] G. Petratos, R. L. Eisele, R. Gearhart, E. Hughes, and C. Young, *Large acceptance magnetic spectrometers for polarized deep inelastic electron scattering*, SLAC-PUB-5678.

[40] T. V. Kuchto and N. M. Shumeiko, Nucl. Phys. B **219**, 412 (1983).

[41] I. V. Akushevich and N. M. Shumeiko, J. Phys. G **20**, 513 (1994).

[42] S. Brodsky, M. Burkhardt, and I. Schmidt, Nucl. Phys. B **441**, 197 (1995).

[43] J. Bartels, B. I. Ermolaev, and M. G. Ryskin, Z. Phys. C **72**, 627 (1996).

[44] E155 Collaboration, *Proposal to add a spectrometer to E155* (1996).

F_2 and Test of the Standard Model at HERA

G. Grindhammer

Max Planck Institut für Physik
Werner Heisenberg Inst.
D-W-8000 München 40, GERMANY

No submission is currently available from the author.

EXPERIMENTAL MEASUREMENTS OF THE ANTIMATTER COMPONENT IN COSMIC RAYS

Presented by Guido Barbiellini
Final Version by Guido Barbiellini and Massimo Zalateu
I.N.F.N. Trieste
Trieste University, Trieste, Italy

Representing the WIZARD Collaboration

ABSTRACT

The antimatter component of the cosmic ray flux is mainly due to secondary production from reactions of the primary proton flux on the galactic interstellar medium (ISM). Searches for other sources of antimatter such as primordial black hole (PBH) evaporation, dark matter decay or annihilation, or from antiparticle leakage from far away antigalaxies are of deep interest. In this lecture, the present experimental status of antimatter searches from balloon flight experiments is presented. The near future experiments are illustrated (long-duration balloon flights); the very long-term data-taking detectors to be sent into space are also briefly reviewed.

© 1996 by Guido Barbiellini.

Introduction

The world in which we live and the part of the world we are able to probe with matter seem to be consistent, at the present average temperature, of being composed mainly of the light quarks u and d, and of electrons. These basic components are bound together by the quanta of the strong and electroweak interactions.

The fantaquantities of $\overline{u}$, $\overline{d}$, and e^+ are found at certain given times and in few places in our planet; for instance, you can find antiprotons ($\overline{p}$) or positrons (e^+) at CERN (Geneva), Fermilab (Chicago), SLAC/Stanford, and a few more places in Japan, the USA, and Europe.

In the cosmic rays of our galaxy, there is a sizable amount of $\overline{p}$ and e^+ ($\overline{p}/p \sim 10^{-4}$; $e^+/e^- \sim 10^{-1}$). The amount of known antimatter in our galaxy is compatible with the production mechanisms (1) and (2) from the interactions of primary protons on the interstellar medium (ISM):

(1) $pp \rightarrow \overline{p} + X$. (2) $pp \rightarrow \pi + Y$

$\hookrightarrow \mu^{\pm} + \nu_{\mu}$

$\hookrightarrow e^{\pm} + \nu_e + \nu_{\mu}$.

If the presence of antimatter in our galaxy and others is only that coming from reactions (1) and (2), then some time between the Big Bang and the 100 GeV temperature, a not well-defined interaction has introduced an asymmetry in the baryons as well as in the leptons.

The search for antimatter in the cosmic ray flux is motivated by the following reasons:

1. Search for predictable sources of positrons (e^+) and antiprotons ($\overline{p}$) to test models of galactic interstellar matter and confining mechanisms.
2. Search for possible excess of e^+ and $\overline{p}$ from possible exotic sources: primordial black hole (PBH) evaporation, supersymmetric dark matter candidate annihilation, or decay.

1 The Discovery of Cosmic Rays

Muons are part of the natural background radiation which was discovered early this century. It was assumed to come from the ground, with the intensity therefore decreasing at higher altitudes. It was a great surprise when Victor Hess in his historical balloon flight (Fig. 1) of 1912 discovered that the intensity increased with the altitude. Hess used an electroscope to measure the ionization as a function of altitude (results from different electroscope measurements are reported in Table 1). He concluded that the increase could best be explained by penetrating radiation incident on the atmosphere from above. It took some years before this conclusion was generally accepted.



Figure 1: Victor F. Hess in the balloon after one of the first successful flights in which cosmic radiation was discovered.

In the tradition of Hess, many more balloon flights have been dedicated to cosmic ray measurements. Studies have been made of the energy spectra and

Altitude (km)	Difference between observed ionization and that at sea-level (ions cm^{-3})
1	−1.5
2	+1.2
3	+4.2
4	+8.8
5	+16.9
6	+28.7
7	+44.2
8	+61.3
9	+80.4

Table 1.

composition. The dominant part (90%) of the cosmic radiation reaching the earth consists of protons. Of the remaining part, 4% is helium, 2% carbon and oxygen, and the rest are heavier elements with a large fraction of iron (if the fluxes are given as particles per GeV per nucleon). The proportions of these components are relatively constant with energy. Their spectra are described by an inverse power law in energy and the differential flux (dN/dE). Figure 2 shows proton cosmic ray energy spectra measured by different flights of the Japan-USA mission BESS.

1.1 Sources of the Antimatter in Cosmic Rays (C.R.)

The predictable amount of antimatter in the C.R. is that due to secondary production from the proton C.R. (see Fig. 2) colliding with the interstellar medium of our galaxy (ISM) and producing secondary pions and antiprotons according to the reactions:

$$p_{CR} + p_{ISM} \rightarrow \pi^{\pm} + X, \qquad p_{CR} + p_{ISM} \rightarrow \overline{p} + Y, \tag{1}$$

where X and Y are a system of pions and baryons. The pion decay [see Introduction section, production mechanism (2)] induces the positron (e^+) component of the C.R. The main uncertainty on the prediction of the absolute flux of positrons (e^+) and antiprotons ($\overline{p}$) comes from the equivalent amount of ISM seen by the primary protons in the containment time of the secondary e^+ and $\overline{p}$.

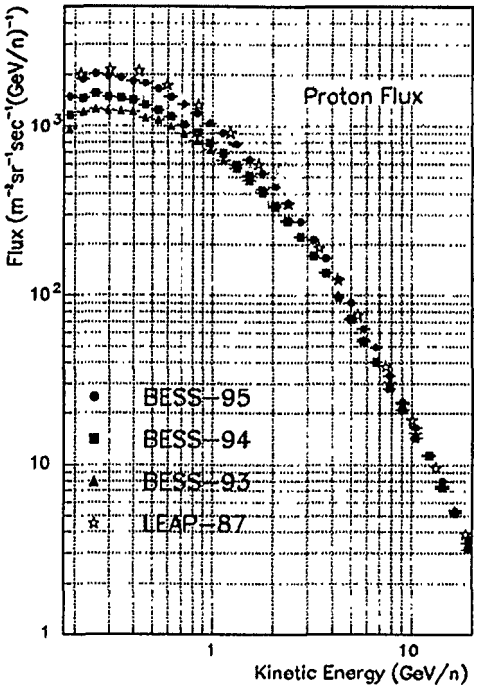


Figure 2: Proton flux measurements in BESS-93, 94, and 95 compared with the LEAP experiment, 1987.

Antimatter is also interesting from the standpoint of cosmology and elementary particle physics. Evidence of primary (not produced in a p-p interaction in the interstellar matter) antiproton components from an extragalactic source would provide the first evidence for large quantities of antimatter in the universe. Furthermore, a primary $\overline{p}$ and e^+ component could also arise from annihilation of dark matter or evaporation of primordial black holes.

2 The Cosmic Ray Positron Component

Measurement of the e^+ component of C.R. started in the early 1970s (Fanselow *et al.*, 1969; Daugherty *et al.*, 1975). The major problems associated with the

balloon-borne positron measurement are:

(a) the e^+ discrimination against the main proton component, and

(b) the correction for e^+ produced in the residual atmosphere and on the top of the balloon.

The very recent data on e^+ in C.R. collected by the CAPRICE Collaboration are reported in the following.

The positron to electron ratio in the cosmic radiation has been measured over more than one decade in energy, from 0.85 to 14 GeV, using the NMSU-WIZARD/CAPRICE balloon-borne magnet spectrometer. The spectrometer uses a solid radiator RICH detector and a silicon-tungsten calorimeter for particle identification. The proton rejection factor of the two instruments combined is better than 2×10^{-6} between 0.6 and 3 GeV/c dropping to 6×10^{-5} at 5 GeV/c and 10^{-4} at 10 GeV/c. The data was collected during 23 hours at a mean residual atmosphere of 4.0 g/cm^2. From a total of 2756 well-identified e^- and 498 e^+, the positron fraction $R = e^+/(e^+ + e^-)$ as a function of energy has been measured with small errors from 0.85 GeV to 14 GeV for the first time. The energy-dependent behavior of R is consistent with the simple leaky box model of the galaxy. The positron fraction in the upper energy bins are in agreement with the latest high-energy measurements.

2.1 Detector System

Figure 3 shows the NMSU-WIZARD/CAPRICE spectrometer that was flown from Lynn Lake, Manitoba, Canada on August 8, 1994. From top to bottom, it includes a RICH detector (Fig. 4), a time-of-flight (ToF) system, a magnet spectrometer of multiwire proportional chambers (MWPC) and drift chambers (DC), and a silicon-tungsten imaging calorimeter.

The RICH detector (Carlson *et al.*, 1994; Carlson *et al.*, 1995), with a threshold Lorentz factor of 1.5, uses a solid NaF radiator and a photosensitive MWPC with pad readout to detect the Cherenkov light image. It was used to measure the velocity of the particles. The ToF system consists of two layers of plastic scintillators, one above and one below the tracking stack. It was used to give a trigger as well as to measure the time-of-flight and dE/dx losses of the particles. The magnet spectrometer (Golden *et al.*, 1991; Hof *et al.*, 1994) measures the rigidity of the particle with an average maximum detectable rigidity of 200 GeV/c.

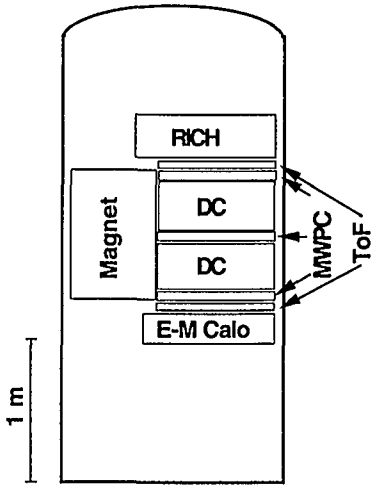


Figure 3: A schematic view of the CAPRICE gondola.

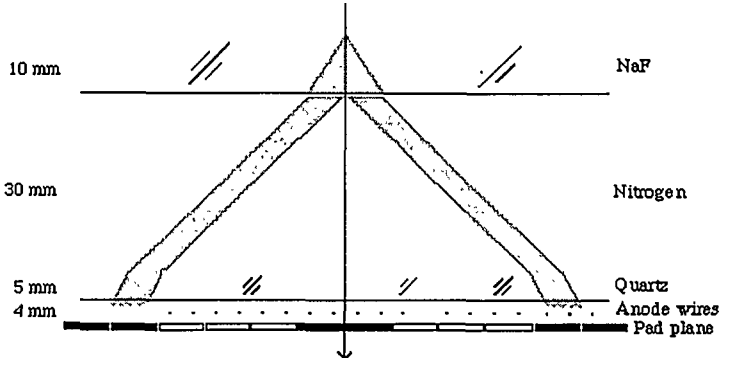


Figure 4: A schematic view of the NaF-RICH detector.

Finally, the electromagnetic calorimeter (Bocciolini *et al.*, 1991) is composed of eight planes of double-sided silicon strip detectors interleaved with seven layers of tungsten converters (each one radiation length thick). The silicon strips are placed perpendicular to each other, giving the energy deposited in each strip. Moreover, this imaging device provides information on the longitudinal as well as the lateral profile of the cascade.

2.2 Data Analysis

During the 23-hour-long flight, more than six million events were recorded at a mean residual atmosphere of 4.0 g/cm^2. Electrons and positrons were selected in the rigidity range between 0.6 and 10 GeV/c. Events with a single track having an acceptable chi-square in the tracking of the spectrometer were accepted. The selected singly charged particles give a signal corresponding to less than 1.7 mips (minimum ionizing particles) in the top ToF scintillator. Albedo events were rejected using both the ToF and the RICH. An electron sample was selected as particles with negative deflection, $\beta = 1$ as detected by the RICH and an electromagnetic shower in the calorimeter.

The cuts imposed on the calorimeter to identify electromagnetic showers have a logarithmic dependence on rigidity and are based on (a) results from an experiment using particle beams at CERN (Bocciolini *et al.*, 1993), (b) simulations, and (c) experience gained from a previous flight with the same instrument (Golden *et al.*, 1996). An electromagnetic shower is characterized by a narrow shower with most of the energy deposited inside four Molière radii around the track. Additional cuts based on the total detected energy, which should match the measured momentum, and on the longitudinal and lateral profiles of the shower were applied. A small number of particles emit a bremsstrahlung photon before entering the calorimeter (e.g., in the RICH or the aluminum cover of the gondola) that was detected in the calorimeter as a parallel shower. These double shower events with a single track in the tracking system are clearly electron/positron events and can be used with looser cuts. The detection efficiency of the calorimeter using the above cuts is rigidity dependent increasing from 80% at 0.6 GeV/c to 85% above 0.7 GeV/c, being constant 85% between 0.7 and 3 GeV/c, then slowly decreasing to 75% at 10 GeV/c.

The RICH was used to measure the velocity (β) of the particles. Due to the high rejection factor of the calorimeter, rather loose cuts were applied on the RICH data in order to maximize the efficiency of selection. Electrons and positrons were selected by the RICH as $\beta = 1$ particles with a well-defined Cherenkov light image and a good agreement between the position determined by the RICH and that from the tracking measurement. With these cuts applied, the RICH has a constant detection efficiency of 72% between 0.6 and 5 GeV/c. Above 5 GeV/c, the RICH is not capable of separating protons from positrons and was not used.

The scintillator cut of $\leq$1.7 mip gave an efficiency of 98% for protons, pions, and muons. Electrons and positrons can emit bremsstrahlung photons which materialize in or above the top scintillator. These events will be rejected by the cuts applied. The efficiency for electrons and positrons is found to decrease from 86% at 0.6 GeV to 81% at 10 GeV due to a small increase in shower multiplicity.

2.3 Results

Table 2 gives the number of electrons and positrons that pass the cuts applied on the RICH, the ToF, and the calorimeter. In order to estimate the number of protons which simulate a positron-like cascade in the calorimeter, we selected a proton sample using the RICH and ToF for rigidities less than 1.4 GeV/c. In this energy region, the RICH acts as a threshold counter and the ToF is able to separate protons from lighter particles. Between 1.4 and 5.0 GeV/c, the RICH can accurately identify protons. On this proton sample, the calorimeter cuts were applied and the surviving protons were used to determine the contamination. The proton contamination was found to be 8×10^{-4} for rigidities between 0.6 and 1.0 GeV/c and less than 1×10^{-4} between 1 and 5 GeV/c. In the energy region from 5 to 10 GeV/c, the contamination is assumed to be the same as that of the bin 3 to 5 GeV/c , that is $(1.1 \pm 0.5) \times 10^{-4}$.

The muon and pion background was estimated using Monte Carlo simulations. The pion contamination was found to be 5×10^{-3} below 1 GeV/c and less than 1×10^{-3} between 1 and 5 GeV/c. However, the abundance of pions is less than 1×10^{-3} of the protons at this small atmospheric depth and hence the pion contamination is insignificant. The muon contamination was negligible at all rigidities.

Energy bin at spectrometer GeV	Observed number of events[a] e^-	e^+	Extrapolated number at ToP[b] e^-	e^+	Atmospheric correction e^-	e^+	Median energy at ToA[c] GeV	$\frac{e^+}{e^+ + e^-}$ at ToA[c]
0.6 - 0.8	396	121	886.4	300.4	125.5	184.8	0.99	0.14 ± 0.03
0.8 - 1.05	415	105	905.7	237.6	67.6	94.6	1.30	0.132 ± 0.021
1.05 - 1.5	554	103	1212.6	212.4	45.9	65.9	1.77	0.113 ± 0.014
1.5 - 2.0	447	65	1040.2	139.2	20	26.6	2.45	0.090 ± 0.016
2.0 - 3.0	455	49	1003.4	88.9	14.8	18.1	3.45	0.076 ± 0.012
3.0 - 5.0	303	28(4)	632.5	49.4	7	8.6	5.37	0.075 ± 0.015
5.0 - 10.0	186	27(7)	414.8	43.9	2.9	3.4	9.56	0.07 ± 0.03

[a]The numbers shown in parentheses are the estimated proton background.

[b]Top of payload.

[c]Top of atmosphere.

Table 2: Summary of electron-positron results.

The number of protons passing the RICH cuts was estimated using a proton sample selected by the ToF below 1 GeV/c, and by the calorimeter above 1 GeV/c by requiring a hadronic interaction. The proton contamination in the RICH was found to be 2×10^{-3} between 0.6 and 1 GeV/c increasing to 2% at 3 GeV/c, 30% at 4 GeV/c, and 60% at 5 GeV/c due to the loose cuts applied. It may be pointed out that the RICH cannot separate muons and pions from electrons and positrons in the energy region of interest in this analysis.

Assuming that the rejection of protons by the RICH and the calorimeter is independent, we get a total proton contamination of less than 2×10^{-6} between 0.6 and 3 GeV/c increasing to 6×10^{-5} at 5 GeV/c and 10^{-4} at 10 GeV/c. The rejection factor of the calorimeter and the RICH is high enough to eliminate all proton, pion, and muon contamination from the positron sample between 0.6 and 3 GeV/c. The proton contamination was found to be 9% and 17% of the positron sample in the rigidity bins 3 to 4 GeV/c and 4 to 5 GeV/c, respectively. In the rigidity region 5 to 10 GeV/c, only the calorimeter has been used, resulting in a proton contamination of 25% of the selected positron sample. This proton contamination is shown in the parentheses in Table 2 and was subtracted from the positron sample.

The secondary positrons and electrons, which are produced in the residual atmosphere above the instrument, were estimated in the following manner. We first determined the energy spectrum of the negative muons. These muons were identified by requiring minimum ionizing, negative curvature particles, which enter the instrument from the top and undergo no interaction in the calorimeter. The efficiency of selecting these particles was found to be 98.2%. We show in Fig. 5 the observed spectrum (number of particles per unit energy) of muons from 0.8 GeV to 15 GeV. The dotted curve shown in this figure is the calculated spectrum at 4 g/cm^2 of residual atmosphere (Stephens, 1981). Note the excellent agreement with data. At the top of the payload (ToP), most secondary electrons and positrons come from decaying muons. We use the normalization constant obtained from the muon spectrum in Fig. 5 to estimate the secondary electron-positron spectra at 4 g/cm^2 (Stephens, 1981).

The observed electron and positron spectra were corrected for the efficiencies and were extrapolated to the top of the payload using bremsstrahlung corrections. These flux values (particles per unit energy) are shown in Fig. 5 as a function of energy. The estimated atmospheric secondary electrons and positrons are also shown by dashed and solid curves, respectively. The number of secondary particles are tabulated in Table 2 along with the extrapolated number of observed electrons and positrons to the top of the payload.

To check the correctness of this procedure, the growth curve of the electrons in the atmosphere from 4 g/cm^2 to 200 g/cm^2 in the energy interval 0.6-0.9 GeV was studied. By normalizing the calculated growth curve (Daniel and Stephens, 1974) for 700 MeV electrons over the depth between 30 and 150 g/cm^2, the fraction of secondary electrons turns out to be 13.2±1.9% at 4 g/cm^2. From Table 2, one can estimate that the fraction of secondary electrons in the energy interval between 0.6 and 0.8 GeV is 15.1±2.3%, assuming a possible 15% uncertainty for the theoretical estimate. This observed consistency between these two independent methods gives us confidence that the corrections made are reliable.

The corrected electron and positron spectra were extrapolated to the top of the atmosphere (ToA) by solving simultaneously the cascade equations describing the propagation of electrons, positrons, and gamma rays that result from bremsstrahlung of the electron component. From this, we obtained the positron to electron ratios that are shown in Table 2 along with the median energy at the top of the atmosphere.

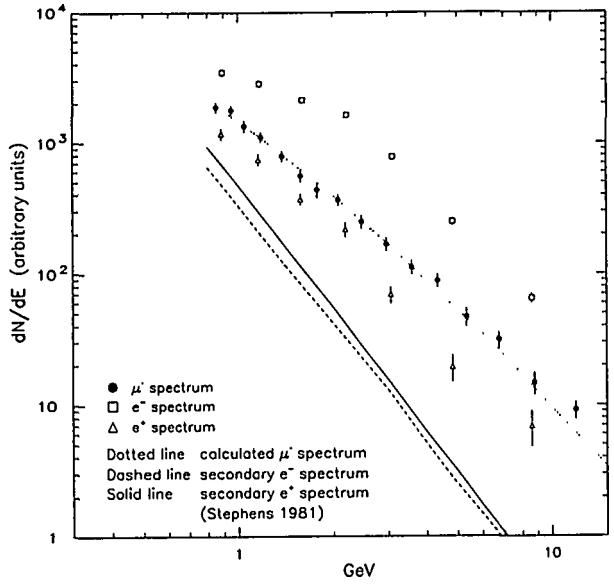


Figure 5: The measured electron and positron flux at the top of the payload, the analytically determined atmospheric background, and the measured muon spectrum with an analytical prediction.

The resulting positron to electron ratio is plotted in Fig. 6 together with previous measurements (Fanselow *et al.*, 1969; Daugherty *et al.*, 1975; Muller and Tang, 1987; Golden *et al.*, 1987; Golden *et al.*, 1994; Barwick *et al.*, 1995; Golden *et al.*, 1996; Agrinier *et al.*, 1969; Clem *et al.*, 1995). The errors shown include both the statistical and the systematic errors. Our results are in agreement with the recent measurements (Golden *et al.*, 1996; Barwick *et al.*, 1995) at the upper energy bins. The positron fraction (R) decreases from 0.14 at 0.8 GeV to 0.075 at 4 GeV and remains nearly constant above this energy. The observed energy dependence of the CAPRICE results is consistent with that expected from the simple leaky box model (Protheroe, 1982). The value of the ratio is dependent on the amount of matter traversed in the interstellar space and on the assumed spectrum of electrons; both of these have large uncertainties. It is essential to obtain the absolute spectra of both electrons and positrons to derive useful information on the origin and propagation of these components. The analysis to obtain absolute fluxes of electrons and positrons is in progress as well as efforts to extend the analysis to lower energies.

3 The Cosmic Ray Antiproton Flux

Antiproton searches started a long time ago following an original idea of L. Alvarez that suggested the possibility of flying a magnetic spectrometer using superconducting coils. Due to the small amount of $\overline{p}$ in C.R. ($\overline{p}/p \sim 10^{-4}$) and because of the large electron background, the progress in this field of C.R. has been quite slow in the past. Recent balloon missions using the most advanced techniques developed in the particle accelerators have improved substantially the experimental status of the art. But for the most relevant progress, future space-based missions are strongly needed. Data from two balloon flight collaborations (CAPRICE and BESS) will be reported in the following.

3.1 CAPRICE Flight 94 for $\overline{p}$ Search

The NMSU-WIZARD/CAPRICE spectrometer described previously for the e^+ data has also collected $\overline{p}$ data.

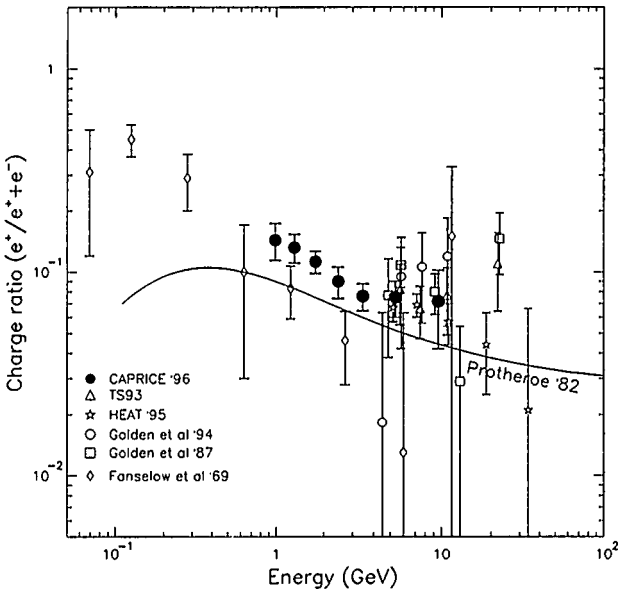


Figure 6: Positron fraction $e^+/(e^+ + e^-)$ as observed in this experiment compared with other published data and a simple leaky box model.

For this data, the 50 × 50 cm^2 RICH detector (Carlson *et al.*, 1994) is essential; other equipment such as time of flight and the imaging calorimeter enhance the antiproton signal among the more copious negative particles e^-, μ^-, ...

3.1.1 Data Analysis

The analysis was based on 18 hours of data collection for a total acquisition time of 60520 seconds under an average residual atmosphere of 4 g/cm^2.

The data analysis must use the information available from the different detectors to safely identify the antiprotons in a very large background of other particles. Albedo particles, as well as the large number of protons and electrons, must be rejected in the antiproton analysis. About 4% of the cosmic ray protons interact in the atmosphere above the spectrometer and produce π^- and μ^- that must be rejected. Interactions in the spectrometer and associated bar structure also results in a background of negatively charged particles. The remaining background in the antiproton sample is carefully estimated using experimental data and simulations. The selection of protons is more straightforward with little background to reject.

Based on the ability of the RICH to reliably identify antiprotons from pions, muons, and electrons, the rigidity range chosen for our analysis was 1.2 to 4.0 GeV/c. This rigidity bin was divided into two: 1.2 to 2.8 GeV/c and 2.8 to 4.0 GeV/c. At 1.2 GeV/c, the RICH (anti)proton selection efficiency becomes higher than 50%. At a rigidity of 2.8 GeV/c, the Cherenkov angle of (anti)protons becomes less than six standard deviations away from the Cherenkov angle of the β (velocity) $\sim$ 1 particles (pions, muons, and electrons). Four GeV/c is the rigidity where the (anti)proton Cherenkov angle becomes less than three standard deviations away from the Cherenkov angle of $\beta \sim 1$ particles. The results are shown in Table 3.

For the first time, the combination of an electromagnetic calorimeter and a ring imaging Cherenkov detector has been used to measure the cosmic ray flux of antiprotons. This combination has made it possible to accurately identify antiprotons in the presence of a large background of lighter, negatively charged particles. It also allows an accurate determination of the contamination within the antiproton sample.

The flux of antiprotons and the ratio of antiprotons to protons increase over the kinetic energy interval 0.6 to 3.2 GeV, see Table 4. In agreement with

other recent data (e.g., Mitchell *et al.*, 1996), it supports the conjecture that the antiprotons in this energy range are produced in the interstellar medium by primary cosmic rays colliding with interstellar gas.

The combination of all available data on the ratio in the energy range 0.3 to 3 GeV (Moiseev *et al.*, 1996; Bogomolov *et al.*, 1987 and 1990; Mitchell *et al.*, 1996; and this work) shows an increase with energy in agreement with calculations by Gaisser and Schaefer (1992). However, the combined data do not rule out a faster increase than calculated. The two measurements that have been reported above 4 GeV by Golden *et al.* (1984) and by the MASS91 experiment (Hof *et al.*, 1996) differ by about three standard deviations, and further measurements are clearly needed in order to rule out any exotic antiproton production. Fortunately, new experiments are in progress.

3.2 Selection Criteria to Identify $\bar{p}$ in CAPRICE Data

3.2.1 Scintillators

Particles with charge one were selected using the measured energy loss in the top scintillator. From the observed distribution of the dE/dx as a function of rigidity, singly charged proton-like events were selected in the following manner.

3.2.2 RICH

The RICH was used to measure the Cherenkov angle of the particle and thereby its velocity. The velocity and the Cherenkov angle resolution which depends on the incidence angle, were determined using a large number of protons selected by the calorimeter and the scintillators. The resolution varied from 8 mrad (perpendicular incidence and $\beta \sim 1$) to about 23 mrad (10° off perpendicular incidence and $\beta = 0.78$). Since the RICH is the only detector capable of clearly identifying antiprotons against a background of muons, pions, and electrons in the rigidity range 1.2 to 4 GeV/c, strict cuts were applied on the RICH data. A good agreement between the particle's impact position as determined by the RICH and the tracking system was required. The difference in x and y should be less than three standard deviations (rigidity dependent), typically < 5 mm. Using these conditions, reliable Cherenkov angle information was obtained.

Rigidity at spectrometer GeV/c	Observed number of events[a] $\bar{p}$	p	Extrapolated number at top of payload $\bar{p}$	p	Atmospheric correction $\bar{p}$	p	$\frac{\bar{p}}{p}$ at TOA[b]
1.2 - 2.8	4(1)	124658	8.6	303433	1.5	8484	$2.5\ (+3.2,-1.9) \times 10^{-5}$
2.8 - 4.0	5(0.7)	25260	17.7	90451	1.4	1662	$1.9\ (+1.6,-1.0) \times 10^{-4}$

[a]The numbers shown in the parentheses are the estimated muon, pion, and electron background.
[b]Top of the Atmosphere. The quoted errors are a combination of statistical and systematic errors.

Table 3: Summary of proton-antiproton results.

Kinetic Energy at TOA[a] GeV	Geometrical factor $(m^2\ sr)^{-1}$	Antiproton flux at TOA[b] $(m^2\ sr\ s\ GeV)^{-1}$	Proton flux at TOA[b] $(m^2\ sr\ s\ GeV)^{-1}$
0.6 - 2.0	179.1 ± 2.8	$1.9\ (+2.4, -1.4) \times 10^{-2}$	743 ± 17
2.0 - 3.2	177.5 ± 2.8	$5.3\ (+4.5, -2.9) \times 10^{-2}$	278 ± 10

[a]Top of the Atmosphere.
[b]The quoted errors are a combination of statistical and systematic errors.

Table 4: Antiproton and proton fluxes at the top of the atmosphere.

3.2.3 Calorimeter

The calorimeter was used to identify electromagnetic showers. The longitudinal and transverse segmentation of the calorimeter combined with the measurement of the energy lost by the particle in each silicon strip resulted in high identification power ($\sim 85\%$) for electromagnetic showers combined with a high rejection power ($\sim 10^4$) for hadronic particles (Barbiellini *et al.*, 1996). In the analysis presented in this paper, the calorimeter was used to reject events with electromagnetic showers initiated by a single electron, possibly accompanied by a bremsstrahlung photon emitted in the RICH or in the dome above the detector stack (see Weber, 1996 for a description of the selection criteria).

Figures 7 and 8 illustrate the calorimeter performance, and show schematic views of two single events in the CAPRICE apparatus. The instrument is shown in the bending (x) view and in the nonbending (y) view. From top to bottom is displayed: the RICH seen from above, the tracking stack of multiwire proportional chambers and drift chambers, and the imaging calorimeter. Note that Figs. 7

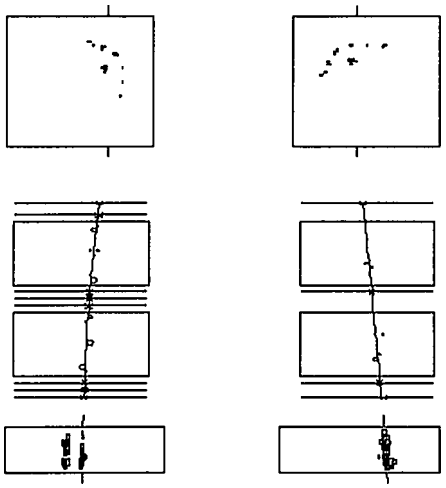


Figure 7: Display of a single 1.3 GeV/c electron traversing the CAPRICE apparatus.

and 8 are not to scale; the calorimeter is significantly thinner than shown in the figure. Figure 7 shows a single 1.3 GeV/c electron traversing the apparatus and emitting a bremsstrahlung photon in the RICH. The RICH shows the detected Cherenkov light image where the ionization of the chamber gas by the electron is shown as a cluster of pads hit in the center surrounded by the signals from the Cherenkov light. Due to total reflection in the NaF crystals, only part of the Cherenkov ring is detected. The tracking stack shows the trajectory of the electron as it is deflected by the strong magnetic field. The calorimeter shows the two electromagnetic showers produced by the electron and the bremsstrahlung photon, respectively. The origin of the bremsstrahlung photon can be located by projecting backward the direction of the shower and determining where it intersects the electron trajectory. More than one-fourth of the electrons in the rigidity region 1.2 to 4 GeV/c were accompanied by a bremsstrahlung photon reconstructed in the calorimeter.

Similarly, Fig. 8 shows a single 2.2 GeV/c antiproton traversing the instrument. The ring of Cherenkov light is clearly seen in the RICH, giving an accurate velocity determination for the particle. The rigidity is measured from the deflection in the

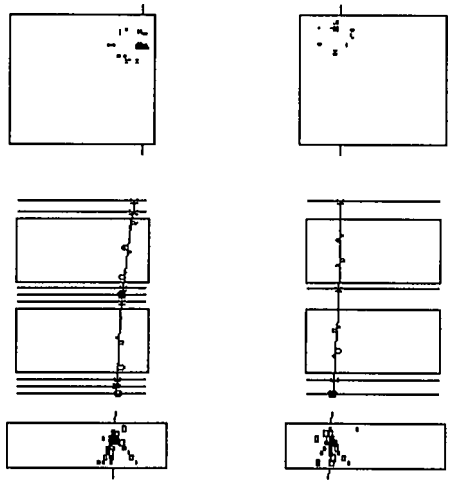


Figure 8: Display of a single 2.2 GeV/c antiproton traversing the CAPRICE apparatus. The antiproton interacts in the calorimeter showing clearly several charged particles emerging from the vertex of interaction; this could be an annihilation in flight.

tracking system. The antiproton interacts in the calorimeter, clearly showing many charged particles emerging from the vertex of interaction; this could be an in-flight annihilation. The interaction probability for a 2.2 GeV/c antiproton is about 40%.

3.2.4 Tracking

The tracking information must be carefully used to eliminate positively charged particles (protons) that have scattered in the tracking system and therefore look like negatively charged particles. Events with more than one track must also be eliminated. To achieve this goal, a set of conditions were imposed on the fitted tracks. These conditions represent a compromise between rejection power and efficiency, and are partly based on experience gained previously using the same tracking system (Mitchell *et al.*, 1996; Hof *et al.*, 1996).

4 BESS-93 to BESS-95 Flights

The largest sample of $\overline{p}$ in C.R. collected so far is the one obtained by the magnetic spectrometer built by the BESS Collaboration.

The BESS experiment has been carried out as a joint research project of the University of Tokyo, National Laboratory for High Energy Physics (KEK), Kobe University, Institute of Space and Astronautical Science (ISAS) in Japan, and National Aeronautics and Space Administration (NASA), New Mexico State University (NMSU), and the University of Maryland in the United States to search for cosmic ray antiparticles and to make precise measurements of cosmic ray spectra.

The BESS spectrometer has been developed since 1987, and three successful scientific flights have been carried out in Canada since 1993.

4.1 BESS Spectrometer and Flights

Figure 9 shows cross sections of the BESS spectrometer. The first two flights were made with configuration (a), and the third flight in 1995 was carried out with configuration (b) after the upgrade of TOF counters with a new pressure vessel. Table 5 gives the latest major spectrometer parameters.

The BESS spectrometer was launched by using 29 MCF balloons, in summers since 1993.

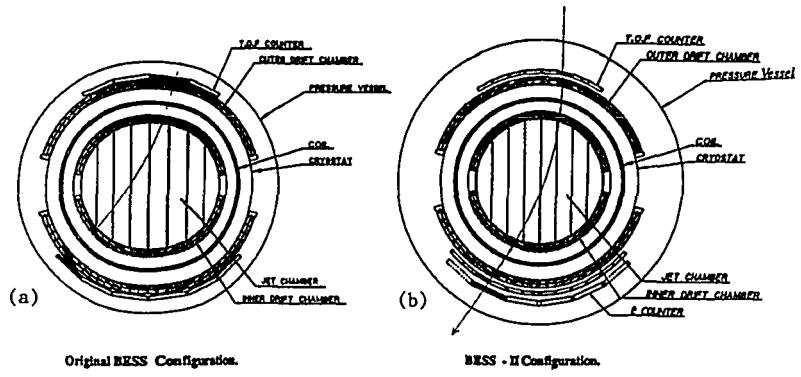


Figure 9: Cross sections of BESS spectrometer.

Geometrical Acceptance	0.4 m^2sr
Maximum Detectable Momentum	200 GeV/c
Momentum Region for Antiproton Search	2 GeV/c ($\gg$ 3 GeV/c)
Momentum Region for Antihelium Search	50 GeV/c
Trigger Rate	1 - 2 kHz
Event Recording Rate	100 - 200 Hz
Sensitivity for Antiparticle Search	10^{-6} - 10^{-7}/one day flight
Transparency of Half Detector Wall	7.5 g/cm^2
Size of Pressure Vessel	1.7 m$\varnothing$ $\times$ 3.6 m
Weight of Payload	2.2 ton
Power Consumption	1.2 kW

Table 5: Main parameters of BESS Spectrometer (II).

4.2 Summary and Further Improvements for Future Flights

The BESS spectrometer has detected more than 40 low-energy antiprotons with precise energy measurement and has resulted in bringing the upper limit of the antihelium to helium ratio down to 2×10^{-6}.

Figures 10 and 11 show the BESS-93 results on the $\bar{p}$ flux and the $\bar{p}/p$ ratio. By making an important improvement in the TOF system, the BESS-95 flight has enlarged the momentum interval for $\bar{p}$'s, consequently increasing the statistics available on the world $\bar{p}$ sample. Figure 12 shows the clean $\bar{p}$ sample in the plane $1/\beta$ versus rigidity (β is the $\bar{p}$ velocity in units of c). Figure 13 and Table 6 give the results on the $\bar{p}$ flux in five and four energy bins.

Energy, MeV	$\bar{p}/p$ ratio	Antiproton flux
200-500	1.3×10^{-5}	0.016
500-700	1.2×10^{-5}	0.013
700-1000	1.6×10^{-5}	0.012
1000-1200	3.3×10^{-5}	0.019

Table 6: Results of the 1995 flight.

4.3 BESS Search for Antihelium

All helium events were carefully checked for an antihelium. Event #1,656,905 from the '95 flight showed good parameters, but unfortunately did not have good consistency of the Z coordinate measured by TOF and by the tracking system, and had a sign of interaction above upper IDC. It does not allow us to accept this event as the first detected nonhydrogen antinucleus.

The BESS Collaboration has computed an $\overline{He}$ limit on the basis of the '93–'94 data.

The presence of the $\overline{He}$ in the cosmic ray would be an important discovery implying the existence of primary antimatter within the universe.

Figure 14 shows the rigidity distribution of the detected cosmic rays. From the absence of candidates with negative charge, the limit shown in the following figure is derived. BESS is planning an infrared detector flight in '97 and possible long-duration flights in '99 and later.

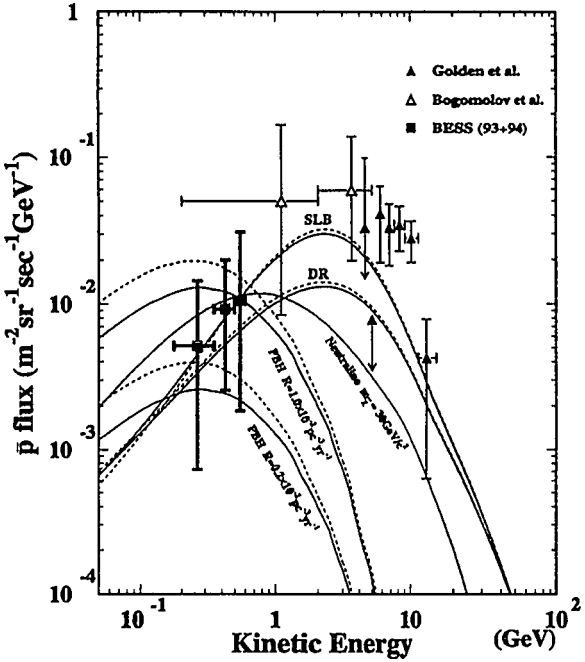


Figure 10: Measured $\bar{p}$ flux in comparision with the results of other experiments and calculations. Filled squares, the present results; filled triangles, Golden *et al.*; open triangles, Bogomolov *et al.* The curves labeled "SLB" and "DR" are recently calculated by Mitsui based on the Standard Leaky Box Model and Diffusive Re-acceleration Model, respectively. The dashed curves are for the minimum solar modulation and the solid are for ϕ = 600 MeV. The curves labeled "PBH" are calculations by Maki *et al.* on the $\bar{p}$ production by primordial black holes for two values of evaporation rate R. The dashed and solid curves are again for the minimum and ϕ = 600 MeV solar modulations. The curve labeled "Neutralino" is calculated by multiplying the model of the proton flux and the $\bar{p}/p$ ratio by Jungman and Kamionkowski based on the $\bar{p}$ production by annihilations of dark matter neutralinos.

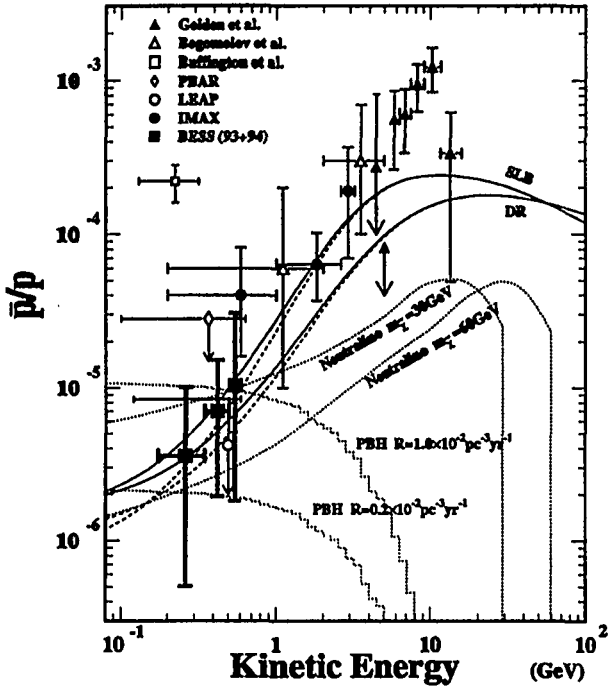


Figure 11: Measured $\bar{p}/p$ ratio in comparision with the other experimental data and calculations. Filled squares, the present result; filled triangles, Golden *et al.*; open triangles, Bogomolov *et al.*; open square, Buffington *et al.*; open diamond, the PBAR experiment; open circle, the LEAP experiment; filled circles, the recent result of IMAX. The dashed curves labeled "SLB" and "DR" are recently calculated by Mitsui based on the Standard Leaky Box Model and Diffusive Reacceleration Model, respectively. The dotted curves labeled "PBH" are predictions of Maki *et al.* for the $\bar{p}$'s produced by primordial black holes with two different assumed evaporation rates R. The dotted lines labeled "Neutralino" are the prediction of Jungman and Kamionkowski for the $\bar{p}$ productions by annihilations of dark matter neutralinos.

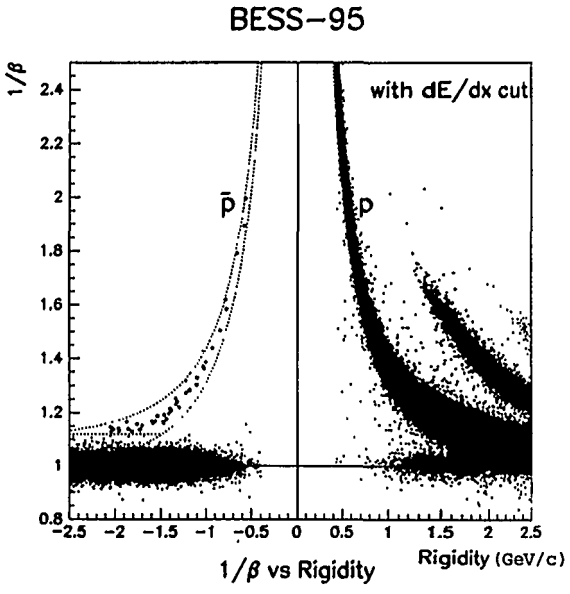


Figure 12: The identification of antiproton events after the dE/dx cut. The antiproton events are marked as solid dots.

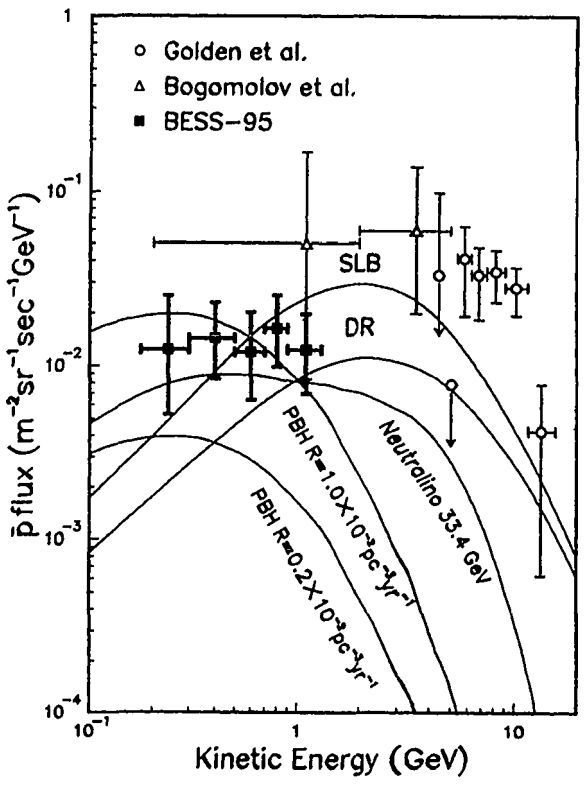


Figure 13: Comparision of the measured $\overline{p}$ flux with the other experiments and theoretical values. Filled squares, the present result; open circles, Golden *et al.*; open triangles, Bogomolov *et al.* The curves labeled "SLB" and "DR" are calculated by Mitsui based on the Standard Leaky Box Model and Diffusive Re-acceleration Model, respectively. The curves labeled "PBH" are calculated by Maki *et al.* for the $\overline{p}$ production by primordial black holes. The curve labeled "Neutralino" is calculated by Jungman and Kamionkowski based on the $\overline{p}$ productions by annihilations of dark matter neutralinos.

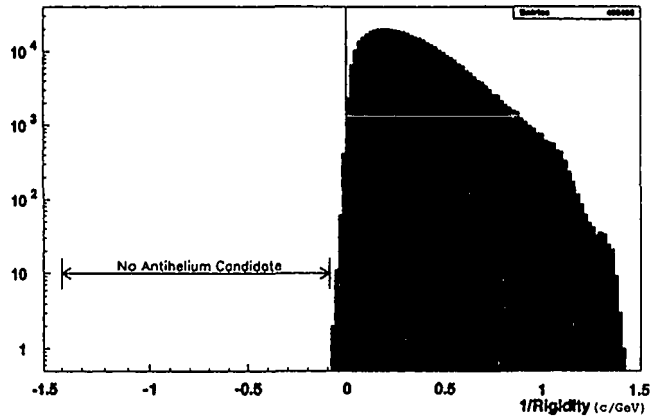


Figure 14: 1/Rigidity distribution.

The expected $\overline{p}$ results from the future activity are shown in Fig. 15. A very comprehensive presentation of the BESS results are published in the *Proceedings of the 6th Workshop on BESS* published as KEK Proceedings 96-9.

4.4 Future

The BESS long-duration flight expectations should lead to an impressive improvement in the experimental knowledge of antimatter within cosmic rays. But the most important step forward is expected to come from future space experiments. Long duration in this case means more than three years, so statistics can increase largely even with an effective area of reduced dimension.

But the experiments in space also benefit from the absence of a residual atmosphere on top of the detector, which introduces an unavoidable background for balloon-borne experiments.

Two projects searching for antimatter in space are in a stage of advanced construction. The basic principles are similar, both using as a basic element a magnetic spectrometer with a permanent magnet to give the magnetic field inside a region where high space accuracy trackers (Si trackers) are inserted. The basic

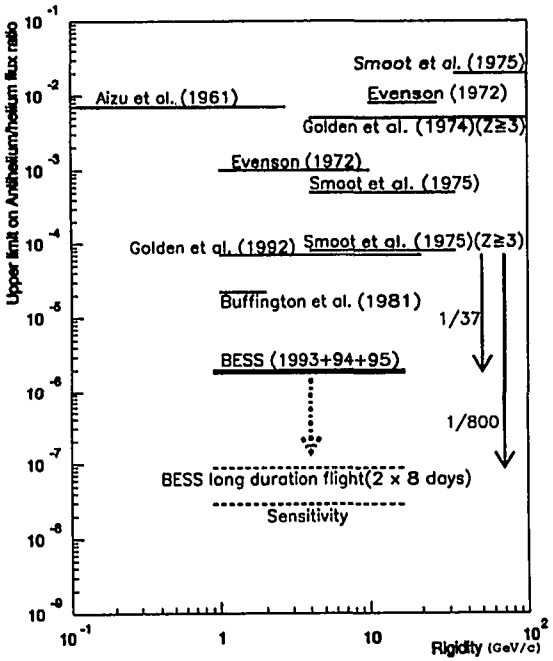


Figure 15: Upper limit on $\overline{\text{He}}$/He flux ratio.

elements of the two experiments are implemented in different ways by particle identification detectors.

The AMS spectrometer will be located in the International Space Station Alpha (ISSA) after a flight test in the shuttle scheduled for 1998. In Figs. 16 and 17 are shown a schematic of the AMS detector, the location of the AMS detector on the shuttle, and on the space station (ISSA). Figure 18 shows the expected improvement of the antimatter-matter ratio obtained by AMS after three years of running on ISSA.

5 PAMELA

PAMELA is part of the Russian Italian Mission (RIM) program, a collaboration between INFN and the VNIIEM Institute of Moscow with the participation of other international institutes, for sending cosmic ray telescopes into space as "piggy-back" on some of their satellites of the Resurs series.

The opportunity is unique both for the very favorable orientation of these satellites (looking to the Earth surface, and indeed out of the Earth on the other side) and for their polar orbit, allowing us to cover the whole energy range down to very low energies, highly enriching the possible physics program. Furthermore, their orbit is quasicircular at about 700 km, which guarantees a very long permanence in flight, and sun-syncronous, which maximizes the electric power availability.

The group headed by Prof. Arkady Galper, of the MEPI of Moscow, acted as interface with the VNIIEM Institute, so that in 1993 the Russian Italian Mission (RIM) program was established, of which the RIM-2 experiment, which we named PAMELA, is the central part.

5.1 The Technical Choices and the Baseline Design

The relative low magnetic field intensity due to use of a permanent magnet can be compensated with the progress made in the recent years in particle localization by the wide application of the silicon microstrip detectors.

The tests made in '94 and '95 of prototypes of the foreseen sensors for the PAMELA tracker guarantee the successful handling of this difficult technique.

The chosen cross section of the magnet gap is 14 × 16 cm^2, matching the optimal use of the four-inch silicon wafers to produce large area silicon microstrip sen-

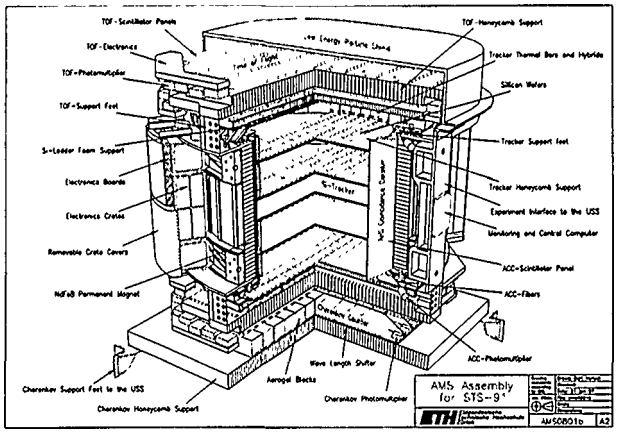


Figure 16.

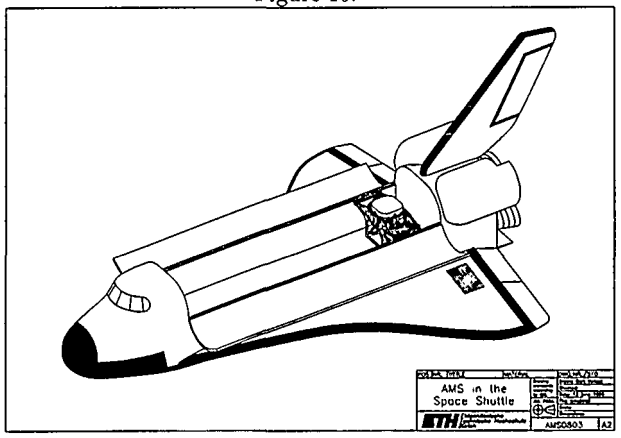


Figure 17.

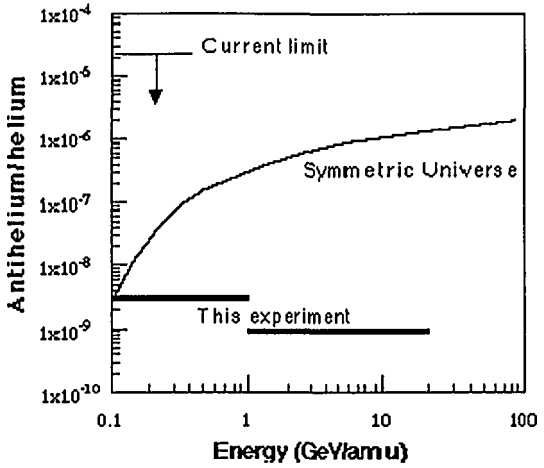


Figure 18: Expected improvements of the antimatter-matter ratio obtained by AMS after three years of running.

sors. For maximizing the MDR, we chose to have a relatively weak field (~0.35 T) on a relatively long magnetic path (44 cm, nearly the maximum allowed by the geometrical constraints to the experiment). The corresponding MDR is ~ 370 GeV/c. The magnetic gap and the magnet length determine the angular acceptance of the telescope, $20.0^\circ \times 17.7^\circ$, corresponding to a geometrical acceptance of 24.5 cm^2 sr.

At low momenta, the MDR is dominated by the multiple scattering of the particle in the silicon sensors and in their supporting structures; afterward it increases linearly with the momentum.

The antiproton counting rate in the given GF is reported in Fig. 19 in two hypotheses: (1) only secondary produced antiprotons according to the Modified Leaky Box Model of the galaxy (MLBM) (lower curve); (2) only secondary produced antiprotons according to the Closed Galaxy Model (CGM). Any primary production mechanism will increase these rates. The counting rate foreseen for the positrons is reported in Fig. 20.

The technical choices for the other detectors are the following:

- silicon microstrip sensors for the imaging calorimeter, interleaved with tungsten plates as absorber; this choice minimizes the volume of the calorimeter

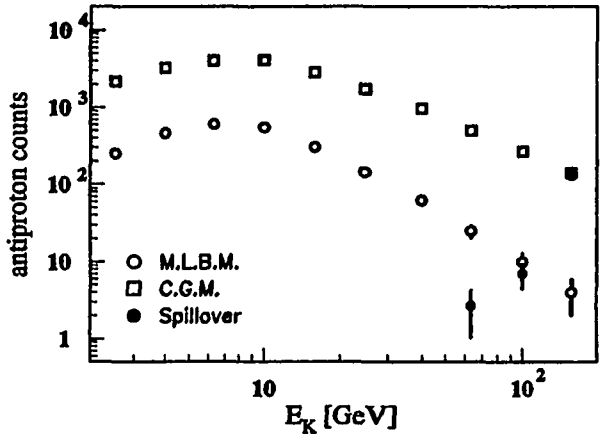


Figure 19.

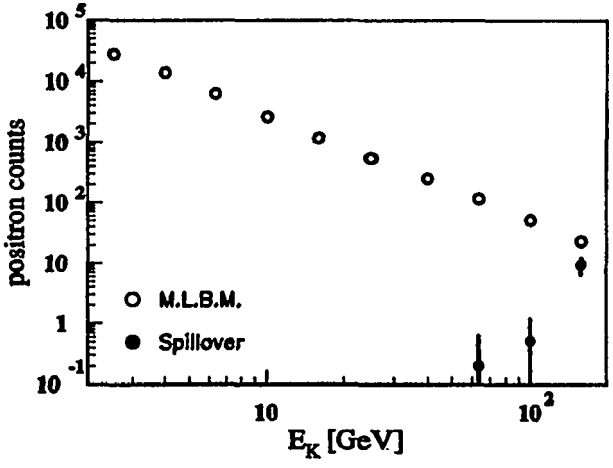


Figure 20.

and maximizes indeed the geometrical acceptance; the high granularity assumed in PAMELA allows a very good separation between electromagnetic showers and interacting or not interacting hadrons; the chosen depth allows a good resolution in the measurement of the energy of electromagnetic particles, further extending the energy spectrum measurements of electrons and positrons;

- several scintillation counter hodoscopes for the construction of the triggers and for the TOF measurements; the use of several hodoscopes allows independent TOF measurements, improving the precision and the safety; the hodoscope structure maximizes the yield of the collected light and the safety of the system; both the hodoscopization and the number of hodoscopes allow a good flexibility in constructing the first-level triggers;
- a Transition Radiation Detector (TRD) for selecting electromagnetic particles from hadrons up to very high energy (~1000 GeV); the TRD is based on small diameter straw tubes arranged in double layer planes interleaved by carbon fiber radiator. The use of the straw tubes allows us to perform many energy loss measurements along the particle trajectory (which brings the selection capability of the instrument down to less than 1 GeV), and to track all particles before their entrance in the magnetic spectrometer, cleaning the sample of the particles accepted at its entrance;
- a sixth scintillator layer will be located below the calorimeter as a penetration detector;
- finally, a set of scintillation counters covering the top edge and the sides of the magnetic spectrometer completes the telescope, for a further labeling of contaminated events.

The PAMELA telescope (see Fig. 21) consists of the following subdetectors (from the top to the bottom):

- two scintillation counter hodoscopes (S11 and S12);
- the TRD counter, occupying 29 cm in height;
- one scintillation counter hodoscope (CAT) on the top of the magnet, labeling the particles not entering the magnet gap;
- the magnet + tracker system, consisting of five permanent magnets, each 8 cm high, interleaving six detection planes of the silicon microstrip tracker,

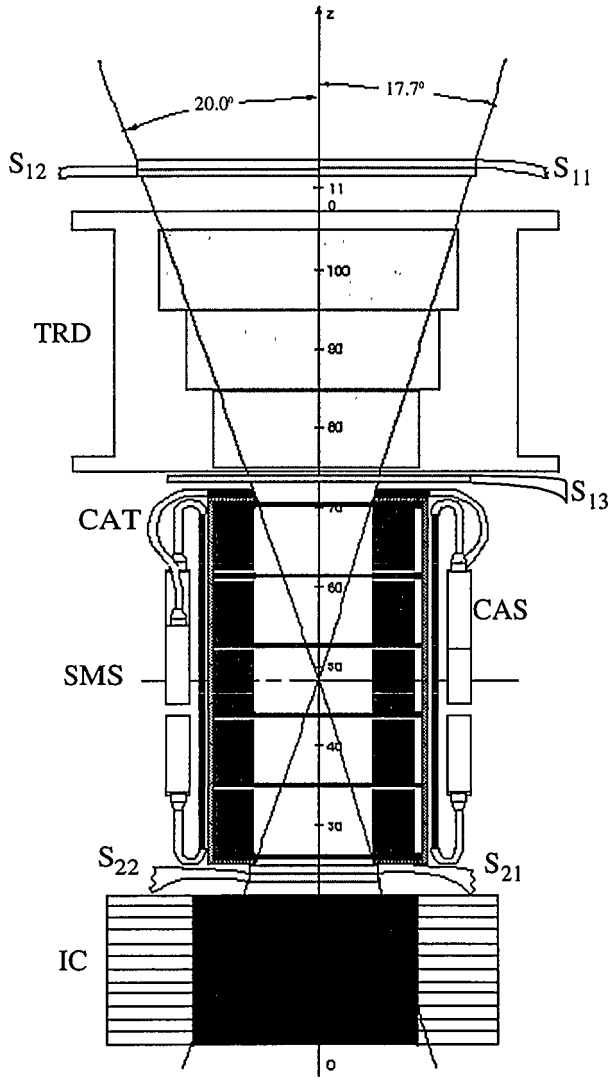


Figure 21: The PAMELA telescope.

each 0.8 cm high, enclosed in a ferromagnetic screen, 0.2 cm thick and surrounded on its sides by a system of scintillation counters (CAS) labeling the particles entering the spectrometer from the sides;

- two scintillation counter hodoscopes (S21 and S22);
- the imaging calorimeter, consisting of 23 planes of silicon microstrip sensors, interleaved by 23 tungsten sheets, whose physical occupancy in height is 19 cm.

The total height of the spectrometer is 113.5 cm. Tables 7 and 8 give technical parameters of PAMELA and the expected rate over the mission time (three years).

protons	3×10^{8}
antiprotons	$\geq3\times10^{4}$
electrons	6×10^{6}
positrons	$\geq3\times10^{5}$
He nuclei	4×10^{7}
Be nuclei	4×10^{4}
C nuclei	4×10^{5}
antinuclei limit (90% c.l.)	7×10^{-8}

Table 7: Expected rates in PAMELA in 10^{8}s.

6 Conclusion

Our understanding of the presence of antimatter in cosmic rays has recently progressed substantially. The future improvement will expand our knowledge, giving hopefully a conclusive result on the origin of antimatter in the universe.

Let me conclude this presentation by mentioning that GLAST (shown in Fig. 22), the next generation gamma ray (γ) telescope, will also contribute to solving the problem of the antimatter search in an indirect way by studying the diffuse γ spectrum, giving a limit to presence in the universe of regions where matter and antimatter are in contact on large scales, and give the typical γ spectrum from π^{o} decay modulated by the red shift due to the distance from our galaxy, as shown in Fig. 23 (De Rújula, 1996).

	Volume (xyz) (cm × cm × cm)	Mass (kg)	R.O.ch (#)	Power (W)
Scintillation counters	45×40×2 + 17×15×3 + 36×32×1	≤33	34	≤32
Trans. rad. detector	40×40×29	23	1,920	≤40
Anticoincidences	(21×6×1)×4+ (9×30×1)×15+ (8×30×1)×5+	13	48	≤5
Silicon tracker	(28×24×0.8)×6	10	36,864	37
Imaging calorimeter	30×24×19	129	3,312	≤60
Fast trigger		5		10
General electronics		≤15		25
Power supply		10		90
Permanent magnet	29×30×47 [(23×24×8)×5+ Fe shielding]	140		
General mechanical structure		25		
Total	45×40×114	≤403	42,178	≤299

Table 8: Main parameters of the elements of the PAMELA telescope.

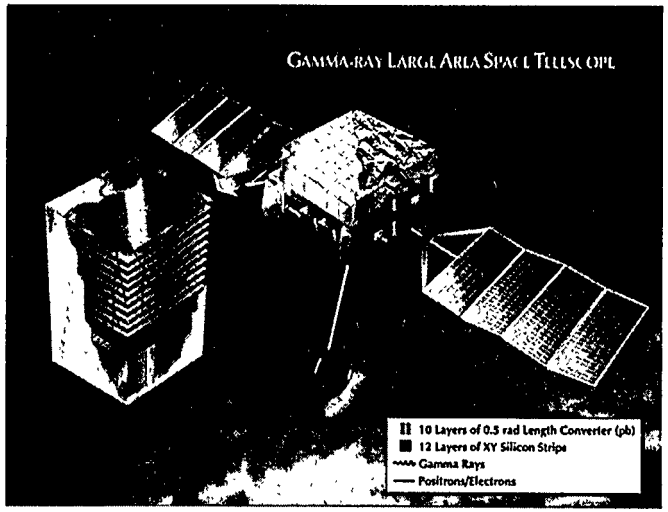


Figure 22.

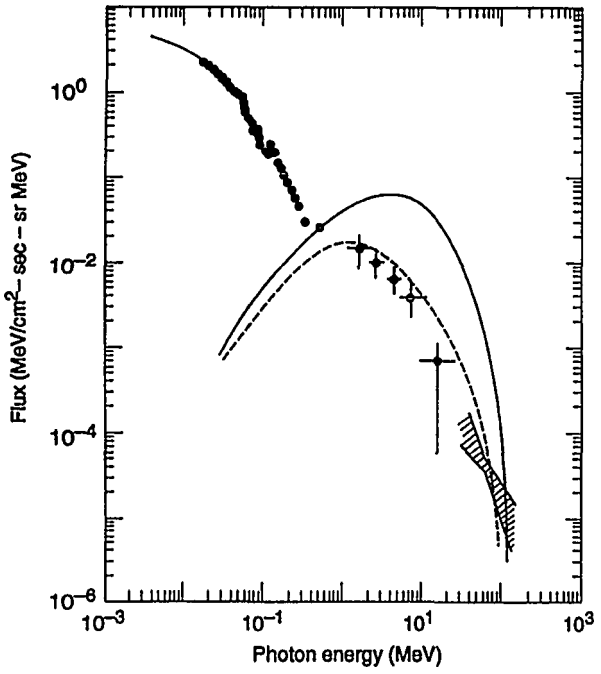


Figure 23: Comparision of the diffuse γ ray energy spectrum with the results of a matter/antimatter symmetric universe for d = Mpc. Dashed (continuous) lines are with (without) reheating by electrons and positrons from $p\overline{p}$ annihilation.

References

- Adriani, O., *et al.*, *Proc. of XXIV ICRC*, Rome, **3**, 591 (1995).
- Agrinier, B., *et al.*, Lett. Nuovo Cimento **1**, 153 (1969).
- Barbiellini, G., *et al.*, Nucl. Instrum. Methods A **371**, 169 [1996(a)].
- Barbiellini, G., *et al.*, A&A **309**, L15 [1996(b)].
- Barwick, S. W., *et al.*, Phys. Rev. Lett. **75**, 390 (1995).
- Bocciolini, M., *et al.*, Nucl. Instrum. Methods A **333**, 77 (1993).
- Bocciolini, M., *et al.*, Nucl. Instrum. Methods A **370**, 403 (1996).
- Bogomolov, E. A., *et al.*, in *Proceedings of the XVI ICRC*, Kyoto, **1**, 330 (1979).
- Bogomolov, E. A. *et al.*, in *Proceedings of the XX ICRC*, Moscow, **2**, 72 (1987).
- Bogomolov, E. A. *et al.*, in *Proceedings of the XXI ICRC*, Adelaide, **3**, 288 (1990).
- Brun, R., *et al.*, "Detector Description and Simulation Tool," CERN program library (1994).
- Buffington, A., Schindler, S. M., and Pennypacker, C. R., Astrophys. J. **248**, 1179 (1981).
- Carlson, P., *et al.*, Nucl. Instrum. Methods A **349**, 577 (1994).
- Carlson, P., *et al.*, to appear in Nucl. Instrum. Methods (1995).
- University of Chicago, 1996, National Science Foundation Grant ATM-9420790, http://astro.uchicago.edu/home/web/pyle/neutron.html.
- Clem, J., *et al.*, in *Proceedings of the 24th Int. Cosmic Ray Conf.*, Rome, Vol. 3, **5** (1995).
- Daniel, R. R. and Stephens, S. A., Rev. Geoph. and Sp. Ph., Vol. 12, **233** (1974).
- Daugherty, J. K., *et al.*, Astrophys. J. **198**, 493 (1975).
- De Rújula, A., "Antimatter in the Universe?" CERN program library (1996).
- Fanselow, J. L., *et al.*, Astrophys. J. **158**, 771 (1969).
- Gaisser, T. K., and Schaeffer, R. K., Astrophys. J. **394**, 174 (1992).
- Gleeson, L. J., and Axford, W. I., Astrophys. J. **154**, 1011 (1968).
- Golden, R. L., *et al.*, Nucl. Instrum. Methods **148**, 179 (1978).
- Golden, R. L., *et al.*, Phys. Rev. Lett. **43**, 1264 (1979).
- Golden, R. L., *et al.*, Astrophys. Lett. **24**, 75 (1984).
- Golden, R. L., *et al.*, A&A **188**, 145 (1987).
- Golden, R. L., *et al.*, Nucl. Instrum. Methods A **306**, 366 (1991).
- Golden, R. L., *et al.*, Astrophys. J. **436**, 769 (1994).
- Golden, R. L., *et al.*, Astrophys. J. **457**, 103 (1996).

- Hof, M., *et al.*, Nucl. Instrum. Methods A **345**, 561 (1994).
- Hof, M., *et al.*, Astrophys. J. **467**, L33 (1996).
- Kiraly, P., Wdowczyk, J., and Wolfendale, A., Nature **293**, 120 (1981).
- Mitchell, J., *et al.*, Phys. Rev. Lett. **76**, 3057 (1996).
- Mitsui, T., Maki, K., and Orito, S., "Expected Enhancement of the Primary Antiproton Flux at the Solar Minimum," UT-ICEPP 96-03, 22 (1996).
- Moiseev, A., *et al.*, 1996, "Cosmic Ray Antiproton Flux in the Energy Range from 200 to 600 MeV," Astrophys. J., to appear in 1997.
- Muller, D., and Tang, K. K., Astrophys. J. **312**, 183 (1987).
- Papini, P., Grimani, C., and Stephens, S. A., Nuovo Cimento **19**, 367 (1996).
- Paradis, P., Ph.D. thesis, New Mexico State University, USA (1996).
- Pfeifer, C., Roesler, S., and Simon, M., Phys. Rev. C **54**, 2, (1996).
- Protheroe, R. J., Astrophys. J. **254**, 391 (1982).
- Rudaz, S., and Stecker, F. W., Astrophys. J. **325**, 16 (1988).
- Silk, J., and Srednicki, M., Phys. Rev. Lett. **53**, 624 (1984).
- Simon, M., *et al.*, Astrophys. J. **456**, 519 (1996).
- Stecker, F. W., Protheroe, R. J., and Kazanas, D., in *Proceedings of the XVII ICRC*, Paris, **9**, 211 (1981).
- Stecker, F. W. and Wolfendale, A. W., Nature **309**, 37 (1984).
- Stephens, S. A., in *Proceedings of the 17th Int. Cosmic Ray Conf.*, Paris, **282**, Vol. 4; *ibid.* **512**, Vol. 2 (1981).
- Stephens, S. A., "Secondary Antiproton Spectrum in the Atmosphere with the Inclusion of Fermi Motion in Air Nuclei," submitted to Astropart. Phys. (1996).
- Sullivan, J. D., Nucl. Instrum. Methods **95**, 5 (1971).
- Weber, N., 1996, "A measurement of the antiproton and proton fluxes in the cosmic rays by the CAPRICE experiment," Ph.D. thesis, KTH Stockholm, Sweden.

DIFFRACTION AT HERA

Nicolò Cartiglia
Columbia University, Nevis Laboratories
136 South Broadway, Irvington, NY, 10533 USA

Representing the H1 and ZEUS Collaborations

ABSTRACT

Recent results on diffraction at HERA, as measured by the H1 and ZEUS Collaborations, are reviewed. Results on the photon-proton total hadronic cross section, on vector meson production both at small and large photon virtuality, and on photon diffraction, are presented. The experimental signature of diffraction at HERA, as well as the selection methods used by the two collaborations, are explained.

© 1996 by Nicolò Cartiglia.

1 Introduction

Photon-proton collisions have been extensively studied in fixed-target experiments up to center-of-mass energies, $W_{\gamma p}$, of about 20 GeV, using both real and virtual photons. At the HERA collider at DESY, 820 GeV protons collide with 27.5 GeV electrons or positrons. The HERA physics program is very rich, ranging from nonperturbative to perturbative QCD, heavy-flavor physics, and to the measurement of the quark and gluon densities in the proton and in the photon. Two general-purpose detectors, H1 (Ref. 1) and ZEUS (Ref. 2), operate at HERA and are instrumented with high-resolution calorimeters and tracking chambers.

The results presented here have been obtained using data collected during 1994 and 1995, for a total of about 9 pb^{-1}. More detailed presentations on individual subjects can be found in many proceedings.[3]

2 Diffraction and Total Cross Section

Historically, hadronic diffraction processes and total cross sections have been described using the concept of "Pomeron exchange." The simplest way to introduce the concept of the Pomeron is within the framework of Regge theory.[4,5] Consider the example shown in Fig. 1: $\pi^- p \to \pi^0 n$ where t is the four-momentum transfer. According to quantum number conservation, this reaction might happen via the exchange of a virtual ρ^0, a_2, or g hadron. If the values of the masses and spins of these particles are plotted on the right-hand side of the spin-t plane (where t is positive), they lie almost on a straight line determining a "trajectory" of particles. The general expression for a straight-line trajectory is:

$$\alpha(t) = \alpha(0) + \alpha' \cdot t,$$

where $\alpha(0)$ is the intercept and α' the slope. The most important trajectories are approximately linear with a universal slope $\alpha' = 0.9$ GeV^2; the first particle on a trajectory gives the name to the trajectory itself (in the above example, the ρ trajectory is exchanged). Regge theory predicts that the properties of a t-channel reaction (that happens on the left-hand side of the spin-t plane, where t is negative, via the exchange of off-mass shell particles), $\pi^- p \to \pi^0 n$ for example, are determined by the parameters of the trajectory formed by the exchanged particles on the right-hand side of the spin-t plane (the ρ trajectory in the case above).

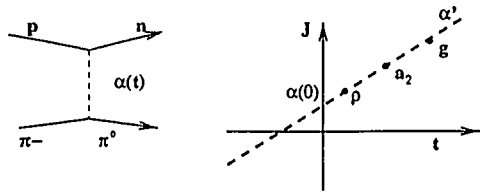


Figure 1: Schematic diagram for $\pi^- p \to \pi^0 n$ scattering and the exchanged trajectory.

Let's consider the dependence of the total cross section (a t-channel process) with the square of the center-of-mass energy s. According to Regge theory, it is parametrized as:

$$\sigma_{tot}(s) \propto \sum_k s^{\alpha_k(0)-1}, \quad (1)$$

where $\alpha_k(0) = 1, \ldots, n$, are the intercepts of the trajectories exchanged. Using only two main trajectories, $\sigma_{tot}(s)$ for $p\bar{p}$, pp, $K^{\pm}p$, $\pi^{\pm}p$, γp have been fitted by Donnachie and Landshoff[6] with an expression of the form:

$$\sigma_{tot}(s) = Xs^{0.0808} + Ys^{-0.4525},$$

where X, Y are parameters which depend on the exchanged field. The first trajectory, called the Pomeron trajectory, has intercept $\alpha_p(0) = 1.0808$ while the second term, which represents an effective meson trajectory, has intercept $\alpha_k(0) = 0.545$. At high enough energy, only the Pomeron term is important. The Pomeron, identified as the first particle of the Pomeron trajectory, is responsible for the rise of the total cross section as a function of the center-of-mass energy. Since the bulk of the processes contributing to the total cross section has very small p_t, the Pomeron exchanged in these reactions is called a "soft Pomeron." The soft Pomeron trajectory has intercept $\alpha_p(0) \simeq 1.08$ and slope $\alpha' \simeq 0.25$ GeV^2.

Figure 2 schematically shows three different types of diffractive reactions: elastic scattering (a), single diffraction (b), where one of the incoming particle dissociates, and double diffraction (c), where both incoming particles dissociate. In diffractive scattering, the hadronization of the final states X and Y with masses M_X^2, M_Y^2 happens independently, as shown in Fig. 2(d). If the center-of-mass energy $\sqrt{s}$ is large enough ($\ln(s) \gg \ln(M_Y^2) + \ln(M_X^2)$), then there is a gap in rapidity between X and Y.

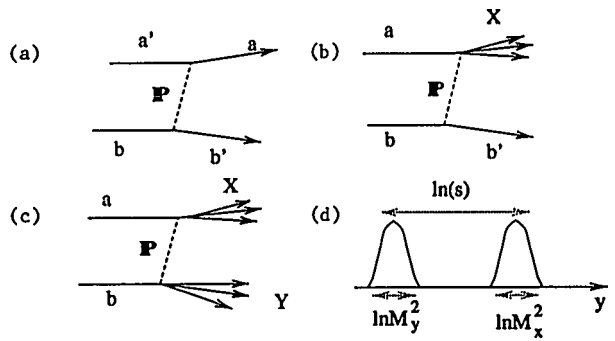


Figure 2: Diagrams for three different types of diffractive reactions: elastic scattering (a), single diffraction (b) where one of the incoming particle fragments, and double diffraction (c). (d) shows energy flow as a function of rapidity for $\ln(s) \gg \ln(M_Y^2) + \ln(M_X^2)$.

3 Total Cross Section at HERA

The values of the total hadronic γp cross section at HERA as measured by the H1 (Ref. 7) and ZEUS (Ref. 8) Collaborations are shown in Fig. 3 together with a compilation of low-energy results. The Donnachie and Landshoff parameterizations including (dotted line) or not (solid line) recent CDF (Ref. 9) results and the ALLM (Ref. 10) parameterization (dashed line) are also shown. The HERA data are in agreement with these predictions, and therefore, with the assumption that also at HERA "soft" Pomeron exchange is responsible for the increase of $\sigma_{tot}^{\gamma p}$ as a function of the center-of-mass energy (see Table 1).

The diffractive cross section represents a large fraction of the total cross section: at HERA, for example, the diffractive and nondiffractive parts are, according to the H1 Collaboration,[7] $\sigma_{dif}^{\gamma p} = 69.2 \pm 13.2\ \mu b$ and $\sigma_{nondif}^{\gamma p} = 96.1 \pm 17.9\ \mu b$, giving $\sigma_{dif}/\sigma_{tot} = (42 \pm 8)\%$, while according to the ZEUS Collaboration,[8] $\sigma_{dif}/\sigma_{tot} = (36 \pm 8)\%$.

Experiment	$W_{\gamma p}$ Range	$W_{\gamma p}$
ZEUS	$167 < W_{\gamma p} < 194$	$\sigma_{tot}^{\gamma p} = 143 \pm 4 \pm 17\ \mu b$
H1	$< W_{\gamma p} > = 200$	$\sigma_{tot}^{\gamma p} = 165 \pm 2 \pm 11\ \mu b$

Table 1: Summary of experimental results on the measurements of σ_{tot} at HERA.

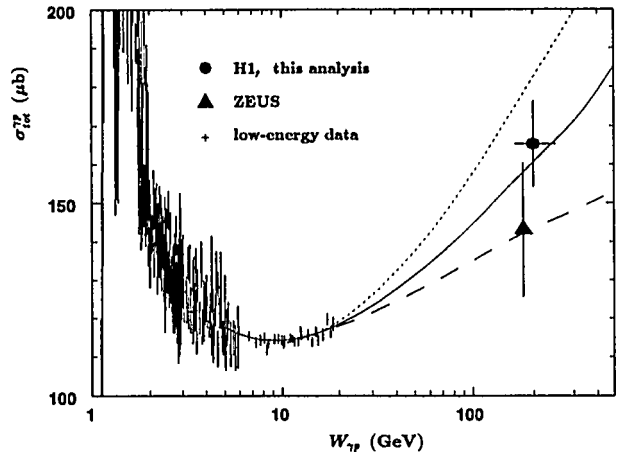


Figure 3: Total γp cross section as a function of $W_{\gamma p}$. The results are shown together with two parameterizations from Donnachie and Landshoff that include (dotted line) or not (solid line) recent CDF results and with the ALLM parameterization (dashed line).

4 Kinematics of Diffractive Events at HERA

In Fig. 4, a diagram for diffractive ep scattering is shown. A photon $\gamma^*(Q^2)$ with virtuality $-q^2 = Q^2$ is emitted at the electron vertex.* Depending on the value of Q^2, the events are divided into two large families: photoproduction, for $Q^2 < 4\ GeV^2$, and deep inelastic scattering (DIS), for $Q^2 > 4\ GeV^2$. $s = (k+p)^2$ is defined as the center-of-mass energy squared of the ep system while ${W_{\gamma p}}^2 = (q+p)^2$ is used to indicate the center-of-mass energy of the virtual photon-proton (γp) system. At large Q^2, in the frame where the proton has infinite momentum, the variable $x_{Bj} = \frac{Q^2}{2p \cdot q}$ represents the fraction of the proton longitudinal momentum

*The symbol γ is used for quasireal photons while the symbol γ^* is used for virtual photons.

carried by the struck quark. In the proton rest frame, $y = Q^2/(sx_{Bj})$ equals the fraction of the electron energy transferred to the proton.

In addition, diffractive events are described by the following variables: t, the square of the four-momentum transfer at the proton vertex, and $x_{\mathbb{P}}$, the momentum fraction of the Pomeron in the proton.

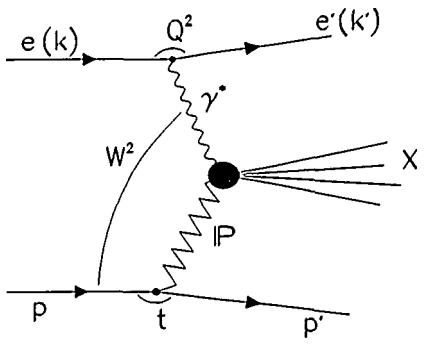


Figure 4: Diagram for diffractive scattering at HERA.

If the reaction is elastic or single diffractive (or photon diffraction as sometimes single diffraction is called for the HERA regime), then the quantities t and $x_{\mathbb{P}}$ can be determined either from the scattered proton or from the system M_X.

If the longitudinal and transverse momentum of the scattered proton, $p'_z, p'_\perp$, are measured, then $x_{\mathbb{P}}$ and t are calculated as:

$$x_L \simeq p'_z/E_p \longrightarrow x_{\mathbb{P}} = 1 - x_L \tag{2}$$

$$t = (P - P')^2 \simeq -\frac{(p'_\perp)^2}{x_L} - m_p^2\frac{(1-x_L)^2}{x_L}, \tag{3}$$

where m_p is the proton mass. If the proton is not observed, a measurement of $x_{\mathbb{P}}$ can be obtained as:

$$x_{\mathbb{P}} = \frac{(P - P')\cdot q}{P\cdot q} \simeq \frac{M_X^2 + Q^2}{W^2 + Q^2 - m_p^2}, \tag{4}$$

where M_X is the mass of the system X. t can be reconstructed from the system X only for some exclusive reactions, such as vector meson production, where the resolution on $p'_\perp$ is accurate enough.

5 Experimental Signature of Diffraction at HERA

One of the main issues concerning diffraction at HERA is the experimental method to separate diffractive from nondiffractive events. For some exclusive reactions, the distinction is actually quite easy. Let's consider, for example, exclusive ρ^0 production and decay:

$$\gamma p \longrightarrow \rho^0 p$$
$$\rho^0 \longrightarrow \pi^+\pi^-.$$

The central detector is empty, except for the two tracks coming from the ρ^0 decay. This topology is very unusual and the background from "non-Pomeron" exchange is negligible. Inclusive γ diffraction, $\gamma p \to Xp$, is on the other hand more difficult to identify. Two quantities can help in the distinction: a rapidity gap in the final state particle production and/or the presence of a highly energetic scattered proton.

5.1 Rapidity Gaps

Figure 5 schematically shows the energy flow as a function of pseudorapidity η for nondiffractive ep scattering at HERA.† Aside from the recoil electron, two main groups of particles can be identified: particles produced at high rapidity in the hadronization of the proton remnant, and particles produced in the hadronization of the photon-parton system, typically at small or negative rapidity. In deep inelastic scattering, for example, the struck parton is deflected and emerges from the proton remnant at an angle θ_q. It is useful to express this angle as the difference in pseudorapidity between the struck parton and the proton remnant:

$$\Delta\eta = \eta_{\text{proton remnant}} - \eta_{\text{parton}}. \tag{5}$$

†The pseudorapidity η is defined as: $\eta = -\ln(\tan(\theta/2))$ Following the HERA convention, the angle θ is measured with respect to the proton beam direction.

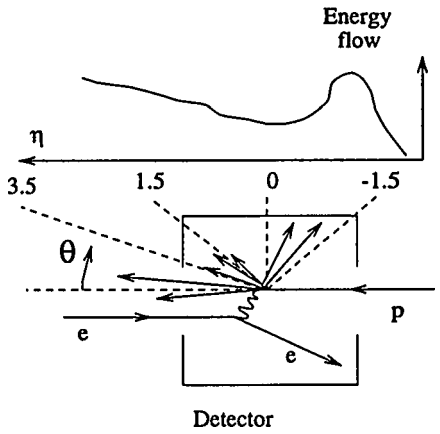


Figure 5: Energy flow vs η for nondiffractive ep scattering at HERA.

Since the pseudorapidity interval covered by a system with center-of-mass energy $\sqrt{s}$ is given by:

$$\Delta\eta \sim \ln(\frac{s}{m_p^2}) \tag{6}$$

with m_p the proton mass, then we can show that the pseudorapidity interval between the proton remnant and the struck quark is:

$$\Delta\eta \sim \ln(\frac{W_{\gamma p}{}^2}{m_p^2}) - \ln(\frac{x_{Bj}W_{\gamma p}{}^2}{m_p^2}) \sim \ln(\frac{1}{x_{Bj}}), \tag{7}$$

where $\ln(\frac{W_{\gamma p}{}^2}{m_p^2})$ is the total rapidity covered by the γ-p system and $\ln(\frac{x_{Bj}W_{\gamma p}^2}{m_p^2})$ is the amount covered by the γ-struck quark system. Due to the color string connecting the struck parton and the proton remnant, the rapidity gap $\Delta\eta$ is filled with particles in the hadronization process. In particular as x_{Bj} decreases, the average hadron multiplicity $< n_h >$ increases faster than the pseudorapidity interval $\Delta\eta$, making it less and less likely for rapidity gaps to be visible.[13] If we assume the produced hadrons fill the rapidity gap according to a Poisson distribution, the probability w_{gap} to have no particles in the gap $\Delta\eta$ has the form:

$$w_{gap} \sim e^{-<n_h>} < e^{-\Delta\eta}. \tag{8}$$

This expression means that rapidity gaps between the proton fragments and the jet produced by the struck quark are exponentially suppressed. For Reggeon or

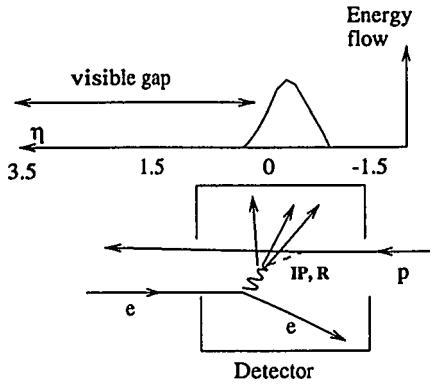


Figure 6: Energy flow vs η for diffractive ep scattering at HERA.

Pomeron exchange, Fig. 6, the probability to have a rapidity gap $\Delta\eta$ depends on the intercept of the exchanged trajectory[14]:

$$p(\Delta\eta) \sim e^{-2(\alpha(0)-1)\Delta\eta}.$$

Let's then consider different possibilities:

$I\!P$ exchange: $\alpha_{I\!P}(0) \sim 1 \Rightarrow p(\Delta\eta) \sim e^0$

ρ, a_2, f_2, ω exchange: $\alpha_R(0) \sim 0.5 \Rightarrow p(\Delta\eta) \sim e^{-\Delta\eta}$

π exchange: $\alpha_\pi(0) \sim 0 \Rightarrow p(\Delta\eta) \sim e^{-2\Delta\eta}$.

Therefore, even though ρ, π, and $I\!P$ are colorless exchanges, only $I\!P$ exchange produces rapidity gaps that are not suppressed as the gap width increases. It is therefore possible to operationally define diffraction[15] by the presence of a rapidity gap: diffractive events are those which lead to a large rapidity gap in final state phase space and are not exponentially suppressed as a function of the gap width.

5.2 Leading Proton in the Final State

In diffractive events, the incoming beam particles, when they do not dissociate, conserve a large fraction of their initial momentum. At HERA, the diffractively scattered proton carries on average more than 99% of its initial momentum. The cross sections for nondiffractive processes to produce such energetic protons is very small compared with the diffractive cross section making the detection of a high-energy proton a clean tag for diffractive physics. Figure 7 schematically shows

the spectra of leading protons generated from different mechanisms: at $x_L \simeq 1$, single diffraction is almost the sole component, while moving away from $x_L = 1$, double diffraction and Reggeon exchange become important. Traditionally, $x_L = 0.9$ has been used to indicate the x_L value at which the diffractive and non-diffractive part of the spectrum are equal. Leading protons can also be produced in "standard" DIS events as part of the proton remnant jet, but they have on average a much lower x_L value. A recent release of the LEPTO Monte Carlo,[16] on the other hand, includes leading proton production in the fragmentation of the proton remnant with a cross section comparable to Reggeon exchange. Note that the distinction between the different mechanisms for leading proton production is somewhat arbitrary and there might be a lot of overlap.

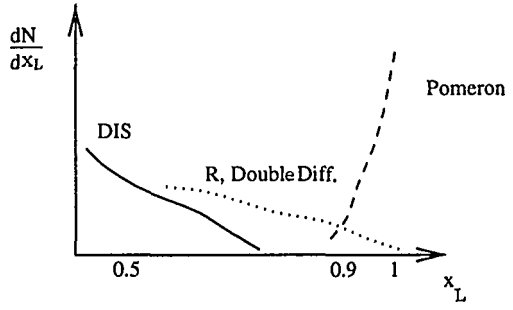


Figure 7: Spectra of leading protons generated from different mechanisms: Pomeron exchange (dashed line), Reggeon exchange and double diffraction (dotted line), and "standard DIS" (solid line) as a function of x_L.

In the transverse plane, leading protons have rather small momentum, with a typical $p_\perp^2$ distribution of the form:

$$\frac{dN}{dp_\perp^2} \sim e^{-b \cdot p_\perp^2}$$

with b = 5–15 GeV^{-2}. This feature makes their detection quite difficult since they tend to stay very close to the beam line. Because of this, movable sections of the beam pipe, called "Roman pots," are used by both the H1 and ZEUS Collaborations to allow the insertion of high-precision detectors down to a few centimeters from the beam line.

6 Models for Diffractive γ^*p Scattering

Several models have been proposed to explain diffractive interactions in ep scattering. In some instances, a connection is made between Regge concepts (like Pomerons) with QCD concepts (like gluons). Here we present a brief description of some of the ideas on which the models are based.

Factorization of vertices and Pomeron structure function: Factorization considers the $\mathbb{P}$p vertex as independent of the $\mathbb{P}\gamma^*$ interaction. A universal Pomeron flux factor $f_{\mathbb{P}/p}(x_{\mathbb{P}}, t)$ characterizes the $\mathbb{P}$p vertex, and parameterizations obtained from fits to pp and $p\bar{p}$ diffractive data can be used in ep collisions. Several different expressions for $f_{\mathbb{P}/p}(x_{\mathbb{P}}, t)$ have been proposed[17–19] which all include an exponential dependence on t of the type $e^{-b|t|}$ with b $\sim$ 5–8 GeV^{-2} and a dependence on the Pomeron longitudinal momentum $x_{\mathbb{P}}$ of the type $\sim 1/x_{\mathbb{P}}$. These models express the diffractive γ^* p cross section as

$$\sigma^{\gamma^* p}(Q^2, \beta, x_{\mathbb{P}}, t) \propto f_{\mathbb{P}/p(x_{\mathbb{P}},t)} \cdot \sigma^{\gamma^* \mathbb{P}}(Q^2, \beta), \tag{9}$$

and describe deep inelastic γ^*p and $\gamma^*\mathbb{P}$ interactions in the same way: the incoming γ^* interacts with one component of the target, leaving behind a remnant. For $\gamma^*\mathbb{P}$ interaction, the scaling variable that plays the same role of x_{Bj} is:

$$\beta = \frac{Q^2}{2x_{\mathbb{P}} p_{proton} \cdot q} \sim \frac{Q^2}{M_X^2 + Q^2}. \tag{10}$$

The $\gamma^*\mathbb{P}$ cross section can then be written as:

$$\sigma_{tot}^{\gamma^* \mathbb{P}}(Q^2, \beta) = \frac{4\pi^2 \alpha_{em}}{Q^2} F_2^{\mathbb{P}}(Q^2, \beta), \tag{11}$$

where $F_2^{\mathbb{P}}(Q^2, \beta)$ is the Pomeron structure function; i.e., the probability for finding a quark of fractional momentum β in the Pomeron.

Factorization breaking and effective Pomeron structure function: The diffractive ep interaction is viewed as photon diffractive dissociation on the proton (some examples are given in Refs. 20, 21, 22, 23, and 24). Consider ep scattering in the proton rest frame. Upstream of the proton, Fig. 8, the incoming γ (or γ^*) fluctuates into different hadronic states, and its wave function can be expressed as:

$$|\gamma> = |\gamma>_{bare} + |q\bar{q}> + |q\bar{q}g> + \ldots.$$

The Pomeron, viewed as two gluon-exchange, couples to these hadronic states in an s-channel interaction, and technically, there is no $\mathbb{P}$ remnant since both gluons interact with the photon. In this approach, the virtual photon couples with more than one Pomeron constituent and the meanings of β and $F_2^{\mathbb{P}}(Q^2,\beta)$ are not well-defined in terms of partons; in particular, factorization is not a natural consequence. To compare the predictions from this approach to those of the previous type of model, an effective $\mathbb{P}$ structure function, $F_{2\,\mathrm{eff.}}^{\mathbb{P}}(Q^2,\beta)$, is introduced. In this picture, the interaction of the $q\bar{q}$ state generates a different value of $\alpha_{\mathbb{P}}$ than the interaction of the $q\bar{q}g$ state[25] with an effective $\alpha_{\mathbb{P}}$ increasing at small $x_{\mathbb{P}}(x_{\mathbb{P}} \simeq 10^{-4})$. Therefore, the $q\bar{q}$ and $q\bar{q}g$ fluctuations have different Pomeron fluxes breaking the factorization mechanism. According to Ref. 26, factorization is also broken by the exchange of longitudinal photons. The states are characterized by the transverse and longitudinal momentum $(k_\perp, z)$ of the $q\bar{q}$ pair (taken as an example) and by the quark mass (m_q). The radius $r_\perp^2$ of the state depends on the inverse of $k_\perp^2 \cdot Q^2$ and m_q^2:

$$\frac{1}{r_\perp^2} \propto \frac{k_\perp^2 \cdot Q^2}{M_X^2}$$

$$\frac{1}{r_\perp^2} \propto m_q^2.$$

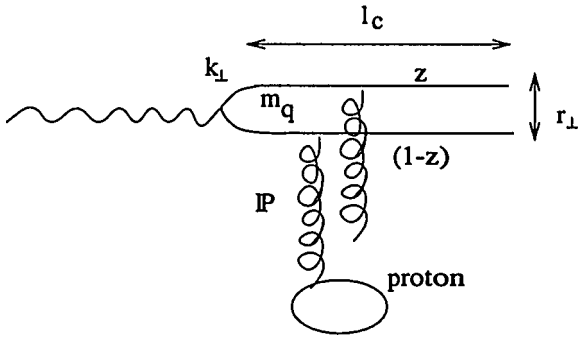


Figure 8: Diffractive γp scattering in the proton rest frame.

If the state has large $r_\perp^2$, both $k_\perp^2 \cdot Q^2$ and m_q^2 are small. In this case, the gluon-quark coupling is large, and pQCD cannot be applied since the photon acts like an extended object providing no information on the microscopic nature of the interaction. Large size fluctuations are thought to be responsible for the rise of the total hadronic cross section with energy and represent the bulk of diffractive events. Large $r_\perp^2$ configurations have small $k_\perp$, and the final state particles tend to be aligned along the photon-Pomeron axis. This phenomenology is known as the Aligned Jet Model.[27]

Conversely, if $r_\perp^2$ is small either because $k_\perp^2 \cdot Q^2$ (high Q^2 DIS events) or m_q^2 (production of charm or bottom $q\bar{q}$ pair) is large, then the gluon-quark coupling is small and pQCD can be applied.

Soft color interaction: In this model,[28] diffractive scattering is viewed as dominated by the exchange of one "hard" gluon plus nonperturbative color interactions to allow a color singlet final state.

7 Vector Meson Production: $\gamma p \rightarrow Vp$

In the range of center-of-mass energy $W_{\gamma p}$ up to 20 GeV covered by pre-HERA experiments, this process has been described very successfully within the framework of the Vector Dominance Model (VDM).[29] In this model, the photon is assumed to fluctuate into a virtual vector meson which then interacts elastically with the proton via the exchange of a Pomeron, Fig. 9(a). From VDM, one expects:

$$\sigma^{\gamma p \rightarrow Vp} = \frac{4\pi\alpha}{f_V^2}\sigma^{Vp \rightarrow Vp}, \tag{12}$$

where $f_V^2/4\pi$ is the photon-vector meson coupling constant, which expresses the fact that the γp cross section should behave as a hadronic cross section. Since vector meson production represents the elastic part of $\sigma_{tot}^{\gamma p}$, we can use the optical theorem to relate the two cross sections at $t = 0$ GeV^2:

$$\left(\frac{d\sigma^{\gamma p \rightarrow Vp}}{dt}\right)_{t=0} = A \cdot \sigma_{tot}^2, \tag{13}$$

with A = constant. Then we can express the elastic cross section at any t value as:

$$\frac{d\sigma^{\gamma p \rightarrow Vp}}{dt}(t) = \left(\frac{d\sigma^{\gamma p \rightarrow Vp}}{dt}\right)_{t=0} \cdot e^{f(t)} = A \cdot \sigma_{tot}^2 \cdot e^{f(t)}, \tag{14}$$

where f(t) is the functional dependence of the cross section on t. For vector meson production, according to Regge theory, f(t) can be written as:

$$f(t) = t \cdot (b_0 + 2\alpha'_{\mathbb{P}} \cdot \ln({W_{\gamma p}}^2/W_0^2)), \tag{15}$$

where b_0 and W_0^2 are parameters. Using Eq. (15) into Eq. (14), integrating over t, and writing explicitly the dependence from the center-of-mass energy $W_{\gamma p}$, we obtain:

$$\sigma^{\gamma p \to Vp}(W_{\gamma p}) \propto \frac{({W_{\gamma p}}^2)^{2\cdot(\alpha_P(0)-1)}}{b_0 + 2\alpha'_P \cdot \ln({W_{\gamma p}}^2/W_0^2)} \simeq {W_{\gamma p}}^{0.22}. \qquad (16)$$

It is very important to note that this reasoning is based on the assumption, supported by pre-HERA data, that the same underlying exchange governs both the total and vector meson cross section.

Recent papers (Refs. 30, 31, and 32) have shown that the situation at HERA, given the large value of $W_{\gamma p}$, might be qualitatively different if a hard scale is present in the interaction. Under these circumstances, the process is calculable in QCD. The approach outlined in Sec. 6 is used: the photon fluctuates into a $q\bar{q}$ pair which first interacts with the target and then the meson is formed, Fig. 9(b). The scale of the interaction is given by the reciprocal of the fluctuation radius $r_\perp^2$,

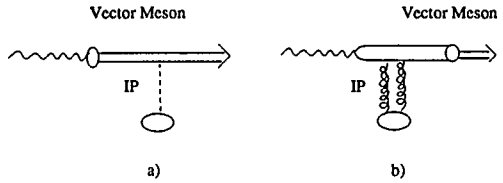


Figure 9: Different models for $\gamma p \to Vp$: (a) vector meson dominance, (b) photon diffraction.

and therefore, if either $k_\perp^2 \cdot Q^2$, t, or m_q^2 is large, the process is hard. Since the transverse momentum $k_\perp^2$ generated at the photon-quark vertex is different for longitudinally and transversely polarized photons, with $\sigma^{\gamma_L \cdot p}$ dominated by large $k_\perp^2$ and $\sigma^{\gamma_\perp \cdot p}$ dominated by small $k_\perp^2$, early papers dealt only with the former photon polarization. Lately,[33] predictions for $\sigma^{\gamma_\perp \cdot p}$ have also been made.

The pQCD approach has been used to calculate the magnitude and energy dependence of the cross section for photoproduction of J/ψ mesons,[30] where the charm mass ensures a hard scale, and production of ρ^0 mesons at high Q^2 (Ref. 31). In both cases, the $q\bar{q}$ pair resolves the gluonic contents of the proton giving a cross section proportional to the proton gluon distribution squared‡:

$$\sigma^{Vp} \propto [\alpha_s(\bar{q}^2)\bar{x}g(\bar{x},\bar{q}^2)]^2. \qquad (17)$$

‡The square comes trivially from the fact that the Pomeron is made of two gluons.

VM Decay Mode	$Q^2 \simeq 0$ GeV^2	Ref.	$Q^2 > 0$ GeV^2	Ref.
$\rho^0 \longrightarrow \pi^+ \pi^-$	X	34, 35, 36, 44	X	37, 38, 45, 4
$\phi \longrightarrow K^+ K^-$	X	39	X	40, 46, 47
$J/\Psi \longrightarrow \mu^+ \mu^-,\ e^+e^-$	X	41, 42, 43	X	38, 46
$\omega \longrightarrow \pi^+ \pi^- \pi^0$	X	49		
$\Psi(2S) \longrightarrow \pi^+ \pi^- J/\Psi$	X	50		
$\rho' \longrightarrow \pi^+ \pi^- \pi^+ \pi^-$			X	51

Table 2: List of decay modes used to identify vector meson production $\gamma p \to Vp$ at HERA.

The energy dependence is therefore no longer determined by the Pomeron intercept but by the rise of the gluon distribution at low x_{Bj}.

7.1 Experimental Signature and Selection Methods for $\gamma p \to Vp$

Vector meson production is characterized by very little activity in the detector since only the vector meson decay products, and for the DIS case, a scattered electron, are present. The processes studied so far by the two collaborations are listed in Table 2.§

General requirements common to the analyses dealing with vector meson production are:

- predictable number of tracks for a given reaction,
- energy clusters in the calorimeter matching the track momenta, with a maximum unmatched energy of $\sim$ 0.5–1 GeV (determined by resolution),
- $W_{\gamma p}$ range restricted to 40–140 GeV. For small (large) $W_{\gamma p}$ values, the tracks are too forward (backward) to be measured in the tracking chamber. For some analyses, higher values of $W_{\gamma p}$ have been achieved using events with the vertex displaced in the forward direction and/or using the calorimeter.

The main sources of systematic errors come from uncertainty on the trigger thresholds, input Monte Carlo distributions, track reconstruction, uncertainties in the mass fit (in particular, for the ρ^0 analysis), nonresonant background subtraction,

§References from Refs. 44 to 51 are contributions to the ICHEP 1996 Conference, Warsaw.

and magnitude of the double dissociation contribution. This last contribution is of particular interest since very little is known about double diffractive production of vector mesons. Figure 10 shows the contamination mechanism: if the mass M_Y of the excited proton system is small ($\leq$1.6 GeV for H1, $\leq$ 2 GeV for ZEUS depending on each detector forward coverage), the event looks elastic and is included in the sample. On the contrary, if M_Y is large, energy deposition in the calorimeter can be used as a veto. The CDF Collaboration[52] measured the mass spectrum of the system Y in $p\bar{p}$ diffraction to be $dN/dM_Y^2 = 1/M_Y^n$ with n = 2.2. This result, however, has not been obtained in the very low mass region and therefore should be used only as an indication. A more direct method used by both the H1 and ZEUS Collaborations is to model the visible energy deposition due to high M_Y states as a function of n to determine which value fits the data best and use it to perform the background subtraction.

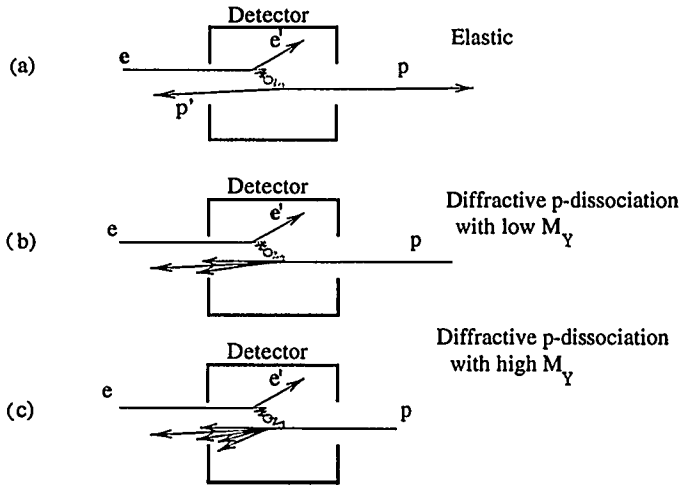


Figure 10: (a) Double dissociation background to single dissociation. (b) If the mass M_Y of the excited proton system is small, the event looks like single diffraction and is included in the sample of elastic vector meson production. (c) For large M_Y, energy deposition in the calorimeter can be used as a veto.

7.2 Light Vector Meson Production at $Q^2 = 0$

The energy dependence of the total cross sections for light mesons (ρ^0, ω, ϕ) and J/ψ photoproduction, as measured by ZEUS and H1, are shown in Fig. 11. The Regge theory prediction $\sigma^{\gamma p \to Vp}(W_{\gamma p}) \propto W_{\gamma p}^{0.22}$ is clearly supported by the data. A summary of experimental results on the measurements of σ_{tot}, b, and r_{00}^{04} in photoproduction is given in Table 3. The b values are consistent with parametrizations of low-energy data and with the "shrinkage mechanism" expected in Regge theory. This mechanism predicts that the value of the slope parameter b increases as a function of the center-of-mass energy like $b(W_{\gamma p}^2) = b_0 + 2\alpha'_{I\!P} \ln(W_{\gamma p}^2)$ where both $\alpha'_{I\!P}$ and b_0, the slope parameter at $W_{\gamma p} = 1$ GeV^2, need to be determined experimentally. This mechanism is called "shrinkage" since as b grows, the area underneath the curve $e^{b \cdot t}$ decreases considering a fixed intercept.

As the experimental results become more precise, it is possible to look for deviations from the pure exponential behavior $d\sigma/dt \sim e^{bt}$ of the t distribution. An exponential with a quadratic term[53] seems to give a good representation of the t dependence for the elastic cross section of many hadronic reactions:

$$\frac{d\sigma}{dt} = A \cdot e^{b \cdot t + c \cdot t^2}, \tag{18}$$

where c is called "curvature." The local slope parameter, defined as:

$$b(t) = \frac{d}{dt}(\ln\frac{d\sigma}{dt}) = b + 2ct \tag{19}$$

is a decreasing function of t. An example is given in Fig. 12 for the case of the ρ^0 meson. Fits to hadronic scattering data yield to very similar results: b = 11.7 GeV^{-2} and c = 3.16 GeV^{-4} for pp scattering and b = 9.9 GeV^{-2} and c = 3.47 GeV^{-4} for πp scattering measured at s = 400 GeV^2 in the interval $0.02 < |t| < 0.66$ GeV^2. The common behavior of the cross section as a function of t is due to the very similar hadronic form factors for pion, proton, and photon.

The parameter b has been recently measured by the ZEUS Collaboration in ρ^0 photoproduction using data from the Leading Proton Spectrometer.[54] This is the first diffractive cross-section measurement at HERA in which the forward scattered proton is detected and its momentum measured. This makes possible a direct determination of the squared four-momentum t exchanged at the proton vertex. The LPS consists of silicon μ-strip detectors placed close to the proton beam by means of reentrant Roman pots and detects forward-going protons scattered at

Reaction	Collab.	$\sigma(\mu b)$	b(GeV^{-2})	r_{00}^{04}
$\gamma p \to \rho^0 p$	ZEUS	$14.7 \pm 0.4 \pm 2.4$	$10.4 \pm 0.6 \pm 1.1$	0.055 ± 0.028
$\gamma p \to \rho^0 p$	$ZEUS_{LPS}$	$5.8 \pm 0.3 \pm 0.7$	$9.9 \pm 0.8 \pm 1.1$	
$\gamma p \to \rho^0 p$	H1	$9.1 \pm 0.9 \pm 2.5$	$10.9 \pm 2.4 \pm 1.1$	-0.11 ± 0.12
$\gamma p \to \rho^0 X$	$ZEUS_{LPS}$		$5.3 \pm 0.8 \pm 1.1$	
$\gamma p \to \omega p$	ZEUS	$1.2 \pm 0.1 \pm 0.2$	$10.0 \pm 1.2 \pm 1.4$	0.11 ± 0.08
$\gamma p \to \phi p$	ZEUS	$0.96 \pm 0.19 \pm 0.2$	$7.3 \pm 1.0 \pm 0.8$	-0.01 ± 0.04

Table 3: Summary of experimental results on the measurements of σ_{tot}, b, and r_{00}^{04} in photoproduction. The b values are determined using a single exponential fit $d\sigma/dt \sim e^{bt}$. The cross section $\gamma p \to \rho^0 p$ measured by the LPS is for a restricted t range.

angles $\lesssim 1$ mrad. The momentum of the proton is measured using the elements (quadrupoles and dipoles) of the proton beam line, and it is reconstructed with a resolution of $\Delta p/p \simeq 0.3\%$ at $p \simeq 820$ GeV/c. The total systematic error on the measurement of b in this analysis is 11%, the main source being the uncertainty on the acceptance ($\sim$ 7%), and the uncertainty coming from the unfolding of the beam transverse momentum spread ($\sim$ 7%). It should be noted that the uncertainty coming from the proton dissociation background is negligible, when compared to analyses which do not make use of the LPS: for LPS tagged events, the contamination has been estimated to be $0.21 \pm 0.15\%$, while a previous ZEUS result estimated the contamination to be $11 \pm 6\%$. Tagging with the LPS, a leading proton with a value of $x_L < 0.97$ has also allowed us to select a clean sample of photoproduction double diffractive ρ^0 events, $\gamma p \to \rho^0 X$. Using the transverse momentum from the decay pions, the slope parameter b has been determined to be $b_{LPS}^{\gamma p \to \rho^0 X} = 5.3 \pm 0.8 \pm 1.1$ GeV^{-2}. Figure 13 and Table 3 show the results for both single and double diffraction.

Fixed-target experiments showed, at much lower $W_{\gamma p}$, that vector mesons retained the helicity of the photon (s-channel helicity conservation, SCHC). This effect was also investigated at HERA. The results can be expressed in terms of the r_{00}^{04} spin-density matrix element which gives the probability for the meson to have zero helicity. As shown in Table 3, all the measurements are consistent with a zero value for r_{00}^{04}, as required by SCHC.

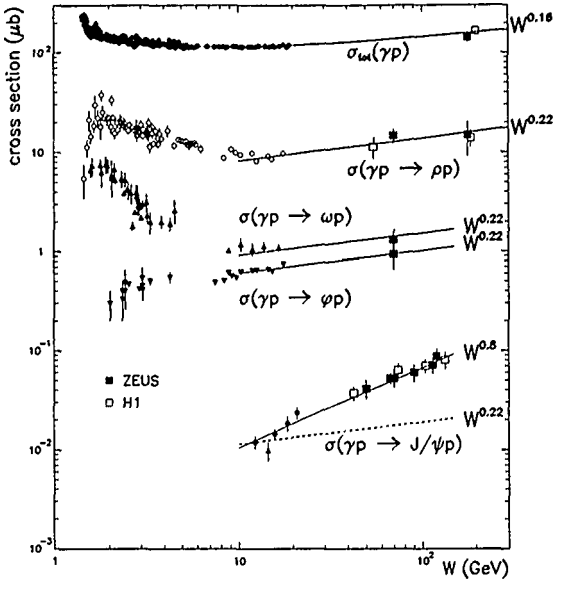


Figure 11: Total and elastic vector meson photoproduction measurements as a function of $W_{\gamma p}$. The curve overlapped to σ_{tot} is the DL parameterization $W_{\gamma p}^{0.16}$. The other lines are curves of the form $W_{\gamma p}^{0.22}$ and $W_{\gamma p}^{0.80}$.

7.3 Vector Meson Production with a Hard Scale

In contrast to the previous results, the cross sections for J/ψ photoproduction and light vector meson production at high Q^2 show a significant rise with $W_{\gamma p}$. In particular, for the J/ψ case, the rise is clearly visible within the range of HERA data, while for the light vector mesons, the rise is observed in comparison with lower energy data. Figure 11 and Fig. 14 show the effect for the J/ψ and ρ^0 case. The rise is inconsistent with the $W_{\gamma p}^{0.22}$ dependence used in the parameterizations of low-energy hadronic data. The measured behavior can be described instead by perturbative QCD models if a rise at small x_{Bj} of the gluon momentum density in the proton is assumed. Both the shape of the rise and the normalization could in principle be used to discriminate between models of the gluon distributions, but since the latter suffers from large theoretical uncertainty, only the shape is

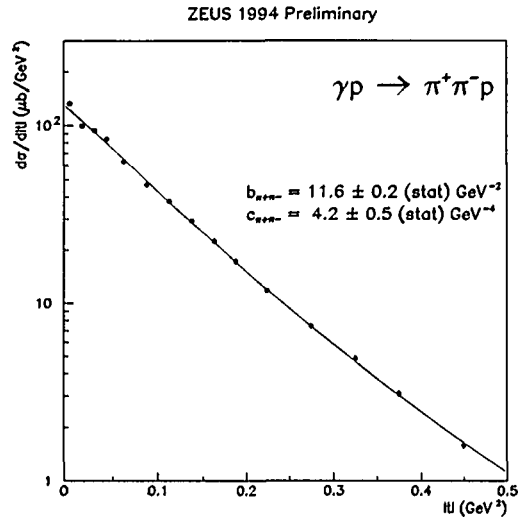


Figure 12: Measurement of the slope parameter for the reaction $\gamma p \rightarrow \rho^0 p$. A quadratic function in t, $\frac{d\sigma}{dt} \propto e^{bt+ct^2}$, was used in the fit.

used. Figure 15 shows the experimental results and the expectation based on different gluon parameterizations for the ρ^0 cross section as a function of x_{Bj} in four different Q^2 bins. The comparison is still dominated by experimental errors, but since the parameterizations are quite different, potentially this approach can be an invaluable tool to rule out many of the current options.

These results show that the cross section for vector meson production in the presence of a hard scale has a steeper energy dependence than the total hadronic γp cross section.

7.3.1 Slope Parameter b and $R = \sigma_L/\sigma_T$ Versus $W_{\gamma p}$ and Q^2

The slope parameter b is related to the effective radius of the interaction R by:

$$R = \sqrt{R_p^2 + R_{VM}^2} \simeq 0.3\, b^{1/2} \text{ fm} \qquad (20)$$

with R_p and R_{VM} the proton and vector meson radius. Given a value of $R_p \simeq 0.7$ fm, the effective vector meson radius in photoproduction, according to Table 3, changes from $R_{VM} \simeq 1.1$ fm for the ρ^0 meson to $R_{VM} \simeq 0.4$ fm for the ϕ meson.

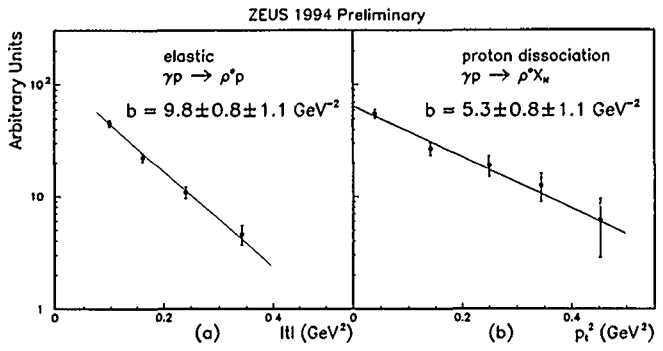


Figure 13: (a) Slope parameter b for the reaction $\gamma p \rightarrow \rho^0 p$ as obtained from the measurement of the scattered proton. The value b = 9.8 has been modified to b = 9.9 in the final analysis. (b) Slope parameter b for the reaction $\gamma p \rightarrow \rho^0 X$ obtained by tagging a low-energy proton in the LPS and measuring p_t^2 in the tracking chamber.

The value of b varies with the meson mass, the photon virtuality Q^2, and the square of the four-momentum transfer t. Figure 16 shows a compilation of the measurements done by both H1 and ZEUS as a function of $Q^2 + M_{VM}^2$. The data show a clear trend toward small b values as $Q^2 + M_{VM}^2$ increases. Note that some authors[55] use an "effective Q^2" instead of the measured Q^2 to set the scale. The drop of b from b $\simeq$ 10 to b $\simeq$ 4–5 GeV^{-2} implies that the size of the system (the $\gamma^* \rightarrow \rho^0$ Pomeron vertex) decreases with $Q^2 + M_{VM}^2$, and that for large $Q^2 + M_{VM}^2$, we do have a short-distance interaction to justify the use of pQCD. The value b $\simeq$ 4–5 GeV^{-2} is approximately equal to what is expected from the size of the proton.

Both the H1 and ZEUS Collaborations have studied the ratio between the longitudinal and transverse cross section for ρ^0 production, $R = \frac{\sigma_L}{\sigma_T}$, as a function of Q^2. A compilation of the results is shown in Fig. 17. The photon polarization, completely transverse at Q^2=0 GeV^2, becomes more longitudinal as Q^2 increases. Different QCD calculations have been done (for a review, see Ref. 33). In particular, the convolution of the $\gamma^* \rightarrow q\bar{q}$ diffractive production with the ρ^0 meson

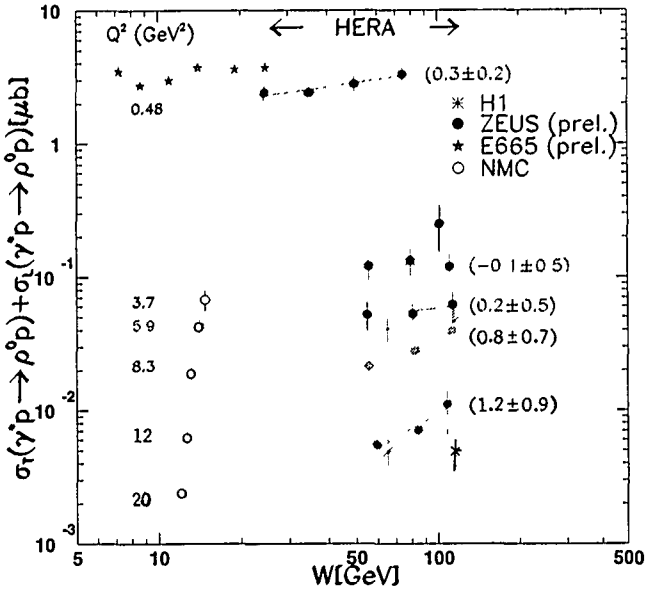


Figure 14: $\gamma p \to \rho^0 p$ cross section as a function of $W_{\gamma p}$ for different $< Q^2 >$ values (as indicated in the picture). The lines are the results of fits to the form $\sigma \propto W_{\gamma p}{}^k$; the values of k are shown in parentheses.

wave function gives:

$$R = \frac{\sigma_L}{\sigma_T} \propto \frac{Q^2}{m_{\rho^0}^2}, \tag{21}$$

which has a much too steep dependence with Q^2. A new approach,[33] based on the parton-hadron duality, couples the rise with Q^2 to the gluon distribution anomalous dimension γ:

$$R = \frac{\sigma_L}{\sigma_\perp} \simeq \frac{Q^2}{M_X^2}\left(\frac{\gamma}{\gamma+1}\right)^2. \tag{22}$$

Since γ decreases with Q^2, a less steep dependence is obtained that seems to fit the data quite well. Within the current experimental accuracy, R does not seem to depend on $W_{\gamma p}$.

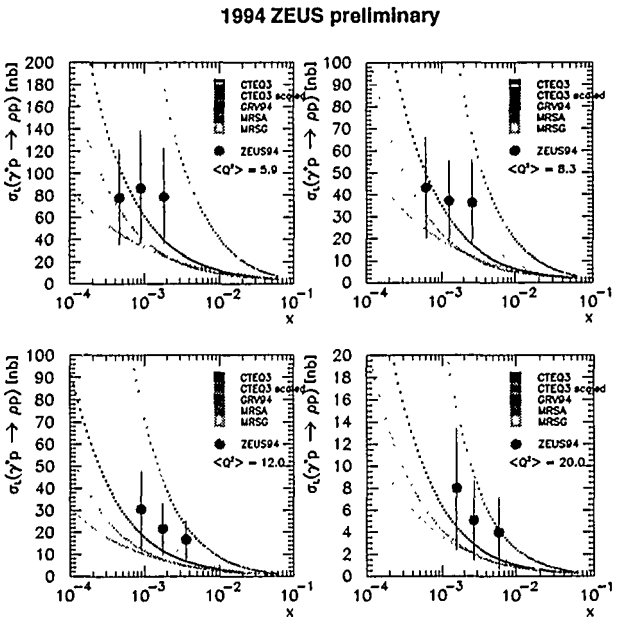


Figure 15: $\gamma p \to \rho^0 p$ cross section as a function of x_{Bj} for different values of $< Q^2 >$. The lines are predictions from a calculation based on pQCD using different gluon distributions.

7.3.2 Determination of $\alpha'_{I\!P}$ at Large Q^2

As we have seen, where Regge theory holds, the value of b should increase with energy according to the "shrinkage" mechanism. The HERA data on photoproduction of ρ^0, ϕ, ω are consistent with this prediction. At high Q^2, there are no pre-HERA measurements of the "shrinkage" mechanism. According to Ref. 56, $\alpha'_{I\!P} \simeq = 0.2$ GeV^{-2} . Therefore, the value of the slope parameter b should increase by ~ 1.5 GeV^{-2} going from low energy, $W_{\gamma p} \sim 10$ GeV, to the HERA regime, $W_{\gamma p} \sim 100$ GeV, for all exclusive reactions of the kind $\gamma^* p \to Vp$. On the other hand, according to Ref. 57, the value of $\alpha'_{I\!P}$ is expected to be $\alpha'_{I\!P} \sim 1/Q^2$ for reactions where the hard QCD regime dominates, leading to a flat behavior of b as a function of W.

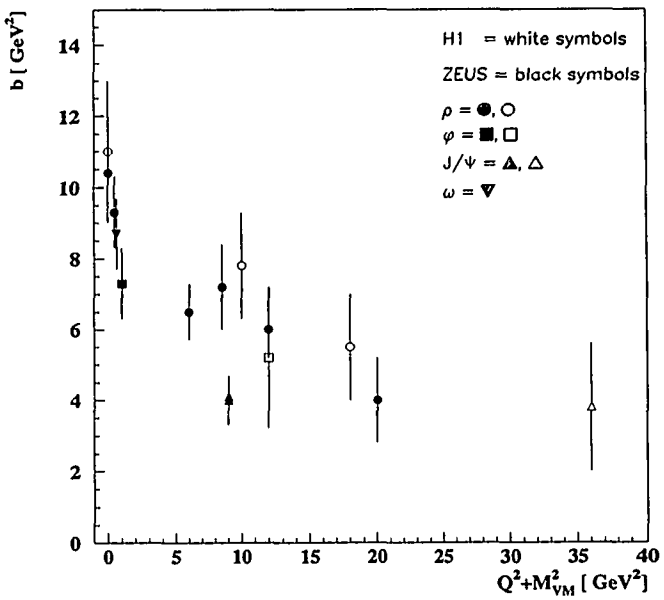


Figure 16: Exponential slope b for vector meson production as a function of $Q^2 + M^2_{VM}$.

Figure 18 shows the b values for the ρ^0 measurements as a function of $W_{\gamma p}$ at high Q^2. The experimental data are still dominated by statistical errors, and therefore no meaningful conclusion can be drawn. On the plot, the expected trend of b versus $W_{\gamma p}$ is plotted if a value of $\alpha'_{I\!P} = 0$ or 0.25 is assumed.

7.3.3 Restoration of SU(4) Symmetry at High Q^2

According to the SU(4) flavor symmetry, when $M_V^2 \ll Q^2$, the ratio among cross sections for diffractive vector meson production should depend only on the meson wavefunction and quark charges[55]:

$$\rho : \omega : \phi : J/\Psi = \left[\frac{1}{\sqrt{2}}(u\bar{u} - d\bar{d})\right]^2 : \left[\frac{1}{\sqrt{2}}(u\bar{u} + d\bar{d})\right]^2 : [s\bar{s}]^2 : [c\bar{c}]^2 = 9 : 1 : 2 : 8. \quad (23)$$

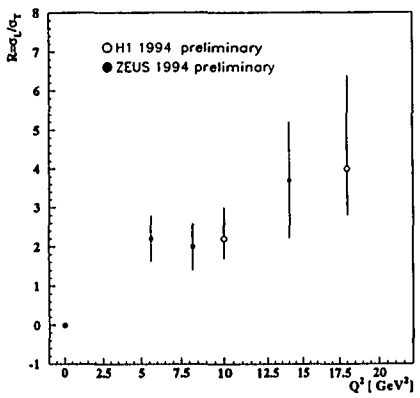


Figure 17: Ratio $R = \sigma_L/\sigma_T$ for the reaction $\gamma p \to \rho^0 p$ as a function of the photon virtuality Q^2.

Besides, QCD dynamics predicts a slow increase of the relative yield of heavy flavor production at small x_{Bj} which modifies the pure SU(4) prediction:

$$\rho : \omega : \phi : J/\Psi = 9 : (1 \times 0.8) : (2 \times 1.2) : (8 \times 3.5). \quad (24)$$

The HERA results are shown in Fig. 19: at $Q^2 \sim 0$ GeV^2, SU(4) symmetry is badly broken, with a suppression factor $\simeq 4$ for ϕ-mesons and $\simeq 25$ for J/ψ-mesons, while at large Q^2, there is a dramatic increase of both the ϕ and J/Ψ cross section compared to ρ^0 meson production. This increase is therefore another indication that the SU(4) symmetry, and therefore perturbative QCD, can be used in these processes at large Q^2.

Cross section ratios between excited and ground states for a meson are also very important quantities because they depend on the internal dynamics of the $q\bar{q}$ wavefunction and can help to determine it. First preliminary results from the H1 Collaboration,[50,51] in agreement with the expectation of Ref. 55, are:

$$\frac{\sigma^{\rho'}}{\sigma^{\rho}} = 0.36 \pm 0.07 \pm 0.11 \text{ at } Q^2 = 4 - 50 \text{ GeV}^2,$$

$$\frac{\sigma^{\Psi(2S)}}{\sigma^{\Psi}} = 0.16 \pm 0.06 \text{ at } Q^2 = 0 \text{ GeV}^2.$$

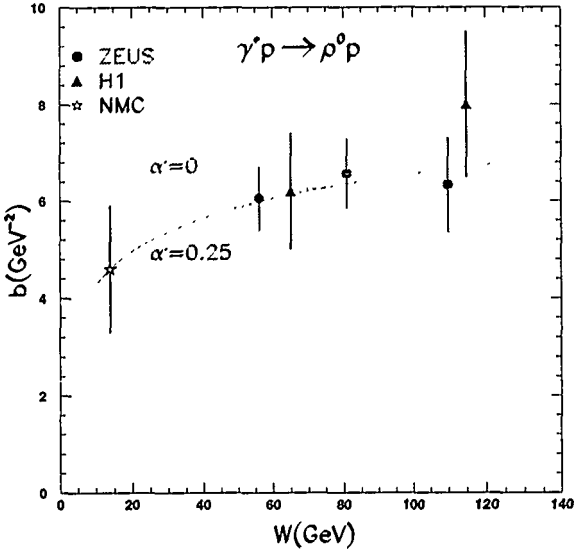


Figure 18: Exponential slope b for the reaction $\gamma p \rightarrow \rho^0 p$ as a function of $W_{\gamma p}$. On the plot, the expected trend of b versus $W_{\gamma p}$ is plotted if a value of $\alpha'_{IP} = 0$ or 0.25 is assumed.

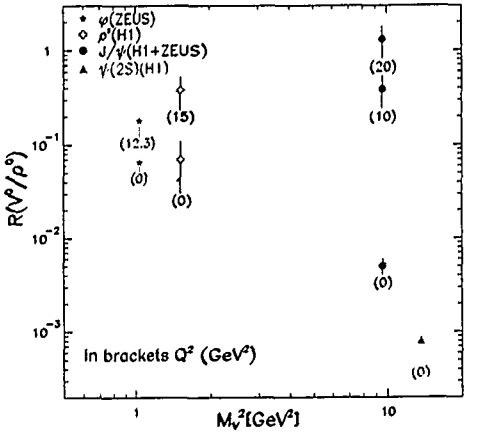


Figure 19: Ratio $R = \sigma^{\gamma p \rightarrow V p}/\sigma^{\gamma p \rightarrow \rho^0 p}$ as a function of the vector meson mass squared M_V^2 at different values of the photon virtuality Q^2 (indicated by the number in parentheses).

8 Photon Diffraction: $\gamma p \rightarrow$X Y

Single and double photon diffraction include all Pomeron-mediated reactions of the kind:

$$\gamma p \longrightarrow XY ,$$

where X is not a vector meson and Y is either a proton or an excited state. These reactions can be divided into two large groups depending on whether a hard scale is present in the scattering process.

8.1 Experimental Signature and Selection Methods for $\gamma p \longrightarrow XY$

As was shown in Sec. 5, diffractive events generally have a rapidity gap and a leading baryon in the final state. Several selection methods have been used by both the H1 and ZEUS Collaborations exploiting their own detectors. In the following, the four most significant methods are presented.

8.1.1 Maximum Pseudorapidity η_{max} (ZEUS, H1)

At HERA, following the first papers on the subject,[58,68] a cut on the pseudorapidity of the most forward[¶] energy deposit in an event has been used to separate diffractive from nondiffractive events. This cut selects as diffractive events all those events whose most forward energy deposit has a rapidity less than 1.5, equivalent to require a visible rapidity gap of at least 2.9 units in the forward direction (ZEUS case). This cut, however, puts strong limitations on the type of events that are selected since it reduces the pseudorapidity interval available for the fragmentation of the system M_X to $\Delta\eta \simeq 4.5$–5.5. Since a system with mass M_X covers a pseudorapidity interval $\Delta\eta \simeq \ln(\frac{M_X^2}{m_p^2})$ with m_p the proton mass, only masses up to $M_X \sim 10$–15 GeV are therefore selected.

8.1.2 Largest Rapidity Gap (H1)

For each event, the largest rapidity gap is identified, Fig. 20. This gap defines two systems, X and Y, with masses M_X and M_Y. If:

(a) $x_{I\!P} = \frac{M_X^2+Q^2}{W_{\gamma p}^2+Q^2} < 0.05$

(b) $M_Y < 1.6$ GeV,

the event is accepted in the diffractive sample. This selection is based on the H1 detector ability of measuring hadronic activity up to $\eta \sim 3.4 \Rightarrow x_{I\!P} < 0.05$ and vetoing activity in the region $3.4 < \eta < 7.5 \Rightarrow M_Y < 1.6$ GeV.

The requirement (a) ensures that only a small fraction of the initial proton longitudinal momentum is present in the detector, while (b) forces the existence of a rapidity gap in the final state. It is important to notice that this selection criteria does not make any assumption on the nature of the interaction but defines a cross section for all events that are selected by (a) and (b).

[¶]As mentioned before, in the HERA convention the proton travels along the z-axis in the positive direction.

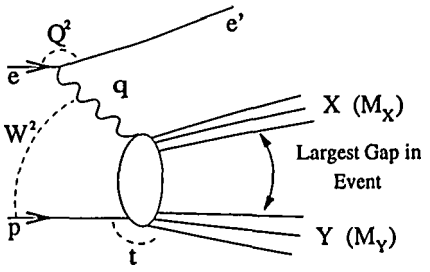


Figure 20: Schematic illustration of the selection method used to define a diffractive cross section by the H1 Collaboration.

8.1.3 Leading Proton Measurement ($ZEUS_{LPS}$)

The cleanest way to identify diffractive events is to tag a scattered proton with a very high fraction x_L of the initial proton momentum. From the leading proton momentum, both t and the hadronic mass M_X can be computed:

$$t \simeq -\frac{p_t^2}{x_L} \tag{25}$$

$$M_X^2 = W_{\gamma p}^2 \cdot (1 - x_L). \tag{26}$$

Figure 21 shows the fraction of DIS events with a leading proton as a function of x_L for $5 < Q^2 < 20$ GeV^2, $45 < W_{\gamma p} < 225$ GeV^2, and $(1 - x_L)^2/x_L < |t| < 0.5$ GeV^2. Comparing this figure with Fig. 7, two different components can be easily identified: the diffractive peak due to $I\!P$ exchange at $x_L \sim 1$ and the continuum due to double dissociation, Reggeon exchange, and nondiffractive DIS scattering rising below $x_L \sim 0.9$. Just below $x_L \sim 1$, the distinction between diffractive and nondiffractive events becomes unclear. From a fit to the x_L spectrum in pp scattering,[60] the value $x_L \sim 0.9$ has been used to identify the point where the Pomeron and non-Pomeron contributions are roughly of the same magnitude. The ZEUS Collaboration, in order to select a very pure diffractive sample, decided to use only protons with $x_L > 0.97$, well within the diffractive peak. Unfortunately, due to the limited LPS acceptance, the number of events with a tagged leading proton is small. Note that the LPS acceptance, at $x_L > 0.95$, starts at $t \sim 0.07$ GeV^2.

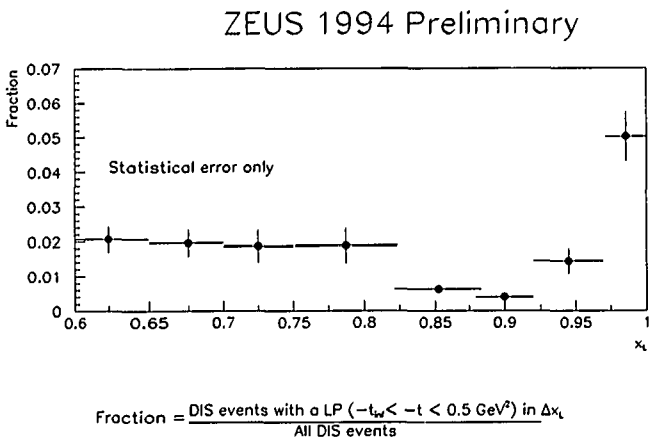


Figure 21: Fraction of DIS events with a leading proton as a function of x_L.

8.1.4 Ln(M_X) Distribution (ZEUS$_{M_X}$)

This method[59] of separating the diffractive and nondiffractive contributions is based on their very different M_X^2 distributions. Nondiffractive events, assuming uncorrelated particle emission, have an exponential fall-off of the ln M_X^2 distribution:

$$\frac{dN^{nondiff}}{d \ln M_X^2} = c \exp(b \ln M_X^2), \tag{27}$$

while diffractive events have a constant value in the ln M_X^2 distribution:

$$\frac{dN}{dM_X^2} \sim \frac{1}{M_X^2} \Longrightarrow \frac{dN}{d \ln M_X^2} = \text{const.} \tag{28}$$

The diffractive sample is therefore defined as the excess contribution in the ln M_X^2 distribution above the exponential fall-off of the nondiffractive peak. In bins of $W_{\gamma p}$, Q^2, and M_X, a fit in the form:

$$\frac{dN}{d \ln M_X^2} = D + c \exp(b \ln M_X^2) \tag{29}$$

is performed allowing the evaluation of the diffractive component. An example of the ln M_X^2 distribution is given in Fig. 22.

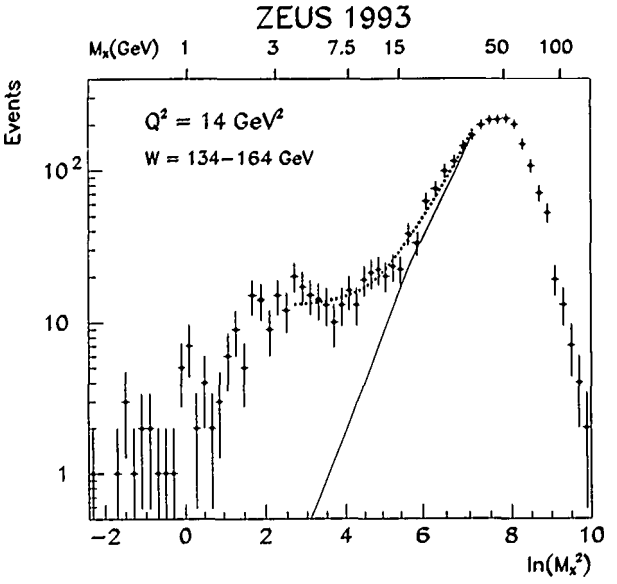


Figure 22: ln M_X^2 distributions for γ^*p scattering. Diffractive events are identified as the excess contribution above the exponential fall-off of the nondiffractive peak.

8.2 Determination of α_P and Test of Factorization

The assumption of factorization implies that the Pomeron structure is independent of the process of emission and that the Pomeron flux is the same in all diffractive processes (see Fig. 23). Its dependence on α_P is given by:

$$f_{P/p}(x_P) \propto (\frac{1}{x_P})^a, \tag{30}$$

with $a = 2\alpha_P(0) - 1$. If factorization holds, the same value of $\alpha_P(0) \simeq 1.08$ measured in many hadronic reactions should also control the Pomeron flux at HERA.

8.2.1 Determination of α_P at $Q^2 \simeq 0$ GeV^2

The value of $\alpha_P(0)$, as shown in Sec. 2, can be measured directly from the behavior of $\sigma_{tot}^{\gamma p}(W)$ as a function of the center-of-mass energy $W_{\gamma p}$. Results from both the

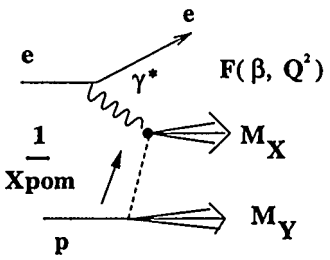


Figure 23: Diffractive ep scattering according to factorization: the flux of the Pomeron and the Pomeron structure function are universal quantities that can be determined separately.

H1 and ZEUS Collaborations are consistent with a value of $\alpha_{I\!P}(0) \simeq 1.08$ (see Sec. 2).

A second method to determine $\alpha_{I\!P}(0)$ is based on the behavior of the differential cross section $\frac{d^2\sigma}{d|t|dM_X^2}$ as calculated in the Regge formalism for the triple Pomeron diagram:

$$\frac{d^2\sigma}{d|t|dM_X^2} \propto (\frac{1}{M_X^2})^{\alpha_{I\!P}(0)} \cdot e^{(b_o+2\alpha'_{I\!P}\ln(\frac{W_{\gamma p}^2}{M_X^2}))\cdot|t|}. \qquad (31)$$

In Table 4, the results from the H1 (Ref. 61) and ZEUS (Ref. 62) Collaborations are presented. Both results suggest a value for $\alpha_{I\!P}(0)$ consistent with Regge phenomenology as already indicated by $\sigma_{tot}^{\gamma p}(W)$ and support the hypothesis that the same "soft Pomeron" used to describe the high-energy behavior of hadron-hadron scattering is also responsible for diffractive photoproduction at HERA.

Collaboration	M_X Interval [GeV]	$\alpha_{I\!P}(0)$
ZEUS	$8 < M_X < 24$	1.14 ± 0.04 (stat) ± 0.08 (syst)
H1	$3 < M_X < 24$	1.11 ± 0.02 (stat) ± 0.07 (syst)

Table 4: $\alpha_{I\!P}(0)$ values in diffractive photoproduction as determined by the H1 and ZEUS Collaborations from a fit to $\frac{d^2\sigma}{d|t|dM_X^2}$.

8.2.2 Determination of $\alpha_{I\!P}$ at Large Q^2

At large Q^2, by analogy with standard deep inelastic scattering, the differential cross section for deep inelastic diffractive scattering can be written as:

$$\frac{d^4\sigma_{diff}}{dQ^2d\beta dx_{I\!P}dt} = \frac{2\pi\alpha^2}{\beta Q^4}(1+(1-y)^2)\,F_2^{D(4)}(Q^2,\beta,x_{I\!P},t). \qquad (32)$$

Using now the assumption that factorization is valid, the t and $x_{I\!P}$ dependence can be separated from the dependence on β and Q^2:

$$F_2^{D(4)}(Q^2,\beta,x_{I\!P},t) = f(x_{I\!P},t)\cdot F_2^{D(2)}(Q^2,\beta).$$

Integrating the Pomeron flux over t and writing the dependence on $x_{I\!P}$ explicitly, $F_2^{D(4)}(Q^2,\beta,x_{I\!P},t)$ becomes:

$$F_2^{D(4)}(Q^2,\beta,x_{I\!P},t) \;\Rightarrow\; (\frac{1}{x_{I\!P}})^a \cdot F_2^{I\!P}(Q^2,\beta). \qquad (33)$$

Following Eqs. (32) and (33), the determination of the DIS diffractive cross section in $x_{I\!P}$ bins provides a method to measure $\alpha_{I\!P}$ as a function of Q^2 and β and to test whether factorization holds.

H1 Determination of $\alpha_{I\!P}$

Figure 25 shows the quantity $x_{I\!P}\cdot F_2^{D(2)}(\beta,Q^2)$ for different Q^2 and β bins as a function of $x_{I\!P}$. The data[64] were fitted with the function:

$$F_2^{D(3)} = (\frac{1}{x_{I\!P}})^a \cdot A(\beta,Q^2)$$

in each β or Q^2 interval. The points clearly show a change in slope going from low to high values of β while no dependence is seen with Q^2, Fig. 24. This analysis, therefore, shows that there is a change in the value of n as a function of $x_{I\!P}$ and β. This experimental factorization breaking, however, does not uniquely indicate a change in the Pomeron flux, but it might also be explained in terms of a presence in the data of a "non-Pomeron" component. If a fit using a meson and a Pomeron component is performed, Fig. 25,

$$F_2^{D(3)} = F_2^{I\!P}(\beta,Q^2)\cdot x_{I\!P}^{\;-a} + C_M \cdot F_2^M(\beta,Q^2)\cdot x_{I\!P}^{\;-n_2},$$

then a single value for "a" gives a good description of the data (preliminary results):

$$a = 1.29 \pm 0.03\,(stat) \pm 0.06(syst) \pm 0.03\,(model)$$

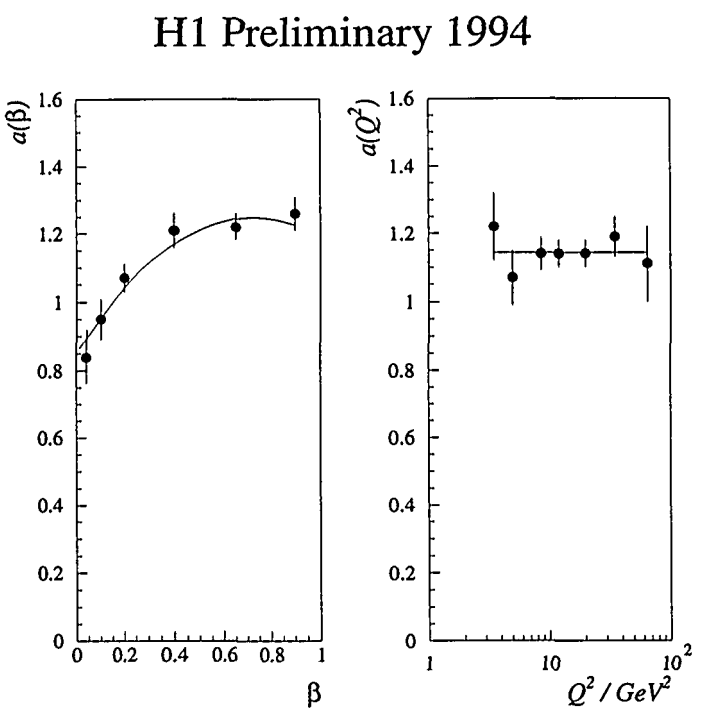


Figure 24: Results for the value of "a" when $F_2^{D(2)}(\beta, Q^2)$ is fitted to the form $(\frac{1}{x_{\mathbb{P}}})^{a(\beta)}$. Statistical and systematic errors are added in quadrature.

$$n_2 = 0.3 \pm 0.3\,(\text{stat}) \pm 0.6\,(\text{syst}) \pm 0.2\,(\text{model})$$

with $\chi^2/\text{ndf} = 170/156$. The value obtained for n_2 is consistent with what is expected from meson exchange. From "a," a value for $\alpha_{\mathbb{P}}$ averaged over the unmeasured t distribution, $\overline{\alpha_{\mathbb{P}}}$, can be obtained, $\overline{\alpha_{\mathbb{P}}} = \frac{a+1}{2}$:

$$\overline{\alpha_{\mathbb{P}}}^{\text{H1}} = 1.15 \pm 0.02\,(\text{stat}) \pm 0.04\,(\text{syst}).$$

To check consistency between results obtained with this method and a previous H1 analysis,[68] the measurement of $\alpha_{\mathbb{P}}$ using a single component has also been performed over the same kinematical range used in Ref. 68, obtaining a result that is compatible within statistical errors with the old one.

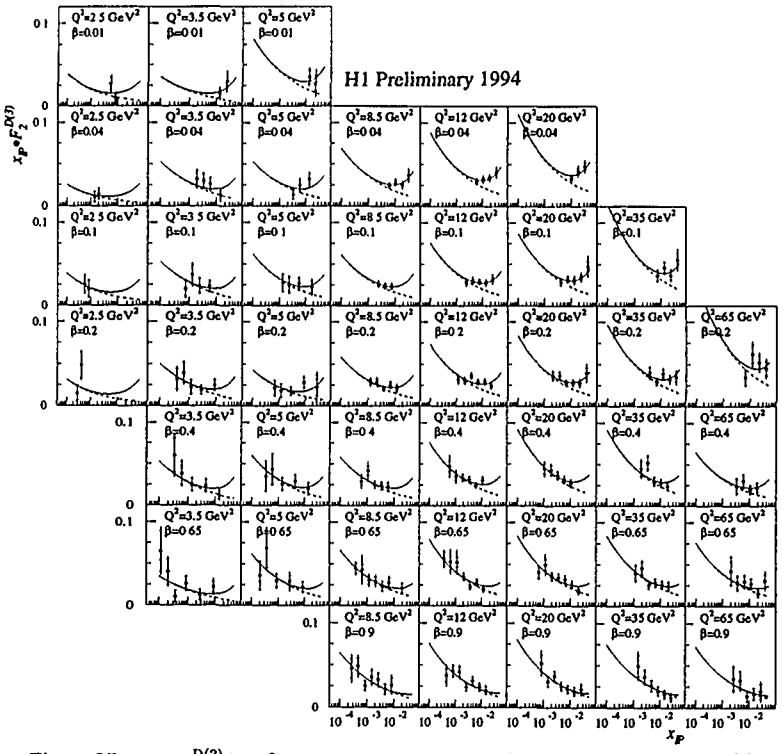


Figure 25: $x_{\mathbb{P}} \cdot F_2^{D(2)}(\beta, Q^2)$ together with a fit in which a Pomeron component with a trajectory $\alpha_{\mathbb{P}}$ contributes together with a meson component with trajectory α_M. On each plot, the bottom line shows the contribution from the Pomeron component while the top line shows the sum of the two components.

ZEUS_{LPS} Determination of $\alpha_{\mathbb{P}}$

The diffractive structure function $F_2^{D(3)}(\beta, Q^2, x_{\mathbb{P}})$ was determined using LPS tagged events[65] in the range $4 < Q^2 < 30$ GeV^2, $0.006 < \beta < 0.5$, $< Q^2 > = 12$ GeV^2, $4 \cdot 10^{-4} < x_{\mathbb{P}} < 3 \cdot 10^{-2}$, and $0.07 < |t| < 0.36$ GeV^2, extending the range to lower β and higher $x_{\mathbb{P}}$ compared to previous ZEUS measurements (Fig. 26). The results are consistent with factorizable $x_{\mathbb{P}}$ dependence in all β bins. Fitting the highest three β bins with the same exponent gives a = 1.28 ± 0.07 (stat.) ± 0.15 (syst.), and therefore:

$$\overline{\alpha_{\mathbb{P}}}^{\text{LPS}} = 1.14 \pm 0.04\,(\text{stat.}) \pm 0.08\,(\text{syst.}).$$

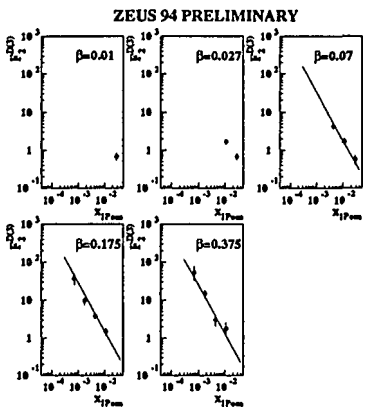


Figure 26: The structure function $F_2^{D(2)}(\beta, Q^2)$ plotted vs $x_{I\!P}$ in bins of β at $< Q^2 > = 12$ GeV^2. The errors are statistical only. The solid line corresponds to the fit described in the text.

ZEUS$_{M_X}$ determination of $\alpha_{I\!P}$

The determination of $\alpha_{I\!P}$ can also be achieved by fitting the energy dependence of the cross section in bins of M_X (Ref. 59). In a Regge-type description,[66,67] the $W_{\gamma p}$ dependence of the diffractive cross section is of the form

$$\frac{d\sigma_{diff}^{\gamma^* p \to XN}(M_X,\ W_{\gamma p},\ Q^2, t)}{dt dM_X} \propto (W_{\gamma p}{}^2)^{2\alpha_{I\!P}(0)-2} \cdot e^{-|t|(b_0+2\alpha'_{I\!P}\ln(W^2_{\gamma p}/(M^2_X+Q^2)))}, \quad (34)$$

where $\alpha_{I\!P}(t) = \alpha_{I\!P}(0) + \alpha'_{I\!P} t$ is the Pomeron trajectory and b_0 and $\alpha'_{I\!P}$ are parameters. The cross sections in each $(M_X,\ Q^2)$ interval is fitted to the form

$$\frac{d\sigma_{diff}^{\gamma^* p \to XN}(M_X,\ W_{\gamma p},\ Q^2)}{dM_X} \propto (W_{\gamma p}{}^2)^{(2\overline{\alpha_{I\!P}}-2)}, \quad (35)$$

allowing a determination of $\overline{\alpha_{I\!P}}$. However, the result obtained with this method is currently under further investigation and is shown only for completeness‖:

$$\overline{\alpha_{I\!P}}^{M_X} = 1.23 \pm 0.02(\text{stat}) \pm 0.04(\text{syst}).$$

8.2.3 Comparison of the Results

In order to compare results obtained at $Q^2 \sim 0$ GeV^2 with results obtained at large Q^2, the influence on the result of the unknown value of $\alpha'_{I\!P}$ in photon diffraction at large Q^2 needs to be evaluated. Note that the value of $\alpha'_{I\!P}$ in photon diffraction at large Q^2 does not have to be the same one measured in vector meson production in the presence of a hard scale. Let's consider, as an example, the $\ln M_X$ analysis. Integrating over t Eq. (34), the expression for the cross section is:

$$\frac{d\sigma_{diff}^{\gamma^* p \to XN}(M_X,\ W_{\gamma p},\ Q^2)}{dM_X} \propto (W_{\gamma p}{}^2)^{2\alpha_{I\!P}(0)-2} \cdot \frac{1}{b_0 + 2\alpha'_{I\!P}\ln(W_{\gamma p}{}^2/(M_X^2+Q^2))}$$
$$e^{-|t|(b_0+2\alpha'_{I\!P}\ln(W^2_{\gamma p}/(M^2_X+Q^2)))} \left|_{|t_{max}|}^{|t_{min}|}\right. . \quad (36)$$

If $\alpha'_{I\!P} \sim 0$ GeV^{-2}, then Eq. (36) simplifies to

$$\frac{d\sigma_{diff}^{\gamma^* p \to XN}(M_X,\ W_{\gamma p},\ Q^2)}{dM_X} \propto (W_{\gamma p}{}^2)^{2\alpha_{I\!P}(0)-2},$$

and comparing this expression with Eq. (35), we obtain $\overline{\alpha_{I\!P}} = \alpha_{I\!P}(0)$. On the other hand, if $\alpha'_{I\!P} > 0$ GeV^{-2}, then two effects change the slope of the $W_{\gamma p}$ dependence:

(1) The denominator of Eq. (36) is a slowly rising function of $W_{\gamma p}$, and therefore, causes $\overline{\alpha_{I\!P}}$ to be smaller than $\alpha_{I\!P}$. This effect has been estimated, for $\alpha'_{I\!P} = 0.25$ GeV^{-2}, to be 0.025–0.03.

(2) If the t range is limited, the last term of Eq. (36) is a decreasing function of $W_{\gamma p}$, causing $\overline{\alpha_{I\!P}}$ to be smaller than $\alpha_{I\!P}$. For the ZEUS$_{LPS}$ analysis, where $|t_{min}| = 0.07$ GeV^2, a value of $\alpha'_{I\!P} = 0.25$ GeV^{-2} reduces the measured $\overline{\alpha_{I\!P}}$ value by ~ 0.02.

‖In the preliminary analysis of the ZEUS '94 data on the diffractive DIS cross sections, a technical mistake has been found in the generation of the Monte Carlo data used for the acceptance correction and resolution unfolding. This mistake led to the mishandling of QED radiative corrections. Its effect is to change the cross sections by typically one systematic error. The ZEUS Collaboration thus has retracted their 1994 preliminary results until further analysis is completed and the effect on the above value of $\overline{\alpha_{I\!P}}^{M_X}$ is currently under study.

In Fig. 27, the compilation of $\alpha_{I\!P}$ values obtained at HERA is shown assuming, for the measurement at large Q^2, (a) $\alpha'_{I\!P} = 0$ GeV^{-2}; or (b) $\alpha'_{I\!P} = 0.25$ GeV^{-2} . The solid line is the statistical error while the dotted line is the systematic error. The values indicated as H1 93 (η_{max}) (Ref. 68) and ZEUS 93 (η_{max}) (Ref. 69) are the first measurement obtained by each experiment, and they were obtained using the selection cut $\eta_{max} < 1.8$ for H1 and $\eta_{max} < 1.5$ for ZEUS.

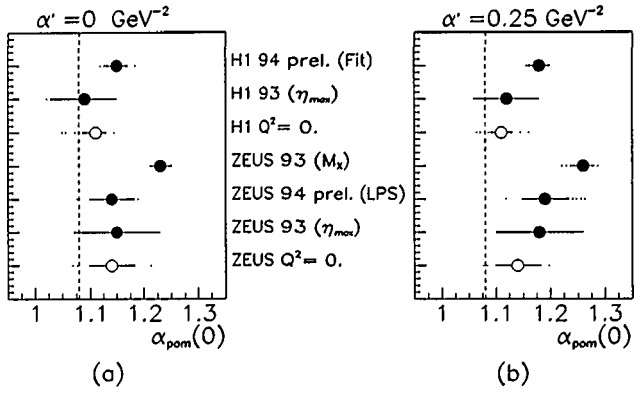


Figure 27: Compilation of $\alpha_{I\!P}(0)$ values obtained at HERA, assuming, for the measurement at large Q^2, (a) $\alpha'_{I\!P} = 0.0$ GeV^{-2}; or (b) $\alpha'_{I\!P} = 0.25$ GeV^{-2}. Empty dots are values obtained at $Q^2 = 0$ GeV^2, full dots at high Q^2. The dashed vertical line is the value $\alpha_{I\!P}(0) = 1.08$. The solid line is the statistical error while the dotted line is the systematic error.

It is possible that the difference in value between $\alpha_{I\!P}{}^{Q^2=0}(0)$ and $\alpha_{I\!P}{}^{Q^2>0}(0)$ is a signal for the presence of a small "hard" Pomeron component in the diffractive sample at high Q^2. How to measure it, its magnitude, and how to enhance it choosing particular final states (for example, see Refs. 70 and 71) is currently under intense theoretical investigation. Note also that the above comparison is done among measurements performed on different t and $x_{I\!P}$ ranges.

8.3 Measurement of the Slope Parameter b in Diffractive DIS

Using the ZEUS leading proton spectrometer, the t distribution of diffractive DIS was measured directly for the first time at HERA.[65] The measurement of t has been performed in the kinematic range: $x_L > 0.97$, $4 < Q^2 < 30$ GeV^2, $< Q^2 >= 12$ GeV^2, $70 < W_{\gamma p} < 210$ GeV, $0.07 < |t| < 0.36$ GeV^2. Assuming an exponential behavior $\frac{d\sigma}{dt} \propto e^{-b|t|}$, b is measured to be:

$$b = 5.9 \pm 1.3\ (stat.)\ ^{+1.1}_{-0.7}\ (syst.)\ \text{GeV}^{-2}.$$

The measured t distribution is shown in Fig. 28. The value of b is similar to the values obtained in single diffraction in pp interactions.

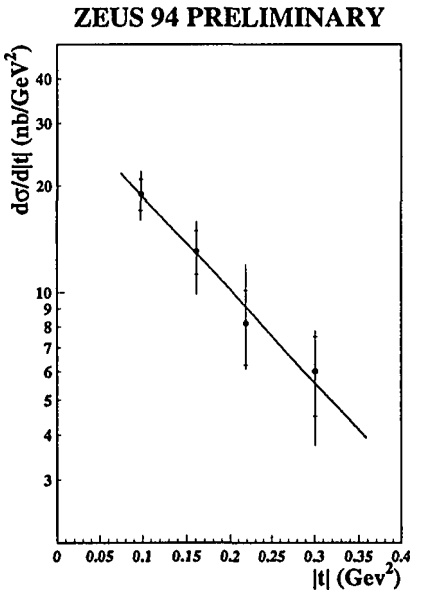


Figure 28: Differential cross section $\frac{d\sigma}{dt}$ for diffractive DIS events with a leading proton detected in the LPS. The error bars represent the statistical and systematic errors added in quadrature, and the line shows the result of the exponential fit.

8.4 Partonic Structure of Diffractive Exchange

8.4.1 QCD Fit to the Diffractive Structure Function

The H1 Collaboration[64] performed a QCD analysis of the diffractive structure function $F_2^{D(3)}(Q^2, \beta, x_{\mathbb{P}})$. The analysis is performed integrating $F_2^{D(3)}(Q^2, \beta, x_{\mathbb{P}})$ over the measured $x_{\mathbb{P}}$ range, and the result interpreted as the deep inelastic structure of the exchanged object averaged over t and $x_{\mathbb{P}}$:

$$\tilde{F}_2^{\mathbb{P}}(Q^2, \beta) = \int_{x_{\mathbb{P}\,min}}^{x_{\mathbb{P}\,max}} (\frac{1}{x_{\mathbb{P}}})^n \cdot F_2^{\mathbb{P}}(Q^2, \beta) \cdot dx_{\mathbb{P}}.$$

The QCD analysis is performed fitting the data using a flavor singlet quark and gluon distribution ($u + \bar{u} + d + \bar{d} + s + \bar{s}$ + gluon) at a starting scale $Q_0^2 = 2.5\,GeV^2$ and then evolving the system according to the DGLAP[72] evolution equation. The results are shown in Fig. 29. The most striking feature in the data is that a rise with $\ln Q^2$ persists to values of β far in excess of the point ($x_{Bj} \simeq 0.15$) at which the structure of the proton is dominated by quarks rather than by gluons, suggesting a strong gluonic component in the structure of the diffractive exchange. The QCD fit supports this interpretation: the analysis has also been done considering only quarks at the starting scale Q_0^2 and a much worse χ^2 value has been obtained. The parton distributions obtained from the fit are shown in Fig. 30. At $Q^2 = 5\ GeV^2$, a "leading" gluon behavior is observed, in which the exchange is dominated by gluons carrying a very large fraction of the longitudinal momentum.

8.4.2 Jet Structure

The question of the constituent content of the Pomeron can also be addressed via measurements of diffractively produced jets, both in photoproduction[73,74] and DIS.[75] The ZEUS Collaboration studied the diffractive dijet cross section:

$$\gamma p \longrightarrow \text{jet} + \text{jet} + X + p$$

and compared its magnitude and shape with different model predictions based on a factorizable model of Pomeron. To ensure diffractive production, a gap in the most forward part of the detector of at least 2.9 units was required. The following Pomeron fractional momentum densities were used in the MC:

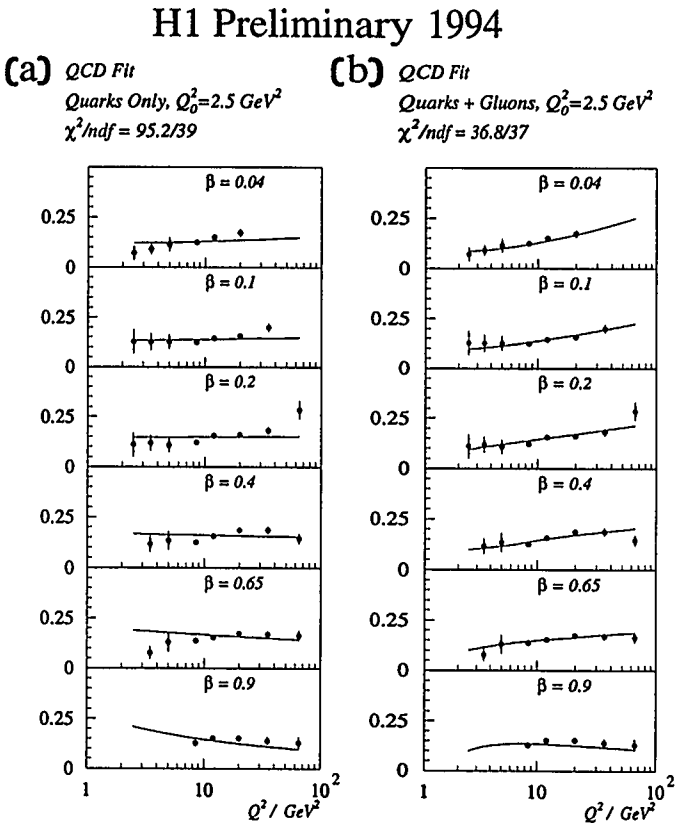


Figure 29: DGLAP QCD comparison of the (β, Q^2) dependence of $\tilde{F}_2^D$: (a) assuming only quarks at the starting scale of $Q_0^2 = 2.5\ GeV^2$, (b) assuming both quarks and gluons at the starting scale of $Q_0^2 = 2.5\ GeV^2$.

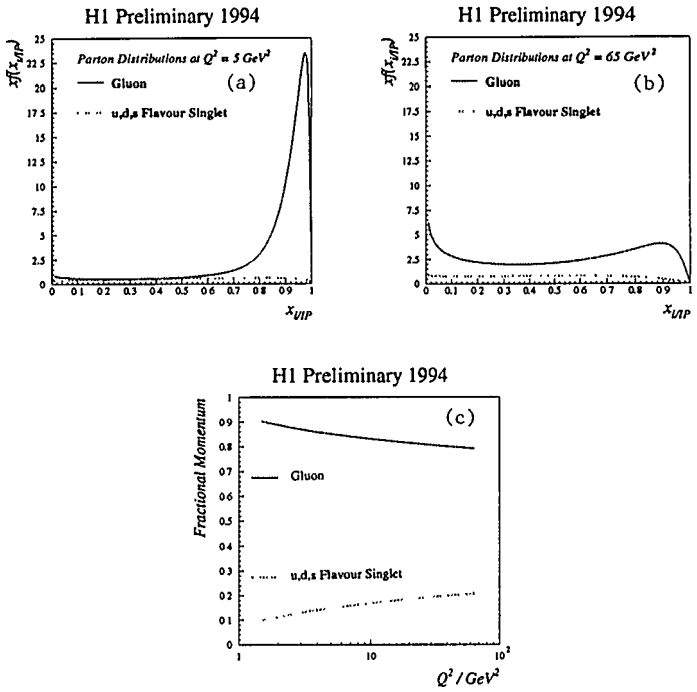


Figure 30: Quark and gluon fractional momentum distributions for diffractive exchange averaged over $x_{I\!P}$ and t extracted using the DGLAP QCD fit at (a) Q^2 = 5 GeV^{2}and (b) Q^2 = 65 GeV^2; (c) fraction of the total momentum carried by quarks and by gluons as a function of Q^2.

- Super-hard gluon: $\beta f_{g/P}(\beta) = \frac{0.1}{(1-\beta)^{0.6}}$
- Hard gluon: $\beta f_{g/P}(\beta) = 6\beta(1-\beta), <\beta> = 1/2$
- Hard-quark (2 flavors): $\beta f_{q/P}(\beta) = \frac{6}{4}\beta(1-\beta)$.

The measured distribution, Fig. 31, is compatible with a Pomeron containing a hard-gluon density. The thick error bars represent the statistical errors of the data, and the thin error bars show the statistical error added in quadrature with the systematic nonassociated with the jet energy scale. Comparison with POMPYT[76] MC calculations for a gluonic (quarkonic) Pomeron are shown, including both direct and resolved contributions and different choices of the parton density. From top to bottom, the curves correspond to super-hard gluon (dashed-dotted), hard gluon, hard quark, and soft gluon. The nondiffractive contribution modelled by PYTHIA[77] is shown as a dashed line.

8.5 $\sigma_{\rm dif}/\sigma_{\rm tot}$ as a Function of Q^2

Figure 32 shows the ratio between the diffractive and total cross section as a function of Q^2. At $Q^2\sim$ 0 GeV^2, the diffractive part of the cross section is $36 \pm 8\%$ ($42 \pm 8\%$) according to the ZEUS (H1) Collaboration of which $23 \pm 6\%$ ($32 \pm 4\%$) is photon diffraction and $13 \pm 5\%$ ($10 \pm 3\%$) is vector meson production. This last component has been measured to fall at least like $d\sigma/dQ^2 \sim 1/(m_{VM}^2 + Q^2)^2$ and therefore becomes negligible as Q^2 increases. Photon diffraction seems to decrease going from Q^2 = 0 to 10 GeV^2, while it stays flat as a function of Q^2 at large Q^2, indicating that diffraction is a leading twist mechanism. It will be very interesting to have more accurate data to see if this decrease, assuming that it is actually confirmed, happens at the same Q^2 values where pQCD starts to be applicable, indicating a change in the nature of the γp diffractive interaction.

9 Central Rapidity Gaps

In high-energy hadronic collisions, the dominant mechanism for jet production is a hard scatter between partons in the incoming hadrons via a quark or gluon propagator. Such jets are said to be "color connected," and this leads to the production of particles throughout the rapidity region between the jets. However, if the hard scattering were mediated by the exchange of a color singlet propagator

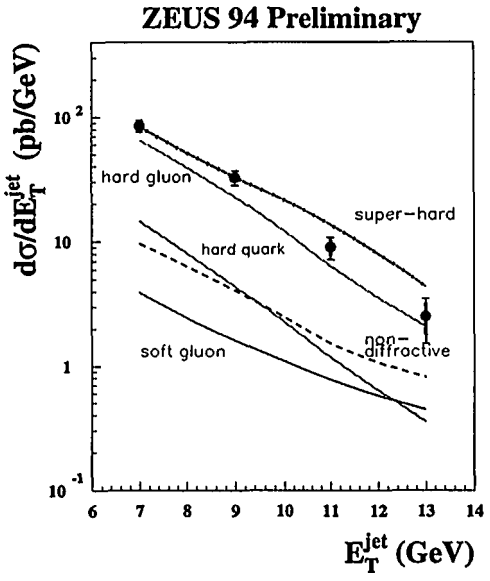


Figure 31: The diffractive dijet cross section as a function of η^{jet} compared to MC predictions for different Pomeron momentum densities.

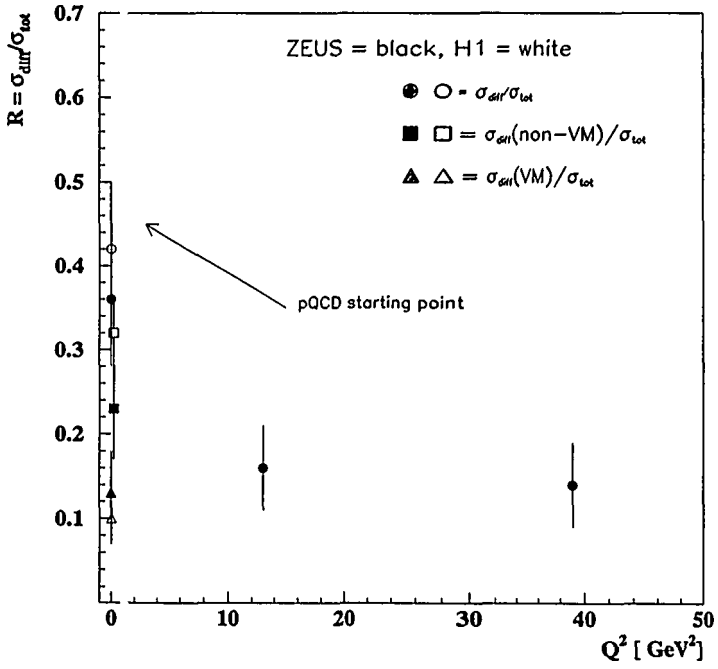


Figure 32: Ratio between the diffractive and total cross section as a function of Q^2.

in the t-channel, each jet would be color connected only to the beam remnant closest in rapidity, and the rapidity region between the jets would contain few final-state particles,[78] Figs. 33(a) and 33(b).

DØ (Ref. 79) and CDF (Ref. 80) have reported the results of searches at $\sqrt{s} = 1.8$ TeV for dijet events in $p\bar{p}$ collisions containing a rapidity gap between the two highest transverse energy (E_T^{jet}) jets. Both collaborations see an excess of gap events over the expectations from color exchange processes. DØ reports an excess of $0.0107 \pm 0.0010(\text{stat.})^{+0.0025}_{-0.0013}(\text{syst.})$, whereas CDF measures the fraction to be 0.0086 ± 0.0012.

At HERA, an equivalent mechanism is possible, with the hadronic fluctuation of the photon acting as one of the hadrons. In order to quantify the rapidity gap events, a gap fraction, $f(\Delta\eta)$, is defined as the ratio of the number of dijet events which have a rapidity gap of width $\Delta\eta$ between the jets to the total number of dijet events. As explained above, for color nonsinglet exchange, the gap fraction is expected to fall exponentially with increasing $\Delta\eta$, while for color singlet exchange, the gap fraction is not expected to depend strongly upon $\Delta\eta$ (Refs. 15 and 81). The situation is illustrated in Fig. 33(d).

The results[82] are shown in Fig. 34. Both the comparison with the default PYTHIA nonsinglet prediction and the fit to an exponential form give an excess of about 0.07 in the gap fraction over the expectation from color nonsinglet exchange. This excess can be interpreted as evidence of hard diffraction: a simple two-gluon model for Pomeron exchange gives $\hat{f}(\Delta\eta) \sim 0.1$ (Ref. 15), thus showing that Pomeron exchange could account for the data.

The magnitude of the squared four-momentum transfer across the rapidity gap as calculated from the jets is large ($|t| \geq (E_T^{jet})^2$). Thus, the color singlet exchange is unambiguously "hard."

10 Conclusions

Diffraction at HERA has provided many measurements in both the soft and perturbative domains.

— The rise of the total γp cross section has been measured to be weak, consistent with the exchange of the same "soft" Pomeron responsible for the rise with energy of hadronic reactions.

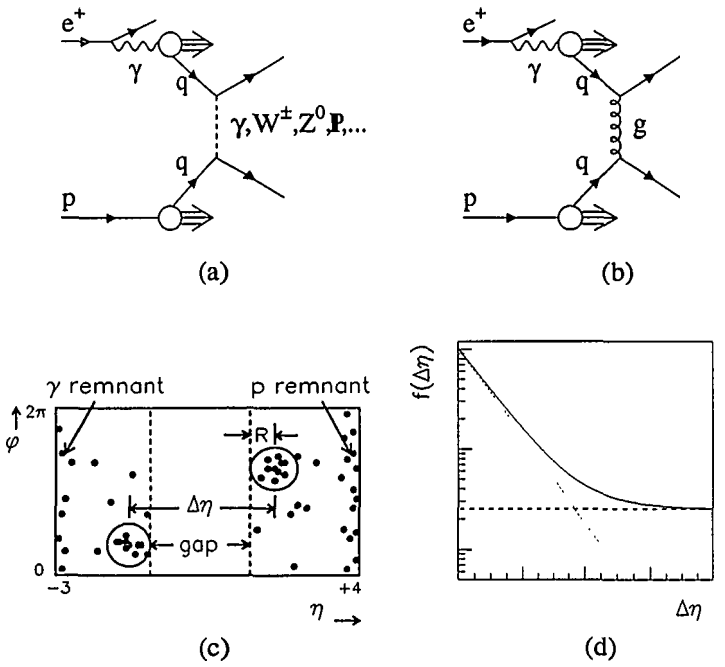


Figure 33: Resolved photoproduction via (a) color singlet exchange and (b) color nonsinglet exchange. The rapidity gap event morphology is shown in (c), where black dots represent final state hadrons and the boundary illustrates the limit of the ZEUS acceptance. Two jets of radius R are shown, which are back-to-back in azimuth and separated by a pseudorapidity interval $\Delta\eta$. An expectation for the behavior of the gap fraction is shown in (d)(solid line). The nonsinglet contribution is shown as the dotted line and the color singlet contribution as the dashed line.

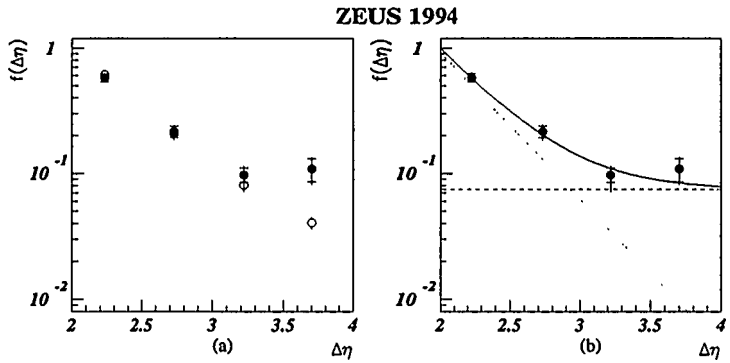


Figure 34: Results from events with central rapidity gaps. (a) Points before (open circles) and after (full circles) detector corrections. (b) Fit as explained in the text.

— Diffractive photoproduction is also governed by soft Pomeron exchange: a value of $\alpha_{\mathbb{P}}(0) \simeq 1.11$-$1.14$ has been measured from the mass spectrum of the dissociated photon in the triple Pomeron regime.

— Elastic vector meson production at HERA shows a clear distinction between two classes of processes. A first group of results, photoproduction of light vector mesons ($\gamma p \to Vp$, $V = \rho^0$, $\phi\,\omega$), exhibits the characteristic features of diffraction, as described by Regge theory: a weak energy dependence of the cross section and a value of the t slope parameter b as observed in hadronic diffractive reactions. They are therefore explained in terms of the same Pomeron that controls the total cross section. A second group, which includes photoproduction of J/ψ and light vector meson production at high Q^2, shows a different pattern: a strong energy dependence of the cross section, values of b consistent with a point-like γ V vertex, and the restoration of the SU(4) flavor symmetry, that indicate a type of dynamic consistent with pQCD predictions.

— Photon diffraction at large Q^2 shows a value of $\alpha_{\mathbb{P}}$ only slightly higher than the values obtained in photoproduction, indicating that the same mechanism used to explain photoproduction processes can be used to explain a large fraction of diffractive dissociation at high Q^2. The partonic structure of the Pomeron has been measured and found to be dominated by hard gluons. Factorization has been found to be valid within the current sensitivity and measurements range.

Acknowledgments

It is a pleasure to thank H. Abramovicz, M. Arneodo, J. Dainton, E. Gallo, G. Iacobucci, A. Levi, R. Nania, J. Phillips, F. Sciulli, A. Solano, and also thanks to Lilian DePorcel for her infinite patience and understanding.

References

[1] H1 Collaboration, DESY 93-103.

[2] ZEUS Collaboration, The ZEUS Detector, Status Report (1993).

[3] G. Iacobucci, talk given at the 1996 Zeuthen Workshop on Elementary Particle Theory, Rheinsberg, Germany (1996);
A. Staiano, talk given at Les Rencontres de la Physique de la Valle d'Aoste, La Thuile (1996);
G. Barbagli, talk given at the 1996 IHEP Conference, Warsaw.

[4] P. D. B. Collins, *An Introduction to Regge Theory and High Energy Physics* (Cambridge University Press, Cambridge, 1977).

[5] M. Perl, *High Energy Hadron Physics* (Wiley & Sons, New York, 1974).

[6] A. Donnachie and P. V. Landshoff, Phys. Lett. B **296**, 227 (1992).

[7] H1 Collaboration, S. Aid *et al.*, Z. Phys. C **69**, 27 (1995).

[8] ZEUS Collaboration, M. Derrick *et al.*, Z. Phys. C **63**, 391 (1994).

[9] CDF Collaboration., F. Abe *et al.*, Phys. Rev. D **50**, 5550 (1994) .

[10] H. Abramowicz *et al.*, Phys. Lett. B **269**, 465 (1991).

[11] ZEUS Collaboration, M. Derrick *et al.*, DESY 96-076 (June 1996).

[12] H1 Collaboration, F. Abe *et al.*, Nucl. Phys. B **470** (1996).

[13] M. Ryskin *et al.*, *Proceedings of the Workshop "Physics at HERA"*, Heavy photon dissociation in DIS (Hamburg, 1991).

[14] B. Kopeliovich *et al.*, hep-ph/9601291.

[15] J. D. Bjorken, Phys. Rev. D **47**, 101 (1992).

[16] M. Przybycien *et al.*, hep-ph/9606294.

[17] A. Donnachie and P. V. Landshoff, Nucl. Phys. B **244**, 322 (1984).

[18] A. Donnachie and P. V. Landshoff, Phys. Lett. B **191**, 309 (1987).

[19] G. Ingelman and P. Schlein, Phys. Lett. B **152**, 256 (1985).

[20] N. N. Nikolaev and B. G. Zakharov, Phys. Lett. B **260**, 414 (1991).

[21] H. Abramowicz *et al.*, in *Proceedings of the 1993 SLAC Summer Institute on Particle Physics,* 539 (1994).

[22] N. Nikolaev *et al.*, Z. Phys. C **53**, 331 (1992).

[23] E. Gotsman *et al.*, hep-ph/9606280.

[24] E. Levin *et al.*, Phys. Rev. D **50**, 4306 (1994).

[25] M. Genovese *et al.*, Sov. Phys. JEPT **81**, 625 (1995).

[26] M. Genovese *et al.*, Phys. Lett. B **380**, 213 (1996).

[27] J. Bjorken, in *AIP Conference Proceedings No. 6*, Particles and Fields Subseries N0. 2, edited by M. Bander, G. Shaw, and D. Wong (AIP, New York, 1972);
J. D. Bjorken and J. Kogut, Phys. Rev. D 8, 1341 (1973);
J. D. Bjorken, preprint SLAC-PUB-7096 (1996), hep-ph/9601363.

[28] W. Buchmuller *et al.*, Phys. Lett. B **355**, 573 (1995).

[29] R. Feynman, *Photon-Hadron Interactions* (Addison-Wesley, 1989).

[30] M. G. Ryskin, Z. Phys. C **57**, 89 (1993).

[31] S.J. Brodsky *et al.*, Phys. Rev. D **50**, 3134 (1994).

[32] J. Nemchik *et al.*, Phys. Lett. B **341**, 228 (1994).

[33] A. D. Martin *et al.*, hep-ph/9609448.

[34] ZEUS Collaboration, M. Derrick *et al.*, Phys. Lett. B **356**, 601 (1995).

[35] H1 Collaboration, F. Abe *et al.*, Nucl. Phys. B **463**, 3 (1996).

[36] ZEUS Collaboration, M. Derrick *et al.*, DESY 96-183, accepted by Z. Phys.–MS 418.

[37] ZEUS Collaboration, M. Derrick *et al.*, Z. Phys. C **69**, 39 (1995).

[38] H1 Collaboration, F. Abe *et al.*, Nucl. Phys. B **468**, 3 (1996).

[39] ZEUS Collaboration, M. Derrick *et al.*, Phys. Lett. B **377**, 259 (1996).

[40] ZEUS Collaboration, M. Derrick *et al.*,Phys. Lett. B **380**, 220 (1996).

[41] H1 Collaboration, F. Abe *et al.*, Phys. Lett. B **338**, 507 (1994).

[42] ZEUS Collaboration, M. Derrick *et al.*, Phys. Lett. B **350**, 120 (1995).

[43] H1 Collaboration, F. Abe *et al.*, Nucl. Phys. B **472**, 3 (1996).

[44] ZEUS Collaboration, M. Derrick *et al.*, ICHEP 1996, pa 02-051.

[45] ZEUS Collaboration, M. Derrick *et al.*, ICHEP 1996, pa 02-053.

[46] ZEUS Collaboration, M. Derrick *et al.*, ICHEP 1996, pa 02-028.

[47] H1 Collaboration, F. Abe *et al.*, ICHEP 1996, pa 02-064.

[48] H1 Collaboration, F. Abe *et al.*, ICHEP 1996, pa 02-085.

[49] ZEUS Collaboration, M. Derrick *et al.*, ICHEP 1996, pa 02-049.

[50] H1 Collaboration, F. Abe *et al.*, ICHEP 1996, pa 02-086.

[51] H1 Collaboration, F. Abe *et al.*, ICHEP 1996, pa 01-088.

[52] CDF Collaboration, F. Abe *et al.*, Phys. Rev. D **50**, 855 (1994), 855 (1995).

[53] A. Schiz *et al.*, Phys. Rev. D **24** (1981) 26.

[54] A. Staiano, "Silicon detectors for the leading proton spectrometer of ZEUS," in *Proceedings of the Third International Workshop on Vertex Detectors*, IUHEE-95-1;
K. O'Shaughnessy *et al.*, Nucl. Instrum. Methods A **342**, 260-263 (1994).

[55] L. Frankfurt *et al.*, Phys. Rev. D **54**, 3194 (1996).

[56] N. N. Nikolaev *et al.*, Phys. Lett. B **366**, 337 (1996).

[57] H. Abramowicz *et al.*, in *Proceedings of "Future Physics at HERA"* (Hamburg, 1996).

[58] ZEUS Collaboration, M. Derrick *et al.*, Phys. Lett. B **315**, 481 (1993).

[59] ZEUS Collaboration, M. Derrick *et al.*, Z. Phys. C **70**, 391 (1996).

[60] K. Goulianos, Phys. Rep. **101**, 169 (1983).

[61] H1 Collaboration, F. Abe *et al.*, ICHEP 1996, pa 02-067.

[62] ZEUS Collaboration, M. Derrick *et al.*, ICHEP 1996, pa 02-048.

[63] ZEUS Collaboration, M. Derrick *et al.*, Z. Phys. C **67**, 227 (1995).

[64] H1 Collaboration, F. Abe *et al.*, ICHEP 1996, pa 02-061.

[65] ZEUS Collaboration, M. Derrick *et al.*, ICHEP 1996, pa02-026.

[66] A. H. Mueller, Phys. Rev. D **2**, 2963 (1970); *ibid.* D **4**, 150 (1971).

[67] R. D. Field and G. Fox, Nucl. Phys. B **80**, 367 (1974).

[68] H1 Collaboration, F. Abe *et al.*, Phys. Lett. B **348**, 681 (1995).

[69] ZEUS Collaboration, M. Derrick *et al.*, Z. Phys. C **68**, 569 (1995).

[70] P. V. Landshoff, talk given at the International Workshop on Deep Inelastic Scattering and Related Phenomena (DIS 96), Rome, Italy, 15-19 Apr. 1996, hep-ph/9605331.

[71] J. Bartels *et al.*, Phys. Lett. B **379**, 239 (1996), ERRATUM-*ibid.* B **382**, 449 (1996).

[72] Y. L. Dokshitzer, JETP **46**, 641 (1977).
V. N. Gribov and L. N. Lipatov, Sov. J. Nucl Phys. **15**, 78 (1972).
G. Altarelli and G. Parisi, Nucl. Phys. B **126**, 298 (1977).

[73] ZEUS Collaboration, M. Derrick *et al.*, Phys. Lett. B **356**, 129 (1995).

[74] ZEUS Collaboration, M. Derrick *et al.*, ICHEP 1996, pa 02-039.

[75] H1 Collaboration, F. Abe *et al.*, ICHEP 1996, pa 02-068.

[76] P. Bruni and G. Ingelman, DESY 93-187.

[77] PYTHIA 5.6: H.-U. Bengtsson and T. Sjöstrand, Comp. Phys. Comm. **46**, 43 (1987).

[78] Y. Dokshitzer, V. Khoze, and S. Troyan, in *Proceedings of the 6th International Conference on Physics in Collisions*, Chicago, Illinois, edited by M. Derrick (World Scientific, Singapore, 1987), p. 417.

[79] DØ Collaboration, S. Abachi *et al.*, Phys. Rev. Lett. **72**, 2332 (1994);
DØ Collaboration, S. Abachi *et al.*, FERMILAB-PUB-95-302-E (1995).

[80] CDF Collaboration, F. Abe *et al.*, Phys. Rev. Lett. **74**, 855 (1995).

[81] V. Del Duca and W.-K. Tang, Phys. Lett. B **312**, 225 (1993).

[82] ZEUS Collaboration, M. Derrick *et al.*, Phys. Lett. B **369**, 55 (1996).

PRECISION STRUCTURE FUNCTION MEASUREMENTS FROM CCFR/NUTEV

Janet Conrad
Columbia University
New York, NY 10027

ABSTRACT

New results from the CCFR Collaboration on the structure functions F_2 and xF_3 are presented. Neutrino scattering structure function measurements offer a unique tool to probe the strong interactions. The parity-violating structure function $xF_3(x, Q^2)$ can only be measured in deep inelastic neutrino scattering. Precise measurements of the structure function $F_2(x, Q^2)$ can also be obtained. The predicted Q^2 evolution of these structure functions can be used to test perturbative Quantum Chromodynamics as well as to measure the strong coupling constant, α_s, and the valence, sea, and gluon parton distributions.

© 1996 by Janet Conrad.

1 Introduction

My talk at the 1996 SLAC Summer Institute reviewed many recent QCD results from the Fermilab deep inelastic scattering muon experiment, E665, and neutrino experiment, CCFR. From E665, the analyses included a measurement of the structure function F_2 at very low x (Ref. 1), the ratio F_2^n/F_2^p (Ref. 2), and a measurement of $xG(x,Q^2)$ from hadronic energy flow.[3] The new results of CCFR included presentation of neutrino differential cross sections,[4] a measurement of the structure function $R(x,Q^2)$ (Ref. 4) and a reanalysis of the data to obtain the structure functions $xF_3(x,Q^2)$ and $F_2(x,Q^2)$. Of these many topics, the reanalysis of $xF_3(x,Q^2)$ and $F_2(x,Q^2)$ from CCFR is the most recent result. As such, it is the one analysis that has not yet been described in detail in conference proceedings or papers. Therefore, this paper will concentrate on this new CCFR result. More information on this analysis can be found in the thesis of William Seligman, Columbia University.[5] A publication will be submitted to PRL by the CCFR Collaboration in the near future.

2 Deep Inelastic Neutrino Scattering

The precision measurements of nucleon structure, as probed by neutrino scattering, are interesting as universal, fundamental measurements, as tests of QCD, and as constraints on the parton distributions of the nucleon. Deep inelastic neutrino scattering experiments provide an opportunity to test QCD evolution and extract the QCD parameter Λ, which sets the scale of the strong interaction. In the kinematic regions where the structure of the nucleon can be interpreted in terms of quarks, neutrino scattering has a high sensitivity to many individual parton distributions. Probing the nucleon with neutrinos is complementary to charged-lepton scattering experiments. Comparisons between neutrino and charged-lepton deep inelastic experiments test the universality of the structure functions and parton distributions. Global analyses which include all of the neutrino data provide the best parameterizations of the individual parton distributions.

Because the topic of this summer school was QCD studies, familiarity with the ideas of QCD is assumed. This section provides a very brief introduction to deep inelastic neutrino scattering.

2.1 Kinematics of Deep Inelastic Scattering (DIS)

The tree-level diagram for charged current neutrino-nucleon scattering is shown in Fig. 1. A neutrino (antineutrino) with incoming four-momentum, k_1, scatters from a quark or antiquark in the nucleon via exchange of a W^+ (W^-) boson, with four-momentum q. In the lab, the variables which can be measured in this interaction are the momentum and angle of the outgoing muon, E_μ and θ_μ, and the energy of the outgoing hadrons E_{had}. These can be used to reconstruct the energy of the incoming neutrino, $E_\nu = E_\mu + E_{had}$. In terms of these variables, the four-vectors shown in Fig. 1 are:

$$\begin{aligned} k_1 &= (E_\nu, 0, 0, E_\nu) \\ k_2 &= (E_\mu, p_\mu \sin\theta_\mu \cos\phi_\mu, p_\mu \sin\theta_\mu \sin\phi_\mu, p_\mu \cos\theta_\mu) \\ p &= (M, 0, 0, 0) \\ q &= k_1 - k_2. \end{aligned}$$

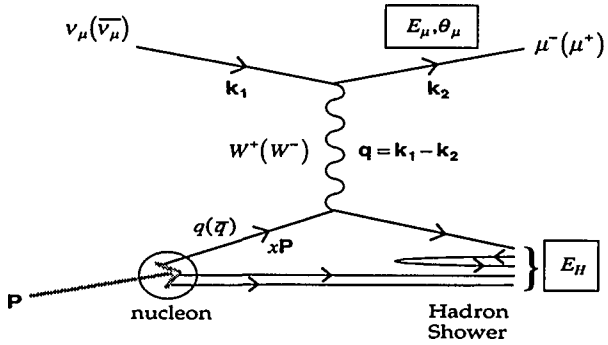


Figure 1: The first-order Feynman diagram for deep inelastic neutrino scattering.

Useful invariant quantities which describe the interaction are:

Energy transfer: $\nu = (p \cdot q)/M$

Fractional Energy Transfer: $y = M\nu/p \cdot k_1$

Negative Squared Four-Momentum: $Q^2 = -q^2$

The Bjorken Scaling Variable: $x = Q^2/(2p \cdot q)$.

In the lab frame, these reduce to:

$$\nu = (E_\nu - E_\mu) = E_{had} - M \quad (1)$$
$$y = \nu/E_\nu \quad (2)$$
$$Q^2 = m_\mu^2 + 2E_\nu(E_\mu - p_\mu \cos\theta_\mu) \quad (3)$$
$$x = Q^2/(2M\nu). \quad (4)$$

For a given beam energy, E_ν, the accessible kinematic region is, in principle, bounded by:

$$0 \leq \nu \leq E_\nu$$
$$0 \leq y \leq 1$$
$$0 \leq Q^2 \leq 2ME_\nu$$
$$0 \leq x \leq 1.$$

In practice, experimental cuts to isolate regions of high acceptance and small corrections may reduce the available range. The accessible kinematic range can be described in the plane of any two of the above variables. The wide band beam of CCFR extended up to 600 GeV and the resulting kinematic range in the x and Q^2 plane is shown in Fig. 2 in comparison to other deep inelastic scattering experiments.

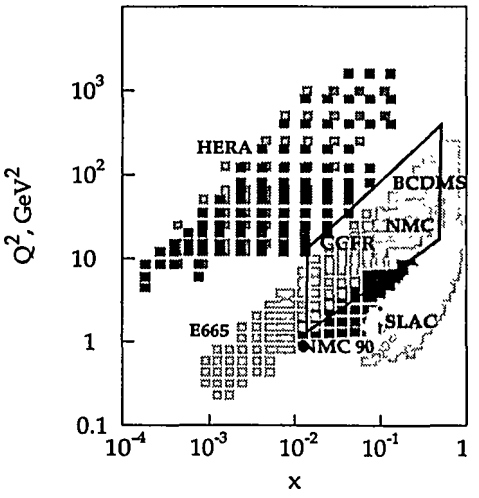


Figure 2: The kinematic region accessible to the CCFR experiment (solid outline) and other deep inelastic scattering experiments.

2.2 The Neutrino-Nucleon Cross Section and the Structure Functions

The general form for the differential cross section depends upon three structure functions, F_2, R, and xF_3:

$$\frac{d^2\sigma^{\nu(\overline{\nu})}}{dxdy} = \frac{G_F^2 M E_\nu}{\pi(1+Q^2/M_W^2)^2}\left[F_2^{\nu(\overline{\nu})}\left(\frac{y^2+(2Mxy/Q)^2}{2+2R^{\nu(\overline{\nu})}}+1-y-\frac{Mxy}{2E_\nu}\right)\right.$$
$$\left.\pm xF_3^{\nu(\overline{\nu})} y\left(1-\frac{y}{2}\right)\right]. \quad (5)$$

The structure functions depend upon the kinematic variables x and Q^2. The functions F_2 and R are also measured in deep inelastic charged lepton scattering. R can be interpreted as the ratio of the longitudinal to transverse virtual boson absorption cross section. The function xF_3 appears only in the cross section for the weak interaction. It is derived from the parity violating term in the product of the leptonic and hadronic tensor.

In the parton model, the neutrino structure functions can be written as functions of the sums and differences of the quark probability distributions. The probability of scattering from a parton with a given fractional momentum x is represented by the quark probability distribution. The structure functions depend on the quark distributions weighted by the fractional momentum and by the squared charge of the quarks, which is unity in the weak interaction. The quark probabilities are related to xF_3 by:

$$xF_3 = x(\sum_i q_i(x) - \overline{q}_i(x)) = x(u_v + d_v), \quad (6)$$

where u_v and d_v are the valence quark distributions. The structure function F_2 is given by:

$$F_2 = x(\sum_i q_i(x) + \overline{q}_i(x)). \quad (7)$$

Within QCD, low transverse momentum quark-gluon interactions may occur at the time of the scatter. Thus, partons with higher fractional momentum may contribute to interactions at any lower x through radiation or gluon splitting. The probability that the interaction resolves such a splitting depends on Q^2. This splitting modifies the structure functions, leading to a Q^2 dependence known as scaling violations. The QCD Dokshitzer-Gribov-Lipatov-Altarelli-Parisi (DGLAP) equations[6] predict the Q^2 dependence of the structure functions and underlying parton distributions.

From the DGLAP equations, the change in the structure functions with Q^2 as a function of x depends on α_s. At next-to-leading order, α_S is given by:

$$\alpha_S(Q^2) = \frac{4\pi}{\beta_0 \ln(Q^2/\Lambda^2)} \left[1 - \frac{\beta_1}{\beta_0} \frac{\ln[\ln(Q^2/\Lambda^2)]}{\ln(Q^2/\Lambda^2)}\right], \tag{8}$$

where $\beta_0 = 11 - 2n_f/3$ and $\beta_1 = 102 - 38n_f/3$, and n_f is the number of quark flavors participating in the interaction at this Q^2. The QCD coupling constant, Λ, must be introduced when the renormalization technique is applied to remove the divergences within QCD. In this analysis, the modified minimal subtraction scheme ($\overline{MS}$) scheme is used.

2.3 Nonperturbative QCD and Nuclear Effects

Nonperturbative QCD processes which might affect the CCFR structure function measurements are collectively termed higher twist effects. These effects occur at low Q^2 where the impulse approximation of scattering from massless noninteracting quarks is no longer valid. Examples include the target mass effects, diquark scattering, and other multiparton effects. The functional form for target mass effects has been determined.[7] The remaining higher twist effects cannot be calculated a priori, but must be measured. A measurement of the contribution of the higher twist terms in charged lepton scattering was made by comparing the SLAC and BCDMS F_2 data to the QCD expectation.[8] Deviations were attributed entirely to higher twist effects and were fit to the form: $F_2^{\text{Measured}}/F_2^{\text{Predicted}} = (1 + C_i/Q^2)$. Separate constants, C_i, were calculated for each x bin. For the CCFR analysis presented below, it was assumed that the measured corrections are applicable to both F_2 and xF_3 in neutrino scattering.

The results presented here are structure functions for neutrino nucleon scattering on iron. The data were corrected to an isoscalar target, but not for nuclear effects. High x bins are expected to be affected by Fermi smearing, and therefore are not included in the fits used to extract the parton distributions and α_s.

2.4 Measurement of the Strange Sea

The flavor-changing quality of the weak interaction allows for the opportunity to directly tag scattering from specific quark flavors. In particular, charged current scattering from strange quarks has the distinct experimental signature of producing two muons of opposite sign, one from the scattered lepton and the other from the semileptonic decay of the produced charm. The strange sea is described by the functions:

$$xs(x) = A_s(1-x)^\alpha [x(\overline{u}(x) + \overline{d}(x))]/2 \tag{9}$$

$$\kappa = \left(\int_0^1 dx[x(s(x) + \overline{s}(x))]\right) / \left(\int_0^1 dx[x(\overline{u}(x) + \overline{d}(x))]\right) \tag{10}$$

$$A_s = \kappa \int_0^1 dx \frac{x\overline{q}(x,Q^2)}{2 + A_s(1-x)^\alpha} / \int_0^1 dx \frac{(1-x)^\alpha x\overline{q}(x,Q^2)}{2 + A_s(1-x)^\alpha}; \tag{11}$$

thus, α represents the relative shape and κ gives the overall normalization relative to the nonstrange sea. The equation for A_s, which relates κ and α, must be solved numerically.

The best measurement to date has come from the dimuon studies of the CCFR Collaboration, where the next-to-leading-order analysis has yielded $\alpha = -0.05 \pm 0.56 \pm 0.10$ and $\kappa = 0.468^{+0.064-0.017}_{-0.051+0.036}$ (Ref. 9). The results of the CCFR measurements at leading and next-to-leading order are used in the analysis described below.

3 The CCFR and NuTeV Experiments

The data presented in this paper were taken by the CCFR Collaboration during the 1985 and 1987 fixed-target runs at Fermilab. The CCFR neutrino beam resulted from decays of pions and kaons produced in interactions of the 800 GeV FNAL proton beam with a beryllium target. This wide-band beam ranged in energy up to 600 GeV and resulted in events of which 86.4% were due to ν_μ's, 11.3% $\overline{\nu}_\mu$'s, and 2.3% ν_e's and $\overline{\nu}_e$'s. Neutrino events were observed in the Lab E neutrino detector,[10] shown in Fig. 3, which consists of a target calorimeter followed by a toroid muon spectrometer. The calorimeter consists of 84 3 m × 3 m × 10 cm

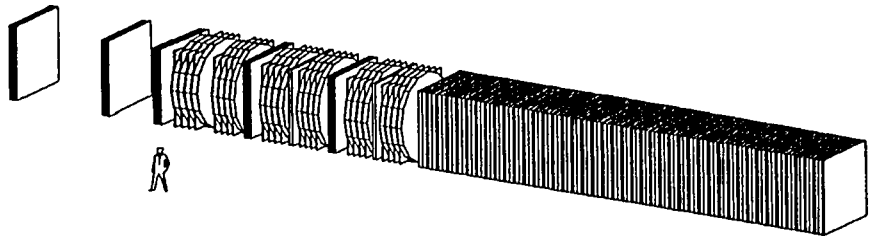


Figure 3: The Lab E neutrino detector.

iron plates, interspersed with scintillators for energy measurement and drift chambers for muon tracking. The toroid spectrometer has five sets of drift chambers for muon tracking as well as hodoscopes for triggering. For the CCFR experiment, the detector was calibrated during special runs using a test beam of pions, electrons, and muons. Details of the CCFR beam and detector can be found in Ref. 10.

NuTeV, the next generation of deep inelastic neutrino scattering experiments at Fermilab, began taking data in May 1996. NuTeV has modified the beamline to select the sign of the charged pions and kaons.[11] The resulting beam is almost purely ν_μ or $\overline{\nu}_\mu$, depending on the sign selection. An increase in the antineutrino-to-neutrino ratio over CCFR will improve several of the QCD measurements. The sign selection also will allow new QCD studies. Separate running will also permit the first high-statistics simultaneous measurements of the electroweak mixing parameter, $\sin^2\theta_W$, and neutral to charged current coupling strength ratio, ρ. The Lab E neutrino detector is being used, after substantial upgrades. To improve sensitivity to a single minimum ionizing particle, we have replaced the scintillator oil and phototubes of the scintillation counters. The drift chambers have been fully refurbished and the TDC/DAQ system has been upgraded. At NuTeV, the detector is calibrated with a test beam of pions, electrons, or muons continuously throughout the running. The new test beam also provides a broader range of hadron and muon energies than the CCFR test beam.

4 The Measurement of the Neutrino Flux

In the analysis described below, the low ν (*i.e.*, low E_{had}) data are used to determine the flux of the incoming neutrinos and antineutrinos. The kinematic cuts on the data used to determine the flux are

$$\begin{aligned} \theta_\mu &< 150\ mr \\ E_\mu &> 15\ GeV \\ 30 < E_\nu &< 360\ GeV \\ E_{had} &< 20\ GeV. \end{aligned}$$

These cuts, in combination with fiducial volume cuts, assured good acceptance for the flux extraction events, while having little overlap with the events used to determine the structure functions.

The CCFR flux is obtained from the y dependence of the data. The relationship between the number of observed events, the flux, and the cross section is:

$$\frac{dN_{\nu,\overline{\nu}}}{dy} = \Phi_{\nu,\overline{\nu}}(E)\frac{d\sigma_{\nu,\overline{\nu}}}{dy}. \tag{12}$$

This can be parametrized as a polynomial in terms of $y = \nu/E_\nu$

$$\frac{dN_{\nu,\overline{\nu}}}{d\nu} = A_{\nu,\overline{\nu}} + B_{\nu,\overline{\nu}}(\nu/E_\nu) + (C_{\nu,\overline{\nu}}/2)(\nu/E_\nu)^2. \tag{13}$$

In this case, A, B, and C are:

$$A = \frac{G^2M}{\pi}\int_0^1 F_2(x,Q^2)\Phi(E_\nu)dx \tag{14}$$

$$B = -\frac{G^2M}{\pi}\int_0^1 (F_2(x,Q^2) \mp xF_3(x,Q^2))\Phi(E_\nu)dx \tag{15}$$

$$C = B - \frac{G^2M}{\pi}\int_0^1 F_2(x,Q^2)\tilde{R}(x,Q^2)dx \tag{16}$$

with

$$\tilde{R}(x,Q^2) \equiv \frac{1+2Mx/\nu}{1+R(x,Q^2)} - \frac{Mx}{\nu} - 1. \tag{17}$$

A, B, and C are assumed to be only dependent upon E_ν. Integrating Eq. (12), the number of events for $\nu < \nu_0$ is:

$$N = \Phi(E) \int_0^{\nu_0} d\nu A \left[1 + \frac{\nu}{E_\nu} \frac{B}{A} - \frac{\nu^2}{2E_\nu^2} \left(\frac{B}{A} - \frac{\int F_2 \tilde{R}}{\int F_2} \right) \right]. \quad (18)$$

Thus, the flux is obtained by binning events in E_ν and $E_{had} < \nu_0$.

CCFR uses an iterative method to determine the flux. Initially, a parton distribution is input to the Monte Carlo to determine A, B, and C. Then the data in the range $\nu < 20$ GeV are used to determine the flux as a function of energy for neutrinos and antineutrinos separately, up to an overall normalization constant. This flux is then used to extract cross sections using $\nu > 10$ GeV data. Thus, the region of overlap between the data used to determine the flux and that used to determine the cross section is small. The data is normalized to the world-average cross section for νFe, as discussed below. Structure functions are then extracted following the prescription described in the following section. Parameterizations of the structure functions are used as input to Monte Carlo for the next iteration. This algorithm usually converges after the second iteration.

The assumption that the integrals over the structure functions are independent of ν, and thus depend only on E_ν, is only approximately true. Recall that $Q^2 = 2M\nu x$; therefore for fixed ν, using F_2 as an example:

$$\int_0^1 F_2(x, Q^2) = \int_0^1 F_2(x, 2M\nu x) \equiv F_2^{int}(\nu). \quad (19)$$

The systematic error introduced by this residual ν dependence was studied by varying the ν range from which the flux was extracted. The systematic error from assuming no ν dependence was found to be less than 0.5%.

Because this algorithm determines the relative shape of the flux distribution with energy, but not the overall normalization, the cross section for νFe scattering is an input to the analysis. The world-average neutrino cross section for iron is $\sigma^\nu/E = (0.677 \pm 0.014) \times 10^{-38}\ cm^2/GeV$ (Ref. 5). While the absolute flux of neutrinos and antineutrinos is not fixed by the CCFR method, the relative neutrino and antineutrino flux in each energy bin is determined. The preliminary ratio of the total cross sections, $\sigma^{\bar{\nu}}/\sigma^\nu$ from the flux extraction method, was found to be 0.509 ± 0.010. The world average including this experiment, which is used to obtain the final relative normalization, is 0.500 ± 0.007. The errors in the averages are included in the systematic error for the determination of the differential cross section and the structure functions.

Figure 4 shows the CCFR flux of neutrinos and antineutrinos.

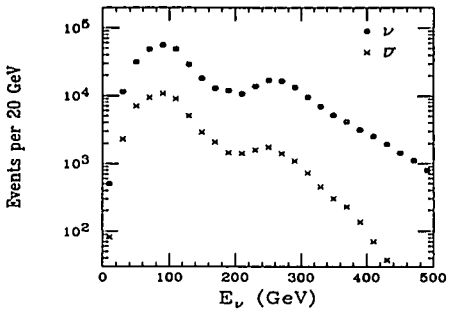


Figure 4: The CCFR neutrino and antineutrino fluxes.

5 The Measurement of F_2 and xF_3

The structure functions F_2 and xF_3 are extracted from the differential cross section given the flux determined by the method described above. The following kinematic cuts were made on the data:

$$\begin{aligned} 30 &< E_\nu < 360\ GeV \\ \theta_\mu &< 150\ mr \\ E_\mu &> 15\ GeV \\ Q^2 &> 1\ GeV^2 \\ E_{had} &> 10\ GeV, \end{aligned}$$

plus fiducial volume cuts, to assure good acceptance. All dimuon events were cut from the sample for two reasons. First, when one muon fails to traverse the toroid, the event could have improperly reconstructed kinematics. Second, at high y, even if both muons traverse the toroid, the algorithm to identify the scattered muon, as versus the charm-decay muon, was not perfectly efficient. The data were corrected for this cut based on the CCFR dimuon measurements discussed above. The data were acceptance corrected. Radiative corrections based on the

calculation by Bardin,[12] which includes muon and quark radiation and the box diagram, were applied. Corrections to an isoscalar target and to remove the charm mass and the propagator effects are included to make the comparison to other experiments straightforward. The number of events in each x and Q^2 bin is related to the differential cross section by:

$$N = \rho L N_A \int_{x-bin} \int_{Q^2-bin} \left[\int_{all\ energies} \frac{d^2\sigma}{dx dQ^2} \Phi(E) dE \right], \tag{20}$$

where ρ is the target density, L is the target length, and N_A is Avogadro's number. The structure functions are extracted from these differential cross sections. For this analysis, R was assumed to be given by the parameterization "R_{Whitlow}."[13]

Many sources of systematic error were considered in this analysis. The hadron energy and muon energy are determined by the test beam data and each is estimated to be known to 1%. The statistical error in the flux extraction was typically also on the order of 1%. There is an error of 2.1% associated with the normalization of the cross section to the world's data. Model-dependent systematic errors included a 15% error on the R_{Whitlow} parameterization, an 18% error on the leading-order charm mass, 26% error on the leading-order strange sea shape, 1.7% on the strange sea normalization, and 7% on the charm branching ratio. Of these sources of systematic error, the calibration errors most strongly affect the QCD analysis.

The data presented here represent a reanalysis of the CCFR data, which differs from the previous analysis[14] in the following ways:

- The hadronic energy and muon calibrations are extracted directly from the test beam data. The previous analysis used a technique of adjusting the measured calibration which was later shown to have large associated systematic uncertainties.
- The muon energy loss in the calorimeter is more accurately modeled in the Monte Carlo simulation of the detector.
- The previously presented data included radiative corrections only for radiation from the muon. The radiative corrections applied to the data presented here also include the contributions from the box diagram.[12]
- The parameterization R_{Whitlow}, which is the most inclusive fit to date, is not identical to R_{SLAC}, which was the best parameterization available for the previous analysis.

Detailed information on each of the improvements can be found in Ref. 5.

Figures 5 and 6 show the preliminary CCFR measurements of F_2 and xF_3 as a function of Q^2 in various bins of x. Only statistical errors are shown. The solid and dashed lines on the plot indicate the QCD fits which are discussed in the following section.

When the final results are obtained, the information will be available in tabular form by contacting SELIGMAN@NEVIS1.COLUMBIA.EDU.

6 QCD Studies and Comparison to Other Experiments

In this section, the preliminary CCFR results are compared to results from other experiments. First, F_2 is compared to that determined by charged lepton deep inelastic scattering. Second, the QCD fits to the CCFR structure functions are described and the extracted value of α_s is compared to the measurements of other experiments. Finally, the gluon distribution from the CCFR global fit is compared to previous results.

6.1 F_2 from Neutrino and Charged Lepton Scattering

The parity-conserving structure function F_2 is measured by both charged and neutral lepton scattering experiments. The definition of F_2 at lowest order is given by:

$$\sum_i e_i^2 q_i(x) + e_i^2 \overline{q}_i(x), \tag{21}$$

where e_i represents the charge associated with the coupling to each quark type i. In neutrino scattering, the "weak charge" is unity. In the case of muon scattering, the coupling is electromagnetic; hence, the definition of F_2 includes the quark charges squared. As a result of the difference in coupling between the electromagnetic and weak interactions, a conversion must be applied in order to compare muon and neutrino experiments. To lowest order, the correction is:

$$F_2^{\mu} = \frac{5}{18} F_2^{\nu} \left[1 - \frac{3(s+\overline{s})}{5(q+\overline{q})} \right]. \tag{22}$$

The strange sea (s, $\overline{s}$) appears explicitly in this equation. This can be precisely measured by charged-current neutrino scattering from strange quarks producing

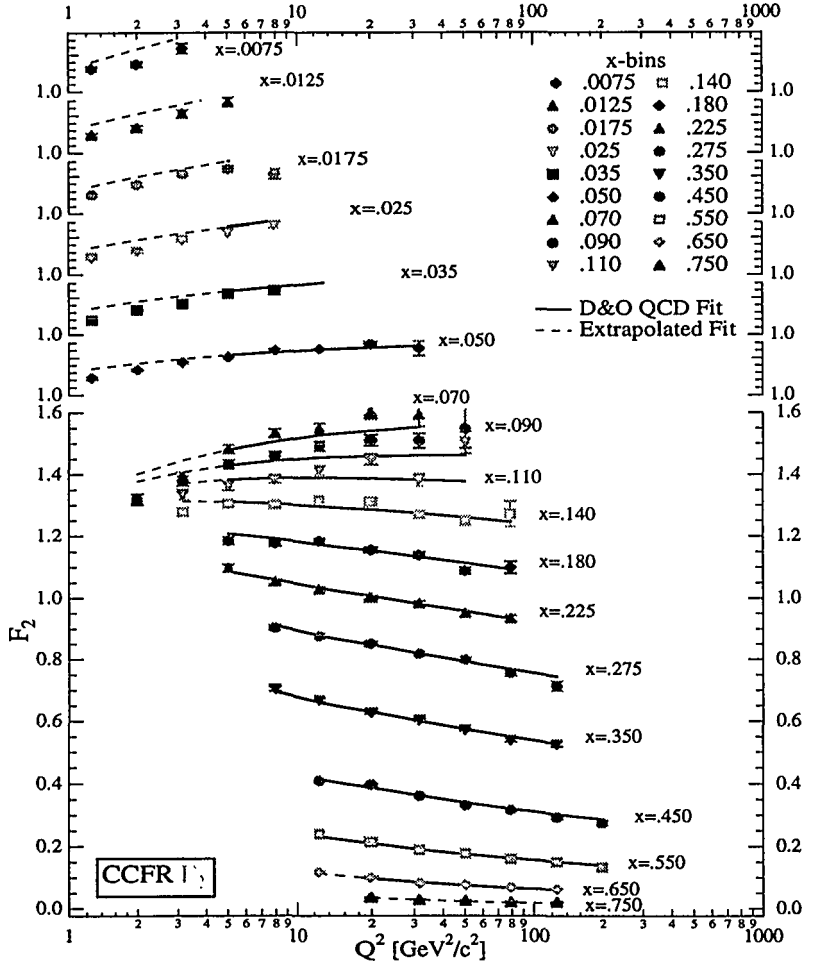


Figure 5: Preliminary CCFR F_2 measurement. Errors are statistical only. Lines indicate the QCD fit discussed in Sec. 6.

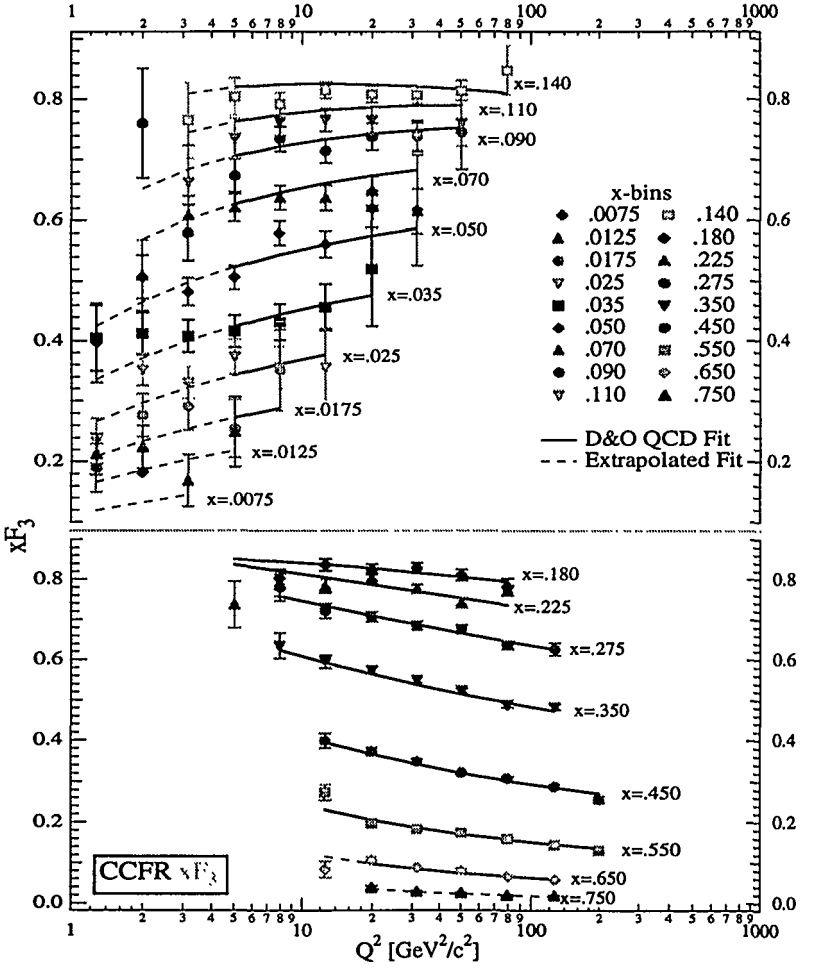


Figure 6: Preliminary CCFR xF_3 measurement. Errors are statistical only. Lines indicate the QCD fit discussed in Sec. 6.

opposite sign dimuons, as discussed in Sec. 2.4 above. The CCFR next-to-leading-order measurement of the strange sea is used to make the corrections in this discussion.[9]

Nuclear effects must also be considered when comparing muon and neutrino measurements of F_2. Neutrino scattering experiments typically use high-density nuclear targets because the neutrino cross section is very small. The CCFR results were obtained with an iron target (bound nucleons). The electromagnetic cross section is reasonably large, and so muon experiments typically use hydrogen and deuterium (free and loosely bound nucleons, respectively). The difference in F_2 between bound nucleons and free nucleons has been studied in charged lepton experiments. The corrections used below are from a fit to NMC, E665, and SLAC data.[15] The fit is compared to the charged lepton results in Fig. 7.

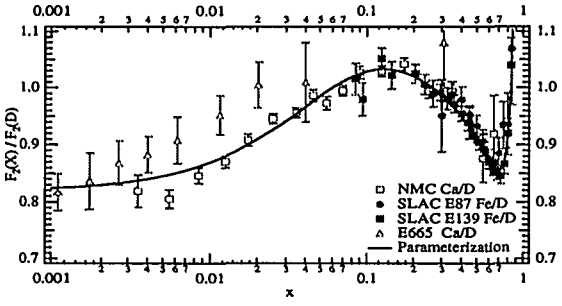


Figure 7: Fit to the NMC, E665, and SLAC nuclear data. The resulting fit is used to correct the charged lepton deuterium data for comparison with the CCFR result.

Figures 8 through 13 compare the preliminary F_2 measured by CCFR and discussed above to the measurements from NMC over a range of x regions.[16] The corrections for charge coupling and nuclear effects have been applied to the muon data. At low x, there appears to be a disagreement between the charged lepton scattering data and the neutrino data. The discrepancy decreases with increasing

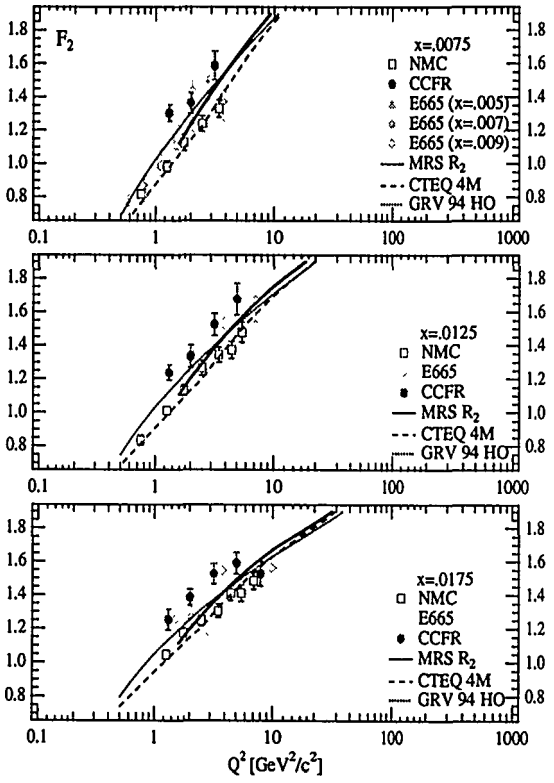


Figure 8: Comparison of the CCFR (ν) measurement of F_2 to the NMC and E665 (μ) results for $x = 0.0075, 0.0125$, and 0.0175. Corrections for definition of F_2 and for nuclear effects (see text) were applied to the NMC data to permit comparison.

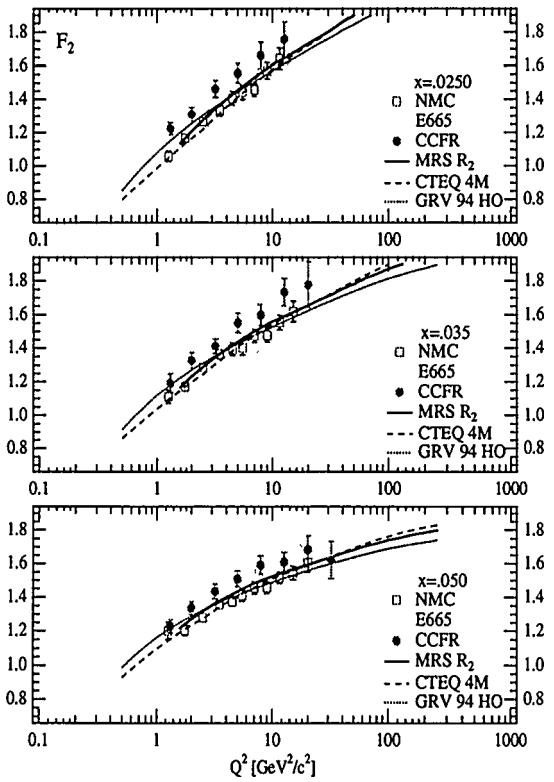


Figure 9: Comparison of the CCFR (ν) measurement of F_2 to the NMC and E665 (μ) results for $x = 0.0250, 0.035$, and 0.050. Corrections for definition of F_2 and for nuclear effects (see text) were applied to the NMC data to permit comparison.

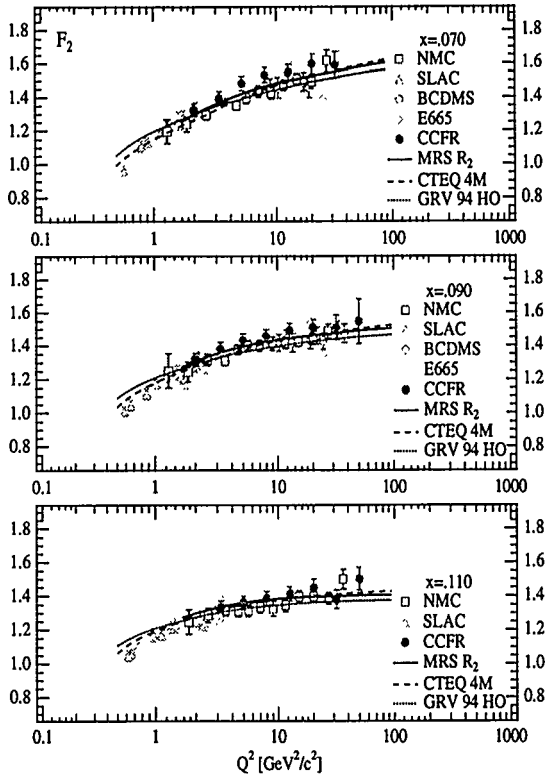


Figure 10: Comparison of the CCFR (ν) measurement of F_2 to the NMC and E665 (μ) results and SLAC (e) results for $x = 0.070, 0.090$, and 0.110. Corrections for definition of F_2 and for nuclear effects (see text) were applied to the NMC data to permit comparison.

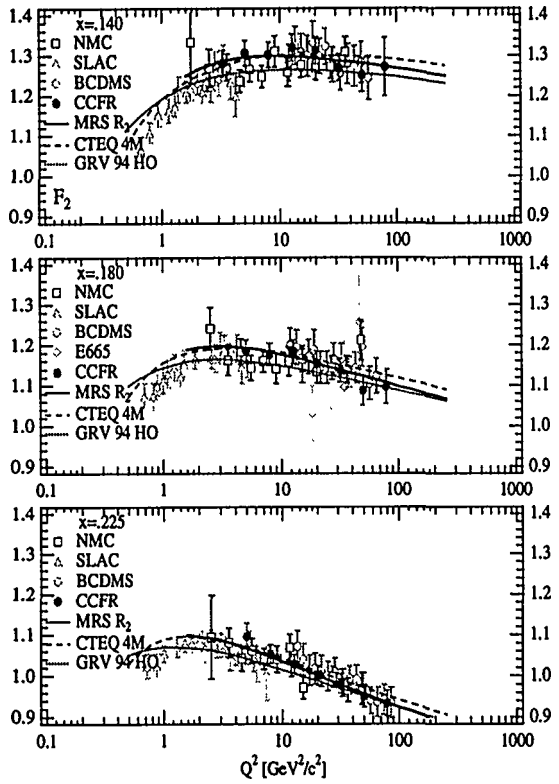


Figure 11: Comparison of the CCFR (ν) measurement of F_2 to the NMC and E665 (μ) results for $x = 0.140, 0.180$, and 0.225. Corrections for definition of F_2 and for nuclear effects (see text) were applied to the NMC data to permit comparison.

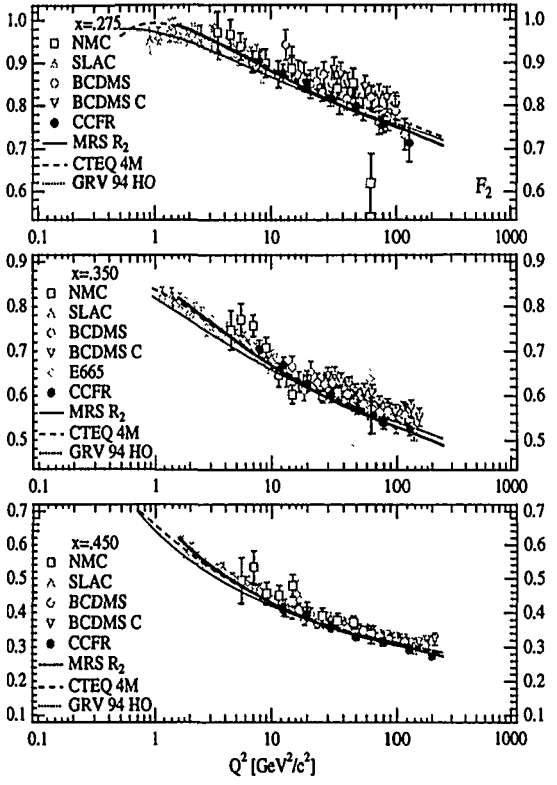


Figure 12: Comparison of the CCFR (ν) measurement of F_2 to the NMC and E665 (μ) results for $x = 0.275, 0.350$, and 0.450. Corrections for definition of F_2 and for nuclear effects (see text) were applied to the NMC data to permit comparison.

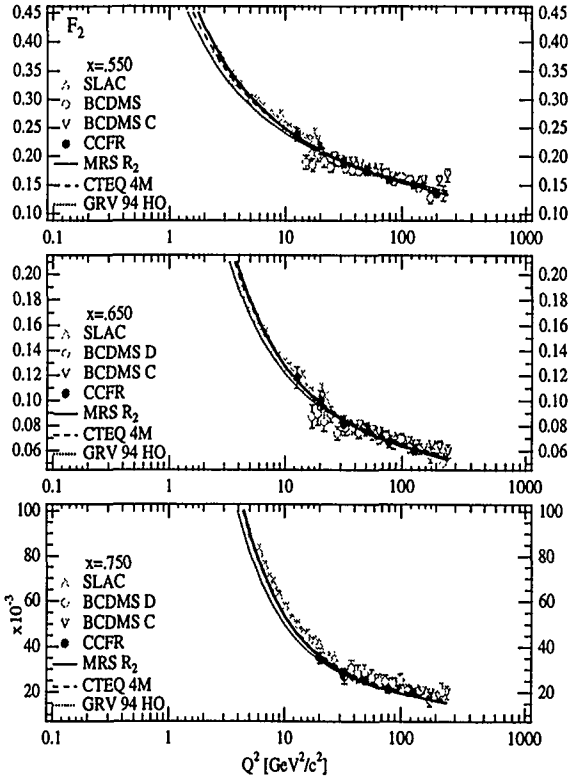


Figure 13: Comparison of the CCFR (ν) measurement of F_2 to the NMC and E665 (μ) results for $x = 0.550, 0.650$, and 0.750. Corrections for definition of F_2 and for nuclear effects (see text) were applied to the NMC data to permit comparison.

x until, in the region of $x \approx 0.070$, the data are in good agreement, which continues to the highest x bins.

The high-statistics data in the region of the discrepancy come from CCFR and NMC. It is possible that one or both experiments have underestimated their systematic errors in this region. The most important systematic error in the CCFR analysis is due to the calorimeter calibration. Extensive studies of the test beam data were undertaken in order to determine the muon and hadron energy calibration, and we believe the systematic error assigned to these are conservative.

Another cause for the disagreement may be the nuclear correction applied to the charged lepton deuterium data in order to allow comparison with the neutrino results. This correction assumes that effects in scattering from bound nucleon targets are the same for muons and neutrinos in the low x ("shadowing") region. However, if shadowing effects are caused by fluctuations of the intermediate virtual boson to mesons, then one might expect differences. The vector-meson-dominance model ascribes the cause of shadowing to fluctuations of the vector boson into mesons leading to strong interactions near the "surface" of the nucleon. In the case of muon scattering, the photon can fluctuate only into vector mesons, while for neutrinos, the W has an axial as well as a vector component. Very little data on shadowing in neutrino scattering has been obtained because of the low event rate for neutrinos in a deuterium target. The best measurements come from the BEBC Collaboration on neon versus deuterium, in which shadowing was found to be consistent with that observed in charged lepton scattering in the $x = 0.02$ and $Q^2 > 1.0\ GeV^2$ region.[17]

Although the NMC and E665 shadowing data which were fit to obtain the nuclear correction are in statistical agreement, there appears to be a systematic shift between the two data sets, as can be seen in Fig. 7. The fit is dominated by the NMC result, which has much smaller errors than the E665 data. However, if only the E665 data are used in a fit which is then applied to the charged lepton deuterium results, then the CCFR/NMC discrepancy is reduced by approximately a factor of two for $x < 0.03$.

Several publications have suggested that the discrepancy is due to an incorrect strange sea correction.[19,18,20] The required distributions to eliminate the discrepancy are inconsistent with, and approximately a factor of two larger at low x, than the CCFR measurement from the dimuon data, as calculated at next-to-leading order by the CTEQ Collaboration.[19] The CCFR measurement of the strange sea,

which is to next-to-leading order and includes corrections for the charm-mass threshold, would have to be incorrect by 5σ to account for the discrepancy. This is shown in Fig. 14, where the solid line is the CCFR measurement, the dotted lines indicate the 1σ systematic and statistical errors on the CCFR result, and the dashed line shows the magnitude of the strange sea required to explain the discrepancy in the F_2 measurements. In this study, the strange and antistrange sea distributions were assumed to be equal.

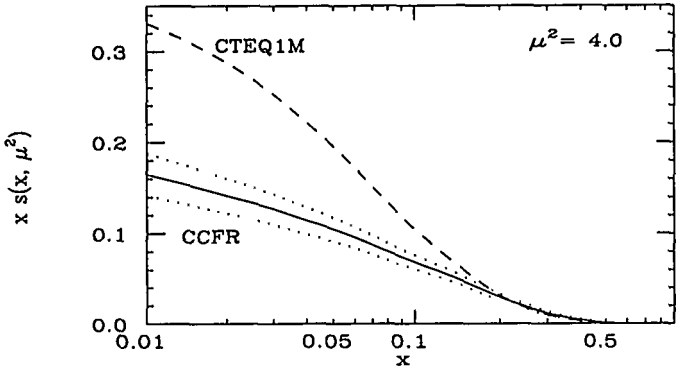


Figure 14: Solid—the strange sea as measured by the CCFR Collaboration from the dimuon data. The surrounding dots show the statistical and systematic errors combined. Dashed—the strange sea required to account for the neutrino-charged-lepton discrepancy, as determined by Ref. 19.

Brodsky and Ma have suggested that the strange and antistrange sea distributions may not be equal.[20] If the proton fluctuates into a virtual $K^+\Lambda$ pair, then the s quark becomes a valence quark of the Λ with a relatively harder momentum distribution than the $\bar{s}$ quark. CCFR has measured the strange and antistrange distributions separately using the dimuon data. The scattered muon was identified using a P_T and energy algorithm, as described in Ref. 9. The sign of the scattered and charm-decay muons identified whether the scatter was from s or $\bar{s}$. The data indicated that the distributions were consistent within the statistical and systematic errors. However, the power-law parameterization which was used for the fits is not the same as the distribution predicted by Brodsky and Ma's model. Therefore, the asymmetric intrinsic strange sea may be masked by the choice of functional form required by the fit. A reanalysis using the functional form of the model is underway.

In order to fully investigate the discrepancy in the F_2 measurements, more data in the low x region are required. The NuTeV experiment, described above, is expected to obtain approximately equal statistical errors on F_2 with substantially reduced systematics. Precise hadron energy calibration will be obtained with the new continuous test beam over a wider range of energies than those covered by CCFR. Also, NuTeV will provide a more accurate measurement of the strange and antistrange seas. This is because the sign selection of the beamline determines the sign of the scattered muon, allowing accurate identification even when only one of the two muons in a dimuon event reaches the toroid spectrometer. Thus, the statistical sample will be larger, and the systematics due to misidentification will be smaller.

6.2 Measurements of α_s and $\Lambda_{\overline{MS}}$

Perturbative QCD can predict the evolution of the structure functions from a starting set of x-dependent distributions,[6] as described in Sec. 2.2. In this analysis, the QCD parameter is determined to next-to-leading order (NLO) for four flavors in the $\overline{MS}$ renormalization scheme: $\Lambda^{NLO\ 4flv}_{\overline{MS}}$.

The QCD evolution of two data sets were examined. First, only the parity-violating structure function xF_3 was used. The advantage of this method is that the evolution of xF_3 is independent of the gluon distribution. Second, a combined xF_3 and F_2 fit to the data was done. This increases the statistical power of the fit, but introduces extra parameters to describe the gluon distribution.

The QCD fits require initial parameterizations of the parton distributions at some Q_0^2. The forms used in this analysis were:

$$xq_{NS}(x,Q_0^2) = A_{NS}x^{\eta_1}(1-x)^{\eta_2} \quad (23)$$

$$xq_S(x,Q_0^2) = xq_{NS}(x,Q_0^2) + A_S(1-x)^{\eta_S} \quad (24)$$

$$xG(x,Q_0^2) = A_G(1-x)^{\eta_G}, \quad (25)$$

where NS and S refer to nonsinglet and singlet, respectively. Because this is a next-to-leading-order analysis, the fermion conservation rule, $\int_0^1 q_{NS}dx = 3$, is modified by a term proportional to $(1-\alpha_s/\pi)$ at next-to-leading order.[21]

	$\Lambda_{\overline{MS}}^{\text{NLO } 4flv}$ from xF_3 only		$\Lambda_{\overline{MS}}^{\text{NLO } 4flv}$ from xF_3 and F_2	
Fit Type:	$\Lambda \pm$ stat $\pm$ sys	χ^2/DOF	$\Lambda \pm$ stat $\pm$ sys	χ^2/DOF
Basic	$336 \pm 41 \pm 84$	82/82	$346 \pm 21 \pm 54$	187/164
Global	$327 \pm 40 \pm 30$	75/82	$309 \pm 19 \pm 15$	167/164

Table 1: Preliminary values of $\Lambda_{\overline{MS}}^{\text{NLO } 4flv}$ determined from fits to the CCFR data.

Also, there is a possible nuclear dependence which could lead to a violation of the fermion conservation rule by approximately 1%. Therefore, for this analysis, the fermion conservation rule was not required. The momentum sum rule, $\int_0^1 (xq(x,Q_0^2) + xG(x,Q_0^2))dx = 1$, is not used to constrain A_G because the gluon distribution is unknown at low x. More complicated parameterizations of the parton distributions were found to have fit results consistent with the parameterizations above.[5] Parameterizations of target mass and higher twist effects, as described in Sec. 2.3 above, were included in the fitting procedure. The results of this fit were shown by the solid line on Figs. 5 and 6. The dashed lines on these figures represent an extrapolation of the parameterization from the global fit to lower Q^2 values.

The data were fit using MINUIT to minimize the χ^2 between the NLO QCD prediction and the data. Fits were for data with $Q^2 > 5$ GeV^2, $W^2 > 10$ GeV^2, and $x < 0.7$. Bins with statistical errors greater than 50% were eliminated. Positive and negative shifts of F_2 and xF_3 were made for each systematic error, and Λ was extracted. For this procedure, the χ^2 can be used to test the validity of QCD to describe the data. The theoretical prediction is based on the Duke and Owens NLO QCD Evolution Program.[22] The results of this fit are listed in Table 1, referred to as "basic." As expected, the fit which uses both the xF_3 and F_2 data have lower statistical and systematic errors because of the increased number of data points in the fit. The good χ^2/DOF indicates that the data are consistent with QCD.

An alternative fit procedure finds the best parameters to describe the data assuming that QCD is valid. For this analysis, a χ^2 fit to the theoretical prediction for the structure functions is compared to the data in each x and Q^2 bin. The prediction from the Duke and Owens program is compared to the data using a χ^2 that includes both statistical and systematic uncertainties with correlations. The systematic uncertainties are handled by introducing a parameter δ_k for each uncertainty k into the χ^2. Defining the structure function vector $\mathbf{F} = (F_2\ xF_3)$ and the structure function error matrix $\mathbf{V} = (\sigma_{ij})$, for $i,j = F_2, xF_3$, then the difference between the theoretical prediction and data and the χ^2 are:

$$\mathbf{F}^{diff} = \mathbf{F}^{data} - \mathbf{F}^{theory} + \textstyle\sum_k \delta_k(\mathbf{F}^k - \mathbf{F}^{data}) \quad (26)$$

$$\chi^2 = (\mathbf{F}^{diff})\mathbf{V}^{-1}(\mathbf{F}^{diff})^T + \textstyle\sum_k \delta_k^2. \quad (27)$$

The results of this fit are listed under "global" in Table 1. The global fit gives a more precise measure of Λ because of the constraint of QCD.

The value of Λ from the global fit using F_2 and xF_3 is equivalent to $\alpha_s(M_Z^2) = 0.117 \pm 0.002(exp) \pm 0.004(theory)$. The theoretical error is due to the renormalization and factorization scale uncertainties.[8] This result is higher than the previous measurement of CCFR: $\alpha_s(M_Z^2) = 0.111 \pm 0.005$. It is also higher than the muon deep inelastic scattering result: $\alpha_s(M_Z^2) = 0.113 \pm 0.005$ (Ref. 23). It is lower than the LEP measurement from event shapes of 0.122 ± 0.007 (Ref. 23). However, all of the above results are consistent within the errors. Figure 15 compares the preliminary CCFR result to results from other experiments.[23]

In the future, several improvements to the measurement of α_s are expected from CCFR/NuTeV. Using the method described above, the NuTeV experiment will make a more precise measurement of α_s by reducing the systematic errors associated with the measurement of the structure functions. A second method of measuring α_s, using the QCD corrections to the Gross-Llewellyn-Smith sum rule,[21] based on the new CCFR results, is also expected in the near future. This analysis extracts α_s at various Q^2 values in the low Q^2 region.[24]

6.3 Extraction of the Gluon Distribution

Fits to xF_3 and F_2, described above, allow one to extract the form of the gluon distribution. The global fit yields the preliminary distribution: $xG(x,Q_0^2 = 5GeV^2) = (2.34 \pm 0.36)(1-x)^{5.02 \pm 0.71}$.

Figure 16 shows this distribution as a function of x, evolved to $Q^2 = 32\ GeV^2$. The shaded region indicates the CCFR $\pm 1\sigma$ errors. For comparison, the crosses show the gluon distribution as measured from jet production at the H1 experiment.[25] The hatched region indicates the E665 gluon distribution measured from

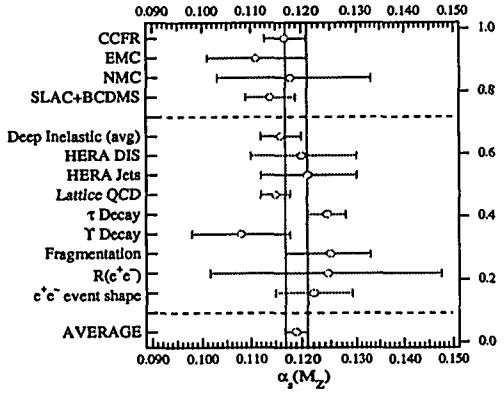


Figure 15: Measurement of α_s from various experiments. The CCFR result is preliminary. Results from other experiments are from Ref. 23.

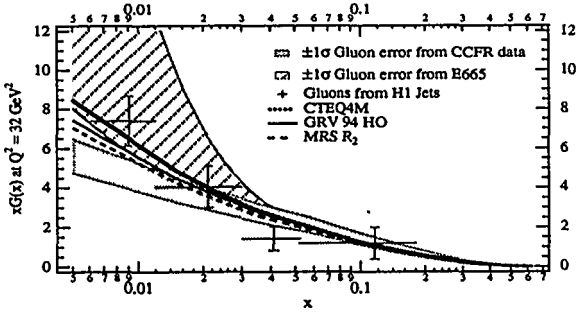


Figure 16: The CCFR gluon distribution evolved to $Q^2 = 32\ GeV^2$. Shaded region shows $\pm 1\sigma$ errors. Crosses show results from HERA jet measurements. Dotted line is CTEQ4M. Solid line is GRV94 HO. Dashed line is MRS R2. Hatched region is gluon distribution from E665 hadronic energy distributions.

the energy distribution of hadrons produced in deep inelastic muon scattering.[3] Also shown are the gluon distributions from fits to data from a wide range of high-energy experiments which are available as parton distribution functions: CTEQ4M (Ref. 26) (dotted), GRV 94 HO (Ref. 27) (solid), and MRS R2 (Ref. 28) (dashed). The gluon distributions from the various experiments agree for the region of $x > 0.01$, the region of the CCFR data.

7 Conclusion

This paper has summarized the re-analysis of the CCFR data, resulting in preliminary new measurements of F_2 and xF_3. Comparisons of F_2 to charged lepton experiments indicate that there may be a discrepancy at low x after quark charge and nuclear corrections are applied. At present, this difference is not understood. The Q^2 evolution of these structure functions agrees with QCD and yields $\Lambda^{\rm NLO\ 4flv}_{\overline{MS}} = 309 \pm 27(exp)\ MeV$. This is equivalent to $\alpha_s(M_Z^2) = 0.117 \pm 0.002(exp) \pm 0.004(theory)$.

References

[1] M. R. Adams *et al.*, Phys. Rev. D **54**, 3006 (1996).

[2] M. R. Adams *et al.*, Phys. Rev. Lett. **75**, 1466 (1995).

[3] M. R. Adams *et al.*, Z. Phys. C **71**, 391 (1996).

[4] U. K. Yang *et al.*, J. Phys. G **22**, 775 (1996).

[5] W. G. Seligman, *A Next-to-Leading-Order QCD Analysis of Neutrino-Iron Structure Functions at the Tevatron,* Columbia University Thesis, CU-398, Nevis report: Nevis-292.

[6] G. Altarelli and G. Parisi, Nucl. Phys. B **126**, 298 (1977); Y. L. Dokshitzer, D. I. Diakonov, and S. I. Troyan, Phys. Lett. B **78**, 290 (1978); Y. L. Dokshitzer, D. I. Diakonov, and S. I. Troyan, Phys. Rep. **58**, 269 (1980); V. N. Gribov and L. N. Lipatov, Sov. J. Nucl. Phys. **15**, 438 (1972).

[7] H. Georgi and H. D. Politzer, Phys. Rev. D **14**, 1829 (1976).

[8] M. Virchaux and A. Milsztajn, Phys. Lett. B **274**, 221 (1992).

[9] A. O. Bazarko *et al.*, Z. Phys. C **65**, 189 (1995).

[10] W. K. Sakamoto *et al.*, Nucl. Instrum. Methods A **294**, 179 (1990).

[11] R. Bernstein *et al.*, Fermilab TM-1884, 1994.

[12] D. Y. Bardin and V. A. Dokchaeva, JINR-ER2-86-260 (1986).

[13] L. W. Whitlow *et al.*, Phys. Lett. B **282**, 475 (1992).

[14] P. Z. Quintas, *Nucleon Structure Functions at the Fermilab Tevatron,* Columbia University Thesis, Nevis Preprint 277 (1992); P. Z. Quintas *et al.*, Phys. Rev. Lett. **71**, 1307 (1993).

[15] P. Amaudruz *et al.*, Z. Phys. C **51**, 387 (1991).

[16] P. Amaudruz *et al.*, Phys. Lett. B **295**, 159 (1992).

[17] P. Allport *et al.*, Phys. Lett. B **232**, 417 (1989).

[18] V. Barone *et al.*, Phys. Lett. B **328**, 143 (1994).

[19] J. Botts *et al.*, Phys. Lett. B **304**, 159 (1993).

[20] S. J. Brodsky and B.-Q. Ma, Phys. Lett. B **381**, 317 (1996).

[21] D. J. Gross and C. H. Llewellyn-Smith, Nucl. Phys. B **14**, 337 (1969).

[22] A. Devoto, D. Duke, and J. Owens, Phys. Rev. D **27**, 508 (1983).

[23] R. M. Barnett *et al.*, Phys. Rev. D **54** (1996).

[24] D. A. Harris *et al.*, FERMILAB-CONF-95-144, in *Proceedings of the 30th Renc. de Mor.* (1995).

[25] S. Aid *et al.*, Nucl. Phys. B **449**, 3 (1995).

[26] H. L. Lai *et al.*, Phys. Rev. D **55**, 1280 (1997).

[27] M. Glück, E. Reya, and A. Vogt, Z. Phys. C **67**, 433 (1995).

[28] A. D. Martin, R. G. Roberts, and W. J. Stirling, Phys. Lett. **B 387**, 419 (1996).

THE BNL RARE KAON DECAY PROGRAM

Laurence Littenberg
Physics 510 A
Brookhaven National Laboratory
Upton, NY 11973-5000

ABSTRACT

The rare kaon decay program at Brookhaven National Laboratory is reviewed. Results from the last round of experiments are briefly discussed. The three experiments currently collecting data are described. Prospects for future experiments are discussed.

© 1996 by Laurence Littenberg.

1 Introduction

After more than a decade of "benign neglect," in which there were no rare K decay experiments at Brookhaven, a new round of experiments was launched in the early 1980s. The motivation for this program was mainly the search for physics beyond the Standard Model (SM).[1] It had been realized in the late 1970s that "lepton flavor violating" (LFV) processes such as $\mu \to e\gamma$ and $K_L \to \mu e$ arise naturally in theoretical attempts to go beyond the Standard Model[2] (BSM). Moreover, it turned out that kaon branching ratios accessible at the AGS correspond to extremely high energy scales for possible new interactions. The classic example is the latter process, $K_L \to \mu e$, which in Fig. 1 is shown mediated by a hypothetical horizontal gauge boson, and compared to the kinematically very similar $K^+ \to \mu^+\nu$ decay.

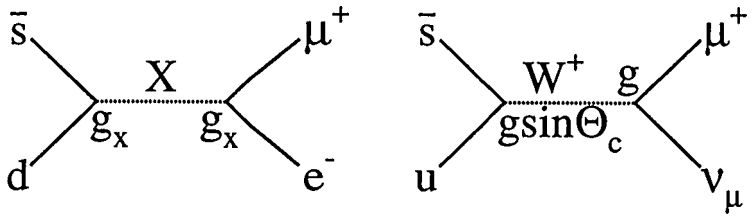


Fig. 1. *Horizontal gauge boson mediating $K_L \to \mu e$, compared with W mediating $K^+ \to \mu^+\nu$.*

Using measured values for M_W, the K_L and K^+ decay rates and $B(K^+ \to \mu^+\nu)$, and assuming a V–A form for the new interaction, one can show

$$M_X \approx 220 \text{ TeV}/c^2 \left[\frac{g_X}{g}\right]^{1/4} \left[\frac{10^{-12}}{B(K_L \to \mu e)}\right]^{1/4} \quad (1)$$

so that truly formidable scales can be probed if $g_X \sim g$. For a V–A interaction, $K_L \to \mu e$ is the most sensitive of kaon decays. If, however, the LFV interaction were pure vector instead, the two-body reaction would be suppressed, and one would be better off searching for $K^+ \to \pi^+\mu^+e^-$, a reaction that also has some advantages in signature with respect to $K_L \to \mu e$. One could also substitute neutral for charged leptons in this last reaction and search for $K^+ \to \pi^+\nu_e\bar{\nu}_\mu$.

Although it has a much worse signature than the decays into charged leptons, a search for this process is also sensitive to the considerable number of proposed BSM processes whose topology is $K^+ \to \pi^+ + \textit{nothing}$ (where *nothing* denotes an undetectable light particle or system of particles[3,4]). Of course, one member of this family, $K^+ \to \pi^+\nu_l\bar{\nu}_l$, is allowed in the SM, but it is suppressed far beyond the experimental limits current in the early 1980s.[5]

Other experiments in this program probed non-SM CP-violating reactions, or searched for a light Higgs or for unexpected enhancements in SM-suppressed decays such as $K_L \to e^+e^-$. Most of the experiments were also capable of studying somewhat more common K decays, and so were able to contribute to the development of new theoretical approaches to long-distance physics, most notably Chiral Perturbation Theory[6] (χPT).

Table 1 lists the first-round experiments. These completed data-taking by 1991.

Table 1. First-round experiments of the BNL Rare K Decay Program. Those denoted by a star were "descendants" of the experiment directly above them in the table.

EXPERIMENT	MODES	INSTITUTIONS
AGS-780	$K_L \to \mu e,\ ee,\ \mu\mu,\ \pi^0e^+e^-$	BNL, Yale
AGS-845*	$K_L \to \pi^0e^+e^-,\ \gamma e^+e^-,\ e^+e^-e^+e^-$	BNL, Yale
AGS-777	$K^+ \to \pi^+e^-\mu^+,\ \pi^+e^+e^-, \ldots$	BNL, SIN, Washington, Yale
AGS-851*	$K^+ \to \pi^+e^+e^-,\ \pi^0 \to e^+e^-$	BNL, SIN, Washington, Yale
AGS-791	$K_L \to \mu e,\ ee,\ \mu\mu, \ldots$	UCI, UCLA, LANL, Stanford, Temple, U. of Texas Austin, William & Mary
AGS-787	$K^+ \to \pi^+\nu\bar{\nu},\ \pi^+\mu^+\mu^-, \ldots$	BNL, Princeton, TRIUMF

Table 2 summarizes the achievements of the first round of experiments. Three very interesting decay modes were seen for the first time: $K_L \to \gamma\gamma e^+e^-$, $K^+ \to$

$\pi^+\mu^+\mu^-$, and $K^+ \to \pi^+\gamma\gamma$. The available data sets of other interesting processes ($K^+ \to \pi^+e^+e^-$ (Ref. 9), $K_L \to \mu^+\mu^-$, $K_L \to \gamma e^+e^-$, etc.) were very significantly increased, and new structure observed in the decay distributions of some of these. Finally, the limits on forbidden and suppressed processes were greatly improved, in a couple of cases, by many orders of magnitude.

Table 2: Results of the first round of the BNL Rare K Decay Program.

Mode	Result	Comment
$K_L \to \mu e$	BR $< 3.3 \times 10^{-11}$/event	BR limit improved by 2×10^5 $M_A > 94$ TeV
$K^+ \to \pi\mu e$	BR $< 2.1 \times 10^{-11}$/event	BR limit improved by 22 $M_V > 39$ TeV
$K^+ \to \pi^+X^0$	BR $< 5.2 \times 10^{-10}$	BR limit improved by 70 $F_{K\pi}^{familon} > 2.2 \times 10^8$ TeV
$K^+ \to \pi^+\nu\bar{\nu}$	BR $< 2.4 \times 10^{-9}$	BR limit improved by 60
$K_L \to \mu^+\mu^-$	> 700 events	previous world supply 27 events
$K_L \to \pi^0e^+e^-$	BR $< 5.5 \times 10^{-9}$	BR limit improved by 360
$K_L \to e^+e^-\gamma\gamma$	$(6.6 \pm 3.2) \times 10^{-7}$	Discovery, changed the course of the study of CP violation
$K^+ \to \pi^+e^+e^-$	512 events	ten-fold improvement, form factor observed, χPT ambiguity broken
$K_L \to \gamma e^+e^-$	$(9.1 \pm 0.4^{+.6}_{-.5}) \times 10^{-6}$	250-fold improvement, form factor deviation observed
$K^+ \to \pi^+\mu^+\mu^-$		discovered
$K^+ \to \pi^+\gamma\gamma$		discovered
$\pi^0 \to e^+e^-$		cleared up a long-standing discrepancy

2 The Current Experiments

The three experiments which constitute the second generation of the AGS Rare Kaon Decay Program are listed in Table 3. Each is the successor of a first-round experiment; in one case, not even the name has changed. The motivation for these

Table 3: Current experiments of the BNL Rare K Decay Program.

EXPERIMENT	MODES	INSTITUTIONS
AGS-787	$K^+ \to \pi^+\nu\bar{\nu}$, π^+X^0, ...	BNL, INS/Tokyo, KEK, Osaka, Princeton, TRIUMF
AGS-865	$K^+ \to \pi^+e^-\mu^+$, π^+ee, ...	Basel, BNL, INR-Moscow, JINR-Dubna, New Mexico, Pittsburgh, PSI, Tbilisi State, Yale, Zurich
AGS-871	$K_L \to \mu e$, ee, $\mu\mu$, ...	UCI, Stanford, U. of Texas Austin, William & Mary

experiments has evolved since the first round was launched. The emphasis is now a little more on SM-suppressed processes and a little less on totally forbidden ones. This is largely because the advances in sensitivity achieved in the first round of experiments have brought some very interesting examples of the former processes into range. It has also been realized that kaon decays can contribute greatly to determining the CKM unitarity triangle. This is illustrated by Fig. 2. All three sides of the triangle can in principle be determined from rare K decays. In Fig. 2, the "primary" reactions are those adjacent to the sides of the triangle. The outlying reactions provide supplementary information needed for interpreting some of the primary reactions, and for evaluating certain possible backgrounds.

Over the past few years, with the addition of a quarter-size booster and a revamped RF-system, the intensity of the AGS has steadily increased to the point where 6×10^{13} protons/spill can routinely be accelerated to 25.2 GeV/c. The K experiments each utilize $1\text{–}2\times10^{13}$ protons/spill, which makes possible unprecedented sensitivities, but which has made necessary radiation-hard beam elements and innovations in production targets, trigger electronics, and high-rate detector design.

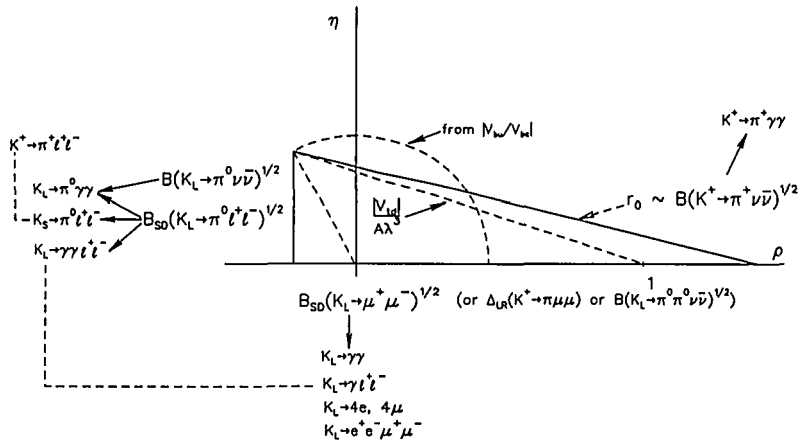


Fig. 2. *Rare K decays and the unitarity triangle.*

2.1 E871

E871 is designed to detect di-lepton decays of the K_L at the 10^{-12} level. This requires a very large flux of K_L and a detector that can make redundant high-resolution measurements. Good particle identification power is also needed. The worst source of background to $K_L \to \mu e$ is $K_L \to \pi e \nu$ ($Ke3$). If the daughter pion decays in flight or is misidentified and the neutrino is soft, one has a background that appears topologically identical to the signal, with kinematics that can closely approach those of the signal. Since a few percent of the pions from $Ke3$ decay in the detector, particle identification *per se* is of limited value in this case. What is essential is excellent kinematic resolution and the ability to recognize track kinks. However, if the $Ke3$ pion is mistaken for an electron and the electron for a muon, the reconstructed two-body mass can exceed (or equal!) M_K. In this case, good kinematic resolution is of limited value but particle identification power is crucial.

The detector is shown in Fig. 3. An intense neutral beam containing $\sim 2 \times 10^8$ K_L/pulse is incident on an 11 m drift space in which about 10% of them decay. The decay products impinge on a two-dipole spectrometer optimized for very high rate operation. Straw chambers using fast gas constitute the first four planes where

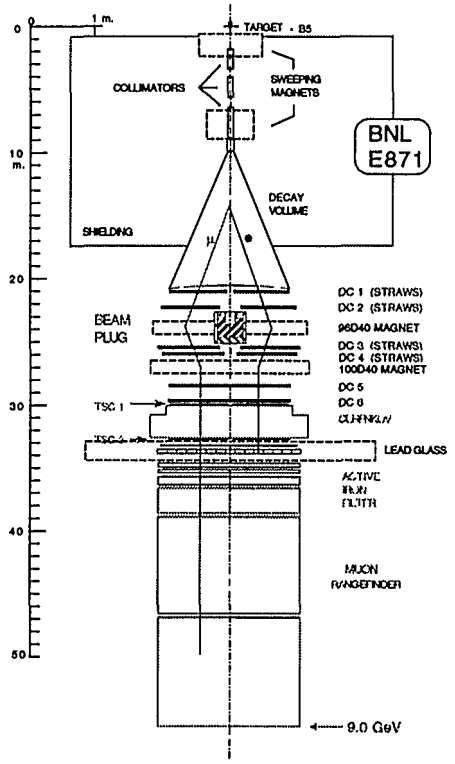


Fig. 3. *Apparatus of AGS E871.*

the rates are highest; conventional drift chambers are deployed in the rear. A novel feature is the beam plug which is designed to absorb the multi-GHz neutral beam part-way through the spectrometer. This eliminates acceptance-eating beam holes in the rear of the spectrometer and provides a quiet environment for the particle ID devices. These include an atmospheric hydrogen Cherenkov counter and a lead glass array for distinguishing electrons from heavier particles, and a muon range finder. The latter consists of planes of proportional wire chambers (and a few scintillator hodoscopes) at intervals of 5% in $\Delta p_\mu/p_\mu$. Muons are identified by the agreement of their momentum and range.

The second spectrometer magnet makes possible a redundant measurement of track momenta. The observed mass resolution for calibration $K_L \to \pi^+\pi^-$ events is $\sigma_{m_{\pi\pi}} = 1.13$ MeV/c^2. The net p_T kick of the spectrometer is set to 220 MeV/c, which tends to make the two-body decays of interest parallel after the last bend, facilitating a simple trigger.

The experiment had long data collection runs in 1995 and 1996. These runs were uncommonly eventful, and the experimenters had to contend with melted production targets, ruptured vacuum windows, and other setbacks that would have confounded ordinary people. However, they prevailed and appear to have reached a sensitivity of $\sim 10^{-12}$/event. Their analysis is in progress and results are expected within a few months. Figure 4 shows the $m_{\mu\mu}$ distribution from a test analysis of a small sample of the 1995 data set. This demonstrates the power of the experiment to pull out a clear signal of a very rare K_L decay [$B(K_L \to \mu^+\mu^-) \sim 7 \times 10^{-9}$]. The experimenters estimate they will reconstruct some 7000 $K_L \to \mu^+\mu^-$'s, to be compared to the present world sample of $\sim$ 1000 events. This should yield a very accurate determination of the branching ratio, potentially allowing this decay to determine the CKM parameter ρ, modulo certain developments in theory and in experimental studies of other K decays[7] (see Fig. 2).

Finally, the expected sensitivity of E871 is sufficient to observe the decay $K_L \to e^+e^-$, which in the Standard Model is expected to occur at about 3×10^{-12}. This would be by far the rarest K decay ever observed. Since the previous upper limit[8] (from the predecessor experiment AGS-791) is 4.1×10^{-11}, there is approximately an order of magnitude in which surprises could lurk.

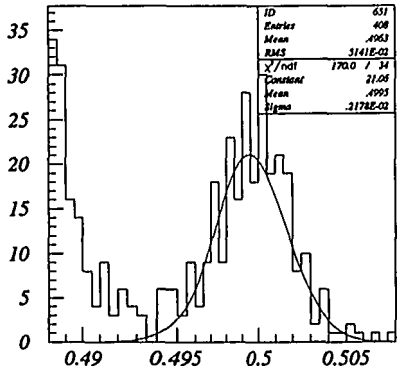


Fig. 4. $K_L \to \mu^+\mu^-$ *signal from a small sample of AGS E871 data.*

2.2 E865

E865 is also primarily a search for LFV, in this case for $K^+ \to \pi^+\mu^+e^-$. In this case, a 6 GeV/c unseparated beam containing 70 MHz of K^+ and about 20 times more pions and protons is incident on a 5 m decay tank. Roughly 10% of the K^+ decay in the tank and the resultant daughter tracks are momentum analyzed by the high-rate proportional chamber spectrometer shown in Fig. 5. The first magnet kicks the decay particles out of the hot beam region and separates them by sign (negative left). This allows the two sides of the detector to be separately optimized for particle identification. A great deal of attention has been paid to particle ID, since this is the most difficult challenge of the experiment. There are two layers of gas Cherenkov counters on each side of the detector. On the left, where it is essential that π^-'s are never mistaken for electrons (the worry is $K^+ \to \pi^+\pi^+\pi^-$; $\pi^+ \to \mu^+\nu$), these counters are filled with hydrogen. On the right, the $\check{\text{C}}$ counters are filled with a lower threshold gas so that positrons are never mistaken for muons (the worry is $K^+ \to \pi^+\pi^0$; $\pi^0 \to e^+e^-\gamma$) or for pions (the worry is $K^+ \to \pi^0\mu^+\nu$; $\pi^0 \to e^+e^-\gamma$). Downstream of the last spectrometer element is a wall of lead-scintillator shower counters. It consists of some 600 11.4 cm x 11.4 cm x 15 r.l. elements read out via wavelength shifting fibers. Downstream of the calorimeter is a muon range stack of alternating proportional tube planes and steel absorber plates.

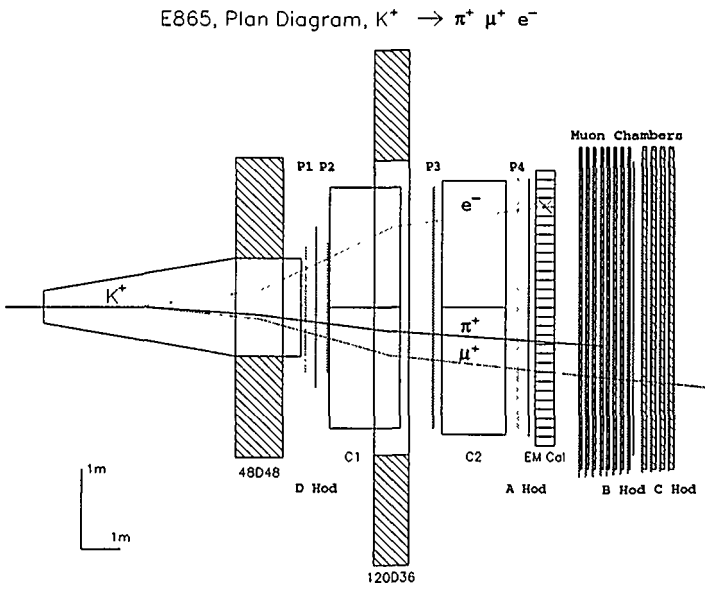


Fig. 5. *Apparatus of AGS E865.*

E865 was commissioned in 1994 and has had significant data collecting runs in the subsequent two years. A sensitivity to $K^+ \to \pi^+\mu^+e^-$ of $\sim 10^{-11}$/event can be expected from this data. This represents an improvement of an order of magnitude over the previous generation of this experiment.[10] The goal of the experiment is to reach $\sim 10^{-12}$/event sensitivity for $K^+ \to \pi^+\mu^+e^-$ and to study many other decay modes. Figure 6 shows preliminary results from the 1995 run on one of these, $K^+ \to \pi^+e^+e^-$. There are about twice as many events in this distribution as in the publication of the previous experiment,[9] and many times this number are expected when E865 completes taking data. Using tagged π^0's from $K^+ \to \pi^+\pi^0$ decay, data on $\pi^0 \to e^+e^-$ and $\pi^0 \to e^+e^-e^+e^-$ has also been collected.

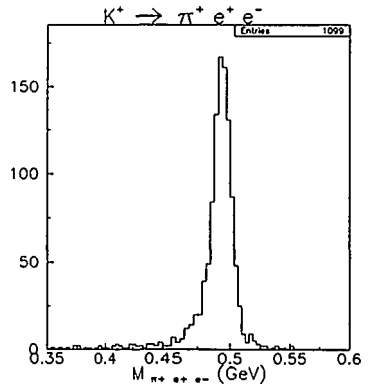


Fig. 6. *Effective mass of $K^+ \to \pi^+e^+e^-$ candidates from E865.*

The experiment has upgraded its DAQ system and is expected to accumulate sensitivity in 1997 at least 30% faster than in 1996. A scintillating pixel device for making beam measurements will be installed in 1997. This will permit the full reconstruction of decay modes with missing neutrinos. Along with improvements to the particle ID and triggering, this should allow many additional decay modes to be studied. In 1997, E865 expects to collect data on $K^+ \to \pi^+\mu^+\mu^-$, $K^+ \to \mu^+\nu e^+e^-$, $K^+ \to e^+\nu e^+e^-$, and $K^+ \to \pi^+\pi^0e^+e^-$. These processes test the predictions of χPT, and the last is a possible locus for CP violation. This experiment may also take a special run to increase the world sample of $K^+ \to \pi^+\pi^-e^+\nu$ events by an order of magnitude. This decay is of primary importance to χPT,

for which it provides much crucial input, and it is a primary source of information on low-energy π–π scattering.

2.3 E787

E787 is now primarily a search for the Standard Model process $K^+ \to \pi^+\nu\bar{\nu}$. This highly GIM-suppressed decay can be very cleanly calculated in terms of SM parameters. As illustrated in Fig. 2, it is particularly sensitive to $|V_{td}|$. The problematic hadronic matrix element that confounds efforts to extract $|V_{td}|$ from B–$\bar{B}$ mixing is in this case determined through the well-known rate of $Ke3$ decay.[11] Long-distance contributions are negligible[12] and QCD corrections are moderate and very well-understood through the next-to-leading logarithmic order calculations of Buchalla and Buras.[13] The first generation[14] of E787 improved the upper limit on $B(K^+ \to \pi^+\nu\bar{\nu})$ from 1.4×10^{-7} to 2.4×10^{-9}. CKM fits[15] tend to predict a branching ratio of $< 2 \times 10^{-10}$, so that there is still about an order of magnitude in which to search for new physics, for which predictions abound.[3,4,16]

$K^+ \to \pi^+\nu\bar{\nu}$ has a far worse signature than most of the processes discussed above. Positive pions are very common decay products of K^+, and there are no kinematic constraints other than $p_\pi < 227$ MeV/c. To detect this process, one basically has to prove one couldn't be seeing *anything else*. This entails excellent kinematic resolution, rejection of μ^+ by $\mathcal{O}(10^9)$, and the ability to veto extra particles by at least 10^3 : 1/particle. The only reason such an experiment is possible at all is that the primary background sources, $K^+ \to \mu^+\nu$ and $K^+ \to \pi^+\pi^0$, are two body decays with very good signatures.

Figure 7 shows the detector[17] which is mounted in a solenoidal magnet with a 2'-thick steel yoke. The necessity for hermetic vetoing and for excellent muon rejection have led all experiments hunting $K^+ \to \pi^+\nu\bar{\nu}$ to employ a stopping geometry. An extremely pure ~ 750 MeV/c beam containing about 10^7 K^+/1.6 second spill is incident on a series of beam identification and tracking devices and loses most of its kinetic energy in a BeO degrader. The K^+ stop in a highly segmented scintillating fiber target and the subsequent decay particles are momentum analyzed in a cylindrical drift chamber with thin-foil cathodes[18] on which a 1-T magnetic field has been imposed. Candidate pions then range out in a cylindrical array of scintillators and straw chambers ("range stack"). This allows their kinetic energy and range to be measured. The range/energy/momentum comparison is a

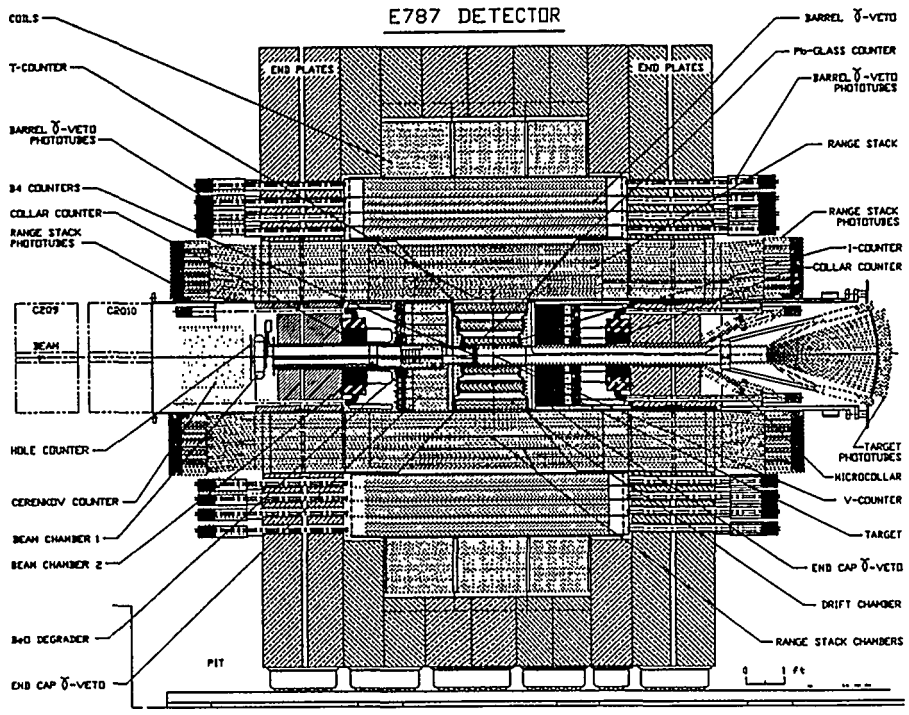


Fig. 7. *Apparatus of AGS E787.*

powerful means of particle ID in this energy range. The pions stop in range stack scintillators and their subsequent $\pi \to \mu \to e$ decay chain is monitored. This allows them to be distinguished from muons, whose decay chain contains only two pulses. Surrounding the range stack and plugging the ends of the device are photon detectors set in veto for $K^+ \to \pi^+ + \textit{nothing}$ events. In combination with the range stack, these form a nearly hermetic photon veto.

The beam and much of the detector was upgraded in '91-94, and commisioned in 1994. Long data runs were taken in 1995 and 1996. Sensitivity corresponding to about five times that of all previous running of E787 was accumulated. Figure 8 summarizes the situation. Data now in hand should yield a sensitivity of $\sim 2 \times 10^{-10}$/event, compared with a central value for recent SM fits of $\sim 10^{-10}$. The limitations of the experiment are now reasonably well-understood, and it is known that the background rejection power of the detector is sufficient to make a measurement at the predicted SM level. The most efficient way to improve the sensitivity of the experiment is to maintain the instantaneous rate of stopping K^+, but increase the duty factor. It is estimated that with long runs under optimum conditions, a sensitivity of 2×10^{-11}/event could be achieved by 1999. This corresponds to ~ 5 events at the central SM prediction. If, on the other hand, no events are observed at this level, the Standard Model must be wrong!

E787 has yielded quite a few interesting results on reactions other than $K^+ \to \pi^+ + \textit{nothing}$. I'll mention of couple of recent ones. The reaction $K^+ \to \pi^+\gamma\gamma$ was initially important to E787 because of its potential as a background to $K^+ \to \pi^+\nu\bar{\nu}$. It is one of the very few possible SM sources of π^+ stiffer than those from $K \to \pi^+\pi^0$ (*i.e.*, in the main kinematic search region of E787). The pre-extant bound[19] on $B(K^+ \to \pi^+\gamma\gamma)$, 8.4×10^{-6}, was high enough to cause concern at the planning stage of E787, before it was clear how well the photon veto would work. In fact, the photon veto power turned out to be $\mathcal{O}(10^3 : 1)/\gamma$ and, in an early measurement,[20] E787 improved the upper limit on $B(K^+ \to \pi^+\gamma\gamma)$ to 10^{-6} (and later[21] to 5×10^{-7}) in the kinematic region of interest. This removed $K^+ \to \pi^+\gamma\gamma$ from the list of significant backgrounds. However, around that time, predictions[22] of χPT indicated that this mode might be detectable by E787. These predictions indicated a very striking $m_{\gamma\gamma}$ distribution. Instead of the smooth phasespace-like distribution predicted by most previous models, there would be a sharp threshold at $m_{\gamma\gamma} \approx 2m_\pi$. Crudely speaking, the idea is that the K^+ decays virtually to three pions, and two of the pions annihilate into a $\gamma\gamma$ final state. The threshold

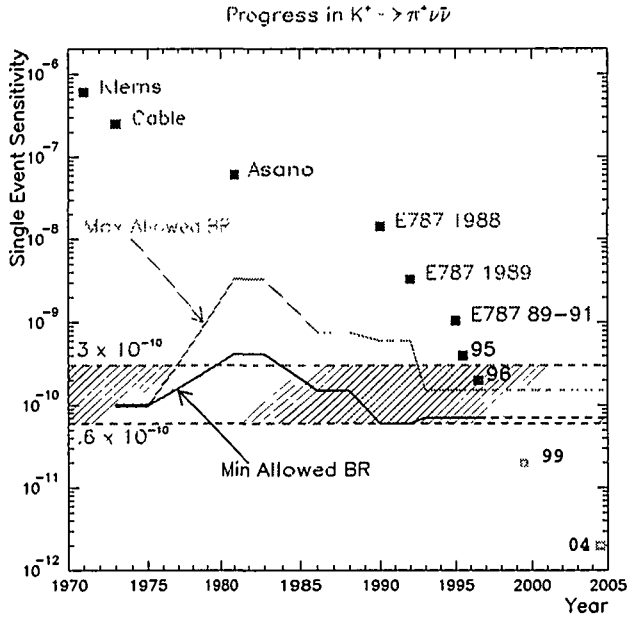


Fig. 8. *Progress of AGS E787. Hatched region is consistent with Standard Model. Solid lines show upper and lower limits of specific fits.*

in $m_{\gamma\gamma}$ corresponds to the region of soft p_{π^+}, which is difficult for E787 because of copious backgrounds from $K^+ \to \pi^+\pi^0$ in which the π^+ is down-shifted in momentum through interaction, and from $K^+ \to \pi^+\pi^0\gamma$ and $K^+ \to \pi^+\pi^0\pi^0$ where photons are lost. A careful analysis was successful in suppressing these backgrounds, and ~ 30 $K^+ \to \pi^+\gamma\gamma$ events were observed. As seen in Fig. 9, they exhibit the predicted threshold behavior.

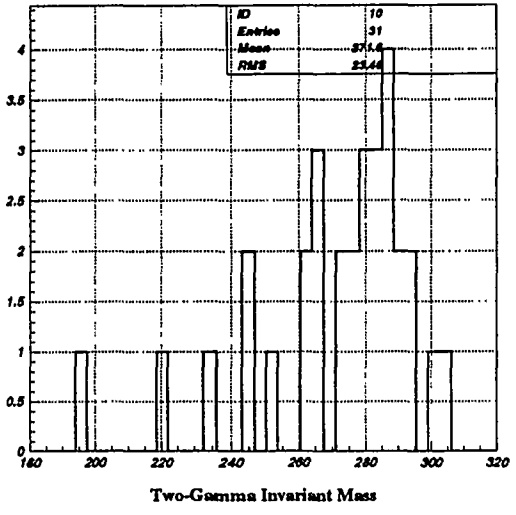


Fig. 9. *$m_{\gamma\gamma}$ distribution of E787 $K^+ \to \pi^+\gamma\gamma$ candidates.*

A second recent result is on the radiative decay $K^+ \to \mu^+\nu\gamma$. This reaction is dominated by inner bremsstrahlung (IB), and was first observed a number of years ago. However, the primary physics interest in this decay is in the much rarer "structure dependent" radiation. A rich panoply of phenomena, including possible CP-violating interferences, have been predicted, but all previous attempts to see anything beside IB in this decay have produced only upper limits.[23] In 1994, a short dedicated run was taken with the upgraded E787 detector. The trigger demanded both a stiff μ^+ and a single γ with energy greater than that of most IB photons. Analysis revealed a clear structure-dependent component in the $K^+ \to \mu^+\nu\gamma$ events collected. This can be seen in Fig. 10 where evidence for ~ 900 non-IB events is exhibited.

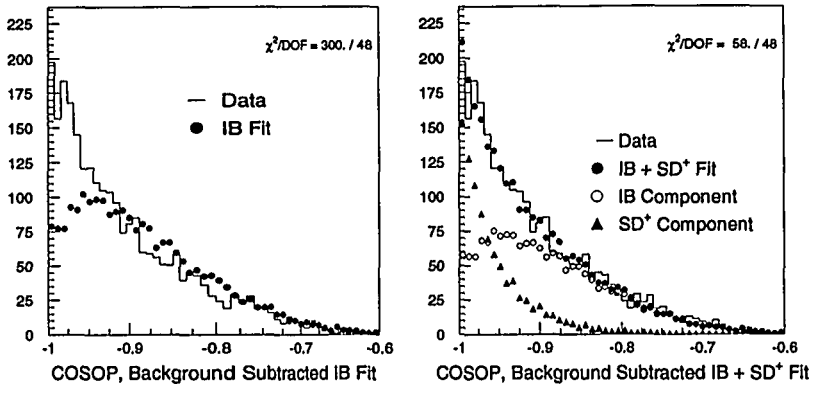


Fig. 10. *Distribution in $cos\theta_{\mu\gamma}$ for E787 $K^+ \to \mu^+\nu\gamma$ candidates. Fit with IB alone is shown in (a), while fit with both IB and structure-dependent radiation is shown in (b).*

A more sophisticated two-dimensional analysis in which interference between various components of the decay was allowed yielded[24] $B(K^+ \to \mu^+\nu\gamma)_{SD+} = (1.331 \pm 0.120 \pm 0.181) \times 10^{-5}$, where the first error is statistical and the second systematic. In terms of the vector and axial vector form factors, this corresponds to $|F_V + F_A| = 0.165 \pm 0.007 \pm 0.011$, which can be compared to the $\mathcal{O}(p^4)$ χPT prediction[25] $F_V + F_A = -0.137 \pm 0.006$. Calculations to $\mathcal{O}(p^6)$ in χPT are in progress.[26]

3 AGS-2000

Although the AGS is slated to become an injector for RHIC in 1999, it will only be needed for this purpose for about two hours per day. The rest of the time, it could be used for proton or heavy ion fixed target experiments. Since the base cost of maintaining the accelerator complex will be borne by RHIC, incremental running would be quite economical. To examine what experiments would be competitive in this situation, in May of 1996 the *AGS-2000* Workshop was held at BNL. Experiments in many areas from muon decay to strangelet production were

considered, but kaon decay was the most active subject. Table 4 lists the decays studied at the workshop. For lack of space, I will discuss only the first three of these. Details of the others may be found in the proceedings.[27]

Table 4. K decays considered by AGS-2000.

$K^+ \to \pi^+\nu\bar{\nu}$	precision measurement of $\|V_{td}\|$
$K_L \to \pi^0\nu\bar{\nu}$	clean measurement of CKM η
$K\mu 3$	T-violating μ polarization tests non-SM CP violation
$K_L \to \pi\pi\nu\bar{\nu}$	clean measurement of CKM ρ
$K^+ \to \pi^+\mu^+\mu^-$	P-violating μ^+ polarization measures ρ, also sensitive to non-SM effects
$K_L \to \mu^+\mu^-$	Longitudinal μ polarization tests non-SM CP violation
$K^+ \to \pi^+\pi^0 e^+ e^-$	CP violation and form factor measurements, sensitive to both SM & non-SM CP violation
$Ke4$	search for non-CKM CP violation
$Ke3$	determines $\|V_{us}\|$ through an improved B.R. measurement

3.1 $K^+ \to \pi^+\nu\bar{\nu}$

A working group devoted itself to $K^+ \to \pi^+\nu\bar{\nu}$ with the object of making a 15% measurement of $|V_{td}|$, without building an entirely new detector. They concluded that this was possible if a higher acceptance, lower momentum K^+ beam were built, the AGS macro duty factor optimized, the beam microbunched at $\sim$ 20 MHz, and certain straightforward improvements made to the E787 detector.

3.2 $K_L \to \pi^0\nu\bar{\nu}$

As indicated in Fig. 2, the branching ratio for the decay $K_L \to \pi^0\nu\bar{\nu}$ is directly related[28] to CKM η. More explicitly,[29] for $m_t = 175$ GeV/c^2,

$$B(K_L \to \pi^0\nu\bar{\nu}) \approx 4.3 \times 10^{-10}\eta^2 A^4. \qquad (2)$$

This corresponds to a predicted branching ratio of $\sim 2 \times 10^{-11}$. The theoretical situation is very clean: there are no significant long-distance contributions, QCD corrections are small and well-understood, the hadronic matrix element is known from $Ke3$, and the effect of indirect CP violation is $\mathcal{O}(1\%)$. This reaction offers a window into the origin of CP violation that is comparable to studies proposed for the B-system and very complementary to them.[29] It is also quite sensitive to new physics beyond the Standard Model.[30] $K_L \to \pi^0\nu\bar{\nu}$ is the most important measurement in the K system, and there are plans to pursue it in at least three laboratories. AGS-2000 stimulated a proposal[31] to measure this process at BNL.

The present experimental upper limit[32] on this decay is 5.8×10^{-5}, so that an increase in sensitivity of at least seven orders of magnitude is necessary in order to make a real measurement. The poor signature makes such a measurement at this level extremely challenging. Therefore, it was proposed to measure everything possible about the reaction: the K_L's velocity as well as its direction, and also the directions of the final state photons (as well as their positions, energies, and arrival times). To measure the K_L velocity, the AGS beam would be tightly bunched so that the time of flight origin of the K_L could be known to $\sim$ 200 ps. The beam can be microbunched on extraction by forcing it between empty RF buckets imposed by a dilution cavity.[33] Tests of this technique in the AGS[34] have so far achieved bunch widths of $<$ 300 ps and are continuing.

To allow an accurate determination of the K_L momentum from its velocity, the K_L must be rather soft. To this end, the beam is produced at a very large angle, *i.e.*, 45°, so that the average K_L momentum is $\sim$ 750 MeV/c. Combined with good timing resolution on the final state photons, this allows a determination of p_K to a few percent. The proposed beam is highly asymmetric with an aperture of 125 mr horizontally and 4 mr vertically, which facilitates collimation and affords an extra kinematic constraint. The proposed detector is shown in Fig. 11. The beam of $\sim 2.5 \times 10^8$ K_L/spill impinges on a 3.5 m decay tank. Decay photons are detected in a wall of directionalizing preconverters composed of ~ 1.5 X_0 of scintillators and low mass chambers. The energy measurement is completed by a lead-scintillating fiber calorimeter similar to that of the KLOE design,[35] but with a larger scintillator/Pb ratio. The remainder of the acceptance, including the beam region, is covered by hermetic photon vetoes.

The leading potential background to $K_L \to \pi^0\nu\bar{\nu}$ is $K_L \to \pi^0\pi^0$, which is almost 10^8 times more copious than the signal. It is very difficult to veto π^0 to this level, hence the importance of the kinematic handle made possible by measuring the K_L momentum. The π^0's from $K_L \to \pi^0\pi^0$ have a unique energy in the K_L center-of-mass system, and so can be eliminated kinematically. In addition to backgrounds due to K decay, it is possible for a beam neutron to

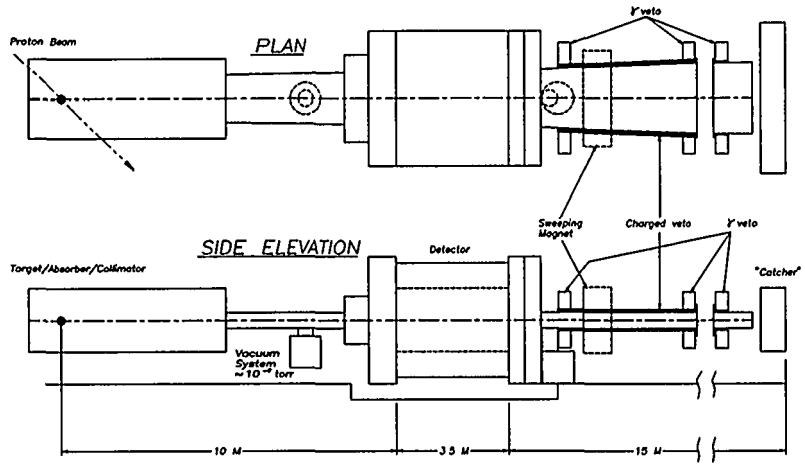


Fig. 11. *Proposed apparatus of AGS E926.*

produce a π^0 off a residual gas molecule without yielding any other visible decay product. This necessitates a vacuum of 10^{-7} Torr in the decay region, adding to the design challenge of this experiment.

In a three-year run, the experiment would collect about 70 $K_L \to \pi^0\nu\bar{\nu}$ events at the central Standard Model prediction, over a background of ≤ 10 events. This would allow a determination of η with a precision of $\leq 15\%$. It would also be possible to get a limit on $K_L \to \pi^0\pi^0\nu\bar{\nu}$, a process which is cleanly sensitive to CKM ρ (Refs. 36 and 37). A number of other interesting decay modes could also be studied, including $K_L \to \gamma\gamma$, $K_L \to \pi^0\gamma\gamma$, and $K_L \to \pi^0\pi^0\gamma$.

3.3 T-Violation in $K^+ \to \pi^0\mu^+\nu$ Decay

The present upper limit on T-violating muon polarization in $K\mu3$ decay ($K^+ \to \pi^0\mu^+\nu$), $-0.009 < P_\mu^T < 0.007$ at 95% C.L., was established by a pair of BNL experiments[38] more than 15 years ago. Since the Standard Model predicts a negligible effect, this reaction is a good place in which to search for BSM CP violation. The observed baryon-antibaryon asymmetry of the universe appears to require sources of CP violation outside the SM, making this a very topical experiment. A number of such models, including those involving multiple Higgs[39] (in some cases arising from supersymmetry[40]), tend to predict detectable effects in $K^+ \to \pi^0\mu^+\nu$. The present limits compare favorably with competing limits available from B decays, so that any improvement in the K limits would yield unique constraints on many models. At AGS-2000, a proposal[41] to improve the sensitivity of this kind of experiment by about a factor of 40 was refined. The proposal attempts to capitalize on the experience of the earlier BNL experiment by retaining the same general philosophy, updated by advances in accelerator, beam, and detector technology. The previous K^+ experiment was mounted in a 4 GeV/c unseparated positive beam. The current proposal utilizes the AGS 2 GeV/c separated beam, which can produce 2×10^7 K^+/pulse with $K : \pi = 1 : 1.2$.

Figure 12 shows the proposed apparatus. The beam is incident on a $\sim$ 5 m decay tank, in which roughly 5×10^6 K^+/spill decay. The π^0 photons from $K\mu3$ are detected in an electromagnetic calorimeter consisting of $\sim$ 500 "Shashlyk" modules. Muons pass through a series of tracking chambers and trigger hodoscopes, and into a cylindrically symmetric polarimeter where they are stopped in radially arrayed graphite wedges. The decay of the stopped muons is detected by wire chambers that abut the absorber wedges. The chambers determine both the muon stop position and the positron direction. The trigger selects events in which the decay plane of the $K\mu3$ coincides with the radial wedges. A T-violating muon polarization then manifests itself as an asymmetry between the number of muons whose decay positrons emerge in a clockwise sense and those whose decay positrons emerge in a counter-clockwise sense. A solenoidal field of $\sim$ 70 G along the beam direction causes the muon spin to precess with a period of about 1 μsec. Reversing the polarity of the field, every spill allows one to cancel many possible systematic errors that might otherwise allow the large in-plane component of polarization to cause a spurious signal.

The calculated analyzing power of the polarimeter is $\sim$ 35%. Collecting 550 events/spill, in a 2000 hour run, one can reach a statistical sensitivity of 1.3×10^{-4} on P_μ^T. This is equivalent to $Im\xi \sim 7 \times 10^{-4}$, where $Im\xi$ is the model-independent T-violating amplitude. In terms of models such as those invoking three Higgs doublets, this is far more sensitive than existing limits from $B(b \to s\gamma)$ or $B(b \to X\tau\nu)$.

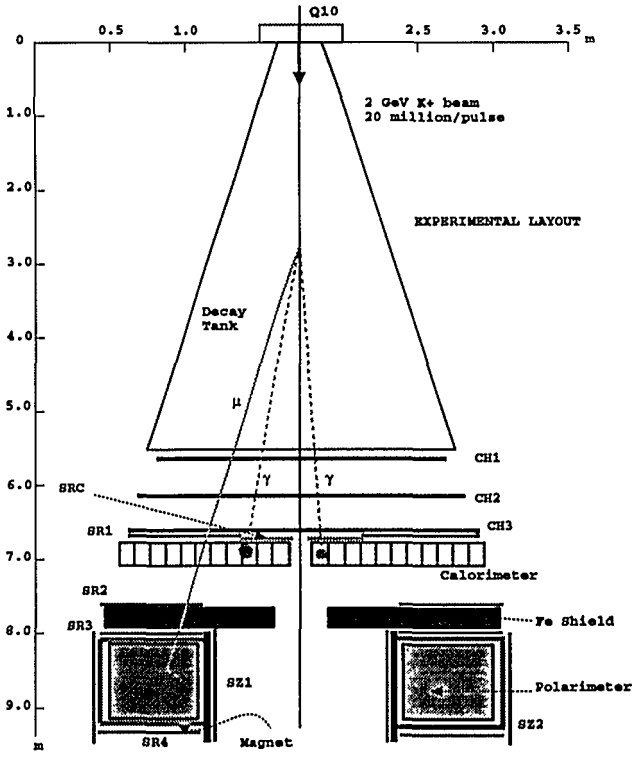


Fig. 12. *Proposed apparatus of AGS E923.*

4 Conclusions

The BNL Rare Kaon Decay Program has yielded a number of interesting discoveries and greatly improved the limits on several processes forbidden by the Standard Model. Experiments in progress now are expected to further improve these limits, and also to produce measurements of certain highly suppressed processes whose rates constrain important Standard Model parameters such as ρ and $|V_{td}|$. Future extensions of the program will be very economical to run after the AGS becomes an injector to RHIC. These could produce accurate measurements of the CKM CP-violation parameter η and probe BSM sources of CP violation in unique ways. Since such experiments are typically sensitive to processes other than their primary quarry, they also offer an opportunity for the kind of completely unexpected discovery that has from time to time graced the history of kaon decay.

Acknowledgments

I would like to thank D. Bryman, A. Buras, M. Diwan, S. Kettell, H. Ma, W. Molzon, J. Ritchie, and M. Zeller for discussions, corrections, access to data, and other assistance with this paper. This work was supported by the U.S. Department of Energy under Contract No. DE-AC02-76CH00016.

References

[1] J. Ritchie and S. Wojcicki, Rev. of Mod. Phys. **65**, 1149 (1993).

[2] W. Buchmüller and D. Wyler, Nucl. Phys. B **268**, 621 (1986); R. Cahn and H. Harari, Nucl. Phys. B **176**, 135 (1980); J. Pati and H. Stemnitzer, Phys. Lett. B **172**, 441 (1986): O. Shanker, Nucl. Phys. B **206**, 253 (1982); A. Acker and S. Pakvasa, Mod. Phys. Lett. A **7**, 1219 (1992); W. J. Marciano and A. Sanda, Phys. Rev. Lett. **38**, 1512 (1977); W. J. Marciano, Phys. Rev. D **45**, R721 (1992); A. Barroso, G. Branco, and M. Bento, Phys. Lett. B **134**, 123 (1984); P. Langacker, S. Uma Sankar, and K. Schilcher, Phys. Rev. D **38**, 2841 (1988).

[3] I. Bigi and F. Gabbiani, Nucl. Phys. B **367**, 3 (1991).

[4] J. Hagelin and L. Littenberg, Prog. Part. Nucl. Phys. **23**, 1 (1989).

[5] Y. Asano *et al.*, Phys. Lett. B **107**, 159 (1981).

[6] A. Pich, Rept. Prog. Phys. **58**, 563 (1995).

[7] L. Littenberg and G. Valencia, Ann. Rev. Nucl. Part. Sci. **43**, 729 (1993).

[8] K. Arisaka *et al.*, Phys. Rev. Lett. **71**, 3910 (1993).

[9] C. Alliegro *et al.*, Phys. Rev. Lett. **68**, 278 (1992).

[10] A. M. Lee *et al.*, Phys. Rev. Lett. **64**, 165 (1990).

[11] W. J. Marciano and Z. Parsa, Phys. Rev. D **53**, 1R (1996).

[12] D. Rein and L. M. Sehgal, Phys. Rev. D **39**, 3325 (1989); M. Lu and M. B. Wise, Phys. Lett. B **324**, 461 (1994); C. Q. Geng, I. J. Hsu, and Y. C. Lin, Phys. Lett. B **55**, 569 (1995).

[13] G. Buchalla and A. J. Buras, Nucl. Phys. B **412**, 106 (1994).

[14] S. Adler *et al.*, Phys. Rev. Lett. **76**, 1421 (1996).

[15] S. Herrlich and U. Nierste, Phys. Rev. D **52**, 6505 (1995).

[16] F. Wilczek, Phys. Rev. Lett. **49**, 1549 (1982).

[17] M. Atiya *et al.*, Nucl. Instrum. Methods A **321**, 129 (1992).

[18] E. W. Blackmore *et al.*, submitted to Nucl. Instrum. Methods A (1996).

[19] Y. Asano *et al.*, Phys. Lett. B **113**, 195 (1982).

[20] M. S. Atiya *et al.*, Phys. Rev. Lett. **65**, 1188 (1990).

[21] S. Adler, "The search for the $K^+ \to \pi^+\gamma\gamma$ decay above the $K_{\pi 2}$ peak using the 1991 data set," State University of New York at Stony Brook thesis (1995).

[22] G. Ecker, A. Pich, and E. de Rafael, Nucl. Phys. B **303**, 665 (1988); G. Ecker, A. Pich, and E. de Rafael, *Phys. Lett.* B **237**, 481 (1990).

[23] Y. Akiba *et al.*, Phys. Rev. D **32**, 2911 (1985); V. S. Demidov *et al.*, Sov. J. Nucl. Phys. **52**, 1006 (1990).

[24] M. Convery, *First Measurement of Structure Dependent* $K \to \mu^+\nu\gamma$, Princeton University Ph.D thesis (1996).

[25] J. Bijnens, G. Ecker, and J. Gasser, Nucl. Phys. B **396**, 81 (1993).

[26] L. Amettler *et al.*, Phys. Lett. B **303**, 140 (1993).

[27] *AGS-2000 Experiments for the 21st Century*, L. S. Littenberg and J. Sandweiss, *Proceedings of the AGS-2000 Workshop*, Brookhaven National Laboratory, May 13-17, 1996, Formal Report.

[28] L. Littenberg, Phys. Rev. D **39**, 3322 (1989).

[29] G. Buchalla and A. J. Buras, Phys. Rev. D **54**, 6782 (1996).

[30] Y. Grossman and Y. Nir, SLAC-PUB-7380, Jan. 1997, hep-ph/9701313.

[31] I.-H. Chiang *et al.*, "Measurement of $K_L \to \pi^0\nu\bar{\nu}$," AGS Proposal 926 (1996).

[32] M. B. Weaver *et al.*, Phys. Rev. Lett. **72**, 3758 (1994).

[33] R. Cappi and C. Steinbach, CERN-PS-OP-81-10, *Particle Accelerator Conference 1981*, 2806.

[34] J. W. Glenn, AGS/AD Technote 426 (1996).

[35] A. Antonelli *et al.*, Nucl. Instrum. Methods A **354**, 352 (1995).

[36] C. Q. Geng, I. J. Hsu, and Y. C. Lin, Phys. Rev. D **50**, 5744 (1994).

[37] L. Littenberg and G. Valencia, Phys. Lett. B **385**, 379 (1996).

[38] M. Schmidt *et al.*, Phys. Rev. Lett. **43**, 556 (1979); W. Morse *et al.*, Phys. Rev. D **21**, 1750 (1980); M. Campbell *et al.*, Phys. Rev. Lett. **47**, 1032 (1981); S. Blatt *et al.*, Phys. Rev. D **27**, 1056 (1983).

[39] R. Garisto and G. Kane, Phys. Rev. D **44**, 2038 (1991); G. Belanger and C. Q. Geng, Phys. Rev. D **44**, 2789 (1991).

[40] G.-H. Wu and J. Ng, TRI-PP-96-57, Oct. 1996, to be published in *Phys. Rev.*

[41] M. V. Diwan *et al.*, "Search for T-Violating Muon Polarization in $K^+ \to \mu^+\pi^0\nu_\mu$ Decay," AGS Proposal 923 (1996).

RECENT RESULTS FROM LEAR

Michael Doser
CERN/PPE
1211 Genève 23, Switzerland

ABSTRACT

Experiments running at LEAR have strongly contributed to many different fields of high-energy physics. The most recent results coming from two experiments in the final year of LEAR running will be presented, and I will indicate where they have improved our understanding of CP violation and of QCD at low energies.

CP, T, and CPT symmetries in the neutral kaon system are studied by the CPLEAR experiment by measuring the decay rates of neutral kaons as a function of the proper time τ. Many of the parameters of these symmetries are measured at a level rivaling the world averages, and some are measured for the first time.

Tests of QCD in the nonperturbative regime via searches for bound states outside of the standard quark model have a long history, but in spite of many observed candidates, no compelling experimental evidence was available until recently. Now however, strong indications exist for non-$\bar{q}q$ states in the scalar sector, and forthcoming data should allow an unambiguous assignment.

© 1996 by Michael Doser.

1. CPLEAR

The aim of the CPLEAR experiment is to study CP, T, and CPT symmetries in the neutral-kaon system. The CPLEAR experiment measures the decay rates of initially tagged neutral kaons as a function of the proper time τ. Physics parameters are extracted from the decay-rate asymmetries

$$A_f(\tau) = \frac{R(\overline{\mathrm{K}}^0 \to \overline{f}) - R(\mathrm{K}^0 \to f)}{R(\overline{\mathrm{K}}^0 \to \overline{f}) + R(\mathrm{K}^0 \to f)} \qquad (1)$$

where f is one of the final states $\pi^+\pi^-$, $\pi^0\pi^0$, $\pi^+\pi^-\pi^0$, $\pi^0\pi^0\pi^0$, and $\pi e\nu$. The asymmetry has the advantage of being only weakly dependent on detector efficiencies. The neutral kaons are produced in the reactions

$$\mathrm{p\overline{p}\ (at\ rest)} \ \to \ \begin{matrix} \mathrm{K^-\pi^+K^0} \\ \mathrm{K^+\pi^-\overline{K}^0}, \end{matrix}$$

with a branching ratio of $\approx 2 \times 10^{-3}$ each. The strangeness of the neutral kaon at its creation is defined by the reconstructed charged kaon.

A detailed description of the experiment can be found elsewhere.[1] Antiprotons of 200 MeV/c are stopped inside a high-pressure gaseous hydrogen target at a rate of about 10^6/s. The cylindrical detector is placed inside a solenoid of 1 m radius, 3.6 m length, which provides a magnetic field of 0.44 T. The tracking system consists of two proportional chambers, six drift chambers, and two layers of streamer tubes. Fast kaon identification is provided by a threshold Cherenkov counter sandwiched between two scintillators (also used for electron/pion separation). A lead/gas sampling calorimeter is used for photon detection. Fast and efficient online data selection is achieved with a multilevel trigger system based on custom-made hardwired processors. The cross section of the CPLEAR detector with a typical event ($\mathrm{K^0} \to \pi^+\pi^-$ decay) is shown in Fig. 1. As an example, from which one can extract the CP-violation parameters η_{+-} and ϕ_{+-}, the rate asymmetry $\mathrm{A_{+-}}$ for the decay to $\pi^+\pi^-$ is shown in Fig. 2 (τ_S is the $\mathrm{K_S}$ mean life).

The current status of the CPLEAR measurements is shown in Table 1 (Ref. 2). For the first time, a violation of T invariance has been directly determined. CPLEAR is able to disentangle CP- and CPT-violating quantities from each other. In many cases, the measurements of CPLEAR are comparable in precision to previous world averages.

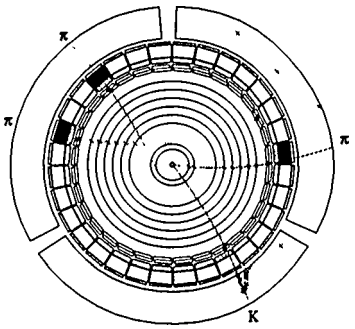


Fig. 1. *Typical CPLEAR event.*

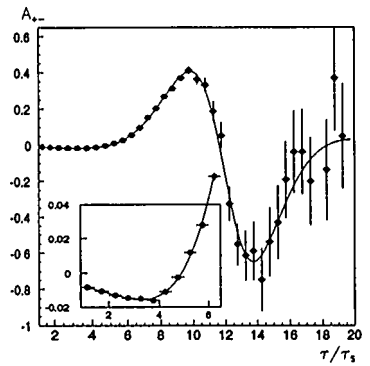


Fig. 2. *The asymmetry* A_{+-}.

Table 1. The current status of the CPLEAR measurements.

Δm	$(529.2 \pm 1.8_{stat} \pm 0.5_{syst})10^7 \hbar s^{-1}$	$\mathrm{K_L - K_S}$ mass difference
$\lvert\eta_{+-}\rvert$	$(2.316 \pm 0.025_{stat} \pm 0.030_{syst})10^{-3}$	CP violation
ϕ_{+-}	$(43.5 \pm 0.5_{stat} \pm 0.5_{syst} \pm 0.4_{\Delta m})^o$	Test of CPT invariance
$\lvert\eta_{00}\rvert$	$(2.49 \pm 0.40_{stat} \pm 0.23_{syst})10^{-3}$	CP violation
ϕ_{00}	$(51.7 \pm 7.1_{stat} \pm 1.5_{syst} \pm 0.4_{\Delta m})^o$	Test of CPT invariance
$Re\eta_{+-0}$	$(-4 \pm 8_{stat} \pm 2_{syst})10^{-3}$	CP violation in $\mathrm{K_S}$ domain
$Im\eta_{+-0}$	$(-3 \pm 10_{stat} \pm 2_{syst})10^{-3}$	CP violation in $\mathrm{K_S}$ domain
$Re\eta_{000}$	$0.15 \pm 0.30_{stat} \pm 0.04_{syst}$	CP violation in $\mathrm{K_S}$ domain
$Im\eta_{000}$	$0.29 \pm 0.40_{stat} \pm 0.03_{syst}$	CP violation in $\mathrm{K_S}$ domain
$\mathrm{A_T}$	$(6.3 \pm 2.1_{stat} \pm 1.8_{syst})10^{-3}$	Direct evidence for T violation
$\mathrm{A_{CPT}}$	$(0.28 \pm 2.1_{stat} \pm 1.8_{syst})10^{-3}$	Direct meas. of CPT invariance
Rex	$(8.5 \pm 7.5_{stat} \pm 6.9_{syst})10^{-3}$	Test of $\Delta S = \Delta Q$ rule
$Im(x+\delta)$	$(0.5 \pm 2.4_{stat} \pm 0.6_{syst})10^{-3}$	Test of $\Delta S = \Delta Q$ rule
α	$(-0.5 \pm 2.8)10^{-17}$ GeV	Test of Quantum Mechanics
β	$(2.5 \pm 2.3)10^{-19}$ GeV	Test of Quantum Mechanics
γ	$(1.1 \pm 2.5)10^{-21}$ GeV	Test of Quantum Mechanics

2. Crystal Barrel

The strong interaction is successfully described by Quantum Chromodynamics, but its distinctive feature—the self-interactions of gluons—has been tested only indirectly and only at high energies through multijet cross sections and angular distributions. At low energies, however, the expected multigluon bound states have been searched for unsuccessfully. If such a state is composed entirely of valence gluons (gg or ggg), the resulting meson is called a glueball; if it is composed of a mixture of valence quarks, antiquarks, and gluons (i.e., $q\bar{q}g$), it is called a hybrid. In addition, $q\bar{q}q\bar{q}$ states are also predicted. An unambiguous confirmation of these states would be an important test of QCD and would give fundamental information on the behavior of this theory in the nonperturbative region.

In the absence of exact calculations, the spectroscopy of the $q\bar{q}$ meson system can best be accounted for by QCD-inspired models. The most complete of these, built by S. Godfrey and N. Isgur[3] in 1985, is able to describe with sufficient accuracy the $q\bar{q}$ spectrum from the pion to the Υ. This model is therefore often used in order to test whether or not a newly discovered resonance belongs to one of the $q\bar{q}$ multiplets.

Recent advances in lattice gauge theory calculations[4] are beginning to shed light on ordering of states, mass scale, and widths of the glueball spectrum. The most recent predictions[4] for the lowest lying 0^{++} and 2^{++} glueballs give masses in the range 1500–1800 MeV and 2200–2500 MeV respectively, and a total width of the 0^{++} of 108 ± 29 MeV. The mass of the 0^{-+} state is predicted to be similar to that of the 2^{++}. While the absolute mass scale is still uncertain at the 10% level, mainly because of uncertainties due to finite lattice spacing, use of the quenched approximation and uncertainties in mapping the string tension to the mass scale, the mass ratio prediction is in line with previous values from various other theoretical models (MIT bag model, potential models, QCD sum rules, flux-tube model).[5] The mass ordering of states is thus: $0^{++} < 2^{++} \sim 0^{-+}$.

The strategy developed over the last years for finding glueballs is based essentially on the comparison of meson spectroscopy from different production mechanisms, with the most recent experimental input concentrating on 0^{-+}, 2^{++}, and 0^{++} states. Given that glueballs may mix with nearby $q\bar{q}$ states with the same quantum numbers, it has also become clear that it will not be possible to identify a glueball in isolation, but that any candidate state has to be understood in the context of the $\bar{q}q$ multiplet with the same J^{PC}. Before proceeding with the identification of a glueball, however, the composition of the corresponding $\bar{q}q$ multiplet must, of course, be known, and much of the discussion is centered on determining this composition.

3. The 0^{++} Multiplet

At present, the most active area in terms of glueball searches is the scalar sector, since the lowest lying glueball is predicted to be a scalar state around 1.5 GeV. Until recently, the number of low-mass scalar states was consistent with the expectations of the quark model. Using the Godfrey-Isgur model as a guide, one can tentatively assign the low-mass scalar states listed in the following table with those making up the 0^{++} multiplet. Although such an assignment is not necessarily unique, it has been shown by Törnqvist[6] that with very few parameters, one can fit the available data on the states in this assignment in the framework of a distorted 0^{++} $q\bar{q}$ nonet. The numbers in square brackets in the following table are the Godfrey-Isgur predictions for the masses (in MeV) for each state.

I=1	I=0	I=1/2
$a_0(980)$ [1090]	$f_0(975)$ [1090] $f_0(1300)$ [1360]	$K_0^*(1430)$ [1240]

This assignment has several problems, and new data suggest a modified composition of the 0^{++} nonet. Much controversy surrounds the $f_0(975)$ and $a_0(980)$, mostly due to the proximity of the $K\bar{K}$ threshold, which suggests that $a_0(980)$ and the $f_0(975)$ might be weakly bound $K\bar{K}$ systems ("molecules") or of other non-$\bar{q}q$ origin.[7] Also, the (mostly elastic) $f_0(1300)$ is seen strongly in further decay modes,[8] indicating at least one further isoscalar scalar state at this mass; in all observations, the dominant decay modes for this state are $\rho\rho$ and $\sigma\sigma$, and the further $\pi^0\pi^0$ and $\eta\eta$ decay modes amount to less than 20% of all decays (Ref. 9). Finally, the situation is confused by the large number of (often low statistics) observations of isoscalar-scalar states below 2 GeV, unfortunately all called "f_0," but with various masses and widths. Recent advances on the experimental and theoretical side have considerably clarified the situation.

3.1 $\pi\pi$ S Wave

The inflation of the number of isoscalar-scalar states coupling to $\pi\pi$ final states has underlined the importance of understanding the $\pi\pi$ S wave, in order to identify clearly the observed resonances (and thus construct the 0^{++} multiplet), and to understand their widths and couplings. Anisovich *et al.*[10] have performed a coupled channel analysis of the Crystal Barrel data[11] on $\bar{p}p \to \pi^0\pi^0\pi^0$, $\eta\eta\pi^0$, $\pi^0\pi^0\eta$ at rest, data on $\pi\pi$ scattering from GAMS[12] ($\pi p \to \pi^0\pi^0 n$), the CERN-Munich[13] ($\pi p \to \pi^+\pi^- n$), and the BNL[14] ($\pi N \to K\bar{K}n$), as well as the inelastic cross section for the $\pi\pi$ interaction[15] to determine the $\pi\pi$ S-wave amplitudes.

In their best fit, four T-matrix poles are found below 1550 MeV, with masses of 1008, 1290, and 1497 MeV as relatively narrow states [identified with the observed scalar states $f_0(975)$, $f_0(1370)$, and $f_0(1500)$—see below], along with a very broad state with a mass between 1300 and 1600 MeV and a width of about 600 MeV [identified with the elastic $f_0(1300)$]. This broad state (referred to as "σ") is needed to account for interferences in most of the above data sets.

The lightest state has a large $\bar{s}s$ component; its partner in the 0^{++} nonet could be the $f_0(1370)$, leaving the very broad state as the first (nonstrange quark) radial excitation ($2\ ^3P_0$), and the $f_0(1500)$ as the lightest glueball. This model predicts the existence of one further $\bar{s}s$-rich state in the region 1550–1850 MeV.

3.2 Experimental Situation: Isoscalar Scalars

Experimental information on the scalar sector comes mainly from new results from $\bar{p}p$ annihilation at rest and reanalysis of radiative J/ψ decays, with supporting information coming from $\gamma\gamma$ collisions and central and diffractive production.

The Crystal Barrel experiment has accumulated very large data samples in a large number of final states in the gluon-rich environment of $\bar{p}p$ annihilation. Partial wave analyses of individual final states, or coupled channel analyses of several final states, have led to the observation of two scalar states, the $f_0(1370)$ and the $f_0(1500)$. The $f_0(1370)$ has been seen as a very broad $(4\pi)^0$ enhancement in nucleon-antinucleon annihilation into five pions by several experiments.[8] The mass and width of this state are compatible with the $f_0(1300)$, but its decay modes—which are compatible with those expected for a $(u\bar{u} + d\bar{d})$ state in the same nonet as $K_0^*(1430)$—are not. This state decays mostly to $\rho\rho$ and $\sigma\sigma$, and to a lesser degree to $\pi^0\pi^0$ and $\eta\eta$ (Ref. 9).

In addition to this state, the Crystal Barrel group has observed a further new scalar state with a mass of 1500 MeV via its $\eta\eta$ and $\pi^0\pi^0$ decays. The band at 2.25 GeV^2 in the $3\pi^0$ Dalitz plot corresponds to the new state. The same scalar $f_0(1500)$ is seen in the $\pi\eta\eta$ Dalitz plot (Fig. 3) as the lower of the two diagonal bands (which correspond to states decaying into $\eta\eta$). In a coupled channel analysis, the following masses and widths for the two isoscalar-scalar resonances are found[16]

$$f_0(1370): \quad m = 1390 \pm 30 \text{ MeV}, \quad \Gamma = 380 \pm 80 \text{ MeV};$$
$$f_0(1500): \quad m = 1500 \pm 10 \text{ MeV}, \quad \Gamma = 154 \pm 30 \text{ MeV}.$$

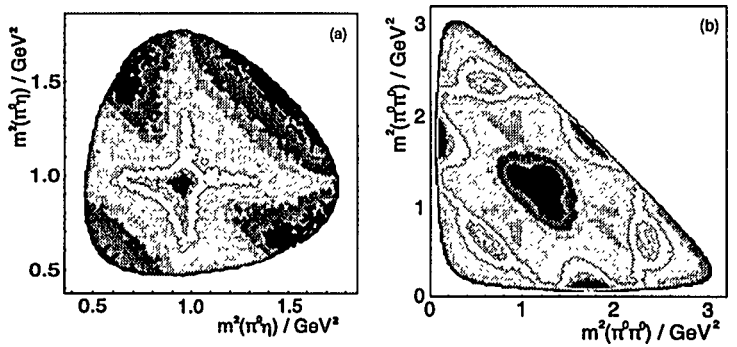


Fig. 3. *(a) Dalitz plot for $\pi^0\eta\eta$ events from the Crystal Barrel. Resonances in the $\eta\pi^0$ system are seen as horizontal and vertical bands, while resonances in the $\eta\eta$ system are seen as diagonal bands. The $f_0(1500)$ corresponds to the lower diagonal band; the $f_0(1370)$ to the upper diagonal band. (b) Dalitz plot for $3\pi^0$ events from the Crystal Barrel. The scalar amplitude $f_0(1500)$ corresponds to the narrow vertical band that crosses the Dalitz plot at $\sim$ 2.3 GeV^2 (and threefold symmetry).*

A state with values for mass and width consistent with those of the $f_0(1500)$ has also been observed in $\bar{p}p$ annihilation at 2.98 GeV (c.m. energy) by E-760 at Fermilab in the channels $\bar{p}p \to \pi^0\eta\eta$ and $\bar{p}p \to \pi^0\pi^0\pi^0$ (Ref. 17); the resulting values are

$$M = (1488 \pm 10 \text{ MeV, resp. } 1525 \pm 10 \text{ MeV}),$$
$$\Gamma = (148 \pm 17 \text{ MeV, resp. } 111 \pm 10 \text{ MeV}),$$

although until a partial wave analysis is performed, identification of either observation with the $f_0(1500)$ is based only on the similarity of the mass, width, and decay channels, and can thus only be tentative.

A third decay of the same state $f_0(1500)$ has been observed[18] in the channel $\bar{p}p \to \pi^0 f_0, f_0 \to \eta\eta'$ as a threshold enhancement. This enhancement is unlikely due to the decay $a_2 \to \eta'\pi^0$, since the corresponding decay $a_2 \to \eta\pi^0$ is not observed in $\pi^0\eta\eta$, and in fact, a spin-parity analysis of this $\eta\eta'$ resonance has confirmed the $f_0(1500)$ assignment.

More recently, the channel $\bar{p}p \to K_L K_L \pi^0$ has been observed [Fig. 5(b)] and a spin-parity analysis performed by the Crystal Barrel experiment.[19] Contrary to previous bubble chamber experiments which only gave an upper limit[20] for the presence of a scalar state at 1500 MeV, this analysis with strongly increased statistics finds a nonzero signal for $f_0(1500) \to \bar{K}K$. At the same time, the $\bar{K}K$ coupling of the $f_0(1370)$ is measured; interestingly, neither state couples strongly to $\bar{K}K$, and neither is thus dominantly $\bar{s}s$.

Finally, the same state is also observed to decay into four pions via intermediate two-pion resonances[21] in the process $\bar{p}p \to 5\pi^0$. By comparing the production of $f_0(1500)$ in all observed decay channels, one finds that the coupling to four pions (i.e., $\rho\rho$ and $\sigma\sigma$) is dominant over all other couplings. Correcting for phase space, the following decay pattern, which is not the one expected for a standard $q\bar{q}$ state, is obtained:

$$f_0(1500) \to \quad \pi\pi : \eta\eta : \eta\eta' : K\bar{K} : 4\pi = 3 : (0.72 \pm 0.37) : (1.05 \pm 0.44) : (0.72^{+0.49}_{-0.34}) : (10.2 \pm 2.4),$$

although these values are somewhat analysis dependent.

Given its many decay channels, it would be surprising if this scalar state $f_0(1500)$ had not been observed before. Although initial analyses of radiative J/ψ decay and central production either ruled out a state at 1500 MeV, or gave different spin parity assignments, recent reanalyses[22] of the same data show clear evidence for a scalar state in the same mass region of $\sim$ 1500 MeV and in several decay modes in radiative J/ψ decay. Supporting evidence comes from central production,[23] where a compatible signal is observed.

In the original analysis of $J/\psi \to \gamma 4\pi$, only $\rho\rho$ decays of a scalar state were allowed, while the reanalysis greatly improves the fit by also allowing $\sigma\sigma$. The fit gives a width of the $f_0(1500)$ of $\Gamma \sim 120$ MeV, and a production branching ratio $\mathrm{BR}(J/\psi \to \gamma X \to \gamma 4\pi) \sim 10^{-3}$.

The $f_0(1500)$ also appears in other final states in radiative J/ψ decays, in particular in Mark III and DM2 data on $J/\psi \to \gamma\pi^0\pi^0$, but also in more recent data from BES. Their $\pi^0\pi^0$ spectrum [Fig. 4(b)] based on 7 $\times 10^6$ J/ψ decays is fitted with five resonances at 1246 $\pm$ 31, 1477 $\pm$ 31, 1724 $\pm$ 36, 2042 $\pm$ 31, and 2230 $\pm$ 35 MeV (Ref. 24). Assigning the 1477 MeV signal in Fig. 4 (b) to the $f_0(1500)$ and taking the known production branching ratio of $4 \pm 0.4 \times 10^{-4}$ for $J/\psi \to \gamma f_2(1270) \to \gamma\pi^0\pi^0$, one obtains a production branching ratio for $J/\psi \to \gamma f_0(1500) \to \gamma\pi^0\pi^0$ of $\sim 2 \times 10^{-4}$. Using the Crystal Barrel couplings of the $f_0(1500)$ to different final states, one then arrives at an independent and consistent estimate for the production branching ratio $\mathrm{BR}(J/\psi \to \gamma X \to \gamma 4\pi) \sim 1 \times 10^{-3}$. Adding all further decay modes observed by the Crystal Barrel would then bring the total branching ratio for $\mathrm{BR}[J/\psi \to \gamma f_0(1500)]$ to $\sim 2 \times 10^{-3}$.

This (high) number allows one to draw conclusions on the nature of this state. Cakir and Farrar[25] have used semiperturbative QCD to derive a relationship between the branching fraction for a resonance in radiative quarkonium decay and its branching fraction into gluons. This analysis has been used in a recent paper by Close, Farrar, and Li[26] to analyze the $\bar{q}q$, respective gluon content of several resonances produced in radiative J/ψ production. In particular, a 0^{++} state with width $\Gamma \sim 100$ MeV should have a branching ratio of $\sim 0.2 \times 10^{-3}$. Branching ratios $\sim 10^{-3}$ require either a large width ($\sim$ 500 MeV) or a large gluonic content.

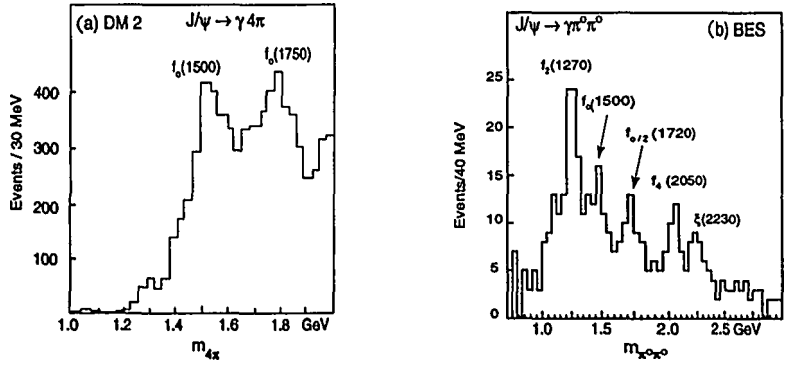


Fig. 4. *Radiative J/ψ decays: (a) Four-pion invariant mass spectrum from $J/\psi \to \gamma 4\pi$ from DM2. (b) Two π^0 invariant mass spectrum from $J/\psi \to \gamma 2\pi^0$ from BES. Both spectra indicate the presence of the $f_0(1500)$ in radiative J/ψ decays.*

The fact that QCD sum rules predict a suppression by one order of magnitude for scalar glueballs relative to tensor glueballs in radiative J/ψ production,[27] coupled to the paucity of the available statistics, explain the initial nonobservation of the $f_0(1500)$ in J/ψ radiative decays. In central production, on the other hand, a signal was observed,[28] but at a lower mass of 1450 MeV; this shift can be explained[23] by interference effects between the $f_0(1370)$ and the $f_0(1500)$. The upward shift in mass of the signal observed at 1590 MeV in $\pi^- p$ by GAMS[29] relative to the 1500 MeV of the $f_0(1500)$ is due to its observation in the final state $\eta\eta'$, where it appears just above the threshold for this channel. Its relative decays are mostly compatible with those of the $f_0(1500)$.

To summarize the isoscalar-scalar situation, recent analyses have shown the presence of two new 0^{++} states, the $f_0(1370)$ and the $f_0(1500)$, neither of which is dominantly $\bar{s}s$, in addition to the already well-known $f_0(980)$ and $f_0(1300)$, while the quark model predicts only two states in the mass region below 1500 MeV.

3.3 Experimental Situation: Isovector Scalars

In addition to the above two new states, the Crystal Barrel group has presented evidence[30] for a new isoscalar-scalar $\pi\eta$ resonance seen in a spin-parity analysis of a high-statistics Dalitz plot for the reaction $\bar{p}p \to \eta\pi^0\pi^0$. The pronounced interference pattern [Fig. 5(a)] is a reflection of the dominance of a single initial state, the $^1S_0$ state of the $\bar{p}p$ atom. The main structures of the Dalitz plot are a $\pi\pi$ S wave [$f_0(975)$ and $f_0(1370)$], an $\eta\pi$ D wave [$a_2(1320)$], and an $\eta\pi$ S wave. This $\eta\pi$ S wave consists of an $a_0(980)$, as well as $a_0(1450)$, although the latter is not observed directly in the $\eta\pi$ spectrum but is a necessary ingredient in the fit. Although the $\bar{K}K$ decay of the $a_0(1450)$ has been searched for in the process $\bar{p}p \to \pi^0 K_L K_L$, the experimental data are not sensitive to this state. This state has however been seen[31] in three other decay channels, $\pi^0 K_L K_L$, $\bar{p}p \to K^0 K^{\pm}\pi^{\mp}$, and $\pi^0\pi^0\eta'$. Fits of Crystal Barrel data on $\bar{p}p \to \eta'\pi^0\pi^0$ accommodate $2.8^{+3.3}_{-0.7}$ % of $a_0(1450) \to \eta'\pi^0$, corresponding to the branching ratios $a_0 \to \eta'\pi$ and $a_0 \to \eta\pi$ of $0.31^{+0.38}_{-0.14}$, whereas SU_3 would predict 0.38 ± 0.06.

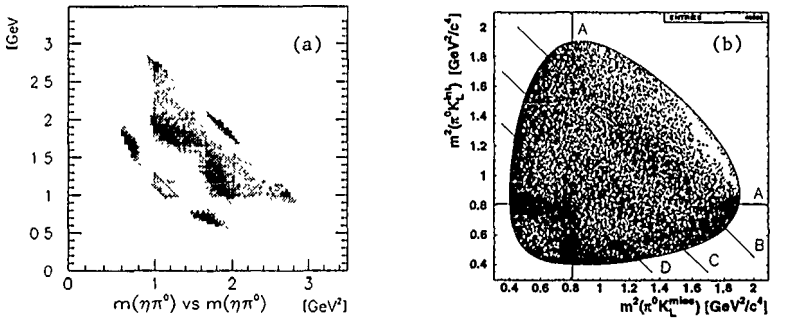


Fig. 5. *(a) Dalitz plot for $\eta\pi^0\pi^0$ events from the Crystal Barrel. (b) Dalitz plot for $\pi^0 K_L K_L$ events from the Crystal Barrel. The lines indicate the positions of the $K\pi$ resonance, $K^*(892)$ (line A), and of the $\bar{K}K$ resonances $f_2(1270)/a_2(1320)$, $f_0(1370)/a_0(1450)$, and $f_0(1500)/f_2(1525)$ (lines B, C, and D).*

3.4 Interpretation of the Scalar States

With the observation of three new scalar states [$f_0(1370)$, $f_0(1500)$, and $a_0(1450)$] in very high statistics experiments, the number of low-mass states exceeds that expected for the scalar nonet. The branching fractions of the $f_0(1370)$ and $f_0(1500)$ into $\pi\pi$, $\eta\eta$, $\eta\eta'$, and $\bar{K}K$ are both inconsistent with being dominantly $\bar{s}s$, and are consistent with both being mostly $\bar{u}u+\bar{d}d$ (although clearly, both cannot belong to the same scalar nonet), while the $\bar{s}s$ is not yet identified. The $f_0(1500)$ is unusual in that it is not observed in $\gamma\gamma$ collisions[32] (although the current upper limits are not sufficient to exclude a $\bar{q}q$ assignment) and in that it is relatively narrow ($\Gamma \sim 120$ MeV). In particular, its $\pi\pi$ partial width is of the order of 20 MeV, while $\bar{q}q$ states—like the $K^*(1430)$ with its dominant decay mode of $K\pi$—have a width of 290 MeV. It is this latter property, along with its various decay modes, that makes it very unlikely that it is the first radial excitation, i.e., the $2\ ^3P_0$ state. Drawing further conclusions requires comparing the properties of all scalar states with those expected for $q\bar{q}$ states individually and for the nonet as a whole, as well as for gg states.

Although several recent approaches, such as the unitarized quark model,[6] or the instanton model,[33] address this problem and are able to account for part of the experimental data, the resulting picture is incomplete since neither model

accounts for all observed states, nor their properties. In the latter, the $f_0(1500)$ is the $(u\bar{u}+d\bar{d})$ member of the scalar nonet (whose $\bar{K}K$ decay mode is suppressed), while the singlet (mostly $s\bar{s}$) state is the $f_0(980)$, leaving the $f_0(1370)$ unexplained. In the unitarized quark model, the roles of $f_0(1500)$ and $f_0(1370)$ are exchanged, leaving the $f_0(1500)$ isolated.

An alternative approach, developed by Amsler and Close,[34] makes testable predictions on couplings and masses of the scalar states. Assuming SU(3), the relative couplings of a $q\bar{q}$ state are calculated for different mixing nonet angles, and they find that seen in isolation, the couplings of the $f_0(1370)$ and of the $f_0(1500)$ are consistent with a dominantly $u\bar{u}+d\bar{d}$ composition. Assigning either state to the scalar nonet leaves the other state isolated and requires that the $\bar{s}s$ state, which has not yet been discovered, be heavier than the $f_0(1500)$. They show that the decay rates of the $f_0(1500)$ are compatible with those of a glueball state with mass intermediate between the $(\bar{u}u+\bar{d}d)$ and $\bar{s}s$ states of the multiplet, whose proximity in mass leads to mixing of the three scalar states. The state $f_0^{\bar{s}s}$ is predicted to lie in the mass range (1600–1800), and should couple mainly to $\bar{K}K$ and $\eta\eta'$. Due to mixing, the width of this state should be reduced relative to the widths of the $K^*(1430)$ or of the $a_0(1450)$. Similar conclusions are reached by V. Anisovitch *et al.*, who find that $f_0(975)$ and $f_0(1600–1800)$ could be the (dominantly) $\bar{s}s$ $1\,^3P_0$ and $2\,^3P_0$ members of the scalar $\bar{q}q$ nonets, while $f_0(1370)$, $f_0(1500)$, and $f_0(400–1400)$ could be a mix of (mostly non-$\bar{s}s$) $1\,^3P_0$, $2\,^3P_0$, and the lowest lying glueball. In their latest analysis,[35] they find that it is the broad resonance $f_0(400–1400)$ which contains the largest (40–50%) glueball component, with the remainder being shared among the narrower resonances $f_0(1370)$ and $f_0(1500)$, which are then mostly the $1\,^3P_0$ and $2\,^3P_0$ states.

4. Conclusions

CPLEAR has directly determined, for the first time, a violation of T invariance and is able to disentangle CP- and CPT-violating quantities from each other. This allows, in particular, the mass and width equality between the K^0 and $\overline{K}^0$ to be tested down to the level of 10^{-19} GeV. Moreover, the precision of the CPLEAR measurements allows us to probe for the first time physics on a scale approaching the Planck mass.

The recent observations of at least three scalar states [$f_0(1370)$, $f_0(1500)$, and $a_0(1450)$] in very high statistics and large acceptance experiments have contributed to a reappraisal of the scalar nonet. Given the masses, widths, and decay patterns of these scalars, it is possible to propose an assignment for the scalar nonet which consists of the mostly $u\bar{u}+d\bar{d}$ isoscalar $f_0(1370)$, and the isovector $a_0(1450)$, whose masses and widths are comparable to the strange member of the scalar nonet, the $K^*(1430)$. The $f_0(1500)$, on the other hand, has a very different and much smaller width than any of these states, but its decays are not those one would naively expect for a glueball. In the model of Amsler and Close, this state is a glueball, but is mixed with the $q\bar{q}$ states in the nonet, both the $f_0(1370)$ and a mostly $s\bar{s}$ isoscalar state, which remains to be discovered. The characteristics of this predicted state (mass, width, and decay pattern) are strongly constrained by this model.

Crucial tests of this assignment are the determination of the nature of the $f_0(975)$, for example, in radiative decays of the ϕ to $f_0(975)$ (Ref. 36), confirmation of the $a_0(1450)$ seen by the Crystal Barrel, a reduction of the systematic errors for the $K\bar{K}$ coupling of the $f_0(1350)$ and $f_0(1500)$ seen by the Crystal Barrel and possibly by E-760, and finally, a detection and study of the predicted $f_0^{\bar{s}s}(1600–1800)$. Given this list of open questions, it is natural that kaonic final states dominate the agenda for the final year of spectroscopy at LEAR.

References

[1] R. Adler *et al.*, Nucl. Instrum. Methods A **379**, 76 (1996).

[2] P. Pavlopoulos, in *Proceedings of the Kaon Workshop*, Orsay, June 1996, and references therein.

[3] S. Godfrey and N. Isgur, Phys. Rev. D **32**, 189 (1985).

[4] G. S. Bali *et al.* (UKQCD Collaboration), Phys. Lett. B **309**, 378 (1993);
J. Sexton, A. Vaccarino, and D. Weingarten, Phys. Rev. Lett. **75**, 4563 (1995);
Nucl. Phys. B (Proc. Suppl.) **42**, 279 (1995);
C. Michael and M. Teper, Nucl. Phys. B **314**, 347 (1989).

[5] See, for example, F. Close, Rep. Prog. Phys. **51**, 833 (1988) for a general review.

[6] N. Törnqvist, Z. Phys. C **68**, 647 (1995).

[7] J. Weinstein and N. Isgur, Phys. Rev. Lett. **48**, 659 (1982); Phys. Rev. D **27**, 588 (1983); Phys. Rev. D **41**, 2236 (1990).

[8] M. Gaspero, Nucl. Phys. A **562**, 407 (1993); Obelix Collaboration, in *Proceedings of Hadron '93*, Como, Italy, June 1993; C. Amsler *et al.*, Phys. Lett. B **322**, 431 (1994).

[9] V. V. Anisovich *et al.* (Crystal Barrel Collaboration), Phys. Lett. B **323**, 233 (1994).

[10] V. V. Anisovich and A. V. Sarantsev, Phys. Lett. B **382**, 429 (1996).

[11] V. A. Anisovich *et al.* (Crystal Barrel), Phys. Lett. B **323**, 233 (1994); C. Amsler *et al.*, Phys. Lett. B **342**, 433 (1995).

[12] A. A. Kondashov *et al.*, in *Proceedings of the 27th International Conference on High Energy Physics* (Glasgow, 1994), p. 1407.

[13] B. Hyams *et al.*, Nucl. Phys. B **64**, 134 (1973).

[14] S. J. Lindenbaum and R. S. Longacre, Phys. Lett. B **274**, 492 (1992); A. Etkin *et al.*, Phys. Rev. D **25**, 1786 (1982).

[15] M. Alston-Garnjost *et al.*, Phys. Lett. B **36**, 152 (1971).

[16] C. Amsler *et al.*, Phys. Lett. B **355**, 425 (1995).

[17] T. A. Armstrong *et al.*, Phys. Lett. B **207**, 394 (1993); T. A. Armstrong *et al.*, Phys. Lett. B **207**, 399 (1993).

[18] C. Amsler *et al.*, Phys. Lett. B **340**, 259 (1995).

[19] C. Amsler *et al.*, Phys. Lett. B **385**, 425 (1996).

[20] L. Gray *et al.*, Phys. Rev. D **27**, 307 (1983).

[21] C. Amsler *et al.*, Phys. Lett. B **380**, 453 (1996).

[22] D. Bugg *et al.*, Phys. Lett. B **353**, 378 (1995).

[23] F. Antinori *et al.*, Phys. Lett. B **353**, 589 (1995).

[24] L. Jin, in *Proceedings of the International Conference on High-Energy Physics* (Warsaw, 1996).

[25] M. B. Cakir and G. Farrar, Phys. Rev. D **50**, 3268 (1994).

[26] F. Close, G. Farrar, and Z. P. Li, "Determining the gluonic content of isoscalar mesons," RAL-96-052, hep-ph/9610280.

[27] V. A. Novikov, M. A. Shifman, A. I. Vainshtein, and V. I. Zakharov, Nucl. Phys. B **165**, 55, 67 (1980); B **191**, 301 (1981).

[28] A. Palano *et al.*, Nucl. Phys. B (Proc. Suppl.) **21**, 49 (1991).

[29] D. Alde *et al.*, Nucl. Phys. B **269**, 485 (1986).

[30] C. Amsler *et al.*, Phys. Lett. B **333**, 277 (1994).

[31] S. Dombrowski, in *Proceedings of the LEAP'96 Conference* (Dinkelsbühl, 1996); S. Resag, in *Proceedings of the LEAP'96 Conference* (Dinkelsbühl, 1996); S. Spanier, in *Proceedings of the LEAP'96 Conference* (Dinkelsbühl, 1996).

[32] M. Feindt and J. Harjes, Nucl. Phys. B (Proc. Suppl.) **21**, 61 (1991), and references therein.

[33] E. Klempt, B. Metsch, C. Munz, and H. Petry, Phys. Lett. B **361**, 160 (1995).

[34] C. Amsler and F. Close, Phys. Rev. D **53**, 295 (1996).

[35] A. V. Anisovich, V. A. Anisovich, and A. V. Sarantsev, "0^{++}-glueball/$\bar{q}q$ mixing in the mass region near 1500 MeV," hep-ph/9611333.

[36] J. Lee-Franzini *et al.*, in *Proceedings of the 27th International Conference on High-Energy Physics* (Glasgow, 1994).

Search for Exotic Mesons in BNL E852

N. Cason

University of Notre Dame
Department of Physics
Notre Dame, IN 46556

No submission is currently available from the author.

PHYSICS AT THE Z POLE WITH SLD

Stéphane Willocq*
Stanford Linear Accelerator Center
Stanford University, Stanford, California 94309

Representing the SLD Collaboration

ABSTRACT

We review recent results from a wide physics program in polarized e^+e^- interactions at the SLC performed by the SLD experiment. Unique and precise measurements of the electroweak parameters A_e, A_b, A_c, and R_b provide valuable constraints on the Standard Model. The excellent 3-D vertexing capabilities of SLD are further exploited to extract precise B^+ and B_d^0 lifetimes, as well as measurements of the time evolution of $B_d^0 - \overline{B_d^0}$ mixing. Finally, the unique capabilities of the SLC/SLD are used to test QCD in new ways. We present results on general properties of particle production in light, c, and b quark events, as well as the first observation of leading particle production in light-quark hemispheres.

*Work supported in part by DOE Contract DE-AC03-76SF00515(SLAC).

©1996 by Stéphane Willocq.

The various measurements presented below rely on the strengths of the SLC and SLD environment. Most important is the fact that the electrons are longitudinally polarized at the interaction point. Average polarizations of $(63.0 \pm 1.1)\%$ and $(77.2 \pm 0.5)\%$ were measured during the 1993 and 1994–95 data taking periods with a Compton Polarimeter. The numbers of hadronic Z^0 decays collected during these periods are approximately 50,000 and 100,000 respectively. Charged particles are tracked and momentum-analyzed by the Central Drift Chamber. The location of these tracks is measured precisely with a pixel-based CCD Vertex Detector. The calorimetry consists of the Liquid Argon Calorimeter (LAC) and the Warm Iron Calorimeter (WIC). The LAC is utilized in the trigger and to reconstruct the event shape (thrust axis and jet finding). It is also used to identify electrons. The WIC is used primarily as a muon finder. Further particle identification is provided by the Cherenkov Ring Imaging Detector which allows separation between π, K, and p over most of the momentum range.

The paper is organized as follows: Electroweak results are described in Sec. 1 with emphasis on the left-right and heavy quark asymmetries. In Sec. 2, two B physics topics are discussed: B^+ and B_d^0 lifetimes, followed by time-dependent B_d^0–$\overline{B_d^0}$ mixing. Several QCD particle production studies are presented in Sec. 3. Finally, a brief summary is given in Sec. 4.

1 Electroweak Physics

In the Standard Model (SM), the $Z^0 \to f\bar{f}$ interaction is governed by a Lagrangian term of the form

$$\frac{-g}{2\cos\theta_W}\,\bar{\psi}\gamma^\mu\left(g_V - g_A\gamma_5\right)\psi Z_\mu, \tag{1}$$

where the vector and axial-vector current coupling constants g_V and g_A are related to the fermion charge Q_f and the third component of its weak isospin T_f^3, as well as the value of $\sin^2\theta_W^{eff}$ as follows:

$$g_V = T_f^3 - 2Q_f \sin^2\theta_W^{eff}\,, \tag{2}$$

$$g_A = T_f^3\,. \tag{3}$$

The differential cross section for $e^+e^- \to Z^0 \to f\bar{f}$ is expressed by

$$\frac{d\sigma}{d\cos\theta} = (1 - P_eA_e)\left(1 + \cos^2\theta\right) + 2\cos\theta\,(A_e - P_e)\,A_f, \tag{4}$$

where $\cos\theta$ is the cosine of the angle between the final state fermion f and the incident electron directions, P_e is the electron beam longitudinal polarization, and A_e and A_f are the asymmetry parameters for the initial and final state fermions, respectively. The asymmetry parameter for a given fermion represents the extent of parity violation at the $Z^0 \to f\bar{f}$ vertex and is defined as

$$A_f = \frac{2g_Vg_A}{g_V^2 + g_A^2} = \frac{g_L^2 - g_R^2}{g_L^2 + g_R^2}, \tag{5}$$

with the left- and right-handed coupling constants $g_L = \frac{1}{2}(g_V + g_A)$ and $g_R = \frac{1}{2}(g_V - g_A)$.

The presence of parity violation introduces a forward-backward asymmetry $A_f^{FB} = \frac{\sigma_f^F - \sigma_f^B}{\sigma_f^F + \sigma_f^B}$ which is equal to $\frac{3}{4}A_eA_f$. At the SLC, the electron beam polarization allows a polarized forward-backward asymmetry to be measured

$$\tilde{A}_f^{FB} = \frac{\left[\sigma_f^F - \sigma_f^B\right]^{\text{left}} - \left[\sigma_f^F - \sigma_f^B\right]^{\text{right}}}{\left[\sigma_f^F + \sigma_f^B\right]^{\text{left}} + \left[\sigma_f^F + \sigma_f^B\right]^{\text{right}}} = \frac{3}{4}P_eA_f. \tag{6}$$

The latter asymmetry provides a *direct* measurement of A_f and yields a statistical enhancement factor of $(P_e/A_e)^2$ over the unpolarized forward-backward asymmetry. This relative enhancement is roughly equivalent to a statistical gain of 25 at the SLC.

Another interesting asymmetry is the left-right cross-section asymmetry

$$A_{LR}^0 = \frac{\sigma_L - \sigma_R}{\sigma_L + \sigma_R} = A_e, \tag{7}$$

which yields a direct measurement of the coupling between the Z^0 and the e^+e^- initial state.

Measurements of partial Z^0 decay widths also provide information regarding the $Z^0 \to f\bar{f}$ couplings. The ratio between the partial decay width into a particular final state fermion and that into any hadron is sensitive to the left- and right-handed coupling constants g_L and g_R of fermion f

$$R_f = \frac{\Gamma(Z \to f\bar{f})}{\Gamma(Z \to \text{hadrons})} \propto g_L^2 + g_R^2\,. \tag{8}$$

Precise measurements of the asymmetry parameters A_f and the partial widths R_f can probe the effect of radiative corrections to the Z^0 propagator or to the $Zf\bar{f}$ vertex. Since the radiative corrections depend on the top and Higgs masses,

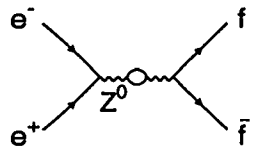


Figure 1: Feynman diagram showing radiative corrections affecting the Z^0 propagator.

precise electroweak measurements can measure or constrain these quantities. Furthermore, such measurements also are sensitive to physics beyond the SM. It is important to measure A_f and R_f for individual fermions since the coupling strengths differ due to differences in electric charge and weak isospin as indicated in Eqs. (2) and (3). Vacuum polarization corrections (Fig. 1) affect the value of $\sin^2\theta_W^{eff}$ which is most precisely measured by the left-right asymmetry

$$A_{LR}^0 = A_e = \frac{2\left[1-4\sin^2\theta_W^{eff}\right]}{1+\left[1-4\sin^2\theta_W^{eff}\right]^2}. \qquad (9)$$

Heavy quark partial widths and asymmetry parameters are most sensitive to vertex corrections (Fig. 2) but with different sensitivity to left- and right-handed coupling constants. In particular, since $g_L^2 \simeq 30\, g_R^2$ for b quarks, R_b is most

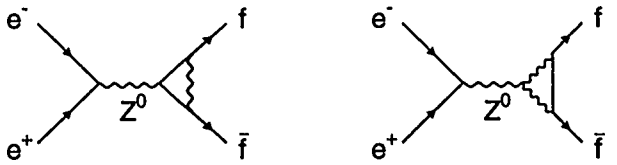


Figure 2: Feynman diagrams showing radiative corrections affecting the Z^0 coupling to the final state fermions.

sensitive to deviations in the left-handed coupling between the Z^0 and b quarks, whereas A_b is more sensitive to deviations in the right-handed coupling. Moreover, vertex corrections involving the top quark only affect the left-handed coupling, in the context of the SM.

1.1 Polarization at the SLC

As indicated above, many unique and powerful measurements can be performed at the SLC by exploiting the high polarization of the electron beam. Here we only summarize the polarization process; further details may be obtained elsewhere.[1] Electrons are photo-emitted from a strained-lattice GaAs photo-cathode using a Ti-Sapphire laser operating at $\lambda = 849$ nm. The laser beam is circularly polarized to produce either left- or right-handed electrons with maximum polarization near 80%. The polarization sign is randomly flipped from pulse to pulse. The polarization axis is rotated to be vertical for the acceleration and damping phases. At the end of the linac, the polarization axis is rotated by a series of betatron oscillations such that it is longitudinal at the e^+e^- Interaction Point (IP).

The electron beam longitudinal polarization is measured 33 m downstream of the IP by a Compton Polarimeter. A Nd:YAG laser produces circularly polarized photons with an energy of 2.33 eV, which are brought to collision with the electron beam. The part of the beam which undergoes Compton scattering is momentum-analyzed with a dipole magnet and detected in a Cherenkov counter. The electron beam polarization is extracted by measuring the asymmetry between parallel and antiparallel configurations of the electron and photon helicities. The polarimeter yields a measurement every three minutes with statistical accuracy near 1%. Two-thirds of the data collected in 1994–95 were dedicated for various calibration checks of the polarimeter. These special runs allow careful control of the systematic uncertainties in the measured polarization. The overall relative systematic uncertainty is estimated to be $\delta P_e/P_e = 1.59\%$ for the 1993 run and 0.67% for the 1994–95 run. The various contributions to this uncertainty are summarized in Table 1; Cherenkov counter linearity is the dominant contribution.

1.2 Left-Right Cross-Section Asymmetry

The measurement of A_{LR} is a simple counting experiment.[2] One needs to count the number of Z^0 produced with left- and right-handed electron beams, and measure the average electron beam polarization. The event selection relies on the Liquid Argon Calorimeter (LAC) and the Central Drift Chamber (CDC) which are also used for the trigger. The selection criteria are chosen to remove two-photon and beam-related background events as well as Z^0 events decaying into e^+e^- final states for which the cross section includes $t-$channel contributions that dilute

Uncertainty	$\delta P_e/P_e$ (%)
Laser polarization	0.20
Detector linearity	0.50
Detector calibration	0.29
Electronic noise	0.20
Compton - IP difference	0.17
Total	0.67

Table 1: Contributions to the polarization systematic uncertainty (1994–95 run).

the left-right asymmetry. The event sample then mostly consists of hadronic Z^0 decays selected with an efficiency of $(89 \pm 1)\%$. In the 1994–95 data, the number of selected events is 52,179 and 41,465 for left- and right-handed electrons respectively. The resulting measured asymmetry is thus $A_m = (N_L - N_R)/(N_L + N_R) = 0.1144 \pm 0.0032(\text{stat})$. To obtain the left-right cross-section asymmetry at the SLC center-of-mass energy of 91.28 GeV, a very small correction $\delta = (0.240 \pm 0.055)\%(\text{syst})$ is applied which takes into account residual contamination in the event sample and slight beam asymmetries. As a result,

$$A_{LR}(91.28\ \text{GeV}) = \frac{A_m}{\langle P_e \rangle}(1+\delta) = 0.1485 \pm 0.0042(\text{stat}) \pm 0.0010(\text{syst}), \quad (10)$$

where the systematic uncertainty is dominated by our systematic understanding of the beam polarization (see Table 1). Finally, this result is corrected for initial and final state radiation as well as for scaling the result to the Z^0 pole energy:

$$A_{LR}^0 = 0.1512 \pm 0.0042(\text{stat}) \pm 0.0011(\text{syst}), \quad (11)$$

$$\sin^2\theta_W^{eff} = 0.23100 \pm 0.00054(\text{stat}) \pm 0.00014(\text{syst}). \quad (12)$$

The 1994–95 measurement can be combined with previous measurements from the 1992 and 1993 running periods[3,4] to yield

$$A_{LR}^0 = 0.1543 \pm 0.0039, \quad (13)$$

$$\sin^2\theta_W^{eff} = 0.23060 \pm 0.00050. \quad (14)$$

The above represents the most precise measurement of $\sin^2\theta_W^{eff}$ by a single experiment.

Analysis	Asymmetry
$\mu\mu$ and $\tau\tau$	$A_e = 0.148 \pm 0.016$
$\mu\mu$	$A_\mu = 0.102 \pm 0.033$
$\tau\tau$	$A_\tau = 0.190 \pm 0.034$
ee Bhabha (Ref. 6)	$A_e = 0.202 \pm 0.038$
Q_{LR} (Ref. 7)	$A_e = 0.162 \pm 0.043$
A_{LR}	$A_e = 0.1543 \pm 0.0039$
Combined	$A_l = 0.1542 \pm 0.0037$

Table 2: Lepton asymmetry parameter measurements from various analyses.

1.3 Lepton Asymmetries

Further information about $\sin^2\theta_W^{eff}$ can be obtained from events with Z^0 decaying into a pair of charged leptons (μ or τ). Here, the $\cos\theta$ dependence of the differential cross section is used (see Eq. 4) and both initial and final state asymmetry parameters can be extracted, i.e., A_e and either A_μ or A_τ. Since the event selection for the left-right asymmetry analysis has poor efficiency for nonhadronic Z^0 decays, analyses utilizing $\mu^+\mu^-$ and $\tau^+\tau^-$ final states are statistically independent.

The event selection employs information from the tracking and calorimetry systems to reject $Z^0 \to e^+e^-$, $Z^0 \to$ hadrons, and two-photon events. Using data from 1993 through 1995, a total of 3,788 events is selected in the $\mu^+\mu^-$ analysis and 3,748 events in the $\tau^+\tau^-$ analysis with respective efficiencies of 95% and 89%. The main background to the $\mu^+\mu^-$ sample originates from $\tau^+\tau^-$ events (0.4%), whereas the background to the $\tau^+\tau^-$ sample comes mainly from Z^0 decays into $\mu^+\mu^-$ (4%) and e^+e^- (1%).

The preliminary results[5] from this analysis are presented in Table 2. Other measurements of lepton asymmetry parameters are also listed for completeness. The uncertainties in all these different measurements are dominated by statistics. If lepton universality is assumed, the measurements may be combined to yield

$$A_l = 0.1542 \pm 0.0037, \quad (15)$$

$$\sin^2\theta_W^{eff} = 0.23061 \pm 0.00047. \quad (16)$$

This value of $\sin^2\theta_W^{eff}$ can be compared with the LEP average[8] of 0.23157 ± 0.00042,

obtained from lepton forward-backward asymmetries and τ polarization measurements. The SLD and LEP lepton averages agree within 1.5 σ.

1.4 Heavy Quark Asymmetries

Measurements of the heavy quark asymmetry parameters A_b and A_c provide complementary information to that obtained from the precise left-right asymmetry measurement. As pointed out earlier, A_b and A_c are particularly sensitive to vertex corrections. Extraction of pure samples of heavy quark events is greatly aided by two unique features of the SLC/SLD. First, the transverse dimensions of the SLC luminous region is of order of 1 μm^2 and the interaction point is very stable over time. Second, SLD is equipped with a high-resolution pixel CCD Vertex Detector[9] (VXD) which provides true three-dimensional information and a single hit resolution of 5.6 μm in the $r\phi$ plane (transverse to the beam axis) and 6.2 μm in the rz plane (containing the beam axis). The inner VXD radius is 2.95 cm and there is a minimum of two hits per track within $|\cos\theta| < 0.74$—the average number of hits is 2.3. Tracking is performed by combining information from the CDC[10] with that from the VXD. The combined impact parameter resolution at high momentum is determined from $Z^0 \to \mu^+\mu^-$ decays to be $\sigma(r\phi) = 11$ μm and $\sigma(rz) = 37$ μm. Multiple scattering yields an additional momentum-dependent contribution parameterized as $\sigma = 70\ \mu\text{m}/(p\ \sin^{3/2}\theta)$, where the momentum p is expressed in GeV/c. The transverse position of the IP is determined using samples of $\sim$ 30 consecutive hadronic Z^0 decays with an accuracy of 7 ± 2 μm. The longitudinal IP position is determined on an event-by-event basis with an accuracy of 32 μm for Z^0 decays into light-flavor quarks (uds), 36 μm for $Z^0 \to c\bar{c}$ decays, and 52 μm for $Z^0 \to b\bar{b}$ decays, as determined from the Monte Carlo (MC). Detailed description of the procedures and performance of the tracking system may be found elsewhere.[11]

Another (almost) unique feature of the SLD is the Cherenkov Ring Imaging Detector[12] (CRID) which allows charged particle identification over most of the momentum range. The CRID contains both a liquid radiator and a gas radiator system (see Fig. 3). The liquid radiator provides low momentum identification with π/K (K/p) separation up to $\sim$ 4 GeV/c ($\sim$ 8 GeV/c), whereas the gas radiator provides π/K (K/p) separation above $\sim$ 2.5 GeV/c ($\sim$ 9 GeV/c).

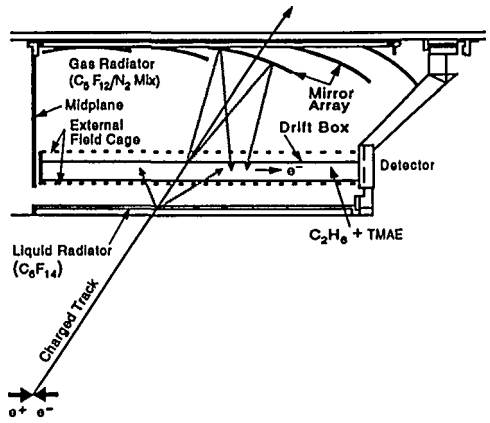


Figure 3: Cross-section view of one CRID quadrant.

Three different techniques have been used to measure the b-quark asymmetry parameter A_b. These differ mostly by the method used to determine which hemisphere contains the primary b-quark: jet charge, kaon charge, or lepton charge. The first step (after hadronic event selection) in each analysis is to tag $Z^0 \to b\bar{b}$ events either by requiring that the number of tracks with two-dimensional impact parameter greater than 3 σ be greater or equal to three, or by utilizing the fact that leptons from B hadron decays have harder p and p_T (with respect to the jet axis) distributions than those from other processes.

A_b is determined with a fit to the $\cos\theta$-dependent differential cross section [Eq. (4)] with the electron beam polarization as input. The thrust axis direction is used to provide the primary quark axis, except for the lepton analysis which uses the jet axis.

1.4.1 A_b with Jet Charge

The first step of the analysis is the selection of $Z^0 \to b\bar{b}$ events by requiring the event to contain at least three tracks with signed normalized $r\phi$ impact parameter $\delta/\sigma_\delta > 3$. This yields a sample with a $b\bar{b}$ purity of 89% and an efficiency of 61%. The $b/\bar{b}$ tag is provided by a momentum-weighted track charge defined as

$$Q_{\text{diff}} = Q_b - Q_{\bar{b}} = -\sum Q_{\text{track}} \left|\vec{p}\cdot\hat{T}\right|^\kappa \text{sign}\left(\vec{p}\cdot\hat{T}\right), \qquad (17)$$

where $\vec{p}$ is the three-momentum of each track and $Q_{\rm track}$ its charge, $\hat{T}$ is the direction of the event thrust axis, signed such as to make $Q_{\rm diff} > 0$, and the coefficient $\kappa = 0.5$ is chosen to maximize the analyzing power of the tag. The quantity $Q_{\rm diff}$ represents the difference between the momentum-weighted charges in the two event hemispheres—separated by the plane perpendicular to the thrust axis. $\hat{T}$ is thus an estimate of the b-quark direction. This tag is commonly referred to as "jet charge". A quantity related to $Q_{\rm diff}$ is the sum of the momentum-weighted charges in the two hemispheres defined as

$$Q_{\rm sum} = Q_b + Q_{\bar{b}} = \sum Q_{\rm track} \left|\vec{p} \cdot \hat{T}\right|^{\kappa}. \tag{18}$$

Due to its high efficiency ($\sim$ 100%), the jet charge tag lends itself to self-calibration, i.e., the analyzing power of the $b/\bar{b}$ tag can be determined directly from the data which reduces the systematic sensitivity to $Z^0 \to b\bar{b}$ modeling in the MC. The self-calibration is performed by comparing the momentum-weighted charges in the two hemispheres or more specifically by comparing the widths of the $|Q_{\rm diff}|$ and $|Q_{\rm sum}|$ distributions. If we make the (excellent) assumption that the momentum-weighted charge obeys a Gaussian distribution, the probability to correctly tag the primary $b/\bar{b}$ quark becomes

$$P_{\rm correct} = \frac{1}{1 + e^{-\alpha_b |Q_{\rm diff}|}}, \tag{19}$$

where the constant α_b is defined in terms of the widths $\sigma_{\rm diff}$ and $\sigma_{\rm sum}$ as determined from the distributions of $|Q_{\rm diff}|$ and $|Q_{\rm sum}|$ observed in the data

$$\alpha_b = \frac{2\sqrt{2\left(\sigma_{\rm diff}/\sigma_{\rm sum} - 1\right)}}{\sigma_{\rm sum}}, \tag{20}$$

$$= 0.253 \pm 0.013 \quad \text{for 1993–95 data.} \tag{21}$$

The average correct tag probability is thus $\langle P_{\rm correct} \rangle = 68\%$. The expression for α_b is modified slightly to take into account correlations between the two hemispheres. The correlation is estimated to be 2.9% by the Monte Carlo simulation. It arises mostly from the correlation between the total charges of the two hemispheres imposed by charge conservation in the event as a whole.

The forward-backward asymmetries obtained for left- and right-handed electron beams are shown in Fig. 4. The magnitude of the asymmetry is clearly more pronounced for the 1994–95 data than for the 1993 data, as expected from the increase in beam polarization for the 1994–95 data. A likelihood analysis using a $|Q_{\rm diff}|$-dependent analyzing power derived from Eq. (19) and including a $\cos\theta$-dependent QCD correction yields

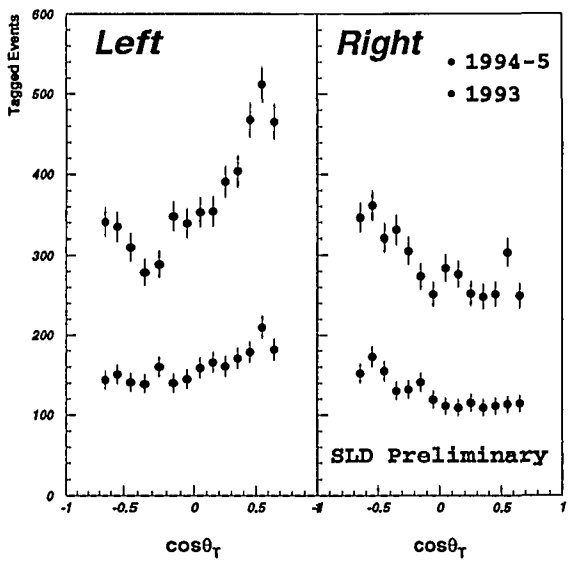


Figure 4: Distributions of the thrust axis $\cos\theta$ for left- and right-handed electron beams. The lower (upper) set of points correspond to 1993 (1994–95) data.

$$A_b = 0.843 \pm 0.046(\text{stat}) \pm 0.051(\text{syst}). \tag{22}$$

The main contributions to the systematic error are: (i) $\delta A_b/A_b = 3.7\%$ from uncertainties in the magnitude of the hemisphere correlation, as determined by comparing different fragmentation models (JETSET 7.4 and HERWIG 5.7); (ii) $\delta A_b/A_b = 3.0\%$ from the statistical uncertainty in determining the value of α_b from the 1993–95 data; (iii) $\delta A_b/A_b = 2.6\%$ from the uncertainties in the event sample composition after the $b\bar{b}$ event tag (mostly uncertainty in R_c).

1.4.2 A_b with Kaons

This analysis proceeds with the same $b\bar{b}$ event tag as the Jet Charge analysis but differs in the technique used to perform the $b/\bar{b}$ tag. Here the tag exploits the dominant $b \to c \to s$ transition in B decays. Therefore, detection of K^- (K^+) mesons tags b ($\bar{b}$) quarks. Right-sign kaon production has been measured by ARGUS[13] in B^+ and B_d^0 decays to be $(85 \pm 5)\%$ and $(82 \pm 5)\%$ respectively. Some dilution is expected due to $b \to c\bar{c}s$ transitions and $s\bar{s}$ production in B or D decays. The analysis presented here is the first application of kaon tagging for a heavy quark asymmetry measurement.

Charged kaon track candidates are required to have signed $r\phi$ normalized impact parameter $\delta/\sigma_\delta > 1.5$ and $3 < p < 20$ GeV/c. These cuts select B decay products preferentially. Kaons are identified with the CRID (gas radiator only). The main uncertainty in the identification comes from knowledge of the rate of charged pions misidentified as kaons. An overall $\pi \to K$ misidentification rate of 7.2% is measured using pure samples of pions from one-prong and three-prong τ decays for which the true $K^\pm$ component is well-measured and small. The cuts yield a sample with 75% kaon purity.

Figure 5 shows the distribution of the cosine of the angle between the thrust axis and the electron beam directions signed by the tagging variable Q_K. This quantity is obtained by computing the difference between the sum of kaon charges in each hemisphere: $Q_K = \sum_i^{Hemi1} Q_i - \sum_j^{Hemi2} Q_j$, where Q_i is the charge of kaon track i. As a result, 30% of the selected events are tagged with a correct $b/\bar{b}$ tag probability estimated to be 71% from the Monte Carlo simulation. A clear forward-backward asymmetry is observed in Fig. 5 (the analysis was only applied to the 1994–95 data). The non-$b\bar{b}$ background is dominated by $c\bar{c}$ events and displays a similar asymmetry to the signal asymmetry. The $b/\bar{b}$ tag analyzing power in the MC is cross-checked in events with a kaon tag in each hemisphere. The fraction with opposite kaon charges is found to be $62.4 \pm 2.9\%$ in the data, in excellent agreement with a fraction of $61.9 \pm 1.5\%$ in the MC.

The measurement of A_b is derived by comparing data and Monte Carlo distributions of the left-right forward-backward asymmetry, as shown in Fig. 6. A binned fit to this distribution yields

$$A_b = 0.91 \pm 0.09(\text{stat}) \pm 0.09(\text{syst}). \qquad (23)$$

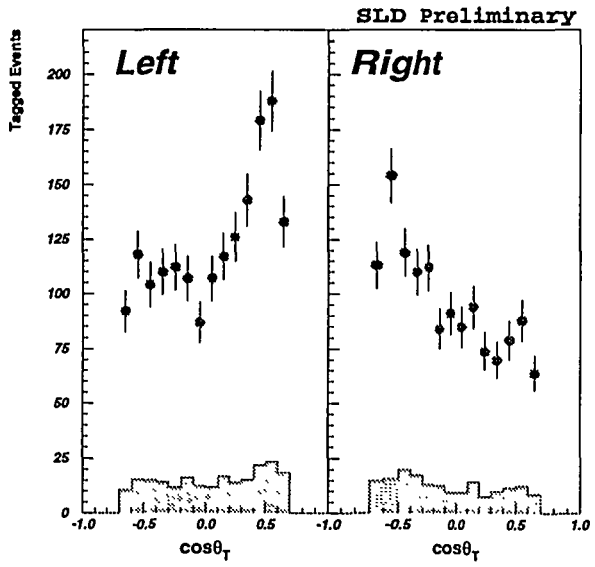


Figure 5: Distribution of the thrust axis $\cos\theta$ for left- and right-handed electron beams. The shaded portions indicate the contributions from non-$b\bar{b}$ events.

The systematic error is dominated by detector uncertainties ($\delta A_b/A_b = 6.2\%$ —mostly due to the uncertainty in the $\pi \to K$ misidentification rate) and by uncertainties in the modeling of B and D production and decay ($\delta A_b/A_b = 7.2\%$).

1.4.3 A_b and A_c with Leptons

Another approach to $b\bar{b}$ event selection and $b/\bar{b}$ tagging is to use leptons from semileptonic decays. The distinctive lepton total and transverse momenta are exploited as well as the charge of the lepton. In this analysis,[14] a measurement of the c-quark asymmetry parameter A_c is also extracted.

Electrons are identified using information from both the CDC and the LAC[15]: track momentum and pointing and energy deposition in the calorimeter. This information is incorporated into a neural network algorithm trained on Monte Carlo electrons. Furthermore, information from the CRID is also added which greatly

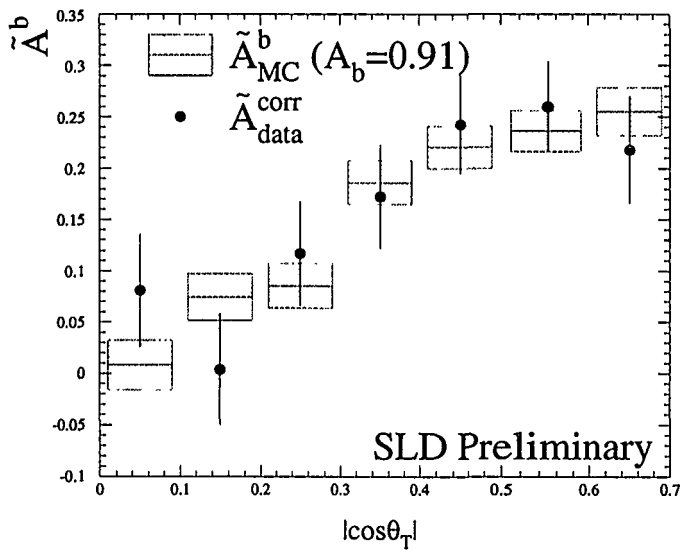


Figure 6: Distribution of the left-right forward-backward asymmetry as a function of the thrust axis $|\cos\theta_T|$ for data (points) and best fit MC (horizontal bands).

improves the electron identification purity at low momentum. The identification efficiency is $\sim 55\%$ with a misidentification rate of less than 2% per charged pion.

Muons are identified using data from the tracking and Warm Iron Calorimeter[16] systems. As in the case of the electron identification, CRID information is added to reject π, K, and p background. The efficiency is $\sim 80\%$ with a charged pion misidentification rate of less than 0.3%.

As was done in the jet charge analysis, the asymmetry parameters A_b and A_c are extracted with an unbinned likelihood analysis using the full differential cross section [Eq. (4)] and which incorporates the sample components ($b \to l$, $b \to c \to l$, $c \to l$, etc.) as a function of lepton p and p_T as determined from the MC. The results for the 1994–95 data are:

$$\text{Muons} \quad A_b = 0.874 \pm 0.107(\text{stat}) \pm 0.044(\text{syst}), \tag{24}$$
$$A_c = 0.633 \pm 0.151(\text{stat}) \pm 0.072(\text{syst}), \tag{25}$$

	$\delta A_b(\mu)$	$\delta A_b(e)$	$\delta A_c(\mu)$	$\delta A_c(e)$
MC statistics	0.022	0.026	0.012	0.035
Jet axis smearing	0.015	0.034	0.003	0.033
Detector simulation	0.022	0.011	0.034	0.045
Physics modeling	0.027	0.026	0.062	0.060
Total	0.044	0.051	0.072	0.089

Table 3: Systematic uncertainties in A_b and A_c measurements with lepton tags.

$$\text{Electrons} \quad A_b = 0.880 \pm 0.107(\text{stat}) \pm 0.051(\text{syst}), \tag{26}$$
$$A_c = 0.620 \pm 0.162(\text{stat}) \pm 0.089(\text{syst}). \tag{27}$$

These measurements can be combined with our previously published results[17] based on the 1993 data to yield

$$A_b = 0.882 \pm 0.068(\text{stat}) \pm 0.047(\text{syst}), \tag{28}$$
$$A_c = 0.612 \pm 0.102(\text{stat}) \pm 0.076(\text{syst}). \tag{29}$$

Systematic uncertainties are summarized in Table 3.

1.5 Combined A_b, A_c, and $Z^0 \to b\bar{b}$ Coupling

The above three A_b analyses have been combined taking into account correlated systematic uncertainties to yield an SLD average of $A_b(\text{SLD}) = 0.863 \pm 0.049$. This value is to be compared with the LEP average unpolarized forward-backward asymmetry for b quarks of $A_b^{FB\,0}(\text{LEP}) = 0.0979 \pm 0.0028$ (Ref. 8). Since the unpolarized asymmetry does not measure A_b directly, one has to use the world average value of $A_e = 0.1500 \pm 0.0025$ from the left-right asymmetry measurement at SLD and the lepton forward-backward asymmetry measurements at LEP.[8] The LEP measurement can then be translated into $A_b(\text{LEP}) = \frac{4}{3}\frac{A_b^{FB}}{A_e} = 0.870 \pm 0.025$. A combined SLD and LEP average value of $A_b = 0.869 \pm 0.022$ is obtained which is about three standard deviations away from the Standard Model prediction of 0.935.

Similarly, the lepton A_c measurement can be combined with a previous measurement[18] based on semiexclusive reconstruction of D^{*+} and D^+ mesons to yield

an SLD average of $A_c(\mathrm{SLD}) = 0.625 \pm 0.084$. This average is in good agreement with both the Standard Model ($A_c = 0.666$) and the LEP average derived from the c-quark forward-backward asymmetry measurements as above.

It is instructive to summarize our knowledge of the $Zb\bar{b}$ coupling in the context of the analysis proposed by Takeuchi, Grant, and Rosner.[19] Deviations from the

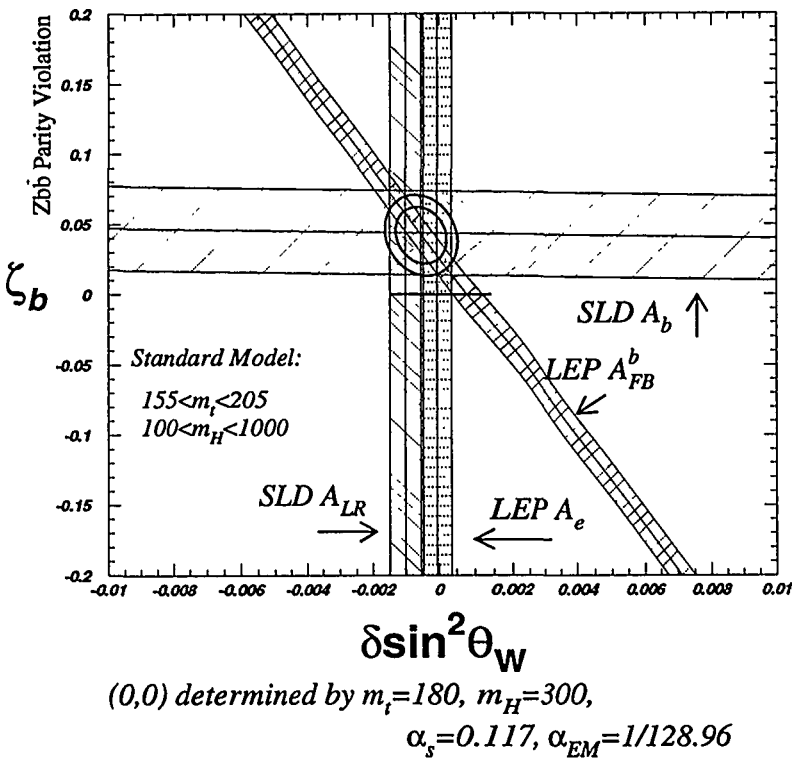


Figure 7: Deviation in the $Z^0 \to b\bar{b}$ coupling parity violation vs the deviation in $\sin^2\theta_W^{eff}$ for the Standard Model and all electroweak data.

Standard Model are parameterized in terms of radiative corrections $\delta \sin^2\theta_W$, ζ_b, and ζ_b. The parameter ζ_b represents deviations in the parity violation of the $Zb\bar{b}$ coupling. As shown in Fig. 7, the A_{LR} and direct A_b asymmetry measurements are complementary, indicating the need for precise measurements of both quantities. The unpolarized forward-backward asymmetry A_b^{FB} measured at LEP cannot alone separate between deviations in $\sin^2\theta_W^{eff}$ and $Z^0 \to b\bar{b}$ parity violation. The Standard Model for $155 < m_t < 205$ GeV/c^2 and $100 < m_H < 1000$ GeV/c^2 is represented by the thin horizontal band passing through the origin ($m_t = 180$ GeV/c^2, $m_H = 300$ GeV/c^2, $\alpha_s = 0.117$, and $\alpha_{em} = 1/128.96$) in the ζ_b vs $\delta \sin^2\theta_W^{eff}$ plane. The best fit to all electroweak data is indicated by the 68% and 90% C.L. contours. This fit displays the discrepancy between A_b measurements and the SM prediction.

1.6 Partial Width R_b

Another observable providing strong constraints on the Standard Model is the partial width of the Z^0 into $b\,\bar{b}$ final states $R_b = \Gamma(Z^0 \to b\bar{b})/\Gamma(Z^0 \to \mathrm{hadrons})$. The measurement proceeds by first selecting a pure sample of $Z^0 \to$ hadrons events. Then each event hemisphere is b-tagged independently for the presence of a B hadron decay. By computing both the rate for tagging a hemisphere (F_s) and the rate for tagging both hemispheres in an event (F_d), one can extract both the value of R_b and the efficiency ϵ_b of the hemisphere tag. These are obtained by solving the following set of equations:

$$F_s = \epsilon_b R_b + \epsilon_c R_c + \epsilon_{uds}(1 - R_b - R_c), \quad (30)$$

$$F_d = \epsilon_b^{dbl} R_b + \epsilon_c^{dbl} R_c + \epsilon_{uds}^{dbl}(1 - R_b - R_c). \quad (31)$$

The Monte Carlo is used to estimate the charm and *uds* efficiencies for tagging hemispheres ϵ_c and ϵ_{uds}, and for tagging both hemispheres ϵ_c^{dbl} and ϵ_{uds}^{dbl}, so it is very important to increase the purity of the b-tag to reduce the potentially large systematic uncertainties mainly due to modeling of the charm production and decay. Correlations between hemispheres imply that the efficiency to tag both hemispheres is not simply ϵ_b^2 but rather $\epsilon_b^{dbl} = \epsilon_b^2 + \lambda_b(\epsilon_b - \epsilon_b^2)$, where λ_b is the correlation parameter to be determined from the MC.

SLD has designed a new approach to achieve high-efficiency and high-purity b-tagging. The excellent 3-D vertexing capabilities of the vertex detector allow B decays to be reconstructed with an inclusive topological technique.[20] Well-measured tracks are parameterized as Gaussian probability tubes in 3-D space [see Fig. 8(a)]. Using these a search is made to find regions in 3-D space with

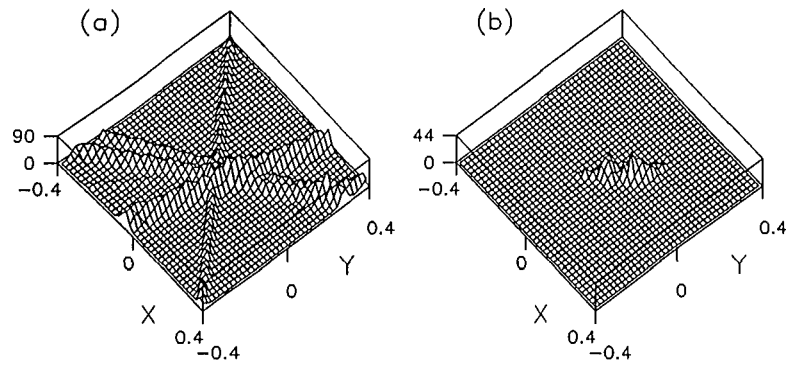


Figure 8: Two-dimensional projection of (a) tracks parameterized as Gaussian tubes and (b) regions of significant track overlap showing primary and secondary vertices.

high "tube overlap" [see Fig. 8(b)]. The significance of the overlap is related to the number of tracks and their extrapolation errors, i.e., the track density. Such an overlap region, or "seed" vertex, is found in $\sim$ 50% of b hemispheres, but only in $\sim$ 15% of c hemispheres and in less than 1% of uds hemispheres. The b hemisphere vertex finding efficiency increases with the decay length D to attain a constant level of 80% for $D > 3$ mm. Due to the typical $B \rightarrow D$ cascade structure of the decays, not all tracks originate from a single space point, and thus, may not be attached to the seed vertex if the D meson travelled sufficiently far from the B decay point. Therefore, an attempt is made to attach isolated tracks to the seed vertex to form the final secondary vertex. Requirements for attachment are: $T < 1$ mm, $L/D > 0.25$, and $L > 1$ mm, where the quantity T represents the minimum distance between a given track and the seed vertex axis, and L is the distance along the vertex axis between the interaction point and the point of closest approach between the track and the vertex axis (see Fig. 9).

The variable used to tag b hemispheres is the mass of the reconstructed vertex. First, the invariant mass M_{raw} of all charged tracks associated with the secondary vertex is computed (tracks are assumed to be pions). A clear separation between b hemispheres and the rest can be observed in Fig. 10(a). In particular, the charm contribution vanishes above the natural cutoff mass of $\sim$ 2 GeV/c^2. Improved

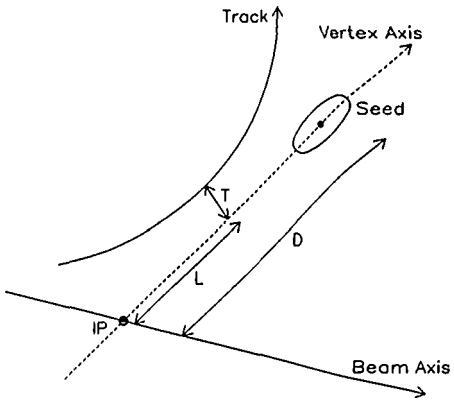


Figure 9: Definition of track variables used to attach isolated tracks to secondary vertices.

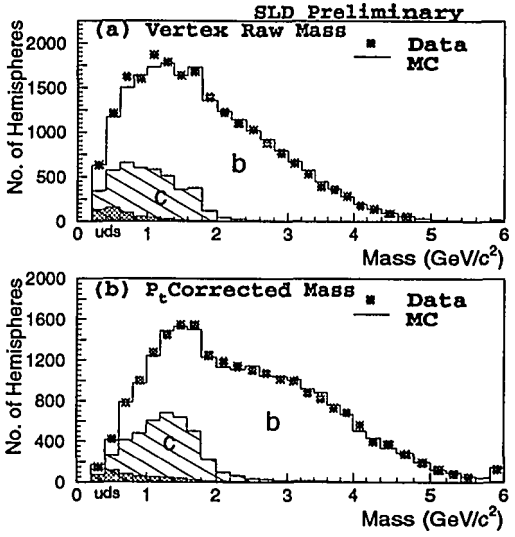


Figure 10: Distributions of (a) raw mass and (b) p_T-added mass for topological vertices.

efficiency for b hemisphere tagging can be obtained by exploiting kinematical information. This is achieved by constructing the p_T-added mass

$$M = \sqrt{M_{raw}^2 + p_T^2} + |p_T|, \tag{32}$$

where p_T is the total momentum of all tracks in the vertex in the plane perpendicular to the vertex axis. The value of p_T is chosen to be the smallest one allowed by the uncertainties in the vertex and IP positions (which affect the direction of the vertex axis). This and the requirement that $M \leq 2\,M_{raw}$ reduces the contamination from non-b hemispheres in the high-mass region. As a result, the b-tag efficiency is enhanced by approximately 40% without significant degradation in purity [see Fig. 10(b)].

For the final analysis, vertices are required to satisfy $D > 1$ mm and $M > 2$ GeV/c^2. The corresponding b-tag purity and the correlation between b hemispheres are estimated from the Monte Carlo to be 97.3% and $\lambda_b = 0.33\%$, respectively. Solving Eqs. (30) and (31) yields

$$\begin{aligned} R_b &= 0.2149 \pm 0.0033(\text{stat}) \pm 0.0021(\text{syst}) \pm 0.0007(R_c), \\ \epsilon_b &= 36.8 \pm 0.6\%. \end{aligned}$$

The value of the mass cut was chosen to minimize the overall uncertainty on R_b as shown in Fig. 11 but is currently dominated by the statistical uncertainty.

The SLD and LEP measurements are compared in Fig. 12. Our measured value is consistent with both the LEP average and the SM prediction.

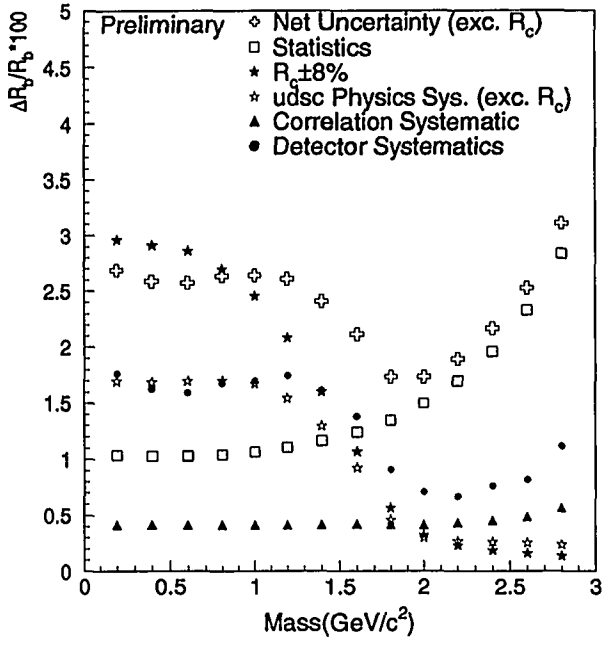


Figure 11: R_b uncertainty components as a function of mass cut.

2 B Physics

Several aspects of the weak interaction can be probed by studying the weak decays of B hadrons. First, by measuring lifetimes, we can test our understanding of B hadron decay dynamics. Second, we can test the Cabibbo-Kobayashi-Maskawa (CKM) quark mixing matrix description within the Standard Model. In particular, this helps constrain CP violation predictions. Measurements of the lifetimes of B^+ and B_d^0 mesons, and of the time dependence of B_d^0–$\overline{B_d^0}$ mixing, are presented below.

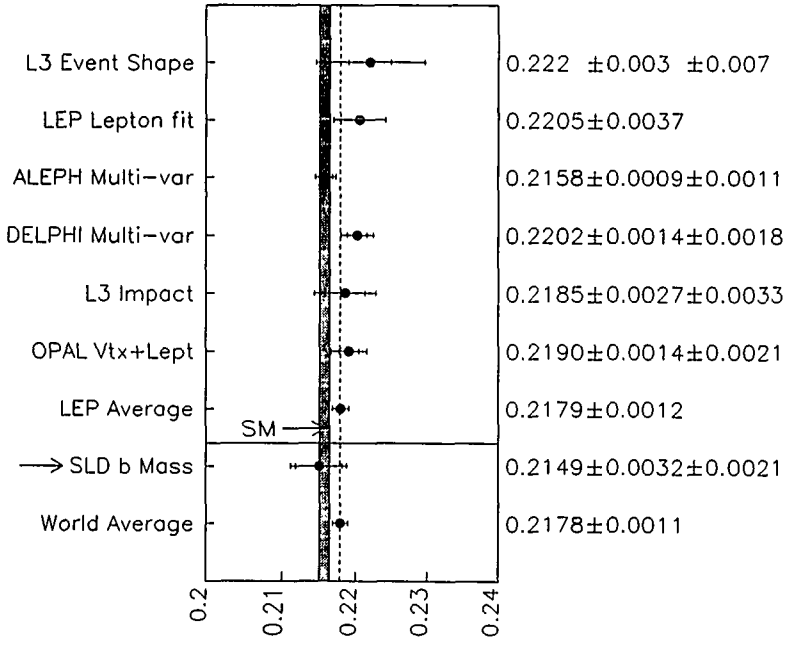


Figure 12: R_b measurements from LEP and SLD.

2.1 B^+ and B_d^0 Lifetimes

As explained above, measurements of the B hadron lifetimes are important to test our understanding of B hadron decay dynamics. In the naive spectator model, all hadrons containing one heavy quark Q are predicted to have the same lifetime. Specifically, one expects $\tau(B^+) = \tau(B_s^0) = \tau(B_d^0) = \tau(\Lambda_b)$. However, a strong hierarchy is observed in the case of charm hadrons: $\tau(D^+) \simeq 2.3\ \tau(D_s) \simeq 2.5\ \tau(D^0) \simeq 5\ \tau(\Lambda_c^+)$. This hierarchy is predicted[21] to scale with $1/m_Q^2$ and is thus expected to yield much smaller lifetime differences for B hadrons. In the case of B^+ and B_d^0, a calculation[21] based on an expansion in terms of $1/m_Q$ predicts $\tau(B^+)/\tau(B_d^0) = 1 + 0.05(f_B/200\text{MeV})^2$, where f_B is the B hadron decay constant. Lifetime differences for different B hadrons are thus predicted to be less than 10%. Exclusive and inclusive B lifetimes are also important because they are necessary inputs to many other measurements, as for example, many electroweak $Z^0 \to b\bar{b}$ measurements, time-dependent B_d^0-$\overline{B_d^0}$ mixing measurements, and precise determinations of the CKM matrix element $|V_{cb}|$.

Several techniques have been used to measure the B^+ and B_d^0 lifetimes. The cleanest method reconstructs samples of B^+ and B_d^0 decays exclusively. However, the branching fractions for such exclusive reconstruction are typically small ($\sim 10^{-4} - 10^{-3}$). Most measurements have relied on samples of semileptonic B decays where the $D^{(*)}$ meson is exclusively reconstructed and intersected with an identified lepton to determine the B decay point. The lifetime measurements then rely on assumptions concerning the B^+ and B_d^0 content of the selected $\overline{D^0}Xl^+\nu$ and $D^{(*)-}Xl^+\nu$ samples.

The two techniques used by SLD take advantage of the excellent 3-D vertexing capabilities of the VXD to reconstruct the decays (semi-) inclusively. The goal is to reconstruct and identify all the tracks originating from the B decay chain. This then allows charged and neutral B mesons to be separated by simply measuring the total charge of tracks associated with the B decay.

The first analysis[22] uses the inclusive topological vertexing technique described earlier (see Sec. 1.6) but the criteria used to attach tracks to seed vertices are slightly different: $T < 1$ mm, $L/D > 0.3$, and no minimum cut on L. In the hadronic Z^0 event sample, we select 9719 B decay candidates by requiring $M_{raw} > 2$ GeV/c^2 and $D > 1$ mm. The minimum vertex mass requirement serves not only as a means to select a 97% pure sample of $b\bar{b}$ events but also as a means to enhance the charge reconstruction purity. The sample is divided into neutral and charged subsamples corresponding to reconstructed decays with total charge $Q = 0$ or $Q = \pm 1, 2, 3$, respectively, where Q is the charge sum of all tracks associated with the vertex. The charged (neutral) sample consists of 6033 (3665) decays. Monte Carlo studies show that the charged (neutral) sample is 97.3% (98.0%) pure in B hadrons. The simulated flavor contents are 54.6% B^+, 30.5% B_d^0, 8.6% B_s^0, and 3.6% B baryons for the charged sample, and 23.3% B^+, 54.5% B_d^0, 14.6% B_s^0, and 5.6% B baryons for the neutral sample*. The sensitivity of this analysis to the individual B^+ and B_d^0 lifetimes can be assessed from the 1.8 (2.3) ratio of B^+ (B_d^0) decays over B_d^0 (B^+) decays in the charged (neutral) sample.

*Reference to a specific state (e.g., B^+) implicitly includes its charge conjugate state (i.e., B^-).

The B^+ and B_d^0 lifetimes are extracted with a simultaneous binned maximum likelihood fit to the decay length distributions of the charged and neutral samples (see Fig. 13). These distributions are compared with MC distributions obtained

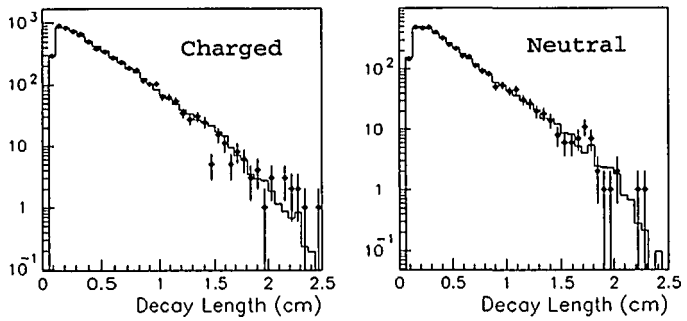


Figure 13: Decay length distributions for data (points) and best fit Monte Carlo (histogram) in the topological analysis.

for a range of values of the B^+ and B_d^0 lifetimes. The maximum likelihood fit yields lifetimes of

$$\tau_{B^+} = 1.69 \pm 0.06(\text{stat}) \pm 0.06(\text{syst}) \text{ ps}, \tag{33}$$

$$\tau_{B_d^0} = 1.63 \pm 0.07(\text{stat}) \pm 0.08(\text{syst}) \text{ ps}, \tag{34}$$

with a lifetime ratio of

$$\frac{\tau_{B^+}}{\tau_{B_d^0}} = 1.04^{+0.08}_{-0.07}(\text{stat}) \pm 0.06(\text{syst}). \tag{35}$$

The main contributions to the systematic error come from uncertainties in the detector modeling, B_s^0 lifetime, fit systematics, and MC statistics.

The second lifetime analysis[23] is restricted to semileptonic decays, which reduces the overall efficiency compared to the topological method but results in an improved charge reconstruction purity. In the semileptonic method, a D decay vertex is reconstructed topologically and the B decay vertex is formed by intersecting the D meson trajectory with that of an identified lepton. An attempt is then made to attach a slow-pion candidate to the B vertex to reconstruct the track topology of B decays into D^{*+} mesons.

The analysis selects identified electrons and muons with momentum transverse to the nearest jet axis > 0.4 GeV/c and results in a sample of 634 charged and 584 neutral decays. Monte Carlo studies show that the remaining charged (neutral) sample is 97.5% (99.1%) pure in B hadrons. The simulated flavor contents are 66.9% B^+, 22.5% B_d^0, 5.7% B_s^0, and 2.4% B baryons for the charged sample, and 19.6% B^+, 60.8% B_d^0, 14.0% B_s^0, and 4.7% B baryons for the neutral sample. The sensitivity of this analysis to the individual B^+ and B_d^0 lifetimes can be assessed from the 3:1 ratio of B^+ (B_d^0) decays over B_d^0 (B^+) decays in the charged (neutral) sample.

As was the case for the topological analysis, the B^+ and B_d^0 lifetimes are extracted from the decay length distributions of the charged and neutral samples (see Fig. 14). The fit yields the following results:

$$\tau_{B^+} = 1.60^{+0.12}_{-0.11}(\text{stat}) \pm 0.06(\text{syst}) \text{ ps},$$

$$\tau_{B_d^0} = 1.55^{+0.13}_{-0.12}(\text{stat}) \pm 0.09(\text{syst}) \text{ ps},$$

with a ratio of

$$\frac{\tau_{B^+}}{\tau_{B_d^0}} = 1.03^{+0.15}_{-0.13}(\text{stat}) \pm 0.08(\text{syst}).$$

As in the case of the topological analysis, the dominant sources of systematic error are due to uncertainties in the detector modeling, B_s^0 lifetime, fit systematics, and MC statistics.

The two analyses described above yield lifetime measurements in agreement with those from other experiments (see Fig. 15) and with the expectation that the B^+ and B_d^0 lifetimes are nearly equal.

2.2 B^0–$\overline{B^0}$ Mixing

The phenomenon of B^0–$\overline{B^0}$ mixing is now well-established. Transitions between flavor states $B^0 \to \overline{B^0}$ take place via second order weak interactions "box diagrams." As in the case of the $K^0 - \overline{K^0}$ system, the weak eigenstates are linear combinations of the flavor eigenstates:

$$|B_L\rangle = \frac{1}{\sqrt{2}}\left(|B^0\rangle + |\overline{B^0}\rangle\right), \tag{36}$$

$$|B_H\rangle = \frac{1}{\sqrt{2}}\left(|B^0\rangle - |\overline{B^0}\rangle\right), \tag{37}$$

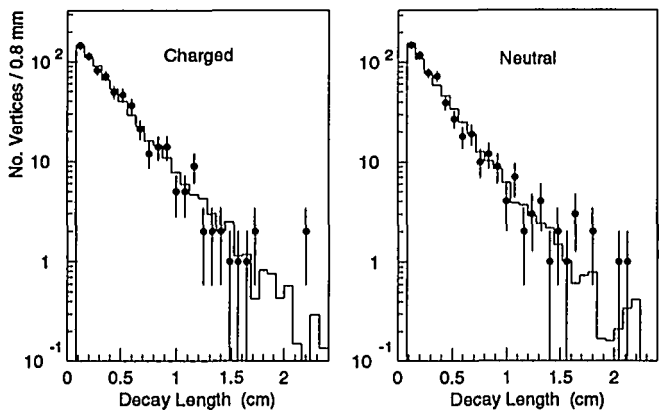


Figure 14: Decay length distributions for data (points) and best fit Monte Carlo (histogram) in the semileptonic analysis.

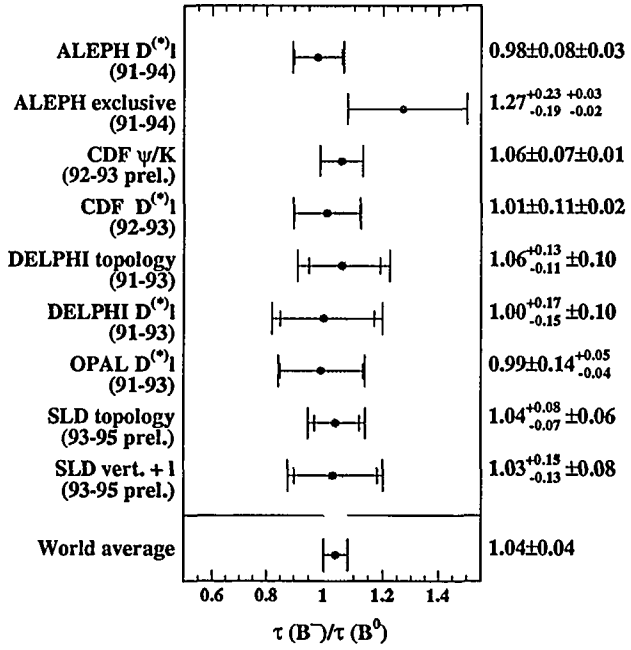


Figure 15: Comparison between measurements of the B^+/B_d^0 lifetime ratio.

where $|B_L\rangle$ and $|B_H\rangle$ represent the light and heavy eigenstates (the effect of CP violation has been neglected). Due to the difference in mass between these eigenstates, they propagate differently in time, which gives rise to time-dependent oscillations between B^0 and $\overline{B^0}$ flavor eigenstates. Given an initial B^0 produced at $t = 0$, the probability that it decays as a B^0 at time t is given by

$$P_{B^0 \to B^0}(t) = \Gamma e^{-\Gamma t} \frac{1}{2} [1 + \cos(\Delta m t)], \tag{38}$$

whereas the probability that it decays as a $\overline{B^0}$ at time t is given by

$$P_{B^0 \to \overline{B^0}}(t) = \Gamma e^{-\Gamma t} \frac{1}{2} [1 - \cos(\Delta m t)], \tag{39}$$

where $\Gamma = 1/\tau$ is the B^0 decay width, Δm is the mass difference between the weak eigenstates and the lifetime difference between the weak eigenstates has been neglected since it is expected to be small. Thus, measuring the oscillation frequency of B^0–$\overline{B^0}$ mixing provides a measurement of Δm. The value of Δm can be calculated from the box diagrams for which the dominant contribution comes from virtual top quark exchange,

$$\Delta m_q = \frac{G_F^2}{6\pi^2} m_t^2 m_{B_q} F(m_t/m_W) \eta_{QCD} f_{B_q}^2 B_{B_q} |V_{tb}^* V_{tq}|, \tag{40}$$

where $q = d, s$ applies to either B_d^0 or B_s^0 mesons. Measuring Δm_q is thus sensitive to the CKM matrix element $|V_{tq}|$ for which little is known experimentally. There are large uncertainties in the theoretical estimates[24] of the term $f_{B_q}^2 B_{B_q}$ but these uncertainties are much reduced for the ratio between Δm_d and Δm_s. Thus, combining measurements of the oscillation frequency of both B_d^0–$\overline{B_d^0}$ and B_s^0–$\overline{B_s^0}$ mixing translates into a measurement of the ratio $|V_{td}|/|V_{ts}|$.

Experimentally, a measurement of the time dependence of B^0–$\overline{B^0}$ mixing requires three ingredients: (i) the B decay and its proper time have to be reconstructed, (ii) the B flavor at production (initial state $t = 0$) needs to be determined, as well as (iii) the B flavor at decay (final state $t = t_{decay}$). At SLD, the time dependence of B_d^0–$\overline{B_d^0}$ mixing has been measured using four different methods. All four use the same initial state tagging but differ by the method used to either reconstruct the B decay or tag its final state.

Initial state tagging takes advantage of the large polarization-dependent forward backward asymmetry in $Z^0 \to b\bar{b}$ decays

$$\tilde{A}_{FB}(\cos\theta_T) = 2A_b \frac{A_e - P_e}{1 - A_e P_e} \frac{\cos\theta_T}{1 + \cos^2\theta_T} \tag{41}$$

which is derived from Eq. (4). This only requires knowledge of the electron beam polarization P_e and the cosine of the angle between the thrust axis direction and the electron beam direction, $\cos\theta_T$. The tag works as follows. For left- (right-) handed electrons and forward (backward) B decay vertices, the initial quark is tagged as a b quark; otherwise, it is tagged as a $\bar{b}$ quark. The initial state tag can be augmented by using the momentum-weighted track charge (see Sec. 1.4.1) in the hemisphere opposite that of the reconstructed B vertex. Figure 16 shows the

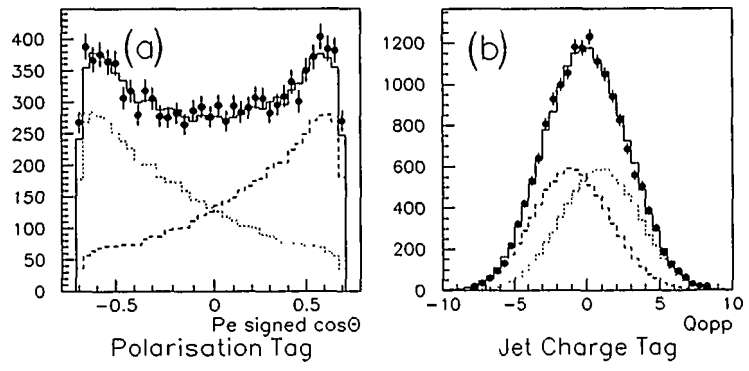


Figure 16: Distributions of (a) polarization-signed $\cos\theta_T$ and (b) opposite hemisphere jet charge for data (points) and MC (solid line). The MC b and $\bar{b}$ components are shown with dotted and dashed lines respectively.

distributions of $\cos\theta_T$ signed by the electron beam helicity and of the opposite hemisphere jet charge. Clear separation between initial b and $\bar{b}$ quarks is observed. The polarized forward-backward asymmetry and the jet charge tags are combined to yield an initial state tag with 100% efficiency and an effective average right-tag probability of 84% (for $\langle P_e \rangle = 77\%$).

The first two B^0_d-$\overline{B^0_d}$ mixing analyses[25] use topological vertexing (see Sec. 1.6) to select the tracks from the B decay and measure its decay length. A sample of 16803 vertices is selected after requiring $M > 2$ GeV/c^2 (no explicit cut is placed on the decay length). The first analysis uses charged kaons from the B decay chain to tag the final state. This tag relies on the fact that most B decays occur via the dominant $b \to c \to s$ transition and is similar to the tag used for the measurement of A_b presented in Sec. 1.4.2. Charged kaons are identified with the

Analysis	Kaon	Dipole	Lept+D	Lept+Trks
Detector simulation	0.036	0.010	0.020	0.013
Physics modeling	0.048	0.027	0.024	0.032
Fit systematics	0.045	0.026	0.038	–
Total	0.075	0.039	0.049	0.035

Table 4: Systematic uncertainties for the different Δm_d measurements (in ps^{-1}).

CRID, but for this analysis, both liquid and gas radiators are used to cover most of the kaon momentum range: 0.8 to 25 GeV/c. The tag variable here consists of the sum of identified kaon charges Q_K for charged tracks in the vertex such that $\Sigma Q_K > 0$ (< 0) tags B^0_d ($\overline{B^0_d}$) decays. The rate of pion misidentification as a function of momentum is calibrated from the data using a pure sample of pions from K^0_s decays. The kaon tag is available for 1/3 of the reconstructed decays and yields a sample of 5694 decays with a correct tag probability of 77% for B^0_d decays.

Measurement of the time dependence of B^0_d-$\overline{B^0_d}$ mixing is extracted by computing the fraction of decays tagged as mixed as a function of decay length. It is not necessary to reconstruct the proper time because of the slow oscillation frequency of B^0_d-$\overline{B^0_d}$ mixing. A decay is tagged as mixed if the initial and final state tags disagree. A binned χ^2 fit is performed by comparing the distributions of the mixed fraction as a function of decay length obtained for the data and the MC for a range of Δm_d values. Figure 17(a) shows the mixed fraction distribution for the charged kaon analysis. A clear oscillation signal is observed. The fit yields a frequency of $\Delta m_d = 0.580 \pm 0.066(\text{stat}) \pm 0.075(\text{syst})$ ps^{-1} with a $\chi^2/\text{dof} = 10.2/10$. The main contributions to the systematic error arise from uncertainties in the $\pi \to K$ misidentification calibration from the data, in the rate of right-sign kaon production in B^+ and B^0_d decays as measured by ARGUS,[13] and in the dependence of the fit results on binning and fit range, as summarized in Table 4.

The second analysis exploits the $B \to D$ cascade charge structure to tag the final state. To enhance the B^0_d fraction in the sample of topological vertices, the total charge of tracks associated with the vertex is required to be equal to zero. This requirement also improves the probability of correctly assigning all of the B^0_d decay tracks. The direction of the vertex axis is adjusted to minimize the impact

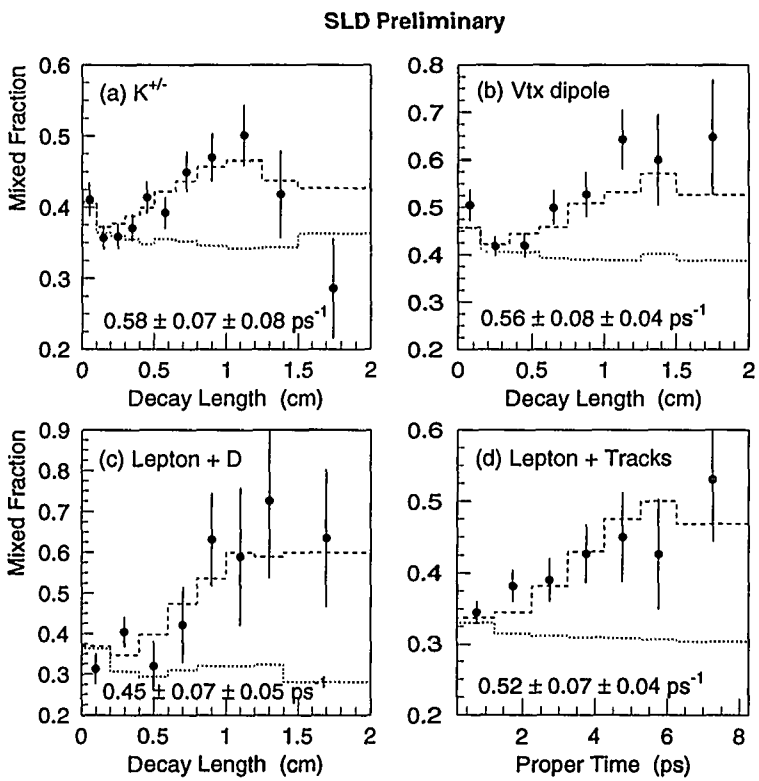


Figure 17: Distributions of the fraction of decays tagged as mixed as a function of decay length or proper time for data (points) and best fit MC (dashed histograms) for the various analyses: (a) charged kaon, (b) charge dipole, (c) lepton + D, and (d) lepton + tracks. The dotted histograms correspond to MC distributions with no B^0_d-$\overline{B^0_d}$ mixing.

parameter sum of the tracks in the vertex and the mean track impact parameter is required to be less than 50 μm at this minimum. A sample of 3291 decays satisfies the selection criteria. The "charge dipole" δq of the vertex is then defined as the relative displacement between the weighted mean location L_i of the positive tracks and of the negative tracks (see Sec. 1.6 for a definition of the quantity L): $\delta q = (\sum^+ w_i L_i)/(\sum^+ w_i) - (\sum^- w_i L_i)/(\sum^- w_i)$, where the first (second) term is a sum over all positive (negative) tracks in the vertex. The weight w_i for each track i is inversely proportional to the uncertainty on the quantity L_i, $w_i = \sin^2\theta_i/\sigma_T$, with θ_i the angle between track i and the vertex axis and σ_T the uncertainty on the impact parameter of the track with respect to the vertex axis. Figure 18

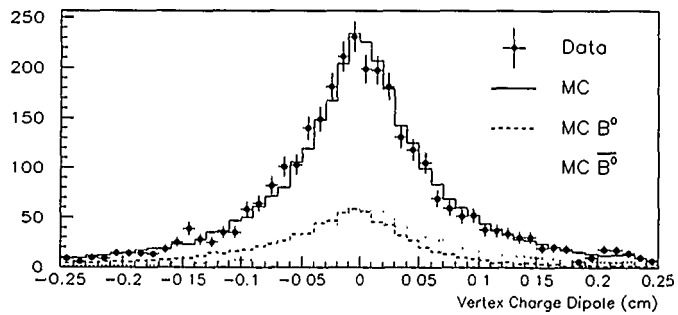


Figure 18: Distribution the vertex charge dipole for data (points) and MC (solid line). The contribution from MC B^0_d and $\overline{B^0_d}$ decays is also indicated by the dashed and dotted histograms, respectively.

shows the distribution of the reconstructed charge dipole for data and MC. Also shown is the separation between B^0_d and $\overline{B^0_d}$ decays. The correct tag probability increases with the magnitude of δq and reaches a maximum of 84% in the tails. This probability can be parameterized as $P_D = 0.84\, e^{-|2.4|\delta q|-0.8|^3}$. A χ^2 fit to the mixed fraction distribution as a function of decay length [Fig. 17(b)] yields $\Delta m_d = 0.561 \pm 0.078(\text{stat}) \pm 0.039(\text{syst})$ ps^{-1} with a $\chi^2/\text{dof} = 8.8/7$. The main contributions to the systematic error come from MC statistics and fit systematics (see Table 4).

The next two analyses select semileptonic decays. The first of these (lepton + D, Ref. 26) is identical to that used to measure the B^+ and B^0_d lifetimes (see Sec. 2.1). As in the case of the charge dipole analysis, a set of neutral vertices is

selected. The sample here consists of 582 neutral decays with a B_d^0 purity of 61%. The charge of the lepton tags the $B_d^0/\overline{B_d^0}$ flavor at decay with a correct tag probability of 85%. As with the above two analyses, a χ^2 fit to the mixed fraction distribution [Fig. 17(c)] yields $\Delta m_d = 0.452 \pm 0.074(\text{stat}) \pm 0.049(\text{syst})$ ps^{-1} with a $\chi^2/\text{dof} = 7.8/7$. The systematic error is dominated by MC statistics and fit systematics (see Table 4).

The last analysis (lepton+tracks, Ref. 27) selects semileptonic decays by identifying electrons and muons with high transverse momentum $p_T > 0.8$ GeV/c with respect to the nearest jet axis. This enhances the fraction of $Z^0 \to b\bar{b}$ events and allows for the use of a fully inclusive vertexing technique. The B decay vertex is estimated by computing an average intersection point between the lepton trajectory and all well-measured tracks in the jet, each track being weighted according to its probability to originate from the decay of a short-lived heavy hadron. This technique is very efficient ($\epsilon = 98\%$) once a high-p_T lepton has been selected and has good decay length resolution. In contrast to the first three analyses described above, the B decay proper time is reconstructed by estimating the B hadron momentum based on track and energy clusters in the calorimeter. The final sample contains 2609 semileptonic decay candidates with an estimated B hadron purity of 93%. The lepton charge provides the final state tag with correct tag probability of 85%.

For this analysis, the value of Δm_d is extracted from an unbinned maximum likelihood analysis with parameterizations estimated from the MC. The fit yields $\Delta m_d = 0.520 \pm 0.072(\text{stat}) \pm 0.035(\text{syst})$ ps^{-1} and the corresponding mixed fraction distribution is shown in Fig. 17(d). The systematic uncertainties are presented in Table 4.

The results from the four analyses described above have been combined, taking into account statistical and systematic correlations between analyses, to produce the following SLD average for the mass difference between the two B_d^0 weak eigenstates:

$$\Delta m_d = 0.525 \pm 0.043(\text{stat}) \pm 0.037(\text{syst}) \text{ ps}^{-1}. \quad (42)$$

As expected, the statistical correlation coefficients are the largest between the kaon and charge dipole analyses, and between the two semileptonic analyses. The SLD average is compared with averages from other experiments in Fig. 19.

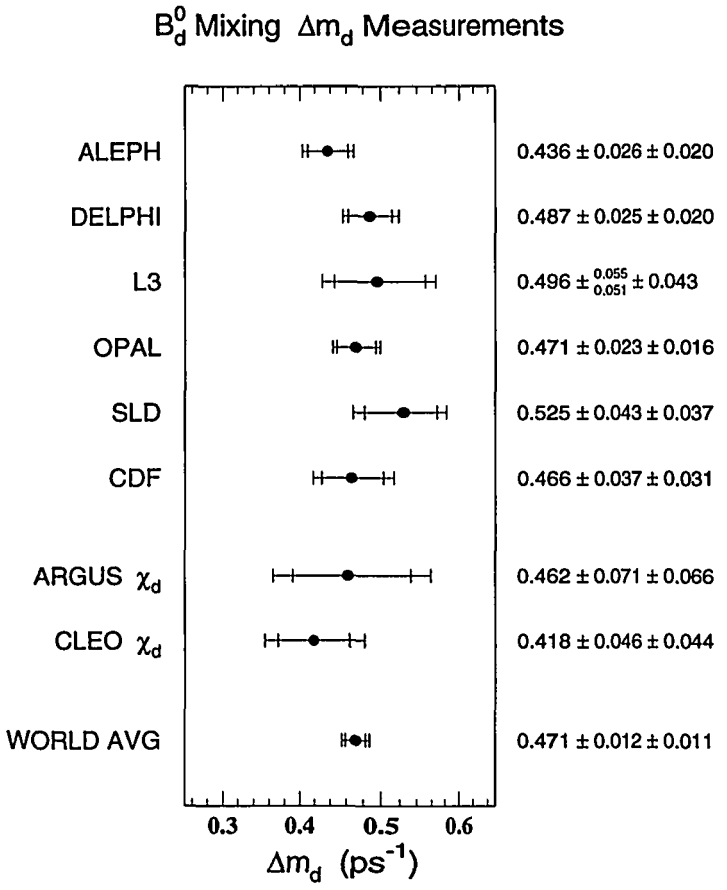


Figure 19: Comparison between the various Δm_d measurements.

3 QCD Physics

Among the QCD analyses performed at SLD, we focus on those addressing the problem of hadronization—the process which turns an initial set of quarks into final state hadrons. Thanks to the unique SLC/SLD environment, quark fragmentation can be studied for differences between light-quark and heavy-quark fragmentation, as well as for differences between quark and antiquark fragmentation.

3.1 Charged Multiplicity in Light-, c-, and b-Quark Events

Perturbative QCD predicts that the difference in average charged multiplicity between heavy-quark Q and light-quark uds events $\Delta n_Q \equiv \bar{n}_Q - \bar{n}_{uds}$ is independent of center-of-mass energy. This prediction has been tested with a technique[28] following three steps: (i) the primary quark flavor is tagged in each event hemisphere, (ii) the number of charged tracks is counted in the opposite hemisphere to minimize the bias due to the quark flavor tag, (iii) the average charged multiplicity in each flavor-tagged sample is unfolded to correct for the purity and bias of the tags. The uds- (b-) tag requires that the hemisphere contains no track (at least three tracks) with signed 2-D impact parameter larger than $3\,\sigma$. Since the impact parameter tag provides a c quark sample of only modest purity, a more exclusive technique is used. For the c-quark tag, high-momentum charged D^* mesons are reconstructed in the $D^{*+} \to D^0\pi^+$, $D^0 \to K^-\pi^+$, and $D^0 \to K^-\pi^+(\pi^0)$ modes (the π^0 is not directly reconstructed), and charged D mesons are reconstructed in the $D^+ \to K^-\pi^+\pi^+$ mode. The number of uds-, c-, and b-tagged hemispheres is 154151, 976, and 9480 respectively with uds, c, and b purities estimated to be 75%, 64%, and 94% respectively.

After unfolding for the tag purities and (small) biases, we find the following multiplicity differences between c-quark and uds-quark, and between b-quark and uds-quark hemispheres:

$$\Delta n_c = 1.07 \pm 0.47(\text{stat})^{+0.36}_{-0.30}(\text{syst}), \quad (43)$$

$$\Delta n_b = 2.93 \pm 0.14(\text{stat})^{+0.30}_{-0.29}(\text{syst}). \quad (44)$$

The main contributions to the systematic errors arise from uncertainties in the detector acceptance and in the modeling of B hadron production and decay. These results are compared with similar measurements performed at lower center-of-mass energies in Fig. 20. The data are consistent with the QCD prediction of energy independence of Δn_Q over center-of-mass energies in the range between 29 and 91 GeV, and with absolute predictions.[29,30]

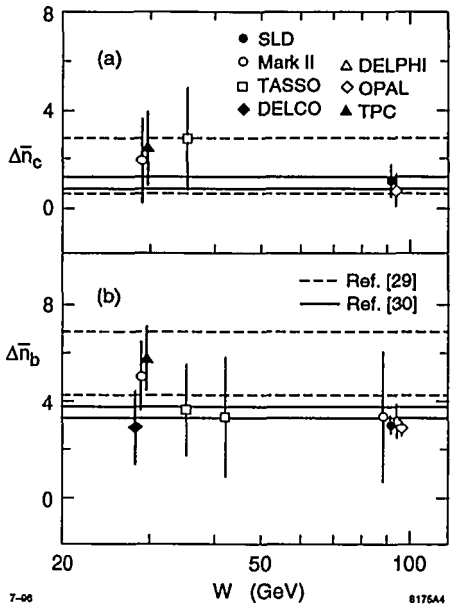


Figure 20: Multiplicity difference measurements as a function of center of mass energy for (a) c-quarks, and (b) b-quarks. Predictions from Refs. 29 and 30 are also indicated.

3.2 Identified Particle Production

Further knowledge about the fragmentation process can be gained by studying the production characteristics of different particle types.[31] Charged hadrons π, K, and p are identified with the CRID. Neutral hadrons are also selected: K^0_s and Λ decays are identified via their two-prong decays, ϕ and K^{*0} are selected with identified charged kaons in the CRID.

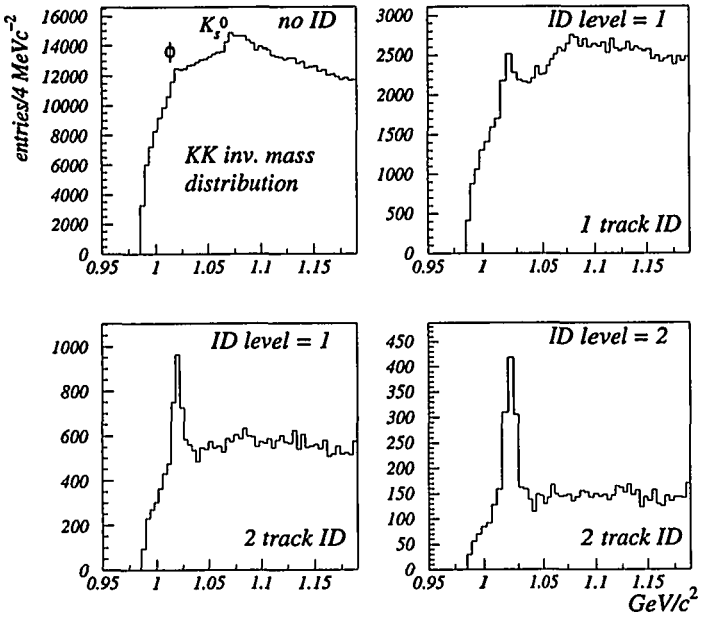


Figure 21: Invariant mass distributions for $\phi \to K^+K^-$ decay candidates without and with various levels of kaon identification.

Figure 21 shows the K^+K^- invariant mass distributions for ϕ decay candidates with increasingly tighter kaon identification requirements. It clearly demonstrates the power of the kaon identification. In order to measure the production rates, it is necessary to accurately determine the identification efficiency for each particle species. Charged particle identification efficiencies (and misidentification rates) are estimated primarily from pure data samples of charged pions from K^0_s and τ decays, whereas proton samples are obtained from Λ decays. Efficiencies for neutral strange particles are estimated from the MC. The differential production rates for the above particle species are shown in Fig. 22 as a function of the scaled momentum variable $x_p = 2p/\sqrt{s}$. Suppression of particles containing strange valence quarks is clearly observed, with an even stronger suppression for ϕ mesons which contain an $s\bar{s}$ valence pair.

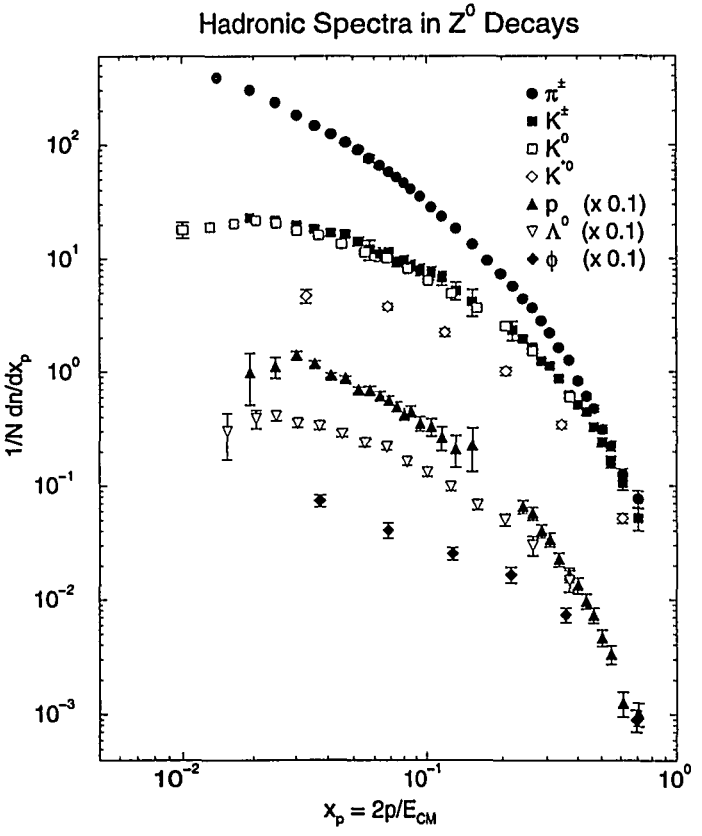


Figure 22: Differential production rates for identified particle species in hadronic Z^0 decays as a function of scaled momentum x_p.

The production rates of $\pi^{\pm}$, $K^{\pm}$, K^0 ($\overline{K^0}$), p ($\overline{\mathrm{p}}$), and Λ ($\overline{\Lambda}$) have also been measured separately in *uds*- and *b*-tagged samples. The *uds* and *b* flavor-tags are identical to the hemisphere tags described in the previous section except that they are applied to the whole event. After unfolding for the tag purity (85% for *uds* and 89% for *b*) and bias, production rates in *uds*- and *b*-quark fragmentation are measured. This allows for a direct comparison of particle production in light- and heavy-quark hemispheres. The measured ratio between *b* and *uds* production of the various identified hadrons is shown in Fig. 23. This is the first such measurement. Meson production is generally higher (lower) for *b* fragmentation at low

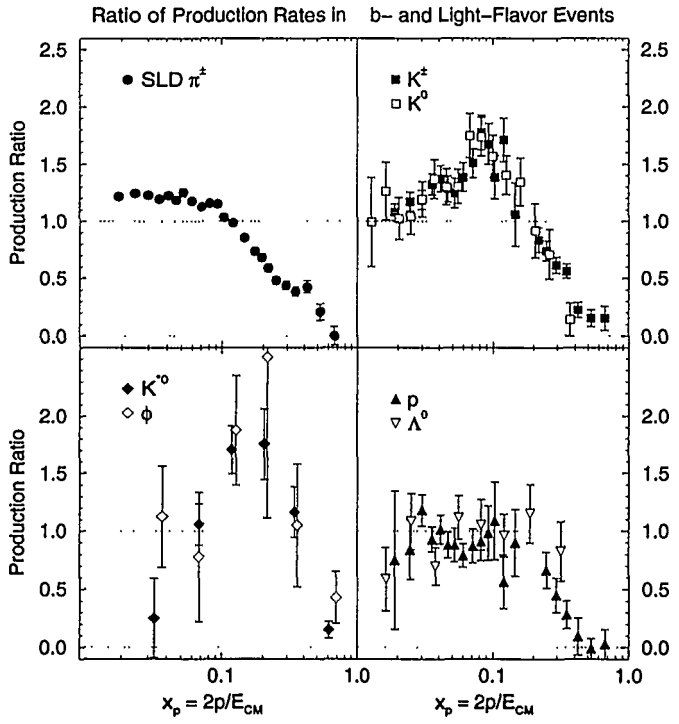


Figure 23: Ratio between the particle production rates in *b*-quark and *uds*-quark hemispheres as a function of scaled momentum for various particle species.

(high) x_p, in agreement with the known characteristics of B hadron production and decay. Baryons are produced equally for $x_p < 0.15$ but are produced less abundantly at larger x_p in *b* fragmentation. Statistical uncertainties in the ratio dominate because the dominant particle identification systematic uncertainties mostly cancel in the ratio. The measured production ratios agree well with the simulation based on JETSET 7.4.

3.3 Leading Particle Effect

Studies of charmed and B hadron production in $e^+e^- \to c\bar{c}$ and $e^+e^- \to b\bar{b}$ indicate that heavy quarks fragment into a single heavy hadron which carries a large fraction of the initial quark momentum. In that sense, there is ample evidence for "leading" particle production in e^+e^- interactions, where a leading particle is defined to be a particle which contains the primary q or $\bar{q}$. However, there is little evidence for leading particle production in light-quark fragmentation.

A unique technique is used to extract such evidence.[32] First, events are required to pass the *uds*-tag selection criteria described earlier. Then, the large polarized forward-backward asymmetry is exploited to tag quark and antiquark hemispheres in a way similar to that used for the B^0_d–$\overline{B^0_d}$ mixing measurements (see Sec. 2.2). A quark-tag purity of 73% is obtained for events with thrust axis $|\cos\theta_T| > 0.2$ for which the asymmetry is sufficiently large. The production rates of π^-, K^-, $\overline{K}^{*0}$, p, and Λ are measured separately in the quark- and antiquark-tagged hemispheres. A small contamination from heavy quarks in the *uds*-tagged event sample is subtracted and a correction is applied to account for the purity of the quark tag.

To compare the production rates $\mathcal{F}^h_q$ for a specific hadron h in quark and antiquark hemispheres, the normalized difference between these rates is computed: $D_h = (\mathcal{F}^h_q - \mathcal{F}^h_{\bar{q}})/(\mathcal{F}^h_q + \mathcal{F}^h_{\bar{q}})$. The distribution of D_h for the various identified hadrons as a function of scaled momentum is shown in Fig. 24. It is observed that more high-momentum protons or Λ's are produced than antiprotons or $\bar{\Lambda}$'s in quark hemispheres. This represents clear evidence for leading baryon production since protons and Λ's contain valence quarks, whereas their antiparticles do not. A higher production of high-momentum K^- and $\overline{K}^{*0}$ in quark hemispheres is also observed. Since mesons contain both valence quarks and antiquarks, one might expect to observe no effect. However, strangeness suppression makes it more likely

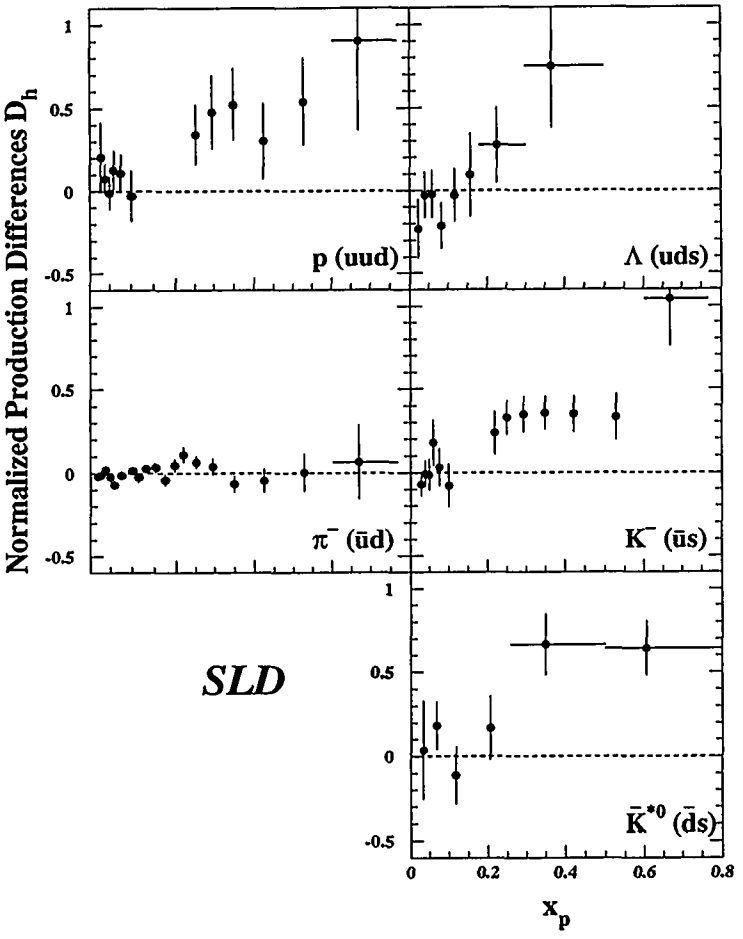


Figure 24: Normalized difference between production rates for a given hadron as a function of scaled momentum.

for a $\overline{K}^{*0}$ (made of a $\bar{d}s$ valence pair) to contain a primary s quark than a primary $\bar{d}$ quark. Thus, the excess of $\overline{K}^{*0}$ over K^{*0} production in quark hemispheres, indicates both the existence of leading $\overline{K}^{*0}$ production and strangeness suppression at the highest momenta. Similarly, an excess of high-momentum K^- over K^+ is observed. There is no difference between π^- and π^+ production in quark hemispheres. The measured behavior measured in Fig. 24 is well-reproduced by the simulation with JETSET 7.4.

4 Summary and Future

Using a sample of $\sim$ 150,000 hadronic Z^0 decays collected between 1993 and 1995, the SLD Collaboration has produced precise and/or unique tests of the Standard Model. These analyses take advantage of the large longitudinal electron beam polarization, the small and stable SLC beam spot, the high-resolution 3-D pixel vertex detector (VXD2), and the particle identification capabilities of the Cherenkov Ring Imaging Detector.

In 1996, SLD installed an improved CCD Vertex Detector (VXD3). As shown in Figs. 25 and 26, this detector is improved in many ways: (i) the angular coverage

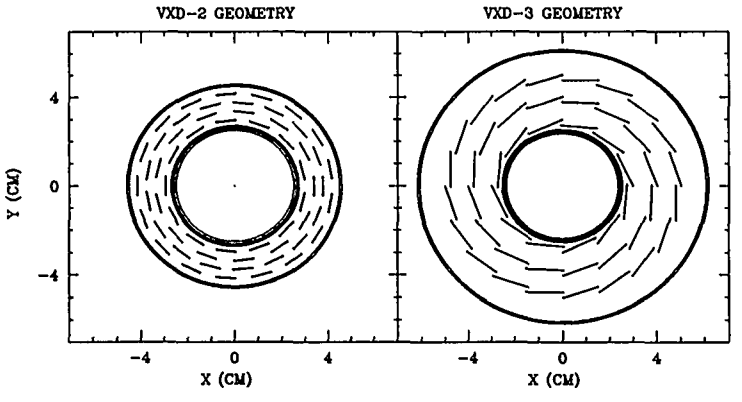


Figure 25: Cross-section views of the old (VXD2) and new (VXD3) vertex detectors.

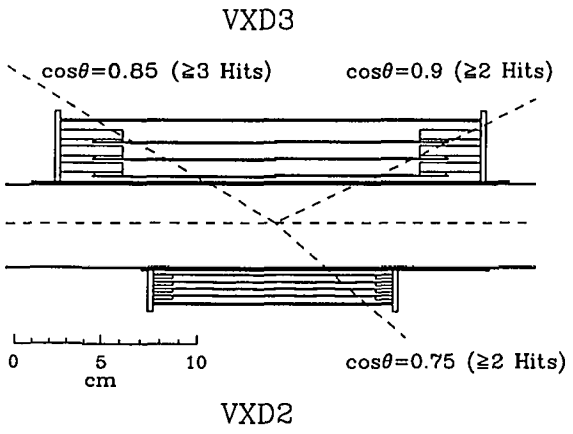


Figure 26: Sideviews of the old (VXD2) and new (VXD3) vertex detectors.

coverage is increased with maximum $|\cos\theta|$ of 0.90 instead of 0.74 for tracks with two hits; (ii) the average number of hits per track is increased from 2.3 to 3.2; (iii) the amount of material is reduced from 1.15% to 0.40% of a radiation length per ladder; (iv) the average distance between the inner and outer layer is increased from 12 to 20 mm to provide an increased lever-arm. These features lead to significant improvements in resolution. In particular, the decay length resolution improves by roughly a factor of two.

Many measurements relying on precise tracking will benefit greatly from the increased resolution and coverage of VXD3. In particular, it is expected that the superior resolution will enable SLD to study the time dependence of B_s^0-$\overline{B_s^0}$ mixing up to very high oscillation frequencies, significantly increasing the reach in Δm_s beyond that currently attained by the LEP experiments.

Acknowledgments

I wish to thank all SLD collaborators who have helped with the preparation for the talk and the proof-reading of this paper. In particular, I would like to thank Su Dong, Dave Muller, Dave Aston, and Ken Baird. Last but not least, I wish to thank the Summer Institute organizers for an enjoyable conference, and especially Lilian DePorcel for her patience with this contribution, among many other things.

References

[1] M. Woods, in *Proceedings of the AIP Conference*, Vol. 343 (1995), p. 230.

[2] E. Torrence, *Determination of Electroweak Parameters at the SLC*, SLAC-PUB-7307, September 1996, to appear in Proc. of ICHEP96, Warsaw, Poland, July 25-31, 1996.

[3] SLD Collab., K. Abe *et al.*, Phys. Rev. Lett. **70**, 2515 (1993).

[4] SLD Collab., K. Abe *et al.*, Phys. Rev. Lett. **73**, 25 (1994).

[5] SLD Collab., K. Abe *et al.*, *Measurement of the Z^0-Lepton Couplings Asymmetries A_l*, SLAC-PUB-7234, July 1996, contribution (PA07-063) to ICHEP96.

[6] SLD Collab., K. Abe *et al.*, Phys. Rev. Lett. **74**, 2880 (1995).

[7] SLD Collab., K. Abe *et al.*, Phys. Rev. Lett. **78**, 17 (1997).

[8] LEP Electroweak Working Group and SLD Heavy Flavor Group, *A Combination of Preliminary LEP and SLD Electroweak Measurements and Constraints on the Standard Model*, LEPEWWG/96-02, July 1996.

[9] C. J. S. Damerell *et al.*, Nucl. Instrum. Methods A **288**, 236 (1990).

[10] M. D. Hildreth *et al.*, IEEE Trans. Nucl. Sci. **42**, 451 (1994).

[11] SLD Collab., K. Abe *et al.*, Phys. Rev. D **53**, 1023 (1996).

[12] K. Abe *et al.*, Nucl. Instrum. Methods A **343**, 74 (1994).

[13] ARGUS Collab., H. Albrecht *et al.*, Z. Phys. C **62**, 371 (1994).

[14] SLD Collab., K. Abe *et al.*, *Measurement of A_b and A_c at the Z^0 Resonance Using a Lepton Tag*, SLAC-PUB-7233, July 1996, contribution (PA10-026) to ICHEP96.

[15] D. Axen *et al.*, Nucl. Instrum. Methods A **328**, 472 (1993).

[16] A. C. Benvenuti *et al.*, Nucl. Instrum. Methods A **290**, 353 (1990).

[17] SLD Collab., K. Abe *et al.*, Phys. Rev. Lett. **74**, 2895 (1995).

[18] D. Su, *Production of Charm and Beauty in e^+e^- with Polarized Electron Beam*, SLAC-PUB-7000, September 1995, *Proc. of 6th Int. Symp. on Heavy Flavor Physics*, Pisa, Italy, June 6-10, 1995.

[19] T. Takeuchi, A. Grant, and J. Rosner in *Proceedings of the 8th Meeting Division of Particles and Fields*, Albuquerque, August, 1994, Vol. 2 (World Scientific, New York, 1995), p. 1231.

[20] D. Jackson, Nucl. Instrum. Methods A **388**, 247 (1997).

[21] See, for example, I. I. Bigi *et al.*, in *B Decays*, edited by S. Stone (World Scientific, New York, 1994), p. 132.

[22] SLD Collab., K. Abe *et al.*, *Measurements of the B^+ and B^0 Lifetimes with Topological Vertexing at SLD*, SLAC-PUB-7227, July 1996, contribution (PA05-085) to ICHEP96.

[23] SLD Collab., K. Abe *et al.*, *Measurements of the B^+ and B^0 Lifetimes from the Semileptonic Decays at SLD*, SLAC-PUB-7226, July 1996, contribution (PA05-084) to ICHEP96.

[24] See, for example, L. K. Gibbons, *Status of Weak Quark Mixing* UR-1494, April 1997, to appear in *Proc. of ICHEP96*, Warsaw, Poland, July 25-31, 1996, and references therein.

[25] SLD Collab., K. Abe *et al.*, *Preliminary Measurements of the Time Dependence of $B^0_d - \overline{B^0_d}$ Mixing with Kaon and Charge Dipole Tags*, SLAC-PUB-7230, July 1996, contribution (PA08-027/028) to ICHEP96.

[26] SLD Collab., K. Abe *et al.*, *Measurement of Time-dependent B^0_d-$\overline{B^0_d}$ Mixing Using Topology and Charge Selected Semileptonic B Decays*, SLAC-PUB-7229, July 1996, contribution (PA08-026B) to ICHEP96.

[27] SLD Collab., K. Abe *et al.*, *Measurement of Time-Dependent B^0_d-$\overline{B^0_d}$ Mixing Using Inclusive Semileptonic Decays*, SLAC-PUB-7230, July 1996, contribution (PA08-026A) to ICHEP96.

[28] SLD Collab., K. Abe *et al.*, Phys. Lett. B **386**, 475 (1996).

[29] B. Schumm *et al.*, Phys. Rev. Lett. **69**, 3025 (1992).

[30] V. A. Petrov and A. V. Kisselev, Z. Phys. C **66**, 453 (1995).

[31] SLD Collab., M. Dima, SLAC-PUB-7199, June 1996, *Production of $\pi^\pm$, $K^\pm$, ρ, K^0_s, Λ^0, K^{*0} and ϕ in Hadronic Z^0 decays*, SLAC-PUB-7280, Aug. 1996, to appear in *Proc. of the 9th Meeting Division of Particles and Fields*, Minneapolis, Minnesota, Aug. 10-15, 1996.

[32] SLD Collab., K. Abe *et al.*, Phys. Rev. Lett. **78**, 3442 (1997).

RECENT RESULTS FROM LEP AT THE Z ON ELECTROWEAK AND HEAVY FLAVOR PHYSICS

Klaus Mönig
CERN/PPE
1211 Genève 23
Switzerland

ABSTRACT

The four LEP experiments ALEPH, DELPHI, L3, and OPAL have collected about four million Z decays each between 1990 and 1995 at energies close to the Z pole. Most of the data have been taken between 1992 and 1995 on the peak and at approximately 2 GeV above and below.

Recent preliminary results, using a large fraction of the full statistics, are presented on electroweak and selected topics of b physics.

© 1996 Klaus Mönig.

1 Introduction

Between 1989 and 1995, LEP has been operated at center-of-mass energies within a few GeV of the Z peak. Each experiment has collected about $4 \cdot 10^6$ hadronic and $4 \cdot 10^5$ leptonic Z decays. Out of this, the luminosity collected at energies a few GeV away from the nominal Z mass is about 40 pb^{-1} per experiment.

Apart from the usual tracking and calorimetry, all experiments are equipped with powerful silicon microvertex detectors allowing for an efficient tagging of b and c quarks.

For the determination of the Z resonance parameters, close to the full statistics have been used. For most other analyses, the data taken up to 1994 are included, which corresponds to more than 80% of the total available statistics.

For all of the electroweak and for some important b-physics quantities, the LEP collaborations have taken a special effort to combine the results in a consistent way, taking into account common systematic uncertainties.

2 The Z Lineshape

The cross section $e^+e^- \to f\bar{f}$, $f \neq e$ near the Z pole at a center-of-mass energy $\sqrt{s}$, can be written as

$$\sigma_f(s) = \frac{12\pi}{m_Z^2} \frac{\Gamma_e \Gamma_f s}{(s-m_Z^2)^2 + \left(\frac{s}{m_Z}\right)^2 \Gamma_Z^2} + \sigma_\gamma + \sigma_{\mathrm{int}} + \text{rad. cor.}$$

The first term describes the dominant contribution from Z exchange; σ_γ and σ_{int} denote the contributions from γ-exchange and $\gamma - Z$ interference which are very much suppressed at center-of-mass energies close to the Z mass. The radiative corrections can be calculated in QED and depend only on the cross section at energies below the center-of-mass energy at which the cross section is measured. Γ_Z stands for the total decay width of the Z and Γ_f for its partial decay width into an $f\bar{f}$ pair. For $f = e$, in addition, the contributions from t-channel γ and Z exchange have to be added.

The LEP experiments extract from the cross sections a set of minimal correlated parameters that are more convenient for averaging and for electroweak fits. These parameters are:

$$\begin{aligned} m_Z & \\ \Gamma_Z & \\ \sigma_0^{\mathrm{had}} &= \frac{12\pi}{m_Z^2} \frac{\Gamma_e \Gamma_{\mathrm{had}}}{\Gamma_Z^2} \\ R_\ell &= \frac{\Gamma_{\mathrm{had}}}{\Gamma_\ell} \quad \ell = e, \mu, \tau. \end{aligned}$$

The maximum correlation between these parameters is 14%.

2.1 Determination of the Beam Energy

The determination of the Z mass and width depends crucially on the accurate knowledge of the LEP beam energy for the off-peak fills. For that reason, at the end of each such fill, an energy calibration using the resonant depolarization technique is attempted, which determines the beam energy to a precision of about 0.2 MeV. However, the total error on the beam energy is significantly larger for several reasons:

- Only a part of the off peak fills are successfully calibrated at the end (40% in 1993, 70% in 1995). For the others, an extrapolation model is needed.
- Imperfections in the RF system make the energies in the interaction points different from the mean energy. These errors are anticorrelated between the different experiments so that they cancel to a large extent in the LEP average.
- The beam energy rises with time due to hysteresis effects in the LEP magnets. This effect has been discovered only during the 1995 scan due to newly installed NMR probes in the LEP tunnel. As illustrated in Fig. 1, these effects are originated by leakage currents through the beam pipe induced by trains in the Geneva region.

A detailed description of the full procedure can be found in Ref. 1. The total error on the Z mass and width from the limited knowledge of the beam energy is $\Delta m_Z = 1.5$ MeV and $\Delta\Gamma_Z = 1.7$ MeV.

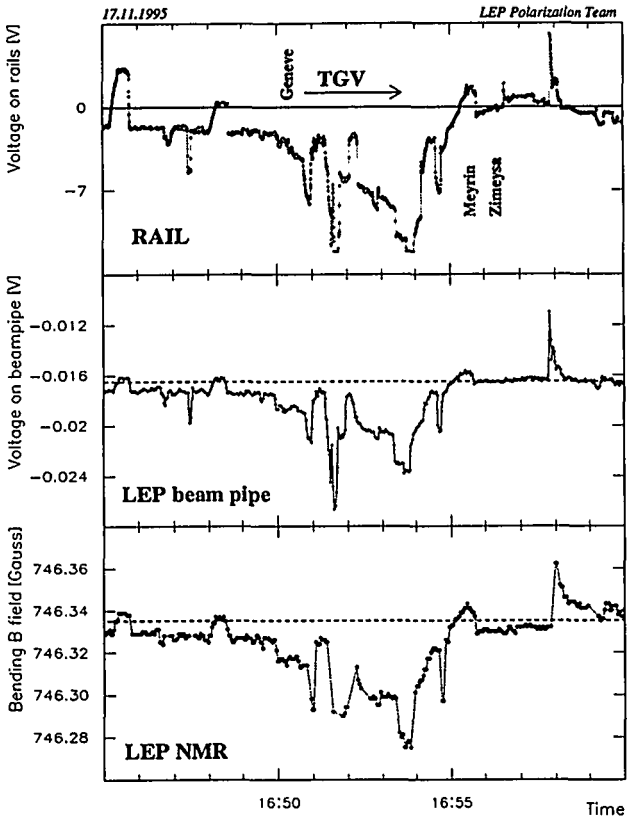


Fig. 1. Effect of trains on the LEP beam energy. The upper plot shows the voltage measured on the rails while a train is passing close to the LEP tunnel. The middle plot shows the voltage measured simultaneously on the LEP beam pipe, and the lower plot shows the field of the dipole magnets measured by an NMR probe.

2.2 Measurement of the Cross Section

Generally, a cross section is given by

$$\sigma = \frac{N}{\mathcal{L}},$$

where N is the acceptance- and background-corrected number of events and $\mathcal{L}$ the integrated luminosity.

The large acceptance of the LEP detectors and the clean environment of the accelerator allow for a determination of the event rate of typically better than 0.1% for $e^+e^- \to$ hadrons and better than 0.5% for the leptonic channels.

The luminosity at LEP is determined from Bhabha scattering at low angles for which the cross section can be calculated reliably in QED. All experiments measure this cross section now to better than 0.1%, and the theoretical calculation is accurate to 0.11%.

2.3 Results

The results on the Z lineshape from the different experiments can be found in Refs. 2–5 and are summarized in Table 1. As an example, the hadronic lineshape measured by the L3 Collaboration is shown in Fig. 2. Combining the four experiments yields:

$$\begin{aligned} m_Z &= 91.1863 \pm 0.0020\,\text{GeV}, \\ \Gamma_Z &= 2.4946 \pm 0.0027\,\text{GeV}, \\ \sigma_0^{\text{had}} &= 41.508 \pm 0.056\,\text{nb}, \\ R_e &= 20.754 \pm 0.057, \\ R_\mu &= 20.796 \pm 0.040, \\ R_\tau &= 20.814 \pm 0.055, \\ R_\ell &= 20.778 \pm 0.029, \end{aligned}$$

where R_ℓ is the result assuming lepton universality, corrected to a massless lepton. From this, the following partial widths can be derived:

$$\begin{aligned} \Gamma_{\text{had}} &= 1743.6 \pm 2.5\,\text{MeV}, \\ \Gamma_e &= 83.96 \pm 0.15\,\text{MeV}, \\ \Gamma_\mu &= 83.79 \pm 0.22\,\text{MeV}, \end{aligned}$$

$$\Gamma_\tau = 83.72 \pm 0.26\,\mathrm{MeV},$$
$$\Gamma_\ell = 83.91 \pm 0.11\,\mathrm{MeV},$$
$$\Gamma_{inv.} = 499.5 \pm 2.0\,\mathrm{MeV}.$$

Taking the ratio of the invisible to the neutrino partial width from the Standard Model yields for the number of light neutrino generations:

$$N_\nu = 2.989 \pm 0.012.$$

	ALEPH	DELPHI	L3	OPAL
m_Z(GeV)	91.1873±0.0030	91.1859±0.0028	91.1883±0.0029	91.1824±0.0039
Γ_Z(GeV)	2.4950±0.0047	2.4896±0.0042	2.4996±0.0043	2.4956±0.0053
σ_0^{had}(nb)	41.576±0.083	41.566±0.079	41.411±0.074	41.53±0.09
R_e	20.64±0.09	20.93±0.14	20.78±0.11	20.82±0.14
R_μ	20.88±0.07	20.70±0.09	20.84±0.10	20.79±0.07
R_τ	20.78±0.08	20.78±0.15	20.75±0.14	20.99±0.12
$A_{FB}^{0,e}$	0.0187±0.0039	0.0179±0.0051	0.0148±0.0063	0.0104±0.0052
$A_{FB}^{0,\mu}$	0.0179±0.0025	0.0153±0.0026	0.0176±0.0035	0.0146±0.0025
$A_{FB}^{0,\tau}$	0.0196±0.0028	0.0223±0.0039	0.0233±0.0049	0.0178±0.0034

Table 1. Lineshape and asymmetry parameters from the data of the four LEP experiments.

2.4 Forward-Backward Lepton Asymmetries

The forward-backward asymmetry for a fermion f is defined as

$$A_{FB}^f = \frac{N_F - N_B}{N_F + N_B},$$

where N_F (N_B) is the number of events, where the fermion f is scattered in the incoming electron (positron) direction. On Born level, the differential cross section with respect to the scattering angle is given by

$$\frac{\partial\sigma}{\partial\cos\theta} = \sigma_{tot}\left(\frac{3}{8}(1+\cos^2\theta) + A_{FB}\cos\theta\right),$$

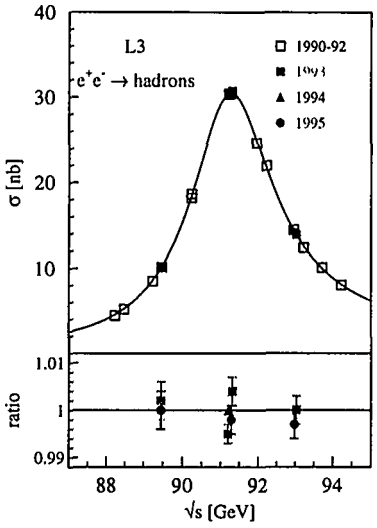


Fig. 2. The hadronic lineshape measured by the L3 Collaboration.

which is only weakly modified by radiative corrections. For pure Z exchange, the forward-backward asymmetry can be expressed as

$$A_{FB}^{0,f} = \frac{3}{4}\mathcal{A}_e\mathcal{A}_f,$$

with $\mathcal{A}_f = \frac{2g_{Vf}g_{Af}}{g_{Vf}^2+g_{Af}^2}$. g_{Vf}, (g_{Af}) denotes the vector (axial vector) coupling of the Z to the fermion f. The ratio of these two couplings is given by the weak mixing angle

$$\frac{g_{Vf}}{g_{Af}} = 1 - 4Q_f\sin^2\theta_{eff}^f.$$

Figure 3 shows the differential cross section $e^+e^- \to \mu^+\mu^-$ at the three energies obtained by DELPHI. The energy dependence of A_{FB} is given by the $\gamma - Z$ interference and contains little information on electroweak quantities. For that reason, the experiments fit the asymmetries at the different energies, together with the lineshape, leaving only $A_{FB}^{0,\ell}$, $\ell = e, \mu, \tau$ as additional free parameters.

The results are described in Refs. 2–5 and included in Table 1. The combined results are:

$$\begin{aligned} A_{\rm FB}^{0,e} &= 0.0160 \pm 0.0024, \\ A_{\rm FB}^{0,\mu} &= 0.0162 \pm 0.0013, \\ A_{\rm FB}^{0,\tau} &= 0.0201 \pm 0.0018, \\ A_{\rm FB}^{0,\ell} &= 0.0174 \pm 0.0010. \end{aligned}$$

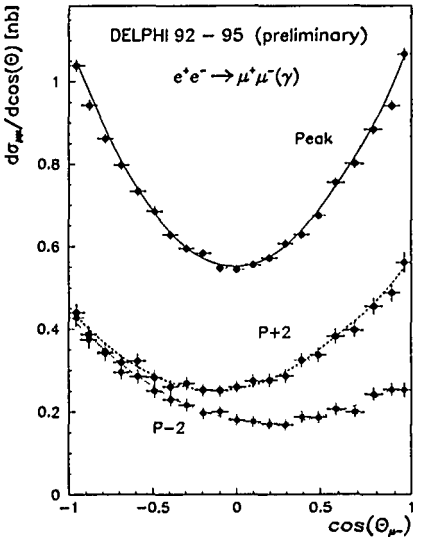


Fig. 3. Differential cross section $e^+e^- \to \mu^+\mu^-$ measured by DELPHI.

2.5 τ Polarization

The mean τ polarization as a function of the scattering angle is given by:

$$\mathcal{P}_\tau(\cos\theta) = -\frac{\mathcal{A}_\tau(1+\cos^2\theta) + 2\mathcal{A}_e\cos\theta}{1+\cos^2\theta + 2\mathcal{A}_\tau\mathcal{A}_e\cos\theta}.$$

From a measurement of the angular dependence of $\mathcal{P}_\tau$, $\mathcal{A}_e$ and $\mathcal{A}_\tau$ can thus be determined separately with almost no correlation.

The τ polarization can be extracted from the energy and decay angles of the τ decay products. This is illustrated for four different decay modes in Fig. 4. Figure 5 shows the polarization as a function of the scattering angle from the L3 analysis.

The results of the different experiments are described in Refs. 6–9 and summarized in Fig. 6. Combining them yields:

$$\begin{aligned} \mathcal{A}_e &= 0.1382 \pm 0.0076, \\ \mathcal{A}_\tau &= 0.1401 \pm 0.0067, \\ \mathcal{A}_\ell &= 0.1393 \pm 0.0050, \end{aligned}$$

where $\mathcal{A}_\ell$ denotes the result assuming lepton universality.

2.6 Z-Lepton Couplings

Since Γ_ℓ depends on the squared sum of the vector and axial-vector couplings $(g_{V\ell}^2 + g_{A\ell}^2)$ and the coupling parameter $\mathcal{A}_\ell$ that determines the asymmetries on the ratio $\left(\frac{g_{V\ell}}{g_{A\ell}}\right)$, the two couplings can be determined separately. Table 2 summarizes the result with and without the assumption of lepton universality. Also shown are the results if the left-right asymmetry measured at SLD[10] is included. The LEP results are shown in Fig. 7 together with the Standard Model prediction and the SLD result. The LEP data agree well with lepton universality. Also, good agreement with the prediction and with the SLD result can be seen.

3 Electroweak Physics with Quarks

b and c quarks can be tagged with high efficiency and purity, so that they can be used for electroweak analyses. Two types of quantities are of basic interest:

- the forward-backward asymmetries $A_{\rm FB}^{\rm b}$, $A_{\rm FB}^{\rm c}$,
- the normalized partial widths $R_{\rm b}^0$, $R_{\rm c}^0$ $(R_q^0 = \frac{\Gamma_q}{\Gamma_{\rm had}})^*$.

As can be seen from Table 3, the quark asymmetries are an efficient measure of $\sin^2\theta_{eff}^l$. The sensitivity is about a factor three larger than for charged leptons, and the total statistics for b and c quarks is each about equal to the sum of all

*The ^{0} always indicates that a quantity is corrected to pure Z exchange.

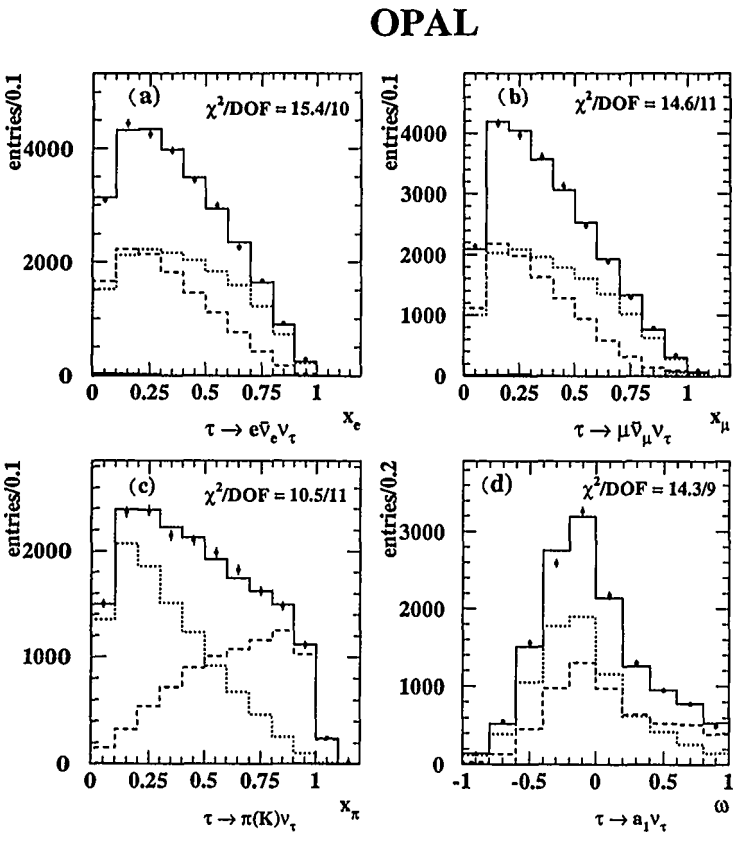


Fig. 4. Polarization-sensitive variables for τ decays in the OPAL analysis for (a) $\tau \to e\bar{\nu}\nu$, (b) $\tau \to \mu\bar{\nu}\nu$, (c) $\tau \to \pi\nu$, and (d) $\tau \to a_1\nu$. For (a)-(c), the sensitive variable plotted is the normalized energy of the charged decay particle. For (d), the variable is an optimized variable constructed from the a_1 energy and the decay angles in the a_1 decay. The points with the error bars represent the data, the dashed line the prediction for positive polarized taus, and the dotted line for negative polarized taus. The solid line is a fit to the data with the polarization left free.

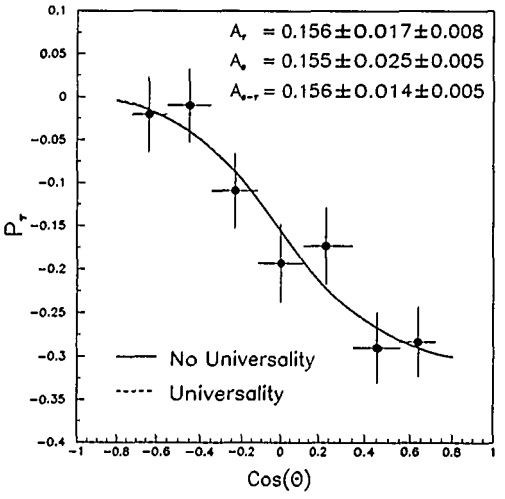


Fig. 5. τ polarization as a function of the scattering angle from the L3 Collaboration. The line represents a fit to the data with (dashed) and without (solid) the assumption of lepton universality.

	Without Lepton Universality:	
	LEP	LEP+SLD
g_{Ve}	-0.0368 ± 0.0015	-0.03828 ± 0.00079
$g_{V\mu}$	-0.0372 ± 0.0034	-0.0358 ± 0.0030
$g_{V\tau}$	-0.0369 ± 0.0016	-0.0367 ± 0.0016
g_{Ae}	-0.50130 ± 0.00046	-0.50119 ± 0.00045
$g_{A\mu}$	-0.50076 ± 0.00069	-0.50086 ± 0.00068
$g_{A\tau}$	-0.50116 ± 0.00079	-0.50117 ± 0.00079
	With Lepton Universality:	
	LEP	LEP+SLD
$g_{V\ell}$	-0.03688 ± 0.00085	-0.03776 ± 0.00062
$g_{A\ell}$	-0.50115 ± 0.00034	-0.50108 ± 0.00034

Table 2. Results for the effective vector and axial-vector couplings derived from the combined LEP data without and with the assumption of lepton universality. For the right column, the SLD measurement of A_{LR} is also included.

	$\frac{\partial A_{FB}}{\partial \sin^2\theta}$	$\frac{\Gamma_f}{\Gamma_Z}$
e, μ, τ	1.7	$3 \times 3.4\%$
c	4.3	12%
b	5.6	15%

Table 3. Sensitivity of A_{FB} to $\sin^2\theta^l_{eff}$ and Z branching ratio for charged leptons, c and b quarks.

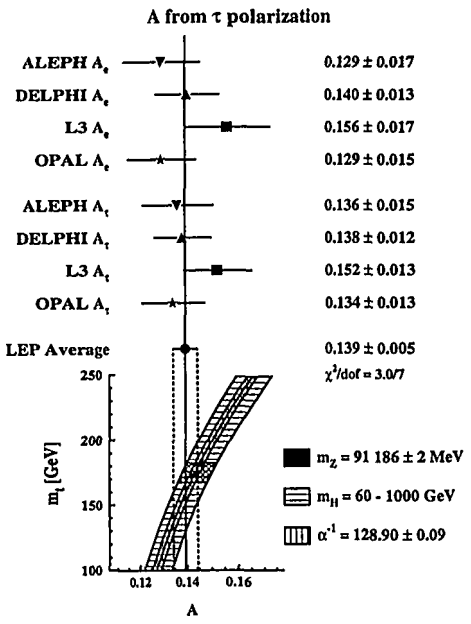


Fig. 6. Measurement of the τ polarization and its asymmetry at LEP.

lepton species. In principle, the forward-backward asymmetries depend on the product of the initial- and final-state coupling. However, if $\sin^2\theta^q_{eff}$ is written as $\sin^2\theta^q_{eff} = \sin^2\theta^l_{eff} + \delta_q$, in the Standard Model δ_c is constant. The variation of δ_b is about the same size as for $\sin^2\theta^l_{eff}$, but the sensitivity of A^b_{FB} to δ_b is two orders of magnitude smaller than the sensitivity to $\sin^2\theta^l_{eff}$.

For R^0_b and R^0_c, practically all QED, QCD, and electroweak propagator corrections cancel, and only corrections to the $Z \to q\bar{q}$ vertex remain. R^0_c is thus predicted by the Standard Model with a very small error. In this model, R^0_b depends only on the top quark mass; however, in supersymmetric extensions, some dependence on the stop and chargino sector also arises.

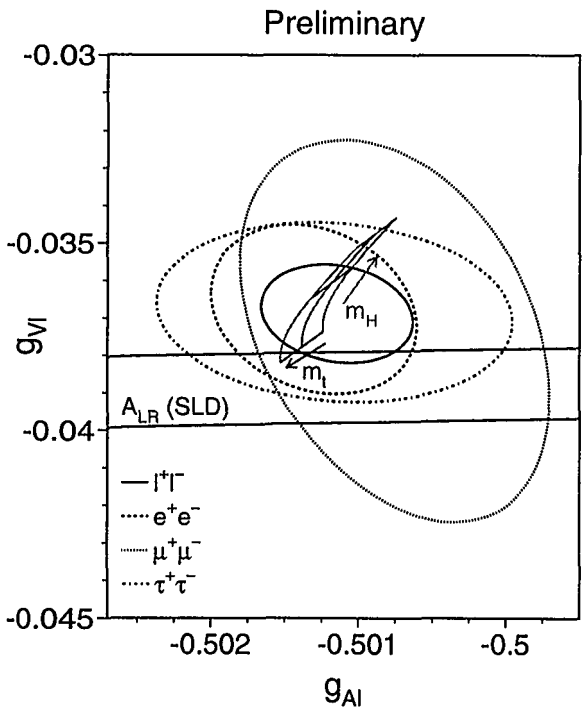


Fig. 7. Contours of 68% probability in the g_{Vl}-g_{Al} plane from LEP measurements. The solid contour results from a fit assuming lepton universality. Also shown is the one standard deviation band resulting from the A_{LR} measurement of SLD. The grid corresponds to the Standard Model prediction for $m_t = 175 \pm 6$ GeV and $m_H = 300^{+700}_{-240}$ GeV. The arrows point in the direction of increasing values of m_t and m_H.

3.1 Tagging Methods

Basically three methods exist to tag b and c quarks:

- lifetime tags, using impact parameters or secondary vertices for b quarks,
- high momentum leptons in jets for b and c quarks,
- exclusively or inclusively reconstructed D mesons, mainly for c quarks.

3.1.1 Lifetime Tags

The lifetime tags provide the purest and most efficient methods to tag b quarks. Basically, two principle methods exist. Either the experiments try to reconstruct secondary vertices and measure the distance of such vertices to the primary one or the beam spot (DELPHI, OPAL), or the presence of tracks with a large impact parameter with respect to the primary vertex is used as the tagging method (ALEPH, DELPHI, L3). For the tagging of b hemispheres, both methods give purities of more than 90% for efficiencies of more than 20%. Recently, ALEPH combined the lifetime tag with a cut on invariant masses and obtained a 98% purity at an efficiency of 23% (Ref. 11). Figure 8 shows the uds and c efficiency for this tag as a function of the b-tagging efficiency.

3.1.2 Lepton Tags

High-momentum leptons in jets have long been used to tag b and c quarks. An almost pure sample from prompt $b \to \ell$ decays can be obtained by cutting on the transverse momentum of the lepton relative to the jet axis. However, a clean separation of leptons from charm and those from b-cascade leptons and misidentified hadrons is not possible.

OPAL recently improved their lepton tagging by the use of additional variables measured from the jet to which the lepton is associated.[21] As can be seen from Fig. 9, this gives a very good purity for $b \to \ell$ and also a reasonable purity for $c \to \ell$.

Although efficiency and purity for the lepton tag are not as good as for the lifetime tags, the lepton measurements still provide the most accurate results on the b asymmetry, since the lepton charge is an efficient indicator of the quark charge.

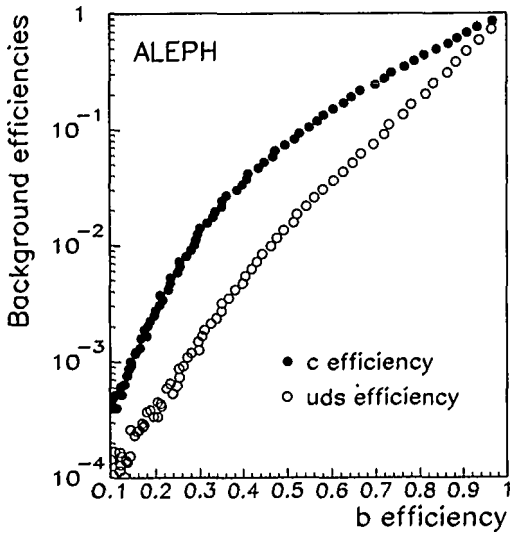


Fig. 8. uds and c efficiency as a function of the b efficiency for the ALEPH lifetime plus mass tag.

3.1.3 D-Meson Tags

D mesons indicate the presence of either c or b quarks. However, the D's from charm tend to have a higher momentum than the ones from B decays. Further separation of the two quark flavors, less dependent on the knowledge of fragmentation properties, is possible using lifetime tags as described above. Three different methods to tag D-mesons are used:

- Exclusive $D^{*\pm}$ reconstruction: First a D^0† is reconstructed and then the D^0 is combined with a π^+ to a D^{*+}. Due to the small $D^{*+} - D^0$ mass difference, the available phase space for the π^+ is very small leading to a good resolution in the mass difference. For this reason, many D^0 decay modes can be used, even some where the D^0 is reconstructed only partially, still giving a small combinatorial background.

†If not mentioned explicitly, charge conjugate modes are always included.

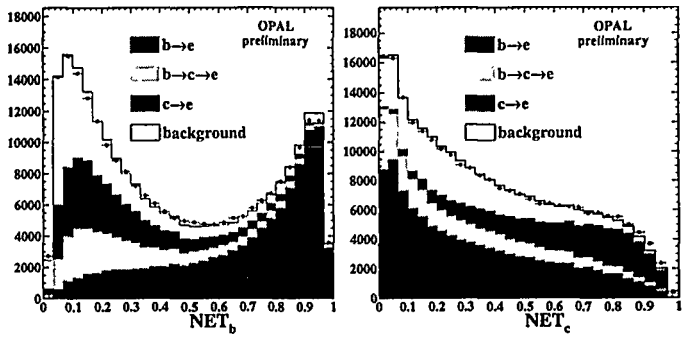


Fig. 9. Network output for the different electron sources in the OPAL lepton tag.

- Inclusive $D^{*\pm}$ reconstruction: Due to the small $D^{*+} - D^0$ mass difference, the π^+ from the D^{*+} decay is forced to follow the D^{*+} flight direction and to have a relatively low momentum. This leads to a small transverse momentum of the decay pion with respect to the jet axis. Due to the large background, an event-by-event tag is not possible with this method. However, the number of D^{*+} mesons in a sample can be obtained from the excess of particles at low p_t in the p_t distribution.
- Exclusive charmed hadron reconstruction: Clean signals can be obtained for basically all weakly decaying charmed hadrons. However, the combinatorial background is rather high for all of these channels.

3.2 Combination of Data

The combination of the LEP heavy flavor data is more complicated than for the lineshape and τ polarization measurements. In some cases, more than one quantity is measured in the same analysis leading to statistical correlations, and in all cases, assumptions on heavy flavor production and decay properties are needed leading to correlations in the systematic errors between different measurements. In addition, some measurements depend explicitly on the values assumed for the other quantities, e.g., the double-tag measurements of R_b depend on the value assumed for R_c. All this makes it necessary to have a well-defined procedure to combine the electroweak results with heavy flavors.

In addition, SLD produces measurements on R_b that are comparable to the ones at LEP and measurements of the polarized forward-backward asymmetries of b and c quarks that are physically independent of the LEP observables, but they need the same assumptions and are therefore systematically correlated with the LEP numbers.

The LEP experiments and SLD have agreed on a common set of input parameters and their errors to be used for the heavy flavor analyses and a procedure to combine the results. A detailed write-up of the full procedure can be found in Ref. 13. The input parameters have been updated recently[14] to take into account new measurements. The main updates are:

- All numbers taken from PDG have been updated with the 96 edition.[15]
- Acceptance biases to the QCD corrections to the forward-backward asymmetries have been evaluated. The experimental cuts select predominantly high momentum quarks. On the contrary, the QCD correction, which has a total size of about 3% of the asymmetry, is mainly due to low momentum quarks with a random direction after hard gluon radiation. The QCD correction is thus reduced by about a factor of two.
- The production rates of charmed hadrons are taken from LEP measurements. These rates enter directly in the interpretation of charmed hadron cross sections in terms of R_c and at second order in the estimate of the charm-background in the R_b analyses. Up to now, these rates have been evaluated from data taken at lower energy. This needed, however, the assumption that the fragmentation process is energy independent.
- The probability that a gluon splits into a $c\bar{c}$ pair is measured by OPAL.[16] This number is used in all the LEP/SLD analyses now. The ratio $\frac{g\to b\bar{b}}{g\to c\bar{c}}$ is still taken from theory but DELPHI has presented a preliminary measurement of the gluon splitting to $b\bar{b}$ which is consistent with the number used.[17]

3.3 Quark Asymmetries

For A_{FB}^b, there are two methods with about equal precision:

- lepton tags,
- lifetime tags combined with a jet charge technique.

The lepton tag analyses measure A_{FB}^b either in a sample of high p and p_t leptons or as a function of the lepton momentum and transverse momentum. In both cases, the Monte Carlo is used to predict the sample composition that is needed to correct the raw asymmetry. In addition, the data have to be corrected for QCD effects and $b\bar{b}$ mixing. However, all corrections are well under control, and the measurements are statistically limited. Most of the needed input parameters like the average mixing and semileptonic branching ratios are measured by the LEP experiments themselves, sometimes even in the same analyses. The results of the experiments on A_{FB}^b with leptons and the lepton fits can be found in Refs. 18–21.

For the lifetime plus jet charge measurements, first a $b\bar{b}$ sample is selected with a lifetime tag and the quark charge is measured from the mean jet charge on a statistical basis. Using the sum and the difference of the two-hemisphere jet charges, the charge tagging efficiency is extracted simultaneously from data. Only corrections due to hemisphere correlations and light quark backgrounds need to be taken from Monte Carlo. Effects from b mixing and QCD are already included in the measured charge tagging efficiency. The results of the four experiments are reported in Refs. 19, 22, and 23.

Figure 10(a) summarizes the results obtained with the two methods. In addition, DELPHI and OPAL report results on A_{FB}^b with D mesons. However, this is basically to take care of the correlation with A_{FB}^c, and the results are not competitive with the analyses presented here.

A_{FB}^c is either measured with leptons together with A_{FB}^b or using D mesons. The results of the D-meson analyses can be found in Refs. 19, 24, and 25. Figure 10(b) summarizes the experimental results.

3.4 R_c

R_c is measured with several methods:

- Leptons (ALEPH, DELPHI): $R_c \cdot \mathrm{BR}(c \to \ell)$ can be obtained from leptons at low p_t. This measurement is systematically limited by $\mathrm{BR}(c \to \ell)$ which has to be inferred from low-energy data.
- Single/double tag (ALEPH, DELPHI): In a single/double-tag measurement, R_c can be extracted without knowing the tagging efficiency. Only Monte Carlo corrections for background and hemisphere correlations are needed.

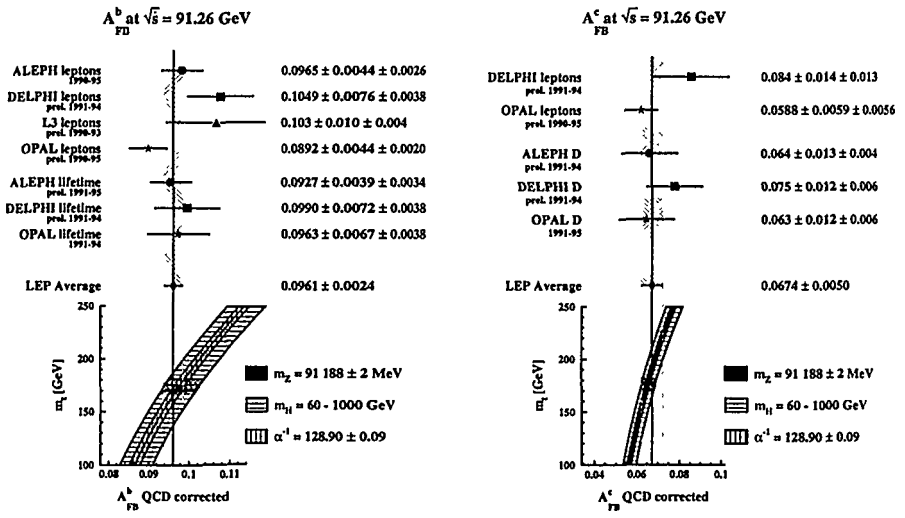


Fig. 10. (a) A^b_{FB} and (b) A^c_{FB} from the LEP experiments compared to the Standard Model prediction.

ALEPH and DELPHI have presented such measurements for R_c. ALEPH uses reconstructed D-mesons, which suffer from the low tagging efficiency. DELPHI uses instead a low p_t pion $D^{*\pm}$ tag. This measurement is, however, limited by the understanding of the background systematics in the single-tag sample.

- Inclusive/exclusive double tag (ALEPH, DELPHI, OPAL): This method tries to overcome the two problems in the single/double-tag measurements described above. In a first step, $R_c \cdot P(c \to D^{*+} \to \pi^+ D^0)$ is measured from exclusively reconstructed $D^{*\pm}$, where $P(c \to D^{*+} \to \pi^+ D^0)$ is the probability that a c quark fragments into a D^{*+} which subsequently decays in $D^0\pi^+$. In a second step, $P(c \to D^{*+} \to \pi^+ D^0)$ is measured from the low p_t pion rate opposite to an exclusively reconstructed $D^{*\pm}$. The disadvantage of this method is that the D^0 reconstruction efficiency in the single-tag sample needs to be known from simulation.

- Charm counting (DELPHI, OPAL): The production rate of a single charmed hadron D is proportional to $R_c \cdot f(D)$ where $f(D)$ is the probability that a charm quark fragments into a hadron D. Since all c quarks end up in a weakly decaying particle, the rates of those hadrons have to add up to one:

$$f(D^0) + f(D^+) + f(D_s) + 1.15 f(\Lambda_c) = 1,$$

where the factor 1.15 accounts for up-to-now-unmeasured charmed strange baryons. If the reconstruction efficiencies are known, R_c can therefore be measured from the sum of four single-tag measurements.

The results of the different measurements are presented in Refs. 26–28 and summarized in Fig. 11.

3.5 R_b

All precise measurements of R_b are single/double-tag measurements using a lifetime tag. In a recent analysis, ALEPH has upgraded this method by using five different tags[11]:

(1) a very pure impact parameter plus mass cut b tag,

(2) a neural net event shape b tag,

(3) a high p_t lepton b tag,

(4) a neural net c tag,

(5) an impact parameter uds tag.

All five single- and 15 double-tag rates are measured in their analysis. If all hemisphere correlations and the background efficiencies for the tag (1) are taken from Monte Carlo, R_b and all other efficiencies can be measured from data. The inclusion of the additional tags does not alter the systematic uncertainty but gives a substantial reduction in the statistical error.

All experiments include their data up to 1994 now, so that most of the LEP 1 statistics is used. However, some substantial improvements in the methods can still be expected. Figure 12 summarizes the results which are presented in Refs. 11, 29–31. Also, the result from SLD[10] is shown and included in the mean.

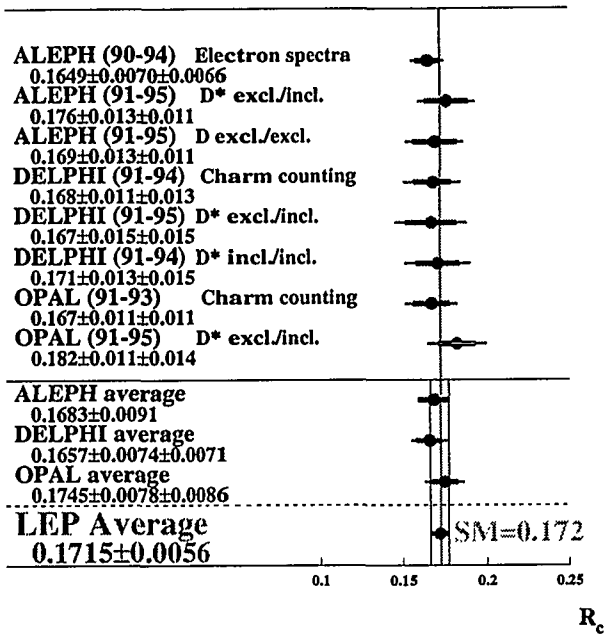


Fig. 11. The measurements of R_c at LEP.

3.6 Results

All measurements presented here and the polarized forward-backward asymmetries from SLD[10] have been combined with the method described in Sec. 3.2. The following results have been obtained:

$$
\begin{aligned}
R_b^0 &= 0.2178 \pm 0.0011, \\
R_c^0 &= 0.1715 \pm 0.0056, \\
A_{FB}^{0,b} &= 0.0979 \pm 0.0023, \\
A_{FB}^{0,c} &= 0.0735 \pm 0.0048, \\
\mathcal{A}_b &= 0.863 \pm 0.049, \\
\mathcal{A}_c &= 0.625 \pm 0.084.
\end{aligned}
$$

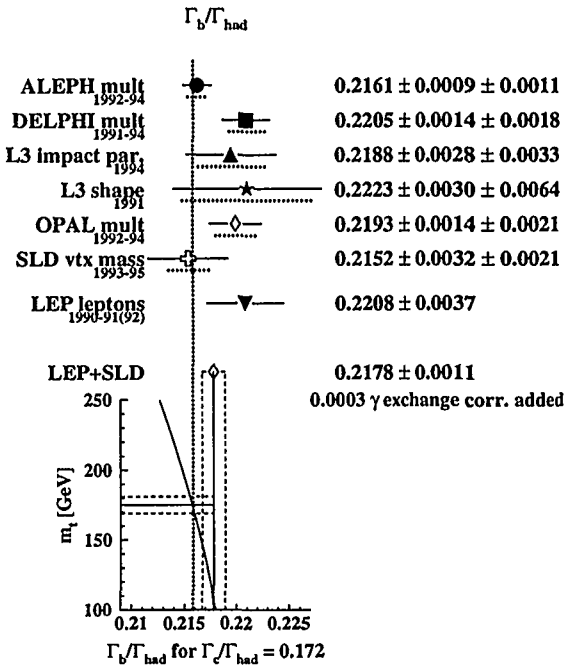


Fig. 12. The measurements of R_b at LEP and SLD.

The correlation matrix can be found in Table 4. The dominant error sources for the four LEP quantities are listed in Table 5. The errors on $\mathcal{A}_b$ and $\mathcal{A}_c$ are completely dominated by statistics and detector-dependent systematics.

4 Interpretation of Electroweak Data

4.1 The Weak Mixing Angle

All asymmetries measured at LEP and SLD can be interpreted in terms of the effective weak mixing angle $\sin^2\theta^l_{eff}$. If new physics appear only via radiative corrections, this is true also for the quark asymmetries, as explained in Sec. 3. The results for $\sin^2\theta^l_{eff}$ from the different observables are summarized in Fig. 13.

	R_b^0	R_c^0	$A_{FB}^{0,b}$	$A_{FB}^{0,c}$	$\mathcal{A}_b$	$\mathcal{A}_c$
R_b^0	1.00	-0.23	0.00	0.00	-0.03	0.01
R_c^0	-0.23	1.00	0.04	-0.06	0.05	-0.07
$A_{FB}^{0,b}$	0.00	0.04	1.00	0.10	0.04	0.02
$A_{FB}^{0,c}$	0.00	-0.06	0.10	1.00	0.01	0.10
$\mathcal{A}_b$	-0.03	0.05	0.04	0.01	1.00	0.12
$\mathcal{A}_c$	0.01	-0.07	0.02	0.10	0.12	1.00

Table 4. The correlation matrix for the electroweak parameters from the heavy-flavor fit.

Source	R_b $\cdot 10^{-3}$	R_c $\cdot 10^{-3}$	A_{FB}^b $\cdot 10^{-3}$	A_{FB}^c $\cdot 10^{-3}$
statistics	0.67	3.7	2.0	4.1
internal syst.	0.53	2.9	0.8	2.2
QCD effects	0.31	0.4	0.3	0.4
$BR(D \to K^0 X)$	0.22	0.3	0	0
D decay mult.	0.29	0.5	0	0
$BR(D^0 \to K^- \pi^+)$	0.03	0.2	0	0
$BR(D^+ \to K^- \pi^+ \pi^+)$	0.10	0.3	0	0
$BR(D_s \to \phi \pi^+)$	0.06	1.1	0	0
Br(c $\to \ell$)	0.03	2.2	0.2	0.3
gluon splitting	0.44	0.8	0	0
b fragmentation	0.15	0.1	0.2	0.1
light quarks	0.17	0.3	0.4	0
total	1.12	5.6	2.3	4.8

Table 5. Dominant error sources of the electroweak parameters. For R_b, the errors are given with R_c fixed to 0.172.

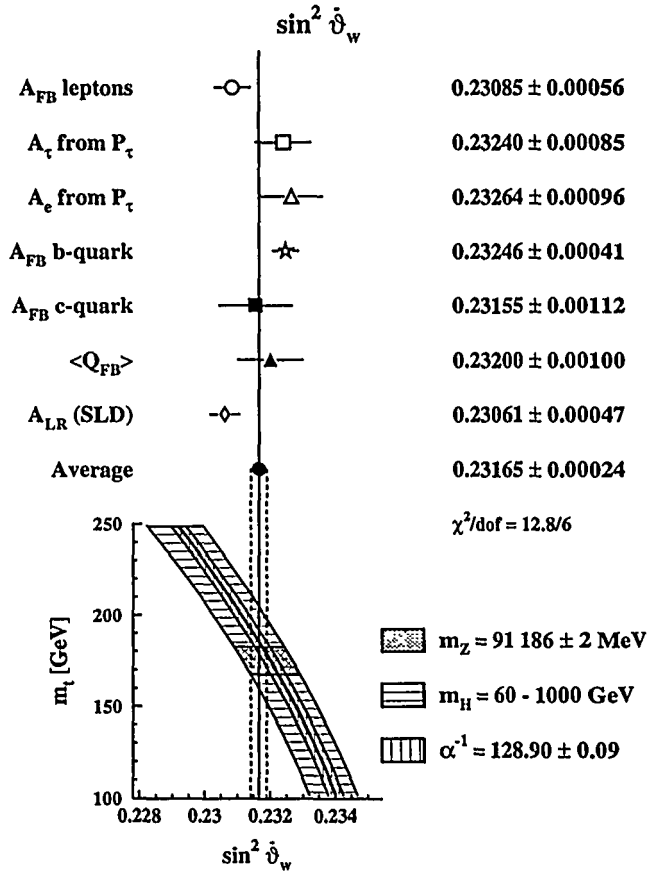


Fig. 13. The measurements of $\sin^2\theta^l_{eff}$ at LEP and SLD.

Their average, using all LEP and SLD results, is

$$\sin^2\theta^l_{eff} = 0.23165 \pm 0.00024.$$

The total χ^2 for the average is 12.8 for six degrees of freedom which corresponds to a probability of about 5%. Approximately equally responsible for the large χ^2 are the left-right asymmetry from SLD and A^b_{FB} from LEP.

In any interpretation of $\sin^2\theta^l_{eff}$, there is an additional uncertainty of 0.00023 coming from the uncertainty in the hadronic vacuum polarization in the running of the electromagnetic coupling constant $\Delta\alpha$. This uncertainty can only be reduced by better measurements of the total hadronic cross section at lower energies.

4.2 Quark Couplings

The polarized forward-backward asymmetries from SLD measure directly the coupling parameter for b and c quarks $\mathcal{A}_b$, $\mathcal{A}_c$. At LEP, these parameters can be obtained from the ratio of the quark asymmetries and $\mathcal{A}_\ell$ from the lepton asymmetries. Table 6 summarizes the quark coupling parameters for the LEP and LEP+SLD data and their Standard Model prediction. For the LEP-only data, the LEP value $\mathcal{A}_\ell = 0.1466 \pm 0.0033$ has been used. For the LEP+SLD, the combined value $\mathcal{A}_\ell = 0.1500 \pm 0.0025$ was used instead.

The bad agreement of $\mathcal{A}_b$ with the prediction is another manifestation of the differences in the $\sin^2\theta^l_{eff}$ results.

4.3 Standard Model Fits

If new physics appears only via radiative corrections, basically all electroweak observables can be expressed in terms of three quantities: Γ_ℓ, $\sin^2\theta^l_{eff}$, and m_W. Figure 14 shows the bands obtained from the world averages of these three quantities in the $\varepsilon_1 - \varepsilon_3$-plane defined by G. Altarelli *et al.*[32] The three bands cross each other in the region predicted by the Standard Model. This suggests that the data are globally consistent with this model.

Since the data agree well with the predictions of the Standard Model, they can be used to constrain its unknown parameters via their effects on the radiative corrections. To constrain the Higgs sector from the electroweak precision data, a global fit to all data has been performed. For the fit, the program ZFITTER[33]

	LEP	LEP+SLD	Standard Model
$\mathcal{A}_b$	0.890 ± 0.029	0.867 ± 0.022	0.935
$\mathcal{A}_c$	0.667 ± 0.047	0.646 ± 0.040	0.667

Table 6. LEP and LEP+SLD results on $\mathcal{A}_b$ and $\mathcal{A}_c$ compared to the Standard Model. Within the given precision, the prediction is without uncertainty.

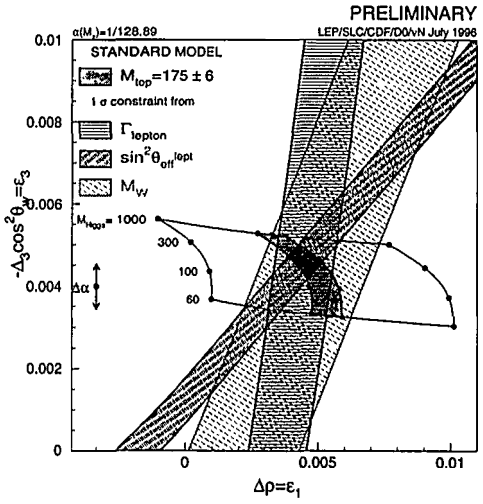


Fig. 14. Experimentally measured bands in the $\varepsilon_1 - \varepsilon_3$ plane from m_W, Γ_ℓ, and $\sin^2\theta^l_{eff}$ compared to the Standard Model prediction.

has been used; however, it has been shown that different programs give identical results.[34,35]

For all parameters apart from R_b, which depends only on m_t, the effects induced by the top and the Higgs particle are strongly correlated. The information on the Higgs boson mass is therefore improved significantly, if the direct measurement of m_t from the Tevatron[36] is imposed in the fit. Apart from the LEP and SLD data, m_W from the Tevatron[37] and $\sin^2\theta = 1 - m_W^2/m_Z^2$ from ν-nucleon scattering[38–40] are also used. The results of the fit are:

$$\begin{aligned} \log(m_H) &= 2.17^{+0.30}_{-0.35} \\ \alpha_s(m_Z^2) &= 0.120 \pm 0.003. \end{aligned}$$

The value of the strong coupling constant agrees well with the world average of 0.118 ± 0.003[15] which was obtained without the observables used here. The χ^2 of the fit is 19 for 14 degrees of freedom, which corresponds to a probability of 16%. From this, it can be concluded that the data agree globally well with each other and with the Standard Model. All data used are summarized in Table 7 together with the Standard Model predictions. The deviations from the prediction follow perfectly the expectation.

Figure 15 shows the variation of the fit χ^2 with the Higgs mass. The shaded band gives an estimate of the theoretical uncertainty. Including the theoretical error, an upper limit of $m_H < 550$ GeV can be derived at 95% confidence level.

5 Measurement of V_{cb} at LEP

The differential decay rate of the decay $\bar{B}^0 \to D^{*+}\ell\bar{\nu}_\ell$ with respect to the velocity of the D^{*+} in the B rest frame can be written as

$$\frac{\partial\Gamma}{\partial\omega} = \frac{G_F^2}{48\pi^2} m_{D^{*+}}^3 (m_{B^0} - m_{D^{*+}})^2 k(\omega)\sqrt{\omega^2-1} \times \mathcal{F}^2(\omega)|V_{cb}|^2,$$

where $k(\omega)$ is a known kinematic function. For the form factor $\mathcal{F}(\omega)$, HQET predicts[41]:

$$\begin{aligned} \mathcal{F}(\omega) &= \mathcal{F}(1)[1 - \rho^2(1-\omega) + c(1-\omega)^2] \\ \mathcal{F}(1) &= 0.91 \pm 0.04, \end{aligned}$$

where ρ^2 and c are in principle free parameters; however, the correlation between the two is also known from HQET with good precision.[41]

	Measurement with Total Error	Standard Model	Pull
LEP			
line shape and lepton asymmetries:			
m_Z [GeV]	91.1863 ± 0.0020	91.1861	0.1
Γ_z [GeV]	2.4946 ± 0.0027	2.4960	−0.5
σ_0^{had} [nb]	41.508 ± 0.056	41.465	0.8
R_ℓ	20.778 ± 0.029	20.757	0.7
$A_{FB}^{0,\ell}$	0.0174 ± 0.0010	0.0159	1.4
+ correlation matrix			
τ polarization:			
$\mathcal{A}_\tau$	0.1401 ± 0.0067	0.1458	−0.9
$\mathcal{A}_e$	0.1382 ± 0.0076	0.1458	−1.0
b and c quark results:			
R_b^0	0.2179 ± 0.0012	0.2158	1.8
R_c^0	0.1715 ± 0.0056	0.1723	−0.1
$A_{FB}^{0,b}$	0.0979 ± 0.0023	0.1022	−1.8
$A_{FB}^{0,c}$	0.0733 ± 0.0049	0.0730	0.1
+ correlation matrix			
$q\bar{q}$ charge asymmetry:			
$\sin^2\theta_{eff}^l$ ($< Q_{FB} >$)	0.2320 ± 0.0010	0.23167	0.3
SLD			
$\sin^2\theta_{eff}^l$ (A_{LR})	0.23061 ± 0.00047	0.23167	−2.2
R_b^0	0.2149 ± 0.0038	0.2158	−0.2
$\mathcal{A}_b$	0.863 ± 0.049	0.935	−1.4
$\mathcal{A}_c$	0.625 ± 0.084	0.667	−0.5
$p\bar{p}$ and νN			
m_W [GeV] ($p\bar{p}$)	80.356 ± 0.125	80.353	0.3
$1 - m_W^2/m_Z^2$ (νN)	0.2244 ± 0.0042	0.2235	0.2
m_t [GeV] ($p\bar{p}$)	175 ± 6	172	0.5

Table 7. The quantities used in the electroweak fit. The second column shows the experimental results, the third column the Standard Model prediction after the fit, and the fourth column the difference, normalized to the experimental error.

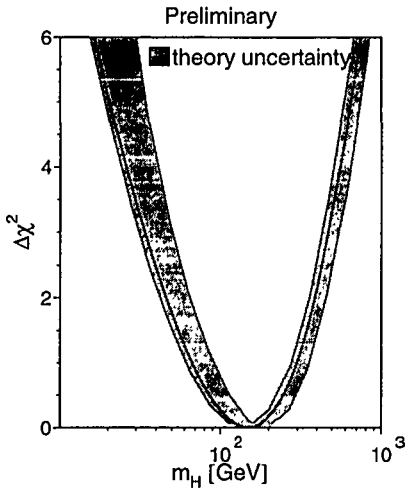


Fig. 15. $\Delta\chi^2$ as a function of the Higgs mass. The shaded band gives an estimate of the theoretical uncertainty.

The same analysis can also be performed at machines running at the $\Upsilon(4S)$, however, in a very complementary way:

- the data sample is typically larger at the $\Upsilon(4S)$-machines;
- at the $\Upsilon(4S)$, the B's are at rest; at LEP, the B momentum needs to be reconstructed;
- at the $\Upsilon(4S)$, the momentum of the pion in the $D^{*+} \to \pi^+ D^0$ decay is very low and its acceptance very small close to the interesting limit $\omega \to 1$; at LEP, however, the π^+ momentum distribution is more or less independent of ω.

ALEPH, DELPHI, and OPAL have performed analyses of V_{cb} using this decay.[42–44] $D^{*+}\ell$ events are selected in different D^0 decay channels with a typical efficiency of about 10% and a purity of about 80% independent of ω.

For the reconstruction of ω, the momentum vectors of the B and the D^{*+} need to be known. Since the D^{*+} is fully reconstructed, its momentum is measured with good precision. The $\bar{B}^0$ direction is reconstructed from the primary and secondary vertex positions. The energy is estimated from the D^{*+} and ℓ energies and from the missing momentum in the hemisphere of the $\bar{B}^0$. With this, a resolution of $\Delta\omega < 0.1$ is obtained.

The data are then fitted with two free parameters, $\mathcal{F}(1)|V_{cb}|$ and ρ^2. Figure 16(a) shows the ALEPH data together with the fit prediction. Figure 16(b) shows the same data and prediction after correction for detector effects and the kinematic terms. Good agreement with the linear dependence predicted by HQET can be observed.

The LEP results on V_{cb} and ρ^2 are summarized in Fig. 17. One obtains[45]

$$\begin{aligned} \mathcal{F}(1)|V_{cb}| &= (34.4 \pm 2.2)10^{-3}, \\ \rho^2 &= 0.56 \pm 0.13. \end{aligned}$$

Applying a scale factor of 1.23 on the error to account for some disagreement between the different experiments yields for the world average[46]:

$$\begin{aligned} \mathcal{F}(1)|V_{cb}| &= 0.0357 \pm 0.0021(\text{exp.}) \pm 0.0014(\text{curv.}), \\ \Longrightarrow \quad |V_{cb}| &= 0.0392 \pm 0.0027(\text{exp.}) \pm 0.0013.(\text{th.}). \end{aligned}$$

The result is in good agreement with the one obtained from the inclusive semileptonic decay rate $\text{Br}(b \to c\ell\nu)$ at LEP:

$$|V_{cb}| = 0.0420 \pm 0.0005(\text{exp.}) \pm 0.0041(\text{th.}),$$

but with much smaller theoretical uncertainty.

6 $B\bar{B}$ Mixing

B^0 and B_s^0 mesons mix with their antiparticles via box diagrams, mainly involving top-quark loops. The probability that a meson, which is produced at the time $t = 0$ as a particle B, decays at time t as its antiparticle $\bar{B}$ is given by

$$P(B \to \bar{B})(t) = \frac{\Gamma}{2} e^{-\Gamma t}(1 - \cos(\Delta m t)),$$

where Γ is the total B-decay width and Δm the mass difference between the two CP eigenstates. Δm depends on the elements of the CKM matrix:

$$\begin{aligned} \Delta m_{B^0} &\propto F_{B^0}|V_{td}V_{tb}^*|^2 \\ \Delta m_{B_s^0} &\propto F_{B_s^0}|V_{ts}V_{tb}^*|^2 \\ \frac{\Delta m_{B_s^0}}{\Delta m_{B^0}} &\propto \frac{F_{B_s^0}}{F_{B^0}}\left|\frac{V_{ts}}{V_{td}}\right|^2. \end{aligned}$$

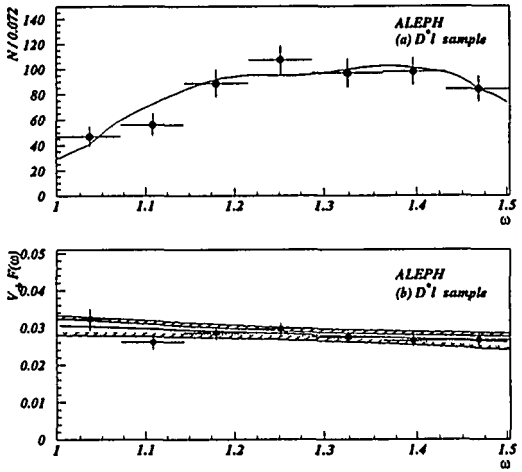


Fig. 16. (a) Differential event rate $dN/d\omega$ after cuts and background subtraction. The points are the data and the solid line is the result of the fit. (b) $\mathcal{F}(\omega)|V_{cb}|$ as a function of ω. The points are the data, corrected for all detector effects and kinematic terms. The solid line is the result of the fit. The shaded area represents its statistical error and the hatched line its systematic uncertainty.

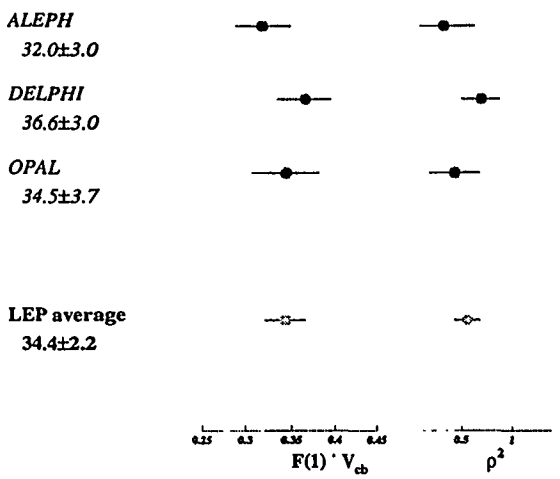


Fig. 17. Measurements of $\mathcal{F}(1)|V_{cb}|$ and ρ^2 at LEP.

The form factors F_{B^0}, $F_{B_s^0}$ need to be calculated from QCD. Some of the uncertainties in the calculation drop out in the ratio.

At LEP, B mesons fly several millimeters with an approximate vertex resolution of about 300 μm. The mixing probability can thus be observed as a function of the B lifetime. To measure B oscillations, one needs to

- identify the b charge at production time,
- identify the b charge at decay time,
- measure the proper time from production to decay.

6.1 B^0 Oscillations

For the measurement of B^0 oscillations, a special B^0 tagging is not needed, since B_s^0 mesons oscillate much faster and all other b hadrons don't oscillate. It is thus sufficient to reject background from light quark events.

6.1.1 Determination of the Production Charge

Generally, the b charge at production time is tagged by measuring the b charge in the opposite hemisphere. Two methods are used:

- a high p_t lepton,
- a jet-charge algorithm combined with a lifetime b tag.

Both methods provide a b purity of $\approx 90\%$ and a charge mistag rate of $\approx 25\%$.

6.1.2 Determination of the Decay Charge

Again, two methods are commonly used:

- a high p_t lepton,
- a $D^{*\pm}$ meson reconstructed either inclusively or exclusively.

6.1.3 Measurement of Proper Time t

The proper time from the production to the decay is given by $(t = \frac{l m_B}{c E_B})$, where l is the B-decay length, m_B the B mass, E_B its energy, and c the speed of light.

l is normally measured from the distance between the fitted primary and secondary vertices. The typical resolution is $\delta l \approx 300$ μm compared to a mean decay length of $\langle l \rangle \approx 3$ mm. In some of the lepton analyses, instead of the decay length, the lepton impact parameter is used, which is on a statistical basis related to the decay length.

The B energy is measured from the tracks attached to the secondary vertex, the missing energy in the hemisphere, and some correction for photons from the B decay. Due to the photon correction, the resolution is worse than in the V_{cb} analyses, typically about 20%.

Figure 18 shows the resolution of the proper time measurement (a) and the resolution normalized to its error (b) for the OPAL $D^{*\pm}\ell$ analysis. Some negative tails due to an imperfect assignment of tracks to the secondary vertex can be observed.

Figure 19 shows the proper time distribution from the ALEPH lepton analysis. The data agree well with the Monte Carlo prediction. All the background is concentrated at small proper times.

6.1.4 Results

To obtain the mixing parameter Δm_d, the experiments fit the fraction of mixed events as a function of the proper time. To reduce the systematic uncertainty, apart from Δm_d, some other parameters describing the background and the tagging efficiencies are left free in the fit.

Figure 20 shows the fraction of mixed events from the DELPHI jet charge-lepton analysis. Good agreement with the fit can be observed. The LEP results are described in Refs. 47–50. All results, including those of CDF and SLD, are summarized in Fig. 21 (Ref. 46). The current world average is

$$\Delta m_d = (0.464 \pm 0.012 \pm 0.013)\ \mathrm{ps}^{-1}.$$

6.2 B_s^0 Oscillations

The B^0 analyses where a lepton is used to tag the decay charge can also be used to search for a high frequency component in the t distribution.

In the $D^{*\pm}$ analyses, the $D^{*\pm}$ is replaced by a D_s. This enriches the sample considerably in B_s^0, reducing the statistical error of the analysis.

When a b quark fragments into a B_s^0 meson, there is a high chance that the free s quark from the fragmentation chain ends up in a kaon of the same charge

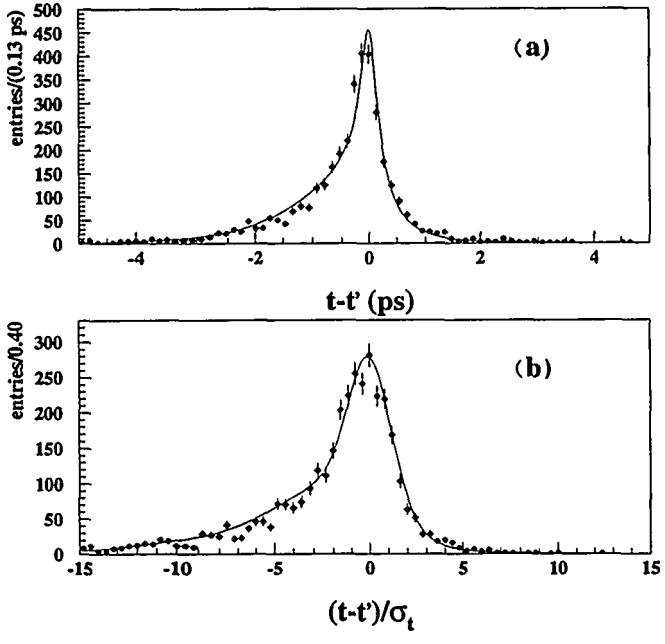


Fig. 18. (a) Difference between the reconstructed proper time t and the true proper time t' in the OPAL $D^{*\pm}\ell$ analysis. The points are the data, and the solid line is the prediction from the Monte Carlo. (b) Same as (a) divided by the calculated error on t.

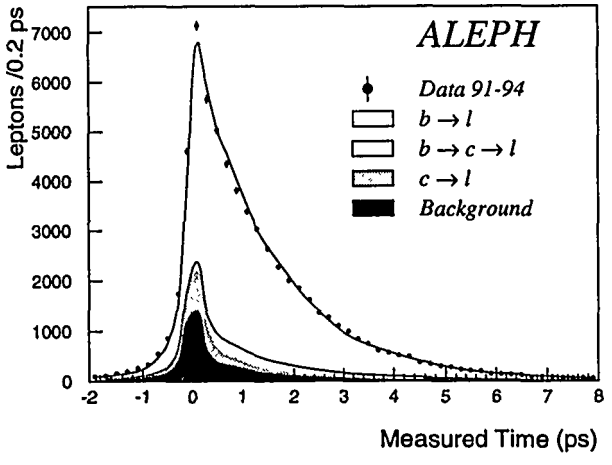


Fig. 19. Reconstructed proper time distribution from the ALEPH lepton-jet charge analysis. The points are the data and the solid line the Monte Carlo prediction. The white area represents the signal and the different shaded areas the background sources.

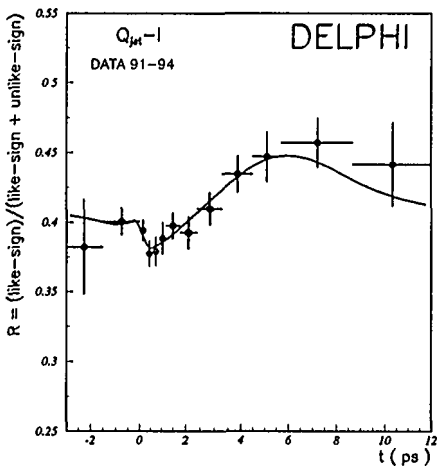


Fig. 20. Fraction of mixed events as a function of the reconstructed proper time from the DELPHI lepton-jet charge analysis.

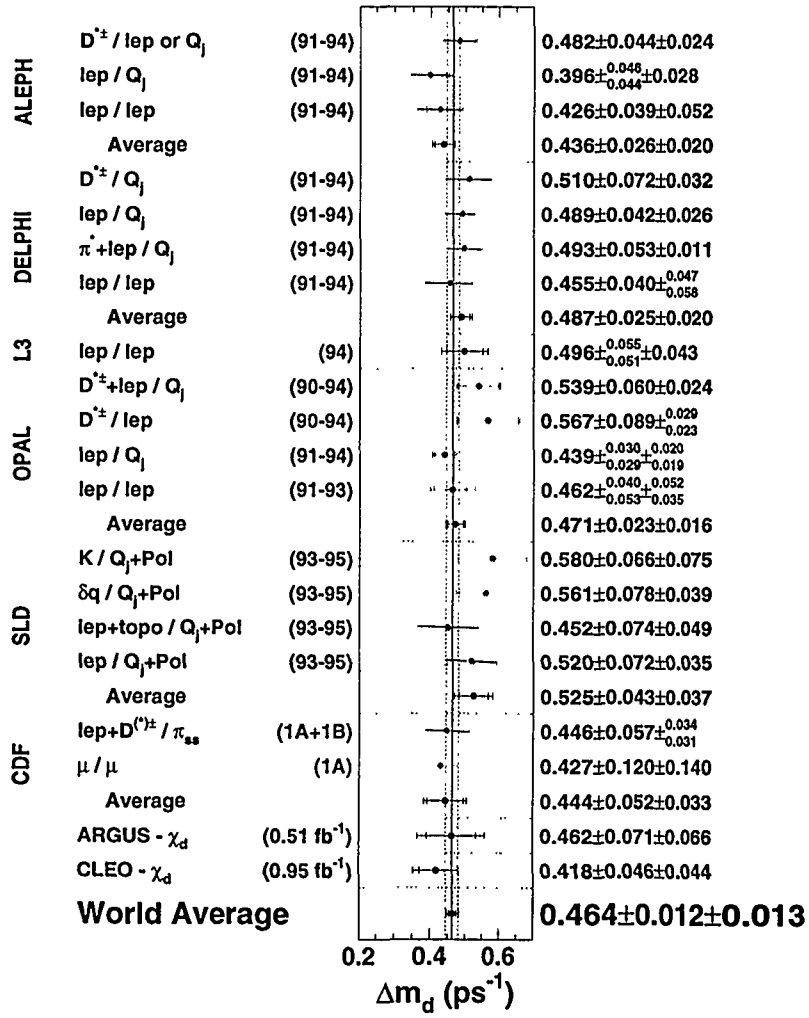


Fig. 21. Summary of Δm_d measurements at LEP, SLD, and CDF.

as the b quark. ALEPH has performed an analysis where such a kaon is used to tag the B_s^0 production charge. However, the sensitivity of this analysis is not yet as large as when the production charge is tagged in the opposite hemisphere.

6.2.1 Combination of Results

Up to now, only lower limits exist for Δm_s. To combine the limits of several analyses inside one experiment, and more of different experiments, the "amplitude method"[51] has been introduced. In this method, the oscillation probability is modified to

$$P(B \to \bar{B})(t) = \frac{\Gamma}{2} e^{-\Gamma t}(1 - A \cdot \cos(\Delta m t)).$$

In the oscillation fit, Δm is fixed to an arbitrary value and A is fitted instead. If Δm is fixed to the correct value, A has to be compatible with 1. In general, $A(\Delta m)$ follows a Breit-Wigner distribution with maximum $A = 1$ in Δm_{true} and width $2/\tau_B$. The assumed Δm can thus be excluded, if the corresponding $A(\Delta m)$ is incompatible with 1. To combine several analyses, measurements of A need simply to be combined in the usual way and the compatibility of the combined A with 1 has to be tested. As an example, Fig. 22 shows the fitted amplitude as a function of Δm_s from the ALEPH analyses alone, and Fig. 23 the combined amplitude from ALEPH and DELPHI.

6.2.2 Results

The analyses of ALEPH, DELPHI, and OPAL are described in Refs. 52–54 and summarized in Fig. 24. Combining ALEPH and DELPHI results in

$$\Delta m_s < 9.2 \text{ ps}^{-1} \quad \text{at 95\% C.L.}$$

OPAL still used the likelihood method, so their result could not easily be combined with the others.

From Fig. 24, it can be seen that there is a significant gain from combining experiments. In addition, one can see that in the case of ALEPH, one analysis has a better exclusion limit than the combination. In fact, with about ten analyses of comparable precision, it is quite probable that one of them excludes the true value of Δm_s with 95% C.L. It is thus wrong to use just the best limit.

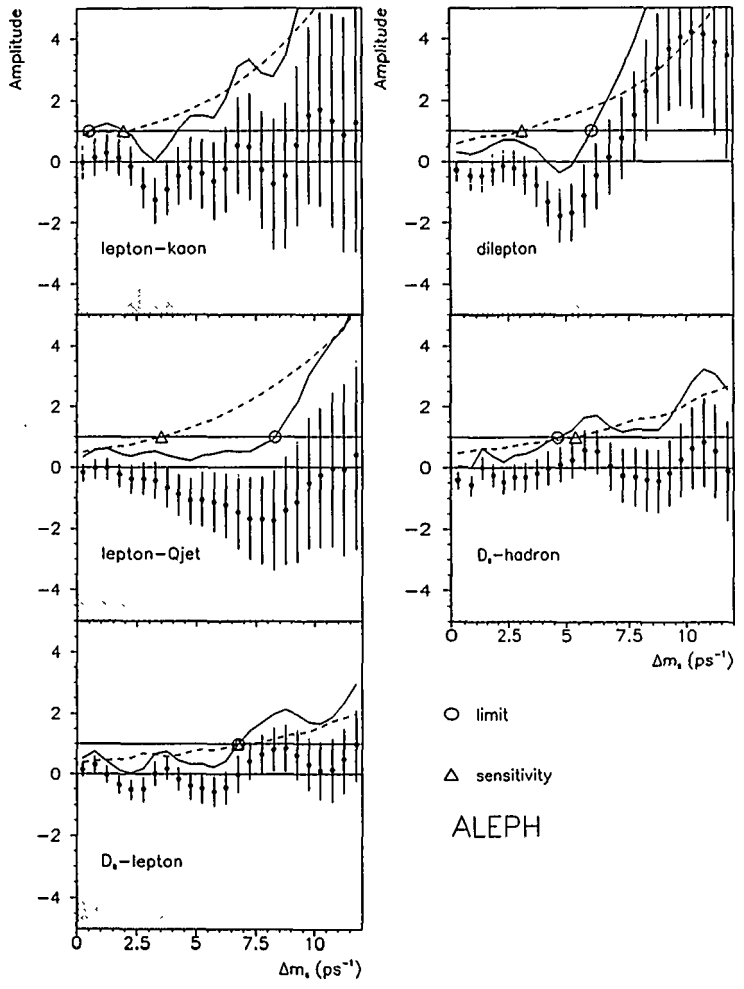


Fig. 22. Fitted amplitude A as a function of the assumed Δm_s for the different ALEPH analyses. The points with the error bars are the fitted amplitudes, the solid line the 95% upper limits derived from them, and the dashed line the sensitivity, i.e., the upper limit if the central value of the amplitude is put to zero.

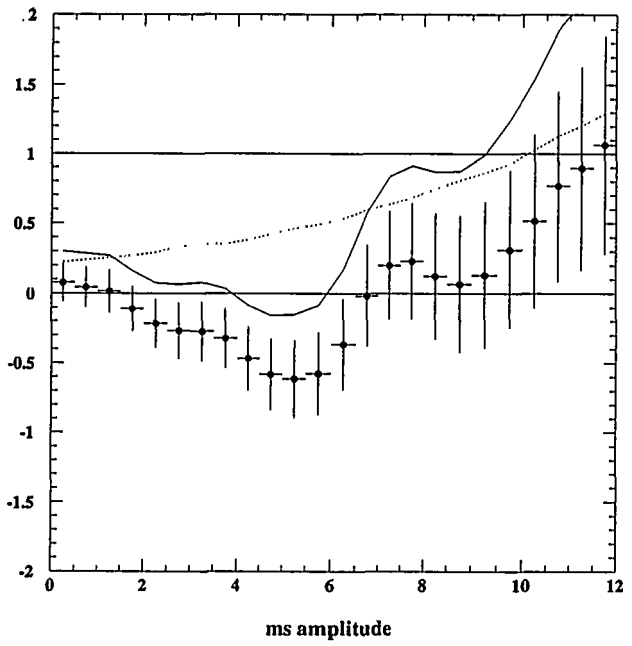


Fig. 23. Combined amplitude from ALEPH and DELPHI. The meaning of the points and lines is as in Fig. 22.

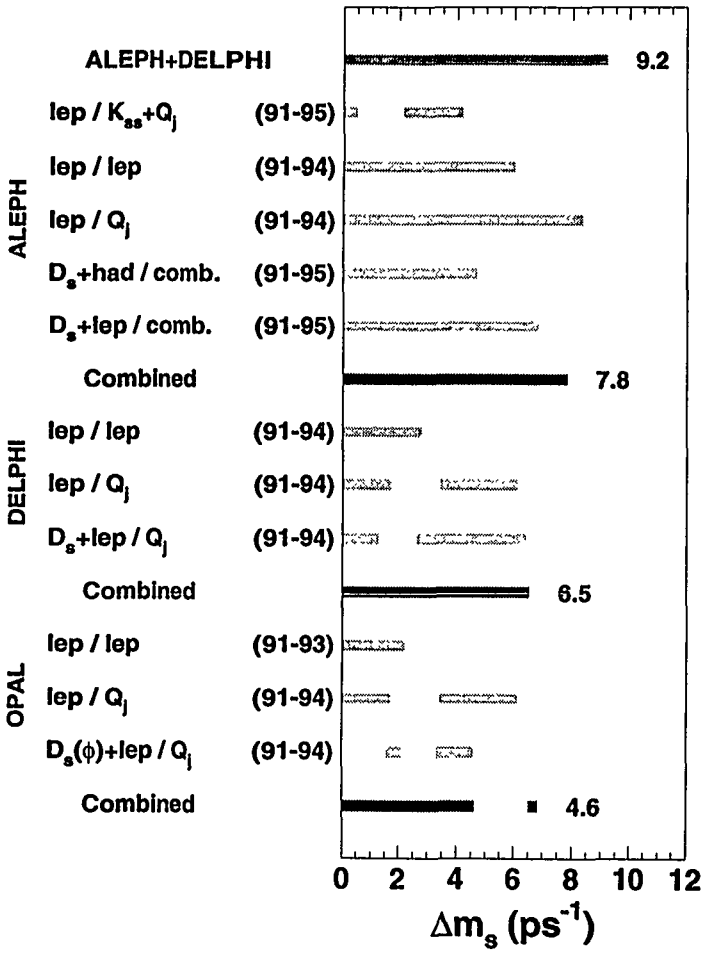


Fig. 24. Δm_s limits from the different LEP analyses.

7 b-Hadron Lifetimes

In the naive spectator model, all b-hadron lifetimes should be equal. It has, however, long been known that the lifetimes of charmed hadrons differ up to a factor of three, because of interference effects between the different assignments of decay and spectator quarks to the final state hadrons. Due to the higher b mass, the lifetime differences in the B sector are expected to be much smaller.

At LEP, all b hadrons are produced and can be tagged via specific decay modes. The analysis techniques are similar to the ones already described for the V_{cb} analyses and for $B\bar{B}$ mixing. For all hadrons, important updates have been presented this summer.

As an example, Fig. 25 shows the B^0 lifetime spectrum from a DELPHI analysis with inclusively reconstructed $D^{*\pm}$ (Ref. 55). The inclusive reconstruction technique permits a high efficiency simultaneously with a high purity and precise estimation of the B momentum. This analysis obtains about the same precision as the current world average. The results for the different b hadrons are summarized in Tables 8, 9, 10, and 11. The averages have been obtained by the LEP B-lifetime group, taking into account common systematic errors.[56] The B^+, B^0, B_s^0, and Λ_b are known to 5% or better by now.

Figure 26 compares the ratios of the b-hadron lifetimes to the B^0 lifetime with the theoretical predictions assuming factorization. The ratios of the B-meson lifetimes agree well with the expectation. The lifetime of the b baryons, however, is about three standard deviations lower than predicted.

8 Conclusions

Using close to the full LEP 1 statistics, results on electroweak and heavy flavor physics have been presented. The electroweak results agree on the per mill level with the predictions from the Standard Model. In the heavy flavor sector, the production of all B species and the large boost allows for competitive results with dedicated B machines.

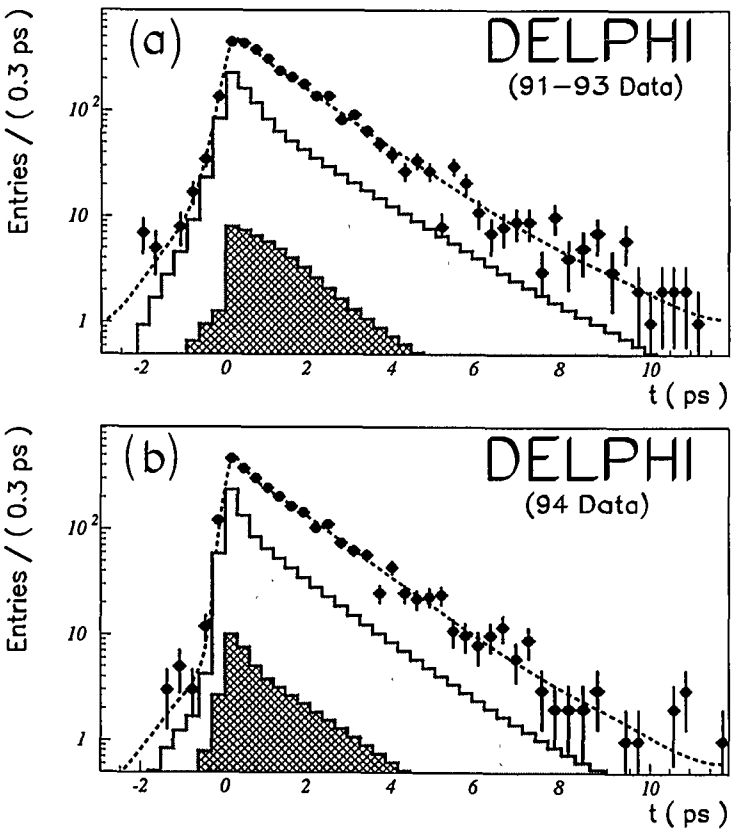


Fig. 25. Reconstructed proper time distribution from the DELPHI B^0 lifetime analysis. Figure (a) is from the 1991-1993 dataset with a two-dimensional silicon vertex detector and (b) for the 1994 dataset with an upgraded three-dimensional detector. The points are the data, the white area represents the Monte Carlo prediction for the signal, and the grey area is the prediction for the background.

Experiment	Method	Data set	τ_{B^0} (ps)	Reference
ALEPH	$D^{(*)}\ell$	91-94	$1.61 \pm 0.07 \pm 0.04$	57
ALEPH	Excl. rec.	91-94	$1.25^{+0.15}_{-0.13} \pm 0.05$	57
ALEPH	Partial rec. $\pi^+\pi^-$	91-94	$1.49^{+0.17+0.08}_{-0.15-0.06}$	57
CDF$^{(p)}$	Excl. $(J/\psi K)$	92-93 & 94-95	$1.58 \pm 0.09 \pm 0.02$	58
CDF	$D^{(*)}\ell$	92-93	$1.54 \pm 0.08 \pm 0.06$	59
DELPHI	$D^{(*)}\ell$	91-93	$1.61^{+0.14}_{-0.13} \pm 0.08$	60
DELPHI	Charge sec. vtx.	91-93	$1.63 \pm 0.14 \pm 0.13$	61
DELPHI	Inclusive $D^* \ell$	91-94	$1.529^{+0.040}_{-0.039} \pm 0.039$	55
OPAL	$D^{(*)}\ell$	91-93	$1.53 \pm 0.12 \pm 0.08$	62
SLD$^{(p)}$	Charge sec. vtx. ℓ	93-95	$1.55^{+0.13}_{-0.12} \pm 0.09$	63
SLD$^{(p)}$	Charge sec. vtx.	93-95	$1.63 \pm 0.07 \pm 0.06$	64
Average			1.55 ± 0.04	

Table 8. Measurements of B^0 lifetime [(p) preliminary].

Experiment	Method	Data set	τ_{B^+} (ps)	Reference
ALEPH	$D^{(*)}\ell$	91-94	$1.58 \pm 0.09 \pm 0.04$	57
ALEPH	Excl. rec.	91-94	$1.58^{+0.21+0.04}_{-0.18-0.03}$	57
CDF$^{(p)}$	Excl. $(J/\psi K)$	92-93 & 94-95	$1.68 \pm 0.07 \pm 0.02$	58
CDF	$D^{(*)}\ell$	92-93	$1.56 \pm 0.13 \pm 0.06$	59
DELPHI	$D^{(*)}\ell$	91-93	$1.61 \pm 0.16 \pm 0.12$	60
DELPHI	Charge sec. vtx.	91-93	$1.72 \pm 0.08 \pm 0.06$	61
OPAL	$D^{(*)}\ell$	91-93	$1.52 \pm 0.14 \pm 0.09$	62
SLD$^{(p)}$	Charge sec. vtx. ℓ	93-95	$1.60^{+0.12}_{-0.11} \pm 0.06$	63
SLD$^{(p)}$	Charge sec. vtx.	93-95	$1.69 \pm 0.06 \pm 0.06$	64
Average			1.65 ± 0.04	

Table 9. Measurements of B^+ lifetime [(p) preliminary].

Experiment	Method	Data set	$\tau_{B_s^0}$ (ps)	Reference
ALEPH	$D_s\ell$	91-95	$1.54^{+0.14}_{-0.13} \pm 0.04$	65
ALEPH	$D_s h$	91-93	$1.61^{+0.30+0.18}_{-0.29-0.16}$	66
CDF$^{(p)}$	$D_s\ell$	92-93 & 94-95	$1.37^{+0.14}_{-0.12} \pm 0.04$	67
CDF	Excl. $J/\psi\phi$	92-93 & 94-95	$1.34^{+0.23}_{-0.19} \pm 0.05$	68
DELPHI$^{(p)}$	$D_s\ell$	91-95	$1.53^{+0.17}_{-0.15} \pm 0.07$	69
DELPHI	$D_s h$	91-94	$1.65^{+0.34}_{-0.31} \pm 0.12$	70
DELPHI	$\phi\ell$	91-94	$1.76 \pm 0.20^{+0.15}_{-0.10}$	70
DELPHI	D_s inclus.	91-94	$1.60 \pm 0.26^{+0.13}_{-0.15}$	70
OPAL	$D_s\ell$	90-94	$1.54^{+0.25}_{-0.21} \pm 0.06$	71
Average			1.52 ± 0.07	

Table 10. Measurements of B_s^0 lifetime [(p) preliminary].

Experiment	Method	Data set	τ_{Λ_b} (ps)	Reference
ALEPH$^{(p)}$	$\Lambda\ell$	91-95	$1.18 \pm 0.08 \pm 0.07$	72
ALEPH$^{(p)}$	$\Lambda_c\ell$	91-95	$1.21^{+0.13}_{-0.12} \pm 0.04$	72
ALEPH	$\Xi\ell$	90-95	$1.35^{+0.37+0.15}_{-0.28-0.17}$	73
CDF	$\Lambda_c\ell$	92-93 & 94-95	$1.32 \pm 0.15 \pm 0.07$	74
DELPHI	$\Lambda\ell\pi$ vtx.	91-94	$1.46^{+0.22+0.07}_{-0.21-0.09}$	75
DELPHI	$\Lambda\mu$ i.p.	91-94	$1.10^{+0.19+0.09}_{-0.17-0.09}$	75
DELPHI	$\Lambda_c\ell$	91-94	$1.19^{+0.21+0.07}_{-0.18-0.08}$	75
DELPHI	$p\mu$	91-93	$1.27^{+0.35}_{-0.29} \pm 0.09$	76
DELPHI	$\Xi\ell$	91-93	$1.5^{+0.7}_{-0.4} \pm 0.3$	77
OPAL	$\Lambda\ell$ i.p.	90-94	$1.21^{+0.15}_{-0.13} \pm 0.10$	78
OPAL	$\Lambda\ell$ vtx.	90-94	$1.15 \pm 0.12 \pm 0.06$	78
OPAL	$\Lambda_c\ell$	90-94	$1.14^{+0.22}_{-0.19} \pm 0.07$	79
Average			1.21 ± 0.06	

Table 11. Measurements of b-baryon lifetime [(p) preliminary]. The ALEPH and DELPHI $\Xi\ell$ results are not included in the quoted average since the selected data sample contains mostly Ξ_b while the selected data sample in the other measurements contain mostly Λ_b.

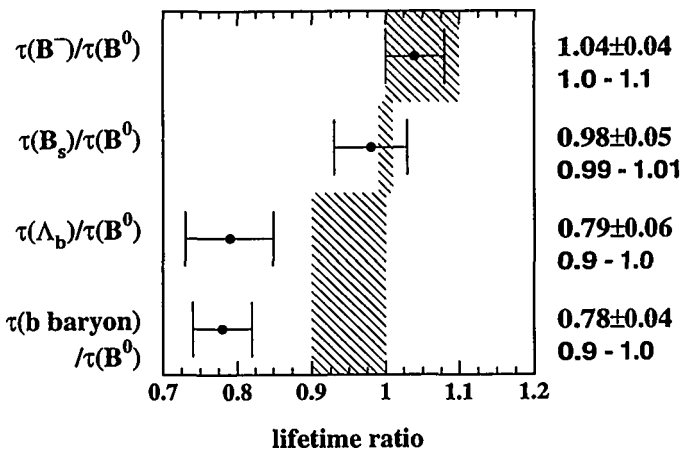


Fig. 26. Ratio of the different b-hadron lifetimes to the B^0 lifetime. The points with the error bars are the world averages and the shaded areas the theoretical prediction.

Acknowledgments

I'd like to thank the LEP collaborations for making their preliminary results available to me. Many thanks to the LEP electroweak and B-lifetime groups for their work combining the data. Also, I'd like to thank the organizers and especially Lilian DePorcel for the superb organization of the Summer Institute.

References

[1] G. Wilkinson, "Measurement of the LEP beam energy," talk presented at ICHEP96, Warsaw, 25-31 July 1996, to appear in the proceedings.

[2] ALEPH Collaboration, "Preliminary results on Z production cross section and lepton forward-backward asymmetries using the 1990-1995 data," contributed paper to ICHEP96, Warsaw, 25-31 July 1996, **PA-07-069**.

[3] DELPHI Collaboration, DELPHI Note 96-118 CONF 65, contributed paper to ICHEP96, Warsaw, 25-31 July 1996, **PA-07-001**.

[4] L3 Collaboration, *Preliminary L3 Results on Electroweak Parameters Using 1990-95 Data*, L3 Note 1980, August 1996, available via http://hpl3sn02.cern.ch/note/note-1980.ps.gz.

[5] OPAL Collaboration, *A Preliminary Update of the Z Line Shape and Lepton Asymmetry Measurements with a Revised 1993-1994 LEP Energy and 1995 Lepton Asymmetry*, OPAL Physics Note PN242, July 1996;
OPAL Collaboration, "Measurements of lepton pair asymmetries using the 1995 data," contributed paper to ICHEP96, Warsaw, 25-31 July 1996, **PA07-015**.

[6] ALEPH Collaboration, D. Buskulic *et al.*, Z. Phys. C **69**, 183 (1996).

[7] DELPHI Collaboration, P. Abreu *et al.*, Z. Phys. C **67**, 183 (1995);
DELPHI Collaboration, "An updated measurement of tau polarisation," DELPHI 96-114 CONF 42, contributed paper to ICHEP96, Warsaw, 25-31 July 1996, **PA07-008**.

[8] L3 Collaboration, O. Acciari *et al.*, Phys. Lett. B **341**, 245 (1994);
L3 Collaboration, "A preliminary update of A_τ and A_e using 1994 data," contributed paper to EPS-HEP Brussels, **eps0094**.
The 1994 data have been combined with the earlier data using a 100% correlation of the systematic errors.

[9] OPAL Collaboration, G. Alexander *et al.*, *A Precise Measurement of the Tau Polarization and Its Forward-Backward Asymmetry at LEP*, CERN-PPE/96-078, submitted to Z. Phys. C.

[10] S. Willocq, *Physics at the Z Pole with SLD*, these proceedings.

[11] ALEPH Collaboration, *Measurement of R_b Using a Lifetime-Mass Tag*, contributed paper to ICHEP96, Warsaw, 25-31 July 1996, **PA10-014**;
ALEPH Collaboration, *A Measurement of R_b Using Mutually Exclusive Tags*, contributed paper to ICHEP96, Warsaw, 25-31 July 1996, **PA10-015**.

[12] OPAL Collaboration, R. Akers *et al.*, Z. Phys. C **60**, 199 (1993);
OPAL Collaboration, R. Akers *et al.*, *Updated Measurement of the Heavy Quark Forward-Backward Asymmetries and Average B Mixing Using Leptons in Multihadronic Events*, OPAL Physics Note PN226, contributed paper to ICHEP96, Warsaw, 25-31 July 1996, **PA05-007**.

[13] The LEP Experiments: ALEPH, DELPHI, L3, and OPAL, Nucl. Instrum. Methods A **378**, 101 (1996).

[14] The LEP Heavy Flavour Group, *Presentation of LEP Electroweak Heavy Flavour Results for Summer 1996 Conferences*, LEPHF/96-01, available from http://www.cern.ch/LEPEWWG/heavy/.

[15] Particle Data Group, M. Barnett *et al.*, Phys. Rev. D **54**, 1 (1996).

[16] OPAL Collaboration, R. Akers *et al.*, Phys. Lett. B **353**, 595 (1995).

[17] DELPHI Collaboration, "Measurement of gluon splitting probability to bottom quark pairs $g_{b\bar{b}}$ in hadronic Z^0 decays," contributed paper to ICHEP96, Warsaw, 25-31 July 1996, **PA01-035**.

[18] ALEPH Collaboration, D. Buskulic *et al.*, Z. Phys. C **62** , 179 (1994);
ALEPH Collaboration, "Measurement of the b forward-backward asymmetries and of the $\bar{\chi}$ mixing parameter using high-p_t leptons," contributed paper to ICHEP96, Warsaw, 25-31 July 1996, **PA10-002**, CERN-PPE/96-072;
ALEPH Collaboration, D. Buskulic *et al.*, "Measurement of the semileptonic b branching ratios from inclusive leptons in Z decays," contributed paper to EPS-HEP-95 Brussels, **eps0404**.

[19] DELPHI Collaboration, P. Abreu *et al.*, Z. Phys C **65**, 569 (1995);
DELPHI Collaboration, P. Abreu *et al.*, Z. Phys C **66**, 341 (1995);
DELPHI Collaboration, "Measurement of the forward-backward asymmetries of $e^+e^- \rightarrow Z \rightarrow b\bar{b}$ and $e^+e^- \rightarrow Z \rightarrow c\bar{c}$," contributed paper to EPS-HEP-95 Brussels, **eps0571**, DELPHI 95-87 PHYS 522.

[20] L3 Collaboration, *L3 Results on A_{FB}^b, A_{FB}^c and χ for the Glasgow Conference*, L3 Note 1624;
L3 Collaboration, *L3 Results on R_b and* Br(b $\rightarrow \ell$) *for the Glasgow Conference*, L3 Note 1625.
The sign of the correlation coefficient arising from the b-semileptonic decay model has been corrected.

[21] OPAL Collaboration, R. Akers *et al.*, Z. Phys. C **60**, 199 (1993);
OPAL Collaboration, R. Akers *et al.*, *Updated Measurement of the Heavy Quark Forward-Backward Asymmetries and Average B Mixing Using Leptons in Multihadronic Events*, OPAL Physics Note PN226, contributed paper to ICHEP96, Warsaw, 25-31 July 1996, **PA05-007**.

[22] ALEPH Collaboration, D. Buskulic *et al.*, Phys. Lett. B **335**, 99 (1994).
ALEPH Collaboration, "An upgraded measurement of A_{FB}^b from the charge asymmetry in lifetime tagged Z decays," contributed paper to ICHEP96, Warsaw, 25-31 July 1996, **PA10-018**.

[23] OPAL Collaboration, R. Akers *et al.*, Z. Phys. C **67**, 365 (1995).

[24] ALEPH Collaboration, D. Buskulic *et al.*, Z. Phys. C **62**, 1 (1994);
ALEPH Collaboration, D. Buskulic *et al.*, "The forward–backward asymmetry for charm quarks at the Z pole: An update," contributed paper to EPS-HEP-95 Brussels, **eps0634**.

[25] OPAL Collaboration, "A measurement of the charm and bottom forward-backward asymmetry using D mesons with the OPAL detector at LEP," contributed paper to EPS-HEP-95 Brussels, **eps0290**, OPAL Physics Note, PN183.

[26] ALEPH Collaboration, "Measurement of the partial decay width of the Z into $c\bar{c}$ quarks," contributed paper to ICHEP96, Warsaw, 25-31 July 1996, **PA10-016**.

[27] DELPHI Collaboration, "Summary of R_c measurements in DELPHI," DELPHI 96-110 CONF 37, contributed paper to ICHEP96, Warsaw, 25-31 July 1996, **PA01-060**.

[28] OPAL Collaboration, R. Akers *et al.*, Z. Phys. C **67**, 27 (1995);
OPAL Collaboration, CERN-PPE/96-51 12, April 1996;
OPAL Collaboration, *A Measurement of $BR(c \rightarrow D^*)$ and $\Gamma_{c\bar{c}}/\Gamma_{had}$ Using a Double Tagging Method*, OPAL Physics Note PN227, contributed paper to ICHEP96, Warsaw, 25-31 July 1996, **PA05-011**.

[29] DELPHI Collaboration, P. Abreu *et al.*, Z. Phys. C 70, 531 (1996).
DELPHI Collaboration, P. Abreu *et al.*, "Measurement of the partial decay width $R_b = \Gamma_{b\bar{b}}/\Gamma_{had}$ with the DELPHI detector at LEP," contributed paper to ICHEP96, Warsaw, 25-31 July 1996, **PA10-061**.

[30] L3 Collaboration, "Measurement of the Z branching fraction into bottom quarks using lifetime tags," contributed paper to ICHEP96, Warsaw, 25-31 July 1996, **PA05-049**.

[31] OPAL Collaboration, Z. Phys. C 65, 17-30 (1995);
"An update of the measurement of $\Gamma_{b\bar{b}}/\Gamma_{had}$ using a double tagging method," contributed paper to EPS-HEP-95 Brussels, **eps0278**, OPAL Physics Note PN181.

[32] G. Altarelli and R. Barbieri, Phys. Lett. B 253, 161 (1991);
G. Altarelli, R. Barbieri, and S. Jadach, Nucl. Phys. B 369, 3 (1992);
G. Altarelli, R. Barbieri, and F. Caravaglios, Nucl. Phys. B 405, 3 (1993).

[33] D. Bardin *et al.*, Z. Phys. C 44, 493 (1989); Comp. Phys. Comm. 59, 303 (1990); Nucl. Phys. B 351, 1 (1991); Phys. Lett. B 255, 290 (1991) and CERN-TH 6443/92 (May 1992).

[34] *Reports of the Working Group on Precision Calculations for the Z Resonance*, edited by D. Bardin, W. Hollik, and G. Passarino, CERN Yellow Report 95-03, Geneva, 31 March 1995.

[35] Electroweak libraries used:
ZFITTER: see Ref. 33;
BHM: G. Burgers, W. Hollik, and M. Martinez; M. Consoli, W. Hollik, and F. Jegerlehner, *Proceedings of the Workshop on Z Physics at LEP I*, CERN Report 89-08 Vol. I, 7; G. Burgers, F. Jegerlehner, B. Kniehl, and J. Kühn, the same proceedings, CERN Report 89-08 Vol. I, 55.
These computer codes have been upgraded recently by including the results of Ref. 34 and references therein.

[36] M. Paulini, *Heavy Flavour Physics—from Top to Bottom*, these proceedings.

[37] C. Klopfenstein, *Electroweak Tests and Searches for New Phenomena from the Tevatron*, these proceedings.

[38] CDHS Collaboration, H. Abramowicz *et al.*, Phys. Rev. Lett. 57, 298 (1986);
CDHS Collaboration, A. Blondel *et al.*, Z. Phys. C 45, 361 (1990).

[39] CHARM Collaboration, J. V. Allaby *et al.*, Phys. Lett. B 177, 446 (1986);
CHARM Collaboration, J. V. Allaby *et al.*, Z. Phys. C 36, 611 (1987).

[40] CCFR Collaboration, C. G. Arroyo *et al.*, Phys. Rev. Lett. 72, 3452 (1994).

[41] I. Caprini and M. Neubert, Phys. Lett. B 380, 376 (1996).

[42] ALEPH Collaboration, "Measurements of $|V_{cb}|$ and form factors and branching ratios of $B^0 \to D^{*+}\ell^-\nu$ and $B^0 \to D^+\ell^-\nu$," contributed paper to ICHEP96, Warsaw, 25-31 July 1996, **PA05-056**.

[43] DELPHI Collaboration, P. Abreu *et al.*, Z. Phys. C 71, 539 (1996).

[44] OPAL Collaboration, "A measurement of $|V_{cb}|$ using $B^0 \to D^{*+}\ell^-\nu$ decays," contributed paper to ICHEP96, Warsaw, 25-31 July 1996, **PA08-008**.

[45] M. Margoni, talk given at the XXVIII ICHEP96, 25-31 July 96, Warsaw, Poland.

[46] L. Gibbons, plenary talk given at the XXVIII ICHEP96, 25-31 July 96, Warsaw, Poland.

[47] ALEPH Collaboration, "Improved measurement of the $B^0_d\bar{B}^0_d$ oscillation frequency," contributed paper to ICHEP96, Warsaw, 25-31 July 1996, **PA05-055**.

[48] DELPHI Collaboration, "Measurement of $B^0_d\bar{B}^0_d$ oscillations," contributed paper to ICHEP96, Warsaw, 25-31 July 1996, **PA01-038**. ICHEP-96 PA01-038,

[49] L3 Collaboration, "Measurement of the B^0_d meson oscillation frequency using dilepton events with the L3 detector," contributed paper to ICHEP96, Warsaw, 25-31 July 1996, PA05-048.

[50] OPAL Collaboration, *A Study of B Meson Oscillations Using Inclusive Lepton Events*, ICHEP-96 PA08-011;
OPAL Collaboration, G. Alexander *et al.*, *A Measurement of the B^0_d Oscillation Frequency Using Leptons and $D^{*\pm}$ Mesons*, CERN–PPE/96–74, submitted to Z. Phys. C.
OPAL Collaboration, R. Akers *et al.*, Z. Phys. C 66, 555 (1995).

[51] H. G. Moser and A. Roussarie, "Mathematical methods for $B^0\bar{B}^0$ oscillation analyses," submitted to Nucl. Instrum. Methods.

[52] ALEPH Collaboration, "Combined limit on the B_s^0 oscillation frequency," contributed paper to ICHEP96, Warsaw, 25-31 July 1996, **PA08-020**.

[53] DELPHI Collaboration, "Search for $B_s^0\bar{B}_s^0$ oscillations," contributed paper to ICHEP96, Warsaw, 25-31 July 1996, **PA01-039**.

[54] OPAL Collaboration, "OPAL combined study of B_s oscillations," contributed paper to ICHEP96, Warsaw, 25-31 July 1996, **PA08-010**.

[55] DELPHI Collaboration, "Accurate measurement of the B_d^0 meson lifetime," contributed paper to ICHEP96, Warsaw, 25-31 July 1996, **PA01-041**.

[56] The LEP B Lifetimes Working Group, *Averaging Lifetimes for B Hadron Species*;
The LEP B Lifetimes Working Group, *Averages of B Hadron Lifetimes*, available from http://wwwcn.cern.ch/ claires/lepblife.html.

[57] ALEPH Collaboration, D. Buskulic *et al.*, Z. Phys. C **71**, 31 (1996).

[58] CDF Collaboration,
http://www-cdf.fnal.gov/physics/new/bottom/bottom.html.

[59] CDF Collaboration, F. Abe *et al.*, Phys. Rev. Lett. **76**, 4462 (1996).

[60] DELPHI Collaboration, P. Abreu *et al.*, Z. Phys. C **68**, 13 (1995).

[61] DELPHI Collaboration, W. Adam *et al.*, Z. Phys. C **68**, 363 (1995).

[62] OPAL Collaboration, R. Akers *et al.*, Z. Phys. C **67**, 379 (1995).

[63] SLD Collaboration, "Measurement of the B^+ and B^0 lifetimes from semileptonic decays at SLD," contributed paper to ICHEP96, Warsaw, 25-31 July 1996, **PA05-084**.

[64] SLD Collaboration, "Measurement of the B^+ and B^0 lifetimes with topological vertexing at SLD," contributed paper to ICHEP96, Warsaw, 25-31 July 1996, **PA05-085**.

[65] ALEPH Collaboration, D. Buskulic *et al.*, Phys. Lett. B **377**, 205 (1996).

[66] ALEPH Collaboration, D. Buskulic *et al.*, Z. Phys. C **69**, 585 (1996).

[67] CDF Collaboration, "Measurement of the lifetime of the B_s^0 meson from $D_s\ell$ correlation," contributed paper to ICHEP96, Warsaw, 25-31 July 1996, **PA05-098d**.

[68] CDF Collaboration, F. Abe *et al.*, Phys. Rev. Lett. **77**, 1945 (1996).

[69] DELPHI Collaboration, "Mean lifetime of the B_s^0 meson," contributed paper to ICHEP96, Warsaw, 25-31 July 1996, **PA01-042**.

[70] DELPHI Collaboration, P. Abreu *et al.*, Z. Phys. C **71**, 11 (1996).

[71] OPAL Collaboration, R. Akers *et al.*, Phys. Lett. B **350**, 273 (1995).

[72] ALEPH Collaboration, "Updated measurement of the b baryon lifetime," contributed paper to ICHEP96, Warsaw, 25-31 July 1996, **PA01-068**.

[73] ALEPH Collaboration, D. Buskulic *et al.*, CERN-PPE/96-081, submitted to Phys. Lett. B.

[74] CDF Collaboration, F. Abe *et al.*, Phys. Rev. Lett. **77**, 1439 (1996).

[75] DELPHI Collaboration, P. Abreu *et al.*, Z. Phys. C **71**, 199 (1996).

[76] DELPHI Collaboration, P. Abreu *et al.*, Z. Phys. C **68**, 375 (1995).

[77] DELPHI Collaboration, P. Abreu *et al.*, Z. Phys. C **68**, 541 (1995).

[78] OPAL Collaboration, R. Akers *et al.*, Z. Phys. C **69**, 195 (1996).

[79] OPAL Collaboration, R. Akers *et al.*, Phys. Lett. B **353**, 402 (1995).

RECENT RESULTS FROM THE VEPP-2M COLLIDER AT NOVOSIBIRSK

E. P. Solodov
Budker Institute of Nuclear Physics, Novosibirsk, 630090, Russia
Representing the CMD-2 Collaboration

ABSTRACT

The e^+e^- collider VEPP-2M at Novosibirsk is the only collider in the energy range 360–1400 MeV. It has a peak luminosity of $\approx 5.0 \times 10^{30}$ cm^{-2} s^{-1} for the ϕ resonance region. Two modern detectors—the general-purpose magnetic detector CMD-2 and the Spherical Neutral Detector (SND)—are taking data at the VEPP-2M collider.

An integrated luminosity of about 10 pb^{-1} has been collected by both detectors. The latest results are described in this paper.

©1996 by E. P. Solodov.

1 VEPP-2M Collider

The VEPP-2M collider at the Budker Institute of Nuclear Physics in Novosibirsk, Russia, shown in Fig. 1, covers the center-of-mass energy range from the two-pion threshold up to 1400 MeV (Ref. 1). Experiments at this collider have yielded a number of important results in e^+e^- physics, including the most precise pion form factor measurements[2] and studies of the ϕ, ω, and ρ meson decays.[3,4]

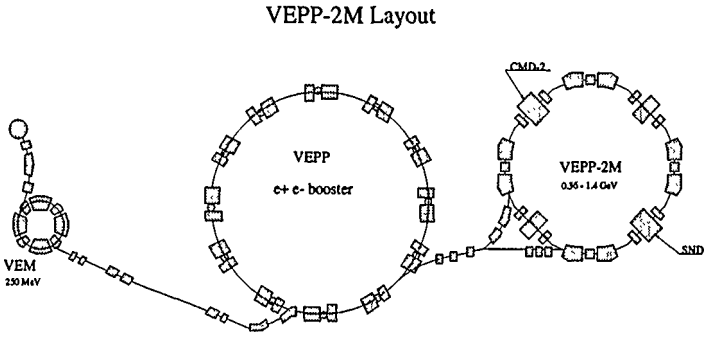


Figure 1: The layout of the VEPP-2M collider at the Budker Institute of Nuclear Physics in Novosibirsk.

During 1988–1992, the collider was upgraded with a new booster to allow higher positron currents and injection of the electron and positron beams directly at the beam energy. After installation of the new booster, VEPP-2M reached a peak luminosity of $L \approx 5.0 \times 10^{30}$ cm^{-2} s^{-1} at the ϕ center-of-mass energy with 40 mA per beam.

2 The CMD-2 Detector

The CMD-2 detector has been described in more detail elsewhere.[5,6] The main systems of the detector are shown in Fig. 2.

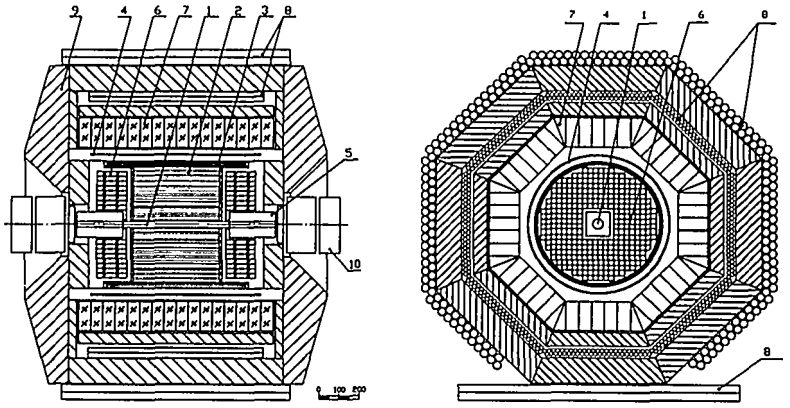


Figure 2: Horizontal and vertical cross sections of the CMD-2 detector. (1) Vacuum chamber; (2) drift chamber; (3) Z chamber; (4) main solenoid; (5) compensating solenoid; (6) BGO end cap calorimeter; (7) CsI barrel calorimeter; (8) muon range system; (9) magnet yoke; (10) collider lenses.

The CsI barrel calorimeter, with 6 x 6 x 15 cm^3 crystal size, is placed outside a 0.4 r.l. superconducting solenoid with a 1 T azimuthally symmetric magnetic field. The endcap calorimeter is made of 2.5 x 2.5 x 15 cm^3 BGO crystals. The drift chamber inside the solenoid has about 250 μ resolution transverse to the beam, and 0.5–0.6 cm resolution longitudinally. The muon range system uses streamer tubes and has 1–3 cm spatial resolution.

The collected sample of Bhabha events was used for calibration and the determination of the reconstruction efficiency of the drift chamber and the calorimeter. A momentum resolution of 5% for 500 MeV/c charged particles, energy resolution of about 10% for gammas in the CsI calorimeter, and about 8% in the BGO calorimeter have been obtained.

Data with integrated luminosity $\approx$ 300 nb^{-1} collected in 1992–1993 at the ϕ were used for the measurement of ϕ meson parameters and branching ratios into four major decay modes.[7]

The integrated luminosity $\approx$ 1500 nb^{-1} around the ϕ mass was collected during the 1993 summer run and was used for studies of rare decay modes of ϕ, coupled

$K_S K_L$ decays, and nuclear interactions of neutral kaons. Some preliminary results have been published in Ref. 8. The latest analyses based on the 1992–1993 data are described below.

The 1994–1995 runs were dedicated mostly to measurements of the total hadronic cross section at energies below the ϕ resonance,[9] where an integrated luminosity of about 500 nb^{-1} was collected. Here, we present preliminary results on the ω meson parameter measurements based on 122 nb^{-1} collected around the ω peak.

An additional 2000 nb^{-1} have been collected around the ϕ peak in the 1996 spring run, and these data are under analysis now.

2.1 Rare ϕ Decay Studies

2.1.1 $\phi \to \eta\gamma$ and $\phi \to \eta'\gamma$

The decay $\phi \to \eta\gamma$ was previously observed only in neutral modes ($\eta \to \gamma\gamma$, $\eta \to 3\pi^0$). The CMD-2 detector gives us the possibility to study the $\phi \to \eta\gamma$ decay in a channel with charged particles, where η decays into $\pi^+\pi^-\pi^0$. The primary photon has the highest energy of all three in the final state—362 MeV at the ϕ meson peak—and was required to be detected in the selected events.

The reconstructed invariant mass of three pions, $M_{\pi^+\pi^-\pi^0}$, was used to select the decay $\phi \to \eta\gamma$; the resulting distribution had a peak around $M_\eta = 547.45$ MeV. After background subtraction, 1100 ± 40 events were selected.

The experimental cross section $\sigma(e^+e^- \to \phi \to \eta\gamma)$ with a fit function is presented in Fig. 3. The parameters of the ϕ meson obtained, $M_\phi = 1019.31 \pm 0.18$ MeV and $\Gamma_\phi = 4.70 \pm 0.25$ MeV, are in good agreement with table values.[10] Using the electron width of the ϕ from Ref. 10, the $Br(\phi \to \eta\gamma)$ was found to be:

$$Br(\phi \to \eta\gamma) = (1.29 \pm 0.07) \times 10^{-2}\,.$$

A search for the decay $\phi \to \eta'\gamma$ was made in the mode where η' decays into $\pi^+\pi^-\eta$ and $\eta \to \gamma\gamma$. Both $\eta\gamma$ and $\eta'\gamma$ final states have two charged particles and three photons. Events detected with all of these particles were used for the constrained fit, and as a result, 481 $\eta\gamma$ events were selected.

The decay into $\eta\gamma$ is the basic background for the $\eta'\gamma$ search. After an anti-$\eta\gamma$ cut, the scatter plot of the invariant mass of the two hardest photons, M_{12}, versus the weakest photon energy ω_3 was studied. For $\eta'\gamma$ events, M_{12} should be close

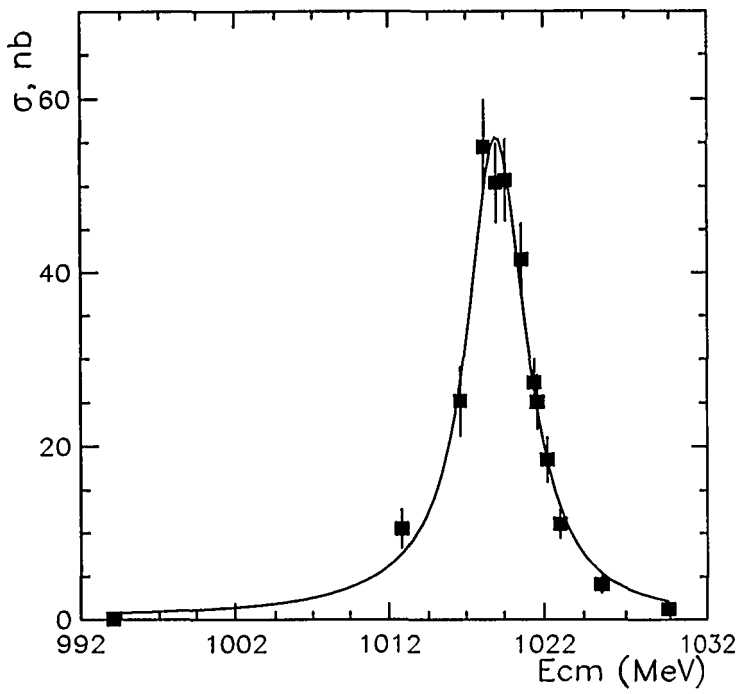


Figure 3: The $\phi \to \eta\gamma$ cross section.

to the η mass 547.5 MeV, while ω_3 is a monochromatic 60 MeV photon. Figure 4 shows the result of the 1992–1993 data together with a simulation of $\phi \to \eta'\gamma$. We have one candidate for an $\eta'\gamma$ event with one event as the estimated background. Using the 90% C.L. upper limit $N_{\eta'\gamma} < 3$ and the efficiencies obtained from the simulation, $\varepsilon_{\eta\gamma} = 14.4\%$ and $\varepsilon_{\eta'\gamma} = 6.4\%$, the following result has been obtained:

$$Br(\phi \to \eta'\gamma) \;<\; 2.4 \cdot 10^{-4}\,.$$

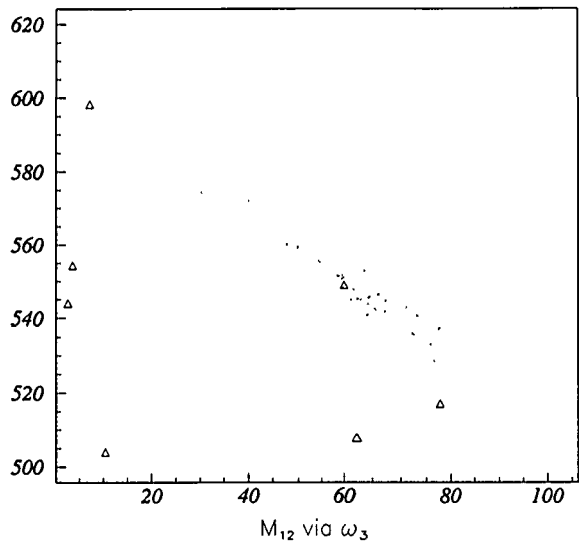


Figure 4: Invariant mass M_{12} (MeV) vs ω_3 (MeV) after the constrained fit. Dots represent simulations, and triangles the experiment.

2.1.2 Search for $\phi \to \pi^+\pi^-\pi^+\pi^-$

Three- and four-track events were selected as candidates for the process $\phi \to \pi^+\pi^-\pi^+\pi^-$. But due to a high background from the main channels of ϕ decaying into three-track events, in the search for the process $\phi \to \pi^+\pi^-\pi^+\pi^-$, only four-track events were used. The ratio of three- and four-track events at the energy points outside the ϕ meson region was used (along with a simulation) to evaluate the detection efficiency.

To extract the number of events from the process $e^+e^- \to \pi^+\pi^-\pi^+\pi^-$, we apply a simple cut to the total momentum of four charged particles (should be around zero) and their total energy (should be around $E_{c.m.}$ energy), assuming that all particles are pions.

The cross section versus energy for the process $e^+e^- \to \pi^+\pi^-\pi^+\pi^-$ is shown in Fig. 5. Only statistical errors are shown. A function which describes interference of a linear background with the amplitude of the process $\phi \to \pi^+\pi^-\pi^+\pi^-$ was used for the fitting, taking into account only this experiment. The result of the

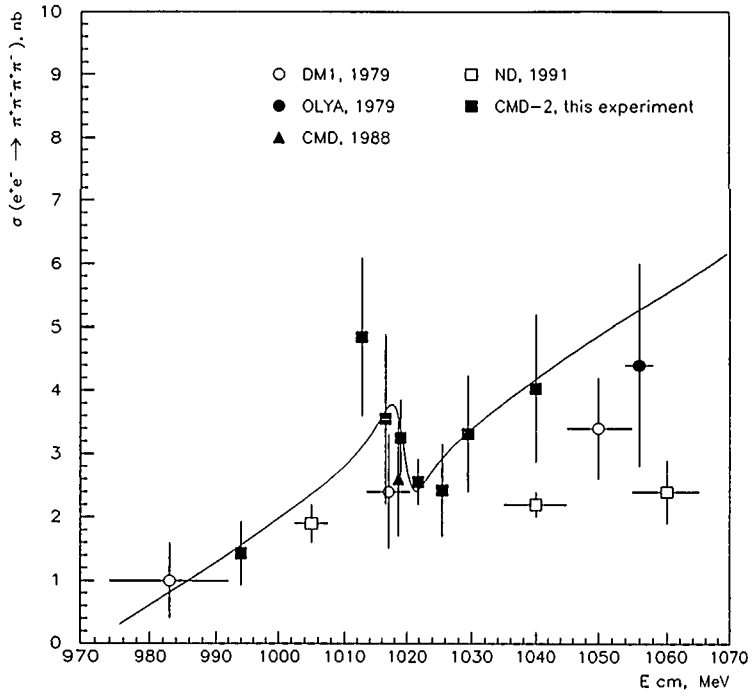


Figure 5: The cross section $e^+e^- \to \pi^+\pi^-\pi^+\pi^-$.

fit is shown in the plot by a smooth line. Using this fit and the uncertainty in the efficiency, one can get

$$Br(\phi \to \pi^+\pi^-\pi^+\pi^-) < 1.0 \times 10^{-4},\ 90\%\ \text{C.L.}$$

2.1.3 Search for $\phi \to f_0(980)\gamma$

The event candidates were selected by a requirement of two charged tracks in the DC and one or two photons with energy greater than 20 MeV in the CsI calorimeter. All particles were required to be within the polar angle range between 0.85 and 2.25 radians to suppress bremsstrahlung processes. The sum of the energy depositions of the two clusters associated with the charged tracks was required to be less than 450 MeV to remove Bhabha events.

The main background for the process studied was the $\phi \to \pi^+\pi^-\pi^0$ decay when one of the gammas from the π^0 escaped detection. To reduce this background, a constrained fit was used. The rest of the 3π background was removed by selecting the gamma energy to lie in the range 20 MeV< E_γ <100 MeV, where the signal of the f_0 was expected. The muon range system was used to remove $\mu^+\mu^-\gamma$ contamination.

Under these conditions, 833 $\pm$ 30 $\pi^+\pi^-\gamma$ events and 846 $\pm$ 31 $\mu^+\mu^-\gamma$ events were selected with the integrated luminosity of 1269 nb^{-1}, determined by Bhabha events. The detection efficiency was found by simulation to be 17%. The experimental cross sections versus center-of-mass energies are presented in Figs. 6(a) and 6(b).

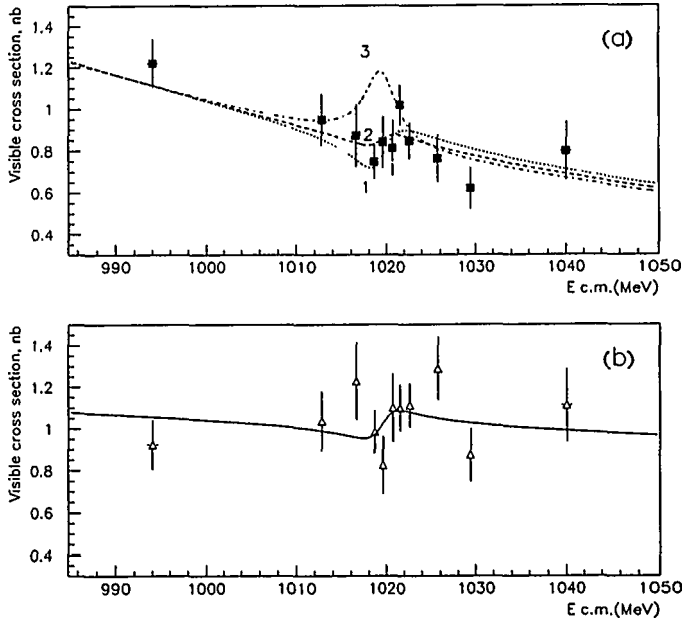


Figure 6: (a) Visible cross section for $e^+e^- \to \pi^+\pi^-\gamma$. Lines are theoretical predictions for the case of no $f_0\gamma$ signal (2), an $f_0\gamma$ signal with B($\phi \to f_0\gamma$) = 2.4 $\times$ 10^{-4} for a negative relative phase (3), and a positive relative phase (1). (b) Visible cross section for $e^+e^- \to \mu^+\mu^-\gamma$, compared with theoretical prediction.

A search for a signal from $\phi \to f_0(980)\gamma$ decay was made using expected interference patterns in the cross section versus energy behavior of the $e^+e^- \to \pi^+\pi^-\gamma$ process, and the difference in the gamma spectra of the selected events at the ϕ peak, with off-peak events near the ϕ region. According to the theoretical calculations,[11] the following interference patterns may be used for an $f_0\gamma$ search: (a) interference of the background process $e^+e^- \to \pi^+\pi^-\gamma$ with the "radiative" decay $e^+e^- \to \phi \to \gamma \to \pi^+\pi^-\gamma$, where f_0 is not present (this is also valid for the $\mu^+\mu^-\gamma$ process); and (b) interference of the above processes with $e^+e^- \to \phi \to f_0\gamma \to \pi^+\pi^-\gamma$, where f_0 was described as a four-quark state. The model predictions are shown in Figs. 6(a) and 6(b) for the cross section, and in Fig. 7 for the difference in gamma spectra.

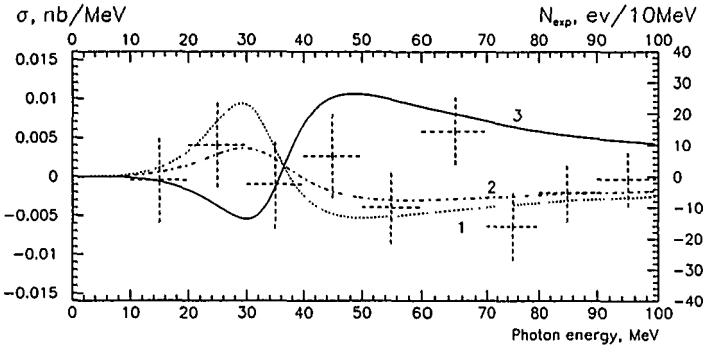


Figure 7: Difference in spectrum for gammas in the "ϕ" and "non-ϕ" regions, normalized to integrated luminosity. The solid lines represent the theoretical prediction for the four-quark model of the 2.4 $\times$ 10^{-4} branching ratio in the case of (1) positive and (3) negative interference signals with a 40 MeV f_0 width. Line (2) is a negative interference signal with a 100 MeV f_0 width.

Using these interference patterns, the following results were obtained at the 90% C.L.:

$$Br(\phi \to \pi^+\pi^-\gamma) < 1.5 \times 10^{-5}\,,$$
$$Br(\phi \to \mu^+\mu^-\gamma) < 2.6 \times 10^{-5}\,,$$
$$Br(\phi \to f_0\gamma) < 7 \times 10^{-4}\,.$$

2.1.4 Search for $\phi \to \eta e^+e^-$

The decay mode $\eta \to \gamma\gamma$ was chosen. The typical characteristics are the invariant mass of the two gammas (0.54 GeV), the small space angle between the two electrons, and the sum of the momenta of the electrons (0.364 GeV). The main backgrounds are: (a) $\phi \to \eta\gamma$ with gamma conversion in the beam pipe and (b) $e^+e^- \to e^+e^-\gamma\gamma$, where the two electrons come from an internal gamma conversion. Full kinematical reconstruction was done and calibrated with $\phi \to \pi^+\pi^-\pi^0$ events with a small angle between the two charged pions. The QED process $e^+e^- \to e^+e^-\gamma$ was used to calibrate the efficiency of the drift chamber for charged particles at small space angle and the photon conversion probability in the beam pipe. The total luminosity was 2085 nb^{-1}, corresponding to 2,715,000 ϕ's.

Figure 8 shows the region around the η mass where 12 events are seen and 4.2 are expected from all backgrounds. The branching ratio was found to be

$$Br(\phi \to \eta e^+e^-) = (1.10 \pm 0.49 \pm 0.19) \times 10^{-4}\,.$$

2.2 Measurements of ω Meson Parameters

The c.m. energy region from 2 × 380 to 2 × 405 MeV has been scanned at 13 energy points with a total integrated luminosity of 122 nb^{-1}. The beam energy in each point has been measured by the resonant depolarization technique[12] and is known to reach an accuracy of better than 10^{-4}.

Events with two noncollinear tracks were selected as candidates for the $\omega \to \pi^+\pi^-\pi^0$ decay. The resulting number of 13489 $\pi^+\pi^-\pi^0$ events was obtained by fitting the missing mass $M^2_{\pi^0}$ parameter to the histogram after background subtraction.

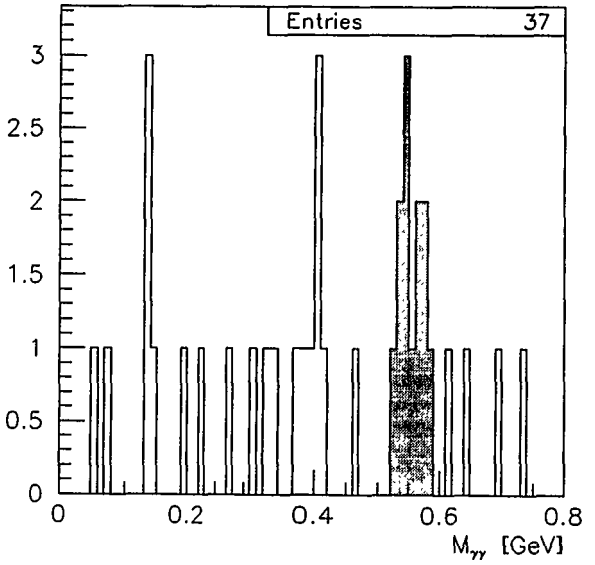


Figure 8: The invariant mass of the two photons after the constrained fit.

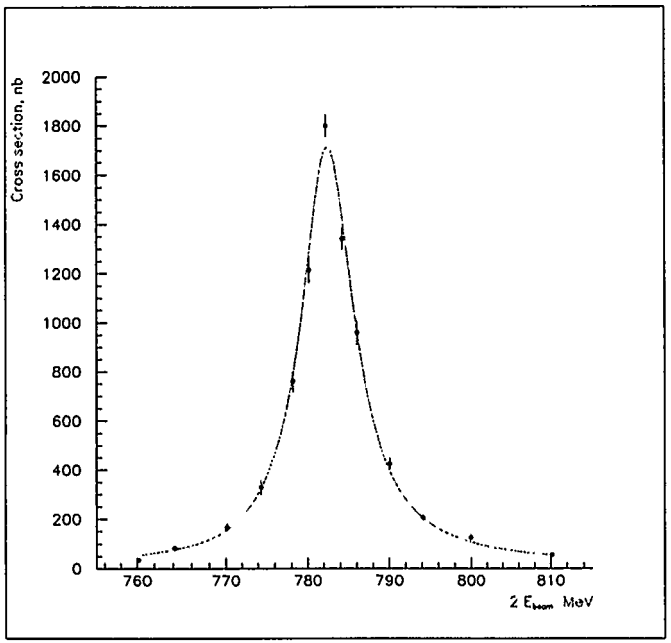


Figure 9: ω meson excitation curve.

Events with two detected gammas from neutral pions were used for the combined trigger and reconstruction efficiency determination, which was found to be 0.91 ± 0.01.

Luminosity was determined by the number of the Bhabha events, selected by the presence of two collinear tracks in the Drift Chamber and high-energy deposition in the CsI barrel calorimeter, with a statistical error at each energy point on the level of 1–2%.

Experimental points together with the fitted excitation curve are shown in Fig. 9.

The following ω-meson parameters were obtained from the fit:

$$\Gamma_{e^+e^-} = 0.62 \pm 0.01 \pm 0.02 \text{ keV},$$
$$\Gamma_{tot} = 8.23 \pm 0.20 \pm 0.30 \text{ MeV}.$$

2.3 K_SK_L Coupled Decays and Interaction Study

It was realized at the very early stages of ϕ meson studies at colliding beam machines that K_SK_L pairs can be used for studying CP and CPT violation. These suggestions, including studies of quantum mechanical correlations, were discussed in Refs. 5 and 13 for experiments at VEPP-2M (Ref. 1), an electron-positron collider at the Budker Institute of Nuclear Physics in Novosibirsk, Russia, and carefully reviewed in Ref. 14.

The ϕ resonance produced in e^+e^- collisions can also be considered as a source of η and η' mesons,[15] and for the low-momenta neutral and charged kaon pairs for studies of nuclear interactions.

The construction of the ϕ factories in Novosibirsk and Frascati[16,17] will facilitate new precise measurements of a possibly direct CP-violating component into the decay $K_L \to \pi^+\pi^-, \pi^0\pi^0$ (ϵ'/ϵ).

The VEPP-2M collider, with peak luminosity $L \approx 5 \times 10^{30}$ cm^{-2} s^{-1}, can be considered as a pre-ϕ factory with the CMD-2 detector, so that some useful measurements can be done to prepare for the running at the ϕ factories. An upgrade of the collider to 10^{32} cm^{-2} s^{-1} luminosity has been planned to investigate the idea of round beams, an important ingredient of the Novosibirsk ϕ-factory project.[18] The 3.4-cm diameter vacuum beam pipe inside the CMD-2 detector, made of Be with a 0.077-cm wall thickness, may be considered as a target for studies of kaon nuclear interactions.

2.3.1 Selection of K_SK_L Coupled Decays

Candidates were selected from a sample in which two vertices, each with two opposite charge tracks, were observed within 15 cm from the beam axes and all tracks were reconstructed. An example of such an event is shown in Fig. 10.

The cuts 470 MeV/c^2 $< M_{inv} <$ 525 MeV/c^2 and 80 MeV/c $< P_{mis} <$ 140 MeV/c, with an additional requirement to have another reconstructed vertex in the P_{mis} direction, select $K_S \to \pi^+\pi^-$ events in one of the vertices. In this case, the K_L is expected to be in the other one.

Figure 11(a) shows the decay length distribution for selected K_S's with the correct 0.55 ± 0.02-cm decay length. The decay radius distribution for the K_L's with two charged tracks in the final state is shown in Fig. 11(b). In the flat region, where reconstruction efficiency is uniform, a peak is seen at the radius of 1.7 cm

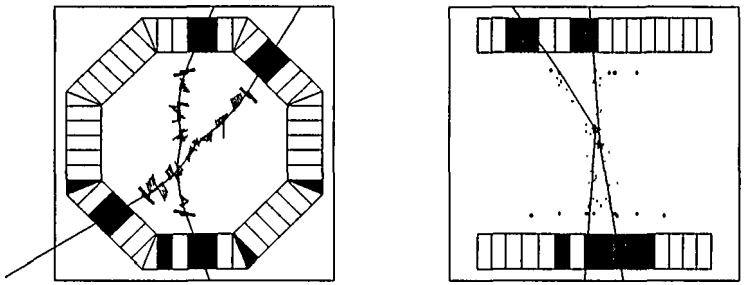


Figure 10: $\phi \to K_S K_L$ event with coupled decay.

corresponding to the 79 $\pm$ 18 K_L's which interacted with nuclei in the Be tube. The remaining 1355 events represent K_L's decaying in flight.

To select candidates for $K_L \to \pi^+\pi^-$ events, an additional cut, requiring the invariant mass of two tracks from a K_L vertex to be in the range of 470–525 MeV/c^2, was applied. The distribution obtained is shown in Fig. 11(d) together with the fit function, where all the parameters, except for the number of events, are fixed values obtained from the distribution in Fig. 11(b). The number of events under the peak drops to 31 $\pm$ 7 and 78 remain from K_L decays in flight. One can apply stronger requirements for these events to satisfy $K_L \to \pi^+\pi^-$ kinematics within the detector resolution; i.e., 80 MeV/c $< P_{mis} <$ 140 MeV/c, and the K_S vertex in the P_{mis} direction. The results of this selection are illustrated in Fig. 11(d) by the shaded histogram. The peak at the Be tube survives with 20 $\pm$ 5 events, and 35 K_L decays in flight remain.

The 28.5 $\pm$ 6.4 events found in the peak after the invariant mass cut and some efficiency corrections are interpreted as regeneration of K_L into K_S with its decay into $\pi^+\pi^-$, and another 50 $\pm$ 17 peak events represent nuclear interactions with two visible charged particles.

Using simulated efficiencies to estimate the full number of K_L's passing the Be tube, the following cross sections for regeneration and visible inelastic scattering have been obtained:

$$\sigma_{reg}^{Be} = 58 \pm 17 \text{ mb.}$$
$$\sigma_{inel}^{vis} = 77 \pm 26 \text{ mb.}$$

The sources of the inelastic scattering events are reactions with Σ and Λ production. To estimate the total cross section, the relative weight of these reactions

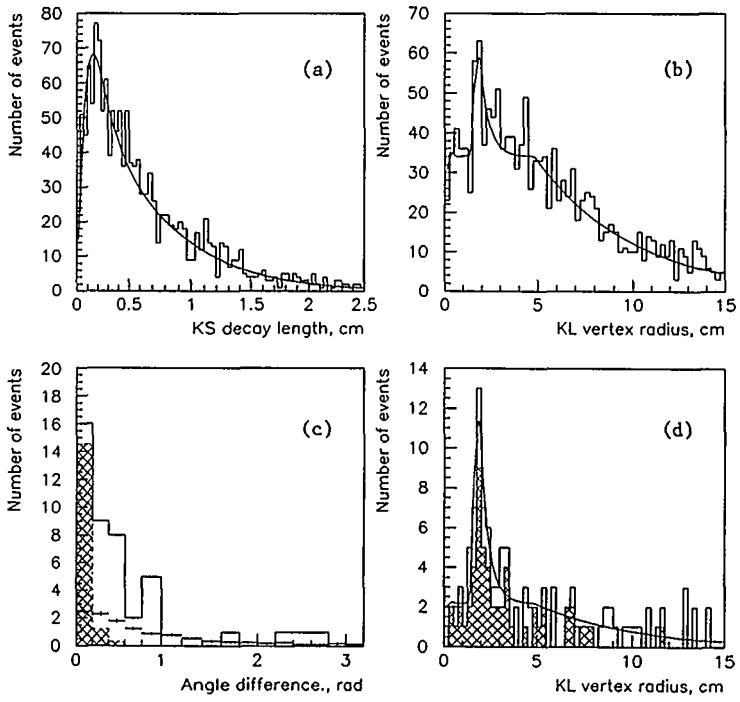


Figure 11: (a) Decay length for K_S. (b) Decay radius for K_L. (c) Projected angular distribution for "tube" events (histogram), K_L semileptonic decays (points with errors), and K_S two-pion decays (shaded). (d) Decay radius for K_L's after M_{inv} cut and after K_S selecting cut (shaded).

was taken to be 0.21 from the CERN GEANT code (NUCRIN). With the ratio $\sigma_{inel}/\sigma_{tot} = 0.52$ (Ref. 19), one can estimate $\sigma_{tot}^{Be} = 705 \pm 238$ mb.

The histogram in Fig. 11(c) shows the projected angular distribution for the regenerated K_S's at the beam pipe along with the background from the semileptonic decays of K_L (dots with errors). The angular distribution obtained is wider than in the case of coherent regeneration, which can be illustrated by comparison with the shaded distribution shown for original K_S decays at the same distance. But, with the available sample, coherent contamination cannot be extracted.

2.3.2 Discussion

The selection of candidates for $K_L \to \pi^+\pi^-$ events faced two problems. The first was a background from the dominant semileptonic K_L decays, which was already discussed in Ref. 20 and seemed to be solvable with better DC resolution.

A second problem was relatively high background from nuclear interactions of K_L and the regeneration effect which was for the first time experimentally observed for slow kaons.

In Fig. 12(a), the experimental regeneration cross section is plotted together with the theoretical calculations for Be and Cu described in Ref. 19. The comparison of the calculated regeneration cross sections for these two different materials shows that at momenta below 200 MeV/c, one cannot scale them by a simple $A^{2/3}$ dependence. The experimental angular distribution of the regenerated K_S after background subtraction is presented in Fig. 12(b), together with the fit function and theoretical prediction,[19] and seems to be narrower than predicted.

The experimental value obtained for the total nuclear cross section in Be for 110 MeV/c kaons is shown in Fig. 13 together with the experimental data at higher momenta[21] and theoretical calculations.[19] The cross sections extracted from the GHEISHA and FLUKA simulation codes are also shown. It is seen that the FLUKA code, as well as the calculations from Ref. 19, are in good agreement with experimental data. The GHEISHA code gives completely wrong absolute values as well as momentum dependence.

After our preliminary results were published,[8] the regeneration influence was discussed for the ϵ'/ϵ measurement planned in the KLOE detector.[19] It was shown that the total regeneration probability in the KLOE drift chamber after an acoplanarity cut (factor of four rejection) was 10^{-4}. This should be compared with

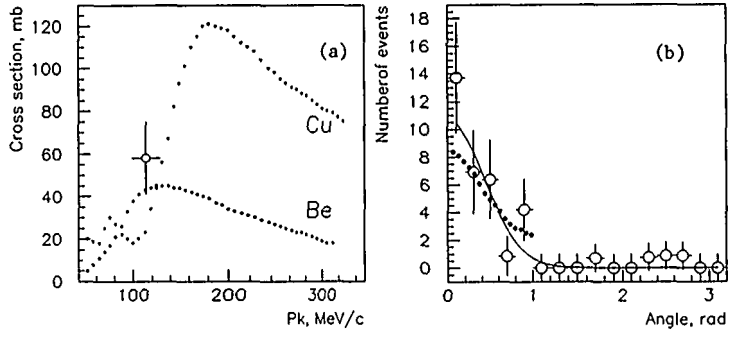


Figure 12: (a) Experimental regeneration cross section and theoretical calculations for Be and Cu. (b) Projected angular distribution of the regenerated K_S with fit function (solid line) and theoretical prediction (dots).

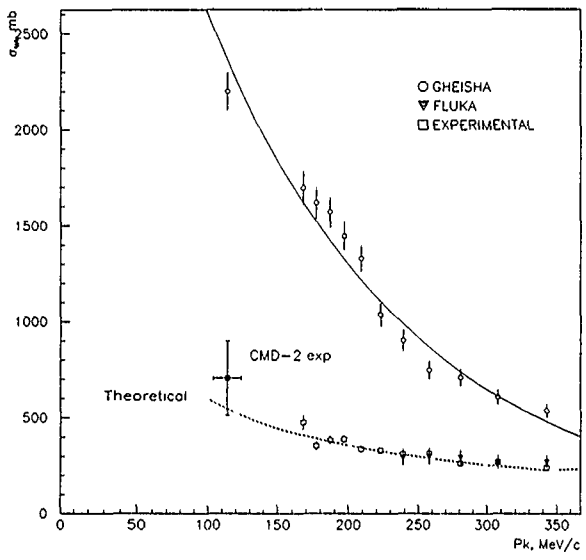


Figure 13: Comparison of the total experimental K_L nuclear interaction cross section in Be with the theoretical calculations and simulation by different codes.

2×10^{-3} probability for the "normal" CP-violating $K_L \to \pi\pi$ decay and $\approx 10^{-6}$ probability for the direct CP-violation decay.

The regeneration itself does not give any of the decay asymmetry expected for the direct CP-violating K_L decay, but the acoplanarity cut as well as another selection cut applied separately to $\pi^+\pi^-$ and $\pi^0\pi^0$ final states with different resolutions (DC for the first and calorimeter for the second) can cause systematic asymmetries due to the broad angular distribution of the regenerated events.

2.4 Search for $\eta \to \pi^+\pi^-$ Decay

As was mentioned before, the radiative $\phi \to \eta\gamma$ decay can be considered as a source of η mesons, accompanied by 362 MeV energy gammas.

In the integrated samples analyzed, 28056 η's were produced. The selected $\pi^+\pi^-\gamma$ events (see above) can be used to search for the CP-violating decay $\eta \to \pi^+\pi^-$. This decay can be seen as a peak in the photon-energy histogram in the 362 MeV region. Figure 14 shows the photon-energy distribution after a constrained fit and some additional cuts to reduce the $\phi \to 3\pi$ background. The shaded histograms show simulated signals from $\eta \to \pi^+\pi^-$ decays before and after the constrained fit. The detection efficiency for these events was found by simulation to be $9.9 \pm 0.9\%$. No signal was seen in the experimental distribution, and the upper limit was found to be:

$$Br(\eta \to \pi^+\pi^-) \; < \; 2.1 \times 10^{-3} \, .$$

2.5 CMD-2 Results Summary

The CMD-2 detector is taking data at the VEPP-2M collider in Novosibirsk. Data collection was performed in the ϕ meson region and over the energy range 600–1000 MeV. About 30% of the collected data have been analyzed to date. The new results for the branching ratios of rare ϕ decays are as follows:

$$\begin{aligned} Br(\phi \to \eta\gamma) &= (1.29 \pm 0.07) \times 10^{-2} \, , \\ Br(\phi \to \eta'\gamma) &< 2.4 \times 10^{-4} \, , \\ Br(\phi \to \pi^+\pi^-\pi^+\pi^-) &< 1.0 \times 10^{-4} \, , \\ Br(\phi \to f_0\gamma) &< 7 \times 10^{-4} \, , \end{aligned}$$

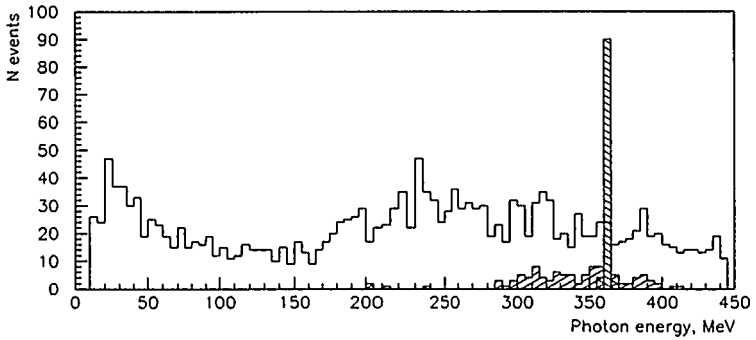


Figure 14: Photon energy for $\phi \to \pi^+\pi^-\gamma$ event searches for $\eta \to \pi^+\pi^-$ decays. Simulated signals before and after constrained fits are shown by the shaded lines.

$$
\begin{aligned}
Br(\phi \to \pi^+\pi^-\gamma) &< 1.5 \times 10^{-5}, \\
Br(\phi \to \mu^+\mu^-\gamma) &< 2.6 \times 10^{-5}, \\
Br(\phi \to \eta e^+e^-) &= (1.10 \pm 0.49 \pm 0.19) \times 10^{-4}.
\end{aligned}
$$

A search for CP-violating decay $\eta \to \pi^+\pi^-$, based on about 23000 η's, gives an upper limit $Br(\eta \to \pi^+\pi^-) < 2.1 \times 10^{-3}$.

With the CMD-2 detector, the coupled $K_S K_L$ decay has been observed for the first time.

The measured values of the cross sections indicate that regeneration will cause an additional background for the CP-violating decays of K_L at ϕ-factory experiments and should be carefully studied to avoid systematic errors.

3 Spherical Neutral Detector

3.1 Introduction

After installation in 1995, experiments with the new SND detector at the e^+e^- collider VEPP-2M have continued. SND is a general-purpose nonmagnetic detector with a spherical NaI(Tl) calorimeter. Its performance parameters, like energy and spatial resolution, background, recording rate, etc., have been obtained during a run in the energy range around $\phi(1020)$, and some preliminary results on $\phi(1020)$ decays, showing detector performance, are presented.

3.2 SND Detector Overview

SND[22] is a general-purpose nonmagnetic detector, consisting of the tracking system, three spherical layers of NaI(Tl) crystals, and an outer system of streamer tubes and plastic scintillation counters (Fig. 15).

The NaI(Tl) calorimeter consists of 1632 individual crystals of 3.6 tons total weight. The calorimeter thickness in the radial direction is 35 cm $\sim$ 13.5 X_0. The angular size of each crystal is $\Delta\phi = \Delta\theta = 9°$; the solid angle coverage of the calorimeter is 90% of 4π. Each crystal is viewed by a vacuum phototriode[23] with a charge-sensitive preamplifier, located on the crystal. The calorimeter calibration procedure is based on the use of cosmic muons.[24]

The tracking system consists of two cylindrical drift chambers. Both chambers are divided into 20 jet-type cells in the azimuthal plane. Each cell contains five

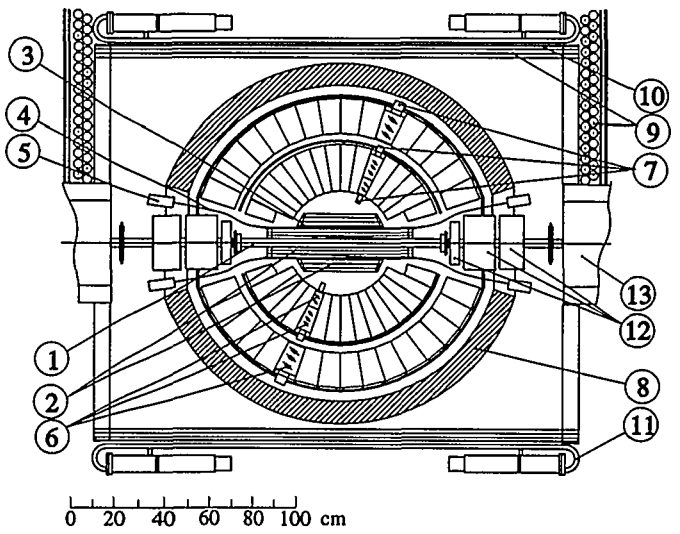


Figure 15: Detector SND—view transverse to the beam. (1) beam pipe, (2) drift chambers, (3) scintillation counters, (4) fiber light guides, (5) PMT's, (6) NaI(Tl) counters, (7) vacuum phototriodes, (8) iron absorber, (9) streamer tubes, (10) 1 cm iron plates, (11) scintillation counters, (12) magnetic lenses, (13) bending magnets.

sensitive wires. The longitudinal coordinate is measured by the charge division method to an accuracy of 3 mm. In addition, a cathode strip readout for inner and outer layers improves the latter value to 0.5 mm.

The muon/veto system consists of plastic scintillator counters and streamer tubes.

3.3 The Physics Program at VEPP-2M

The physics program for SND includes the following processes:

- Radiative decays of $\rho, \omega, \phi \to \pi^0\gamma, \eta\gamma$; $\phi \to \eta'\gamma$; $\phi \to a_0\gamma, f_0\gamma, \pi\pi\gamma, \eta\pi\gamma$; $\rho, \omega \to \pi\pi\gamma$.
- OZI and G-parity suppressed decays $\phi \to \omega\pi, \pi\pi, \eta\pi\pi$; $\rho \to 3\pi$; $\omega \to 2\pi$.
- Electromagnetic decays $\rho, \omega, \phi \to \eta e^+e^-, \pi^0 e^+e^-$.
- e^+e^- annihilation into hadrons $e^+e^- \to 2\pi, 3\pi, 4\pi, 5\pi$; $e^+e^- \to \omega\pi, \eta\pi\pi, \phi\pi$; $e^+e^- \to K^+K^-, K_SK_L, KK\pi$.
- Tests of QED $e^+e^- \to 3\gamma, e^+e^-\gamma$ $(2 \to 3)$; $e^+e^- \to 4\gamma, e^+e^-\gamma\gamma, 4e$ $(2 \to 4)$; $e^+e^- \to 5\gamma, 3\gamma e^+e^-, 4e\gamma$ $(2 \to 5)$.
- Search for rare K_S decays $K_S \to 2\gamma, 3\pi^0, 2\pi^0\gamma, \pi^0\gamma\gamma, \pi^0 e^+e^-$.
- Search for rare η decays $\eta \to 3\gamma, e^+e^-, 4e, 2\pi^0$.
- Search for C-even reactions $e^+e^- \to \eta', a_0, f_0, a_2, f_2$.

The search for electric dipole radiative decays like $\phi \to a_0\gamma$, $f_0\gamma$ can clarify the structure of the lightest scalar mesons and help determine whether or not they are mixed with four-quark states.

Accurate measurement of e^+e^- annihilation cross sections into hadrons is important for precise theoretical calculations of the hadron contribution to the muon anomalous magnetic moment (AMM). In the energy range $2E < 1$ GeV, the total hadron production cross section should be measured with an uncertainty of 0.5%. The corresponding error in AMM calculations would be 0.2 ppm.

The hadronic cross section is also of great importance to solve the problem of existence and location of radial excitations of the light vector mesons ρ, ω, ϕ. This cross section also contributes significantly to measuring some decay spectra and branching ratios of the τ lepton, and the D and B mesons.

3.4 1995 Test Run[25]

The goal of the test run was to minimize background rates, adjust trigger components, and calibrate the calorimeter and drift chambers. At that time, the collider operated in the energy range 660–800 MeV with the CMD-2 detector, and the average luminosity was about 2×10^{29} cm^{-2} sec^{-1}. We installed lead shields around the beam pipe and found optimum trigger components, which allowed us to reduce the trigger rate to the level of 5×10^4 events × nb. The average event length on the tape was about 0.5 kByte. Using Bhabha scattering and two-photon annihilation events, we measured the energy resolution of the SND calorimeter for 400 MeV electromagnetic showers to be 8% (σ), which should be compared with the Monte Carlo value of 4%. Such a strong disagreement showed that the calorimeter calibration procedure was unsatisfactory at that time. The drift chamber system operated with a gas mixture Ar + 10% CO_2. The spatial resolution measured using Bhabha events was about 0.2 mm in the r–ϕ plane, which was close to the expected value.

3.5 1996 $\phi(1020)$ Run

The energy range $2E$ = 984–1034 MeV around the maximum $\phi(1020)$ peak was scanned with a total integrated luminosity of 4 pb^{-1}. The number of produced ϕ's was estimated to be about 5×10^6. The VEPP-2M average luminosity was slightly above 10^{30} cm^{-2} sec^{-1}. The normalized trigger rate was 10^7 events × pb. After improvement of the energy calibration procedure, the calorimeter energy resolution reached $\sigma/E = 5.8\%$ for 500 MeV photons (Fig. 16), which is still larger than the expected value of 4.2%. The measured σ of the effective mass spectra of π^0, η, and K_s mesons, produced in the ϕ peak and decaying into photon final states, was 13, 18, and 26 MeV, respectively (Figs. 17, 18, and 19).

Another important feature is the SND event reconstruction together with charged particles and photons. For example, in the decay $\phi \to \eta\gamma \to \pi^+\pi^-\pi^0\gamma$, the reconstructed η mass has a width of $\sigma_{M_\eta} = 20$ MeV.

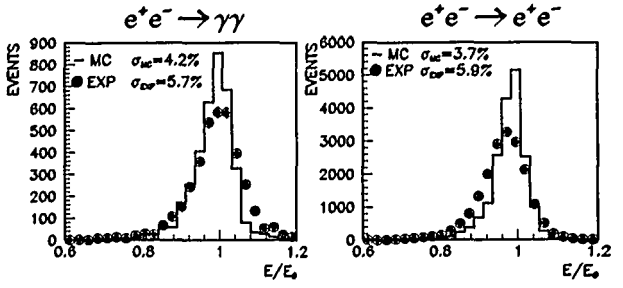


Figure 16: Energy spectra of electrons and photons for $e^+e^- \to e^+e^-$ and $e^+e^- \to \gamma\gamma$ reactions at E_{beam} = 517 MeV.

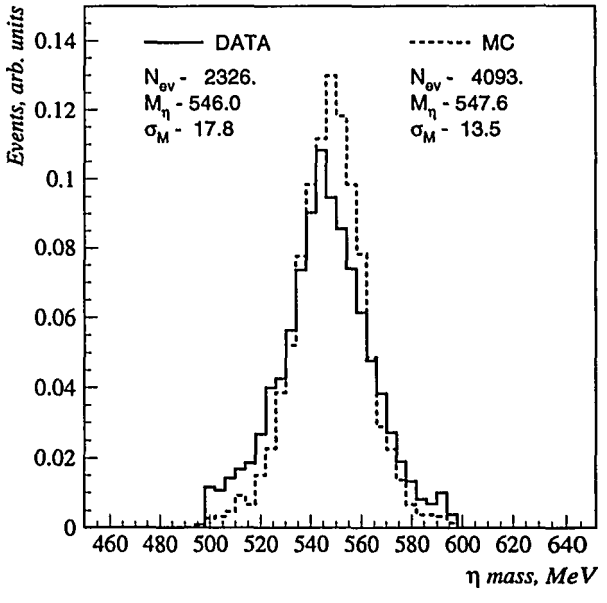


Figure 17: Effective mass spectrum of two photons from the $e^+e^- \to \eta\gamma \to 3\gamma$ reaction.

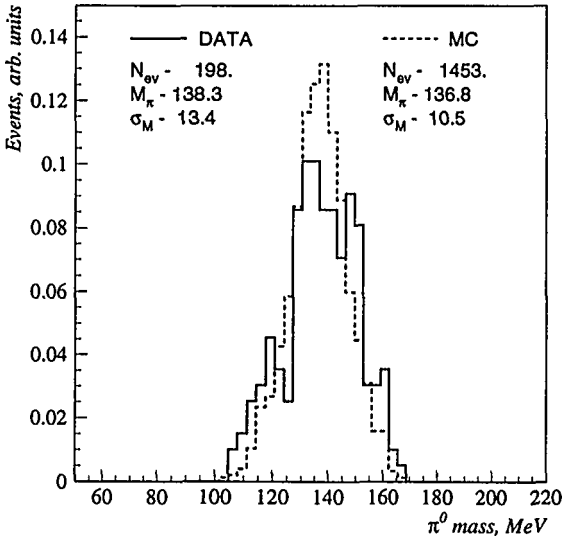


Figure 18: Effective mass spectrum of two photons from the $e^+e^- \to \pi^0\gamma \to 3\gamma$ reaction.

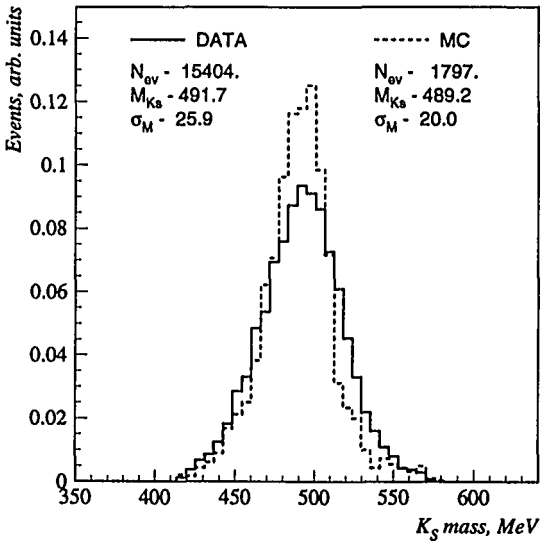


Figure 19: Effective mass spectrum of four photons from $K_S \to 2\pi^0$ decay.

3.6 Preliminary Physics Results

By June 1996, about 10% of the collected data sample, corresponding to an integrated luminosity of 0.4 pb^{-1}, was processed. We selected the main $\phi(1020)$ event decays, i.e., $\phi \to K^+K^-, K_SK_L, \eta\gamma$, etc. (examples are shown in Fig. 20).

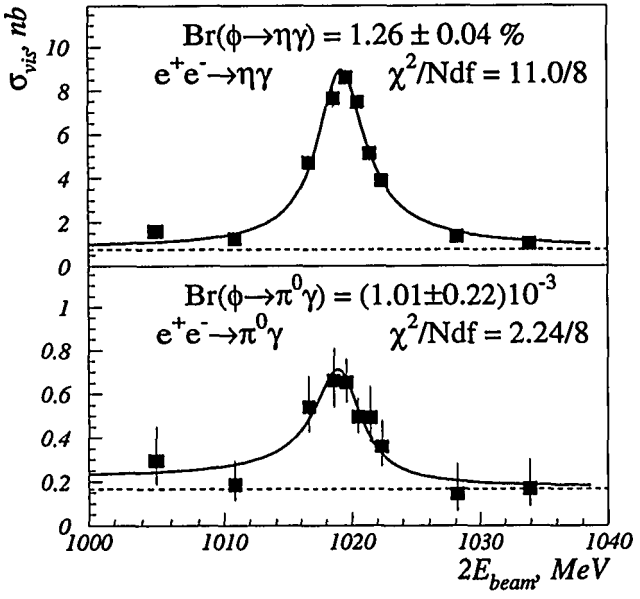


Figure 20: Visible cross section of $e^+e^- \to \eta\gamma$ and $e^+e^- \to \pi^0\gamma$ reactions.

After fitting the data with the standard routine using a Breit-Wigner curve, and the Monte Carlo efficiency for particular channels, we obtained the following preliminary results:

$$
\begin{aligned}
B(\phi \to \eta\gamma) &= (1.26 \pm 0.08)\% \text{ (from } \eta \to 2\gamma \text{ mode)}, \\
B(\phi \to \eta\gamma) &= (1.15 \pm 0.10)\% \text{ (from } \eta \to 3\pi^0 \text{ mode)}, \\
B(\phi \to \pi^0\gamma) &= (0.10 \pm 0.02)\%,
\end{aligned}
$$

$$
\begin{aligned}
B(\phi \to f_0(975)\gamma) &< 9 \times 10^{-4} \text{ (from } f_0 \to 2\pi^0 \text{ mode), (90\% C.L.)}, \\
B(\phi \to a_0(980)\gamma)B(a_0 \to \pi^0\eta) &< 9 \times 10^{-4} \text{ (from } \eta \to 2\gamma \text{ mode), (90\% C.L.)}.
\end{aligned}
$$

The obtained data still has larger errors than in the tables and can be considered as a first step, showing the SND ability to produce new physics results.

3.7 SND Summary

In Novosibirsk, experiments with the new SND detector at the low-energy collider VEPP-2M are continuing. SND is a general-purpose nonmagnetic detector, the main part of which is the three-layer NaI(Tl) spherical calorimeter with 1632 individual crystals. SND provides a good opportunity to study processes with multiple photons in final state. In the summer of 1996, a data-taking run in the vicinity of the $\phi(1020)$, with an integrated luminosity of about 4 pb^{-1}, was performed. The measured photon energy resolution and mass resolution for π^0, η, and K_S show the feasibility of studying e^+e^- processes at VEPP-2M with SND. First preliminary physics results have been obtained for $\phi(1020)$ decays.

Acknowledgments

I would like to thank R. Baldini and A. Michetti for their advice and useful discussions on nuclear interaction studies.

The work is supported in part by the U.S. Department of Energy, U.S. National Science Foundation, and the International Science Foundation under grants RPT000 and RPT300.

This work is also supported in part by the Soros Foundation, Grants No. RPX000 and RPX300; and the RFBR Fund, Grants No. 95-02-04587 and 96-02-19192.

References

[1] V. V. Anashin *et al.*, preprint Budker INP 84-114, Novosibirsk, 1984.

[2] L. M. Barkov *et al.*, Nucl. Phys. B **364**, 199 (1985).

[3] A. D. Bukin *et al.*, Sov. J. Nucl. Phys. **27**, 516 (1978).

[4] S. I. Dolinsky *et al.*, Phys. Report **202**, 99 (1991).

[5] G. A. Aksenov *et al.*, preprint Budker INP 85-118, Novosibirsk, 1985.

[6] E. V. Anashkin *et al.*, ICFA Instrumentation Bulletin **5** (1988), p.18.

[7] R. R. Akhmetshin *et al.*, Phys. Lett. B **364**, 199 (1995).

[8] R. R. Akhmetshin *et al.*, preprint Budker INP 95-62, Novosibirsk 1995.

[9] G. V. Fedotovich (CMD-2 Collaboration), in *Proceedings of the Workshop on Physics and Detectors for DAΦNE'95*, Frascati, April 4-7, 1995, p. 571.

[10] L. Montanet *et al.*, Phys. Rev. D **54**, 341 (1996).

[11] N. N. Achasov, V. Gubin, and E. P. Solodov, hep-ph/9610282.

[12] A. Lysenko *et al.*, Nucl. Instrum. Methods A **359**, 419 (1995).

[13] V. N.Bayer, Russian ZETP **17**, 446 (1973).

[14] J. L. Rosner, I. Dunietz, and J. Hauser, Phys. Rev. D **35**, 2166 (1987).

[15] S. Eidelman, E. Solodov, and J. Thompson, Nucl. Phys. B **24**, 174 (1991).

[16] A. N. Skrinsky, in *Proceedings of the Workshop on Physics and Detectors for DAΦNE*, Frascati, April 1991, p. 67.

[17] G. Vignola, in *Proceedings of the Workshop on Physics and Detectors for DAΦNE*, Frascati, April 1991, p. 11.

[18] A. N. Filippov *et al.*, in *Proceedings of the XVth Int. Conf. on High Energy Accelerators*, Hamburg, Germany, 1991, World Scientific, V. II, p. 1145.

[19] R. Baldini and A. Michetti, KLOE Memo 30, July 1995.

[20] G. Barbellini and C. Santoni, CERN-EP/89-8 and CERN-PPE/90-09.

[21] G. A. Sayer and E. F. Beall, Phys. Rev. D **169**, 1045 (1968).

[22] V. M. Aulchenko *et al.*, in *Proceedings of the Workshop on Physics and Detectors for DAΦNE*, Frascati, April 1991, p. 605; V. M. Aulchenko *et al.*, *The 6th International Conference on Hadron Spectroscopy*, Manchester, UK, 10–14 July 1995, p. 295.

[23] P. M. Beschastnov *et al.*, Nucl. Instrum. Methods A **342**, 477 (1994).

[24] M. N. Achasov *et al.*, "Absolute energy calibration of the SND detector calorimeter by cosmic muons," to be published in *Proceedings of the VI International Conference on Instrumentation for Experiments at e^+e^- Colliders*, Novosibirsk, 1996.

[25] V. M. Aulchenko *et al.*, *Beginning of the Experiments with SND Detector at e^+e^- Collider VEPP-2M*, preprint Budker INP 95-56, 1995.

SOME RECENT RESULTS FROM CLEO II

Richard Kass*
Department of Physics
The Ohio State University, Columbus, Ohio 43210

Representing the CLEO Collaboration

ABSTRACT

The CLEO experiment has been operating for several years now collecting e^+e^- annihilation data at and near the $\Upsilon(4S)$ resonance ($E_{cm} \approx$ 10.6 GeV). The accumulated event sample contains several million $B\bar{B}$ and $\tau^+\tau^-$ pairs. This data is used to explore rare b, c, and τ decays. In this report, several recent CLEO results in the area of B-meson and τ decay are presented. The topics covered include: penguin decays of B-mesons, measurement of exclusive $b \to u$ semileptonic transitions, τ decays with an η in the final state, precision measurement of the Michel parameters in leptonic τ decay, and a search for lepton number violation using τ's.

*Supported by DOE grant DE-FG02-91ER40690.

© 1996 by Richard Kass.

1 Introduction

In this report, B-meson and τ lepton physics results from the CLEO Collaboration will be discussed. The CLEO experiment occupies the sole interaction region at the Cornell Electron-Positron Storage Ring (CESR). To date, CLEO has collected a total integrated luminosity in excess of 5 fb^{-1}, with $\approx$ two-thirds of the data collected at the $\Upsilon(4S)$ ($\sqrt{s}$ =10.58 GeV) [Ref. 1], and the rest at energies slightly below the $\Upsilon(4S)$. This luminosity corresponds to the production of $\approx 3 \times 10^6$ $B\bar{B}$ and 5×10^6 τ-pairs.

The CLEO II detector,[2] shown in Fig. 1, emphasizes precision charged particle tracking, high resolution electromagnetic calorimetry, and good lepton identification. The various subsystems that make up the detector are described in Table 1. All detector subsystems, with the exception of the muon chambers, reside in a 1.5 T solenoidal magnetic field. The momentum of a charged particle is measured by reconstructing its trajectory as it traverses the three drift chamber systems (PTL,VD, DR). The energy and angle of electrons and photons is measured using a calorimeter (BCC, ECC) that consists of $\approx$ 8000 CsI crystals.

The identification of electrons is primarily accomplished by comparing the momentum measured by the drift chamber with the energy measured in the CsI calorimeter. Muons are identified by their ability to penetrate a significant amount of iron without undergoing an inelastic collision. Thus charged particles which traverse the drift chambers, calorimeter, magnet iron, and match up with hits in the muon chambers are labeled muons. The lepton identification efficiencies and fake rates are summarized in Table 2. Finally, charged hadrons (π, K, p) are identified over a limited momentum region using an array of scintillation counters to measure their time of flight and the main drift chamber to measure their average ionization energy loss (dE/dx).

2 B-Meson Physics

The production and subsequent decay of the $\Upsilon(4S)$ provides the B-mesons for the CLEO experiment. This source of B-mesons has several attractive features for the experimentalist including:

- The $\Upsilon(4S)$ decays exclusively into a pair of B-mesons; no extra particles are produced.

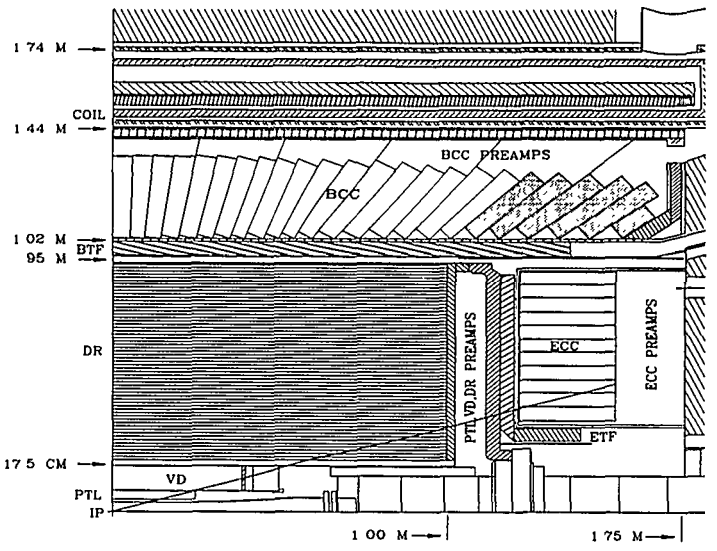


Figure 1: Quarter section of the CLEO II detector.

- To the accuracy that it can be measured, $B^0\bar{B}^0$ and B^+B^- pairs are produced in equal numbers.
- The energy of a B-meson is given by the CESR beam energy and hence is determined to a higher accuracy than if it were to be measured by CLEO.
- The mass resolution of a B-meson is improved by using the beam energy in place of the measured energy of a B candidate, i.e., $M_B = \sqrt{E^2_{beam} - p^2}$, with p the measured momentum of the B decay products.
- A B-meson free sample of data can be obtained by running CESR at a center-of-mass energy below the mass of the $\Upsilon(4S)$.
- The cross section for producing B-mesons from the decay of the $\Upsilon(4S)$ is about 1/3 the continuum hadronic cross section ($e^+e^- \rightarrow q\bar{q}$).

The fact that $m_{\Upsilon(4S)} \approx 2m_B$ is a mixed blessing. Since the B's are practically at rest ($\beta \approx 0.06$) when they decay, the particles produced in these events tend to populate the detector in an isotropic fashion. This is in contrast to the "jet-like"

Table 1: The detector subsystems of the CLEO detector.

Device	#	R(cm)	$\|z\|$(cm)	$\|cos\theta\|$	Resolution
PTL	6	4.7-7.2	25	0.96	50μm (DME @ 6 mm H_2O)
Inner VD Cath	1	7.6	19	0.92	1.3 mm (5.85 mm strips)
VD	10	8.5-16	35	0.91	90μm (Ar/Et @ 6 PSIG)
Outer VD Cath	1	17.1	33	0.90	1.3 mm (6.85 mm strips)
Inner DR Cath	1	18.6	48	0.92	1.3 mm (1cm strips)
DR	1	19.9-90.1	97	0.71	120μm (Ar/Et @6 mm H_2O)
Outer DR Cath	1	96.1	91	0.71	1.3 mm (1cm strips)
Combined CD	67/4	47-90.1	-	0.92	$\sigma_p/p(\%) = \sqrt{(0.15p)^2 + 0.5^2}$
					$\sigma_{dE/dx}(e) = 6.3\%$ @ 5 GeV
TF-Barrel	64	96-101	140	0.77	$\sigma_t(\pi)$ =154 ps
					2σ $\pi - K$ for p_t <1.1 GeV/c
TF-Endcap	2 x 28	31-89	120-125	0.81-0.96	$\sigma_t(\pi)$ =240 ps
CC-Barrel	6144	102-132	167	0.82	$\frac{\sigma_E}{E}(\%) = \frac{0.35}{E^{0.75}} + 1.9 - 0.1E$
					σ_ϕ(mrad)=$2.8/\sqrt{E}$+1.9
CC-Endcap	2 x 828	33-91	125-155	0.81-0.98	$\sigma_E/E(\%) = 0.26/E + 2.5$
Mu-Barrel	3	210, 246, 282	240	0.71	≈4 cm @ 5GeV
Mu-Endcap	2 x 1	160-310	280	0.67-0.85	≈5 cm @ 5GeV

Table 2: Lepton identification efficiencies and fake rates.

Lepton	p (GeV)	ϵ(%)	Fake rate/track (%)
electron	0.4-5.3	95	0.3
muon	1.5-2.1	70-93	0.7(π)/1.0(K)
	2.1-5.3	93	1.2(π)/1.7(K)

structure of events produced via $e^+e^- \to q\bar{q}$. This difference in event shape can be exploited when a B-meson rich event sample is desired.

There are, however, two drawbacks to having the B's decay at rest. First, since the particles tend to be produced isotropically, it is very difficult to associate a given particle with its parent B. This is in contrast to the situation at LEP and/or SLC where the B decay products tend to follow the direction of the parent B. Second, the mean decay length of a B is $\approx$ 30 μm, too short for silicon vertex detectors to separate the primary and secondary vertices. Again, this is in contrast to the situation at LEP/SLC where the mean decay length is several mm.

2.1 $B^0 \to D^{(*)+}D^{(*)-}$

Two-body decays of the form $B^0 \to D^{(*)+}D^{(*)-}$ are thought to be good modes for the observation of CP violation with sensitivity in $sin2\beta$ comparable to the decay $B \to \psi K_s^o$ (Ref. 3). The branching fractions for these decay modes can be estimated using the measured rates for the analog reactions where the D is replaced with a Cabibbo favored D_s. Making the appropriate substitutions, we have:

$$\frac{\mathcal{B} \to D^{(*)+}D^{(*)-}}{\mathcal{B} \to D_s^{(*)+}D_s^{(*)-}} \approx (f_{D^{(*)}}/f_{D_s^{(*)}})^2 tan^2\theta_c \approx \frac{1}{20}(0.9)^2 .$$

Table 3 gives the expected $B^0 \to D^{(*)+}D^{(*)-}$ branching fractions where the CLEO measurements for the D_s modes have been used.[4]

Table 3: $B^0 \to D^{(*)+}D^{(*)-}$ branching ratio estimates.

Mode	BR of D_s mode (%)	Estimated BR (%)
$B^0 \to D^{*+}D^{*-}$	2.4	0.097
$B^0 \to D^{*+}D^- + D^+D^{*-}$	2.0	0.081
$B^0 \to D^+D^-$	1.1	0.045

An integrated luminosity of 3.09 fb^{-1} ($3.3 \times 10^6 B\bar{B}$ pairs) taken at the Υ(4S) was used for this analysis. Charged tracks were required to be consistent with originating from a primary vertex in both the $r-\phi$ and $r-z$ planes. Photon candidates were required to have energies greater than 30 MeV if $|cos\theta| < 0.71$ (θ = polar angle) and greater than 50 MeV for other regions of the CsI calorimeter.

Pairs of photons with invariant mass within $\pm 2.5\sigma$ of the nominal π^0 mass were kept for further consideration. Both dE/dx and time-of-flight information were used to distinguish charged kaons from pions.

Candidate D^{*+}'s were reconstructed using the $D^{*+} \to \pi^+ D^0$ mode while D^0's were reconstructed using the modes $D^0 \to K^-\pi^+$, $K^-\pi^+\pi^0$, and $K^-\pi^-\pi^+\pi^+$. Only the mode $D^+ \to K^-\pi^+\pi^+$ was used for D^+ candidates. The $D^* - D$ mass resolution for modes containing a D^{*+} decay into all charged tracks was improved by performing a vertex constrained fit.

Backgrounds from non-B sources were minimized using the beam constrained mass and energy difference ($\Delta E = E_B - E_{beam}$). Since the decays under study here are all of the form $Pseudoscalar \to Vector + Pseudoscalar$, a cut of $|cos\theta_{helicity}| > 0.5$ was used in the analysis. Background events are expected to have a flat $|cos\theta_{helicity}|$ distribution.

The results of this analysis are displayed in Fig. 2 where ΔE vs m_B is plotted for the three decay modes. In each case, the signal region is given by the box, and the sideband regions lie above and below the dotted lines. Table 4 gives a summary of the event yields and 90% confidence level upper limits for each mode. The probability that the expected background of 0.022 ± 0.011 events in the $B^0 \to D^{*+}D^{*-}$ channel fluctuates up to or exceeds the observed one event is $\approx 2.2\%$. If we interpret this one event to be a signal, then the corresponding branching fraction is:

$$\mathcal{B}(B^0 \to D^{*+}D^{*-}) = [6.0^{+8.1}_{-4.2}(stat) \times 10^{-4}] \times [1 \pm 0.18(syst)]\,,$$

where the systematic error is largely due to uncertainties in the D and D^* branching fractions, and tracking efficiencies. No significant excess of events is found in the other two modes.

2.2 Nonresonant Three-Body Hadronic B-Meson Decays

Decays of charged B mesons to three charged hadrons are of interest as they may exhibit CP violation. In particular, decays of the form $B^+ \to h^+h^-h^+$ where h can be a $\pi^\pm, K^\pm, p$, or $\bar{p}$ may have CP asymmetries as large as 10% when the h^+h^- invariant mass is close to the η_c or χ_{c0} mass.[5] The nonresonant decay $B^+ \to \pi^+\pi^-\pi^+$ is predicted[6] to have a branching fraction in the range (1.5–8.4) $\times\ 10^{-5}$. Here the authors point out that interference between the nonresonant

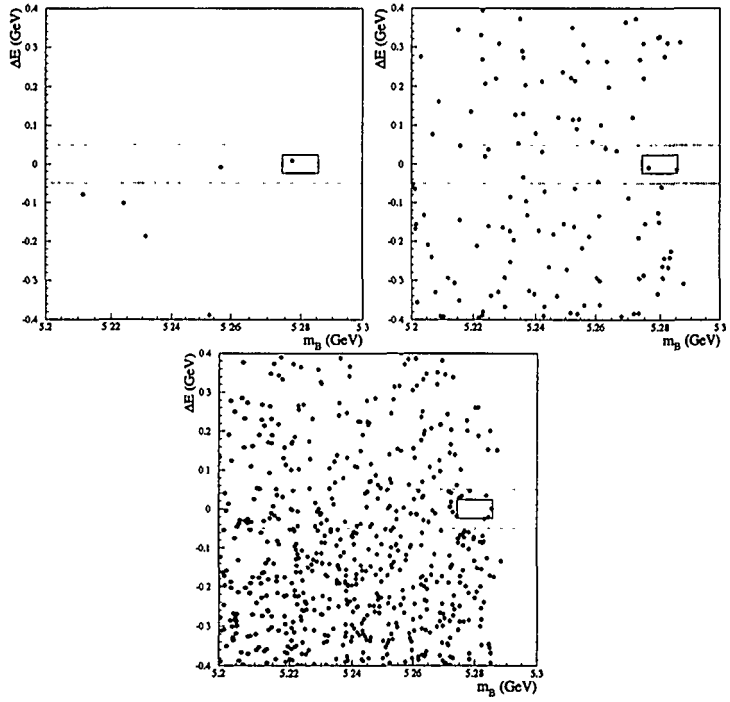


Figure 2: ΔE vs m_B for data. The signal region is indicated by the box. The sideband region lies above and below the dotted lines.

Table 4: Summary of $B^0 \to D^{(*)+}D^{(*)-}$ analysis.

Mode	Evts. in ΔE sidebands	Pred. Bkgd. in signal region	Evts. in signal region	Upper Limit 90% CL
$D^{*+}D^{*-}$	4	0.022±0.11	1	2.5×10^{-3}
$D^{*+}D^{-} + D^{+}D^{*-}$	117	0.64±0.10	2	2.0×10^{-3}
$D^{+}D^{-}$	539	2.64±0.34	3	1.3×10^{-3}

amplitude [with $m(\pi^+\pi^-) \approx 3.4$ GeV] and $B \to \chi_{c0}$, $\chi_{c0} \to \pi^+\pi^-$ could lead to a CP asymmetry of $(0.4\text{-}0.8)sin\gamma$, with $\gamma = \arg V_{ub}^*$. If this is so, then γ can be measured at an e^+e^- facility operating at the $\Upsilon(4S)$.

The CLEO Collaboration has searched for these decays using 3.2 fb^{-1} of data taken at the $\Upsilon(4S)$ and 1.1 fb^{-1} of data taken at energies about 60 MeV below the $\Upsilon(4S)$. The continuum event background (non-$B\bar{B}$ events) is greatly reduced using a combination of event shape cuts and kinematic based criteria optimized for three-body B decay. Charged tracks in hadronic events are identified as $\pi^{\pm}, K^{\pm}, p$, or $\bar{p}$ using dE/dx information from the central drift chamber system. B-meson related backgrounds (e.g., $B \to \psi K$) are suppressed by vetoing any event where a charged track is identified as either an electron or muon or the invariant mass of oppositely charged tracks is within 60 (40) MeV of the ψ (D^0) mass. The detection efficiency of each mode listed in Table 5 is determined using a GEANT[7] based Monte Carlo simulation. In all cases, the energy of the B-meson is constrained to be the same as the beam energy.

The mass distributions for the various decay modes are shown in Fig. 3. The signal region for each mode is shown between the arrows. Unfortunately, there is no signal in any of the mass plots. The details of the analysis are summarized in Table 5 and 90% confidence level upper limits are given in Table 6. While this analysis does not find any evidence for these decay modes, it does rule out a substantial range of the predicted branching fraction for $B^+ \to \pi^+\pi^-\pi^+$ and provides improved limits in all other cases.

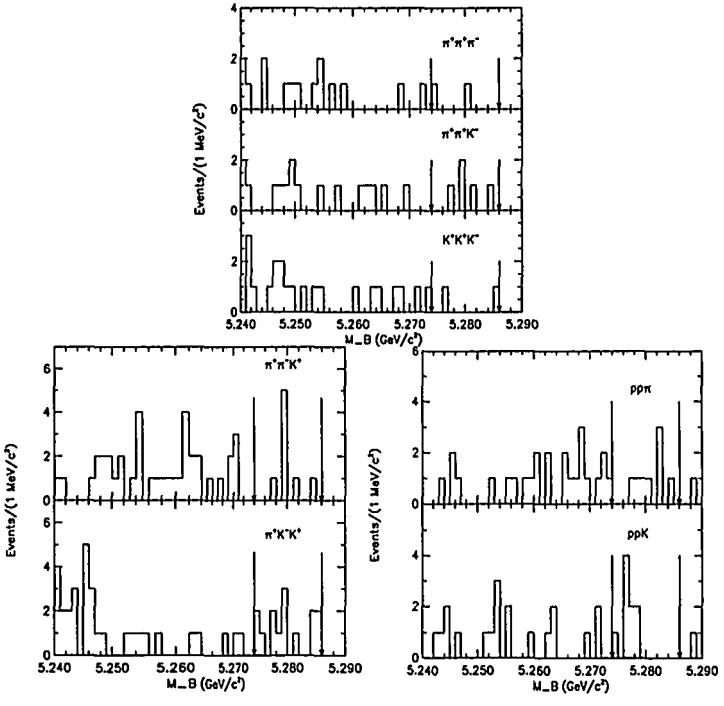


Figure 3: Mass distributions for the various $B^+ \to h^+h^-h^+$ modes. In all cases, the signal region is between the arrows.

Table 5: Summary of $B^+ \to h^+h^-h^+$ analysis.

Mode	Signal Yield	Estimated Background	Efficiency (%)	90% CL Upper Limit No. Events
$B^+ \to \pi^+\pi^-\pi^+$	2	1.2±1.2	4.5±0.66	5.3
$B^+ \to \pi^+\pi^+K^-$	5	3.9±1.8	4.5±0.66	7.2
$B^+ \to \pi^+\pi^-K^+$	8	13.0±4.0	7.1±1.1	5.6
$B^+ \to \pi^+K^-K^+$	14	8.8±3.0	6.7±0.98	14.3
$B^+ \to K^+K^+K^-$	2	3.9±2.0	3.6±0.54	3.9
$B^+ \to p\bar{p}\pi^+$	8	8.6±2.4	4.8±0.7	7.2
$B^+ \to p\bar{p}K^+$	9	4.3±1.5	4.5±0.66	11.4

2.3 Electromagnetic Penguin Decays of the B-Meson

The first direct observation of penguin mediated B-meson decay was by CLEO in 1993 (Ref. 11) with the observation of $B \to K^*\gamma$. Precision measurements of this decay rate, as well as other penguin decays, give a new window into and perhaps beyond the Standard Model, as they involve internal loops with heavy mass quarks and vector bosons (Fig. 4). In addition, the mode $B \to K^*\gamma$ is important as it can be used to constrain the models used to estimate form factors in semileptonic $b \to u$ decay, e.g., $B \to \rho l\nu$. The decay $B \to \rho\gamma$ is similar to $B \to K^*\gamma$ but has a decay rate that is dependent on the CKM matrix element $|V_{td}|$ rather than $|V_{ts}|$. Given the difficulty with measuring direct t-quark decays, the simultaneous measurement of $B \to \rho\gamma$ and $B \to K^*\gamma$ offers the best opportunity to determine $|V_{td}|/|V_{ts}|$ for the near term future.

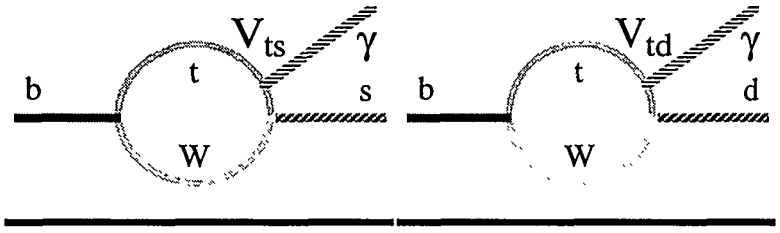


Figure 4: Electromagnetic penguin decay.

Table 6: Comparison of branching fractions with previous results and theoretical predictions.

Mode	90% CL Upper Limit (10^{-5})	Previous Best Limit (10^{-5})	Prediction (10^{-5})
$B^+ \to \pi^+\pi^-\pi^+$	4.1	5.0[8]	1.5-8.4[6]
$B^+ \to \pi^+\pi^+K^-$	5.6	-	-
$B^+ \to \pi^+\pi^-K^+$	2.8	19[9]	-
$B^+ \to \pi^+K^-K^+$	7.5	-	-
$B^+ \to K^+K^+K^-$	3.8	20[10]	-
$B^+ \to p\bar{p}\pi^+$	5.3	8.4[8]	-
$B^+ \to p\bar{p}K^+$	8.9	-	-

The CLEO Collaboration has updated its electromagnetic penguin decay analysis by using a larger data set than that used in the 1993 analysis. This new analysis uses 2.4 fb^{-1} of data taken at the $\Upsilon(4S)$ and 1.1 fb^{-1} of data taken at energies about 60 MeV below the $\Upsilon(4S)$. Candidate B-mesons are formed by combining a vector meson (ρ, ω, or K^*) with a high-energy photon. The mass resolution of a candidate B is improved using the beam energy in place of the measured energies. In Fig. 5, the invariant mass of $B \to K^*\gamma$ candidates for the various K^* modes is shown. Backgrounds to this analysis arise from processes that produce either high-energy photons or high-energy π^0's and η's that are reconstructed as single showers in the calorimeter. High-energy photons are produced by initial state radiation (ISR), while high energy π^0's and η's can be present in nonresonant e^+e^- annihilation events ($Q\bar{Q}$). Extreme care is taken in this analysis to suppress backgrounds from these sources. A combination of event shape cuts (Fox-Wolfram moment R_2, thrust axis) and a Fisher discriminant (Fig. 6) effectively remove contamination from ISR and $Q\bar{Q}$ events.

The $B \to K^*\gamma$ analysis is also subject to contamination from $B \to \rho\gamma$ events where a charged pion is misidentified as a kaon. In order to distinguish between these two types of B decay, a neural network is employed. The neural network uses the following inputs: $\Delta E_{\pi\pi}$, $M_{K\pi}$, $M_{\pi\pi}$, and $cos\theta_\rho$. Here θ_ρ is the angle found by transforming the momentum vector of the ρ's daughter with the larger momentum into the ρ's rest frame and measuring the angle between this trans-

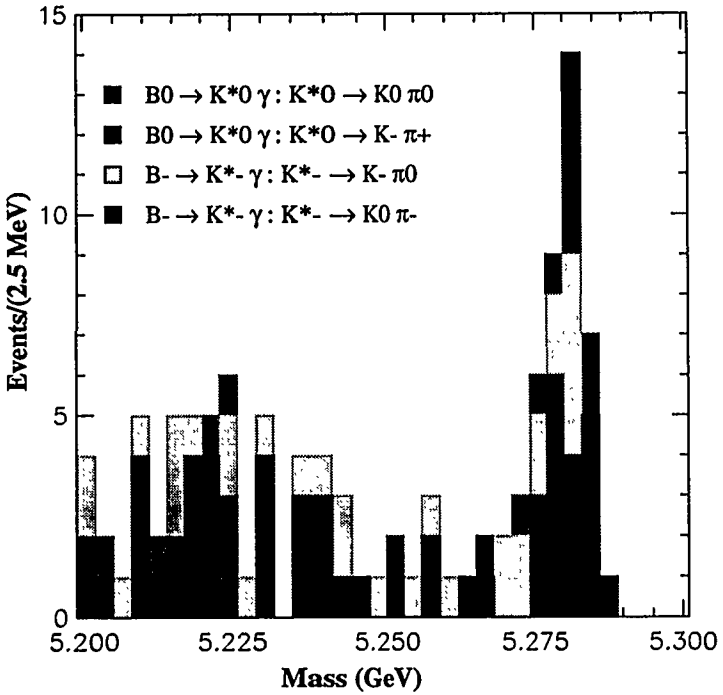


Figure 5: Mass plot for $B \to K^*\gamma$ candidates.

formed momentum vector and the flight direction of the ρ in the lab frame. In Fig. 7, the output from the neural network for $B \to K^*\gamma$ (peak at -1) and $B \to \rho\gamma$ (peak at +1) Monte Carlo events is shown.

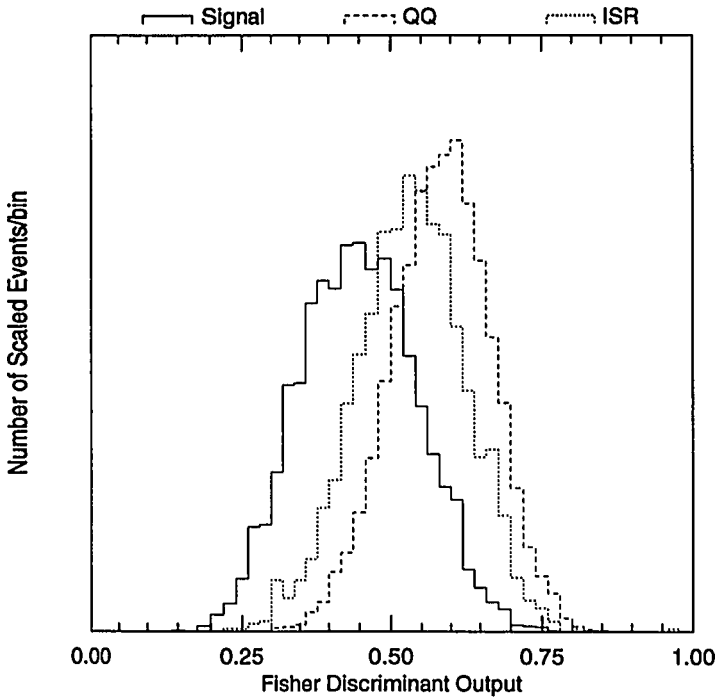


Figure 6: The distribution of the Fisher discriminant output for a Monte Carlo sample of $B^0 \to K^{*0}\gamma(K^{*0} \to K^+\pi^-)$ signal, $Q\bar{Q}$, and initial state radiation (ISR) events. The histograms all have equal area.

In Fig. 8, the data is shown for the various K^* decay modes. The box in each figure represents the signal region in the ΔE, M_B plane. A maximum likelihood fit using M_B, $M_{K\pi}$, ΔE, and the Fisher discriminant is used to determine the signal and background for each K^* mode. Table 7 gives the number of signal events, efficiency, and branching fraction for each K^* mode. The first error on the branching fraction is from the maximum likelihood fit and includes statistical and systematic errors. The second error is due to the uncertainty in the efficiency. In

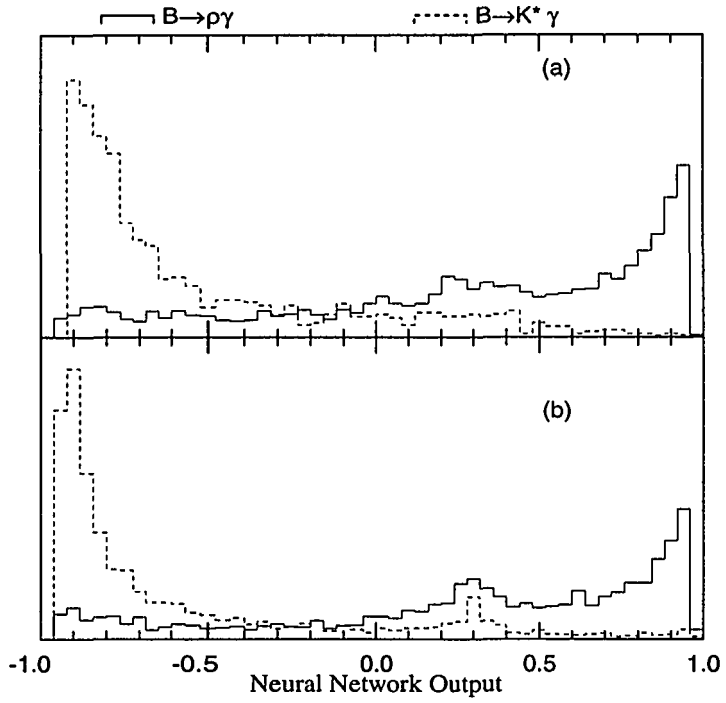


Figure 7: Distribution of the output of the neural network for Monte Carlo samples of (a) $B^0 \to \rho^0\gamma$ and $B^0 \to K^{*0}\gamma$ ($K^{*0} \to K^+\pi^-$) and (b) $B^- \to \rho^-\gamma$ and $B^- \to K^{*-}\gamma$ ($K^{*-} \to K^-\pi^0$).

Table 8, the combined $B \to K^*\gamma$ branching fraction is given for both the old and new analysis. The new results are in good agreement with the previous CLEO results.

Table 7: Individual $B \to K^*\gamma$ branching ratios.

K^* Mode	Signal Evts.	Signal Eff. (%)	Branching Ratio (10^{-5})
$K^+\pi^-$	$24.2^{+6.1}_{-5.6}$	22.3±2.0	$4.2^{+1.1}_{-1.0} \pm 0.4$
$K^0\pi^0$	$2.8^{+2.0}_{-1.5}$	1.8±0.2	$6.1^{+4.2}_{-3.3} \pm 0.8$
$K^0\pi^-$	$6.3^{+3.0}_{-2.5}$	5.7±0.6	$4.3^{+2.1}_{-1.7} \pm 0.5$
$K^-\pi^0$	$4.6^{+4.4}_{-3.0}$	6.9±0.7	$2.6^{+2.5}_{-1.7} \pm 0.3$

Table 8: Comparison of old and new $B \to K^*\gamma$ branching ratios.

Mode	New Branching Ratio (10^{-5})	Old Branching Ratio (10^{-5})
$B^0 \to K^{*0}\gamma$	$4.4 \pm 1.0 \pm 0.6$	$4.0 \pm 1.7 \pm 0.8$
$B^- \to K^{*-}\gamma$	$3.8^{+2.0}_{-1.7} \pm 0.5$	$5.7 \pm 3.1 \pm 1.1$
$B \to K^*\gamma$	$4.2 \pm 0.8 \pm 0.6$	$4.5 \pm 1.5 \pm 0.9$

There are many predictions[12] for the ratio $\mathcal{B}(B \to K^*\gamma)/\mathcal{B}(B \to s\gamma)$ as shown in Fig. 9. By combining CLEO's previous measurement[13] of

$$\mathcal{B}(B \to s\gamma) = (2.32 \pm 0.57 \pm 0.35) \times 10^{-4}$$

with these new results, we obtain:

$$\frac{\mathcal{B}(B \to K^*\gamma)}{\mathcal{B}(B \to s\gamma)} = 0.181 \pm 0.068.$$

This result is shown in Fig. 9 along with a number of theoretical predictions for this ratio. Clearly, more precise measurements and calculations are needed to discriminate between the models.

The $B \to (\rho\omega)\gamma$ analysis suffers from a lack of statistics in comparison to the $B \to K^*\gamma$ analysis. Since the candidate sample is so small, signals (or limits) are

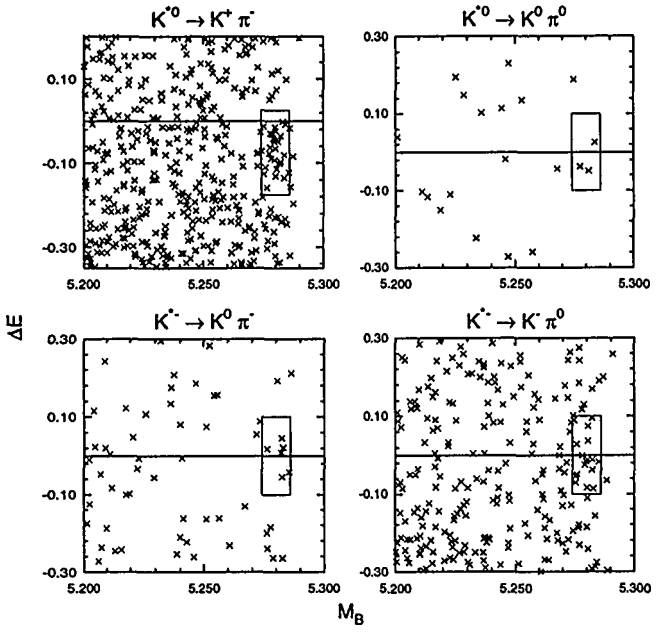


Figure 8: Distribution of $B \to K^*\gamma$ events in the M_B and ΔE plane.

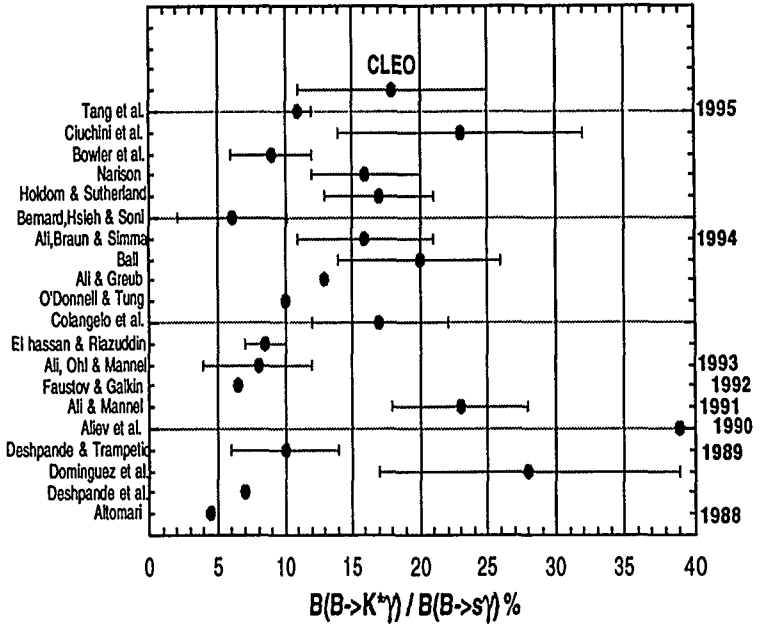


Figure 9: Summary of $\frac{\mathcal{B}(B\to K^*\gamma)}{\mathcal{B}(B\to s\gamma)}$ predictions and the CLEO result.

extracted by cutting on variables rather than performing a maximum likelihood analysis. In Fig. 10, events which pass all cuts are plotted in the M_B, ΔE plane. The events within the signal region (rectangle in Fig. 10) as well the various background estimates are given in Table 9. There is no signal apparent in the $B \to \rho^-\gamma$ and $B \to \omega\gamma$ channels. While there are four events in the signal region for $B \to \rho^0\gamma$, these events all have low values of ΔE and neural net output values marginally consistent with that expected from true $B \to \rho^0\gamma$ events. Hence these four events are not to be taken as evidence for $B \to \rho^0\gamma$. The 90% upper limit confidence levels for these decay modes are given in Table 10. The upper limit for $B \to \rho^-\gamma$ is still about an order of magnitude higher than the theoretical estimates from Soares[14] ((0.04-0.07)$\times 10^{-5}$) and Greub *et al.*[15] ((0.12-0.30)$\times 10^{-5}$).

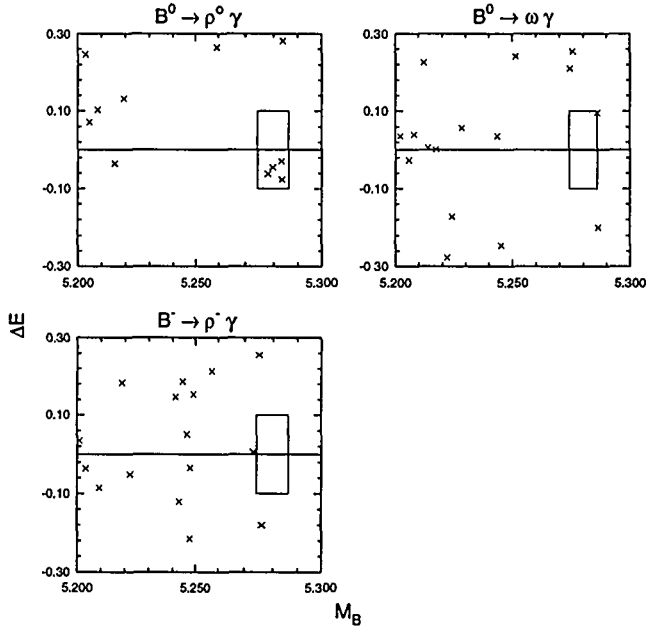


Figure 10: Distribution of $B \to (\rho\omega)\gamma$ events in the M_B and ΔE plane.

Table 9: Events and background estimates.

	$B \to \rho^0\gamma$	$B \to \omega\gamma$	$B \to \rho^-\gamma$
Events	4	0	0
QQ	0.23±0.08	0.56±0.18	0.40±0.11
ISR	0.18±0.12	0.14±0.10	0.12±0.09
$B \to K^*\gamma$	0.45±0.11	0.0	0.27±0.06
SUM	0.85±0.17	0.70±0.14	0.79±0.14

Table 10: Branching fraction upper limits at 90% CL.

Mode	Signal Events	Eff. (%)	Branching Fraction (10^{-5})
$B \to \rho^0\gamma$	4(7.99)	9.2±1.3	< 3.9
$B \to \omega\gamma$	0(2.30)	8.9±1.2	< 1.3
$B \to \rho^-\gamma$	0(2.30)	9.2±1.3	< 1.1

The ratio of rates for $B \to K^*\gamma$ and $B \to (\rho\omega)\gamma$ can be related to the CKM matrix elements $|V_{ts}|$ and $|V_{td}|$ through:

$$\frac{\mathcal{B}(B^- \to \rho^-\gamma)}{\mathcal{B}(B^- \to K^{*-}\gamma)} = \frac{\mathcal{B}(B^0 \to \rho^0\gamma) + \mathcal{B}(B^0 \to \omega\gamma)}{\mathcal{B}(B^0 \to K^{*0}\gamma)} = |\frac{V_{td}}{V_{ts}}|^2 \Omega\xi \ .$$

Here we neglect contributions from long-distance effects. In the above equation, ξ accounts for $SU(3)$ symmetry breaking and Ω accounts for the difference in phase space. An upper limit combining all the modes can be calculated if one assumes that $\mathcal{B}(B \to K^{*0}\gamma) = \mathcal{B}(B \to K^{*-}\gamma)$. Doing so, we obtain:

$$\frac{\mathcal{B}(B \to (\rho\omega)\gamma)}{\mathcal{B}(B \to K^*\gamma)} < 0.19 \ .$$

The phase space factor Ω can be estimated using[16]:

$$\Omega = \frac{(m_b^2 + m_d^2)}{(m_b^2 + m_s^2)} \frac{(m_B^2 + m_\rho^2)^3}{(m_B^2 + m_{K^*}^2)^3} \ .$$

Assuming m_b =5 GeV, m_s=300 MeV, m_d=100 MeV, and the nominal masses for m_B, m_{K^*}, and m_ρ, we obtain $\Omega = 1.02 \pm 0.02$. The SU(3) term ξ has been evaluated by several groups. In Table 11, estimates of ξ as well as the upper limits on the ratio $|V_{td}|/|V_{ts}|$ are given. These limits are comparable to recent ALEPH results[18] which rely on B_s^0 oscillations.

Table 11: Upper limits for $|V_{td}|/|V_{ts}|$.

Group	Model	ξ	Upper Limit
Ali *et al.*[16]	QCD Sum Rule	0.58	< 0.56
Soares[14]	BSW Formalism	0.72-0.90	$< (0.45 - 50)$
Narison[17]	Hybrid QCD Sum Rule	0.77	< 0.49

2.4 Search for $b \to s$ Gluonic Penguins Using Inclusive η' and K^0_s Decays

To date, there is no experimental evidence for gluonic penguin decay in the b-quark sector. Unlike the photon radiated in an electromagnetic penguin decay, the gluon is not directly observable in the CLEO detector. This greatly complicates the search strategy for these decays. One way to look for gluonic penguin decay is to take advantage of the kinematics of the underlying $b \to sg$ reaction and search for events in a phase space region forbidden to $b \to c$ decays. For example, $b \to sg \to s\bar{s}s$ can hadronize into $B \to \eta' X_s$ (X_s a meson system containing a strange quark) and produce an η' with momentum larger than that possible from the analog charm reaction $B \to \eta' X_c$. Another such example is $b \to sg \to s\bar{d}d$ which can hadronize to $B \to K_s X$ (X a meson containing no strange quarks), the K_s produced with momentum greater than that possible from $B \to K_s X_c$.

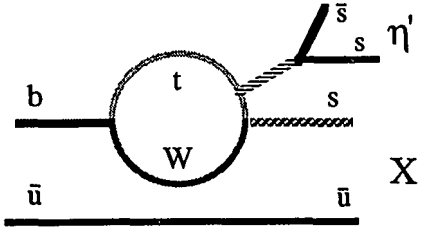


Figure 11: Penguin decay of $b \to \eta' X$.

Inclusive searches for $b \to sg$ have two possible advantages over exclusive searches. First, the rate for inclusive $b \to sg$ can be reliably calculated and is not subject to the same uncertainties as the exclusive calculations. Second, the rate for inclusive $b \to sg \to sq\bar{q}$ (with $q = u, d, s$) is expected to be of order 1% (Refs. 19 and 20) with $b \to s\bar{s}s$ expected to be $\approx 0.2\%$ (Ref. 20). This is in contrast to two-body exclusive modes such as $\bar{B}^0 \to \phi K_s$ or $\bar{B}^0 \to K^-\pi^+$ which have rates estimated to be in the 10^{-5} range.

The signature for a $B \to \eta' X_s$ gluonic penguin decay is an η' with $2.0 < p_{\eta'} < 2.7$ GeV/c. This kinematic region eliminates most of the η''s produced by $b \to c$ transitions. Backgrounds from $b \to c$ transitions (e.g., $B \to D^{(*)0}\eta'$) can only contribute to the region $2.0 < p_{\eta'} < 2.34$ GeV/c.

There are many sources of K_s's in B decay including $B \to D_s X$, $B \to D^0 X$, $B \to D^+ X$, and $B \to \Lambda_c X$. However, these sources produce K_s's with $p_{K_s} < 2$ GeV/c. Thus a signature for $b \to sg$ is an excess of K_s's produced in B decay with $p_{K_s} > 2$ GeV/c. The most important background in this momentum region is from the Cabibbo suppressed internal spectator decay $B \to K_s D^{(*)}$.

The data sample used in this analysis consists of 3.1 fb^{-1} ($3.3 \times 10^6 B\bar{B}$ pairs) of data taken at the $\Upsilon(4S)$ and 1.6 fb^{-1} of data taken at energies below the $\Upsilon(4S)$. Hadronic continuum events are suppressed using a combination of event shape cuts and a Fisher discriminant. To reconstruct an η', first the η is reconstructed through the $\eta \to \gamma\gamma$ mode and then the η is combined with pairs of oppositely charged pions. The K_s decays are reconstructed through the $K_s \to \pi^+\pi^-$ mode. For convenience, the analysis is done using the scaled momentum of the meson (η', K_s):

$$x = \frac{p_{meson}}{\sqrt{E^2_{beam} - m^2_{meson}}}$$

to aid in the continuum subtraction. In terms of x, the region $0.45 < x_{\eta'} < 0.52$ is heavily populated by $b \to sg \to \eta' X_s$ while for $b \to sg \to K_s X$ the interesting region is $0.46 < x_{K_s} < 0.54$.

In Fig. 12, the inclusive continuum subtracted x spectrum of K_s's and η''s from B-meson decay is shown. There is no apparent $b \to sg$ signal in the K_s x spectrum. The data can be used to calculate 90% upper limit confidence levels of:

$$\mathcal{B}(B \to K_s X) < 7.5 \times 10^{-4}$$

for $0.40 < x_{K_s} < 0.54$ and

$$\mathcal{B}(B \to K_s X) < 2.1 \times 10^{-4}$$

for $0.46 < x_{K_s} < 0.54$.

For $B \to \eta' X$, there is a modest excess ($\approx 2\sigma$) of η''s in the region of interest. However, this is not compelling evidence for $b \to sg$ at this time, so we quote 90% upper limit confidence levels of:

$$\mathcal{B}(B \to \eta' X) < 7.4 \times 10^{-4}$$

for $0.45 < x_{\eta'} < 0.52$ and

$$\mathcal{B}(B \to \eta' X) < 17 \times 10^{-4}$$

for $0.39 < x_{\eta'} < 0.52$.

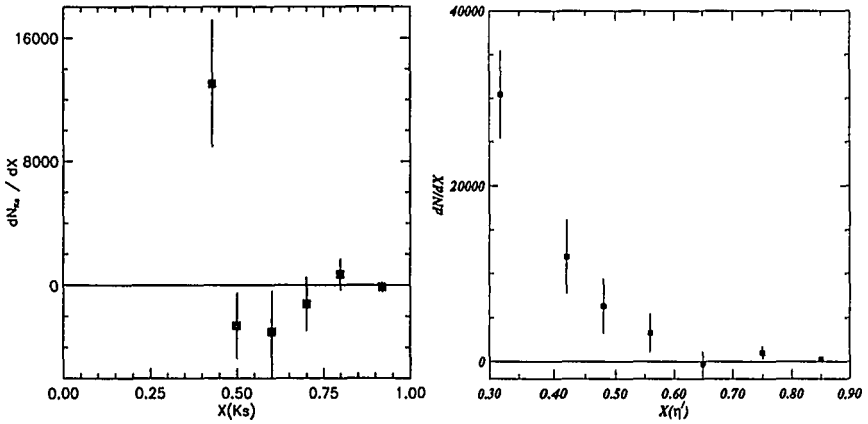


Figure 12: The continuum subtracted yield of K_s's and η''s as a function of the scaled momentum x.

2.5 Search for $B^+ \to \omega h^+$ and $B^+ \to \eta h^+$

Two-body decays of B-mesons into final states containing either an ω or η and a charged pion or kaon are sensitive probes of the Standard Model, as they can be described by either hadronic penguin or spectator $b \to u$ graphs. For example, as shown in Fig. 13, $B^+ \to \omega\pi^+$ can occur as the result of a spectator $b \to u$ decay while $B^+ \to \omega K^+$ can result from gluonic penguin decay. Theoretical predictions[21] for these decays range from 3×10^{-7} to 1.1×10^{-5}, while previous experimental upper limits are in the 10^{-4} range.[1]

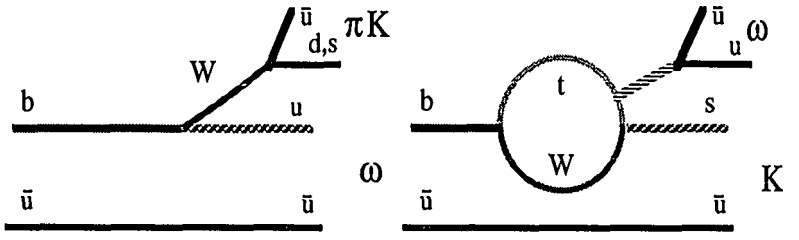


Figure 13: $B^- \to \omega h^-$ via spectator and penguin graphs.

The data used in this analysis consist of 3.1 fb^{-1} ($3.3 \times 10^6 B\bar{B}$ pairs) taken at the $\Upsilon(4S)$ and 1.6 fb^{-1} of data taken at energies slightly below the $\Upsilon(4S)$. As in many other CLEO analyses, continuum suppression is achieved by a combination of event shape cuts and use of a Fisher discriminant. Both the η's and ω's were reconstructed using the $\pi^+\pi^-\pi^0$ decay mode. Charged pion candidates were required to have drift chamber dE/dx within 3σ of their expected value. However, no particle identification cuts were applied to the h^+ in these decays. Candidates for $B^+ \to \omega h^+$ and $B^+ \to \eta h^+$ were formed by combining reconstructed η's and ω's with a charged track. Here the beam energy and known B mass was substituted for the measured quantities. The events passing all selection criteria are shown in Fig. 14. In these figures, the signal region is the area inside the box.

The results of this analysis are presented in Table 12. There are no $B \to \eta h^+$ candidates which lead to a 90% confidence level upper limit on the branching fraction of $< 3.0 \times 10^{-5}$. There are ten events in the signal region for $B \to \omega h^+$ with a predicted background of only two events. Assuming binomial statistics, the probability of the observed signal to be a background fluctuation is only 1.2×10^{-4}. This observed excess over the background corresponds to a branching fraction of $(2.8 \pm 1.0 \pm 0.5) \times 10^{-5}$, where the first error is due to statistics and the second is due to systematics. A more detailed analysis using particle identification to extract the individual branching fractions for $B^+ \to \omega K^+$ and $B^+ \to \omega\pi^+$ is currently in progress.

Table 12: Results for $B^+ \to \omega h^+$ and $B \to \eta h^+$.

Mode	Background	Eff. (%)	Events	Branching Ratio(10^{-5})
ωh^+	2.0±0.3	8.5±1.6	10	2.8±1.0 ± 0.5
ηh^+	0.7±0.2	2.8±0.5	0	<3.0 (90% CL)

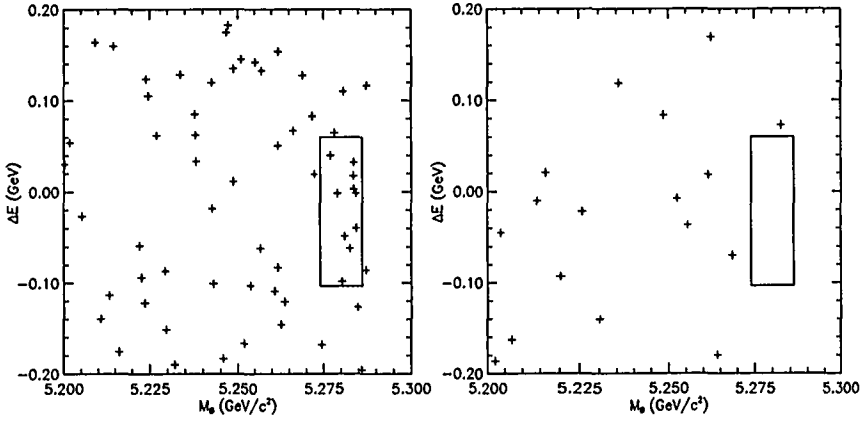


Figure 14: Candidate events for $B^+ \to \omega h^+$ (left) and $B^+ \to \eta h^+$ (right). The boxes indicate the signal regions.

2.6 Measurement of $|V_{ub}|$ Using Exclusive B-Meson Decays

In order to determine the origin of CP violation, it is important to measure as precisely as possible the elements of the CKM matrix. The matrix element $|V_{ub}|$ plays an important role in the search for CP violation in the b-quark sector. That $|V_{ub}|$ is not zero was demonstrated first by CLEO[22] and shortly thereafter by ARGUS.[23] Both experiments found evidence for $b \to u$ transitions by studying the lepton momentum spectrum above the $b \to c$ kinematic endpoint. While this method is fine for demonstrating a nonzero value for $|V_{ub}|$, theoretical uncertainties in the lepton momentum spectrum prevent a precise determination of $|V_{ub}|$ with this technique. CLEO has recently side-stepped this problem by explicitly reconstructing several semileptonic $b \to u$ decay modes including $B \to \pi l\nu$, $B \to \rho l\nu$, and $B \to \omega l\nu$.

The data used in this analysis consist of 2.66 fb^{-1} (2.84 $\times$ $10^6 B\bar{B}$ pairs) taken at the Υ(4S). The hermiticity of CLEO is exploited to select Υ(4S) decays where only a single neutrino goes undetected. Here the neutrino energy and momentum is given by $E_\nu = 2E_{beam} - \sum E_i$ and $\vec{p}_\nu = -\sum \vec{p}_i$ respectively. B-mesons decaying via the modes listed above should also satisfy the following constraints, $\Delta E \equiv (E_\nu + E_l + E_m) - E_{beam} = 0$ and $M_{ml\nu} = [E^2_{beam} - (\vec{p}_\nu + \vec{p}_l + \vec{p}_m)^2]^{1/2} = M_B$ where $m = \pi, \rho, \omega$. From Monte Carlo studies (Fig. 15), the resolution in $\vec{p}_\nu$ is determined to be 110 MeV/c.

Electrons are identified by combining drift chamber dE/dx, time of flight, and calorimeter information. Muons are identified by their ability to penetrate the magnet iron. Pairs of photons which have invariant masses within $\pm 2\sigma$ of the π^0 mass are kept for further study and are used in decay modes with ρ's and ω's in the final state.

Care must be taken to reduce background without losing too much of the signal. A ten-fold reduction in continuum related backgrounds is achieved using the thrust axis of the ml pair. Additional background reduction is achieved by using only high momentum leptons ($p_l > 1.5$ GeV for π modes and $p_l > 2$ GeV for ρ, ω modes) to discriminate against $b \to c \to sl\nu$ decays and to some extent $b \to cl\nu$ decays. Finally, non-$B\bar{B}$ contributions were determined using data taken at energies below the Υ(4S).

In order to extract the decay rate for each mode, the data was binned into 11 regions in the $M_{ml\nu}$, ΔE ($5.1075 \leq M_{ml\nu} < 5.2875$ GeV, $|\Delta E| < 75$ MeV) plane. For the $\rho l\nu$ ($\omega l\nu$) modes, the yield was further subdivided into four (five) bins over the 2π (3π) mass range. For all decay modes, Monte Carlo simulations were used to provide signal, $b \to c$ backgrounds, cross feed, and feed down from higher mass $B \to ul\nu$ states. The isospin and quark symmetry relations $\Gamma(B^0 \to \pi^- l^+\nu) = 2\Gamma(B^+ \to \pi^0 l^+\nu)$ and $\Gamma(B^0 \to \rho^- l^+\nu) = 2\Gamma(B^+ \to \rho^0 l^+\nu) \approx 2\Gamma(B^+ \to \omega l^+\nu)$ are used to constrain the B^+ rates relative to B^0. Prior to fitting, the data was corrected for backgrounds due to residual continuum and sources of fake leptons. In Fig. 16, the data along with the various background estimates is shown separately for the $B \to \pi l\nu$ and $B \to (\rho, \omega) l\nu$ modes. Here the ISGWII[24] model is used for the normalization. A clear signal over the background is present

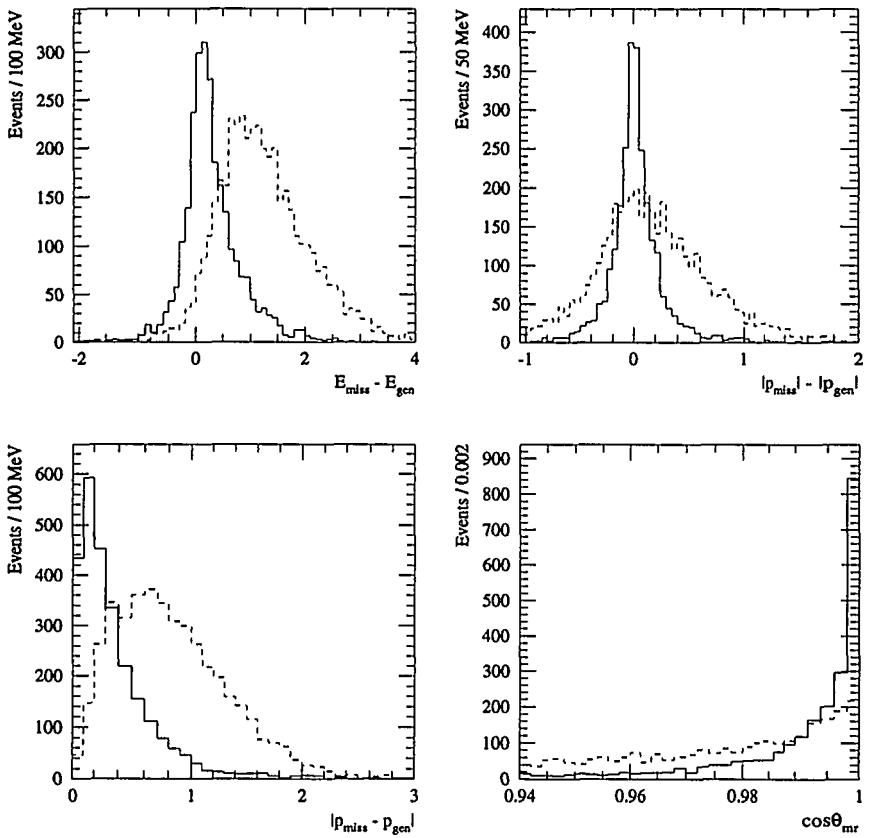


Figure 15: The resolution of neutrino energy, momentum, and angle from $B^0 \to \pi^- l^+ \nu$ Monte Carlo events. The solid histograms are distributions when no K_L^0 and/or extra neutrinos are present in the event. The dashed histograms had at least one K_L^0 and/or extra neutrinos in the event.

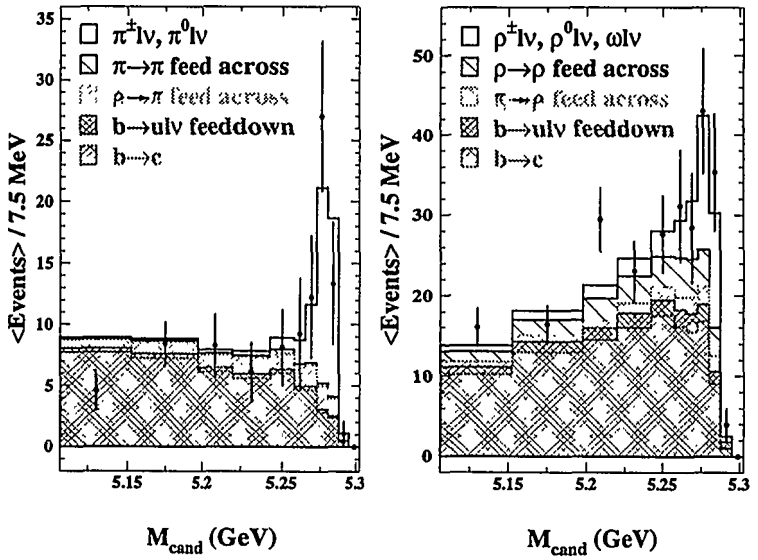


Figure 16: The M_{cand} mass distribution in the ΔE signal band for the combined π and vector meson modes. The data points have been corrected for continuum and background fakes. The ISGWII model is used for normalization.

in both plots. A summary of the data yields for the ISGWII fit is given in Table 13. There are many models of semileptonic $b \to u$ decay.[24-28] For each of these models, a simultaneous fit for the number of $B \to \pi l\nu$ events (N_π) and $B \to \rho l\nu$ events (N_ρ) is performed. In Fig. 17, the results of such fits are shown. The KS[26] model gives a poor fit to the data (confidence level $< 0.5\%$) while the other models give acceptable fits. Results from these fits are used to calculate the branching fractions shown in Fig. 18. Values for $|V_{ub}|$ are calculated for each model assuming $\tau_{B^0} = 1.56 \pm 0.05$ ps and $\tau_{B^0}/\tau_{B^+} = 1.02 \pm 0.04$. Averaging over the models, a value of $|V_{ub}| = (3.3 \pm 0.2^{+0.3}_{-0.4} \pm 0.7) \times 10^{-3}$ is obtained where the uncertainties are statistical, systematic, and model dependent. This value of $|V_{ub}|$ is in good agreement with the previous results using the endpoint of the lepton spectrum (see Fig. 19).

Table 13: Summary of event yields using the ISGWII model.

Yield	$\pi^\pm$	π^0	$\rho^\pm$	ρ^0	ω
Raw	46	19	47	73	7
Corrected	26.6	8.6	19.5	15.1	3.5
Eff.$\times 10^{-2}$	2.3	1.5	1.5	2.4	0.6

3 τ Lepton Physics

The CLEO detector is also well-suited for the study of τ decay. Its fine grained electromagnetic calorimeter reconstructs π^0's and η's with high efficiency and low background. This combined with excellent charged particle tracking and particle identification (e, μ, π, K^+, K^0, p) over a large momentum range allows for many detailed studies of τ final states.

At the center-of-mass energies available to CLEO, τ leptons are produced through the reaction $e^+e^- \to \tau^+\tau^-$. The cross section for this reaction is "large," approximately 1 *nb*. To date, CLEO has accumulated $\approx 10^7$ τ decays, by far the world's largest data sample. If we neglect initial and final state radiation, then each τ is produced with energy equal to the beam energy. Thus, like the situation with B-mesons, the τ's energy and momentum is *a priori* accurately known.

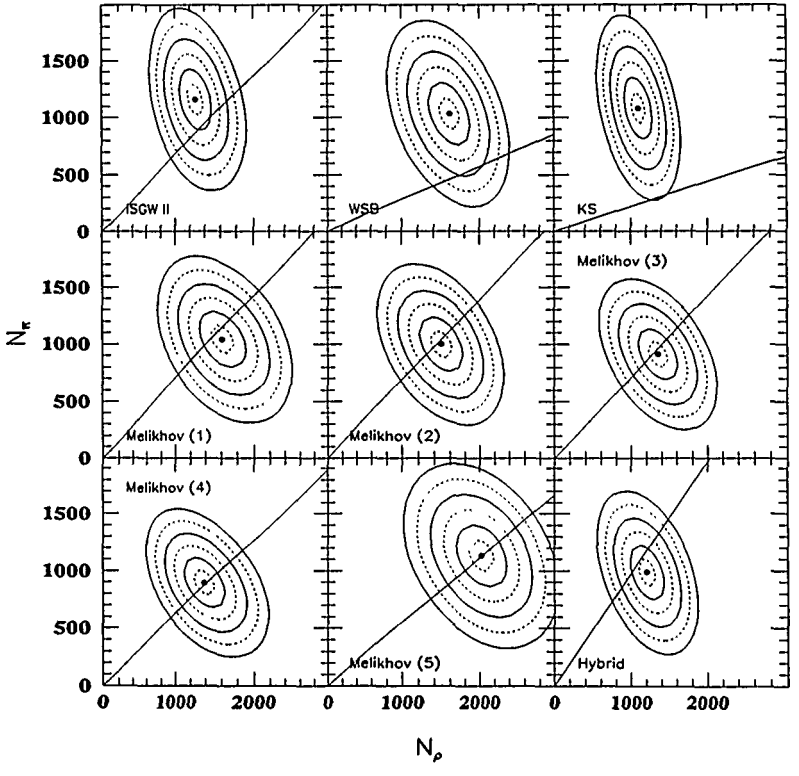


Figure 17: The half sigma contours in the fit parameters N_π vs N_ρ for the various models. The lines are the ρ/π rates predicted by each model.

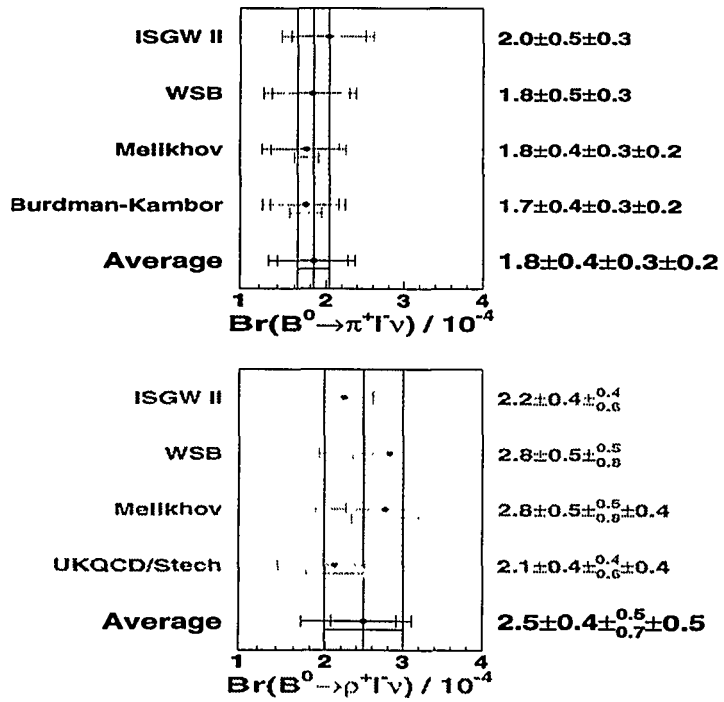


Figure 18: The results for the branching ratios for several models. The central vertical line is the average of the models.

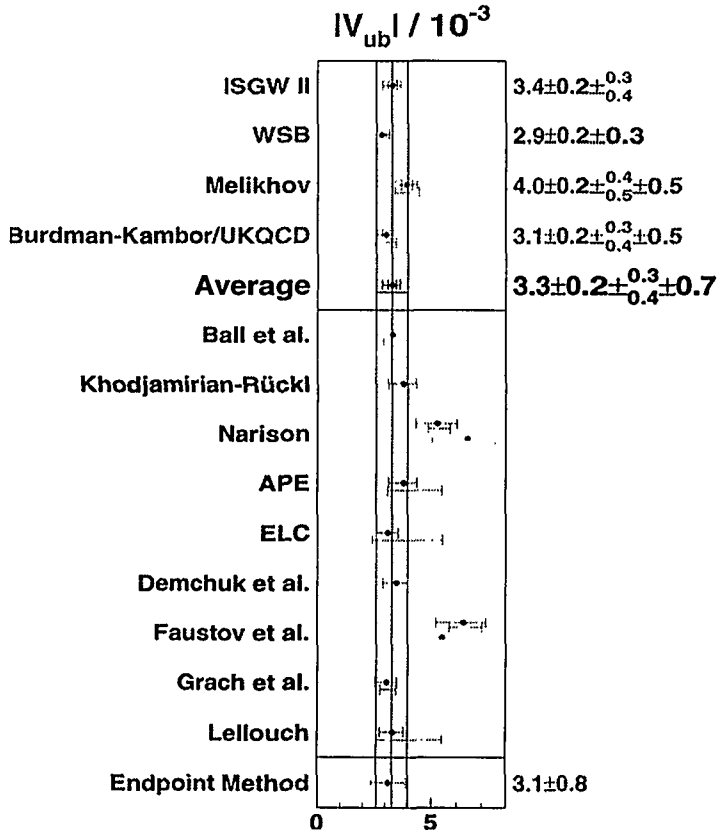


Figure 19: The values of $|V_{ub}|$ from several models of $B \to \pi l\nu$ and $B \to \rho l\nu$ decay. Also included is the value of $|V_{ub}|$ from the lepton endpoint technique. The vertical line is the average of the top four models.

Even at CLEO's center-of-mass energy, the τ event topology is jet-like. In addition, a τ event has four or fewer charged tracks $\approx 98\%$ of the time. These two characteristics make it easy to separate $\tau^+\tau^-$ events from $B\bar{B}$ events. A more serious background comes from low multiplicity hadronic events produced via $e^+e^- \to q\bar{q}$ (continuum events). However, with a judicious choice of total energy and momentum cuts and particle identification, even the continuum hadronic background can be kept below 1%. The CLEO experiment is therefore in the enviable position of having a high statistics, low background sample of τ's to work with. This has allowed CLEO to become the first experiment to perform detailed studies of τ decays with branching fractions in the $10^{-4} - 10^{-5}$ range and search for decay modes with branching fractions $\mathcal{O}(10^{-6})$.

3.1 τ Decays with an η in the Final State

Decays of the τ with an η in the final state are of interest as they provide both valuable information concerning the behavior and violation of several hadronic symmetries, and a new system for the study of the weak hadronic current. There is very little information available on these final states due to their small branching fractions. In fact, the Particle Data Group[1] only lists exclusive branching fractions for $\mathcal{B}(\tau^- \to \eta\pi^-\pi^0\nu)$ ($(0.17\pm0.02\pm0.02)\%$ [Ref. 29]) and $\mathcal{B}(\tau \to \eta K^-\nu)$ ($(0.026\pm0.002\pm0.002)\%$ [Ref. 30]). Other $\tau \to \eta$ modes are expected to be severely suppressed by the chiral anomaly term and phase space.

The CLEO experiment has recently measured the branching fraction of the decay $\tau^- \to \eta h^- h^+ h^- \nu$ at a rate two orders of magnitude larger than predicted.[31] The analysis uses $4.86 fb^{-1}$ (4.27×10^6 τ pairs) of data collected at energies at and slightly below the $\Upsilon(4S)$. Events that are consistent with the one-versus-three topology are searched for η's decaying via $\eta \to \gamma\gamma$ and $\eta \to 3\pi^0$. In Fig. 20, there are clear η signals in both decay modes.

Care must be taken to ensure that these events with η's are from τ's and not hadronic in origin. Therefore, the η signal is studied as a function of the one-prong tag as shown in Table 14. Backgrounds from τ events feeding into this decay mode are estimated using Monte Carlo simulations based on the KORALB[32] and TAUOLA[33] computer routines. The CLEO experiment is modeled using the GEANT[7] package. The contribution to the sample from hadronic and two-photon events is estimated using data rather than Monte Carlo. As listed in Table 14,

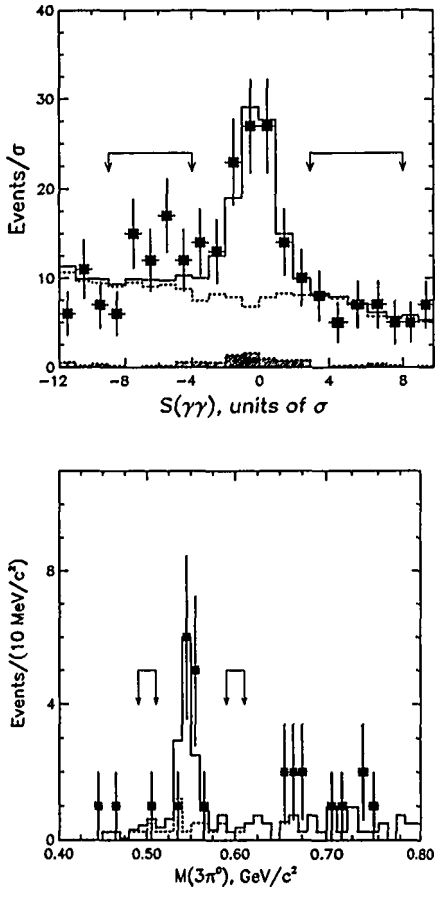


Figure 20: The η signals in the $\eta \to \gamma\gamma$ (top) and $\eta \to 3\pi^0$ (bottom) modes. For both plots, the solid line is a fit including signal and random photon background (dashed line). The arrows indicate the range used for sideband subtraction. The contamination from $e^+e^- \to q\bar{q}$ events is given by the hatched area.

Table 14: CLEO results for $\tau^- \to h^-h^+h^-\eta\nu$.

Mode	Tags	Events	Backgd.	BR$\times 10^{-4}$
$\eta \to \gamma\gamma$	$e, \mu, h/\rho$	65.1±12.9	5.0±1.1	3.8±0.8
$\eta \to 3\pi^0$	e, μ	11.2±3.7	-	5.1±1.7

there is small contamination in the $\eta \to \gamma\gamma$ sample (from hadronic events) and negligible background in the $3\pi^0$ sample. The detection efficiencies are calculated separately for each one-prong tag and η branching mode. The branching fractions for the two η decay modes are listed in Table 14. Since these results are statistically independent, we can average them and find:

$$\mathcal{B}(\tau^- \to \eta h^-h^+h^-\nu) = (4.1 \pm 0.7 \pm 0.7) \times 10^{-4}\,.$$

The second error above is the systematic uncertainty in the branching fraction. It includes contributions from background modeling, π^0 and η reconstruction, spectral functions, tracking, luminosity, and cross sections. It is interesting to note that this measurement is $\approx 100\times$ larger than the prediction from Pich![31]

An effort is underway to look for resonant substructure in these $\tau^- \to \eta h^-h^+h^-\nu$ events. In Fig. 21 (top), the $\eta\pi^+\pi^-$ mass is plotted (two entries per event) for the $\eta \to \gamma\gamma$ events. There is an enhancement at the mass of the $f_1(1285)$. In the lower part of Fig. 21 (top), a scatterplot of $m_{\eta\pi^+\pi^-}$ versus $m_{\eta\pi^\pm}$ is presented (four entries per event). This plot suggests that the η is produced through an intermediate state, $a_0(980)$, and the overall decay chain is: $\tau^- \to f_1(1285)\pi^-\nu$, $f_1(1285) \to a_0^+(980)\pi^-$, $a_0^+(980) \to \eta\pi^+$. A fit to the data yields 30.4±8.8 events. To convert these events into a branching fraction, we use $\mathcal{B}(f_1(1285) \to \eta\pi\pi) = 0.54 \pm 0.15$ (Ref. 1), and the isospin prediction that $\eta\pi^+\pi^-$ is 2/3 of the $\eta\pi\pi$ state. We find:

$$\mathcal{B}(\tau^- \to f_1(1285)\pi^-\nu) = (6.0 \pm 1.7 \pm 2.1) \times 10^{-4}.$$

The second error quoted above is the systematic, and it has components similar to the $\eta 3\pi$ analysis.

The decay $\tau^- \to f_1(1285)\pi^-\nu$ can also be present in one-prong τ decays through $\tau \to \eta\pi^-\pi^0\pi^0\nu$. A sample of events consistent with this topology was isolated using similar π^0 and η criteria as in the three-prong case. In Fig. 21 (top, right), the invariant mass of the $\eta\pi^0\pi^0$ system is plotted (one entry per event).

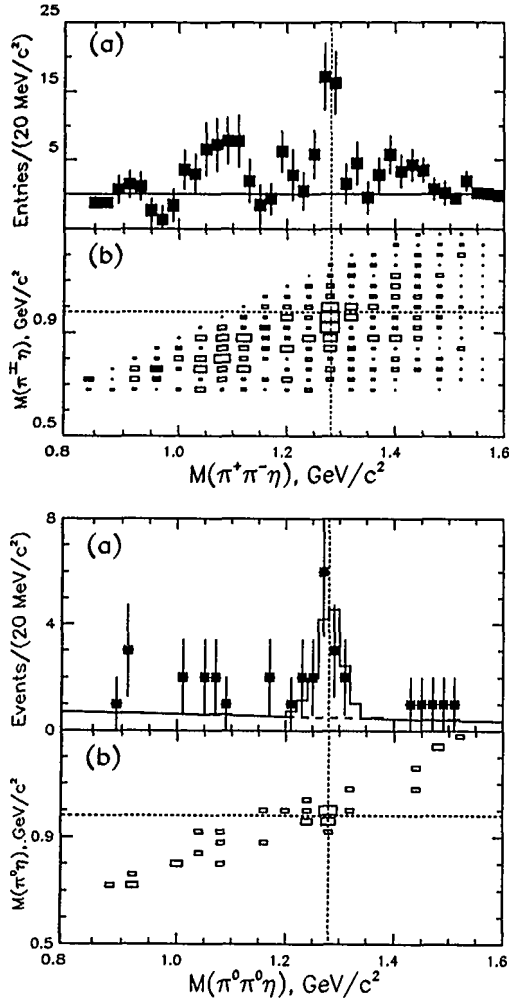


Figure 21: Mass of $\eta\pi^+\pi^-$ (a, top) and $\eta\pi^0\pi^0$ (a, bottom) system. Lower plots (b) are $M_{\eta\pi\pi}$ vs $M_{\eta\pi}$. The dotted lines show the expected positions of the $f_1(1285)$ and $a_o(980)$ resonances.

There is a clear enhancement at the $f_1(1285)$ mass. The scatterplot (Fig. 21, bottom, right), of $m_{\eta\pi^0}$ versus $m_{\eta\pi^0\pi^0}$ also resembles the three-prong case, as there appears to be an enhancement at the $a_0(980)$ mass. The branching fraction extracted from this analysis is:

$$\mathcal{B}(\tau^- \to f_1(1285)\pi^-\nu) = (8.1 \pm 2.6 \pm 2.6) \times 10^{-4}.$$

This result is in good agreement with and independent of the three-prong result. The two results can be combined to give:

$$\mathcal{B}(\tau^- \to f_1(1285)\pi^-\nu) = (6.7 \pm 1.4 \pm 2.2) \times 10^{-4}.$$

Using this result, we find that a large component of $\tau^- \to \eta h^- h^+ h^- \nu$ contains an $f_1(1285)$, i.e.,

$$\frac{\mathcal{B}(\tau^- \to f_1(1285)\pi^-\nu)}{\mathcal{B}(\tau^- \to \eta h^- h^+ h^-\nu)} = 0.59 \pm 0.17.$$

These results have implications for CVC predictions for $\tau \to 6\pi\nu$ using $e^+e^- \to 6\pi$ data. The above results imply that $\tau \to 3\pi^\pm 3\pi^0\nu$ and $\tau \to 5\pi^\pm\pi^0\nu$ have significant contributions from the $\tau \to \eta 3\pi\nu$ mode. Since this mode has G parity opposite to that of direct 6π decays and proceeds through the axial-vector current, it must be subtracted before applying isospin or CVC to compare with e^+e^- annihilation data.

3.2 Measurement of the Michel Parameters in Leptonic τ Decay

The leptonic decays of the τ, $\tau^- \to e^-\nu_\tau\bar{\nu}_e$, and $\tau^- \to \mu^-\nu_\tau\bar{\nu}_\mu$ can provide detailed information on the $\tau W\nu_\tau$ vertex. Since these decays are not clouded by the strong interaction, they are ideal laboratories to explore the Lorentz structure of the $\tau W\nu_\tau$ current. Neglecting radiative corrections, the distribution of the scaled energy ($x = E_l/E_{max}$) of the charged lepton in the τ rest frame can be written as:

$$\frac{1}{\Gamma}\frac{d\Gamma}{dx} = x^2 \frac{12(1-x) + \frac{4\rho}{3}(8x-6) + 24\eta m\frac{(1-x)}{x}}{1+4\eta m}.$$

In the above equation, ρ and η are the spectral shape Michel Parameters[34] and m is the scaled lepton mass $m = m_l/m_\tau$. In the Standard Model, $\rho = 3/4$ and $\eta = 0$. At CLEO center-of-mass energies, τ pairs are produced with no net polarization, hence the scaled energy spectrum is insensitive to the two other Michel Parameters, ξ and δ. It is important to measure ρ and η as accurately as possible, since nonstandard electroweak models predict values other than $\rho = 3/4$, $\eta = 0$. For example, $\eta \neq 0$ suggests the presence of a scalar boson that couples a right-handed τ to a left-handed l. Another example is the Two Higgs Doublet Model[35] with a charged Higgs. Here η_μ (measured using $\tau \to \mu\nu\bar{\nu}$) is related to the ratio of vacuum expectation values of the neutral components of the Higgs doublet (β) and the mass of the Higgs (m_H) by

$$\eta_\nu = -(m_\tau m_\mu tan^2\beta)/2m_H^2.$$

The sample of τ's used in this analysis were taken from 3.5 fb^{-1} (3.2×10^6 τ pairs) of data collected at $E_{cm} \approx 10.6$ GeV. The decay mode $\tau^- \to h^-\pi^0\nu$ ($h^- = \pi^-$, K^-) was used as a tag in order to obtain a clean, high statistics sample of τ events.

Pairs of photons with polar angles (θ) satisfying $|cos\theta| < 0.71$ are used to form π^0's if their invariant mass is within 3σ of the nominal π^0 mass. Electrons with momentum above 0.5 GeV/c are identified using a combination of dE/dx and tracking information from the drift chamber and energy measurements from the calorimeter. The background in this electron sample is estimated to be $(0.178 \pm 0.026)\%$. Muons with momentum above 1.5 GeV/c are identified as charged particles which are tracked through the inner and outer detector and pass through at least three absorption lengths of material. The background in this muon sample is estimated as $(1.08 \pm 0.16)\%$. Muons with momentum 0.5–1.5 GeV/c are identified by kinematically eliminating all other τ decay hypotheses ($\pi\nu$, $K\nu$, $e\nu\bar{\nu}$, $h\pi^0\nu$). This muon sample contains a small amount of background from π/K, $h\pi^0\nu$, and $e\nu\bar{\nu}$ events ($\approx 4\%$ total).

The τ rest frame is the ideal Lorentz frame for simultaneously measuring ρ and η. CLEO, however, measures the momentum of the electrons and muons in the LAB frame. Unfortunately, there is no unambiguous way to transform from the LAB frame to the τ rest frame due to the unmeasured neutrinos in the event. This lack of information can in part be compensated for using information from the "tag" τ. In the absence of initial or final state radiation, the two τ's in an event are produced back-to-back, each with the energy of the beam. In a $\tau^- \to h^-\pi^0\nu$ decay, the angle (α) between the hadronic system ($H \equiv h\pi^0$) and

the τ can be calculated using:

$$m_\tau^2 + m_H^2 - 2E_\tau E_H + 2p_\tau p_H cos\alpha = m_\nu^2.$$

In the above equation, E_H, p_H, and m_H are calculated quantities while we assume $m_\nu = 0$ and $E_\tau = E_{beam}$. As $cos\alpha \to 1$, the ambiguity in ϕ disappears and the momentum vector of the $h\pi^0$ system gives a good estimate of the $\tau \to l\nu\bar{\nu}$ direction. Thus, events with $cos\alpha > 0.970$ are used to transform the lepton momentum spectra to a pseudo rest frame (PRF). After the $cos\alpha$ cut, there are 18587 electrons and 12580 (2931) high momentum (low, $p < 1.5$ GeV/c) muons left in the sample. The x spectrum for electrons and muons passing all cuts is shown in Fig. 22. In order to extract η and ρ values from the data, a χ^2 fit is performed using three binned Monte Carlo x spectrums. The three individual x spectrums are generated with (ρ, η) values: (3/4,0), (0,0), and (3/4,1). The data spectrum is then represented by:

$$N\frac{dN}{dx}(\rho,\eta) = N_{3/4,0}\epsilon_{V-A}\frac{dN}{dx}(3/4,0) + N_{0,0}\epsilon_{V+A}\frac{dN}{dx}(0,0) + N_{3/4,1}\epsilon_{\eta=1}\frac{dN}{dx}(3/4,1)$$

with:

$$N = N_{(3/4,0)} + N_{(0,0)} + N_{(3/4,1)} = \frac{4\rho/3-\eta}{1+4\eta m} + \frac{1-4\rho/3}{1+4\eta m} + \frac{\eta(1+4m)}{1+4\eta m}.$$

The ϵ's are efficiency corrections for each Monte Carlo x spectrum. The τ Monte Carlo spectrums are generated using the simulation packages KORALB,[32] TAUOLA,[33] and PHOTOS.[36] The CLEO II detector is simulated using GEANT.[7] All effects due to radiation, resolution, and efficiency are included in these spectra. The events which passed the $cos\alpha$ cut are analyzed in the PRF frame. An additional 12981 (9186) electron (muon) events which do not satisfy the $cos\alpha$ cut are analyzed in the LAB frame.

The results from fitting the spectra are given in Table 15. A detailed study of systematic errors leads to the uncertainties quoted in this table. Using lepton universality, a simultaneous fit to the electron and muon data is performed resulting in the values of $\rho^\tau_{e\mu}$ and $\eta^\tau_{e\mu}$ given in Table 15. In Fig. 23, the results from the individual and combined modes are displayed as well as the prediction from the Standard Model. All measurements are consistent with a $V-A$ Lorentz structure for the current in τ decay. In Fig. 24, the CLEO results along with other measurements of ρ and η are presented. The CLEO results are consistent with, but more

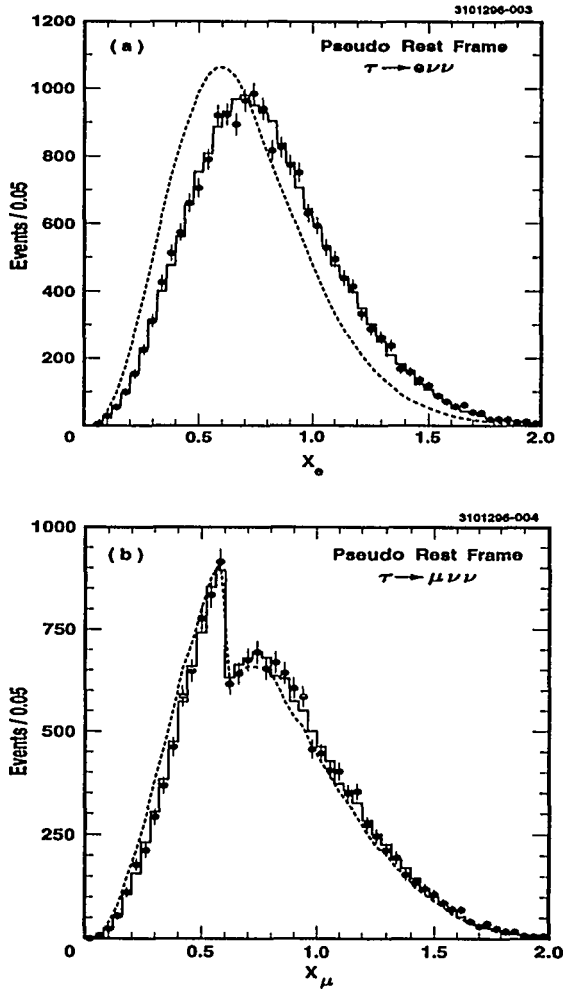


Figure 22: Scaled energy spectrum (x) for electrons (a) and muons (b) in the pseudo rest frame of the τ. The dotted line in (a) is a $V+A$ Monte Carlo calculation, while the dotted line in (b) is a Monte Carlo calculation of the muon spectrum assuming $\eta = 1$. Events with $x > 1$ are the result of imperfect reconstruction of the τ direction. The discontinuity in (b) at $x = 0.6$ is due to low momentum muons.

Table 15: CLEO results along with the corresponding previous world average results.

Parameter	CLEO II	World Average
ρ_e^τ	0.732±0.014 ± 0.009	0.736±0.028
ρ_μ^τ	0.747±0.048 ± 0.044	0.74±0.04
η_μ^τ	0.010±0.149 ± 0.171	-0.24±0.29
$\rho_{e\mu}^\tau$	0.735±0.013 ± 0.008	0.742±0.027
$\eta_{e\mu}^\tau$	-0.015±0.061 ± 0.062	-0.01±0.14

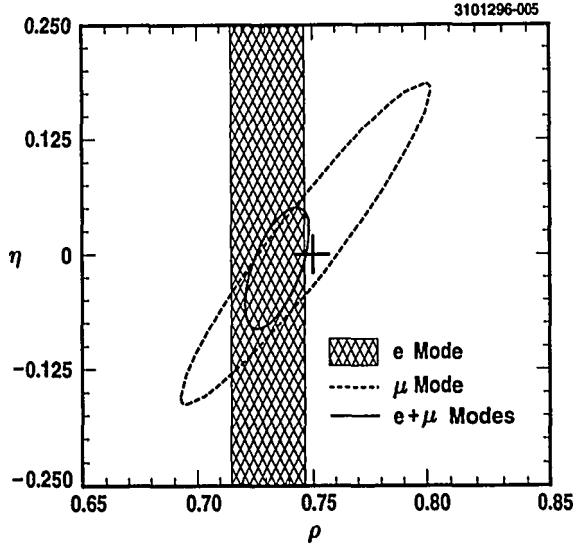


Figure 23: ρ vs η for electron, muon, and combined modes. The Standard Model prediction is given by the cross.

Table 15: CLEO results along with the corresponding previous world average results.

Parameter	CLEO II	World Average
ρ_e^τ	0.732±0.014 ± 0.009	0.736±0.028
ρ_μ^τ	0.747±0.048 ± 0.044	0.74±0.04
η_μ^τ	0.010±0.149 ± 0.171	-0.24±0.29
$\rho_{e\mu}^\tau$	0.735±0.013 ± 0.008	0.742±0.027
$\eta_{e\mu}^\tau$	-0.015±0.061 ± 0.062	-0.01±0.14

precise than, previous measurements. Finally, the measurement of η leads to the model-dependent limit on the charged Higgs mass of $M_{H^\pm} > (0.97 \times tan\beta)$ GeV at the 90% confidence level.

3.3 Search for $\tau \to e^-\gamma$ and $\tau \to \mu^-\gamma$

The Standard Model does not contain a symmetry associated with lepton number. Therefore, one expects that lepton number violating decays should be present in nature. Clearly, the rate of these decays is small, as shown by the experimental upper limits[1] for lepton number violation in muon decay ($\mathcal{B}(\mu \to e\gamma) < 4.9 \times 10^{-11}$, $\mathcal{B}(\mu \to eee) < 1 \times 10^{-12}$). Although it is not possible to collect τ data samples comparable to those used to obtain the limits from muon decay, there are reasons to use τ's as a probe of lepton number violation. For example, there are models which relate lepton number violation to mass-dependent couplings. One such model[37] favors τ decay and predicts an enhancement of $\mathcal{B}(\tau \to \mu\gamma) = 2 \times 10^5 \mathcal{B}(\mu \to e\gamma)$.

Lepton number violation in τ decay has been studied extensively for close to two decades now. The 1996 version of the *Review of Particle Properties*[1] gives limits on 37 different lepton number violating τ decay modes. The most stringent limit in the list is a result from CLEO,[38] $\mathcal{B}(\tau \to \mu\gamma) < 4.2 \times 10^{-6}$. Here we update this CLEO result and present a new upper limit for $\mathcal{B}(\tau \to e\gamma)$.

The data in this analysis consists of 4.68 fb^{-1} ($\approx 4.24 \times 10^6 \tau^+\tau^-$ pairs) of data taken at energies at and slightly below the mass of the $\Upsilon(4S)$. Events that are consistent with the one-versus-one topology (i.e., oppositely charged tracks in different hemispheres) are kept for further consideration. Requirements on the

tag hemisphere are minimal and all standard one-prong τ decays are used. Event selection criteria were developed from a study of Monte Carlo events incorporating both KORALB[32] and GEANT.[7]

This analysis relies heavily on lepton (electron and muon) identification both for isolating a signal and rejecting background. The standard CLEO lepton identification software package is used here. Electrons are identified with a combination of calorimeter, drift chamber tracking and dE/dx, and time-of-flight information. Identified muons are charged tracks that are tracked from the inner drift chambers all the way through the magnet iron. Since radiative Bhabhas and μ-pairs are backgrounds to this analysis, events can have only one identified electron or one identified muon.

Additional background suppression is achieved by examining both the missing momentum and transverse momentum in the event. Since there must be at least one undetected neutrino on the tag side of the event, the missing momentum in a τ event should lie in the tag hemisphere. However, the missing momentum in QED background processes will be randomly oriented with respect to the "tag" track. Thus, only events where the cosine of the angle between the tag track's momentum vector and the missing momentum vector is greater than 0.4 are kept for further study. A cut on transverse momentum ($p_{trans} > 0.3$ GeV/c) is made to eliminate backgrounds from the two-photon process.

The events that pass all selection criteria are shown in Fig. 25. The signature for $\tau \to e\gamma$ or $\tau \to \mu\gamma$ is an $l\gamma$ combination with measured energy and invariant mass consistent with the beam energy and τ mass respectively. For convenience, the variables $\Delta E = E_{l\gamma} - E_{beam}$ and $m_{l\gamma} - m_\tau$ are used in this analysis. The central box in both plots of Fig. 25 shows the signal region in the $(\Delta E, m_{l\gamma})$ plane. The boundaries of the signal region were determined using a Monte Carlo simulation (two body phase space) of the decays $\tau \to e\gamma$, $\tau \to \mu\gamma$ (open circles in Fig. 25). There are no candidate events for the $e\gamma$ channel and three candidates for the $\mu\gamma$ channel. From a study of the sideband regions in Fig. 25, two (5.5) background events are predicted for the $e\gamma$ ($\mu\gamma$) channel. A Monte Carlo study suggests that the $\mu\gamma$ background events originate from generic τ decays. The results of the analysis are summarized in Table 16. The upper limits presented here include systematic uncertainties calculated according to the prescription of Cousins and Highland.[39] Thus, the strictest limit on lepton number violation in τ decay now belongs to the $e\gamma$ mode.

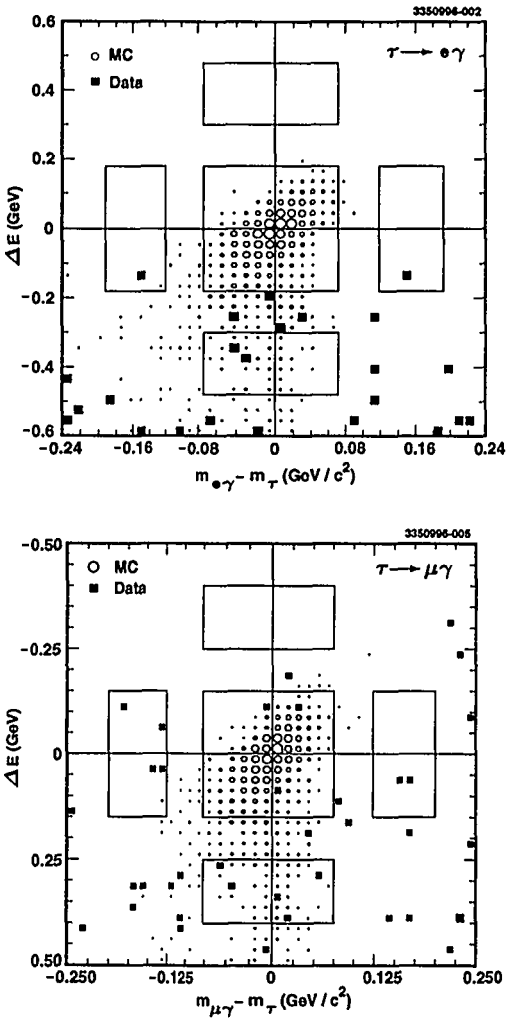


Figure 25: The ΔE vs $m_{l\gamma} - m_\tau$ distributions for $\tau \to e\gamma$ and $\tau \to \mu\gamma$. The solid squares are the data while the open circles are the Monte Carlo signal events.

Table 16: Efficiencies, observed events (n_0), background events (μ_B), calculated number of events including systematic error for 90% confidence level upper limits (λ), and the 90% confidence level upper limits for $\tau \to e\gamma$ and $\tau \to \mu\gamma$.

Channel	MC Efficiency	n_0	μ_B	λ	Upper Limit at 90% CL
$\tau \to e\gamma$	10.1	0	2.0	2.3	2.7×10^{-6}
$\tau \to \mu\gamma$	14.4	3	5.5	3.7	3.0×10^{-6}

4 Future Plans, CLEO III

The CLEO experiment is currently taking data at the $\Upsilon(4S)$ with a recently (summer 1995) installed three-layer silicon vertex detector. Data taking with this detector configuration is expected to continue until early 1998 when the experiment and CESR will shut down for major renovation. Installed in place of the present detector will be CLEO III (Fig. 26). This detector features a new silicon vertex detector (four layers), a new main drift chamber, and a ring imaging Cherenkov detector (RICH). The present calorimeter, magnet, and muon detector are also used in this version of CLEO. The main advantage of CLEO III over CLEO II is in the area of particle identification. The RICH detector should be able to provide $\geq 3\sigma$ π/K separation over the entire momentum region of interest for B-meson decay. Upgrades to CESR should put the instantaneous luminosity in excess of 10^{33} cm^{-2} s^{-1}. This combination of detector and accelerator will increase the physics reach of CLEO by over an order of magnitude in the areas of b, c, and τ physics. In fact, it may even allow for the first observation of CP violation in the b-quark sector.

5 Acknowledgments

It is a pleasure to acknowledge the efforts of my colleagues in the CLEO Collaboration and the staff of CESR. A special word of thanks to the many people who made the SLAC Summer Institute a most enjoyable experience.

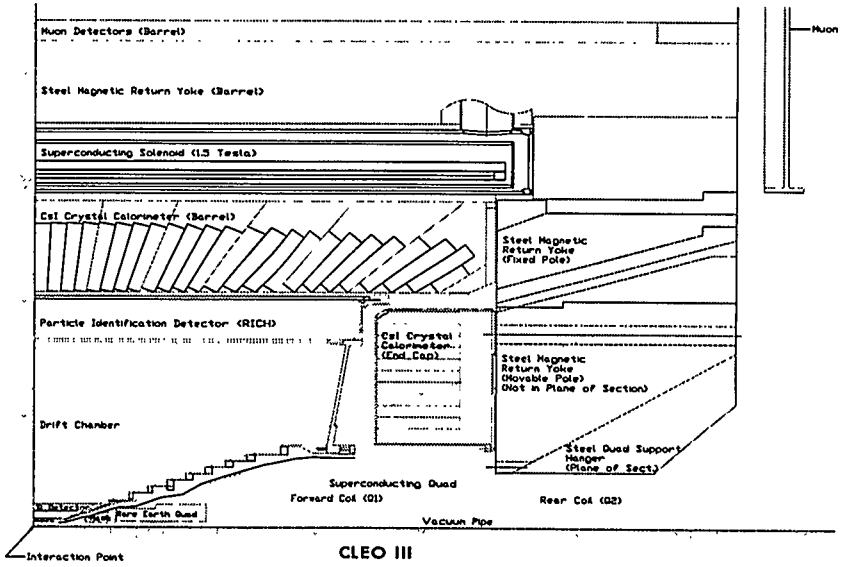


Figure 26: Quarter section of the CLEO III detector.

References

[1] Particle Data Group, R. Barnett *et al.*, Phys. Rev. D **54**, 1 (1996).

[2] Y. Kubota *et al.*, Nucl. Instrum. Meth. **320**, 66 (1992).

[3] R. Aleksan *et al.*, Phys. Lett. B **317**, 173 (1993); The *BaBar* Collaboration, TDR, SLAC-R-95-457 (1995); K. Lingel *et al.*, "Physics Rationale for a B Factory," CLNS-91-1043 (1991).

[4] D. Gibaut *et al.*, Phys. Rev. D **53**, 4734 (1996).

[5] G. Eilam *et al.*, Phys. Rev. Lett. **74**, 4984 (1995).

[6] N. G. Deshpande *et al.*, Phys. Rev. D **52**, 5354 (1995).

[7] R. Brun *et al.*, CERN dd/ee/84-1.

[8] ALEPH Collaboration, in *Proceedings of the International Conference on High Energy Physics*, Warsaw, 1996 (Report No. PA-05-057).

[9] P. Avery *et al.*, Phys. Lett. B **223**, 470 (1989).

[10] DELPHI Collaboration, W. Adam *et al.* (to be published).

[11] R. Ammar *et al.*, Phys. Rev. Lett. **71**, 674 (1993).

[12] T. Altomari, Phys. Rev. D **37**, 677 (1988); N. G. Deshpande *et al.*, Z. Phys. C **40**, 369 (1988); C. A. Dominguez *et al.*, Phys. Lett. B **214**, 459 (1988); N. G. Deshpande and J. Trampetic, Ann. N. Y. Acad. Sci., **578**, 424 (1989); T. M. Aliev *et al.*, Phys. Lett. B **237**, 569 (1990); A. Ali and T. Mannel, Phys. Lett. B **264**, 447 (1991); R. N. Faustov and V. O. Galkin, Mod. Phys. Lett. A **7**, 2111 (1992); A. Ali, T. Ohl, and T. Mannel, Phys. Lett. B **298**, 195 (1993); El hassan, El aaoud, and Riazuddin, Phys. Rev. D **47**, 1026 (1993); P. Colangelo *et al.*, Phys. Lett. B **317**, 183 (1993); P. J. O'Donnell and H. K. K. Tung, Phys. Rev. D **48**, 2145 (1993); A. Ali and C. Greub, Z. Phys. C **60**, 433 (1993); P. Ball, TUM-T31-43/93; A. Ali, V. M. Braun, and H. Simma, Z. Phys. C **63**, 437 (1994); C. Bernard, P. Hsieh, and A. Soni, Phys. Rev. Lett. **72**, 1402 (1994); B. Holdom and M. Sutherland, Phys. Rev. D **49**, 2356 (1994); S. Narison, Phys. Lett. B **327**, 354 (1994); K. C. Bowler *et al.*, Edinburgh-94-544 (1994); M. Ciuchini *et al.*, Phys. Rev. D **51**, 137 (1994); J. Tang *et al.*, Phys. Rev. D **51**, 3501 (1995).

[13] M. S. Alam, *et al.*, Phys. Rev. Lett. **74**, 2885 (1995).

[14] J. M. Soares, Phys. Rev. D **49**, 283 (1994).

[15] C. Greub, H. Simma, and D. Wyler, Nucl. Phys. B **434**, 39 (1995).

[16] A. Ali, V. M. Braun, and H. Simma, Z. Phys. C **63**, 437 (1994).

[17] S. Narison, Phys. Lett. B **327**, 354 (1994).

[18] D. Buskulic *et al.*, Phys. Lett. B **356**, 409 (1995).

[19] R. Grigjanis, P. J. O'Donnell, M. Sutherland, and H. Navelet, Phys. Lett. B **224**, 209 (1989).

[20] N. G. Deshpande, X.-G. He, and J. Trampetic, Phys. Lett. B **377**, 161 (1996).

[21] L.-L. Chau *et al.*, Phys. Rev. D **43**, 2176 (1991); A. Deandrea *et al.*, Phys. Lett. B **318**, 549 (1993); A. Deandrea *et al.*, Phys. Lett. B **320**, 170 (1994); D. Du and L. Guo, BIHEP-TH-95-28.

[22] R. Fulton *et al.*, Phys. Rev. Lett. **64**, 16 (1990); J. Bartelt *et al.*, Phys. Rev. Lett. **71**, 4111 (1993).

[23] H. Albrecht *et al.*, Phys. Lett. B **234**, 409 (1990); **255**, 297 (1991).

[24] N. Isgur and D. Scora, Phys. Rev. D **52**, 2783 (1995).

[25] M. Wirbel, B. Stech, and M. Bauer, Z. Phys. C **29**, 637 (1985).

[26] J. G. Körner and G. A. Schuler, Z. Phys. C **38**, 511 (1988).

[27] D. Melikhov, Phys. Rev. D **53**, 2460 (1996).

[28] G. Burdman and J. Kambor, FNAL Report No. FERMILAB-Pub-96/033-T, 1996; J. M. Flynn *et al.*, Nucl. Phys. B **461**, 327 (1996); B. Stech, Phys. Lett. B **354**, 447 (1995).

[29] M. Artuso *et al.*, Phys. Rev. Lett. 69, 3278 (1992).

[30] J. Bartelt *et al.*, Phys. Rev. Lett. **76**, 4119 (1996).

[31] A. Pich, Phys. Lett. B **196**, 561 (1987).

[32] S. Jadach and Z. Was, Comp. Phys. Commun. **64**, 267 (1991); S. Jadach *et al.*, Comp. Phys. Commun. **76**, 361 (1993).

[33] S. Jadach, J. H. Kühn, and Z. Was, CERN-TH-5856/90 (1990).

[34] L. Michel, Proc. Phys. Soc. London A **63**, 514 (1950).

[35] A. Stahl, Phys. Lett. B **324**, 121 (1994).

[36] E. Barberio, B. van Eijk, and Z. Was, CERN-TH-5857/90 (1990).

[37] R. Arnowitt and P. Nath, Phys. Rev. Lett. **66**, 2708 (1991).

[38] J. Bartelt *et al.*, Phys. Rev. Lett. **73**, 1890 (1994).

[39] R. Cousins and V. Highland, Nucl. Instrum. Methods A **320**, 331 (1992).

HEAVY FLAVOR PHYSICS FROM TOP TO BOTTOM

Manfred Paulini
Lawrence Berkeley National Laboratory
MS 50B-5239, Berkeley, California 94720

(Representing the CDF and DØ Collaborations)

ABSTRACT

We review the status of heavy flavor physics at the Fermilab Tevatron collider by summarizing recent top quark and B-physics results from CDF and DØ. In particular, we discuss the measurement of the top quark mass and top production cross section as well as B-meson lifetimes and time-dependent $B\bar{B}$ mixing results. An outlook of perspectives for top and B physics in Run II starting in 1999 is also given.

© 1996 by Manfred Paulini.

1 Introduction

In this article, we review recent heavy flavor physics results from the Tevatron $p\bar{p}$ collider at Fermilab, where heavy flavor refers to the top quark as well as the bottom quark. After a brief historical overview, we summarize the status of top quark physics at CDF and DØ in Sec. 2. In particular, we discuss the measurement of the top production cross section and the top quark mass. Section 3 is devoted to recent B-physics results at a hadron collider, where we concentrate on B hadron lifetimes and latest time-dependent $B\bar{B}$ mixing results. A brief look to the future, summarizing the prospects for top quark physics as well as B physics and CP violation in Run II starting in 1999, is given in Sec. 4. We conclude with Sec. 5.

1.1 Historical Overview

In 1977, the bottom quark was discovered as a resonance in the dimuon mass spectrum in 400 GeV proton-nucleus collisions at Fermilab.[1] Soon after the discovery, the so-called Υ resonances at a mass of about 9.5 GeV/c^2 were confirmed in e^+e^- collisions at the DORIS storage ring at DESY.[2] From the narrow resonance observed at (9.46 ± 0.01) GeV/c^2, the PLUTO and DASP detectors were able to determine the electronic width Γ_{ee}, which implied a charge assignment of $-1/3$ for the b quark. It took a few years until decays of B mesons, bound states of a b quark and a light quark, were observed in 1983 by the CLEO Collaboration.[3] The weak isospin of the b quark was first extracted from the forward-backward asymmetry A_{FB} in $e^+e^- \to b\bar{b}$ at PETRA,[4] where the measurement of $A_{FB} = (-22.8 \pm 6.0 \pm 2.5)\%$ at $\sqrt{s} = 34.6$ GeV was found to be consistent with the Standard Model prediction of $A_{FB} = -25\%$ assuming $I_3 = -1/2$ for the weak isospin of the b quark. This indicated that the bottom quark has a partner, and it can be counted as the first evidence for the existence of the top quark. Finally, concluding this brief historical overview with a link between top and B physics, $B^0\bar{B}^0$ mixing was first observed by the ARGUS Collaboration in 1987 (Ref. 5). The measurement of a large mixing parameter x_d was the first indication of a large top quark mass.

Why are we discussing the history of b-quark physics? A certain pattern can be observed after the discovery of a new quark. This pattern appears to repeat itself after the discovery of the top quark. It looks like right after the discovery of the b quark, an attempt was made to confirm the discovery in a different environment like e^+e^- collisions. Then the fundamental quantities of the newly discovered quark, like its charge and isospin, were determined. After sufficient statistics were accumulated, rare phenomena like $B\bar{B}$ oscillations were searched for. Nowadays, B physics is fully explored at e^+e^- colliders and rare phenomena like $b \to u$ transitions or $b \to s\gamma$ penguin decays are also studied.[6] This raises the question of why B physics is studied at a $p\bar{p}$ hadron collider which is a much more difficult environment for studying low p_t physics. We shall discuss this issue further on, in Sec. 3.

1.2 Early Searches for the Top Quark

The experimental search for the top quark begun soon after the discovery of the b quark. Between 1979 and 1984, measurements of R, the ratio of the cross sections $\sigma(e^+e^- \to \text{hadrons})$ to $\sigma(e^+e^- \to \mu^+\mu^-)$, were performed at the PETRA e^+e^- storage ring up to a center-of-mass energy of 46.8 GeV. The value of R was found to be consistent with Standard Model predictions without a top quark contribution, setting a lower bound on the top quark mass[7] of 23.3 GeV/c^2. Later searches at e^+e^- colliders were also negative and limits on m_{top} of half of the center-of-mass energy were set. These limits from TRISTAN[8] as well as SLC[9] and LEP[10] are listed in Table 1.

With the advantage of higher mass regions being accessible, the search for the top quark was soon dominated by $p\bar{p}$ colliders, first the SPS collider ($\sqrt{s} =$ 630 GeV) at CERN and then the Tevatron ($\sqrt{s} = 1.8$ TeV) at Fermilab. Initial results reported in 1984 by the UA1 Collaboration[11] at the SPS seemed to be consistent with the production of a top quark of mass (40 ± 10) GeV/c^2 in $p\bar{p} \to W \to t\bar{b}$. The results were based on the observation of 12 isolated lepton plus two-jet events with an expected background of approximately 3.5 events in 200 $n\text{b}^{-1}$. However, these first results were not supported by a subsequent UA1 analysis[12] with a higher statistics data sample setting a lower limit on m_{top} of > 52 GeV/c^2. More sensitive searches were performed later on by UA2 (Ref. 13) and with the start of the Tevatron. CDF (Refs. 14 and 15) and DØ (Ref. 16) finally increased the limit on the mass of the top quark to 131 GeV/c^2 in 1994 (see Table 1).

Year	Location	Mass limit (95% CL)	Ref.
1979	e^+e^-: PETRA	> 23.3 GeV/c^2	7
1987	e^+e^-: TRISTAN	> 30.2 GeV/c^2	8
1989	e^+e^-: SLC & LEP	> 45.8 GeV/c^2	9,10
1984	$p\bar{p}$: UA1	(40 ± 10) GeV/c^2	11
1988	$p\bar{p}$: UA1	> 52 GeV/c^2	12
1990	$p\bar{p}$: UA2	> 69 GeV/c^2	13
1990	$p\bar{p}$: CDF	> 77 GeV/c^2	14
1992	$p\bar{p}$: CDF	> 91 GeV/c^2	15
1994	$p\bar{p}$: DØ	> 131 GeV/c^2	16

Table 1: Historical overview of searches for the top quark and limits on the top quark mass.

However, in April 1994 the CDF Collaboration presented evidence for top quark production[17,18] with the observation of 12 events consistent with either two W bosons, or a W boson and at least one b jet. The probability that the measured yield was consistent with the expected background was 0.26%, corresponding to a $2.8\,\sigma$ effect. Finally, in February 1995 the top quark was discovered by the CDF experiment[19] and the DØ experiment[20] at the same time. Although top quark physics is still a relatively young field at the time of this conference, a lot of progress has been made in understanding the top quark and its characteristics.

2 Status of Top Quark Physics at CDF and DØ

2.1 The Tevatron with the CDF and DØ Detectors

At the Fermilab Tevatron, proton-antiproton collisions take place at a center-of-mass energy of $\sqrt{s} = 1.8$ TeV. The Tevatron Run I started delivering data in December 1992 and finished in February 1996. During this period, a total of about 110 pb^{-1} and 100 pb^{-1} of data were accumulated by the CDF and DØ experiments, respectively. All results presented in this paper refer to the full Run I statistics unless otherwise noted. The running period was divided up in a so-called Run Ia from December 1992 through August 1993 and Run Ib from December 1993 to February 1996. The collected integrated luminosities by CDF and DØ were ≈ 19.3 pb^{-1} and ≈ 15 pb^{-1} for Run Ia as well as ≈ 90 pb^{-1} and ≈ 85 pb^{-1} for Run Ib, respectively. During that time, the Tevatron operated with six bunches of protons and six bunches of antiprotons crossing every 3.5 μs at the experiments' interaction regions. During Run Ib, the highest instantaneous luminosities, which were reached, were around $2.5 \cdot 10^{31}$ cm^{-2} s^{-1}. At this luminosity, on average two interactions occurred per beam crossing.

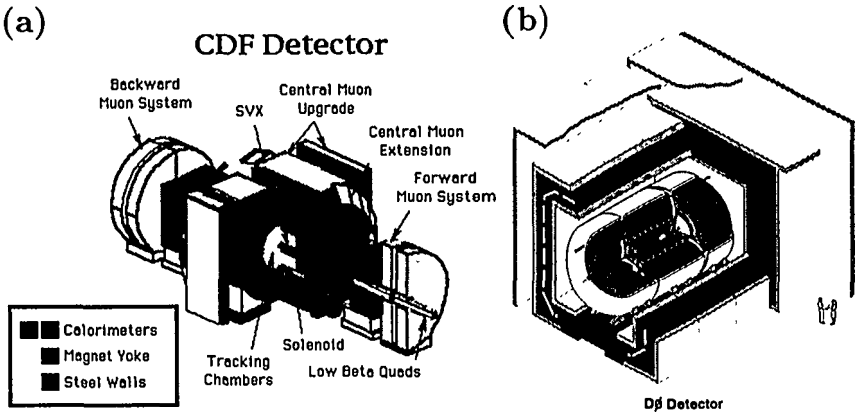


Figure 1: Schematic view of (a) the CDF detector and (b) the DØ detector.

2.1.1 The CDF Detector

The Collider Detector at Fermilab (CDF) is a general-purpose detector to efficiently identify leptons and hadronic jets, as well as charged particles in $p\bar{p}$ collisions.[21] A schematic view of the CDF detector is shown in Fig. 1(a). Three devices inside the 1.4 T solenoid are used for the tracking of charged particles: the silicon vertex detector (SVX), a set of vertex time projection chambers (VTX), and the central tracking chamber (CTC).

The SVX consists of four layers of silicon microstrip detectors located at radii between 3.0 cm and 7.9 cm from the interaction point, and provides spatial measurements in the r-φ plane with a resolution of 13 μm, giving a track impact parameter resolution of about $(13 + 40/p_t)$ μm (Ref. 22), where p_t is the transverse momentum of the track in GeV/c. Throughout this article, φ is the azimuthal angle, θ is the polar angle measured from the proton direction, and r is the radius from the beam axis (z-axis). The geometric acceptance of the SVX is $\sim$ 60%

as it extends to only ± 25 cm from the nominal interaction point, whereas the Tevatron beam has an RMS width of ~ 30 cm along the beam direction. The transverse profile of the beam is circular and has an RMS of ~ 25–35 μm.

The VTX reconstructs intermediate tracks in the r-z plane and is used to determine the primary interaction vertex. Surrounding the SVX and VTX is the CTC, a cylindrical drift chamber containing 84 layers grouped into nine alternating superlayers of axial and stereo wires. It covers the pseudorapidity interval $|\eta| < 1.1$, where $\eta = -\ln[\tan(\theta/2)]$. The p_t resolution of the CTC combined with the SVX is $\sigma(p_t)/p_t = ((0.0066)^2 + (0.0009\,p_t)^2)^{1/2}$, with p_t measured in GeV/c.

Outside the solenoid are electromagnetic (CEM) and hadronic (CHA) calorimeters ($|\eta| < 1.1$) that employ a projective tower geometry with a segmentation of $\Delta\eta \times \Delta\varphi \sim 0.1 \times 15°$. The sampling medium is composed of scintillators layered with lead and steel absorbers. A layer of proportional wire chambers (CES) is located near shower maximum in the CEM and provides a measurement of electromagnetic shower profiles in both the φ and z directions. Plug and forward calorimeters instrument the region of $1.1 < |\eta| < 4.2$ and consist of gas proportional chambers as active media, and lead and iron as absorber materials. The overall resolution for the CDF central calorimeter is $\sigma_E/E = (13.5\%/\sqrt{E_t}) + 2\%$ for electromagnetic showers and $\sigma_E/E = (75\%/\sqrt{E_t}) + 3\%$ for hadrons.

Several muon subsystems in the central region are used. The central muon chambers (CMU) and the central muon upgrade chambers (CMP) cover 80% for $|\eta| \leq 0.6$, while the central muon extension chambers (CMX) extend the coverage up to $|\eta| < 1.1$. The CMP chambers are located behind eight interaction lengths of material.

2.1.2 The DØ Detector

The DØ detector[23] consists of three primary systems: a nonmagnetic tracking device, a uranium-liquid argon calorimeter, and a muon spectrometer. A perspective view of the DØ detector can be seen in Fig. 1(b). The tracking system consists of four detector subsystems: a three-layer vertex drift chamber, a transition radiation detector for additional electron identification, a four-layer central drift chamber, and two forward drift chambers. The tracking system provides charged particle tracking over the region $|\eta| < 3.2$.

The hermetic, compensating, uranium-liquid argon sampling calorimeter is divided into three parts: a central calorimeter and two end calorimeters. They each consist of an electromagnetic section, a fine hadronic section, and a coarse hadronic section, housed in a steel cryostat. The calorimeter covers the pseudorapidity range $|\eta| < 4.2$ with fine longitudinal segmentation (eight depth segments) and fine transverse segmentation ($\Delta\eta \times \Delta\phi = 0.1 \times 6°$, and $\Delta\eta \times \Delta\phi = 0.05 \times 6°$ in the third depth segment of the electromagnetic calorimeter). The overall resolution for the DØ calorimeter is $\sigma_E/E = (15\%/\sqrt{E}) + 0.4\%$ for electromagnetic showers and $\sigma_E/E = (50\%/\sqrt{E})$ for hadrons.

The muon system, used for the identification of muons and determination of their trajectories and momenta, consists of five separate solid-iron toroidal magnets, together with sets of proportional drift tube chambers. The muon system covers $|\eta| < 3.3$. The material in the calorimeter and iron toroids combined varies between 13 and 19 interaction lengths. The achieved momentum resolution is $\sigma_p/p = 0.2 + 0.003\,p$ (with p measured in GeV/c) for the rapidity range $|\eta| < 3.3$.

2.2 Top Quark Production at the Tevatron

In $p\bar{p}$ collisions at $\sqrt{s} = 1.8$ TeV, the dominant top quark production mechanism is $t\bar{t}$ pair production through $q\bar{q}$ annihilation. Gluon-gluon fusion, which will be the main production mechanism at LHC energies, contributes at a level of about 10% at the Tevatron. The production of single top quarks through the creation of a virtual W boson is estimated to be about one order of magnitude lower than the $t\bar{t}$ pair production at $\sqrt{s} = 1.8$ TeV.

During the Tevatron Run I, about $5 \cdot 10^{12}$ $p\bar{p}$ collisions occurred within the CDF and DØ detectors but only about 500 $t\bar{t}$ pairs have been produced. The top quark production cross section is about ten orders of magnitude lower than the total inelastic cross section at the Tevatron. Comparing $\sigma_{t\bar{t}}$ to other physics processes like W boson production shows that $\sigma_{t\bar{t}}$ is still three orders of magnitude lower than the W cross section. This means the challenge in discovering and studying top quarks is to separate them from backgrounds in hadron collisions.

2.3 Top Quark Decay Signature

Within the Standard Model, each of the pair-produced top quarks decays almost exclusively into a W boson and a b quark as shown in Fig. 2. The W boson decays

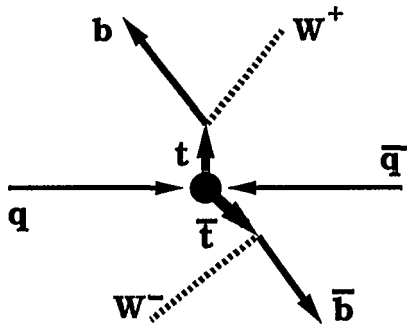


Figure 2: Top decay signature within the Standard Model.

into either a lepton-neutrino or quark-antiquark pair. The top decay signature depends primarily on the decay of the W boson. Events are classified by the number of W's that decay leptonically. In this context, lepton refers to an electron or a muon.

If both W bosons decay leptonically into $W \to \ell\nu$, we call it the "dilepton channel," where the final state consists of $\ell^-\bar{\nu}\ell^+\nu b\bar{b}$ as can be seen in Fig. 3(a). This means there will be two leptons and two jets originating from b quarks in the event. Due to both W's decaying semileptonically, this top decay mode has a small branching fraction of about 5%.

If one of the W bosons decays leptonically into $W \to \ell\nu$ and the other into $W \to q\bar{q}'$, we call it the "lepton plus jets channel," where the final state consists of $\ell\nu q\bar{q}'b\bar{b}$ as shown in Fig. 3(b). In this case, one lepton and four jets, where two jets originate from b quarks, can be seen in the event. This decay mode happens in about 30% of the time.

If both W bosons decay into quark pairs as $W \to q\bar{q}'$, we call it the "all hadronic channel." The final state consists of $q\bar{q}'q\bar{q}'b\bar{b}$ (see Fig. 4). In this case, we can find six jets in the event, where two jets originate from b quarks. This top decay mode occurs at a large rate of about 44%.

In addition, there are about 21% of $t\bar{t}$ decays to final states containing τ leptons. According to the τ decay, these top decays are either classified as dilepton or lepton plus jet events, if the tau decays into e or μ, or as all hadronic events if the tau decays hadronically. In the following, we are going to use these decay channels to discuss top decays at the Tevatron.

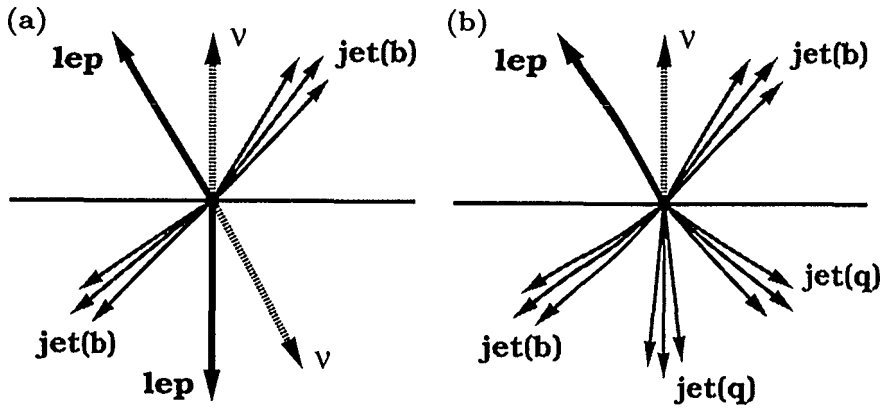


Figure 3: Top decay signature of (a) the dilepton channel and (b) the lepton plus jets channel.

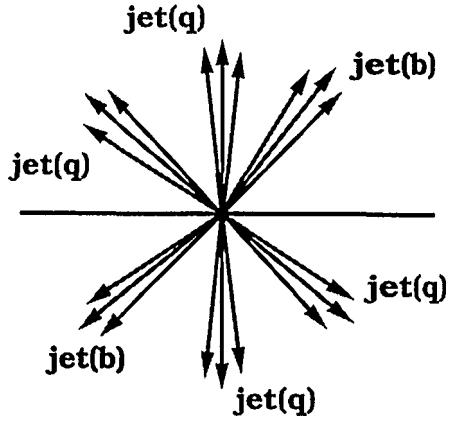


Figure 4: Top decay signature of the all hadronic channel.

Sample	DØ	CDF
$e\mu$	3	7
Background	0.4 ± 0.1	0.76 ± 0.21
Expected Yield	1.7 ± 0.3	2.4 ± 0.2
ee or $\mu\mu$	2	2
Background	1.2 ± 0.4	1.23 ± 0.36
Expected Yield	1.4 ± 0.1	1.6 ± 0.2
e or $\mu + \tau$	2	4
Background	1.4 ± 0.5	1.96 ± 0.35
Expected Yield	1.4 ± 0.1	0.7 ± 0.1

Table 2: Event summary for the dilepton channel. The expected yield is based on determinations of the top cross section[24] for a top quark mass of 175 GeV/c^2.

2.4 The Top Dilepton Channel

The signature of the dilepton channel [see Fig. 3(a)] is two isolated high p_t leptons (e or μ) and missing energy ($\not\!\!E_t$) from the two neutrinos that escape the detector unobserved. In addition, two or more jets can be found in the event. The event selection also relies on kinematic requirements. The dominant backgrounds are from WW diboson production plus jet activity where both W's decay leptonically and from jet plus Z production with $Z \to \tau\tau$ followed by subsequent leptonic τ decays. Events where the e^+e^- or $\mu^+\mu^-$ invariant mass is within 75 GeV/c^2 < $m_{\ell\ell}$ < 105 GeV/c^2 are considered as $Z \to \ell\ell$ candidates and removed in the event selection. Fake leptons and Drell-Yan production of lepton pairs are further sources of background. These backgrounds are estimated from data as well as Monte Carlo predictions.

The dilepton channel has a good signal to background ratio, but low statistics. Due to the two neutrinos, this channel is not ideal for a determination of the top quark mass. The dilepton event summary for the CDF and DØ experiments is shown in Table 2. Both experiments find a few events on small backgrounds in the $e\mu$, ee or $\mu\mu$, and e or μ plus τ mode. The expected division of the dilepton signal events is consistent with the data observed by CDF and DØ. For example, in the case of CDF, 58% $e\mu$, 27% $\mu\mu$, and 15% ee events are expected. In Table 2, the expected yield from $t\bar{t}$ production is also listed. It is based on determinations of the top cross section[24] for a top quark mass of 175 GeV/c^2.

2.5 The Top Lepton plus Jets Channel

The signature of the lepton plus jets channel [see Fig. 3(b)] is one isolated high p_t lepton (e or μ), missing energy ($\not\!\!E_t$) from the neutrino, and four jets where two of them are from b quarks. The dominant backgrounds are from W plus jet production including W plus $b\bar{b}$ production. In this channel, it is important to reduce the backgrounds ($S : B \approx 1 : 4$), where both experiments follow different strategies.

To reduce background, CDF tags the b jets in the event through a so-called "soft lepton tag" and a "SVX tag." The first technique identifies b jets by searching for a lepton from $b \to \ell X$ or $b \to c \to \ell X$ decays, which have branching fractions of about 10% each. Since these leptons typically have lower momenta than the leptons from the primary W decay, this technique is known as the "soft lepton tag" (SLT). It looks for electrons and muons by matching tracks from the central drift chamber with electromagnetic energy clusters in the calorimeter or track segments in the muon chambers. The p_t threshold is at 2 GeV/c. The efficiency for SLT tagging a $t\bar{t}$ event is $(18 \pm 2)\%$, and the typical fake rate per jet is about 2%. Details of the SLT algorithm can be found in Ref. 18.

The second, more powerful b-tagging technique exploits the finite lifetime of b hadrons by searching for a secondary decay vertex with CDF's silicon vertex detector. This technique is known as the "SVX tag." The algorithm begins by searching for displaced vertices containing three or more tracks which satisfy a loose set of track quality requirements. If no such vertices are found in an event, two-track vertices that satisfy more stringent quality cuts are accepted. A jet is defined to be tagged if it contains a secondary vertex which is displaced from the primary vertex with a significance of greater than three. The efficiency for SVX tagging a $t\bar{t}$ event is $(41 \pm 4)\%$, while the fake rate is only $\approx 0.5\%$. More information on the SVX tag can be found in Refs. 18 and 19. An example of a SVX-tagged event display can be found in Fig. 5. Both b jets are SVX tagged and well-separated from the primary interaction vertex by 2.2 mm and 4.5 mm, respectively.

The DØ experiment makes use of two different approaches to reduce the background in the lepton plus jets channel. DØ uses kinematic and topological cuts as well as b tagging via soft muon tagging. The first approach exploits the fact that the large top quark mass gives rise to kinematically different events. Jets

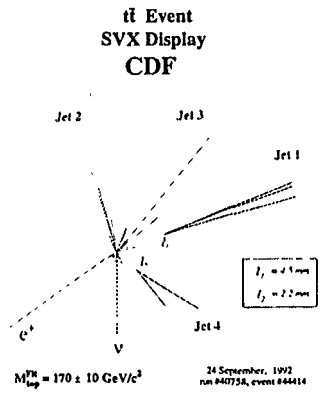


Figure 5: Example of a SVX-tagged event where both b jets are SVX tagged.

from $t\bar{t}$ decays tend to be more energetic and more central than those from typical QCD background events. In addition, $t\bar{t}$ events as a whole are more spherical while QCD jet production results in more planar event shapes. Top-enriched data samples can therefore be selected with a set of topological and kinematic cuts like the total hadronic activity in the event, $H_T = \sum E_t^{\rm jet}$, which can be combined with the aplanarity $\mathcal{A}$ of the W plus jets system. A value of $\mathcal{A} = 0$ indicates a planar event shape, while $\mathcal{A} = 1/2$ reflects a spherical event shape. In addition, a third kinematic variable with discriminating power, the total leptonic transverse energy, $E_t^L = E_t^{\rm lep} + \not\!\!E_t$, is also used. The second D$\emptyset$ approach uses b tagging via muon tags through $b \to \mu X$ and $b \to c \to \mu X$ decays. The typical fake rate for background events is at the $\approx 2\%$ level for tagging muons of $p_t > 4$ GeV/c. For more details on both techniques, see Ref. 20.

The lepton plus jets event summary for the CDF and D$\emptyset$ experiments is shown in Table 3. CDF finds 34 events with at least one SVX tag on a background of (8.0 ± 1.4) events, while (19.8 ± 4.0) events are expected from $t\bar{t}$ production, where a top quark mass of 175 GeV/c^2 has been assumed. The CDF event shape analysis is based on only 67 pb^{-1}.

Sample	D$\emptyset$	CDF
Event Shape:		
Observed	21	22
Background	9.2 ± 2.4	7.2 ± 2.1
Expected Yield	12.9 ± 2.1	-
Lepton Tag (SLT):		
Observed	11	40
Background	2.5 ± 0.4	24.3 ± 3.5
Expected Yield	5.2 ± 1.0	9.6 ± 1.7
Displaced Vertex (SVX tag):		
Observed	-	34
Background	-	8.0 ± 1.4
Expected Yield	-	19.8 ± 4.0

Table 3: Event summary for the lepton plus jets channel. The expected yield is based on determinations of the top cross section[24] for a top quark mass of 175 GeV/c^2.

2.6 The Top All Hadronic Channel

The signature of the all hadronic channels (see Fig. 4) is nominally six jets where two of them are from b quarks, no leptons, and low $\not\!\!E_t$. Since not all jets are always observed, a jet multiplicity of at least five is required. In order to overcome the huge background from QCD multijet production, b tagging alone is not sufficient and kinematic cuts are used in addition. If the backgrounds can be controlled, the all hadronic channel would be the ideal way to determine the top mass because no neutrinos are present and all objects of the top decay are measured in the detector.

After a set of kinematic cuts is applied in the CDF all hadronic analysis, at least five jets are required, where the leading jets have to pass an aplanarity cut. In addition, at least one jet has to be SVX tagged. The efficiency of a SVX tag in a $t\bar{t}$ event is $(47 \pm 5)\%$ in the all hadronic mode, slightly larger than in the lepton plus jets channel due to the presence of additional charm tags from $W \to c\bar{s}$. CDF observes 192 events on a predicted background of 137 ± 11 events as can be seen in Table 4.

Sample	DØ	CDF
Observed	15	192
Background	11 ± 2	137.1 ± 11.3
Expected Yield	4.5 ± 0.5	26.6 ± 9.1

Table 4: Event summary for the all hadronic channel. The expected yield is based on determinations of the top cross section[24] for a top quark mass of 175 GeV/c^2.

Recently, DØ also reported on a search for $t\bar{t}$ pairs in the all hadronic channel. They require at least six jets within $|\eta| < 2$ and use several additional kinematic quantities. Finally, a soft muon tag has to be present in at least one of the jets. Fifteen μ tagged events are observed for an expected background of 11 ± 2 events (see Table 4).

In summary, we explored top quark production through three different top decay modes, the dilepton, the lepton plus jets, and the all hadronic channel. We reviewed the current yield of top decays in these three decay modes observed by the CDF and DØ experiments. As was true after the discovery of the bottom quark, the top quark has been confirmed in different decay modes. In the following, we use these top event candidates to measure the fundamental quantities of the top quark: the top production cross section $\sigma_{t\bar{t}}$ and the top quark mass $m_{\rm top}$.

2.7 The Top Production Cross Section

The measurement of the top production cross section $\sigma_{t\bar{t}}$ is of interest for several reasons. It checks QCD calculations of top production, which have been performed by several groups,[24–27] and it provides an important benchmark for estimating top yields in future high statistics experiments at the Tevatron and LHC. In addition, a value of the top cross section significantly different from the QCD prediction could indicate nonstandard top production or decay mechanisms.

The measurement of the top production cross section $\sigma_{t\bar{t}}$ is straightforward:

$$\sigma_{t\bar{t}} = \frac{N_{\rm obs} - N_{\rm bkg}}{A\,\mathcal{L}}. \qquad (1)$$

The number of predicted background events $N_{\rm bkg}$ is subtracted from the number of observed top candidates $N_{\rm obs}$ and divided by the acceptance A of the sample selection and the integrated luminosity $\mathcal{L}$ of the used data set. The measurement of $\sigma_{t\bar{t}}$ has been determined in each decay channel individually as detailed in Fig. 6.

The results of the different $\sigma_{t\bar{t}}$ measurements from CDF and DØ can be compared to each other and to theoretical predictions indicated by the dark band also shown in Fig. 6. The width of the theory band is given by the spread in the theoretical predictions of Laenen *et al.*,[24] Nason *et al.*,[25] Berger *et al.*,[26] and Catani *et al.*[27] From all these measurements of $\sigma_{t\bar{t}}$, a world average top production cross section

$$\sigma_{t\bar{t}} = (6.4^{+1.3}_{-1.2})\ pb \qquad (2)$$

can be determined, which is slightly larger but in good agreement with the theoretical predictions.

2.8 Measurement of the Top Quark Mass

The top quark mass $m_{\rm top}$ is a fundamental parameter in the Standard Model. A precise determination of $m_{\rm top}$ is therefore the most important measurement of the CDF and DØ experiments in Run I. The goal is to use as many decay modes as possible and to measure $m_{\rm top}$ as accurately as possible. The use of several methods also allows cross checking of the different techniques and studying of systematic uncertainties. An incredible amount of work exploring these issues has been done by both experiments. This resulted in significantly improved measurements of $m_{\rm top}$ since the discovery publications.[19,20] The uncertainties on the top quark mass measurements by CDF and DØ have been improved by a factor of more than two. In such a short time, this is a respectable amount of progress in understanding the newly discovered top quark.

The primary dataset for measuring the top quark mass is the lepton plus jets sample. This is the decay mode with the most power. The background in the all hadronic channel is too large, and the statistics of the dilepton mode is too weak, together with the additional complication of two missing neutrinos. Thus, the preferred method of determining $m_{\rm top}$ by both experiments, is a constrained fit to the lepton plus four-jet events arising from the process $t\bar{t} \to WbW\bar{b} \to \ell\nu J_1 J_2 J_3^b J_4^{\bar{b}}$. The task is to assign the observed particles, jets, and $\not\!\!E_t$ in these events one-to-one to the decay products of the t and $\bar{t}$. However, the problem remains that we don't know *a priori* how to map the observed jets to the partons from the $t\bar{t}$ decay. This is illustrated in Fig. 7, where, for example, in Fig. 7(a) jet J_1 is combined with the lepton and neutrino to originate from one top quark, while jets J_2 through J_4 are assigned to the $\bar{t}$ quark. Figure 7(b) shows another possible assignment, which

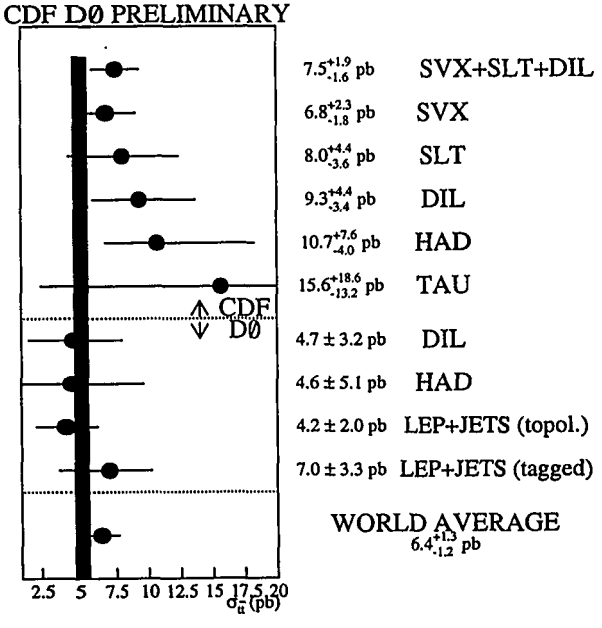


Figure 6: Summary of the CDF and DØ top quark production cross section measurements in different decay channels.

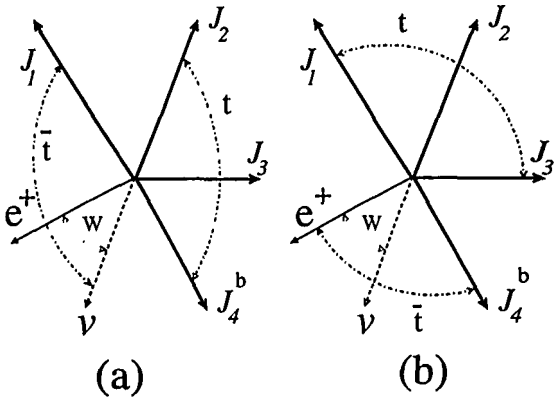


Figure 7: Illustration of different assignments of the observed objects in a $t\bar{t}$ decay to the originating partons.

might as well be the result of a $t\bar{t}$ decay. In total, there are 12 possible jet-parton assignments which are reduced to six combinations if one b jet is tagged. If there are two b tags in the event, there are still two possible combinations from assigning the two b jets to the t or $\bar{t}$ quark. In addition, this combinatorics gets doubled, because there is a two-fold ambiguity for p_z^ν since only the transverse component of the missing energy $\not\!\!E_t$ is reconstructed by the experiments.

To select the best combination, CDF and DØ use a likelihood method that exploits the many constraints in the system. Each event is fitted individually to the hypothesis that three of the jets come from one top quark through its decay into Wb, and that the lepton, $\not\!\!E_t$, and the remaining jet come from the other top quark. In addition, b-tagged jets are assigned as b quarks in the fit; the invariant dijet mass has to equal the W boson mass, and $m_t = m_{\bar{t}}$ is required. CDF chooses the solution with the best fit χ^2, while DØ takes a weighted average of the three best solutions, where each solution has to satisfy a minimum χ^2 cut. The result is a distribution of the best fit top mass from each candidate event. The final value of the top mass is then extracted by fitting this distribution to a set of Monte Carlo templates from $t\bar{t}$ production and background. There are several reasons why a MC simulation of the kinematic fitting is necessary. At first, there is the need to relate the jet energies to parton energies, where the experimental smearing, predominantly in the jet energies, has to be taken into account. In

addition, the four most energetic jets in the event may not be directly related to the $t\bar{t}$ decay products, if, for example, a hard gluon radiation produced an energetic jet. Finally, the fit solution with the lowest χ^2 may not have the correct jet assignment.

2.8.1 CDF Top Quark Mass Measurement

CDF has a good signal to background ratio in the lepton plus jets channel, where one of the jets is SVX tagged. This sample of lepton plus four-jet events with at least one SVX tag provided the original top mass measurement at CDF.[19] Recent optimization studies indicate a reduced error on $m_{\rm top}$, if the tagged events are subdivided into different tagging classes and a set of no-tagged events is added. The following four data samples are used for this optimized determination of the top quark mass: (a) events with one SVX tag (15 events), (b) events with two SVX tags (five events), (c) events with a SLT tag but no SVX tag (14 events), and (d) events with no tag but all four leading jets having $E_{\rm t} > 15$ GeV (48 events).

These four subsamples are orthogonal to each other and a top mass can be extracted from each sample individually. These top mass distributions for the four samples are shown separately in Fig. 8(a). For each of the subsamples, an expected background fraction was estimated, and predicted top signal distributions were obtained from Monte Carlo events at several values of $m_{\rm top}$. A likelihood fit was performed for each subsample, which is shown in the inserts of the distributions in Fig. 8(a). Since the likelihood values from the four subsamples are essentially independent, a combined result is obtained by taking the product of the four likelihood values. The sums of the four distributions, as well as the likelihood product versus top mass, are shown in Fig. 8(b), where the solid line represents the data, while the dashed line is the predicted sum of background plus expected signal. The shaded area just represents the background contribution.

From the distribution of the likelihood product versus $m_{\rm top}$, a top mass value of $m_{\rm top} = (176.8 \pm 4.4 \pm 4.8)$ GeV/c^2 has been extracted. The systematic errors are detailed in Table 5. The largest contribution (± 3.6 GeV/c^2) comes from soft gluon radiation plus jet energy scale uncertainties in estimating the true jet energy from the observed energy. The systematic error due to hard gluon effects

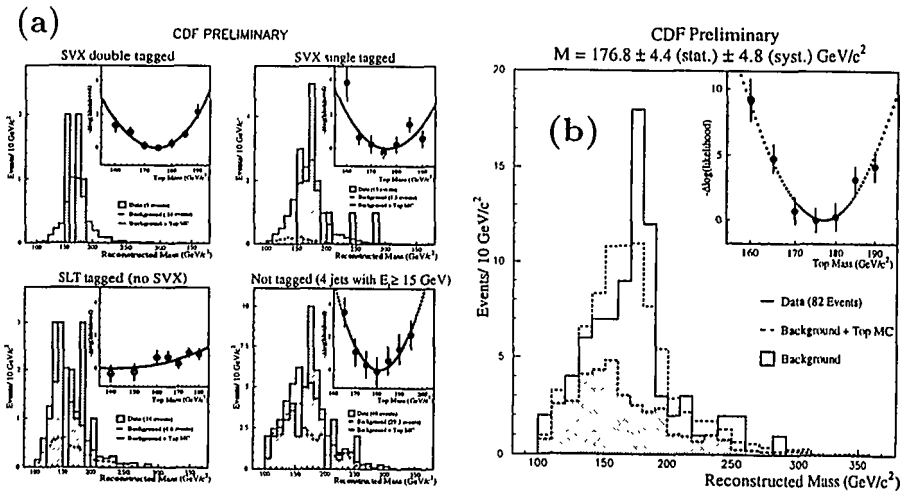


Figure 8: CDF top mass distributions: (a) For the four subsamples discussed in the text. The shaded area represents the data, while the solid line is the predicted sum of background plus expected signal. The dashed line just represents the background contribution. The inserts show the obtained likelihood function versus top mass. In (b), the combined top mass distribution is shown. The solid line represents the data, while the dashed line is the predicted sum of background plus expected signal. The shaded area represents the background contribution. The insert shows the obtained likelihood function versus top mass.

CDF Lepton plus Jets Mass Systematics	$\Delta m_{\rm top}$
Soft Gluon + Jet E_t Scale	3.6 GeV/c^2
Different MC Generators	1.4 GeV/c^2
Hard Gluon Effects	2.2 GeV/c^2
Kin. & Likelihood Fitting Method	1.5 GeV/c^2
b-Tagging Bias	0.4 GeV/c^2
Background Spectrum	0.7 GeV/c^2
Monte Carlo Statistics	0.8 GeV/c^2
Total	4.8 GeV/c^2

Table 5: Systematic uncertainties of the CDF top quark mass measurement.

reflects the uncertainty in how often one of the four leading jets is associated with a hard gluon rather than directly with a parton in a top decay. All other systematic errors contribute less than 1.5 GeV/c^2 (see Table 5).

2.8.2 DØ Top Quark Mass Measurement

As already discussed, the power to extract a top quark mass from the lepton plus four-jet events depends on the suppression of the background. The DØ experiment combines four kinematic variables into one top likelihood discriminant $\mathcal{D}$, which provides a distinct separation power between top signal and background without biasing the analysis. For example, a straight cut on the total hadronic energy H_T would push both background and signal distributions towards higher values of $m_{\rm top}$ and make the background look like signal. The top likelihood discriminant $\mathcal{D}$ combines $\not\!\!E_t$, the aplanarity $\mathcal{A}$ of the W plus jets system, the fraction of the E_t of the W plus jets system which is carried by the W (H'_{T2}), and the E_t weighted RMS η of the W and jets ($K'_{T_{min}}$). Some of the distributions of these variables, as well as the combined top likelihood discriminant $\mathcal{D}$, are shown in Fig. 9(a). As can be seen, there is separation between a top signal predicted from Monte Carlo (light shaded area) and background expectations (dark shaded area). After applying a cut of $\mathcal{D} > 0.43$, 32 events have been selected for the fit of $m_{\rm top}$.

The distribution of the fitted top mass values is shown in Fig. 9(b) as the solid histogram. The solid crosses represent the prediction for background plus expected signal, which is in good agreement with the data. The dashed crosses in Fig. 9(b) show the background expectation only. A measurement of the top quark

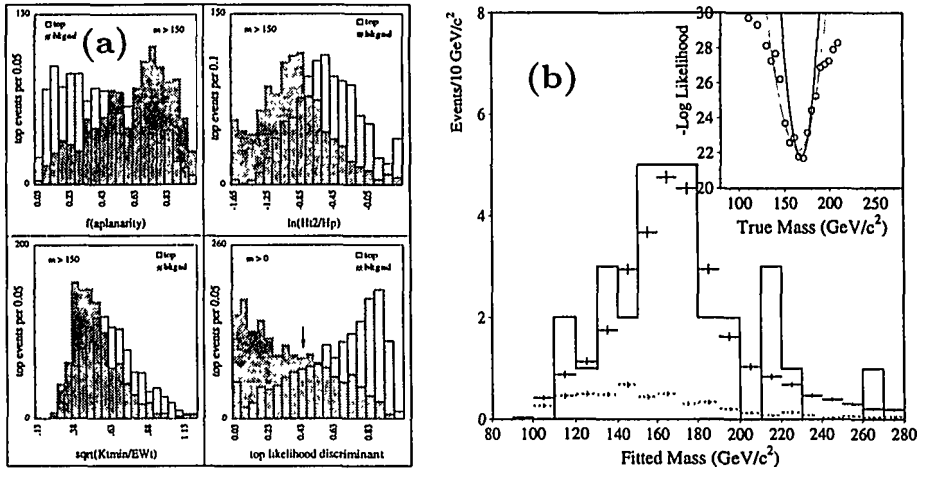


Figure 9: DØ top mass measurement: (a) Distribution of MC top (light) and background (dark) lepton plus four-jet events for different kinematic parameters like aplanarity, H'_{T_2}, $K'_{T_{min}}$, and the combined top likelihood discriminant $\mathcal{D}$ (from top left to bottom right). (b) Observed (solid) top quark mass distribution, where the solid crosses represent the prediction for background plus signal. The dashed crosses are just the background expectation. The curves in the insert are used to determine the top quark mass and its statistical error.

DØ Lepton plus Jets Mass Systematics	Δm_{top}
Jet Energy Correction	7.3 GeV/c^2
Monte Carlo Model	3.3 GeV/c^2
Fitting Method	2.0 GeV/c^2
Total	8 GeV/c^2

Table 6: Systematic uncertainties of the DØ top quark mass measurement.

mass of $m_{top} = (168 \pm 8 \pm 8)$ GeV/c^2 has been extracted from this distribution. The insert in Fig. 9(b) shows the obtained likelihood as a function of true m_{top} as well as the curves used to determine the top quark mass and its statistical error. The systematic errors on the DØ top mass measurement are detailed in Table 6. The largest systematic uncertainty results from the jet energy correction.

2.8.3 World Average Top Quark Mass

An attempt can be made to combine the CDF and DØ top quark mass measurements to a world average top mass. For this purpose, the reported mass measurements from the lepton plus jets channel have been used. CDF measured $m_{top} = (176.8 \pm 4.4 \pm 4.8)$ GeV/c^2, while the DØ measurement results in $m_{top} = (169 \pm 8 \pm 8)$ GeV/c^2. In the determination of the world average top mass, the conservative assumption has been made that all the systematic errors, except for the energy scale, the b-tagging bias, and the Monte Carlo statistics, are fully correlated between both experiments. This results in a world average top quark mass of

$$m_{top} = (175.0 \pm 3.9 \pm 4.5) \text{ GeV}/c^2. \quad (3)$$

It is worthwhile to note that knowing the top quark mass with a combined statistical and systematic error of ± 6 GeV/c^2 (a 3.4% relative error) is a big accomplishment of both Tevatron experiments in Run I.

2.8.4 Summary of Top Quark Mass Measurements

A summary of all top quark mass measurements performed by CDF and DØ is given in Fig. 10. Top mass measurements from other top decay modes like the dilepton channel or the all hadronic channel are also shown. They are in good agreement with the measurement from the lepton plus four-jet samples, which has

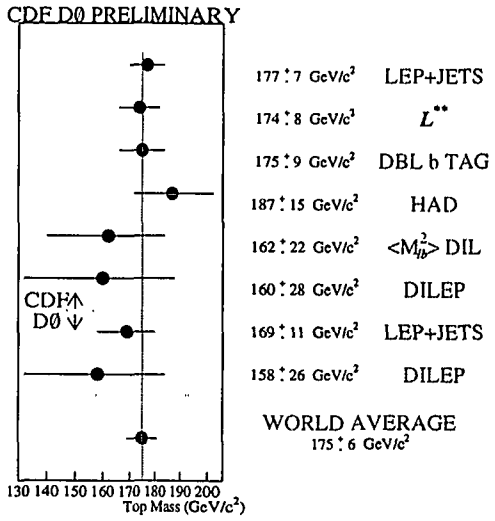


Figure 10: Summary of the CDF and DØ top quark mass measurements in different decay channels.

been discussed in the previous sections in more detail. This decay mode represents the most precise determination of the top mass for each experiment.

The knowledge of the top quark mass plays an important role in calculations of radiative corrections that relate electroweak parameters. For example, higher order radiative corrections relate the W boson mass m_W to the top quark mass m_{top}. This relationship also depends on the mass of the Higgs boson m_{Higgs}, which can also participate in these higher order loops. The relationship between M_W and m_{top} is displayed in Fig. 11. The well-known dependence on the Higgs mass is shown through the different bands for several assumptions of m_{Higgs}. Although m_W and m_{top} are precisely known, the sensitivity on the Higgs boson mass is still too poor. A precise measurement of the top quark mass together with m_W is therefore a high priority of both collider experiments in Run II.

3 B Physics at a Hadron Collider

The principal interest in studying B hadrons in the context of the Standard Model arises from the fact that B-hadron decays provide valuable information on the

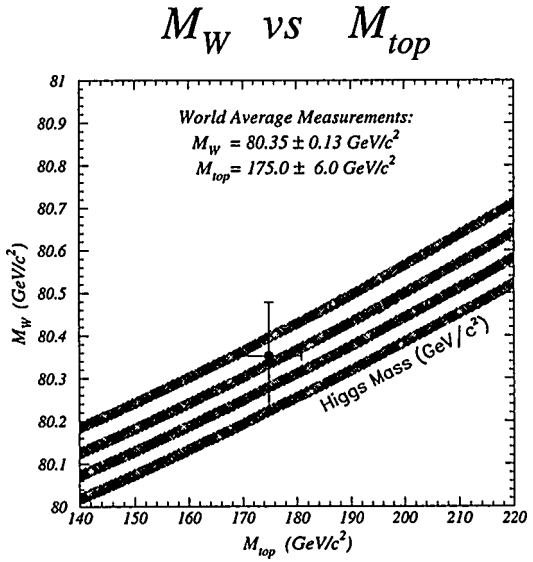


Figure 11: Relation between the top quark mass and the W boson mass. The dependence on the Higgs mass is shown through the different bands for several assumptions of m_{Higgs}.

weak mixing matrix, the Cabibbo-Kobayashi-Maskawa (CKM) matrix.[28] In fact, B decays determine five of the nine CKM matrix elements: V_{cb}, V_{ub}, V_{td}, V_{ts}, and V_{tb}. The future interest in B physics certainly lies in the study of CP violation in the system of neutral B mesons, which will be discussed further in Sec. 4.2.

Traditionally, B physics has been the domain of e^+e^- machines, but already the UA 1 Collaboration has shown that B physics is feasible at a hadron collider.[29] However, the combination of a better mass resolution and vertex detection enables the CDF experiment to perform a broader B-physics program. The D$\emptyset$ experiment has also published several B-physics results,[30] but due to the lack of a precision momentum measurement of charged particles within a magnetic field and the absence of a precision microvertex detector, D$\emptyset$ is not ideally suited to do B physics. Since we concentrate in this presentation on recent results from B hadron lifetimes and time-dependent $B^0\bar{B}^0$ oscillations, we shall report only on measurements from the CDF experiment.

One advantage of B physics at a hadron collider compared to an e^+e^- machine at the $\Upsilon(4S)$ is that all B-hadron species are produced. Another advantage in doing B physics at hadron colliders can be seen by comparing the B-production cross section, which is about 1 nb at the $\Upsilon(4S)$, while at the Z^0 pole $\sigma(B\bar{B}) \approx 6$ nb. However, at the Tevatron, the b-quark production cross section is quite large with $\sigma_b \sim 50$ μb within the central region of rapidity less than 1 ($|\cos\theta| < 1$). This is a huge cross section which resulted in about $5 \cdot 10^9$ $b\bar{b}$ pairs being produced in Run I within the Tevatron detectors. But the total inelastic cross section is still about three orders of magnitude larger. This puts certain requirements on the trigger system to find B-decay products. In addition, the total integrated b-quark production cross section is a rapidly falling cross section, which drops by about two orders of magnitude for a b quark p_t^b greater than about 8 GeV/c compared to p_t^b greater than about 20 GeV/c. This means in terms of trigger thresholds for b decay products, one likes to go as low as possible in p_t in order to increase the amount of recorded B triggers. Of course, the experiment's DAQ bandwidth is the limiting factor.

All B physics triggers at CDF are based on leptons. Dilepton and single lepton triggers both exist. Exploiting the steeply falling b quark production cross section, CDF was able to maintain low p_t thresholds throughout Run I without increasing the experiment deadtime during data taking.

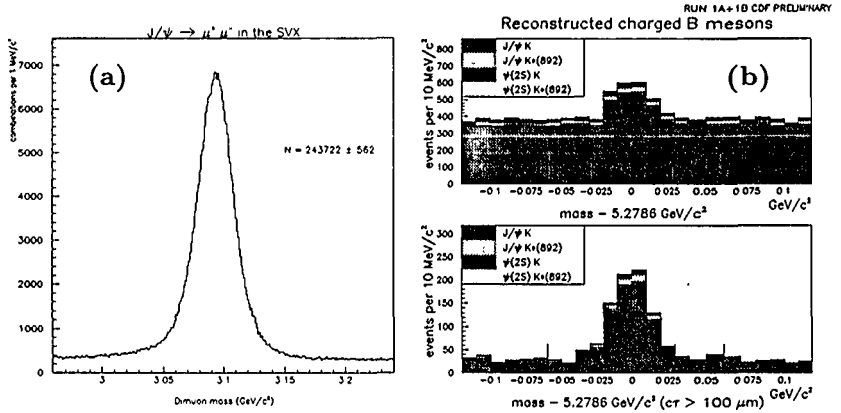


Figure 12: Invariant mass distribution of (a) dimuon trigger in the J/ψ mass region and (b) $B^+ \to J/\psi K^+$ candidates without (top) and with a $c\tau > 100$ μm requirement (bottom).

CDF's dilepton triggers consist of a dimuon trigger with $p_t > 2$ GeV/c for both muon legs, and an $e\mu$ trigger with $p_t^\mu > 3$ GeV/c and $E_t^e > 5$ GeV. The dimuon trigger is the source of CDF's J/ψ sample. Both dilepton trigger samples are also starting points for B mixing analyses. The thresholds for the single lepton triggers are higher with $p_t > 7.5$ GeV/c for muons and $E_t > 8$ GeV for electrons. Analyses involving semileptonic B decays are based on these single lepton datasets. The given p_t thresholds are representative for Run Ib but similar for Run Ia.

The basis of CDF's B-physics program is the good tracking and vertexing capabilities of the CTC and the SVX. This is demonstrated in Fig. 12. The invariant dimuon mass from CDF's dimuon trigger sample is shown in Fig. 12(a). From all Run I data, a prominent signal of about 240,000 J/ψ candidates with both muons in the SVX can be found with a low background. The mass resolution of the observed signal is about 16 MeV/c^2. One handle to reduce backgrounds with the help of CDF's silicon vertex detector is demonstrated in Fig. 12(b). Here, J/ψ candidates are paired with another track in the event, which is assumed to be a kaon, in order to fully reconstruct $B^+ \to J/\psi K^+$ decays. The top plot shows the invariant $J/\psi K^+$ mass distribution, where a B^+ signal is observed above a large background. This background is drastically reduced after a displaced B vertex with, e.g., $c\tau > 100$ μm as measured in the SVX, is required [see Fig. 12(b)].

3.1 B-Hadron Lifetimes

The lifetimes of B hadrons are fundamental properties of these particles and can be used to test theoretical models of heavy flavor decays. Predictions for B-hadron lifetimes and their ratios have been made by several groups.[31,32] Bigi *et al.*[31] predict the charged B lifetime to be longer than the B^0 lifetime by about 5%

$$\frac{\tau(B^+)}{\tau(B^0)} \simeq 1.0 + 0.05 \cdot \frac{f_B^2}{(200\ \mathrm{MeV})^2}, \tag{4}$$

and expect the lifetime of the Λ_b^0 baryon to be shorter than $\tau(B^0)$ with a ratio of $\tau(\Lambda_b^0)/\tau(B^0)$ not smaller than about 0.9. On the other hand, using the heavy quark expansion, Neubert[32] obtains:

$$\frac{\tau(B^+)}{\tau(B^0)} = 1.0 + \mathcal{O}(1/m_b^3), \tag{5}$$

$$\frac{\tau(\Lambda_b^0)}{\tau(B^0)} = 0.98 + \mathcal{O}(1/m_b^3), \tag{6}$$

where the estimate for $\tau(\Lambda_b^0)/\tau(B^0)$ includes corrections that arise at order $1/m_b^2$. Although these ratios might appear to be close to unity, Neubert argues that the $1/m_b^3$ corrections might be large due to phase space enhancement from effects involving the u, d spectator quark. He concludes that theoretical uncertainties allow a lifetime ratio in the range between 0.8 and 1.2.

This subject is controversial, and best solved by precisely measuring all the B-hadron lifetimes. As we shall see, the uncertainties on the individual B lifetimes have reached a level of a few percent. In the following, we review the latest B-hadron lifetime results from CDF and also compare them to other experiments.

3.1.1 B^+ and B^0 Lifetimes with Fully Reconstructed B Mesons

The analysis principle for the B lifetime measurement using fully reconstructed B^+ and B^0 mesons is as follows. All Run I dimuons forming a J/ψ candidate, as shown in Fig. 12(a), are used. All possible decay modes $B \to \Psi \mathbf{K}$ have been investigated, where Ψ is mainly a J/ψ but can also be a $\psi(2S) \to \mu\mu$. $\mathbf{K}$ represents the different kaon states K^+ and $K^*(892)^+$ for the charged B lifetime measurement, as well as K_S^0 and $K^*(892)^0$ for the $\tau(B^0)$ determination. The vertex and mass constrained J/ψ candidates are vertexed with the $\mathbf{K}$ candidates yielding the two-dimensional decay length L_{xy}. Together with the known B transverse momentum p_t, the proper

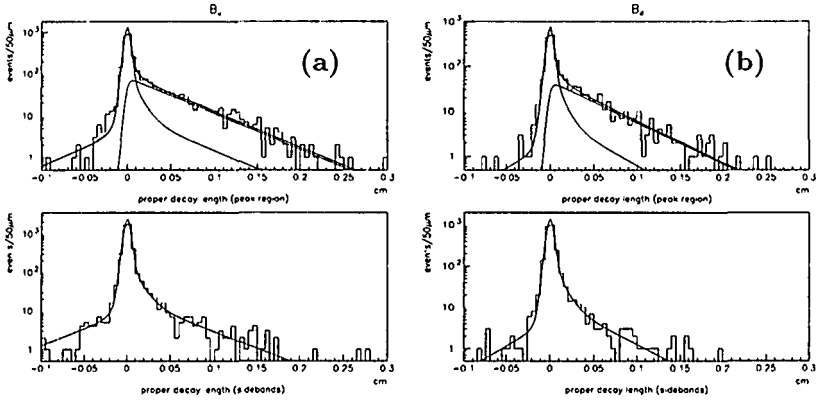


Figure 13: Proper time distributions of (a) charged and (b) neutral B mesons, which were fully reconstructed through $B \to \Psi K$. The bottom plots represent the background $c\tau$ distributions as obtained from the B sidebands.

time distributions, shown in Fig. 13 for (a) charged and (b) neutral B candidates, are obtained. The bottom $c\tau$ distributions represent the background as obtained by fitting the B sideband regions to a Gaussian with exponential tails. Using this background shape, an unbinned likelihood fit of the signal, which is assumed to be an exponential convoluted with a Gaussian, is performed. The following lifetimes are obtained:

$$\tau(B^+) = (1.68 \pm 0.07 \pm 0.02)\ ps \tag{7}$$

$$\tau(B^0) = (1.58 \pm 0.09 \pm 0.02)\ ps \tag{8}$$

$$\tau(B^+)/\tau(B^0) = 1.06 \pm 0.07 \pm 0.01. \tag{9}$$

The exclusive B lifetime measurement is still statistics dominated. One way to increase the number of B candidates is to not fully reconstruct the B meson. This is done in the semiexclusive analysis described in the next section.

3.1.2 B^+ and B^0 Lifetimes with Partially Reconstructed B Mesons

The B-lifetime analysis using partially reconstructed B mesons exploits the semileptonic decays $B \to D^{(*)}\ell X$ and starts with the single lepton trigger data. In a

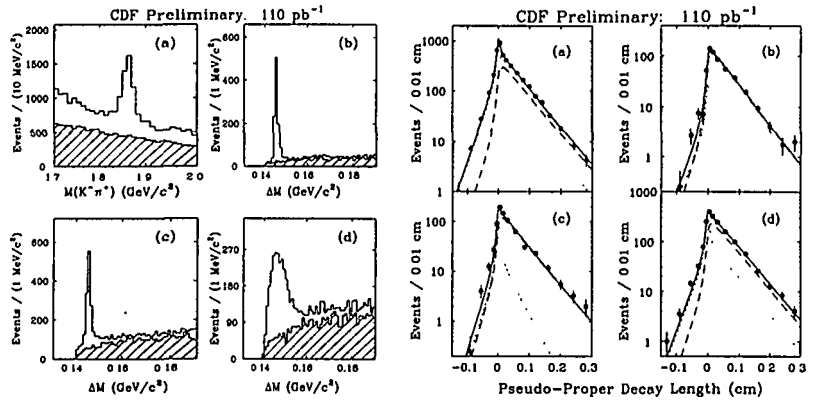


Figure 14: Invariant mass distribution of $D^{(*)}$ candidates (left-hand side) and proper time distributions (right-hand side) from the B-lifetime analysis using partially reconstructed $B \to D^{(*)}\ell X$ decays with (a) $D^0 \to K^-\pi^+$, where the D^0 is not from a D^{*+}. (b) $D^{*+} \to D^0\pi^+$, $D^0 \to K^-\pi^+$. (c) $D^{*+} \to D^0\pi^+$, $D^0 \to K^-\pi^+\pi^+\pi^-$. (d) $D^{*+} \to D^0\pi^+$, $D^0 \to K^-\pi^+\pi^0$.

cone around the trigger electron or muon, $D^{(*)}$ meson candidates are reconstructed through their decay modes:

1. $D^0 \to K^-\pi^+$, where the D^0 is not from a D^{*+},
2. $D^{*+} \to D^0\pi^+$, $D^0 \to K^-\pi^+$,
3. $D^{*+} \to D^0\pi^+$, $D^0 \to K^-\pi^+\pi^+\pi^-$,
4. $D^{*+} \to D^0\pi^+$, $D^0 \to K^-\pi^+\pi^0$, where the π^0 is not reconstructed.

The $D^{(*)}$ candidates are intersected with the lepton to find the B decay vertex. Since the B meson is not fully reconstructed, its $c\tau_B$ cannot be directly determined. A correction has to be applied to scale from the $D^{(*)}\ell$ momentum to $p_t(B)$. This $\beta\gamma$ correction is obtained from a Monte Carlo simulation.

The final $D^{(*)}$ candidates can be seen on the left-hand side of Fig. 14 for (a) $D^0 \to K^-\pi^+$, where the D^0 is not from a D^{*+}; (b) $D^{*+} \to D^0\pi^+$, $D^0 \to K^-\pi^+$; (c) $D^{*+} \to D^0\pi^+$, $D^0 \to K^-\pi^+\pi^+\pi^-$; and (d) $D^{*+} \to D^0\pi^+$, $D^0 \to K^-\pi^+\pi^0$. Although the resolution of the D^{*+} mass peak is worse in mode (d) compared to the other channels, it is still good enough to be used in this analysis.

Note that the charm signals in Fig. 14 are quite clean and rather competitive with $D^{(*)}$ signals found at e^+e^- machines. This demonstrates the feasibility of B physics in a hadron collider environment without using J/ψ's.

The obtained lifetime distributions from $\ell^+\bar{D}^0$ and ℓ^+D^{*-} are used to determine the individual B^+ and B^0 lifetimes. A $\ell^+\bar{D}^0$ combination usually originates from a charged B meson while ℓ^+D^{*-} comes from a B^0. This simple picture is complicated by the existence of D^{**} states which are the source of $\bar{D}^0$ (D^{*-}) mesons that originate from a decay $B^0 \to D^{**-}\ell^+$, $D^{**-} \to \bar{D}^0X$ ($B^+ \to \bar{D}^{**0}\ell^+$, $\bar{D}^{**0} \to D^{*-}X$). This cross talk from D^{**} resonances has been decomposed using Monte Carlo. A combined lifetime fit, as shown on the right-hand side of Fig. 14, yields the following B lifetimes:

$$\tau(B^+) = (1.64 \pm 0.06 \pm 0.05)\ ps \tag{10}$$

$$\tau(B^0) = (1.48 \pm 0.04 \pm 0.05)\ ps \tag{11}$$

$$\tau(B^+)/\tau(B^0) = 1.11 \pm 0.06 \pm 0.03. \tag{12}$$

3.1.3 B^+ and B^0 Lifetime Comparison

A comparison of the CDF B^+ and B^0 lifetime measurements with other experiments, as presented at the 28th International Conference on High Energy Physics, Warsaw, Poland (ICHEP'96),[33] can be found in Figs. 15 and 16, respectively. A comparison of the CDF lifetime ratio measurements is presented in Fig. 17. The B-lifetime analysis using partially reconstructed $B \to D^{(*)}\ell X$ decays is a new result comprising the full Run I statistics and updates the 1992-93 measurement. These new measurements were not yet available at the time of the ICHEP'96 conference and have been added to Figs. 15 through 17. This comparison shows that the CDF B-lifetime measurements are competitive with the results from the Z pole at LEP and SLC.

The combination of the presented B lifetime results using fully and partially reconstructed B decays yields the following combined CDF B-lifetime average:

$$\tau(B^+) = (1.66 \pm 0.05)\ ps \tag{13}$$

$$\tau(B^0) = (1.52 \pm 0.06)\ ps \tag{14}$$

$$\tau(B^+)/\tau(B^0) = 1.09 \pm 0.05. \tag{15}$$

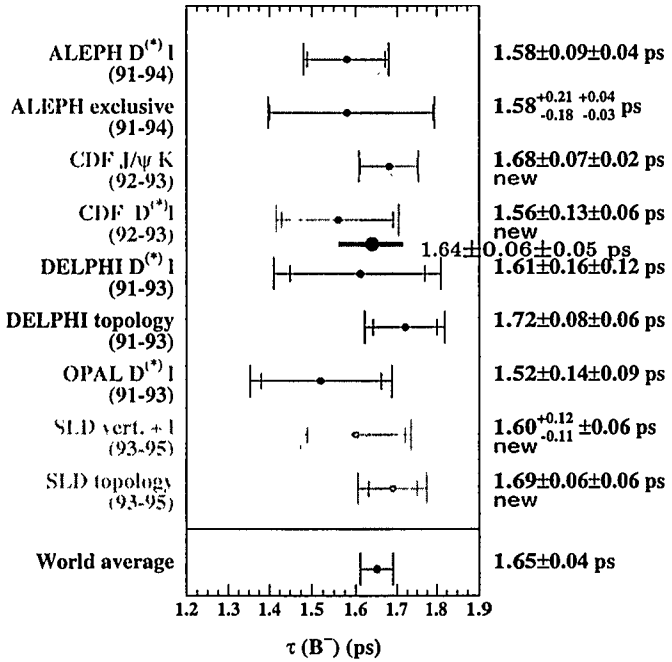


Figure 15: Comparison of the CDF B^+ lifetime measurements with other experiments.

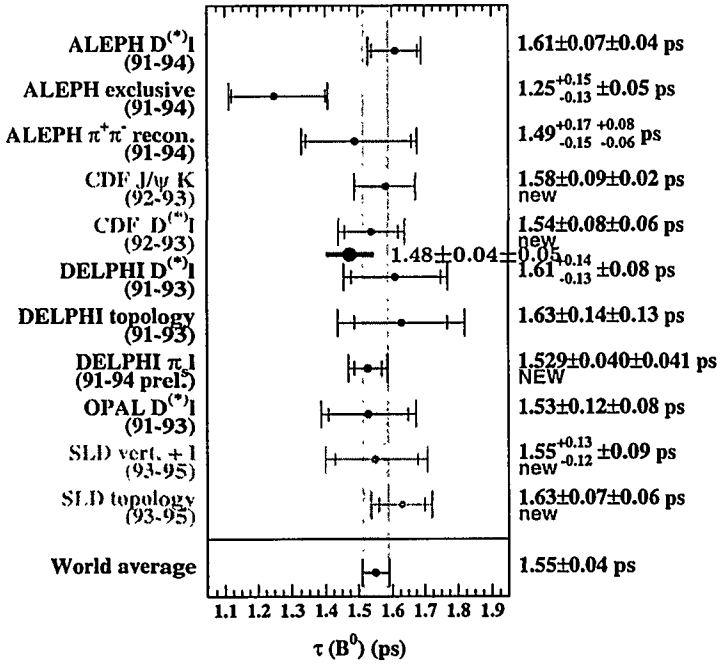


Figure 16: Comparison of the CDF B^0 lifetime measurements with other experiments.

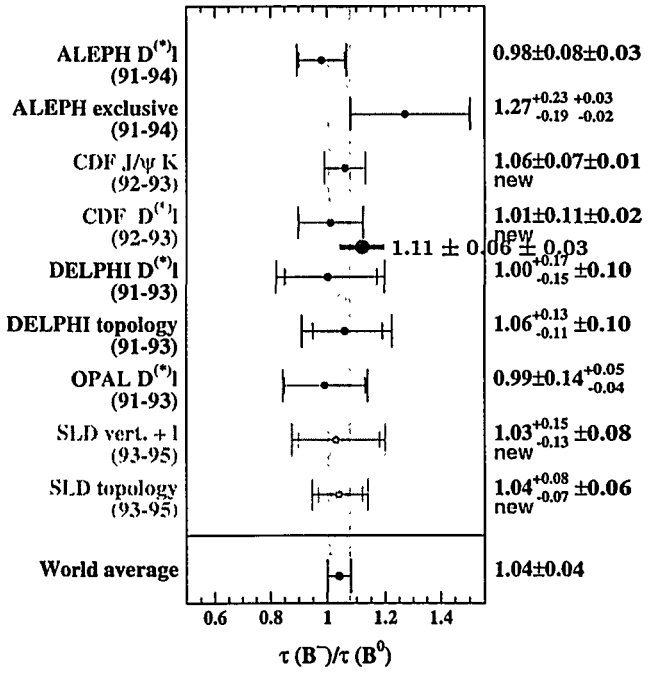


Figure 17: Comparison of the CDF $\tau(B^+)/\tau(B^0)$ lifetime ratio measurements with other experiments.

The error is the sum of statistical and systematic errors, where the correlated systematic errors are taken into account. It appears that the lifetime ratio measurement is different from unity by almost two standard deviations.

3.1.4 B Lifetimes: B^0 Meson

The lifetime of the B_S^0 meson is measured at CDF using the semileptonic decay $B_S^0 \to D_S^- \ell^+ \nu X$, where the D_S^- is reconstructed through its decay mode $D_S^- \to \phi\pi^-$, $\phi \to K^+K^-$. The analysis starts again with the single lepton (e, μ) trigger data searching for $D_S^- \to \phi\pi^-$ candidates in a cone around the lepton. The D_S^- candidates are intersected with the lepton to find the B_S^0 decay vertex from where the analysis follows the description of the B-lifetime measurement using partially reconstructed B mesons (see Sec. 3.1.2). A signal of (254 ± 21) $D_S^- \ell^+$ candidates is found as shown in Fig. 18(a), where the $\phi\pi^-$ invariant mass distribution for right sign $D_S^- \ell^+$ combinations is plotted. The shaded histogram shows the wrong sign $D_S^- \ell^-$ distribution. Using these events, the B_S^0 meson lifetime is determined to be

$$\tau(B_S^0) = (1.37\ ^{+0.14}_{-0.12} \pm 0.04)\ ps. \qquad (16)$$

A comparison of the CDF B_S^0 lifetime measurement with other experiments at LEP and SLC can be found in Fig. 18(b).

3.1.5 B Lifetimes: Λ^0 Baryon

The analysis principle for the Λ_b^0 lifetime measurement is very similar to the B_S^0 lifetime analysis at CDF. The Λ_b^0 baryon is reconstructed through the semileptonic decay $\Lambda_b^0 \to \Lambda_c^+ \ell^- \nu X$, with the subsequent decay $\Lambda_c^+ \to pK^-\pi^+$. The analysis again uses the single lepton trigger data, searching for $\Lambda_c^+ \to pK^-\pi^+$ candidates in a cone around the lepton. The Λ_c^+ candidates are intersected with the lepton to find the Λ_b^0 decay vertex. A signal of (197 ± 25) Λ_c^+ candidates is obtained as shown in Fig. 19(a), where the $pK\pi$ invariant mass distribution for right sign $\Lambda_c^+ \ell^-$ combinations is plotted. The shaded histogram shows the wrong sign $\Lambda_c^- \ell^-$ distribution. Using these events, the Λ_b^0 lifetime is determined to be

$$\tau(\Lambda_b^0) = (1.32 \pm 0.15 \pm 0.07)\ ps\,. \qquad (17)$$

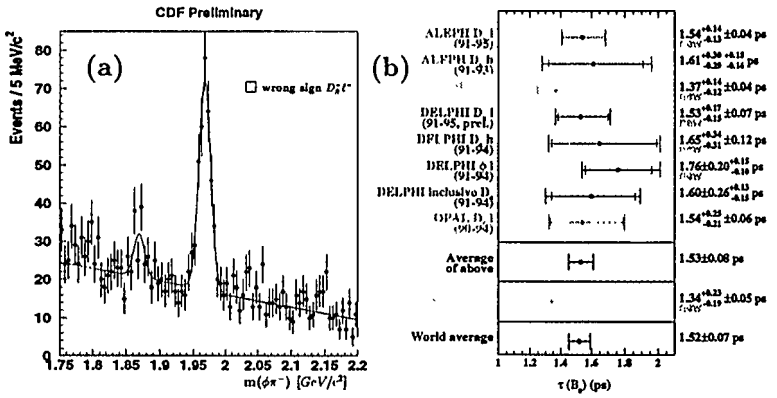


Figure 18: B_S^0 lifetime measurement: (a) Invariant $\phi\pi^-$ mass distribution for right sign $D_S^- \ell^+$ combinations. The shaded histogram shows the wrong sign distribution. (b) Comparison of the CDF B_S^0 lifetime measurement with other experiments.

A comparison of the CDF Λ_b^0 lifetime measurement with LEP results can be seen in Fig. 19(b). The CDF Λ_b^0 lifetime is competitive with the LEP measurements in precision, but tends to be longer compared to the LEP results.

3.1.6 B Lifetimes: Summary

A summary of the B lifetime measurements at CDF is given in Table 7. As we have seen, CDF's B lifetime results are very competitive with the LEP and SLC measurements where a precision of a few percent is reached. Although CDF's measurement of the B^+/B^0 lifetime ratio appears to be different from unity by almost two standard deviations, the precision is still not yet sufficient to distinguish between theoretical approaches. The Λ_b^0 lifetime lies closer to the B^0 lifetime at CDF with a ratio of $\tau(\Lambda_b^0)/\tau(B^0) = 0.87 \pm 0.11$, while the LEP experiments report a ratio of 0.78 ± 0.04 (Ref. 33). Theory favors the value for this ratio to be closer to 0.9–1.0 in good agreement with the CDF measurement.

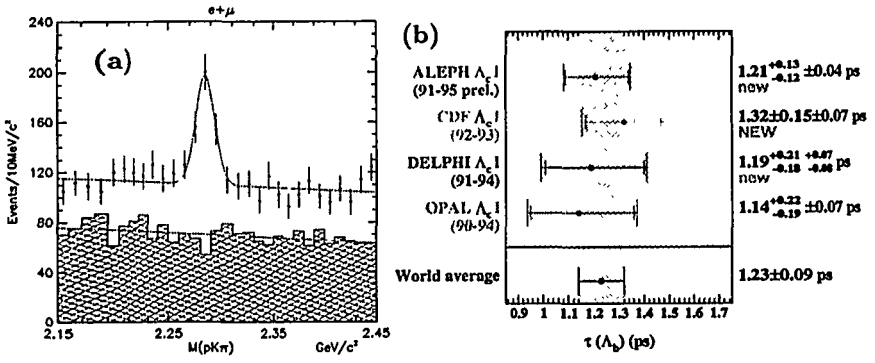


Figure 19: Λ_b^0 lifetime measurement: (a) Invariant $pK\pi$ mass distribution for right sign $\Lambda_c^+\ell^-$ combinations. The shaded histogram shows the wrong sign distribution. (b) Comparison of the CDF Λ_b^0 lifetime measurement with LEP results.

3.2 $B\bar{B}$ Oscillations

In the Standard Model, $B\bar{B}$ mixing occurs through the electroweak box diagram, where the dominant contribution is through the top quark loop. The size of the oscillation is expressed in terms of the mixing parameter $x = \Delta m/\Gamma$, where Δm is the difference in mass between the two B-meson eigenstates and Γ refers to the average lifetime of both B states $\tau_B = \hbar/\Gamma$. For a beam initially pure in B^0 mesons (at $t = 0$), the numbers of B^0 and $\bar{B}^0$ mesons at proper time t, $N(t)_{B^0\to B^0}$ and $N(t)_{B^0\to\bar{B}^0}$, respectively, are given by:

$$N(t)_{B^0\to B^0} = \frac{1}{2\tau_B} e^{-t/\tau_B}(1 + \cos\Delta m_d\, t) \qquad (18)$$

CDF B-Lifetime Summary		
$\tau(B^+)$	=	(1.66 ± 0.05) ps
$\tau(B^0)$	=	(1.52 ± 0.06) ps
$\tau(B^+)/\tau(B^0)$	=	1.09 ± 0.05
$\tau(B_s^0)$	=	(1.37 ± 0.14) ps
$\tau(\Lambda_b^0)$	=	(1.32 ± 0.17) ps

Table 7: Summary of CDF B-hadron lifetime results.

$$N(t)_{B^0\to\bar{B}^0} = \frac{1}{2\tau_B} e^{-t/\tau_B}(1 - \cos\Delta m_d\, t). \qquad (19)$$

Measurements of the frequencies of B^0 and B_s^0 oscillations can potentially constrain the magnitudes of the CKM matrix elements V_{td} and V_{ts}, where in the ratio of $\Delta m_d/\Delta m_s$ several theoretical uncertainties cancel out

$$\frac{\Delta m_d}{\Delta m_s} = \frac{m_{B^0}}{m_{B_s^0}} \frac{\eta_{B^0}^{\rm QCD}}{\eta_{B_s^0}^{\rm QCD}} \frac{f_{B^0}^2 B_{B^0}}{f_{B_s^0}^2 B_{B_s^0}} \frac{|V_{td}|^2}{|V_{ts}|^2}. \qquad (20)$$

Here, f_B is the weak B decay constant, B_B the bag parameter of the B meson, and $\eta^{\rm QCD}$ are QCD corrections which are of the order of one.

In general, a time-dependent mixing measurement requires the knowledge of the flavor of the B meson at production and at decay, as well as the proper decay time of the B meson. Experimentally, the flavor of the B meson is determined at the time of its decay from the observed decay products like the charge of the lepton from a semileptonic B decay. The flavor at production time can be determined in various ways, employing either the second b-flavored hadron in the event, or the charge correlation with particles produced in association with the B meson. We report about two recent time dependent $B\bar{B}$ mixing results from CDF, which exploit these two ways of tagging the B flavor at the origin.

3.2.1 $B\bar{B}$ Mixing in $e\mu$ Events

For this analysis, the $e\mu$ trigger data are used, where both leptons are assumed to come from the semileptonic decay of both b hadrons in the event: $b_1 \to eX$ and $b_2 \to \mu X$. This means the flavor of the B meson at decay is tagged by its semileptonic decay, while the semileptonic decay of the other b hadron in the event tags the B flavor at production. The requirement $m_{e\mu} > 5$ GeV/c^2 ensures that both leptons originate from two b hadrons and not from a sequential decay of one b hadron: $b \to c\ell_1 X$, with $c \to \ell_2 X$.

The principle of this analysis is to search for an inclusive secondary vertex associated with one of the leptons. The decay length of this vertex and the momenta of the tracks associated with the lepton provide an estimate of the $c\tau$ of the B meson. The boost resolution for this technique is about 21% for electrons and about 24% for muons. In order to search for an inclusive secondary vertex, a modified version of the SVX b-tagging algorithm, which was successfully used in the search for b tags in top quark events (see Sec. 2.5), has been used. This

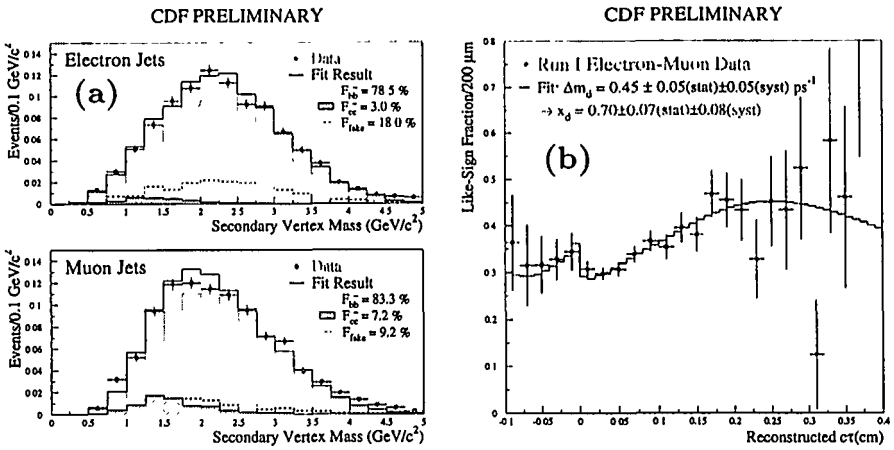


Figure 20: (a) Example of the determination of the sample composition in the $e\mu$ mixing analysis using the invariant mass of the secondary vertex. The fitted fractions from $b\bar{b}$, $c\bar{c}$, and fake events are shown. The terms "e Jet" and "μ Jet" indicate that the secondary vertex is associated with the electron or muon. In (b), the fit to the like-sign fraction versus $c\tau$ is displayed.

algorithm has been tuned for high efficiency near $c\tau = 0$, with the efficiency reaching a plateau of about 40% for $c\tau > 500$ μm according to a MC study.

The important task of this analysis is to determine the sample composition, the fraction of events which come from $b\bar{b}$ decays with respect to events from $c\bar{c}$ or background events with at least one fake lepton. We find to a good approximation that the fake electron events are a subset of the fake muon events due to the higher p_t cut. Other backgrounds arise from sequential $b \to c \to \ell$ decays. The sample composition has been estimated from several kinematic quantities, like the p_t^{rel} distribution or the invariant mass of the tagged secondary vertex. Here, p_t^{rel} is defined as the transverse momentum of the lepton with respect to the highest p_t track in a cone around the lepton. An example of the determination of the sample composition is shown in Fig. 20(a). The fitted fractions from $b\bar{b}$, $c\bar{c}$, and fake events are displayed. The final sample composition is given in Table 8, which shows that more than 80% of the events originate from $b\bar{b}$ decays.

Component	e Jet	μ Jet
Fake e with Real μ	$\leq 1\%$	$\leq 1\%$
Fake μ Fraction	$(15 \pm 4)\%$	$(7 \pm 3)\%$
$c\bar{c}$ events	$(2 \pm 2)\%$	$(4 \pm 3)\%$
$b\bar{b}$ events	$(83 \pm 5)\%$	$(89 \pm 4)\%$
Sequential e	$(8.8 \pm 1.3)\%$	$(7.9 \pm 1.2)\%$
Sequential μ	$(13.6 \pm 2.0)\%$	$(16.5 \pm 2.5)\%$

Table 8: Final sample composition of the $e\mu$ mixing analysis. The terms "e Jet" and "μ Jet" indicate that the secondary vertex is associated with the electron or muon. The sequential fractions are part of the $b\bar{b}$ component.

From a fit to the like-sign lepton fraction as a function of $c\tau$, the mixing frequency Δm_d is extracted as shown in Fig. 20(b). The fit includes components for direct and sequential b decays, $c\bar{c}$, and fake events. In about 16% of the events with a secondary vertex around one lepton, a secondary vertex is also found around the other lepton. These events enter the like-sign fraction distribution twice, and we allow for a statistical correlation between the two entries. The final fit result is

$$\Delta m_d = (0.45 \pm 0.05 \pm 0.05)\ ps^{-1}, \tag{21}$$

where the dominant systematic error arises from the uncertainty in the sample composition.

3.2.2 $B\bar{B}$ Mixing in $\ell D^{(*)}$ Events

For this analysis, B mesons are reconstructed through their semileptonic decays $B \to D^{(*)}\ell X$ (see also Sec. 3.1.2). The analysis starts with the single lepton trigger data and reconstructs $D^{(*)}$ meson candidates in a cone around the trigger electron or muon in the following channels:

$$\begin{aligned}
&\bar{B}^0 \to D^{*+}\ell^-\nu, \quad D^{*+} \to D^0\pi^+, \qquad D^0 \to K^-\pi^+,\\
&\qquad\qquad\qquad\qquad\qquad\qquad\quad D^0 \to K^-\pi^+\pi^+\pi^-,\\
&\qquad\qquad\qquad\qquad\qquad\qquad\quad D^0 \to K^-\pi^+\pi^0, \ (\pi^0 \text{ not reconstructed})\\
&\bar{B}^0 \to D^+\ell^-\nu, \quad D^+ \to K^-\pi^+\pi^+,\\
&B^- \to D^0\ell^-\nu, \quad D^0 \to K^-\pi^+ \qquad (\text{veto } D^{*+} \text{ candidates}) .
\end{aligned}$$

Tracks with impact parameters significantly displaced from the primary vertex are selected in order to decrease combinatorial backgrounds. The signals are identified

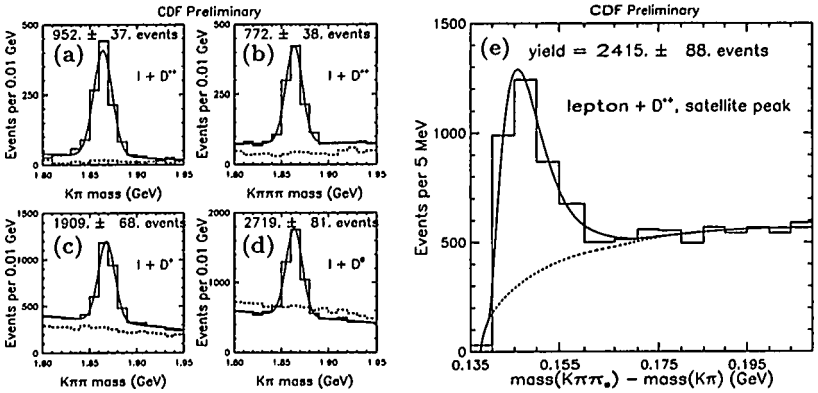


Figure 21: Invariant mass distribution of $D^{(*)}$ candidates used in the B-mixing analysis using partially reconstructed $B \to D^{(*)}\ell X$ decays: (a) ℓD^{*+} with $D^{*+} \to D^0\pi^+$, $D^0 \to K^-\pi^+$, (b) ℓD^{**+} with $D^{**+} \to D^0\pi^+$, $D^0 \to K^-\pi^+\pi^+\pi^-$, (c) ℓD^+ with $D^+ \to K^-\pi^+\pi^+$, (d) ℓD^0 with $\ell D^0 \to K^-\pi^+$, where the D^0 is not from a D^{*+}, and (e) ℓD^{**+} with $D^{**+} \to D^0\pi^+$, $D^0 \to K^-\pi^+\pi^0$, where the π^0 is not reconstructed.

as peaks in the invariant mass spectra of the charm decay products as shown in Fig. 21 for the different $D^{(*)}$ decay modes.

The $D^{(*)}$ candidates are intersected with the lepton to find the B decay vertex. Since the B meson is not fully reconstructed, its $c\tau_B$ cannot be directly obtained. The boost of the B meson is determined from the observed decay products and a $\beta\gamma$ correction is applied as obtained from a Monte Carlo simulation.

In order to tag the B flavor at production, we use a "same side tagging" (SST) algorithm, which exploits the correlation between the B flavor and the charge of tracks from either the fragmentation process or B^{**} resonances.[34] In this analysis, no attempt is made to differentiate the sources of correlated pions. To study the correlation between the flavor of the B meson and the charged particles produced in association with it, we consider all tracks that are within an η-ϕ cone of radius 0.7 centered around the direction of the B candidate. Since the B meson is only partially reconstructed, we approximate this direction with the momentum sum of the lepton and charm hadron.

The tracks considered as tags should be consistent with the hypothesis that they originate from the fragmentation chain or the decay of B^{**} mesons, i.e., that they originate from the primary vertex of the event. All tracks with transverse momentum $p_t > 0.4$ GeV/c are therefore required to satisfy $d_0/\sigma_{d_0} < 3$, where d_0 is the distance of closest approach of the track trajectory to the estimated B-production position, and σ_{d_0} is the estimated error on this quantity.

String fragmentation models indicate that the velocity of the fragmentation particles, that we seek for our tag, is close to the velocity of the B meson. Similarly, pions from B^{**} decays should also have a velocity that is close to the velocity of the B meson. In particular, the relative-transverse momentum ($p_t^{\rm rel}$) of the particle with respect to the combined momentum of the B momentum plus particle momentum, should be small. Of the candidate tracks, we select as the tag the track that has the minimum component of momentum $p_t^{\rm rel}$ orthogonal to the momentum sum of that track, the lepton, and the D meson. The efficiency for finding such a tag is about 72% for this algorithm.

Since we know the flavor of the B meson at decay from the $D^{(*)}\ell$ signature, we compare the number of right-sign (N_{RS}) correlations to the number of wrong-sign (N_{WS}) tags as a function of $c\tau$. For the B^0 meson, we expect the asymmetry $A(t)$ to be:

$$A(t) = \frac{N_{RS}(t) - N_{WS}(t)}{N_{RS}(t) + N_{WS}(t)} = D \cdot \cos(\Delta m_d\, t), \tag{22}$$

where D is the dilution of the same side tagging algorithm. D is also often expressed in terms of the mistag fraction w as $D = 1 - 2w$. In our analysis, we fit for both Δm_d and D.

To obtain the asymmetry for B^0 and B^+ mesons, we correct for the fact that each $D^{(*)}\ell$ signal has contributions from both neutral and charged B mesons via D^{**} decays. We correct for this cross talk by performing a fit bin by bin in $c\tau$. The inputs to the fit are the raw asymmetries as measured in each sample for a given $c\tau$ bin, and parameters describing the D^{**} composition in semileptonic B decays. We fit the corrected B^0 asymmetry as a function of $c\tau$ to a cosine convoluted with the $c\tau$ resolution function and extract the mixing frequency Δm_d as well as the dilution D of the same side tagging algorithm as shown in Fig. 22(a). We also determine the asymmetry for the charged B meson, which is flat in $c\tau$ as expected. We measure

$$\Delta m_d = (0.45 \pm 0.06 \pm 0.03)\ ps^{-1}, \tag{23}$$

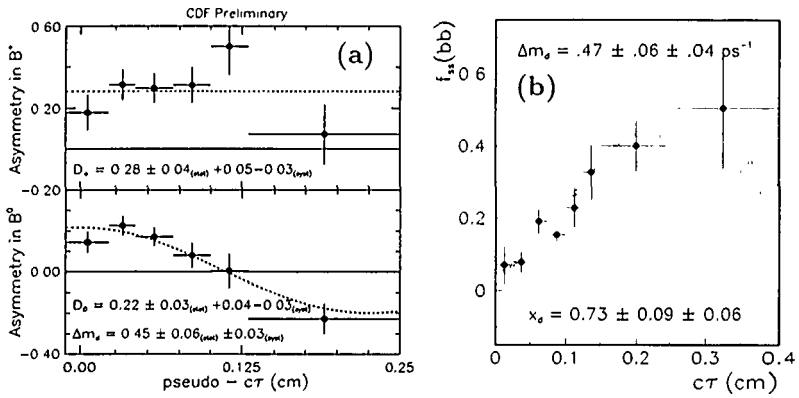


Figure 22: (a) Time-dependent asymmetry for the $D^{(*)}\ell$ mixing analysis, where the top plot shows the measured asymmetry for B^+ while the bottom plot represents the asymmetry for B^0. (b) Fitted like-sign fraction versus $c\tau$ for a B-mixing analysis using a jet charge and soft lepton tag.

and find $D = 0.22 \pm 0.04^{+0.04}_{-0.03}$. We also determine the effective tagging efficiency to be $\varepsilon D^2 = (3.4 \pm 1.0^{+1.2}_{-0.9})\%$. The dominant systematic error arises from the uncertainty in the fraction of D^{**} in semileptonic B decays.

In summary, we have reported two measurements of Δm_d at CDF using $D^{(*)}\ell$ events with a same side tag as well as $e\mu$ dilepton events. There are more time-dependent $B\bar{B}$ oscillation measurements in preparation at CDF, like a mixing analysis using a soft lepton tag (see Sec. 2.5) and a jet charge tag as shown in Fig. 22(b). The result from this analysis is

$$\Delta m_d = (0.47 \pm 0.06 \pm 0.04)\ ps^{-1}\ . \qquad (24)$$

Since there is an event overlap of about 10% between this analysis and the $e\mu$ analysis, a combined CDF average has not yet been determined, but CDF's mixing results start to become competitive with the LEP measurements.[35]

4 A Brief Look to the Future

In Run I, the luminosity of the Tevatron was limited by the antiproton current. The Fermilab accelerator complex is undergoing an upgrade to produce an order of magnitude higher luminosities in the Tevatron. The largest change will be to replace the Main Ring with the new Main Injector, which will be housed in a new tunnel. The Main Injector will provide higher proton intensity onto the antiproton production target, and larger aperture for the antiproton transfer into the Tevatron. After the completion and commissioning of the Main Injector, the Tevatron is scheduled to deliver luminosity again in the summer of 1999. The center-of-mass energy will then be at 2.0 TeV. Luminosities of $2.0 \cdot 10^{32}\ cm^{-2}s^{-1}$ will be reached yielding an integrated luminosity of 2 fb^{-1} delivered to the collider experiments within two years. The physics projections for Run II presented here assume 2 fb^{-1} of integrated luminosity. In addition to the Tevatron upgrade, the CDF and DØ experiments will undergo major detector upgrades, which are described in detail elsewhere.[36,37]

4.1 Top Physics in Run II

In Run II, both collider detectors will be equipped with new and improved silicon vertex detectors which will, for example, enhance the efficiency to detect top decays. In addition, the Tevatron's center-of-mass energy will be at 2.0 TeV, which will increase the top quark production cross section by 40%. The estimated yield per experiment will be about 160 dilepton events, 990 lepton plus four-jet events with one or more b tags, and for the top mass measurement, about 240 lepton plus four-jet events where both b jets are tagged. This will result in a statistical uncertainty on the top quark mass measurement of 1–2 GeV/c^2. The top production cross section will be known with a precision of better than 10%. In addition, single top production can be studied, top polarization measurements can be performed, and rare top decays will be searched for. A more detailed overview of top quark physics in Run II can be found in Ref. 38.

4.2 B Physics in Run II

In this section, we concentrate on reviewing the future of B physics at CDF by summarizing the prospects of measuring CP violation in Run II. The B-physics goal is to measure the CP asymmetry in $B^0 \to J/\psi K^0_S$ and $B^0 \to \pi^+\pi^-$, determining $\sin 2\beta$ and $\sin 2\alpha$, respectively. CDF plans to also look for CP violation in $B_S \to D_S K$ and $B \to DK$, probing $\sin 2\gamma$.

CDF has the advantage of being an existing experiment that took plenty of data in Run I. We can use these data to study the ingredients for a future CP violation measurement, e.g., in $B^0 \to J/\psi K^0_S$. One input is the knowledge of the expected number of $J/\psi K^0_S$ events, which can be extrapolated from the $J/\psi K^0_S$ yield in CDF's current data. The second ingredient is the knowledge of the B flavor at production. For this purpose, CDF studies several B flavor tagging methods at a hadron collider environment. The figure of merit to compare flavor tagging algorithms is the effective tagging efficiency εD^2, where ε is the efficiency of how often a flavor tag is applicable and D is the dilution $D = (N_{RS} - N_{WS})/(N_{RS} + N_{WS}) = 1 - 2w$. Here, N_{RS} and N_{WS} are the numbers of right and wrong sign tags, while w is the mistag fraction (see also Sec. 3.2.2).

Figure 23 shows the invariant $J/\psi K^0_S$ mass distribution from CDF's current data corresponding to about 110 pb^{-1}. About 240 signal events with a signal-to-noise ratio better than 1:1 are observed. This is currently the world's largest sample of $B^0 \to J/\psi K^0_S$ and serves as proof that $B^0 \to J/\psi K^0_S$ decays can be fully reconstructed in a hadron collider environment in a well understood way.

4.2.1 B Flavor Tagging Studies in Run I

Several B flavor tagging methods are studied with CDF data. One is referred to as "same side tagging" (SST) which is described in more detail in Sec. 3.2.2. This method exploits charge correlations between B mesons and charged particles produced in the fragmentation of the b quarks. Such correlations are expected to arise from particles produced in the fragmentation chain and from decays of the $L = 1$ B mesons (the B^{**} mesons).[34] Another way of tagging the flavor of a B meson at production is to exploit the flavor of the other B meson in the event. This can be done through a B semileptonic decay (lepton tagging) or by counting the charge of the other b jet (jet-charge tagging). CDF has preliminary results on the effective tagging efficiency of these three methods.

Using a high statistics sample of partially reconstructed B mesons from ℓD^0 (B^+ signature) and $\ell D^+/\ell D^{*+}$ (B^0 signature) combinations, charge correlations between the B candidate and tracks in its vicinity are studied as detailed in Sec. 3.2.2. In the case of charged B mesons, we measure $\varepsilon D^2 = (5.7 \pm 1.5^{+2.0}_{-1.2})\%$ ($D = (28 \pm 4^{+5}_{-3})\%$) for the same side tagging algorithm. For the neutral B meson, we obtain $\varepsilon D^2 = (3.4 \pm 1.0^{+1.2}_{-0.9})\%$ with $D = (22 \pm 3^{+4}_{-3})\%$. The proof that this

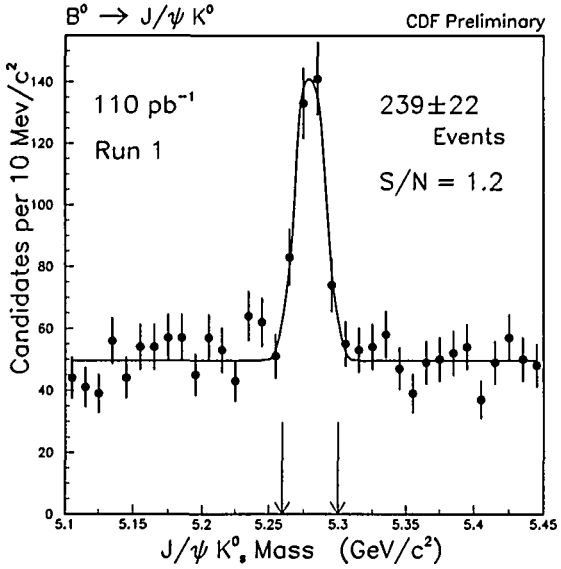


Figure 23: Run I signal of $B^0 \to J/\psi K^0_S$ at CDF.

tagging method actually works is shown in Fig. 22(a), where the asymmetry of right minus wrong sign tags normalized to the sum of both is plotted versus the $c\tau$ of the B meson. The top plot is for B^+ candidates and shows a flat behavior as expected. The bottom plots shows the same distribution for B^0 mesons and exhibits an oscillatory behavior as expected from $B\bar{B}$ mixing. This means applying same side tagging to a sample of partially reconstructed B meson results in a measurement of time-dependent B^0 mixing. We also studied same side tagging with a sample of fully reconstructed $B \to J/\psi K^{(*)}$ decays. The results of $\varepsilon D^2 = (4.0 \pm 1.9)\%$ ($D = (33 \pm 8)\%$) and $\varepsilon D^2 = (1.5 \pm 3.0)\%$ ($D = (19 \pm 19)\%$) for B^+ and B^0 mesons, respectively, are somewhat limited by statistics.

CDF also studied opposite side lepton tagging and obtains an effective tagging efficiency of $\varepsilon D^2 = (0.6 \pm 0.1)\%$ for soft muon tagging and $\varepsilon D^2 = (0.3 \pm 0.1)\%$ for soft electron tagging. The tagging algorithms are similar to the ones used in the top quark search as described in Sec. 2.5. The preliminary result for the effective tagging efficieny of jet charge tagging is $(1.0 \pm 0.3)\%$, which makes use of information from the silicon vertex detector. The proof that jet charge and soft lepton tagging actually works is shown in Fig. 22(b), where the time-dependent B-mixing measurement using these two tags is displayed. Combining the existing measurements on B flavor tagging from Run I results in an effective tagging efficiency of $\approx 3.4\%$.

4.2.2 CP Asymmetry in $B^0 \to J/\psi K^0$: $\sin 2\beta$

For the measurement of $\sin 2\beta$ in $B^0 \to J/\psi K^0_S$, CDF expects about 15,000 $J/\psi K^0_S$ events. This event number will be obtained with a lower muon trigger threshold of $p_t > 1.5$ GeV/c compared to about 2.0 GeV/c in Run I, improved muon coverage, and by also triggering on $J/\psi \to e^+e^-$. The effective tagging efficiencies are expected to improve with the upgraded detector. We expect $\varepsilon D^2 \approx 2\%$ for lepton tagging due to a better coverage for the lepton identification. For same side tagging, we expect $\varepsilon D^2 \approx 2\%$ from a cleaner selection of fragmentation tracks with SVX II. Finally, for jet charge tagging, we expect $\varepsilon D^2 \approx 3\%$ from an improved purity of the algorithm with three-dimensional vertexing and the extended coverage of SVX II. Considering the overlap of all three tags by combining them, we expect a total εD^2 of about 5.5% resulting in an uncertainty on $\sin 2\beta$ of $\Delta \sin 2\beta = 0.09$.

4.2.3 CP Asymmetry in $B^0 \to \pi^+\pi$: $\sin 2\alpha$

The key to measuring the CP asymmetry in $B^0 \to \pi^+\pi^-$ is to trigger on this decay mode in hadronic collisions. CDF plans to do this with a three-level trigger system. On Level 1, two oppositely charged tracks with $p_t > 2$ GeV/c found with a fast track processor yield an acceptance rate of about 16 kHz. This will be reduced to about 20 Hz on Level 2 using impact parameter information ($d > 100$ μm). On Level 3, the full event information is available, further reducing the trigger rate to about 1 Hz. With this trigger, we expect about 10,000 $B^0 \to \pi^+\pi^-$ events in 2 fb^{-1}. Assuming the same effective tagging efficiency of 5.5%, we expect an uncertainty on $\sin 2\alpha$ of $\Delta \sin 2\alpha = 0.10$. Backgrounds from $B \to K\pi$ and $B \to KK$ decays can be extracted from the untagged signal by making use of the invariant mass distribution as well as CDF's dE/dx capability in the central tracking chamber.

4.2.4 CP Asymmetry in $B_S \to D_S K$: $\sin 2\gamma$

The CP asymmetry in $\sin 2\gamma$ completes the test of the unitarity triangle. The angle γ can be probed via the decay $B^0_S \to D^-_S K^+$ and $D^+_S K^-$, where both the mixed and the unmixed amplitudes can decay to the same final $D^+_S K^-$ state. The interference between both amplitudes results in the weak phase γ, but also in a relative QCD phase which is expected to be small but a priori unknown. This measurement requires an all hadronic trigger with similar requirements as for $B^0 \to \pi^+\pi^-$. We expect an overall efficiency times acceptance of $\approx 3 \cdot 10^{-4}$. Because of rapid B^0_S oscillations, a time-dependent analysis is required, but only a small sample of tagged events is expected at CDF in Run II.

The CP asymmetry in $\sin 2\gamma$ can also be explored via $B \to DK$. In this case, the decays are self-tagging and a time-integrated analysis can be performed, but the theoretical uncertainties are large. Thus, performing a measurement of $\sin 2\gamma$ through both modes will be a challenge at CDF in Run II.

5 Conclusion

In this article, we have reviewed recent heavy flavor physics results from the Tevatron $p\bar{p}$ collider at Fermilab. We summarized the status of top quark physics at CDF and DØ. The top production cross section has been measured to be

$$\sigma_{t\bar{t}} = (6.4^{+1.3}_{-1.2})\ \mathrm{pb}\ ,$$

and the top quark mass is known with a precision of

$$m_{\mathrm{top}} = (175.0 \pm 3.9 \pm 4.5)\ \mathrm{GeV}/c^2.$$

We also discussed recent B physics results from the CDF Collaboration. We summarized CDF's B hadron lifetime measurements, which are very competitive with the LEP and SLC results, and discussed latest time-dependent $B\bar{B}$ mixing results from CDF.

We also reviewed future prospects of top and B physics at the Tevatron. In Run II, starting in 1999, both experiments will measure the top quark mass with a statistical uncertainty of 1–2 GeV/c^2. The top production cross section will be known with a precision of better than 10%. The future prospects of B physics at CDF will concentrate on the discovery of CP violation in the B system. CDF expects to measure $\sin 2\beta$ in $B^0 \to J/\psi K^0_S$ with a precision of $\Delta \sin 2\beta = 0.09$. CDF will also search for CP violation in $B^0 \to \pi^+\pi^-$ and expects to measure $\sin 2\alpha$ with a precision of $\Delta \sin 2\alpha = 0.10$. A measurement of $\sin 2\gamma$ will be challenging in Run II.

Acknowledgments

It is a pleasure to thank all friends and colleagues from the CDF and DØ Collaborations for their excellent work and their help in preparing this talk. Special thanks go to L. Galtieri, J. Lys, and B. Winer. A constant source of inspiration and support is my wife Ann, who I would like to thank for her continuous understanding about the life of a physicist.

I would like to thank the CDF and DØ technical support staff at all CDF and DØ institutions for their hard work and dedication. I also thank the Fermilab Accelerator Division for their hard and successful work in commissioning the machine for this physics run. The CDF and DØ experiments are supported by the U.S. Department of Energy; the U.S. National Science Foundation; the Istituto Nazionale di Fisica Nucleare, Italy; the Ministry of Science, Culture, and Education of Japan; the Natural Sciences and Engineering Research Council of Canada; the National Science Council of the Republic of China; the Commissariat à L'Energie Atomique in France; the Ministry for Atomic Energy and the Ministry of Science and Technology Policy in Russia; CNPq in Brazil; the Departments of Atomic Energy and Science and Education in India; Colciencias in Colombia; CONA-CyT in Mexico; the Ministry of Education, Research Foundation and KOSEF in Korea; and the A. P. Sloan Foundation.

I gratefully acknowledge the organizers of this inspiring meeting which was a genuine pleasure to attend. I am sorry for the late submission of this manuscript but as Albert Einstein already pointed out, time is relative: *"Put your hand on a hot stove for a minute, and it seems like an hour. Sit with a pretty girl for an hour, and it seems like a minute. THAT's relativity."*

References

[1] S. W. Herb *et al.*, Phys. Rev. Lett. **39**, 252 (1977).

[2] C. Berger *et al.*, (PLUTO), Phys. Lett. B **76**, 243 (1978);
C. W. Darden *et al.*, (DASP), Phys. Lett. B **76**, 246 (1978).

[3] S. Behrends *et al.*, (CLEO), Phys. Rev. Lett. **50**, 881 (1983).

[4] W. Behrends *et al.*, (JADE), Phys. Lett. B **146**, 437 (1984).

[5] H. Albrecht *et al.*, (ARGUS), Phys. Lett. B **192**, 245 (1987).

[6] Particle Data Group, Phys. Rev. D **54**, 1 (1996).

[7] D. P. Barber *et al.*, (MARK-J), Phys. Lett. B **85**, 463 (1979);
Phys. Rev. Lett. **44**, 1722 (1980);
C. Berger *et al.*, (PLUTO), Phys. Lett. B**86**, 413 (1979);
Phys. Rev. Lett. **45**, 1533 (1980);
W. Bartel *et al.*, (JADE), Phys. Lett. B **88**, 171 (1979); B **89**, 136 (1979);
Phys. Lett. B **99**, 277 (1981);
R. Brandelik *et al.*, (TASSO), Phys. Lett. B **133**, 499 (1983);
B. Adeva *et al.*, (MARK-J), Phys. Rev. Lett. **50**, 799 (1983); **51**, 433 (1983);
Phys. Lett. B **152**, 439 (1985); Phys. Rev. D **34**, 681 (1986);

M. Althoff *et al.*, (TASSO), Phys. Lett. B **138**, 441 (1984);
Z. Phys. C **22**, 307 (1984);
H. J. Behrend *et al.*, (CELLO), Phys. Lett. B **144**, 297 (1984).

[8] H. Yoshida *et al.*, (VENUS), Phys. Lett. B **198**, 570 (1987);
H. Sagawa *et al.*, (AMY), Phys. Rev. Lett. **60**, 93 (1988);
I. Adachi *et al.*, (TOPAZ), Phys. Rev. Lett. **60**, 97 (1988);
S. Igarashi *et al.*, (AMY), Phys. Rev. Lett. **60**, 2359 (1988);
K. Abe *et al.*, (VENUS), Phys. Lett. B **234**, 382 (1990).

[9] G. S. Abrams *et al.*, (MARK II), Phys. Rev. Lett. **63**, 2447 (1989).

[10] M. Z. Akrawy *et al.*, (OPAL), Phys. Lett. B **236**, 364 (1990);
D. Decamp *et al.*, (ALEPH), Phys. Lett. B **236**, 511 (1990);
P. Abreu *et al.*, (DELPHI), Phys. Lett. B **242**, 536 (1990);
O. Adriani *et al.*, (L3), Phys. Rep. **236**, 1 (1993).

[11] G. Arnison *et al.*, (UA1), Phys. Lett. B **147**, 493 (1984).

[12] C. Albajar *et al.*, (UA1), Z. Phys. C **37**, 505 (1988).

[13] T. Akesson *et al.*, (UA2), Z. Phys. C **46**, 179 (1990).

[14] F. Abe *et al.*, (CDF), Phys. Rev. Lett. **64**, 174 (1990).

[15] F. Abe *et al.*, (CDF), Phys. Rev. Lett. **68**, 447 (1992);
Phys. Rev. D **45**, 3921 (1992).

[16] S. Abachi *et al.*, (DØ), Phys. Rev. Lett. **72**, 2138 (1994).

[17] F. Abe *et al.*, (CDF), Phys. Rev. Lett. **73**, 225 (1994).

[18] F. Abe *et al.*, (CDF), Phys. Rev. D **50**, 2966 (1994).

[19] F. Abe *et al.*, (CDF), Phys. Rev. Lett. **74**, 2626 (1995).

[20] S. Abachi *et al.*, (DØ), Phys. Rev. Lett. **74**, 2632 (1995).

[21] F. Abe *et al.*, (CDF), Nucl. Instrum. Methods A **271**, 387 (1988), and references therein.

[22] D. Amidei *et al.*, (CDF), Nucl. Instrum. Methods A **350**, 73 (1994).

[23] S. Abachi *et al.*, (DØ), Nucl. Instrum. Methods A **338**, 185 (1994), and references therein.

[24] E. Laenen, J. Smith, and W. L. Van Neerven, Nucl. Phys. B **369**, 543 (1992);
Phys. Lett. B **321**, 254 (1994).

[25] P. Nason, S. Dawson, and R. K. Ellis, Nucl. Phys. B **303**, 607 (1988).

[26] E. L. Berger and H. Contopanagos, Phys. Rev. D **54**, 3085 (1996).

[27] S. Catani *et al.*, Phys. Lett. B **378**, 329 (1996).

[28] N. Cabibbo, Phys. Rev. Lett. **10**, 531 (1963);
M. Kobayashi and T. Maskawa, Prog. Theor. Phys. **49**, 652 (1973).

[29] C. Albajar *et al.*, (UA 1), Phys. Lett. B **186**, 247 (1987);
Phys. Lett. B **256**, 221 (1991); erratum: ibid, B **262**, 497 (1991).

[30] S. Abachi *et al.*, (DØ), Phys. Rev. Lett. **74**, 3548 (1995);
Phys. Lett. B **370**, 239 (1996).

[31] I. I. Bigi, Nuovo Cim. A **109**, 713 (1996).

[32] M. Neubert, Int. J. Mod. Phys. A **11**, 4173 (1996).

[33] J. D. Richman, in *Proceedings of the 28th International Conference on High Energy Physics*, 25-31 July 1996, Warsaw, Poland.

[34] M. Gronau, A. Nippe, and J. Rosner, Phys. Rev. D **47**, 1988 (1993).

[35] L. Gibbons, in *Proceedings of the 28th International Conference on High Energy Physics*, 25-31 July 1996, Warsaw, Poland.

[36] The CDF Collaboration, FERMILAB-Pub-96/390-E (1996).

[37] The DØ Collaboration, PAC-Report, Sept. 1996.

[38] Report from the TeV2000 Study Group, FERMILAB-Pub-96/082-E (1996).

NEW ACCURATE IDEAS ON FLAVOR FORMATION IN HADRONIZATION AND CONNECTIONS TO QCD

C. D. Buchanan and Sebong Chun
UCLA, Los Angeles, CA 90024

Presented by C. D. Buchanan

ABSTRACT

Our work strongly suggests a paradigm shift in understanding flavor creation within relativistic string approaches, a paradigm shift to a viewpoint in which suppression of heavy particle formation (kaon, η, ρ, ϕ, proton, Λ, etc.) predominantly comes directly from the final state hadronic mass, not from the virtual $q\bar{q}$ production level (s/u, qq/q, ...) nor from the hadronic formation level (vector/all, ...). Our predictions are especially clean and accurate for the production of various flavored mesons, the most fundamental and elementary tests of colorfield behavior. Our approach also forms an excellent "platform" for future understanding of baryon formation, P_T effects, etc. The central feature of our approach is a simple *Event Weight Function* which, on the one hand, leads with very few assumptions to predictions agreeing quite well with e^+e^- hadronization data, and on the other hand, connects persuasively to strong-coupled soft nonperturbative QCD and forms a "target" for calculations within this regime.

© 1996 by C. D. Buchanan.

1 Introduction

It is commonly believed that QCD may well be the appropriate underlying theory for the "hadronization process" (how hadrons are produced). Hadronization can occur in many different arenas: hadron-hadron interactions, lepton-hadron interactions, etc. The cleanest arena in which to study it is electron-positron interactions in which the electroweak annihilation creates an almost asymptotically free initial quark-antiquark pair at very large Q^2, with a QCD colorfield emerging between the pair as they separate. The system then evolves from its initial condition, in which perturbative QCD can be used to calculate intermediate-state gluon emission, into a very soft low-Q^2 nonperturbative regime in which the hadrons are finally created. The most fundamental and elementary testing ground for hadronization ideas is meson formation and distributions.

The conceptual path from QCD to accurate predictions of e^+e^- data is sketched in Fig. 1.

The central feature for our UCLA approach is an *Event Weight Function* (dW_f) which can be written for any final state of specified hadrons—that is, where the flavor (and, therefore, mass) and three-momentum of each hadron is specified—and which provides the probability of that specific event occurring relative to other possible final states. The nomenclature of such an event is shown in Fig. 2.

In our present view, we now conceptualize the path as moving logically from QCD to dW_f to dP_1 (the fragmentation function for an "outside-in, one-hadron-at-a-time" implementation) to comparisons with data (see Fig. 1). However, historically, quite the reverse is true: We first noted in 1987 (Ref. 1) that if the Lund Symmetric Fragmentation Function[2,3]

$$f(z, P_{T_h}^2) = N \frac{(1-z)^a}{z} e^{-b\left(m_h^2 + P_{T_h}^2\right)/z} \tag{1}$$

was used as a hadronic production density (i.e., with constant normalization N for all hadrons), then the predicted rates agreed rather well with measured ones. In this approach, the suppression of heavy hadrons arose from the $\exp(-bm_H^2/z)$ factor rather than from suppression factors such as s/u and Vector/All as used, for example, in the Lund implementation. After this initial phenomenological success, we then began, with some guidance from the Lund group, to develop the idea and form of the *Event Weight Function*[4] which not only leads to the idea of

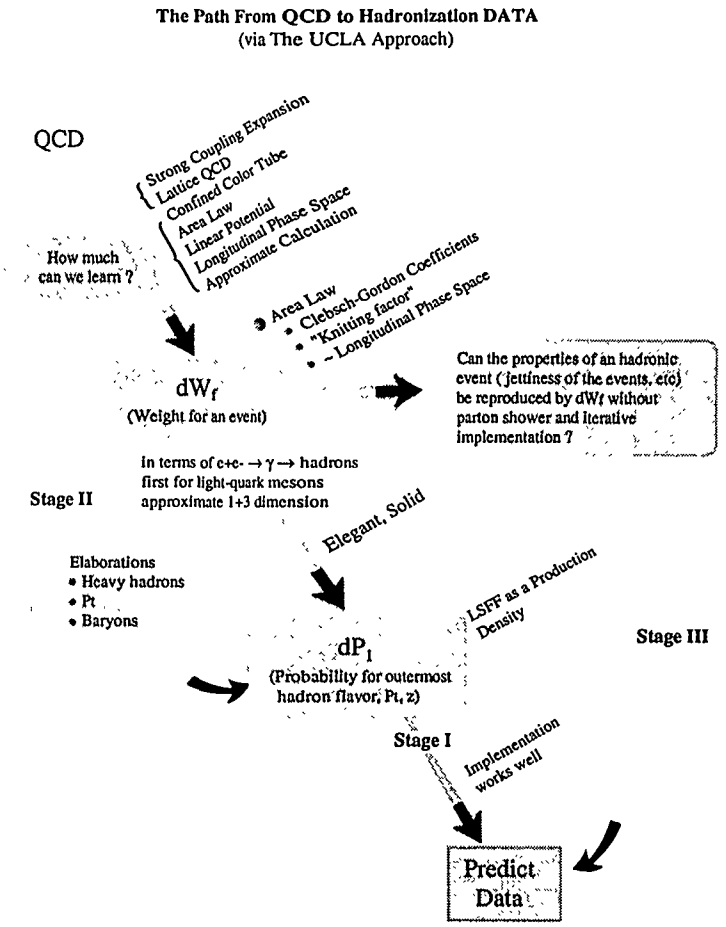


Fig. 1. The conceptual flow of the UCLA approach from QCD to the *Event Weight Function* to the *Fragmentation Function* to predictions of data. [Note, however, that the historical development proceeded in roughly the opposite sequence.]

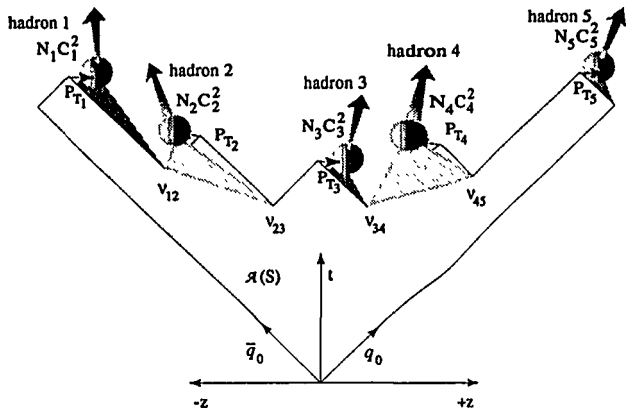


Figure 2: Five hadrons are produced with small intrinsic P_T relative to a *"planar"* hadronic event of e^+e^- annihilation. These P_T's distort the plane of the event in such a way that the resulting area becomes slightly larger than for the planar event. See text for description of ν_{ij}, C_i^2, N_i, and of our UCLA assumptions for these.

using the Lund Symmetric Fragmentation Function with constant normalization, but also begins to connect with QCD for which it potentially forms a "target" for approximate calculations, lattice work, etc.

The *Event Weight Function* involves very simple principles: An area law[5] in space-time (which almost any strong-coupled theory will suggest), approximately longitudinal phasespace, the possibility of suppression "penalties" in creating massive quark-antiquark pairs from the colorfield (ν_{ij} in Fig. 2), Clebsch-Gordon coefficients to describe the flavor and spin combination of a quark and antiquark as they coalesce into a meson or of three quarks into a baryon (C_i^2), and "knitting factors" to describe the combinations into the spatial wave functions of the hadron to be created (N_i). In our UCLA modeling, we make the simplest possible assumptions within this structure:

(i) that there is no appreciable suppression for creating light-quark pairs from the colorfield (namely, $\nu_{ij} \simeq 1.0$ for $u\bar{u}$, $d\bar{d}$, and $s\bar{s}$ virtual pairs from the colorfield), and

(ii) that the spatial "knitting factors" for forming all hadrons are approximately the same [namely, all $N_i \simeq (75\ \mathrm{MeV})^{-2} = (2.7\ \mathrm{fm})^2$].

How should we go about testing our *Event Weight Function* hypothesis against experimental data? The ideal way would be to have a computer big enough and fast enough that, for a given E_{CM}, a library of *Event Weight Functions* could be calculated for each possible set of final state hadrons within a grid of the flavor (mass), longitudinal momentum, and transverse momentum of each hadron produced. This, unfortunately, is not practical, but it is useful to remind the reader that the goal is a method to simulate this ideal. The practical technique to carry this out is to use a Monte Carlo program in which one hadron at a time is picked in such a way that an event as a whole is eventually constructed appropriately.

The program we use is an adaptation of the relativistic string Monte Carlo JETSET7.4 (Ref. 6) written by Dr. Torbjorn Sjöstrand of Lund University, Sweden (with many thanks to him for making it available to us and aiding us in using it). The program uses an "outside-in" implementation, that is, first picking the outermost hadron containing the initial quark, and then working its way inward.

Thus, it is necessary for us, beginning with an *Event Weight Function* for an event, to derive the fragmentation function—i.e., the probability (dP_1)—for the flavor and momentum of a first outermost hadron (see, e.g., Fig. 2). When we perform this derivation, we find that our simple UCLA assumptions for the *Event Weight Function* vertex suppression and knitting factors yield essentially the phenomenology which we originally found to be successful: namely, using the Lund Symmetric Fragmentation Function as a hadronic production density in the outside-in JETSET implementation framework!

2 The Event Weight Function dW_f for Meson Formation

Referring to Fig. 2, the Event Weight Function for an event with a final state f is written as:

$$
\begin{aligned}
dW_f^{q_0\bar{q}_0} &= \frac{N_1 C_1^2}{(2\pi)^3} dE_1 dP_{z_1} dP_{x_1} dP_{y_1} \delta\left(E_1^2 - P_1^2 - m_1^2\right) \nu_{12} \times \ldots \\
&\times \frac{N_{n-1} C_{n-1}^2}{(2\pi)^3} dE_{n-1} dP_{z_{n-1}} dP_{x_{n-1}} dP_{y_{n-1}} \delta\left(E_{n-1}^2 - P_{n-1}^2 - m_{n-1}^2\right) \nu_{n-1,n} \\
&\times \frac{N_n C_n^2}{(2\pi)^3} dE_n dP_{z_n} dP_{x_n} dP_{y_n} \delta\left(E_n^2 - P_n^2 - m_n^2\right) \\
&\times (2\pi)^4 \delta\left(\mathbf{E} - \sum_i E_i\right) \delta\left(\mathbf{P}_z - \sum_i P_{z_i}\right) \delta\left(\mathbf{P}_x - \sum_i P_{x_i}\right) \delta\left(\mathbf{P}_y - \sum_i P_{y_i}\right) \\
&\times e^{-b' \mathcal{A}_{\text{world-surface}}},
\end{aligned}
\tag{2}
$$

where

$$
\left(\frac{1}{2\pi}\right)^3 dE_i dP_{z_i} dP_{x_i} dP_{y_i} \delta\left(E_i^2 - P_{z_i}^2 - P_{x_i}^2 - P_{y_i}^2 - m_i^2\right) \tag{3}
$$

is just the four-dimensional phasespace

$$
\left(\frac{1}{2\pi}\right)^3 d^4P_i \delta\left(P_i^2 - m_i^2\right) = \left(\frac{1}{2\pi}\right)^3 \frac{d^3P_i}{2E_i}
$$

for the i-th meson and

$$
(2\pi)^4 \delta\left(\mathbf{E} - \sum_i E_i\right) \delta\left(\mathbf{P}_z - \sum_i P_{z_i}\right) \delta\left(\mathbf{P}_x - \sum_i P_{x_i}\right) \delta\left(\mathbf{P}_y - \sum_i P_{y_i}\right) \tag{4}
$$

is overall four-momentum conservation. The bold face $\mathbf{E}$ signifies E^{total}, etc. The factor $\exp(-b'\mathcal{A}_{\text{world-surface}})$ is the QCD-inspired space-time area law factor and the ν_{ij}'s are the vertex suppression factors possible at the production of each virtual $q\bar{q}$ pair from the colorfield.

We include a structure to describe the probability that a quark from one virtual vertex and an antiquark from an adjacent vertex combine to form the state function of a final meson. This involves both Clebsch-Gordon coefficients to control the flavor and spin parts (the C_i^2's) and a "knitting factor" N_i for the spatial part of the hadron state function.

The factor $\exp(-b'\mathcal{A}_{\text{world-surface}})$ is the area law behavior which, as will be discussed in Sec. 7, most approaches to strong-coupling situations (such as that of hadronization in its later stages) lead to, where b' is a parameter which is related to the string constant and $\mathcal{A}$ is the area swept out in a space-time diagram such as Fig. 2. Because the JETSET implementation provides a good recipe for iterating past a gluon-induced string kink, Eq. (2) is rewritten relative to a straight relativistic string using

$$
\mathcal{A}_{\text{world-surface}} \simeq \mathcal{A}_{plane} + \sum_i \frac{\chi_i}{b'} P_{T_i}^2,
$$

where $\mathcal{A}_{plane}$ is the area of world-surface projected to a plane. This yields

$$
\begin{aligned}
dW_f^{q_0\bar{q}_0} &= \frac{N_1 C_1^2}{(2\pi)^3} dE_1 dP_{z_1} dP_{x_1} dP_{y_1} \delta\left(E_1^2 - P_1^2 - m_1^2\right) e^{-\chi\left(P_{x_1}^2 + P_{y_1}^2\right)} \nu_{12} \times \ldots \\
&\times \nu_{n-1,n} \frac{N_n C_n^2}{(2\pi)^3} dE_n dP_{z_n} dP_{x_n} dP_{y_n} \delta\left(E_n^2 - P_n^2 - m_n^2\right) e^{-\chi\left(P_{x_n}^2 + P_{y_n}^2\right)} \\
&\times (2\pi)^4 \delta\left(\mathbf{E} - \sum_i E_i\right) \delta\left(\mathbf{P}_z - \sum_i P_{z_i}\right) \delta\left(\mathbf{P}_x - \sum_i P_{x_i}\right) \delta\left(\mathbf{P}_y - \sum_i P_{y_i}\right) \\
&\times e^{-b' \mathcal{A}_{plane}}.
\end{aligned}
\tag{5}
$$

This *Event Weight Function* structure can be used to analyze both the Lund and the UCLA approaches to the situation.

The UCLA assumptions are:

(i) The ν_{ij}'s for $u\bar{u}$, $d\bar{d}$, and $s\bar{s}$ are all ≈ 1.0; that is, there is no substantial penalty for creating any $q\bar{q}$ pair, at least as long as the quark mass is below the QCD scale of ≈ 1 GeV. This also recognizes that at this stage, the event is very close (in time or virtuality) to the actual final state hadrons and that

the virtual quark pair production from the colorfield is being "pulled" by the configurations of allowable final state hadrons.

(ii) The Clebsch-Gordon coefficients for creating mesons are remarkably simple, flowing from three aspects of our approach:

(a) Only sets of final state hadrons are allowed which correspond to local flavor conservation in creating virtual pairs in the colorfield. That is, virtual $u\bar{u}$, $d\bar{d}$, and $s\bar{s}$ pairs can be created locally in the colorfield, but $u\bar{d}$, $u\bar{s}$, and $d\bar{s}$ pairs cannot.

(b) If, for example, a K^+ meson is part of a hypothesized *local-flavor-conserva-tion-allowed chain*, then the $u\bar{s}$ pair needed to form the K^+ is simply available. The flavor coupling, then, of this "available" $u\bar{s}$ pair into the K^+ flavor state function, whose only flavor composition is $u\bar{s}$, is simply 1.0. Note, however, for example, that a π^0 has equal terms in both $u\bar{u}$ and $d\bar{d}$ composition. Thus, if a $u\bar{u}$ mesonic combination is allowed by a hypothesized local-flavor-conservation chain, then this $u\bar{u}$'s coupling to the π^0's flavor state function would be 0.5. Similarly, the couplings which we use into either an η or into an η' have strength 0.25 from $u\bar{u}$, 0.25 from $d\bar{d}$, and 0.5 from $s\bar{s}$.

(c) The spins of the final state hadrons are presumed to be (at least, approximately) independent. Given the intense amount of spin angular momentum in the gluons of the colorfield, this would seem to be a plausible approximate assumption. Therefore, the colorfield couples in spin to a final state hadron simply with the hadron's spin degrees of freedom.

Thus, to summarize, the colorfield couples to a final state meson in flavor and spin with simply the spin-counting of the meson's spin degrees of freedom, except for neutral mesons where the additional content of the meson's flavor state function must also be coupled to by the quark-antiquark combination allowed by local flavor conservation.

(iii) The "knitting factors" N_i express the difficulty or probability of a quark and its "neighbor" antiquark coupling into the spatial wave function of a particular hadron. [It is conceptually somewhat akin to a hadronic decay factor in reverse]. We presume that all such knitting factors, whether the meson be a pion, kaon, η, η', ρ, ω, K^*, ϕ, etc., are all approximately the same. The units for N_i, as can be seen from the *Event Weight Function* expression, are $(Energy)^{-2}$. The unitarity normalization constraint from the probability for the outermost hadron, as we shall see in Sec. 3, establishes all $N_i \simeq (75\ \text{MeV})^{-2} \simeq (2.7\ \text{fm})^2$.

(iv) The transverse situation is described in terms of P_T of the observed hadrons, compatible with the description and handling of $A_{\text{world-surface}}$ above. (See Sec. 3 for our particular approach to possible local P_T compensation.)

In our modeling, the suppression of heavier particles arises from the mass of the hadron (as will be seen in Sec. 3), rather than from suppression factors at the quark pair production level and smaller knitting factors for vector mesons as, for example, Lund presumes.

The Lund modeling, by contrast, assumes:

(i) At the virtual $q\bar{q}$ production stage, there is vertex suppression of $s\bar{s}$ production (the famous $s/u \simeq 0.3$), based on a WKB tunneling sort of argument; that is,

$$\nu_{u\bar{u}} \simeq \nu_{d\bar{d}} \simeq 1.0 \quad \text{and} \quad \nu_{s\bar{s}} \simeq 0.3.$$

Also, for baryon production, the qq/q factor of ≈ 0.09 is introduced as a vertex suppression.

(ii) As in our UCLA treatment, Clebsch-Gordon factors are different from 1.0 only, for example, to decide whether a $u\bar{u}$ state is to be coupled into a π^0, η, or η'.

(iii) The knitting factors are used, via some detailed wave function arguments, for the Vector/All suppressions, with different parameters for light quarks, strange quarks, and heavy quarks. The final state phase-space spin-counting is also incorporated at this stage.

(iv) The Lund modeling conceptually originates the P_T structure from balanced nonzero transverse momenta of a virtual quark-antiquark pair as it is created from the colorfield; however, this can be incorporated into the general description of Eq. (5).

3 Deriving the Fragmentation Function dP_1 for the Outermost Meson from dW_f

- Define the *Total Weight* for all possible final state configurations at some value $S = E_{CM}^2$ by

$$g^{q_0\bar{q}_0}(S) = \sum\!\!\!\!\!\!\int_f dW_f^{q_0\bar{q}_0}(S), \tag{6}$$

where $\sum\!\!\!\!\!\!\int$ sums over all possible final state flavors and multiplicities and integrates over all possible momenta.

- Then:

$$dP_f^{q_0\bar{q}_0}(S) \equiv \frac{dW_f^{q_0\bar{q}_0}(S)}{g^{q_0\bar{q}_0}(S).} \tag{7}$$

is a properly normalized probability for an event of specified final state f such that

$$\sum\!\!\!\!\!\!\int_f dP_f^{q_0\bar{q}_0}(S) = 1.$$

- Integrate Eq. (5) over the azimuthal angle of each hadron, introduce light cone variables W_+, W_-, and define

$$z_i \equiv \frac{(E_i + P_{z_i})_h}{(E + P_z)_{q_0}} \equiv \frac{W_{+i}}{W_+} = \frac{l_1}{l_0}. \tag{8}$$

That is, z_i is the fraction of the initial quark's energy plus longitudinal momentum which the hadron carries. As is explained in the caption of Fig. 3, the last step in Eq. (8) is due to the proportionality between the length and energy via a presumed approximately constant *string tension*.

Note:

$$\delta\left(\mathbf{E} - \sum_i E_i\right)\ \delta\left(\mathbf{P}_z - \sum_i P_{zi}\right) = 2\delta\left(1 - \sum_i z_i\right)\ \delta\left(S - \frac{\sum_i (m_i^2 + P_{Ti}^2)}{z_i}\right),$$

where the **bold face** signifies **total** quantity as before.

- This yields

$$\begin{aligned} dW_f^{q_0\bar{q}_0}(S) = {} & \frac{N_1 C_1^2}{(4\pi)^2}\frac{dz_1}{z_1} e^{-\chi P_{T_1}^2} dP_{T_1}^2\ \nu_{12} \times \ldots \\ & \times \nu_{n-1,n}\ \frac{N_n C_n^2}{(4\pi)^2}\frac{dz_n}{z_n} e^{-\chi P_{T_n}^2} dP_{T_n}^2 \cdot (2\pi)^4 \delta\left(1 - \sum_{i=1}^n z_i\right) \\ & \times \delta\left(S - \sum_{i=1}^n \frac{m_{T_i}^2}{z_i}\right) \delta\left(\mathbf{P}_x - \sum_{i=1}^n P_{x_i}\right) \delta\left(\mathbf{P}_y - \sum_{i=1}^n P_{y_i}\right)\ e^{-b' A_{plane}}. \end{aligned} \tag{9}$$

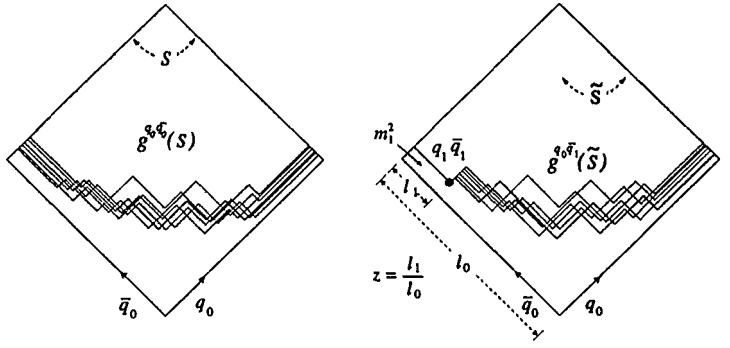


Figure 3: The probabilty that the first hadron is produced with a specific energy-momentum and flavor can be extracted by comparing $g^{q_0\bar{q}_1}(\tilde{S})$ (an *integration/summation* of the weight function for the rest of the system) to $g^{q_0\bar{q}_0}(S)$ (an *integration/summation* of the weight function for the original system). The primary $q_0\bar{q}_0$ with kinetic energy E will stretch until all kinetic energy is converted to potential energy, i.e., $2E = \kappa d$ where κ is the string tension (presumed constant) and d is the maximum separation between the primary $q_0\bar{q}_0$. This enables one to write distance and area in terms of energy and energy-squared, respectively. For example, the energy-momentum fraction of the hadron z can be written in terms of the lengths l_1 and l_0 and the mass-squared of the first hadron can be recognized as the area labeled m_1^2 in the figure.

- Next, one derives the outermost fragmentation function $dP_1^{q_0}(S)$ by writing out $dP_f^{q_0\bar{q}_0}(S)$ and then *integrating/summing* over all possible flavors, multiplicities, and momenta of all particles except the first (outermost) one. But this *integration/summation* is simply $g^{q_0\bar{q}_0}(\tilde{S})$ where $\tilde{S} = \left(S - m_{T_1}^2/z_1\right)(1 - z_1)$ is the E_{CM}^2 of the system excluding the first hadron. The situation is indicated in Figs. 3(a) and 3(b).

- Thus,

$$dP_1^{q_0}(z_1, P_{T_1}^2, m_1^2) = \frac{N_1 C_1^2}{(4\pi)^2}\,\nu_{12}\,e^{-bm_1^2/z_1}\frac{dz_1}{z_1}\,e^{-\chi P_{T_1}^2}dP_{T_1}^2\,\frac{g^{q_1\bar{q}_0}(\tilde{S})}{g^{q_0\bar{q}_0}(S)}, \qquad (10)$$

where $b = b'/\kappa^2$, $\kappa \simeq 1$ GeV/fm is the string tension, and m_1^2/z_1 is the part of the original area $\mathcal{A}(S)$ which is excluded from the new remaining area $\mathcal{A}(\tilde{S}) = \tilde{\mathcal{A}}$.

- The reason to introduce the *Event Weight Function* $dW_f^{q_0\bar{q}_0}(S)$, instead of using the probability $dP_f^{q_0\bar{q}_0}(S)$, is that a very useful theorem can be proven for $g^{ij}(S)$ (Ref. 7):

  Take the natural log of both sides of Eq. (10). Differentiate with respect to S. Make the crucial assumption that the fragmentation function $dP_1^{q_0}(S)$ is, in fact, independent of S when S is large enough. Then, one obtains at large S

$$\frac{S}{g^{q_0\bar{q}_0}(S)}\,\frac{dg^{q_0\bar{q}_0}(S)}{dS} = \frac{\tilde{S}}{g^{q_0\bar{q}_1}\left(\tilde{S}\right)}\,\frac{dg^{q_0\bar{q}_1}\left(\tilde{S}\right)}{d\tilde{S}}.$$

  Separation of variables implies

$$g^{q_0\bar{q}_0}(S) = d_{q_0\bar{q}_0}S^a \quad \text{and} \quad g^{q_1\bar{q}_0}(S) = d_{q_1\bar{q}_0}S^a, \qquad (11)$$

  where all systems have the same power *"a"* of S^a and the coefficients d_{ij} depend on the flavors of the system.

- Thus, finally our fragmentation function for the outermost hadron is (as derived from dW_f with the one assumption that $dP_1^{q_0}(S)$ is independent of S at large S):

$$dP_1^{q_0}(z_1, P_{T_1}^2, m_1^2) = \frac{N_1 C_1^2}{(4\pi)^2}\,\nu_{12}\,(1 - z_1)^a\left(1 - \frac{m_1^2}{Sz_1}\right)^a e^{-bm_1^2/z_1}\frac{dz_1}{z_1}e^{-\chi P_{T_1}^2}dP_{T_1}^2 \times\frac{d_{q_1\bar{q}_0}}{d_{q_0\bar{q}_0}}, \qquad (12)$$

where we have used $\tilde{S} = \left(S - m_{T_1}^2/z_1\right)(1 - z_1)$.
Note that an absolute normalization $N_1 C_1^2 \nu_{12}/(4\pi)^2$ is indicated for the fragmentation function in this derivation.

Though Eq. (12), with all $\nu_{ij} \simeq 1.0$ and all N_i approximately the same, is the primary structure to be used in the outside-in iterative implementation of our UCLA modeling, there are several important subtleties to be mentioned in its implementation:

Equation (12) contains an exponential suppression of P_T, carried over from the *Event Weight Function* of Eq. (5). At this stage in our work, we want simply to use some approximate P_T treatment which works so that we can focus on the question of meson production rates. We note that if one simply replaced m_H^2 by the transverse mass squared $m_T^2 = m_H^2 + P_T^2$, this would set $\chi = b/z$. However, one can show[8] that, if there are local compensation correlations between hadrons, then the subsequent P_T distributions will be narrower than the "natural" distribution. In particular, in an outside-in implementation, if the P_T of one hadron is compensated for by the next n hadrons, then one can show that a factor of $n/(n-1)$ is introduced as a coefficient of P_T^2 in the exponential. We find that the following works reasonably well and use it as an approximate treatment for the time being: (a) We use $n = 2$ (the most local compensation possible on the hadron level) so that the suppression factor is $\exp(-2bP_T^2/z)$; (b) after one hadron's P_T is picked, the next hadron's P_T is centered at -1/2 of the remaining P_T imbalance. This, as will be seen, gives an adequate description of the data. We also note, however, that a different factor in $exp(-2bP_T^2/z)$ from $exp(-bm_H^2/z)$ leads to a small deviation from $Left - Right$ symmetry.[2]

In Fig. 2, we have presumed that the initial $q_0\bar{q}_0$ pair are quite light and essentially travel along the light cone. This is a good approximation for up, down, and even strange quarks. However, it is a poor approximation for charm and bottom quarks, which travel in a hyperbolic path inside the light cone. This is indicated in Fig. 4. Focusing on area-law considerations, we presume that z_{eff} is really m_H^2/(comparison area) of Fig. 4. This modifies the definition of the energy-momentum fraction z to be used in the exponential of Eq. (12),

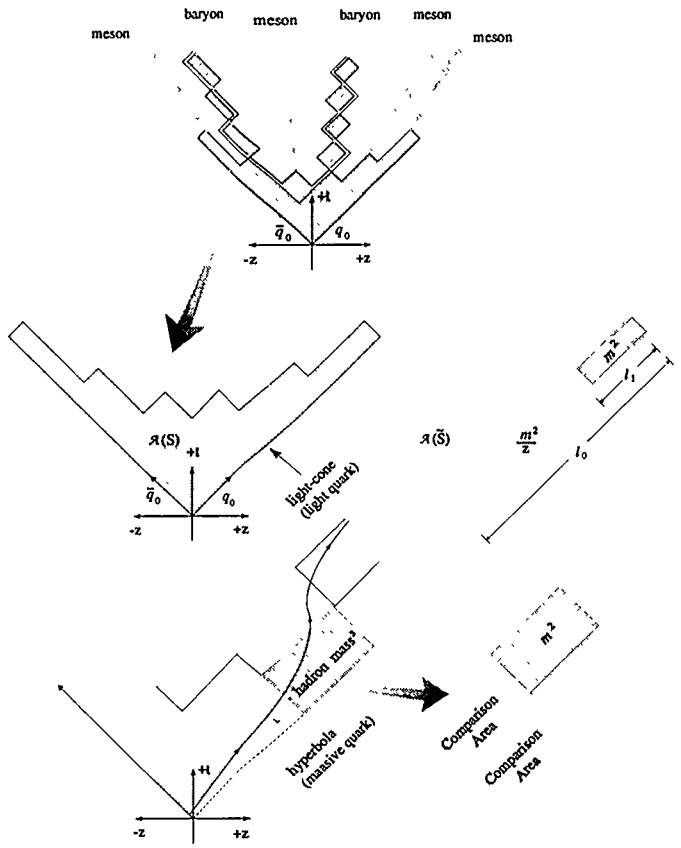


Figure 4: Various geometrical definitions to be used in deriving the outermost hadron's fragmentation function dP_1 are displayed. A heavy initial quark travels along a hyperbola rather than a light-cone, which affects the area involved. One has to modify the definition of z in order to incorporate this change.

which arises from the area-law. The result is

$$z_{\rm eff} = \frac{z}{1 - \frac{\mu^2 z}{m^2} - \frac{\mu^2 z}{m^2}\log\left(\frac{m^2}{\mu^2 z}\right)}, \tag{13}$$

where μ is the current quark mass and m is the hadron mass. This has little effect on light and strange hadrons, but softens the predicted spectra for b and c hadrons in a manner which gives substantially better agreement with experimental spectra than otherwise.

The ratio $d_{q_1\bar{q}_0}/d_{q_0\bar{q}_0}$ correctly expresses a procedure which was clearly called for in our original phenomenological approach. Consider Fig. 2: Let $\bar{q}_0$ be a $\bar{u}$, where we want to focus on properly picking meson #1 using our fragmentation function weights of Eq. (12). If $vertex_{12}$ is either $u\bar{u}$ or $d\bar{d}$, then meson #1 is nonstrange. However, if $vertex_{12}$ is $s\bar{s}$, then *both* meson #1 and meson #2 are strange, and therefore heavier than otherwise, and therefore provide more suppression to the event via the $exp(-bm^2/z)$ factors. In our iterative phenomenological implementation, as we consider meson #1, we must *"look ahead"* at meson #2 also and incorporate the effects of the quark-antiquark flavor at $vertex_{12}$ on the mass of meson #2; that is, we include a factor of

$$\sum\!\!\!\!\!\!\int_{z,P_T} \frac{N_i C_i^2}{(4\pi)^2}\,\frac{(1-z)^a}{z}\left(1-\frac{m_i^2}{Sz}\right)^a e^{-b\left(m_i^2+2P_T^2\right)/z}\,dz dP_T^2$$

from each appropriate meson #2 into the weight for each possible meson #1. The d_{ij} factors in Eq. (12) explicitly summarize and require this procedure. More precisely, Eq. (12) can be recast into an eigenvector problem for the d_{ij}'s with the knitting factor N related to the eigenvalue: Since some first hadron must be created, there is a probability unitarity constraint of:

$$\sum\!\!\!\!\!\!\int_{\substack{z,P_T,\\ flavor}} dP_1^{q_0}(z,P_T^2,m^2) = 1,$$

where the summation over $flavor$ is for the flavor of the hadrons containing a quark q_0. Carrying out this *sum/integration* over possible hadron flavors, z's, and P_T's and generalizing to any combination of initial quark and antiquark flavors leads to a set of coupled equations:

$$d_{ij} = \sum\!\!\!\!\!\!\int_{\substack{z,P_T\\ flavor}} \frac{NC_{ik}^2}{(4\pi)^2}\,\frac{(1-z)^a}{z}\left(1-\frac{m_{ik}^2}{Sz}\right)^a e^{-b\left(m_{ik}^2+2P_T^2\right)/z}\,dz dP_T^2\ \cdot d_{kj}.$$

The factor quoted above which we use in the weight for hadron #1 from appropriate hadrons #2 is just the first step in an iterative solution to this eigenvector problem for the d_{ij}'s. Solving the eigenvector problem directly for our best fit values of $a = 1.65$ and $b = 1.18$ GeV^{-2}, we find

$$d_{u\bar{u}} \simeq d_{d\bar{d}} \simeq d_{u\bar{d}} = d_{d\bar{u}},$$

$$d_{s\bar{u}} = d_{u\bar{d}} \simeq d_{s\bar{d}} = d_{d\bar{s}} \simeq 0.47\ d_{u\bar{u}},$$

$$d_{s\bar{s}} \simeq 0.47\ d_{s\bar{u}}.$$

These, of course, to first order are simply the factors we have used for the hadron #2 weighting.

The solution to the eigenvalue problem also gives an intriguing new piece of information, namely, an eigenvalue for the knitting factor:

$$N \simeq 160 \sim 220\ \text{GeV}^{-2} \simeq (68 \sim 80\ \text{MeV})^{-2} \simeq (2.5 \sim 2.9\ \text{fm})^2.$$

The knitting factor appears to be a new and interesting concept, which may in some manner be related to the inverse of a hadronic decay constant.

We note, in fact, that $N \simeq (2/f_\pi)^2$ for typical hadronic decay constants f_π of $110 \sim 160$ MeV.

4 Baryon Formation

During our hadronization studies, as we have come to understand meson formation as apparently a very simple process, we have also come to view baryon formation as a much more complicated process: (1) three quarks must somehow coalesce into a baryon wave function; (2) whereas a quark and antiquark define a one-dimensional line between them in forming a meson, three quarks can have a more complex two-dimensional structure in forming a baryon; (3) one or more "popcorn" mesons can be formed between the baryon and antibaryon; and (4) because of the multiple popcorn meson formations possible, there are many more combinations possible in the flavor chain of an event.

Recognizing this much-increased complexity for baryon formation, we extend our approach for mesons to baryon formation in as simple a manner as possible. The following approach works encouragingly well, though we currently must introduce at least one *"ad hoc"* parameter in order to reach fairly reasonable agreement with baryon rate, distribution, and correlation data:

(1) For any given final state of hadrons with specified flavors and three-momenta, now including baryons and antibaryons, we assign a weight via the Event Weight Function approach. For this weight function, we presume:

(2) The area law approach (and likewise proper kinematics) is valid.

(3) The same values of *"a"* and *"b"* are used in the fragmentation function for baryons as for mesons.

(4) There is no significant suppression for creating any number of virtual $u\bar{u}$, $d\bar{d}$, and $s\bar{s}$ pairs from the colorfield, as we also assumed for mesons.

(5) To knit quarks into baryons:

- Proper Clebsch-Gordon coefficients should be used for creating baryons as well as for mesons.
- The spatial knitting factors to form baryons are assumed to be the same as for the mesons, where the *universal* value is found to be $\approx 1/(75\ \text{MeV}^2)$ from data and probability conservation, as is discussed in Sec. 3.

The Clebsch-Gordon coefficients for flavor and spin couplings are as simple for baryons as they are for mesons, presuming the three assumptions made in Sec. 2: (1) local flavor conservation in creating virtual $q\bar{q}$ pairs from the colorfield; (2) virtual $q\bar{q}$ pairs are available "for free" from the colorfield; and (3) the spins of the final state hadrons are (at least, approximately) independent. Given these assumptions, the flavor coupling of whatever quarks are needed into the final state baryon flavor state is simply 1.0 and the spin coupling is simply the final state baryon spin degrees of freedom, i.e., 2.0 for spin 1/2 baryons and 4.0 for spin 3/2 baryons. The only difference between mesons and baryons is in the neutral sector: Mesons such as π^0, η, ρ^0, ϕ, etc., contain superpositions of different $q\bar{q}$ flavor states (i.e., $u\bar{u}$, $d\bar{d}$, and $s\bar{s}$), and therefore a given state of flavored $q\bar{q}$ (e.g., $u\bar{u}$) couples into a neutral meson flavor state with less than 1.0. By contrast, for example, every term in the Λ and Σ^0 flavor state is uds. Thus, the flavor coupling of quarks within the colorfield into *each* of the Λ and Σ^0 is 1.0.

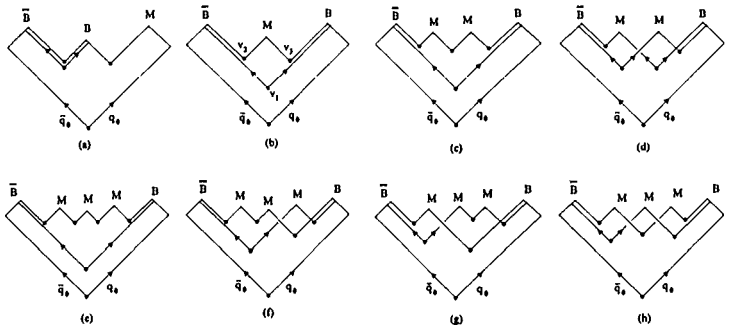


Fig. 5. (a) The baryon and antibaryon pair are produced adjacent to each other. (b) One popcorn meson is produced between the baryon and antibaryon. (c) and (d) Two possible ways of producing two mesons between the baryon and antibaryon. (e) to (h) Four possible ways of producing three mesons between the baryon and antibaryon. As more popcorn mesons are produced, the number of possible diagrams increases rapidly.

In terms of area law treatment, because baryons contain three quarks, there is a new spatial degree of freedom. Whereas quarks and antiquarks in a meson always define a one-dimensional line between them, the three quarks in a baryon can form a two-dimensional spatial structure. As the three quarks propagate forward in time, an area law structure can take either a "Y" structure or a "Δ" structure connecting them.[9] In our current treatment, we presume that the area law for baryons can be treated in an approximate manner where the "Y" or "Δ" structure has been collapsed into a 1+1 dimensional structure (partially reminiscent of a diquark approach), as for mesons.

Even within the context of our presumed 1+1 dimensional treatment for baryons, another new degree of freedom emerges: namely, events where "popcorn" mesons are "popped out" between the baryon and antibaryon. Figure 5 shows (a) the baryon and antibaryon are adjacent and share two virtual $q\bar{q}$ pairs; (b) there is one intermediate popcorn meson and the baryon and antibaryon share one virtual $q\bar{q}$ pair; (c) there are two popcorn mesons and the baryon and antibaryon share one virtual pair (where the "first" virtual pair must "live a long time" before the rest of the baryon-antibaryon formation occurs); (d) there are two popcorn mesons in a "crossed" diagram where the baryon and antibaryon share no virtual $q\bar{q}$ pairs; and (e)–(h) various diagrams with three popcorn mesons. Hypothetically, the popcorn diagrams, with ever increasing complexity, could extend to very many popcorn mesons. Note that the popcorn diagrams introduce new baryonic degrees of freedom which are otherwise unachievable, e.g., a $\bar{p} - \Xi$ (baryon-antibaryon) pair, and thus increase the density of final states for baryon production.

We find, in fact, that the series diverges as one increases the number of popcorn mesons. Thus, we must introduce a parameter to effectively cut off long popcorn chains. We are led by the fact that strong interaction theory suggests a perimeter law as well as an area law (see Sec. 7). In the case of popcorn diagrams, where in fact the perimeters are longer than for nonpopcorn diagrams, this suggests the use of a suppression of the form $exp(-\eta \cdot m_{popcorn})$. This works well phenomenologically with $\eta \simeq 3.5/\text{GeV}$.

5 Comparisons of Predictions with Data

Within the context of using JETSET7.4 (an outside-in iterative Monte Carlo program) to implement our approach, the comparisons of our model predictions with data and the associated tuning of parameters naturally divide into five "sectors" which are fairly separable, though there is some "parameter cross-talk" between the sectors: (A) the parton shower; (B) P_T effects; (C) heavy-quark hadrons (containing c or b quarks); (D) light-quark baryons; and (E) light-quark mesons. Our main thrust in this paper is to make sure that (A)–(D) are well-tuned so that they create negligible biases and we can study the main focus of our investigation, namely (E), the light-quark meson production rates and distributions.

Comparisons are made at e^+e^- center-of-mass energies sufficiently high for hadronization studies, where there are large data samples from more than one detector, namely 91 GeV, 29 GeV, and 10 GeV (continuum). Data used include flavored multiplicities and distributions for the light-quark meson and baryon sectors, as well as for various topological and single particle distributions for the parton shower, P_T, and heavy-quark sectors.

SECTOR	PARAMETERS	VALUE
Parton Shower	Λ (QCD strength)	0.32 GeV
	Q_0 (Cuts off shower)	2.0 GeV
P_T	n (Local correlations)	2
Heavy-quark Hadrons	(None needed)	
Light-quark Baryons	η (Controls popcorn)	3.5 GeV^{-1}
Light-quark Mesons	a (Growth of g(s))	1.65
	b (related to the *string tension*)†	1.18 GeV^{-2}

† $b = b'/\kappa^2$ where κ and b' are the *real* and the *imaginary* part (which allows a system to decay into the final state hadrons) of the string tension, respectively.

Table 1: Parameters for UCLA and their tuned values. Note that this set of parameters are tuned to span 10 GeV, 29 GeV, and 91 GeV.

For multiplicities, all relevant data through Summer 1996 have been included. At 10 GeV and 29 GeV, we use the data review by E. C. Berg and C. D. Buchanan[10]; at 91 GeV, we use the 1995 data review by A. De Angelis[11], updated by publications and papers up through the ICHEP Conference at Warsaw in July 1996 (Ref. 12). For the flavored distributions and for the topological and single particle distributions, a comprehensive (but not exhaustive) sample of relevant distributions gleaned from the same sources is presented. We concentrate most of these distribution displays at E_{CM} of 91 GeV where the data is most copious.

Our predictions have been tuned simultaneously for all three center-of-mass energies with only the one set of energy-independent parameters cited in Table 1, which lists each *sector*, the major parameters used in tuning that sector, and the best-tune values of those parameters.

Once (A)–(D) (above) are reasonably well-tuned, we reach our major conclusion in sector (E): *there are no significant deviations between our predictions and data at all three center-of-mass energies for all the various flavored light-quark meson rates and distributions studied, using only the two parameters—"a" and "b"—natural to the light-quark meson sector.*

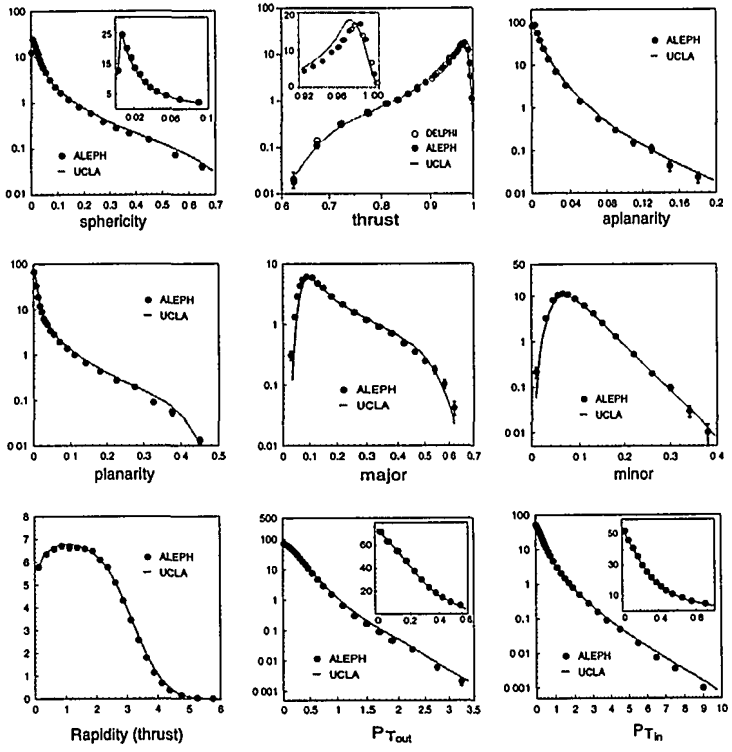


Figure 6: UCLA predictions for various topological variables and charged particle distributions are compared to LEP experiments at $E_{CM} = 91$ GeV.

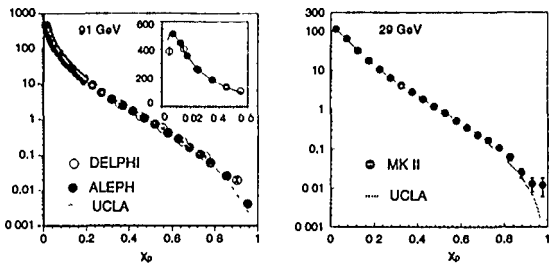


Fig. 7. UCLA predictions for $X_P = P_{hadron}/P_{beam}$ of charged particles are compared to experiments at $E_{CM} = 29,\ 91$ GeV.

It is also worthy of note that: (D) our current predictions for light-quark baryons, developed following an extension of our approach used for mesons, are approximately accurate (though not as good as for light-quark mesons) using only one additional *ad hoc* parameter; (C) our predictions for spectra of heavy-quark hadrons, which are substantially influenced by the area-law approach in our use of $z_{\rm eff}$, are rather good and require no additional parameters; and (A and B) our predictions for the topological distributions (dependent on the JETSET parton shower treatment and using the two major parameters therein) and for the various P_T distributions (using one *ad hoc* parameter) are also rather reasonable.

It is worth noting in the comparisons that there are some deviations between our predictions and data. The important questions to bear in mind are: (1) "Are the deviations in the other sectors significant enough to affect the light-quark meson comparisons?" and (2) "Are the deviations in the light-quark meson sector big enough to affect our conclusions?" We feel that the answer to each of these questions is "No." We also note that there are other treatments in the JETSET7.4 program which are approximations and which can affect the comparisons slightly. These include: the parton shower, the treatment during iteration to move past a gluon-created string-kink, the treatment of the final two hadrons at the end of the iteration, and the tables used to decay higher mass hadrons into those ultimately observed in a detector. Our very rough estimation is that these effects can lead to $2 \sim 10\%$ biases in the flavored multiplicities predicted.

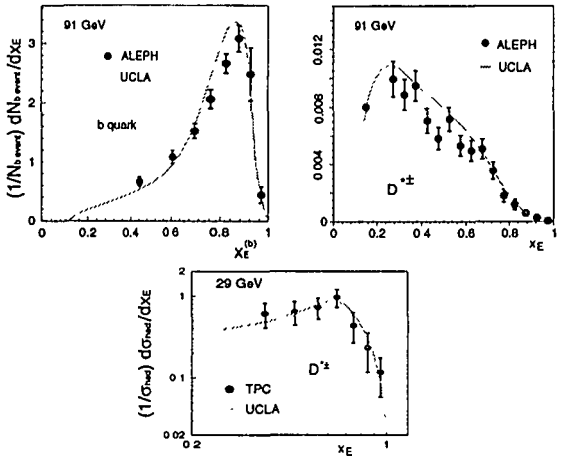


Fig. 8. UCLA predictions for the heavy-quark hadrons are compared to experiments at $E_{CM} = 29,\ 91$ GeV.

5.1 Comparisons for Parton Shower, P_T, and Heavy-Quark Hadrons

5.1.1 Parton Shower

We use the parton shower option of JETSET7.4. This is a recipe which incorporates leading log parton shower structure with a weighting function to allow mimicking of the matrix element calculations for the first two perturbatively calculated gluon emissions. It employs two somewhat correlated parameters Λ controlling the QCD running strength and Q_0 controlling the low-virtuality cutoff at the end of the shower. Various "topological" distributions, such as sphericity, thrust, aplanarity, planarity, and major and minor eigenvalues of the sphericity tensor can be used to tune these parameters. A potpourri of such topological plots, as well as single-charged particle distributions for rapidity and x_p, are displayed in Figs. 6 and 7. The overall agreement seems quite acceptable, though there are minor discrepancies apparent at high thrust, high and low major values, and possibly high x_p.

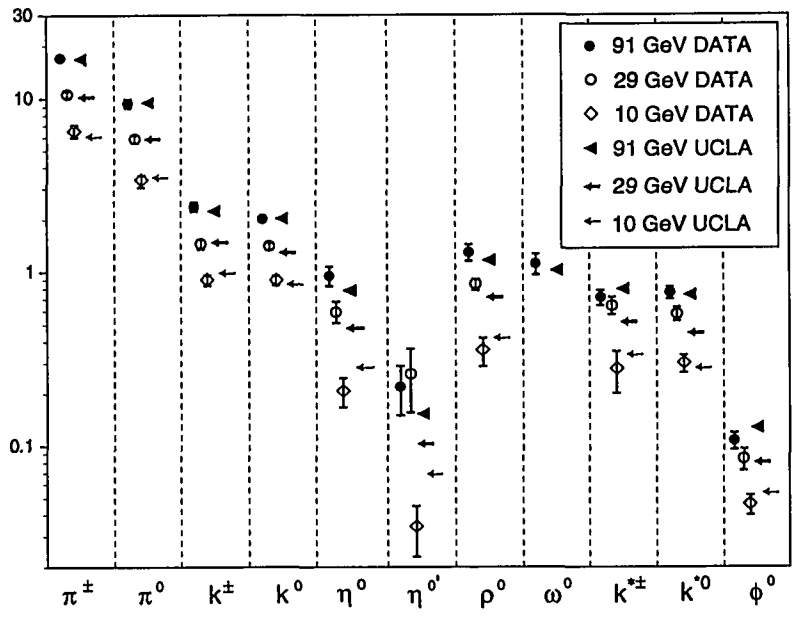


Fig. 9. Comparison of the experimental and predicted absolute production rates per event for various flavored light-quark mesons at $E_{CM} = 10$, 29, and 91 GeV.

5.1.2 P_T Effects

If only transverse mass were involved in P_T effects, then we would use $\chi = b/z$ in Eq. (5) and Eq. (12). However, local P_T compensation between nearby hadrons, such as is discussed in Sec. 3, suggests a factor greater than "one." We use $\chi = 2b/z$, which approximates the most local P_T correlation possible. Agreement (see Fig. 6) with data seem acceptably good, though our predictions might be a little high at high P_T values.

5.1.3 Spectra for Heavy-Quark Hadrons

Our use of the area-law to derive $z_{\rm eff}$, as described in Sec. 3, leads to considerably softer spectra for heavy-quark hadrons than would otherwise be predicted.

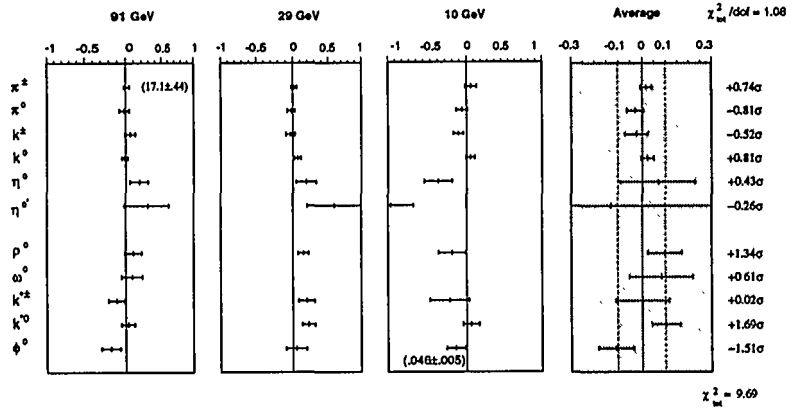


Fig. 10. The summary of experimental data vs the UCLA prediction for mesons at $E_{CM} = 10$, 29, and 91 GeV. On the right, in an *expanded* scale, the comparison is shown for each flavor meson averaged over all three energies.

Using this, we find reasonable agreement with the observed spectra in both peak positions and in shapes (see Fig. 8). This internally consistent treatment would seem to eliminate the need to switch to the Peterson fragmentation function[13] for heavy-quark mesons.

5.2 Comparisons for Light-Quark Mesons

[Note: We defer the discussion of light-quark baryons, which are influenced by *"a"* and *"b"* of the fragmentation function as well as by the ad hoc *popcorn* parameter η, until after the light-quark meson discussion. Roughly speaking, the light-quark meson data are used to tune *"a"* and *"b"* and then η is used to tune the baryon data.]

This light-quark meson sector is our most important study of *"elementary fundamental"* behavior of the colorfield. This sector is predominantly controlled by only the two "natural" parameters of the fragmentation function for the modeling—

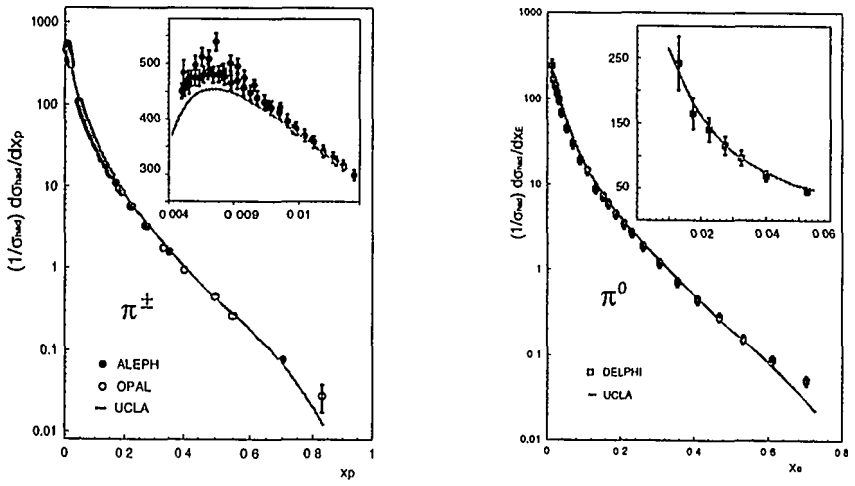


Fig. 11. UCLA predictions for π mesons are compared to experiments at E_{CM} = 91 GeV.

"a" from the growth of g(S) with S and "b" which is related to the imaginary part of the string tension which allows the system to decay.

Our predicted multiplicities are compared with data for various pseudoscalar and vector mesons at E_{CM} = 91, 29, and 10 GeV in Table 2 and in Figs. 9 and 10. Figure 9 compares the absolute magnitudes of predicted and measured multiplicities and gives an overall view of the range of rates over which prediction and experiment are compared. Figure 10 provides a finer grain comparison by suppressing the absolute rates and displaying deviations simultaneously in both percent and standard deviations. We use "data minus prediction" to determine the ± sign in our presentations of standard deviations.

	91 GeV			29 GeV			10 GeV		
	DATA	UCLA	*STD*†	DATA	UCLA	*STD*†	DATA	UCLA	*STD*†
N_{ch}	20.92 ±0.24	20.62	0.94σ	12.57 ±0.26	12.79	-0.76σ	8.48 ±0.42	7.59	2.08σ
$\pi^{\pm}$	17.06 ±0.44	16.88	0.32σ	10.60 ±0.36	10.41	0.45σ	6.53 ±0.51	6.13	0.75σ
π^0	9.39 ±0.53	9.56	-0.31σ	5.84 ±0.28	5.96	-0.40σ	3.33 ±0.26	3.55	-0.82σ
$k^{\pm}$	2.37 ±0.13	2.24	0.88σ	1.444±0.080	1.490	-0.51σ	0.897±0.058	1.001	-1.63σ
k^0	2.012±0.033	2.038	-0.38σ	1.402±0.048	1.308	1.47σ	0.899±0.049	0.854	0.80σ
η	0.95 ±0.11	0.79	1.29σ	0.593±0.075	0.484	1.31σ	0.207±0.038	0.289	-2.05σ
η'	0.22 ±0.07	0.15	1.00σ	0.260±0.103	0.105	1.49σ	0.034±0.011	0.070	-3.22σ
ρ^0	1.29 ±0.13	1.16	0.93σ	0.846±0.054	0.723	1.93σ	0.353±0.064	0.425	-1.10σ
ω^0	1.11 ±0.14	1.02	0.61σ						
$k^{*\pm}$	0.713±0.056	0.791	-1.10σ	0.641±0.062	0.518	1.69σ	0.276±0.073	0.342	-0.88σ
k^{*0}	0.759±0.041	0.736	0.38σ	0.574±0.039	0.448	2.42σ	0.299±0.029	0.280	0.56σ
ϕ^0	0.107±0.009	0.126	-1.53σ	0.084±0.010	0.080	0.33σ	0.046±0.005	0.053	-1.13σ

† Decay table uncertainties are incorporated into the calculation of the number of standard deviations between the data and predictions, the column labeled "*STD.*" (See text.)

Table 2: UCLA predictions for mesons at 10 GeV, 29 GeV, and 91 GeV are compared to experiments.

Though the uncertainties quoted for the data in Table 2 are simply the experimental uncertainties, in the comparisons with predictions in Table 2 (the column labeled *"STD"*) and in Figs. 9 and 10, we have included in quadrature estimations of the effects on the multiplicity-comparison uncertainties arising from the decay table uncertainties. (That is, if the decay table rate of a particle decaying into a relevant particle is incorrect, then the predicted rate for that relevant daughter particle will be biased. If the decay table rate is incorrect for a decay mode used experimentally to reconstruct the multiplicity for a relevant particle, then the experimental rate found will be biased. We have presumed the uncertainties in multiplicity comparisons from these decay table uncertainties to be: ± 2% for pions; ± 3% for kaons; ± 4% for ρ^0 and ω^0; ± 6% for η, η', K^0, and $K^{\pm}$; and ±8% for ϕ; also, ±1% for N_{charged}.)

Comparing data and predictions over the range of meson multiplicities from 17.1 $\pi^{\pm}$ at 91 GeV to 0.046 ϕ's at 10 GeV (a range of $\sim$ 400), we arrive at our

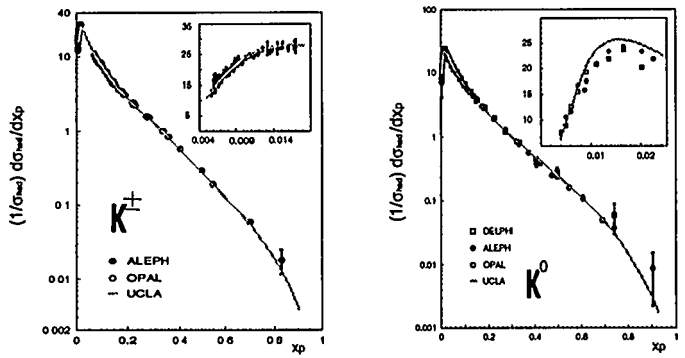


Fig. 12. UCLA predictions for K mesons are compared to experiments at E_{CM} = 91 GeV.

report's most important conclusion, namely: *Over this broad range, there are no deviations which seem truly significant.*

If we presume that our model is accurate (and the deviations appear to be fairly randomly distributed), then we can treat the comparisons of the same meson at different energies as different measurements of the same quantity. Using both fractional deviations and standard deviations, these can be combined appropriately to give an overall comparison for each meson. This is displayed in the right-hand column of Fig. 10, which employs an *expanded* scale, since the deviations are small. As displayed, there is very little difference between data and prediction; each flavor is typically within $\pm 10\%$ and/or $\pm 1.0\ \sigma$. These energy-averaged flavor comparisons have an overall $\chi^2/d.o.f. = 9.69/9 = 1.08$ or an average of ~ 1.0 standard deviation.

Figures 11—14 display sample energy and momentum distributions for various flavors at $E_{CM} = 91$ GeV. Again, though there are minor differences, the overall agreement seems good.

Overall, we find that our predictions for light-quark meson rates and distributions are reasonably accurate and appear to display no significant deviations from the data over integrated multiplicity rates ranging from 17/event to .046/event (a

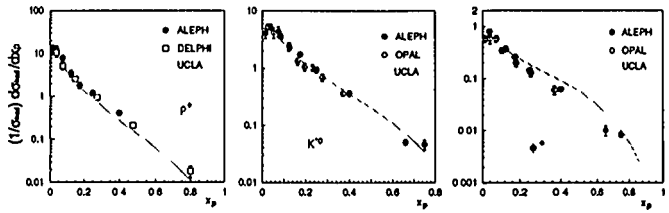


Fig. 13. UCLA predictions for ρ^0, K^{*0}, and ϕ mesons are compared to the experiments at $E_{CM} = 91$ GeV.

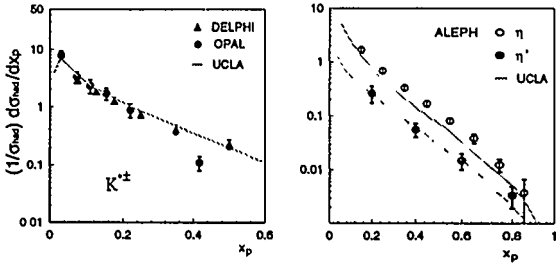


Fig. 14. UCLA predictions for $K^{*\pm}$, η, and η' mesons are compared to experiments at $E_{CM} = 91$ GeV.

range of ≈ 400) and over differential rates in $1/\sigma_{\rm TOT} \cdot d\sigma/dx_p$ ranging from 500 to 0.01 (a range of $\approx 50,000$).

5.3 Comparisons for Light-Quark Baryons

Baryons are much more complicated objects than mesons, and their physical dynamics are much less clear, e.g., three virtual quark-antiquark pairs must be created from the colorfield, and via some dynamics, the three quarks must knit together into a baryon; *popcorn* mesons can be formed between the baryon and antibaryon, which radically increases the number of ways in which a given set of final state hadron flavors and momenta can be achieved.

For baryon production, we follow an extrapolation of our successful meson production approach in order to see whether this sort of approach makes sense for baryon production: we use our Event Weight Function (a) incorporating the area-law, (b) presuming no suppression for creating any number of $u\bar{u}$, $d\bar{d}$, or $s\bar{s}$ virtual pairs from the colorfield, (c) assuming the spatial knitting factors for baryon formation are the same as for meson formation, and (d) developing the necessary Clebsch-Gordon coupling apparatus for the flavor and spin coupling. Since we follow a Fermi Golden Rule addition of final states type of approach, the possibility of long chains of *popcorn* mesons increases the rates of baryon production. Currently, we introduce a parameter η in $\exp(-\eta\, m_{pop})$, motivated by QCD-inspired perimeter law arguments (see Sec. 4), to cut off these long chains.

Our goals currently in studying baryons are: (1) to show that this sort of approach has potential merit, (2) to tune the baryon sector predictions to the data well enough that they won't create any biases in the meson studies, and (3) to point the way toward the kind of data needed to really understand baryon production.

We find that indeed this approach works rather well. Thus, our baryon modeling, though clearly not yet as fundamental as for mesons, provides a very good platform for further developing our understanding of baryon formation on a fundamental level as significantly higher quality data becomes available.

Our baryon multiplicity comparisons are summarized in Table 3 and Figs. 15 and 16, paralleling Table 2 and Figs. 9 and 10 for light-quark mesons. The decay table uncertainties presumed are: $\pm 3\%$ for protons and lambdas; $\pm 5\%$ for $\Sigma^{\pm}$,

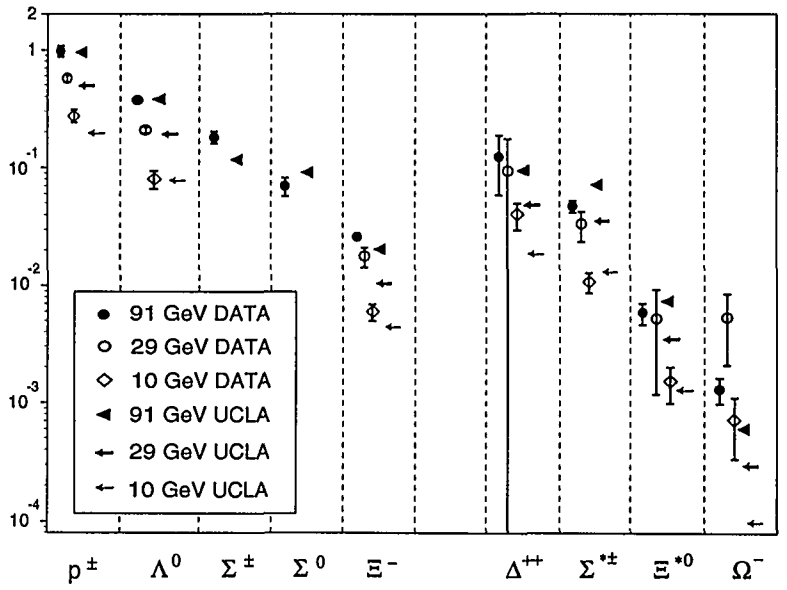


Fig. 15. Comparison of the experimental and predicted absolute production rates for various flavored baryons at E_{CM} = 10, 29, and 91 GeV.

Σ^0, Ξ^-, Δ^{++}, and $\Sigma^{*\pm}$; and $\pm 8\%$ for Ξ^{*0} and Ω^-. Figures 17–18 display various single baryon distributions.

	91 GeV			29 GeV			10 GeV		
	DATA	UCLA	$STD^\dagger$	DATA	UCLA	$STD^\dagger$	DATA	UCLA	$STD^\dagger$
P	0.98 ±0.10	0.97	0.09σ	0.570 ±0.036	0.498	1.81σ	0.275 ±0.034	0.196	2.26σ
Λ^0	0.373 ±0.008	0.383	-0.70σ	0.209 ±0.010	0.197	1.02σ	0.080 ±0.014	0.079	0.07σ
$\Sigma^\pm$	0.182 ±0.019	0.119	3.01σ						
Σ^0	0.070 ±0.012	0.092	-1.79σ						
Ξ^-	0.0262±0.0010	0.0204	3.52σ	0.0176±0.0034	0.0106	2.99σ	0.0059 ±0.0009	0.0045	1.48σ
Δ^{++}	0.124 ±0.065	0.094	0.46σ	0.094 ±0.094	0.049	0.48σ	0.040 ±0.010	0.019	2.06σ
$\Sigma^{*\pm}$	0.047 ±0.005	0.074	-4.86σ	0.0330±0.0094	0.0359	-0.30σ	0.0107 ±0.0020	0.0133	-1.26σ
Ξ^{*0}	0.0058±0.0011	0.0073	-1.25σ	0.0052±0.0040	0.0035	0.42σ	0.0015 ±0.0005	0.0013	0.40σ
Ω^-	0.0013±0.0003	0.0006	2.19σ	0.0053±0.0032	0.0003	1.56σ	0.00072±0.00038	0.00010	1.62σ

† The decay table uncertainties are incorporated into the calculation of the number of standard deviations between the data and predictions, the column labeled "*STD*." (See text.)

Table 3: UCLA predictions for the baryons at 10 GeV, 29 GeV, and 91 GeV are compared to experiments.

Figure 19 displays the baryon-antibaryon rapidity correlation for $\Lambda\bar{\Lambda}$ pairs.[14] Table 4 displays baryon-antibaryon, baryon-baryon, baryon-meson, and meson-meson correlation rates.

	DATA	UCLA
$\Lambda\Lambda/evt.$	0.089 ±0.007	0.114
$\{(\Xi^-\bar{\Lambda} - \Xi^-\Lambda) + (\bar{\Xi}^+\Lambda - \bar{\Xi}^+\bar{\Lambda})\}/evt.$	0.0096 ±0.0023	0.0146
$\{\Xi^-\bar{\Xi}^+ - (\Xi^-\Xi^- + \bar{\Xi}^+\bar{\Xi}^+)\}/evt.$	0.00038±0.00067	0.00128
$(\Lambda\Lambda + \bar{\Lambda}\bar{\Lambda})/evt.$	0.0249 ±0.0022	0.0272
$(\Lambda K_s^0 + \bar{\Lambda}K_s^0)/evt.$	0.403 ±0.029	0.394
$K_s^0K_s^0/evt.$	0.593 ±0.036	0.628

Table 4: Baryon-antibaryon, baryon-baryon, baryon-meson, and meson-meson correlation rates at $E_{CM} = 91$ GeV.

The single-particle rates vary from ≈ 1.0 for protons at 91 GeV to $\approx .001$ for Ω^- at 10 GeV. Generally, the predictions follow the data fairly well. However, we seem systematically to *underpredict* the rates for Ξ^-'s and Ω^-'s, and possibly protons, and to *overpredict* the rates for $\Sigma^{*\pm}$.

Other intriguing deviations in baryon production include: (a) As displayed in Figs. 17 and 18, we consistently *overpredict* the baryon production above $x_p \simeq 0.5$. (This phenomenon leads to the *"leading baryon suppression"* factor recently introduced into JETSET.) (b) Our predicted $\Lambda - \bar{\Lambda}$ rapidity correlation in Fig. 19 is not sharp enough and is too broad (e.g., suggesting somewhat too much popcorn in our Monte Carlo). However, (c) our predictions of the absolute baryon-antibaryon correlation rates (see Table 4) are too high, suggesting too little popcorn (whereas we note that our predicted baryon-baryon, baryon-meson, and meson-meson correlation rates agree adequately with the data).

To bring the understanding of baryon formation to the same, apparently fundamental, level as our current meson formation understanding will require $\approx 10^8$ e^+e^- annihilation events with good, relatively unbiased, efficiency and particle identification in order to obtain flavor-identified three-body baryon-meson-antibaryon rapidity correlations. This appears to be achievable only with the continuum events from one of the high-luminosity B factories currently being built.

6 Connections with QCD

When one has a successful phenomenology, there are two possible approaches toward deeper understanding: (1) Working *"backwards"* from the phenomenology with as few assumptions as possible to see what kind of a theory might justify the phenomenology, or (2) hypothesizing a theory and then working *"forward"* to see if (or under what conditions) it leads to the phenomenology. Since QCD exists as a very strong candidate for the theory underlying hadronization, we will work primarily in the second mode to see to what extent QCD can justify our *Event Weight Function* for hadronization.

There are two main questions to try to answer from QCD:

- To justify the structure of the *Event Weight Function*: i.e., the space-time area law, the limited transverse phase-space, the possible vertex suppression factors, and the Clebsch-Gordon and spatial knitting factors.
- To estimate the sizes of the vertex suppression factors and knitting factors.

Ultimately, one would then hope to extend the treatment to include understanding of P_T, of baryon formation, etc.

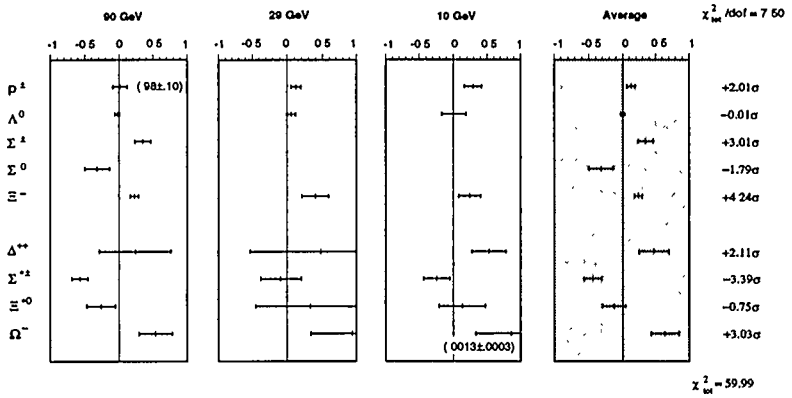


Fig. 16. The summary of UCLA prediction vs experiments for the baryons at E_{CM} =10, 29, and 91 GeV. On the right, the comparison is shown for each flavor baryon averaged over all three energies.

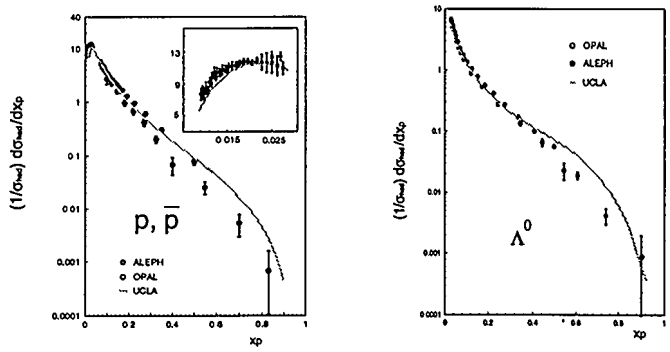


Fig. 17. UCLA predictions for protons and Λ baryons are compared to experiments at $E_{CM} = 91$ GeV.

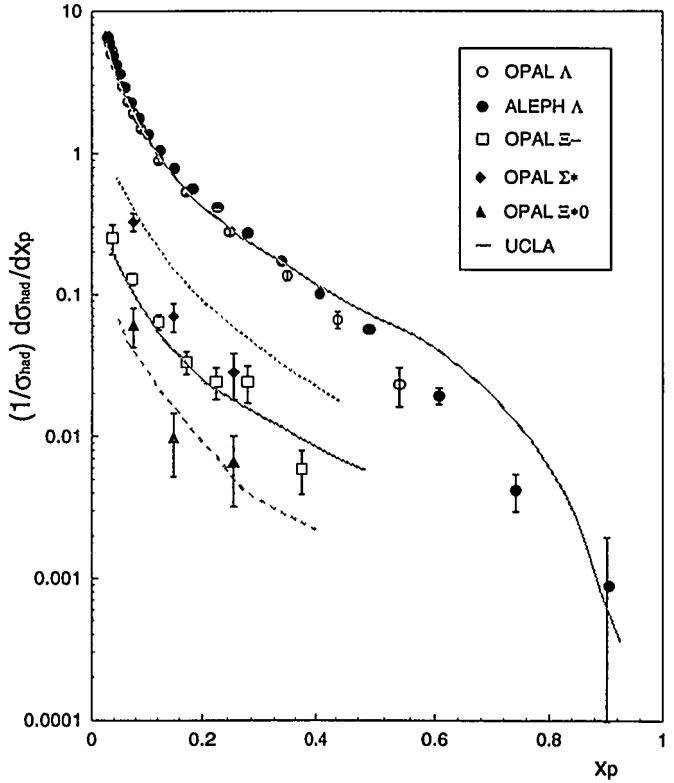


Fig. 18. UCLA predictions for various strange baryons are compared to experiments at $E_{CM} = 91$ GeV.

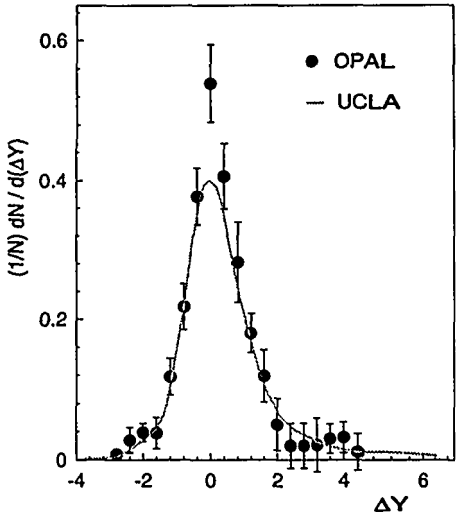


Fig. 19. UCLA prediction for the rapidity correlation of the Λ and $\bar{\Lambda}$ baryon pair is compared to experiments at $E_{CM} = 91$ GeV.

Lattice QCD work[15] within a Euclidean space-time metric indicates that, as a quark and antiquark separate, the color-field begins to collapse into a narrow tube-like structure—approximately a *"string."* There is some very preliminary lattice-work indication[16] that, if virtual quark-antiquark pair production is allowed from the colorfield, then the energy density near the center of the string begins to drop—that is, the string begins to break. This, of course, is also bolstered by the very strong intuition that as a string stretches, a string broken by a quark-antiquark pair represents a lower energy state and therefore that *the string prefers to break.*

Even if one can't expect truly quantitative results from this analytic tool due to the difficulties of extracting the behavior in the continuum limit and of extrapolating from a Euclidean metric to a Minkowskian one, the strong coupling expansion can provide some insights about the physics typical to the strong coupling domain which otherwise would not be possible. For this purpose, we sketch (below) the relevant results of lattice QCD without extensive derivation or justification in order to demonstrate what *lattice QCD* can suggest. (See Ref. 17, accepted for publication in *Physics Reports,* for a more extensive discussion.)

To the lowest order in QED, the cross section $e^+e^- \to f$, where f is a final state of hadrons with particular momenta and flavors can be written as

$$\sigma_{e^+e^-\to f} = \frac{8\pi^2\alpha^2}{S^3}(2\pi)^2\delta\left(P_1 + P_2 - P_f\right) l_{\mu\nu}\langle f|J^\mu(0)|0\rangle\langle f|J^\nu(0)|0\rangle^*, \qquad (14)$$

where $l_{\mu\nu}$ is the lepton current of an electron and J^μ is an electromagnetic current. The matrix element $\langle f|J^\mu(0)|0\rangle$ is related to an *n-point Green's function.* For example, as displayed in Fig. 20, a four-point function, with a loose notation, can be written as

$$\langle f|J^\mu(0)|0\rangle \sim \langle 0|T\bar{\psi}_0\psi_0\bar{\psi}_1\psi_1\bar{\psi}_2\psi_2\bar{\psi}_3\psi_3|0\rangle \sim G\left(x_0, x_1, x_2, x_3\right), \qquad (15)$$

where indices for the quark fields 1, 2, 3 indicate the production points of hadrons and 0 indicates the origin where the virtual photon couples to the current J^μ. The next step is to evaluate the n-point Green's function in Euclidean Lattice QCD.

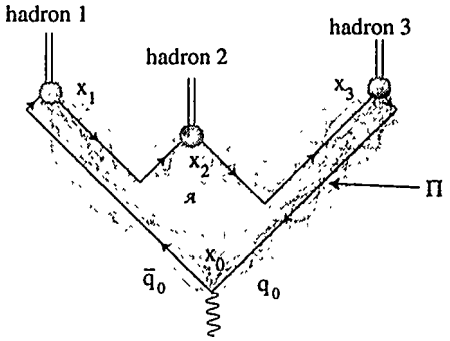


Fig. 20. The virtual photon created by the e^+e^- annihilation decays into the initial $q_0\bar{q}_0$ at x_0. Three hadrons are produced at x_1, x_2, x_3 where the solid straight lines Π depict the classical trajectories of massless fermions (quark or antiquark) whereas gray lines depict all possible loops connecting the four points x_0, x_1, x_2, x_3.

In general, there are many different ways to construct QCD action on the lattice space-time; the *Wilson action* is[18]

$$\begin{aligned} S(U,\bar{\psi},\psi) &= \frac{6}{g^2}\sum_{\square}\left(1-\frac{1}{3}Tr\left(U_{\square}+U_{\square}^{\dagger}\right)\right)+a^3\sum_n \bar{\psi}_n(4+ma)\psi_n \\ &-\frac{a^3}{2}\sum_{n,\mu}\bar{\psi}_n\{(1+\gamma_\mu)\,U\,(n+\hat{\mu},-\mu)\,\psi_{n+\hat{\mu}}+(1-\gamma_\mu)\,U\,(n-\hat{\mu},\mu)\,\psi_{n-\hat{\mu}}\} \\ &=\sum_{i,j}\bar{\psi}_i K_{ij}(U)\psi_j+S_G, \end{aligned} \tag{16}$$

where $U_{\square}$ is the product of links connecting four nearest sites (a *"plaquette"*), μ denotes the space-time index, a is the lattice spacing, and g is the bare coupling constant. The matrix

$$K_{ij}\equiv(8+2ma)\delta_{ij}-(1+\hat{e}_\mu\gamma_\mu)U_{ij}=\frac{1}{\kappa}(\delta_{ij}-\kappa M_{ij})$$

was introduced with the hopping parameter $\kappa=1/(8+2ma)$ in Eq. (16).

Upon introducing source terms $(\rho,\bar{\rho})$ and integrating out the fermion fields, the n-point Green's function becomes

$$\begin{aligned} Z(\rho,\bar{\rho}) &= \int(dU)\ det\ K\ \exp\left(\sum_{ij}\bar{\rho}_i K_{ij}^{-1}\rho_j\right)\ e^{-S_G(U)} \\ &= \int(dU)\ \exp\left(\sum_{ij}\bar{\rho}_i K_{ij}^{-1}\rho_j\right)\ e^{-S_G(U)}, \end{aligned} \tag{17}$$

where the *quenched approximation* (*det* $K=1$; that is, no closed internal quark loops) was used in the last step.

Then, the four-point function Eq. (15) can be written using Eq. (17) as:

$$\begin{aligned} G(x_0,x_1,x_2,x_3) &= \frac{1}{Z}\int\left(dUd\bar{\psi}d\psi\right)T\left(\bar{\psi}_0\psi_0\bar{\psi}_1\psi_1\bar{\psi}_2\psi_2\bar{\psi}_3\psi_3\right)\ e^{-S(\psi,\bar{\psi},\rho,\bar{\rho},U)} \\ &= \frac{1}{Z(\rho,\bar{\rho})}\frac{\partial Z(\rho,\bar{\rho})}{\partial\rho_0\cdots\partial\rho_3\partial\bar{\rho}_0\cdots\partial\bar{\rho}_3}\bigg|_{\rho=0} \\ &= \int(dU)\left(K_{01}^{-1}\cdots K_{30}^{-1}+\text{permutations}\right)e^{-S_G}. \end{aligned} \tag{18}$$

By an iteration, the inverse matrix K^{-1} identically becomes

$$K_{ij}^{-1}=\kappa\left(\delta_{ij}+K_{ik}^{-1}M_{kj}\right)=\kappa\left(\sum_{l=0}^{\infty}\kappa^l M^l\right)_{ij}. \tag{19}$$

Thus, K^{-1} will include the product of $(1\pm\gamma_\mu)\,U$. One, then, finds the important result that Eq. (18) becomes

$$\begin{aligned} G(x_0,x_1,x_2,x_3) &\propto \sum_C \kappa^m\int(dU)\ Tr\ (U\cdots U)_C\ e^{-S_G} \\ &= \sum_C \kappa^m\left\langle P\ e^{ig\oint_C dx^\mu A_\mu}\right\rangle_{gluon}, \end{aligned} \tag{20}$$

where m is the perimeter p of the loop C in lattice units, A_μ is the gauge field, and P stands for *path ordered product*. The summation runs over all the loops connecting the four points. The quantity in brackets $\langle\cdots\rangle$ is the expectation value of the *Wilson Loop* over the *gluon field*.

Now, when the coupling gets weak (and therefore the lattice spacing gets small), the perimeter dependence still persists, in the form of $e^{-\mu p/a}$, since it represents the dependence of the fermion's internal energy, while the area dependence collapses and the overall Wilson Loop average yields *Coulomb's law*. So, for weak

coupling (the early perturbative region), the exponent diverges as $a \to 0$ and dominates the Green's function in this limit. The energy of the initial $q_0\bar{q}_0$ pair is so large that their coupling to gluons can be considered to be small. Therefore, this perimeter dominance overwhelmingly chooses the light-cone as its trajectory in order to minimize the perimeter. Thus, this eliminates all other terms in Eq. (20) except a term with a loop Π which goes through the light-cone as in Fig. 20, i.e.,

$$\begin{aligned} G(x_0, x_1, x_2, x_3) &\propto \sum_C \kappa^m \int (dU)\, Tr\, (U \cdots U)_C\, e^{-S_G} \\ &\simeq \kappa^m \left\langle P\, e^{ig \oint_\Pi dx^\mu A_\mu} \right\rangle_{gluon}. \end{aligned} \tag{21}$$

Next, once the initial $q_0\bar{q}_0$ are separated far away from each other defining a *loop* Π, the coupling rapidly becomes strong, leading toward the hadronization process. The expectation value of the Wilson Loop over the gluon field in Eq. (21) should be evaluated considering that the coupling is a mixture of weak (near the edge of the primary $q_0\bar{q}_0$) and strong (in the middle) over the configuration Π in Fig. 20. But the expectation value of the Wilson loop over the gluon field evaluated over the weak coupling region is essentially *common* to all events with different hadronic final states [see below for the comments about UCLA "stage 3"]; hence the expectation value over the gluon field in Eq. (21) can be evaluated as if the coupling is strong in all regions of configuration Π in Fig. 20 using the *strong coupling expansion*. [Note that the expectation value of the Wilson loop evaluated over the weak coupling region can be considered as a *weak coupling correction* to the expectation value of the Wilson loop evaluated using strong coupling throughout the configuration Π. Further, since this *correction* factor is essentially *common* to all hadronic final states (in 1+1 dimensions, it is exact), it therefore cancels in comparing the *relative* weights of the *Event Weight Function* for different final states or when using the *fragmentation function* Eq. (12).]

This yields an area dependence

$$\left(g^2\right)^{-\mathcal{A}/a^2}$$

Thus, finally, one finds the important result in Euclidean space-time with lattice spacing a:

$$G(x_0, x_1, x_2, x_3) = \kappa^{p/a} \left(g^2\right)^{-\mathcal{A}/a^2}, \tag{22}$$

where $\mathcal{A}$ is the minimal area enclosed by the loop Π, p is its perimeter, and a is the lattice spacing.

The above procedure is, in fact, a dual expansion in terms of $1/(4 + ma)$ (a *hopping parameter*) which gives a multiplication of successive link variables (the perimeter dependence) and a coupling constant g which gives a rule for tiling the surface with *plaquettes* (the area dependence). So, one can see there is always a competition between area dependence and perimeter dependence.

The fact that the expectation value of the Wilson loop over the gluon field evaluated over the weak coupling region is essentially *common* to all events with different hadronic final states raises a very interesting possibility. It suggests that the *Event Weight Functions* for all the final states can be evaluated by the expectation value of a fermion loop along the classical path in strong coupling which involves only the area of world surface determined by the fermion loop. According to this picture, events with hadrons which have big P_T's will be suppressed since the events have large world surface area and will be suppressed by $e^{-b'\mathcal{A}}$. Thus, the picture is qualitatively capable of explaining the fact that jetty events are preferred to nonjetty events and two-jet events are preferred to three- or more jet events. In the future development of the UCLA model (UCLA "stage 3"), it will be attempted to construct the *Event Weight Function* for a given final state from such a *warped area-law* approach, which subsumes the parton shower treatment into the area-law approach, and to simulate whole events at a time rather than an iterative implementation.

7 Summary and Future Work

The hadronization process is a very interesting challenge from a QCD viewpoint in that (a) it is a fundamental QCD process, (b) it can be studied experimentally extensively in a detailed clean fashion in e^+e^- interactions and with particularly simple fundamental probes in the form of flavored meson rates and distributions, and (c) it is a transition, as the initial quark and antiquark rapidly separate, from an original high-virtuality state where perturbative calculations can be performed to a very soft low-virtuality nonperturbative regime, traditionally the domain of lattice work and strong-coupling expansion calculations.

We have shown and discussed the steps in an emerging conceptual and calculational path from QCD to successful predictions of e^+e^- annihilation rates and distributions into hadrons (the simplest arena in which to study quark-colorfield

behavior). Central to this path is construction of an *Event Weight Function* which, for our stringent UCLA assumptions, depends only on a QCD-motivated space-time area law, approximate longitudinal phase-space, and factors to knit quarks into hadronic wave functions (Clebsch-Gordon coefficients for flavor and spin, and a universal *"knitting"* factor for spatial wave functions).

Our approach is particularly successful in predicting data on light-quark meson production, thereby contributing to our understanding of this simplest manifestation of colorfield behavior. It also forms a foundation for further understanding of more sophisticated colorfield behavior—e.g., baryon formation, P_T effects, spin-spin correlations, etc.—as larger samples of more detailed data become available in the future.

The *Event Weight Function*—a simple phenomenological model—also performs the valuable role of a *"target"* for physicists interested in various QCD theoretic approaches to hadronization—e.g., Euclidean-space lattice work, relativistic string modeling, approximate Minkowski-space calculations using new emerging techniques such as world-line formalism—to use as possible verification of their work.

Work to be done in the future includes:

(1) Accumulation of large flavor-identified data samples such that accurate two- and three-particle distributions can be studied in order to understand baryon formation, P_T effects, spin-spin correlations, etc., on the same level as the present understanding of meson formation.

(2) More highly developed phenomenological Monte Carlo modeling, in particular, of phenomena such as popcorn production and local P_T compensation, in order to help interpret the data on these phenomena.

(3) Continued lattice work to understand the shape and possible decay of the colorfield between a quark and antiquark.

(4) As QCD calculational techniques continue to improve, attempts to derive the Event Weight Function structure (or modifications of it) and then to predict the parameter values within this structure, in particular (a) the vertex suppression factors, which our UCLA model assumes are all approximately 1.0 for $u\bar{u}$, $d\bar{d}$, $s\bar{s}$ and 0.0 for $c\bar{c}$ and $b\bar{b}$, and (b) the knitting factors, which UCLA assumes are all approximately equal and for which probability unitarity of the *integrated/summed* fragmentation function leads to a value around $1/(75\ \mathrm{MeV})^{-2} \simeq (2.7\ \mathrm{fm})^2$.

(5) Attempts to calculate and/or understand, either from a QCD-basis or from other physical mechanisms, the values of the "natural" constants "a" and "b"; e.g., using spin-and-spectator-quark counting arguments from deep inelastic crossing symmetry to estimate "a" values for mesons and baryons.

(6) Attempts to develop the "Initial-to-Final-State Global" approach (UCLA "stage 3") described in Sec. 6 in which the parton shower is treated as an unobserved intermediate state and an area law type of approach is applied to the entire transverse momentum (combining P_T from gluons and P_T from the finite colorfield width) of a set of specified final state hadrons.

For those interested in working with our model, the program and manual can be found at *www.physics.ucla.edu/~chuns*.

Acknowledgments

We are deeply indebted to members of the Lund group: Bo Anderson, Hans-Uno Bengtsson, Gösta Gustafson, Gunnar Ingleman, Torbjörn Sjöstrand—for many important and illuminating conversations in the development of this ansatz. We gratefully acknowledge stimulating and useful discussions with Zvi Bern, Siegfried Bethke, Dick Blankenbecler, Stan Brodsky, Phil Burrows, Mike Cornwall, Brent Corbin, Glen Cowan, Alessandro deAngelis, Eric D'Hoker, Tom Gottschalk, Werner Hofmann, J. K. Kim, Duncan Morris, Roberto Peccei, Ina Sarcevic, Terry Tomboulis, Douglas Toussaint, and Bryan Webber. We especially want to thank Rick Berg (who compiled the "world average" data used at 10 GeV and 29 GeV), Sahak Khacheryan (who suggested the heavy quark modification leading to z_{eff}), James Yentang Oyang (who participated extensively in several phases of the work), and Hiroaki Yamamoto (who presented many illuminating challenges to the ansatz).

References

[1] C. D. Buchanan and S.-B. Chun, Phys. Rev. Lett. **59**, 1997 (1987).

[2] B. Anderson *et al.*, Z. Phys. C **20**, 317 (1983).

[3] B. Anderson *et al.*, Phys. Rep. **97**, 33 (1983)

[4] S.-B. Chun and C. D. Buchanan, Phys. Lett. B **308**, 153 (1993).

[5] K. Wilson, Phys. Rev. D **10**, 2445 (1974).

[6] T. Sjöstrand, Comp. Phys. Comm. **82**, 74 (1994).

[7] This solution was first implicitly used by the Lund group in Ref. [2], where they showed that the assumption of $g(S) \propto S^a$ for large S connected the area law with the Lund Symmetric Fragmentation Function, which they had derived from a left-right symmetry requirement. A rigorous proof can be found in Ref. [17].

[8] Private communication from Gösta Gustafson, Lund.

[9] J. M. Cornwall, UCLA/96/TEP/15 (unpublished).

[10] E. C. Berg and C. D. Buchanan, UCLA-HEP-95-01 (unpublished).

[11] A. De Angelis, CERN-PPE/95-135.

[12] XXVIII International Conference on High Energy Physics, July 1996, Warsaw, Poland.

[13] C. Peterson *et al.*, Phys. Rev. D **27**, 105 (1983).

[14] P. D. Acton *et al.*, Phys. Lett. B **305**, 415 (1993).

[15] G. S. Bali, K. Schilling, and C. Schichter, CERN-TH 7413/94;
The UK QCD Collaboration, Phys. Lett. B **275**, 424 (1992);
R. W. Haymaker *et al.*, LSUHE 94-159;
Y. Peng and R. W. Haymaker, Nucl. Phys. B **34**, 266 (1994).

[16] W. Feilmair and H. Markum, Nucl. Phys. B **370**, 299 (1992).

[17] Sebong Chun and Charles Buchanan, "A Simple Plausible Path from QCD to Successful Prediction of $e^+e^- \rightarrow$ *Hadronization* Data," accepted for publication by *Physics Reports*. UCLA-HEP-97-01.

[18] K. Wilson, Phys. Rep. **23**, 331 (1975).

NONRELATIVISTIC EFFECTIVE THEORY FOR QUARKONIUM PRODUCTION IN HADRON COLLISIONS

Martin Beneke
Theory Division, CERN
CH–1211 Genève 23, Switzerland

ABSTRACT

I review recent progress in understanding inclusive quarkonium production in hadron collisions. The first part focuses on nonrelativistic QCD as an effective theory. I discuss its differences from and similarities with effective theories describing bound states of a single heavy quark, as far as matching calculations beyond tree-level and power counting are concerned. The second part summarizes predictions for charmonium and bottomonium production at collider and fixed target experiments and their comparison with data. The emphasis here is on novel signatures due to color octet production, polarization of quarkonia, and the χ_1/χ_2 ratio in fixed target collisions.

© 1996 by Martin Beneke.

1 Introduction

The discovery of charmonium bound states[1] opened the world of heavy flavors, its wonderful variety and complexity. Since then, the focus has shifted to decays of bound states of a single heavy quark, their implications for CP violation, and perhaps, "New Physics." Quarkonia, due to their leptonic decay signature, on the other hand have become important tagging modes in hadron collisions and may become so for the quark-gluon plasma phase. For a theorist, therefore, the interest in quarkonia is mostly of intrinsic nature. The experimental data are there, and we are challenged to explain them.

Quarkonia are the "atoms" of the strong force. If their Rydberg energy were larger than Λ, the dynamical low-energy scale of the strong interaction, quarkonia would be weakly coupled bound states of a heavy quark and antiquark, tractable in perturbation theory just as positronium is in electrodynamics. Neither charm nor bottom quarks are heavy enough to satisfy this requirement. And the top quark decays so rapidly that toponium has barely time to form. The binding of charmonia and bottomonia must be described nonperturbatively. Once the simplicity of a Coulombic bound state is foregone, having two heavy quarks to bind rather than a heavy and a light quark adds complications. Apart from the mass scale m_Q, set by the mass of the heavy quark, a quarkonium bound state involves three essential "small" (compared to m_Q) scales: $m_Q v$, the typical three-momentum of the constituents in the quarkonium rest frame or the inverse quarkonium size; $m_Q v^2$, the scale of binding energies and Λ. In a heavy-light meson, there is no other dimensionless ratio of scales besides Λ/m_Q. Although none of the nonperturbative properties of quarkonia are calculated in the approach described in the sequel, the multitude of low-energy scales entails more complicated power counting rules than those applicable to heavy-light mesons. One may envisage different power counting schemes, depending on the relation of the low-energy scales.

The success of nonrelativistic potential models in describing static properties of the charmonium and bottomonium family suggests that these states are indeed nonrelativistic and that v^2 could be used as a parameter for systematically expanding about the nonrelativistic limit. With v^2 being small, quarkonium production involves two different time scales: the scale $1/m_Q$ on which a $Q\bar{Q}$ pair is produced* and the scale $1/(m_Q v^2)$ on which the heavy quark pair binds into a quarkonium. Provided that the two stages of the production process can be separated and assuming that perturbation theory is valid at the scale m_Q, the heavy quark production part could be computed perturbatively; anything related to quarkonium formation could then be factorized into quarkonium-specific, but production process-independent, nonperturbative parameters.

A systematic realization of these ideas has been developed by Bodwin, Braaten, and Lepage.[2] It is based on an effective field theory, called nonrelativistic QCD (NRQCD), combined with the methods of perturbative factorization, and provides us with a tool to calculate inclusive quarkonium production cross sections as a double expansion in α_s and v^2, and to leading order in Λ/m_Q in production processes with (light) hadrons in the initial state. This development is summarized in Sec. 2.

For phenomenology, the most important insight[3] following from the NRQCD description of quarkonium production is that relativistic effects are very large in the production of ${}^3S_1$ states. Because v^2 is not very small, the radiation of gluons late in the production process, when the $Q\bar{Q}$ pair has already expanded to the quarkonium size, turns out to be favored as compared to the radiation from an almost point-like $Q\bar{Q}$ pair. As a consequence, the $Q\bar{Q}$ pair can remain in a color octet state at distances of order $1/m_Q$, a possibility that is ignored in the earlier color singlet model. The importance of these color octet contributions is supported by the large direct J/ψ and ψ' cross sections observed in $p\bar{p}$ collisions at the Tevatron.[4]

Subsequent to this initial success, almost all quarkonium production processes have been reconsidered in the light of NRQCD. The coverage of all production processes is beyond the scope of this presentation, and I am restricting myself to an overview of the current status of inclusive quarkonium production at colliders and fixed target in Secs. 3 and 4, respectively. A discussion of other interesting production processes, such as photoproduction, e^+e^- annihilation, Z^0 or B decay, together with a (by now incomplete) list of references, can be found in Refs. 5–7. There is also an increasing interest in polarization phenomena, as quarkonium polarization provides calculable quantities in NRQCD, and sometimes a striking

*The scale $1/m_Q$ need not appear if the quarkonium is produced through a weak interaction. Compare $B \to J/\psi X$ mediated by a $b \to c\bar{c}s$ transition with $B_c \to J/\psi X$ mediated by a $b \to c\bar{u}d$ transition. In the latter case, the $c\bar{c}$ pair is produced at distances of order of the B_c radius.

signature of color octet production. I believe that although the above choice of production processes is selective, it covers, on the one hand, the most dramatic new production mechanisms, and on the other hand, illustrates the difficulties connected with a quantitative confirmation of the universality of long-distance parameters, as assumed in NRQCD. Especially for charmonium production, quarkonium binding effects that are at the center of tests of NRQCD factorization can rarely be exhibited in isolation from other QCD effects that reside in the short-distance part or are neglected, such as small-x and soft gluon effects (colliders, photoproduction), BFKL-type situations (photoproduction, $z \to z_{\max} \approx 1$), higher twist effects (fixed target, photoproduction), and parton-hadron duality (B decay). Everything taken together makes for an intricate combination of QCD phenomena. Beyond any doubt, NRQCD is the correct theory for quarkonium systems in the heavy quark limit. Whether the charm quark mass is large enough to justify an expansion around this limit, will be decided by confronting predictions with experiments. As of now, we are only beginning to assess theoretical uncertainties and to sort out those observables that eventually will stand as solid tests of NRQCD.

2 Effective Theory and Factorization in Quarkonium Production

2.1 Nonrelativistic QCD

Let me assume that indeed $m_Q \gg m_Q v, m_Q v^2, \Lambda$. In this situation of well-separated scales, it is intuitive that a quarkonium production cross section should factorize into the production cross section of a $Q\bar{Q}$ pair times the probability that this $Q\bar{Q}$ pair forms a specific quarkonium state.

To make the scale separation explicit, one may think of integrating out all high momentum modes in the path integral down to a factorization scale μ in between m_Q and $m_Q v$. The result would be an effective action, which is highly nonlocal on distances $1/m_Q$. But since the low momentum modes that dominate a quarkonium bound state cannot resolve such small distances, this effective action could be expanded in an infinite series of local interactions. This expansion would realize an expansion in v^2; to all orders, it would be exactly equivalent to QCD. In practice, this procedure can be carried out only in very simplified situations. However, as long as the strong coupling α_s is small enough at the scale μ, the effective Lagrangian can be constructed perturbatively to a specified accuracy.

First, one identifies the low-energy degrees of freedom. In the nonrelativistic limit, intermediate states (in the sense of time-ordered perturbation theory) containing heavy quark pairs are suppressed and integrated out. The heavy quark field Q splits into a two-spinor quark field ψ and a two-spinor antiquark field χ. The effective Lagrangian a priori consists of the most general Lagrangian, including nonrenormalizable operators, consistent with the symmetries of QCD.[†] The coefficients of the operators are then tuned to reproduce QCD by comparing on-shell Green functions computed in QCD with those computed with the NRQCD Lagrangian. The desired accuracy and the values of $\alpha_s(\mu)$ and v^2 determine which operators have to be kept in NRQCD and to what loop-order the comparison has to be done. Note that since the "matching" is carried out at a scale much above the bound state scales, only scattering diagrams have to be computed. By construction, the NRQCD Lagrangian already has the same infrared behavior as QCD. This implies in particular that the result of matching is independent of how the small scales $m_Q v$, $m_Q v^2$, and Λ are related. However, their relation does have some consequences for which operators have to be kept in NRQCD to achieve the desired accuracy.

Nonrelativistic effective theory has first been introduced by Caswell and Lepage[8] as a tool to manage bound state calculations in QED. This application is particularly transparent, as both the short-distance matching and the long-distance contributions can be calculated perturbatively. The main advantage of nonrelativistic QED compared to the Bethe-Salpeter approach is that the physics above the scale m_e is encoded once and forever in the effective Lagrangian. Because NRQED still contains two scales, $m_e\alpha$ and $m_e\alpha^2$, the scale separation is still not complete, but separating m_e already entails great simplifications. See Ref. 9 for a state-of-the-art calculation in NRQED.

The NRQCD Lagrangian takes the form

$$\mathcal{L}_{\rm NRQCD} = \mathcal{L}_2 + \mathcal{L}_4 + \mathcal{L}_{glue} + \ldots . \qquad (1)$$

[†]The NRQCD Lagrangian is usually written in the heavy quark rest frame and is therefore constrained only by rotational symmetry. Of course, the result of any calculation is Lorentz invariant. The "hidden" full Lorentz symmetry constrains some of the coefficient functions in the Lagrangian.

The light quark and gluon part of the QCD Lagrangian remains unaltered and is not indicated. The contribution to the effective Lagrangian that involves two heavy quark fields can be obtained at tree-level from a Foldy-Wouthuysen-Tani transformation, generalized to the non-Abelian case (see, e.g., Ref. 10):

$$\begin{aligned}\mathcal{L}_2 &= \psi^\dagger\left[iD_0+\frac{\vec{D}^2}{2m_Q}\right]\psi+\frac{1}{8m_Q^3}\psi^\dagger\vec{D}^4\psi+\frac{c_1}{2m_Q}\psi^\dagger\vec{\sigma}\cdot g\vec{B}\psi \\ &\quad+\frac{c_2}{8m_Q^2}\psi^\dagger(\vec{D}\cdot g\vec{E}-g\vec{E}\cdot\vec{D})\psi+\frac{c_3}{8m_Q^2}\psi^\dagger(i\vec{D}\times g\vec{E}-g\vec{E}\times i\vec{D})\psi \quad (2)\\ &\quad+\ldots+\text{ charge-conjugated for the antiquark.}\end{aligned}$$

The leading term in square brackets describes a nonrelativistic Schrödinger field theory. To reproduce the on-shell Green functions in QCD at order v^2, the four subsequent terms have to be included. Radiative corrections due to hard gluons shift their coefficients away from their tree level values $c_i = 1$. The ellipses stand for higher order terms in v^2. To reproduce Green functions with $2n$ external heavy quark fields, NRQCD must contain local operators with $2n$ quark fields. In the following, only operators with four quark fields are of interest. The generic form of $\mathcal{L}_4$ is

$$\begin{aligned}\mathcal{L}_4 &= \sum_i \frac{d_i}{m_Q^2}(\psi^\dagger\kappa_i\chi)(\chi^\dagger\kappa_i'\psi) \quad (3)\\ &\quad+\text{ four quark scattering operators,}\end{aligned}$$

where κ_i (κ_i') is a matrix in spin and color indices and may also contain factors of spatial derivatives $\vec{D}/m_Q$ in case of higher dimension operators. The coefficients d_i of the annihilation operators are complex. Their imaginary parts describe the annihilation decay of quarkonium states.[2] Finally, integrating out heavy quark loops leads to higher dimension operators in gluon fields, $\mathcal{L}_{glue}$, the non-Abelian analogue of the Euler-Heisenberg effective Lagrangian.

The NRQCD Lagrangian $\mathcal{L}_2+\mathcal{L}_{glue}$ coincides with the Lagrangian of heavy quark effective theory (HQET).[11] Nevertheless, the two effective theories are different, because their power counting schemes are different. Because Λ is the only low-energy scale in heavy-light mesons, the importance of operators in the HQET Lagrangian is ordered strictly by dimension. Consequently, the kinetic energy operator $\psi^\dagger\vec{D}^2/(2m_Q)\psi$ is suppressed by Λ/m_Q and the leading effective Lagrangian $\psi^\dagger iD_0\psi$ describes a static quark. In a nonrelativistic bound state, we expect $\vec{D}\sim m_Q v$, but $D_0\sim m_Q v^2$ and the kinetic term cannot be neglected. A more compelling argument arises, if one begins to compute Green functions in the quark-antiquark sector of NRQCD. In the following I will implicitly assume the Coulomb gauge, which makes the physics of nonrelativistic bound states most transparent. The amplitude for a $Q\bar{Q}$ pair created in a point and then interacting through exchange of a Coulomb gluon (see Fig. 1), the "00" component of the gluon propagator in this gauge, is given by

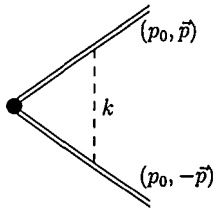


Figure 1: Coulomb correction to point-like $\psi^\dagger\chi$ creation.

$$I=iC_Fg_s^2\int\frac{d^4k}{(2\pi)^4}\frac{1}{\vec{k}^2}\frac{1}{\left[p_0+k_0-\frac{(\vec{p}+\vec{k})^2}{2m_Q}+i\epsilon\right]}\frac{1}{\left[-p_0+k_0+\frac{(\vec{p}+\vec{k})^2}{2m_Q}-i\epsilon\right]}. \quad (4)$$

On-shell, $p_0=\vec{p}^2/(2m_Q)$. The integral is done most easily by closing the contour in the complex k_0-plane and picking up the residues of the enclosed poles. The poles are located at $k_0=p_0-(\vec{p}+\vec{k})^2/(2m_Q)+i\epsilon$ and $k_0=-p_0+(\vec{p}+\vec{k})^2/(2m_Q)-i\epsilon$, one on each side of the real axis. Then

$$I=C_Fg_s^2\int\frac{d^3k}{(2\pi)^3}\frac{m_Q}{\vec{k}^2(\vec{k}^2+2\vec{p}\cdot\vec{k}-i\epsilon)}=\frac{C_F\pi\alpha_s}{4}\frac{m_Q}{|\vec{p}|}+\text{ imaginary.} \quad (5)$$

The imaginary part is divergent and related to the Coulomb phase; the real part exhibits the well-known Coulomb divergence close to threshold.

In the static approximation, the "kinetic term" in the propagators in Eq. (4) would be dropped and the on-shell condition reads $p_0=0$. In this limit, the integration contour becomes pinched between the two poles and the integral becomes ill-defined. Thus, the kinetic term must be kept in the propagator to regulate the pinch-singularity. If one of the quarks were light, as in physical processes to which HQET applies, the static limit can be taken. Although the static propagator pole lies on the real axis, the contour can be deformed away from the pole.

From Eq. (5), it follows that the effective coupling for the exchange of Coulomb gluons is $\alpha_s m_Q/|\vec{p}|$. At small momenta $|\vec{p}| \sim m_Q\alpha_s$, Coulomb exchange cannot be treated as a perturbation, even at weak coupling α_s. The result of resumming Coulomb gluons is, of course, well-known and leads to Coulomb bound state poles in the quark Green function. On the other hand, HQET contains only strongly-coupled bound states. Note that, for the purpose of matching, it is sufficient to use free NRQCD propagators. Being of infrared origin, the Coulomb-enhanced terms cancel in the matching coefficients at every order. The integral in Eq. (5) contains only one scale $|\vec{p}| = m_Q v$. Thus, its finite real part is dominated by gluons with momenta $m_Q v$.‡

Because the leading order Lagrangian contains m_Q in NRQCD, NRQCD does not lead to flavor symmetry. The nonperturbative properties of charmonia and bottomonia remain unrelated even in the nonrelativistic limit. On the other hand, the NRQCD Lagrangian exhibits heavy-quark spin symmetry at leading order in v^2, which turns out to be useful to reduce the number of nonperturbative parameters that describe quarkonium binding.

I started out with quarkonium production, but the effective Lagrangian above does not yet allow quarkonia to be produced. One could not have expected that, because the short-distance part of a production process depends on the initial particles (hadrons, photons, Z bosons, ...) that initiate it. But for every production process, the separation of short and long distances can be performed in the same way as for the effective Lagrangian above. I will elaborate on this in the following subsection.

At this point, let me pause for a discussion of the scales m_Q, $m_Q v$, and $m_Q v^2$ in charmonium and bottomonium systems. They are shown in Table 1, together with those for positronium for comparison. The values of v^2 are based on potential models, which describe the spectrum of quarkonia reasonably accurately. For positronium, $v \sim \alpha$. In a quantum field theoretic context, v^2 could be defined as the expectation value of a derivative operator that scales like v^2 according to the scaling rules to be described later. In general, v^2 will be a complicated function of m_Q and Λ. In the limit $m_Q \to \infty$, the binding becomes Coulombic and $v \sim 1/\ln(m_Q/\Lambda)$. Neither charmonia nor bottomonia are Coulombic, because the energy scale $m_Q v^2$ is of order Λ for both quarkonium families. The same conclusion can be obtained from the observation that with $r \sim 1/(m_Q v)$, the contribution of the linear term in the Cornell potential[12]

$$V(r) = -\frac{C_F\alpha_s(m_Q)}{r} + a^2 r \tag{6}$$

is nonnegligible with respect to the Coulomb term. (The string tension is $a \approx 430\,\text{MeV}$ and $C_F = 4/3$.) Let me stress that NRQCD does not rely in any way on a Coulombic system. It is enough that m_Q is large compared to all bound state scales. The values in Table 1 should be understood for the ground state of each family. Excited states are more nonrelativistic, and at the same time, even less Coulombic. It is possible that the hierarchy of $m_Q v$ and $m_Q v^2$ with respect to Λ changes as one considers higher excited quarkonium states. Different power counting rules would then apply to different members of the onium family. Comparing the different onium systems, note that relativistic corrections (governed by the parameter v^2) are exceedingly small for positronium, comparable to radiative corrections (governed by the parameter $\alpha_s(m_Q)/\pi$) for bottomonium, and definitely large for charmonium.

	$c\bar{c}$	$b\bar{b}$	e^+e^-
m_Q	1.5 GeV	5 GeV	0.5 MeV
$m_Q v$	750 MeV	1.4 GeV	3.7 keV
$m_Q v^2$	400 MeV	400 MeV	25 eV
v^2	0.25	0.08	$5 \cdot 10^{-5}$
$\alpha(m_Q)/\pi$	0.1	0.07	$2 \cdot 10^{-3}$

Table 1: Scales in onium systems and the expansion parameters of the nonrelativistic approximation.

2.2 Factorization and Matching

The factorization of a quarkonium production process, suggested in Ref. 2, begins with the observation that the creation of the $Q\bar{Q}$ pair requires an energy larger than $2m_Q$, and therefore, some of the propagators of the diagram are off-shell by at least m_Q^2, much larger than the typical off-shellness in a quarkonium bound

‡However, they cannot be thought of as on-shell intermediate states in time-ordered perturbation theory, and in this sense, they are not "dynamical."

state. These propagators can be "contracted to a point," and the remainder of the diagram, sensitive to distances larger than $1/m_Q$, is then associated with an operator matrix element in NRQCD. This is true, provided the production process is inclusive,

$$A + B \to \psi(P, \lambda) + X, \tag{7}$$

where X denotes light hadrons and λ the quarkonium polarization state. If it is not inclusive, the process is sensitive to the details of the hadronic final state and its long-distance contributions cannot be absorbed in quarkonium-specific objects alone.

The short-distance coefficients can be computed by replacing the quarkonium in the final state by a perturbative $Q\bar{Q}$ state at small relative momentum, because the short-distance coefficient by construction does not depend on those effects that bind such a quark state into the quarkonium. Hence, one can (and should) use on-shell quark states, and instead of Eq. (7), one considers

$$A + B \to Q(p)\bar{Q}(\bar{p}) + \text{gluons, light quarks}, \tag{8}$$

where

$$p = \left(\sqrt{m_Q^2 + \vec{q}_1^{\,2}}, \vec{q}_1\right), \qquad \bar{p} = \left(\sqrt{m_Q^2 + \vec{q}_2^{\,2}}, \vec{q}_2\right) \tag{9}$$

in the frame where the $Q\bar{Q}$ pair is almost at rest. (We may think of this frame as the quarkonium rest frame.) The amplitude squared is then expanded in the small quantities $\vec{q}_1$, $\vec{q}_2$, and the external heavy quark spinors are expressed in terms of two-component spinors ξ and η. For a quarkonium not at rest, one applies a Lorentz boost to the vectors p and $\bar{p}$. For the case $\vec{q}_2 = -\vec{q}_1$, explicit formulae for the reduction of the amplitude to rest frame two-spinors can be found in Ref. 13. The simplest example of tree-level matching is shown in Fig. 2. Evaluating the

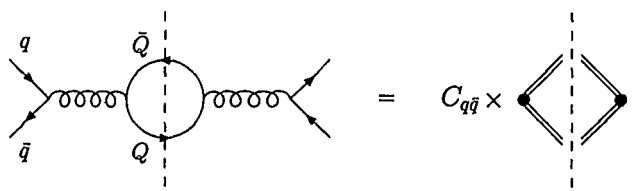


Figure 2: Trivial example of factorization.

cut diagram and summing over all polarizations results in

$$\frac{16\pi^3\alpha_s^2}{27(2m_Q)^3}\,\delta(\hat{s} - 4m_Q^2) \times \eta^\dagger\sigma^i T^a \xi\, \xi^\dagger\sigma^i T^a\eta + O(\vec{q}_1^{\,2}, \vec{q}_2^{\,2}, \vec{q}_1\cdot\vec{q}_2), \tag{10}$$

where $\hat{s}$ is the cms energy of the $q\bar{q}$ pair. The spinor product can be identified with the tree-level evaluation of the matrix element

$$\langle \mathcal{O}_8^\psi(^3S_1)\rangle \equiv \sum_{X,\lambda} \langle 0|\chi^\dagger\sigma^i T^a\psi|\psi(\lambda) + X\rangle\langle\psi(\lambda) + X|\psi^\dagger\sigma^i T^a\chi|0\rangle, \tag{11}$$

where ψ is again replaced by a $Q\bar{Q}$ pair at small relative momentum. Equation (11) displays the structure of a quarkonium production matrix element. In general, the $Q\bar{Q}$ pair can be in various color and spin states. Evidently, in our example, the $Q\bar{Q}$ pair must be in a color octet and spin-one state as expressed by the product $\sigma^i T^a$ in Eq. (11). Further terms in the expansion in $\vec{q}_1$ and $\vec{q}_2$ can be associated with operators similar in form, but with derivatives. It is natural to combine these into "relative" and "cms" derivatives, such that the following identifications can be made

$$\begin{aligned} (q_1 - q_2)_k\, \xi^\dagger\eta &\to \psi^\dagger\left(i\overleftrightarrow{D}_k\right)\chi \\ (q_1 + q_2)_k\, \xi^\dagger\eta &\to iD_k\left(\psi^\dagger\chi\right). \end{aligned} \tag{12}$$

Operators with one relative derivative on each fermion bilinear can be decomposed as ^3P_J with $J = 0, 1, 2$. It is important that the quantum numbers of the $Q\bar{Q}$ pair in the operator need not coincide with the quantum numbers of the quarkonium ψ, because they refer to the $Q\bar{Q}$ state at a time $\tau \sim 1/m_Q$ (in the quarkonium rest frame), long before the quarkonium is formed. In between, gluons with energies less than m_Q can be emitted (so that X becomes nontrivial) and change the color and spin of the $Q\bar{Q}$ pair. By the nature of factorization, these low-energy gluons have to be and are included in the definition of the nonperturbative parameters above.

Operators with cms derivatives are usually neglected, because they are suppressed in v^2 according to the power counting rules discussed below.[§] These operators are important to resolve an ambiguity that arises at leading order in v^2 and which is apparent in Eq. (10): the phase space restrictions ($\hat{s} = 4m_Q^2$) are expressed in terms of partonic variables, such as the quark mass, and do not reflect

[§]For quarkonium decays, such operators were introduced by Mannel and Schuler.[14]

the physical phase space for a quarkonium state with mass different from $4m_Q^2$. It must be like this, because the phase space is part of the short-distance coefficient and therefore can depend only on short-distance parameters. It is also consistent, because $M_\psi - 2m_Q \sim m_Q v^2$ and the mass difference can be neglected at leading order in v^2. This negligence is certainly unjustified, if an observable is sensitive to the kinematic boundaries of phase space and leads to large ambiguities even in fully inclusive (and p_t-integrated) hadroproduction cross sections at high energies, because of the steep rise of the gluon distribution at small x. In the example of Fig. 2, $\vec{q}_1 + \vec{q}_2$ enters the phase-space delta-function. Expansion in $\vec{q}_1 + \vec{q}_2$ leads to a series of higher-dimension operators with increasingly singular coefficients, schematically written as

$$\sum_n c_n \, \delta^{(n)}(\hat{s} - 4m_Q^2) \, (\chi^\dagger \sigma^i T^a \psi) \, (\vec{D})^n \, (\psi^\dagger \sigma^i T^a \chi), \tag{13}$$

where the superscript on the delta-function denotes derivatives. The resummation of this series leads to a (nonperturbative) distribution function[15] with support properties such that its convolution with the short-distance coefficient reproduces the physical phase space constraints.¶ We will meet a particular application of this in Sec. 3.1.

So far, I have discussed only tree-level matching. Factorization becomes nontrivial when one computes radiative corrections, for instance, to the leading-order $q\bar{q}$ annihilation process in Fig. 2:

$$q + \bar{q} \to Q(p)\bar{Q}(\bar{p}) + g. \tag{14}$$

When the $Q\bar{Q}$ pair is in a P-wave state, the cross section is infrared divergent, when the gluon is soft.[18] (I assume that collinear singularities from emission off the initial quarks have already been absorbed into redefined partons.) For a long time, this infrared divergence has shed doubt on the perturbative calculability of P-wave quarkonium decay or production. Within the NRQCD approach, this problem finds its natural solution:[19] the infrared divergence indicates that the soft gluon emission is sensitive to bound state scales and therefore should be factored in a NRQCD matrix element. Since the $Q\bar{Q}$ pair is in a color octet, spin-one state before gluon emission, the only candidate is $\langle \mathcal{O}_8^\psi(^3S_1) \rangle$. Indeed, since this matrix element appeared at leading order [Fig. 2 and Eq. (10)], a complete matching calculation includes the α_s correction to this matrix element, computed in a perturbative $Q\bar{Q}$ state at small relative momentum. This contribution is both ultraviolet and infrared divergent. The ultraviolet divergence can be absorbed into a renormalization of $\langle \mathcal{O}_8^\psi(^3S_1) \rangle$, which becomes explicitly factorization scale dependent. The infrared divergence cancels the infrared divergence in the calculation of the process of Eq. (14). The short-distance coefficient of the P-wave matrix element is now infrared finite, but contains a scale-dependent $\ln(m_Q/\mu)$. The scale dependence cancels with the scale dependence of the octet matrix element $\langle \mathcal{O}_8^\psi(^3S_1) \rangle(\mu)$.

Note that before the advent of NRQCD, the infrared logarithm $\ln m_Q/\lambda$ was sometimes treated as an adjustable nonperturbative parameter, see, for instance, Ref. 20. When this is done consistently in all production processes, this procedure is fully equivalent to taking into account the color octet contribution $\langle \mathcal{O}_8^\psi(^3S_1) \rangle$ in NRQCD. It is for this reason that the leading color octet contributions in NRQCD for P-wave production do not lead to significant differences compared to the color singlet model[21] at next-to-leading order. Ironically, color octet contributions turn out to be more important for S-wave quarkonia, precisely because they are suppressed in v^2 and not intertwined with the leading color singlet term through (logarithmic) operator mixing.

It is quite instructive to go into some details of the NRQCD part of the matching calculation. As an example, let me consider the one-loop mixing of $\langle \mathcal{O}_8^\psi(^3S_1) \rangle$ into $\langle \mathcal{O}_1^\psi(^3P_0) \rangle$. To get a nonzero contribution, a transverse gluon must be cut. The dimensions work out correctly, because a transverse gluon couples proportional to $\vec{p}/m_Q$. One of the diagrams is shown in Fig. 3; it leads to an integral

$$I = \int \frac{d^3k}{(2\pi)^3} \frac{1}{2|\vec{k}|} \frac{1}{m_Q^2} \frac{\vec{p}\cdot\vec{p}' - (\vec{p}\cdot k)(\vec{p}'\cdot k)/\vec{k}^2}{\left[|\vec{k}| - \frac{2\vec{k}\cdot\vec{p}+\vec{k}^2}{2m_Q} + i\epsilon\right]\left[|\vec{k}| - \frac{2\vec{k}\cdot\vec{p}'+\vec{k}^2}{2m_Q} + i\epsilon\right]}. \tag{15}$$

The integral is divergent and has to be regularized. One would like to use dimensional regularization, because it makes matching calculations particularly simple. Dimensional regularization is fine, as long as the effective theory contains only one low-energy scale, such as HQET. Then all integrals in the effective theory are scaleless and vanish identically. NRQCD integrals such as Eq. (15) are not of this type.

¶In the context of quarkonium decays, the breakdown of the NRQCD expansion near boundaries of phase space is discussed in Refs. 16 and 17.

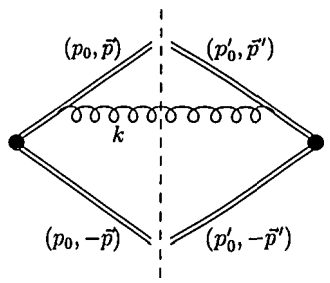


Figure 3: Contribution to mixing of $\langle \mathcal{O}_8^\psi(^3S_1)\rangle$ into $\langle \mathcal{O}_1^\psi(^3P_0)\rangle$.

To see how such integrals are evaluated, let me consider the following simplified version of Eq. (15), both with a cut-off and dimensional regularization:

$$J_{\Lambda_c} = \int_\lambda^{\Lambda_c} \frac{dk}{k} \frac{m_Q^2}{(m_Q+p+k)^2}$$
$$J_d = \mu^{-\epsilon} \int_\lambda^{\infty} \frac{dk}{k^{1-\epsilon}} \frac{m_Q^2}{(m_Q+p+k)^2}. \qquad (16)$$

I will only consider the logarithmically divergent and finite contributions in the limit of small infrared cut-off λ. Because NRQCD is an effective theory below the scale m_Q, the ultraviolet cut-off must be chosen such that $p \ll \Lambda_c \ll m_Q$. Therefore, taking the integral J_{Λ_c} and expanding it in Λ_c/m_Q and p/m_Q, one gets

$$J_{\Lambda_c} = \left(1-\frac{2p}{m_Q}\right)\ln\frac{\Lambda_c}{\lambda} - \frac{2\Lambda_c}{m_Q} + \ldots. \qquad (17)$$

The same result would have been obtained if the integrand had been first expanded in p/m_Q and k/m_Q, which are both small for $k < \Lambda_c$. Note the logarithmic term in the cut-off Λ_c, which would correspond to mixing of $\langle \mathcal{O}_8^\psi(^3S_1)\rangle$ into $\langle \mathcal{O}_1^\psi(^3P_0)\rangle$ in the real case. The dimensionally regulated integral, in the limit $\epsilon \to 0$, evaluates to

$$J_d = \frac{m_Q^2}{(m_Q+p)^2}\left(\ln\frac{m_Q+p}{\lambda} - 1\right) \qquad (18)$$

and seems to have no ultraviolet divergence. The problem here is that dimensional regularization does not know about the physical requirement $p \ll \Lambda_c \ll m_Q$, which expresses that the factorization scale is smaller than m_Q, and treats the cut-off as if it were larger than m_Q. Indeed, up to power-like cut-off dependence, Eq. (18) coincides with the result for J_{Λ_c} evaluated for $\Lambda_c \gg m_Q$. We can force dimensional regularization to treat m_Q larger than all other scales by expanding the integral in m_Q before integration. The result is

$$J_d = \left(1-\frac{2p}{m_Q}\right)\left(\frac{1}{\epsilon} - \ln\frac{\lambda}{\mu}\right) + \ldots, \qquad (19)$$

in agreement with Eq. (17) up to power-like terms in the cut-off which are always zero in dimensional regularization. Thus, in dimensional regularization, one must expand the integrand before integration, while with a cut-off integrating before or after expansion yields the same result, provided $\Lambda \ll m_Q$. The calculation may be simplified even further when the infrared divergence is also regulated dimensionally. After expansion of the integrand, all integrals are scaleless and vanish in dimensional regularization. This technique has been used in Ref. 22 to obtain the NRQCD Lagrangian up to order α_s/m_Q^3 in the single heavy-quark sector.

Expanding the integrand works for matching calculations to all loops in the single heavy-quark sector, but fails in the quark-antiquark sector. Indeed, we know already from Eq. (5) that some matrix elements in the effective theory must be nonvanishing, so that the Coulomb divergence cancels in the matching. Integrands containing Coulomb singularities cannot be expanded in m_Q before integration over k_0. While at one-loop it is easy to separate the Coulomb contributions explicitly, a general matching scheme based on dimensional regularization that would treat diagrams with mixed Coulomb and transverse gluon exchanges has not yet been devised. Since the problem does not appear in matching calculations with a cut-off,‖ it is not related with the effective NRQCD Lagrangian per se. See, however, Ref. 23 for an alternate view of the problem.

Summarizing the discussion of this subsection, the differential quarkonium production cross section in a hadron-hadron collision, $A+B \to \psi(P,\lambda)+X$, can be factorized as

$$d\sigma = \sum_{i,j}\int dx_1 dx_2\, f_{i/A}(x_1) f_{j/B}(x_2) \sum_n d\hat{\sigma}_{i+j\to Q\bar{Q}[n]+X}\,\langle \mathcal{O}_n^{\psi(\lambda)}\rangle. \qquad (20)$$

This equation is diagrammatically represented in Fig. 4, where I have replaced hadron B by a virtual photon for graphical simplicity. Each factor in Eq. (20)

‖NRQED calculations are naturally done in such a scheme, see, e.g., Ref. 9. Otherwise, the bound state diagrams would also have to be evaluated in dimensional regularization.

corresponds to a subgraph in Fig. 4 and a momentum scale that dominates this subgraph. The amplitude squared for $A \to i +$ remnant J is given by the parton distribution $f_{i/A}(x_1)$. The typical virtualities in this subgraph are of order Λ^2. Parton i then participates in a hard collision H, in which a $Q\bar{Q}$ pair in a certain state n is produced. This involves energies of order m_Q. The $Q\bar{Q}$ pair (and, in general, additional gluons) connects to the quarkonium subgraph, represented by the NRQCD matrix element $\langle \mathcal{O}_n^{\psi(\lambda)} \rangle$, which contains all soft lines that are sensitive to the bound state scale $m_Q v^2$. After factorizing initial state singularities into redefined parton distributions and performing the NRQCD matching as described above, the short-distance cross section $d\hat{\sigma}_{i+j \to Q\bar{Q}[n]+X}$ is infrared finite, but depends on the collinear and NRQCD factorization scale. The scale dependence cancels in the product [Eq. (20)].

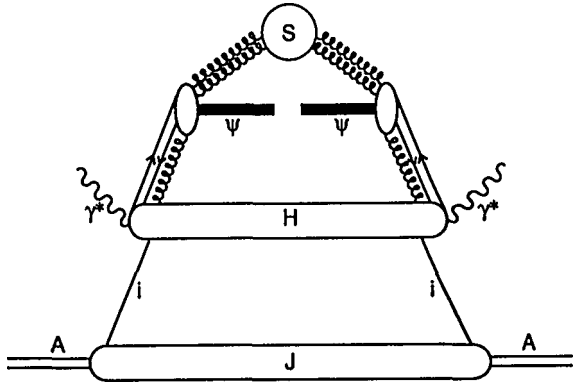


Figure 4: Diagrammatic representation of factorization in $\gamma^* + A \to \psi + X$. For the cross section, the diagram has to be cut.

Note that the factorization formula above implies complete factorization between the final and initial state; all lines connecting both run through the hard part of the diagram. The cancellation of soft gluons, that could connect the quarkonium and remnant jet part, is believed, but not yet really proven, to hold perturbatively for inclusive quarkonium production. This is quite intuitive, if the quarkonium is scattered at large transverse momentum with respect to the colliding hadrons. It holds also for the total quarkonium production cross section even though the bulk cross section is from quarkonia at small transverse momentum. This is intuitive only in the Coulombic limit $m_Q v^2 \gg \Lambda$, in which quarkonium formation has terminated long before the time-scale of a second interaction with the remnant. Since perturbative matching is insensitive to the relation of low energy scales, factorization should thus hold in perturbation theory. The calculation of next-to-leading corrections to total P-wave production cross sections[24] confirms factorization at the one-loop level. The mathematical statement of factorization is thus that all corrections to Eq. (20) scale as some power of $1/m_Q$, or another kinematic scale larger than m_Q, as $m_Q \to \infty$. (Recall that relativistic and radiative corrections scale as $1/\ln m_Q$ in this limit.) Corrections should then be suppressed as Λ divided by potentially any other scale in the process. Since $m_Q v^2 \sim \Lambda$ for charmonium and bottomonium, one may expect large "higher twist" corrections in fixed-target collisions, when the heavy quark-antiquark pair moves parallel with a remnant jet and remains in its hadronization region over a time $1/\Lambda$ in the quarkonium rest frame. Even if higher twist effects scale only as Λ^2/m_c^2 for charmonium, they can be expected to be nonnegligible for total cross sections.

2.3 Power Counting (Velocity Scaling)

The factorization formula (20) contains an infinite series of nonperturbative production matrix elements $\langle \mathcal{O}_n^{\psi(\lambda)} \rangle$ and would be useless, if it could not be truncated after a finite number of terms. A first indication comes from the dimension of the operators, since any power of $1/m_Q$ in the coefficient of an operator can be compensated only by one of the low-energy scales $m_Q v$, $m_Q v^2$, or Λ. However, the matrix elements can have additional suppressions beyond their dimension, because of the particular structure of a nonrelativistic bound state.

The standard power counting (or "velocity scaling") rules are due to Ref. 25. For example, heavy quark fields scale as $(m_Q v)^{3/2}$, because $\int d^3r\, \psi^\dagger \psi$ counts heavy quark number and $r \sim 1/|\vec{p}| \sim 1/(m_Q v)$. The Virial theorem relates the potential to the kinetic energy $E \sim m_Q v^2$ and leads to $g\vec{E} \sim m_Q^2 v^3$ for the electric field inside a quarkonium. From the equation of motion for the vector potential, $g\vec{B} \sim m_Q^2 v^4$ follows for the magnetic field. As a consequence, the "dipole interaction" $\psi^\dagger(g\vec{A} \cdot \vec{\partial}/m_Q^2)\psi$ and "magnetic interaction" $\psi^\dagger(g\vec{B} \cdot \vec{\sigma}/(2m_Q))\psi$ in the NRQCD Lagrangian both scale as v^2 relative to the Coulomb interaction.

It follows that a matrix element such as $\langle \mathcal{O}_1^{J/\psi}(^3S_1) \rangle$ scales as v^3, because a $Q\bar{Q}$ pair in a color singlet $^3S_1$ state overlaps with the leading Fock state wavefunction

of a J/ψ without need of soft gluon emission.** In the following, the scaling of all matrix elements will be considered relative to $\langle \mathcal{O}_1^{J/\psi}(^3S_1)\rangle$; that is, I put $\langle \mathcal{O}_1^{J/\psi}(^3S_1)\rangle \sim 1$. To estimate the scaling of other matrix elements, the multipole suppression of gluon emission with momentum $\vec{k} \sim m_Q v^2 \ll \vec{p} \sim m_Q v$ has to be taken into account as a consequence of the two low-energy scales present in NRQCD. (In the context of NRQED, the separation of photons with momenta $|\vec{k}| \sim m_e v$ and $|\vec{k}| \sim m_e v^2$ and the power counting for the two momentum regions has been analyzed in detail by Labelle.[26])

Consider the P-wave matrix element $\langle \mathcal{O}_8^{J/\psi}(^3P_0)\rangle$ in a J/ψ state. A nonzero overlap requires the emission of gluons into the final state. For a single gluon emission, one such diagram looks exactly like Fig. 3. The $Q\bar{Q}$ vertex carries a derivative for the P-wave operator, and the transverse gluon also couples proportional to $\vec{p}/m_Q$ from the dipole interaction term above. Thus, $\langle \mathcal{O}_8^{J/\psi}(^3P_0)\rangle$ scales as $p^4/m_Q^4 \sim v^4$ relative to $\langle \mathcal{O}_1^{J/\psi}(^3S_1)\rangle$, to which diagrams without radiation would contribute.

Consider now $\langle \mathcal{O}_8^{J/\psi}(^1S_0)\rangle$, which requires a spin-flip transition. As the chromomagnetic interaction is proportional to the gluon momentum, a diagram such as Fig. 3 leads to [cf. Eq. (15)]

$$\begin{aligned} I &= \frac{\alpha_s}{4m_Q^2}\int^{\Lambda_c}\frac{d^3k}{(2\pi)^3}\frac{1}{2|\vec{k}|}\frac{P_{ij}\,(\vec{k}\times\vec{\sigma})_i\,(\vec{k}\times\vec{\sigma})_j}{\left[p_0+|\vec{k}|-\frac{(\vec{p}+\vec{k})^2}{2m_Q}+i\epsilon\right]\left[p_0'+|\vec{k}|-\frac{(\vec{p}'+\vec{k})^2}{2m_Q}+i\epsilon\right]} \\ &\sim \alpha_s\frac{\Lambda_c^2}{m_Q^2} + \text{magnetic dipole contribution}, \end{aligned} \tag{21}$$

where $P_{ij} = \delta_{ij} + k_i k_j/\vec{k}^2$. In the second line, I have (schematically) separated the contribution from the region $|\vec{k}| \sim m_Q v$. In this region, the $|\vec{k}|$ terms in the quark propagators dominate; the integrand becomes independent of the bound state structure and results in a pure (power-like) cut-off term. The contribution from $|\vec{k}| \sim m_Q v^2$ is denoted as "magnetic dipole" and scales as

$$\frac{\alpha_s}{m_Q^2}|\vec{k}|^2 \sim v^2\lambda^2 \sim v^4, \tag{22}$$

where for $|\vec{k}| \sim m_Q v^2$, the coupling α_s must be counted as 1. $\lambda \equiv k/p \sim v$ corresponds to the ratio of the size of the quarkonium and the wavelength of the emitted gluon, and provides the expansion parameter for the multipole expansion. In general, once gluons of momentum $m_Q v$ are separated, the interaction vertices of NRQCD can be multipole-expanded. This is true beyond perturbation theory and justifies the single-gluon approximation which I used for illustration. Thus, $\langle \mathcal{O}_8^{J/\psi}(^1S_0)\rangle$ scales as v^4, if the cut-off term in Eq. (21) could be discarded. If one identifies $\Lambda_c \sim m_Q v$ and α_s at the scale $m_Q v$ with v, as suggested by a Coulombic limit, the cut-off term scales as[27,28] v^3. Being pure cut-off, however, it should not be taken into account to estimate the scaling of low-energy matrix elements. It would be cancelled with a contribution to the coefficient function, if it were evaluated with the same cut-off. In dimensional regularization, the contribution from $|\vec{k}| \sim m_Q v$ gives a tadpole-like integral and would be set to zero naturally.

The multipole suppression is effective as long as $m_Q v \gg \Lambda \sim m_Q v^2$ holds. If, on the other hand, $m_Q v \sim \Lambda \gg m_Q v^2$, the typical momenta of (soft) gluons would be Λ and the multipole expansion would not work, as $\lambda = 1$. We can keep λ as a free parameter and conceive an intermediate case for J/ψ or, in particular, ψ'. The power counting for the most important $Q\bar{Q}$ states is summarized in Tables 2 and 3 for S- and P-wave quarkonia, respectively. For each $Q\bar{Q}$ state, there exist v^2 corrections due to operators with two and more derivatives on a single bilinear of fermion fields. Since their coefficient functions are not enhanced by fewer powers of α_s compared to the leading operator in each channel, I will not discuss them further. Like operators with cms derivatives, these operators can be important in specific kinematic regions.

	$\langle \mathcal{O}_1^{\psi}(^3S_1)\rangle$	$\langle \mathcal{O}_8^{\psi}(^3S_1)\rangle$	$\langle \mathcal{O}_8^{\psi}(^1S_0)\rangle$	$\langle \mathcal{O}_8^{\psi}(^3P_0)\rangle$
NRQCD	1	v^4	$v^2\lambda^2$	v^4
CEM	1	1	1	v^2

Table 2: Velocity scaling in NRQCD and the color evaporation model (CEM) relative to $\langle \mathcal{O}_1^{\psi}(^3S_1)\rangle$ for S-wave quarkonia. The "standard" velocity counting is recovered for $\lambda = v$.

Before closing this section, I would like to mention the color evaporation model[29] (CEM), the only remaining potential competitor of NRQCD.†† In the

**Up to corrections in v^2, this matrix element coincides with the wavefunction at the origin squared. Keeping only this contribution, NRQCD reproduces the color singlet model for S-wave quarkonia.

††As alluded to earlier, the color singlet model has been swallowed by NRQCD and lost its justification hence after.

	$\langle \mathcal{O}_1^\psi(^3P_J)\rangle$	$\langle \mathcal{O}_8^\psi(^3S_1)\rangle$	$\langle \mathcal{O}_8^\psi(^3P_{J'})\rangle$	$\langle \mathcal{O}_8^\psi(^1P_1)\rangle$	$\langle \mathcal{O}_1^\psi(^3S_1)\rangle$	$\langle \mathcal{O}_8^\psi(^3D_{J''})\rangle$
NRQCD	v^2	v^2	v^6	$v^4\lambda^2$	v^6	v^6
CEM	v^2	1	v^2	v^2	1	v^4

Table 3: Velocity scaling in NRQCD and the color evaporation model (CEM) relative to $\langle \mathcal{O}_1^\psi(^3S_1)\rangle$ for P-wave quarkonia with total angular momentum J. The "standard" velocity counting is recovered for $\lambda = v$.

CEM, the NRQCD expansion on the right-hand side of Eq. (20) becomes replaced by an average,

$$\sum_n d\hat{\sigma}_{i+j\to Q\bar{Q}[n]+X}\,\langle \mathcal{O}_n^{\psi(\lambda)}\rangle \to f_\psi \int_{2m_Q}^{2m_{Q_\theta}} dM\, d\hat{\sigma}_{i+j\to Q\bar{Q}(M)+X}/dM, \qquad (23)$$

i.e., the open heavy quark cross section is integrated over the invariant mass M of the $Q\bar{Q}$ pair up to the open heavy flavor threshold. It is then assumed that the quarkonium production cross section is a universal (for each ψ) fraction f_ψ of the subthreshold cross section.

Spiritually, the CEM is close to NRQCD in that it also allows a $Q\bar{Q}$ pair in a color octet state in the hard collision to hadronize into a quarkonium. It is also clear that, because the NRQCD expansion arises from an expansion of the open $Q\bar{Q}$ production amplitude at small relative $Q\bar{Q}$ momentum and because $m_{Q_\theta} - m_Q \ll m_Q$, the CEM is very similar to NRQCD as far as kinematic dependences of the production cross section are concerned. The difference arises in the importance that is assigned to the various terms that arise in the expansion close to threshold. In terms of NRQCD matrix elements, this difference can be summarized by the statement that the power counting implied by the CEM would assign v^{2d-6} to any dimension d operator, independent of the color and spin state of the $Q\bar{Q}$ pair (see Tables 2 and 3). The usual argument is that the emission of soft gluons in the hadronization of a $Q\bar{Q}$ pair randomizes spin and color, so that by the time the quarkonium forms, any information on the state of the initial $Q\bar{Q}$ pair has been lost. The problem with the argument is that soft gluons do not flip a heavy quark spin easily, a piece of information that is incorporated in NRQCD via spin symmetry but disregarded in the CEM. Moreover, the CEM treats a quarkonium as if its size were that of a light hadron, in which case the multipole expansion is not valid. The CEM also does not incorporate the heavy quark limit, in which the binding becomes Coulombic. This does not impede the color evaporation model from providing a description that is phenomenologically successful in some cases, in particular as—in contrast to the color singlet model—the correct kinematic dependences are incorporated. In general, with only one parameter f_ψ, the CEM is too restrictive. Its predictions are universal $\chi/(J/\psi)$-ratio $f_\chi/f_{J/\psi}$, which is not supported by the comparison of quarkonium production in fixed target collisions, photoproduction, and B decay. Note that the CEM (like NRQCD) is based on a leading-twist approximation to the heavy quark production cross section.

2.4 Quarkonium Polarization

NRQCD factorization also predicts the polarization of the produced quarkonia, although, in general, at the expense of introducing further nonperturbative matrix elements that do not appear in the cross section summed over all ψ polarization states ("unpolarized cross section"). Let me sketch the decomposition of matrix elements for the case of a S-wave, spin-triplet quarkonium.[30,31,13]

After expansion of the $Q\bar{Q}$ production amplitude squared in relative momentum, and after decomposing color indices into color singlet and a color octet term, and spin indices in a spin singlet and triplet term, the cross section can be written as a sum [compare with Eq. (20)]

$$\sum_n C_{n;ij}(\mu)\,\langle \mathcal{O}_{n;ij}^{\psi(\lambda)}\rangle, \qquad (24)$$

where the short-distance part C is still coupled to the matrix elements through three-vector indices that arise in the expansion in relative momentum. To decouple these indices, one writes down the most general decomposition of the Cartesian tensor $\langle \mathcal{O}_{n;ij}^{\psi(\lambda)}\rangle$ incorporating rotational invariance and the fact that the rest frame matrix elements can depend only on the polarization vector (in general, tensor) of the quarkonium.

The constraints from spin symmetry are incorporated as follows. Because of spin symmetry, spin and orbital angular momentum are separately good quantum numbers at leading order in the velocity expansion. The angular momentum part of the quarkonium wave function is thus a direct product $S \times L_i$ (i may be a multi-

index for orbital angular momentum greater than 1) in spin and orbital angular momentum, and can be represented as

$$\begin{aligned} {}^1S_0 \quad & 1 \\ {}^3S_1 \quad & \epsilon_a(\lambda)\,\sigma^a \\ {}^1P_1 \quad & \epsilon_i(\lambda) \\ {}^3P_J \quad & \sum_{\alpha,\rho}\langle J\lambda|1\rho;1\alpha\rangle\,\epsilon_i(\rho)\epsilon_a(\alpha)\,\sigma^a \end{aligned} \tag{25}$$

in the quarkonium rest frame, where $\langle J\lambda|1\rho;1\alpha\rangle$ denotes a Clebsch-Gordon coefficient and $\epsilon(\lambda)$ an angular momentum-one polarization vector. A general NRQCD matrix element can then be written as

$$\begin{aligned} &\sum_X \langle 0|\chi^\dagger \kappa D_{i_n}\ldots D_{i_n}\psi|\psi(\lambda)+X\rangle\langle\psi(\lambda)+X|\psi^\dagger\kappa' D_{j_n}\ldots D_{j_m}\chi|0\rangle \\ &\quad = \mathrm{tr}(\kappa S)\,\mathrm{tr}(\kappa' S)\,L_i L_j\,\xi_{iji_1\ldots i_n j_1\ldots j_m}, \end{aligned} \tag{26}$$

where κ is a matrix in spin and color indices and

$$\begin{aligned} \xi_{kl} &= a\,\delta_{kl} \\ \xi_{klmn} &= b_0\delta_{kl}\delta_{mn}+b_1\delta_{km}\delta_{ln}+b_2\delta_{kn}\delta_{lm}, \end{aligned} \tag{27}$$

etc. a, b_i are scalar nonperturbative parameters. Some of them can be expressed in terms of those that appear in unpolarized production by taking contractions or summing over polarizations. For an S-wave quarkonium, the orbital angular momentum part is trivial and it is straightforward to obtain

$$\begin{aligned} &\sum_X \langle 0|\chi^\dagger\sigma^a\psi|\psi(\lambda)+X\rangle\langle\psi(\lambda)+X|\psi^\dagger\sigma^b\chi|0\rangle = \frac{1}{3}\langle\mathcal{O}_1^\psi({}^3S_1)\rangle\,\epsilon^{a*}(\lambda)\epsilon^b(\lambda) \\ &\sum_X \langle 0|\chi^\dagger\sigma^a T^A\psi|\psi(\lambda)+X\rangle\langle\psi(\lambda)+X|\psi^\dagger\sigma^b T^a\chi|0\rangle = \frac{1}{3}\langle\mathcal{O}_8^\psi({}^3S_1)\rangle\,\epsilon^{a*}(\lambda)\epsilon^b(\lambda) \\ &\sum_X \langle 0|\chi^\dagger\sigma^a T^A\left(-\frac{i}{2}\overleftrightarrow{D}_i\right)\psi|\psi(\lambda)+X\rangle\langle\psi(\lambda)+X|\psi^\dagger\sigma^b T^A\left(-\frac{i}{2}\overleftrightarrow{D}_j\right)\chi|0\rangle \\ &\qquad = \langle\mathcal{O}_8^\psi({}^3P_0)\rangle\,\delta_{ij}\,\epsilon^{a*}(\lambda)\epsilon^b(\lambda) \\ &\sum_X \langle 0|\chi^\dagger T^A\psi|\psi(\lambda)+X\rangle\langle\psi(\lambda)+X|\psi^\dagger T^A\chi|0\rangle = \frac{1}{3}\langle\mathcal{O}_8^\psi({}^1S_0)\rangle. \end{aligned} \tag{28}$$

The matrix elements on the right-hand side include implicitly a sum over polarization as in the definition of Ref. 2 and in Eq. (11). For the last line, zero would be obtained in the spin-symmetry limit. The factor 1/3 here follows from rotational invariance. Note that the decomposition of P-wave operators in the third and fourth lines is not diagonal in the angular momentum basis JJ_z. As a consequence, for S-wave production, the total angular momentum of an intermediate quark pair in a P-wave state is not a good quantum number. In this basis, interference terms between states with different total angular momentum have to be included to obtain a factorized form of polarized production cross sections.[30] These interference terms vanish when all polarizations are summed over.

Notice that after applying spin symmetry, no new nonperturbative matrix elements had to be introduced to describe polarized S-wave quarkonium production as compared to unpolarized production at this order in the velocity expansion. For P-wave quarkonia, this is also true at leading order in v^2, but—in contrast to S-wave states—no longer there for v^4 corrections.

3 Quarkonium Production at the Tevatron

In this present section, I discuss the comparison of predictions for S-wave production with Tevatron data,[4,32] which inspired to a large extent the theoretical development described above. In Sec. 4, fixed-target data will be revisited in the NRQCD approach.

3.1 Cross Sections

Let me follow the chronology of the development of theory and data. When CDF measured, for the first time, separately J/ψ and ψ' production not coming from B decay ("prompt"), they found much larger cross sections than expected.[4] The expectation then was based on the color singlet process

$$g+g\to c\bar{c}[{}^3S_1^{(1)}]+g: \qquad \alpha_s^3\frac{(4m_c^2)^2}{p_t^8} \tag{29}$$

for the direct production of S-wave states, with additional contributions to J/ψ from radiative decays of χ_{c1} and χ_{c2}. As indicated, this lowest order process leads to a very steep p_t-spectrum $d\hat{\sigma}/dp_t^2$ of the short-distance cross section. On the other hand, at $p_t \gg 2m_Q$ the quarkonium mass can be considered small and the inclusive production cross section, like any single-particle inclusive cross section in QCD, should exhibit scaling: $d\hat{\sigma}/dp_t^2 \sim 1/p_t^4$ up to logarithms. Such processes can be described by convoluting a (properly factorized) parton production cross

section with a fragmentation function $D_{i\to H}(z)$, where z denotes the fraction of i's momentum transferred to the hadron H. Braaten and Yuan[33] noted that for quarkonia, the dependence of fragmentation functions on z can be calculated in the NRQCD approach. Since the hadronization of the $Q\bar{Q}$ pair takes place by emission of gluons with momenta of order $m_Q v^2$ in the quarkonium rest frame, the energy fraction of the quarkonium relative to the fragmenting parton differs from that of the $Q\bar{Q}$ pair only by an amount $\delta z \sim v^2 \ll 1$. They argued that the higher-order color singlet process

$$g + g \to \left[c\bar{c}[^3S_1^{(1)}] + gg\right] + g: \qquad \alpha_s^5 \frac{1}{p_t^4} \tag{30}$$

exceeds Eq. (29) for $p_t > 7$ GeV as is relevant for most of the Tevatron data. This expectation was born out by detailed analyses.[34] At this point, taking also into account fragmentation production of P-wave states and their subsequent decay, theory and data seemed to agree for J/ψ production, but showed a factor of 30 discrepancy in overall normalization for ψ', a discrepancy then referred to as the ψ'-anomaly. The discrepancy in normalization indicated that an additional fragmentation contribution had been missed. Braaten and Fleming[3] suggested that the color octet fragmentation process

$$g + g \to c\bar{c}[^3S_1^{(8)}] + g: \qquad \alpha_s^3 v^4 \frac{1}{p_t^4}, \tag{31}$$

where a gluon fragments as $g \to c\bar{c}[^3S_1^{(8)}]$, could make up for the missing piece. The price to pay is a new parameter $\langle \mathcal{O}_8^{\psi'}(^3S_1)\rangle$ that had to be fitted to the data. Because Eq. (31) has two powers of α_s/π less than Eq. (30), the magnitude of $\langle \mathcal{O}_8^{\psi'}(^3S_1)\rangle$ turned out to be consistent with its v^4 suppression according to the scaling given in Table 2. Subsequently, CDF was able to remove χ feed-down from J/ψ production. The same discrepancy as for ψ' appeared in the J/ψ cross section and could be explained as for ψ' by color octet fragmentation.[35]

With this explanation of the ψ'-anomaly at hand, further studies focused on finding additional consistency checks of the color octet hypothesis beyond the consistent size of the octet matrix element. One such check derives from polarization and will be described in the next subsection. Others come from different charmonium production processes. Apart from fixed-target production discussed in the following section, I do not undertake such a comparison in this article, a comparison that would in any case be still preliminary. Let me instead continue with the Tevatron analysis and discuss the uncertainties in the theoretical prediction.

At moderate $p_t \sim 2m_Q$, two further octet production channels, which do not have a fragmentation interpretation at order α_s^3,

$$g + g \to c\bar{c}[^1S_0^{(8)}, ^3P_J^{(8)}] + g: \qquad \alpha_s^3 v^4 \frac{4m_c^2}{p_t^6}, \tag{32}$$

need to be considered, too, even though they seem to be suppressed by v^4 with respect to the color singlet process [Eq. (29)]. (I'll come back to this point later.) These contributions have been calculated in Refs. 36 and 37, and turn out to be significant for $p_t < 10$ GeV. In this region (and taking $m_c = 1.5$ GeV), the transverse momentum distribution is sensitive only to the combination $M_{3.5}^{\psi}(^1S_0^{(8)}, ^3P_0^{(8)})$ defined as

$$M_k^{\psi}(^1S_0^{(8)}, ^3P_0^{(8)}) \equiv \langle \mathcal{O}_8^{\psi}(^1S_0)\rangle + \frac{k}{m_c^2}\langle \mathcal{O}_8^{\psi}(^3P_0)\rangle. \tag{33}$$

This matrix element appears as a second fit parameter. The fits to the CDF data[32] are shown in Figs. 5 and 6. These fits are based on a combined fit of J/ψ and ψ' data, keeping the ratios of octet matrix elements for J/ψ and ψ' fixed. See Ref. 37 for further details. The values of the matrix elements with parameters as specified for Fig. 5 are found to be

$$\begin{aligned}
&\langle \mathcal{O}_8^{J/\psi}(^3S_1)\rangle = 1.06 \cdot 10^{-2}\ \text{GeV}^3\\
&\langle \mathcal{O}_8^{J/\psi}(^1S_0)\rangle + \frac{3.5}{m_c^2}\langle \mathcal{O}_8^{J/\psi}(^3P_0)\rangle = 4.38 \cdot 10^{-2}\ \text{GeV}^3\\
&\langle \mathcal{O}_8^{\psi'}(^3S_1)\rangle = 0.44 \cdot 10^{-2}\ \text{GeV}^3\\
&\langle \mathcal{O}_8^{\psi'}(^1S_0)\rangle + \frac{3.5}{m_c^2}\langle \mathcal{O}_8^{\psi'}(^3P_0)\rangle = 1.80 \cdot 10^{-2}\ \text{GeV}^3.
\end{aligned} \tag{34}$$

Note that Figs. 5 and 6 include only α_s^3 processes. The leading color singlet process at large p_t, Eq. (30), is not included but would fall below the data by a factor of 30 as mentioned above.

It is not surprising that a good fit of the data can be obtained with two contributions to the fit that scale as $1/p_t^4$ and $1/p_t^6$ at large p_t. It is not at all clear how accurate the fitted matrix elements are, however, as any effect that modifies the slope of the p_t spectrum would affect the relative weight assigned to the two matrix elements $\langle \mathcal{O}_8^{\psi}(^3S_1)\rangle$ and $M_{3.5}^{\psi}(^1S_0^{(8)}, ^3P_0^{(8)})$. Some uncertainties that enter the theoretical prediction can be enumerated:

1. One may vary the parameters of the calculation such as α_s, the renormalization and/or factorization scale, as well as the parton distribution set. A

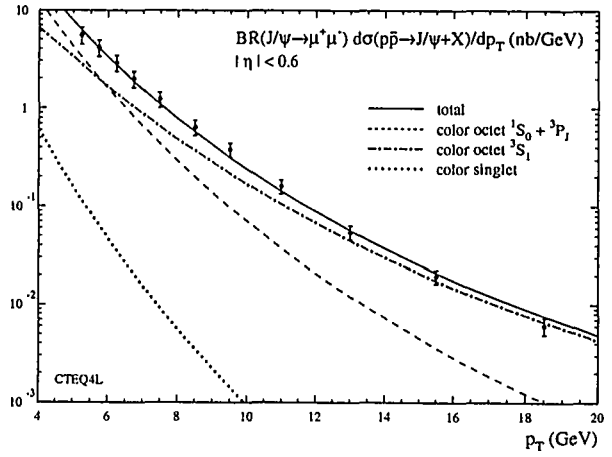


Figure 5: Fit of color octet contributions to direct J/ψ production data from CDF ($\sqrt{s}$ = 1.8 TeV, pseudorapidity cut $|\eta| < 0.6$). Theory: CTEQ4L parton distribution functions, the corresponding Λ_4 = 235 MeV, factorization scale $\mu = (p_t^2 + 4m_c^2)^{1/2}$, and m_c = 1.5 GeV. Taken from Ref. 37.

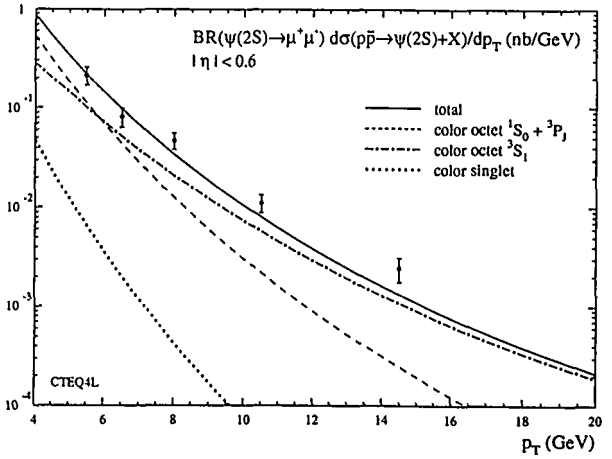


Figure 6: Same as Fig. 5 for prompt ψ' production.

different value of α_s modifies the overall normalization and also the slope of the p_t-distribution, because the coupling is evaluated at $\mu = \sqrt{4m_c^2 + p_t^2}$.

The parametrization of the gluon density affects the prediction in a systematic way. Roughly, we may estimate the typical proton momentum fractions of the gluons that participate in the hard collision as $x_g \sim 2\sqrt{p_t^2 + 4m_c^2}/\sqrt{s}$ for a given value of p_t. A gluon density with steeper small-x behavior therefore steepens the p_t-spectrum for the ${}^3S_1^{(8)}$ component. As a consequence, the $M_{3.5}^{\psi}({}^1S_0^{(8)}, {}^3P_0^{(8)})$ component, whose magnitude depends crucially on the data being somewhat steeper than the ${}^3S_1^{(8)}$ component, decreases for a steeper gluon density.

The combined effect of a lower α_s and flatter small-x gluon distribution is clearly seen in Table 4 by comparing the value of $M_{3.5}^{\psi}({}^1S_0^{(8)}, {}^3P_0^{(8)})$ obtained with MRS(R2) distributions with the one obtained from CTEQ4L or GRV. In contrast, the value of $\langle \mathcal{O}_8^{J/\psi}({}^3S_1) \rangle$ is rather insensitive to the parton distribution set, but absorbs most of the uncertainty in overall normalization obtained by varying the factorization scale μ within a factor of two about $\sqrt{4m_c^2 + p_t^2}$ (see the second error in Table 4). From these variations alone, one can conclude that none of the two matrix elements is determined to an accuracy better than a factor of two and that $M_{3.5}^{\psi}({}^1S_0^{(8)}, {}^3P_0^{(8)})$ is particularly sensitive to any effect that influences the slope of the p_t distribution.

	CTEQ4L	GRV (1994) LO	MRS(R2)
$\langle \mathcal{O}_8^{J/\psi}({}^3S_1) \rangle$	$1.06 \pm 0.14^{+1.05}_{-0.59}$	$1.12 \pm 0.14^{+0.99}_{-0.56}$	$1.40 \pm 0.22^{+1.35}_{-0.79}$
$M_{3.5}^{J/\psi}({}^1S_0^{(8)}, {}^3P_0^{(8)})$	$4.38 \pm 1.15^{+1.52}_{-0.74}$	$3.90 \pm 1.14^{+1.46}_{-1.07}$	$10.9 \pm 2.07^{+2.79}_{-1.26}$
$\langle \mathcal{O}_8^{\psi'}({}^3S_1) \rangle$	$0.44 \pm 0.08^{+0.43}_{-0.24}$	$0.46 \pm 0.08^{+0.41}_{-0.23}$	$0.56 \pm 0.11^{+0.54}_{-0.32}$
$M_{3.5}^{\psi'}({}^1S_0^{(8)}, {}^3P_0^{(8)})$	$1.80 \pm 0.56^{+0.62}_{-0.30}$	$1.60 \pm 0.51^{+0.60}_{-0.44}$	$4.36 \pm 0.96^{+1.11}_{-0.50}$

Table 4: NRQCD matrix elements in $10^{-2}\,\mathrm{GeV}^3$. First error statistical, second error due to variation of scale. Ratio of ψ' to J/ψ fixed. Parton densities from Ref. 38.

2. The variation of renormalization and factorization scales gives some insight into the magnitude of higher order corrections in α_s only for those contributions that have the same kinematic dependence as the leading-order term. In high-energy processes or at not so large transverse momentum, this may be rather misleading.

   Looking at Fig. 5 or 6, we may wonder why at $p_t \sim 2m_c$, the contribution from color octet ${}^3P_J$ and ${}^1S_0$ $c\bar{c}$ pairs exceeds the color singlet contribution by about a factor 20, although from the scaling rules, the color octet contribution would have been expected to be suppressed by $v^4 \sim 1/10$. Since the ratio of matrix elements is indeed $M_{3.5}^{\psi}({}^1S_0^{(8)}, {}^3P_0^{(8)})/\langle \mathcal{O}_1^{\psi}({}^3S_1)\rangle \sim 4 \cdot 10^{-2}$, the short-distance coefficient of the octet term must be three orders of magnitude larger than the coefficient of the singlet term. Examining the short-distance coefficients at $p_t = 2m_c$, one finds approximately

$$\frac{d\hat{\sigma}/dp_t^2[{}^3P_J^{(8)}]}{d\hat{\sigma}/dp_t^2[{}^3S_1^{(1)}]} \sim 81 \frac{\hat{s}^2}{(2m_c)^4}, \tag{35}$$

   where $\hat{s}$ is the partonic cms energy. The constant 81 is a large numerical factor, partly accidental, partly related to color factors and the larger number of P-wave intermediate states. The parametric ratio $\hat{s}^2/(2m_c)^4$ follows from the fact that diagrams with t-channel gluon exchange do not contribute to the leading order color singlet amplitude. Thus, all propagators in the color singlet amplitude are off-shell by $\hat{s}$, while the octet amplitude is dominated by t-channel exchange that allows propagators to be off-shell by only $4m_c^2$. Because the gluon density favors small-x gluons, $\hat{s}$ is not tremendously large at the Tevatron. Nevertheless, at $p_t = 2m_c$, the lower kinematic limit specifies $\hat{s} \geq (1+\sqrt{2})^2\,(2m_c)^2 \sim 5.8\,(2m_c)^2$ and the ratio $\hat{s}^2/(2m_c)^4$ provides a further significant enhancement of the amplitude. This rough estimate approximately coincides with the factor 10^3 estimated from Fig. 5.

   It follows from this discussion that the next-to-leading α_s^4 color singlet contribution to which t-channel exchange diagrams contribute should be strongly enhanced as well and lead to large K factors that increase with increasing transverse momentum, rather similar to photoproduction.[39] At $p_t \gg 2m_c$, this contribution falls as $1/p_t^6$, slower than the lowest order contribution [but still faster than the fragmentation component Eq. (30)], and is rather similar in shape to the ${}^3P_J$ and ${}^1S_0$ octet components. The value of $M_{3.5}^{\psi}({}^1S_0^{(8)}, {}^3P_0^{(8)})$ will therefore decrease to compensate for the additional singlet contribution.

   Another source of potentially large higher-order corrections is related to initial state radiation. These effects, like intrinsic transverse momentum, would primarily modify the p_t-distribution in the small-p_t region, up to at least several GeV. Initial state radiation could be treated either by analytic resummation or estimated by Monte Carlo event generators. A first step in this direction has been taken.[40] The bulk effect seems to be an enhanced short-distance coefficient that leads to a decrease of both fitted color octet matrix elements. For a comparison of $\langle \mathcal{O}_8^{\psi}({}^3S_1)\rangle$ in Ref. 40 and those quoted here and in Ref. 36, one has to take into account that the evolution of the fragmentation function in the ${}^3S_1^{(8)}$ channel has not been incorporated in Ref. 40. Evolution depletes the fragmentation function at large z and consequently increases the fitted value of $\langle \mathcal{O}_8^{\psi}({}^3S_1)\rangle$ by about a factor of two.

3. Apart from higher-order radiative corrections, higher order corrections in v^2, the parameter of the nonrelativistic expansion, can be important close to boundaries of partonic thresholds, as discussed in Sec. 2.2. Such a situation occurs for the color octet fragmentation function that enters the most important fragmentation process [Eq. (31)] at large p_t. At the scale $2m_c$, it is given by[3]

$$D_{g\to\psi}(z, 2m_c) = \frac{\pi\alpha_s(2m_c)}{24m_c^3}\,\delta(1-z)\,\langle \mathcal{O}_8^{\psi}({}^3S_1)\rangle. \tag{36}$$

   The delta-function clearly neglects that a fraction $\delta z \sim v^2$ of the gluon momentum is transferred to light hadrons in the "hadronization" of the color octet intermediate state. Because of the steep p_t-distribution, negligence of this nonperturbative softening of the fragmentation function introduces a systematic bias[6,24,41] towards a too low fitted value of $\langle \mathcal{O}_8^{\psi}({}^3S_1)\rangle$.

   The momentum taken by the light degrees of freedom (light hadrons) is incorporated into the velocity expansion of NRQCD through operators with cms derivatives. Resumming the leading contribution results in[15]

$$D_{g\to\psi}(z, 2m_c) = \frac{\pi\alpha_s(2m_c)}{24m_c^3} \int dy_+\,\delta(1-z-y_+)\,f_{\psi}[{}^3S_1^{(8)}](y_+), \tag{37}$$

where

$$f_\psi[^3S_1^{(8)}](y_+) \;=\; \sum_{X,\lambda}\langle 0|\chi^\dagger\sigma^i T^a\psi|\psi(\lambda)+X\rangle\,\delta\Big(y_+ - [\Lambda\cdot(iD)]_+/k_+\Big)\,\langle\psi(\lambda)+X|\psi^\dagger\sigma^i T^a\chi|0\rangle. \tag{38}$$

D denotes a (cms) derivative in the quarkonium rest frame, Λ the Lorentz boost that transforms it into a moving frame, "+" the light-cone "plus"-component of a four-vector, and k is the four-momentum of the "hadronizing" color octet $c\bar{c}$ pair. The distribution $f_\psi[^3S_1^{(8)}](y_+)$ can be interpreted as a distribution of light-cone momentum fraction y_+ taken by light hadrons in the process[‡‡]:

$$c\bar{c}[^3S_1^{(8)}] \to \psi + \text{light hadrons}. \tag{39}$$

After resummation, the octet fragmentation function is expressed in terms of a new unknown function and all predictivity seems to be lost. However, we know that $f_\psi[^3S_1^{(8)}](y_+)$ should have support mainly in a region $y_+ \sim v^2$. Moreover, it is a universal function that could in principle be extracted from other processes not necessarily related to fragmentation. Once such a universal function is isolated, one can also try to model it and check the consistency of the ansatz in different production processes.

Summarizing this discussion, I think that regarding the numerical values of the matrix elements in Eq. (34) as accurate within a factor of two or less for $M_{3.5}^{\psi}(^1S_0^{(8)}, ^3P_0^{(8)})$ would not be overly conservative. It is worth noting that the color evaporation model mentioned earlier can reproduce the Tevatron data rather reasonably.[42] This is no surprise for the shape of the p_t distribution, as the CEM includes a fragmentation component. It is less obvious that this works (again within factors of two) with the same values of normalization factors f_ψ required to describe fixed-target data. From the point of view of NRQCD, such agreement would be considered coincidental, perhaps related to the fact that the octet matrix elements relevant to both processes all scale equally as v^4.

Prompt S-wave bottomonium production has also been measured by CDF, although a χ_b component could not yet be separated. A comparison with predictions can be found in Ref. 36. As $v^4 \sim 1/100$ for bottomonium, color octet contributions are less relevant than for charmonium in the region $p_t < 15\,\text{GeV}$ of the Tevatron data. Given the uncertainties in the color singlet contribution discussed above and the octet matrix elements for bottomonium, the necessity of color octet contributions is not yet as firmly established as for charmonium production. A realistic description of the p_t spectrum requires the resummation of soft gluon radiation, which has not yet been undertaken.

[‡‡]While writing this review, I learned of related ideas by M. Mangano, who introduces a similar distribution function on phenomenological grounds outside the context of the NRQCD expansion.

3.2 Polarization

Perhaps the most decisive test of the NRQCD picture of quarkonium production will come from a polarization measurement of direct J/ψ and ψ' at the Tevatron at large quarkonium transverse momentum. Recall that at large p_t, the production cross section is dominated by gluon fragmentation into $c\bar{c}[^3S_1^{(8)}]$. It was first noted by Cho and Wise[43] that the $c\bar{c}$ pair is transversely polarized, because the coupling of longitudinal gluons is suppressed by $4m_c^2/p_t^2$. Furthermore, to leading order in the velocity expansion, the subsequent transition [Eq. (39)] takes place via a double electric dipole transition, which does not flip the heavy quark spin. Consequently, at large transverse momentum, one should observe transversely polarized quarkonia. The polarization can be observed in the angular distribution of decay leptons from $\psi \to l^+l^-$, which can be written as

$$\frac{d\Gamma}{d\cos\theta} \propto 1 + \alpha\cos^2\theta, \tag{40}$$

with θ the angle between the lepton three-momentum in the ψ rest frame and the polarization axis, and the ψ direction in the hadronic cms frame (lab frame). Pure transverse polarization would imply $\alpha = 1$.

Corrections to the asymptotic limit come from three sources, corresponding to the three small parameters v^2, α_s/π, and $4m_c^2/p_t^2$ that characterize quarkonium production at the Tevatron.* Since spin symmetry is violated by higher order interaction terms in the NRQCD Lagrangian, longitudinal polarization can arise if the transition [Eq. (39)] proceeds via two magnetic dipole transitions. These corrections scale as v^4 and do not vanish in the limit of large transverse momentum. According to the power counting estimate,[30] they could reduce α to 0.85.

The second source of corrections comes from α_s corrections to the fragmentation function, since radiation of a hard gluon can change the $c\bar{c}$ pair's polariza-

*I am ignoring higher twist corrections which are suppressed in the small ratio Λ/p_t.

tion. This correction decreases with p_t as $1/(\ln p_t)$. All relevant fragmentation functions into longitudinally polarized quarkonia have been computed[30] and were found to yield about 5% longitudinal polarization at $p_t = 20\,\text{GeV}$. The corrections turned out to be rather small, mainly because the fragmentation functions can only be softer than the leading term [Eq. (36)] that produces transverse charmonia. After convolution with the short-distance cross section, this leads to suppression of the higher order contribution. If added to the first correction, the second still implies that $\alpha > 0.65$ at $p_t = 20\,\text{GeV}$. This estimate is based on $\langle \mathcal{O}_8^\psi(^3P_0)\rangle/m_c^2 \approx \langle \mathcal{O}_8^\psi(^3S_1)\rangle$, consistent with Table 4 (CTEQ4L).

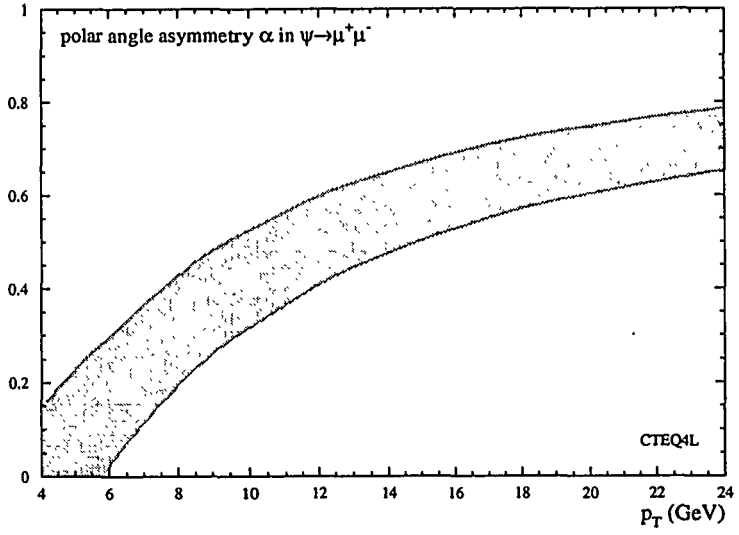


Figure 7: α as a function of p_t. Taken from Ref. 37.

Below $p_t \sim 15\,\text{GeV}$, the dominant source of depolarization is due to nonfragmentation contributions,[37] because they have large short-distance coefficients as seen above. The size of these depends crucially on the magnitude of the parameter $M_{3.5}^\psi(^1S_0^{(8)}, ^3P_0^{(8)})$. With the value taken from Table 4, the prediction for the parameter α in the polar angle distribution is shown in Fig. 7. The band is based on the nonfragmentation corrections and α_s corrections to the fragmentation functions, but neglects the depolarization due to spin symmetry breaking of order $\delta\alpha \sim 0.1$. It is important that the band reflects only the uncertainties in the extraction of NRQCD matrix elements due to statistical errors in the data of the unpolarized cross section. It does not include any of the theoretical uncertainties that could systematically affect the extraction of these matrix elements. In particular, if $M_{3.5}^\psi(^1S_0^{(8)}, ^3P_0^{(8)})$ is smaller than assumed here, which is not unlikely, the transverse polarization fraction would increase. Nevertheless, at $p_t \sim 5\,\text{GeV}$, Fig. 7 shows that no remnant of transverse polarization may be expected. As p_t increases, the angular distribution becomes rapidly more anisotropic. If above $p_t \sim 20\,\text{GeV}$ a substantial fraction of transverse polarization is not observed in future (run II) Tevatron data, we will definitely know that NRQCD, or at least spin symmetry, is not applicable at the charm mass scale. If it is observed, the color evaporation model will have lost most of its remaining appeal.

4 Quarkonium Production at Fixed Target

It has long been known, and highlighted most recently in Refs. 20 and 44, that the color singlet model does not give a satisfactory description of all quarkonium production cross sections at fixed target energies. The discrepancies arise for direct J/ψ and χ_1, both of which cannot be produced by gluon-gluon fusion at leading order in the color singlet channel. When the overall normalization of the color singlet cross section is adjusted to the data, one also predicts a significant fraction of transverse polarization, $\alpha \approx 0.25$ in the notation of Eq. (40) and in the Gottfried-Jackson frame. No polarization is observed. As compared to the Tevatron "ψ'-anomaly," these discrepancies are less dramatic and the theoretical uncertainties could always be stretched, and higher twist effects invoked, to make them appear even less incisive. Nevertheless, these discrepancies must be reassessed in the light of the NRQCD factorization approach.

4.1 Cross Sections

Fixed target quarkonium cross sections have been calculated by several collaborations.[31,45,46] The spin and color states that can be produced in parton-parton

collisions at order α_s^2 are as follows:

$$\begin{aligned} gg &\to c\bar{c}[n]: \quad n = {}^1S_0^{(1,8)}, {}^3P_{0,2}^{(1,8)}, {}^1P_1^{(8)}, D\text{-waves}, \ldots \\ q\bar{q} &\to c\bar{c}[n]: \quad n = {}^3S_1^{(8)}, D\text{-waves}, \ldots . \end{aligned} \tag{41}$$

At order α_s^3, after hard gluon radiation, no stringent helicity and color constraints remain. Adopting a value for $\langle \mathcal{O}_8^\psi({}^3S_1)\rangle$ on the order of those shown in Table 4, the quark annihilation channel turns out to be insignificant at energies far enough from the $c\bar{c}$ threshold such that $x_1 x_2 \sim 4m_c^2/s \ll 1$ for the product of parton momentum fractions. The cross sections are then dominated by gluon-gluon fusion for both pion and proton beams. Keeping the intermediate $c\bar{c}$ states that are leading according to the scaling rules of Table 2, the direct J/ψ and ψ' production cross section is given by

$$\begin{aligned} &\hat{\sigma}(gg \to \psi') = \\ &\frac{5\pi^3\alpha_s^2}{12(2m_c)^3 s}\,\delta\!\left(x_1x_2 - \frac{4m_c^2}{s}\right)\left[\langle \mathcal{O}_8^\psi({}^1S_0)\rangle + \frac{3}{m_c^2}\langle \mathcal{O}_8^\psi({}^3P_0)\rangle + \frac{4}{5m_c^2}\langle \mathcal{O}_8^\psi({}^3P_2)\rangle\right] \\ &+ \frac{20\pi^2\alpha_s^3}{81(2m_c)^5}\,\Theta\!\left(x_1x_2 - \frac{4m_c^2}{s}\right)\langle \mathcal{O}_1^\psi({}^3S_1)\rangle\, z^2\left[\frac{1-z^2+2z\ln z}{(1-z)^2} + \frac{1-z^2-2z\ln z}{(1+z)^3}\right], \end{aligned} \tag{42}$$

where $z \equiv (2m_c)^2/(sx_1x_2)$, $\sqrt{s}$ is the center-of-mass energy, and α_s is normalized at the scale $2m_c$. The third line gives the color singlet cross section that enters at order α_s^3. Using spin symmetry to relate $\langle \mathcal{O}_8^\psi({}^3P_J)\rangle = (2J+1)\langle \mathcal{O}_8^\psi({}^3P_0)\rangle$, the leading color octet contributions are proportional to $M_7^\psi({}^1S_0^{(8)}, {}^3P_0^{(8)})$ defined as in Eq. (33).

A comparison of the predicted energy dependence and normalization of the cross section (including the $q\bar{q}$ annihilation channel) with data is shown in Figs. 8 and 9 for ψ' and J/ψ production, respectively. The solid curves are obtained with

$$\begin{aligned} M_7^{\psi'}({}^1S_0^{(8)}, {}^3P_0^{(8)}) &\equiv \langle \mathcal{O}_8^{\psi'}({}^1S_0)\rangle + \frac{7}{m_c^2}\langle \mathcal{O}_8^{\psi'}({}^3P_0)\rangle = 0.56 \cdot 10^{-2}\,\mathrm{GeV}^3 \\ M_7^{J/\psi}({}^1S_0^{(8)}, {}^3P_0^{(8)}) &\equiv \langle \mathcal{O}_8^{J/\psi}({}^1S_0)\rangle + \frac{7}{m_c^2}\langle \mathcal{O}_8^{J/\psi}({}^3P_0)\rangle = 3.0 \cdot 10^{-2}\,\mathrm{GeV}^3, \end{aligned} \tag{43}$$

with $m_c = 1.5\,\mathrm{GeV}$, which is assumed in this analysis. The color singlet contributions to the direct production cross section is shown separately. Note that since the $q\bar{q}$ annihilation channel is insignificant, the P-wave feed-down incorporated for J/ψ is entirely color singlet, because relativistic corrections to χ_1 production have been neglected. I will discuss χ production in more detail in Sec. 4.2.

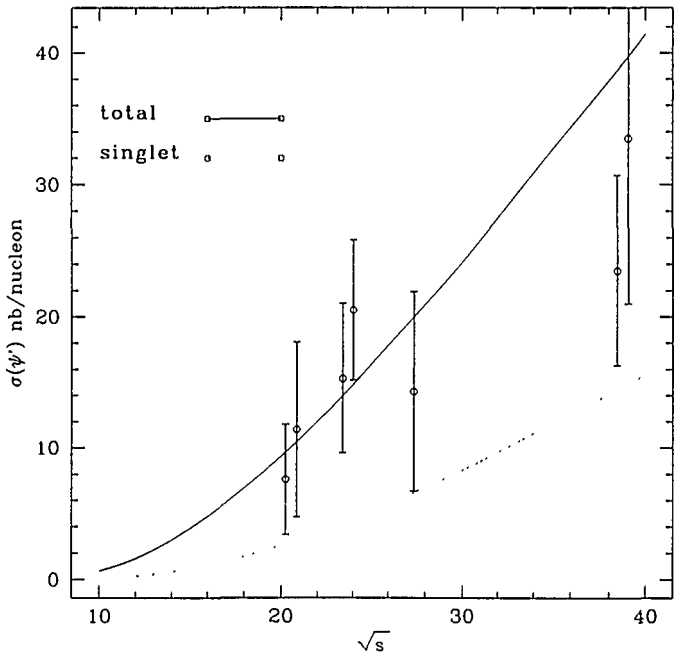


Figure 8: Total (solid) and singlet only (dotted) ψ' production cross section ($x_F > 0$) in proton-nucleon collisions. The solid line is obtained with $M_7^{\psi'}({}^1S_0^{(8)}, {}^3P_0^{(8)}) = 5.2 \cdot 10^{-3}\,\mathrm{GeV}^3$.

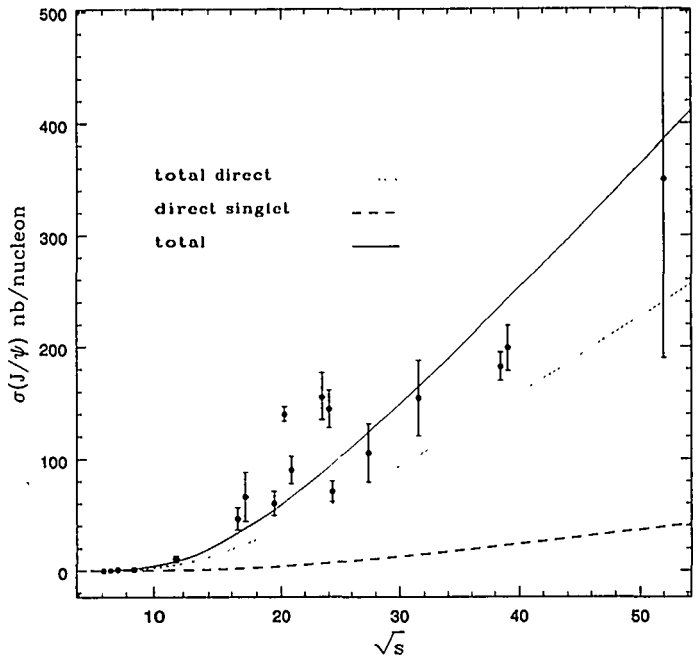


Figure 9: J/ψ production cross sections ($x_F > 0$) in proton-nucleon collisions. Solid line: Fit to the total cross section including radiative feed-down from the χ_{cJ} and ψ' with $M_7^{J/\psi}(^1S_0^{(8)},^3P_0^{(8)}) = 3.0 \cdot 10^{-2}$ GeV^3. Dashed line: Direct J/ψ cross section. Dotted line: Direct J/ψ production, color singlet only.

Turning first to ψ' production, one notes that given the uncertainties inherent to leading order QCD predictions (no K factors have been introduced), their renormalization scale-dependence, as well as the dependence on m_c, and the relevance of color octet contributions is far from obvious. This is mainly due to the fact that the color singlet cross section is dramatically enhanced compared to Ref. 44, because it is expressed in terms of $2m_c = 3\,\mathrm{GeV}$ rather than the significantly larger ψ' mass. Expressing the cross section in terms of quark masses implies a product x_1x_2 smaller by 50% than its physical value and enhances the cross section as a consequence of the rising gluon density at small x. As noted earlier, this intrinsic ambiguity of a leading order calculation in v^2 would be alleviated by resumming higher dimension operators. In the present case, it is likely that the effect would be a reduction of the color singlet cross section, indicating more stringently a missing additional production mechanism. The short-distance coefficients of color octet production would be likewise affected by implementing the physical phase space constraints. In fact, as the invariant mass of the final state containing ψ' and light hadrons is even larger than $m_{\psi'}$, an even more significant reduction would be expected. A fit of the normalization to data would then require a larger $M_7^{\psi'}(^1S_0^{(8)},^3P_0^{(8)})$ than the one quoted in Eq. (43), which would be desirable in view of the apparent discrepancy between Eq. (43) and Eq. (34). Given these uncertainties, we can conclude that the sizes of color octet contributions as deduced from Tevatron and fixed target data are consistent with each other as far as order of magnitude is concerned, and that one could not have hoped for more than that.

For J/ψ, Fig. 9, we have a clear deficit in the color singlet direct production cross section. The difference with respect to ψ' comes from the fact that $m_{J/\psi}$ is not much larger than $2m_c$. While this does not remove the ambiguity with the choice of m_c, one would at least seem to be already closer to the physical phase space. If we assume that the P-wave feed-down is determined by leading order color singlet cross sections, an absolute prediction is obtained for the direct J/ψ cross section, once the unknown parameter $M_7^{J/\psi}(^1S_0^{(8)},^3P_0^{(8)})$ is fitted to the total J/ψ cross section. One finds that $\sigma(J/\psi)_{\mathrm{dir}}/\sigma(J/\psi) \approx 0.6$ in good agreement with experiment. On the other hand, this ratio comes out a factor of three too small with color singlet contributions only. The result $\sigma(J/\psi)_{\mathrm{dir}}/\sigma(J/\psi) \approx 0.6$ is still somewhat problematic, because it relies on the assumption that the χ feed-down is accurately reproduced and understood. But, as discussed in the

following subsection, the χ_1/χ_2 composition of the χ feed-down assumed here conflicts with experiment in that there are too few χ_1 predicted. Thus, there should be an additional but neglected χ production mechanism that would then upset the nice agreement found for $\sigma(J/\psi)_{\rm dir}/\sigma(J/\psi)$ (and make the color singlet model look even worse). This, however, can be compensated by taking into account the larger mass of χ states in the same way as for ψ'. Thus, it seems that color octet contributions in fixed target production are natural candidates to remove large discrepancies in overall normalizations, but the remaining uncertainties preclude a straightforward test of the universality of color octet matrix elements by comparison with Tevatron data. In particular, one cannot exclude the possibility of significant "higher twist" contributions that would have to be added on top of color octet contributions. The numerical situation will be considerably improved by the soon available next-to-leading QCD calculation of all relevant octet and singlet production channels. For P-waves, this analysis has been reported in Ref. 24.

A comparison of cross sections in experiments with pion beams, using Eq. (43) extracted from proton beam experiments, shows that the former are then systematically underpredicted by a factor of about two. The resolution of this discrepancy, already known in the context of color singlet model predictions,[20] is clearly outside the scope of NRQCD, which assumes factorization of the hadronic initial from the hadronic final state.

The analysis of bottomonium S-wave cross sections suffers from the lack of sufficient experimental data, and in particular, the absence of any experimental information on χ_b cross sections. Using color singlet wave functions and an estimate of color octet matrix elements, one finds[31] a larger indirect contribution to S-wave cross sections than for charmonium. The observation of $\Upsilon(3S)$ comparable to $\Upsilon(1S)$ in the E772 experiment[47] then indicates the existence of yet undetected $\chi_b(3P)$ states below the open bottom threshold.

In addition to integrated cross sections, x_F (Ref. 48) and p_t (Ref. 49) distributions may be analyzed. Since the x_F distribution is determined by the gluon flux, the distributions are identical for color singlet and octet contributions and do not lead to further insight. Note that at large x_F, the NRQCD expansion breaks down and higher twist corrections become large.[50] A realistic comparison of p_t distributions in the range of available fixed target data requires accounting of soft gluon effects.

4.2 The χ_1/χ_2 Ratio

As noted in Eq. (41), the leading-order gluon-gluon fusion process cannot produce a spin-1 P-wave state. Consequently, at energies where $q\bar{q}$ annihilation is irrelevant,

$$R \equiv \frac{\sigma(\chi_1)}{\sigma(\chi_2)} = O\left(\frac{\alpha_s}{\pi}\right) \sim 0.05 \qquad \text{(color singlet)}, \tag{44}$$

with the numerical value from Ref. 31. The data[51] compiled in Table 5 clearly show more copious χ_1 production.

Experiment	Beam/Target	$\sqrt{s}$/GeV	R
E673	pBe	19.4/21.7	0.24 ± 0.28
E705	pLi	23.7	0.09
E771	pSi	38.8	0.34 ± 0.16
WA11	πBe	18.63	0.7 ± 0.2
E673	πBe	18.88	0.96 ± 0.64
E673	πBe	20.55	0.9 ± 0.4
E705	πLi	23.72	0.53
E672/706	πBe	31.08	0.57 ± 0.19

Table 5: Experimental data on the χ_1/χ_2 ratio R. Data compiled from Ref. 51. In view of the experimental errors, no attempt has been made to rescale older measurements to account for the latest χ branching fractions.

In the context of the color singlet model, the χ_1 production cross section has sometimes been boosted by taking into account an exclusive quark-antiquark fusion mechanism[52] $q\bar{q} \to \chi_{cJ}$ at order α_s^4, see, e.g., the cross sections displayed in Fig. 16 of Ref. 20. As this mechanism produces χ_{cJ} states in the ratio 0:4:1, it raises R at low energies, especially in πN and $\bar{p}N$ collisions. The justification for keeping this higher order contribution derives from the presence of two infrared logarithms, so that this contribution is of order $\alpha_s^4 \ln^2(m_c/\lambda)$, where $\ln(m_c/\lambda)$ is interpreted as a nonperturbative parameter. This bears some similarity with the infrared logarithm in $q\bar{q} \to \chi_{cJ} + g$ which, as discussed, could be interpreted as $q\bar{q} \to c\bar{c}[^3S_1^{(8)}] \to \chi_{cJ} + X$ in the framework of NRQCD factorization. This simi-

larity is superficial though because the double logarithm above is not regularized by the quarkonium binding energy and cannot be absorbed into a NRQCD matrix element. Thus, if it existed, it would contradict NRQCD factorization. However, it seems clear that the origin of the double logarithm is the exclusive final state considered. The relevant cut diagram at order α_s^4 contains other cuts related to interfering $q\bar{q}g$ final states, which would cancel the infrared logarithms in agreement with NRQCD factorization. Thus, there is no infrared enhancement in the quark-antiquark fusion mechanism, and it cannot help to raise the χ_1/χ_2 ratio.

The next candidates are relativistic corrections in the velocity expansion.[31,53] Indeed, since they dominate direct J/ψ production, which suffers from the same suppression as χ_1 in the color singlet gluon-gluon fusion channel, they should naturally also be large for χ_1 production. The contributions that scale as v^4 relative to the leading order contribution for P-wave production are listed in Table 3. (In each channel, there exist v^2 corrections due to operators with spatial derivatives squared.) To get an estimate with no pretense of accuracy, let me consider only the octet ${}^3P_{J'}$ intermediate states. They yield

$$\frac{\sigma(\chi_1)\,\text{from}\,{}^3P_{J'}^{(8)}}{\sigma(\chi_2)\,\text{from}\,{}^3P_2^{(1)}} = \frac{15}{8}\,\frac{\langle \mathcal{O}_8^{\chi_1}({}^3P_2)\rangle + 15/4\langle \mathcal{O}_8^{\chi_1}({}^3P_0)\rangle}{\langle \mathcal{O}_1^{\chi_2}({}^3P_2)\rangle} \sim \frac{1}{3}, \tag{45}$$

where I assumed that $\langle \mathcal{O}_8^{\chi_1}({}^3P_2)\rangle/\langle \mathcal{O}_1^{\chi_2}({}^3P_2)\rangle \sim 1/10$ according to the scaling $v^4 \sim 1/10$. If we multiply this ratio by two to account for the intermediate S- and D-wave states, we obtain a χ_1 production cross section an order of magnitude larger than Eq. (44). Since the new production channels contribute also to χ_2 production, let me assume that they contribute to χ_1 and χ_2 in the ratio 3:5. Then

$$R \approx 0.3. \tag{46}$$

I emphasize again that this is a very crude estimate.† The estimate is in agreement with the χ_1/χ_2 ratio measured in pN collisions, but is lower than the measurement in πN collisions. If the trend of larger R for pion collisions exhibited by the measurements shown in Table 5 is confirmed, the real problem would no longer be the χ_1/χ_2 ratio per se, but the difference between proton and pion beam experiments. Unless there is an unknown enhancement of the $q\bar{q}$ annihilation channel, such a difference would violate the initial/final state factorization of NRQCD and would have to be attributed to a "higher twist" effect. Note that as long as the $q\bar{q}$ annihilation channel can be neglected, the χ_1/χ_2 ratio should be approximately energy independent.

4.3 Polarization

Polarization measurements have been performed for both ψ and ψ' production in pion scattering fixed target experiments.[55,56] Both experiments observe an essentially flat angular distribution in the decay $\psi \to \mu^+\mu^-$ ($\psi = J/\psi, \psi'$),

$$\frac{d\sigma}{d\cos\theta} \propto 1 + \alpha\cos^2\theta\,, \tag{47}$$

where the angle θ is defined as the angle between the three-momentum vector of the positively charged muon and the beam axis in the rest frame of the quarkonium. The observed values for α are 0.02 ± 0.14 for ψ', measured at $\sqrt{s} = 21.8\,\text{GeV}$ in the region $x_F > 0.25$, and 0.028 ± 0.004 for J/ψ measured at $\sqrt{s} = 15.3\,\text{GeV}$ in the region $x_F > 0$. In both cases, the errors are statistical only.‡

Compared to these measurements, the color singlet contributions alone yield $\alpha \approx 0.25$ for the direct S-wave production cross section.[44] The polarization yield of octet contributions has been considered in Ref. 31.§ The $c\bar{c}[{}^3S_1^{(8)}]$ intermediate state yields pure transverse polarization, but is insignificant for the total cross section, because it occurs only in $q\bar{q}$ annihilation. The $c\bar{c}[{}^1S_0^{(8)}]$ intermediate state results in unpolarized quarkonia while the $c\bar{c}[{}^3P_J^{(8)}]$ intermediate states prefer transverse to longitudinal polarization by a ratio 6:1. The longitudinal polarization fraction is therefore proportional to $M_3^{\psi}({}^1S_0^{(8)}, {}^3P_0^{(8)})$, different from the combination that enters the cross section summed over all polarizations. Con-

†The short-distance coefficients of all v^4 suppressed intermediate states have recently been calculated.[54] Nevertheless, the significant number of new matrix elements makes it difficult to improve on the crude estimate given here. The estimate of R given in Ref. 54 is larger than the one quoted here, because for unknown reasons, the authors choose to omit the dominant color singlet channel in χ_2 production. Accounting for it makes their estimate consistent with Eq. (46).

‡Contemplating Fig. 11 of Ref. 55, I am strongly tempted to assume that the error is misprinted and that the measurement should read 0.028 ± 0.04.

§Polarization has also been treated in Ref. 45. However, in the first reference of Ref. 45 and the preprint version of the second, it was assumed that the ${}^1S_0^{(8)}$ production channel yields pure transverse polarization rather than no polarization, which leads to results significantly different from Ref. 31. This has been corrected in the published version of the second reference.

straining $\langle \mathcal{O}_8^\psi(^1S_0)\rangle$ and $\langle \mathcal{O}_8^\psi(^3P_0)\rangle$ to be positive, the range

$$0.15 < \alpha < 0.44 \tag{48}$$

is obtained for ψ' production at $\sqrt{s} = 21.8\,\mathrm{GeV}$. (The energy dependence is rather mild.) The lower bound is attained if $\langle \mathcal{O}_8^{\psi'}(^3P_0)\rangle = 0$ and could be as low as 0.08, since, as discussed in Sec. 4.1, the color singlet fraction in ψ' production is likely to be lower than that shown in Fig. 8. Thus, the prediction can be consistent with data within experimental errors, if $\langle \mathcal{O}_8^{\psi'}(^3P_0)\rangle$ is small compared to $\langle \mathcal{O}_8^{\psi'}(^1S_0)\rangle$. Such a scenario would be realized in case that the multipole suppression of $\langle \mathcal{O}_8^{\psi'}(^1S_0)\rangle$ is not effective ($\lambda \sim 1$ in Table 2).

The discussion for direct J/ψ production follows the ψ' case. To compare with the measurement, the polarization yield from χ and ψ' feed-down has to be computed. One then obtains

$$0.31 < \alpha < 0.62, \tag{49}$$

the larger value of α being related to the fact that only color singlet mechanisms to χ production were considered (so that the feed-down is almost purely χ_2, in conflict with experiment) and that χ_2 is produced only in a helicity ± 2 state in gluon-gluon fusion at leading order. The feed-down therefore yields an almost purely transversely polarized component to the J/ψ cross section. Equation (49) is incompatible with the observed flat angular distribution. As a prediction, it should, however, be taken with due caution. Taking the estimate of Sec. 4.2 literally, only one-third of the χ feed-down is due to χ_2 produced in a color singlet state, while the polarization yield of the remainder is unknown. Thus, it does not seem excluded that the total χ feed-down is largely unpolarized, in which case α can be as small as 0.1. To resolve this issue, a measurement of χ polarization would be desirable. In particular, one would like to know to what extent χ_{c2} is produced with helicity ± 2. Meanwhile, the situation remains unclear and one may speculate on the role of higher twist final state interactions without impunity.

The comparison with polarization data, as well as the compatibility of matrix elements determined from large-p_t and fixed target production, Eqs. (34) and (43), could be ameliorated, if, as has been suggested,[57] $\langle \mathcal{O}_8^\psi(^3P_0)\rangle$ is actually negative. This is indeed possible in principle for the renormalized matrix element, because of operator mixing, and in particular, a quadratic divergence, that would appear in schemes with an explicit factorization scale. However, phenomenologically, a negative value is unacceptable. The quadratic divergence implies that in any process, $\langle \mathcal{O}_8^\psi(^3P_0)\rangle$ appears as a combination

$$\langle \mathcal{O}_8^\psi(^3P_0)\rangle + k\alpha_s\mu^2\langle \mathcal{O}_1^\psi(^3S_1)\rangle, \tag{50}$$

where μ denotes the factorization scale and the constant k follows from separating and including only the soft gluon contribution to the color singlet cross section. As this combination enters a physical cross section, it must be positive in any factorization scheme. On the other hand, in all phenomenological applications, the higher order color singlet piece is not included into the theoretical prediction or is argued to be smaller than the octet contribution. Consequently, the phenomenologically extracted value of $\langle \mathcal{O}_8^\psi(^3P_0)\rangle$ alone must satisfy the positivity constraint. If a fit prefers this matrix element to be negative, it must be attributed to uncertainties in either theory or data.

4.4 Beyond NRQCD

As emphasized in Sec. 2.2, the NRQCD factorization approach is leading twist and neglects potential interactions of the intermediate heavy quark pair with the beam or target remnants, as well as any production mechanism that involves multiparton interactions in the initial state. Quarkonium production cross sections in fixed target experiments, where most quarkonia escape at small angle with the beam axis, would be especially vulnerable to such corrections. In this subsection, I list some of such phenomena, that cannot be described by NRQCD. For more comprehensive discussions and references, see the overviews given by Brodsky[58] and by Hoyer.[59]

Nuclear dependence. Charmonium production on nuclear targets shows suppression with increasing nucleon number, which is parametrized by $\sigma = \sigma_0 A^\alpha$, where $\alpha \approx 0.9 - 0.92$ for cross sections integrated over positive x_F. Since $\alpha \approx 1$ for open charm production, this nuclear dependence cannot be attributed to shadowing in parton distributions. NRQCD cannot account for such a nuclear dependence due to rescattering of a $c\bar{c}$ pair with the nucleus. Since for bottomonia $\alpha \sim 0.97$, nuclear suppression is consistent with being higher twist. Note that in the nucleus rest frame, the charmonium formation time is long in a high-energy collision and charmonium forms only after the $c\bar{c}$ pair has left the nucleus. Since most J/ψ are now believed to originate from a $c\bar{c}$ pair originally produced in a

color octet state, the rescattering cross section is that of an octet rather than a singlet $c\bar{c}$ pair. A further consequence is that despite their different sizes, the nuclear dependence should be the same for J/ψ and ψ' as is indeed observed.

Comover interactions. A $c\bar{c}$ pair that moves with nearly equal velocity as light quarks from the hadron remnants may find it preferable to produce open charm rather than charmonium. Comover interactions responsible for this effect would be expected to be largest in the nuclear fragmentation region ($x_F < 0$), because of the larger number of potential comovers. Consequently, α should decrease for $x_F < 0$, an effect that is observed for both charmonium and bottomonium.

Large-x_F phenomena. The region $x_F \to 1$ is particularly interesting, because the usual hard scattering picture breaks down in this region.[50] One way to visualize this is to note that all partons of the projectile have to be correlated in order that all momentum can be transferred to a single parton, that subsequently transfers all momentum of the projectile to the $c\bar{c}$ pair. Such a correlation is rather short-lived, and at large x_F, its lifetime can approach the hard interaction time scale set by $1/m_c$. A hard collision at large x_F then takes a snapshot of a compact Fock state component of the projectile, for which multiparton interactions are not suppressed. Such effects may explain the turnover to longitudinal polarization at large x_F seen by the Chicago-Iowa-Princeton Collaboration, and also a decrease of α towards 0.7 at large x_F, since the soft parton in the projectile stopped after transferring its momentum to the $c\bar{c}$ and might then scatter only from the surface of the target nucleus. If the hadron wave function contains an intrinsic charm component (which it certainly does at some level), it would also naturally show itself at large x_F, as the intrinsic $c\bar{c}$ pair preferentially carries most of the projectile momentum. Charmonium production due to intrinsic charm is suppressed as Λ^2/m_c^2 (but can be sizable in narrow kinematic regions) and is not included in NRQCD.

5 Conclusion

In this lecture, I have tried to convey a topical overview on nonrelativistic QCD as an effective theory and some of its applications. As with any effective theory, NRQCD relies on the presence of different mass scales, here the quark mass m_Q and the quark's typical velocity $m_Q v$ and energy $m_Q v^2$ in a nonrelativistic bound state. Assuming perturbation theory at the scale m_Q, NRQCD allows us to organize a calculation as an expansion in $\alpha_s(m_Q)$ and v^2. NRQCD shares many features with heavy quark effective theory and yet has a much richer structure owing to the existence of several low-energy scales $m_Q v$, $m_Q v^2$, and Λ. As a consequence, the power counting in the effective theory is also complicated and one cannot rely on the dimension of operators alone. The velocity scaling rules of NRQCD are simple and unique in the Coulombic limit $m_Q v^2 \gg \Lambda$. If this limit were realized, our use of NRQCD would mimic nonrelativistic QED and the bound state properties of quarkonia would be amenable to a perturbative treatment. As Λ is close to any of the two other bound state scales for charmonium, the velocity scaling is more delicate (and perhaps the most debated issue in NRQCD) and must in principle be assessed for every quarkonium state anew.

To describe quarkonium production, NRQCD has to be amalgamated with the concept of factorization in perturbative QCD. This opens tremendous perspectives on phenomenology, of which only a fraction could be reported here. New insights into quarkonium production followed from recognizing the importance of color octet and fragmentation production mechanisms, both of which are crucial in accounting for the charmonium cross sections observed in the Fermilab Tevatron experiments.

Nevertheless, NRQCD is not a "Theory of Everything" in quarkonium production. The factorization formula for quarkonium production can be compared to the factorization theorem for Drell-Yan processes, with higher twist corrections due to, for example, initial and final state multiparton interactions neglected in both cases. Such corrections may be more or less severe depending on the production process, but would affect fixed target and forward photoproduction in particular. The comparison of leading twist predictions with fixed target data showed significant improvement in all aspects compared to the color singlet model, although some features such as χ production and ψ polarization could be made just consistent with data only upon straining the theory to its limits, which does not appear entirely satisfactory. In any case, even without higher twist corrections, theoretical uncertainties remain appreciable and complicate a verification of the universality of long-distance matrix elements in NRQCD. It seems, at least in my opinion, that at this moment there is no discrepancy in any process, including those not discussed here, that could not be attributed to one or another difficulty in the theoretical prediction, and which thus is understood, even if it is not easily remedied. As concerns fixed target experiments, much clarity could be obtained

from measurements of χ polarization, polarization of $\Upsilon(nS)$, and separate χ_b cross sections.

For any theory, the question "Can it be wrong?" is at least as important as "Is it correct?" Since, in the asymptotic limit $m_Q \to \infty$, NRQCD is evidently as correct as QCD itself, one should ask whether it could generally be inapplicable at the charmonium scale. Here, at last, the situation is clear: ψ' or direct J/ψ polarization at the Tevatron at large transverse momentum will evidence dramatic success or failure of NRQCD for charmonium production.

Acknowledgments

I wish to thank Michael Krämer and Ira Rothstein for their collaboration on quarkonia, and Gerhard Schuler for many discussions and careful reading of the manuscript.

References

[1] J. J. Aubert *et al.*, Phys. Rev. Lett. **33**, 1404 (1974); J.-E. Augustin *et al.*, Phys. Rev. Lett. **33**, 1406 (1974).

[2] G. T. Bodwin, E. Braaten, and G. P. Lepage, Phys. Rev. D **51**, 1125 (1995).

[3] E. Braaten and S. Fleming, Phys. Rev. Lett. **74**, 3327 (1995).

[4] F. Abe *et al.*, Phys. Rev. Lett. **69**, 3704 (1992).

[5] E. Braaten, S. Fleming, and T. C. Yuan, Ann. Rev. Nucl. Part. Sci. **46**, 197 (1996).

[6] M. Beneke, in *Proceedings of the Second Workshop on Continuous Advances in QCD*, Minneapolis, edited by M. Polikarpov (World Scientific, Singapore, 1996), p. 12 [hep-ph/9605462].

[7] A comprehensive overview as of summer 1996 can be found in the *Proceedings of the Quarkonium Physics Workshop*, University of Illinois, Chicago, June 1996.

[8] W. E. Caswell and G. P. Lepage, Phys. Lett. B **167**, 437 (1986).

[9] T. Kinoshita and M. Nio, Phys. Rev. D **53**, 4909 (1996); M. Nio and T. Kinoshita, CLNS97/1463 [hep-ph/9702218].

[10] J. G. Körner and G. Thompson, Phys. Lett. B **264**, 185 (1991); S. Balk, J. G. Körner, and D. Pirjol, Nucl. Phys. B **428**, 499 (1994).

[11] E. Eichten and B. Hill, Phys. Lett. **234**, 511 (1990); B. Grinstein, Nucl. Phys. B **339**, 253 (1990); H. Georgi, Phys. Lett. B **240**, 253 (1990).

[12] E. Eichten *et al.*, Phys. Rev. D **17**, 3090 (1977).

[13] E. Braaten and Y.-Q. Chen, Phys. Rev. D **54**, 3216 (1996).

[14] T. Mannel and G. A. Schuler, Z. Phys. C **67**, 159 (1995).

[15] M. Beneke, I. Z. Rothstein, and M. B. Wise, in preparation.

[16] T. Mannel and S. Wolf, TTP 97-02 [hep-ph/9701324].

[17] I. Z. Rothstein and M. B. Wise, UCSD-97-02 [hep-ph/9702404].

[18] R. Barbieri *et al.*, Phys. Lett. B **95**, 43 (1980); Nucl. Phys. B **192**, 61 (1981).

[19] G. T. Bodwin, E. Braaten, and G. P. Lepage, Phys. Rev. D **46**, 1914 (1992).

[20] G. A. Schuler, "Quarkonium production and decays," CERN-TH-7170-94 [hep-ph/9403387].

[21] C.-H. Chang, Nucl. Phys. B **172**, 425 (1980); E. L. Berger and D. Jones, Phys. Rev. D **23**, 1521 (1981); R. Baier and R. Rückl, Phys. Lett. B **102**, 364 (1981) and Ref. 20 for a review.

[22] A. V. Manohar, UCSD/PTH 97-01 [hep-ph/9701294].

[23] B. Grinstein and I. Z. Rothstein, UCSD-97-06 [hep-ph/9703298].

[24] M. Mangano and A. Petrelli, CERN-96-293 [hep-ph/9610364], to appear in the *Proceedings of the Quarkonium Physics Workshop*, University of Illinois, Chicago, June 1996.

[25] G. P. Lepage *et al.*, Phys. Rev. D **46**, 4052 (1992).

[26] P. Labelle, McGill/96-33 [hep-ph/9608491].

[27] G. T. Bodwin, E. Braaten, and G. P. Lepage, erratum to Ref. 2, January 1997.

[28] G. A. Schuler, CERN-TH/97-12 [hep-ph/9702230], to appear in the *Proceedings of the Quarkonium Physics Workshop*, University of Illinois, Chicago, June 1996.

[29] H. Fritzsch, Phys. Lett. B **67**, 217 (1977); F. Halzen, Phys. Lett. B **69**, 105 (1977).

[30] M. Beneke and I. Z. Rothstein, Phys. Lett. B **372**, 157 (1996) [Erratum: *ibid.* B **389**, 789 (1996)].

[31] M. Beneke and I. Z. Rothstein, Phys. Rev. D **54**, 2005 (1996) [Erratum: *ibid.* D **54**, 7082 (1996)]; I. Z. Rothstein, UCSD-96-22 [hep-ph/9609281], to appear in the *Proceedings of the Quarkonium Physics Workshop*, University of Illinois, Chicago, June 1996.

[32] M. W. Bailey (for the CDF Collaboration), FERMILAB-CONF-96-235-E; A. Sansoni (for the CDF Collaboration), FERMILAB-CONF-96-221-E; V. Papdimitriou (for the CDF Collaboration), to appear in the *Proceedings of the Quarkonium Physics Workshop*, University of Illinois, Chicago, June 1996.

[33] E. Braaten and T. C. Yuan, Phys. Rev. Lett. **71**, 1671 (1993).

[34] M. Cacciari and M. Greco, Phys. Rev. Lett. **73**, 1586 (1994); E. Braaten, M. Doncheski, S. Fleming, and M. Mangano, Phys. Lett. B **333**, 548 (1994); D. P. Roy and K. Sridhar, Phys. Lett. B **339**, 141 (1994).

[35] M. Cacciari, M. Greco, M. L. Mangano, and A. Petrelli, Phys. Lett. B **356**, 560 (1995).

[36] P. Cho and A. K. Leibovich, Phys. Rev. D **53**, 150 (1996); D **53**, 6203 (1996).

[37] M. Beneke and M. Krämer, CERN-96-310 [hep-ph/9611218], to appear in Phys. Rev. D.

[38] M. Glück, E. Reya, and A. Vogt, Z. Phys. C **67**, 433 (1995); A. D. Martin, R. G. Roberts, and W. J. Stirling, Phys. Lett. **387**, 419 (1996) 419; H. L. Lai *et al.*, Phys. Rev. D **55**, 1280 (1997).

[39] M. Krämer, Nucl. Phys. B **459**, 3 (1996).

[40] B. Cano-Coloma and M. A. Sanchis-Lozano, IFIC/97-1 [hep-ph/9701210].

[41] P. Ernström, L. Lönnblad, and M. Vänttinen, NORDITA-96-78-P [hep-ph/9612408].

[42] J. Amundson *et al.*, Phys. Lett. **390**, 323 (1997); G. A. Schuler and R. Vogt, Phys. Lett. B **387**, 181 (1996).

[43] P. Cho and M. B. Wise, Phys. Lett. B **346**, 129 (1995).

[44] M. Vänttinen, P. Hoyer, S. J. Brodsky, and W.-K. Tang, Phys. Rev. D **51**, 3332 (1995).

[45] W.-K. Tang and M. Vänttinen, Phys. Rev. D **53**, 6203 (1996); Phys. Rev. D **54**, 4349 (1996).

[46] S. Gupta and K. Sridhar, Phys. Rev. D **54**, 5545 (1996).

[47] D. M. Alde *et al.*, Phys. Rev. Lett. **66**, 2285 (1991).

[48] S. Gupta and K. Sridhar, Phys. Rev. D **55**, 2650 (1997).

[49] L. Slepchenko and A. Tkabladze, contribution to the 3rd German-Russian Workshop on Progress in Heavy Quark Physics, Dubna, Russia, May 1996 [hep-ph/9608296].

[50] S. J. Brodsky *et al.*, Nucl. Phys. B **369**, 519 (1992).

[51] Y. Lemoigne *et al.*, Phys. Lett. B **113**, 509 (1982); S. R. Hahn *et al.*, Phys. Rev. D **30**, 671 (1984); D. A. Bauer *et al.*, Phys. Rev. Lett. **54**, 753 (1985);

L. Antoniazzi *et al.*, Phys. Rev. D **49**, 543 (1994); V. Koreshev *et al.*, Phys. Rev. Lett. **77**, 4294 (1996); K. Hagan (for the E771 Collaboration), to appear in the *Proceedings of the Quarkonium Physics Workshop*, University of Illinois, Chicago, June 1996.

[52] J. H. Kühn, Phys. Lett. B **89**, 385 (1980).

[53] S. Gupta and P. Mathews, TIFR/TH/96-53 [hep-ph/9609504], to appear in Phys. Rev. D.

[54] S. Gupta and P. Mathews, TIFR/TH/97-08 [hep-ph/9703370].

[55] C. Akerlof *et al.*, Phys. Rev. D **48**, 5067 (1993).

[56] J. G. Heinrich *et al.*, Phys. Rev. D **44**, 1909 (1991).

[57] S. Fleming *et al.*, Phys. Rev. D **55**, 4098 (1997).

[58] S. J. Brodsky, SLAC-PUB-7306 [hep-ph/9609415], to appear in the *Proceedings of the Quarkonium Physics Workshop*, University of Illinois, Chicago, June 1996.

[59] P. Hoyer, NORDITA-97-8-P [hep-ph/9702385], talk given at the 2nd ELFE Workshop, St. Malo, France, September 1996.

ELECTROWEAK TESTS AND SEARCHES FOR NEW PHENOMENA FROM THE TEVATRON

Chris Klopfenstein
Physics Department
University of California at Davis
Davis, CA 95616

Representing the DØ and CDF Collaborations

ABSTRACT

Recent results in precision electroweak measurements and searches for new phenomena from the DØ and CDF experiments at the Fermilab Tevatron collider are reviewed.

©1996 by Chris Klopfenstein.

1 Introduction

The Fermilab Tevatron $\bar{p}p$ collider, the world's highest energy accelerator (1.8 TeV), has recently completed a very successful run. Here we review results from the two major collider experiments, CDF and DØ, in the areas of electroweak measurements and precision tests of the Standard Model (SM), and searches for new phenomena beyond the SM.

In the period 1992–1996, the Tevatron delivered an integrated luminosity to both experiments of $\approx$ 130 pb^{-1}. The run was divided into two distinct running periods: $\approx$ 20 pb^{-1} was delivered in 1992–93 (referred to as run 1A), and $\approx$ 110 pb^{-1} in 1994–96 (run 1B). Most (but not all) results from run 1A given here have been previously published, while most run 1B results are preliminary.

The two detectors are both general-purpose collider detectors. The CDF detector[1] features a superconducting solenoid, tracking system consisting of a central drift chamber and silicon strip vertex detector, scintillator and gas-based calorimetry, and muon detectors. The DØ detector[2] includes central tracking chambers (without magnetic field), a uranium/liquid argon calorimeter, and magnetized iron toroids and drift tubes for muon detection. Both detectors provide excellent measurement of leptons, jets, and missing energy.

The large data sample now available provides considerably higher precision in tests of the SM, and significantly higher reach in searches for new particles and processes than previous experiments. In this paper, we present a selection of results—measurements of production properties of W and Z bosons, determination of the W mass, results of searches for diboson final states, and searches for a zoo of nonstandard particles.

2 W and Z Production Properties

Production properties of W and Z bosons provide stringent tests of the SM, and constraints on parton distribution functions (pdf's). Here we review measurements of W and Z cross sections, determinations of the W width, and charge asymmetries in W and Z production and decay.

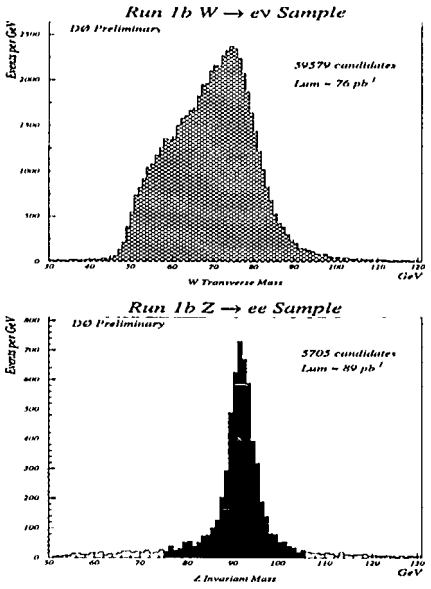


Figure 1: W and Z distributions.

2.1 W and Z Production Cross Sections

W and Z bosons are identified in hadron collider experiments through their leptonic decays. The signature for a $W \to l\nu$ decay is a high p_T lepton (electron or muon) together with a large missing transverse energy ($\not\!\!E_T$), signalling a high p_T neutrino. $Z \to l^+l^-$ decays are detected by reconstructing the invariant mass of lepton pairs. The main backgrounds to these signals come from QCD multijet production (where one or more jets fake an electron), cosmic rays (for muon channels), and W and Z decays to final states containing τ leptons. Figure 1 shows the distribution in transverse mass

$$M_T = \sqrt{2E_T^l \not\!\!E_T (1 - cos\Delta\phi)}$$

for $W \to e\nu$ candidates, and the invariant mass distribution of $Z \to ee$ candidates from DØ.

Measured values of the W and Z cross sections are shown in Fig. 2: published run 1A results and preliminary run (1A+1B) results for both electron and muon

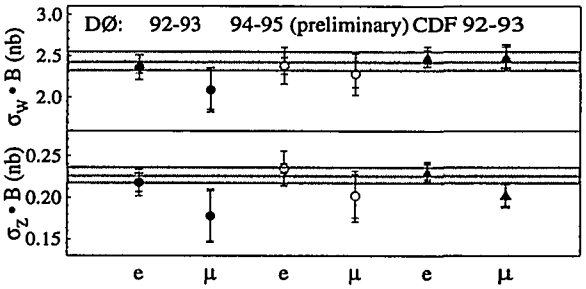


Figure 2: Measurements of W and Z cross sections.

channels from DØ (Ref. 3), and published run 1A electron results and preliminary run 1A muon results from CDF.[4] The shaded band shows the prediction of an order α_s^2 calculation.[5,6] CDF measures

$$\sigma_W \cdot B(W \to e\nu) = 2.49 \pm 0.02(stat) \pm 0.08(sys) \pm 0.09(lum)\ nb$$

$$\sigma_Z \cdot B(Z \to e^+e^-) = 0.231 \pm 0.006(stat) \pm 0.007(sys) \pm 0.008(lum)\ nb.$$

DØ reports

$$\sigma_W \cdot B(W \to e\nu) = 2.38 \pm 0.01(stat) \pm 0.09(sys) \pm 0.20(lum)\ nb$$

$$\sigma_Z \cdot B(Z \to e^+e^-) = 0.235 \pm 0.003(stat) \pm 0.005(sys) \pm 0.020(lum)\ nb$$

$$\sigma_W \cdot B(W \to \mu\nu) = 2.28 \pm 0.04(stat) \pm 0.16(sys) \pm 0.19(lum)\ nb$$

$$\sigma_Z \cdot B(Z \to \mu^+\mu^-) = 0.202 \pm 0.016(stat) \pm 0.020(sys) \pm 0.017(lum)\ nb.$$

2.2 Indirect and Direct Determinations of Γ_W

The measurements of the W and Z cross sections can be combined to determine the ratio

$$R = \frac{\sigma_W \cdot B(W \to l\nu)}{\sigma_Z \cdot B(Z \to l^+l^-)}.$$

Many systematic errors in the individual measurements cancel, at least partially, in the ratio. In particular, errors in luminosity cancel completely. Figure 3 shows the R value as determined in several measurements, both by the Fermilab experiments, and by UA1 and UA2 at the CERN collider.

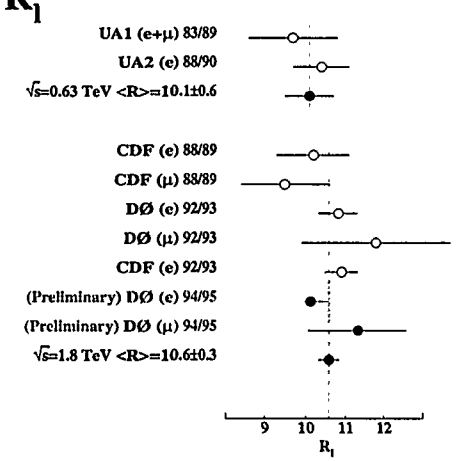


Figure 3: Measurements of R.

The cross-section ratio can be used to indirectly determine the width of the W. Using theoretical predicted values[6,7] for $\sigma_W/\sigma_Z = 3.33 \pm 0.03$ and $\Gamma(W \to l\nu) = 225.2 \pm 1.5$ MeV together with measurements of $BR(Z \to l^+l^-)$ from LEP/SLC[8] allows Γ_W to be extracted. CDF using electron data from run 1A determines $\Gamma_W = 2.06 \pm 0.09$ GeV. DØ obtains $\Gamma_W = 2.159 \pm 0.092$ GeV using electrons and muons from the full run 1 data set.

CDF has also measured Γ_W directly,[9] by fitting the high mass tail of the M_T distribution of $W \to e\nu$ events. The fit is shown in Fig. 4. The result is $\Gamma_W = 2.11 \pm 0.28(stat) \pm 0.16(sys)$ GeV. This result is less precise than the indirect determinations, but has the advantage of model independence. All measurements are consistent with the SM prediction $\Gamma_W = 2.077 \pm 0.014$ GeV.

2.3 W and Z Charge Asymmetries

Decay products of W and Z bosons produced in $\bar{p}p$ collisions display charge asymmetries due to asymmetries in production (for $W^\pm$) and in decay (for both W and Z). The charge asymmetry in W production arises from the imbalance in momentum carried by u and d quarks in the proton—u quarks carry a larger momentum fraction than d quarks. Thus, W^+ are preferentially produced in the proton direction. This production asymmetry is diluted by a decay asymmetry—the charged

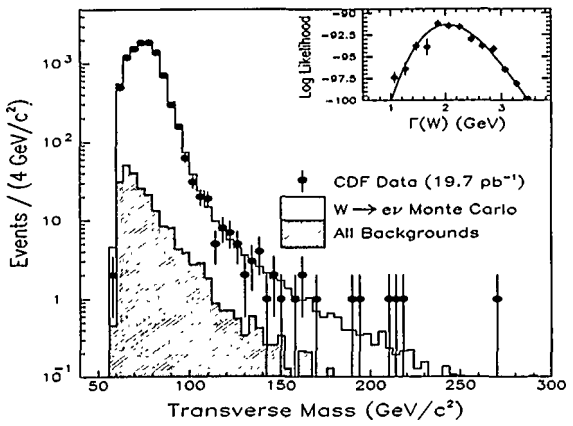


Figure 4: Direct determination of Γ_W.

lepton in the decay $W \to l\nu$ is preferentially emitted opposite the direction of the W, due to the $(V - A)$ coupling of W to quarks and leptons. The observed distribution of leptons in pseudorapidity $\eta = -ln(tan(\frac{\theta}{2}))$ is sensitive to the pdf's $u(x)$ and $d(x)$, and in particular to the slope of the ratio $u(x)/d(x)$. The folded distributions of charged leptons from W decay[10,11] are shown in Fig. 5, compared to predicted distributions from various pdf sets.[12] CDF measures the asymmetry for both muon and electron channels, since DØ does not measure the sign of electrons; they use only the muon channel.

Decays of Z bosons also exhibit a charge asymmetry, which is sensitive both to pdf's and to the V and A couplings of the Z to quarks and leptons. While the asymmetry is small at the Z pole itself, it is substantial off-peak. This asymmetry is also sensitive to various non-SM effects, *e.g.*, a heavy Z' boson. Figure 6 shows CDF's preliminary measurement[13] of the forward-backward asymmetry of e^+e^- pairs as a function of the mass of the pair, compared to a Standard Model prediction calculated using MRSA pdf's. No significant deviation is observed.

3 Measurement of the W Mass

Since W bosons are produced in $\overline{p}p$ collisions with an unknown (and typically large) longitudinal momentum, only the transverse momenta of the decay products

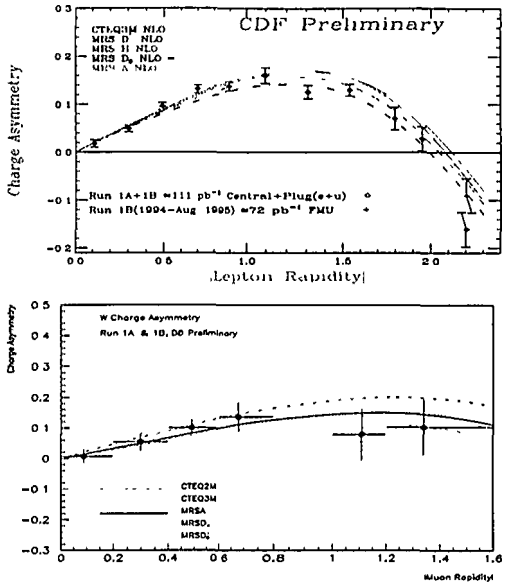


Figure 5: $A = \frac{N_+(\eta) - N_-(\eta)}{N_+(\eta) + N_-(\eta)}$.

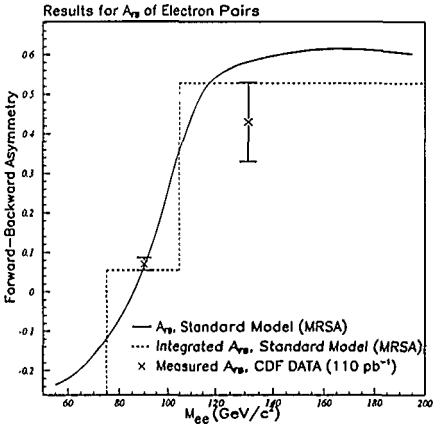


Figure 6: Z charge asymmetry (CDF preliminary).

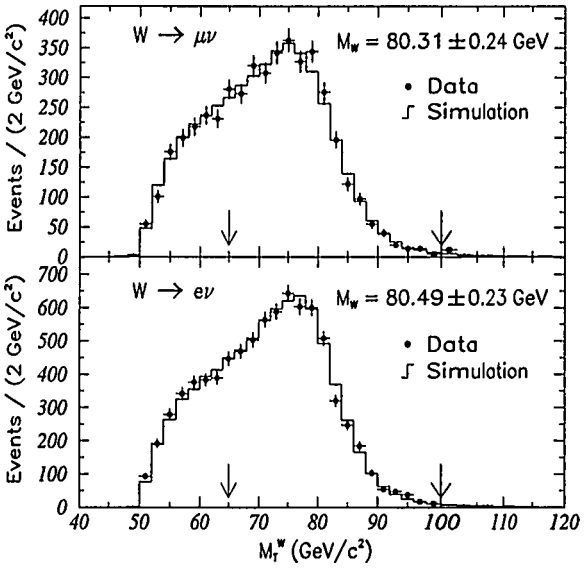


Figure 8: CDF $M_T(l\nu)$, run 1A published.

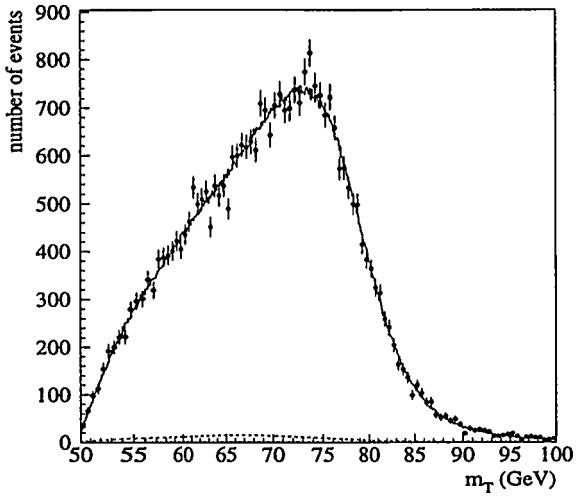


Figure 9: DØ run 1B $M_T(e\nu)$ (preliminary).

Analysis of run 1B data is in progress, and an error $\delta(M_W)$ less than ≈ 100 MeV is expected.

DØ's M_T distribution of $W \to e\nu$ events from run 1B is shown in Fig. 9. The W mass is determined to be

$$M_W = 80.38 \pm 0.07(Wstat) \pm 0.08(Zstat) \pm 0.13(sys) \text{ GeV}.$$

Combining this with the DØ run IA result gives

$$M_W = 80.37 \pm 0.15 \text{ GeV}.$$

The dominant systematic errors are energy scale (due mainly to Z statistics), energy underlying the electron, multiple interaction effects, and the W production model.

The CDF and DØ results can be combined with the earlier UA2 measurement[17] to give a world average value from $\overline{p}p$ experiments

$$M_W = 80.35 \pm 0.13 \text{ GeV } (CDF + D\emptyset + UA2).$$

The recent measurement of M_W in e^+e^- collisions is presented elsewhere in these proceedings.[18]

can be used practically to determine the W mass. While the p_T distributions of charged leptons and of neutrinos (as measured by $\not\!\!E_T$) can be used to determine M_W, these distributions are quite sensitive to the p_T distribution of the W, and therefore to pdf's. The transverse mass of the $l\nu$ pair is considerably less sensitive to the $P_T(W)$ distribution, and we use this distribution to determine M_W.

Here, we discuss the measurements of M_W from fits to the $M_T(l\nu)$ distribution from CDF[14] and DØ (Ref. 15), and also a preliminary result from DØ of an alternative determination, using the ratio of $M_T(W)$ to a "transverse mass" of the Z (Ref. 16).

In the standard approach, $M_T(l\nu)$ distributions are simulated by Monte Carlo for various values of M_W, and this ensemble of spectra is then used to fit the observed distribution from data. The main systematic errors come from uncertainties in lepton energy/momentum response and resolution, the W production model (pdf's), recoil momentum response and resolution, effects of underlying events, efficiency and acceptance effects, and backgrounds. The W production model is checked with the measured W and Z cross sections and asymmetries. Recoil momentum response is determined using Z+jet events.

3.1 Energy Scale Calibration

CDF and DØ calibrate lepton response in quite different ways. CDF uses a sample of $\approx$ 60,000 $J/\psi \to \mu^+\mu^-$ events to calibrate the momentum scale of their central tracker to an accuracy of $\approx$ 6 parts in 10^4, corresponding to an error in M_W of $\approx$ 50 MeV. The energy scale of the calorimeter is then determined by the E/p distribution of good electrons (in fact, the $W \to e\nu$ sample is used). This transfers the momentum calibration to the calorimeter; the resulting error in M_W is $\approx$ 105 MeV. The calibration is checked using Z and Υ events.

DØ calibrates their calorimeter's electron response using $Z \to e^+e^-$, $J/\psi \to e^+e^-$, and π^0 samples. The EM energy response is parameterized in terms of a scale α and an offset δ. The measured $M(ee)$ of Z and J/ψ events together with the distribution of $E(e)$ as a function of opening angle provide constraints on α and δ. Although the two photons from π^0 decay are not separated in the calorimeter, a sample of π^0 events in which both photons convert can be used to determine a "symmetric mass,"

$$M_{sym} = \sqrt{\frac{E(\pi^0)^2}{2}(1 - cos\omega)},$$

where ω is the opening angle between the two tracks. The M_{sym} distribution is then fit for $M(\pi^0)$. Figure 7 shows the constraints on energy scale and offset. The diagonal ellipse is the constraint from Z events; the near-vertical ellipse is from the π^0 data. The small oval shows the overlap of all constraints. The resulting error in M_W from the energy scale is $\approx$ 75 MeV.

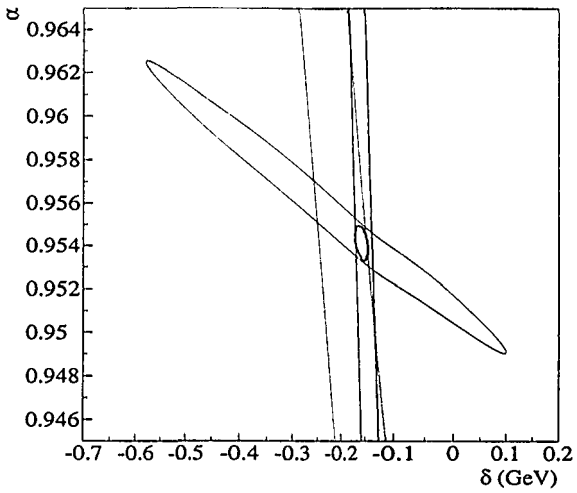


Figure 7: DØ preliminary EM scale and offset.

3.2 M_W Results

The M_T distributions for $W \to e\nu$ and $W \to \mu\nu$ events from CDF's run 1A data sample are shown in Fig. 8. They determine the following values:

$$M_W = 80.490 \pm 0.145(stat) \pm 0.175(sys) \text{ GeV } (e)$$

$$M_W = 80.310 \pm 0.205(stat) \pm 0.130(sys) \text{ GeV } (\mu)$$

$$M_W = 80.41 \pm 0.18 \text{ GeV } (combined).$$

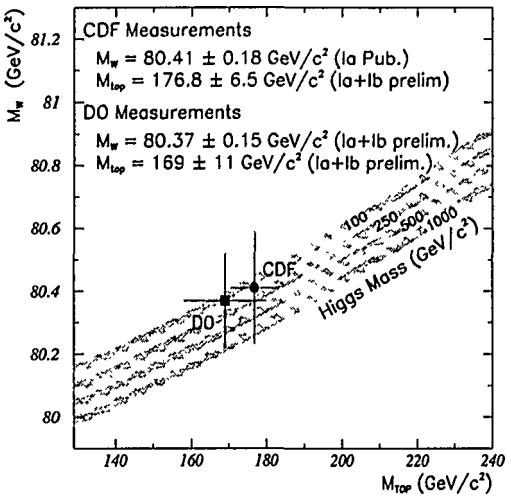


Figure 10: M_W vs m_t.

The ratio M_W/M_Z is related by radiative corrections to the measured value of $sin^2\theta_W$ from LEP/SLC and other sources, to the top mass, and to the mass of the Higgs boson. Figure 10 shows the measured values of M_W and m_t from CDF and DØ; the shaded bands show the corresponding values of M_H.

3.3 Transverse Mass Ratio of W and Z

DØ has also analyzed their $W \to e\nu$ data using an alternative approach: a comparison between the W transverse mass distribution and a distribution of "transverse mass" of $Z \to ee$ events. For each Z event, one electron is removed and replaced by missing energy. The transverse mass of the remaining electron and the $\not\!\!E_T$ is then calculated. (Each $Z \to ee$ event is used twice.) The ratio M_W/M_Z is then determined by scaling the $M_T(Z)$ distribution and fitting to the $M_T(W)$ distribution. Since the W and Z p_T distributions are related, this direct comparison is somewhat less sensitive to the W production model than the standard $M_T(W)$ analysis. Figure 11 shows the $M_T(W)$ and scaled $M_T(Z)$ distributions. The fit result using run 1A data, electron data only, is

$$M_W = 80.160 \pm 0.360(stat) \pm 0.075(sys)\ \text{GeV},$$

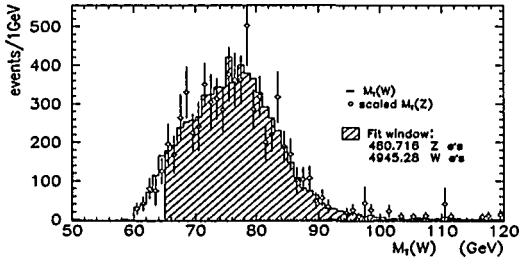


Figure 11: W, Z, and M_T ratio (DØ preliminary).

where the statistical error is dominated by Z statistics (it includes the scale error). The dominant systematic errors come from uncertainty in energy underlying the electrons, and multiple interaction effects.

4 Diboson Final States

Measurement of cross sections and distributions of final states containing two electroweak gauge bosons (W, Z, γ) provides a sensitive test of gauge couplings. These processes are sensitive to anomalous triple boson couplings. Since unitarity requires that these couplings take their SM values in the limit of high energy, all anomalous couplings are assumed to be modified by form factors $1/(1+\hat{s}/\Lambda^2)^n$, where Λ is the form factor scale.

4.1 $W\gamma$ Production

$W\gamma$ final states can be produced both via $WW\gamma$ and $W\gamma\gamma$ vertices, and by initial or final state radiation. Anomalous $WW\gamma$ couplings are described by parameters $\Delta\kappa$ and λ; both are zero in the SM. $\Delta\kappa$ measures the anomalous magnetic moment of the W, and λ measures the W electric quadrupole moment. Nonzero anomalous couplings lead to both an increase in the $W\gamma$ cross section and a harder $P_T(\gamma)$ spectrum.

DØ (Ref. 19) and CDF[20] have both measured $W\gamma$ production in ($l+\gamma+\not\!\!E_T$) channels. Isolation cuts are applied to photons to reduce contributions from final state radiation. Constraints on $\Delta\kappa$ and λ derived from the cross-section measurements and fits to the $P_T(\gamma)$ spectra are shown in Fig. 12, along with constraints from CLEO measurements.[21]

4.2 $Z\gamma$ Production

$ZZ\gamma$ and $Z\gamma\gamma$ couplings vanish at tree level in the SM. Anomalous values of these couplings are characterized by parameters h_i^V, $i=1-4$, $V=Z,\gamma$. The $h_{1,2}^V$ violate CP, while $h_{3,4}^V$ are CP conserving. DØ (Ref. 22) and CDF[20] have measured $Z\gamma$ production in both the $ee\gamma$ and $\mu\mu\gamma$ channels, and derived limits on the h_i^V parameters from cross sections and P_T spectra.

A preliminary analysis from DØ (Ref. 22) has searched in the run 1A data sample for $Z\gamma$ production in the $Z\to\nu\nu$ mode. This mode has the advantages of

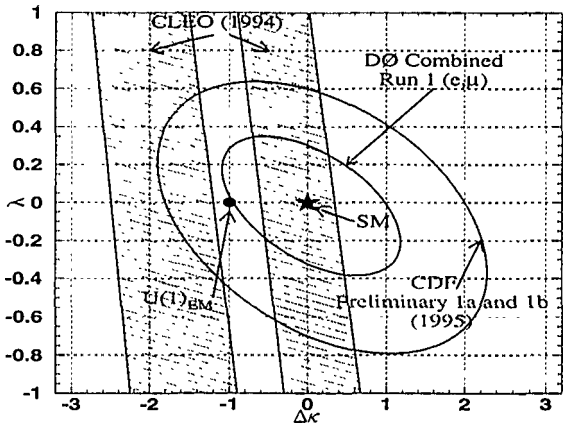


Figure 12: Limits on W anomalous couplings.

a factor of six increase in branching ratio relative to $Z\to ee$, and of no final state radiation. The signature for this final state is a single $\gamma+\not\!\!E_T$. The principal backgrounds are (1) $W\to e\nu$ events, where the electron track is undetected, and (2) bremsstrahlung photons from cosmic ray or beam halo muons. The first background is reduced by requiring $E_T(\gamma)>40$ GeV, above the endpoint of the W electron spectrum. The second background is reduced by using the photon shower shape to reconstruct the photon's direction, and require that the photon be consistent with the event vertex, both along and transverse to the beam axis. The final sample contains four events. Figure 13 shows the photon p_T spectrum.

Figure 14 shows limits on anomalous couplings $h_{3,4}^Z$ derived from the various measurements. The tightest limits to date come from the $\nu\nu\gamma$ measurement, although only the run 1A data has been analyzed so far. Analysis of the full data set is in progress.

4.3 WW and WZ Production

Searches for WW and WZ final states have also been carried out, with some candidates seen. Figure 15 shows CDF results[20] for cross sections for diboson final states. DØ has set limits[19] on the sum of WW and WZ cross sections, using searches in dilepton and (e + jets + $\not\!\!E_T$) channels.

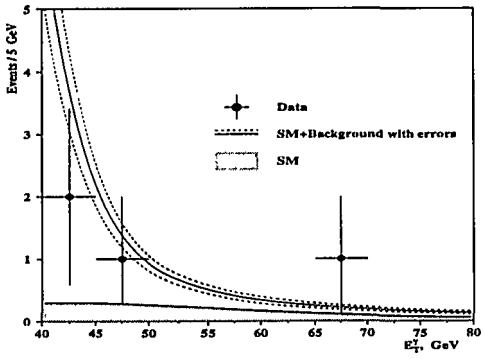


Figure 13: $P_T(\gamma)$ spectrum of $\nu\nu\gamma$ candidates.

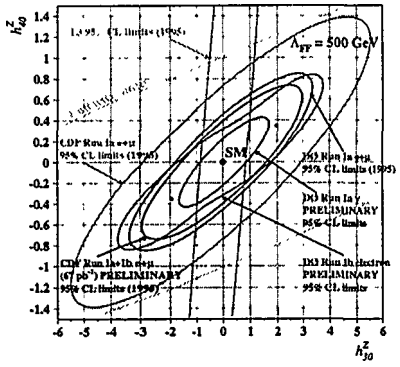


Figure 14: Limits on $Z\gamma$ anomalous couplings.

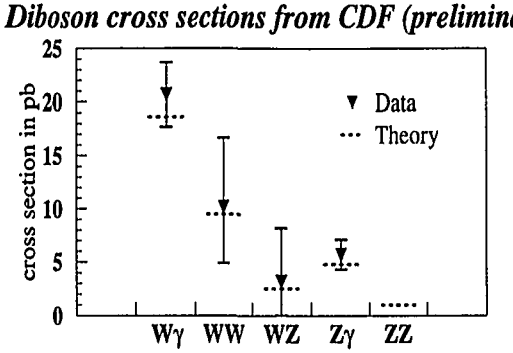


Figure 15: CDF diboson cross sections.

5 Searches for W' and Z'

Many extensions to the SM predict additional gauge bosons with decays similar to W and Z bosons. Searches for W' decays to $l\nu$ have been carried out for both light and heavy neutrinos. A recently published DØ result[23] reports a search for a right-handed W with associated heavy ν_R. If the ν_R is undetected, the W' can be detected as a Jacobian peak in the electron p_T spectrum. Decays $\nu_R \to e+$ 2 jets are also searched for, in the final state $ee+$ 2 jets. Limits in the $M(W_R)$ vs $M(\nu_R)$ are shown in Fig. 16. Other searches for W' decays to a light neutrino have been previously reported.

Searches for $Z' \to l^+l^-$ have also been carried out. The most stringent limit at present is a preliminary CDF result[31] $M(Z') > 690$ GeV, assuming SM couplings for the Z'.

6 Supersymmetry Searches

Supersymmetric (SUSY) theories predict partners for all SM particles. SUSY particles are assumed to be pair produced, with the lightest SUSY particle (LSP) stable. Final states will contain LSP's, and a general signal for SUSY particles is $\not\!\!E_T$. The partners of W, Z, and Higgs bosons can mix, and these particles are referred to as charginos $\widetilde{\chi^+}$ and neutralinos $\widetilde{\chi^0}$. The lightest neutralino $\widetilde{\chi_1^0}$ is often assumed to be the LSP. While the parameter space (particle spectra

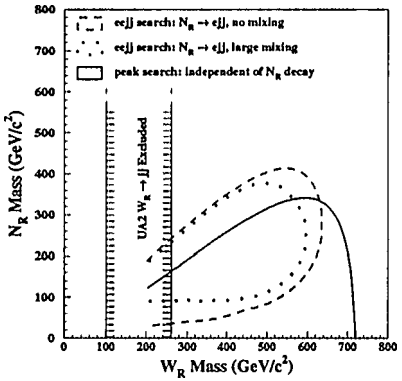


Figure 16: DØ right-handed W search.

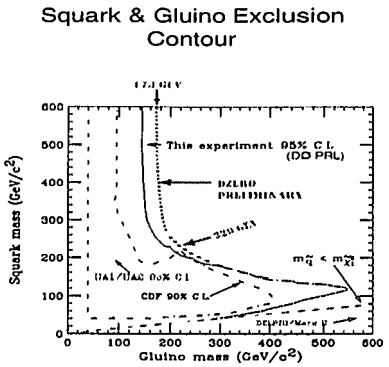


Figure 17: Squark, gluino limits.

and couplings) of SUSY models is quite large, many results are interpreted in the framework of the "minimal SUSY standard model" (MSSM), or supergravity (SUGRA) inspired models. The parameter space in these models is somewhat more restricted than the general case.

6.1 Squark, Gluino, and Stop Squark Searches

Searches for partners of quarks and gluons (squarks $\tilde{q}$ and gluinos $\tilde{g}$) have been carried out. Decays $\tilde{q}, \tilde{g} \to q, g +$ LSP are searched for in multijet + $\not\!\!E_T$final states, and cascade decays $\tilde{q}, \tilde{g} \to q, g + \tilde{\chi}$, where the $\tilde{\chi}$ decays to W or Z + LSP are searched for in ll + jets + $\not\!\!E_T$ final states. A representative plot of limits[34] in the $m(\tilde{q}), m(\tilde{g})$ plane is shown in Fig. 17.

DØ has also searched for a light partner of the top quark, the stop ($\tilde{t}$) (Ref. 24). If the $\tilde{t}$ is lighter than the top quark, decays to top are not kinematically allowed, and the stop could decay via a flavor-changing neutral current to a c quark and the $\widetilde{\chi}_1^0$. If the $\widetilde{\chi}_1^0$ is the LSP, then stop pair production would result in a final state with 2 jets + $\not\!\!E_T$. No signal above background is observed in the search and a region of the $M(\tilde{t})$, $M(\widetilde{\chi}_1^0)$ plane is excluded.

6.2 Chargino/Neutralino Searches

Searches for partners of W/Z/Higgs bosons have been carried out in the mode $\widetilde{\chi}_1^+\widetilde{\chi}_2^0 \to W + Z + 2\widetilde{\chi}_1^0$. The signature is a final state containing three leptons + $\not\!\!E_T$. Both CDF[25] and DØ (Ref. 26) have set limits as functions of masses and the branching ratio for $\widetilde{\chi}_1^+\widetilde{\chi}_2^0$ decay to trileptons. Figure 18 shows preliminary DØ limits on the cross section versus chargino mass.

6.3 $ee\gamma\gamma\not\!\!E_T$ Event

CDF's observation[27] of a single event containing two high p_T electrons, two high p_T photons, and a large $\not\!\!E_T$ has aroused considerable speculation.[28] Several scenarios have been suggested in which this event is interpreted as an example of production of a selectron $\tilde{e}$ (electron partner) pair. CDF[27] and DØ (Ref. 29) have carried out searches in a related channel for $\gamma\gamma + \not\!\!E_T$ final states, with null results. No positive confirmation for a SUSY signal has been found to date, but the single event is difficult to interpret within the SM.

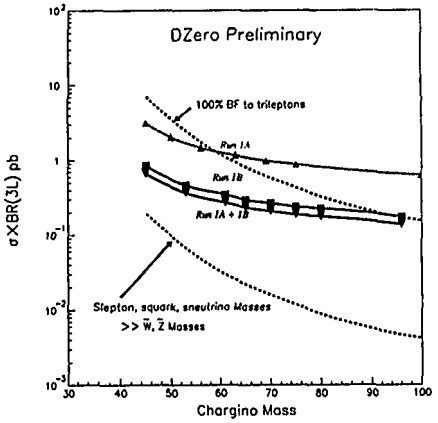


Figure 18: Limits on $\tilde{\chi}^+\tilde{\chi}^0 \to lll$.

7 Dijet Resonances

A number of exotic particles might be detected as resonances in the dijet mass spectrum. Examples include technicolor particles, excited quarks, and (possibly) Higgs bosons.

7.1 Searches for Excited Quarks

Both DØ (Ref. 30) and CDF[31] have searched for resonances in their inclusive dijet mass spectra. No bumps have been found; CDF excludes an excited quark q^* decaying to qg in the mass region 20–750 GeV. DØ sets a slightly lower limit.

7.2 Search for $W+$ Dijet Resonance

DØ has searched for dijet resonances produced in association with a W boson.[32] A signal in this channel could indicate Higgs production. No signal above background is observed, and limits on resonance cross section versus mass are set both from the number of events observed, and a fit to event shape. The level of sensitivity is not sufficient to exclude a SM Higgs, but can exclude some non-SM models.

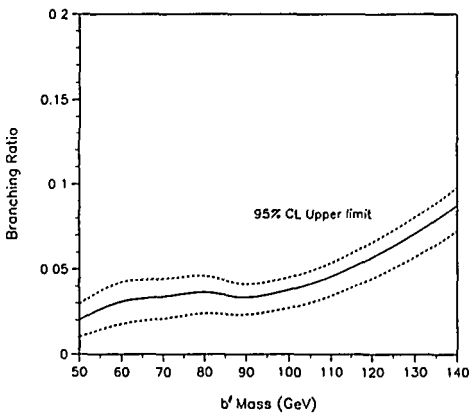


Figure 19: b' search (DØ preliminary).

8 Fourth Generation Particles

Searches have been carried out for pair-produced fourth generation particles. DØ has reported[33] results of a search for a b' quark with mass $m_{b'} < m_t$. The dominant decay for the b' in this mass region is by a flavor-changing neutral current, $b' \to b + (\gamma \text{ or } g)$. Searches are performed for final states $\gamma + 3$ jets, with at least one jet tagged with a muon, and for $2\gamma + 2$ jets. Limits are set on $BR(b' \to b + \gamma)$ as a function of $m_{b'}$. Figure 19 shows limits derived from the $2\gamma + 2$ jet mode.

DØ has also searched for a fourth generation neutrino ν_4 (Ref. 34) decaying via mixing to a $W + e$ final state. No candidates are observed, and limits are set as a function of $m(\nu_4)$ versus the mixing parameter.

9 Search for Heavy, Stable Charged Particles

CDF has searched for production of heavy, stable charged particles.[31] The experimental signature for such particles would be a high p_T penetrating charged particle moving slowly. With a requirement of large ionization energy loss in both the silicon vertex detector and central tracking chamber, no candidates are

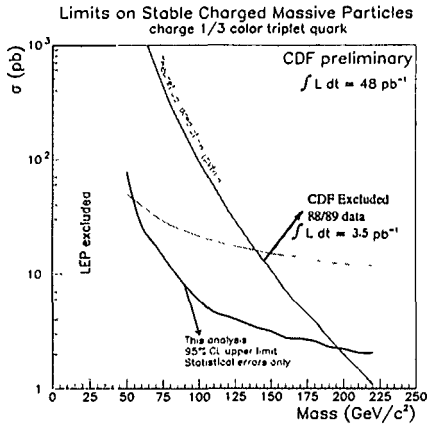


Figure 20: Limit on a heavy, stable particle.

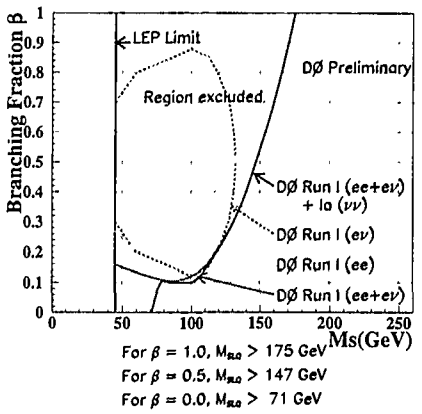


Figure 21: First generation leptoquark limits.

found in a data sample of 48 pb^{-1}. This result can be interpreted as a limit on production cross section for a variety of non-SM particles. Figure 20 shows the cross-section limit for a color triplet charge-1/3 quark compared to a model prediction. Analysis of the full run 1 data set is underway.

10 Leptoquark Searches

Leptoquarks are (hypothetical) particles carrying both quark and lepton quantum numbers, predicted in a number of extensions to the SM. Leptoquarks could be pair produced in $\overline{p}p$ collisions and detected through decays $LQ \rightarrow l^+q$ or $LQ \rightarrow \nu q$. Separate searches are conducted for first (eq), second (μq), and third (τq) generation leptoquarks. Limits are expressed in terms of a parameter $\beta = BR(LQ \rightarrow l^+q)$.

Searches for final states ll+ 2 jets and l + jets + $\not\!\!E_T$ have been carried out. The $\nu\nu qq$ mode can also be searched for, via a jets + $\not\!\!E_T$ signature. DØ reports a preliminary limit[35] on a first generation scalar leptoquark $M(LQ1) > 147$ GeV for $\beta = 0.5$, from a search in the ee + 2 jet and E + jets + $\not\!\!E_T$ modes in the run (1A+1B) data set, and a search for $\nu\nu jj$ in the run 1A data only. Figure 21 shows 95% CL limits on the production cross section, compared to several models. CDF reports a preliminary limit[31] on a second generation scalar leptoquark $M(LQ2) > 141$ GeV for $\beta = 0.5$, from the $\mu\mu$ + 2 jet channel, using their full run 1 data set. CDF has also searched for third generation leptoquarks.[31] The search is carried out in the channel $\tau\tau$ + 2 jets, where one τ decays to a lepton and the other decays hadronically.

11 Compositeness Limits

Quark and/or lepton compositeness would lead to several observable effects in $\overline{p}p$ collisions. Jet production in collisions of composite quarks would be modified by an effective four-fermion contact interaction, characterized by a compositeness scale Λ. Such a contact interaction could be detected as an excess in the jet cross section at very high p_T, and modifications in dijet angular distributions. Limits on quark compositeness from these processes are discussed elsewhere in these proceedings.[36]

If quarks and leptons were composite, an effective ($llqq$) contact term would modify the mass spectrum of Drell-Yan lepton pairs. Figure 22 shows the mass spectrum of electron and muon pairs measured by CDF.[37] No deviation from the SM prediction is observed. The individual ee and $\mu\mu$ spectra can be fit to derive limits on the scale of $eeqq$ and $\mu\mu qq$ contact terms. If the $llqq$ interaction

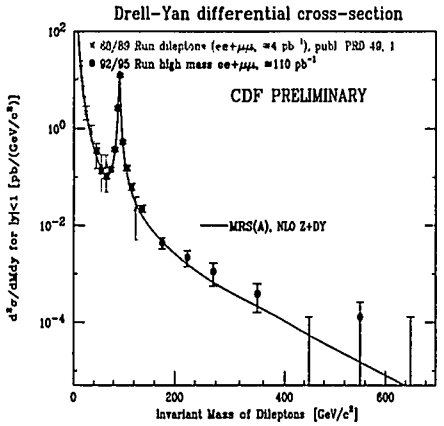


Figure 22: CDF Drell-Yan lepton mass spectrum.

is assumed to be universal, a combined limit $\Lambda_- > 2.9$ TeV, $\Lambda_+ > 3.8$ TeV is obtained (where $+, -$ refer to the sign of the contact term).

12 Conclusions

A very large data set from the Tevatron's 1992–1996 run has been collected and is still in the process of analysis. Results obtained so far include precise determinations of W and Z cross sections, a new measurement of the W mass, $M_W = 80.35 \pm 0.13$ GeV, and measurements of diboson production in a variety of channels, with corresponding limits on anomalous gauge couplings. Many searches for new phenomena have been carried out. Improved mass limits are placed on a number of nonstandard particles, including heavy gauge bosons, leptoquarks, and SUSY particles. In the near future, we can expect improved results as the analysis of the full run 1 data is completed, and systematic errors are reduced.

In the longer term, we can look forward to Tevatron run II. A major upgrade to the accelerator, replacement of the Main Ring with a new Main Injector, is underway. This will provide an increase in luminosity of about a factor ten. The next run is planned to begin in 1999 and is expected to deliver an integrated luminosity of $\approx 2\ fb^{-1}$. Both detectors are being upgraded as well. CDF will have a new tracking chamber and silicon detector, improved calorimetry in the forward region, and extended muon coverage. DØ will replace their tracking systems, add a solenoid, and upgrade muon systems. The 20-fold increase in luminosity along with enhanced detector capabilities will provide significant improvements. Mass reach for searches will be greatly extended, and higher precision electroweak measurements can be expected. The resulting precision in the measurement of the W mass is expected to reach $\delta(M_W) \approx 40$–50 MeV, which may be competitive with LEP II.

Acknowledgments

I would like to thank my colleagues in the DØ and CDF Collaborations for their help in preparing this paper. I would also like to thank the organizers of the Summer Institute.

References

[1] F. Abe *et al.* (CDF Collaboration), Nucl. Instrum. Methods A **271**, 387 (1988).

[2] S. Abachi *et al.* (DØ Collaboration), Nucl. Instrum. Methods A **338**, 185 (1994).

[3] J. Tarazi (DØ Collaboration), in *Proceedings of the Divisional Meeting of the Division of Particles and Fields*, American Physical Society, Minneapolis, MN, August 10-15, 1996.

[4] F. Abe *et al.* (CDF Collaboration), Phys. Rev. Lett. **76**, 3070 (1996).

[5] H. Hamberg, T. Matsuura, and W. L. van Neerven, Nucl. Phys. B **345**, 331 (1990).

[6] H. Hamberg *et al.*, Nucl. Phys. B **359**, 343 (1991); W. L. van Neerven and E. B. Zijlstra, Nucl. Phys. B **382**, 11 (1992).

[7] J. L. Rosner, M. P. Worah, and T. Takeuchi, Phys. Rev. D **49**, 1363 (1994).

[8] Particle Data Group, L. Montanet *et al.*, Phys. Rev. D **50**, 1173 (1994).

[9] F. Abe *et al.* (CDF Collaboration), Phys. Rev. Lett. **74**, 341 (1995).

[10] H. Budd (CDF Collaboration), in *Proceedings of the Divisional Meeting of the Division of Particles and Fields*, American Physical Society, Minneapolis, MN, August 10-15, 1996.

[11] A. Narayanan (DØ Collaboration), in *Proceedings of the Divisional Meeting of the Division of Particles and Fields*, American Physical Society, Minneapolis, MN, August 10-15, 1996.

[12] A. D. Martin, R. G. Roberts, and W. J. Sterling, RAL-94-055, 1994; A. D. Martin, R. G. Roberts, and W. J. Sterling, Phys. Lett. B **306**, 147 (1993) and erratum *ibid.* B **309**, 492 (1993); CTEQ Collaboration, MSU-HEP/41024.

[13] L. Nodulman (CDF Collaboration), in *Proceedings of the 28th International Conference on High Energy Physics (ICHEP'96)*, Warsaw, Poland, July 25-31, 1996; F. Abe *et al.* (CDF Collaboration), Phys. Rev. Lett. **77**, 2616 (1996).

[14] F. Abe *et al.* (CDF Collaboration), Phys. Rev. D **52**, 4784 (1995).

[15] A. V. Kotwal (DØ Collaboration), in *Proceedings of the Divisional Meeting of the Division of Particles and Fields*, American Physical Society, Minneapolis, MN, August 10-15, 1996.

[16] S. Rajagopalan (DØ Collaboration), in *Proceedings of the Divisional Meeting of the Division of Particles and Fields*, American Physical Society, Minneapolis, MN, August 10-15, 1996.

[17] J. Alitti *et al.* (UA2 Collaboration), Phys.Lett. B **276**, 354 (1992).

[18] J. Mnich, these proceedings.

[19] M. Kelly (DØ Collaboration), in *Proceedings of the Divisional Meeting of the Division of Particles and Fields*, American Physical Society, Minneapolis, MN, August 10-15, 1996.

[20] L. Nodulman (CDF Collaboration), in *Proceedings of the 28th International Conference on High Energy Physics (ICHEP'96)*, Warsaw, Poland, July 25-31, 1996.

[21] S. Playfer *et al.* (CLEO Collaboration), Int. J. Mod. Phys. A **10**, 4107 (1995).

[22] G. Landsberg (DØ Collaboration), in *Proceedings of the Divisional Meeting of the Division of Particles and Fields*, American Physical Society, Minneapolis, MN, August 10-15, 1996.

[23] S. Abachi *et al.* (DØ Collaboration), Phys. Rev. Lett. **76**, 3271 (1996).

[24] S. Abachi *et al.* (DØ Collaboration), Phys. Rev. Lett. **76**, 2222 (1996).

[25] J. Done (CDF Collaboration), in *Proceedings of the Divisional Meeting of the Division of Particles and Fields*, American Physical Society, Minneapolis, MN, August 10-15, 1996.

[26] D. M. Norman (DØ Collaboration), in *Proceedings of the Divisional Meeting of the Division of Particles and Fields*, American Physical Society, Minneapolis, MN, August 10-15, 1996.

[27] D. Toback (CDF Collaboration), in *Proceedings of the Divisional Meeting of the Division of Particles and Fields*, American Physical Society, Minneapolis, MN, August 10-15, 1996.

[28] S. Dimopoulos *et al.*, Phys. Rev. Lett. **76**, 3494 (1996); S. Ambrosanio *et al.*, Phys. Rev. Lett. **76**, 3498 (1996); G. Kane and J. Wells, Phys. Rev. Lett. **76**, 4458 (1996).

[29] S. Abachi *et al.* (DØ Collaboration), Fermilab preprint FERMILAB-PUBF-96/446-E, submitted to Phys. Rev. Lett.

[30] I. A. Bertram (DØ Collaboration), in *Proceedings of the Divisional Meeting of the Division of Particles and Fields*, American Physical Society, Minneapolis, MN, August 10-15, 1996.

[31] K. Maeshima (CDF Collaboration), in *Proceedings of the 28th International Conference on High Energy Physics (ICHEP'96)*, Warsaw, Poland, July 25-31, 1996.

[32] P. Tamburello (DØ Collaboration), in *Proceedings of the Divisional Meeting of the Division of Particles and Fields*, American Physical Society, Minneapolis, MN, August 10-15, 1996.

[33] S. Abachi *et al.* (DØ Collaboration), Fermilab preprint FERMILAB-PUB-96/430-E, submitted to Phys. Rev. Lett.

[34] K. W. Merritt (DØ Collaboration), in *Proceedings of the Divisional Meeting of the Division of Particles and Fields*, American Physical Society, Minneapolis, MN, August 10-15, 1996.

[35] G. Wang (DØ Collaboration), in *Proceedings of the Divisional Meeting of the Division of Particles and Fields*, American Physical Society, Minneapolis, MN, August 10-15, 1996.

[36] M. Albrow, these proceedings.

[37] L. Nodulman (CDF Collaboration), in *Proceedings of the 28th International Conference on High Energy Physics (ICHEP'96)*, Warsaw, Poland, July 25-31, 1996.

THE STRONG COUPLING CONSTANT IN GRAND UNIFIED THEORIES

Damien M. Pierce*
Stanford Linear Accelerator Center
Stanford University, Stanford, CA 94309

ABSTRACT

The prediction for the strong coupling constant in grand unified theories is reviewed, first in the Standard Model, then in the supersymmetric version. Various corrections are considered. The predictions in both supergravity-induced and gauge-mediated supersymmetry breaking models are discussed. In the region of parameter space without large fine tuning, the strong coupling is predicted to be $\alpha_s(M_Z) \gtrsim 0.13$. Imposing $\alpha_s(M_Z) = 0.118$, we require a unification scale threshold correction of typically -2%, which is accommodated by some GUT models but in conflict with others.

*Work supported by Department of Energy Contract DE–AC03–76SF00515.

© 1996 by Damien M. Pierce.

1 Introduction

In the Standard Model, given values of the three gauge couplings, the Yukawa couplings, the Higgs boson self-coupling, and a dimensionful observable (e.g., the muon lifetime, a gauge boson mass, or a quark mass), any other observable can then be computed. In a grand unified theory (GUT), one need only input two of the gauge couplings, then the third one can be predicted, as well as other observables.

Thus, GUT theories are more predictive. Because the SU(2) and U(1) couplings are measured quite precisely, we will examine the prediction of the strong coupling constant in grand unified theories, both in the Standard Model and in supersymmetric models. We start with the one-loop results and then proceed to discuss the next higher-order corrections. The inclusion of these corrections leads to a precise prediction of the strong coupling constant.

2 Renormalization Group Equations

We are interested in measuring gauge couplings at the weak scale or below, and running the gauge couplings up to higher scales. The solution of the renormalization group equations (RGE's) accurately describes the evolution of the couplings, even as they are evolved over many decades. At one-loop, the renormalization group equations for the gauge couplings are

$$\frac{dg_i}{dt} = \frac{b_i}{16\pi^2} g_i^3, \qquad t = \ln \frac{Q}{Q_0} , \tag{1}$$

where the b_i are the one-loop beta-constants. These constants receive contributions from every particle which circulates in the one-loop gauge-boson self-energy diagram. For example, for a fermion doublet (ν, e), $\Delta b_2 = 1/3$.

The one-loop renormalization group equation is easily solved. The inverse of the gauge coupling evolves linearly with the log of the scale,

$$\alpha_i^{-1}(Q) = \alpha_i^{-1}(Q_0) - \frac{b_i}{2\pi} \ln \frac{Q}{Q_0} . \tag{2}$$

If we assume that the couplings do unify at some scale, we have

$$\frac{b_1 - b_2}{\alpha_3(Q)} + \frac{b_2 - b_3}{\alpha_1(Q)} + \frac{b_3 - b_1}{\alpha_2(Q)} = 0 . \tag{3}$$

This equation is valid for any scale Q between the weak scale and the unification scale. Next, we deduce the $\overline{\rm MS}$ values of the U(1) and SU(2) gauge couplings from the quantities $\hat{\alpha}^{-1} = 127.90 \pm 0.09$ and $\hat{s}^2 = 0.2315 \pm 0.0004$ (Ref. 1) ($\hat{\alpha}$ and $\hat{s}^2$ are the $\overline{\rm MS}$ values of the electromagnetic coupling and the sine-squared of the weak mixing angle evaluated at M_Z)

$$\alpha_1^{-1}(M_Z) = 58.97 \pm 0.05 , \qquad \alpha_2^{-1}(M_Z) = 29.61 \pm 0.05 . \tag{4}$$

Given the Standard Model values of the one-loop beta-constants

$$b_1 = \frac{41}{10} , \qquad b_2 = -\frac{19}{6} , \qquad b_3 = -7 , \tag{5}$$

we determine the prediction of the strong coupling constant in the Standard Model

$$\alpha_s(M_Z) = 0.07 \qquad \text{(Standard Model, one-loop)} \tag{6}$$

with negligible error. Comparing with the measured value as quoted by the Particle Data Group,[1] $\alpha_s(M_Z) = 0.118 \pm 0.003$, we see that the Standard Model prediction of the strong coupling constant is about 16 standard deviations too small. Including higher order corrections cannot help repair this situation by more than a few standard deviations. In order to remedy this huge discrepancy, we need to go beyond the Standard Model, adding matter to change the beta-constants b_i. We also need to specify the mass scale of the new matter.

Rather than determining what additional matter content will lead to successful gauge coupling unification in an ad hoc fashion, we will examine the implications of a motivated model. It is widely accepted that the Standard Model is an effective theory. Some new physics must become manifest at scales below the multi-TeV scale. A promising model of new physics is supersymmetry,[2] which, among other virtues, explains how a theory with a weak-scale elementary Higgs boson is stable with respect to the Planck scale. Supersymmetry also naturally explains the breaking of electroweak symmetry,[3] and it typically contains a natural dark matter candidate.[4]

In order to make the Standard Model supersymmetric, we are required to add a specific set of new particles, the superpartners. For every Standard Model gauge boson, we must add a spin-1/2 majorana particle, a gaugino. And for every Standard Model fermion, we must add a spin-0 partner, a squark or a slepton. In order to give both up- and down-type fermions a mass, and to ensure anomaly

cancellation, we must also add an additional Higgs doublet. We refer to the two Higgs doublets as "up-type" and "down-type." This additional particle content defines the Minimal Supersymmetric Standard Model (MSSM). In the simplest and most often considered versions of the MSSM with high-energy inputs, the entire supersymmetric spectrum scales with one or two parameters which must be near the weak scale by naturalness considerations.

Given this new matter content and the superpartner mass scale, which we take to be M_Z for the moment, we can take a first-order look at the prediction of the strong coupling constant in the MSSM. As before, we use Eq. (3) to solve for $\alpha_s(M_Z)$ as a function of $\alpha_1(M_Z)$ and $\alpha_2(M_Z)$. Now the beta-constants are different. Because of the new matter content, we have the following changes from the Standard Model values

$$b_1 = 4.1 \longrightarrow 6.6\,, \qquad b_2 = -3.2 \rightarrow 1\,, \qquad b_3 = -7 \rightarrow -3\,. \tag{7}$$

We use the central values and errors in Eq. (4) to find

$$\alpha_s(M_Z) = 0.116 \pm 0.001 \qquad \text{(MSSM, one-loop)}. \tag{8}$$

The new matter content mandated by supersymmetry brings the prediction for the strong coupling constant to the measured value (0.118 ± 0.003) within one standard deviation! This could be a coincidence, or it could be a hint that we are on the right track by considering minimal low-energy supersymmetry. Next we will consider corrections to the prediction of α_s in the MSSM.

3 Corrections to the Prediction of α_s

In this section, we consider two sources of corrections to the prediction of the strong coupling constant in the MSSM. The first involves improving the evolution of the couplings from their initial values at the grand unification scale to the weak scale (or, the supersymmetry breaking scale). We simply extend the renormalization group equations to one higher loop order. This means that in addition to resumming logarithms of the form $[\alpha/4\pi \ln(M_{\rm GUT}/M_Z)]^n$ from the one-loop RGE, we now resum logarithms of the form $[(\alpha/4\pi)^2 \ln(M_{\rm GUT}/M_Z)]^n$ from the two-loop terms. At two loops, it is necessary to run both the gauge and Yukawa couplings together, as they form a coupled set of differential equations. The general form for either a gauge or Yukawa coupling RGE at two-loops is[5]

$$\frac{dg_i}{dt} = g_i\left\{\frac{b_{ij}}{16\pi^2}g_j^2 + \frac{b_{ijk}}{(16\pi^2)^2}g_j^2 g_k^2\right\}. \tag{9}$$

Since we can safely ignore the small Yukawa couplings of the first two generations, the set g_i includes $\{g_1,\ g_2,\ g_3,\ \lambda_t,\ \lambda_b,\ \lambda_\tau\}$. The equations are readily solved numerically. The correction due to the two-loop RGE's is large and positive. The prediction of $\alpha_s(M_Z)$ increases by about 0.01.

The second source of corrections we will consider in this section are the supersymmetric threshold corrections. These are divided into two types, the logarithmic corrections and the finite (i.e., nonlogarithmic) corrections. We will discuss these in turn.

When we arrived at prediction (8), we assumed that the masses of the superpartners were equal to M_Z. However, we know from collider searches that many of the superpartner masses must be heavier than M_Z, and in general, they could be an order of magnitude heavier without straining naturalness considerations too much. As we evolve the gauge couplings down from high scales, we must decouple each superpartner contribution in turn as we cross the mass threshold. Hence, we arrive at logarithmic corrections of the form $\Delta b_i \ln(M_{\rm susy}/M_Z)$. From these corrections, we determine the shift in the prediction of the strong coupling and find, in general, for a particle of mass $M > M_Z$ with Δb_i contributions to the beta-constants

$$\Delta\alpha_s^{-1}(M_Z) = -\frac{1}{2\pi(b_1-b_2)}\Big[(b_2-b_3)\Delta b_1 + (b_3-b_1)\Delta b_2 + (b_1-b_2)\Delta b_3\Big]\ln\frac{M}{M_Z}. \tag{10}$$

Note that the beta-constants b_i in this equation *include* the entire superpartner spectrum. Plugging in all the superpartners, we arrive at the following supersymmetric threshold correction

$$\begin{aligned}\Delta\alpha_s^{-1}(M_Z) \;=\; & \frac{1}{28\pi}\Big[3\ln\frac{M_L^3 M_Q^7}{M_D^3 M_E^2 M_U^5} + 32\ln\frac{M_2}{M_Z} - 28\ln\frac{M_3}{M_Z} \\ & +\; 3\ln\frac{M_H}{M_Z} + 12\ln\frac{|\mu|}{M_Z}\Big]\,.\end{aligned} \tag{11}$$

In the first term, M_Q and M_L (M_U, M_D, and M_E) denote the left-handed (right-handed) squark and slepton masses. This term is easily modified to account for generation-dependent masses.

There are a few aspects of this equation worth pointing out. First, notice that the first term does not contain M_Z. This is because the squarks and sleptons are

in complete SU(5) multiplets, and degenerate complete multiplets do not affect α_s at one loop. It happens that this particular combination of soft squark and slepton masses is near unity in the entire parameter space of both of the models that we consider in the following section. Hence, the squarks and sleptons do not significantly affect the prediction of $\alpha_s(M_Z)$.

Another point is that the SU(2) and SU(3) gauginos contribute corrections which largely combine into the term $(1/\pi)\ln M_2/M_3$. In GUT models, the gaugino masses are degenerate above the unification scale. At one-loop, they are renormalized proportional to the corresponding gauge couplings, so the ratio $M_2/M_3 = \alpha_2/\alpha_3$. At the weak scale, this ratio is about $8/30 \simeq 0.27$. Hence, this term contributes about $+0.006$ to $\alpha_s(M_Z)$, independent of parameter space.

The remaining terms include the residual term from the SU(2) gaugino mass, and the contributions of the heavy Higgs bosons and Higgsinos. If we take these three masses to be characterized by a single scale $M_{\rm susy}$, then these terms combine to give

$$\Delta\alpha_s^{-1}(M_Z) = \frac{19}{28\pi}\ln\frac{M_{\rm susy}}{M_Z}\ . \qquad (12)$$

Hence, as we increase the supersymmetric mass scale, the prediction of the strong coupling constant decreases. This makes sense, since in the limit that the entire supersymmetric spectrum is raised above $M_{\rm GUT}$, we should recover the prediction of the Standard Model. [In fact $(0.116)^{-1} + (19/28\pi)\ln M_{\rm GUT}/M_Z = (0.064)^{-1}$.] If $M_{\rm susy} = 1$ TeV, this correction yields $\Delta\alpha_s(M_Z) = -0.007$. Note that the largest contribution to Eq. (12) is due to the $\ln(|\mu|/M_Z)$ term. Because we impose electroweak symmetry breaking, $|\mu|/M_Z$ is a measure of the fine tuning necessary to obtain the Z-mass from the input mass parameters. The predicted strong coupling is larger in the region of no fine tuning ($|\mu|/M_Z \lesssim 2$) than in the region of appreciable fine tuning ($|\mu|/M_Z \gtrsim 10$).

There is one last point about Eq. (11). Because of the particle content of the supersymmetric standard model, the particles which are charged under SU(2) always come into the expression for $\Delta\alpha_s^{-1}$ with a positive coefficient in front of the logarithm of the mass. The SU(2) singlets always come with a negative coefficient. Hence, heavy SU(2) doublets, for example, $\tilde{W}$, H, or $\tilde{H}$, will decrease α_s, and heavy SU(2) singlets, e.g., the gluino, will increase the prediction of the strong coupling.

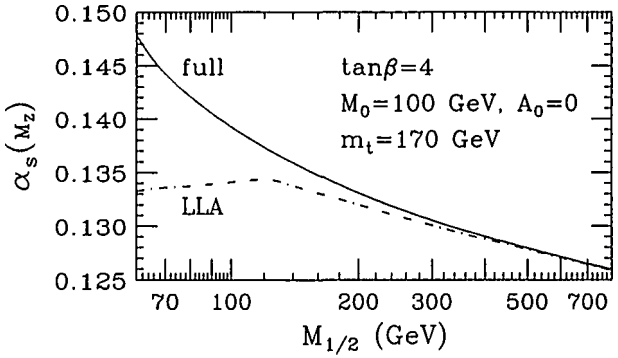


Fig. 1. The prediction of $\alpha_s(M_Z)$ with (solid) and without (dot-dashed) including the finite corrections. From Ref. 10.

Besides the logarithmic corrections of Eq. (11), there are also finite corrections. These arise when the full one-loop correction to $\hat{s}^2$ is taken into account. Taking the electromagnetic constant, the Z-boson mass, and the muon lifetime as inputs, we determine the $\overline{\rm DR}$ (Ref. 6) renormalized weak mixing angle,[7]

$$\hat{s}^2\hat{c}^2 = \frac{\pi\hat{\alpha}}{\sqrt{2}G_\mu M_Z^2(1-\Delta\hat{r})}\ , \qquad \Delta\hat{r} = \frac{\hat{\Pi}_{WW}(0)}{M_W^2} - \frac{\hat{\Pi}_{ZZ}(M_Z^2)}{M_Z^2} + \delta_{\rm vb}\ . \qquad (13)$$

The correction $\Delta\hat{r}$ is comprised of the real and transverse $\overline{\rm DR}$ gauge-boson self-energy contribution (the oblique correction), and the vertex and box diagram contributions, $\delta_{\rm vb}$ (the non-universal part).[8] The oblique correction contains both logarithmic and finite contributions, while $\delta_{\rm vb}$ is purely finite. The finite contributions decouple as $M_Z^2/M_{\rm susy}^2$ for large supersymmetric masses.

In the regions of parameter space where some SU(2) nonsinglet particles are of order M_Z, the finite corrections to the weak mixing angle can substantially increase the prediction of the strong coupling constant.[9,10] We illustrate this in Fig. 1. We show the prediction of the strong coupling with and without taking the finite corrections into account in the supergravity model described below. If all the supersymmetric particles are above a few hundred GeV, the finite corrections are negligible. In that case, the low-energy threshold corrections are well-approximated by the logarithms in Eq. (11).

4 $\alpha_s(M_Z)$ at Two Loops in Two Supersymmetric Models

Utilizing the two-loop renormalization group equations and the weak-scale threshold corrections, we are now in a position to present the improved prediction of the strong coupling constant in the supersymmetric case. We still need to specify the supersymmetric particle spectrum. In what follows, we consider two models in turn, first a minimal supergravity model, then a simple model with gauge-mediated supersymmetry breaking.

4.1 Minimal Supergravity Model

In the minimal supergravity model, there are universal soft-supersymmetry breaking parameters induced at the grand unification scale. These include a gaugino mass $M_{1/2}$, a scalar mass M_0, and a trilinear scalar coupling A_0. Also, we require that electroweak symmetry is broken radiatively.[3] This happens naturally, as the large top-quark Yukawa coupling drives the up-type Higgs mass-squared negative near the weak scale. Given the Z-boson mass and $\tan\beta$ [the ratio of up-type Higgs boson vacuum expectation value (vev) to down-type], we impose electroweak symmetry breaking, and this allows us to solve for the masses of the heavy Higgs bosons and their superpartners, M_H and $|\mu|$.

In Fig. 2, we show the prediction of the strong coupling in the M_0, $M_{1/2}$ plane. After including the corrections, the supersymmetric prediction is not as consistent with the measured value 0.118 ± 0.003. We find that for squark masses below about 1 TeV (where the model is more natural), α_s is predicted to be greater than 0.127. For the smallest supersymmetric masses, we find numbers larger than 0.140. The predicted value is three to seven standard deviations larger than the measured value.

The prediction of α_s depends slightly on m_t. It changes by about 0.001 if m_t changes by 10 GeV. Of the three input parameters M_Z, G_μ, and $\hat{\alpha}$, only $\hat{\alpha}$ has an appreciable error. Changing $\hat{\alpha}$ by 1-σ changes α_s by about 0.001. The prediction weakly depends on $\tan\beta$ because at small (~ 1) or large ($\gtrsim 30$) $\tan\beta$, the top, bottom, and/or tau-Yukawa couplings become large, and they enter into the two-loop renormalization group equations of the gauge couplings. The prediction for

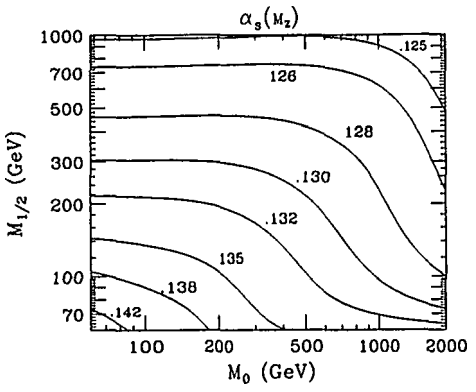


Fig. 2. The prediction of $\alpha_s(M_Z)$ in the M_0, $M_{1/2}$ plane, with $\tan\beta = 2$ and $A_0 = 0$. From Ref. 10.

$\alpha_s(M_Z)$ can be lowered by about 0.002 at the extreme values of $\tan\beta$.* The strong coupling is also insensitive to the sign of the Higgsino mass term μ. In Fig. 2 and the following figures, we set $\mu > 0$.

Hence, we find that we cannot avoid the large values of α_s shown in Fig. 2. We will give an interpretation of these large numbers after discussing the gauge-mediated case.

4.2 Minimal Gauge-Mediated Model

Models with gauge-mediated supersymmetry breaking are an attractive alternative to the supergravity models. In the supergravity model we considered, we chose universal boundary conditions, which suppress dangerous squark- and slepton-mediated flavor changing neutral currents. However, there is no symmetry which protects this choice of boundary conditions, and hence it is an artificial imposition. The advantage of the gauge-mediated models is that flavor changing neutral currents are automatically suppressed, since the soft supersymmetry breaking masses which are induced by the gauge interactions are flavor diagonal and generation independent.

*The change -0.002 is due solely to the Yukawa couplings entering into the two-loop RGE's. There may be an additional dependence because the particle spectrum depends on $\tan\beta$.

In the simplest models with gauge-mediated supersymmetry breaking,[11] there is a messenger sector with the superpotential interaction

$$W = \lambda S M \overline{M} \ , \tag{14}$$

where S is a Standard Model singlet superfield, M and $\overline{M}$ are a pair of messenger fields which are vector-like under the Standard Model gauge group, and λ is the messenger Yukawa coupling. In a grand unified theory, M and $\overline{M}$ come in full SU(5) representations. We will consider n_5 $5 + \overline{5}$ pairs and n_{10} $10 + \overline{10}$ representations. Perturbative unification of the gauge couplings is ensured if we allow at most $(n_5, n_{10}) = (1, 1)$ or $(4, 0)$.

In these models, the singlet superfield S couples to a sector in which supersymmetry is dynamically broken, and as a result, it acquires both a vev (S) and an F-term (F). This in turn generates supersymmetry-conserving diagonal entries and supersymmetry-violating off diagonal entries in the M, $\overline{M}$ scalar mass matrix. The M and $\overline{M}$ fields enter into loop diagrams with Standard Model fields on the external legs, thereby generating soft supersymmetry breaking masses for the superpartners and the Higgs bosons. The gaugino and scalar masses are generated at one- and two-loops, respectively, and in the limit $F \ll \lambda S^2$ are given by[11]

$$M_i(M) = (n_5 + 3n_{10}) \frac{\alpha_i(M)}{4\pi} \Lambda \ , \tag{15}$$

$$\tilde{m}^2(M) = 2(n_5 + 3n_{10}) \sum_{i=1}^{3} C_i \left(\frac{\alpha_i(M)}{4\pi} \right)^2 \Lambda^2 \ , \tag{16}$$

where $M = \lambda S$ is the messenger mass scale, $\Lambda = F/S$, and $C_i = 3Y^2/5, 3/4, 4/3$ for fundamental representations and zero for singlet representations.

The mass parameters [Eqs. (15) and (16)] serve as boundary conditions for the renormalization group equations at the messenger scale. In order to determine the superparticle spectrum, we run these parameters from the messenger scale to the weak scale using the two-loop renormalization group equations. As before, we impose radiative electroweak symmetry breaking and determine the Higgs boson and Higgsino masses M_H and $|\mu|$ for a given $\tan\beta$. Hence, the parameter space of the model under consideration is

$$\tan\beta, \quad M, \quad \Lambda, \quad n_5, \quad n_{10}, \quad \lambda, \quad \mathrm{sgn}(\mu),$$

where λ is the value of the messenger Yukawa coupling at the grand unification scale (we assume a single Yukawa coupling). Note that a physical messenger spectrum requires $M > \Lambda$.

After we determine the superpartner spectrum at the weak scale, we apply the same weak-scale gauge coupling threshold corrections as in the supergravity model. However, the messenger sector gives rise to additional corrections. Not only are the one- and two-loop renormalization group equations altered above the messenger scale,[12] but there are also new threshold corrections at the scale M. A degenerate SU(5) multiplet does not affect the prediction of α_s at one loop. However, the evolution of the messenger Yukawa couplings from the grand unification scale down to the messenger scale splits the messenger multiplets. If we decompose a $5 + \overline{5}$ pair of messenger fields into their doublet and triplet components, respectively denoted L and D, then the messenger sector superpotential below the grand unification scale becomes

$$W = \lambda_L S M_L \overline{M}_L + \lambda_D S M_D \overline{M}_D \ . \tag{17}$$

Thus, the messenger doublet (triplet) ends up with mass $\lambda_L S$ ($\lambda_D S$). According to Eq. (10), this mass splitting leads to the threshold correction [the $10 + \overline{10}$ fields decompose into [SU(2), SU(3)] representations $Q(2, 3)$, $U(1, 3)$, and $E(1, 1)$][†]

$$\Delta\alpha_s^{-1}(M) = \frac{9n_5}{14\pi} \ln\frac{\lambda_L}{\lambda_D} + \frac{n_{10}}{14\pi} \left(15 \ln\frac{\lambda_Q}{\lambda_U} + 6 \ln\frac{\lambda_Q}{\lambda_E} \right) \ . \tag{18}$$

The Yukawa couplings are evaluated at the messenger scale, either $\lambda_L S \simeq \lambda_D S$ or $\lambda_Q S \simeq \lambda_U S \simeq \lambda_E S$. Note that at one loop order $\Delta\alpha_s^{-1}(M_Z) = \Delta\alpha_s^{-1}(M)$.

To determine the messenger Yukawa couplings at the messenger scale, we solve the renormalization group equations which are of the form[12]

$$\frac{d\lambda_i}{dt} = \frac{\lambda_i}{16\pi^2} \left(\sum_j c_j \lambda_j^2 - \sum_k a_k g_k^2 \right) + \cdots \ , \tag{19}$$

where the dots indicate that there may be extra contributions due to interactions of the singlet with the supersymmetry breaking sector fields. These extra contributions are the same for all the messenger fields so they do not affect the ratios of Yukawa couplings. Note that for a large initial value of the messenger Yukawa coupling, the renormalization group evolution is initially dominated by the Yukawa term, which leads to the same evolution for the various messenger fields. Hence, there will be less splitting if the initial value is large. We illustrate

[†]There is an additional negligible correction due to the splitting within each U(1), SU(2), or SU(3) multiplet. Each logarithm in Eq. (18) is replaced according to $\ln(\lambda_1/\lambda_2) \to \ln(\lambda_1/\lambda_2) + (1/12) \ln[1 - (F/\lambda_1 S^2)^2]/[1 - (F/\lambda_2 S^2)^2]$.

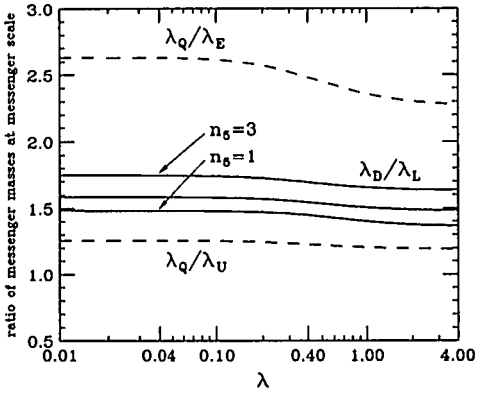


Figure 3: The ratios of the messenger masses at the messenger scale vs the value of the Yukawa coupling at the unification scale. Both the $n_{10} = 1$ (dashed) and $n_5 = 1, 2, 3$ (solid) cases are shown.

this in Fig. 3 where we show the ratio of messenger Yukawa couplings at the messenger scale versus the starting value at the grand unification scale. In the $10+\overline{10}$ case, we see that λ_Q/λ_U (λ_Q/λ_E) varies from 1.2 to 1.3 (2.3 to 2.6). Hence, the splitting is small and confined to a narrow range of values. Plugging this splitting into Eq. (18), we find that the messenger threshold correction results in at most $\Delta\alpha_s(M_Z) = -0.003$ for $n_{10} = 1$, $+0.001$ for $n_5 = 1$, and $+0.005$ for $n_5 = 3$.

Combining all the effects together, we show the full result for the prediction of $\alpha_s(M_Z)$ in the gauge-mediated model in the M/Λ, Λ plane in Fig. 4, with $\tan\beta = 4$, $n_5 = 1$, and $\lambda = 3$. We see slightly smaller numbers than in the supergravity case (Fig. 2). Relative to other choices of n_5, n_{10}, and λ, this case results in the smallest values of $\alpha_s(M_Z)$. As before, the result is not very sensitive to the value of $\tan\beta$. Changing the value of the messenger Yukawa coupling does not change the value of the strong coupling significantly.

The dashed lines in Fig. 4 indicate that the region of parameter space with the least fine tuning ($|\mu|/M_Z \simeq 2$) corresponds to the largest value of $\alpha_s(M_Z) \simeq 0.137$. The strong coupling can be reduced significantly at the cost of fine tuning. In the fine tuned region $|\mu|/M_Z \simeq 10$, $\alpha_s(M_Z) \simeq 0.125$.

We summarize the predicted values of α_s in the gauge-mediated models in Table 1. Here we set $m_t = 175$ GeV, $\tan\beta = 4$, and $\mu > 0$. We find that

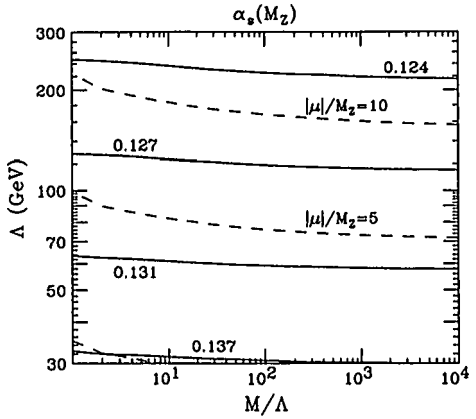


Figure 4: Contours of $\alpha_s(M_Z)$ in the gauge mediated model with $n_5 = 1$, $\tan\beta = 4$, and $\lambda = 3$. The dashed lines show contours of $|\mu|/M_Z = 2$, 5, and 10.

if $|\mu| < 10M_Z$, $\alpha_s(M_Z)$ is greater than 0.124. This is two standard deviations larger than the measured value. Hence, we are faced with the fact that, like the Standard Model, supersymmetric models do not predict that the gauge couplings meet. However, the discrepancy in the Standard Model case is enormous. The small discrepancy in the MSSM can be accounted for, and is required by, threshold corrections at the grand unification scale.

	$\|\mu\| < 10M_Z$		$\|\mu\| < 2M_Z$	
	$\lambda = 0.01$	$\lambda = 3$	$\lambda = 0.01$	$\lambda = 3$
$n_5 = 1$	> 0.125	> 0.124	> 0.137	> 0.136
$n_5 = 3$	> 0.126	> 0.125	> 0.139	> 0.136
$n_{10} = 1$	> 0.127	> 0.128	> 0.137	> 0.140

Table 1: Summary of predictions for $\alpha_s(M_Z)$ in the gauge-mediated models.

5 GUT Threshold Corrections

At the GUT scale, there are incomplete SU(5) multiplets (most notably the color triplet Higgs bosons) and there can be split multiplets as well. These fields give

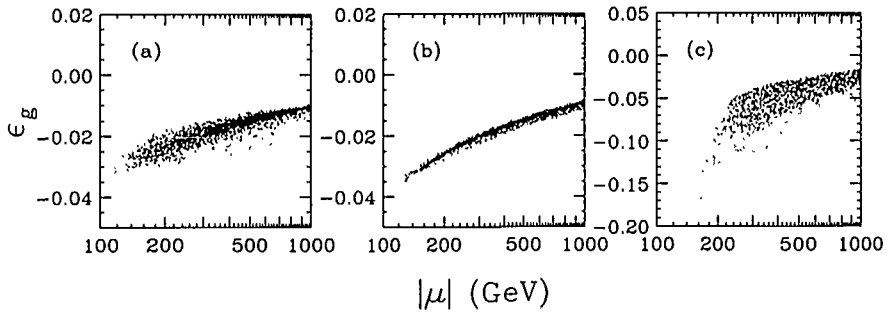


Fig. 5. The discrepancy ε_g with $\alpha_s(M_Z) = 0.118$ vs $|\mu|$ in (a) the supergravity model, and the messenger model with (b) $n_5 = 1$ and (c) $n_5 = n_{10} = 1$.

rise to threshold corrections which are expected to be of order of a couple of percent (or larger if $\alpha_{\rm GUT}$ is larger).

If we take all three gauge couplings as input at the weak scale and run them up to the grand unification scale $M_{\rm GUT}$ (which is defined to be the scale where g_1 and g_2 meet), we find a discrepancy between the value of g_3 and $g_1 = g_2$. We define the discrepancy ε_g as

$$g_3(M_{\rm GUT}) = g_2(M_{\rm GUT})(1 + \varepsilon_g) \ . \tag{20}$$

If we fix $\alpha_s(M_Z) = 0.118$, the discrepancy is negative. We show a scatter plot of the discrepancy in Fig. 5 for three different models: the supergravity model, the messenger model with $n_5 = 1$, and the messenger model with $n_5 = n_{10} = 1$ (Ref. 13). For the supergravity model and the messenger model with $n_5 = 1$, ε_g varies from about -3 to -1% as $|\mu|$ varies from 100 to 1000 GeV. For the messenger model with $n_5 = n_{10} = 1$, ε_g is larger because $\alpha_{\rm GUT}$ is larger.

In a grand unified theory, there will be a discrepancy due to the grand unification threshold corrections.[‡] In any particular model of grand unification, we can calculate ε_g as a function of the GUT model parameter space. By varying the parameters over their allowed range, we can see whether the model is consistent with the "measured" values of ε_g shown in Fig. 5. Here we give two examples, the minimal SU(5) model[14] and the missing doublet SU(5) model.[15]

[‡]There are possibly additional corrections due to higher dimension operators suppressed by $M_{\rm GUT}/M_{\rm Planck}$. See Ref. 17 for a discussion.

In the minimal SU(5) model, we find the correction[10,16]

$$\varepsilon_g = \frac{3\alpha_{\rm GUT}}{10\pi} \ln \frac{M_{H_3}}{M_{\rm GUT}} \ , \tag{21}$$

where M_{H_3} is the triplet Higgs boson mass. It is constrained to be larger than about 10^{16} GeV by the lower limits on the nucleon lifetimes.[18] Both $M_{\rm GUT}$ and the bound on M_{H_3} are functions of the supersymmetric parameter space. The bound on M_{H_3} is typically such that $M_{H_3} > M_{\rm GUT}$, so that in most of the minimal SU(5) model parameter space, ε_g is positive. From Fig. 5, we know that in order to be compatible with gauge coupling unification, ε_g must be negative. Hence, the minimal SU(5) model is not compatible with coupling constant unification.

The minimal SU(5) model contains a $5 + \overline{5}$ of Higgs fields. The doublet parts are the MSSM Higgs fields with order M_Z masses. The triplet parts mediate nucleon decay via dimension five operators. In order to be compatible with the lower bound on the nucleon lifetimes, the triplet Higgs particles must have GUT scale masses. In general, it is problematic to find a GUT model which naturally yields light Higgs doublets and heavy triplets. In the minimal SU(5) model, this doublet-triplet splitting is imposed by fine tuning superpotential parameters. The missing doublet model elegantly solves the doublet-triplet splitting problem by a judicious choice of Higgs representations. The 75, 50, and $\overline{50}$ representations are employed, and when the 75 gets a vev, the superpotential term 75 50 5 generates a mass for the triplet, but not for the doublet.

In the missing doublet model, we find[10,19]

$$\varepsilon_g = \frac{3\alpha_{\rm GUT}}{10\pi} \left\{ \ln \frac{M_{H_3}^{\rm eff}}{M_{\rm GUT}} - 9.72 \right\} . \tag{22}$$

We have defined an effective triplet Higgs mass $M_{H_3}^{\rm eff}$ which enters into the nucleon decay amplitude in the same way as in the minimal SU(5) model, so the same bounds apply. However, the splitting in the 75-dimensional representation gives rise to a negative correction, such that in the missing doublet model, the discrepancy ε_g is negative, just as it must be in order to be consistent with the measured values of $g_1(M_Z)$, $g_2(M_Z)$, and $g_3(M_Z)$. In fact, in each of the three models shown in Fig. 5, the allowed range of ε_g in the missing doublet model just about overlaps the required values. Hence, the missing doublet model is consistent with gauge coupling unification.

6 Conclusion

In the end, what we really do when we investigate gauge coupling unification is constrain the physics at the grand-unification scale. The weak-scale measurements of the gauge couplings imply that ε_g is negative. We can calculate ε_g in various grand unified models to see whether the grand unified model parameter space can accommodate the required value. Here, we showed that this is not possible in the minimal SU(5) model, but that it is possible in the missing doublet SU(5) model. In other words, the missing doublet model requires that ε_g is negative, which corresponds with the measured values of the gauge couplings. Similarly, there are SO(10) models which can accommodate the "measured" ε_g, and others which cannot. Gauge coupling unification remains an effective constraint on model building.

References

[1] Particle Data Group Review of Particle Properties, Phys. Rev. D **54**, 1 (1996).

[2] For a review, see e.g., H. P. Nilles, Phys. Rep. **110**, 1 (1984); H. E. Haber and G. L. Kane, Phys. Rep. **117**, 75 (1985).

[3] K. Inoue, A. Kakuto, H. Kamatsu, and S. Takeshita, Prog. Theo. Phys. **68**, 927 (1982); L. Alvarez-Gaumé, J. Polchinkski, and M. B. Wise, Nucl. Phys. B **221**, 495 (1983); J. Ellis, J. S. Hagelin, D. V. Nanopoulos, and K. Tamvakis, Phys. Lett. B **125**, 275 (1983); L. E. Ibañez and C. Lopez, Nucl. Phys. B **233**, 511 (1984); L. E. Ibañez, C. Lopez, and C. Muñoz, Nucl. Phys. B **250**, 218 (1985).

[4] For a review, see G. Jungman, M. Kamionkowski, and K. Griest, Phys. Rep. **267**, 195 (1996).

[5] M. E. Machacek and M. T. Vaughn, Nucl. Phys. B **222**, 83 (1983); *ibid.*, B **236**, 221 (1984); *ibid.*, B **249**, 70 (1985); I. Jack, Phys. Lett. B **147**, 405 (1984); Y. Yamada, Phys. Rev. D **50**, 3537 (1994); I. Jack and D. R. T. Jones, Phys. Lett. B **333**, 372 (1994); S. Martin and M. Vaughn, Phys. Lett. B **318**, 331 (1993); *ibid.*, Phys. Rev. D **50**, 2282 (1994).

[6] W. Siegel, Phys. Lett. B **84**, 193 (1979); D. M. Capper, D. R. T. Jones, and P. van Nieuwenhuizen, Nucl. Phys. B **167**, 479 (1980); I. Jack, D. R. T. Jones, S. P. Martin, M. T. Vaughn, and Y. Yamada, Phys. Rev. D **50**, 5481 (1994).

[7] G. Degrassi, S. Fanchiotti, and A. Sirlin, Nucl. Phys. B **351**, 49 (1991), and references therein.

[8] D. M. Pierce, J. A. Bagger, K. T. Matchev, and R.-J. Zhang, hep-ph/9606211, to be published in Nucl. Phys. B, and references therein.

[9] P. Chankowski, Z. Pluciennik, and S. Pokorski, Nucl. Phys. B **439**, 23 (1995).

[10] J. Bagger, K. Matchev, and D. Pierce, Phys. Lett. B **348**, 443 (1995).

[11] M. Dine and A. Nelson, Phys. Rev. D **48**, 1277 (1993); M. Dine, A. Nelson, and Y. Shirman, Phys. Rev. D **51**, 1362 (1995); M. Dine, A. Nelson, Y. Nir, and Y. Shirman, Phys. Rev. D **53**, 2658 (1996).

[12] J. A. Bagger, K. T. Matchev, D. M. Pierce, and R.-J. Zhang, hep-ph/9611229, to appear in Phys. Rev. Lett., and references therein.

[13] In the scatter plots, we set $m_t = 175$ GeV, $\mathrm{sgn}(\mu) = \pm 1$, we allow $\tan\beta$ to take any value consistent with perturbative unification and electroweak symmetry breaking, and we vary the inputs as follows: in the supergravity model $M_{1/2} \leq 500$ GeV, $M_0 \leq 1000$ GeV, and $|A_0| \leq 3\sqrt{M_0^2 + 4M_{1/2}^2}$. In the gauge-mediated models, $\Lambda \leq 300$ TeV, $1.03 \leq M/\Lambda \leq 10^4$, and $0.03 \leq \lambda \leq 3$. We impose that the (first or second generation) squark masses be greater than 220 GeV, $m_{\tilde{\chi}^+} > 65$ GeV, $m_{\tilde{g}} > 170$ GeV, $m_{\tilde{l}} > 45$ GeV, and $m_h > 60$ GeV. For references on these bounds, see Ref. 8.

[14] S. Dimopoulos and H. Georgi, Nucl. Phys. B **193**, 150 (1981); N. Sakai, Z. Phys. C **11**, 153 (1981).

[15] S. Dimopoulos and F. Wilczek, in *The Unity of the Fundamental Interactions*, edited by A. Zichichi (Plenum, 1983); A. Masiero, D. V. Nanopoulos, K. Tamvakis, and T. Yanagida, Phys. Lett. B **115**, 380 (1982); B. Grinstein, Nucl. Phys. B **206**, 387 (1982); J. Hisano, T. Moroi, K. Tobe, and T. Yanagida, Phys. Lett. B **342**, 138 (1995).

[16] M. B. Einhorn and D. R. T. Jones, Nucl. Phys. B **196**, 475 (1982); I. Antoniadis, C. Kounnas, and K. Tamvakis, Phys. Lett. B **119**, 377 (1982).

[17] P. Langacker and N. Polonsky, Phys. Rev. D **47**, 4028 (1993).

[18] J. Hisano, H. Murayama, and T. Yanagida, Nucl. Phys. B **402**, 46 (1993).

[19] K. Hagiwara and Y. Yamada, Phys. Rev. Lett. **70**, 709 (1993); Y. Yamada, Z. Phys. C **60**, 83 (1993).

RECENT RESULTS FROM LEP

Joachim Mnich
CERN, PPE-L3
CH-1211 Genève 23

Representing the LEP Collaborations

ABSTRACT

In this article, recent preliminary results of the four LEP experiments, ALEPH, DELPHI, L3, and OPAL, from running at energies above the Z resonance are presented. LEP was operated at center-of-mass energies between 130 and 140 GeV at the end of 1995 and at the $e^+e^- \rightarrow W^+W^-$ threshold of 161 GeV in 1996. Studies are performed on fermion pair production and the energy evolution of QCD observables. From the measured W pair cross section at 161 GeV, a value for the mass of the W is obtained. The new energy regime in e^+e^- collision is also exploited to extend searches for particles predicted by Supersymmetry and other extensions of the Standard Model.

© 1996 by Joachim Mnich.

1 Introduction

The Large Electron-Positron Collider (LEP) at CERN in Geneva has been operated since 1989 at center-of-mass (cms) energies close to the mass of the Z. This first phase (LEP I) has been concluded in 1995. Each of the four experiments, ALEPH, DELPHI, L3, and OPAL, has collected approximately four million Z decays allowing very precise tests of the Standard Model (SM) of electroweak interactions and the determination of many of its parameters. Significant contributions are made to Quantum Chromodynamics, b-quark and tau physics, as well as the search for new particles and phenomena. In particular, the SM Higgs boson is ruled out in the entire mass range from 0–65 GeV by the LEP experiments.

In preparation of the second phase (LEP II), marked by running at energies above the W pair production cross section, LEP was operated at cms energies between 130 and 140 GeV in November 1995 (LEP 1.5). This has been possible after installation of additional super-conducting (SC) radio frequency cavities required by the higher energy loss due to synchrotron radiation at higher beam energies. A total luminosity of about 6 pb^{-1} was delivered by LEP to each of the four experiments. Besides serving as a pilot run for the machine and the experiments to get accustomed to the very different running conditions as compared to the Z, this run also provided interesting physics results, in particular, the search for Supersymmetry, which are discussed below.

In 1996 after installation of more cavities, LEP ran at a cms energy of 161 GeV. The main merit of this run is the determination of the W mass from the measured cross section $e^+e^- \to W^+W^-$ at the threshold. Also, new kinematic regions in the search for new particles are explored. Preliminary results from about one-third of the data collected at this energy were available at the time of the conference and are included here.

2 Status of LEP

The energy upgrade of the LEP machine requires most importantly the increase of the accelerating power which is achieved by the addition of SC cavities. The average energy loss per turn of the circulating particles increases from about 130 MeV at the Z pole to 1 900 MeV for a beam energy E_b = 90 GeV. By October 1995, in total, 64 SC cavities were installed increasing the maximum

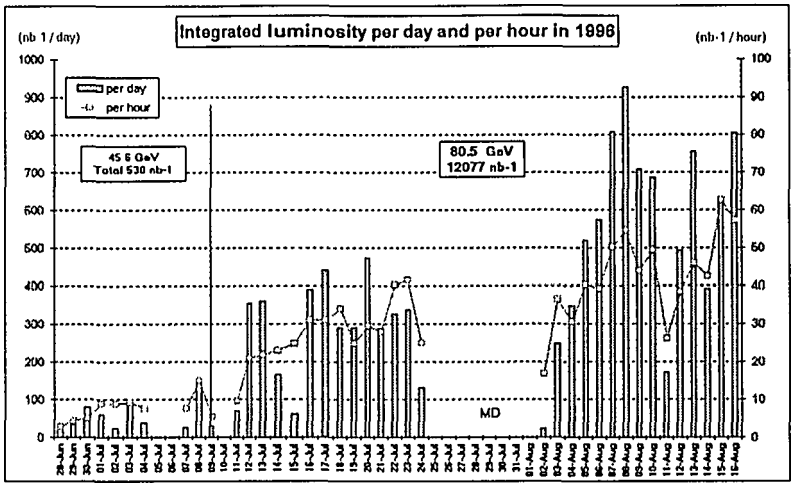


Figure 1: Day-by-day development of the integrated luminosity per day and per hour delivered by LEP to each experiment from the end of June to August 1996.

beam energy to E_b = 70 GeV. During the winter shutdown, 80 more units were installed allowing for beam energies above 80 GeV and hence crossing the W pair threshold. In October 1996, a total number of 172 SC cavities will have been installed, which will increase the operational energy to E_b = 86 GeV. The successful operation of the machine so far demonstrated the reliable performance of the SC cavity system at its design gradient of 6 MV/m (Refs. 1 and 2).

The performance of the LEP machine is illustrated in Fig. 1, which shows the delivered integrated luminosity as a function of time from June to August 1996. The setup of the machine was done at the Z pole which provided calibration data for the experiments. In the last week of running at $\sqrt{s}$ = 161 GeV, average daily luminosities of 0.6 pb^{-1} were provided to each of the four experiments.

The installation of more cavities is foreseen such that in 1998 the beam energy can be raised to 96 GeV. The goal is to provide an integrated luminosity of 500 pb^{-1} above the W pair threshold to each of the four experiments by the year 2000.

3 Total Cross Sections and Forward-Backward Asymmetries

The LEP experiments study fermion pair production at the new cms energies far above the Z pole. Total cross section measurements are performed for the four reactions

$$e^+e^- \to \text{hadrons}, \quad e^+e^- \to e^+e^-, \quad e^+e^- \to \mu^+\mu^-, \quad e^+e^- \to \tau^+\tau^- . \quad (1)$$

In the leptonic final states, the forward-backward asymmetry, A_{FB}, is determined as well.

Cross sections at LEP 1.5 and at LEP II are about two orders of magnitude smaller than at the Z pole. Figure 2 shows the cross section $e^+e^- \to q\bar{q}$ as a function of the cms energy. The approximate energy range of current and previous e^+e^- colliders is also indicated. The luminosity of 5–6 pb^{-1} collected at 130–140 GeV corresponds to about 1 600 hadron events per experiment. Approximately the same number of events has been observed in 11 pb^{-1} at 161 GeV.

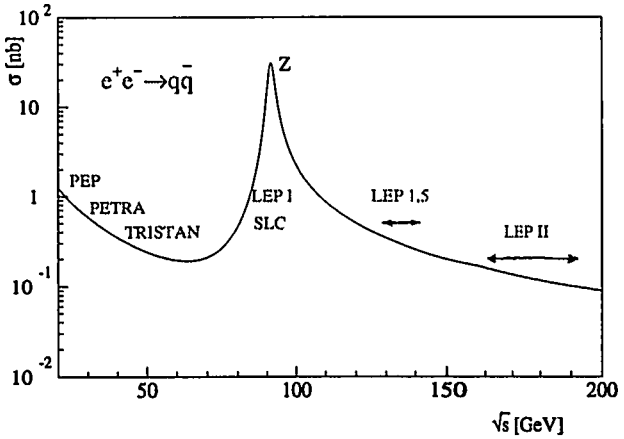


Figure 2: The cross section $e^+e^- \to q\bar{q}$ as a function of the cms energy. The approximate energy ranges of previous and current e^+e^- colliders are indicated.

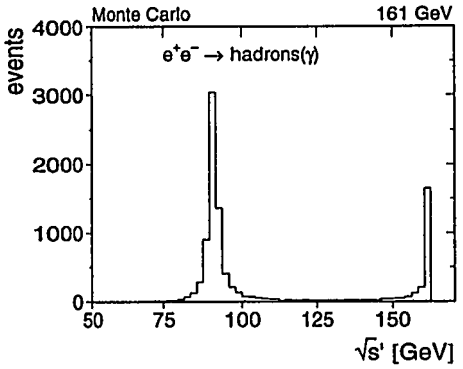


Figure 3: Distribution of the effective cms energy, $\sqrt{s'}$, in the reaction $e^+e^- \to$ hadrons, obtained from MC calculation at $\sqrt{s} = 161$ GeV.

3.1 Radiative Return to the Z

At cms energies above the Z pole, initial state radiation (ISR) plays an important role. Radiation of photon(s) by the incoming electrons removes energy from the annihilation process and the fermion production takes place at a lower effective cms energy, $\sqrt{s'}$, where the cross section is different. In particular, if the remaining energy in the e^+e^- system is close to the mass of the Z, m_Z, the annihilation cross section is very high. Consequently, this provides a major contribution to the total cross section $e^+e^- \to f\bar{f}$ and it is called "Radiative Return to the Z." The importance of the return to the Z is illustrated in Fig. 3 which shows the distribution of the effective cms energy of the final-state quark pair in $e^+e^- \to q\bar{q}$ as obtained from a Monte Carlo (MC) calculation for $\sqrt{s} = 161$ GeV. Besides the usual peak at the nominal cms energy with a smooth tail towards lower energies from the radiation of soft photons, one observes that the majority of the events is actually produced at $\sqrt{s'} \approx m_Z$.

Table 1 gives the fraction of events with the fermion pair produced at lower energy ($\sqrt{s'} < 110$ GeV) calculated with the JETSET[3] and KORALZ[4] programs. The relative contribution of events radiated back to the Z becomes smaller with increasing cms energy as the required energy for the ISR photon is higher. In the hadron sample, the fraction of events produced at $\sqrt{s'} \approx m_Z$ is higher than in the muon and tau samples because the ratio of hadron to charged lepton production at the Z is higher than above the Z as the Z couples more strongly to quarks than

	$\sqrt{s}$	140 GeV	161 GeV
$e^+e^- \to$ hadrons		80%	70%
$e^+e^- \to \mu^+\mu^-$		65%	50%

Table 1: Fraction of events with effective cms energies $\sqrt{s'} < 110$ GeV for hadron and muon final states at two cms energies.

to charged leptons. For the process $e^+e^- \to e^+e^-$, the t-channel boson exchange is dominant above the Z pole. Hence, the resonant s-channel production at the Z is less important for this process (see below).

Because of the different nature of events produced at, or close to, the nominal cms energy and those stemming from decays of real Z bosons, the LEP experiments measure two sets of cross sections and forward-backward asymmetries: for the total sample and the high energy events separated by a cut in the reconstructed $\sqrt{s'}$ value. The definition of high-energy events differs among the experiments.

3.2 Determination of $\sqrt{s'}$

The effective cms energy is reconstructed assuming a three-body final state, i.e., only one ISR photon (Fig. 4). Then $\sqrt{s'}$ is given by the photon energy E_γ:

$$s' = s - 2E_\gamma\sqrt{s}\,. \tag{2}$$

If the ISR photon is detected, its measured energy can be used to obtain $\sqrt{s'}$. However, in general, photons are emitted at small angles by the incoming electron or positron, and thus often escape detection through the beam pipe. In this case, the photon energy can be determined from the polar angles of the outgoing

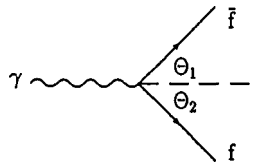


Figure 4: Reconstruction of the photon energy from the polar angles of the outgoing fermion-antifermion pair.

fermions, Θ_1 and Θ_2 (Fig. 4):

$$E_\gamma = \sqrt{s}\,\frac{|\sin(\Theta_1+\Theta_2)|}{\sin\Theta_1+\sin\Theta_2+|\sin(\Theta_1+\Theta_2)|}\,. \tag{3}$$

Higher order effects like multiple photon emission are taken into account by correcting the cross section and A_{FB} measurements with factors obtained from MC studies. Hadron events are forced into two jets and the quark directions are approximated by the jet axes. A kinematic fit taking into account direction and energy measurements improves the resolution on E_γ and thus $\sqrt{s'}$.

An event $e^+e^- \to$ hadrons $+\,\gamma$ recorded with the DELPHI detector at $\sqrt{s} =$ 130 GeV is shown in Fig. 5. In this example, the ISR photon is emitted at a relatively large angle and observed in the forward calorimeter of the detector.

The effective cms energy, reconstructed as described above by L3, for the four final states of Eq. (1) is shown in Fig. 6. The data correspond to a luminosity of 4.3 pb^{-1} at $\sqrt{s} = 161$ GeV. High-energy events are clearly separated from the ones produced with $\sqrt{s'} \approx m_Z$. The shapes of the observed distributions are well-described by MC simulations. As mentioned above, the radiative return to the Z is much less pronounced in the e^+e^- final state because the cross section is dominated by t-channel boson exchange.

3.3 Results on Total Cross Sections

The measurements of cross sections at LEP 1.5 are described in Refs. 5–8. Most of the luminosity was taken at cms energies of 130 and 136 GeV and only a small amount at 140 GeV. A total number of about 1600 hadron events has been recorded by each experiment. Recent preliminary results from the 161 GeV run are presented in Ref. 9.

The results of the hadronic cross-section measurements above the Z pole are shown in Fig. 7 for both the total event sample and the high-energy events alone. For the sake of comparison, the results of the four experiments are scaled to the common definition $\sqrt{s'} > 110$ GeV for the high-energy sample.[9] The measurements are compared to the SM expectations as calculated with the program ZFITTER 4.9 (Ref. 10), and they are found to be in good agreement.

Measurements of leptonic cross sections above the Z pole are shown in Fig. 8. Here the results for $e^+e^- \to \mu^+\mu^-$ and $e^+e^- \to \tau^+\tau^-$ are averaged over the four experiments after being adjusted to a common $\sqrt{s'}$ cut. For comparison also, the

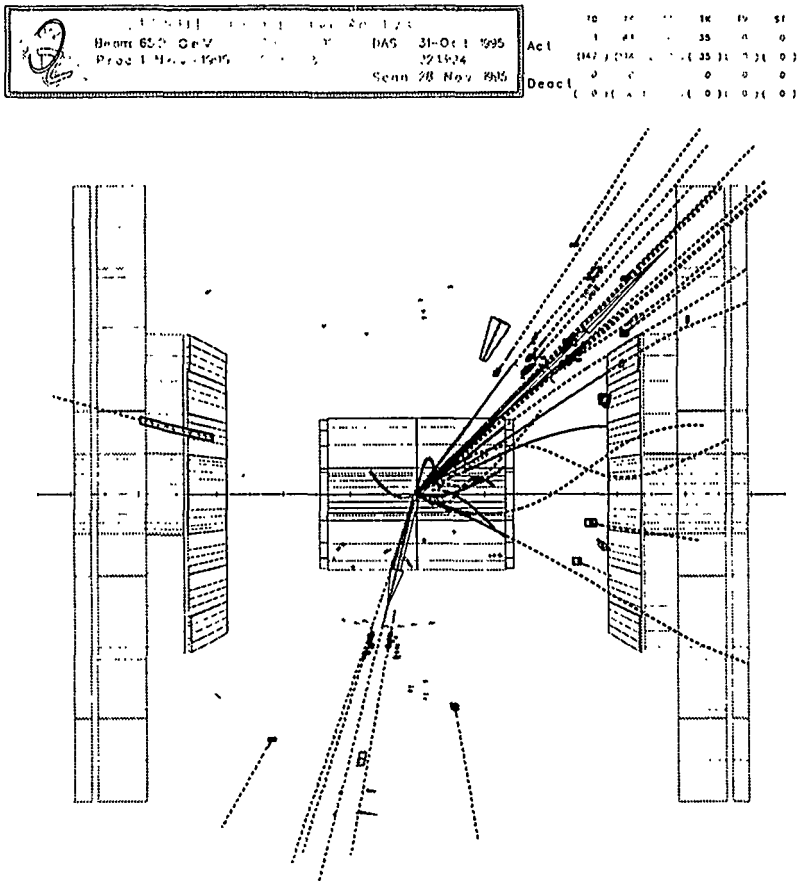


Figure 5: Example of an event $e^+e^- \to$ hadrons$+\gamma$ in the DELPHI detector (side view). Here the initial state photon is observed in the left forward region of the detector.

high-precision measurements at cms energies close to m_Z are displayed. For both reactions, the total cross sections as well as the cross sections for the inclusive high-energy samples are in good agreement with the SM prediction.

3.4 Results on Forward-Backward Asymmetries

The forward-backward asymmetry is defined as

$$A_{FB} = \frac{N_F - N_B}{N_F + N_B}, \tag{4}$$

where N_F and N_B are the number of events in the forward and backward hemispheres. Above the Z, a large fraction of the events is produced with a large acollinearity angle. This creates an ambiguity in the definition of the asymmetry because both final state leptons are often scattered into the same hemisphere. Forward and backward events are defined either by the hemisphere of the negative lepton or by calculating the polar angle in the $\ell^+\ell^-$ rest frame. Different definitions of A_{FB} used by the experiments make it difficult to compare experimental results, especially for the asymmetry of the total sample which includes the radiative return to the Z.

As an example, experimental results from OPAL from the Z pole up to recent measurements based on about 3 pb^{-1} at 161 GeV are shown in Fig. 9 and compared to the SM expectations. Figure 9(a) shows the asymmetry in e^+e^- as a function of the cms energy for electron scattering angles $|\cos\Theta_{e^-}| < 0.7$. For most of the energy range, t-channel boson exchange dominates and leads to a large positive forward-backward asymmetry. The effect of resonant Z production at $\sqrt{s} = m_Z$, where the asymmetry is small, is clearly visible.

The reactions $e^+e^- \to \mu^+\mu^-$ and $e^+e^- \to \tau^+\tau^-$ which are expected to have similar asymmetries are combined in Fig. 9(b). The SM expectation for the total sample is shown as a solid line and for the high energy events $\sqrt{s'/s} > 0.8$ as a dotted line; the latter is close to the Born-level asymmetry without radiative corrections (broken line). Radiative corrections are huge above the Z pole since the total sample is a mixture of events from high energy with large asymmetry and events at the Z where the asymmetry is small. The observed polar angle distributions for the three lepton species at 161 GeV are shown in Figs. 9(c)–9(e). All measurements are in good agreement with the theoretical expectations.

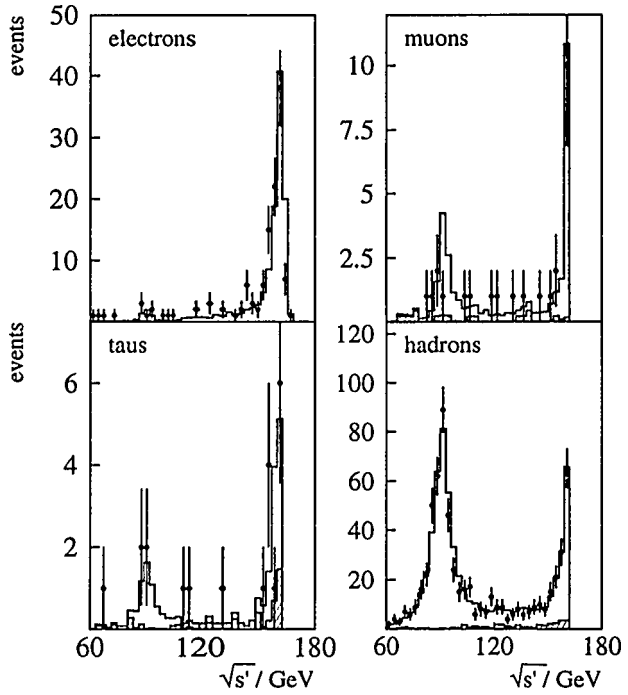


Figure 6: Distributions of the reconstructed effective cms energy $\sqrt{s'}$ for the four reactions of Eq. (1) obtained at $\sqrt{s} = 161$ GeV by L3. The points with error bars represent the data. Signal and background MC expectations are shown as open and hatched histograms, respectively.

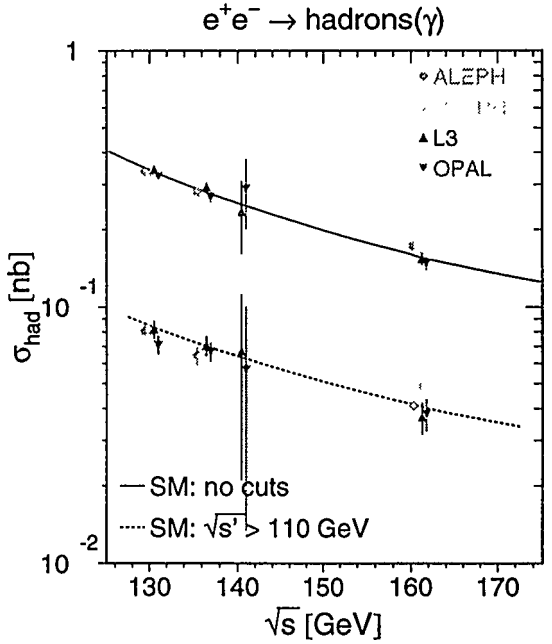


Figure 7: Cross section $e^+e^- \to$ hadrons measured by the LEP experiments between 130 and 161 GeV. The total cross section as well as the cross section at high $\sqrt{s'}$ are shown and compared to the SM expectation (solid and broken line, respectively).

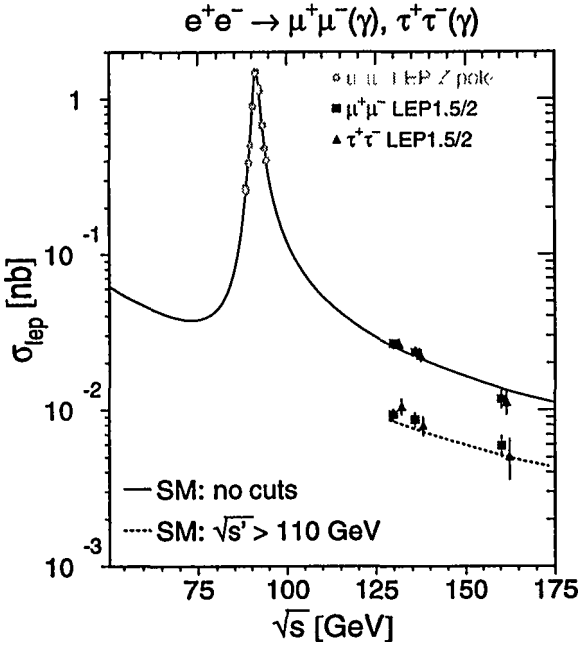


Figure 8: Cross sections $e^+e^- \to \mu^+\mu^-$ and $e^+e^- \to \tau^+\tau^-$ averaged over the four LEP experiments as a function of $\sqrt{s}$ from the Z pole to 161 GeV. The total cross sections as well as the cross sections for high $\sqrt{s'}$ are shown and compared to the SM expectation (solid and broken line, respectively).

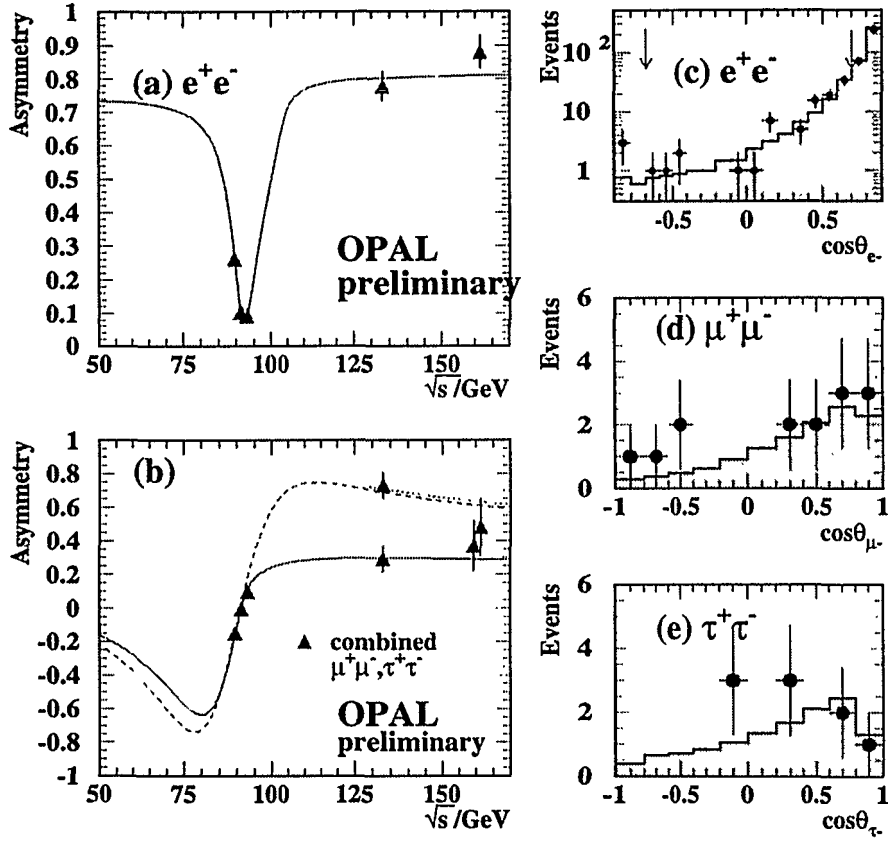


Figure 9: Measured e^+e^- forward-backward asymmetry (a) for $|\cos\Theta_{e^-}| < 0.7$ as a function of the cms energy as obtained by OPAL. (b) shows the combined muon and tau asymmetry as a function of energy for the total and the high-energy samples ($\sqrt{s'/s} > 0.8$). The SM expectations are represented as solid lines for the total, and a dotted line for the high-energy sample. The broken line shows the Born-level asymmetry. The polar angle distributions at 161 GeV of the negative leptons are shown in plots (c)-(e).

The measurements at the highest e^+e^- energies can be compared to results obtained by experiments at lower energies. Figure 10 shows a compilation of forward-backward asymmetry measurements in $e^+e^- \to \mu^+\mu^-$ performed at e^+e^- colliders operating below the Z resonance (see Ref. 11 and references therein) together with L3 measurements at and above the Z. Measurements in the gap between the TRISTAN cms energy and m_Z are performed using events collected at $\sqrt{s} = m_Z$ which are radiated down to lower energies.[12] Good agreement between the measurements and the SM prediction is observed over the entire energy range up to $\sqrt{s} = 161$ GeV.

4 Determination of the γZ Interference

The total $e^+e^- \to f\bar{f}$ cross section, σ_{tot}, is composed of three terms

$$\sigma_{tot} = \sigma_\gamma + \sigma_Z + \sigma_{int} \tag{5}$$

describing the contributions of the photon and Z exchange and their interference, σ_{int}. While running at the Z pole, the LEP experiments mainly measured the Z contribution whereas the other two represented small corrections preventing their precise measurement. In particular, the γZ interference contributes significantly only below and above the Z pole. This can be seen from Fig. 11 which shows the relative contribution of σ_{int} to the total hadronic cross section. Above the Z pole, most of the sensitivity is contained in the part of the cross section at high effective cms energy.

In lowest order, the contribution of the γZ interference can be written as

$$\begin{aligned} \sigma_{int} &= \frac{4\pi\alpha^2}{3} J_f \frac{s - m_Z^2}{(s - m_Z^2)^2 + s^2\Gamma_Z^2/m_Z^2} \\ J_f &= \frac{G_F m_Z^2}{\sqrt{2}\,\pi\,\alpha} q_e q_f g_V^e g_V^f \end{aligned} \tag{6}$$

with Γ_Z denoting the total width of the Z, α the QED, and G_F the Fermi coupling constants. The interference term J_f is proportional to the product of the charge, q_f, and the vector coupling constants g_V^f of the fermions involved.

Of special interest is the hadronic interference term defined as the sum over the five quark flavors produced at LEP energies

$$J_{had} = \sum_{u,d,c,s,b} J_q \,. \tag{7}$$

	J_{had}
LEP $\sqrt{s} \approx m_Z$	$+0.18 \pm 0.34$
incl. $130 - 140$ GeV	-0.21 ± 0.20
incl. TOPAZ	-0.07 ± 0.16
Standard Model	$+0.22$

Table 2: LEP results on the hadronic interference term J_{had} from fits in the S-matrix framework using different data sets. The last line shows the SM expectation.

About 90% of the Z decays recorded by the LEP experiments are hadronic final states which therefore dominate the results on parameters like the mass and total width of the Z. When determining Z parameters from a Breit-Wigner fit to the measured cross sections at the Z resonance, the hadronic interference term usually is set to its SM expectation. This way, the quark couplings, and hence, the flavor composition of hadronic Z decays, are prescribed to their SM expectations. This introduces some model dependence into the determination of Z parameters.

Alternatively, the hadronic interference term can be measured by treating it as a free parameter in the fit. For instance, this is done in the S-matrix approach.[13] In Table 2, the results on J_{had} averaging over the four LEP experiments are shown with and without using the data collected at LEP 1.5. One notices that the few hundred hadron events at high energy collected per experiment significantly improve the precision on J_{had} as compared to the Z data alone. Further improvement is achieved when including the measurement of the hadron cross section at $\sqrt{s} = 57.8$ GeV performed by the TOPAZ Collaboration.[14] The measurements of J_{had} agree reasonably well with the SM expectation.

At the Z pole, the γZ interference contribution changes its sign. Varying the hadronic interference term would therefore change the position of the peak while leaving the width and height of the resonance curve unchanged. Figure 12 shows the correlation of m_Z and J_{had} as obtained from a fit to LEP data in the S-matrix framework.[15] Both 68% contours, with and without including LEP 1.5 data, are shown. The improvement on J_{had} translates hence to a reduction of the error on m_Z determined this way, which depends less on the validity of the SM (Table 3).

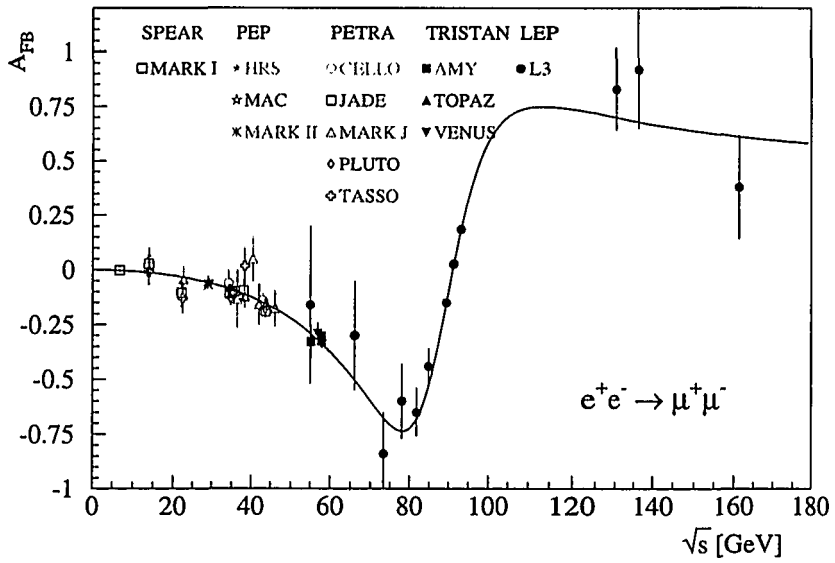


Figure 10: Measurements of the forward-backward asymmetry in $e^+e^- \to \mu^+\mu^-$ as a function of the cms energy performed by experiments at various e^+e^- colliders. The solid line represents the Born-level expectation.

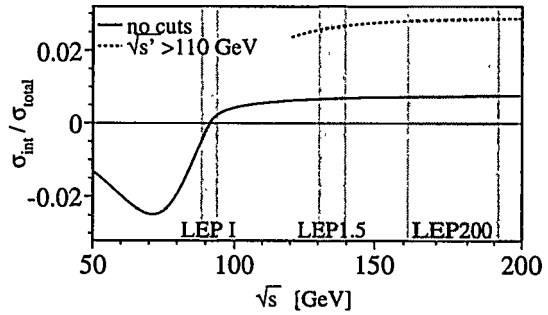


Figure 11: The relative contribution of the γZ interference to the total hadronic cross section as a function of the cms energy. The broken line shows this ratio for the cross section at high effective cms energies.

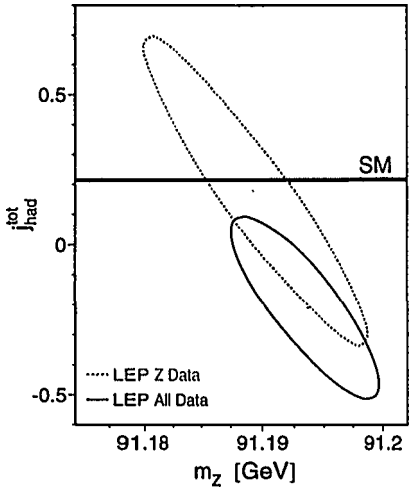


Figure 12: Contours (68% C.L.) in the m_Z-J_{had} plane using LEP data at the Z pole only (broken line) as well as including LEP 1.5 results (solid line). The horizontal line shows the SM expectation for J_{had}.

	m_Z [MeV]
LEP $\sqrt{s} \approx m_Z$	$91\,189.3 \pm 6.2$
incl. $130 - 140$ GeV	$91\,193.6 \pm 4.0$
J_{had} fixed to SM	$91\,191.3 \pm 2.0$

Table 3: LEP results on the Z mass obtained in the S-matrix framework, with and without including measurements at 130–140 GeV, and compared to the result obtained with a fixed hadronic interference term.[15]

For comparison, the combined LEP Z mass obtained with a J_{had} fixed to its SM value is quoted as well.[16]

5 Studies of QCD in $e^+e^- \rightarrow$ hadrons

The hadronic events recorded during the runs at $130 \leq \sqrt{s} \leq 161$ GeV are used to perform studies on the energy evolution of observables and to compare them to the predictions based on QCD. For these studies, events radiated to lower effective cms energies are excluded. Details on the QCD tests performed with the data collected at $130 \leq \sqrt{s} \leq 140$ GeV can be found in Refs. 17–20. Some examples of these studies are presented here.

A first example is the measurement of the average charged particle multiplicity in hadronic events, $<n_{ch}>$. The DELPHI experiment, using their hadron sample with $\sqrt{s'} > 122$ GeV, finds for $\sqrt{s} = 130$ GeV (Ref. 18)

$$<n_{ch}> = 23.84 \pm 0.91 \pm 0.52, \qquad (8)$$

where the first error is statistical and the second systematic.

In Fig. 13, this result is compared to measurements at lower cms energies. The evolution of the average charged particle multiplicity is well-described by QCD including next-to-leading log corrections up to the new measurement when using $\alpha_s(130 \text{ GeV}) = 0.105$.

In addition to counting charged particles from quark fragmentation, the momentum spectrum is studied at the new cms energies. From the particle momentum, p, normalized to the beam energy, one defines the quantity

$$\xi_p = -\ln x_p \qquad \text{with } x_p = \frac{p}{E_b} \qquad (9)$$

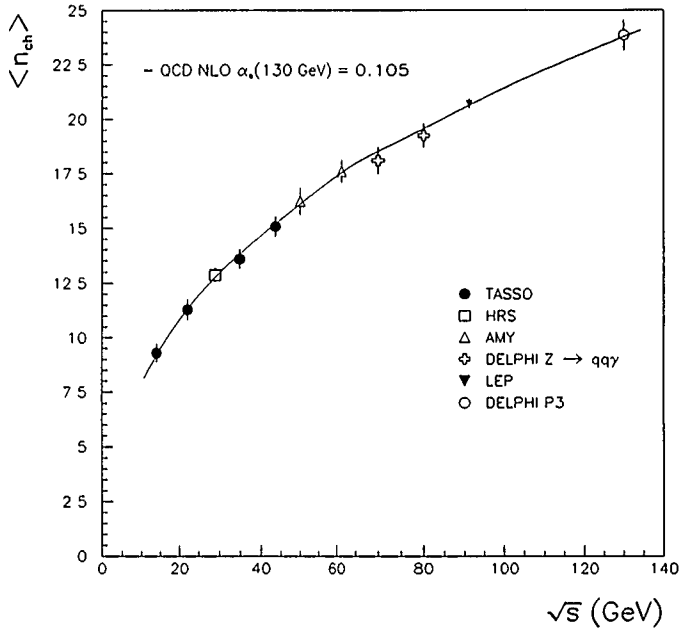


Figure 13: The average charged particle multiplicity in $e^+e^- \rightarrow$ hadrons measured by DELPHI at 130 GeV compared to measurements at lower energies and to the QCD expectation.[18]

thus emphasizing the low-energy part of the spectrum. The distribution obtained by OPAL from the first part of their 161 GeV data is shown at the top of Fig. 14. The observed spectrum is compared to the PYTHIA[21] MC program and to a QCD fit in next-to-leading log approximation. From the fit, the position of the maximum, ξ_0, is obtained which can be calculated in QCD. At the bottom of Fig. 14, measurements of ξ_0 at different energies are compared to the QCD calculation. Again, the new measurements are in good agreement with the expected energy evolution up to $\sqrt{s} = 161$ GeV.

The LEP experiments determine the average thrust in $e^+e^- \rightarrow$ hadron events at the new energies. The ALEPH result is compared to measurements at $\sqrt{s} = m_Z$ and other experiments at lower energies in Fig. 15. These data are compared

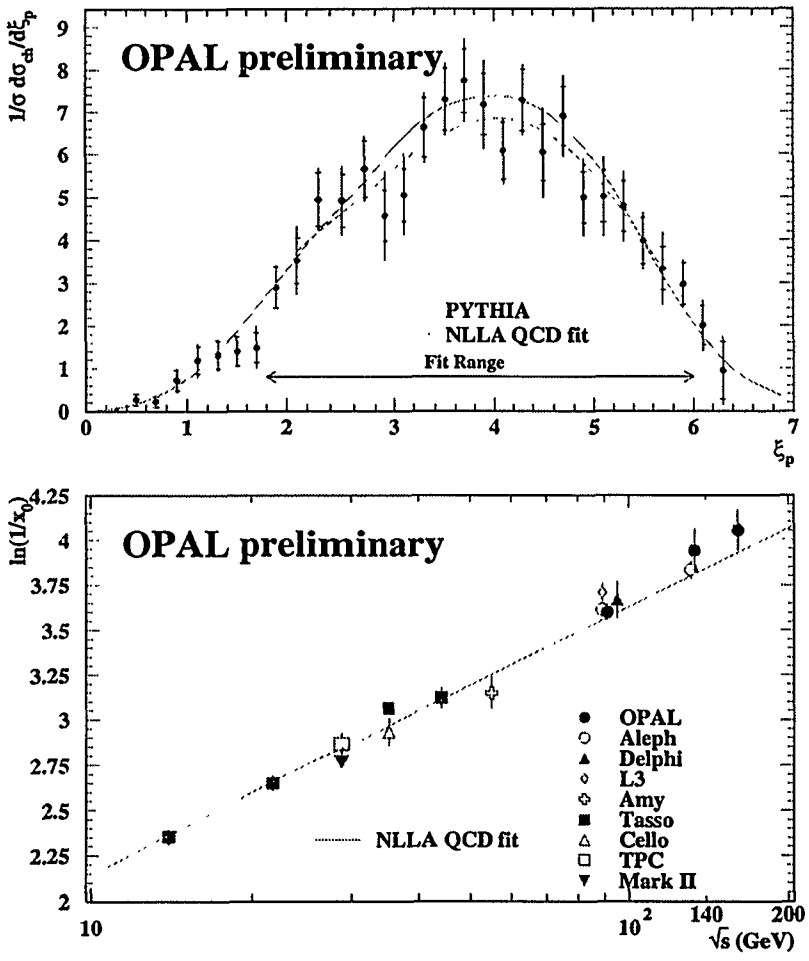


Figure 14: Top: The distribution of ξ_p observed at 161 GeV by OPAL compared to the PYTHIA program and next-to-leading log QCD calculation.
Bottom: Measurements of the peak of the ξ_p distribution at various energies compared to a QCD fit.

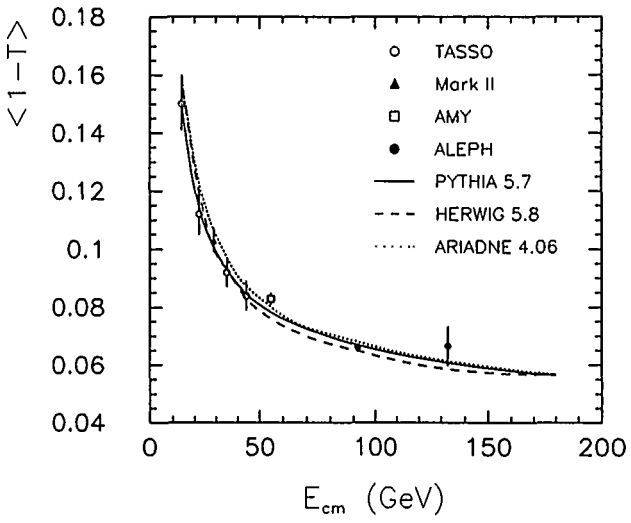


Figure 15: Evolution of the average thrust in $e^+e^- \rightarrow$ hadron events.[17] The ALEPH result at 133 GeV is compared to measurements at lower energies and various MC calculations.

to several MC models predicting the narrowing of jets at higher energies. The measurement at 133 GeV is in agreement with the expectation.

All QCD observables investigated at high energies are consistent with their expected energy evolution using the α_s value measured by the LEP experiments at the Z pole. Hence, the new measurements can be used to extract α_s at higher energy. Table 4 summarizes the results on α_s obtained from various event shape variables at the average LEP 1.5 energy of $\sqrt{s} = 133$ GeV. As expected, these α_s values are smaller than $\alpha_s(m_Z)$, but the statistical errors are still large. Detailed investigations of error correlations on the experimental and theoretical side should allow us to confirm the running of α_s from the Z up to the new cms energies.

Measurements of the strong coupling constant α_s at different momentum transfer Q are compared in Fig. 16. The experimental results are in agreement with the expected running of α_s.

	α_s(133 GeV)
ALEPH	0.119 ± 0.008
DELPHI	0.119 ± 0.008
L3	0.107 ± 0.008
OPAL	0.110 ± 0.010

Table 4: Measurements of α_s at $\sqrt{s}$ = 133 GeV using hadronic event shape variables.[17–20]

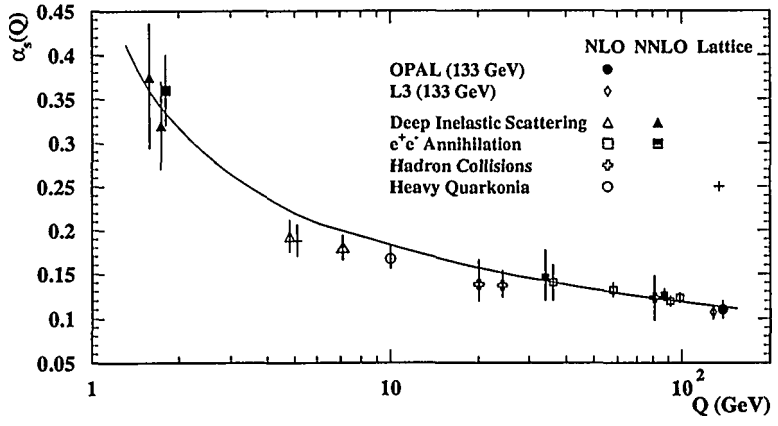


Figure 16: Measurement of the strong coupling constant α_s at different energies. New LEP measurements at $\sqrt{s}$ = 133 GeV are compared to measurements at the Z and various other determinations at lower energies. The solid line represents the second order QCD prediction for $\alpha_s(m_Z) = 0.120$ (Ref. 20).

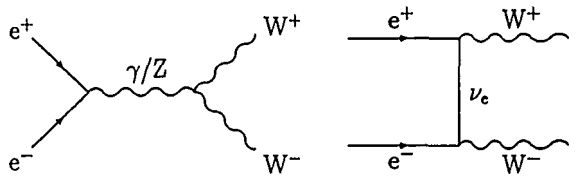


Figure 17: Feynman diagrams contributing to the reaction $e^+e^- \rightarrow W^+W^-$ in lowest order.

6 W Pair Production at LEP

The second phase of the LEP program, marked by the increase of the cms energy above the threshold for the process $e^+e^- \rightarrow W^+W^-$, has started in 1996. This reaction proceeds by the two Feynman diagrams depicted in Fig. 17: s-channel photon or Z exchange and t-channel electron neutrino exchange. Both individual diagrams diverge at high energies, and only their sum with the couplings predicted by the SM preserves unitarity. Of particular interest are the couplings at the three boson vertices arising from the non-Abelian structure of the SM of electroweak interactions. These will be tested experimentally to the percent level during the next years at LEP II (Ref. 22).

The first goal is to determine the mass of the W, m_W, from the measured cross section at the threshold. Figure 18 shows the cross section as a function of the cms energy around threshold for five different W mass values. These mass values are chosen 200 MeV apart and in the vicinity of the combined measurement from $p\bar{p}$ colliders. The curves are calculated with the program GENTLE,[23] which includes initial state radiative corrections and the finite width of the W. The best separation between the curves and hence the highest sensitivity for m_W is achieved for a cms energy of 161 GeV. The point with error bars indicates the statistical precision on m_W one experiment would have with 25 pb^{-1} luminosity and an average selection efficiency for W^+W^- final states of 50%.

6.1 Selection of W Pairs

The branching fractions of the W into hadrons and into each of the lepton generations has been measured at $p\bar{p}$ colliders to be[24]

$$BR(W \rightarrow q\bar{q}') = 67.9 \pm 1.5\%$$

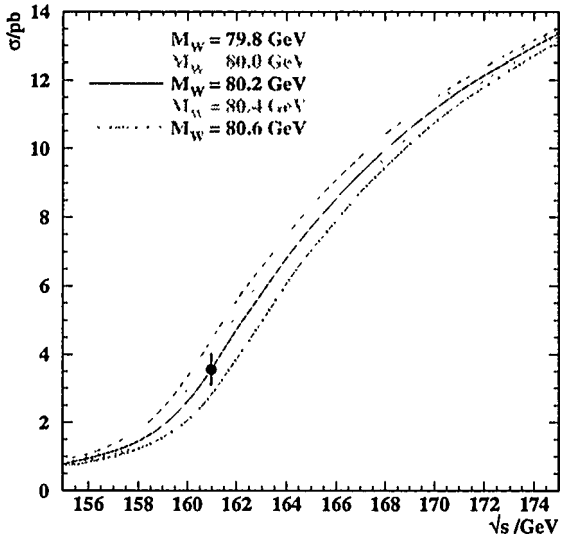


Figure 18: The cross section $e^+e^- \to W^+W^-$ in the threshold region for different W mass values. The point indicates the statistical precision obtainable with an integrated luminosity of 25 pb^{-1} and 50% selection efficiency.

$$BR(W \to \ell\nu) \;=\; 10.8 \pm 0.4\%, \qquad (10)$$

in agreement with the SM prediction. In the reaction $e^+e^- \to W^+W^-$, one distinguishes three event classes as observed in the detector which are listed in Table 5 with their relative fractions.

Events where both W bosons decay into quarks are selected as four-jet hadron events. To suppress four-jet background from $e^+e^- \to \gamma/Z \to$ *hadrons*, the jet-pair masses are required to be close to m_W. Usually, kinematic fits are performed to increase the resolution on the jet-pair mass. It should be noted that for $\sqrt{s} =$ 161 GeV, the total hadronic cross section is about 50 times larger than the cross section for W pair production.

The second event class is marked by the presence of two jets with a jet-pair mass of approximately m_W, an energetic charged lepton, and large missing energy due to the neutrino. To keep background from two-fermion production under control, events are retained only if the lepton is isolated from the jets. The decay

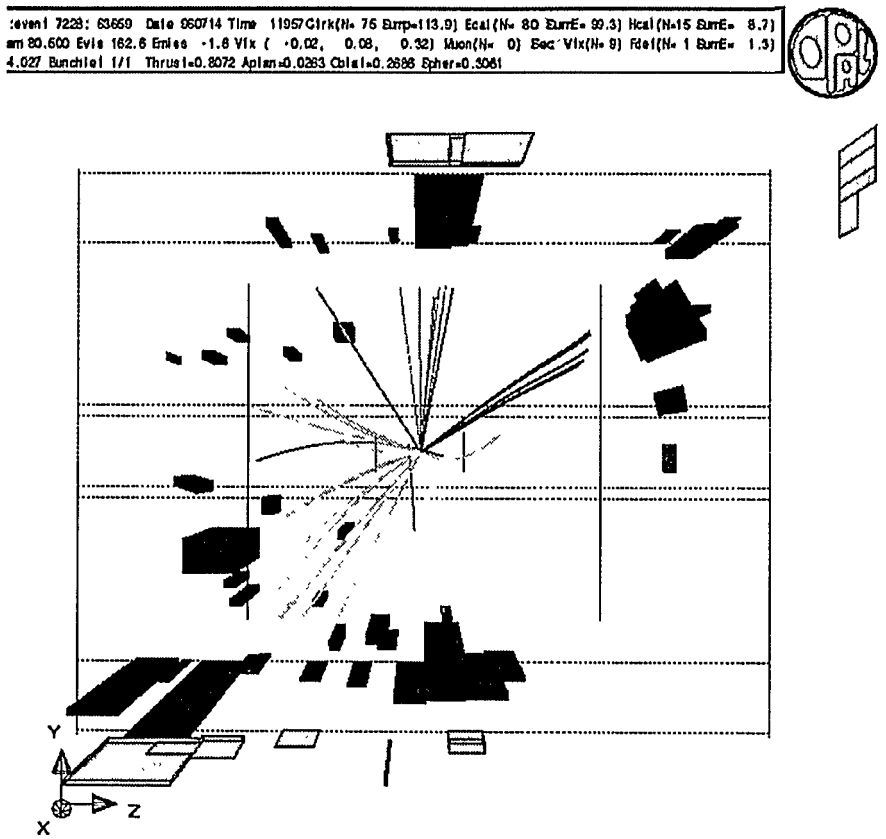


Figure 19: Candidate event $e^+e^- \to W^+W^- \to$ 4 jets observed in the OPAL detector.

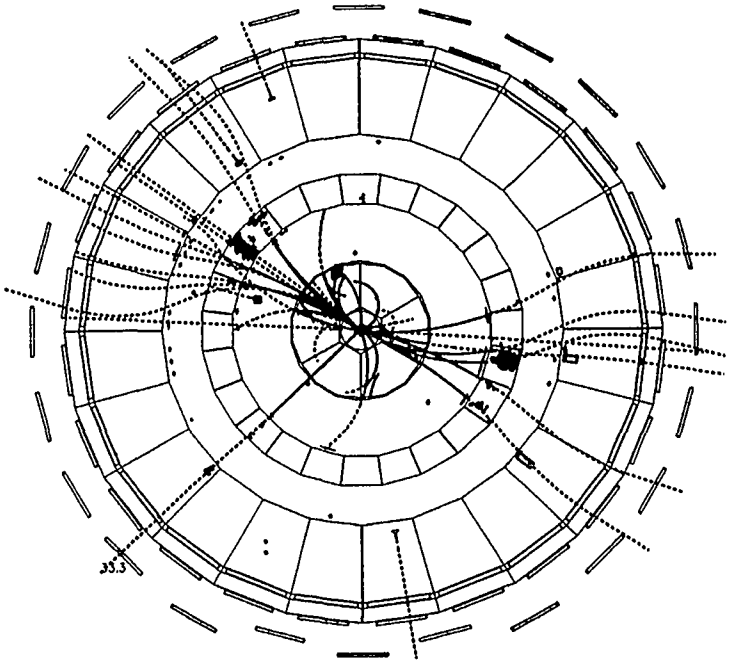


Figure 20: Candidate event $e^+e^- \to W^+W^- \to q\bar{q}'\,\mu^-\bar{\nu}_\mu$ observed in the DELPHI detector. The isolated high momentum track in the lower left part stems from the muon.

$W^+ \to \tau^+\nu_\tau$ can be identified by the hadronic decay of the τ lepton giving rise to a narrow jet containing one or three charged hadrons.

If both W bosons decay into leptons, two oppositely charged leptons are seen in the detector. The process $e^+e^- \to \ell^+\ell^-$ is suppressed by requiring missing energy and the two lepton candidates to be acoplanar.

Figures 19, 20, 21, and 22 show some examples of $e^+e^- \to W^+W^-$ events selected by the LEP Collaborations in the first part of the 1996 run at 161 GeV.

	Event class	Fraction
$e^+e^- \to W^+W^-$	$\to$ 4 jets	46%
	$\to \ell\nu + 2$ jets	44%
	$\to \ell\nu + \ell'\nu'$	10%

Table 5: Classes of W pair events as observed in the detectors and their relative abundance (ℓ = e, μ, τ).

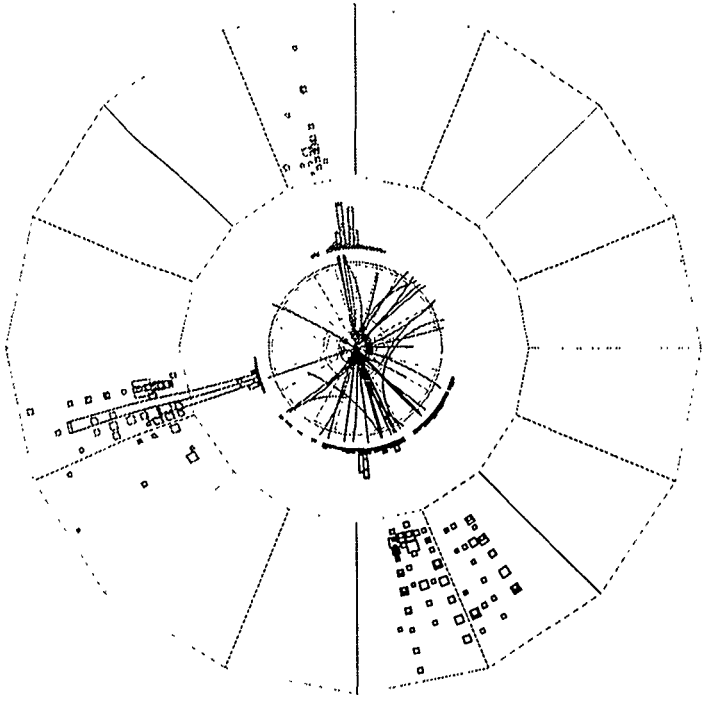


Figure 21: Candidate event $e^+e^- \to W^+W^- \to q\bar{q}'\,\tau^-\bar{\nu}_\mu$ observed in the L3 detector. The narrow jet containing one charged particle on the left side is interpreted as the tau lepton from W decay.

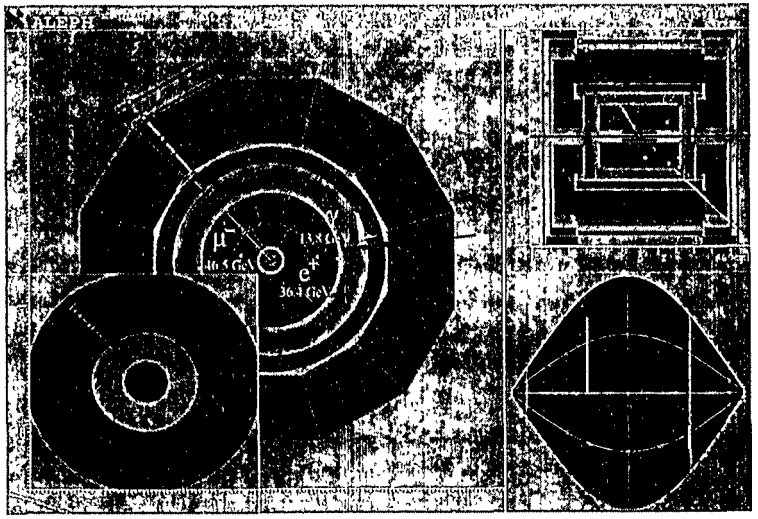


Figure 22: Candidate event $e^+e^- \to W^+W^- \to e^+\nu_e\,\mu^-\bar{\nu}_\mu$ observed in the ALEPH detector.

Experiment	$\int \mathcal{L}\,dt$ [pb^{-1}]	σ_{WW} [pb]
ALEPH	3	$4.9^{+1.9}_{-1.6}$
DELPHI	5	$3.5^{+1.5}_{-1.3}$
L3	6	$2.9^{+1.3}_{-1.1}$
OPAL	3	$3.9^{+1.8}_{-1.4}$

Table 6: Integrated luminosity analyzed by the time of the conference and results on the $e^+e^- \to W^+W^-$ cross section as obtained by the LEP experiments.

6.2 First Results on $e^+e^- \to W^+W^-$ Cross Section

Preliminary results on the W pair cross section at the threshold obtained by the LEP experiment using the first part of the 1996 data are summarized in Table 6. The luminosity analyzed so far corresponds to 5–10 events seen by each experiment. These results can be combined to an average value of[25]

$$\sigma_{WW} = 3.6 \pm 0.7 \qquad \text{at } \sqrt{s} = 161.3 \pm 0.2 \text{ GeV}. \tag{11}$$

It should be noted that the total luminosity collected by the four LEP experiments during the summer of 1996 is about 11 pb^{-1} per experiment, such that very soon more precise measurements of the $e^+e^- \to W^+W^-$ cross section at 161 GeV will be available.

6.3 W Mass Determined from Threshold Cross Section

The LEP average on the W pair cross section [Eq. (11)] can be converted into a value of the W mass. This method intrinsically implies the validity of the SM, in particular, the couplings at the three-boson vertex. Figure 23 shows the $e^+e^- \to W^+W^-$ cross section as a function of m_W for the average LEP cms energy of $\sqrt{s} = 161.3$ GeV. From the curve, one reads the preliminary LEP result on m_W (Ref. 25)

$$m_W = 80.4 \pm 0.3 \pm 0.1 \text{ (LEP) GeV}. \tag{12}$$

The second error represents the current precision on the knowledge of the LEP beam energy as obtained from preliminary magnet calibrations.[26] Both errors are expected to be reduced in near future.

The result presented in Eq. (12) is in good agreement with the measurement of m_W from Fermilab[27] and the mass value that can be inferred from the precise

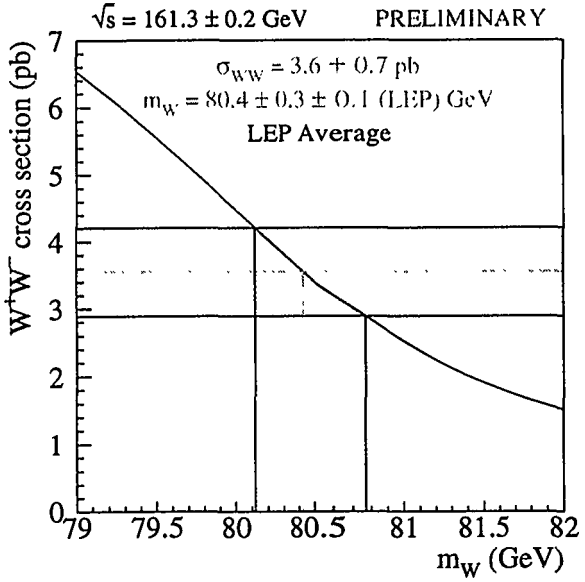


Figure 23: The cross section $e^+e^- \to W^+W^-$ as a function of the W mass for $\sqrt{s} = 161.3$ GeV calculated with GENTLE.[23] The band shows the combined LEP result [Eq. (11)] and the derived W mass.

measurements of electroweak radiative corrections at LEP I and SLC[16]:

$$\begin{aligned} m_W &= 80.37 \pm 0.15 \text{ GeV} \quad \text{Fermilab} \\ m_W &= 80.36 \pm 0.05 \text{ GeV} \quad \text{LEP I \& SLC.} \end{aligned} \tag{13}$$

7 Search for Supersymmetry

The search for new particles predicted by Supersymmetry[28] (SUSY) has been carried out by the LEP experiments at the Z resonance. No experimental evidence for SUSY has been found, and limits on particle masses and model parameters are set.[24] For most of the presumed SUSY particles, the kinematic range accessible has been explored at LEP I, and further improvements cannot be expected from more luminosity at $\sqrt{s} = m_Z$ (Ref. 29).

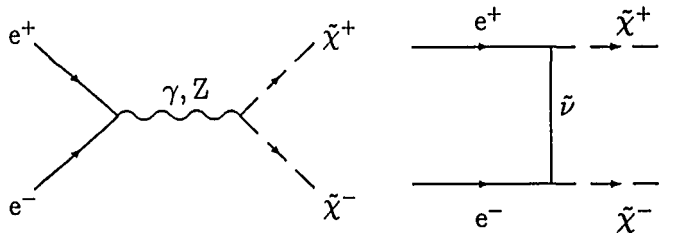


Figure 24: Feynman diagrams contributing to SUSY chargino pair production.

High cross sections on the order of several picobarns are expected for a wide range of SUSY parameter space in the kinematically accessible region at LEP 1.5 and in the 1996 run at 161 GeV, in particular, for chargino pair production $e^+e^- \to \tilde{\chi}^+\tilde{\chi}^-$. This very fact was one of the motivations for a short run at 130–140 GeV at the end of 1995 because already with a modest integrated luminosity of several inverse picobarns, the chargino could be discovered if it existed or else the saturated LEP I limits could be improved.

Here some results on SUSY searches in the framework of the Minimal Supersymmetric Model (MSSM) are presented. Searches for charginos and neutralinos at LEP 1.5 are published in Refs. 30–35.

The free parameters of the MSSM are the gaugino mass at the weak scale M_2, the mass scale of the scalar partners of the fermions m_0, and the mixing parameter of the two Higgs field doublets μ and $\tan\beta$ which is the ratio of the vacuum expectation values associated to the neutral Higgs bosons (h and A). Values around $\tan\beta = 1.5$ and 35 are favored by cosmological arguments.

7.1 Chargino Search

Pair production of charginos, the superposition of the fermionic W partners (winos) and the charged Higgs (higgsino), in e^+e^- collisions as predicted by the MSSM is depicted in Fig. 24. Two diagrams contribute: s-channel boson exchange and t-channel exchange of a sneutrino, $\tilde{\nu}$, the massive supersymmetric partner of the neutrino. For most of the parameter space usually considered, these two diagrams interfere destructively such that predicted cross sections are generally higher if a large mass for the sneutrino is assumed.[36]

Expected cross sections at LEP 1.5 energies for chargino pair production as a function of the chargino mass are shown in Fig. 25 (Ref. 32). The two plots correspond to a very high sneutrino mass and to a light $\tilde{\nu}$ compatible with the lower bounds obtained at LEP I. The parameters of the MSSM are varied in the range $0 < M_2 < 800$ GeV, $-400 < \mu < 400$ GeV and $\tan\beta = 1,\ 1.5,\ 35$. In addition, the chargino is assumed to be at least 10 GeV heavier than the neutralino. Under these assumptions, cross sections in the $\mathcal{O}$(pb) are expected (Fig. 25) and a luminosity of a few inverse picobarns at high energy would allow the discovery of the chargino or pushing the mass limits beyond the LEP I range.

The chargino is assumed to decay via W radiation into a neutralino, $\tilde{\chi}_1^0$, the lightest SUSY particle, which interacts only weakly and hence escapes the detector undetected (Fig. 26). The signature of chargino production is thus missing energy from the $\tilde{\chi}_1^0$, and eventually the neutrino from the W decay, and the decay products of the two W's: an acoplanar lepton pair, two jets, and an isolated lepton or acoplanar jets with missing energy.

In addition to the background at lower energies, fermion pair production and two-photon collisions, new important background sources for SUSY searches play a role at $\sqrt{s} = 161$ GeV. W pairs with one of the bosons decaying leptonically have similar signatures as charginos. Also, single W production, as depicted in Fig. 27, with the electron escaping through the beam pipe can fake the SUSY signature. Figure 28 shows one candidate found by L3 in the search for SUSY at 161 GeV, which can be explained in the SM by single W production. For a total luminosity of 5.5 pb^{-1} analyzed at the time of the conference, this was the only candidate event found with 1.9 background events from SM processes expected. The new background sources require more stringent experimental cuts and hence reduce efficiency for the SUSY signal.

The data between 130 and 161 GeV show no evidence for SUSY. The results can be converted into experimental upper limits on cross sections. As an example, Fig. 29 shows the experimental upper limit on the cross section $e^+e^- \to \tilde{\chi}^+\tilde{\chi}^-$ at 161 GeV obtained by ALEPH. The plot shows the range of $\tilde{\chi}^\pm$ masses not explored at LEP I. The results of LEP 1.5 are included in the plot by applying appropriate phase space factors. The shaded area is excluded kinematically and by requiring that the neutralino is lighter than the chargino.

A low cross section ($\sigma_{\tilde{\chi}^+\tilde{\chi}^-} \leq 0.7$ pb) is excluded in the region $m_{\tilde{\chi}^\pm} \approx 50$ GeV and $m_{\tilde{\chi}^0} \approx 20$ GeV where the kinematic conditions are favorable providing high

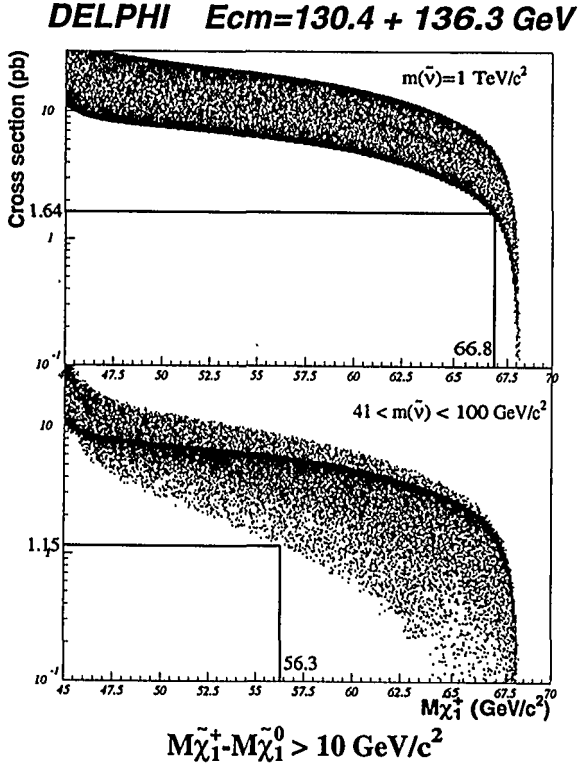


Figure 25: Expected cross sections for chargino pair production as a function of the chargino mass.[32]

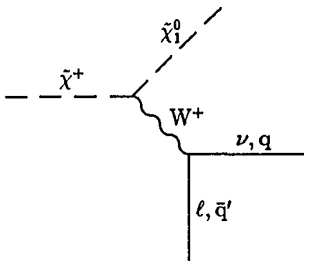


Figure 26: Chargino decay into the lightest neutralino and a W boson.

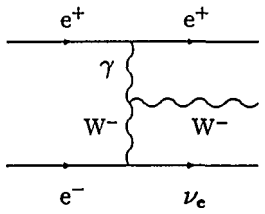


Figure 27: Single W production $e^+e^- \rightarrow W^-e^+\nu_e$ at LEP II.

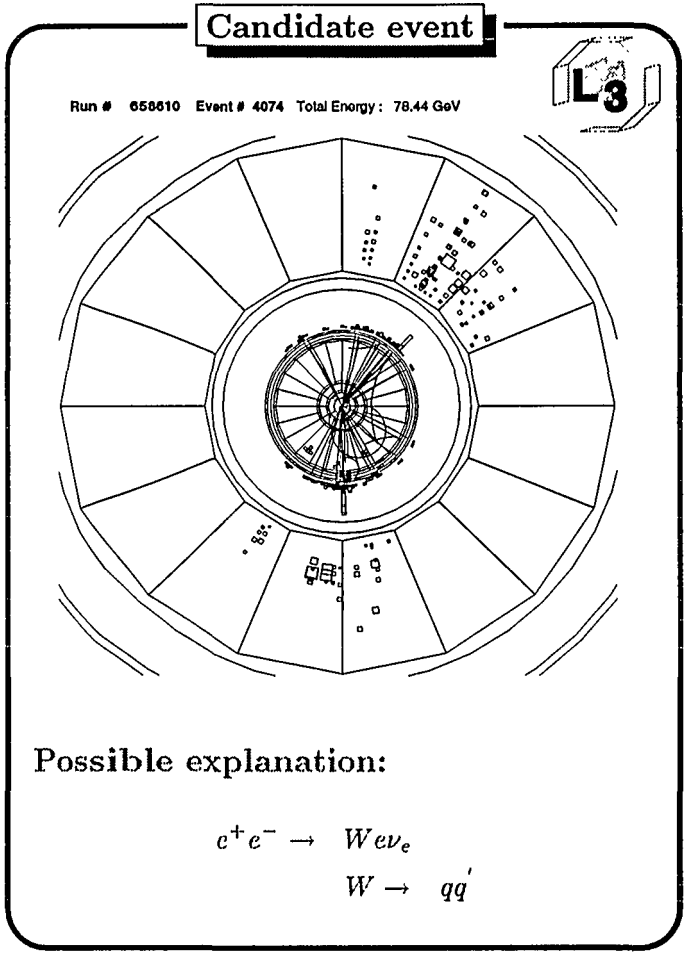


Figure 28: Two-jet hadronic event with missing energy observed by L3 at $\sqrt{s} =$ 161 GeV. The SM explanation for this event is single W production with the electron escaping detection through the beam pipe (Fig. 27).

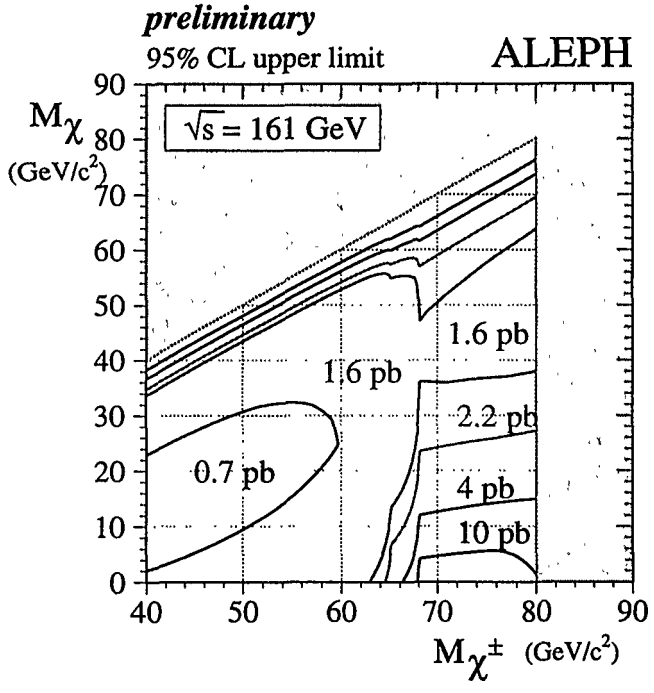


Figure 29: Experimental upper limits (95% C.L.) on the cross section $e^+e^- \to \tilde{\chi}^+\tilde{\chi}^-$ at $\sqrt{s} = 161$ GeV in the mass plane of the chargino and the lightest neutralino, here denoted χ, obtained by ALEPH. The shaded area is kinematically inaccessible and the remaining area is subdivided into five regions with different experimental upper cross-section limits.

detection efficiency and good background suppression. Limits on the cross section become worse as the neutralino mass approaches the mass of the chargino because the visible energy in the detector becomes lower and thus reduces the detection efficiency. Also, background from two photon processes is larger there. Similarly, if the mass difference between the chargino and neutralino becomes large, the missing energy is reduced and chargino events resemble more and more ordinary fermion pairs. This makes background suppression difficult, and consequently, only higher cross sections can be excluded.

This way of presenting search results is less model dependent as it makes only assumptions about the decay of SUSY particles, e.g., the chargino decay in Fig. 26, which is needed for the calculation of detection efficiencies. For the interpretation in terms of limits on SUSY parameters, like the chargino mass, one calculates chargino pair cross sections for different sets of SUSY parameters and compares them to the experimental cross section limit as shown in Fig. 29. The exclusion limit on the chargino mass is only valid in the range of SUSY parameters considered. Figure 30 shows the exclusion in the $m_{\tilde{\chi}^\pm} - m_{\tilde{\chi}^0}$ plane obtained by DELPHI at LEP 1.5 using the calculated cross sections shown in Fig. 25 and the parameter space considered there. With the assumption of a heavy sneutrino, chargino masses close to the kinematic limit can be ruled out.

7.2 Neutralino Search

The MSSM predicts the existence of four weakly interacting neutralinos $\tilde{\chi}_i^0$ with the index i ordering them by mass. Assuming R parity conservation and following cosmological arguments, the lightest neutralino, $\tilde{\chi}_1^0$, must be stable and invisible.

The production of a pair of kinematically allowed, but not necessarily identical, neutralinos in e^+e^- annihilation is depicted in Fig. 31. The decay of a heavier neutralino into $\tilde{\chi}_1^0$ proceeds by radiation of a Z and thus gives rise to missing energy and a pair of jets or leptons (Fig. 32). The decay through photon radiation is also possible and has been searched for.[34]

The nonobservation of a signal can be expressed in terms of cross-section limits on neutralino production. Similar to Fig. 29, the experimental upper limit of the cross section $e^+e^- \to \tilde{\chi}_2^0\tilde{\chi}_1^0$ at $\sqrt{s} = 161$ GeV as a function of the masses of the two lightest neutralinos is shown in Fig. 33.

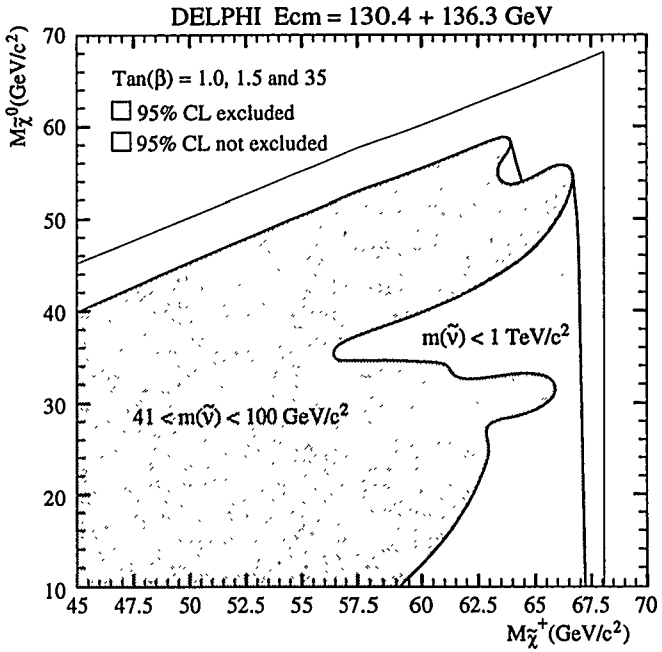


Figure 30: Limits set by DELPHI on the chargino mass from LEP 1.5 shown in the $m_{\tilde{\chi}^\pm} - m_{\tilde{\chi}^0}$ plane.[32]

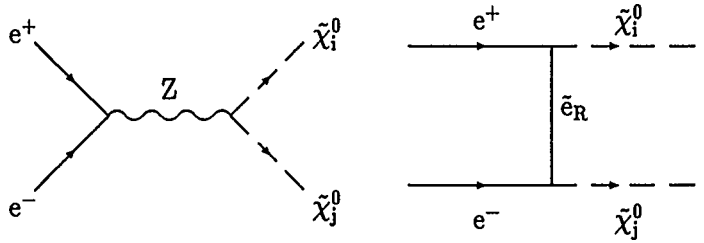


Figure 31: Feynman diagrams contributing to SUSY neutralino pair production.

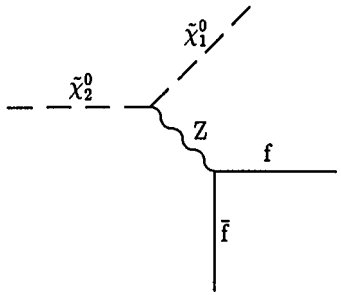


Figure 32: Decay of the second lightest into the lightest neutralino by radiating a Z boson.

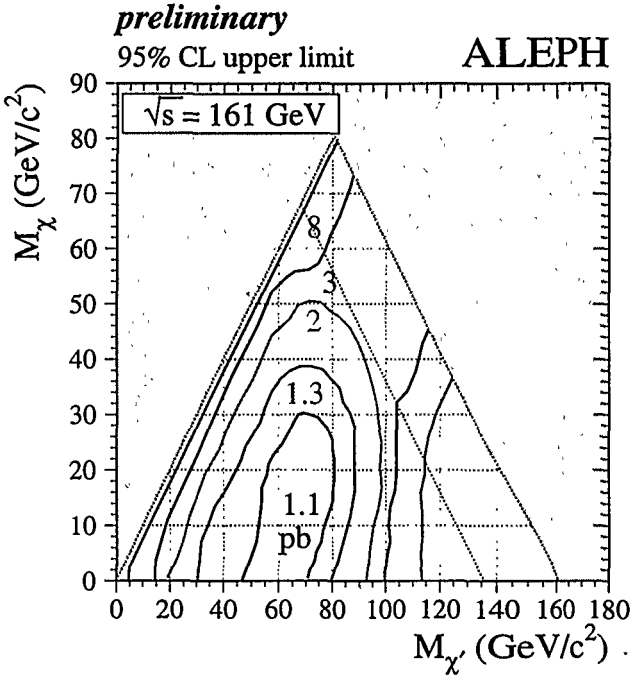


Figure 33: Same as Fig. 29 for the cross section $e^+e^- \to \tilde{\chi}_2^0 \tilde{\chi}_1^0$ (here labeled χ' and χ).

Again interpretation in terms of SUSY parameters requires more assumptions about the model. The cross section limits on neutralino pair production can be interpreted in terms of mass limits for the right-handed supersymmetric partner of the electron, $\tilde{e}_R$. Figure 34 shows the L3 result from LEP 1.5 assuming MSSM parameters in the range $0 < M_2 < 200$ GeV, $-200 < \mu < 200$ GeV, and $\tan\beta = 1$. The high-energy data enlarge the excluded region in the $m_{\tilde{e}_R} - m_{\tilde{\chi}_1^0}$ plane as compared to the limits obtained at LEP I owing to the relatively high sensitivity due to the t-channel contribution to neutralino pair production (Fig. 31).

For the other bosonic partners of the SM fermions, the LEP I limits are not improved. From a combined analysis of the data taken at the Z resonance and at 130–140 GeV, the ALEPH Collaboration sets a lower mass limit for the lightest neutralino $m_{\tilde{\chi}_1^0} > 12.8$ GeV (Ref. 31).

The results on SUSY searches are often presented in an exclusion plot for the μ and M_2 parameters. Figure 35 shows the result obtained by OPAL using about 3 pb^{-1} at 161 GeV and including those regions already excluded at LEP I and LEP 1.5. The two plots are obtained assuming two different values for $\tan\beta$ and the mass scale for the scalar partners of the fermions to be $m_0 = 1$ TeV.

8 Four-Jet Events at $\sqrt{s} \geq 130$ GeV

A detailed study of four-jet hadronic events at LEP 1.5 has been reported by the ALEPH Collaboration.[37] From selected four-jet events, the invariant masses of jet pairs are computed, and out of the three jet combinations, the one with the lowest difference in jet-pair masses is retained. The distribution of the sum of these two jet-pair masses is shown in Fig. 36. Not only is the total number of four-jet events observed by ALEPH at 130–140 GeV larger than expected from QCD, but this excess is contained in a narrow window around 105 GeV for the sum of the jet-pair masses. In this window, about two times the width of the estimated resolution, nine events are observed with only 0.8 events expected from QCD. Detailed discussion of this observation can be found in Ref. 37.

Similar analyses have been performed by the other three LEP experiments on their LEP 1.5 data, and all find agreement with the QCD expectation.[38,35] No anomaly either in the total four-jet rate nor in the jet-pair mass distribution is seen by any of the other experiments. Combining the four LEP experiments, one obtains the distribution shown in Fig. 37 (Ref. 39). However, with the limited

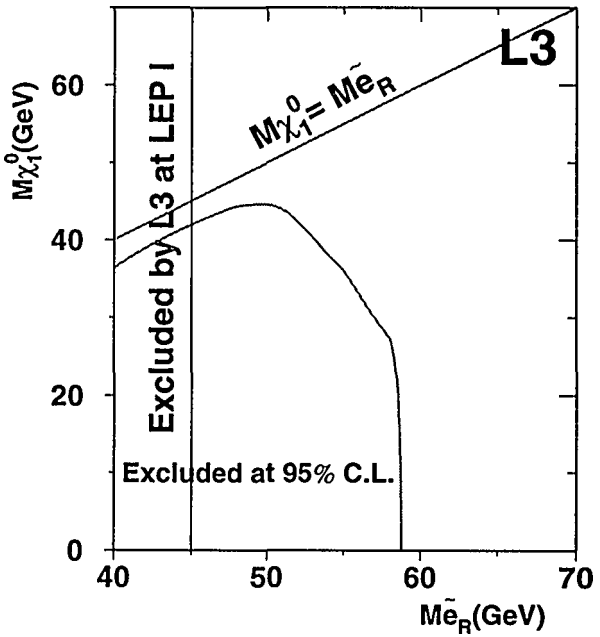


Figure 34: Mass limit for the right-handed supersymmetric partner of the electron in the $m_{\tilde{e}_R} - m_{\tilde{\chi}_1^0}$ plane obtained at LEP 1.5 as compared to the LEP I result.

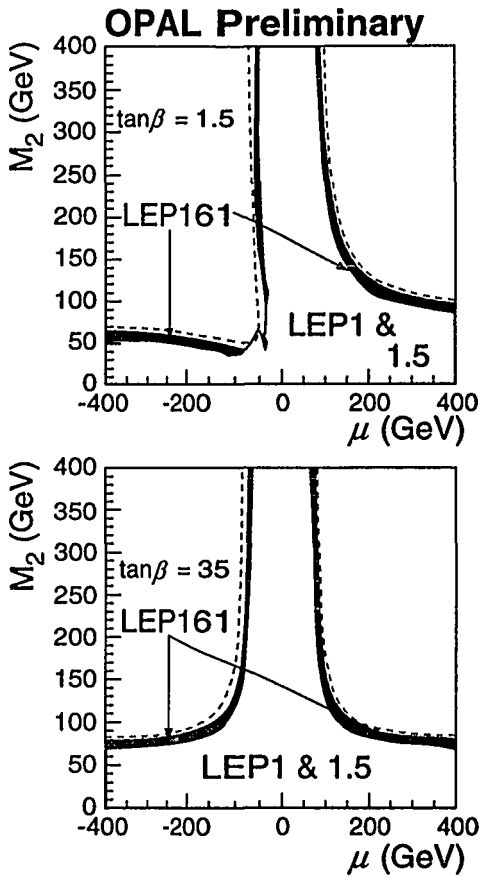


Figure 35: Exclusion (95% C.L.) of SUSY parameters μ and M_2 for two different values of $\tan\beta$ and for $m_0 = 1$ TeV from OPAL. The limits obtained from 161 GeV are compared to the combined limits from LEP I and LEP 1.5. The broken lines indicate the kinematic limit at 161 GeV for chargino pair production.

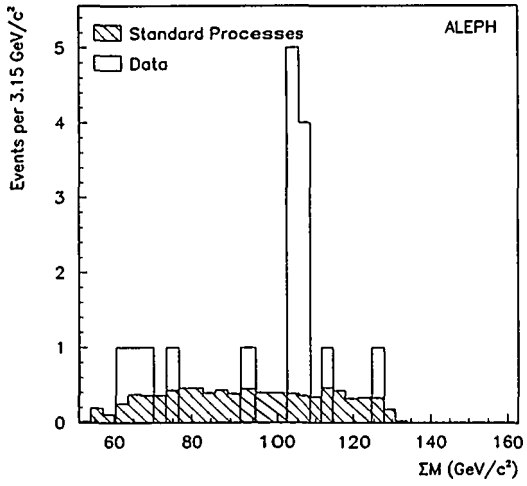


Figure 36: Sum of jet-pair masses in four-jet hadronic events as observed by ALEPH for cms energies of 130–140 GeV.

statistics, a possible signal cannot be ruled out. By averaging the four experiments, a cross section for four-jet events with the sum of the jet-pair mass equaling 105 GeV can be derived[39]:

$$\sigma(\Sigma\, m_{ij} = 105 \text{ GeV}) = 1.2 \pm 0.4 \text{ pb}. \qquad (14)$$

Neutral SUSY Higgs boson production $e^+e^- \to h\,A$ is not likely to explain the surplus of four-jet events at $\sum m_{ij} = 105$ GeV, as the expected cross section is much lower and there is no evidence for b-quark enrichment in the nine ALEPH events. The latter argument would not apply for charged SUSY Higgs boson $e^+e^- \to H^+H^- \to c\bar{s}\,\bar{c}s$, but in this case, $c\bar{s}\,\tau^-\bar{\nu}_\tau$ final states should also be observed. Clarification of the ALEPH observation is expected from more luminosity at energies $\sqrt{s} \geq 130$ GeV. The first results reported from the 161 GeV run are in agreement with the SM expectation.[39]

9 Studies of Photon Final States

Every time a new energy domain is experimentally accessible, studies of events with hard photons draw much attention since many extensions of the SM predict significant additional sources of photon production. Compositeness of SM particles is just one example. The studies of single and multiphoton final states at LEP 1.5 are described in Refs. 40–43.

Single-photon final states have been used at LEP I to determine the number of light neutrino generations (Fig. 38). At energies above the Z pole, the energy spectrum of the observed photon is very much different since the return to the Z gives rise to very energetic photons. Figure 39 shows the spectrum measured by the L3 experiment at 161 GeV. One clearly sees the peak at $E_\gamma = 55$ GeV which is just the energy of the ISR photon which leaves $\sqrt{s'} = m_Z$ for the annihilating e^+e^- system. The rate and the energy distribution of the single photon events are in good agreement with the SM expectation.

Two-photon final states in the reaction $e^+e^- \to \gamma\gamma$ are mediated by t-channel exchange of an electron. The reaction can be used to test the point-like structure of electrons because the existence of an excited electron, e^*, would lead to a different angular distribution of the photons. Deviations from QED are parametrized by

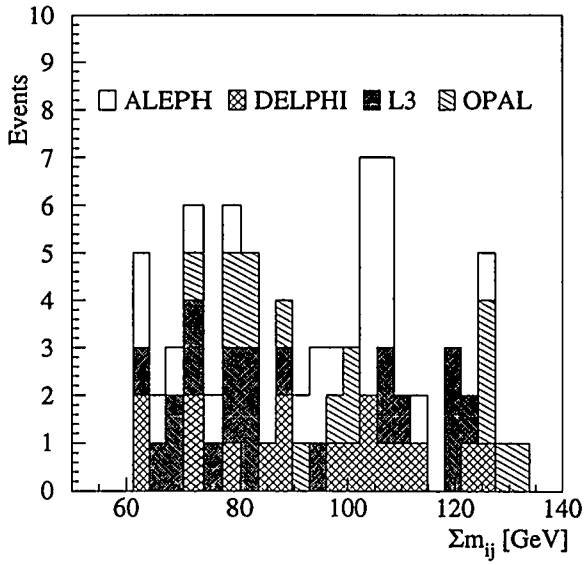


Figure 37: Distribution of the sum of jet-pair masses in four-jet hadronic events as observed by the four LEP experiments at cms energies of 130–140 GeV.

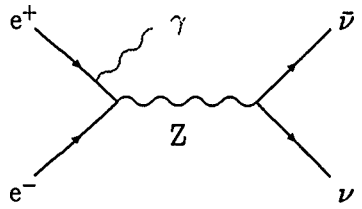


Figure 38: Feynman diagram contributing to the single photon reaction in the SM.

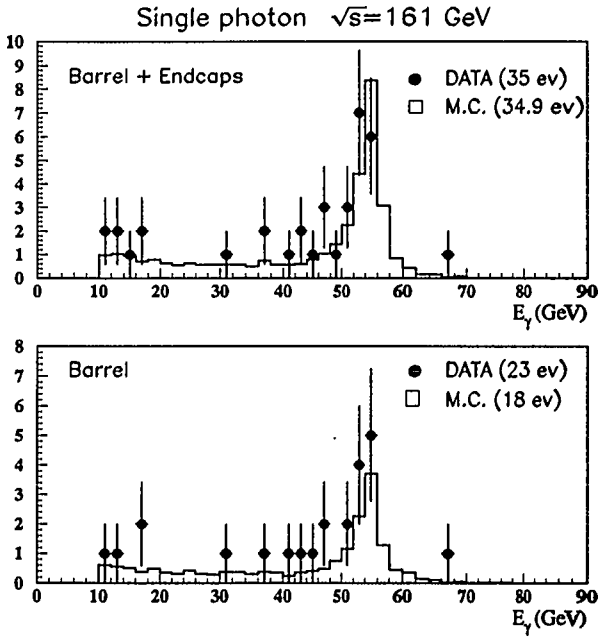


Figure 39: Spectrum of single photon events observed by L3 at $\sqrt{s} = 161$ GeV. The top plot shows the total sample and the bottom plot the events at large polar angles ($44° \leq \Theta \leq 136°$). The points are the data, and the histograms show the SM expectations.

two cutoff parameters $\Lambda_\pm$

$$\frac{d\sigma}{d\Omega} = \left(\frac{d\sigma}{d\Omega}\right)_{QED} \left(1 \pm \frac{s^2}{2\Lambda_\pm^4}\left(1 - \cos^2\Theta^*\right)\right), \qquad (15)$$

with Θ^* being the scattering angle in the two-photon rest frame. As an example, Fig. 40 shows the result obtained by ALEPH at LEP 1.5. The plot shows the ratio of measured to QED differential cross section as a function of the scattering angle. Good agreement is observed, and 95% C.L. limits of the cutoff parameters of 132 and 169 GeV, respectively, are derived.

No deviation from QED in this reaction has yet been reported from the data at $\sqrt{s} = 161$ GeV which would allow us to further increase the limits on $\Lambda_\pm$ by about 30 GeV.

10 Search for Excited and Heavy Leptons

The LEP experiments have searched for excited states of the known fundamental charged and neutral leptons, e^*, μ^*, τ^*, and ν^*. Excited leptons can be produced either in pairs ($e^+e^- \to \ell^*\ell^*$) or singly ($e^+e^- \to \ell\ell^*$). As the excited leptons are thought to decay radiatively into their ground states, their existence would lead to anomalies in the observed $\ell^+\ell^-\gamma$ and $\ell^+\ell^-\gamma\gamma$ final states. If produced in pairs, the expected cross section is, apart from kinematic suppression, assumed to be the same as for ordinary lepton pairs. Therefore, excited leptons can be excluded up to the kinematic limit of $m_{\ell^*} \approx E_b$ with a relatively small luminosity. In principle, exclusion up to $m_{\ell^*} \approx \sqrt{s}$ can be achieved from single ℓ^* production. This, however, depends on assumptions about coupling constants.

The decay of excited leptons through Z and W radiation has also been investigated. Details of the analysis at LEP 1.5 can be found in Refs. 44–47. As an example, the excluded mass of a charged excited lepton as a function of the coupling parameter λ is shown in Fig. 41 as obtained at LEP 1.5 by ALEPH.

The precision measurements of Z parameters at LEP have shown that there are only the three fermion generations with light neutrinos ($m_\nu < m_Z/2$). However, there still could exist a fourth generation with all fermions being heavy. Searches for neutral (L^0) and charged ($L^\pm$) heavy leptons are performed at LEP. These particles are assumed to be produced in pairs, and they decay through W radiation into known fermions: $L^0 \to \ell^\pm W^\mp$ and $L^\pm \to \nu_L W^\pm$. No sign for these new

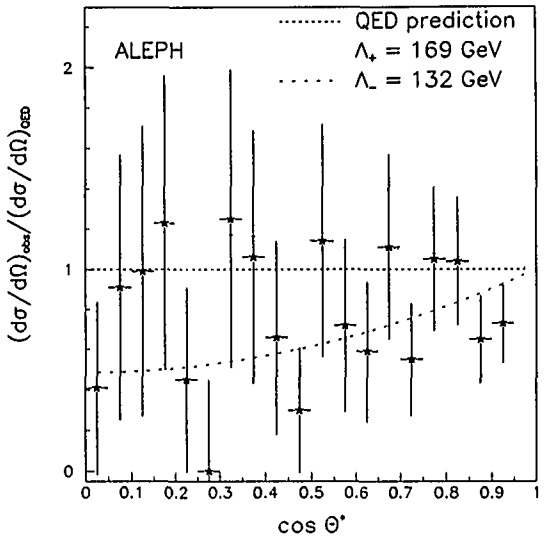


Figure 40: Ratio of the experimental and QED expected differential cross section of the reaction $e^+e^- \to \gamma\gamma$ as measured by ALEPH at cms energies between 130 and 140 GeV (Ref. 40). The two lines show the maximum deviation experimentally allowed according to the parameterization of Eq. (15) from which limits for $\Lambda_\pm$ are derived.

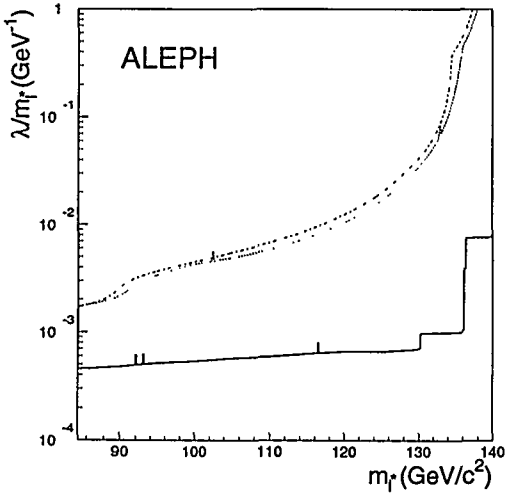


Figure 41: Exclusion limits (95% C.L.) in the mass-coupling plane for singly produced charged leptons ℓ^* as obtained by ALEPH at LEP 1.5. The solid, dotted, and dot-dashed lines are for e^*, μ^*, and τ^*, respectively.[44]

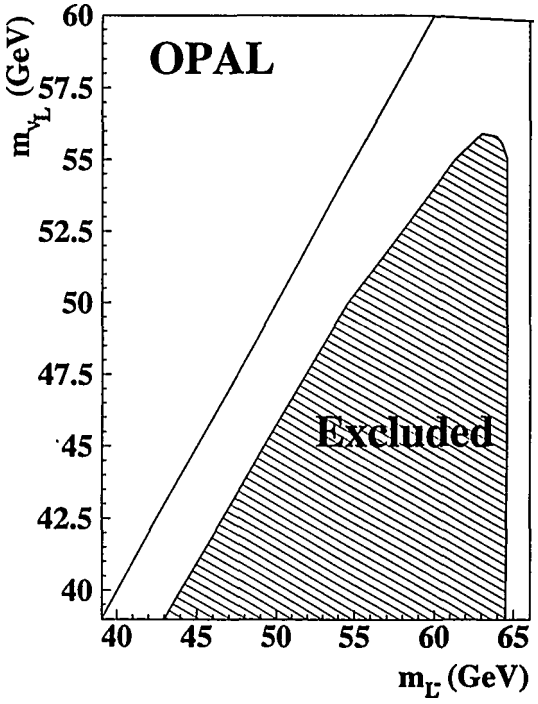


Figure 42: The excluded region (95% C.L.) in the mass plane of the charged and neutral heavy lepton. The neutral heavy lepton ν_L is assumed to be stable.

particles has been observed so far. Details can be found in Refs. 48–50. Figure 42 shows the result of OPAL at LEP 1.5 in the mass plane of the charged and neutral heavy lepton.

11 Conclusions

The second phase of the LEP program has started in October 1995 with cms energies of 130–140 GeV, and it continued in June 1996 at $\sqrt{s} = 161$ GeV at the $e^+e^- \to W^+W^-$ threshold. The energy upgrade was successful, and good luminosity and background conditions were provided to the experiments.

From the measured cross section at the threshold using the first part of the 161 GeV data, the LEP experiments determine the mass of the W boson to be

$$m_W = 80.4 \pm 0.3 \pm 0.1(\text{LEP}) \text{ GeV},$$

in excellent agreement with the value measured at $p\bar{p}$ colliders and the mass derived from precise measurement of electroweak corrections at the Z pole.

For the first time, fermion pair production in e^+e^- annihilation has been studied above the Z resonance. This provides a much improved determination of the γZ interference as compared to the LEP I data.

The search for new physics has been extended into a new energy regime. No sign of Supersymmetry has been observed at LEP, and lower mass limits have been improved, in particular, for the chargino.

The Standard Model of electroweak and strong interactions is confirmed up to an energy of 161 GeV.

The energy of LEP will be further increased in steps up to $\sqrt{s} = 192$ GeV with the goal of collecting 500 pb^{-1} per experiment, which will allow us the determination of W parameters and to extend the search for new particles, in particular for the Higgs boson up to $m_H \approx 100$ GeV.

Acknowledgments

I would like to thank my colleagues from the LEP experiments for providing preliminary results from the recent run. In particular, I am grateful to A. Blondel, D. Charlton, R. Faccini, M. Grünewald, S. Mele, C. Paus, M. Schmitt, U. Uwer, and G. Wilkinson for their help in preparing my talk. I thank A. Böhm and S. Wynhoff for the careful reading of the manuscript.

References

[1] S. Myers, "Conclusions of the Sixth LEP Performance Workshop," preprint CERN-SL-96-06-DI, CERN, 1996.

[2] C. Wyss, "Status of LEP2," presentation at the LEPC meeting, May 1996, CERN.

[3] T. Sjöstrand, Comp. Phys. Comm. **39**, 347 (1986);
T. Sjöstrand and M. Bengtsson, Comp. Phys. Comm. **43**, 367 (1987);
T. Sjöstrand, *PYTHIA 5.6 JETSET 7.3 Physics and Manual,* preprint CERN-TH 6488/92, CERN (1992).

[4] S. Jadach, B. F. L. Ward, and Z. Wąs, Comp. Phys. Comm. **66**, 276 (1991).

[5] ALEPH Collaboration, D. Buskulic *et al.*, Phys. Lett. B **378**, 373 (1996).

[6] DELPHI Collaboration, M. Bigi *et al.*, contributed paper to the XXVIII International Conference on High Energy Physics, Warsaw, 1996, ICHEP'96, Ref. pa07-001.

[7] L3 Collaboration, M. Acciarri *et al.*, Phys. Lett. B **370**, 195 (1996).

[8] OPAL Collaboration, G. Alexander *et al.*, Phys. Lett. B **376**, 232 (1996).

[9] U. Uwer, talk given at the XXVIII International Conference on High Energy Physics, Warsaw, 1996, to appear in the proceedings.

[10] D. Bardin *et al.*, *FORTRAN Package ZFITTER*, preprint CERN-TH 6443/92;
D. Bardin *et al.*, Z. Phys. C **44**, 493 (1989); D. Bardin *et al.*, Nucl. Phys. B **351**, 1 (1991); D. Bardin *et al.*, Phys. Lett. B **255**, 290 (1991).

[11] J. Mnich, Phys. Rep. **271**, 181 (1996).

[12] L3 Collaboration, M. Acciarri *et al.*, Phys. Lett. B **374**, 331 (1996).

[13] A. Leike, T. Riemann, and J. Rose, Phys. Lett. B **273**, 513 (1991); T. Riemann, Phys. Lett. B **293**, 451 (1992).

[14] TOPAZ Collaboration, K. Miyabayashi *et al.*, Phys. Lett. B **347**, 171 (1995).

[15] The LEP Electroweak Working Group, "An investigation of the interference between photon and Z-boson exchange," internal note; see also presentations at the XXVIII International Conference on High Energy Physics, Warsaw, 1996.

[16] The LEP Electroweak Working Group, "A combination of preliminary LEP and SLD electroweak measurements and constraints on the Standard Model," CERN PPE preprint in preparation.

[17] ALEPH Collaboration, D. Buskulic *et al.*, "Studies of QCD in $e^+e^- \to Hadrons$ at E_{cm} = 130 and 136 GeV," preprint CERN-PPE/96-043, CERN, 1996, preprint CERN-PPE/96-05, CERN, 1996, submitted to Phys. Lett. B.

[18] P. Abreu *et al.*, "Charged particle multiplicity in e^+e^- interactions at $\sqrt{s}$ = 130 GeV," preprint CERN-PPE/96-05, CERN, 1996, submitted to Phys. Lett. B.

[19] L3 Collaboration, M. Acciarri *et al.*, Phys. Lett. B **371**, 137 (1996).

[20] OPAL Collaboration, G. Alexander *et al.*, "QCD studies with e^+e^- annihilation data at 130 and 136 GeV," preprint CERN-PPE/96-047, CERN, 1996, submitted to Z. Phys.

[21] T. Sjöstrand, *PYTHIA 5.6 JETSET 7.3 Physics and Manual*, CERN-TH 7112/93, CERN (1993), revised August 1995; T. Sjöstrand, Comp. Phys. Comm. **82**, 74 (1994).

[22] G. Gounaris, J. L. Kneur, and D. Zeppenfeld, "Triple gauge boson couplings," in *Physics at LEP2*, CERN 96-01, Vol. 2, edited by G. Altarelli, T. Sjöstrand, and F. Zwirner.

[23] D. Bardin, D. Lehner, A. Leike, and A. Olchevski, "GENTLE/4fan" in *Physics at LEP2*, CERN 96-01, Vol. 2, edited by G. Altarelli, T. Sjöstrand, and F. Zwirner.

[24] Particle Data Group, "Review of Particle Properties," Phys. Rev. D **54**, 1 (1996).

[25] The LEP Electroweak W Mass Working Group, "Updated LEP WW cross-sections and W mass for DPF96," internal note, CERN, 1996; see also presentations at XXVIII International Conference on High Energy Physics, Warsaw, 1996, and at DPF96, Minneapolis, 1996.

[26] The Working Group on LEP Energy Calibration (private communication).

[27] C. Klopfenstein, these proceedings.

[28] P. Fayet, Phys. Lett. B **64**, 159 (1976); P. Fayet, Phys. Lett. B **69**, 489 (1977); P. Fayet and S. Ferrara, Phys. Rep. C **32**, 249 (1977); H. P. Nilles, Phys. Rep. **110**, 1 (1984); H. Haber and G. Kane, Phys. Rep. **117**, 75 (1985).

[29] S. Mele, talk given at the XXVIII International Conference on High Energy Physics, Warsaw, 1996, to appear in the proceedings.

[30] ALEPH Collaboration, D. Buskulic *et al.*, Phys. Lett. B **373**, 246 (1996).

[31] ALEPH Collaboration, D. Buskulic *et al.*, "Mass limit for the lightest neutralino," preprint CERN-PPE/96-083, CERN, 1996, submitted to Z. Phys.

[32] DELPHI Collaboration, P. Abreu *et al.*, "Search for the lightest chargino at $\sqrt{s}$ = 130 and 136 GeV," preprint CERN-PPE/96-75, CERN, 1996, submitted to Phys. Lett. B.

[33] L3 Collaboration, M. Acciarri *et al.*, "Search for Supersymmetric Particles at 130 GeV < $\sqrt{s}$ < 140 GeV at LEP," preprint CERN-PPE/96-29, CERN, 1996, submitted to Phys. Lett.

[34] OPAL Collaboration, G. Alexander *et al.*, Phys. Lett. B **377**, 181 (1996).

[35] OPAL Collaboration, G. Alexander *et al.*, "Searches for supersymmetric particles and anomalous four-jet production at $\sqrt{s}$ = 130 and 136 GeV," preprint CERN-PPE/96-096, CERN, 1996, submitted to Z. Phys.

[36] C. Dionisi, "Supersymmetric particles," in *Proceedings of the ECFA Workshop on LEP 200*, Aachen 1987, CERN 87-08, Vol. 2, edited by A. Böhm and W. Hoogland.

[37] ALEPH Collaboration, D. Buskulic *et al.*, Z. Phys. C **71**, 179 (1996).

[38] DELPHI Collaboration, W. Adam *et al.*, "Search for Pair Production of Heavy Objects in 4-Jet Events at $\sqrt{s}$ = 130 – 136 GeV," preprint CERN-PPE/96-119, CERN, 1996, submitted to Z. Phys.

[39] P. Mättig, "Searches for new particles," talk given at the XXVIII International Conference on High Energy Physics, Warsaw, 1996, to appear in the proceedings.

[40] ALEPH Collaboration, D. Buskulic *et al.*, "A study of single and multi-photon production in e^+e^- collisions at centre-of-mass energies of 130 and 136 GeV," preprint CERN-PPE/96-053, CERN, 1996, submitted to Phys. Lett. B.

[41] DELPHI Collaboration, W. Adam *et al.*, "Search for anomalous production of single photons at $\sqrt{s}$ =130 and 136 GeV," preprint CERN-PPE/96-61, CERN, 1996, submitted to Phys. Lett. B.

[42] L3 Collaboration, M. Acciarri *et al.*, "Observation of Multiple Hard Photon Final States at $\sqrt{s}$ = 130–140 GeV at LEP," preprint CERN-PPE/96-48, CERN, 1996, submitted to Phys. Lett.

[43] OPAL Collaboration, G. Alexander *et al.*, Phys. Lett. B **377**, 222 (1996).

[44] ALEPH Collaboration, D. Buskulic *et al.*, "Search for excited leptons at 130–140 GeV," preprint CERN-PPE/96-087, CERN, 1996," submitted to Phys. Lett. B.

[45] DELPHI Collaboration, P. Abreu *et al.*, "Study of radiative leptonic events with hard photons and search for excited charged leptons at $\sqrt{s}$ = 130–136 GeV," preprint CERN-PPE/96-60, CERN, 1996, submitted to Phys. Lett. B.

[46] L3 Collaboration, M. Acciarri *et al.*, Phys. Lett. B **370**, 211 (1996).

[47] OPAL Collaboration, G. Alexander *et al.*, "Search for excited leptons in e^+e^- collisions at $\sqrt{s}$ = 130 and 136 GeV," preprint CERN-PPE/96-094, CERN, 1996, submitted to Phys. Lett. B.

[48] ALEPH Collaboration, D. Buskulic *et al.*, "Search for heavy lepton pair production in e^+e^- collisions at center-of-mass energies of 130 and 136 GeV," preprint CERN-PPE/96-080, CERN, 1996, submitted to Phys. Lett. B.

[49] L3 Collaboration, M. Acciarri *et al.*, "Search for unstable sequential neutral and charged heavy leptons in e^+e^- annihilation at $\sqrt{s}$ = 130 and 136 GeV," preprint CERN-PPE/96-38, CERN, 1996, submitted to Phys. Lett.

[50] OPAL Collaboration, G. Alexander *et al.*, "Search for unstable neutral and charged heavy leptons in e^+e^- Collisions at $\sqrt{s}$ = 130 and 136 GeV," preprint CERN-PPE/96-093, CERN, 1996, submitted to Phys. Lett. B.

APPENDICES

1996 SLAC SUMMER INSTITUTE PARTICIPANTS

Kenji Abe
Nagoya University
Department of Physics
Furo-cho, Chikusa-ku
Nagoya-shi 464, JAPAN
Phone: 415-926-2746
E-Mail: ABEKE@SLAC.STANFORD.EDU

Perry Anthony
SLAC
Mail Stop 42
P.O. Box 4349
Stanford, CA 94309
Phone: 415-926-4354
E-Mail: ANTHONY@SLAC.STANFORD.EDU

Joe Ballam
SLAC
Mail Stop 78
P.O. Box 4349
Stanford, CA 94309
Phone: 415-926-2794
E-Mail: JBALLAM@SLAC.STANFORD.EDU

Lorenzo Bellagamba
Istituto Naz. Fis. Nucleare
Via Imerio 46
I-40126 Bologna, Italy
Phone: 39-5135-1082
E-Mail: BELLAGAMBA@BO.INFN.IT

Chris Adolphsen
SLAC
Mail Stop 65
P.O. Box 4349
Stanford, CA 94309
Phone: 415-926-3560
E-Mail: STAR@SLAC.STANFORD.EDU

David Aston
SLAC
Mail Stop 62
P.O. Box 4349
Stanford, CA 94309
Phone: 415-926-2457
E-Mail: DYAEB@SLAC.STANFORD.EDU

Guido Barbiellini
Universita di Trieste
Dipt. di Fisica
Via A. Valerio 2
I-34100 Trieste, Italy
E-Mail: BARBIELLINI@TRIESTE.INFN.IT

Martin Beneke
SLAC
Mail Stop 81
P.O. Box 4349
Stanford, CA 94309
Phone: 415-926-4421
E-Mail: MBENEKE@SLAC.STANFORD.EDU

Takashi Akagi
SLAC
Mail Stop 96
P.O. Box 4349
Stanford, CA 94309
Phone: 415-926-4091
E-Mail: AKAGI@SLAC.STANFORD.EDU

David Atwood
Jefferson Lab
12000 Jefferson St.
Newport News, VA 23606
Phone: 804-249-7412
E-Mail: ATWOOD@CEBAF.GOV

Timothy L. Barklow
SLAC
Mail Stop 65
P.O. Box 4349
Stanford, CA 94309
Phone: 415-926-3199
E-Mail: TIMB@SLAC.STANFORD.EDU

Corinne Berat
Inst. des Sciences Nucleaires de Grenoble
Univ. de Grenoble
53, Ave. des Martyrs
F-38026 Grenoble, CEDEX, France
Phone: 33-7628-4128
E-Mail: CORINNE@ISN5M1.IN2P3.FR

Michael Albrow
Fermilab, MS 318
P.O. Box 500, Wilson Rd.
Batavia, IL 60510
Phone: 630-840-8618
E-Mail: ALBROW@FNALD.FNAL.GOV

William Atwood
SLAC
Mail Stop 98
P.O. Box 4349
Stanford, CA 94309
Phone: 415-926-2698
E-Mail: ATWOOD@SLAC.STANFORD.EDU

Johannes M. Bauer
University of Mississippi
Department of Physics and Astronomy
University, MS 38677
Phone: 415-926-4202
E-Mail: BAUERJ@SLAC.STANFORD.EDU

Stefano Bettarini
Istituto Naz. Fis. Nucleare
Via Livornese, 1291
San Piero a Grado
I-56010 Pisa, Italy
Phone: 01139-50-880-274
E-Mail: BETTARIN@GALILEO.PI.INFN.IT

Marta Ambrogiani
Istituto Naz. Fis. Nucleare
Via Paradiso 12
I-44100 Ferrara, Italy
Phone: 39-532-781879
E-Mail: AMBROGIANI@VAXFE.FE.INFN.IT

Mark Bachman
University of California
Department of Physics and Astronomy
Irvine, CA 92717
Phone: 714-824-3817
E-Mail: MBACHMAN@UCI.EDU

Heiko M. Beier
Deutsches Elektronen Synchrotron
Notkestr. 85
D-22603 Hamburg, Germany
Phone: 49-40-8998-2002
E-Mail: BEIER@DESY.DE

Ciro Bigongiari
Istituto Naz. Fis. Nucleare
Via Livornese, 1291
San Piero a Grado
I-56010 Pisa, Italy
Phone: 39-050-880-283
E-Mail: BIGONGIARI@AXPIA.PI.INFN.IT

Farhang Amiri
Weber State University
Department of Physics
Ogden, UT 84408-2508
Phone: 801-626-6199
E-Mail: FAMIRI@WEBER.EDU

Kenneth G. Baird
Rutgers University
P.O. Box 849
Serin Physics Lab
Piscataway, NJ 08855-0849
Phone: 415-926-2728
E-Mail: BAIRD@SLAC.STANFORD.EDU

Andrew Bell
Birmingham University
School of Physics and Space Research
P.O. Box 363
Birmingham B15 2TT, England
Phone: 41-22-767-8181
E-Mail: ANB@HEP.PH.BHAM.AC.UK

James Bjorken
SLAC
Mail Stop 81
P.O. Box 4349
Stanford, CA 94309
Phone: 415-926-4426
E-Mail: BJORKEN@SLAC.STANFORD.EDU

Elliott Bloom
SLAC
Mail Stop 98
P.O. Box 4349
Stanford, CA 94309
Phone: 415-926-2469
E-Mail: ELLIOTT@SLAC.STANFORD.EDU

Leonida Bucci
Laboratori Nazionali, Frascati
Via E. Fermi, 40
I-00044 Frascati, Rome, Italy
Phone: 39-6-940-32728
E-Mail: BUCCI@LNF.INFN.IT

James Bloomer
Birmingham University
School of Physics and Space
P.O. Box 363
Birmingham B15 2TT, England
Phone: 41-22-767-8181
E-Mail: JBLOOMER@HPOPB1.CERN.CH

Charles Buchanan
University of California
Department of Physics
Los Angeles, CA 90024
Phone: 310-825-7466
E-Mail: BUCHANAN@PHYSICS.UCLA.EDU

Peter Bosted
American University
Department of Physics
4400 Massachusetts Ave., N.W.
Washington, D.C. 20016
Phone: 415-926-2319
E-Mail: BOSTED@SLAC.STANFORD.EDU

Michel Buenerd
SLAC
Mail Stop 20
P.O. Box 4349
Stanford, CA 94309
Phone: 415-926-4205
E-Mail:BUENERD@SLAC.STANFORD.EDU

Gary Bower
SLAC
Mail Stop 71
P.O. Box 4349
Stanford, CA 94309
Phone: 415-926-2460
E-Mail: GRB@SLAC.STANFORD.EDU

Fatin Bulos
SLAC
Mail Stop 78
P.O. Box 4349
Stanford, CA 94309
Phone: 415-926-2766
E-Mail: FYBEC@SLAC.STANFORD.EDU

Christian Bradtke
University Bonn
Physikalisches Inst.
Nussallee 12
D-53115 Bonn, Germany
Phone: 0049-228-732-230
E-Mail: BRADTKE@PIB1.PHYSIK.UNI-BONN.DE

David L. Burke
SLAC
Mail Stop 65
P.O. Box 4349
Stanford, CA 94309
Phone: 415-926-2853
E-Mail: DAVEB@SLAC.STANFORD.EDU

Stanley J. Brodsky
SLAC
Mail Stop 81
P.O. Box 4349
Stanford, CA 94309
Phone: 415-926-2644
E-Mail: SJBTH@SLAC.STANFORD.EDU

Philip Burrows
Massachusetts Institute of Technology
Lab. for Nuclear Science
Cambridge, MA 02139
Phone: 415-926-2683
E-Mail: BURROWS@SLAC.STANFORD.EDU

Mihaela Buza
NIKHEF
High Energy Phys.
P.O. Box 41882
NL-1009 DB Amsterdam, Netherlands
Phone: 31-0-20-592-5128
E-Mail: T912OTELLO.NIKHEF.NL

Suyong Choi
Seoul National University
Ctr. for Theoretical Phys.
San 56-1, Shinrim-dong, Kwanak-gu
Seoul 151-742, Korea
Phone: 630-840-4595
E-Mail: SUYONG@FNAL.FNAL.GOV

Dave Calloway
SLAC
Mail Stop 78
P.O. Box 4349
Stanford, CA 94309
Phone: 415-926-3115
E-Mail: CALLOWAY@SLAC.STANFORD.EDU

Chih-Lung Chou
SLAC
Mail Stop 81
P.O. Box 4349
Stanford, CA 94309
Phone: 415-926-4425
E-Mail: ALEXCHOU@LELAND.STANFORD.EDU

Michela Canepa
Universita di Genova
Dipt. di Fisica
Via Dodecaneso 33
I-16146 Genoa, Italy
Phone: 39-10-3536339
E-Mail: CANEPAM@ASGEDH.GE.INFN.IT

Ernesto Cocca
Istituto Naz. Fis. Nucleare
Via Livornese, 1291
San Piero a Grado
I-56010 Pisa, Italy
Phone: 39-50-880-239
E-Mail: COCCA@AXPIA.PI.INFN.IT

Nicolo Cartiglia
Columbia University
Nevis Labs, P.O. Box 137
Irvington on Hudson, NY 10533
E-Mail: CARTIGLIA@VXDESY.DESY.DE

Janet Conrad
Columbia University
Department of Physics
New York, NY 10027
Phone: 630-840-3266
E-Mail: CONRAD@NEVIS1.NEVIS.COLUMBIA.EDU

Jorge Casaus
CIEMAT
Div. de Fisica de Particulas
Avda. Complutense, 22
E-28040 Madrid, Spain
Phone: 41-22-767-3779
E-Mail: JORGEC@HPL3.CERN.CH

Dave Coupal
SLAC
Mail Stop 95
P.O. Box 4349
Stanford, CA 94309
Phone: 415-926-2836
E-Mail: COUPAL@SLAC.STANFORD.EDU

Neal M. Cason
University of Notre Dame
Department of Physics
Notre Dame, IN 46556
Phone: 219-631-6305
E-Mail: CASON@UNDHEP.HEP.ND.EDU

Ray F. Cowan
Massachusetts Institute of Technology
Lab. for Nuclear Science
Cambridge, MA 02139
Phone: 415-926-4560
E-Mail: RFC@SLAC.STANFORD.EDU

Piergiorgio Cerello
Istituto Naz. Fis. Nucleare
Via Pietro Giuria 1
I-10125 Turin, Italy
Phone: 39-11-6707416
E-Mail: CERELLO@TO.INFN.IT

David Coward
SLAC
Mail Stop 95
P.O. Box 4349
Stanford, CA 94309
Phone: 415-926-2419
E-Mail: DHC@SLAC.STANFORD.EDU

Nicolo DeGroot
SLAC
Mail Stop 96
P.O. Box 4349
Stanford, CA 94309
Phone: 415-926-4794
E-Mail: NICOLO@SLAC.STANFORD.EDU

Tulay Cuhadar
Bogazici University
Department of Physics
Bebek, P.K. 2
Istanbul, Turkey
Phone: 41-22-767-6527
E-Mail: TULAY@NA47SUN05.CERN.CH

Roberto DellaMarina
Eidgenossische Tech. Hochschule
Inst. of High Energy Physics
Honggerberg
CH-8093 Zurich, Switzerland
Phone: 41-38-205-352
E-Mail: DELLAMAR@VXCERN.CERN.CH

Lee Curtis
University of Glasgow, Rm. 456
Department of Physics & Astronomy
Glasgow G12 8QQ, Scotland
Phone: 44-141-339-8855, x. 8305
E-Mail: LEE.CURTIS@CERN.CH

Hobey DeStaebler
SLAC
Mail Stop 17
P.O. Box 4349
Stanford, CA 94309
Phone: 415-926-2416
E-Mail: HOBEY@SLAC.STANFORD.EDU

Gerd Dahlinger
Universitaet Dresden
Institut fuer Kern- und Teilchenphysik
Mommsen-Str. 13
D-01062 Dresden, Germany
Phone: 49-351-463-4110
E-Mail: DAHLINGR@PKTW03.PHY.TU-DRESDEN.DE

Gian DiLoreto
Michigan State University
Department of Physics
East Lansing, MI 48824
Phone: 630-840-5034
E-Mail: GIAN@D0TNG.FNAL.GOV

Mourad Daoudi
SLAC
Mail Stop 78
P.O. Box 4349
Stanford, CA 94309
Phone: 415-926-4566
E-Mail: DAOUDI@SLAC.STANFORD.EDU

Michael Dirkmann
University Dortmund
Department of Physics
Otto-Hahn-Strasse 4
Postfach 500500, D-44227 Dortmund
Germany
Phone: 49-231-755-4534
E-Mail: MICHAEL@PHYSIK.UNI-DORTMUND.DE

Tom DeGrand
University of Colorado
Department of Physics
P.O. Box 390
Boulder, CO 80309
Phone: 303-492-8602
E-Mail:DEGRAND@AURINKO.COLORADO.EDU

Lance Dixon
SLAC
Mail Stop 81
P.O. Box 4349
Stanford, CA 94309
Phone: 415-926-2627
E-Mail: LANCE@SLAC.STANFORD.EDU

Thomas Doeker
Tel Aviv University
School of Physics and Astronomy
Ramat Aviv
Tel Aviv 69978, Israel
Phone: 972-3-640-8376
E-Mail: THOMAS@ALZT.TAU.AC.IL

Sidney Drell
SLAC
Mail Stop 80
P.O. Box 4349
Stanford, CA 94309
Phone: 415-926-2664
E-Mail: DRELL@SLAC.STANFORD.EDU

Simone Donati
Istituto Naz. Fis. Nucleare
Via Livornese, 1291
San Piero a Grado
I-56010 Pisa, Italy
Phone: 39-50-880-305
E-Mail: DONATI@AXPIA.PI.INFN.IT

William Dunwoodie
SLAC
Mail Stop 62
P.O. Box 4349
Stanford, CA 94309
Phone: 415-926-2729
E-Mail: WMD@SLAC.STANFORD.EDU

Danning Dong
Massachusetts Institute of Technology
Lab. for Nuclear Science
Cambridge, MA 02139
Phone: 415-926-2918
E-Mail: DNDONG@SLAC.STANFORD.EDU

Robin Erbacher
SLAC
Mail Stop 78
P.O. Box 4349
Stanford, CA 94309
Phone: 415-926-3607
E-Mail: ROBINE@SLAC.STANFORD.EDU

Jonathan M. Dorfan
SLAC
Mail Stop 17
P.O. Box 4349
Stanford, CA 94309
Phone: 415-926-5322
E-Mail: JONATHAN@SLAC.STANFORD.EDU

Tom Fahland
Brown University
Department of Physics
182 Hope St.
Providence, RI 02912
Phone: 630-840-2722
E-Mail: FAHLAND@FNALD0.FNAL.GOV

Tommaso Dorigo
Istituto Naz. Fis. Nucleare
Via Marzolo 8
I-35100 Padua, Italy
Phone: 0039-49-827-7215
E-Mail: DORIGO@FNALD.FNAL.GOV

Adam Falk
Johns Hopkins University
3400 N. Charles St.
Department of Physics
Baltimore, MD 21218
Phone: 410-516-7817
E-Mail: FALK@JHU.EDU

Michael Doser
CERN/PPE Division
CH-1211 Geneva 23, Switzerland
Phone: 41-22-767-6552
E-Mail: MICHAEL.DOSER@CERN.CH

Jorge P. Fernandez
University of California
College 10/SCIPP
Santa Cruz, CA 95064
Phone: 426-1041
E-Mail: JPFERNAN@SCIPP.UCSC.EDU

Ted H. Fieguth
SLAC
Mail Stop 20
P.O. Box 4349
Stanford, CA 94309
Phone: 415-926-2529
E-Mail: FIEGUTH@SLAC.STANFORD.EDU

Clive Field
SLAC
Mail Stop 65
P.O. Box 4349
Stanford, CA 94309
Phone: 415-926-2694
E-Mail: SARGON@SLAC.STANFORD.EDU

Kevin Flood
University of Massachusetts
Department of Physics and Astronomy
Amherst, MA 01003
Phone: 415-926-2787
E-Mail: KFLOOD@PHAST.UMASS.EDU

Andrew Foland
Cornell University
Lab. of Nuclear Studies
Ithaca, NY 14853
Phone: 607-255-4882
E-Mail: ADF4@CORNELL.EDU

David Fryberger
SLAC
Mail Stop 20
P.O. Box 4349
Stanford, CA 94309
Phone: 415-926-2768
E-Mail: DAFRA@SLAC.STANFORD.EDU

Frank Gaede
Max Planck Inst. fuer Phys.
Werner-Heisenberg Inst. fuer Phys.
Postfach 40 12 12
D-80333 Munich, Germany
Phone: 40-8998-3293
E-Mail: GAEDE@REC06.DESY.DE

Philipp Geiger
Max Planck Inst. fuer Kernphysik
Postfach 103 980
D-69029 Heidelberg, Germany
Phone: 49-6221-516-432
E-Mail: PGEIGER@HERMES.DESY.DE

Gary Godfrey
SLAC
Mail Stop 98
P.O. Box 4349
Stanford, CA 94309
Phone: 415-926-2919
E-Mail: GODFREY@SLAC.STANFORD.EDU

Douglas Graham
Imperial College
Blackett Lab.
Prince Consort Road
London, SW7 2AZ, England
Phone: 41-22-767-4942
E-Mail: GRAHAMDJ@CERNVM.CERN.CH

Christoph Greub
SLAC
Mail Stop 81
P.O. Box 4349
Stanford, CA 94309
Phone: 415-926-4411
E-Mail: GREUB@SLAC.STANFORD.EDU

Guenter Grindhammer
Max Planck Inst. fuer Phys.
Werner-Heisenberg Inst. fuer Phys.
Postfach 40 12 12
D-80333 Munich, Germany
Phone: 49-40-8998-2590
E-Mail: GUENTERG@DESY.DE

John Groves
528 38th Avenue
Santa Cruz, CA 95062
Phone: 408-464-7049
E-Mail: RAJAYOGA.AOL.COM

Arthur Hebecker
SLAC
Mail Stop 81
P.O. Box 4349
Stanford, CA 94309
Phone: 415-926-4430
E-Mail: HEBECKER@SLAC.STANFORD.EDU

Fritz-Herbert Heinsius
Lawrence Berkeley Lab
One Cyclotron Rd.
Mail Stop 7-222
Berkeley, CA 94720
Phone: 510-486-5021
E-Mail: FHHEINSIUS@LBL.GOV

Fabian Heitsch
University Bonn
Physikalisches Inst.
Nussallee 12
D-53115 Bonn, Germany
Phone: 49-228-217-162
E-Mail: HEITSCH@CIPS01.PHYSIK.UNI-BONN.DE

JoAnne Hewett
SLAC
Mail Stop 81
P.O. Box 4349
Stanford, CA 94309
Phone: 415-926-4424
E-Mail: HEWETT@SLAC.STANFORD.EDU

Michael E. Huffer
SLAC
Mail Stop 71
P.O. Box 4349
Stanford, CA 94309
Phone: 415-926-4269
E-Mail: MEHSYS@SLAC.STANFORD.EDU

Michael Ingram
Manchester University
Department of Physics
Schuster Lab.
Manchester M13 9PL, England
Phone: 41-22-767-5918
E-Mail: MICHAELI@HPOPM1.CERN.CH

Ovid Jacob
SLAC
Mail Stop 81
P.O. Box 4349
Stanford, CA 94309
Phone: 415-926-2734
E-Mail: JACOB@SLAC.STANFORD.EDU

Jamal Jalilian-Marian
University of Minnesota
School of Physics and Astronomy
Minneapolis, MN 55455
Phone: 612-624-6345
E-Mail: JAMAL@MNHEP.HEP.UMN.EDU

John A. Jaros
SLAC
Mail Stop 96
P.O. Box 4349
Stanford, CA 94309
Phone: 415-926-2852
E-Mail: JOHN@SLAC.STANFORD.EDU

Zhi-Yu (John) Jiang
SLAC
Mail Stop 65
P.O. Box 4349
Stanford, CA 94309
Phone: 415-926-2308
E-Mail: JIANG@SLAC.STANFORD.EDU

Anthony S. Johnson
SLAC
Mail Stop 71
P.O. Box 4349
Stanford, CA 94309
Phone: 415-926-2278
E-Mail: TONY_JOHNSON@SLAC.STANFORD.EDU

Aurelio Juste
University Autonoma de Barcelona
Inst. de Fisica d'Altes Energies
E-08193 Bellaterra, Barcelona
Spain
Phone: 34-3-581-2834
E-Mail: JUSTE@IFAE.ES

Marek Karliner
Tel Aviv University
Department of Physics
Tel Aviv 69978
ISRAEL
Phone: 415-926-2266
E-Mail: MAREK@VM.TAU.AC.IL

Jiro Kodaira
Hiroshima University
Department of Physics
1-3 Kagamiyama
Higashi-Hiroshima 739, Japan
Phone: 824-24-7362
E-Mail: KODAIRA@THEO.PHYS.SCI.HIROSHIMA-U.AC.JP

Richard Kass
Ohio State University
Department of Physics
174 W.18th Ave.
Columbus, OH 43210
E-Mail: KASS@OHSTPY.MPS.OHIO-STATE.EDU

Yuri Kovchegov
Columbia University
Department of Physics
New York, NY 10027
Phone: 212-854-3960
E-Mail: YURI@CUPHY3.PHYS.COLUMBIA.EDU

Hideaki Kawahara
SLAC
Mail Stop 62
P.O. Box 4349
Stanford, CA 94309
Phone: 415-926-2810
E-Mail: KAWAHARA@SLAC.STANFORD.EDU

Thomas Kraemerkaemper
University Dortmund
Department of Physics
Otto-Hahn-Strasse 4
Postfach 500500, D-44227 Dortmund, Germany
Phone: 49-231-755-3662
E-Mail: KRAEMERK@PHYSIK.UNI-DORTMUND.DE

Hiroyuki Kawamura
Kyoto University
Department of Fundamental Sci., FIHS
Yoshida
Kyoto-shi 606-01, JAPAN
Phone: 081-75-753-6806
E-Mail: KAWAMURA@PHYS.H.-KYOTO-U.AC.JP

Stefan Kretzer
University Dortmund
Department of Physics
D-44221 Dortmund
GERMANY
Phone: 49-231-755-3699
E-Mail: KRETZER@HAL1.PHYSIK.UNI-DORTMUND.DE

Mohsen Khakzad
York University
Department of Physics
4700 Keele St.
Downsview, ON, Canada M3J 1P3
Phone: 49-40-8998-3053
E-Mail: MOHSEN@ZEEMAN.DESY.DE

Paul Kunz
SLAC
Mail Stop 62
P.O. Box 4349
Stanford, CA 94309
Phone: 415-926-2884
E-Mail: PAUL_KUNZ@SLAC.STANFORD.EDU

Chris Klopfenstein
University of California
Department of Physics
Davis, CA 95616-8677
Phone: 916-752-6702
E-Mail: KLOPFENSTEIN@UCDAVIS.EDU

Tibor Kurca
DESY
Inst. fuer Hochenergiephysik
Platanenallee 6
D-15738 Zeuthen, Germany
Phone: 49-40-8998-3135
E-Mail: KURCA@DICE2.DESY.DE

Xinhua Li
Institute for High Energy Physics
Academia Sinica
P.O. Box 918
Beijing 100039, CHINA
Phone: 415-926-2662
E-Mail: LIXH@SLAC.STANFORD.EDU

Nicola Labanca
Istituto Naz. Fis. Nucleare
Via Celoria 16
I-20133 Milan, Italy
Phone: 39-2-239-2363
E-Mail: LABANCA@VAXMI.MI.INFN.IT

Vincenzo Lia
Massachusetts Institute of Technology
Lab. for Nuclear Science
Cambridge, MA 02139
Phone: 415-926-2502
E-Mail: LIA@SLACVX.SLAC.STANFORD.EDU

Sabine Lang
University of Durham
Department of Physics
South Road
Durham DH1 3LE, England
Phone: 44-191-374-2174
E-Mail: S.C.LANG@DURHAM.AC.UK

Lawrence Littenberg
Brookhaven National Lab
Upton, NY 11973
E-Mail: LITTENBE@BNL.GOV

Frank Lehner
Deutsches Elektronen Synchrotron
Notkestr. 85
D-22607 Hamburg, Germany
Phone: 49-40-8998-3269
E-Mail: LEHNERF@DICE2.DESY.DE

William Lockman
Universityof California
Department of Physics
Santa Barbara, CA 93106
Phone: 415-926-3435
E-Mail: LOCKMAN@SLAC.STANFORD.EDU

David Leith
SLAC
Mail Stop 80
P.O. Box 4349
Stanford, CA 94309
Phone: 415-926-2663
E-Mail: LEITH@SLAC.STANFORD.EDU

Heather Logan
University of California
Inst. for Particle Physics
Santa Cruz, CA 95064
Phone: 408-469-4811
E-Mail: LOGAN@PHYSICS.UCSC.EDU

Claire Lewis
University of Durham
Department of Physics
South Road
Durham DH1 3LE, England
Phone: 44-191-374-2180
E-Mail: C.A.M.LEWIS@DURHAM.AC.UK

William Loinaz
University of Pittsburgh
Department of Physics
Pittsburgh, PA 15260
Phone: 412-624-9056
E-Mail: LOINAZ@PITT.EDU

Vera G. Luth
SLAC
Mail Stop 95
P.O. Box 4349
Stanford, CA 94309
Phone: 415-926-2702
E-Mail: LUTH@SLAC.STANFORD.EDU

David MacFarlane
McGill University
Physics Dept., Rutherford Bldg.
3600 University Ave.
Montreal, PQ, Canada M3A 2T8
Phone: 415-926-3406
E-Mail: DBMACF@SLAC.STANFORD.EDU

Tom Markiewicz
SLAC
Mail Stop 96
P.O. Box 4349
Stanford, CA 94309
Phone: 415-926-2668
E-Mail: TWMARK@SLAC.STANFORD.EDU

Helmut Marsiske
SLAC
Mail Stop 95
P.O. Box 4349
Stanford, CA 94309
Phone: 415-926-4333
E-Mail: MARSISKE@SLAC.STANFORD.EDU

Sean Mattingly
University of Wisconsin
Department of Physics
Madison, WI 53706
Phone: 49-40-8998-2489
E-Mail: MATTING@AMZEUS.DESY.DE

Tom Mattison
SLAC
Mail Stop 17
P.O. Box 4349
Stanford, CA 94309
Phone: 415-926-2802
E-Mail: MATTISON@SLAC.STANFORD.EDU

Mark A. McDougald
SLAC
Mail Stop 95
P.O. Box 4349
Stanford, CA 94309
Phone: 415-926-2707
E-Mail: MARK_MCDOUGALD@SLAC.STANFORD.EDU

Maurizio Melis
Istituto Naz. Fis. Nucleare
Via Ada Negri 18
I-09127 Cagliari, Italy
Phone: 39-70-670833-4-5-6
E-Mail: MELIS@VAXCA.CA.INFN.IT

Sven Menke
University of Bonn
Physikalisches Inst.
Nussallee 12
D-53115 Bonn, Germany
Phone: 0228-732-275
E-Mail: SVEN.MENKE@CERN.CH

Arnd Meyer
University of Hamburg
Inst. Physik
Luruper-Chaussee 149
D-22761 Hamburg, Germany
Phone: 49-40-8998-3490
E-Mail: MEYERA@DICE2.DESY.DE

Jens Meyer
DESY/F-OPAL
Notkestr. 85
D-22603 Hamburg, Germany
Phone: 49-40-8998-3426
E-Mail: MEYER@OPL03.DESY.DE

Peer-Oliver Meyer
Rhein-Westf. Tech. Hochschule
III Physikalisches Inst.
Physikzentrum
Sommerfeldstr. D-52074 Aachen, Germany
Phone: 49-40-8998-4551
E-Mail: MEYERPO@DICE2.DESY.DE

Michiko Miyamoto
Kobe College
11-2, 1-chome, Yamate
Nakasuji, Takarazuka-City
Hyogo-Prefecture, Japan (665)
Phone: 0798-52-0955

Joachim Mnich
CERN/PPE Division
CH-1211 Geneva 23, Switzerland
Phone: 41-22-767-6487
E-Mail: JOACHIM.MNICH@CERN.CH

Juergen Moeck
Max Planck Inst. fuer Phys.
Werner-Heisenberg Inst. fuer Phys.
Postfach 40 12 12
D-80333 Munich, Germany
Phone: 49-0-89-32354-219
E-Mail: JUM@MPPMU.MPG.DE

Klaus Moenig
CERN/PPE Division
CH-1211 Geneva 23, Switzerland
Phone: 41-22-76-77161
E-Mail: KLAUS_MONIG@CERN.CH

Kenneth C. Moffeit
SLAC
Mail Stop 78
P.O. Box 4349
Stanford, CA 94309
Phone: 415-926-2772
E-Mail: MOFFEIT@SLAC.STANFORD.EDU

Teresa Monteiro
Deutsches Elektronen Synchrotron
Notkestr. 85
D-22603 Hamburg, Germany
Phone: 49-40-8998-2003
E-Mail: MONTEIRO@DESY.DE

Thomas Moore
Yale University
Department of Physics
New Haven, CT 06511
Phone: 415-926-2918
E-Mail: TBMOORE@SLAC.STANFORD.EDU

Al Mueller
Columbia University
Department of Physics
New York, NY 10027
Phone: 212-854-3338
E-Mail: ARB@CUPHY.PHYS.COLUMBIA.EDU

Dieter Mueller
Sektion Physik
Leipzig Universitaet
Karl-Marx-Platz
D-04103 Leipzig, Germany
Phone: 49-341-973-2429
E-Mail: MUELLER@SERVER1.RZ.UNI-LEIPZIG.DE

David Muller
SLAC
Mail Stop 62
P.O. Box 4349
Stanford, CA 94309
Phone: 415-926-3590
E-Mail: MULLER@SLAC.STANFORD.EDU

Gregory J. Mushial
10870 North Stelling Road
Apt. 27G
Cupertino, CA 95014
Phone: 415-926-3176
E-Mail: GJM@SLAC.STANFORD.EDU

Freedy Nang
University of Arizona
Department of Physics
Tucson, AZ 85721
Phone: 630-840-3835
E-Mail: NANG@FNALD0.FNAL.GOV

Takashi Nasuno
Hiroshima University
Department of Physics
1-3 Kagamiyama
Higashi-Hiroshima 739, Japan
Phone: 81-(0)824-24-7361
E-Mail: NASUNO@THEO.PHYS.SCI.HIROSHIMA-U.AC.JP

H. Pierre Noyes
SLAC
Mail Stop 81
P.O. Box 4349
Stanford, CA 94309
Phone: 415-926-2665
E-Mail: NOYES@SLAC.STANFORD.EDU

Manfred Paulini
Lawrence Berkeley Lab
MS 50B-5239
One Cyclotron Road
Berkeley, CA 94720
Phone: 510-486-6926
E-Mail: PAULINI@LBL.GOV

Odd Magne Ogreid
University of Bergen
Department. of Physics
Allegaten 55
N-5007 Bergen, Norway
Phone: 47-55582771
E-Mail: OGREID@VSFYS1.FI.UIB.NO

Tomas J. Pavel
SLAC
Mail Stop 95
P.O. Box 4349
Stanford, CA 94309
Phone: 415-926-2543
E-Mail: PAVEL@SLAC.STANFORD.EDU

Noritsugu Oishi
Nagoya University
Department of Physics
Furo-cho, Chikusa-ku
Nagoya-shi 464, JAPAN
Phone: 415-926-2746
E-Mail: NORITSUG@SLAC.STANFORD.EDU

Hardy Pawletta
Rhein-Westf. Tech. Hochschule
III Phys. Inst., Physikzentrum
Sommerfeldstr.
D-52056 Aachen, GERMANY
Phone: 49-241-807-306
E-Mail: PAWLETTA@PHYSIK.RWTH-AACHEN.DE

Michael Olson
Kent State University
Department of Physics
Kent, OH 44242
Phone: 415-926-5188
E-Mail: MOLSON@SLAC.STANFORD.EDU

Michael Peskin
SLAC
MS 81
P.O. Box 4349
Stanford, CA 94309
Phone: 415-926-3250
E-Mail: MPESKIN@SLAC.STANFORD.EDU

Patrick Palmen
Rhein-Westf. Tech. Hochschule
III Physikalisches Inst.
Physikzentrum
Sommerfeldstr. D-52074 Aachen, Germany
Phone: 49-0-241-807-306
E-Mail: PALMEN@PHYSIK.RWTH-AACHEN.DE

Alexey A. Petrov
University of Massachusetts
Department of Physics and Astronomy
Amherst, MA 01003
Attn: High Energy Theory Group
Phone: 413-545-0559
E-Mail: PETROV@HET.PHAST.UMASS.EDU

W. K. H. Panofsky
SLAC
Mail Stop 76
P.O. Box 4349
Stanford, CA 94309
Phone: 415-926-3988
E-Mail: BEERBOHM@SLAC.STANFORD.EDU

Peter Pfeifenschneider
Rhein-Westf. Tech. Hochschule
III Physikalisches Inst.
Physikzentrum
Sommerfeldstr. D-52074 Aachen, Germany
Phone: 49-241-807-265
E-Mail: PETERP@PHYSIK.RWTH-AACHEN.DE

Daniela Piccioni
University of Bristol
H. H. Wills Physics Lab.
Royal Fort, Tyndall Ave.
Bristol BS8 1TL, England
Phone: 040-8998-2609
E-Mail: PICCIONI@DESY.DE

Arvind Rajaraman
SLAC
Mail Stop 81
P.O. Box 4349
Stanford, CA 94309
Phone: 415-926-4422
E-Mail: ARVINDRA@LELAND

Damien Pierce
SLAC
Mail Stop 81
P.O. Box 4349
Stanford, CA 94309
Phone: 415-926-4427
E-Mail: PIERCE@SLAC.STANFORD.EDU

Johan Rathsman
Uppsala University
Department of Radiation Sciences
P.O. Box 535
S-75121 Uppsala, Sweden
Phone: 46-18-18-38-54
E-Mail: RATHSMAN@TSL.UU.SE

Rainer Pitthan
SLAC
Mail Stop 20
P.O. Box 4349
Stanford, CA 94309
Phone: 415-926-3467
E-Mail: RAINER@SLAC.STANFORD.EDU

Per Lasse Reinertsen
University of California
Inst. for Particle Physics
Santa Cruz, CA 95064
E-Mail: PLASSE@SCIPP.UCSC.EDU

Alyssa Prinz
SLAC
Mail Stop 78
P.O. Box 4349
Stanford, CA 94309
Phone: 415-926-2800
E-Mail: AAPRINZ@LELAND.STANFORD.EDU

Burton Richter
SLAC
Mail Stop 80
P.O. Box 4349
Stanford, CA 94309
Phone: 415-926-2601
E-Mail: BRICHTER@SLAC.STANFORD.EDU

Betsy Pugel
University of Michigan
Department of Physics
Ann Arbor, MI 48109
Phone: 313-669-6168
E-Mail: DRUID@UMICH.EDU

Thomas Gerard Rizzo
SLAC
Mail Stop 81
P.O. Box 4349
Stanford, CA 94309
Phone: 415-926-4420
E-Mail: RIZZO@SLAC.STANFORD.EDU

Christopher Purves
University of Bristol
H. H. Wills Physics Lab.
Royal Fort, Tyndall Ave.
Bristol BS8 1TL, England
Phone: 44-117-928-9000
E-Mail: PURVES@CMS.CERN.CH

Leon Rochester
SLAC
Mail Stop 96
P.O. Box 4349
Stanford, CA 94309
Phone: 415-926-2695
E-Mail: LSREA@SLAC.STANFORD.EDU

Stefan Roesler
University of Siegen
Fachbereich fuer Physik
D-57068 Siegen, Germany
Phone: 49-271-740-4533
E-Mail: SROESLER@AFSMAIL.CERN.CH

Stephen F. Schaffner
SLAC
Mail Stop 95
P.O. Box 4349
Stanford, CA 94309
Phone: 415-926-3133
E-Mail: SSCHAFF@SLAC.STANFORD.EDU

Reiner Seitz
SLAC
Mail Stop 61
P.O. Box 4349
Stanford, CA 94309
Phone: 415-926-4191
E-Mail: RSE@SLAC.STANFORD.EDU

Evgeny Solodov
Russian Acad. Sci., Siberian Div.
Budker Inst. of Nuclear Physics
Novosibirsk 630090, Russia
E-Mail: SOLODOV@VXINPZ.INP.NSK.SU

Daniel Roff
Bristol University
H. H. Wills Physics Lab.
Royal Fort, Tyndall Ave.
Bristol BS8 1TL, England
Phone: 49-40-8998-2609
E-Mail: DROFF@ZOW.DESY.DE

William Schmidke
York University
Department of Physics
4700 Keele St.
Downsview, ON, Canada M3J 1P3
Phone: 040-8998-3653
E-Mail: SCHMIDKE@VXDESY.DESY.DE

Marina Shmakova
SLAC
Mail Stop 81
P.O. Box 4349
Stanford, CA 94309
Phone: 415-926-4409
E-Mail: SHMAKOVA@SLAC.STANFORD.EDU

Andrew Sonnenschein
University of California
Department of Physics
Santa Barbara, CA 93106
Phone: 415-926-2069

Simona Rolli
Istituto Naz. Fis. Nucleare
Via Bassi 6
I-27100 Pavia, Italy
Phone: 630-840-4464
E-Mail: ROLLI@FNAL.GOV

Maik Schramm
Tech. University Dresden
Sektion Physik
Zellescher Weg 17
D-01062 Dresden, Germany
Phone: 49-351-463-4129
E-Mail: SCHRAMM@PKTW01.PHY.TU-DRESDEN.DE

Adrian Signer
SLAC
Mail Stop 81
P.O. Box 4349
Stanford, CA 94309
Phone: 415-926-4433
E-Mail: ADRIAN@SLAC.STANFORD.EDU

Davison Soper
University of Oregon
Department of Physics
Eugene, OR 97403
Phone: 541-346-5162
E-Mail: SOPER@OREGON.UOREGON.EDU

Aura Marilena Rosca
Laboratori Nazionali, Frascati
Via E. Fermi, 40
C.P. 13
I-00044 Frascati, Rome, Italy
Phone: 39-6-940-32645
E-Mail: ARS@VXCERN.CERN.CH

Bruce Schumm
SLAC
Mail Stop 78
P.O. Box 4349
Stanford, CA 94309
Phone: 415-926-3621
E-Mail: SCHUMM@SLAC.STANFORD.EDU

Wesley Smith
University of Wisconsin
Department of Physics
1150 University Ave.
Madison, WI 53706
Phone: 608-262-4690
E-Mail:WSMITH@WISHEP.PHYSICS.WISC.EDU

Juergen Spiekermann
University of Dortmund
Department of Physics
Otto-Hahn-Strasse 4
Postfach 500500, D-44227 Dortmund, Germany
Phone: 49-40-8998-2384
E-Mail: SPIEKERMANN@H1D01.DESY.DE

Ester Ruiz-Morales
SLAC
Mail Stop 81
P.O. Box 4349
Stanford, CA 94309
Phone: 415-926-4413
E-Mail: MERUIZ@UNIXHUB.SLAC.STANFORD.EDU

Jochen Schwiening
SLAC
Mail Stop 62
P.O. Box 4349
Stanford, CA 94309
Phone: 415-926-3593
E-Mail: JOCHEN@SLAC.STANFORD.EDU

Rob Snihur
Northwestern University
Department of Physics and Astronomy
Evanston, IL 60208
Phone: 708-840-5222
E-Mail: SNIHUR@FNAL.GOV

Jens Staeck
Southern Methodist University
Department of Physics
Dallas, TX 75275
Phone: 607-254-2778
E-Mail: STAECK@LNS62.LNS.CORNELL.EDU

Kuruganti V. L. Sarma
Tata Inst. of Fundamental Res.
Homi Bhabha Road
Mumbai 400005, India
Phone: 215-2971, ext. 2214
E-Mail: KVLS@THEORY.TIFR.RES.IN

Gabriella Sciolla
SLAC
Mail Stop 95
P.O. Box 4349
Stanford, CA 94309
Phone: 415-926-2706

Arthur Snyder
SLAC
Mail Stop 95
P.O. Box 4349
Stanford, CA 94309
Phone: 415-926-2701
E-Mail: SNYDER@SLAC.STANFORD.EDU

Hermann Staengle
Colorado State University
Department of Physics
Fort Collins, CO 80521
Phone: 970-491-1581
E-Mail: STAENGLE@LAMAR.COLOSTATE.EDU

Achim Stahl
SLAC
Mail Stop 61
P.O. Box 4349
Stanford, CA 94309
Phone: 415-926-3480
E-Mail: STAHL@SLAC.STANFORD.EDU

Pedro Teixeira-Dias
University of Glasgow
Department of Physics & Astronomy
Glasgow G12 8QQ, Scotland
Phone: 44-141-330-5893
E-Mail: PEDROTD@PHYSICS.GLA.AC.UK

Beate Stockhausen
University of Bonn
Physikalisches Inst.
Nussallee 12
D-53111 Bonn, Germany
Phone: 49-0-228-733-231
E-Mail: BEATE.STOCKHAUSEN@CERN.CH

Oliver Thilmann
Max Planck Inst. fuer Kernphysik
Postfach 103 980
D-69029 Heidelberg, Germany
Phone: 49-6221-516461
E-Mail: OTH@DXNHDC.MPI-HD.MPG.DE

Linda Stuart
SLAC
Mail Stop 78
P.O. Box 4349
Stanford, CA 94309
Phone: 415-926-2887
E-Mail: STUART@SLAC.STANFORD.EDU

James Tickner
Oxford University
Department of Theoretical Physics
1 Keble Road
Oxford OX1 3NP, England
Phone: 49-40-8998-3133
E-Mail: TICKNER@ZUKAL01.DESY.DE

Dong Su
SLAC
Mail Stop 61
P.O. Box 4349
Stanford, CA 94309
Phone: 415-926-2284
E-Mail: SUDONG@SLAC.STANFORD.EDU

Walter Toki
Colorado State University
Department of Physics
Fort Collins, CO 80523
Phone: 970-491-1548
E-Mail: TOKI@LAMAR.COLOSTATE.EDU

Bernd Surrow
DESY/ZEUS-F1
Notkestr. 85
D-22603 Hamburg, Germany
Phone: 49-40-8998-3062
E-Mail: SURROW@ZOW.DESY.DE

Yung-Su Tsai
SLAC
Mail Stop 81
P.O. Box 4349
Stanford, CA 94309
Phone: 415-926-2632
E-Mail: YSTTH@SLAC.STANFORD.EDU

Richard E. Taylor
SLAC
Mail Stop 96
P.O. Box 4349
Stanford, CA 94309
Phone: 415-926-2417
E-Mail: RETAYLOR@SLAC.STANFORD.EDU

Dennis Ugolini
SLAC
Mail Stop 61
P.O. Box 4349
Stanford, CA 94309
Phone: 415-926-3791
E-Mail: UGOLINI@SLAC.STANFORD.EDU

Tracy Usher
SLAC
Mail Stop 96
P.O. Box 4349
Stanford, CA 94309
Phone: 415-328-5545
E-Mail: USHER@SLAC.STANFORD.EDU

Klaus Vorwalter
Max Planck Inst. fuer Kernphysik
Postfach 103 980
D-69029 Heidelberg, Germany
Phone: 49-6221-516-461
E-Mail: KVO@DXNHD1.MPI-HD.MPG.DE

Jaroslav Va'vra
SLAC
Mail Stop 62
P.O. Box 4349
Stanford, CA 94309
Phone: 415-926-2658
E-Mail: JJV@SLAC.STANFORD.EDU

Maneesh Wadhwa
University of Basel
Inst. fuer Physik
Klingelbergstr. 82
CH-4056 Basel, Switzerland
Phone: 41-89-201-01-65
E-Mail: WADHWA@HPL3.CERN.CH

Tony Vaiciulis
University of Wisconsin
Department of Physics
Madison, WI 53706
Phone: 49-40-8998-3140
E-Mail: VAICIULIS@VXDESY.DESY.DE

Steve Wagner
SLAC
Mail Stop 95
P.O. Box 4349
Stanford, CA 94309
Phone: 415-926-2921
E-Mail: STEVEW@SLAC.STANFORD.EDU

Paolo Valente
Universita di Roma II, Tor Vergata
Dipt. di Fisica
Via E. Carnevale
I-00173 Rome, Italy
Phone: 39-6-7259-4761
E-Mail: PVALENTE@LNF.INFN.IT

James Walden
Carnegie Mellon University
Department of Physics
Nuclear Theory Group
Pittsburgh, PA 15213
Phone: 412-268-2737
E-Mail: WALDEN@DEFOE.PHYS.CMU.EDU

Jeroen J. vanHunen
Nat. Inst. Nuclear
High Energy Physics
P.O. Box 41882
NL-1009 DB Amsterdam, Netherlands
Phone: 31-020-592-2089
E-Mail: JEROENVH@NIKHEFK.NIKHEF.NL

Dieter Walz
SLAC
Mail Stop 20
P.O. Box 4349
Stanford, CA 94309
Phone: 415-926-2786
E-Mail: DWALZ@SLAC.STANFORD.EDU

Lorenzo Vitale
Istituto Naz. Fis. Nucleare
Via Fabia Severo 158
I-34100 Trieste, Italy
Phone: 39-40-375-6233
E-Mail: VITALE@TRIESTE.INFN.IT

Roy Wang
SLAC
Mail Stop 61
P.O. Box 4349
Stanford, CA 94309
Phone: 415-926-3442
E-Mail: RWANG@SLAC.STANFORD.EDU

David Waters
Oxford University
Nuclear Physics Lab.
Keble Road
Oxford OX1 3RH, England
Phone: 49-40-8998-3133
E-Mail: WATERS@ZOW.DESY.DE

Matthew Williams
Imperial College
Blackett Lab.
Prince Consort Road
London, SW7 2AZ, England
Phone: 41-22-767-6475
E-Mail: MATHEW@ALOHA.CERN.CH

Tom Weber
SLAC
Mail Stop 53
P.O. Box 4349
Stanford, CA 94309
Phone: 415-926-4146
E-Mail: WEBER@SLAC.STANFORD.EDU

Stephen H. Williams
SLAC
Mail Stop 80
P.O. Box 4349
Stanford, CA 94309
Phone: 415-926-2276
E-Mail: STEVE@SLAC.STANFORD.EDU

Marvin Weinstein
SLAC
Mail Stop 81
P.O. Box 4349
Stanford, CA 94309
Phone: 415-926-2214
E-Mail: NIV@SLAC.STANFORD.EDU

Stephane Willocq
SLAC
Mail Stop 62
P.O. Box 4349
Stanford, CA 94309
Phone: 415-926-3362
E-Mail: WILLOCQ@SLAC.STANFORD.EDU

James Wells
SLAC
Mail Stop 81
P.O. Box 4349
Stanford, CA 94309
Phone: 415-926-4415
E-Mail: JWELLS@SLAC.STANFORD.EDU

William Wisniewski
SLAC
Mail Stop 61
P.O. Box 4349
Stanford, CA 94309
Phone: 415-926-4890
E-Mail: WJW@SLAC.STANFORD.EDU

Robert C. Welsh
University of Michigan
Department of Physics
Ann Arbor, MI 48109
Phone: 313-763-6926
E-Mail: RCWELSH@UMICH.EDU

James Wiss
University of Illinois
Department of Physics
1110 W. Green St.
Urbana, IL 61801
Phone: 217-333-4873
E-Mail: JEW@UIUC.EDU

Joseph L. White
SLAC
Mail Stop 95
P.O. Box 4349
Stanford, CA 94309
Phone: 415-926-3525
E-Mail: JLW@SLAC.STANFORD.EDU

Markus Wobisch
Rhein-Westf. Tech. Hochschule
III Physikalisches Inst.
Physikzentrum
Sommerfeldstr. D-52074 Aachen, Germany
Phone: 49-40-8998-4551
E-Mail: WOBISCH@DICE2.DESY.DE

David Woods
Kansas State University
Department of Physics
Cardwell Hall
Manhattan, KS 66502
Phone: 913-532-1699
E-Mail: WOODS@HEP.PHYS.KSU.EDU

XiaoFan Zhou
SLAC
Mail Stop 61
P.O. Box 4349
Stanford, CA 94309
Phone: 415-926-3791
E-Mail: ZHOUF@SLAC.STANFORD.EDU

Michael B. Woods
SLAC
Mail Stop 78
P.O. Box 4349
Stanford, CA 94309
Phone: 415-926-3609
E-Mail: MWOODS@SLAC.STANFORD.EDU

Mihir Worah
SLAC
Mail Stop 81
P.O. Box 4349
Stanford, CA 94309
Phone: 415-926-4416
E-Mail: WORAH@SLAC.STANFORD.EDU

Shimon Yankielowicz
SLAC
Mail Stop 81
P.O. Box 4349
Stanford, CA 94309

Charles C. Young
SLAC
Mail Stop 96
P.O. Box 4349
Stanford, CA 94309
Phone: 415-926-2669
E-Mail: YOUNG@SLAC.STANFORD.EDU

Brad Youngman
SLAC
Mail Stop 20
P.O. Box 4349
Stanford, CA 94309
Phone: 415-926-3627
E-Mail: YOUNGMAN@SLAC.STANFORD.EDU

THE SLAC SUMMER INSTITUTE ON PARTICLE PHYSICS
1973 - 1995

1973 DEEP INELASTIC ELECTROPRODUCTION

"Hadron Production in Deep Inelastic Processes"	J.D. Bjorken
"Hadron Production in the Collision of Virtual Photons with Nucleons–an Experimental Review"	M. Perl
"Phenomenological Analysis"	F.J. Gilman
"Asymptotic Behavior and Short Distance Singularities"	Y. Frishman

WEAK CURRENTS AND INTERACTIONS

"Raw Notes of Lectures on Current Algebra and PCAC"	S. Drell
"Experimental Phenomenology"	M. Schwartz S. Wojcicki
"Gauge-Theories of Weak and Electromagnetic Interaction"	T. Appelquist
"How to Transform Current Quarks to Constituent Quarks and Try to Predict Hadron Decays"	J. Primack K. Kugler

1974 THE STRONG INTERACTIONS

"Diffractive Processes"	D.W.G.S. Leith
"Amplitude Structure in Two- and Quasi-Two-Body Processes"	M. Davier
"Resonances: Experimental Review"	R.J. Cashmore
"Resonances: A Quark View of Hadron Spectroscopy and Transitions"	F.J. Gilman
"Lectures on Inclusive Hadronic Processes"	D. Sivers
"Large Momentum Transfer Processes"	R. Blankenbecle
"Hadron Dynamics"	H.D.I. Abarbane

1975 DEEP HADRONIC STRUCTURE AND THE NEW PARTICLES

"Leptons as a Probe of Hadronic Structure"	F.J. Gilman
"Lepton Scattering as a Probe of Hadronic Structure"	E.D. Bloom
"High $p\perp$ Dynamics"	J.D. Bjorken
"Hadronic Collision and Hadronic Structure (An Experimental Review)"	M. Davier
"The New Spectroscopy"	H. Harari
"The New Spectroscopy (An Experimental Review)"	G.H. Trilling

1976 WEAK INTERACTIONS AT HIGH ENERGY AND THE PRODUCTION OF NEW PARTICLES

"Weak Interaction Theory and Neutral Currents"	J.D. Bjorken
"Weak Interactions at High Energy"	S.G. Wojcicki
"ψ Spectroscopy"	G.J. Feldman
"A New Lepton?"	G.J. Feldman
"Lectures on the New Particles"	J.D. Jackson
"New Particle Production"	D. Hitlin

1977 QUARK SPECTROSCOPY AND HADRON DYNAMICS

"Quarks and Leptons"	H. Harari
"Quark Confinement"	S.D. Drell
"Hadron Spectroscopy"	F.J. Gilman
"Lectures on the Quark Model, Ordinary Mesons, Charmed Mesons, and Heavy Leptons"	M.L. Perl
"Quarks and Particle Production"	K.C. Moffeit

1978 WEAK INTERACTIONS–PRESENT AND FUTURE

"Accelerator Neutrino Experiments"	D.H. Perkins
"Weak Interactions at High Energies"	J. Ellis
"Gauge Theories of the Weak Interactions"	H. Quinn
"Weak Decays"	S. Wojcicki

1979 QUANTUM CHROMODYNAMICS

"Lepton Nucleon Scattering"	W.G. Atwood
"Massive Lepton Pair Production"	R. Stroynowski
"QCD Phenomenology of the Large P_T Processes"	R. Stroynowski
"Perturbative Quantum Chromodynamics"	S.J. Brodsky
"Elements of Quantum Chromodynamics"	J.D. Bjorken

1980 THE WEAK INTERACTIONS

"Gauge Theories of Weak Interactions"	M.J. Veltman
"Neutrinos and Neutrino Interactions"	F.J. Sciulli
"Weak Decays of Strange and Heavy Quarks"	D. Hitlin
"From the Standard Model to Composite Quarks and Leptons"	H. Harari
"Physics of Particle Detectors"	D.M. Ritson J. Jaros J. Marx H.A. Gordon R.S. Gilmore W.B. Atwood

1981 THE STRONG INTERACTIONS

"Quark-Antiquark Bound State Spectroscopy and QCD"	E.D. Bloom
"Meson Spectroscopy: Quark States and Glueballs"	M.S. Chanowitz
"Quantum Chromodynamics and Hadronic Interactions at Short Distances"	S.J. Brodsky
"Untangling Jets from Hadronic Final States"	G. Fox
"Heavy Flavor Production from Photons and Hadrons"	C.A. Heusch
"Design Constraints and Limitations in e^+e^- Storage Rings"	J. LeDuff
"Linear Colliders: A Preview"	H. Wiedemann

1982 PHYSICS AT VERY HIGH ENERGIES

"Expectations for Old and New Physics at High Energy Colliders"	R.N. Cahn
"Beyond the Standard Model in Lepton Scattering and Beta Decay"	M. Strovink
"Grand Unification, Proton Decay, and Neutrino Oscillations"	H.H. Williams
"e^+e^- Interactions at Very High Energy: Searching Beyond the Standard Model"	J. Dorfan
"The Hierarchy Gauge Susskind Problem, Technicolor, Supersymmetry, and All That"	L. Susskind
"Composite Models for Quarks and Leptons"	H. Harari
"Electron-Proton Colliding Beams: The Physics Programme and Machine"	B.H. Wiik

1983 DYNAMICS AND SPECTROSCOPY AT HIGH ENERGY

"Jets in QCD: A Theorist's Perspective"	S. Ellis
"Jets in e^+e^- Annihilation"	R. Hollebeek
"Jet Production in High Energy Hadron Collisions"	R.F. Schwitters
"Aspects of the Dynamics of Heavy-Quark Systems"	M.E. Peskin
"Heavy Particle Spectroscopy and Dynamics B's to Z's"	M.G.D. Gilchriese
". . . And for Our Next Spectroscopy?"	J. Ellis
"Review of the Physics and Technology of Charged Particle Detectors"	A.H. Walenta
"A Review of the Physics and Technology of High-Energy Calorimeter Devices"	P.M. Mockett

1984 THE SIXTH QUARK

"The Last Hurrah for Quarkonium Physics: The Top System"	E. Eichten
"Developments in Solid State Vertex Detectors"	C.J.S. Damerell
"Experimental Methods of Heavy Quark Detection"	T. Himel
"Production and Uses of Heavy Quarks"	G.L. Kane
"Weak Interactions of Quarks and Leptons: Experimental Status"	S. Wojcicki
"The Experimental Method of Ring-Imaging Cherenkov (RICH) Counters"	T. Ekelöf
"Weak Interactions of Quarks and Leptons (Theory)"	H. Harari

PIEF-FEST

"Pief"	S. Drell
"Accelerator Physics"	R.R. Wilson
"High Energy Theory"	T.D. Lee
"Science and Technology Policies for the 1980s"	F. Press
"Inclusive Lepton-Hadron Experiments"	J. Steinberger
"Forty-Five Years of e^+e^- Annihilation Physics: 1956 to 2001"	B. Richter
"We Need More Piefs"	J. Wiesner

1985 SUPERSYMMETRY

"Introduction to Supersymmetry"	J. Polchinski
"Signatures of Supersymmetry in e^+e^- Collisions"	D. Burke
"Properties of Supersymmetric Particles & Processes"	R.M. Barnett
"Supersymmetry: Experimental Signatures at Hadron Colliders"	P. Darriulat
"Superworld/Hyperworlds"	M.E. Peskin
"Very High Energy Colliders"	B. Richter
"Some Issues Involved in Designing a 1 TeV (c.m.) $e^{\pm}$ Linear Collider Using Conventional Technology"	G.A. Loew
"Wake Field Accelerators"	P.B. Wilson
"Plasma Accelerators"	R.D. Ruth & P. Chen
"Collider Scaling and Cost Estimation"	R.B. Palmer

1986 PROBING THE STANDARD MODEL

"Electroweak Interactions–Standard and Beyond"	H. Harari
"CP and Other Experimental Probes of Electroweak Phenomena"	B. Winstein
"Perturbative QCD: K-Factors"	R. Field
"Experimental Tests of Quantum Chromodynamics"	J. Dorfan
"Phenomenology of Heavy Quark Systems"	F. Gilman
"Heavy Quark Spectroscopy and Decay"	R. Schindler
"Some Aspects of Computing in High Energy Physics"	P. Kunz
"Data Acquisition for High Energy Physics Experiments"	M. Breidenbach

DRELL-A-BRATION

"Topics in Arms Control"	M. Goldberger
"Compositeness Below 1 TeV"	R. Jaffe
"Our Changing View of Hadron Structure"	J. Bjorken

1987 LOOKING BEYOND THE Z

"Theory of e^+e^- Collisions at Very High Energy"	M.E. Peskin
"Prospects for Physics at e^+e^- Linear Colliders"	G.J. Feldman
"Physics with Polarized Electron Beams"	M.L. Swartz
"Electron-Proton Physics at HERA"	G. Wolf
"Hadron Colliders Beyond the Z^0"	C. Quigg
"Physics at Hadron Colliders (Experimental View)"	J.L. Siegrist
"The Dialogue Between Particle Physics and Cosmology"	B. Sadoulet
"Requirements for Detectors at SSC"	M.G.D. Gilchriese*

1988 PROBING THE WEAK INTERACTION: CP VIOLATION AND RARE DECAYS

"Results on b-Decay in e^+e^- Collisions, with Emphasis on CP Violation"	K. Berkelman
"Precious Rarities–On Rare Decays of K, D and B Mesons"	I. Bigi
"Superconducting Detectors for Monopoles and Weakly Interacting Particles"	B. Cabrera
"Cosmic Relics from the Big Bang"	L. Hall
"Double Beta Decay"	M.S. Witherell
"Neutrino Masses and Mixings"	L. Wolfenstein
"The Bottom Quark: A Key to 'Beyond Standard' Physics"	H. Harari*
"b-Physics in Fixed Target Experiments"	J. Sandweiss*
"Experimental Searches for Rare Decays"	A.J.S. Smith*

1989 PHYSICS AT THE 100 GeV MASS SCALE

"Heavy Quarks-Experimental"	R. Hollebeek
"The Theory of Heavy Flavour Production"	R.K. Ellis
"Precision Experiments in Electroweak Interactions (Experimental)"	M. Swartz
"Theory of Precision Electroweak Measurements"	M. Peskin
"Applications of QCD to Hadron-Hadron Collisions: Experimental"	M.D. Shapiro
"Applications of QCD to Hadron-Hadron Collisions: Theoretical"	I. Hinchcliffe
"W^+W^- Interactions and the Search for the Higgs Boson"	M.E. Levi
"Electroweak Symmetry Breaking: Higgs/Whatever"	M.S. Chanowitz
"Electron-Positron Storage Rings as Heavy Quark Factories"	R.H. Siemann
"Prospects for Next-Generation e^+e^- Linear Colliders"	R.D. Ruth
"Current Prospects for Hadron Colliders"	H. Edwards
"Hadron Colliders Beyond the SSC"	M. Tigner

1990 GAUGE BOSONS AND HEAVY QUARKS

"Z Decays and Tests of the Standard Model"	R. Cahn
"Future Experiments at LEP I and LEP II"	D. Treille
"Experimental Studies of Electroweak Gauge Bosons"	D. Burke
"Top Quark Topics"	G. Kane
"The Next Linear Collider"	R. Ruth
"Theoretical Aspects of B-Physics"	J. Bjorken
"Fundamental Aspects of B-Physics"	P. Drell
"B-Factory Storage Ring Design"	J. Rees

1991 LEPTON-HADRON SCATTERING

"A Historical Review of Lepton-Photon Scattering"	R. Taylor
"Uses of Superconductivity in Particle Accelerators"	R. Siemann
"Theoretical Aspects of Lepton-Hadron Scattering"	S. Drell
"Lepton-Hadron Scattering from Scaling Violation through HERA"	F. Sciulli
"Experimental Studies on QCD"	T. Hansl-Kozanecka
"HERA: The New Frontier"	J. Feltesse
"Topics in Calorimetry for High Energy Physics"	R. Hollebeek
"High Energy Lepton Hadron Scattering as a Probe of QCD"	R. Peccei

1992 THE THIRD FAMILY AND THE PHYSICS OF FLAVOR

"Predicting Quark and Neutrino Masses and Mixings"	L.J. Hall
"Experimental Techniques for B Physics"	N.A. Roe
"Experimental Aspects of CP Violation"	H.N. Nelson
"CP Violation"	Y. Nir
"Trigger and Data Acquisition at High-Rate Colliders"	A.J. Lankford
"Vertex Detectors"	V. Luth
"Tau Physics"	M.L. Perl
"Experimental Searches for the Top Quark"	R. Hollebeek
"Top-ology"	M. Peskin

1993 SPIN STRUCTURE IN HIGH ENERGY PROCESSES

"Spin, Mass, and Symmetry"	M.E. Peskin
"Physics with Polarized Z^0s"	P. Rowson
"Spin and Precision Electroweak Physics"	W.J. Marciano
"Polarized Electron Sources"	R. Prepost
"Polarization Phenomena in Quantum Chromodynamics"	S.J. Brodsky
"Polarized Lepton-Nucleon Scattering"	E. Hughes
"Polarized Targets in High Energy Physics"	G.D. Cates, Jr.
"Spin Dynamics in Storage Rings and Linear Accelerators"	J. Irwin
"Spin Formalism and Applications to New Physics Searches"	H.E. Haber

1994 PARTICLE PHYSICS, ASTROPHYSICS & COSMOLOGY

"Cosmology: Standard and Inflationary"	M.S. Turner
"Gravitational Waves"	K.S. Thorne
"Gravity Wave Experiments"	R. Weiss
"Neutrino Masses and Mixing"	S. Mishra
"A Dielectric-Based GeV/m Crossed-Laser-Beam Electron Linear Accelerator"	R. Byer
"Dark Matter and Large-Scale Structure"	J. Primack
"Searches for Baryonic Dark Matter via Microlensing"	C. Alcock
"Low-Noise Detectors in Astrophysics"	B. Sadoulet
"Investigating High-Field Gravity Using Astrophysical Techniques"	E.D. Bloom
"Dark Matter Candidates: Front Runners and Dark Horses"	M. Srednicki

1995 THE TOP QUARK & THE ELECTROWEAK INTERACTION

"Theory of Top Quark Production and Decay"	J.H. Kühn
"Top Quark Stidoes at Hadron Colliders"	P.K. Sinervo
"Top at Future Linear e^+e^- Colliders"	K. Fujii
"Review of Precision Electroweak Data"	M. Swartz
"Vertex Detectors: The State of the Art and Future Prospects"	C.J. S. Damerell
"The Role of Top in Heavy Flavor Physics"	J.L. Hewett
"Techniques for Particle Identification"	T. Ypsilantis
"The Heavy Top Quark and Supersymmetry"	L.J. Hall

AUTHOR INDEX

Albrow, M. G. 67

Barbiellini, G. 315
Beneke, M. 549
Bjorken, J. D. 1
Buchanan, C. D. 525
Burrows, P. N. 101

Cartiglia, N. 337
Cason, N. 403
Conrad, J. 365

DeGrand, T. 169
Doser, M. 395

Falk, A. F. 43

Grindhammer, G. 313

Kass, R. 473
Klopfenstein, C. 575

Littenberg, L. 381

Mnich, J. 599
Mönig, K. 429
Mueller, A. H. 237

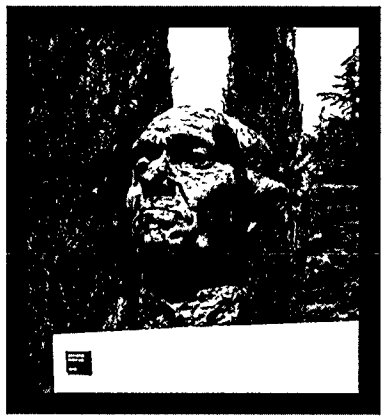
Paulini, M. 499
Pierce, D. M. 589

Smith, W. H. 203
Solodov, E. P 457
Soper, D. E. 15

Toki, W. 141

Welsh, R. C. 297
Willocq, S. 405
Wiss, J. 251












YAMAHA